

dc\_1955\_21

**Dr. Edit Mátyus**

From molecular spectroscopy  
to molecular physics

*submitted in partial fulfillment of the requirements for  
the Doctor of the Hungarian Academy of Sciences title*

Budapest, 11 November 2022

## CONTENTS

I. Introductory thoughts about molecular quantum theory	4
II. Exact quantum dynamics developments for floppy molecular systems and complexes	5
A. Introduction	5
B. Theoretical framework for quantum nuclear motion theory	6
1. Nuclear Schrödinger equation and coordinate transformation	6
2. Geometrical constraints and reduced-dimensionality models	12
3. A variational rovibrational approach: basis set and integration grid for the matrix representation of the Hamiltonian	12
4. Computational bottleneck of the variational vibrational methodology	15
5. A possible strategy for efficient vibrational computations: Smolyak quadrature and pruning	15
6. Other possible strategies for efficient vibrational computations	18
7. Efficient rotational-vibrational computations	19
C. Assignment of the rovibrational states	20
1. Vibrational parent analysis	21
2. Rotational parent analysis	21
3. Coupled-rotor decomposition	22
D. Simulating rovibrational infrared and Raman spectra	22
1. Infrared transition moments	23
2. Raman transition moments	23
E. Summary and conclusions	24
III. The Bethe–Salpeter QED wave equation for bound-state computations of atoms and molecules	24
A. Introduction: a historical line-up	24
B. The Bethe–Salpeter equation and the Salpeter–Sucher exact equal-time approach	26
1. Introductory ideas and propagators	26
2. Coordinate and Fourier transformation: the total and relative time and energy	28
3. Construction of the interaction kernels using energy-momentum translation operators, the instantaneous part of the interaction	30
4. A practical wave equation: the exact equal-times Bethe–Salpeter equation and emergence of the no-pair Dirac–Coulomb(–Breit) Hamiltonian	32
5. Phenomenology: why and when the equal-time equation is useful?	36
C. Prospects regarding $\mathcal{H}_\Delta$	37
D. Numerical solution of the no-pair Dirac–Coulomb–Breit eigenvalue equation	40
E. An overview of numerical results	44
1. Variational vs. perturbation theory: perturbative benchmark for the no-pair energies through $\alpha$ scaling	45
F. Summary of the current status and outlook to future work	46
IV. In lieu of a summary: Quo vadis theoretical molecular physics and spectroscopy?	46
References	47

## Acknowledgment

I start this thesis by acknowledging my post-doctoral scientific advisors, Markus Reiher (ETH Zürich) and Stuart Althorpe (University of Cambridge), for allowing me to join their groups for 2-2 years. During both periods, I have collected long lasting experiences. The start of my independent research career in 2016 was made possible by a grant of the Swiss National Science Foundation (No. IZ11Z0\_166525). The fundamental molecular physics research direction (Chapter III) currently benefits from financial support of an ERC Starting Grant (No. 851421). Most recently, the exact quantum dynamics direction (Chapter II) gained a little momentum from the Hungarian NKFIH (No. 142869). ELTE, my alma mater, hosted all this research and has provided me absolute scientific freedom. As to the actual research developments, I am grateful to my closest co-workers at ELTE during the past couple of years, most importantly, Dávid Ferenc, (Dr.) Alberto Martín Santa Daría, Dr. Péter Jeszenszki, Dr. Gustavo Avila, and (Dr.) Ádám Margócsy. Their names appear in the authors list of the published articles reviewed in this thesis, and this documents their contribution to my, in fact, to our joint research. For me, it has been an extraordinary scientific journey together with all of you! Thank you for your hard work and enthusiasm! Finally, I am grateful to colleagues from the Institute of Physics at ELTE, most importantly, Dániel Nógrádi and also Antal Jakovác for early discussions about relativistic QED with potential use for molecular spectroscopic computations.

## I. INTRODUCTORY THOUGHTS ABOUT MOLECULAR QUANTUM THEORY

Application of quantum mechanics to atoms and molecules is as old as quantum mechanics itself. The characteristic ‘energy resolution’ of a typical wet-lab chemical experiment (*e.g.*, experiments of the great Emil Fischer) has been determined by the value of  $kT$ , the Boltzmann constant times the room temperature, to be ca. 0.03 eV or  $0.001 E_h = 1 mE_h$  for activation barriers or conformational energy differences, etc. This also means that for any prediction to be useful for traditional chemical transformations, the relevant molecular energy difference must be accurate within ca.  $1 mE_h$ .

This requirement naturally led quantum theorists during the 1920s, immediately after the new theory has turned out to be useful to explain atomic spectra, to start adapting it to molecular systems. A plausible assumption was the separability of the quantum mechanical motion of the electrons and atomic nuclei. Nowadays, this separation is connected to the great pioneer of quantum mechanics, Max Born and his doctoral student, Robert Oppenheimer [1], although the idea of this separability was ‘in the air’ already during the years of the ‘old quantum theory’.

Another very natural ‘decision’ was to ‘immediately’ start using Schrödinger’s [2] (Born’s, Jordan’s, and Heisenberg’s [3–5]) *non-relativistic* quantum mechanics to describe molecules as many-particle quantum systems, in fact, as many-electron quantum systems, in the fixed Coulomb field of the atomic nuclei. It is very well understandable that the pioneers did not consider for this purpose Dirac’s (Lorentz covariant) at-the-time new one-electron equation [6, 7], which was problematic to generalize to many-electron systems [8–10]. Furthermore, the Dirac equation had only a ‘minor’ energetic effect in comparison with the energy resolution of chemical-molecular experiments available at that time.

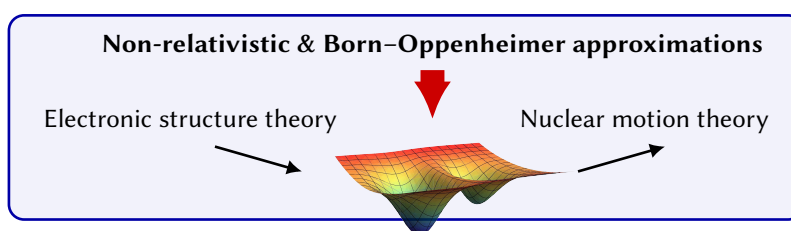


Figure 1. Present-day quantum chemistry with the two major fields: electronic structure theory and nuclear motion theory that are defined by the two fundamental approximations. The potential energy surface computed by electronic structure theory provides the ‘effective’ interaction for the motion of the atomic nuclei.

Based on these foundations (Figure 1), quantum chemistry has taken off, to conquer almost all experimental laboratories around the world within a hundred years. This 100 years was spent with hard work in theoretical and computational chemistry laboratories to systematically develop (or sometimes just to accidentally find) theoretical, algorithmic, and computational methodologies and to write computer programs for later use by millions of educated practitioners. Initially, the chemist community had reservations about the new computational tool, it was not a simple plug-and-play formula, but required heavy mathematics and computer algebra, or at least use of digital computers, understood in detail only by the expert. By the beginning of the 21st century, ordinary citizens, including the chemists themselves, have got used to ‘black-box’ gadgets in every-day life, and the lab-PC equipped with one of the modern quantum chemistry packages happened to be just another ‘gadget’, which was found to be useful in every-day research.

Although the non-relativistic and the Born–Oppenheimer (BO) approximations define two major fields for quantum chemistry (Fig. 1), electronic structure theory and quantum nuclear motion theory, it was primarily the electronic energy that was essential to have meaningful energetic predictions in relation with (organic) chemistry experiments. In addition, local minima of the electronic energy with respect to the nuclear configurations made it possible to compute and picture the (classical) structure of molecules, which, in spite of, having problematic origins in quantum theory [11–13], was wonderfully in agreement with the chemist’s mental picture of molecules invented by organic chemistry much before quantum mechanics [14].

In the meanwhile, molecular experiments also developed, and the molecular world became ‘visible’ in great more detail. It is widely appreciated that the nuclei also move, and their motion must be described also by quantum mechanics. At the same time, the simplest quantum harmonic oscillator model about a local minimum had remained sufficient for a long time. The first (correct) quantum harmonic oscillator calculation, which later served as a simplest model also for molecular vibrations, is due to Born and Jordan in 1925 [4], one year before Schrödinger’s partial differential equation [2].

Modern molecular experiments do see ‘effects’ which can be understood only by rigorous solution of the nuclei’s Schrödinger equation with an accurate potential energy surface (PES). For molecular interactions, experimental spectroscopy in conjunction with quantum nuclear motion theory has become a stringent tool to test the interaction representation of dimers and larger clusters. Molecular quantum dynamical databases, collecting the rovibrational energy differences and corresponding transition moments, are required and used by other branches of science, most importantly, by astrophysics, atmospheric modelling, and strong-field laser science. All these directions require the development of so-called exact quantum dynamics methodologies (quantum nuclear motion theory) both in terms of (a) completeness, *i.e.*, by extending the energetic coverage of the database; as well as in terms of (b) molecular system size and complexity, which makes it necessary to improve the ‘scaling’ of the computational cost with the number of

vibrational degrees of freedom. The theoretical background and recent developments realized in my group in these directions are reviewed in Chapter II.

Furthermore, there is a third, (c) dimension of computational molecular spectroscopy: the accuracy of predictions. A computed molecular spectrum, but most importantly the line positions are directly comparable with the experimental data. If the computed result agrees with the experimental result, *within the uncertainty of both*, and over a reasonably wide range of energies and systems, then, we can say that the molecular theory most likely covers all relevant physical processes (and can be used for predictions where experiment may not be feasible).

For understanding, interpreting an experimental molecular spectrum, a good albeit non-perfect agreement may be sufficient, unless the spectral density of the experiment is very high. Obviously, the accuracy of the PES is a limiting factor for the accuracy of quantum-nuclear motion computations, but assuming that the PES representation is sufficiently good, the two fundamental approximations, BO and non-relativistic, remain that will ultimately limit the accuracy of the computations in comparison with high-resolution spectroscopy experiments.

With recent developments of precision spectroscopy techniques and manipulation of atomic and molecular quantum states, extraordinarily precise spectral information is becoming available for a range of calculable systems. Calculable means that, the system is so small, that the underlying equations can be solved, evaluated to an almost 'arbitrary' numerical precision. Hence, the accuracy of the computation is determined by the fundamental equations and relations used to describe atoms and molecules and our ability to use them. Hence, the increasing amount of very high-quality experimental data challenges us to revise the fundamental theory of molecular matter, by abandoning the two approximations that had been central to quantum chemistry over the past hundred years.

Development of a (non-relativistic) pre-Born–Oppenheimer theory does not have major fundamental difficulties, although there are a few theoretically interesting aspects [11–13, 15], and the main challenge lies with converging the solutions of the known equations to the necessary numerical precision [15–20]. On the contrary, going beyond the non-relativistic approximation, with the aim of helping precision spectroscopy and creating a useful and versatile methodological and computational framework, has been truly challenging. I have been thinking about this direction over the past decade (12 years), for many years without any visible research output. In the meanwhile, I have learned how to pinpoint the known perturbative relativistic and leading-order QED correction values with a precision necessary for spectroscopy. It has only been during the past 3–4 years that a promising research direction to pursue practical relativistic QED developments for atoms and molecules has started to emerge.

I have reviewed my pre-Born–Oppenheimer research a few years ago [13], so it is not presented in a great detail in this thesis. Instead, Chapter III is fully devoted to recent progress and my near-future plans in relation with the development of a computational (BO or pre-BO) relativistic QED framework for atoms and molecules in relation with precision spectroscopy, and ultimately, for testing and further developing the fundamental theory of molecular matter.

## II. EXACT QUANTUM DYNAMICS DEVELOPMENTS FOR FLOPPY MOLECULAR SYSTEMS AND COMPLEXES

Molecular rotation, vibration, internal rotation, isomerization, tunneling, intermolecular dynamics of weakly and strongly interacting systems, intra-to-inter-molecular energy transfer, hindered rotation and hindered translation over surfaces are important types of molecular motions. Their fundamentally correct and detailed description can be obtained by solving the nuclear Schrödinger equation on a potential energy surface. Many of the chemically interesting processes involve quantum nuclear motions which are 'delocalized' over multiple potential energy wells. These 'large-amplitude' motions in addition to the high dimensionality of the vibrational problem represent challenges to the current (ro)vibrational methodology. A review of the quantum nuclear motion methodology is provided, current bottlenecks of solving the nuclear Schrödinger equation are identified, and solution strategies are reviewed based on Ref. 21. Technical details, computational results, and analysis of these results in terms of limiting models and spectroscopically relevant concepts are highlighted for selected numerical examples.

### A. Introduction

Molecules are never at rest, they constantly vibrate and rotate, and most interesting molecular phenomena involve nuclear motions extending over multiple potential energy wells. These multi-well motions are called large-amplitude motions that is in contrast to small-amplitude motions that correspond to small nuclear displacements localized to the bottom of a single potential energy well. Although atomic nuclei are 'heavy' particles and several types of molecular motion exhibit (semi-)classical features, the fundamentally correct theoretical description of molecules in motion [22] is based on quantum mechanics [23].

The basic quantum mechanical models of the most common types of nuclear motion, *i.e.*, rotation and small-amplitude vibration, are the rigid rotor and the harmonic oscillator approximations that are almost as old as quantum mechanics [4] and they are taught in established chapters of the undergraduate curriculum [24]. The equilibrium rotational constants and harmonic frequencies are built-in features in most quantum chemical program packages and are often computed to obtain theoretical guidance in relation with experimentally recorded spectra. Perturbative corrections [25] to these equilibrium quantities can be computed in electronic structure packages, but the

simplest approach has limitations. As to the corrections of the harmonic frequencies, if there are several zeroth-order vibrational states close in energy, which is a common situation in polyatomic molecules, ‘resonance effects’ introduce erroneous shifts in the perturbative correction. Furthermore, the quantum harmonic oscillator approximation is qualitatively wrong for large-amplitude motions that are common and important types of motions in molecular systems.

A straightforward solution to the beyond-harmonic-oscillator-problem accounting for large-amplitude motions, anharmonicities, mode coupling, etc., which is free of resonances, is offered by variational-type approaches. A direct variational solution of the rovibrational Schrödinger equation provides the direct or numerically ‘exact’ solution corresponding to a given potential energy surface (PES). Hence, the common name, ‘exact quantum dynamics’ is used to distinguish this approach from other techniques trying to ‘simulate’ quantum ‘effects’ by extending classical mechanical simulation of the nuclear motion. Quantum effect simulations by (imaginary-time) path-integral techniques have a favorable scaling property with the system size, but—apart from very special exceptions—they can have large errors on the vibrational band origins.

On the contrary, exact quantum dynamics methods can be used to systematically approach the numerically exact solutions of the nuclear Schrödinger equation. The severe shortcoming of the exact quantum approach is connected with an unfavorable, exponential scaling of the computational cost with the vibrational dimensionality.

This chapter starts with a general theoretical framework for the (ro)vibrational methodology, the Hamiltonian and curvilinear coordinates (Secs. II B 1 and II B 2), basis functions and matrix representation (Secs. II B 3) and lists some common algorithmic elements. This introduction leads us to identify the main bottlenecks (Sec. II B 4), and to review possible strategies to eliminate or at least attenuate the computational cost increasing rapidly with the dimensionality (Secs. II B 5 and II B 6). The review is continued with analysis tools and spectroscopic limiting models for the computed rovibrational states (Sec. II C), simulation of (ro)vibrational infrared and Raman spectra (Sec. II D). To respect the length limitations and to avoid unnecessary repetition of already documented material (cited in the reference list), computational results from our own recent work are showcased during the course of the presentation of the theoretical and algorithmic background.

## B. Theoretical framework for quantum nuclear motion theory

### 1. Nuclear Schrödinger equation and coordinate transformation

The time-independent Schrödinger equation is considered for the motion of the atomic nuclei on a potential energy surface (PES,  $V$ ),

$$(\hat{T} + V)\Psi = E\Psi . \quad (1)$$

The direct solution of this differential (eigenvalue) equation can provide all stationary states of the system. The  $\hat{T}$  nuclear kinetic energy operator for  $N$  nuclei (in Hartree atomic units) is

$$\hat{T} = - \sum_{i=1}^N \frac{1}{2m_i} [\hat{p}_{iX}^2 + \hat{p}_{iY}^2 + \hat{p}_{iZ}^2] , \quad (2)$$

where  $\hat{p}_{i\alpha} = -i\partial/\partial R_{i\alpha}$  are the nuclear momenta conjugate to the  $R_{i\alpha}$ ,  $\alpha = X, Y, Z$  laboratory-frame (LF) Cartesian coordinates.

For an isolated system, the PES is invariant to the molecule’s translation (and rotation), so it is convenient to separate the overall translation from the internal motion by defining  $\mathbf{r}_i$  translationally invariant, body-fixed Cartesian coordinates [26],

$$\mathbf{R}_i = \mathbf{O}(\Omega)\mathbf{r}_i + \mathbf{R}_{\text{CM}} , \quad i = 1, \dots, N , \quad (3)$$

where translational invariance means that  $\mathbf{r}_i$  is a function of the laboratory coordinates which remain invariant to an overall translation of the system,

$$\mathbf{r}_i = \mathbf{f}_i(\mathbf{R}) = \mathbf{f}_i(\mathbf{R}') \quad \text{with} \quad \mathbf{R}'_j = \mathbf{R}_j + \mathbf{d}, \quad \forall \mathbf{d} \in \mathbb{R}^3 . \quad (4)$$

The overall translation of the system is described by the center of mass coordinates of the nuclei,

$$\mathbf{R}_{\text{CM}} = \sum_{i=1}^N \frac{m_i}{m_{12\dots N}} \mathbf{R}_i \quad \text{with} \quad m_{12\dots N} = \sum_{i=1}^N m_i , \quad (5)$$

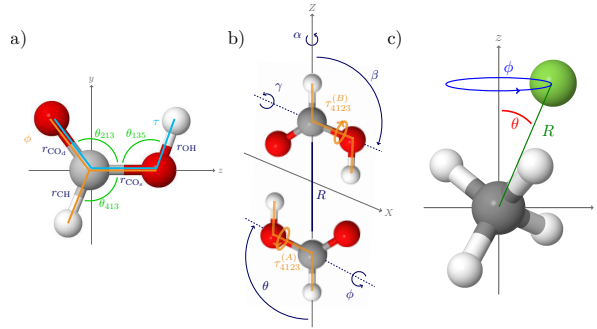


Figure 2. Examples for internal coordinates: (a) full 9D model for the formic acid monomer [29]; (b) intermolecular-plus-torsional, 8D model for the formic acid dimer [30]; (c) full 12D model of the  $\text{CH}_4\text{-F}^-$  complex using the  $q_1, \dots, q_9$  normal coordinates for the methane fragment and  $(R, \theta, \phi)$  spherical polar coordinates for the relative ion-methane motion [31–34].

and the center of the body-fixed frame can be fixed at the origin,

$$\sum_{i=1}^N m_i \mathbf{r}_i = 0 \quad (6)$$

with the  $m_i$  masses associated to the nuclei. In Eq. (3),  $\mathbf{O}(\Omega)$  with  $\Omega = (\omega_1, \omega_2, \omega_3)$  describes the 3-dimensional rotation which connects the orientation of the body-fixed (BF) frame [27] and the laboratory frame.

The commonly used normal coordinates (coordinates underlying the harmonic oscillator approximation) are defined as the linear combination of the  $\mathbf{r}_i$  Eckart's [28] body-fixed Cartesian coordinates with respect to a reference structure fixed at a PES minimum, and minimize the kinetic and potential couplings at the reference structure (Sec. II B 7) [24].

For an efficient description of quantum nuclear motion beyond small-amplitude vibrations about a local minimum, non-linear functions of  $\mathbf{r}_i$  are commonly defined,

$$q_k = g_k(\mathbf{r}), \quad k = 1, \dots, 3N - 6 \quad (7)$$

to efficiently describe the (extended) internal motion.  $g_k(\mathbf{r})$  is typically a function of scalar products of the  $\mathbf{r}_i$  body-fixed Cartesian coordinates (hence independent of the frame definition), distance- and angle-type variables (Fig. 2). It has been shown that beyond four-particle systems,  $3N - 6$  distance- and angle-type variables are not sufficient to uniquely characterize all molecular structures [35]. So, beyond  $N = 4$ , torsion-like coordinates (including some vector-type product of  $\mathbf{r}_i$ 's) must be also included to uniquely characterize the internal structure with  $3N - 6$  variables.

The variable change

$$\begin{aligned} (X_1, Y_1, Z_1, X_2, Y_2, Z_2, \dots, X_{3N}, Y_{3N}, Z_{3N}) &\Rightarrow \\ (\xi_1, \dots, \xi_{3N}) &= (q_1, q_2, \dots, q_{3N-6}, \omega_1, \omega_2, \omega_3, X_{\text{CM}}, Y_{\text{CM}}, Z_{\text{CM}}) \end{aligned} \quad (8)$$

corresponds to a curvilinear coordinate ‘transformation’, which can be characterized by the Jacobi matrix. The Jacobi matrix collects derivatives of the ‘old’ coordinates with respect to the ‘new’ ones,  $J_{ik} = \partial \mathbf{R}_i / \partial \xi_k$ . For a vibrational degree of freedom,  $\xi_k = q_k$  ( $k = 1, \dots, 3N - 6$ ), the Jacobian elements can be written as

$$J_{ik} = \frac{\partial \mathbf{R}_i}{\partial \xi_k} = \frac{\partial [\mathbf{O} \mathbf{r}_i + \mathbf{R}_{\text{CM}}]}{\partial q_k} = \mathbf{O} \frac{\partial \mathbf{r}_i}{\partial q_k} = \mathbf{O} \mathbf{t}_{ik}, \quad (9)$$

where we defined the ‘vibrational  $t$ -vector’ as

$$\mathbf{t}_{ik} = \frac{\partial \mathbf{r}_i}{\partial q_k}, \quad k = 1, 2, \dots, 3N - 6. \quad (10)$$

For a rotational degree of freedom,  $\xi_{3N-6+a} = \omega_a$ , which is a rotation angle about the  $a = 1(x), 2(y), 3(z)$  axis of the body-fixed frame, we can write

$$\begin{aligned} J_{i,3N-6+a} &= \frac{\partial \mathbf{R}_i}{\partial \xi_{3N-6+a}} = \frac{\partial [\mathbf{O}(\Omega) \mathbf{r}_i + \mathbf{R}_{\text{CM}}]}{\partial \omega_a} \\ &= \frac{\partial \mathbf{O}(\omega_1, \omega_2, \omega_3)}{\partial \omega_a} \mathbf{r}_i = \mathbf{O}[\mathbf{e}_a \times \mathbf{r}_i] = \mathbf{O} \mathbf{t}_{i,3N-6+a}, \end{aligned} \quad (11)$$

where the ‘rotational  $t$ -vector’ was defined as

$$\mathbf{t}_{i,3N-6+a} = \mathbf{e}_a \times \mathbf{r}_i, \quad a = 1(x), 2(y), 3(z), \quad (12)$$

and  $\mathbf{e}_a$  is the unit vector pointing along the (positive direction of the) coordinate axis,  $(\mathbf{e}_a)_n = \delta_{an}$  ( $n = 1, 2, 3$ ).

To obtain Eq. (11), we used the following relation regarding the derivative of an abstract three-dimensional rotational operation, written in the Euler–Rodrigues’ form, with respect to the rotation angle  $\omega$  about the axis pointing in the direction of the unit vector  $\mathbf{k} = (k_x, k_y, k_z)$  with  $|\mathbf{k}| = 1$ :

$$\frac{\partial}{\partial \omega^{(\mathbf{k})}} \mathbf{O} = \frac{\partial}{\partial \omega} [\mathbf{I} + \mathbf{K} \sin \omega + \mathbf{K}(1 - \cos \omega)] = \mathbf{K} \cos \omega + \mathbf{K}^2 \sin \omega, \quad (13)$$

where  $\mathbf{I}$  is the three-dimensional unit matrix and  $\mathbf{K}$  is the ‘cross product matrix’,  $\mathbf{K}\mathbf{r}_i = \mathbf{k} \times \mathbf{r}_i$ ,

$$\mathbf{K} = \begin{pmatrix} 0 & -k_z & k_y \\ k_z & 0 & -k_x \\ -k_y & k_x & 0 \end{pmatrix}. \quad (14)$$

Then, by using the  $\mathbf{K}^3 = -\mathbf{K}$  identity, we can write

$$\begin{aligned} \mathbf{O}\mathbf{K} &= [\mathbf{I} + \mathbf{K} \sin \omega + \mathbf{K}(1 - \cos \omega)] \mathbf{K} \\ &= \mathbf{K} + \mathbf{K}^2 \sin \omega + \mathbf{K}^3(1 - \cos \omega) \\ &= \mathbf{K} \cos \omega + \mathbf{K}^2 \sin \omega, \end{aligned} \quad (15)$$

and hence, the relation, used in Eq. (11), is obtained as

$$\frac{\partial}{\partial \omega^{(\mathbf{k})}} \mathbf{O}\mathbf{r}_i = \mathbf{O}\mathbf{K}\mathbf{r}_i = \mathbf{O}(\mathbf{k} \times \mathbf{r}_i). \quad (16)$$

Finally, for a translational-type degree of freedom in the laboratory frame,  $\xi_{3N-3+\alpha} = R_{\text{CM},\alpha}$ ,  $\alpha = 1(X), 2(Y), 3(Z)$ , we can write

$$J_{i,3N-3+\alpha} = \frac{\partial \mathbf{R}_i}{\partial \xi_{3N-3+\alpha}} = \frac{\partial [\mathbf{O}(\omega_1, \omega_2, \omega_3)\mathbf{r}_i + \mathbf{R}_{\text{CM}}]}{\partial R_{\text{CM},\alpha}} = \mathbf{e}_\alpha. \quad (17)$$

Having the Jacobi-matrix elements at hand, Eqs. (9), (11), and (17), we can calculate the mass-weighted metric tensor elements,

$$g_{kl} = \sum_{i=1}^N m_i \frac{\partial \mathbf{R}_i^\top}{\partial \xi_k} \frac{\partial \mathbf{R}_i}{\partial \xi_l}, \quad (18)$$

where the introduction of the mass weights corresponds to mass-scaled Cartesian coordinates,  $\tilde{\mathbf{R}}_i = \sqrt{m_i}\mathbf{R}_i$ .

For the rotation-vibration block of  $\mathbf{g}$ ,  $k, l = 1, 2, \dots, 3N - 3$ , is

$$\begin{aligned} g_{kl} &= \sum_{i=1}^N m_i \frac{\partial \mathbf{R}_i^\top}{\partial \xi_k} \frac{\partial \mathbf{R}_i}{\partial \xi_l} \\ &= \sum_{i=1}^N m_i \mathbf{t}_{ik}^\top \mathbf{O}^\top \mathbf{O} \mathbf{t}_{il} \\ &= \sum_{i=1}^N m_i \mathbf{t}_{ik}^\top \mathbf{t}_{il}, \end{aligned} \quad (19)$$

where orthogonality of the rotation matrix,  $\mathbf{O}^\top \mathbf{O} = \mathbf{I}$ , allowed us to express the rovibrational  $g_{kl}$  elements solely in terms of body-fixed quantities, *i.e.*, using the vibrational and rotational  $t$ -vectors, Eqs. (10) and (12), respectively. Regarding the translation-vibration and translation-rotation blocks, we use the fact that the translational Jacobi matrix elements are coordinate independent (constant), and we fixed the origin of the body-fixed frame at the nuclear center of mass,



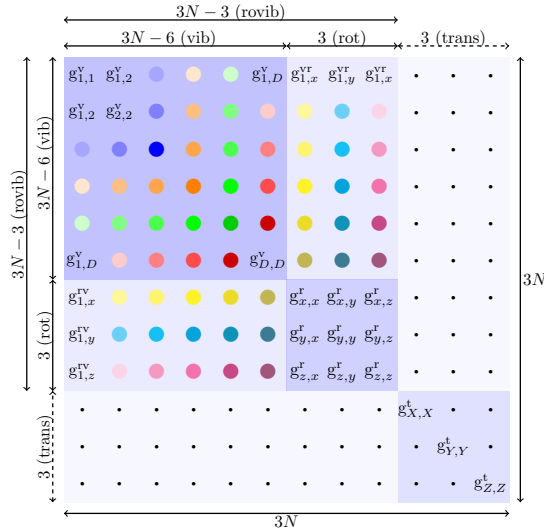


Figure 3. Mass-weighted metric tensor: vibrational (v), rotational (r), rovibrational (rv, vr), and translational (t) blocks of  $\mathbf{g}$ . The dots stand for '0' entries, *i.e.*, the kinetic coupling is exactly zero between the rovibrational and the translational degrees of freedom.

Eq. (6),  $\alpha = 1(X), 2(Y), 3(Z)$  and  $l = 1, 2, \dots, 3N - 3$ ,

$$\begin{aligned}
 g_{3N-3+\alpha, l} &= \sum_{i=1}^N m_i \frac{\partial \mathbf{R}_i^T}{\partial \xi_{3N-3+\alpha}} \frac{\partial \mathbf{R}_i}{\partial \xi_l} \\
 &= \sum_{i=1}^N m_i \mathbf{e}_\alpha^T \frac{\partial \mathbf{O} \mathbf{r}_i}{\partial \xi_l} \\
 &= \mathbf{e}_\alpha^T \frac{\partial}{\partial \xi_l} \mathbf{O} \sum_{i=1}^N m_i \mathbf{r}_i = 0.
 \end{aligned} \tag{20}$$

The translational matrix elements are

$$g_{3N-3+\alpha, 3N-3+\beta} = \sum_{i=1}^N m_i \mathbf{e}_\alpha^T \mathbf{e}_\beta = m_{12\dots N} \delta_{\alpha\beta}. \tag{21}$$

The resulting structure of the mass-weighted metric tensor,  $\mathbf{g}$ , is highlighted in Fig. 3.

Next, let us define the  $3N$ -dimensional gradient operator,  $(\text{grad}_{\tilde{\mathbf{R}}})_{i\alpha} = \partial_{i\alpha} = \partial / \partial \tilde{R}_{i\alpha}$ , and write the nuclear Schrödinger equation, Eq. (1), as

$$2(V - E)\Psi = \text{div}_{\tilde{\mathbf{R}}} \text{grad}_{\tilde{\mathbf{R}}} \Psi = \text{div}_{\xi} \text{grad}_{\xi} \Psi, \tag{22}$$

which is understood with the normalization of  $\Psi$  is written as

$$1 = \int \Psi^* \Psi \, d\tilde{\mathbf{R}} = \int \Psi^* \Psi \, \tilde{g}^{1/2} \, d\xi. \tag{23}$$

In the second equation, due to the coordinate change, the determinant of the Jacobi matrix,  $\det \mathbf{J}$ , appears, which equals the square root of the determinant of the metric tensor,  $\det \mathbf{J} = \tilde{g}^{1/2}$  with  $\tilde{g} = \det \mathbf{g}$ . We can say in short that the 'volume element' corresponding to integration in the new coordinates is

$$dV' = \tilde{g}^{1/2} \, d\xi_1 d\xi_2 \dots d\xi_{3N}. \tag{24}$$

In curvilinear coordinates, the divergence of an  $\mathbf{F}$  vector field is written (using Einstein's summation convention and the covariant and contravariant labelling) as

$$\text{div}_{\xi} \mathbf{F} = \tilde{g}^{-1/2} \partial_k \tilde{g}^{1/2} F^k, \tag{25}$$

and the gradient of a  $\phi$  scalar field is

$$\text{grad}_{\xi}\phi = \partial^k\phi = g^{kl}\partial_l\phi, \quad (26)$$

where  $g^{kl}$  is the contravariant metric tensor, which is the inverse of the (covariant) metric tensor, Eq. (18). As a result, we can write the ‘divgrad’ operator in curvilinear coordinates as

$$\text{div}_{\xi}\text{grad}_{\xi}\Psi = \tilde{g}^{-1/2}\partial_k\tilde{g}^{1/2}g^{kl}\partial_l\Psi, \quad (27)$$

and the integrals are calculated ‘with’ the  $dV'$  volume element, Eq. (24). A more symmetric form of the differential operator appears, if we ‘merge’ (the square root of) the Jacobi determinant in the wave function, so that we can use the simple normalization condition

$$1 = \int \psi^*\psi d\xi_1 \dots d\xi_{3N}. \quad (28)$$

This implies that  $\Psi = \tilde{g}^{-1/4}\psi$ , and we obtain the Schrödinger equation for  $\psi$  as

$$2(V - E)\Psi = \tilde{g}^{-1/2}\partial_k\tilde{g}^{1/2}g^{kl}\partial_l\Psi \quad (29)$$

$$2(V - E)\tilde{g}^{-1/4}\psi = \tilde{g}^{-1/2}\partial_k\tilde{g}^{1/2}g^{kl}\partial_l\tilde{g}^{-1/4}\psi \quad (30)$$

$$2(V - E)\psi = \tilde{g}^{-1/4}\partial_k\tilde{g}^{1/2}g^{kl}\partial_l\tilde{g}^{-1/4}\psi, \quad (31)$$

which can be rearranged to

$$\left[ -\frac{1}{2}\tilde{g}^{-1/4}\partial_k\tilde{g}^{1/2}g^{kl}\partial_l\tilde{g}^{-1/4} + V \right] \psi = E\psi \quad (32)$$

or written in the more traditional form,

$$\left[ \frac{1}{2} \sum_{k=1}^{3N} \sum_{l=1}^{3N} \tilde{g}^{-1/4} \hat{p}_k \tilde{g}^{1/2} G_{kl} \hat{p}_l \tilde{g}^{-1/4} + V \right] \psi = E\psi \quad (33)$$

with the  $\hat{p}_k = -i\partial/\partial\xi_k$  ‘generalized momenta’ and the ‘big’  $\mathbf{G}$  matrix

$$\mathbf{G} = \mathbf{g}^{-1}. \quad (34)$$

In the physical chemistry literature, the Eq. (33) form of the kinetic energy operator is commonly referred to as the ‘Podolsky form’ [36]. In 1928, Boris Podolsky drew Paul Dirac’s attention to the correct form of the Laplace (‘divgrad’) operator in curvilinear coordinates (that had been known in mathematics for decades). Podolsky’s choice for the normalization of the wave function resulted in a symmetric form of the operator, which is convenient for variational-type applications of the Schrödinger equation in curvilinear coordinates.

It is important to note that the curvilinear form of the operator can be expressed with the metric tensor, and it is not necessary to use the Jacobian matrix. Eqs. (19), (20), and (21) (see also Fig. 3) show that the metric tensor can be calculated from body-fixed quantities, *i.e.*, rotational and vibrational  $t$ -vectors and the constant masses associated to the nuclei, and it depends neither on the rotation angles, nor the translational coordinates. The metric tensor can be written as a function of the vibrational coordinates and of the body-fixed frame definition ( $\mathbf{e}_a$  vectors).

Due to the block-diagonal structure of  $\mathbf{g}$  in terms of the rovibrational and the translational coordinates (Fig. 3) and since  $\tilde{g}$  does not depend on the translational coordinates, the kinetic energy operator is the sum of a rovibrational and a translational part,

$$\left[ \frac{1}{2} \sum_{k=1}^{3N-3} \sum_{l=1}^{3N-3} \tilde{g}^{-1/4} \hat{p}_k \tilde{g}^{1/2} G_{kl} \hat{p}_l \tilde{g}^{-1/4} + \frac{1}{2m_{12\dots N}} \mathbf{P}_{\text{CM}}^2 + V \right] \psi = E\psi \quad (35)$$

with  $P_{\text{CM},\alpha} = -i\partial/\partial R_{\text{CM},\alpha}$ . The complete Eq. (35) must be used to describe molecules in interaction with solid materials or their motion in cages [37, 38].

At the same time, for an isolated molecular system,  $V$  is independent of the translational degrees of freedom, and then, it is convenient to subtract the center-of-mass kinetic energy,  $\mathbf{P}_{\text{CM}}^2/(2m_{12\dots N})$  from the operator and separate the

continuum spectrum of free translation. Thereby, we obtain the rovibrational Hamiltonian for an isolated molecule as

$$\hat{H}^{rv,P} = \frac{1}{2} \sum_{k=1}^{D+3} \sum_{l=1}^{D+3} \tilde{g}^{-1/4} \hat{p}_k \tilde{g}^{1/2} G_{kl} \hat{p}_l \tilde{g}^{-1/4} \quad (36)$$

$$\begin{aligned} &= \frac{1}{2} \sum_{k=1}^D \sum_{l=1}^D \tilde{g}^{-1/4} \hat{p}_k G_{kl} \tilde{g}^{1/2} \hat{p}_l \tilde{g}^{-1/4} \\ &\quad + \frac{1}{2} \sum_{k=1}^D \sum_{a=1}^3 (\hat{p}_k G_{k,D+a} + G_{k,D+a} \hat{p}_k) \hat{J}_a \\ &\quad + \frac{1}{2} \sum_{a=1}^3 G_{D+a,D+a} \hat{J}_a^2 \\ &\quad + \frac{1}{2} \sum_{a=1}^3 \sum_{b>a}^3 G_{D+a,D+b} [\hat{J}_a, \hat{J}_b]_+ + V, \end{aligned} \quad (37)$$

where  $D = 3N - 6$  applies. Eq. (37) was obtained from Eq. (36) by exploiting the fact that  $\tilde{g}$  does not depend on the rotational coordinates [39]. Furthermore, we used that the derivative with respect to the  $a$ th rotational angle, is the body-fixed angular momentum component,  $\hat{J}_a = -i\partial/\partial\omega_a$ .  $[\hat{J}_a, \hat{J}_b]_+$  labels the anti-commutator of  $\hat{J}_a$  and  $\hat{J}_b$  [40]. We also note that the body-fixed angular momentum operators satisfy the (anomalous) commutation relations, expressed with the  $\epsilon_{abc}$  Levi-Civita symbol,

$$[\hat{J}_a, \hat{J}_b] = -i\epsilon_{abc} \hat{J}_c, \quad a, b, c = 1(x), 2(y), 3(z) \quad (38)$$

The  $\hat{H}^P$  Podolsky form of the rovibrational Hamiltonian was found to be advantageous in some computer implementation [41], because it was possible to arrive at a stable numerical code using only first-order coordinate derivatives (vibrational  $t$ -vectors computed by finite differences). Efficient use of the Podolsky form assumes that the truncated resolution of identity in the finite vibrational basis provides an accurate matrix representation ( $Mx$ ) for the operator identity  $Mx(\hat{p}_k^2) \approx Mx(\hat{p}_k) \cdot Mx(\hat{p}_k)$  for the vibrational derivative operators ( $k = 1, \dots, D$ ).

If this approximation is inaccurate in the vibrational basis, then, it is better to use the ‘fully-rearranged’ form of the Hamiltonian [31, 32, 42, 43], which is obtained from the vibrational Podolsky form by mathematically equivalent manipulations,

$$\hat{H}^v = -\frac{1}{2} \sum_{k=1}^D \sum_{l=1}^D G_{kl} \frac{\partial}{\partial q_k} \frac{\partial}{\partial q_l} - \frac{1}{2} \sum_{l=1}^D B_l \frac{\partial}{\partial q_l} + U + V, \quad (39)$$

where

$$B_l = \sum_{k=1}^D \frac{\partial}{\partial q_k} G_{kl}, \quad (40)$$

and the potential-like term [41, 43],

$$U = \frac{1}{32} \sum_{k=1}^D \sum_{l=1}^D \left[ \frac{G_{kl}}{\tilde{g}^2} \frac{\partial \tilde{g}}{\partial q_k} \frac{\partial \tilde{g}}{\partial q_l} + 4 \frac{\partial}{\partial q_k} \left( \frac{G_{kl}}{\tilde{g}} \frac{\partial \tilde{g}}{\partial q_l} \right) \right] \quad (41)$$

are functions of the vibrational coordinates only (similarly to  $G_{kl}$  and  $V$ ).

Evaluation of  $B_l$  and  $U$  assumes the evaluation of higher-order coordinate derivatives (vibrational coordinate derivatives of the  $t$ -vectors, up to third order, *i.e.*,  $\partial^3 \mathbf{r}_i / \partial q_k \partial q_l \partial q_m$ ). In this case, evaluation of the derivatives by finite differences requires the use of increased precision arithmetic (quadruple precision in Fortran) [41], alternatively analytic derivatives, *e.g.*, for  $Z$ -matrix coordinates [43], or automated differentiation [44] can be used.

The idea of developing a general and unifying approach to the rovibrational kinetic energy operator has an at least half-a-century history, and we only cite here some of the prominent examples [42, 43, 45–48]. During the rest of this work, developments will be reviewed in relation with the numerical kinetic energy operator approach of Ref. 41 and its applications within the GENIUSH (GENERAL Internal-coordinate USer-defined Hamiltonians) program [41, 49–51].

## 2. Geometrical constraints and reduced-dimensionality models

The number of vibrational degrees of freedom increase linearly with the number of atoms in the system and result in a rapid scale-up of the computational cost of variational applications (Secs. II B 3–II B 5). To attenuate this growth, it is possible to introduce constraints on the motion of the nuclei.

Geometrical constraints, *e.g.*, fixing certain bond lengths or angles, can be implemented in the outlined formalism by ‘deleting’ the corresponding rows and columns of the  $\mathbf{g}$  matrix corresponding to the constrained coordinate [41]. Zeroing rows and columns in the  $\mathbf{G}$  matrix does not correspond to imposing a rigorous geometrical constraint, but it corresponds to fixing the ‘generalized’ momenta corresponding to the selected coordinate. Although ‘zeroing’ in the  $\mathbf{G}$  matrix (within some specific computational setup) may result in a better numerical approximation to the full-dimensional result, the numerical values depend on the coordinate representation used for the *constrained fragment*, which is conceptually problematic.[41]

The (ro)vibrational Hamiltonians corresponding to rigorous geometrical constraints take the same form as in Eqs. (36), (37) and (39), but  $D < 3N - 6$  and it labels the number of the active vibrational degrees of freedom. The  $\tilde{g}$  and  $\mathbf{G}$  functions in the Hamiltonian are obtained by (a) constructing the full  $\mathbf{g} \in \mathbb{R}^{(3N-3) \times (3N-3)}$  matrix (the block-diagonal translational block can be inverted separately, if needed); (b) deleting the last  $D_{\text{fixed}}$  rows and columns of the full  $\mathbf{g}$  corresponding to the constrained degrees of freedom; (c) the remaining  $D$ -dimensional ‘reduced’  $\mathbf{g}$  matrix is used to calculate  $\tilde{g}$  and to obtain  $\mathbf{G}$  by inversion.

Experience shows these reduced dimensionality-models (with fixed geometrical parameters) can be useful in weakly interacting systems [31, 32, 51–54], but they can introduce large errors within bound molecules [29]. It remains a question to be explored whether the error of (a qualitatively meaningful) reduced-dimensionality model is introduced due to the lack of ‘quantum coherence’ of the discarded modes with the active degrees of freedom or it is rather a structural effect due to the dissection of a certain  $D$ -dimensional cut of the full-dimensional PES corresponding to some fixed coordinate values.

All in all, ideally we can aim for an systematically improvable (series of) approximate solution(s) of the nuclear Schrödinger equation by including all vibrational degrees of freedom as dynamical variable.

## 3. A variational rovibrational approach: basis set and integration grid for the matrix representation of the Hamiltonian

In bound-state quantum mechanics, a common and powerful approach for solving the wave equation, a differential equation with no known analytic solution, is provided by the variational method. This method can be straightforwardly applied to the rovibrational problem, since the rovibrational Hamiltonian is bounded from below. According to Walther Ritz’ [55] linear variational procedure from 1909, the variationally best linear combination coefficients of a fixed (orthonormal) basis set are obtained by diagonalization of the matrix-eigenvalue problem

$$\mathbf{H}\mathbf{c}_n = E_n\mathbf{c}_n, \quad (42)$$

which provides the best approximation to the exact wave function over the space spanned by the  $\Phi_I$  basis functions,

$$\psi_n = \sum_{I=1}^{N_b^{(rv)}} c_{n,I} \Phi_I \quad (43)$$

and  $E_n$  approaches the  $n$ th exact eigenvalue from above.

These rigorous variational properties apply if the Hamiltonian matrix is constructed exactly, which assumes evaluation of integrals for the Hamiltonian with the pre-defined basis functions

$$H_{IJ} = \langle \Phi_I | \hat{H} | \Phi_J \rangle. \quad (44)$$

In all applications reviewed in this work, the  $\langle \Phi_I | \Phi_J \rangle = \delta_{IJ}$  orthonormality applies.

The  $\Phi_I$  multi-dimensional basis functions are often defined as

$$\Phi_I = \Phi_{iK\tau}^{(JM)}(q_1, \dots, q_D, \Omega) = \Phi_i(q_1, \dots, q_k) \Theta_{K\tau}^{(JM)}(\Omega), \quad (45)$$

where  $\Theta_{K\tau}^{(JM)}(\Omega)$  and  $\Phi_i(q_1, \dots, q_k)$  label rotational and vibrational basis functions, respectively. The choice of the rotational and vibrational basis functions is motivated by analytically solvable quantum mechanical models, and most importantly, those of the rigid rotor and the harmonic oscillator approximations [24, 56].

*a. Rotational basis functions and matrix elements* Basis functions for the rotational part are obtained from eigenfunctions of the symmetric top problem,  $|J\bar{K}M\rangle$  ( $\bar{K} = -J, \dots, J$ ) [56]. The  $J = 0, 1, \dots$  and  $M = -J, \dots, J$  quantum numbers correspond to the total rotational angular momentum and its laboratory-frame projection, which are exact quantum numbers for isolated molecules. For every  $JM$  pair, the  $2J + 1$  symmetric top eigenfunctions corresponding to different  $\bar{K} = -J, \dots, J$  values span the rotational subspace.

For a variational-like computation, the matrix representation of the Hamiltonian, Eq. (37), must be constructed over the basis set. Matrix elements including the  $\hat{J}_a$  angular momentum operators and the  $|J\bar{K}M\rangle$  rigid-rotor functions are [40, 49, 56]

$$\langle J\bar{K}M|\hat{J}_x|J(\bar{K} \pm 1)M\rangle = \frac{1}{2}\sqrt{J(J+1) - \bar{K}(\bar{K} \pm 1)} \quad (46)$$

$$\langle J\bar{K}M|\hat{J}_y|J(\bar{K} \pm 1)M\rangle = \mp \frac{i}{2}\sqrt{J(J+1) - \bar{K}(\bar{K} \pm 1)} \quad (47)$$

$$\langle J\bar{K}M|\hat{J}_z|J\bar{K}M\rangle = \bar{K} . \quad (48)$$

To avoid complex-valued Hamiltonian matrix elements, instead of  $|J\bar{K}M\rangle$ , their linear combination, the so-called called Wang-functions [57] are used,  $K = |\bar{K}| = 0, \dots, J$ ,

$$\Theta_{K\tau}^{(JM)} = \begin{cases} \frac{1}{\sqrt{2}} [ |J\bar{K}M\rangle + |J - \bar{K}M\rangle ], & \text{for even } \bar{K}, \tau = 0 \\ \frac{1}{\sqrt{2}} [ |J\bar{K}M\rangle - |J - \bar{K}M\rangle ], & \text{for even } \bar{K}, \tau = 1 \\ \frac{1}{\sqrt{2}} [ |J\bar{K}M\rangle - |J - \bar{K}M\rangle ], & \text{for odd } \bar{K}, \tau = 0 \\ \frac{1}{\sqrt{2}} [ |J\bar{K}M\rangle + |J - \bar{K}M\rangle ], & \text{for odd } \bar{K}, \tau = 1 \end{cases} \quad (49)$$

*b. Vibrational basis functions and matrix elements* A common and straightforward choice for a multi-dimensional vibrational basis function is a product form,

$$\Phi_i(q_1, \dots, q_D) = \prod_{k=1}^D \varphi_{i_k}^{(k)}(q_k) , \quad (50)$$

where the  $\varphi_{i_k}^{(k)}$  ( $i_k = 1, \dots, N_b, k$ ) functions are 1-dimensional (1D) functions of the vibrational coordinates forming an orthonormal basis set, e.g., Hermite functions, obtained from the analytic solution of the harmonic oscillator eigenproblem [24, 56].

As to the matrix representation of the Hamiltonian, the matrix representation for the  $\hat{p}_k$  differential operator is known in analytic form for all commonly used 1D basis function types. At the same time, the potential energy is, in general, a complicated  $(3N - 6)$ -dimensional function, and its matrix elements can be computed only by numerical integration, unless some special form is assumed for the function representing the potential energy (Sec. II B 6). For special coordinate choices, the curvilinear kinetic energy operator can be written in a closed analytic form, which can be integrated by analytic expressions for the vibrational basis. But, if we aim for a ‘black-box-type’ vibrational procedure, we consider  $G_{kl}$ ,  $\tilde{g}$ ,  $B_i$ , and  $U$  as general, vibrational-coordinate dependent functions, similar to the  $V$  potential energy, which is integrated by numerical techniques. Furthermore, the coordinates which are most convenient for fitting the potential, most commonly, interatomic distances, do not represent a good choice for doing the rovibrational computation.

A 1D numerical integral,

$$\int_a^b w(q)F(q) dq = \sum_{i=1}^k w_i F(q_i) \quad (51)$$

can be most efficiently calculated by some Gaussian quadrature. If an appropriate Gaussian quadrature rule ( $w_i$  weights and the  $q_i$  points) exists for the  $a$  and  $b$  boundaries and the  $w$  weight function, then, the numerical result is exact if  $F$  is at most a  $(2k - 1)$ -order polynomial of  $q$ , and  $2k - 1$  is called the (1D) accuracy of the Gaussian quadrature [58]. A straightforward generalization of 1D quadratures to multi-dimensional integration relies on forming a multi-dimensional, direct-product quadrature of the 1D rules,

$$\begin{aligned} & \int_{a_1}^{b_1} \dots \int_{a_D}^{b_D} w^1(q_1) \dots w^D(q_D) F(q_1, \dots, q_D) dq_1 \dots dq_D \\ & \approx \sum_{i_1=1}^{k_1^q} \dots \sum_{i_D=1}^{k_D^q} w_{1,i_1} \dots w_{D,i_D} F(q_{1,i_1}, \dots, q_{D,i_D}) \end{aligned} \quad (52)$$

with the  $w_{k,i_k}$  weights and  $q_{k,i_k}$  points ( $k = 1, \dots, D$ ) corresponding to the 1D quadrature rule of the  $k$ th degree of freedom. We note, that in some cases (for periodic coordinates), we do not use orthogonal polynomial functions, but sine and cosine functions. Integrals of periodic functions can be very efficiently integrated by a trapezoidal (equidistant) quadrature that converges exponentially fast with respect to the number of grid points.

In the vibrational methodology, a finite basis and finite grid representation used to construct the Hamiltonian matrix is called the finite basis representation (FBR). Since we assume a general  $V$  function representing the PES, the

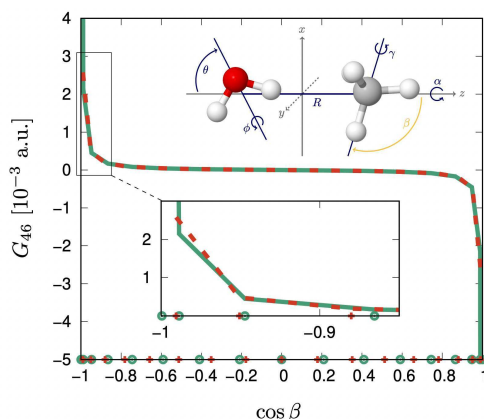


Figure 4. Singular behaviour of a  $\mathbf{G}$  matrix element, ‘ $G_{46}$ ’, for the example of the  $\text{CH}_4\text{-H}_2\text{O}$  dimer along the  $\cos \beta$  coordinate. The definition of the intermolecular coordinates,  $(R, \theta, \phi, \alpha, \beta, \gamma)$ , is also shown. The cot-DVR points [64] (green) have a higher density than Legendre DVR (red) near the singularities,  $\cos \beta = -1$  and  $+1$ .

integration is in general non-exact, but the exact value of the integrals for the basis set can be approached (arbitrarily close) by increasing the number of quadrature points.

For the special case of an equal number of basis functions and quadrature points for the  $k$ th degree of freedom ( $N_b k = k_k^n$ ), it is possible to define a similarity transform of the finite basis with the prescription that the transformed basis functions diagonalize the  $q_k$  coordinate operator matrix. This choice results in the discrete variable representation (DVR) of the basis, and the eigenvalues of the coordinate operator provide us with the DVR grid points [59–61]. This representation became popular in the vibrational community in conjunction with the approximation

$$(\mathbf{q}_k^n)_{ij} \approx (\mathbf{q}_k \cdot \dots \cdot \mathbf{q}_k)_{ij} = q_{k,i}^n \delta_{ij}, \quad (53)$$

which relies on multiple  $(n - 1)$  insertion of the truncated resolution of identity (in the finite basis), and allows us to approximate any function of the coordinates by a diagonal matrix. For a finite grid (and basis), this is certainly an approximation, which spoils the rigorous variational property (and convergence of the eigenvalues from ‘above’) of the computations. In practice, beyond a certain minimal number of grid points, the eigenvalues properly converge to their ‘numerically’ exact value upon a systematic increase of the number of grid points (equal to the number of basis functions). Eq. (53) allows to straightforwardly include any complicated function of the coordinates in a ‘black-box’ fashion. Complicated functions of the coordinates, *e.g.*,  $V$ ,  $G_{kl}$ ,  $\tilde{g}$ ,  $B_l$ ,  $U$  (Sec. II B 1), are ubiquitous in the vibrational theory. These general coordinate-dependent functions do not need to be explicitly represented with polynomials of the coordinates, but it is assumed that they are smooth functions of the coordinates and their change with the coordinates is characterized by not too high-order polynomials (the maximal polynomial order is not too high), and hence, the numerically exact results can be systematically approached by increasing the number of quadrature points. This is generally the case for the  $V$  PES corresponding to an isolated electronic state over the dynamically relevant coordinate range. Certain terms in the kinetic energy operator ( $G_{kl}$ , ...) may become singular over the dynamically relevant coordinate range, which commonly happens in floppy molecular systems (singularity of some elements of the  $\mathbf{G}$  matrix is highlighted for the example of the methane-water dimer in Fig. 4). In practice, this singular behaviour can be determined (either from the analytic formulation of the kinetic energy or) by numerically ‘measuring’ the behaviour upon the change of the coordinates [31]. Most often an appropriate (Gaussian-)quadrature can be found, in which the weight function, Eq. (51), corresponds to this singular behaviour. Ref. 31 presents an example, when this is not the case, and the DVR-FBR approach used. Another option would be to deal with singularities using special functions of multiple coordinates. Most importantly, singularities due to spherical motion can be treated by using spherical harmonics [62] or Wigner  $D$ -functions [63], but this alternative would mean losing a product basis set (of one-particle basis functions), which allows a general implementation.

The size of the direct-product basis and the direct-product grid grows exponentially with the number of active vibrational degrees of freedom. The corresponding computational cost can be mitigated by efficient algorithmic and implementation techniques, most importantly by (a) evaluating nested sums, *e.g.*, Eq. (52), sequentially [63, 65–70]; (b) using an iterative (Lanczos) eigensolver [71, 72], which requires only multiplication of a trial vector with the Hamiltonian matrix without storage or even explicit construction of the full matrix [41, 72, 73]. Nevertheless, even in the most efficient implementation, a few vectors of the total size of the basis (and the grid) must be stored, which grows exponentially with the vibrational dimensionality. The matrix-vector multiplication can be parallelized with the OpenMP protocol (as it is described in Ref. 73, for example).

During the course of the Lanczos eigensolver iterations, one eigenpair is converged after the other. The computational effort, which is determined by the number of matrix-vector products is determined by the number of required eigenvalues, which means that, in practice, up to a few hundred (a thousand) states can be efficiently computed. The

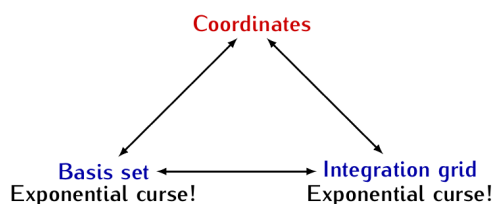


Figure 5. Complexity of the vibrational problem. In general, the PES is a multi-dimensional function.

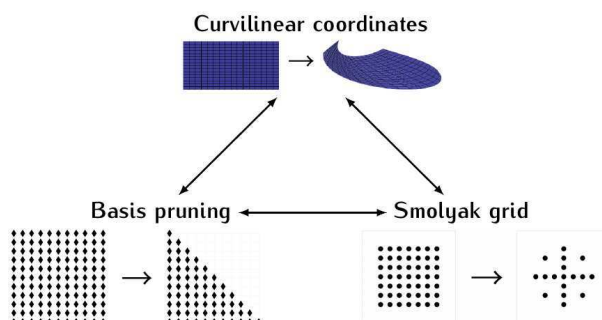


Figure 6. Illustration of a possible strategy to attenuate the double-exponential scale-up of the vibrational problem: system-adapted curvilinear coordinates, basis pruning, and grid pruning.

smallest (or largest) eigenvalues of the Hamiltonian matrix can be efficiently computed. To compute a spectral window (from an arbitrarily chosen range of the entire spectrum), there is currently no known methodology that would be more efficient than computing all states up to the desired range [73]. A truly efficient computation of solely a spectral window is still an open problem.

An efficient implementation and available computing power typically allows us to use this simple, ‘direct’(-product) methodology up to 6–10 fully coupled vibrational degrees of freedom [30, 50–53, 74].

To be able to solve the vibrational Schrödinger equation beyond this system size (or for challenging floppy systems up to a higher energy range already with up to ca. 10 degrees of freedom), it is necessary to develop vibrational methodologies which attenuate the rapid increase of the computational cost with the dimensionality.

#### 4. Computational bottleneck of the variational vibrational methodology

While the electronic structure problem scales exponentially with respect to the basis size, the general vibrational problem suffers from a *double* exponential scale-up: the computational effort grows exponentially fast with the dimensionality with respect to the basis set size *and* also with respect to the integration grid size (Fig. 5).

This double exponential scale-up is due to the fact that the potential energy surface (PES) is in general a multi  $(3N-6)$  dimensional function, for which the matrix representation must be constructed by means of numerical integration (hence, the exponentially growing integration grid).

Over the past decade, there have been important developments in the quantum nuclear motion methodology that make it possible to attenuate the exponential scaling of the vibrational problem in a systematic manner. In the following subsection (Sec. II B 5), we present a strategy that we used and developed during the past few years, and it is followed by a short overview of other possible strategies in Sec. II B 6.

#### 5. A possible strategy for efficient vibrational computations: Smolyak quadrature and pruning

A possible strategy to attenuate the rapidly increasing computational cost of solving the vibrational Schrödinger equation relies on a systematically improvable reduction of both the basis set size and the integration grid size.

The foundations of this direction were laid down by Avila and Carrington about a decade ago [75–77]. More recently, we have ‘embedded’ this approach, originally used for semi-rigid systems, in computations involving both floppy and semi-rigid parts [29, 31–33].

The strategy is highlighted in Fig. 6. An initial pre-requisite for practical usefulness of this approach is to find good curvilinear coordinates, which make the kinetic and potential coupling small.

*a. Towards optimal internal coordinates* To be able to efficiently truncate the product basis set, Eq. (50), we need good coordinates. For good coordinates, both the kinetic and the potential energy coupling is small. For semi-rigid molecules, like methane,  $\text{CH}_4$ , and ethene,  $\text{C}_2\text{H}_4$ , a reasonably good coordinate representation is immediately provided

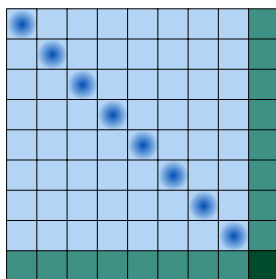


Figure 7. Optimized coordinates ensure small coupling (light blue).

by the commonly used rectilinear coordinates. By construction (*vide infra*) both the kinetic and the potential coupling is zero at the equilibrium structure, and since the vibrations are of small amplitude, the coupling remains small over the dynamically relevant coordinate range. Hence efficient basis pruning is possible, and grid pruning was introduced for these systems used as examples in Refs. 75–77.

At the same time, finding optimal coordinates for floppy systems is non-trivial. Fortunately, a very broad and chemically important class of floppy molecular systems have just a few large-amplitude motions (LAMs) and many small-amplitude motions (SAMs), examples include,  $\text{NH}_3$ , methanol,  $\text{CH}_3\text{OH}$  [78], ethane,  $\text{CH}_3\text{CH}_3$ , ethanol,  $\text{CH}_3\text{CH}_2\text{OH}$ , or glycine,  $\text{NH}_2\text{CH}_2\text{COOH}$ . For these types of systems, a simple strategy is to accept that a small number of vibrational degrees of freedom, *i.e.*, the LAMs, are strongly coupled (among themselves and with the small-amplitude ones), and hence basis and grid truncation is inefficient. At the same time, the remaining coordinates are small-amplitude motions for which good coordinates can be constructed (Fig. 7). For doing this, we need to abandon the equilibrium structure as reference, and use instead a reference path (surface, volume, hyper-volume...) which depends on the LAMs. With respect to this (multi-dimensional) reference ‘path’, we can define linear combination of the small-amplitude coordinates, which minimize both the kinetic and the potential energy coupling among the small-amplitude modes. These ‘good’ small-amplitude coordinates are constructed similarly to the (curvilinear) normal coordinates.[25, 79, 80]

Papušek and co-workers pioneered this direction of research starting from the 1970s with first applications for the ammonia molecule described by one large-amplitude and many (5) small-amplitude degrees of freedom [25, 81]. For the case of using rectilinear normal coordinates for representing the small-amplitude vibrations and a one-dimensional path, the ‘so-called’ reaction-path Hamiltonian [82] has been formulated and used in many applications [82, 83], whereas for two large-amplitude degrees of freedom, the reaction-surface Hamiltonian [84] has been formulated, but never used in computations to the best of our knowledge.

Anharmonicities of one-dimensional bond-stretching and bending-type motions are better represented by the curvilinear bond stretching- and bending-type coordinates, than by rectilinear ‘analogues’ [29], and this motivates the definition of *curvilinear* normal (c-normal) coordinates,  $\mathbf{Q}$ . Although the analytic kinetic energy operator is not immediately available for these coordinates, the kinetic energy coefficients can be straightforwardly computed over a grid using ideas of Sec. II B 1.

So, let us consider some physically motivated ‘primitive’ internal coordinates,  $\rho_i$  (bond distances, angles, etc.), to describe the small-amplitude vibrations. Then, the curvilinear normal coordinates,  $Q_k$ , are defined with respect to the reference structure,  $\rho^{(0)}$ , obtained as the minimum of the PES for a selected value of the LAM coordinates,  $\tau$ ,

$$\rho(\tau) = \rho^{(0)}(\tau) + \mathbf{L}(\tau)\mathbf{Q}, \quad (54)$$

where the linear combination coefficient matrix,  $\mathbf{L}$ , solves the  $\mathbf{L}^{-1}\mathbf{G}\mathcal{F}\mathbf{L} = \mathbf{A}$  equation with normalization  $\mathbf{L}^T\mathbf{G}^{-1}\mathbf{L} = \mathbf{I}$ , and thereby minimize the coupling both in the potential and in the kinetic energy near the  $\rho^{(0)}$  reference structure [25].  $\mathbf{G}(\rho^{(0)}, \tau)$  is the small-amplitude block of the ‘big’  $\mathbf{G}$  matrix, Eq. (34), corresponding to the reference structure for  $(\rho^{(0)}, \tau)$ , and  $(\mathcal{F})_{ij} = \partial^2 V / \partial \rho_i \partial \rho_j |_{(\rho^{(0)}, \tau)}$  is the force-constant matrix at the same structure.

Whether it is necessary to determine  $\mathbf{L}(\tau)$  for ‘every’  $\tau$  (in practice, carried out over a grid and interpolated or fitted to have a functional representation) [29] or some ( $\tau$  independent) averaged  $\bar{\mathbf{L}}$  is sufficient for the relevant  $\tau$  range of the dynamics, depends on the system and energy range, and, in principle, should be always checked (numerically).

The more common rectilinear normal coordinates [24],  $\bar{Q}_i$  could be obtained as

$$\mathbf{r} = \mathbf{r}^{(0)} + \mathbf{I}\mathbf{Q}, \quad (55)$$

where  $\mathbf{I} = \mathbf{T}^{(0)}\mathbf{L}$ , and  $(\mathbf{T}^{(0)})_{ik} = t_{ik}^{(0)}$  collects the vibrational t-vectors, Eq. (10), corresponding to the semi-rigid degrees of freedom at structure  $(\rho^{(0)}, \tau)$ .

For practical computations with c-normal coordinates, it is necessary to pay attention to the domain of the various coordinates. The primitive internal coordinates are typically angle- and distance-type coordinates, and they are calculated as linear combination of the c-normal coordinates, defined on the entire real axis,  $Q_k \in \mathbb{R}$ . ‘Mapping



functions' were used in Ref. 29 to ensure that the calculated coordinate values are in the mathematically correct range.

*b. Basis pruning* If good coordinates are found, which ensure that the coupling of the different degrees of freedom is small (off-diagonal Hamiltonian matrix elements less than ca. 30 % of the corresponding diagonal elements), then, some product basis functions are not required in order to converge the lowest energy levels and they can be discarded [85, 86], assuming that reasonably good one-dimensional basis functions can be found. We note that for basis (and grid) pruning, we use FBR, since (unfortunately), there is no known efficient way to prune a DVR, in which the basis and grid representations are inherently coupled.

Discarding basis functions from a direct-product basis means that instead of writing the vibrational ansatz as

$$\Psi_i(q_1, \dots, q_D) = \sum_{n_1=1}^{n_1^{\max}} \dots \sum_{n_D=1}^{n_D^{\max}} c_{i,n_1,\dots,n_D} \prod_{k=1}^D \varphi_{n_k}(q_k), \quad (56)$$

we choose an  $f(n_1, \dots, n_D)$  function of the basis function 'excitation' indices to define basis combinations of one-dimensional basis functions, which are important,

$$\Psi_i(q_1, \dots, q_D) = \sum_{f(n_1,\dots,n_D) \leq b} c_{i,n_1,\dots,n_D} \prod_{k=1}^D \varphi_{n_k}(q_k), \quad (57)$$

and discard the rest without losing from the accuracy of the results. The simplest possible pruning function is the sum of the basis excitation indices,

$$f(n_{q_1}, \dots, n_{q_D}) = \sum_{i=1}^D n_{q_i} = n_{q_1} + \dots + n_{q_D}. \quad (58)$$

This function can be improved by weighting 'down' the contribution from the  $n_{q_i}$  excitation 'quanta' of the lowest-energy ( $D - 1$ )th and  $D$ th) vibrations, e.g.,

$$f(n_{q_1}, \dots, n_{q_D}) = n_{q_1} + \dots + \frac{1}{2} n_{q_{D-1}} + \frac{1}{3} n_{q_D}. \quad (59)$$

For an *a priori* assessment of the importance of a basis function, the following considerations can be made. Regarding the (un)importance of an  $|\mathbf{n}'\rangle$  basis state ( $\mathbf{n}'$  collects the basis indexes) in a wave function dominated by the  $|\mathbf{n}\rangle$  basis state, the largeness (smallness) of the ratio,

$$\frac{\langle \mathbf{n} | \hat{H} | \mathbf{n}' \rangle}{E_{\mathbf{n}}^{(0)} - E_{\mathbf{n}'}^{(0)}} \approx 0 \quad (60)$$

can be indicative. The ratio is small, *i.e.*, the  $|\mathbf{n}'\rangle$  basis function can be neglected, either if (a) the coupling through the Hamiltonian matrix (nominator) is small, or (b) the zeroth-order energy difference (denominator) is large. The order of magnitude of the Hamiltonian matrix element can be estimated by considering the Taylor expansion of the potential and the kinetic energy written in good coordinates. Pruning is almost a separate field within theoretical spectroscopy, since there are infinitely many possible choices (and many possible physically motivated arguments). For example, there are pruning choices that are effective only to compute fundamental vibrations and other pruning choices are useful to compute thousands of states [87–89].

*c. Grid pruning* Reducing the basis size allows us to tackle part of the problem (Figs. 5, 6), the exponential scale-up of the overall variational procedure can be attenuated only if the integration grid is also pruned. A general approach to the variational grid-size problem is provided by the non-product Smolyak quadrature grid approach first introduced by Avila and Carrington [75] in vibrational computations, and, since then, it has been used to efficiently describe the semi-rigid skeleton of a variety of systems [29, 31, 32, 76–78, 90].

In an abstract manner, we can write the direct-product quadrature rule as

$$\hat{Q}(D, k_1^{\max}, \dots, k_D^{\max}) = \sum_{i_1=1}^{k_1^{\max}} \dots \sum_{i_D=1}^{k_D^{\max}} \hat{Q}_{q_1}^{i_{q_1}} \otimes \dots \otimes \hat{Q}_{q_D}^{i_{q_D}}, \quad (61)$$

to generate the sum in Eq. (52). This direct-product quadrature could be used to integrate all matrix elements of the full, direct-product basis, Eq. (56), but it is 'too good' to integrate the matrix elements of a pruned basis. It is also important to note that the basis pruning, Eq. (57), has some structure, determined by the  $f(n_1, \dots, n_D)$  function, and typically, the products of multiple high-order polynomials are discarded. So, in the pruned basis, it is sufficient to integrate functions including high-order polynomials for only one (or a few) degrees of freedom at a time. The products of the highest-order polynomials for multiple (all) degrees of freedom are discarded in the pruned basis, and thus, the corresponding part

of the grid, which would be necessary to integrate these high-order polynomial products can also be discarded.

A systematic formulation and implementation of this idea was provided by Avila and Carrington [75] by using a non-product Smolyak quadrature, which can be defined as a linear combination of direct-product quadratures rules as

$$\hat{Q}(D, H) = \sum_{\sigma_s(i) \leq H} C_{i_{q_1}, \dots, i_{q_D}} \hat{Q}_{q_1}^{i_{q_1}} \otimes \dots \otimes \hat{Q}_{q_D}^{i_{q_D}},$$

$$i_\chi = 1, 2, 3, 4, \dots \quad \text{and} \quad \chi = 1, \dots, D, \quad (62)$$

where  $H$  is a grid-pruning parameter and  $\sigma_s(i)$  is the grid-pruning function, for which the simplest form is

$$\sigma_s(i) = s^{(q_1)}(i_{q_1}) + \dots + s^{(q_D)}(i_{q_D}) \leq H. \quad (63)$$

With this non-product grid, the number of points kept for the accurate integration of the potential and kinetic integrals is (much) smaller than the direct product grid that we would need to evaluate the same integrals with the same accuracy. There are three factors that can be tuned to modify and improve the accuracy of the Smolyak integration grid, namely: (a) The grid pruning functions,  $s^{(q_k)}(i_k)$ , which must be monotonic increasing functions, i.e.,  $s^{(q_k)}(i_k) \geq s^{(q_k)}(i_k - 1)$ . (b) The grid-pruning parameter,  $H$ . The larger  $H$ , the better the convergence, but the grid is larger. (c) The underlying grid sizes of the nested quadrature rules. For a nested quadrature, all points of the  $j$ th quadrature rule are within the  $(j+1)$ th quadrature rule. These quadratures do not have a Gaussian accuracy. For harmonic basis functions, we use a sequence of quadrature rules explained by Heiss and Winschel [91]. Nested quadratures are necessary to have a structure for the Smolyak grid, and thereby, to be able to calculate the Hamiltonian matrix-vector product in a sequential way.

So, we can write a multi-dimensional integral of an  $F(x_1, \dots, x_D)$  multivariate function as

$$\int \dots \int F(x_1, \dots, x_D) dx_1 \dots dx_D \approx$$

$$\sum_{k_1=1}^{k_1^{\max}} \dots \sum_{k_D=1}^{k_D^{\max}} W^{\text{Smol}}(k_1, \dots, k_D) F(x_1^{k_1}, \dots, x_D^{k_D}), \quad (64)$$

where  $W^{\text{Smol}}(k_1, \dots, k_D)$  is the Smolyak weight for every  $(k_1, \dots, k_D)$  point. The Smolyak grid structure appears in the summation indexes  $k_c^{\max}$  as follows:  $k_1$  depends on  $H$ ,  $k_2^{\max}$  depends on  $H$  and  $k_1^{\max}$ ,  $k_3^{\max}$  depends on  $H$ ,  $k_1^{\max}$  and  $k_2^{\max}$ , etc. Due to this special structure, the matrix-vector products can be computed using sequential summations [31–33, 75, 77]. The implementation details of the matrix-vector multiplication in relation with a pruned Smolyak integration was described in Refs. [31, 75, 77].

Finally, we note that Lauvergnat and co-workers use a somewhat different grid-pruning approach [78, 90, 92].

## 6. Other possible strategies for efficient vibrational computations

*a. Other efficient variational strategies* Instead of pruning the multi-dimensional direct product basis, it is possible to reduce the number of multi-dimensional basis functions by ensuring that the number of one-particle basis functions remains very small, which is possible by using optimized 1D basis functions in the direct-product expansion. This idea is realized in the multi-configurational time-dependent Hartree approach (MCTDH) [93], which ensures that the 1D basis functions are optimal by using time-dependent basis functions. Alternatively, one can build a compact multi-dimensional basis set by using contracted basis functions obtained from solving the (reduced-dimensionality) subsystems' Schrödinger equation [94–100].

Similarly to the basis-size problem, there are different strategies to tackle the grid-size problem of multi-dimensional numerical integration, including: (a) a Sum-Of-Products (SOP) expansion [101–103] of the Hamiltonian, which allows to construct the multi-dimensional integrals from 1D integrals; and (b) a truncated  $n$ -mode expansion [86, 104–106] of the Hamiltonian, which replaces the  $D$ -dimensional integrals with a combination of maximum  $n$ -dimensional integrals ( $n \ll D$ ).

Aiming for a precise representation of the PES, the number of terms in a sum-of-products expansion may grow rapidly, and the overall computational cost increases significantly. Regarding the  $n$ -mode expansion, the variational computations can be made very efficient up to 3-4-modes, but (going beyond) 4-mode coupling has been found to be important for spectroscopic precision [107]. Furthermore, the multi-mode expansion of the PES is carried out about a single reference structure (typically the equilibrium structure). For floppy systems this expansion is not efficient, but the more general high-dimensional model representation (HDMR), [108] which has been successfully used for PES development, [109, 110] can be used, in principle. The  $n$ -mode expansion about a single equilibrium structure can be considered as a special case of HDMR ('cut-HDMR').

*b. A non-variational approach* A fundamentally different and promising direction is about fully abandoning the variational approach and aiming to solve the eigenvalue equation as a differential equation using numerical (finite element) methods. This approach, called 'collocation', has been introduced and pursued by Carrington and co-workers

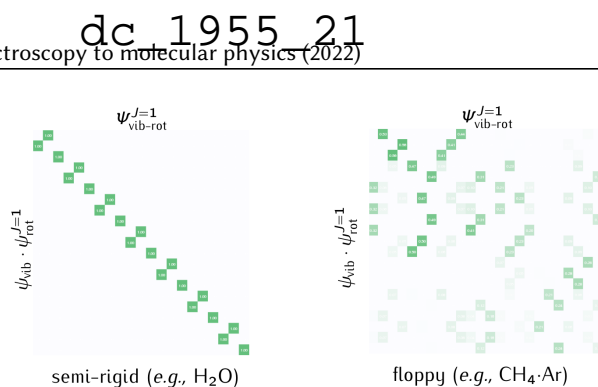


Figure 8. Vibrational parent assignment for a semi-rigid vs. floppy system.

for solving the vibrational Schrödinger equation over the past decade [111–117]. A great advantage of collocation is that it does not require the computation of any integrals, so the computational burden (and unfavorable scale-up with the vibrational dimensionality) of the evaluation of multi-dimensional integrals is completely avoided. It can be efficiently used if a very good basis set is available. Its current technical ‘difficulty’ is connected with an efficient computation of many eigenvectors for a (generalized) non-symmetric (real) matrix eigenvalue problem.

*c. Prospects for quantum hardware* As to further possible strategies, we mention the popular direction of considering alternative hardware, *i.e.*, use of future quantum computers for quantum dynamics [118]. For these types of applications, it is convenient to construct the second-quantized form of the vibrational Hamiltonian following Christiansen [118, 119]. For a QC implementation, it appears to be the most advantageous if we have a very sparse matrix over the multi-dimensional basis constructed from one-dimensional basis functions, for which the entries can be ‘assembled’ from lower-dimensional objects. The multi-dimensional (product) basis size does not enter the problem, only the sum of the number of the one-dimensional basis functions (instead of their product, which builds up the exponential growth of the ‘classical’ computational effort). If these conditions are realized, then, we may speculate that a DVR representation will be advantageous (which we abandoned due the exponential scale-up of the matrix size over the one-particle basis and grid). Furthermore, if a sufficiently accurate  $d < 3N - 6$  dimensional HDMR representation can be found for the system, then it is possible to cut the exponential growth of the storage (memory) requirement. So, based on this speculation, a DVR-HDMR( $d$ ), where  $d$  is ideally not (much) larger than 4, may turn out to be an efficient representation of the vibrational problem on a quantum computer.

### 7. Efficient rotational-vibrational computations

Let us assume that all vibrational states have been computed for the dynamically relevant energy range. If the rovibrational coupling is small, then the rovibrational states with rotational quantum number  $J$  can be well approximated with a linear combination of products of the vibrational eigenfunction and the rigid rotor functions,

$$\psi_i^{(JM)} = \sum_{n=1}^{N_{\text{vib}}} \sum_{K=0}^J \sum_{\tau=0,1} c_{i,nK\tau}^{(JM,i)} \psi_n^{\text{v}} \Theta_{K\tau}^{(JM)}, \quad (65)$$

and precise variational results can be obtained by diagonalizing a (small) rovibrational Hamiltonian matrix constructed over the  $JM$  rotational basis (consisting of  $2J + 1$  basis functions) and the vibrational eigenstates up to the energetically relevant region.

The rovibrational coupling can be made small for semi-rigid systems by using the Eckart frame as a body-fixed frame, *i.e.*, by choosing the  $\mathbf{r}_i$  coordinates (molecular orientation) so that they satisfy, in addition to the center of mass condition, Eq. (6), also the rotational (Eckart) condition [28],

$$\sum_{i=1}^N m_i \mathbf{c}_i \times \mathbf{r}_i = 0, \quad (66)$$

where  $\mathbf{c}_i$  is some reference structure, typically the relevant equilibrium structure on the PES. Fulfillment of these conditions ensures that the rovibrational coupling remains small near  $\mathbf{c}_i$ , which is sufficient for an efficient rovibrational computation of not too high rotational and vibrational excitation of semi-rigid systems (see, for example, Ref. 120), for which the dynamically relevant coordinate range remains in the proximity of the equilibrium structure.

Let us choose the  $\mathbf{c}_i$  Cartesian reference configuration and solve the orientational Eckart condition at Cartesian structures which belong to the  $\delta_i^{(\pm k)}$  Cartesian displacements by making small changes in the  $q_k \pm \varepsilon$  internal coordinates

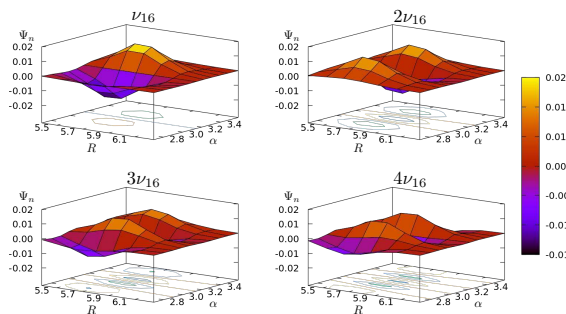


Figure 9. Assignment of vibrational excitation based on counting the nodes of the wave function for the example of the formic acid dimer. Reproduced from Ref. 30 with permission from the PCCP Owner Societies.

about the reference structure,  $\mathbf{c}_i$ . So, we solve the Eckart condition at  $\mathbf{r}_i^{(\pm k)} = \mathbf{c}_i \pm \delta_k$ :

$$\sum_{i=1}^N m_i \mathbf{c}_i \times \mathbf{r}_i^{(+k)} = 0 \quad (67)$$

$$\sum_{i=1}^N m_i \mathbf{c}_i \times \mathbf{r}_i^{(-k)} = 0. \quad (68)$$

Then, the rovibrational block of the  $\mathbf{g}$  matrix reads as

$$\begin{aligned} g_{D+a,k} &= \sum_{i=1}^N m_i [\mathbf{e}_a \times \mathbf{r}_i] \cdot \frac{\partial \mathbf{r}_i}{\partial q_k} \\ &= \mathbf{e}_a \cdot \sum_{i=1}^N m_i \left[ \mathbf{r}_i \times \frac{\partial \mathbf{r}_i}{\partial q_k} \right] \\ &= \lim_{\varepsilon \rightarrow 0} \mathbf{e}_a \cdot \sum_{i=1}^N m_i \left[ \mathbf{r}_i \times \frac{\mathbf{r}_i^{(+k)} + \mathbf{r}_i^{(-k)} - 2\mathbf{r}_i}{\varepsilon} \right] \\ &= \lim_{\varepsilon \rightarrow 0} \frac{1}{\varepsilon} \left( \mathbf{e}_a \cdot \sum_{i=1}^N m_i \mathbf{r}_i \times \mathbf{r}_i^{(+k)} + \mathbf{e}_a \cdot \sum_{i=1}^N m_i \mathbf{r}_i \times \mathbf{r}_i^{(-k)} \right), \end{aligned} \quad (69)$$

which shows the known result that the Eckart condition ensures that the rovibrational coupling vanishes at the reference point with  $\mathbf{r}_i = \mathbf{c}_i$ . Unfortunately, it is impossible to make the rovibrational coupling vanish over an extended part (beyond finite many points) of the configuration space [27]. Nevertheless, it may be possible to reduce the rovibrational coupling by numerical methods.

In order to make the rovibrational coupling small,  $\mathbf{G}^{rv}$  ( $= (\mathbf{G}^{vr})^T$ ) must be small, where the ‘rv’ and ‘vr’ blocks are understood similarly to the blocks of  $\mathbf{g}$  in Fig. 3.  $\mathbf{G}^{rv}$  depends on the choice of the  $\mathbf{r}_i$  body-fixed Cartesian coordinates, and in principle, the coupling can be modified by defining an optimal shape-dependent body-fixed frame by rotating the system from some initial orientation,  $\mathbf{r}_i^{(0)}$ , by a 3D rotation, described by a rotation matrix  $\mathbf{C}$  and parameterized by three angles, which depend on the  $\mathbf{q}$  shape coordinates,  $\boldsymbol{\alpha}(\mathbf{q}) = (\alpha(\mathbf{q}), \beta(\mathbf{q}), \gamma(\mathbf{q}))$ :

$$\mathbf{r}_i = \mathbf{C}[\boldsymbol{\alpha}(\mathbf{q})] \mathbf{r}_i^{(0)}. \quad (70)$$

### C. Assignment of the rovibrational states

Variational (ro)vibrational computations provide list of energies and corresponding wave functions (stationary states) that can be used to simulate spectral patterns (Sec. II D 1) or time-dependent phenomena [121, 122]. It is nevertheless a relevant aim to characterize the computed (hundreds or thousands of) stationary states.

A simple characterization of a state is possible by visual inspection of (1D and 2D cuts of) its wave function and counting the nodes (nodal surfaces), which carry information about the vibrational excitation along the relevant degrees of freedom. As an example, we show 2D cuts of the formic acid dimer vibrational states corresponding to the fundamental vibration and overtones of the twisting mode (Fig. 9) [30]. Node counting is (a) least model independent

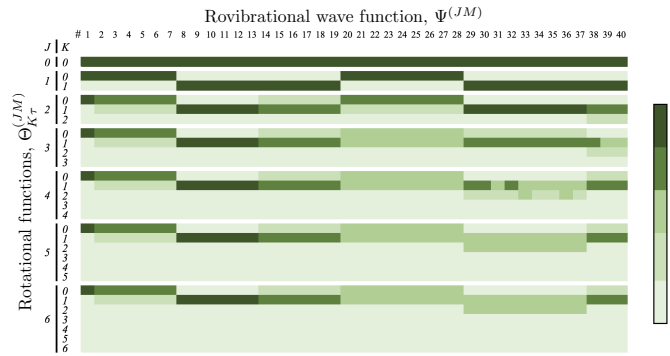


Figure 10. Assignment of  $K\tau$  labels of the rotational functions to the intermolecular-rotational states of  $(\text{CH}_4)_2$  computed with GENIUSH using the 6D intermolecular coordinates (similar to methane-water in Fig. 4) and the PES of Ref. 124.

way of characterizing a wave function.

Further assignment options include ‘measuring’ the similarity of the variational wave function with simple models (of rotation and vibration). In the most common representation, a rovibrational wave function can be considered as a linear combination of rigid-rotor or Wang functions and the lowest  $N_{\text{vib}}$  vibrational eigenfunctions used as a vibrational basis, Eq. (65).

### 1. Vibrational parent analysis

If there is a single, dominant  $\Psi_n^{\text{v}}$  vibrational state in the expansion, Eq. (65), then we may say that it is the ‘vibrational parent’, from which we can ‘derive’ the rovibrational state by ‘rotational excitation’. As a measure for this property, the rigid-rotor decomposition (RRD) [123] scheme was defined, which amounts to computing the overlap between the  $m$ th rovibrational wave function  $\Psi_m^{(J>0)}$ , with the product of a vibrational wave function and a rigid-rotor function,

$$S_{nK\tau,m} = \langle \psi_n^{\text{v}} \Theta_{K\tau}^{(JM)} | \Psi_m^{(J>0)} \rangle. \quad (71)$$

Figure 8 exemplifies that the low-energy states shown in the figure for the (semi-rigid) water molecule have clear, dominant RRD coefficients, whereas the floppy methane-argon dimer (from a 3D computation [54]) strong mixing is visible already in the low-energy range. We note that the RRD coefficients depend on the body-fixed frame, which is a computational ‘parameter’ (Sec. II B 7).

### 2. Rotational parent analysis

Similarly to the vibrational parent assignment, we can ask whether there is any dominant  $\Theta_{K\tau}^{(JM)}$  Wang function in the Eq. (65) expansion of a rovibrational state. This question may be relevant even if there is no dominant vibrational parent, which is often the case for floppy systems.

As a measure of the importance of  $\Theta_{K\tau}^{(JM)}$  in the rovibrational wave function, we have integrated the product of the vibrational ‘sub-blocks’ (corresponding to different Wang functions) of the rovibrational wave function with respect to the  $\mathbf{q}$  vibrational coordinates,

$$\tilde{\kappa}_{K\tau}^{(JM)} = \langle \psi_{K\tau}^{(JM)} | \psi_{K\tau}^{(JM)} \rangle_{\mathbf{q}}. \quad (72)$$

To have a measure only for the  $K$  label, we can sum for the  $\tau = 0, 1$  contributions

$$\kappa_K^{(JM)} = \sum_{\tau=0,1} \tilde{\kappa}_{K\tau}^{(JM)}. \quad (73)$$

Due to the normalization of the rovibrational wave function  $\sum_{K=0}^J \kappa_K^{(JM)} = 1$ .

Figure 10 shows for the example of the lowest-energy states of the  $(\text{CH}_4)_2$  dimer, for which the equilibrium structure on the used PES [124] is a symmetric top. The  $K\tau$  labels can be unambiguously assigned up to  $J = 1(2)$ , but beyond  $J > 2$  this is not always possible due to the strong rovibrational coupling.

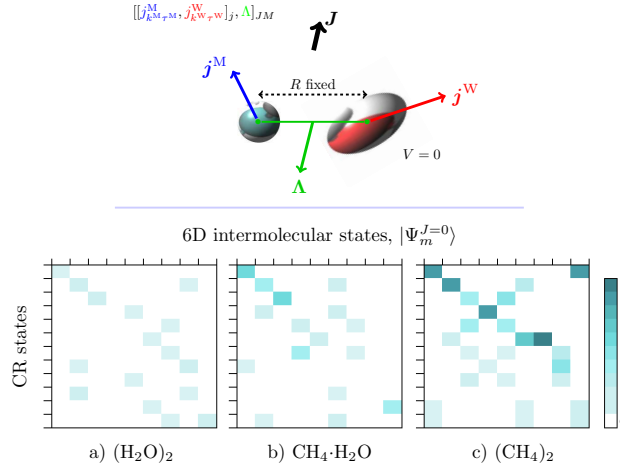


Figure 11. Coupled-rotor decomposition coefficients computed for the  $J = 0$  states of the  $(\text{CH}_4)_2$  dimer.

### 3. Coupled-rotor decomposition

For the analysis of rovibrational states of floppy molecular dimers, it is useful to assign subsystems' angular momenta to the dimer state according to the coupling of the angular momenta of monomer  $A$ , ( $\mathbf{j}^A$ ), monomer  $B$ , ( $\mathbf{j}^B$ ), and the effective diatom,  $\mathbf{\Lambda}$  to a dimer state with  $JM$  angular momentum quantum numbers corresponding to the overall rotation,  $\mathbf{J}$ , and its projection to a space-fixed axis,  $J_Z$ , (Fig. 11a)

$$[[j_{k^A \tau^A}^A, j_{k^B \tau^B}^B]_j, \Lambda]_{JM}. \quad (74)$$

Since during the computations performed with GENIUSH [51–54] (with DVR), we did not use monomer rotational basis functions, we computed the overlap, called coupled rotor decomposition (CRD) [53], of the intermolecular rovibrational state,  $\Psi_{m,k}^{(JM)}$  and the coupled rotor (CR) function with a fixed monomer distance and without the PES (Fig. 11a),

$$\text{CRD}_{nm}^{(J)} = \sum_{r=1}^{N_R} \left| \sum_{k=-J}^J \sum_{o=1}^{N_\Omega} \tilde{\Psi}_{m,k}^{(J)}(\rho_r, \omega_o) \cdot \tilde{\varphi}_{n,k}^{(J)}(\omega_o) \right|^2, \quad (75)$$

where  $\tilde{\Psi}_m^{(J)}$  is the  $m$ th rovibrational state and  $\tilde{\varphi}_n^{(J)}$  is the  $n$ th CR function in the DVR representation used in the cited references.

The CRD overlaps were used to assign the rovibrational states to irreducible representations of the molecular symmetry (MS) group, by using the formal symmetry properties of the CR functions [53, 54].

### D. Simulating rovibrational infrared and Raman spectra

We can consider interaction of (non-relativistic) molecular matter with external electromagnetic fields, not accounted for in the description, by using the rovibrational eigenstates as a basis. To account for the effect of 'external fields', weak-field spectroscopies, strong-field interactions, or for corrections 'within the system' beyond the Coulomb interactions, *i.e.*, hyperfine [125, 126], we have implemented the evaluation of the transition moments connecting the rovibrational states  $\Psi_{j'M'\nu'}^{\text{rv}}$  and  $\Psi_{j''M''\nu''}^{\text{rv}}$ , for a  $T_A^{(\text{LF})}$  general tensorial property of rank  $\Omega$ , where  $A$  collects the LF Cartesian indexes, according to [127]

$$\langle \Psi_{j'M'\nu'}^{(J'M')} | T_A^{(\text{LF})} | \Psi_{j''M''\nu''}^{(J''M'')} \rangle = \sum_{\omega=0}^{\Omega} \mathcal{M}_{A\omega}^{(J'M',JM)} \mathcal{K}_{\omega}^{(J''M'',J)} \quad (76)$$

with

$$\begin{aligned} \mathcal{M}_{A\omega}^{(J'M',JM)} &= (-1)^{M'} \sqrt{(2J'+1)(2J+1)} \\ &\times \sum_{\sigma=-\omega}^{\omega} [U^{(\Omega)}]_{A,\omega\sigma}^{-1} \begin{pmatrix} J & \omega & J' \\ M & \sigma & -M' \end{pmatrix} \end{aligned} \quad (77)$$

and

$$\begin{aligned} \mathcal{K}_\omega^{(J',i',j,i)} &= \sum_{\substack{n,K,\tau \\ n',K',\tau'}} [c_{n'K'\tau'}^{(J',i')}]^* c_{nK\tau}^{(J,i)} \sum_{\pm K', \pm K} [d_{K'}^{(\tau')}]^* d_K^{(\tau)} \\ &\times (-1)^{K'} \sum_{\sigma=-\omega}^{\omega} \sum_a \begin{pmatrix} J & \omega & J' \\ K & \sigma & -K' \end{pmatrix} U_{\omega\sigma,a}^{(\Omega)} \langle \psi_{n'}^{\nu} | T_a^{(\text{BF})} | \psi_n^{\nu} \rangle, \end{aligned} \quad (78)$$

where  $c_{nK\tau}^{(J,i)}$  are the linear combination coefficients of Eq. (65) and  $d_K^{(\tau)}$  correspond to the Wang combination coefficients, Eq. (49). The vibrational integrals  $\langle \psi_{n'}^{\nu} | T_a^{(\text{BF})} | \psi_n^{\nu} \rangle$  are computed in the body-fixed (BF) frame using (the DVR or FBR) vibrational wave functions  $\psi_n^{\nu}$  and the  $T_a^{(\text{BF})}$  ‘property’ hypersurface available from *ab initio* electronic structure theory (in a fitted or interpolated functional form). The  $\mathcal{K}_\omega$  coefficients correspond to the rank- $\Omega$  tensor in the body-fixed frame and the corresponding rovibrational wave functions, so they can be evaluated separately and stored for every  $\omega$  value.

This implementation has been reported and was tested for the example of electric dipole transitions (for  $\Omega = 1$ ) of the methane-water complex [51] in comparison with the transition moments reported by Wang and Carrington [63].

In what follows, the expressions are summarized for rovibrational infrared ( $\Omega = 1$ ) and Raman ( $\Omega = 2$ ) experiments.

### 1. Infrared transition moments

Intensities of infrared spectroscopy experiments can be simulated by using the electric dipole moment, which is an  $\Omega = 1$  rank property, including the  $U_{\omega\sigma,\alpha}^{(1)}$  matrix elements [51, 127]. The working formula for dipole moment transitions is obtained after some manipulation from the general expressions, Eqs. (76)–(78), [127, 128]

$$\begin{aligned} \mathcal{R}_1 &= g_{\text{ns}} \sum_{M,M'} \sum_{A=X,Y,Z} |\langle \Psi_{J'M'i'}^{\text{rv}} | T_A^{(\text{LF})} | \Psi_{JMi}^{\text{rv}} \rangle|^2 \\ &= g_{\text{ns}} (2J' + 1)(2J + 1) \\ &\times \left| \sum_{\substack{n,K,\tau \\ n',K',\tau'}} [c_{n'K'\tau'}^{(J',i')}]^* c_{nK\tau}^{(J,i)} \sum_{\pm K', \pm K} [d_{K'}^{(\tau')}]^* d_K^{(\tau)} \right. \\ &\times (-1)^{K'} \sum_{\sigma=-1}^1 \sum_{\alpha} \begin{pmatrix} J & 1 & J' \\ K & \sigma & -K' \end{pmatrix} U_{\omega\sigma,\alpha}^{(1)} \langle \psi_{n'}^{\nu} | \mu_{\alpha}^{(\text{BF})} | \psi_n^{\nu} \rangle \left. \right|^2. \end{aligned}$$

### 2. Raman transition moments

Another important technique in rovibrational spectroscopy is Raman scattering. For computing Raman intensities, the relevant property is the rank  $\Omega = 2$  polarizability matrix,  $\alpha$ . It is convenient to distinguish to types of transition moments, the isotropic (independent of the molecular orientation) with  $\omega = 0$  and the anisotropic with  $\omega = 2$  components. By using the general expressions in Eqs. (76)–(78), the isotropic ( $\omega = 0$ ) component can be written as [129]

$$\begin{aligned} \mathcal{R}_0 &= \delta_{JJ'} g_{\text{ns}} (2J' + 1)(2J + 1) \\ &\times \left| \sum_{\substack{n,K,\tau \\ n',K',\tau'}} [c_{n'K'\tau'}^{(J',i')}]^* c_{nK\tau}^{(J,i)} \sum_{\pm K', \pm K} [d_{K'}^{(\tau')}]^* d_K^{(\tau)} \right. \\ &\times (-1)^{K'} \sum_{ab} \begin{pmatrix} J & 0 & J' \\ K & 0 & -K' \end{pmatrix} U_{00,ab}^{(2)} \langle \psi_{n'}^{\nu} | \alpha_{ab}^{(\text{BF})} | \psi_n^{\nu} \rangle \left. \right|^2, \end{aligned} \quad (79)$$

where the  $3J$ -symbol vanishes unless  $J = J'$ , leading to the selection rule  $\Delta J = 0$  for the isotropic transition moments, incorporated in the equations with the Kronecker delta,  $\delta_{JJ'}$ . For the anisotropic contribution ( $\omega = 2$ ), the working

equation is

$$\begin{aligned}
 \mathcal{R}_2 = & g_{ns}(2J' + 1)(2J + 1) \\
 & \times \left| \sum_{\substack{n,K,\tau \\ n',K',\tau'}} [c_{n'K'\tau'}^{(J',i')}]^* c_{nK\tau}^{(J,i)} \sum_{\pm K', \pm K} [d_{K'}^{(\tau')}]^* d_K^{(\tau)} \right. \\
 & \left. \times (-1)^{K'} \sum_{\sigma=-2}^2 \sum_{ab} \begin{pmatrix} J & 2 & J' \\ K & \sigma & -K' \end{pmatrix} U_{2\sigma,ab}^{(2)} \langle \psi_{n'}^v | \alpha_{ab}^{(BF)} | \psi_n^v \rangle \right|^2.
 \end{aligned} \tag{80}$$

The non-zero matrix elements of  $U_{\omega\sigma,\alpha\beta}^{(2)}$  have been collected in Ref. 127. The non-vanishing value of 3J-symbols gives the  $\Delta J = 0, 1, 2$  selection rules for the anisotropic component. The current procedure makes it possible to compute polarizability transition moments connecting rovibrational states of floppy systems that are relevant for high-resolution Raman scattering experiments.

### E. Summary and conclusions

We have reviewed the theoretical and methodological (ro)vibrational framework developed by ourselves or in close collaboration with colleagues over the past decade. The reviewed methodology is implemented in GENIUSH program, which was used to carry out the highlighted computations.

The focus of this chapter was on (ro)vibrational spectroscopy of isolated floppy molecules and complexes, presenting the numerically exact solution of the (ro)vibrational Schrödinger equation on a potential energy surface, analysis of the computed wave function, assignment of the computed stationary states, and evaluating electric dipole and polarizability transition moments for simulating (weak-field) high-resolution infrared and Raman spectra of (semi-rigid or) floppy molecular systems and complexes. The methodology can be straightforwardly extended to compute molecules in cages and at surfaces.

An important methodological challenge, which is currently at the focus of our main efforts, is the increase of the vibrational dimensionality of feasible computations. Exact quantum dynamics computations of molecular systems with up to 20–30 fully coupled vibrational degrees of freedom, allowing for a few large-amplitude motions, which carry lots of interesting chemistry, will be an important next milestone to reach in the next couple of years. We aim to pursue these developments by developing general,  $N$ -atomic,  $D$ -dimensional approaches, *i.e.*, pushing the frontier of a black-box-type rovibrational research program. Thereby, as available computational power increases, in parallel with the methodological developments, rovibrational computations of spectroscopic quality become possible for higher-dimensional ( $> 12D$ ) floppy molecular systems.

## III. THE BETHE–SALPETER QED WAVE EQUATION FOR BOUND-STATE COMPUTATIONS OF ATOMS AND MOLECULES

Interactions in atomic and molecular systems are dominated by electromagnetic forces and the theoretical framework must be in the quantum regime. The physical theory for the combination of quantum mechanics and electromagnetism, quantum electrodynamics has been ‘established’ by the mid-twentieth century, primarily as a scattering theory. To describe atoms and molecules, it is important to consider bound states. In the non-relativistic quantum mechanics framework, bound states can be efficiently computed using robust and general methodologies with systematic approximations developed for solving *wave equations*. With the sight of the development of a computational quantum electrodynamics framework for atomic and molecular matter, the field theoretic Bethe–Salpeter wave equation expressed in space-time coordinates, its exact equal-time variant and emergence of a relativistic wave equation is reviewed. A computational framework, with initial applications and future challenges in relation with precision spectroscopy, is also highlighted based on Ref. 130.

### A. Introduction: a historical line-up

Dirac’s one-electron space-time equation was an ingenious departure from Schrödinger’s time-dependent wave equation to have a Lorentz covariant description, but it was strange due to the introduction of hole theory that seemed a bit artificial [6, 7]. In a recorded discussion from 1982, Dirac modestly admitted to Hund that for him, ‘it took a year, perhaps two, to understand the role of the negative-energy states’ [131].

Breit attempted a two-particle generalization of Dirac’s one-electron theory in a series of papers between 1928 and 1931 [8–10, 132], by adopting Darwin’s 1920 calculation of the classical electromagnetic interaction for two moving charges [133] and the quantum mechanical velocity operator obtained with Dirac’s formalism [10].



Already from the beginning, it was apparent that the Breit equation was not Lorentz covariant. Nevertheless, Breit used this ‘quasi-relativistic’ equation in a perturbation theory approach imposing the Pauli approximation to the four-(sixteen-)component wave function. Good agreement with experiment was obtained after discarding a term from the result ‘by hand’ [9, 132]. This procedure was later explained based on Dirac’s hole theory by Brown and Ravenhall [134].

The problem, called Brown–Ravenhall (BR) disease, related to the artificial coupling of the positive- and negative-energy states of Dirac’s theory when naïvely applied to two-particle systems, survived also in the modern literature and it is commonly used to explain the failure of the two-(many-)particle Breit equation. A recent numerical study demonstrated that bound states of helium-like two-electron systems represented by the Breit equation have (unphysical) finite lifetimes (of order  $\alpha^3 E_h$ , where  $\alpha$  is the fine-structure constant) [135, 136]. It has been also discussed [137] that there was no BR dissolution problem for isolated two-particle systems, like positronium, when modelled with the Breit equation, and it was numerically demonstrated by a finite-element computation [138] that the energy levels of the two-particle Breit equation (with Coulomb interactions, no external fields) are ‘stable’. Nevertheless, the two-particle Breit equation is still incorrect, or in other words, ‘correct only up to order  $\alpha^2 E_h$ ’ [136].

A consistent and Lorentz covariant many-particle theory was put forward by the development of quantum electrodynamics (QED). As a natural continuation of Feynman’s two papers in 1949 on the reinterpretation of the mathematical solutions of the Dirac equation [139] and the development of the space-time approach to quantum electrodynamics [140], Salpeter and Bethe in 1951 published a Lorentz-covariant wave equation for two interacting particles (with stating that generalization to more than two particles is straightforward) [141]. It is interesting to note that the same equation was written at the end of a paper without explanation by Nambu already in 1950 [142], and it was formulated by Schwinger [143] and also by Gell-Mann and Low [144] during 1951. In 1952, Salpeter used this equation for the hydrogen atom in combination with perturbation theory and an instantaneous interaction kernel. Probably, this was the first formulation of the exact equal-time equation for two-particle systems [145]. Salpeter reported results for the hydrogenic case (of one heavy and one light particle,  $M \gg m$ ) up to the  $\alpha^3(m/M)E_h$  order, and he stated that the calculation can be generalized to any masses. In 1954, Fulton and Martin calculated the energy levels for an arbitrary two-fermion system, such as positronium, up to  $\alpha^3 E_h$  order [146].

In 1958, Sucher’s PhD thesis represented another important step forward using the formalism and extending Salpeter’s work to a two-electron system in an external Coulomb field, for the example of the helium atom [147]. Sucher’s final  $\alpha^3 E_h$ -order correction formulae were identical with those reported by Araki [148] a year earlier, but we can build on the fundamental ideas explained in Sucher’s work for further developments.

In 1974, Douglas and Kroll [149] started their paper on the  $\alpha^4 E_h$ -order corrections to the fine-structure splitting of helium with a good review of Sucher’s work by extending the formalism with explicitly writing also the radiative terms in the wave equation (Sucher only highlighted the steps at the end of his work).

Then, in 1989, Adkins elaborated this direction for positronium, still relying on a perturbative expansion with respect to the non-relativistic reference for practical calculations [150]. During the 1990s, Zhang worked on higher-order corrections to the fine-structure splitting ( $\alpha^5 E_h$ ) and energy levels ( $\alpha^4 E_h$ ) of helium.

Pachucki initiated a different approach starting from the late 1990s [151–155]. This approach is based on performing a Foldy–Wouthuysen transformation [156] of the Dirac operator in the Lagrangian density—thereby linking the formalism to the non-relativistic theory from the outset, and then, collecting corrections to the poles of the equal-time Green function [157] to the required  $\alpha$  order. In 2006, Pachucki reported the complete  $\alpha^4 E_h$ -order corrections to the energy levels of singlet helium [158], thereby extending the 1974 work of Douglas and Kroll valid only for triplet states, as well as work from Yelkhovsky [159] and computations from Korobov and Yelkhovsky [160] in 2001 for  $\alpha^4 E_h$ -order corrections of singlet helium. In 2016, the complete  $\alpha^4 E_h$ -order corrections derived by Pachucki were used for the ground electronic state of the  $H_2$  molecule with fixed protons [161]. Most recently, the ‘Foldy–Wouthuysen–Pachucki’ approach has been used to derive  $\alpha^5 E_h$ -order contributions for triplet states of helium [162, 163].

In contrast to using a non-relativistic reference (as in all previous work), we aim for a *relativistic* QED approach, in which some (well-defined, many-particle) relativistic wave equation is first solved to high precision and used as a reference for computing ‘QED’ (retardation, pair, and radiative) corrections up to a required accuracy. Such an approach appears to be feasible along the lines formally started by Bethe, Salpeter, Sucher, Douglas and Kroll. These authors performed calculations by hand, so in the end, they had to rely on approximations based on the non-relativistic formalism. Nowadays, we can use the power of modern computers to first numerically solve a many-particle relativistic wave equation, and then, compute corrections to the relativistic energy. It is also necessary to add that there have been several articles on understanding and solving the original, space-time Bethe–Salpeter (BS) equation [164–168].

For atomic and molecular computations, the exact equal-time form of the BS equation, as introduced by Salpeter and Sucher [145, 147], appears to be more promising. In this approach, a *two-particle* relativistic Hamiltonian and corresponding wave equation emerges, for which numerical strategies for solving wave equations, including the variational method, can be used. During the 1980s, Sucher [137, 169, 170] published review articles about the (formal) connection of the equal-time BS wave equation with the relativistic quantum chemistry framework and computational methodologies, e.g., [171, 172]. In this context, it is necessary to mention the excellent book of Lindgren who further developed these ideas for orbital-based many-body applications in chemistry [173].

We consider the renormalized, ‘mixed gauge’, two-particle Bethe–Salpeter equation as the starting point for a theoretical framework of atoms and molecules and with relevance for spectroscopic applications. This theoretical

framework is reviewed in the first part of the paper by relying on work by Sucher [147], Douglas and Kroll [149], as well as Salpeter [145]. The second part of the chapter highlights our recent work [174–179], algorithmic details of a computer implementation and numerical results for two spin-1/2 particles with and without a fixed, external Coulomb field, *i.e.*, with relevance for relativistic Born–Oppenheimer (BO) as well as relativistic pre-Born–Oppenheimer (pre-BO) computations. Although in the present review, we focus on the theory and a numerical procedure for two-particle systems, we mention Sucher’s series of papers [137, 169, 170] from the 1980s implying a possible generalization and Broyles’ work from 1987 [180] about presenting a line of thoughts connecting field theory and an  $N$ -particle no-pair Dirac–Coulomb–Breit wave equation.

Regarding a relativistic QED approach, we also mention the quasi-potential method, which originates from Logunov, Tavkhelidze, and Faustov working during the 1960-70s [181, 182], and the corresponding two-time (equal-time) Green function idea developed by Shabaev [157]. Comparison of the Salpeter–Sucher approach with the quasi-potential method is left for future work.

## B. The Bethe–Salpeter equation and the Salpeter–Sucher exact equal-time approach

### 1. Introductory ideas and propagators

The Dirac equation for a particle of mass  $m_1$  and  $x_1 = (\mathbf{r}_1, t_1)$  space-time coordinates is

$$\left[ i \frac{\partial}{\partial t_1} - H_1^{(0)} \right] \varphi_n^{(1)}(x_1) = 0 \quad (81)$$

with the free-particle Hamiltonian

$$H_1^{(0)} = -i\alpha_1 \nabla_1 + \beta_1 m_1 \quad (82)$$

and the  $\alpha_1$  and  $\beta_1$  Dirac matrices. Feynman pointed out in 1949 [139] that instead of working with the Hamiltonian equation, it is often more convenient to use the corresponding Green function or propagator

$$\left[ i \frac{\partial}{\partial t_1} - H_1^{(0)} \right] G_1^{(0)}(x_1, x'_1) = i\beta_1 \delta(x_1 - x'_1). \quad (83)$$

For a Dirac particle in an external scalar field,  $\Phi_1$

$$\left[ i \frac{\partial}{\partial t_1} - H_1 \right] G_1(x_1, x'_1) = i\beta_1 \delta(x_1 - x'_1) \quad (84)$$

with

$$H_1 = H_1^{(0)} + z_1 e \Phi_1 = H_1^{(0)} + U_1, \quad (85)$$

$z_1 \in \mathbb{Z}$  and  $e$  standing for the charge number of the active particle and the elementary charge, respectively. Simple calculation [139] shows that the  $G_1$  propagator can be obtained from the  $G_1^{(0)}$  free-particle propagator through the integral equation (corresponding to subsequent interaction events of the particle with the external field) as

$$G_1(x_1, x'_1) = G_1^{(0)}(x_1, x'_1) - i \int G_1^{(0)}(x_1, y_1) \beta_1 U_1(y_1) G_1(y_1, x'_1) dy_1. \quad (86)$$

According to Feynman’s combination of the electronic and positronic theory in a consistent manner [139], the propagator is expressed with the eigenvalues and eigenfunctions of the Dirac Hamiltonian as the sum over positive-energy (electronic) states moving forward in time, and the negative sum over negative-energy (positronic) states moving backward in time. Feynman defined the free-particle propagator this way corresponding to Eq. (83). The arguments can be taken over for a particle in an external field, Eq. (84), which is known as the ‘Furry picture’ [183], and the propagator is

$$G_1(x_1, x'_1) = \begin{cases} \sum_{E_n^{(1)} > 0} \phi_n^{(1)}(\mathbf{r}_1) \bar{\phi}_n^{(1)}(\mathbf{r}'_1) e^{-iE_n^{(1)}(t_1 - t'_1)}, & t_1 > t'_1 \\ - \sum_{E_n^{(1)} < 0} \phi_n^{(1)}(\mathbf{r}_1) \bar{\phi}_n^{(1)}(\mathbf{r}'_1) e^{-iE_n^{(1)}(t_1 - t'_1)}, & t_1 < t'_1 \end{cases}, \quad (87)$$

where  $\bar{\phi}_n^{(1)} = \phi_n^{(1)*} \beta_1$  is the Dirac adjoint. The  $G_1^{(0)}(x_1, x'_1)$  free-particle propagator is recovered for eigenvalues and eigenfunctions of the Dirac equation with  $\Phi_1 = 0$ . Regarding the external field in the present work, only the scalar

potential due to the Coulomb field of the fixed nuclei will be relevant, e.g., for helium-like systems with the nucleus fixed at the origin and with  $Z$  nuclear charge number, the interaction energy is

$$U_1(\mathbf{r}_1) = z_1 \frac{Z\alpha}{|\mathbf{r}_1|}, \quad (88)$$

where  $\alpha = e^2/(4\pi)$  is the fine-structure constant in natural units ( $\hbar = c = \epsilon_0 = 1$ ).

To describe a two-particle system, we can consider the  $G(x_1, x_2; x'_1, x'_2)$  two-particle propagator or amplitude which describes that particles 1 and 2 get from  $x'_1, x'_2$  to  $x_1, x_2$  space-time points. For non-interacting particles, the two-particle propagator is the simple product of the one-particle propagators,  $G_1(x_1, x'_1)G_2(x_2, x'_2)$ . For interacting two-particle systems Salpeter and Bethe [141], following Feynman [139, 140], devised an integral equation, called Bethe–Salpeter (BS) equation,

$$G(x_1, x_2; x'_1, x'_2) = G_1(x_1, x'_1)G_2(x_2, x'_2) - i \int dy_1 dy_2 dy'_1 dy'_2 G_1(x_1, y_1)G_2(x_2, y_2)K(y_1, y_2; y'_1, y'_2)G(y'_1, y'_2; x'_1, x'_2), \quad (89)$$

where  $K$  is the interaction function. In particular,  $K$  must contain only the so-called ‘irreducible’ interactions, since the corresponding consecutive, so called ‘reducible’, interactions are already included, ‘iterated’ to all orders by the integral equation.

The simplest interaction function,  $K^{(1)}$ , corresponds to the single photon exchange (see also Sec. III B 3) with  $\gamma_i^\mu = \beta_i(\alpha_i, 1)$

$$K^{(1)}(x_1, x_2; x'_1, x'_2) = \alpha z_1 z_2 \gamma_{1\mu} \gamma_{2\nu} D_F^{\mu\nu} [(x_1 - x_2)^2] \delta^4(x_1 - x'_1) \delta^4(x_2 - x'_2), \quad (90)$$

where  $D_F^{\mu\nu}$  is the photon propagator, which takes a simple, manifestly covariant form in Feynman gauge,

$$D_F^{\mu\nu} [(x_1 - x_2)^2] = - \int \frac{d^4 k}{(2\pi)^4} \frac{g^{\mu\nu}}{k^2 + i\Delta} e^{-ik \cdot (x_1 - x_2)}. \quad (91)$$

To describe the inter-particle interaction in atoms and molecules, it is more convenient to use the Coulomb gauge, in which the interaction is the sum of the Coulomb (C, the dominant part) and the transverse (T) contributions,

$$K^{(1)}(x_1, x_2; x'_1, x'_2) = [K_C^{(1)}(x_1, x_2) + K_T^{(1)}(x_1, x_2)] \delta(x_1 - x'_1) \delta(x_2 - x'_2) \quad (92)$$

with

$$K_C^{(1)}(x_1, x_2) = \alpha z_1 z_2 \beta_1 \beta_2 \int \frac{d^4 k}{(2\pi)^4} \frac{4\pi}{\mathbf{k}^2} e^{-ik(x_1 - x_2)} = \beta_1 \beta_2 \frac{\alpha z_1 z_2}{|\mathbf{r}_1 - \mathbf{r}_2|} \delta(t_1 - t_2) \quad (93)$$

$$K_T^{(1)}(x_1, x_2) = \alpha z_1 z_2 \beta_1 \beta_2 \int \frac{d^4 k}{(2\pi)^4} \frac{4\pi \tilde{\alpha}_1^i \tilde{\alpha}_2^i}{\omega^2 - \mathbf{k}^2 + i\Delta} e^{-ik(x_1 - x_2)}, \quad (94)$$

where

$$\tilde{\alpha}^i(\mathbf{k}) = \left( \delta^{ij} - \frac{k^i k^j}{\mathbf{k}^2} \right) \alpha^j \quad (95)$$

refers to the transverse components of  $\alpha$  perpendicular to  $\mathbf{k}$ . (In Eq. (93), we highlighted the well-known coordinate-space form of the Coulomb interaction, the primarily important interaction term in quantum chemistry).

If radiative corrections are accounted for, the one-electron (one-particle) propagator is replaced by [141, 147, 149, 184]

$$G'_1 = G_1 + G_1 \Sigma_1 G_1 + G_1 \Sigma_1 G_1 \Sigma_1 G_1 + \dots = G_1 + G'_1 \Sigma_1 G_1, \quad (96)$$

or equivalently,

$$(G'_1)^{-1} = G_1^{-1} - \Sigma_1, \quad (97)$$

where  $\Sigma_1$  is the sum of the one-electron self-energy contributions. Douglas and Kroll [149], following the last chapter of Sucher’s work [147], formulated the two-electron equations by formally including all radiative corrections. This formulation also relies on the work of Mathews and Salam [185] who explained that the Bethe–Salpeter equation can

be renormalized with the replacement of  $G'_1, G'_2, \gamma_{1\mu}, \gamma_{2\mu}$ , and the  $D_F$  photon propagator by [147, 149]

$$G_1'^* = G_1 + G_1 \Sigma_1^* G_1 + \dots, \quad (98)$$

$$\Gamma_{1\mu}^* = \gamma_{1\mu} + \Lambda_{1\mu}^*, \quad (99)$$

$$D_F^* = D_F + D_F \Pi^* D_F + \dots. \quad (100)$$

We note that Mathews and Salam mostly formulated their renormalization approach based on series expansion, whereas Källen [186] and Lehmann [187] defined renormalization terms without the use of power series expansion in the interaction constant. Karplus and Kroll [188] and Jauch and Rohrlich [189] carried out explicit calculations for the  $\Sigma_1^*, \Pi^*, \Lambda_{1\mu}^*$  renormalized electron self-energy, photon self-energy, and vertex correction operators to order  $\alpha$  for the case of no external potentials.

For renormalization, it is necessary to work in the Feynman gauge, Eq. (91). At the same time, binding of the particles in atomic and molecular systems is dominated by the Coulomb interaction, Eq. (93), which can be identified by writing the interaction operators in the Coulomb gauge.

According to Sucher's arguments [147, 149] (following the field theoretical derivation of the BS equation by Gell-Mann and Low [144]), it is valid to perform renormalization of the radiative terms in the Feynman gauge, and then, use the resulting expressions for the interacting problem, written in the Coulomb gauge. This special procedure is known as the mixed-gauge representation.

## 2. Coordinate and Fourier transformation: the total and relative time and energy

Eq. (89) can be rewritten for the wave function of a bound state (e.g., Ch. 6 of [190] or Ch. 12 of [191]), formally including now also the radiative effects [149], as

$$\Psi_T(x_1, x_2) = -i \int dy_1 dy_2 dy_1' dy_2' G_1'(x_1, y_1) G_2'(x_2, y_2) K(y_1, y_2; y_1', y_2') \Psi_T(y_1', y_2'), \quad (101)$$

or in short,

$$\Psi_T = -i G_1' G_2' K \Psi_T, \quad (102)$$

which, using Eq. (97), can be rearranged to (we note the missing imaginary unit in Ref. 149)

$$G_1^{-1} G_2^{-1} \Psi_T = -i [K + i G_1^{-1} \Sigma_2 + i G_2^{-1} \Sigma_1 - i \Sigma_1 \Sigma_2] \Psi_T = -i K' \Psi_T, \quad (103)$$

where the full 'interaction' kernel, containing also the radiative corrections, was defined as

$$K' = K + i G_1^{-1} \Sigma_2 + i G_2^{-1} \Sigma_1 - i \Sigma_1 \Sigma_2. \quad (104)$$

From rearrangement of the operator form of Eq. (84),  $G_1^{-1} = -i \beta_1 [i \partial / \partial t_1 - H_1]$  and using  $\beta_1 \beta_1 = \beta_2 \beta_2 = 1$ , we obtain

$$\left[ i \frac{\partial}{\partial t_1} - H_1 \right] \left[ i \frac{\partial}{\partial t_2} - H_2 \right] \Psi = i \beta_1 \beta_2 K' \Psi_T, \quad (105)$$

which is a (space-time) wave equation which accounts for (non-radiative) interactions and radiative corrections on an equal footing.

Since Eq. (105) includes the 'own' time for both particles, but the  $U$  external interaction (if any) is time independent in our frame of reference, we can write the two-particle wave function as

$$\Psi_T(x_1, x_2) = e^{-iET} \Psi(\mathbf{r}_1, \mathbf{r}_2, t), \quad (106)$$

where the average ('total') time and relative time was introduced as

$$T = \frac{1}{2}(t_1 + t_2) \quad \text{and} \quad t = t_1 - t_2. \quad (107)$$

It is important to note that  $E$  is the total energy of the two-particle system and it corresponds to the  $T$  total time, Eq. (106). Similarly to  $T$  and  $t$ , we define

$$T' = \frac{1}{2}(t_1' + t_2') \quad \text{and} \quad t' = t_1' - t_2'. \quad (108)$$

Then, we obtain the following equation for the  $\Psi(\mathbf{r}_1, \mathbf{r}_2, t)$  space- and relative-time wave function,

$$\begin{aligned} & \left[ \frac{E}{2} + i \frac{\partial}{\partial t} - H_1 \right] \left[ \frac{E}{2} - i \frac{\partial}{\partial t} - H_2 \right] \Psi(\mathbf{r}_1, \mathbf{r}_2, t) \\ & = i\beta_1\beta_2 \int K'_t(\mathbf{r}_1, \mathbf{r}_2, t; \mathbf{r}'_1, \mathbf{r}'_2, t') \Psi(\mathbf{r}'_1, \mathbf{r}'_2, t') d\mathbf{r}'_1 d\mathbf{r}'_2 dt' \end{aligned} \quad (109)$$

with the interaction kernel depending only on the relative time variables,

$$K'_t(\mathbf{r}_1, \mathbf{r}_2, t; \mathbf{r}'_1, \mathbf{r}'_2, t') = \int_{-\infty}^{+\infty} K'(x_1, x_2; x'_1, x'_2) e^{iE(T-T')} dT', \quad (110)$$

where it is exploited that the external field is time independent, *i.e.*,  $K'(x_1, x_2; x'_1, x'_2)$  depends on  $T$  and  $T'$  only through the  $T' - T$  difference, and  $T$  represents only a constant shift for the  $T'$  integration variable.

Both Sucher [147] and Douglas and Kroll [149] continued the calculation in momentum space, and we follow this line of thought. The  $\mathbf{r}_1, \mathbf{r}_2$  space coordinates of the two particles and the  $t$  relative time are replaced with the  $\mathbf{p}_1, \mathbf{p}_2$  momenta and the  $\varepsilon$  relative energy. The relative-time and relative-energy wave functions are connected by the seven-dimensional Fourier transformation,

$$\Psi(\mathbf{r}_1, \mathbf{r}_2, t) = \frac{1}{(2\pi)^{\frac{7}{2}}} \int_{\mathbb{R}^7} e^{i(\mathbf{p}_1\mathbf{r}_1 + \mathbf{p}_2\mathbf{r}_2 - \varepsilon t)} \psi(\mathbf{p}_1, \mathbf{p}_2, \varepsilon) d\mathbf{p}_1 d\mathbf{p}_2 d\varepsilon, \quad (111)$$

while the interaction kernel in momentum space is defined as

$$\begin{aligned} & \mathcal{K}'(\mathbf{p}_1, \mathbf{p}_2, \varepsilon, \mathbf{p}'_1, \mathbf{p}'_2, \varepsilon') = \\ & \frac{\beta_1\beta_2}{(2\pi)^6} \int e^{-i[(\mathbf{p}_1\mathbf{r}_1 + \mathbf{p}_2\mathbf{r}_2 - \varepsilon t) - (\mathbf{p}'_1\mathbf{r}'_1 + \mathbf{p}'_2\mathbf{r}'_2 - \varepsilon' t')]} K'_t(\mathbf{r}_1, \mathbf{r}_2, t, \mathbf{r}'_1, \mathbf{r}'_2, t') d\mathbf{r}_1 d\mathbf{r}_2 dt d\mathbf{r}'_1 d\mathbf{r}'_2 dt', \end{aligned} \quad (112)$$

and it acts as an integral operator,

$$\mathcal{K}'f(\mathbf{p}_1, \mathbf{p}_2, \varepsilon) = \int \mathcal{K}'(\mathbf{p}_1, \mathbf{p}_2, \varepsilon, \mathbf{p}'_1, \mathbf{p}'_2, \varepsilon') f(\mathbf{p}'_1, \mathbf{p}'_2, \varepsilon') d\mathbf{p}'_1 d\mathbf{p}'_2 \frac{d\varepsilon'}{-2\pi i}. \quad (113)$$

Then, Eq. (109) can be rewritten as

$$\mathcal{F}\psi(\mathbf{p}_1, \mathbf{p}_2, \varepsilon) = \mathcal{K}'\psi(\mathbf{p}_1, \mathbf{p}_2, \varepsilon) \quad (114)$$

and

$$\mathcal{F} = \mathcal{F}_1\mathcal{F}_2 \quad (115)$$

with

$$\mathcal{F}_1 = \frac{E}{2} + \varepsilon - \mathcal{H}_1(\mathbf{p}_1) \quad (116)$$

$$\mathcal{F}_2 = \frac{E}{2} - \varepsilon - \mathcal{H}_2(\mathbf{p}_2) \quad (117)$$

and their inverse define the one-particle propagators (for the  $E$  total and  $\varepsilon$  relative energy), which will be used in later sections,

$$S_1(p_1) = \mathcal{F}_1^{-1} = \left[ \frac{E}{2} + \varepsilon - \mathcal{H}_1(\mathbf{p}_1) \right]^{-1} \quad (118)$$

$$S_2(p_2) = \mathcal{F}_2^{-1} = \left[ \frac{E}{2} - \varepsilon - \mathcal{H}_2(\mathbf{p}_2) \right]^{-1} \quad (119)$$

with the four-vector variables  $p_1 = (\mathbf{p}_1, \varepsilon)$  and  $p_2 = (\mathbf{p}_2, -\varepsilon)$ .  $\mathcal{H}_1$  (and similarly  $\mathcal{H}_2$ ) is the momentum-space form of the one-particle Dirac Hamiltonian, Eq. (85). In this representation, the interaction operators are integral operators, as it was indicated in Eq. (113) for  $\mathcal{K}'$ .  $\mathcal{U}_1$  (and  $\mathcal{U}_2$ ) labels the external-field Coulomb operator. For the example of a single

nucleus fixed at the origin, Eq. (88), [147, 149]

$$\mathcal{U}_1 f(\mathbf{p}_1, \mathbf{p}_2, \varepsilon) = z_1 \frac{Z\alpha}{2\pi^2} \int \frac{1}{\mathbf{k}^2} f(\mathbf{p}_1 - \mathbf{k}, \mathbf{p}_2, \varepsilon) d\mathbf{k} \quad (120)$$

$$\mathcal{U}_2 f(\mathbf{p}_1, \mathbf{p}_2, \varepsilon) = z_2 \frac{Z\alpha}{2\pi^2} \int \frac{1}{\mathbf{k}^2} f(\mathbf{p}_1, \mathbf{p}_2 + \mathbf{k}, \varepsilon) d\mathbf{k}. \quad (121)$$

### 3. Construction of the interaction kernels using energy-momentum translation operators, the instantaneous part of the interaction

According to Eq. (104), the full interaction kernel contains contributions both from ‘inter-particle’ interactions and from radiative contributions,

$$\mathcal{K}' = \mathcal{K}_1 + \mathcal{K}^{\text{rad}}. \quad (122)$$

In what follows, we focus on the construction of the  $\mathcal{K}_1$  inter-particle kernel, which is obtained as the sum of  $\mathcal{K}_1^{(j)}$  operators corresponding to *irreducible* ‘diagrams’ [141, 147].

Action of the interaction kernel for a single-photon exchange (written in the Coulomb gauge), Eqs. (92)–(94), on some  $f(\mathbf{p}_1, \mathbf{p}_2, \varepsilon)$  two-particle function depending also on the  $\varepsilon$  relative energy can be written in the momentum-space representation as

$$\mathcal{K}_C f(\mathbf{p}_1, \mathbf{p}_2, \varepsilon) = z_1 z_2 \frac{\alpha}{2\pi^2} \int \frac{1}{\mathbf{k}^2} f(\mathbf{p}_1 - \mathbf{k}, \mathbf{p}_2 + \mathbf{k}, \varepsilon - \omega) d\mathbf{k} \frac{d\omega}{-2\pi i} \quad (123)$$

$$\mathcal{K}_T f(\mathbf{p}_1, \mathbf{p}_2, \varepsilon) = z_1 z_2 \frac{\alpha}{2\pi^2} \int \frac{\tilde{\alpha}_1^i \tilde{\alpha}_2^j}{\omega^2 - \mathbf{k}^2 + i\Delta} f(\mathbf{p}_1 - \mathbf{k}, \mathbf{p}_2 + \mathbf{k}, \varepsilon - \omega) d\mathbf{k} \frac{d\omega}{-2\pi i}. \quad (124)$$

A more compact operator form of  $\mathcal{K}_C$  and  $\mathcal{K}_T$  is obtained by using  $k = (\mathbf{k}, \omega)$  momentum-energy translation operators. The one-particle translation operators are

$$\eta_1(\mathbf{k}) f(\mathbf{p}_1, \mathbf{p}_2, \varepsilon) = f(\mathbf{p}_1 - \mathbf{k}, \mathbf{p}_2, \varepsilon) \quad (125)$$

$$\eta_2(-\mathbf{k}) f(\mathbf{p}_1, \mathbf{p}_2, \varepsilon) = f(\mathbf{p}_1, \mathbf{p}_2 + \mathbf{k}, \varepsilon), \quad (126)$$

the two-particle translation operator is,

$$\eta(k) f(\mathbf{p}_1, \mathbf{p}_2, \varepsilon) = f(\mathbf{p}_1 - \mathbf{k}, \mathbf{p}_2 + \mathbf{k}, \varepsilon - \omega), \quad (127)$$

and for later convenience, we also define the notation

$$\eta(k) = \eta(\mathbf{k}, \omega) = \eta_1(\mathbf{k}) \eta_2(-\mathbf{k}) \eta_\varepsilon(\omega). \quad (128)$$

Then, the Coulomb and transverse parts of the one-photon exchange, Eqs. (123) and (124), can be written as

$$\mathcal{K}_C f(\mathbf{p}_1, \mathbf{p}_2, \varepsilon) = \int \kappa_C \eta(\mathbf{k}, \omega) f(\mathbf{p}_1, \mathbf{p}_2, \varepsilon) d\mathbf{k} \frac{d\omega}{-2\pi i} \quad (129)$$

with

$$\kappa_C(\mathbf{k}, \omega) = z_1 z_2 \frac{\alpha}{2\pi^2} \frac{1}{\mathbf{k}^2} \quad (130)$$

and

$$\mathcal{K}_T f(\mathbf{p}_1, \mathbf{p}_2, \varepsilon) = \int \kappa_T \eta(\mathbf{k}, \omega) f(\mathbf{p}_1, \mathbf{p}_2, \varepsilon) d\mathbf{k} \frac{d\omega}{-2\pi i} \quad (131)$$

with

$$\kappa_T(\mathbf{k}, \omega) = z_1 z_2 \frac{\alpha}{2\pi^2} \frac{\tilde{\alpha}_1^i \tilde{\alpha}_2^j}{\omega^2 - \mathbf{k}^2 + i\Delta}. \quad (132)$$

It is interesting to note that the Coulomb interaction carries only a trivial shift in the relative-energy dependence, and this corresponds to saying that the Coulomb interaction acts through momentum transfer and the interaction is instantaneous. At the same time, the transverse part has a non-trivial relative-energy dependence, and this is related to the finite propagation speed of the overall interaction (retardation). At the same time, the retardation contribution to

the transverse part is small and it is convenient to separate the instantaneous part, which is called the Breit interaction,

$$\mathcal{K}_B f(\mathbf{p}_1, \mathbf{p}_2, \varepsilon) = \int \kappa_B \eta(\mathbf{k}, \omega) f(\mathbf{p}_1, \mathbf{p}_2, \varepsilon) d\mathbf{k} \frac{d\omega}{-2\pi i} \quad (133)$$

with

$$\kappa_B(\mathbf{k}, \omega) = z_1 z_2 \frac{\alpha}{2\pi^2} \frac{\tilde{\alpha}_1^i \tilde{\alpha}_2^i}{-\mathbf{k}^2}. \quad (134)$$

The remainder, *i.e.*, difference of the transverse and the Breit interactions, is the retarded part, which we label as

$$\mathcal{K}_\tau = \mathcal{K}_T - \mathcal{K}_B, \quad (135)$$

while the instantaneous contributions (Coulomb–Breit) can be handled ‘together’,

$$\mathcal{K}_{CB} = \mathcal{K}_C + \mathcal{K}_B. \quad (136)$$

To write down the mathematical expression for more complicated  $\mathcal{K}_1^{(j)}$  interactions including multiple (Coulomb and/or transverse) photons (*e.g.*, Fig. 12), Sucher derived and summarized the following simple rules.

First,

- (a) label each interaction line with four vectors,  $k, k', k'',$  etc. with assigning each line a specific sense (convenient to choose the same for all lines), *e.g.*, from 2 to 1;
- (b) label the final parts of the world lines of the fermions 1 and 2 with  $p_1 = (\mathbf{p}_1, \varepsilon)$  and  $p_2 = (\mathbf{p}_2, -\varepsilon)$ ;
- (c) label all remaining electron lines with conserving the four-momentum.

Second, for a fully labelled diagram,  $\mathcal{K}_1^{(j)}$  can be formulated by writing

1.  $\tilde{\alpha}_1^i$  or  $\tilde{\alpha}_2^i$  for a transverse interaction vertex;
2. a factor  $S_1(p_1 - k)$  for an intermediate electron line labelled with  $p_1 - k$  on the path of 1 and a factor  $S_2(p_2 + k')$  for an intermediate electron line labelled with  $p_2 + k'$  on the path of 2; while writing down the factors, it is necessary to preserve the order of events along a world line, *i.e.*, factors for ‘later’ events along a world line stand to the left of factors corresponding to ‘earlier’ events;
3. to the *right* of these expressions a factor  $\kappa_C(k)$  for a Coulomb interaction line labelled with  $k = (\mathbf{k}, \omega)$  and a factor  $\kappa_T(k')$  for a transverse interaction line with  $k' = (\mathbf{k}', \omega')$ ;
4. in addition to each  $\kappa_C$  and  $\kappa_T$ , an  $\eta(k)/(-2\pi i)$  factor appears, if the interaction is from 2 to 1 (or, an  $\eta(-k)/(-2\pi i)$  factor, if the interaction is from 1 to 2).

It is also useful to note that the effect of the  $\eta(k) = \eta(\mathbf{k}, \omega)$  four-momentum translation on the one-particle propagators, Eqs. (118)–(119), is

$$\eta(k) S_1(p_1) \eta(-k) = S_1(p_1 - k) = \left[ \frac{E}{2} + \varepsilon - \omega - \mathcal{H}_1(\mathbf{p}_1 - \mathbf{k}) \right]^{-1} \quad (137)$$

$$\eta(k) S_2(p_2) \eta(-k) = S_2(p_2 + k) = \left[ \frac{E}{2} - \varepsilon + \omega - \mathcal{H}_2(\mathbf{p}_2 + \mathbf{k}) \right]^{-1}, \quad (138)$$

where the  $\mathbf{k}$ -translation of the one-particle Hamiltonians gives

$$\mathcal{H}_1(\mathbf{p}_1 - \mathbf{k}) = \eta_1(\mathbf{k}) \mathcal{H}_1(\mathbf{p}_1) \eta_1(-\mathbf{k}) = \alpha_1(\mathbf{p}_1 - \mathbf{k}) + \beta_1 m + \mathcal{U}_1 \quad (139)$$

$$\mathcal{H}_2(\mathbf{p}_2 + \mathbf{k}) = \eta_2(-\mathbf{k}) \mathcal{H}_2(\mathbf{p}_2) \eta_2(\mathbf{k}) = \alpha_2(\mathbf{p}_2 + \mathbf{k}) + \beta_2 m + \mathcal{U}_2. \quad (140)$$

Sucher calculated corrections to the energy up to order  $\alpha^3 E_h$ , Douglas and Kroll calculated the fine-structure splitting up to order  $\alpha^4 E_h$ , and they have included the following interactions,

$$\mathcal{K}_I = \mathcal{K}_C + \mathcal{K}_T + \mathcal{K}_{C \times C} + \mathcal{K}_{T \times C} + \mathcal{K}_{T \times T} + \mathcal{K}_{T \times C^2}. \quad (141)$$

It is necessary to compile ‘by hand’ only the irreducible interactions, and all reducible diagrams are automatically included in the solution of the BS equation [141].

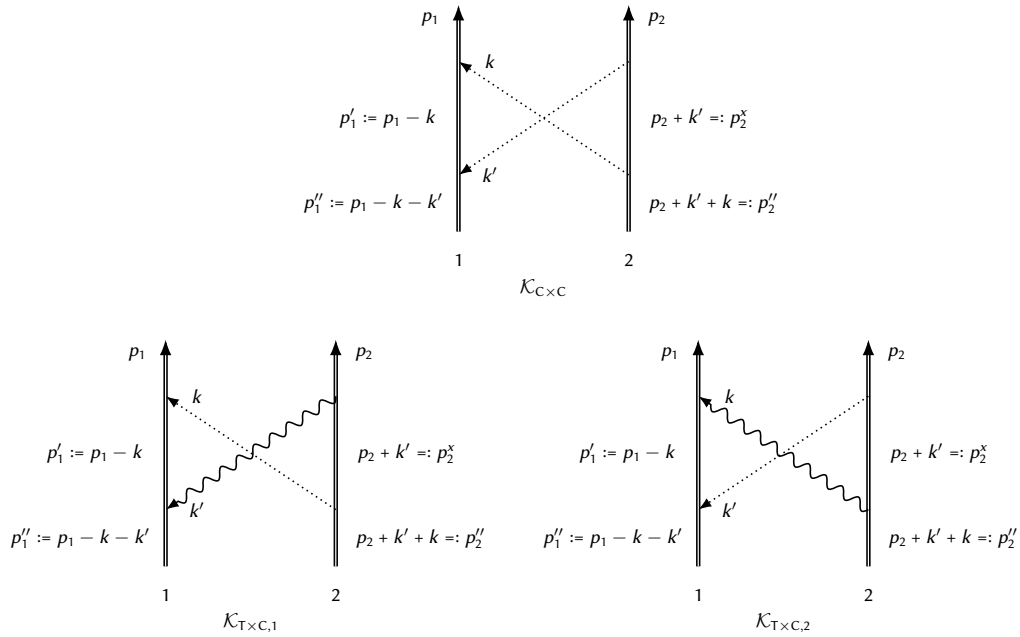


Figure 12. Example interaction diagrams including four-momentum labels

4. A practical wave equation: the exact equal-times Bethe–Salpeter equation and emergence of the no-pair Dirac–Coulomb(–Breit) Hamiltonian

Let’s exploit the fact that, in atoms and molecules, the dominant part of the interaction is instantaneous (Coulomb or Coulomb–Breit), so, it is convenient to write the kernel as the sum of a  $\mathcal{K}_i$  instantaneous part and the ‘rest’,

$$\mathcal{K}_1 = \mathcal{K}_i + \mathcal{K}_\Delta . \quad (142)$$

The instantaneous part,  $\mathcal{K}_i$ , induces only a trivial shift for the  $\varepsilon$  relative energy, and hence the effect of the relative energy can be integrated out

$$\begin{aligned} \mathcal{K}_i \psi(\mathbf{p}_1, \mathbf{p}_2, \varepsilon) &= \int \int \kappa_i(\mathbf{k}) \psi(\mathbf{p}_1 - \mathbf{k}, \mathbf{p}_2 + \mathbf{k}, \varepsilon - \omega) \, \mathbf{d}\mathbf{k} \frac{d\omega}{-2\pi i} \\ &= \frac{1}{-2\pi i} \int \kappa_i(\mathbf{k}) \Phi(\mathbf{p}_1 - \mathbf{k}, \mathbf{p}_2 + \mathbf{k}) \, \mathbf{d}\mathbf{k} \\ &= \frac{1}{-2\pi i} \mathcal{I}_i \Phi(\mathbf{p}_1, \mathbf{p}_2) , \end{aligned} \quad (143)$$

where  $\mathcal{I}_i$  is only a momentum shift integral operator,

$$\mathcal{I}_i \Phi(\mathbf{p}_1, \mathbf{p}_2) = \int \kappa_i(\mathbf{k}) \Phi(\mathbf{p}_1 - \mathbf{k}, \mathbf{p}_2 + \mathbf{k}) \, \mathbf{d}\mathbf{k} \quad (144)$$

with

$$\kappa_i(\mathbf{k}) = \begin{cases} z_1 z_2 \frac{\alpha}{2\pi^2} \frac{1}{k^2} , & \text{for the Coulomb interaction, } i = C \\ z_1 z_2 \frac{\alpha}{2\pi^2} \frac{1}{k^2} (1 - \tilde{\alpha}_1^i \tilde{\alpha}_2^i) , & \text{for the Coulomb–Breit interaction, } i = CB . \end{cases} \quad (145)$$

In Eq. (143), it is also important to note the emergence of the equal-time wave function,

$$\Phi(\mathbf{p}_1, \mathbf{p}_2) = \int_{-\infty}^{\infty} \psi(\mathbf{p}_1, \mathbf{p}_2, \varepsilon) \, d\varepsilon . \quad (146)$$

Next, we rearrange Eq. (114) and separate the instantaneous part of the interaction as

$$\begin{aligned} (\mathcal{F} - \mathcal{K}_\Delta) \psi(\mathbf{p}_1, \mathbf{p}_2, \varepsilon) &= \mathcal{K}_i \psi(\mathbf{p}_1, \mathbf{p}_2, \varepsilon) \\ \psi(\mathbf{p}_1, \mathbf{p}_2, \varepsilon) &= (\mathcal{F} - \mathcal{K}_\Delta)^{-1} \mathcal{K}_i \psi(\mathbf{p}_1, \mathbf{p}_2, \varepsilon) . \end{aligned} \quad (147)$$



By integrating both sides with respect to the relative energy and using Eqs. (143) and (146), we obtain

$$\begin{aligned} \int d\varepsilon \psi &= \int d\varepsilon (\mathcal{F} - \mathcal{K}_\Delta)^{-1} \mathcal{K}_i \psi \\ \Phi &= \int \frac{d\varepsilon}{-2\pi i} (\mathcal{F} - \mathcal{K}_\Delta)^{-1} \mathcal{I}_i \Phi \\ \Phi &= \int \frac{d\varepsilon}{-2\pi i} \mathcal{F}^{-1} \mathcal{I}_i \Phi + \int \frac{d\varepsilon}{-2\pi i} \mathcal{F}^{-1} \mathcal{K}_\Delta (\mathcal{F} - \mathcal{K}_\Delta)^{-1} \mathcal{I}_i \Phi, \end{aligned} \quad (148)$$

where the operator identity was used in the last step,

$$(A - B)^{-1} = A^{-1} + A^{-1} B (A - B)^{-1}. \quad (149)$$

Next, we define the one-particle positive- and negative-energy projection operators for particles  $i = 1$  and  $2$  by

$$\mathcal{L}_{i\pm} = \frac{1}{2} [1 \pm \mathcal{H}_i(\mathbf{p}_i) \mathcal{E}_i^{-1}(\mathbf{p}_i)], \quad (150)$$

which is, at this point, contains a purely formal definition for the one-particle Hamiltonian absolute value operator,

$$\mathcal{E}_i(\mathbf{p}_i) = |\mathcal{H}_i(\mathbf{p}_i)|, \quad (151)$$

which also means that

$$\mathcal{E}_i(\mathbf{p}_i) \phi_n^{(i)}(\mathbf{p}_i) = |E_n^{(i)}| \phi_n^{(i)}(\mathbf{p}_i). \quad (152)$$

In short, we can also write

$$\mathcal{H}_i \mathcal{L}_{i\pm} = \pm \mathcal{E}_i \mathcal{L}_{i\pm}. \quad (153)$$

If there is no external field, *e.g.*, pre-BO description of two spin-1/2 particles, then,  $\mathcal{L}_{i\pm}$  reduces to the free-particle projector [192]

$$\mathcal{L}_{i\pm}(\mathbf{p}_i) = L_{i\pm}(\mathbf{p}_i) = \frac{1}{2} \left[ 1 \pm \frac{\boldsymbol{\alpha}_i \mathbf{p}_i + \beta_i m_i}{\sqrt{p_i^2 + m_i^2}} \right] \quad (\text{for } U_i = 0), \quad (154)$$

since for  $U_i = 0$ ,  $\mathcal{H}_i = \mathcal{H}_i^{(0)} = \boldsymbol{\alpha}_i \mathbf{p}_i + \beta_i m_i$  and the eigenvalues of the Hamiltonian absolute value operator are  $|E_p^{(i)}| = +\sqrt{p_i^2 + m_i^2}$ .

Using the  $\mathcal{E}_1$  and  $\mathcal{E}_2$  notation, we can write the  $\mathcal{F}_1^{-1}$  and  $\mathcal{F}_2^{-1}$  propagators in  $\mathcal{F}^{-1}$  as

$$S_1 = \mathcal{F}_1^{-1} = \left[ \frac{E}{2} + \varepsilon - \mathcal{H}_1 \right]^{-1} = \frac{\mathcal{L}_{1+}}{\frac{E}{2} + \varepsilon - \mathcal{E}_1 + i\delta} + \frac{\mathcal{L}_{1-}}{\frac{E}{2} + \varepsilon + \mathcal{E}_1 - i\delta}, \quad (155)$$

and similarly,

$$S_2 = \mathcal{F}_2^{-1} = \left[ \frac{E}{2} - \varepsilon - \mathcal{H}_2 \right]^{-1} = \frac{\mathcal{L}_{2+}}{\frac{E}{2} - \varepsilon - \mathcal{E}_2 + i\delta} + \frac{\mathcal{L}_{2-}}{\frac{E}{2} - \varepsilon + \mathcal{E}_2 - i\delta}, \quad (156)$$

according to Feynman's prescription [139] of adding a complex number with a small negative imaginary value to the mass and the limit is taken from the positive side for a consistent electron-positron theory (here, the energy replaces Feynman's mass and  $\delta > 0$  with  $\delta \rightarrow 0+$ ).

The first term in Eq. (148) contains a relative-energy integral, but  $\mathcal{I}_i$  and  $\Phi$  are independent of  $\varepsilon$ , so we only need to

calculate

$$\begin{aligned}
 \int \frac{d\varepsilon}{-2\pi i} \mathcal{F}^{-1} &= \int \frac{d\varepsilon}{-2\pi i} \mathcal{F}_2^{-1} \mathcal{F}_1^{-1} \\
 &= \int \frac{d\varepsilon}{-2\pi i} \left( \frac{\mathcal{L}_{2+}}{\frac{\varepsilon}{2} - \varepsilon - \mathcal{E}_2 + i\delta} + \frac{\mathcal{L}_{2-}}{\frac{\varepsilon}{2} - \varepsilon + \mathcal{E}_2 - i\delta} \right) \\
 &\quad \left( \frac{\mathcal{L}_{1+}}{\frac{\varepsilon}{2} + \varepsilon - \mathcal{E}_1 + i\delta} + \frac{\mathcal{L}_{1-}}{\frac{\varepsilon}{2} + \varepsilon + \mathcal{E}_1 - i\delta} \right) \\
 &= \int \frac{d\varepsilon}{-2\pi i} \frac{1}{\frac{\varepsilon}{2} - \varepsilon - \mathcal{E}_2 + i\delta} \frac{1}{\frac{\varepsilon}{2} + \varepsilon - \mathcal{E}_1 + i\delta} \mathcal{L}_{++} \\
 &\quad + \int \frac{d\varepsilon}{-2\pi i} \frac{1}{\frac{\varepsilon}{2} - \varepsilon - \mathcal{E}_2 + i\delta} \frac{1}{\frac{\varepsilon}{2} + \varepsilon + \mathcal{E}_1 - i\delta} \mathcal{L}_{-+} \\
 &\quad + \int \frac{d\varepsilon}{-2\pi i} \frac{1}{\frac{\varepsilon}{2} - \varepsilon + \mathcal{E}_2 + i\delta} \frac{1}{\frac{\varepsilon}{2} + \varepsilon - \mathcal{E}_1 - i\delta} \mathcal{L}_{+-} \\
 &\quad + \int \frac{d\varepsilon}{-2\pi i} \frac{1}{\frac{\varepsilon}{2} - \varepsilon + \mathcal{E}_2 - i\delta} \frac{1}{\frac{\varepsilon}{2} + \varepsilon + \mathcal{E}_1 - i\delta} \mathcal{L}_{--}
 \end{aligned} \tag{157}$$

with the two-particle projectors,  $\mathcal{L}_{\sigma\sigma'} = \mathcal{L}_{1\sigma} \mathcal{L}_{2\sigma'}$  ( $\sigma, \sigma' = +$  or  $-$ ).

To evaluate these  $\varepsilon$  integrals, we use Cauchy's residue theorem,

$$\oint_{\gamma} f(z) dz = \text{sgn}(\gamma) 2\pi i \sum_{k \in \text{poles}} \text{Res}(f, a_k), \tag{158}$$

where the summation goes through the poles of  $f$  within the domain surrounded by the simple closed curve  $\gamma$ . We can choose the positive  $\gamma$  contour ( $O_{\gamma}$  counterclockwise,  $\text{sgn}\gamma = +1$ ), but identical results are obtained from using the negative  $\gamma'$  contour ( $O_{\gamma'}$  clockwise,  $\text{sgn}\gamma' = -1$ ). Since this is

an important step of the calculation, we proceed term by term with the evaluation of Eq. (157).

$$\begin{aligned}
 \lim_{\delta \rightarrow 0^+} \mathcal{L}_{++} & \int \frac{d\varepsilon}{-2\pi i} \underbrace{\frac{-1}{\varepsilon - \frac{E}{2} + \mathcal{E}_2 - i\delta}}_{\varepsilon = \frac{E}{2} - \mathcal{E}_2 + i\delta \text{ in } O_{\gamma'}} \underbrace{\frac{1}{\varepsilon + \frac{E}{2} - \mathcal{E}_1 + i\delta}}_{\varepsilon = -\frac{E}{2} + \mathcal{E}_1 - i\delta \text{ in } O_{\gamma'}} \\
 & = \begin{cases} \text{for } O_{\gamma} : \lim_{\delta \rightarrow 0^+} \mathcal{L}_{++} \frac{-2\pi i}{-2\pi i} \frac{-1}{\frac{E}{2} - \mathcal{E}_2 + i\delta + \frac{E}{2} - \mathcal{E}_1 + i\delta} \\ \text{for } O_{\gamma'} : \lim_{\delta \rightarrow 0^+} \mathcal{L}_{++} \frac{-2\pi i}{-2\pi i} \frac{-1}{-\frac{E}{2} + \mathcal{E}_1 - i\delta - \frac{E}{2} + \mathcal{E}_2 - i\delta} \end{cases} \\
 & = \mathcal{L}_{++} \frac{1}{E - \mathcal{E}_1 - \mathcal{E}_2} \\
 & = \mathcal{L}_{++} (E - \mathcal{H}_1 - \mathcal{H}_2)^{-1} \tag{159}
 \end{aligned}$$

$$\begin{aligned}
 \lim_{\delta \rightarrow 0^+} \mathcal{L}_{+-} & \int \frac{d\varepsilon}{-2\pi i} \underbrace{\frac{-1}{\varepsilon - \frac{E}{2} - \mathcal{E}_2 - i\delta}}_{\varepsilon = \frac{E}{2} + \mathcal{E}_2 + i\delta \text{ in } O_{\gamma'}} \underbrace{\frac{1}{\varepsilon + \frac{E}{2} - \mathcal{E}_1 - i\delta}}_{\varepsilon = -\frac{E}{2} + \mathcal{E}_1 + i\delta \text{ in } O_{\gamma'}} \\
 & = \begin{cases} \text{for } O_{\gamma} : \lim_{\delta \rightarrow 0^+} \mathcal{L}_{+-} \frac{-2\pi i}{-2\pi i} \left[ -\frac{1}{\frac{E}{2} + \mathcal{E}_2 + i\delta + \frac{E}{2} - \mathcal{E}_1 - i\delta} + \frac{-1}{-\frac{E}{2} + \mathcal{E}_1 + i\delta - \frac{E}{2} - \mathcal{E}_2 - i\delta} \right] = 0 \\ \text{for } O_{\gamma'} : 0 \end{cases} \\
 & = 0 \tag{160}
 \end{aligned}$$

$$\begin{aligned}
 \lim_{\delta \rightarrow 0^+} \mathcal{L}_{-+} & \int \frac{d\varepsilon}{-2\pi i} \underbrace{\frac{-1}{\varepsilon - \frac{E}{2} + \mathcal{E}_2 - i\delta}}_{\varepsilon = \frac{E}{2} - \mathcal{E}_2 + i\delta \text{ in } O_{\gamma'}} \underbrace{\frac{1}{\varepsilon + \frac{E}{2} + \mathcal{E}_1 - i\delta}}_{\varepsilon = -\frac{E}{2} - \mathcal{E}_1 + i\delta \text{ in } O_{\gamma'}} \\
 & = \begin{cases} \text{for } O_{\gamma} : \lim_{\delta \rightarrow 0^+} \mathcal{L}_{-+} \frac{-2\pi i}{-2\pi i} \left[ -\frac{1}{\frac{E}{2} - \mathcal{E}_2 + i\delta + \frac{E}{2} + \mathcal{E}_1 - i\delta} + \frac{-1}{-\frac{E}{2} - \mathcal{E}_1 + i\delta - \frac{E}{2} + \mathcal{E}_2 - i\delta} \right] = 0 \\ \text{for } O_{\gamma'} : 0 \end{cases} \\
 & = 0 \tag{161}
 \end{aligned}$$

$$\begin{aligned}
 \lim_{\delta \rightarrow 0^+} \mathcal{L}_{--} & \int \frac{d\varepsilon}{-2\pi i} \underbrace{\frac{-1}{\varepsilon - \frac{E}{2} - \mathcal{E}_2 + i\delta}}_{\varepsilon = \frac{E}{2} + \mathcal{E}_2 - i\delta \text{ in } O_{\gamma'}} \underbrace{\frac{1}{\varepsilon + \frac{E}{2} + \mathcal{E}_1 - i\delta}}_{\varepsilon = -\frac{E}{2} - \mathcal{E}_1 + i\delta \text{ in } O_{\gamma'}} \\
 & = \begin{cases} \text{for } O_{\gamma} : \lim_{\delta \rightarrow 0^+} \mathcal{L}_{--} \frac{-2\pi i}{-2\pi i} \frac{-1}{-\frac{E}{2} - \mathcal{E}_1 + i\delta - \frac{E}{2} - \mathcal{E}_2 + i\delta} = -\mathcal{L}_{--} \frac{1}{E + \mathcal{E}_1 + \mathcal{E}_2} \\ \text{for } O_{\gamma'} : \lim_{\delta \rightarrow 0^+} \mathcal{L}_{--} \frac{-2\pi i}{-2\pi i} (-1)^2 \frac{1}{\frac{E}{2} + \mathcal{E}_2 - i\delta + \frac{E}{2} + \mathcal{E}_1 - i\delta} = -\mathcal{L}_{--} \frac{1}{E + \mathcal{E}_1 + \mathcal{E}_2} \end{cases} \\
 & = -\mathcal{L}_{--} \frac{1}{E + \mathcal{E}_1 + \mathcal{E}_2} \\
 & = -\mathcal{L}_{--} (E - \mathcal{H}_1 - \mathcal{H}_2)^{-1} \tag{162}
 \end{aligned}$$

The result of this short calculation can be summarized as operator identities [147, 149]

$$\int \frac{d\varepsilon}{-2\pi i} \frac{1}{\varepsilon - A + i\delta} \frac{1}{\varepsilon + B - i\delta} = \frac{1}{A + B} \tag{163}$$

$$\int \frac{d\varepsilon}{-2\pi i} \frac{1}{\varepsilon - A + i\delta} \frac{1}{\varepsilon + B + i\delta} = 0, \tag{164}$$

where the second identity holds in general, the first is valid only for commuting  $A$  and  $B$  operators. All in all, we obtain

$$\int \frac{d\varepsilon}{-2\pi i} \mathcal{F}^{-1} = (E - \mathcal{H}_1 - \mathcal{H}_2)^{-1} (\mathcal{L}_{++} - \mathcal{L}_{--}) = \mathcal{D}^{-1} (\mathcal{L}_{++} - \mathcal{L}_{--}), \tag{165}$$

where the short notation is introduced,

$$\mathcal{D} = E - \mathcal{H}_1 - \mathcal{H}_2. \tag{166}$$

Using this result, we can re-write Eq. (148),

$$\begin{aligned}
 \Phi & = (E - \mathcal{H}_1 - \mathcal{H}_2)^{-1} (\mathcal{L}_{++} - \mathcal{L}_{--}) \mathcal{I}_i \Phi + \int \frac{d\varepsilon}{-2\pi i} \mathcal{F}^{-1} \mathcal{K}_{\Delta} (\mathcal{F} - \mathcal{K}_{\Delta})^{-1} \mathcal{I}_i \Phi \\
 E\Phi & = [\mathcal{H}_1 + \mathcal{H}_2 + (\mathcal{L}_{++} - \mathcal{L}_{--}) \mathcal{I}_i] \Phi + \mathcal{D} \int \frac{d\varepsilon}{-2\pi i} \mathcal{F}^{-1} \mathcal{K}_{\Delta} (\mathcal{F} - \mathcal{K}_{\Delta})^{-1} \mathcal{I}_i \Phi, \tag{167}
 \end{aligned}$$

and finally obtain, the exact, equal-time Bethe-Salpeter (eBS) equation

$$E\Phi = (\mathcal{H}_1 + \mathcal{H}_2 + \mathcal{L}_{++}\mathcal{I}_i\mathcal{L}_{++} + \mathcal{H}_\Delta)\Phi \quad (168)$$

with

$$\mathcal{H}_\Delta = \mathcal{L}_{++}\mathcal{I}_i(1 - \mathcal{L}_{++}) - \mathcal{L}_{--}\mathcal{I}_i + \mathcal{D} \int \frac{d\varepsilon}{-2\pi i} \mathcal{F}^{-1}\mathcal{K}_\Delta(\mathcal{F} - \mathcal{K}_\Delta)^{-1}\mathcal{I}_i. \quad (169)$$

Eq. (168) is the central equation to our work. It is obtained by equivalent mathematical manipulations from the original space-time Bethe–Salpeter equation, Eq. (89), it is a homogeneous, linear equation for the equal-time wave function,  $\Phi$ , which depends only on the momenta (or coordinates) of the two fermions. At the same time, the exact equal-time equation is a non-linear eigenvalue equation for the  $E$  energy, since the  $\mathcal{H}_\Delta$  term also depends on  $E$  (through  $\mathcal{F}$ ). We can arrive at a useful initial description of atoms and molecules, by first neglecting  $\mathcal{H}_\Delta$ , and starting with the solution of the positive-energy projected or no-pair Dirac–Coulomb(–Breit) equation,

$$E\Phi = (\mathcal{H}_1 + \mathcal{H}_2 + \mathcal{L}_{++}\mathcal{I}_i\mathcal{L}_{++})\Phi. \quad (170)$$

It is important to note that in the present derivation [145, 147, 149], the projector is defined according to Eqs. (150) and (154), and it is connected to the emergence of the no-pair two-particle Dirac Hamiltonian, Eqs. (157)–(166). Variants of the no-pair DC(B) equation are commonly used in relativistic quantum chemistry. Sucher [137, 170] analyzed the connection to relativistic quantum chemistry methodologies, in which the Dirac–Hartree–Fock projector is a popular (and natural) choice, and came to the conclusion that the use of that projector is also valid, but then, during the evaluation of the  $\mathcal{H}_\Delta$  corrections, one has to correct for the difference (which may be complicated).

During our work, we stick to the original definition, Eq. (150) for two particles in an external field and Eq. (154) for an isolated two-fermion system. Corresponding numerical results (for helium- and for positronium-like systems) are reviewed in Sec. III E.

During the present calculation, which follows closely the work by Salpeter [145], Sucher [147], and Douglas and Kroll [149], it was critical to retain the relative energy between the particles. Integration for the relative energy resulted in the emergence of the no-pair, two-electron Dirac Hamiltonian with instantaneous (Coulomb or Coulomb–Breit) interactions. Emergence of the two-particle Hamiltonian naturally occurs for a certain choice of the projector. At the moment, we understand  $\mathcal{H}_\Delta$  in Eq. (169) as some ‘quasi potential’ for a DC(B) interacting reference. The DC(B) reference, *i.e.*, numerical solution of Eq. (170), already contains all reducible interaction diagrams of the instantaneous kernel [141], *i.e.*, the full Coulomb(–Breit) ladder.

##### 5. Phenomenology: why and when the equal-time equation is useful?

In atoms and molecules, the interaction of electrons and atomic nuclei (considered now as point-like, quasi-elementary particles) are dominated by electromagnetic forces. To capture most of the binding energy in these systems, it is convenient to work in the Coulomb gauge, since the instantaneous Coulomb interaction dominates the binding. Subtle magnetic effects can be accounted for by including also the instantaneous Breit interaction in the treatment.

We can define an equal-time equation, a simple, linear  $H\Psi = E\Psi$ -type wave equation, by retaining the instantaneous part (Coulomb or Coulomb–Breit) of the interaction mediated by (subsequent exchanges of) a single photon (at a time) and the positive-energy solutions of matter. The remaining part of the exact equal-time equation can be obtained by integrating through the relative energy (relative time) of the interacting particles (in addition to a simple energy-independent correction term for double-pair instantaneous corrections in the first two terms of Eq. (169)).

The exact equal-time equation form is useful, if the correction obtained from the relative-energy integral is small. In atoms and molecules, it can be anticipated that it is small, because the electromagnetic interaction is relatively weak. During the ‘infinitely’ long lifetime of bound systems, infinitely many photon exchanges occur, but these exchanges are mostly consecutive, there are not ‘many photons’ present at the same time. The binding of atoms and molecules is dominated by a single photon exchange at a time, and during the lifetime of the system, there is an infinite ladder of single-photon exchanges, the Coulomb ladder or the Coulomb–Breit ladder with non-crossing steps. The effect of crossing photons can be identified under a high-energy resolution, and as a small effect it can potentially be accounted for as a (low-order) perturbative correction to the interaction ladder.

If the interaction was much stronger ( $\alpha$  was larger), there were more interaction-mediating particles present at the same time, crossed diagrams would be more important, and the equal-time separation and the no-pair approximation would be less useful.

### C. Prospects regarding $\mathcal{H}_\Delta$

The equal-time two-particle wave equation with instantaneous interactions could be formulated at the price of the appearance of a complicated potential energy-like term, which contains an integral with respect to the relative energy of the particles, and which can be considered as some effective potential due to the full-fledged description of the photon field for an interacting two-particle reference (no-pair DC or DCB).

Sucher [147] formulated low-order perturbative corrections to the no-pair DC(B) energy using Brillouin–Wigner perturbation theory (BWPT). The advantage of the BWPT energy formula is that it remains formally unchanged for an energy-dependent perturbation (here  $\mathcal{H}_\Delta(E)$ ),

$$\begin{aligned} E - E_i &= \langle \Phi_i | \mathcal{H}_\Delta (1 - \Gamma \mathcal{H}_\Delta)^{-1} \Phi_i \rangle \\ &= \langle \Phi_i | \mathcal{H}_\Delta \Phi_i \rangle + \langle \Phi_i | \mathcal{H}_\Delta \Gamma \mathcal{H}_\Delta \Phi_i \rangle + \langle \Phi_i | \mathcal{H}_\Delta \Gamma \mathcal{H}_\Delta \Gamma \mathcal{H}_\Delta \Phi_i \rangle + \dots, \end{aligned} \quad (171)$$

where the no-pair Hamiltonian is

$$\mathcal{H}_i = \mathcal{H}_1 + \mathcal{H}_2 + \mathcal{L}_{++} \mathcal{I}_i \mathcal{L}_{++} \quad (172)$$

and  $\Gamma(E, \Phi_i)$  stands for the (reduced) resolvent

$$\Gamma(E; \Phi_i) = \sum_n \frac{|\Phi_{i,n}\rangle \langle \Phi_{i,n}|}{E - E_n} - \frac{|\Phi_i\rangle \langle \Phi_i|}{E - E_i} = (E - \mathcal{H}_i)^{-1} (1 - |\Phi_i\rangle \langle \Phi_i|). \quad (173)$$

The  $\Phi_{i,n}$  functions are eigenfunctions of the  $\mathcal{H}_i$  no-pair Hamiltonian with instantaneous (i) interactions.

A useful relation for the quasi-Green function is obtained as follows. Using the  $1 = \mathcal{L}_{++} + \mathcal{L}_{+-} + \mathcal{L}_{-+} + \mathcal{L}_{--}$  completeness relation, we can write

$$\begin{aligned} &(E - \mathcal{H}_i)^{-1} (1 - |\Phi_i\rangle \langle \Phi_i|) \\ &= (E - \mathcal{H}_i)^{-1} (\mathcal{L}_{++} - |\Phi_i\rangle \langle \Phi_i|) + (E - \mathcal{H}_i)^{-1} (\mathcal{L}_{+-} + \mathcal{L}_{-+} + \mathcal{L}_{--}) \\ &= (E - \mathcal{H}_i)^{-1} (\mathcal{L}_{++} - |\Phi_i\rangle \langle \Phi_i|) + (E - \mathcal{H}_1 - \mathcal{H}_2 - \mathcal{L}_{++} \mathcal{I}_i \mathcal{L}_{++})^{-1} (\mathcal{L}_{+-} + \mathcal{L}_{-+} + \mathcal{L}_{--}) \\ &= (E - \mathcal{H}_i)^{-1} (\mathcal{L}_{++} - |\Phi_i\rangle \langle \Phi_i|) + (E - \mathcal{H}_1 - \mathcal{H}_2)^{-1} (\mathcal{L}_{+-} + \mathcal{L}_{-+} + \mathcal{L}_{--}) \\ &= (E - \mathcal{H}_i)^{-1} (\mathcal{L}_{++} - |\Phi_i\rangle \langle \Phi_i|) + \mathcal{D}^{-1} (\mathcal{L}_{+-} + \mathcal{L}_{-+} + \mathcal{L}_{--}). \end{aligned} \quad (174)$$

Thus, the quasi-Green function can be written as

$$\Gamma(E; \Phi_i) = (E - \mathcal{H}_i)^{-1} (\mathcal{L}_{++} - |\Phi_i\rangle \langle \Phi_i|) + \mathcal{D}^{-1} (1 - \mathcal{L}_{++}). \quad (175)$$

Aiming for a given order result, simplifications are possible. In Sucher's  $\alpha^3 E_h$  calculation [147], it was sufficient to consider only the first two terms in the expansion of Eq. (171), furthermore, the exact energy could be approximated by  $E \approx E_i$ , i.e.,  $\mathcal{H}_\Delta(E) \approx \mathcal{H}_\Delta(E_i)$  and  $\Gamma(E, \Phi_i) \approx \Gamma(E_i, \Phi_i)$ . These approximations essentially led to first- and second-order Rayleigh–Schrödinger-type correction formulae.

For the inclusion of  $\mathcal{H}_\Delta$  in numerical computations, it is convenient to write it as the sum of two terms,

$$\mathcal{H}_\Delta = \mathcal{H}_\delta + \mathcal{H}_\varepsilon. \quad (176)$$

$\mathcal{H}_\delta$  is algebraically straightforward, and corresponds to (non-crossing) pair corrections,

$$\mathcal{H}_\delta = \mathcal{L}_{++} \mathcal{I}_i (1 - \mathcal{L}_{++}) - \mathcal{L}_{--} \mathcal{I}_i. \quad (177)$$

The technically more involved part includes an integral for the  $\varepsilon$  relative energy and carries retardation and crossed-photon contributions (e.g.,  $\mathcal{K}_{C \times C}$ ,  $\mathcal{K}_{T \times C, 1}$  and  $\mathcal{K}_{T \times C, 2}$  in Fig. 12),

$$\mathcal{H}_\varepsilon = \mathcal{D} \int \frac{d\varepsilon}{-2\pi i} \mathcal{F}^{-1} \mathcal{K}_\Delta (\mathcal{F} - \mathcal{K}_\Delta)^{-1} \mathcal{I}_i. \quad (178)$$

For numerical computations, the inverse can be expanded as

$$\begin{aligned}
 \mathcal{H}_\varepsilon &= \mathcal{D} \int \frac{d\varepsilon}{-2\pi i} \mathcal{F}^{-1} \mathcal{K}_\Delta (\mathcal{F} - \mathcal{K}_\Delta)^{-1} \mathcal{I}_i \\
 &= \int \frac{d\varepsilon}{-2\pi i} \mathcal{D} \mathcal{F}^{-1} \mathcal{K}_\Delta \mathcal{F}^{-1} (1 - \mathcal{K}_\Delta \mathcal{F}^{-1})^{-1} \mathcal{I}_i \\
 &= \int \frac{d\varepsilon}{-2\pi i} \mathcal{D} \mathcal{F}^{-1} \mathcal{K}_\Delta \mathcal{F}^{-1} [1 + \mathcal{K}_\Delta \mathcal{F}^{-1} + \mathcal{K}_\Delta \mathcal{F}^{-1} \mathcal{K}_\Delta \mathcal{F}^{-1} + \dots] \mathcal{I}_i \\
 &= \int \frac{d\varepsilon}{-2\pi i} [\mathcal{D} \mathcal{F}^{-1} \mathcal{K}_\Delta \mathcal{F}^{-1} + \mathcal{D} \mathcal{F}^{-1} \mathcal{K}_\Delta \mathcal{F}^{-1} \mathcal{K}_\Delta \mathcal{F}^{-1} + \mathcal{D} \mathcal{K}_\Delta \mathcal{F}^{-1} \mathcal{K}_\Delta \mathcal{F}^{-1} + \dots] \mathcal{I}_i.
 \end{aligned} \tag{179}$$

We can start by considering the first term of the expansion,

$$\mathcal{H}_\varepsilon^{(1)} = \mathcal{D} \left[ \int \frac{d\varepsilon}{-2\pi i} \mathcal{F}^{-1} \mathcal{K}_\Delta \mathcal{F}^{-1} \right] \mathcal{I}_i, \tag{180}$$

where the  $\varepsilon$  integral is within the square brackets, since it is surrounded by equal-time quantities (without any relative-energy dependence, cf. Eqs. (168) and (169)). Eq. (180) can be considered as the next-order term to the known relation, Eq. (165),

$$\int \frac{d\varepsilon}{-2\pi i} \mathcal{F}^{-1} = \mathcal{D}^{-1} (\mathcal{L}_{++} - \mathcal{L}_{--}). \tag{181}$$

A useful identity for the inverse of the product of the one-particle propagators:

$$\begin{aligned}
 \mathcal{F}^{-1} &= \mathcal{F}_1^{-1} \mathcal{F}_2^{-1} \\
 &= (\mathcal{F}_1^{-1} + \mathcal{F}_2^{-1}) (\mathcal{F}_1 + \mathcal{F}_2)^{-1} \\
 &= (\mathcal{F}_1^{-1} + \mathcal{F}_2^{-1}) \mathcal{D}^{-1} = \mathcal{D}^{-1} (\mathcal{F}_1^{-1} + \mathcal{F}_2^{-1})
 \end{aligned} \tag{182}$$

$$= (\mathcal{S}_1 + \mathcal{S}_2) \mathcal{D}^{-1} = \mathcal{D}^{-1} (\mathcal{S}_1 + \mathcal{S}_2). \tag{183}$$

Then, using Eq. (182), we can write

$$\begin{aligned}
 \mathcal{H}_\varepsilon^{(1)} &= \mathcal{D} \left[ \int \frac{d\varepsilon}{-2\pi i} \mathcal{F}^{-1} \mathcal{K}_\Delta \mathcal{F}^{-1} \right] \mathcal{I}_i \\
 &= \mathcal{D} \left[ \int \frac{d\varepsilon}{-2\pi i} \mathcal{D}^{-1} (\mathcal{F}_1^{-1} + \mathcal{F}_2^{-1}) \mathcal{K}_\Delta (\mathcal{F}_1^{-1} + \mathcal{F}_2^{-1}) \right] \mathcal{D}^{-1} \mathcal{I}_i \\
 &= \left[ \int \frac{d\varepsilon}{-2\pi i} (\mathcal{F}_1^{-1} + \mathcal{F}_2^{-1}) \mathcal{K}_\Delta (\mathcal{F}_1^{-1} + \mathcal{F}_2^{-1}) \right] \mathcal{D}^{-1} \mathcal{I}_i \\
 &= \left[ \int \frac{d\varepsilon}{-2\pi i} (\mathcal{S}_1 + \mathcal{S}_2) \mathcal{K}_\Delta (\mathcal{S}_1 + \mathcal{S}_2) \right] \mathcal{D}^{-1} \mathcal{I}_i,
 \end{aligned} \tag{184}$$

where in the last step, we used the short notation for the one-electron propagators, Eqs. (155)–(156). It is convenient to consider the propagators as the sum of electronic and positronic contributions,  $\mathcal{S}_1 = \mathcal{S}_{1+} + \mathcal{S}_{1-}$  and  $\mathcal{S}_2 = \mathcal{S}_{2+} + \mathcal{S}_{2-}$ . Even for complicated  $\mathcal{K}_\Delta$  kernels with multiple photon exchanges, remembering the sign of the imaginary component of the  $\varepsilon$  pole (positive for  $\mathcal{S}_{1-}, \mathcal{S}_{2+}$  and negative for  $\mathcal{S}_{1+}, \mathcal{S}_{2-}$ ) is useful for the identification of non-vanishing contributions. Furthermore, depending on the actual  $\mathcal{K}_\Delta$  interaction, one can make arguments (following Sucher [147] and Douglas & Kroll [149]) about the relative importance of the contribution from the electronic and positronic subspaces.

A useful relation regarding  $\mathcal{D}_i^{-1} \mathcal{I}_i \Phi_i$ :

If  $E_i$  and  $\Phi_i$  is the eigenvalue and eigenfunction of the no-pair Hamiltonian, Eq. (170), then

$$\begin{aligned}
 (\mathcal{H}_1 + \mathcal{H}_2 + \mathcal{L}_{++} \mathcal{I}_i \mathcal{L}_{++}) \Phi_i &= E_i \Phi_i \\
 \mathcal{L}_{++} \mathcal{I}_i \mathcal{L}_{++} \Phi_i &= (E_i - \mathcal{H}_1 - \mathcal{H}_2) \Phi_i \\
 (E_i - \mathcal{H}_1 - \mathcal{H}_2)^{-1} \mathcal{L}_{++} \mathcal{I}_i \mathcal{L}_{++} \Phi_i &= \Phi_i \\
 \mathcal{D}_i^{-1} \mathcal{L}_{++} \mathcal{I}_i \mathcal{L}_{++} \Phi_i &= \Phi_i \\
 \mathcal{D}_i^{-1} \mathcal{L}_{++} \mathcal{I}_i \Phi_i &= \Phi_i,
 \end{aligned} \tag{185}$$

where the last step can be made, since  $\Phi_i \in \text{Span}(\mathcal{L}_{++})$ . This relation with the  $\mathcal{D} \approx \mathcal{D}_i = E_i - \mathcal{H}_1 - \mathcal{H}_2$  approximation is used during the calculations.

To proceed, we can first consider a first-order perturbative correction to the no-pair eigenfunction (of Eq. (170)),

$$\begin{aligned}
 \langle \Phi_i | \mathcal{H}_\varepsilon^{(1)} | \Phi_i \rangle &= \langle \Phi_i | \mathcal{D} \left[ \int \frac{d\varepsilon}{-2\pi i} \mathcal{F}^{-1} \mathcal{K}_\Delta \mathcal{F}^{-1} \right] \mathcal{I}_i | \Phi_i \rangle \\
 &= \langle \Phi_i | \left[ \int \frac{d\varepsilon}{-2\pi i} (\mathcal{F}_1^{-1} + \mathcal{F}_2^{-1}) \mathcal{K}_\Delta (\mathcal{F}_1^{-1} + \mathcal{F}_2^{-1}) \right] \mathcal{D}^{-1} \mathcal{I}_i | \Phi_i \rangle \\
 &= \langle \Phi_i | \left[ \int \frac{d\varepsilon}{-2\pi i} (\mathcal{S}_1 + \mathcal{S}_2) \mathcal{K}_\Delta (\mathcal{S}_1 + \mathcal{S}_2) \right] \mathcal{D}^{-1} (\mathcal{L}_{++} + \mathcal{L}_{+-} + \mathcal{L}_{-+} + \mathcal{L}_{--}) \mathcal{I}_i | \Phi_i \rangle \\
 &\approx \langle \Phi_i | \left[ \int \frac{d\varepsilon}{-2\pi i} (\mathcal{S}_1 + \mathcal{S}_2) \mathcal{K}_\Delta (\mathcal{S}_1 + \mathcal{S}_2) \right] \mathcal{D}_i^{-1} \mathcal{L}_{++} \mathcal{I}_i | \Phi_i \rangle \\
 &= \langle \Phi_i | \left[ \int \frac{d\varepsilon}{-2\pi i} (\mathcal{S}_1 + \mathcal{S}_2) \mathcal{K}_\Delta (\mathcal{S}_1 + \mathcal{S}_2) \right] | \Phi_i \rangle \\
 &= \langle \Phi_i | \left[ \int \frac{d\varepsilon}{-2\pi i} \mathcal{L}_{++} (\mathcal{S}_1 + \mathcal{S}_2) \mathcal{K}_\Delta (\mathcal{S}_1 + \mathcal{S}_2) \mathcal{L}_{++} \right] | \Phi_i \rangle \\
 &= \langle \Phi_i | \left[ \int \frac{d\varepsilon}{-2\pi i} (\mathcal{S}_{1+} + \mathcal{S}_{2+}) \mathcal{K}_\Delta (\mathcal{S}_{1+} + \mathcal{S}_{2+}) \right] | \Phi_i \rangle, \tag{186}
 \end{aligned}$$

where we used the approximation  $\mathcal{D}^{-1} \approx \mathcal{D}_i^{-1} = (E_i - \mathcal{H}_1 - \mathcal{H}_2)^{-1}$ , and retained only the positive-energy space contribution between  $\mathcal{D}^{-1}$  and  $\mathcal{I}_i$ , furthermore, we inserted the relationship of Eq. (185), and exploited the fact that  $\Phi_i$  is the solution of the no-pair equation.

*a. Transverse and retardation correction* If we consider the solution of the no-pair DC equation,  $\Phi_i = \Phi_C$  and approximate the total energy in the correction with the no-pair DC energy,  $E \approx E_C$ , then we can proceed for  $\mathcal{K}_\Delta = \mathcal{K}_T$  (Fig. 12) by using the fact that the  $\varepsilon$  integral for the ‘homogeneous’ terms (1 + 1+ and 2 + 2+) gives zero contributions (the  $\varepsilon$ -poles are either both in the positive or in the negative imaginary half plane), and only the mixed (1 + 2+ and 2 + 1+) terms have a non-vanishing contribution,

$$\begin{aligned}
 \Delta E_{T++} &= \langle \Phi_C | \left[ \int \frac{d\varepsilon}{-2\pi i} (\mathcal{S}_{1+} + \mathcal{S}_{2+}) \mathcal{K}_T (\mathcal{S}_{1+} + \mathcal{S}_{2+}) \right] | \Phi_C \rangle \\
 &= \langle \Phi_C | \left[ \int \frac{d\varepsilon}{-2\pi i} \{ \mathcal{S}_{1+} \mathcal{K}_T \mathcal{S}_{2+} + \mathcal{S}_{2+} \mathcal{K}_T \mathcal{S}_{1+} \} \right] | \Phi_C \rangle \\
 &= \langle \Phi_C | \int \frac{d\varepsilon}{-2\pi i} \left\{ \frac{\mathcal{L}_{1+}}{\frac{E_C}{2} + \varepsilon - \mathcal{E}_1 + i\delta} \mathcal{K}_T \frac{\mathcal{L}_{2+}}{\frac{E_C}{2} - \varepsilon - \mathcal{E}_2 + i\delta} \right. \\
 &\quad \left. + \frac{\mathcal{L}_{2+}}{\frac{E_C}{2} - \varepsilon - \mathcal{E}_2 + i\delta} \mathcal{K}_T \frac{\mathcal{L}_{1+}}{\frac{E_C}{2} + \varepsilon - \mathcal{E}_1 + i\delta} \right\} | \Phi_C \rangle. \tag{187}
 \end{aligned}$$

Furthermore,  $\mathcal{L}_{1+}$  and  $\mathcal{L}_{2+}$  can be suppressed next to the  $\Phi_C$  no-pair wave function (and we assume  $z_1 z_2 = +1$  for simplicity),

$$\begin{aligned}
 \Delta E_{T++}^{(12)} &= \langle \Phi_C | \int \frac{d\varepsilon}{-2\pi i} \frac{\mathcal{L}_{1+}}{\frac{E_C}{2} + \varepsilon - \mathcal{E}_1 + i\delta} \mathcal{K}_T \frac{-\mathcal{L}_{2+}}{\frac{E_C}{2} + \varepsilon + \mathcal{E}_2 - i\delta} | \Phi_C \rangle \\
 &= \frac{\alpha}{2\pi^2} \int d\mathbf{k} \int \frac{d\omega}{-2\pi i} \langle \Phi_C | \int \frac{d\varepsilon}{-2\pi i} \frac{1}{\varepsilon + \frac{E_C}{2} - \mathcal{E}_1 + i\delta} \frac{\tilde{\alpha}_1^i \tilde{\alpha}_2^j}{\omega^2 - \mathbf{k}^2 + i\Delta} \eta(\mathbf{k}, \omega) \frac{-1}{\varepsilon - \frac{E_C}{2} + \mathcal{E}_2 - i\delta} | \Phi_C \rangle \\
 &= \frac{\alpha}{2\pi^2} \int d\mathbf{k} \int \frac{d\omega}{-2\pi i} \langle \Phi_C | \eta_2(-\mathbf{k}) \tilde{\alpha}_2^j \frac{1}{\omega^2 - \mathbf{k}^2 + i\Delta} \left[ \int \frac{d\varepsilon}{-2\pi i} \frac{1}{\varepsilon + \frac{E_C}{2} - \mathcal{E}_1 + i\delta} \frac{-1}{\varepsilon - \omega - \frac{E_C}{2} + \mathcal{E}_2 - i\delta} \right] \tilde{\alpha}_1^i \eta_1(\mathbf{k}) | \Phi_C \rangle \\
 &\quad \varepsilon = -\frac{E_C}{2} + \mathcal{E}_1 - i\delta \\
 &= \frac{\alpha}{2\pi^2} \int d\mathbf{k} \int \frac{d\omega}{-2\pi i} \langle \Phi_C | \frac{2\pi i}{-2\pi i} \eta_2(-\mathbf{k}) \tilde{\alpha}_2^j \frac{1}{\omega^2 - \mathbf{k}^2 + i\Delta} \frac{-1}{-\frac{E_C}{2} + \mathcal{E}_1 - \omega - \frac{E}{2} + \mathcal{E}_2} \tilde{\alpha}_1^i \eta_1(\mathbf{k}) | \Phi_C \rangle \\
 &= -\frac{\alpha}{2\pi^2} \int d\mathbf{k} \int \frac{d\omega}{-2\pi i} \langle \Phi_C | \eta_2(-\mathbf{k}) \tilde{\alpha}_2^j \frac{1}{\omega^2 - \mathbf{k}^2 + i\Delta} \frac{1}{E_C - \mathcal{E}_1 - \mathcal{E}_2 + \omega} \tilde{\alpha}_1^i \eta_1(\mathbf{k}) | \Phi_C \rangle. \tag{188}
 \end{aligned}$$

Then, we proceed along the counter-clockwise integration contour for calculating the  $\omega$  integral in Eq. (188), and find one pole at  $\omega = -k(+i\Delta)$  with  $k = |\mathbf{k}|$ , and thus, obtain,

$$\begin{aligned}
 \Delta E_{T++}^{(12)} &= -\frac{\alpha}{2\pi^2} \int d\mathbf{k} \frac{2\pi i}{-2\pi i} \langle \Phi_C | \eta_2(-\mathbf{k}) \tilde{\alpha}_2^j \frac{1}{2k} \frac{1}{E_C - \mathcal{E}_1 - \mathcal{E}_2 - k} \tilde{\alpha}_1^i \eta_1(\mathbf{k}) | \Phi_C \rangle \\
 &= \frac{\alpha}{2\pi^2} \int d\mathbf{k} \frac{1}{2k} \langle \Phi_C | \eta_2(-\mathbf{k}) \tilde{\alpha}_2^j \frac{1}{E_C - \mathcal{H}_0 - k} \tilde{\alpha}_1^i \eta_1(\mathbf{k}) | \Phi_C \rangle, \tag{189}
 \end{aligned}$$

where  $\mathcal{H}_0 = \mathcal{H}_1 + \mathcal{H}_2$  is the non-interacting two-particle Hamiltonian. A similar calculation can be carried out for

exchanged 1 and 2, and thus, the full, positive-energy transverse correction to the no-pair DC wave function is

$$\Delta E_{T_{++}} = \frac{\alpha}{2\pi^2} \int d\mathbf{k} \frac{1}{2k} \langle \Phi_C | \left\{ \tilde{\alpha}_2^i \eta_2(-\mathbf{k}) \frac{1}{E_C - \mathcal{H}_0 - k} \eta_1(\mathbf{k}) \tilde{\alpha}_1^i + \tilde{\alpha}_1^i \eta_1(\mathbf{k}) \frac{1}{E_C - \mathcal{H}_0 - k} \eta_2(-\mathbf{k}) \tilde{\alpha}_2^i \right\} \Phi_C \rangle, \quad (190)$$

which reproduces Sucher's result, Eq. (5.26) of Ref. [147].

With further manipulation, Sucher obtained the Coulomb ladder correction to  $T_{++}$  resulting in the appearance of the interacting no-pair DC Hamiltonian in the resolvent,

$$\Delta E_{T(C)_{++}} = \frac{\alpha}{2\pi^2} \int d\mathbf{k} \frac{1}{2k} \langle \Phi_C | \left\{ \tilde{\alpha}_2^i \eta_2(-\mathbf{k}) \frac{1}{E_C - \mathcal{H}_C - k} \eta_1(\mathbf{k}) \tilde{\alpha}_1^i + (1 \leftrightarrow 2) \right\} \Phi_C \rangle. \quad (191)$$

The important part of this correction is due to the retardation of the interaction, which can be obtained by separating the instantaneous part according to (p. 75 of Ref. [147])

$$\frac{1}{E_C - \mathcal{H}_C - k} = -\frac{1}{k} + \frac{1}{k} \frac{E_C - \mathcal{H}_C}{E_C - \mathcal{H}_C - k}, \quad (192)$$

where the first term gives rise to the Breit operator (*cf.*, Eq. (133)–(134)),

$$B = -\frac{\alpha}{2\pi^2} \int d\mathbf{k} \frac{1}{k^2} \tilde{\alpha}_1^i \tilde{\alpha}_2^i \eta_1(\mathbf{k}) \eta_2(-\mathbf{k}) \quad (193)$$

and the second term gives the perturbative retardation correction,

$$\Delta E_{\text{ret}} = \frac{\alpha}{2\pi^2} \int d\mathbf{k} \frac{1}{2k^2} \langle \Phi_C | \tilde{\alpha}_1^i \eta_1(\mathbf{k}) \frac{E_C - \mathcal{H}_C}{E_C - \mathcal{H}_C - k} \tilde{\alpha}_2^i \eta_2(-\mathbf{k}) \Phi_C \rangle + (1 \leftrightarrow 2). \quad (194)$$

In 1958, Sucher did not have access to the numerical solution of the no-pair DC equation, so he introduced a series of approximations (including the Pauli approximation) to have final expressions for the non-relativistic wave function. Nowadays, computer power allows us to compute and converge to 'high precision' the numerical solution of the no-pair eigenvalue equation (Sec. III D), so it is a challenge to develop algorithms and computational procedures using an accurate relativistic wave function for the evaluation of perturbative corrections of  $\mathcal{H}_\Delta$ .

For future research, it will be a task to find practical expressions and procedures for the evaluation of the correction terms. Since the correction terms are written in an operator form (without making assumptions about using some special, *e.g.*, one-particle, basis representation), it remains a technical and computational task to evaluate the integrals for a basis representation allowing high-precision numerical results (Secs. III D and III E). For general, many-(two-) particle basis functions it may turn out to be convenient to group certain terms together (*e.g.*, retardation and self energy), which would otherwise be evaluated separately (*i.e.*, in computations with one-particle basis functions).

*b. Initial thoughts about crossed photon corrections*  $\mathcal{K}_{C \times C}$  is the simplest crossed-photon correction (Fig. 12). Using Sucher's rules (Sec. III B 3), we can formulate the correction integral to first-order perturbation theory (and using the  $E \approx E_i$  approximation),

$$\begin{aligned} \Delta E_{C \times C} &= \langle \Phi_i | \left[ \int \frac{d\varepsilon}{-2\pi i} (S_{1+} + S_{2+}) \mathcal{K}_{C \times C} (S_{1+} + S_{2+}) \right] \Phi_i \rangle \\ &= \int \Phi_C^\dagger(\mathbf{p}_1, \mathbf{p}_2) \int \frac{d\varepsilon}{-2\pi i} \frac{d\omega}{-2\pi i} \frac{d\omega'}{-2\pi i} [S_{1+}(p_1) + S_{2+}(p_2)] \\ &\quad S_1(p_1 - k) S_2(p_2 + k') \kappa_C(\mathbf{k}) \kappa_C(\mathbf{k}') \eta(k) \eta(k') \\ &\quad [S_{1+}(p_1) + S_{2+}(p_2)] \Phi_C(\mathbf{p}_1, \mathbf{p}_2) d\mathbf{k} d\mathbf{k}' d\mathbf{p}_1 d\mathbf{p}_2, \end{aligned} \quad (195)$$

which can be simplified by repeated use of the residue theorem [147]. Direct evaluation (or possible approximation) of the remaining integrals is a future task for precise no-pair wave functions computed by numerical solution of the no-pair wave equation (Secs. III D–III E).

#### D. Numerical solution of the no-pair Dirac–Coulomb–Breit eigenvalue equation

This section provides a brief overview of the practical aspects for solving the no-pair Dirac–Coulomb or Dirac–Coulomb–Breit equation with explicitly correlated trial functions [174–177]. Explicitly correlated, *i.e.*,



two-particle, basis functions make it possible in practice to converge the energy to a precision where comparison of the sixteen-component results with precise and accurate perturbative computations (non-relativistic QED) established in relation with precision spectroscopy is interesting and has been unexplored until recently. For the sake of this comparison, we focus on atoms and molecules of light elements, but in principle, the theoretical and algorithmic framework presented in this work is not limited to low  $Z$  systems (unlike finite-order nrQED).

Starting from this section, we replace the natural units ( $\hbar = c = \epsilon_0 = 1$ ), used in the previous section and common in molecular physics, with Hartree atomic units ( $\hbar = e = 1/(4\pi\epsilon_0) = m_e = 1$ ), convenient for quantum chemistry computations. We also note that it is not assumed that the mass of the spin-1/2 particles equals the electron mass, and so, we continue to explicitly write out the particle mass.

Furthermore, the practical solution of the no-pair wave equation, Eq. (170), is carried out in coordinate space, instead of using the momentum-space representation, which was useful for writing down the interactions (Sec. III B 3) and working with the propagators (Secs. III B 4).

*a. No-pair Hamiltonian* In the coordinate-space representation, the no-pair Dirac–Coulomb–Breit (DCB) Hamiltonian, Eq. (170), is

$$H^{[16]} = \mathcal{L}_{++}^{[16]} \left( H_1^{[4]} \boxtimes I^{[4]} + I^{[4]} \boxtimes H_2^{[4]} + V I^{[16]} + B^{[16]} \right) \mathcal{L}_{++}^{[16]}, \quad (196)$$

where we wrote the projectors around the entire operator, not only around the interaction, so, we can deal with only the positive-energy block, which was decoupled from the Brown–Ravenhall (+– and –+) and negative-energy (––) blocks already in Eq. (170).

$H_i^{[4]}$  ( $i = 1, 2$ ) is the single-particle Dirac Hamiltonian of Eq. (85) shifted by the  $m_i c^2$  rest energy,

$$H_i^{[4]} = c(\boldsymbol{\alpha}^{[4]} \cdot \mathbf{p}_i) + (\beta^{[4]} - I^{[4]})m_i c^2 + U_i I^{[4]}, \quad (197)$$

and the  $U_i$  external potential is due to the nuclei with  $Q_A = Z_A$  electric charge, fixed at position  $\mathbf{R}_A$ ,

$$U_i = \sum_{A=1}^{N_{\text{nuc}}} \frac{z_i Z_A}{|\mathbf{r}_i - \mathbf{R}_A|}, \quad (198)$$

and  $z_i$  refers to the electric charge of  $i$ th active particle.

The third term of  $H^{[16]}$  stands for the Coulomb interaction of the particles (with  $r_{12} = |\mathbf{r}_1 - \mathbf{r}_2|$ )

$$V I^{[16]} = \frac{Z_1 Z_2}{r_{12}} I^{[16]}, \quad (199)$$

while the last term represents the instantaneous Breit interaction in coordinate representation, cf. Eq. (133)–(134) and (193):

$$B^{[16]} = -\frac{Z_1 Z_2}{2r_{12}} \left[ \boldsymbol{\alpha}^{[4]} \boxtimes \boldsymbol{\alpha}^{[4]} + \frac{1}{r_{12}^2} (\boldsymbol{\alpha}^{[4]} \cdot \mathbf{r}_{12}) \boxtimes (\boldsymbol{\alpha}^{[4]} \cdot \mathbf{r}_{12}) \right]. \quad (200)$$

The symbol  $\boxtimes$  stands for a block-wise direct product (also called Tracy–Singh product [193–196]), which allows us to retain in the many-particle quantities the block structure of the one-particle Dirac matrix expressed with the  $\sigma_i$  ( $i = 1, 2, 3$ ) Pauli matrices,

$$\alpha_i^{[4]} = \begin{pmatrix} 0^{[2]} & \sigma_i^{[2]} \\ \sigma_i^{[2]} & 0^{[2]} \end{pmatrix} \quad \text{and} \quad \beta^{[4]} = \begin{pmatrix} I^{[2]} & 0^{[2]} \\ 0^{[2]} & -I^{[2]} \end{pmatrix}. \quad (201)$$

Furthermore, we explicitly indicate the ( $k \times k$ ) dimensionality of the matrices by the  $[k]$  superscript. For the numerical implementation, we write the Hamiltonian with the  $\sigma_i$  Pauli matrices,

$$H(1, 2) = \mathcal{L}_{++}^{[16]} \begin{pmatrix} V_1^{[4]} + U_1^{[4]} & c\boldsymbol{\sigma}_2^{[4]} \cdot \mathbf{p}_2 & c\boldsymbol{\sigma}_1^{[4]} \cdot \mathbf{p}_1 & B^{[4]} \\ c\boldsymbol{\sigma}_2^{[4]} \cdot \mathbf{p}_2 & V_1^{[4]} + (U - 2m_2 c^2)1^{[4]} & B^{[4]} & c\boldsymbol{\sigma}_1^{[4]} \cdot \mathbf{p}_1 \\ c\boldsymbol{\sigma}_1^{[4]} \cdot \mathbf{p}_1 & B^{[4]} & V_1^{[4]} + (U - 2m_1 c^2)1^{[4]} & c\boldsymbol{\sigma}_2^{[4]} \cdot \mathbf{p}_2 \\ B^{[4]} & c\boldsymbol{\sigma}_1^{[4]} \cdot \mathbf{p}_1 & c\boldsymbol{\sigma}_2^{[4]} \cdot \mathbf{p}_2 & V_1^{[4]} + (U - 2m_2 c^2)1^{[4]} \end{pmatrix} \mathcal{L}_{++}^{[16]}, \quad (202)$$

where neglecting the  $B$  Breit term (zeroing the anti-diagonal blocks) defines the no-pair Dirac–Coulomb (DC) Hamiltonian,  $H_{\text{DC}}^{[16]}$ .

Regarding the  $\mathcal{L}_{++}^{[16]}$  projector, it is important to remember that the two-particle Dirac operator with instantaneous (Coulomb or Coulomb–Breit) interactions emerges from the Bethe–Salpeter equation with the  $\mathcal{L}_{++}^{[16]}$  operator projecting

onto the positive-energy states of the non-interacting problem (Sec. III B 4). In this context, a two-particle operator without this projector appears to be an *ad hoc* construct without simple connection to quantum electrodynamics.

*b. Kinetic balance condition and its implementation as a metric* The no-pair Hamiltonian, Eq. (196), is bounded from below, and thus, development of (precise) variational procedures to solve its eigenvalue equation is highly relevant for practical application of the theory. To define a good basis set, it is important to ensure a faithful matrix representation of the  $\mathbf{p}_i^2 = \mathbf{p}_i \cdot \mathbf{p}_i$  identity [197]. During our work, fulfillment of this relation is ensured by using the so-called ‘restricted kinetic balance’ condition, relying on the  $(\boldsymbol{\sigma}^{[2]} \cdot \mathbf{a})(\boldsymbol{\sigma}^{[2]} \cdot \mathbf{b}) = (\mathbf{a} \cdot \mathbf{b})I^{[2]} + i(\mathbf{a} \times \mathbf{b})\boldsymbol{\sigma}^{[2]}$  property of the Pauli matrices,

$$X_i^{[4]} = \begin{bmatrix} I^{[2]} & \mathbf{0}^{[2]} \\ \mathbf{0}^{[2]} & \frac{(\boldsymbol{\sigma}^{[2]} \cdot \mathbf{p}_i)}{2m_i c} \end{bmatrix}. \quad (203)$$

The simple generalization of this one-particle balance to the two-particle case is

$$X_{12}^{[16]} = X_1^{[4]} \otimes X_2^{[4]} = \begin{bmatrix} I^{[4]} & \mathbf{0}^{[4]} & \mathbf{0}^{[4]} & \mathbf{0}^{[4]} \\ \mathbf{0}^{[4]} & \frac{(\boldsymbol{\sigma}_2^{[4]} \cdot \mathbf{p}_2)}{2m_2 c} & \mathbf{0}^{[4]} & \mathbf{0}^{[4]} \\ \mathbf{0}^{[4]} & \mathbf{0}^{[4]} & \frac{(\boldsymbol{\sigma}_1^{[4]} \cdot \mathbf{p}_1)}{2m_1 c} & \mathbf{0}^{[4]} \\ \mathbf{0}^{[4]} & \mathbf{0}^{[4]} & \mathbf{0}^{[4]} & \frac{(\boldsymbol{\sigma}_1^{[4]} \cdot \mathbf{p}_1)(\boldsymbol{\sigma}_2^{[4]} \cdot \mathbf{p}_2)}{4m_1 m_2 c^2} \end{bmatrix}, \quad (204)$$

where  $\boldsymbol{\sigma}_1^{[4]} = \boldsymbol{\sigma}^{[2]} \otimes I^{[2]}$  and  $\boldsymbol{\sigma}_2^{[4]} = I^{[2]} \otimes \boldsymbol{\sigma}^{[2]}$  and  $\otimes$  denotes the usual Kronecker product.

We have implemented the kinetic balance condition in an operator form, *i.e.*, as a ‘metric’, [174–177, 196, 198]

$$H_{\text{KB}}^{[16]} = X_{12}^{[16]\dagger} H^{[16]} X_{12}^{[16]} \quad \text{and} \quad I_{\text{KB}}^{[16]} = X_{12}^{[16]\dagger} X_{12}^{[16]}, \quad (205)$$

and detailed operator expressions can be found in Refs. [174–177].

*c. Spatial and spinor basis* Finding the spectrum of  $H^{[16]}$  (in the X-KB metric) numerically requires a finite set of basis functions, which we first define as the product of a (two-particle) spatial function and an elementary spinor (vector),

$$|\chi_{iq}^{(16)}\rangle = \varphi_i |e_q^{(16)}\rangle. \quad (206)$$

Regarding the spatial part, two-particle functions can be efficiently represented in the floating explicitly correlated Gaussian (ECG) basis [13, 196, 199],

$$\varphi_i(\mathbf{r}_1, \mathbf{r}_2) = \exp\left[-(\mathbf{r} - \mathbf{s}_i)^T (\mathbf{A}_i^{[2]} \otimes I^{[3]})(\mathbf{r} - \mathbf{s}_i)\right], \quad i = 1, \dots, N_b, \quad (207)$$

where  $\mathbf{r} = (\mathbf{r}_1, \mathbf{r}_2)^T \in \mathbb{R}^6$ . The  $\mathbf{s}_i \in \mathbb{R}^6$  shift vector and the positive-definite  $\mathbf{A}_i^{[2]}$  matrix elements are parameters of each ECG to be determined via variational optimization (*vide infra*). The main advantage of working with ECGs lies in the fact that ECG matrix elements of various operators can be calculated analytically.

Regarding the spinor part,  $4^2 = 16$  elementary spinors can be constructed, they are of the form

$$|e_q^{(16)}\rangle = |\lambda(1)\rangle \otimes |\lambda(2)\rangle \otimes |\sigma_m(1)\rangle \otimes |\sigma_m(2)\rangle, \quad q = 1, \dots, 16, \quad (208)$$

with  $\lambda = l, s$  (corresponding to the large and small components) and  $m = \pm 1/2$  (corresponding to the spin projection,  $s_z$ ),

$$|l\rangle = \begin{bmatrix} 1 \\ 0 \end{bmatrix}, \quad |s\rangle = \begin{bmatrix} 0 \\ 1 \end{bmatrix} \quad \text{and} \quad |\sigma_{+\frac{1}{2}}\rangle = \begin{bmatrix} 1 \\ 0 \end{bmatrix}, \quad |\sigma_{-\frac{1}{2}}\rangle = \begin{bmatrix} 0 \\ 1 \end{bmatrix}. \quad (209)$$

In Eq. (208), the ‘(1)’ and ‘(2)’ symbols are shown to highlight the particle index, which is defined by the position of the vector in the Kronecker product.

Instead of the elementary spin representation, we can use a spinor basis which is adapted to the two-particle spin eigenstates ( $S = 0, M_S = 0$  singlet and  $S = 1, M_S = 0, +1, -1$  triplet), *i.e.*,

$$|\tilde{e}_q^{(16)}\rangle = \varphi_i |\tilde{e}_q^{(16)}\rangle \quad (210)$$

with

$$|\tilde{e}_q^{(16)}\rangle = |\lambda(1)\rangle \otimes |\lambda(2)\rangle \otimes |\Sigma_{S, M_S}(1, 2)\rangle, \quad q = 1, \dots, 16, \quad (211)$$

and

$$|\Sigma_{0,0}\rangle = \frac{1}{\sqrt{2}} \begin{bmatrix} 0 \\ 1 \\ -1 \\ 0 \end{bmatrix}, \quad |\Sigma_{1,0}\rangle = \frac{1}{\sqrt{2}} \begin{bmatrix} 0 \\ 1 \\ 1 \\ 0 \end{bmatrix}, \quad |\Sigma_{1,+1}\rangle = \begin{bmatrix} 1 \\ 0 \\ 0 \\ 0 \end{bmatrix}, \quad |\Sigma_{1,-1}\rangle = \begin{bmatrix} 0 \\ 0 \\ 0 \\ 1 \end{bmatrix}. \quad (212)$$

Spin-adapted functions are useful both from an interpretational and also from a practical point of view, as they make a direct connection with non-relativistic results. This direct connection to non-relativistic computations can be exploited for systems in which relativistic effects are small and the non-relativistic basis parameterization provides a good starting point for relativistic computations [174–178].

*d. Symmetry-adaptation of the basis* For identical spin-1/2 fermions, anti-symmetrized basis functions must be used,

$$|\psi_{iq}^{(16)}\rangle = \mathcal{A}^{[16]} |\chi_{iq}^{(16)}\rangle, \quad (213)$$

where the  $\mathcal{A}^{[16]}$  anti-symmetrizer acts both on the coordinate and spinor space [174, 175],

$$\mathcal{A}^{[16]} = \frac{1}{2} [I^{[16]} - (P^{[4]} \otimes P^{[4]})\mathcal{P}_{12}] = \frac{1}{2} \begin{bmatrix} I^{[4]} - P^{[4]}\mathcal{P}_{12} & 0^{[4]} & 0^{[4]} & 0^{[4]} \\ 0^{[4]} & I^{[4]} & -P^{[4]}\mathcal{P}_{12} & 0^{[4]} \\ 0^{[4]} & -P^{[4]}\mathcal{P}_{12} & I^{[4]} & 0^{[4]} \\ 0^{[4]} & 0^{[4]} & 0^{[4]} & I^{[4]} - P^{[4]}\mathcal{P}_{12} \end{bmatrix}, \quad (214)$$

where  $\mathcal{P}_{12}$  exchanges coordinate space labels and

$$P^{[4]} = \begin{bmatrix} 1 & 0 & 0 & 0 \\ 0 & 0 & 1 & 0 \\ 0 & 1 & 0 & 0 \\ 0 & 0 & 0 & 1 \end{bmatrix} \quad (215)$$

acts on the spinor components. In particular,  $(P^{[4]}\mathcal{P}_{12})(\sigma_1^{[4]} \cdot \mathbf{p}_1) = P^{[4]}(\sigma_1^{[4]} \cdot \mathbf{p}_2)\mathcal{P}_{12} = (\sigma_2^{[4]} \cdot \mathbf{p}_2)(P^{[4]}\mathcal{P}_{12})$ . In two-particle computations with different spin-1/2 particles, the anti-symmetrization step is, of course, omitted [179].

Furthermore, if the system in consideration possesses additional spatial symmetries carried by elements of point group  $G$ , then, it is useful to adapt the basis functions also to these symmetries. A  $P_G^{[16]}$  operation projecting onto an irreducible representation of  $G$  can be realized by accounting for both the spatial and spin part of the problem [175, 178].

*e. A variational procedure* We approximate eigenfunctions of  $H^{[16]}$  in the  $\{|\psi_{iq}^{(16)}\rangle\}$  basis by the linear combination,

$$|\Psi\rangle = \sum_{i=1}^{N_b} \sum_{q=1}^{16} c_{iq} |\psi_{iq}^{(16)}\rangle, \quad (216)$$

which results in the generalized eigenvalue equation,

$$\mathbf{Hc} = \mathbf{E}\mathbf{S}\mathbf{c}, \quad (217)$$

where the Hamiltonian and the overlap matrix elements are calculated as

$$(\mathbf{H})_{jp,iq} = \langle \psi_{jp}^{(16)} | H_{\text{KB}}^{[16]} | \psi_{iq}^{(16)} \rangle \quad \text{and} \quad (\mathbf{S})_{jp,iq} = \langle \psi_{jp}^{(16)} | I_{\text{KB}}^{[16]} | \psi_{iq}^{(16)} \rangle. \quad (218)$$

This is a linear variational problem for the  $c_{iq}$  coefficients and a non-linear variational problem for the basis function parameters,  $\{\mathbf{A}_i^{[2]}, \mathbf{s}_i\}$ . The coefficients are found by solving Eq. (217) with a given set of parameters, and the parameters can be refined by minimization of the energy for a selected eigenstate. This optimization procedure, along with (analytic) evaluation of ECG integrals has been implemented in the QUANTEN program package [13, 19, 174–177, 200–204].

For calculating the matrix elements of Eq. (218), the positive-energy projection of the Hamiltonian must be carried out. The matrix representation of the  $\mathcal{L}_{++}^{[16]}$  projector is constructed by using the positive-energy eigenstates of the non-interacting two-particle Hamiltonian,  $H_1^{[4]} \boxtimes I^{[4]} + I^{[4]} \boxtimes H_2^{[4]}$ , represented as a matrix over the actual basis space [174–177, 179]. Selection of the ‘positive-energy’ two-electron states can be realized approximately by ‘cutting’ the non-interacting spectrum based on some energetic condition [174, 175], or more precisely, by rotating the spectrum to the complex plane via complex rescaling of the electron coordinates. This complex rotation (CR) allows us to distinguish three different ‘branches’ of the non-interacting two-electron system (positive-, Brown–Ravenhall, and negative-energy states), in principle, for any finite rotation angle [205]. In practice, an optimal range for the angle can be found by some

numerical experimentation (considering the finite precision arithmetic and the finite basis set size). For the low- $Z$  end of the helium isoelectronic series, the cutting and the CR approaches resulted in practically identical energies, with a relative difference (much) less than one parts-per-billion (ppb) [174, 175].

*f. Perturbative inclusion of  $B^{[16]}$*  Since the energetic contribution of the Breit to Coulomb interaction is small, the  $B^{[16]}$  term of the DCB Hamiltonian can be treated as a perturbation to the DC problem, which corresponds to the  $H^{[16]} = H_{\text{DC}}^{[16]} + \mathcal{L}_{++}^{[16]} B^{[16]} \mathcal{L}_{++}^{[16]}$  partitioning. The Rayleigh–Schrödinger-type perturbative corrections to the DC energy (up to first or second order) [176, 177] are evaluated as

$$E_{\text{DC(B)},n}^{++} = E_{\text{DC},n}^{++} + \langle \Psi_n | B_{\text{KB}}^{[16]} | \Psi_n \rangle, \quad (219)$$

and

$$\mathcal{P}_n^{(2)}\{\text{B}\} = E_{\text{DC},n}^{++} + \langle \Psi_n | B_{\text{KB}}^{[16]} | \Psi_n \rangle - \sum_{k \neq n} \frac{|\langle \Psi_k | B_{\text{KB}}^{[16]} | \Psi_n \rangle|^2}{E_{\text{DC},k}^{++} - E_{\text{DC},n}^{++}}, \quad (220)$$

where  $\{|\Psi_n\rangle\}$  and  $E_{\text{DC},n}^{++}$  are eigenfunctions and eigenvalues of the no-pair DC Hamiltonian, and  $B_{\text{KB}}^{[16]} = X_{12}^{[16]\dagger} B^{[16]} X_{12}^{[16]}$ . Brown–Ravenhall states do not require any further caution in the perturbative calculations either, since the  $\Psi_n$  zeroth-order states are within the positive-energy ( $++$ ) space.

For low nuclear charge numbers (low  $Z$ ), the (second-order) perturbative and variational inclusion of the Breit interaction resulted in very small energy differences (on the order of a few ppb relative difference) [176, 177], which means that the one- and two-Breit photon exchange dominates the ‘magnetic part’ of the interaction. For higher values of the nuclear charge, the difference between the two approaches is anticipated to be larger (to be explored in later work), as higher-order perturbative corrections become more important. These effects are automatically included in the variational solution, which, after all, can be thought of as the infinite-order summation of ladder diagrams.

On the other hand, it is interesting to note that higher-order corrections due to the ‘Coulomb ladder’ are significant already beyond  $Z = 1$  [175] (Sec. III E 1), which indicates the relevance of the development of a variational relativistic procedure.

*g. Extension to a pre-Born–Oppenheimer relativistic framework* We have originally formulated and implemented the equations for two-electron systems with fixed external charges, *i.e.*, for Born–Oppenheimer-like relativistic computations [174–177]. Most recently, it became possible to generalize these ideas to two-particle systems without external charges, *i.e.*, pre-Born–Oppenheimer-like [15, 16, 19, 20] relativistic computations, by using a center-of-momentum frame, by considering the operators and definition of the projector according to Sec. III B 4, which result in the emergence of a sixteen-component no-pair DC(B) Hamiltonian for the relative (internal) motion. The formalism, implementation details, and numerical results, tested with respect to available perturbative corrections according to Sec. III E, are reported in Ref. [179].

## E. An overview of numerical results

Before our work, a few ‘high-precision’ Dirac–Coulomb computations have been reported in the literature for helium-like ions [135, 196, 205, 206], but the different computational procedures (with slightly different technical and theoretical details) delivered (slightly) different numerical results. Direct (and useful) comparison of these results with high-precision atomic experiments was not possible due to other, important missing (*e.g.*, radiative and nuclear recoil) corrections.

At the same time, many questions and concerns appeared in the literature regarding the Dirac–Coulomb(–Breit) ‘model’ taken as a ‘starting point’ and its use in a variational-type approach [135, 136, 205, 207–209], the role and the correct form of the kinetic balance condition [196, 208, 209], the ‘choice’ of a good projector for correlated computations [205, 206, 210]. There had been even more controversy (and fewer solid data or formal result) regarding the inclusion of the Breit interaction in a variational treatment. Most of the observations have their own right in their own context, but the literature was very fragmented and the proper origins for a Dirac–Coulomb-based variational-type procedure with potential utility for precision spectroscopy had been obscure. At the same time, it is important to add that (various) Dirac–Coulomb(–Breit) Hamiltonian-based computational procedures have already been successfully used for compounds of heavier elements in relativistic quantum chemistry and in relation with (lower) chemical energy resolution, *e.g.*, [171, 172].

We have in mind (high) precision spectroscopy experiments for ‘calculable’ systems, calculable to an in principle ‘arbitrary’ precision, if the fundamental equations are known. So, we have had anticipated that a precise solution of some (appropriate) variant of a DC(B)-type wave equation is an important step, but it is at most halfway to the solution of the full problem, *i.e.*, for delivering values for direct comparison with precision spectroscopy experiments. For this reason, it was of utmost importance to find good anchors for our work to established results and to the (more) complete

theory, *i.e.*, relativistic quantum electrodynamics.

The primary and essential ‘anchor’ for our work was, of course, the connection to the field theoretic Bethe–Salpeter equation that was reviewed in Sec. III B. This formal connection clearly defines the form of the operator, the projector, and the (wave) equation which we solve, as well as, in principle, all correction terms due to retardation, pair, and radiative effects.

In addition to this formal ‘benchmark’, it was necessary to establish numerical benchmarks to be able to check ‘intermediate’ numerical results. Extensive testing of numerical results became possible by finding connections to (part of) the already established perturbative relativistic and QED approach based on a non-relativistic reference. This perturbative route, sometimes called non-relativistic QED (nrQED), is currently the state of the art for compounds of light elements, which are ‘calculable’ systems to an almost ‘arbitrary precision’, and has been extensively tested in relation with precision spectroscopy experiments [211–217]. The fundamental limitation of nrQED is connected with the finite-order of the available corrections in  $\alpha$  (including also  $Z\alpha$ ), which limits the overall accuracy of the results, and this limitation provided the motivation for the present research program.

### 1. Variational vs. perturbation theory: perturbative benchmark for the no-pair energies through $\alpha$ scaling

Using a computer implementation of the algorithmic details summarized in Sec. III D, we computed the no-pair DC and DCB energies for a series of two-electron atomic and molecular systems with fixed nuclei [174–177], as well as for two-particle positronium-like systems without external charges [179]. Are these numerical results correct? Do they (with the corresponding wave functions) represent a solid intermediate step for further potential computation of increasingly accurate relativistic QED energies for these systems? Direct comparison with experiment, due to missing corrections carried by  $\mathcal{H}_\Delta$  (and the nuclear motion for the BO-type computations), is not relevant at the current stage. Numerical results of (more) ‘complete’ nrQED computations have been extensively tested with respect to experiments, and apart from known (and conjectured) limitations of the nrQED framework, these results provide us current numerical benchmarks.

At the same time, comparison of our variational no-pair Dirac–Coulomb(–Breit) energies with nrQED is not immediately obvious. In nrQED, the total (electronic) energy is written as the sum of the non-relativistic (nr) energy and correction terms for increasing orders of the  $\alpha$  fine-structure constant,

$$E = \underline{E}_{\text{nr}} + \alpha^2 \underline{\varepsilon}_2 + \alpha^3 \underline{\varepsilon}_3 + \alpha^4 \underline{\varepsilon}_4 + \alpha^5 \underline{\varepsilon}_5 + \dots \quad (221)$$

The  $\varepsilon_2$  correction has been known as the Breit–Pauli Hamiltonian expectation value basically since Breit’s work during 1928–1931 [8–10, 132], the complete  $\varepsilon_3$  correction was first reported by Araki [148] in 1957 and Sucher [147] in 1958, the  $\varepsilon_4$  correction to triplet states of helium was derived by Douglas and Kroll [149] in 1974 and also for singlet states by Yelkhovsky [159] (and computations with Korobov [160]) in 2001 and by Pachucki [158] in 2006. There are currently ongoing efforts [162, 163] for the computation of the  $\varepsilon_5$  correction to triplet states of helium-like systems. Furthermore, for comparison with experiment, the effect of the nuclear motion is also accounted for in addition to Eq. (221). A recent review provides an overview of the current status for positronium-like systems [218].

At the same time, a precise variational solution of the no-pair DCB equation provides us with the no-pair or positive-energy projected energy to all orders of  $\alpha$  (all orders of  $Z\alpha$ ), for which the following  $\alpha$  series can be formally written as

$$\underline{E}^{++} = E_{\text{nr}} + \alpha^2 \varepsilon_2 + \alpha^3 \varepsilon_3^{++} + \alpha^4 \varepsilon_4^{++} + \alpha^5 \varepsilon_5^{++} + \dots \quad (222)$$

In Eqs. (221) and (222), we underlined the quantities that are primarily computed.

In a variational computation, we obtain  $E^{++}$  to a certain numerical precision, and we want to check these computations, for *testing* the (correctness of the result of a complex) implementation and computational (work) and for gaining more *insight and understanding* to the numbers. We do not directly have access to the formal  $\alpha$  expansion of the no-pair energy (right-hand side of Eq. (222)), but by computing  $E^{++}(\alpha)$  for a series of slightly varied  $\alpha$  values, we can fit an  $\alpha$ -polynomial to the result [175, 176]. Coefficients of this fitted polynomial deliver us values for  $\varepsilon_2, \varepsilon_3^{++}, \varepsilon_4^{++}, \dots$  resulting from (a series of) variational computations, and these values can be directly compared (tested) with respect to the relevant (part of the) nrQED corrections (right-hand side of Eq. (221)).

The second-order term in Eq. (222),  $\varepsilon_2$ , is the same as in Eq. (221). Beyond second order, the  $\varepsilon_n^{++}$  term contains only part of the  $\varepsilon_n$  ‘complete’  $n$ th order nrQED contribution. Sucher calculated perturbative corrections to the non-relativistic energy [147] (in this sense, similar in spirit to nrQED), but fortunately, he reported also the no-(and single- and double-)pair part of the contributions. So, we could easily use his no-pair corrections and compare with our  $\alpha^3$ -order coefficient from variational results of helium-like ions (and two-electron molecules) [175–177]. Similar  $\alpha^3 E_n$ -order results are available for hydrogen- and positronium-like two-particle systems from Fulton and Martin [146].

All implementation details and extensive comparison with the perturbative results have been reported in Refs. [174–177], and in the more recent papers, Ref. [178] regarding triplet contributions, and in Ref. [179] about a Dirac relativistic pre-Born–Oppenheimer framework for two-particle systems without external charges.

In a nutshell, an excellent agreement of the no-pair (BO and pre-BO) variational results [174–179] is observed through the  $\alpha$  scaling procedure for a series of systems, which represents an important milestone for the development of a computational relativistic QED framework for future use in relation with precision spectroscopy.

#### F. Summary of the current status and outlook to future work

With relevance for testing and development of the fundamental theory of atomic and molecular matter, a relativistic quantum electrodynamics framework for two-spin-1/2 fermion systems (with or without external fixed nuclei) has been reviewed starting from the field theoretic Bethe–Salpeter (BS) equation. By exploiting the fact that the dominant part of the interaction (Coulomb or Coulomb–Breit) is instantaneous, it is convenient to re-write the original BS equation to an exact equal-time form, which contains the no-pair Dirac–Coulomb(–Breit) Hamiltonian and a correction term, which carries retardation, pair, and radiative corrections. Since this correction term is anticipated to be small, a perturbative treatment has been considered. Initial ideas have been reviewed for such a perturbative treatment assuming that a highly precise approximation to the DC(B) wave function, solution of the no-pair equation including the instantaneous Coulomb(–Breit) interaction ladder, is available.

For computing highly precise approximations to the no-pair DC(B) energy and wave function, implementation details have been reviewed for an explicitly correlated, variational, no-pair DC(B) computational procedure with the Born–Oppenheimer approximation as well as for extension to a pre-Born–Oppenheimer relativistic framework. The computed variational no-pair energies are tested through their  $\alpha$  fine-structure constant dependence with respect to the relevant parts of the order-by-order computed non-relativistic QED (nrQED) corrections.

Regarding future work, it is important to realize and implement the evaluation of perturbative corrections for the retardation, pair, and radiative corrections using the variational no-pair DC(B) wave functions already computed for a series of two-particle systems.

Further important work will include generalization of the theoretical framework to  $N$ -particle systems (including electron, positron, muon, and spin-1/2 nuclei), *i.e.*, which appears to be feasible through the following steps: (a) starting from an  $N$ -particle Bethe–Salpeter wave equation; (b) identification of the relevant irreducible interaction kernels; (c) exploitation of the instantaneous character of the dominant part of the interaction; (d) emergence of the  $N$ -particle no-pair DCB wave equation for the non-interacting projectors plus a correction term including integral(s) for the relative energy; (e) solution of the no-pair DCB wave equation to high precision using explicitly correlated basis functions and a variational procedure; (f) accounting for the retardation, pair, and radiative corrections by perturbation theory; (g) testing the intermediate results with respect to the relevant terms (if known) from nrQED; (+ $\diamond$ ) accounting for the motion of the nuclei (for systems with spin-1/2-nuclei, *e.g.*,  $H_2^+$ ,  $H_2$  or  $H_3^+$ ), by using a many-particle pre-Born–Oppenheimer no-pair DCB approach through generalization of Ref. [179]. At the moment, this endeavour appears to define an extensive research program. The present work reviewed a promising starting point based on the fundamental theory (QED) and outlined necessary practical steps. Various technical and conceptual difficulties can be foreseen.

Nevertheless, the success of many-particle Dirac–Coulomb(–Breit) methodologies in relativistic quantum chemistry targeting a much lower, *i.e.*, chemical energy resolution, as well as the limitations due to finite-order nrQED expressions suggest that the development of a computational relativistic QED framework, targeting the spectroscopic energy resolution for testing and further developing the fundamental theory of atomic and molecular matter, is relevant.

#### IV. IN LIEU OF A SUMMARY: QUO VADIS THEORETICAL MOLECULAR PHYSICS AND SPECTROSCOPY?

This is not the end, but a new beginning. So, I list goals and questions in relation with the presented material to be met and answered in the (near) future. I can see molecular physics and spectroscopy living its renaissance and anticipate major progress in the future along the following directions.

*a. Floppy molecular motions are the most chemically interesting, but the scaffold also matters* Floppy systems are chemically interesting, but the floppy part is most often connected to a large, semi-rigid part. This semi-rigid part is not completely rigid, complete freezing would mean a crude approximation. So, it will be important to develop quantum dynamical ‘embedding’ methods in the future.

*b. For quantum nuclear motion theory, the real challenge is the great variety of experimental applications* After all, quantum nuclear motion theory provides the link between the electronic quantities (almost correct), with experimental observables (the nuclei also move!). And there is a great variety of experiments that can probe molecular motion or use information (databases) from molecular quantum dynamics. The main challenge is to develop quantum dynamics methods that can meet all experimental requirements, in terms of energy resolution, complexity of the system, energetic-dynamical range of the experiment, etc. In any case, the present-day quantum chemistry set-up provides us with an extremely powerful modeling framework (ingeniously relying on powerful error cancellation) that we can use to explore the structure and dynamics of molecular systems to a great detail, help to explain and understand experimental observations, and produce data for use by other branches of science and technology.

c. *Will quantum computers help solving the quantum nuclear motion problem?* We will see. If we need to solve a fully coupled  $3N - 6$  dimensional problem, the answer is most likely: ‘no’. If sum of lower-mode surfaces provide a faithful representation, by some powerful and automated implementation of high-dimensional model representation, then the answer is ‘maybe’. According to some researchers, the entire electron-nucleus (pre-Born–Oppenheimer) problem should be considered on a quantum computer, since the non-relativistic molecular Hamiltonian is guaranteed to be sum of at most two-body terms. Furthermore, without introducing the BO approximation, we are freed from the trouble of having to fit, and then, integrate a multi-dimensional hypersurface. So, this is an appealing direction, but probably a very long way to go.

d. *Testing physics with atoms and molecules* We can aim for more than just modelling or reproducing or explaining experimental results. Precision spectroscopy and molecular quantum theory can, hand in hand, test and improve. To pursue this direction, we – theorists – are responsible for developing molecular quantum theory. The current challenge is to abandon the two approximations underlying present-day quantum chemistry. I foresee the development of a computational (BO or pre-BO) relativistic QED framework. It must be a proper theory with equations that remain valid over the entire periodic system (and not just a numerical recipe to compute correction terms for special systems). We have just scratched the surface (Ch. III), it is still some way to go and not without difficulties, but there will be some fruits and flowers at almost every step. Ultimately, it will bridge precision spectroscopy and relativistic quantum chemistry. And then? Well, in the one hand, we will have the best possible description of molecular matter, which can then be reliably used to study molecular systems under extreme environments, e.g., ultra-strong laser fields. Or even more interestingly, to study atoms and molecules in gravitational fields (of our Earth or in the outer space, maybe near a black hole) and think about relativistic QED and gravity...

Finally, I cite Theodor Hänsch [219]

*‘Precision measurements have always appealed to me as one of the most beautiful aspects of physics. With better measuring tools, one can look where no one has looked before. More than once, seemingly minute differences between measurement and theory have led to major advances in fundamental knowledge. The birth of modern science itself is intimately linked to the art of accurate measurements.’*

- 
- [1] M. Born and R. Oppenheimer, *Ann. der Phys.* **84**, 457 (1927).
  - [2] E. Schrödinger, *Phys. Rev.* **28**, 1049 (1926).
  - [3] W. Heisenberg, *Z. Phys.* **33**, 879 (1925).
  - [4] M. Born and P. Jordan, *Z. Phys.* **34**, 858 (1925).
  - [5] M. Born, W. Heisenberg, and P. Jordan, *Z. Phys.* **35**, 557 (1926).
  - [6] P. A. M. Dirac, *Proc. Roy. Soc. Lon. A* **117**, 610 (1928).
  - [7] P. A. M. Dirac, *Proc. Roy. Soc. Lon. A* **118**, 351 (1928).
  - [8] G. Breit, *Proc. Nat. Acad. Sci.* **14**, 553 (1928).
  - [9] G. Breit, *Phys. Rev.* **34**, 553 (1929).
  - [10] G. Breit, *Proc. Nat. Acad. Sci.* **17**, 70 (1931).
  - [11] E. Mátyus, J. Hutter, U. Müller-Herold, and M. Reiher, *Phys. Rev. A* **83**, 052512 (2011).
  - [12] E. Mátyus, J. Hutter, U. Müller-Herold, and M. Reiher, *J. Chem. Phys.* **135**, 204302 (2011).
  - [13] E. Mátyus, *Mol. Phys.* **117**, 590 (2019).
  - [14] A. J. Rocke, *Image & Reality: Kekulé, Kopp, and the Scientific Imagination (Synthesis)*, A Series in the History of Chemistry (The University of Chicago Press, Chicago and London, 2010).
  - [15] E. Mátyus, *J. Phys. Chem. A* **117**, 7195 (2013).
  - [16] E. Mátyus and M. Reiher, *J. Chem. Phys.* **137**, 024104 (2012).
  - [17] A. Muolo, E. Mátyus, and M. Reiher, *J. Chem. Phys.* **149**, 184105 (2018).
  - [18] A. Muolo, E. Mátyus, and M. Reiher, *J. Chem. Phys.* **151**, 154110 (2019).
  - [19] D. Ferenc and E. Mátyus, *Phys. Rev. A* **100**, 020501(R) (2019).
  - [20] E. Saly, D. Ferenc, and E. Mátyus, (2022), 10.48550/arXiv.2210.09653.
  - [21] E. Mátyus, A. M. S. Daría, and G. Avila, *Chem. Comm.* (in press), 10.1039/D2CC05123K.
  - [22] M. Quack, *Chimia* **55**, 753 (2001).
  - [23] M. Quack and F. Merkt, eds., *Handbook of High-resolution Spectroscopy* (John Wiley & Sons, Chichester, 2011).
  - [24] E. B. Wilson, Jr., J. C. Decius, and P. C. Cross, *Molecular Vibrations: The Theory of Infrared and Raman Vibrational Spectra* (McGraw-Hill Book Company, Inc., 1955).
  - [25] D. Papousek and M. R. Aliev, *Molecular Vibrational-rotational Spectra* (1982).
  - [26] B. Sutcliffe, “Coordinate Systems and Transformations,” in *Handbook of Molecular Physics and Quantum Chemistry*, ed. S. Wilson. Vol. 1: Fundamentals (John Wiley & Sons, Ltd., 2002) Chap. 31, pp. 485–500.
  - [27] R. G. Littlejohn and M. Reinsch, *Rev. Mod. Phys.* **69**, 213 (1997).
  - [28] C. Eckart, *Phys. Rev.* **47**, 552 (1935).
  - [29] A. Martín Santa Daría, G. Avila, and E. Mátyus, *J. Mol. Spectrosc.* **385**, 111617 (2022).
  - [30] A. Martín Santa Daría, G. Avila, and E. Mátyus, *Phys. Chem. Chem. Phys.* **23**, 6526 (2021).
  - [31] G. Avila and E. Mátyus, *J. Chem. Phys.* **150**, 174107 (2019).
  - [32] G. Avila and E. Mátyus, *J. Chem. Phys.* **151**, 154301 (2019).
  - [33] G. Avila, D. Papp, G. Czako, and E. Mátyus, *Phys. Chem. Chem. Phys.* **22**, 2792 (2020).

- [34] D. Papp, V. Tajti, G. Avila, E. Mátyus, and G. Czakó, *Mol. Phys.*, e2113565 (2022).
- [35] K. C. Thompson, M. J. T. Jordan, and M. A. Collins, *J. Chem. Phys.* **108**, 8302 (1998).
- [36] B. Podolsky, *Phys. Rev.* **32**, 812 (1928).
- [37] D. Lauvergnat, P. Felker, Y. Scribano, D. M. Benoit, and Z. Bačić, *J. Chem. Phys.* **150**, 154303 (2019).
- [38] P. M. Felker, D. Lauvergnat, Y. Scribano, D. M. Benoit, and Z. Bačić, *J. Chem. Phys.* **151**, 124311 (2019).
- [39] E. Mátyus, T. Szidarovszky, and A. G. Császár, *J. Chem. Phys.* **141**, 154111 (2014).
- [40] R. N. Zare, *Angular Momentum: Understanding Spatial Aspects in Chemistry and Physics* (Wiley-Interscience, New York, 1998).
- [41] E. Mátyus, G. Czakó, and A. G. Császár, *J. Chem. Phys.* **130**, 134112 (2009).
- [42] D. Luckhaus, *J. Chem. Phys.* **113**, 1329 (2000).
- [43] D. Lauvergnat and A. Nauts, *J. Chem. Phys.* **116**, 8560 (2002).
- [44] A. Yachmenev and S. N. Yurchenko, *J. Chem. Phys.* **143**, 014105 (2015).
- [45] R. Meyer and H. H. Günthard, *J. Chem. Phys.* **50**, 353 (1969).
- [46] R. Meyer, *J. Mol. Spectrosc.* **76**, 266 (1979).
- [47] D. Luckhaus, *J. Chem. Phys.* **118**, 8797 (2003).
- [48] S. N. Yurchenko, W. Thiel, and P. Jensen, *J. Mol. Spectrosc.* **245**, 126 (2007).
- [49] C. Fábri, E. Mátyus, and A. G. Császár, *J. Chem. Phys.* **134**, 074105 (2011).
- [50] J. Sarka and A. G. Császár, *J. Chem. Phys.* **144**, 154309 (2016).
- [51] A. Martín Santa Daría, G. Avila, and E. Mátyus, *J. Chem. Phys.* **154**, 224302 (2021).
- [52] J. Sarka, A. G. Császár, S. C. Althorpe, D. J. Wales, and E. Mátyus, *Phys. Chem. Chem. Phys.* **18**, 22816 (2016).
- [53] J. Sarka, A. G. Császár, and E. Mátyus, *Phys. Chem. Chem. Phys.* **19**, 15335 (2017).
- [54] D. Ferenc and E. Mátyus, *Mol. Phys.* **117**, 1694 (2019).
- [55] W. Ritz, *J. rein. angew. Math.* **135**, 1 (1909).
- [56] P. R. Bunker and P. Jensen, *Molecular Symmetry and Spectroscopy, 2nd Edition* (NRC Research Press, Ottawa, 1998).
- [57] S. C. Wang, *Phys. Rev.* **34**, 243 (1929).
- [58] G. H. Golub and J. H. Welsch, *Math. Comp.* **23**, 221 (1969).
- [59] V. Szalay, *J. Chem. Phys.* **105**, 6940 (1996).
- [60] Z. Bacic and J. C. Light, *J. Chem. Phys.* **85**, 4594 (1986).
- [61] J. C. Light and T. Carrington Jr., “Discrete-Variable Representations and their Utilization,” in *Adv. Chem. Phys.* (John Wiley & Sons, Ltd, 2000) Chap. 14, pp. 263–310.
- [62] X.-G. Wang and T. Carrington Jr, *J. Chem. Theo. Comp.* **2**, 599 (2003).
- [63] X.-G. Wang and J. T. Carrington, *J. Chem. Phys.* **154**, 124112 (2021).
- [64] G. Schiffel and U. Manthe, *Chem. Phys.* **374**, 118 (2010).
- [65] M. J. Bramley and T. Carrington, *J. Chem. Phys.* **99**, 8519 (1993).
- [66] M. J. Bramley and T. Carrington Jr, *J. Chem. Phys.* **101**, 8494 (1994).
- [67] P.-N. Roy and T. Carrington Jr, *Chem. Phys. Lett.* **257**, 98 (1996).
- [68] X.-G. Wang and T. Carrington, *J. Phys. Chem. A* **105**, 2575 (2001).
- [69] X.-G. Wang and T. Carrington Jr, *J. Chem. Phys.* **118**, 6946 (2003).
- [70] T. Carrington Jr and X.-G. Wang, *Wiley Interdis. Rev.: Comp. Mol. Sci.* **1**, 952 (2011).
- [71] C. Lanczos, *J. Res. Natl. Bur. Stand.* **45**, 255 (1950).
- [72] M. J. Bramley and T. Carrington, Jr., *J. Chem. Phys.* **101**, 8494 (1994).
- [73] E. Mátyus, J. Šimunek, and A. G. Császár, *J. Chem. Phys.* **131**, 074106 (2009).
- [74] C. Fábri, J. Sarka, and A. G. Császár, *J. Chem. Phys.* **140**, 051101 (2014).
- [75] G. Avila and T. Carrington, *J. Chem. Phys.* **131**, 174103 (2009).
- [76] G. Avila and T. Carrington, *J. Chem. Phys.* **134**, 054126 (2011).
- [77] G. Avila and T. Carrington, *J. Chem. Phys.* **135**, 064101 (2011).
- [78] D. Lauvergnat and A. Nauts, *Spectrochim. Acta A* **119**, 18 (2014).
- [79] Y. Zhang, S. J. Klippenstein, and R. A. Marcus, *J. Chem. Phys.* **94**, 7319 (1991).
- [80] E. Castro, G. Avila, S. Manzhos, J. Agarwal, H. F. Schaefer, and T. Carrington, Jr, *Mol. Phys.* **115**, 1775 (2017).
- [81] D. Papoušek, J. Stone, and V. Špirko, *J. Mol. Spectrosc.* **48**, 17 (1973).
- [82] W. H. Miller, N. C. Handy, and J. E. Adams, *J. Chem. Phys.* **72**, 99 (1980).
- [83] J. M. Bowman, X. Huang, N. C. Handy, and S. Carter, *J. Phys. Chem. A* **111**, 7317 (2007).
- [84] T. Carrington and W. H. Miller, *J. Chem. Phys.* **81**, 3942 (1984).
- [85] R. J. Whitehead and N. C. Handy, *J. Mol. Spectrosc.* **55**, 356 (1975).
- [86] J. M. Bowman, S. Carter, and X. Huang, *Int. Rev. Phys. Chem.* **22**, 533 (2003).
- [87] T. Halverson and B. Poirier, *Chem. Phys. Lett.* **624**, 37 (2015).
- [88] T. Halverson and B. Poirier, *J. Phys. Chem. A* **119**, 12417 (2015).
- [89] J. Sarka and B. Poirier, *J. Chem. Theo. Comp.* **17**, 7732 (2021).
- [90] A. Chen and D. Lauvergnat, *arXiv preprint arXiv:2111.13655* (2021), 10.48550/arXiv.2111.13655.
- [91] F. Heiss and V. Winschel, *J. Econometrics* **144**, 62 (2008).
- [92] A. Nauts and D. Lauvergnat, *Mol. Phys.* **116**, 3701 (2018).
- [93] M. H. Beck, A. Jäckle, G. A. Worth, and H.-D. Meyer, *Phys. Rep.* **324**, 1 (2000).
- [94] Z. Bačić and J. C. Light, *Ann. Rev. Phys. Chem.* **40**, 469 (1989).
- [95] J. R. Henderson and J. Tennyson, *Chem. Phys. Lett.* **173**, 133 (1990).
- [96] X.-G. Wang and T. Carrington Jr, *J. Chem. Phys.* **121**, 2937 (2004).
- [97] X.-G. Wang and T. Carrington Jr, *J. Chem. Phys.* **148**, 074108 (2018).
- [98] P. M. Felker and Z. Bačić, *J. Chem. Phys.* **151**, 024305 (2019).
- [99] P. M. Felker and Z. Bačić, *J. Chem. Phys.* **153**, 074107 (2020).
- [100] Y. Liu, J. Li, P. M. Felker, and Z. Bačić, *Phys. Chem. Chem. Phys.* **23**, 7101 (2021).



- [101] A. Jäckle and H.-D. Meyer, *J. Chem. Phys.* **104**, 7974 (1996).
- [102] P. S. Thomas and T. Carrington Jr, *J. Chem. Phys.* **146**, 204110 (2017).
- [103] P. S. Thomas, T. Carrington Jr, J. Agarwal, and H. F. Schaefer III, *J. Chem. Phys.* **149**, 064108 (2018).
- [104] S. Carter, S. J. Culik, and J. M. Bowman, *J. Chem. Phys.* **107**, 10458 (1997).
- [105] S. Carter, J. M. Bowman, and N. C. Handy, *Theor. Chem. Acc.* **100**, 191 (1998).
- [106] B. Ziegler and G. Rauhut, *J. Phys. Chem. A* **123**, 3367 (2019).
- [107] X. Wang, S. Carter, and J. M. Bowman, *J. Phys. Chem. A* **119**, 11632 (2015).
- [108] H. Rabitz and O. F. Alis, *J. Math. Chem.* **25**, 197 (1999).
- [109] S. Manzhos and T. Carrington, *J. Chem. Phys.* **125**, 084109 (2006).
- [110] S. Manzhos and T. Carrington, *J. Chem. Phys.* **127**, 014103 (2007).
- [111] S. Manzhos, K. Yamashita, and T. Carrington, *Chem. Phys. Lett.* **511**, 434 (2011).
- [112] G. Avila and T. Carrington, *J. Chem. Phys.* **139**, 134114 (2013).
- [113] G. Avila and T. Carrington, *J. Chem. Phys.* **143**, 214108 (2015).
- [114] G. Avila and T. Carrington, *J. Chem. Phys.* **147**, 064103 (2017).
- [115] R. Wodraszka and T. Carrington Jr, *J. Chem. Phys.* **150**, 154108 (2019).
- [116] R. Wodraszka and T. Carrington, *J. Chem. Phys.* **154**, 114107 (2021).
- [117] T. Carrington, *Spectrochim. Acta A* **248**, 119158 (2021).
- [118] P. J. Ollitrault, A. Baiardi, M. Reiher, and I. Tavernelli, *Chem. Sci.* **11**, 6842 (2020).
- [119] O. Christiansen, *J. Chem. Phys.* **120**, 2140 (2004).
- [120] C. Fábri, E. Mátyus, T. Furtenbacher, L. Nemes, B. Mihály, T. Zoltáni, and A. G. Császár, *J. Chem. Phys.* **135**, 094307 (2011).
- [121] A. Owens, E. Zak, K. Chubb, S. N. Yurchenko, J. Tennyson, and A. Yachmenev, *Sci. Rep.* **7**, 45068 (2017).
- [122] T. Szidarovszky and K. Yamanouchi, *Mol. Phys.* **115**, 1916 (2017).
- [123] E. Mátyus, C. Fábri, T. Szidarovszky, G. Czakó, W. D. Allen, and A. G. Császár, *J. Chem. Phys.* **133**, 034113 (2010).
- [124] M. P. Metz, K. Szalewicz, J. Sarka, R. Tóbiás, A. G. Császár, and E. Mátyus, *Phys. Chem. Chem. Phys.* **21**, 13504 (2019).
- [125] P. A. Coles, A. Owens, J. Küpper, and A. Yachmenev, *Astrophys. J.* **870**, 24 (2018).
- [126] A. Yachmenev, G. Yang, E. Zak, S. Yurchenko, and J. Küpper, *J. Chem. Phys.* **156**, 204307 (2022).
- [127] A. Owens and A. Yachmenev, *J. Chem. Phys.* **148**, 124102 (2018).
- [128] S. Erfort, M. Tschöpe, and G. Rauhut, *J. Chem. Phys.* **152**, 244104 (2020).
- [129] S. Erfort, M. Tschöpe, and G. Rauhut, *J. Chem. Phys.* **156**, 124102 (2022).
- [130] E. Mátyus, D. Ferenc, P. Jeszenszki, and Ádám Margócsy, [arXiv:2211.02389](https://arxiv.org/abs/2211.02389).
- [131] "Paul Dirac interviewed by Friedrich Hund, Institut für den Wissenschaftlichen Film, Göttingen, 1982."
- [132] G. Breit, *Phys. Rev.* **36**, 383 (1930).
- [133] C. G. Darwin, *Phil. Mag.* **39**, 537 (1920).
- [134] G. E. Brown and D. G. Ravenhall, *Proc. Roy. Soc. Lon. A* **208**, 552 (1951).
- [135] G. Pestka, M. Bylicki, and J. Karwowski, *J. Phys. B* **39**, 2979 (2006).
- [136] G. Pestka, M. Bylicki, and J. Karwowski, *J. Phys. B* **40**, 2249 (2007).
- [137] J. Sucher, "Foundations of the relativistic theory of many-electron systems," in *Relativistic Effects in Atoms, Molecules, and Solids*, edited by G. L. Malli (Springer US, Boston, MA, 1983) pp. 1–53.
- [138] T. C. Scott, J. Shertzer, and R. A. Moore, *Phys. Rev. A* **45**, 4393 (1992).
- [139] R. P. Feynman, *Phys. Rev.* **76**, 749 (1949).
- [140] R. P. Feynman, *Phys. Rev.* **76**, 769 (1949).
- [141] E. E. Salpeter and H. A. Bethe, *Phys. Rev.* **84**, 1232 (1951).
- [142] Y. Nambu, *Prog. Theor. Phys.* **5**, 614 (1950).
- [143] J. Schwinger, *Proc. Nat. Acad. Sci.* **37**, 455 (1951).
- [144] M. Gell-Mann and F. Low, *Phys. Rev.* **84**, 350 (1951).
- [145] E. E. Salpeter, *Phys. Rev.* **87**, 328 (1952).
- [146] T. Fulton and P. C. Martin, *Phys. Rev.* **95**, 811 (1954).
- [147] J. Sucher, "Energy levels of the two-electron atom, to order  $\alpha^3$  Rydberg (Columbia University)," (1958).
- [148] H. Araki, *Prog. of Theor. Phys.* **17**, 619 (1957).
- [149] M. Douglas and N. M. Kroll, *Ann. Phys.* **82**, 89 (1974).
- [150] G. S. Adkins, *AIP Conf. Proc.* **189**, 65 (1989).
- [151] K. Pachucki, *Phys. Rev. A* **56**, 297 (1997).
- [152] K. Pachucki, *Phys. Rev. Lett.* **79**, 4120 (1997).
- [153] K. Pachucki and S. G. Karshenboim, *Phys. Rev. Lett.* **80**, 2101 (1998).
- [154] K. Pachucki, *Hyperfine Int.* **114**, 55 (1998).
- [155] K. Pachucki, *Phys. Rev. A* **71**, 012503 (2005).
- [156] L. L. Foldy and S. A. Wouthuysen, *Phys. Rev.* **78**, 29 (1950).
- [157] V. Shabaev, *Phys. Rep.* **356**, 119 (2002).
- [158] K. Pachucki, *Phys. Rev. A* **74**, 022512 (2006).
- [159] A. Yelkhovsky, *Phys. Rev. A* **64**, 062104 (2001).
- [160] V. Korobov and A. Yelkhovsky, *Phys. Rev. Lett.* **87**, 193003 (2001).
- [161] M. Puchalski, J. Komasa, P. Czachorowski, and K. Pachucki, *Phys. Rev. Lett.* **117**, 263002 (2016).
- [162] V. Patkóš, V. A. Yerokhin, and K. Pachucki, *Phys. Rev. A* **101**, 062516 (2020).
- [163] V. Patkóš, V. A. Yerokhin, and K. Pachucki, *Phys. Rev. A* **103**, 012803 (2021).
- [164] G. C. Wick, *Phys. Rev.* **96**, 1124 (1954).
- [165] R. E. Cutkosky, *Phys. Rev.* **96**, 1135 (1954).
- [166] C. Schwartz, *Phys. Rev.* **137**, B717 (1965).
- [167] N. Nakanishi, *Prog. Theor. Phys. Suppl.* **43**, 1 (1969).

- [168] K. Ladányi, *Acta Phys. Hung.* **62**, 161 (1987).
- [169] J. Sucher, *Phys. Rev. A* **22**, 348 (1980).
- [170] J. Sucher, *Int. J. Quant. Chem.* **25**, 3 (1984).
- [171] T. Saue, R. Bast, A. S. P. Gomes, H. J. A. Jensen, L. Visscher, I. A. Aucar, R. Di Remigio, K. G. Dyall, E. Eliav, E. Fasshauer, T. Fleig, L. Halbert, E. D. Hedegård, B. Helmich-Paris, M. Iliaš, C. R. Jacob, S. Knecht, J. K. Laerdahl, M. L. Vidal, M. K. Nayak, M. Olejniczak, J. M. H. Olsen, M. Pernpointner, B. Senjean, A. Shee, A. Sunaga, and J. N. P. van Stralen, *J. Chem. Phys.* **152**, 204104 (2020).
- [172] L. Belpassi, M. De Santis, H. M. Quiney, F. Tarantelli, and L. Storchi, *J. Chem. Phys.* **152**, 164118 (2020).
- [173] I. Lindgren, *Relativistic Many-Body Theory*, Springer Series on Atomic, Optical, and Plasma Physics, Vol. 63 (Springer, New York, NY, 2011).
- [174] P. Jeszenszki, D. Ferenc, and E. Mátyus, *J. Chem. Phys.* **154**, 224110 (2021).
- [175] P. Jeszenszki, D. Ferenc, and E. Mátyus, *J. Chem. Phys.* **156**, 084111 (2022).
- [176] D. Ferenc, P. Jeszenszki, and E. Mátyus, *J. Chem. Phys.* **156**, 084110 (2022).
- [177] D. Ferenc, P. Jeszenszki, and E. Mátyus, *J. Chem. Phys.* **157**, 094113 (2022).
- [178] P. Jeszenszki and E. Mátyus, “Relativistic two-electron atomic and molecular energies using *LS* coupling and double groups: role of the triplet contributions to singlet states,” (2022).
- [179] D. Ferenc and E. Mátyus, “Pre-Born–Oppenheimer Dirac–Coulomb–Breit computations for two-body systems: positronium, muonium, hydrogen atom, and muonic hydrogen,” (2022).
- [180] A. A. Broyles, *Phys. Rev. A* **38**, 1137 (1987).
- [181] A. A. Logunov and A. N. Tavkhelidze, *Il Nuovo Cim.* **29**, 380 (1963).
- [182] R. N. Faustov, *Theor. Math. Phys.* **3**, 478 (1970).
- [183] W. H. Furry, *Phys. Rev. A* **81**, 115 (1951).
- [184] F. J. Dyson, *Phys. Rev.* **75**, 486 (1949).
- [185] P. T. Matthews and A. Salam, *Phys. Rev.* **94**, 185 (1954).
- [186] G. Källen, *Helv. Phys. Acta* **25**, 417 (1952).
- [187] H. Lehmann, *Il Nuovo Cim.* **11**, 342 (1954).
- [188] R. Karplus and N. M. Kroll, *Phys. Rev.* **77**, 536 (1950).
- [189] J. M. Jauch and F. Rohrlich, *The Theory of Photons and Electrons* (Springer Berlin Heidelberg, 1976).
- [190] W. Greiner and J. Reinhardt, *Quantum Electrodynamics* (Springer-Verlag, Berlin Heidelberg, 2009).
- [191] F. Gross, *Relativistic Quantum Mechanics and Field Theory* (John Wiley & Sons, Inc., New York, 1999).
- [192] G. Hardekopf and J. Sucher, *Phys. Rev. A* **30**, 703 (1984).
- [193] S. Tracy and P. Singh, *Stat. Neerl.* **26**, 143 (1972).
- [194] Z. Li, S. Shao, and W. Liu, *J. Chem. Phys.* **136**, 144117 (2012).
- [195] S. Shao, Z. Li, and W. Liu, in *Handbook of Relativistic Quantum Chemistry*, edited by W. Liu (Springer, Berlin, Heidelberg, 2017) pp. 481–496.
- [196] B. Simmen, E. Mátyus, and M. Reiher, *J. Phys. B* **48**, 245004 (2015).
- [197] W. Schwarz and H. Wallmeier, *Mol. Phys.* **46**, 1045 (1982).
- [198] W. Kutzelnigg, *Int. J. Quant. Chem.* **25**, 107 (1984).
- [199] Y. Suzuki and K. Varga, *Stochastic Variational Approach to Quantum-Mechanical Few-Body Problems* (Springer-Verlag, Berlin, Heidelberg, 1998).
- [200] D. Ferenc and E. Mátyus, *J. Chem. Phys.* **151**, 094101 (2019).
- [201] R. Ireland, P. Jeszenszki, E. Mátyus, R. Martinazzo, M. Ronto, and E. Pollak, *ACS Phys. Chem. Au* **2**, 23–37 (2021).
- [202] P. Jeszenszki, R. T. Ireland, D. Ferenc, and E. Mátyus, *Int. J. Quant. Chem.* **122**, e26819 (2022).
- [203] E. Mátyus and D. Ferenc, *Mol. Phys.* , e2074905 (2022).
- [204] D. Ferenc and E. Mátyus, “Evaluation of the Bethe logarithm: from atom to chemical reaction,” (2022).
- [205] M. Bylicki, G. Pestka, and J. Karwowski, *Phys. Rev. A* **77**, 044501 (2008).
- [206] F. A. Parpia and I. P. Grant, *J. Phys. B* **23**, 211 (1990).
- [207] H. A. Bethe and E. E. Salpeter, *Quantum Mechanics of One- and Two-Electron Atoms* (Springer, Berlin, 1957).
- [208] M. J. Esteban, M. Lewin, and E. Séré, *Bull. Amer. Math. Soc.* **45**, 535 (2008).
- [209] M. Lewin and E. Sere, *Proc. Lond. Math. Soc.* **100**, 864 (2010).
- [210] A. Almoukhalalati, S. Knecht, H. J. A. Jensen, K. G. Dyall, and T. Saue, *J. Chem. Phys.* **145**, 074104 (2016).
- [211] M. Haidar, Z.-X. Zhong, V. I. Korobov, and J.-P. Karr, *Phys. Rev. A* **101**, 022501 (2020).
- [212] S. Alighanbari, G. S. Giri, F. L. Constantin, V. I. Korobov, and S. Schiller, *Nature* **581**, 152 (2020).
- [213] M. Germann, S. Patra, J.-P. Karr, L. Hilico, V. I. Korobov, E. J. Salumbides, K. S. E. Eikema, W. Ubachs, and J. C. J. Koelemeij, *Phys. Rev. Res.* **3**, L022028 (2021).
- [214] N. Hölsch, M. Beyer, E. J. Salumbides, K. S. E. Eikema, W. Ubachs, C. Jungen, and F. Merkt, *Phys. Rev. Lett.* **122**, 103002 (2019).
- [215] M. Puchalski, J. Komasa, P. Czachorowski, and K. Pachucki, *Phys. Rev. Lett.* **122**, 103003 (2019).
- [216] D. Ferenc, V. I. Korobov, and E. Mátyus, *Phys. Rev. Lett.* **125**, 213001 (2020).
- [217] L. Semeria, P. Jansen, G.-M. Camenisch, F. Mellini, H. Schmutz, and F. Merkt, *Phys. Rev. Lett.* **124**, 213001 (2020).
- [218] G. Adkins, D. Cassidy, and J. Pérez-Ríos, *Phys. Rep.* **975**, 1 (2022).
- [219] T. W. Hänsch, *Rev. Mod. Phys.* **78**, 1297 (2006).



Contents lists available at ScienceDirect

## Journal of Molecular Spectroscopy

journal homepage: [www.elsevier.com/locate/jmbsp](http://www.elsevier.com/locate/jmbsp)

## Variational vibrational states of HCOOH

Alberto Martín Santa Daría, Gustavo Avila, Edit Mátyus\*

ELTE, Eötvös Loránd University, Institute of Chemistry, Pázmány Péter sétány 1/A, 1117 Budapest, Hungary

## ARTICLE INFO

## Keywords:

Formic acid  
Large-amplitude motion  
Curvilinear normal coordinate  
Variational vibrational computation  
Smolyak quadrature

## ABSTRACT

Vibrational states of the formic acid molecule are converged using the GENIUSH–Smolyak approach and the potential energy surface taken from Tew and Mizukami (2016). The quantum nuclear motion is described by using the *cis-trans* torsional coordinate and eight curvilinear normal coordinates defined with respect to an instantaneous reference configuration changing as a function of the torsional degree of freedom. Harmonic oscillator basis functions are used for the curvilinear normal coordinates, a Fourier basis for the torsional coordinate, and a simple basis pruning condition is combined with a Smolyak integration grid. *Trans*, *cis*, and *delocalized* vibrational states are reported up to and slightly beyond the isomerization barrier.

## 1. Introduction

This paper is dedicated to the memory of J. K. G. Watson, the father of the Watson Hamiltonian, a compact, analytic formulation of the rovibrational kinetic energy operator in normal coordinates. In this paper, we also use normal coordinates, but we adapt these coordinates to the *cis-trans* isomerization of the formic acid molecule. There is no known analytic formulation for the corresponding kinetic energy operator available, and we use computer power to construct the kinetic energy coefficients where they are needed.

Over the past decade, we have observed a rapid and fundamentally important development of exact quantum dynamics techniques to solve the (ro)vibrational problem. Development is observed in several directions: (a) coordinate representation and the kinetic energy operator [1–7]; (b) contraction techniques [8–12]; (c) grid pruning techniques [13–18]; (d) collocation [19–21]; (e) accurate potential energy representations for high-dimensional systems [22–24]; (f) highly parallel computation of ten thousands or millions of vibrational states [25–27].

Regarding the formic acid molecule, there are two full-dimensional, high-level *ab initio* potential energy surfaces (PESs) [28,29] that have been used in sophisticated (variational or perturbative) vibrational computations. Tew and Mizukami used their PES in a variational vibrational computation with a five-mode representation and the internal-coordinate path Hamiltonian (ICPH) approach [28]. Richter and Carbonnière used a similar PES [29], computed vibrational energies using a valence-coordinate representation of the kinetic energy operator and the multi-configuration time-dependent Hartree approach, and they reported significant deviations from Ref. [28] for the vibrational states of the *cis* potential energy well. Last year, Nejad and Sibert used both

PESs and sixth-order canonical Van Vleck perturbation theory (CVPT) in curvilinear normal coordinates localized in one of the potential energy wells (*trans* or *cis*) of the molecule [30].

In the present work, we focus on the vibrational methodology and define an efficient setup that can be used to converge (better than  $5\text{ cm}^{-1}$ ) all vibrational states of the formic acid molecule up to and possibly beyond the isomerization barrier (Fig. 1). During the course of the development of a benchmark-quality variational vibrational setup, we use the Tew–Mizukami PES [28] (henceforth labeled as TM16-PES). It is left for future work, when well-converged vibrational energies can be ‘routinely’ computed for the relevant energy range of this system, to decide which PES representation performs better in comparison with experiment (gas-phase overtone and combination bands). Vibrational band origins are available from experimental infrared and Raman observations, a review and an extensive list of references can be found in the introduction of Ref. [30].

The present work is organized as follows. Section 2 reports the development of a torsional-curvilinear normal coordinate representation. Section 3 describes the construction of the corresponding kinetic energy operator coefficients using the numerical kinetic energy operator approach as it is implemented in the GENIUSH computer program [2]. Section 4 defines the harmonic oscillator basis functions for the curvilinear normal coordinates, the Fourier basis and torsional functions for the torsional degree of freedom, and discusses basis pruning strategies. Section 5 describes the Smolyak non-product grid technique that is used to compute multi-dimensional integrals. In Section 6, vibrational energies are presented and discussed in relation with earlier computations [28,30], and further necessary development and computational work is outlined.

\* Corresponding author.

E-mail addresses: [Gustavo\\_Avila@telefonica.net](mailto:Gustavo_Avila@telefonica.net) (G. Avila), [edit.matyus@ttk.elte.hu](mailto:edit.matyus@ttk.elte.hu) (E. Mátyus).

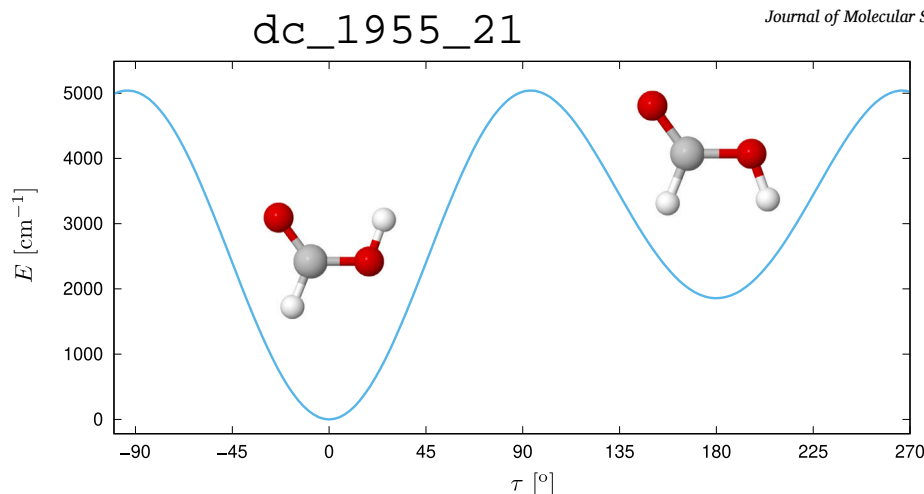


Fig. 1. 1-dimensional cut of the TM16-PES [28] along the torsional angle ( $\tau$ ) that describes the conversion between the *trans* and the *cis* conformers of the formic acid molecule.

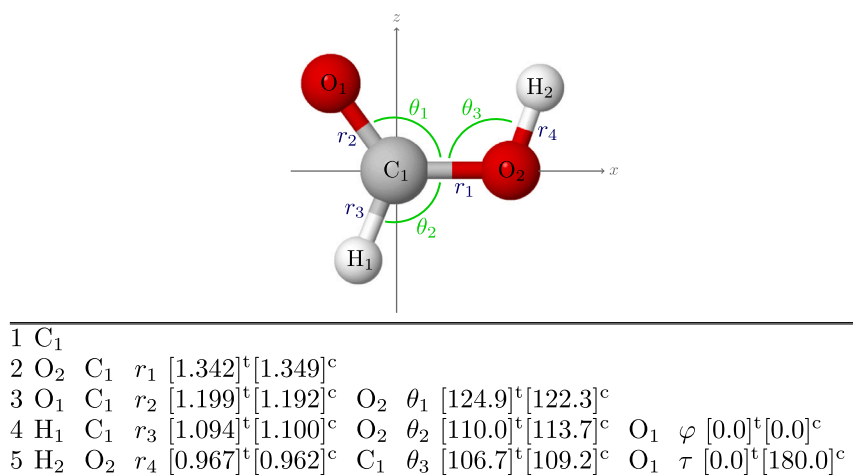


Fig. 2. Visualization of the internal coordinates, Eq. (1), for the example of the *trans*-formic acid molecule in its equilibrium structure. The equilibrium values of the distances, in Å and the angles, in degree, corresponding to the *cis* (°) and the *trans* (°) conformers on the TM16-PES are shown in brackets.

## 2. Vibrational coordinates

### 2.1. Internal coordinates

The body-fixed Cartesian coordinates of HCOOH are defined in terms of the  $r_i \in [0, \infty)$  distances, the  $\theta_i \in [0, \pi]$  angles, the  $\varphi \in [-\pi, \pi)$  out-of-plane bending, and the  $\tau \in [0, 2\pi)$  torsional angle according to the following expressions:

$$\begin{aligned} \mathbf{r}_{\text{C}_1} &= \mathbf{0}, & \mathbf{r}_{\text{O}_2} &= \begin{pmatrix} 0 \\ 0 \\ r_1 \end{pmatrix}, & \mathbf{r}_{\text{O}_1} &= \begin{pmatrix} 0 \\ r_2 \cos(\theta_1 - \pi/2) \\ -r_2 \sin(\theta_1 - \pi/2) \end{pmatrix}, \\ \mathbf{r}_{\text{H}_1} &= \begin{pmatrix} r_3 \cos(\theta_2 - \pi/2) \sin \varphi \\ -r_3 \cos(\theta_2 - \pi/2) \cos \varphi \\ -r_3 \sin(\theta_2 - \pi/2) \end{pmatrix}, \\ \mathbf{r}_{\text{H}_2} &= \mathbf{r}_{\text{O}_2} + \begin{pmatrix} r_4 \cos(\theta_3 - \pi/2) \sin \tau \\ r_4 \cos(\theta_3 - \pi/2) \cos \tau \\ r_4 \sin(\theta_3 - \pi/2) \end{pmatrix}. \end{aligned} \quad (1)$$

The coordinate definition and the corresponding  $Z$ -matrix including the equilibrium values at the *trans* and the *cis* minima of the TM16-PES are summarized in Fig. 2. For later use, a compact notation of the coordinates is introduced as

$$\xi = (\xi_1, \dots, \xi_9) = (r_1, r_2, r_3, r_4, \theta_1, \theta_2, \theta_3, \varphi, \tau). \quad (2)$$

### 2.2. Rectilinear normal coordinates

The body-fixed Cartesian coordinates and displacements with respect to the  $c_{i\alpha}$  reference (equilibrium) geometry of an  $N$ -atomic molecule can be written in terms of the  $Q_k \in \mathbb{R}$  normal coordinates as

$$\begin{aligned} r_{i\alpha} &= c_{i\alpha} + d_{i\alpha} \quad \text{with} \\ d_{i\alpha} &= \frac{1}{m_i^{1/2}} \sum_{k=1}^{\bar{D}} l_{i\alpha,k} Q_k, \quad i = 1, \dots, N, \quad \text{and } \alpha = x, y, z. \end{aligned} \quad (3)$$

The  $l_{i\alpha,k}$  coefficients are the elements of the eigenvectors of the  $GF$  matrix [31] evaluated at the reference (equilibrium) structure. In this work, the normal coordinate calculation has been performed at both minima (*trans* and *cis*) of HCOOH, hence, there are two parameter sets. The  $F$  Hessian matrix has been computed by finite differences of the PES at both (*trans* and *cis*) equilibrium structures with respect to the displacements along the  $3N$  Cartesian coordinates. The numerical derivatives and related mathematical manipulations were evaluated using the Wolfram Mathematica symbolic algebra program [32].

HCOOH is an  $N = 5$ -atomic molecule and its total number of vibrational degrees of freedom is  $3N - 6 = 9$ . We used Eq. (3) with  $\bar{D} = 9$  (Fig. 3), but we also used it with  $\bar{D} = 8$  while the  $\tau$  torsional degree of freedom was excluded from the harmonic analysis that is necessary to have a good description for the *cis-trans* isomerization.

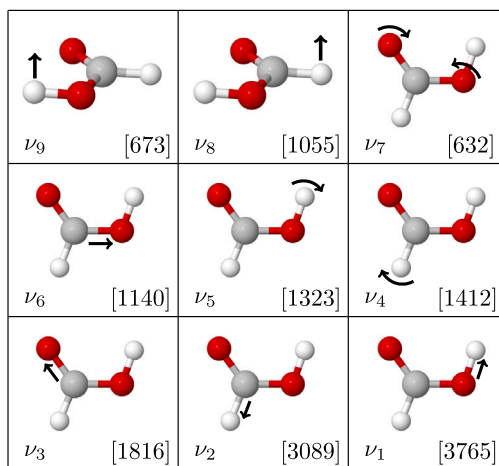


Fig. 3. Visualization of the normal modes corresponding to the global minimum (*trans*) of HCOOH. The harmonic frequencies, in  $\text{cm}^{-1}$ , are shown in brackets.

### 2.3. Curvilinear normal coordinates

Instead of using rectilinear displacement coordinates,  $d_{i\alpha}$ , a better vibrational representation can be obtained [33], if we use (curvilinear) internal coordinates (Fig. 2), for which curvilinear displacement (*c*-displacement) coordinates can be defined with respect to some reference (equilibrium, eq) value as

$$\Delta\xi_i = \xi_i - \xi_i^{(\text{eq})}. \quad (4)$$

We define linear combinations of these curvilinear displacement coordinates, and we call them curvilinear (*c*-normal) normal coordinates,

$$Q = \mathcal{L}^{-1}(\Delta\xi) \quad (5)$$

such that the kinetic and potential energy coupling (near the reference structure) is reduced. Hence, similarly to the rectilinear normal coordinates, the linear combination coefficients can be obtained using the *GF* method:

$$\mathcal{L}^{-1}GF\mathcal{L} = A \quad (6)$$

and the eigenvectors, in  $\mathcal{L}$ , of the *GF* matrix provide us the linear combination coefficients of the *c*-normal coordinates.  $F$  is the Hessian matrix of the PES

$$F_{ij} = \left( \frac{\partial^2 V}{\partial \xi_i \partial \xi_j} \right)_{\text{eq}} \quad (7)$$

computed with respect to the  $\xi_i$  curvilinear coordinates at the equilibrium (eq) structure. The matrix  $G$  is obtained as

$$G = \mathbf{B}\mathbf{M}^{-1}\mathbf{B}^T, \quad (8)$$

where  $\mathbf{M}$  is a  $3N \times 3N$  diagonal matrix containing the masses,  $m_a$  ( $a = 1, \dots, N$ ), of the atomic nuclei

$$\mathbf{M}^{-1} = \begin{pmatrix} 1/m_1 & & & & 0 \\ & 1/m_1 & & & \\ & & 1/m_1 & & \\ & & & \ddots & \\ 0 & & & & 1/m_N \end{pmatrix} \quad (9)$$

and  $\mathbf{B}$  is a  $\bar{D} \times 3N$  matrix that contains the derivatives of the internal coordinates with respect to the rectilinear displacements ( $\partial \xi_i / \partial d_{j\alpha}$ )<sub>eq</sub> ( $i = 1, \dots, \bar{D}$ ,  $j = 1, \dots, N$ ,  $\alpha = x, y, z$ ) and satisfy the following relation:

$$\begin{pmatrix} \xi_1 \\ \xi_2 \\ \vdots \\ \xi_{\bar{D}} \end{pmatrix} = \mathbf{B} \begin{pmatrix} d_{1x} \\ d_{1y} \\ d_{1z} \\ \vdots \\ d_{Nz} \end{pmatrix}. \quad (10)$$

To have a good description of the *cis-trans* torsional motion, we exclude the  $\tau$  torsional degree of freedom from the *GF* calculation and the *c*-normal coordinates are defined for the remaining  $\bar{D} = 8$  (displacement) internal coordinates that exhibit small(er) amplitude motions.

For a given value of the  $Q_k$  *c*-normal coordinates, the value of the  $\xi_i$  internal coordinates can be calculated using the eigenvectors in  $\mathcal{L}$  and the  $\xi_i^{(\text{eq})}$  equilibrium values:

$$\xi_i = \xi_i^{(\text{eq})} + \sum_{k=1}^{\bar{D}} \mathcal{L}_{i,k}^{(\text{eq})} Q_k, \quad k = 1, \dots, \bar{D} (= 8) \quad (11)$$

Since HCOOH has two equilibrium configurations, we have two parameter sets:  $\{\xi^{(\text{c})}, \mathcal{L}^{(\text{c})}\}$  and  $\{\xi^{(\text{t})}, \mathcal{L}^{(\text{t})}\}$  (the parameters are deposited as Supplementary data).

### 2.4. Relaxed curvilinear normal coordinates along the torsional motion

Since we are interested in the overall vibrational dynamics of HCOOH, we cannot restrict the description to the *cis* or the *trans* well. Hence, we repeated the *c*-normal mode computation (with  $\bar{D} = 8$  degrees of freedom) along the large-amplitude motion at several points (*vide infra*) over the entire range of  $\tau \in [0, 2\pi)$ . During this computation, we relaxed the molecular structure along  $\tau$  by minimizing the potential energy (Fig. 4). The relaxed values of the internal coordinates that correspond to the minimal potential energy as a function of  $\tau$  are shown in Fig. 5. These relaxed internal coordinate structures are considered as the ‘equilibrium structure’,  $\xi^{(\text{eq})}(\tau)$ , for the 8-dimensional *c*-normal-mode computation that is repeated for several  $\tau$  values.

In practice, the *c*-normal coordinates are computed (similarly to Section 2.3) at 24 equally distributed values of  $\tau = t_n$  with  $t_n = (n-1)360^\circ/24$ ,

$$\xi_i(\tau) = \xi_i^{(\text{eq})}(\tau) + \sum_{j=1}^8 \tilde{\mathcal{L}}_{i,j}(\tau) \tilde{Q}_j, \quad i = 1, \dots, 8. \quad (12)$$

Using the value of the coefficients at the  $t_n$  ( $n = 1, \dots, 24$ ) points, we interpolate  $\tilde{\mathcal{L}}_{i,j}(\tau)$  by solving a system of linear equations,

$$\tilde{\mathcal{L}}_{i,j}(t_n) = \sum_{k=1}^{24} c_k^{ij} f_k(t_n), \quad n = 1, \dots, 24. \quad (13)$$

For the  $f_k$  functions, we have considered the following functions of the Fourier basis

$$1, \cos(\tau), \sin(\tau), \cos(2\tau), \sin(2\tau), \dots, \cos(12\tau). \quad (14)$$

All coordinates can be expanded using only cosine functions of  $\tau$ , except for the  $\varphi$  out-of-plane bending (that is also a torsion-like, but small-amplitude vibration).  $\varphi$  is an odd function of  $\tau$  (Fig. 5), and hence sine basis functions are used for its interpolation.

As a result, we have relaxed equilibrium internal coordinates,  $\xi^{(\text{eq})}(\tau)$  and relaxed *c*-normal (rc-normal) mode  $\tilde{\mathcal{L}}_{i,j}(\tau)$  coefficients as a function of  $\tau$  (Figs. 5 and 6). The rc-normal coordinates incorporate in the coordinate definition the optimal structural changes along the  $\tau$  large-amplitude motion, while the kinetic and potential energy coupling is minimized among the small amplitude (normal) coordinates. This construct is expected to provide an almost ideal coordinate representation for this system. Results of convergence tests are reported in Section 6.

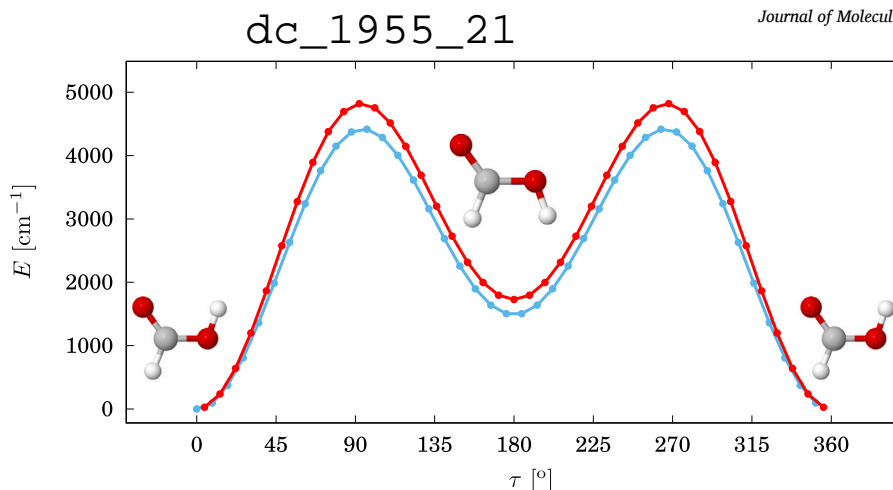


Fig. 4. 1-dimensional cut of the PES along the  $\tau$  torsional coordinate with (a) the non-torsional coordinates fixed at their equilibrium value at the global minimum (red); (b) relaxed non-torsional coordinates minimizing the potential energy (blue).

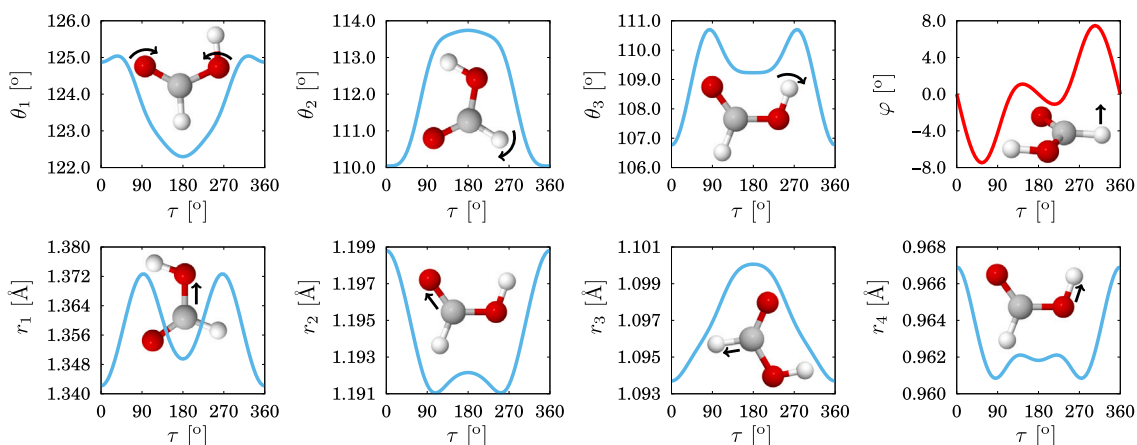


Fig. 5. Minimized equilibrium values for the internal coordinates as a function of the  $\tau$  torsional angle. The relaxed bond length and bond angle functions are symmetric with respect to  $\tau = 180^\circ$  (blue). The relaxed out-of-plane bending angle,  $\varphi$ , is anti-symmetric with respect to  $\tau = 180^\circ$  (red).

### 3. Quantum Hamiltonian

The (ro)vibrational kinetic energy operator (KEO) corresponding to the torsional-relaxed-curvilinear-normal coordinate representation  $q = (\tilde{Q}, \tau)$  is constructed using the numerical KEO approach as implemented in the GENIUSH computer program [2]. The core of the program is based on the evaluation of the mass-weighted metric tensor at coordinate points:

$$g_{kl} = \sum_{i=1}^N m_i \mathbf{t}_{ik}^T \mathbf{t}_{il}; \quad k, l = 1, 2, \dots, 3N - 3, \quad (15)$$

where the so-called vibrational and rotational t-vectors are

$$\mathbf{t}_{ik} = \frac{\partial \mathbf{r}_i}{\partial q_k}; \quad k = 1, 2, \dots, 3N - 6 \quad (16)$$

$$\mathbf{t}_{i,3N-6+a} = \mathbf{e}_a \times \mathbf{r}_i; \quad a = 1(x), 2(y), 3(z), \quad (17)$$

respectively. For the computation of the t-vectors, and using them to construct the  $g \in \mathbb{R}^{(3N-3) \times (3N-3)}$  matrix, it is necessary to know the body-fixed Cartesian coordinates  $\mathbf{r}_i$  ( $i = 1, \dots, N$ ) as a function of the generalized vibrational coordinates  $q_k$  ( $k = 1, \dots, 3N - 6$ ). We expect that an efficient representation can be obtained with the relaxed-curvilinear-normal coordinate plus torsion choice (Section 2)

$$q_i = \tilde{Q}_i, \quad i = 1, \dots, 8$$

$$q_{3N-6} = \tau. \quad (18)$$

The corresponding  $\mathbf{r}_i$  vs.  $q_k$  relations can be obtained from Eqs. (1) and (12). This coordinate choice results in an arrow-like structure of the  $G$  matrix (Fig. 7), *i.e.*, the coupling of the  $\tau$  large-amplitude motion and the  $\tilde{Q}$  small-amplitude coordinates is not necessarily small (can be large), but the coupling among the small-amplitude  $\tilde{Q}$  coordinates is small for all  $\tau$  values.

The derivatives of the  $\mathbf{r}_i$  Cartesian coordinates with respect the  $q_k$  generalized internal coordinates are obtained by using the two-sided finite difference formula. The  $G \in \mathbb{R}^{(3N-3) \times (3N-3)}$  matrix is obtained by inversion of  $g \in \mathbb{R}^{(3N-3) \times (3N-3)}$ :

$$G = g^{-1}. \quad (19)$$

In most applications of GENIUSH [2–4,34–38], the discrete variable representation [39] was used, and in that representation the Podolsky (P) form of the general vibrational KEO

$$\hat{H}^{v,P} = \frac{1}{2} \sum_{k=1}^D \sum_{l=1}^D \tilde{g}^{-1/4} \hat{p}_k G_{kl} \tilde{g}^{1/2} \hat{p}_l \tilde{g}^{-1/4} \quad \text{with } \tilde{g} = \det g \quad (20)$$

is an advantageous choice, because it requires only first-order coordinate derivatives.

In this work, we use a finite basis representation of the Hamiltonian (Sections 4 and 5), and for this purpose the ‘fully rearranged’ form [16,

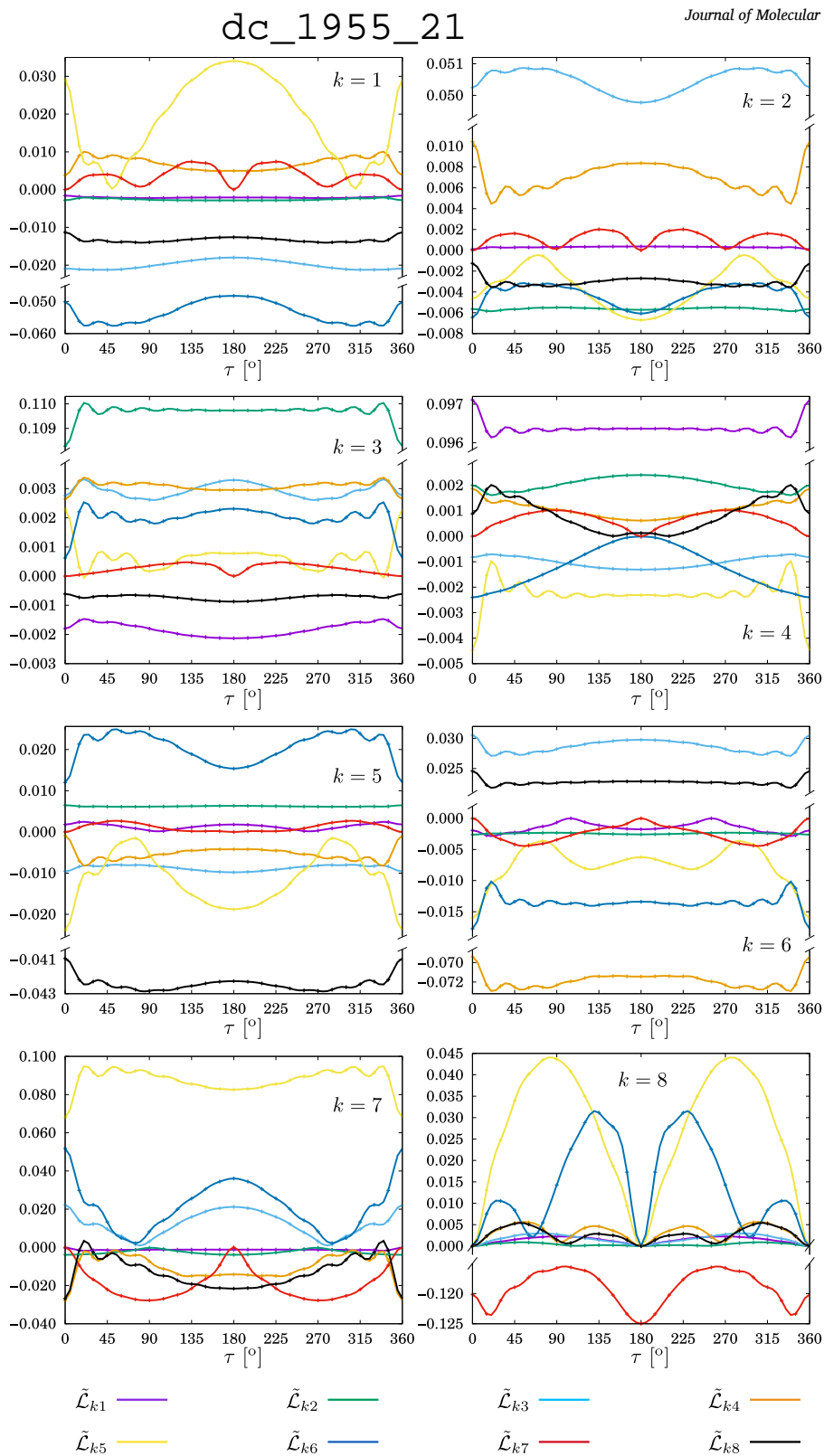


Fig. 6. Curvilinear normal coordinate coefficients, Eq. (12), as a function of the  $\tau$  torsional angle.

17,40] is more convenient

$$\hat{H}^V = -\frac{1}{2} \sum_{i=1}^{3N-6} \sum_{j=1}^{3N-6} G_{ij} \frac{\partial}{\partial q_i} \frac{\partial}{\partial q_j} - \frac{1}{2} \sum_{i=1}^{3N-6} B_i \frac{\partial}{\partial q_i} + U + V \quad (21)$$

where  $G_{ij}$ ,  $B_i$ ,  $U$ , and  $V$  are functions of the vibrational coordinates,

$$B_i = \sum_{k=1}^{3N-6} \frac{\partial}{\partial q_k} G_{ki} \quad (22)$$

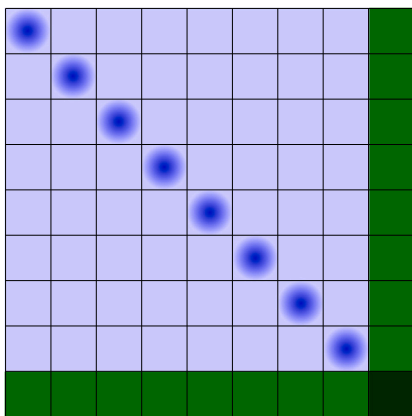


Fig. 7. Visualization of the  $G$  matrix, Eqs. (15) and (19), for a (any) grid point from the dynamically relevant range. The eight rc-normal modes are weakly coupled among each other (light blue), but their weak coupling with the large amplitude motion ( $\tau$ ) is *not* assumed (dark green). The relaxation of the reference structure and the  $GF$  diagonalization along  $\tau$  ensures that the coupling among the rc-normal coordinates remains small (light blue) for any value of  $\tau$  (see also Figs. 5 and 6).

and the pseudo-potential term is

$$U = \frac{1}{32} \sum_{kl=1}^{3N-6} \left[ \frac{G_{kl}}{\tilde{g}^2} \frac{\partial \tilde{g}}{\partial \xi_k} \frac{\partial \tilde{g}}{\partial \xi_l} + 4 \frac{\partial}{\partial \xi_k} \left( \frac{G_{kl}}{\tilde{g}} \frac{\partial \tilde{g}}{\partial \xi_l} \right) \right]. \quad (23)$$

#### 4. Basis functions and truncation of the direct-product basis

We start expanding the wave function over a direct product of basis functions of the selected coordinates

$$\Psi_i(q_1, \dots, q_8, \tau) = \sum_{n_{q_1}=0}^b \dots \sum_{n_{q_8}=0}^b \sum_{n_\tau=0}^{N_\tau^{\max}} C_{n_{q_1}, \dots, n_{q_8}, n_\tau}^i \prod_{i=1}^8 \psi_{n_{q_i}}^{(i)}(q_i) \psi_{n_\tau}^{(\tau)}(\tau). \quad (24)$$

In this work, we use harmonic oscillator basis functions, for the (dimensionless)  $q_1, \dots, q_8$  rc-normal coordinates,

$$\psi_n(q) = A_n H_n(q) e^{-q^2/2} \quad \text{with } q \in (-\infty, +\infty), \quad (25)$$

where  $H_n(q)$  is the  $n$ th-order Hermite polynomial and  $A_n$  is a normalization constant. Section 5.1 provides further important technical details regarding the range of the different coordinate choices. Regarding the  $\tau$  torsional coordinate, we use a Fourier basis including the following functions,

$$1, \cos(\tau), \sin(\tau), \dots, \cos(n_\tau \tau), \sin(n_\tau \tau), \quad \tau \in [0, 2\pi] \quad (26)$$

to solve the 1-dimensional (1D) torsional Schrödinger equation,

$$\hat{H} = G_{\tau\tau} \frac{\partial^2}{\partial \tau^2} + \frac{\partial G_{\tau\tau}}{\partial \tau} \frac{\partial}{\partial \tau} + V_\tau, \quad (27)$$

where the pseudo-potential term, Eq. (23), is neglected. As a result, we obtain torsional functions that can be identified as *trans*, *cis*, or *delocalized* torsional functions explained and discussed in detail in Section 6. We use this 1D torsional basis set to solve the 9D vibrational problem of formic acid.

An accurate product basis set representation for the lowest vibrational levels of HCOOH requires values of  $N_\tau^{\max} > 30$  and  $b \geq 8$ . The number of functions in a direct product basis with  $N_\tau^{\max} = 30$  and  $b = 8$  is  $9^8 \cdot 31 \approx 1.3 \cdot 10^9$  that is too large for practical computations, and still not sufficient for good convergence. Since the couplings of the eight (relaxed) curvilinear normal coordinates was made small over the entire range of  $\tau$  (Section 2), we may expect that the basis set can be efficiently pruned according to

$$\Psi_i = \sum_{n_\tau=0}^{N_\tau^{\max}} \sum_{f(n_{q_1}, \dots, n_{q_8}) \leq b} C_{n_{q_1}, \dots, n_{q_8}, n_\tau}^i \prod_{i=1}^8 \psi_{n_{q_i}}^{(i)}(q_i) \psi_{n_\tau}^{(\tau)}(\tau) \quad (28)$$

$$\text{with } f(n_{q_1}, \dots, n_{q_8}) = n_{q_1} + \dots + n_{q_8}, \quad (29)$$

where certain basis functions have been discarded from the direct product. Eq. (29) gives the simplest possible pruning function. Poirier and co-workers [25–27] have studied more elaborate pruning conditions targeting very highly excited states.

Since the  $\psi_{n_{q_1}}(q_1) \cdot \dots \cdot \psi_{n_{q_8}}(q_8)$  product function provides a good representation for the small-amplitude (non- $\tau$ ) dynamics, we can discard basis functions based on simple physical arguments. For an *a priori* assessment about the importance of a basis function  $|n'\rangle$  ( $n'$  collects the basis indexes) in a wave function dominated by the  $|n\rangle$  basis state, the smallness of the ratio of the Hamiltonian matrix element with respect to the difference of the zeroth-order energies,

$$\frac{\langle n_1, \dots, n_8, n_\tau | \hat{H} | n'_1, \dots, n'_8, n'_\tau \rangle}{E_{n_1, \dots, n_8, n_\tau}^{(0)} - E_{n'_1, \dots, n'_8, n'_\tau}^{(0)}} \approx 0 \quad (30)$$

can provide a good indication about the unimportance of  $|n'\rangle$  for the variational result. The ratio is small, if (a) the Hamiltonian matrix element is small, and/or (b) the zeroth-order energy difference is large. The order of magnitude of the Hamiltonian matrix element can be estimated by considering the fast convergence of the Taylor expansion of the potential and the kinetic energy in rc-normal coordinates.

If the zeroth-order energy for a multi-dimensional basis function is very large, then the contribution of the function to the lowest-energy wave functions is negligible. For example, in order to compute the ground vibrational wave function, the 8D basis functions

$$\mathbf{0} = (0, 0, 0, 0, 0, 0, 0, 0) \quad \text{and} \quad 1_1, 2_1, 3_1, 4_1, 5_1, 6_1, 7_1, 8_1 \quad (31)$$

are necessary, since  $\langle \mathbf{0}, n_\tau | \hat{H} | n'_1, \dots, n'_8, n'_\tau \rangle$  is not small. In Eq. (31), we have introduced a short notation, we list only the degrees of freedom for which the basis function index (‘vibrational quantum number’) is larger than 0, e.g.,  $3_1 = (0, 0, 1, 0, 0, 0, 0, 0)$ .

Furthermore, less important, but still significant contribution to the ground vibrational state may be expected from the following 8D basis functions:

$$\begin{aligned} &1_2, 2_2, 3_2, 4_2, 5_2, 6_2, 7_2, 8_2, \\ &1_1 2_1, 1_1 3_1, 1_1 4_1, 1_1 5_1, 1_1 6_1, 1_1 7_1, 1_1 8_1, \\ &2_1 3_1, 2_1 4_1, 2_1 5_1, 2_1 6_1, 2_1 7_1, 2_1 8_1, \\ &3_1 4_1, 3_1 5_1, 3_1 6_1, 3_1 7_1, 3_1 8_1, \\ &4_1 5_1, 4_1 6_1, 4_1 7_1, 4_1 8_1, \\ &5_1 6_1, 5_1 7_1, 5_1 8_1, \\ &6_1 7_1, 6_1 8_1, \\ &7_1 8_1, \end{aligned} \quad (32)$$

where we note that the functions with  $8_1$  contribution can be discarded for the present system (HCOOH) due to symmetry reasons. At the same time, the basis function  $1_1 2_1 3_1 4_1 5_1 6_1 7_1 8_1$  gives a negligible contribution to the lowest-energy states in comparison with the basis functions listed in Eqs. (31) and (32), since both the Hamiltonian matrix elements are expected to be small and the zeroth-order energy differences are large.

These kinds of arguments do not apply for discarding torsional functions, since the coupling of the  $\tau$  coordinate and the curvilinear normal modes (the Hamiltonian matrix element) may be large and the zeroth-order torsional energies are small, *i.e.*, both (a)–(b) pruning ‘criteria’ below Eq. (30) fail. Therefore, we retain all torsional basis functions in the basis set.

All in all, using the simplest pruning function in Eq. (29), the direct-product basis, Eq. (24), including  $1.3 \cdot 10^9$  functions can be reduced to  $4 \cdot 10^5$  functions, while the lowest (few hundred) vibrational states can be computed accurately.



For future work, we consider more elaborate pruning conditions. Based solely on the harmonic frequencies, the following condition could be formulated,

$$0 \leq 2n_{q_1} + 2n_{q_2} + \frac{3}{2}n_{q_3} + n_{q_4} + n_{q_5} + n_{q_6} + \frac{1}{2}n_{q_7} + n_{q_8} \leq b. \quad (33)$$

This condition accounts only for the denominator of Eq. (30). Since the higher-frequency harmonic oscillator modes correspond to the stretching degrees of freedom, the coupling through the Hamiltonian matrix element, numerator of Eq. (30), may be large. A ‘safe’ improvement of Eq. (29), reads as

$$0 \leq n_{q_1} + n_{q_2} + n_{q_3} + n_{q_4} + n_{q_5} + n_{q_6} + \frac{1}{2}n_{q_7} + n_{q_8} \leq b \quad (34)$$

that corresponds to increasing the number of basis functions of the lowest-frequency (totally symmetric) harmonic mode (O–C–O bending). We plan to use Eq. (34) in future work (see also Section 6).

## 5. Multi-dimensional integration

### 5.1. Coordinate ranges for curvilinear normal coordinates

Since we use harmonic oscillator basis functions, Eq. (25), it will be appropriate to use a set of (nested) Hermite quadratures to evaluate integrals for the matrix elements. Before doing that we need to address the question of the coordinate range for rc-normal coordinates.

The range of the harmonic oscillator functions and also of the Hermite quadrature is  $(-\infty, \infty)$ , whereas the range of the internal coordinates is more restricted:  $[0, \infty)$  for a stretching and  $[0, \pi]$  for a bending. At the same time, if we calculate the value of the curvilinear coordinates,  $\xi_i$ , using the values of rc-normal coordinates,  $\tilde{Q}_k$  (at grid points) according to Eq. (12), it can happen that we obtain a value that is outside the coordinate range (e.g., negative value for a distance). Fortunately, this does not happen for grid points near the origin, but at the edges of the multi-dimensional grid, there are points that return internal coordinate values outside their range. For rectilinear normal coordinates, this does not happen, since the body-fixed Cartesian coordinates are also defined over  $(-\infty, +\infty)$ .

To handle the problematic points of the rc-normal coordinate grid, we define mapping functions which ensure that the result is in the good range:

$$\mathcal{F} \left[ \xi_i^{(\text{eq})} + \sum_{k=1}^D \tilde{\mathcal{L}}_{ik} \tilde{Q}_k \right] \in \text{Range}(\xi_i). \quad (35)$$

Furthermore, we expect that a good mapping function behaves as a linear (an almost trivial) mapping within the good range, but it ensures that at the ‘edges’ of the multi-dimensional grid meaningful values are returned.

For a sigmoid-like mapping function,  $x \mapsto \arctan(x)$  and  $x \mapsto \tanh(x)$  are the most common examples. Unfortunately, outside the  $[-0.5, 0.5]$  interval, these functions significantly deviate from  $x \mapsto x$ , and we would like to find a function that is close to  $x \mapsto x$  over almost the entire coordinate range, but ensures that the ‘edges’ also have meaningful values. For these reasons, we decided to use

$$\mathcal{F}(x) = \frac{x}{(1 + |x|^k)^{1/k}} \quad (36)$$

with  $k = 8$ . The procedure is simple. For a quadrature point  $\tau^{k\tau}$  and  $q_1^{k_1}, \dots, q_8^{k_8}$ , the internal coordinates of the reference structure and the corresponding displacements are calculated. Their sum provides the ‘raw’ internal coordinate value that is mapped to the final value of the coordinate within the correct range. The following parameterization is used for the stretching ( $r_i$ ), bending ( $\theta_i$ ), and out-of-plane bending (oop,  $\varphi$ ) types of coordinates (Fig. 8)

$$\mathcal{F}_{\text{stre}}(x) = \frac{x - 3.5}{(1 + |(x - 3.5) \cdot 0.34|^8)^{1/8}} + 3.5, \quad (37)$$

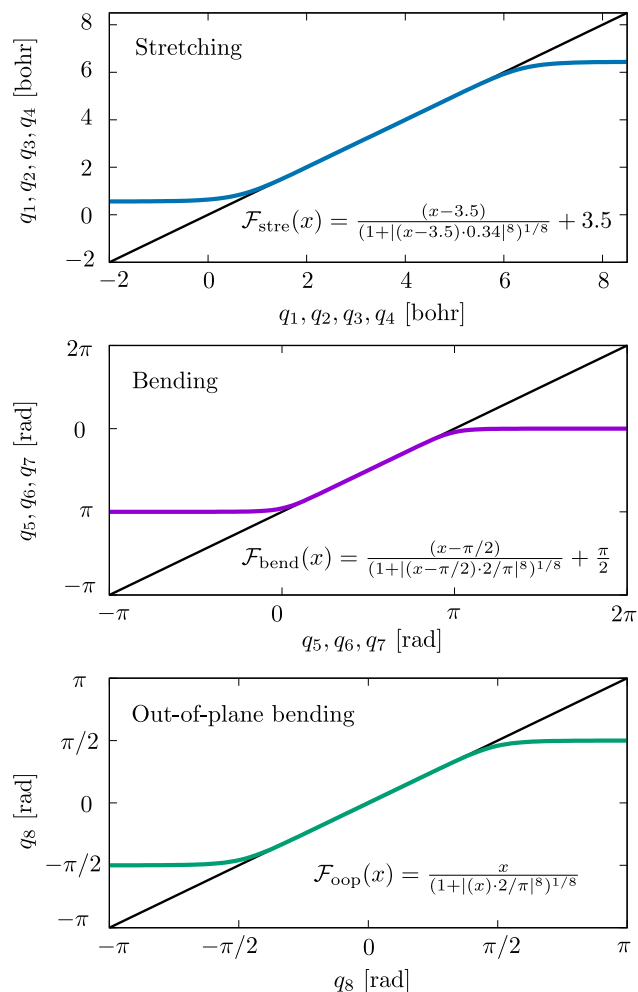


Fig. 8. Functions used for the stretching, bending, and out-of-plane bending coordinates to map the  $(-\infty, +\infty)$  range of the curvilinear normal coordinates to the mathematically appropriate and dynamically relevant range of HCOOH.

$$\mathcal{F}_{\text{bend}}(x) = \frac{x - \pi/2}{(1 + |(x - \pi/2) \cdot 2/\pi|^8)^{1/8}} + \frac{\pi}{2}, \quad (38)$$

and

$$\mathcal{F}_{\text{oop}}(x) = \frac{x}{(1 + |(x) \cdot 2/\pi|^8)^{1/8}}, \quad (39)$$

respectively. These functions ensure that the ‘final’ value for the stretching coordinates is within the  $[0.56, 6.44]$  bohr interval, which is the relevant dynamical range for all stretches in HCOOH, the value of the bending coordinate is within  $[0, \pi]$ , and the out-of-plane bending is within  $[-\pi/2, \pi/2]$ . Although  $\varphi$  is a torsion-like coordinate and is defined on  $[-\pi, \pi]$ , it is a small(er) amplitude vibration of formic acid, and the relevant dynamical range is within  $[-\pi/2, \pi/2]$ .

Regarding Eq. (36), we decided to use  $k = 8$  because it appears to be a good compromise between a faithful mapping (of the good range) and numerical integrability of the matrix elements with a reasonable number of points. Nevertheless, we have checked values up to  $k = 14$  using a pruned basis set with  $b = 8$  (Section 4), and we obtained the vibrational energies within  $0.03 \text{ cm}^{-1}$  from the  $k = 8$  values (using the same basis) up to  $3000 \text{ cm}^{-1}$  beyond the zero-point energy.

### 5.2. Smolyak quadrature

We use the Smolyak approach [6,13–15,18,41] to construct efficient non-product grids for the pruned basis set, Eqs. (28)–(29), that can

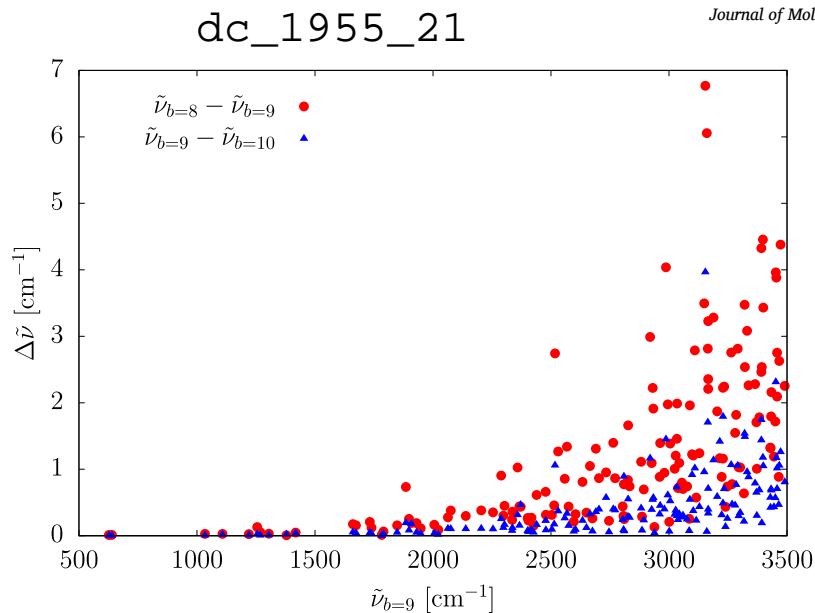


**Fig. 9.** Assessment of the convergence of the vibrational band origin obtained with a  $b = 9$  pruned basis set, Eqs. (28)–(29), using relaxed curvilinear (rc-) normal coordinates for the non-torsional degrees of freedom. The vibrational energies are compared with smaller ( $b = 8$ ) and larger ( $b = 10$ ) basis-set results. The zero-point energy with  $b = 8, 9$ , and  $10$  is  $\tilde{\nu}_0 = 7350.84, 7350.82$ , and  $7350.81$   $\text{cm}^{-1}$ , respectively.

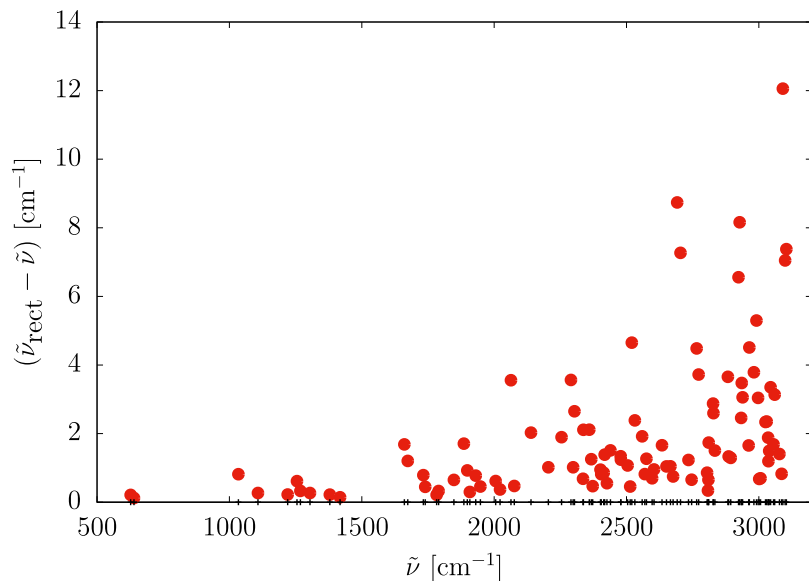


**Fig. 10.** Difference between the vibrational energies obtained using rectilinear,  $\tilde{\nu}_{\text{rect}}$ , and relaxed curvilinear (rc-),  $\tilde{\nu}$ , normal coordinates for the non-torsional degrees of freedom. In both cases the pruned basis set corresponds to the  $b = 8$  parameter, Eqs. (28)–(29). The corresponding ZPVEs are  $\tilde{\nu}_0 = 7350.84$   $\text{cm}^{-1}$  and  $\tilde{\nu}_{\text{rect},0} = 7350.91$   $\text{cm}^{-1}$ .

be used to evaluate the multi-dimensional integrals appearing in the kinetic energy coefficients, Eq. (21), and in the PES. The Smolyak quadrature for nine dimensions is defined as

$$Q(9, H) = \sum_{\sigma_s(i) \leq H} \otimes \prod_{\chi=1}^9 \Delta \hat{Q}_{\chi}^{i_{q_{\chi}}}, \quad i_{\chi} = 1, 2, 3, 4, \dots, \chi = 1, \dots, 9$$

with  $\sigma_s(i) = s^{\tau}(i_{\tau}) + s^{q_1}(i_{q_1}) + \dots + s^{q_8}(i_{q_8})$ , (40)

where  $H$  is a grid-pruning parameter,  $\sigma_s(i)$  is a grid-pruning function, and the incremental operator is defined as

$$\Delta \hat{Q}_{\chi}^{i_{\chi}} = \hat{Q}_{\chi}^{i_{\chi}} - \hat{Q}_{\chi}^{i_{\chi}-1} \quad (41)$$

with  $\hat{Q}_{\chi}^0 = 0$  and the 1D quadrature rules,

$$\hat{Q}_{\chi}^{i_{\chi}} f(q_{\chi}) = \sum_{m=1}^{m_{i_{\chi}}} w_{\chi,m}^{i_{\chi}} f(q_{\chi,m}^{i_{\chi}}), \quad i_{\chi} = 1, 2, 3, 4, \dots \quad (42)$$

Equivalently, we can also write the Smolyak quadrature as a linear combination of product quadratures with different 1-dimensional accuracies as

$$Q(9, H) = \sum_{\sigma_s(i) \leq H} C_i \left( \otimes \prod_{\chi=1}^9 \hat{Q}_{\chi}^{i_{\chi}} \right), \quad i_{\chi} = 1, 2, 3, 4, \dots, \chi = 1, \dots, 9, \quad (43)$$

$$\text{with } \sigma_s(i) = s^{\tau}(i_{\tau}) + s^{q_1}(i_{q_1}) + \dots + s^{q_8}(i_{q_8}). \quad (44)$$

$Q(9, H)$  has a smaller number of points, than the direct product grid,  $\hat{Q}_{q_1}^{i_{q_1}^{\max}} \otimes \dots \otimes \hat{Q}_{q_8}^{i_{q_8}^{\max}} \otimes \hat{Q}_{\tau}^{i_{\tau}^{\max}}$ , and its accuracy depends on three factors, (a) the form of the  $s^{\chi}(i_{\chi})$  grid pruning functions, for which  $s^{\chi}(i_{\chi}) \geq s^{\chi}(i_{\chi}-1)$  must hold; (b) the grid-pruning parameter  $H$ ; and (c) the number of the  $m_{i_{\chi}}$  grid points, for which  $m_{i_{\chi}} \geq m_{i_{\chi}-1}$  must hold.

For constructing the Smolyak grid in the present work, we define the  $s^{\chi}(i_{\chi})$  functions as follows:

$$\chi = \tau : \quad s^{\chi}(i_{\chi}) = 10 \quad (45)$$

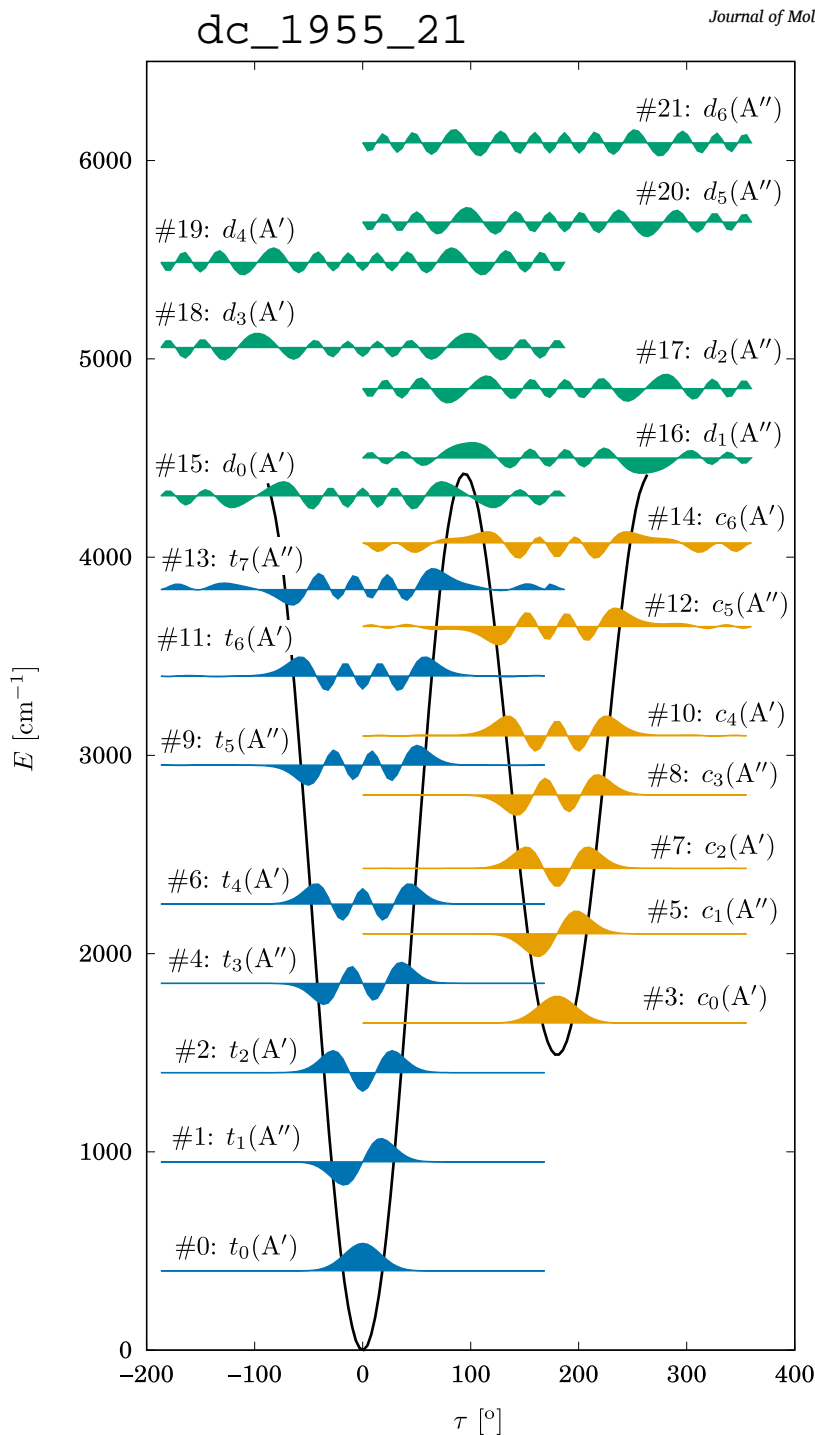


**Fig. 11.** Visualization of the *trans*- (blue), the *cis*- (yellow), and the lowest-energy *delocalized* (green) 1D torsional functions that were obtained by solving the 1D torsional Schrödinger equation, Eq. (27). The symmetry properties of the functions with respect to reflection to the plane defined by the equilibrium structures ( $\tau = 0^\circ$  and  $180^\circ$  in the figure) are collected in Table 1.

$$\chi = q_1, \dots, q_8 : s^\chi(i_\chi) = 10i_\chi, \quad i_\chi = 1, 2, 3, \dots \quad (46)$$

The value of  $H$ , which sets an upper limit on the sum of the  $s$  function values, is chosen according to this definition. The sequences of quadrature rules  $\hat{Q}_\chi^{i_\chi}$  are chosen as

$$\chi = \tau : \hat{Q}_\tau^{i_\tau} = \hat{Q}_{M_\tau^{\max}}^{\text{trap}}, \quad i_\tau = 1, 2, 3, \dots$$

$$\chi = q_1, \dots, q_8 : \hat{Q}_\chi^{i_\chi} = \hat{Q}_{m_{i_\chi}}^{\text{Her}}, \quad i_\chi = 1, 2, 3, \dots$$

with

$$m_{i_\chi} = 1, 3, 3, 7, 9, 9, 9, 9, 17, 19, 19, 19, 31, 33, 41, 41, \dots \quad (47)$$

where  $\hat{Q}_{M_\tau^{\max}}^{\text{trap}}$  is a trapezoidal quadrature rule of  $M_\tau^{\max}$  points and a maximum degree of  $d_\tau = 2M_\tau^{\max} - 1$ , while  $\hat{Q}_{m_{i_\chi}}^{\text{Her}}$  are nested quadrature rules for Hermite polynomials with a maximum degree of  $d_{i_\chi} = 1, 5, 5, 7, 15, 15, 15, 15, 17, 29, 29, 29, 31, 33, 61, 61, \dots$  corresponding to  $i_\chi = 1, 2, 3, \dots$  [42] Nesting means that all quadrature points of the quadrature rule  $\hat{Q}^j$  appear in the higher-order quadrature rule,  $\hat{Q}^{j+1}$ .

Using this construct with  $M_\tau = 11$  trapezoidal points and  $H = 150$ , we can integrate exactly all overlap matrix elements for the pruned basis set with  $0 \leq n_\tau \leq 4$  and  $0 \leq n_{q_1} + \dots + n_{q_8} \leq 8$  conditions. For  $H = 170$ , the Smolyak grid includes  $1\,230\,251 \approx 1.2 \cdot 10^6$  points. The

**Table 1**

Plane reflection symmetry ( $C_s$  point group) with respect to the equilibrium structures of the one-dimensional basis functions used in the computations (Section 4). The first 22 1-dimensional (1D) torsional functions ( $c, t, d$ ) are plotted in Fig. 11. ( $n = 0, 1, 2, \dots, m = 1, 2, \dots$ ).

$A'$	$A''$
$1_n, 2_n, 3_n, 4_n, 5_n, 6_n, 7_n$	–
$8_0, 8_2, \dots, 8_{2n}$	$8_1, 8_3, \dots, 8_{2n+1}$
$t_0, t_2, t_4, t_6$	$t_1, t_3, t_5, t_7$
$c_0, c_2, c_4, c_6$	$c_1, c_3, c_5$
$d_0, d_3, d_4, \dots, d_{4m-1}, d_{4m}$	$d_1, d_2, d_5, d_6, \dots, d_{4m-3}, d_{4m-2}$

smallest 9D direct-product Gauss grid that integrates correctly the same overlap matrix would have  $11 \cdot 9^8 \approx 4.7 \cdot 10^8$  points.

The Smolyak algorithm using nested sequences of quadrature rules allows us to use a non-product grid that has a structure, *i.e.*, a multi-dimensional integral of a function  $F(x_1, \dots, x_9)$  can be written as

$$\int F(x_1, \dots, x_9) dx_1 \dots dx_9 \approx \sum_{k_1=1}^{k_1^{\max}} \dots \sum_{k_9=1}^{k_9^{\max}} W^{\text{smol}}(k_1, \dots, k_9) F(x_1^{k_1}, \dots, x_9^{k_9}), \quad (48)$$

where  $W^{\text{Smolyak}}(k_1, \dots, k_9)$  is the multi-dimensional Smolyak weight and the points are sorted according to the sequence of quadrature rules. The structure appears in the  $k_c^{\max}$  indexes.  $k_1$  depends on  $H$ ,  $k_2$  depends on  $H$  and  $k_1$ , etc. and thus, matrix–vector products can be computed by sequential summation [13,15–17,40,43–45]. Eigenvalues and eigenvectors are computed using a Lanczos iterative eigensolver that requires only the multiplication of the Hamiltonian matrix with a vector. Implementation details regarding the matrix–vector multiplication has been described in Refs. [13,15,16].

## 6. Numerical results

We have computed the vibrational energies using the basis set and pruning condition defined in Eqs. (28) and (29). The number of torsional basis functions was 55 and we used 79 grid points for this degree of freedom. Regarding the 8-dimensional (8D) rc-normal coordinate part of the problem, three basis set sizes were used with the  $b = 8, 9$ , and 10 basis pruning parameter and with the  $H = 190, 200$ , and 210 grid pruning parameter, respectively. As a result, the 9D basis sets with  $b = 8, 9$ , and 10 included 707 850, 1 337 050, and 2 406 690 basis functions, respectively. The size of the corresponding non-product Smolyak quadrature grid was 42 223 623, 72 656 063 and 132 043 839.

The value of  $H$  was selected to be able to exactly integrate the Hamiltonian matrix elements up to 5th order (in a hypothetical Taylor expansion) with the highest-excited basis functions in the pruned basis set. Of course, we have checked the effect of using a larger  $H$  value. For  $H = 200$  (instead of  $H = 190$ ) with  $b = 8$ , the eigenvalues up to  $5000 \text{ cm}^{-1}$ , beyond the zero-point vibrational energy (ZPVE), changed at most by  $0.001 \text{ cm}^{-1}$ . Based on these observations, we think that the procedure is almost perfectly variational, which corresponds to an exact integration and provides rigorous energy upper bounds. Further computations with the more elaborate pruning condition in Eq. (34), with larger basis and grid sizes are in progress and will allow us to have access to well-converged vibrational energies beyond  $2000 \text{ cm}^{-1}$  above the ZPVE.

Convergence properties have been tested with respect to the basis set size (Fig. 9) and the coordinate representation (Fig. 10). Fig. 9 shows that the vibrational energies with  $b = 9$  are converged better than  $1 \text{ cm}^{-1}$  up to ca.  $2500 \text{ cm}^{-1}$ , and within ca.  $2 \text{ cm}^{-1}$  up to  $3500 \text{ cm}^{-1}$  beyond the ZPVE.

Fig. 10 highlights the efficiency of the rc-normal coordinates (Section 2) in comparison with the rectilinear normal coordinates (for the non-torsional degrees of freedom). For the  $b = 8$  basis, the rectilinear

normal coordinate vibrational energies differ (are less accurate) by  $8\text{--}10 \text{ cm}^{-1}$  from the rc-normal coordinate results.

We have also tested the coordinate definition of Lauvergnat and Nauts who computed the vibrational states of the methanol molecule in full dimensionality (12D) [6]. They did not relax and interpolate the normal coordinate coefficients along the large-amplitude coordinate, but they calculated the average of the (curvilinear) normal coordinate coefficients at the two local minima, hence we may call their coordinates averaged, curvilinear (ac-) normal coordinates. For HCOOH, we have performed computations both with ac- and rc-normal coordinates with the  $b = 8$  basis set. We have found that (for the present system) the relaxed curvilinear (rc-) normal coordinates slightly outperform simple averaging (ac-normal coordinates), but the difference is typically less than  $0.5 \text{ cm}^{-1}$  in the higher energy range. Hence, the ac-normal coordinates appear to be an excellent choice and they are technically much simpler to construct than the rc-normal coordinates used in the present work. Nevertheless, if there are multiple minima, stronger coupling of the large-amplitude motion with the ‘rest’ of the molecule, or more than one large-amplitude motions, then we can anticipate that the relaxation-interpolation approach used in the present work is, in principle, more efficient.

### 6.1. Torsional assignment

Since the computation is not localized to one of the wells of the PES (Fig. 11), it is a relevant question to ask whether a given state can be assigned to the *trans* or the *cis* conformer. The torsional assignment of the 9D wave functions was performed based on the contribution of the 1D torsional basis functions (Fig. 11). Unless the torsional energy is very high, the torsional functions are localized in the *trans* or in the *cis* well, *i.e.*, they have a well-defined number of nodes beyond the ground state in ‘their’ well. The 1D torsional functions are eigenfunctions of the Schrödinger equation with the 1D torsional Hamiltonian, Eq. (27). There are eight 1D *trans* torsional functions ( $t_0, t_1, \dots, t_7$ ) and there are seven 1D *cis* torsional functions ( $c_0, c_1, \dots, c_6$ ). Beyond these states, the torsional functions have nodes in both wells and we call them *delocalized* functions. Each torsional function has a well-defined parity with respect to reflection to the plane of the equilibrium structures (Table 1). The torsional assignment of a 9D vibrational state was performed based on the assignment of the dominant torsional function. The plane reflection symmetry of the 9D vibrational wave function can be determined by the symmetry of the torsional functions and the symmetry of the out-of-plane vibrational mode (Table 1).

Regarding the *trans* states computed with the GENIUSH-Smolyak approach ( $b = 9$  and 10), we observe an overall good agreement with the internal-coordinate path Hamiltonian (ICPH) [28] and a very good agreement with the 6th-order canonical van Vleck perturbation theory (CVPT) [30] results (Fig. 12). The present variational computations systematically improve upon the CVPT results by  $5\text{--}10\text{--}(25) \text{ cm}^{-1}$  up to  $4000 \text{ cm}^{-1}$  beyond the ZPVE. The good agreement of the *trans* vibrational energies (and assignments) with CVPT is interesting, since the CVPT computation was based on a single-well description and the *cis* zero-point vibration is only  $1418 \text{ cm}^{-1}$  higher than the *trans* ZPVE, but it can be explained by the relatively high *cis-trans* isomerization barrier (Fig. 11).

The current (almost perfectly variational) computation improves the CVPT results by  $1\text{--}5 \text{ cm}^{-1}$  in the range up to ca.  $2500 \text{ cm}^{-1}$ , and by ca.  $5\text{--}15 \text{ cm}^{-1}$  in the  $2500\text{--}4000 \text{ cm}^{-1}$  range. We can spot one important outlier from this favorable comparison at around  $3808 \text{ cm}^{-1}$  (Fig. 12). For this state the GENIUSH-Smolyak ( $b = 9$ ) energy is by  $25 \text{ cm}^{-1}$  higher than the CVPT energy, and by comparing the  $b = 9$  and 10 energies, it is unlikely that some further enlargement of the basis set ( $b = 11, 12$ ) reduces this deviation to a value below  $5 \text{ cm}^{-1}$ . This state is unambiguously assigned to  $7_6t_0$  in both computation, which is the 6th excitation of the lowest-energy, totally symmetric harmonic mode ( $\nu_7$ ). By considering the currently used pruning condition, Eq. (29),

Table 2

*Trans*-HCOOH: vibrational excitation energies,  $\tilde{\nu}$  in  $\text{cm}^{-1}$ , computed with the GENIUSH-Smolyak approach in comparison with the sixth-order canonical van Vleck perturbation theory (CVPT) [30] and the internal-coordinate reaction-path Hamiltonian (ICPH) [28] results. (The footnotes are below Table 3.)

# <sup>a</sup>	Assign. <sup>b</sup>	$\tilde{\nu}$	$(\delta_{10}, \delta_3)^c$	CVPT	ICPH	# <sup>a</sup>	Assign. <sup>b</sup>	$\tilde{\nu}$	$(\delta_{10}, \delta_3)^c$	CVPT	ICPH
1	ZPV- $t_0$	7351	(0, 0)	[n.a.]	7354	71	$6_2 7_1 t_0$	2827	(1, 2)	2826	2825
2	$7_1 t_0$	627	(0, 0)	627	627	72	$6_2 t_1$	2833	(0, 1)	2836	2829
3	$t_1$	639	(0, 0)	640	638	73	$7_1 8_1 t_2$	2882	(0, 1)	2885	2890
4	$8_1 t_0$	1034	(0, 0)	1035	1034	74	$3_1 6_1 t_0$	2886	(0, 0)	2884	2886
5	$6_1 t_0$	1108	(0, 0)	1108	1108	75	$6_1 t_3$	2893	(0, 1)	2894	2902
6	$t_2$	1220	(0, 0)	1221	1222	76	$7_3 8_1 t_0$	2920	(1, 3)	2919	2925
7	$7_2 t_0$	1255	(0, 0)	1256	1256	77	$[7_1 t_4, 6_1 7_1 t_2]$	2926	(0, 1)	2934	2952
8	$7_1 t_1$	1268	(0, 0)	1269	1268	79	$7_2 8_1 t_1$	2934	(1, 2)	2934	2940
9	$5_1 t_0$	1304	(0, 0)	1305	1305	80	$2_1 t_0$	2938	(0, 0)	2940	2938
10	$4_1 t_0$	1379	(0, 0)	1380	1379	81	$[7_1 t_4, 6_1 7_1 t_2]$	2961	(0, 1)	2964	3066
12	$7_1 8_1 t_0$	1661	(0, 0)	1661	1661	82	$5_1 7_1 8_1 t_0$	2963	(0, 1)	2965	2965
13	$8_1 t_1$	1673	(0, 0)	1675	1672	83	$5_1 8_1 t_1$	2980	(0, 1)	2983	2981
14	$6_1 7_1 t_0$	1732	(0, 0)	1732	1733	84	$6_1 7_3 t_0$	2987	(1, 4)	2986	2996
15	$6_1 t_1$	1739	(0, 0)	1741	1739	85	$6_1 7_2 t_1$	2995	(1, 2)	2996	3004
16	$3_1 t_0$	1783	(0, 0)	1783	1783	86	$3_1 t_2$	3001	(0, 0)	3002	3003
17	$t_3$	1790	(0, 0)	1793	1795	88	$3_1 7_2 t_0$	3024	(0, 1)	3025	3027
18	$7_1 t_2$	1848	(0, 0)	1850	1855	89	$[5_1 6_1 7_1 t_0]$	3028	(0, 1)	3030	3033
19	$7_3 t_0$	1885	(0, 1)	1886	1890	91	$[5_1 6_1 t_1]$	3034	(0, 2)	3038	3036
20	$7_2 t_1$	1898	(0, 0)	1900	1903	92	$3_1 7_1 t_1$	3038	(0, 1)	3040	3041
22	$5_1 7_1 t_0$	1930	(0, 0)	1932	1933	93	$4_1 7_1 8_1 t_0$	3043	(0, 1)	3044	3046
23	$5_1 t_1$	1948	(0, 0)	1950	1947	94	$[7_1 t_1, 7_2 t_3]$	3055	(0, 1)	3057	[3109]
24	$4_1 7_1 t_0$	2006	(0, 0)	2006	2006	95	$4_1 8_1 t_1$	3059	(0, 1)	3061	3058
25	$4_1 t_1$	2022	(0, 0)	2024	2021	96	$[5_1 t_3]$	3077	(0, 1)	3080	3084
26	$8_2 t_0$	2063	(0, 0)	2066	2063	97	$3_1 5_1 t_0$	3086	(0, 0)	3087	3087
28	$6_1 8_1 t_0$	2139	(0, 0)	2139	2139	98	$8_3 t_0$	3089	(1, 2)	3094	3090
29	$6_2 t_0$	2205	(0, 0)	2204	2205	100	$4_1 6_1 7_1 t_0$	3103	(0, 1)	3103	3105
30	$8_1 t_2$	2254	(0, 0)	2257	2257	101	$[7_3 t_2]$	3109	(1, 3)	3112	[3144]
31	$7_2 8_1 t_0$	2289	(0, 1)	2290	2290	102	$4_1 6_1 t_1$	3115	(0, 1)	3117	3115
32	$[t_4, 6_1 t_2, 5_1 t_2]$	2298	(0, 0)	2305	2312	103	$[5_2 7_1 t_0]$	3129	(0, 1)	3135	[3159]
33	$7_1 8_1 t_1$	2303	(0, 0)	2304	2302	105	$7_3 t_0$	3154	(4, 7)	3149	
34	$[t_4, 6_1 t_2]$	2336	(0, 0)	2338	2358	106	$3_1 4_1 t_0$	3160	(0, 6)	3160	3161
35	$5_1 8_1 t_0$	2337	(0, 0)	2338	2338	107	$7_4 t_1$	3165	(2, 3)	3164	
36	$6_1 7_2 t_0$	2358	(0, 1)	2359	2361	109	$4_1 t_3$	3166	(0, 2)	3171	
37	$6_1 7_1 t_1$	2366	(0, 0)	2368	2369	110	$6_1 8_2 t_0$	3166	(0, 3)	3166	
39	$[5_1 6_1 t_0]$	2401	(0, 0)	2405	2406	111	$5_1 7_3 t_0$	3189	(1, 3)	3192	
40	$3_1 7_1 t_0$	2404	(0, 0)	2402	2402	112	$5_1 7_2 t_1$	3204	(1, 2)	3209	
41	$[3_1 t_1, 4_1 8_1 t_0]$	2414	(0, 0)	2418	2420	114	$4_1 7_1 t_2$	3223	(0, 1)	3226	
42	$4_1 8_1 t_0$	2417	(0, 0)	2416	2415	115	$[5_2 7_1 t_0, 5_1 7_1 t_2]$	3229	(2, 1)	3235	
43	$3_1 t_1$	2426	(0, 0)	2427	2420	117	$6_2 8_1 t_0$	3234	(1, 2)	3232	
49	$7_4 t_0$	2517	(1, 3)	2517	2517	119	$[5_2 t_1]$	3247	(0, 1)	3255	
50	$7_3 t_1$	2530	(0, 1)	2531	[2543]	120	$4_1 7_3 t_0$	3263	(1, 3)	3264	
51	$5_1 7_2 t_0$	2558	(0, 1)	2561	2568	121	$t_6$	3267	(0, 1)	3295	
53	$5_1 7_1 t_1$	2575	(0, 0)	2579	2579	122	$4_1 7_2 t_1$	3280	(0, 2)	3283	
54	$4_1 t_2$	2597	(0, 0)	2598	2600	123	$8_2 t_2$	3285	(1, 2)	3290	
55	$[5_2 t_0, 5_1 t_2]$	2604	(0, 0)	2608	2608	124	$6_3 t_0$	3291	(1, 3)	3289	3292
56	$4_1 7_2 t_0$	2633	(0, 1)	2634	2636	126	$[4_1 5_1 7_1 t_0]$	3301	(0, 1)	3305	
57	$4_1 7_1 t_1$	2650	(0, 0)	2653	2652	127	$[4_1 5_1 t_1]$	3318	(0, 1)	3322	
59	$4_1 5_1 t_0$	2676	(0, 0)	2678	2678	128	$7_2 8_2 t_0$	3320	(2, 3)	3320	3321
60	$7_1 8_2 t_0$	2690	(0, 1)	2692	2690	130	$7_1 8_2 t_1$	3331	(1, 3)	3335	
61	$8_2 t_1$	2703	(0, 1)	2707	2702	131	$[8_1 t_4, 7_1 8_2 t_1, 8_2 t_2]$	3337	(1, 2)	3340	
63	$4_2 t_0$	2746	(0, 0)	2747	2746	132	$5_1 8_2 t_0$	3365	(1, 2)	3368	
64	$6_1 7_1 8_1 t_0$	2764	(0, 1)	2763	2764	133	$[8_1 t_4, 6_1 8_1 t_2]$	3370	(1, 2)	3374	
65	$6_1 8_1 t_1$	2772	(0, 1)	2773	2771	134	$4_2 7_1 t_0$	3372	(0, 1)	3373	
66	$t_5$	2804	(0, 0)	2818	2818	135	$[6_1 t_4]$	3383	(1, 2)	3386	
69	$3_1 8_1 t_0$	2810	(0, 0)	2810	2810	136	$6_1 7_2 8_1 t_0$	3391	(2, 2)	3389	
70	$8_1 t_3$	2826	(0, 1)	2830	2834	138	$4_2 t_1$	3393	(0, 3)	3396	

and the  $b = 8, 9, 10$  (11, 12) values of the pruning parameters (that are computationally feasible), we think that for this state our result is in an error and CVPT makes a (probably) good prediction. We can improve the GENIUSH-Smolyak results, without significantly increasing the computational cost, by using the more elaborate pruning condition in Eq. (34). The Eq. (34) pruning simply allows to double the number of basis functions for the totally symmetric, lowest-frequency mode, while keeping the size of the multi-dimensional basis within reasonable limits. Further work in this direction is in progress and will be reported in the future.

Regarding the *cis* states, the computed fundamentals agree well from all computations (GENIUSH-Smolyak, ICPH, and CVPT). We note that the highest energy  $c_1$  vibration is not (yet) available from the GENIUSH-Smolyak computations (this work), nor from ICPH Ref. [28].

Although CVPT results are available for all *cis* fundamental vibrations [30], combination and overtone bands have not been reported.

Fig. 13 shows the comparison for *cis* states up to two excitations (based on the wave function assignments, Tables 4–5) of the GENIUSH-Smolyak ( $b = 9, 10$ ) and the ICPH [28] results. Similarly to the *trans* energies, there is an overall good agreement, but several ICPH energies are too high (by 10–40  $\text{cm}^{-1}$ ).

Beyond 3700  $\text{cm}^{-1}$  (above the *trans*-ZPVE), we can see mixed *cis-trans* states, in which torsional functions corresponding to the *trans* and other functions corresponding to the *cis* well are entangled (Tables 4–5). Several *cis-trans* entangled states come in pairs corresponding to + and – combinations of *cis* and *trans* basis functions. The corresponding ‘tunneling’ splittings, which we currently compute to be  $< 1 - 5(-10)$   $\text{cm}^{-1}$ , are smaller or on the borderline with respect to the convergence uncertainty of the  $b = 9$  basis in the relevant energy range

**Table 3**  
*Trans*-HCOOH. (Table 2 continued, CVPT [30], ICPH [28].)

# <sup>a</sup>	Assign. <sup>b</sup>	$\tilde{\nu}$	( $\delta_{10}, \delta_8$ ) <sup>c</sup>	CVPT	ICPH	# <sup>a</sup>	Assign. <sup>b</sup>	$\tilde{\nu}$	( $\delta_{10}, \delta_8$ ) <sup>c</sup>	CVPT	ICPH
140	6,7,8,1 <sub>t1</sub>	3400	(1, 3)	3399		198	[4,1 <sub>t4</sub> ]	3705	(0, 1)	3712	
141	[7,1 <sub>t3</sub> ]	3430	(1, 1)	3448		199	3,5,7,1 <sub>t0</sub>	3706	(0, 1)	3708	
142	3,7,8,1 <sub>t0</sub>	3430	(0, 1)	3431		200	[5,7,1 <sub>t3</sub> , 7,1 <sub>t3</sub> ]	3706	(1, 2)	3707	
143	[6,1 <sub>t4</sub> , 6,2 <sub>t2</sub> ]	3433	(1, 2)	3433		201	4,5,1,8,1 <sub>t0</sub>	3711	(1, 2)	3713	
144	[5,1,6,8,1 <sub>t0</sub> ]	3434	(1, 2)	3434		202	7,1,8,3 <sub>t0</sub>	3717	(2, 5)	3719	
145	3,1,8,1 <sub>t1</sub>	3445	(0, 1)	3447		204	4,6,1,7,2 <sub>t0</sub>	3730	(2, 1)	3729	
146	4,1,8,2 <sub>t0</sub>	3451	(1, 2)	3452		205	8,3 <sub>t1</sub>	3730	(2, 4)	3735	
147	6,2,7,2 <sub>t0</sub>	3453	(2, 4)	3450		206	3,1,5,1 <sub>t1</sub>	3730	(0, 5)	3732	
149	[6,2,7,1 <sub>t1</sub> ]	3458	(1, 2)	3461		207	4,1,6,1,7,1 <sub>t1</sub>	3743	(1, 2)	3745	
150	[7,1,8,1 <sub>t3</sub> ]	3458	(1, 3)	3461		208	[7,1 <sub>t2</sub> ]	3745	(4, 10)	3744	
154	[5,1,6,2 <sub>t0</sub> ]	3490	(1, 2)	3491		213	[4,1,5,1,6,1 <sub>t0</sub> ]	3764	(1, 2)	3770	
155	3,1,6,1,7,1 <sub>t0</sub>	3504	(0, 1)	3503		214	[5,3 <sub>t0</sub> ]	3777	(1, 2)	3785	
156	[3,1,6,1,1,7,2,8,1 <sub>t2</sub> ]	3511	(1, 2)	3514		215	3,1,4,7,1 <sub>t0</sub>	3781	(0, 1)	3781	
157	[4,1,6,1,8,1 <sub>t0</sub> ]	3512	(1, 3)	3511		216	4,2,8,1 <sub>t0</sub>	3784	(0, 2)	3785	
158	[4,1,6,1,8,1 <sub>t0</sub> ]	3515	(1, 2)	3514		217	[4,1,7,1 <sub>t3</sub> ]	3792	(2, 1)	3797	
159	[3,1,6,1,1,7,1,1 <sub>t3</sub> ]	3522	(1, 2)	3514		218	6,1,7,8,2 <sub>t0</sub>	3793	(2, 6)	3790	
161	[5,2,8,1 <sub>t0</sub> ]	3536	(1, 2)	3539		219	6,1,8,2 <sub>t1</sub>	3801	(9, 5)	3801	
162	3,2 <sub>t0</sub>	3546	(0, 0)	3545	3547	220	7,5 <sub>t1</sub>	3805	(6, 2)	3797	
163	7,1,8,1 <sub>t0</sub>	3556	(4, 5)	3550		221	3,1,4,1 <sub>t1</sub>	3805	(6, 11)	3807	
164	[7,2,1 <sub>t4</sub> ]	3557	(1, 9)	3564		222	7,6 <sub>t0</sub>	3808	(3, 14)	3783	
165	[4,1,6,2 <sub>t0</sub> ]	3563	(1, 3)	3563		225	[5,1,7,4 <sub>t0</sub> ]	3825	(5, 10)	3825	
166	2,1,7,1 <sub>t0</sub>	3566	(1, 3)	3568	3566	227	3,1,8,2 <sub>t0</sub>	3833	(1, 4)	3835	3833
167	7,3,8,1 <sub>t1</sub>	3567	(1, 2)	3565		229	4,2,6,1 <sub>t0</sub>	3835	(1, 8)	3835	3836
168	3,1 <sub>t3</sub>	3568	(0, 4)	3570		230	[5,1,7,3 <sub>t1</sub> ]	3837	(2, 9)	3841	
169	4,1,6,2 <sub>t0</sub>	3571	(1, 2)	3565		234	6,2,7,1,8,1 <sub>t0</sub>	3858	(3, 5)	3854	
170	1,1 <sub>t0</sub>	3576	(0, 0)	3576	3575	235	[8,2 <sub>t3</sub> ]	3859	(2, 5)	3864	
171	2,1 <sub>t1</sub>	3578	(0, 0)	3581	3579	237	[6,2,8,1 <sub>t1</sub> ]	3865	(2, 4)	3854	
173	[6,1,7,2,2,7,2,1 <sub>t4</sub> ]	3588	(1, 3)	3592		239	[5,2,7,1,1 <sub>t1</sub> ]	3873	(1, 3)	3884	
174	5,1,7,2,8,1 <sub>t0</sub>	3592	(2, 4)	3593		240	[6,1 <sub>t5</sub> ]	3882	(1, 3)	3890	
178	[5,1,7,1,8,1,1 <sub>t1</sub> ]	3607	(1, 4)	3611		247	4,1,7,4 <sub>t0</sub>	3898	(1, 8)	3895	
179	[5,1,1 <sub>t4</sub> , 5,2,6,1,1 <sub>t0</sub> ]	3612	(1, 2)	3615		249	3,1,6,1,8,1 <sub>t0</sub>	3911	(1, 2)	3909	
180	6,1,7,4 <sub>t0</sub>	3622	(6, 4)	3615		250	4,1,7,3 <sub>t1</sub>	3913	(2, 5)	3914	
181	3,1,7,1 <sub>t2</sub>	3625	(0, 9)	3626		251	[7,1,8,2,2,5,1,7,1,8,2 <sub>t0</sub> ]	3914	(3, 4)	3916	
182	6,1,7,3 <sub>t1</sub>	3627	(3, 9)	3625		254	[6,3 <sub>t1</sub> ]	3918	(2, 6)	3919	
183	[4,1,8,1,1 <sub>t2</sub> ]	3634	(1, 3)	3636		255	[6,1,8,1,1 <sub>t3</sub> ]	3928	(2, 4)	3929	
184	[4,1,5,1,8,1,1 <sub>t0</sub> ]	3635	(1, 5)	3638		256	[4,1,5,1,7,2 <sub>t0</sub> ]	3930	(1, 4)	3934	
185	3,1,7,3 <sub>t0</sub>	3649	(1, 4)	3649		257	[4,1,5,1,7,1,1 <sub>t1</sub> ]	3944	(1, 2)	3951	
186	[5,1,6,1,7,2 <sub>t0</sub> ]	3656	(2, 5)	3656		258	2,1,8,1 <sub>t0</sub>	3952	(3, 1)	3954	3952
187	[5,1,6,1,7,1,1,7,1,1 <sub>t3</sub> ]	3659	(1, 3)	3659		260	7,3,8,2 <sub>t0</sub>	3955	(3, 3)	3949	
189	3,1,7,2 <sub>t1</sub>	3664	(1, 2)	3664		262	[4,2,2,2,4,2,5,1,1 <sub>t0</sub> ]	3959	(0, 7)	3965	
190	[4,1 <sub>t4</sub> ]	3672	(1, 1)	3670		263	[7,2,8,2 <sub>t1</sub> ]	3962	(3, 7)	3963	
191	4,1,7,2,8,1 <sub>t0</sub>	3672	(1, 4)	3672		264	[4,1,5,2 <sub>t0</sub> , 4,2 <sub>t2</sub> ]	3965	(1, 6)	3977	
192	1 <sub>t7</sub>	3679	(1, 2)	3679		265	[7,2,8,2 <sub>t1</sub> ]	3969	(3, 8)	3963	
194	[7,3 <sub>t3</sub> ]	3687	(1, 3)	3688		266	3,1,6,2 <sub>t0</sub>	3978	(1, 2)	3975	3978
195	4,1,7,1,8,1 <sub>t1</sub>	3688	(1, 3)	3690		268	[6,2,1 <sub>t3</sub> ]	3985	(2, 4)	3984	
196	[5,1,6,1,1 <sub>t2</sub> ]	3693	(1, 2)	3698		269	5,1,7,8,2 <sub>t0</sub>	3993	(3, 6)	3994	

<sup>a</sup> #: Number of the state in the full vibrational energy list including *cis*, *trans*, and *delocalized* states.

<sup>b</sup> Excitation number for the *rc*-normal modes, 1<sub>*n*</sub>, 2<sub>*n*</sub>, 3<sub>*n*</sub>, 4<sub>*n*</sub>, 5<sub>*n*</sub>, 6<sub>*n*</sub>, 7<sub>*n*</sub>, 8<sub>*n*</sub> (*n* = 0, 1, ...), zero excitation is not shown. For the 9th degree of freedom, the type of torsional function (Fig. 11) and the excitation number is indicated, *t<sub>n</sub>/c<sub>n</sub>/d<sub>n</sub>* with *n* ≥ 0. ‘[...]’ labels the largest contribution(s) from strongly mixed states. The symmetry behavior with respect to plane reflection can be derived from the properties of the 1D basis functions according to Table 1 by multiplication of the characters.

<sup>c</sup> ( $\delta_{10}, \delta_8$ ) = ( $\tilde{\nu}_{b=9} - \tilde{\nu}_{b=10}, \tilde{\nu}_{b=8} - \tilde{\nu}_{b=9}$ ) is shown for assessment of the convergence. The reported  $\tilde{\nu}$  values and the assignment correspond to the *b* = 9 basis set.

(indicated by ( $\delta_{10}, \delta_8$ ) in the tables), and we plan to determine these splittings more precisely in future work.

Beyond 3900  $\text{cm}^{-1}$  (above the *trans*-ZPVE), non-negligible contribution from delocalized torsional states (Fig. 11) can be observed. Table 6 shows the lowest-energy vibrational states with a significant delocalized contribution (see also Tables 4–5). These states have an energy close to the *cis-trans* isomerization barrier height (Fig. 11) and in this range the *cis-trans-delocalized* functions strongly mix and for their good description a variational procedure appears to be necessary. Further, better converged results will be reported in future work.

## 7. Summary, conclusion, and outlook

Variational vibrational excitation energies have been reported for the formic acid molecule up to ca. 4700  $\text{cm}^{-1}$ , which is slightly beyond the top of the *cis-trans* isomerization barrier, using system-adapted curvilinear coordinates in the GENIUSH-Smolyak approach developed in the present work and a high-level *ab initio* potential energy surface (PES) taken from Ref. [28].

The results confirm (within 1–5  $\text{cm}^{-1}$ ) up to 2500  $\text{cm}^{-1}$ , and improve (by 5–10  $\text{cm}^{-1}$ ) between 2500 and 4000  $\text{cm}^{-1}$  the 6th-order canonical van Vleck perturbation theory (CVPT) energies [30] that were obtained from a computation localized on the *trans* PES well. Both the *cis* and *trans* energies computed with the GENIUSH-Smolyak approach are in an overall good agreement, but improve (by 10–40  $\text{cm}^{-1}$ ) upon the internal-coordinate path Hamiltonian (ICPH) results that similarly to the present work account for both the *cis* and *trans* wells of the PES. There exists another potential energy surface and multi-configuration time-dependent Hartree (MCTDH) computations have been reported using that PES [29,46]. Direct comparison with those results have not been reported in this work, because our current focus was on the development of a computational procedure that can be used to provide benchmark quality vibrational energies up to and possibly beyond the isomerization barrier of the formic acid molecule. We think that we have almost achieved this goal, further necessary work with larger basis sets and an improved basis pruning condition is in progress and results will be reported in future work.

Table 4

Cis-HCOOH (including contributions from *trans* and *delocalized* states): vibrational energies,  $\tilde{\nu}$  in  $\text{cm}^{-1}$  referenced to the *trans*-ZPVE, computed with the GENIUSH-Smolysk approach in comparison with the internal-coordinate reaction-path Hamiltonian (ICPH) results [28]. (The footnotes are below Table 5.)

# <sup>a</sup>	Assign. <sup>b</sup>	$\tilde{\nu}$	( $\delta_{10}, \delta_8$ ) <sup>c</sup>	ICPH	# <sup>a</sup>	Assign. <sup>b</sup>	$\tilde{\nu}$	( $\delta_{10}, \delta_8$ ) <sup>c</sup>	ICPH
11	ZPV- $c_0$	1418	(0, 0)	1412	245	[ $c-t$ mixed]	3897	(3, 2)	
21	$c_1$	1908	(0, 0)	1904	246	[ $c+t$ mixed]	3898	(1, 4)	
27	$7_1c_0$	2076	(0, 0)	2080	248	[ $5_1c_3, 6_1c_3$ ]	3902	(2, 10)	[3915]
38	$c_2$	2372	(0, 0)	2400	252	[ $c_6-t$ mixed, $d_0$ ]	3914	(2, 5)	
44	$8_1c_0$	2439	(0, 1)	2450	253	[ $c_6+t$ mixed, $d_0$ ]	3916	(2, 7)	
48	$5_1c_0$	2514	(0, 0)	2514	259	$8_2c_1$	3953	(2, 4)	
52	$7_1c_1$	2568	(0, 1)	2577	261	$4_17_1c_1$	3956	(2, 4)	
58	$6_1c_0$	2665	(0, 1)	2667	267	[ $7_3c_0, 6_17_2c_0$ ]	3980	(2, 8)	
62	$7_2c_0$	2733	(1, 1)	2759	276	[ $5_18_1c_1, 6_18_1c_1$ ]	4027	(3, 5)	
67	$4_1c_0$	2807	(0, 0)	2806	277	[ $6_1c_3 + 3_18_1t_2$ ]	4029	(3, 7)	
68	$c_3$	2809	(1, 1)	278	278	[ $6_1c_3 - 3_18_1t_2$ ]	4029	(2, 7)	
78	$8_1c_1$	2931	(1, 2)	2937	281	[ $d_2, c, t$ mixed]	4036	(2, 7)	
87	$5_1c_1$	3005	(1, 1)	3009 <sup>†</sup>	283	$4_16_1c_0$	4049	(1, 2)	4061
90	$7_1c_2$	3034	(1, 1)		286	$7_4c_0$	4054	(2, 8)	
99	$7_18_1c_0$	3098	(1, 1)	3133	299	[ $5_16_1c_1, 5_2c_1$ ]	4096	(2, 9)	
104	$6_1c_1$	3149	(1, 3)	3159 <sup>†</sup>	306	$7_18_2c_0$	4116	(2, 7)	
108	[ $5_17_1c_0, 6_17_1c_0$ ]	3166	(1, 2)	3179	312	[ $5_17_1c_2, 6_17_1c_2$ ]	4135	(2, 3)	
113	$c_4$	3215	(1, 1)		314	$7_2c_3$	4142	(4, 6)	
116	$7_2c_1$	3229	(0, 2)		321	$4_2c_0$	4166	(0, 2)	4170
118	$3_1c_0$	3239	(0, 0)	3235	324	[ $6_18_1c_1, 5_18_1c_1$ ]	4178	(1, 3)	
125	$4_1c_1$	3296	(0, 1)	3299	327	[ $5_17_18_1c_0, 6_17_18_1c_0$ ]	4187	(3, 5)	
129	[ $6_17_1c_0$ ]	3321	(1, 3)		328	$3_1c_2$	4189	(2, 4)	
137	$7_3c_0$	3391	(1, 4)		329	[ $c, t$ mixed]	4189	(1, 4)	
139	$8_1c_2$	3398	(1, 4)		332	$4_1c_3$	4192	(2, 5)	
148	$8_2c_0$	3455	(1, 4)	3486	349	[ $6_2c_1, 5_2c_1$ ]	4243	(5, 11)	
151	$4_17_1c_0$	3465	(0, 1)	3475	350	[ $7_1c_5, 8_1c_4$ ]	4247	(2, 7)	
152	$5_1c_2$	3467	(1, 3)	3638	352	[ $5_16_17_1c_0, 5_27_1c_0$ ]	4250	(1, 7)	
153	$7_1c_3$	3473	(1, 4)		353	$3_18_1c_0$	4254	(1, 3)	4274
160	$5_18_1c_0$	3531	(1, 2)	3536	355	[ $7_28_1c_1 - 4_16_1t_3$ ]	4259	(4, 4)	
172	$c_5$	3582	(2, 2)	3570 <sup>*,†</sup>	356	[ $7_28_1c_1 + 4_16_1t_3$ ]	4259	(4, 9)	
175	$7_18_1c_1$	3594	(3, 3)		357	[ $7_1c_5, 8_1c_4$ ]	4260	(3, 8)	
176	[ $5_16_1c_0, 5_2c_0$ ]	3601	(1, 3)	3595 <sup>†</sup>	362	[ $6_17_1c_2, 7_2c_2$ ]	4273	(10, 10)	
177	[ $6_1c_2, 5_1c_2$ ]	3605	(2, 6)	3638	369	$2_1c_0$	4291	(1, 10)	4292
188	[ $5_17_1c_1, 7_18_1c_1$ ]	3661	(2, 3)		372	[ $c, t$ mixed]	4299	(1, 8)	
193	$6_18_1c_0$	3686	(2, 3)	3715 <sup>†</sup>	374	[ $5_1c_4, 6_1c_4$ ]	4303	(2, 13)	
197	$7_2c_2$	3698	(4, 4)		380	[ $5_17_2c_1, 6_17_2c_2$ ]	4320	(3, 9)	
203	$3_1c_1$	3727	(0, 1)	3733	383	[ $c, t$ mixed]	4325	(2, 7)	
209	[ $6_2c_0, 5_2c_0$ ]	3753	(2, 4)	3761 <sup>*,†</sup>	384	$4_18_1c_1$	4325	(2, 7)	
210	$4_1c_2 - [t$ mixed]	3757	(2, 2)		387	[ $3_15_1c_0, 3_16_1c_0$ ]	4330	(1, 4)	4322
211	$4_1c_2 + [t$ mixed]	3757	(1, 4)		391	[ $6_17_18_1c_0, 7_28_1c_0$ ]	4346	(4, 10)	
212	$7_28_1c_0$	3758	(1, 6)		398	$7_3c_2$	4366	(5, 12)	
223	$6_17_1c_1$	3811	(5, 14)		399	[ $d_3, c, t$ mixed]	4371	(5, 9)	
224	[ $5_17_2c_0, 6_17_2c_0$ ]	3820	(2, 15)		404	[ $6_2c_1, 5_16_1c_1$ ]	4378	(2, 7)	
226	[ $c, t$ mixed]	3833	(2, 4)		405	$3_17_1c_1$	4382	(2, 6)	
228	$4_18_1c_0$	3833	(1, 4)	3854	407	[ $3_17_1c_1, 4_15_1c_1$ ]	4388	(5, 3)	
231	[ $8_1c_3, 8_1t_5$ ]	3842	(2, 12)		416	[ $6_27_1c_0, 5_17_2c_0$ ]	4408	(5, 10)	
232	[ $c+t$ mixed]	3850	(1, 7)		419	[ $c-t$ mixed]	4420	(4, 5)	
233	[ $c-t$ mixed]	3854	(1, 4)		420	[ $c+t$ mixed]	4420	(3, 9)	
236	[ $c, t$ mixed]	3860	(2, 5)		421	$4_17_1c_2$	4421	(4, 10)	
238	[ $c, t$ mixed]	3873	(1, 2)		422	$7_38_1c_0$	4423	(5, 10)	
241	$7_1c_4$	3883	(2, 6)		424	$8_2c_2$	4427	(-, 9)	
242	[ $3_17_1c_0, 4_15_1c_0$ ]	3890	(2, 2)		437	$8_3c_0$	4467	(-, 8)	
243	$7_3c_1$	3891	(3, 4)		441	[ $7_3c_1, 6_17_2c_1$ ]	4477	(-, 12)	
244	[ $3_17_1c_0, 6_2c_0$ ]	3892	(2, 7)	3908	444	[ $5_27_2c_0, 6_17_3c_0, 5_17_3c_0$ ]	4479	(-, 15)	

Already in the present paper, *cis-trans* entangled states, corresponding ‘tunneling’ splittings, and the (*cis* or *trans*) localized to *delocalized* transition taking place near the top barrier were shortly discussed. Benchmark quality computed data (limited by the quality of the PES) on these interesting features will become available soon with the outlined theoretical, computational progress. We are not aware of detailed experimental data of these phenomena in HCOOH, and we look forward to developments from the experimental side.

#### CRedit authorship contribution statement

**Alberto Martín Santa Daría:** Software, Methodology, Investigation, Computations, Writing – original draft, Visualization. **Gustavo Avila:** Software, Methodology, Investigation, Computations, Writing – original draft. **Edit Mátyus:** Funding acquisition, Conceptualization, Methodology, Validation, Supervision, Writing – original draft, Review & editing.

#### Acknowledgment

We thank the financial support of the Swiss National Science Foundation (PROMYS Grant, No. IZ11Z0\_166525). The authors are indebted to Tucker Carrington, Attila Császár, and their co-workers for joint work and discussions over the past decade that had resulted in ideas and developments necessary to accomplish the present research. We also thank Martin Suhm and Arman Nejad who made us interested in working on this system.

#### Appendix A. Supplementary data

Normal coordinate coefficients and computed vibrational states. Supplementary material related to this article can be found online at <https://doi.org/10.1016/j.jms.2022.111617>.

Table 5

Cis-HCOOH (including contributions from *trans* and *delocalized* states). (Table 4 continued, ICPH [28].)

# <sup>a</sup>	Assign. <sup>b</sup>	$\tilde{\nu}$	$(\delta_{10}, \delta_8)^c$	ICPH	# <sup>a</sup>	Assign. <sup>b</sup>	$\tilde{\nu}$	$(\delta_{10}, \delta_8)^c$	ICPH
446	[3 <sub>1</sub> 6 <sub>1</sub> c <sub>0</sub> ]	4483	(-, 16)	4496	492	[7 <sub>1</sub> c <sub>6</sub> , c, d, t mixed]	4583	(-, 8)	
447	[c + t mixed]	4485	(-, 14)		496	[4 <sub>1</sub> c <sub>4</sub> + 3 <sub>1</sub> 6 <sub>2</sub> 7 <sub>1</sub> t <sub>0</sub> ]	4596	(-, 7)	
448	[c - t mixed]	4490	(-, 12)		497	[4 <sub>1</sub> c <sub>4</sub> - 3 <sub>1</sub> 6 <sub>2</sub> 7 <sub>1</sub> t <sub>0</sub> ]	4597	(-, 7)	
452	4 <sub>1</sub> 7 <sub>1</sub> 8 <sub>1</sub> c <sub>0</sub>	4493	(-, 17)		498	4 <sub>1</sub> c <sub>4</sub>	4598	(-, 7)	
453	[5 <sub>1</sub> 8 <sub>1</sub> c <sub>2</sub> , 6 <sub>1</sub> 8 <sub>1</sub> c <sub>2</sub> ]	4495	(-, 17)		508	4 <sub>1</sub> 7 <sub>2</sub> c <sub>1</sub>	4618	(-, 9)	
454	[c, t mixed]	4496	(-, 19)		509	[5 <sub>2</sub> 8 <sub>1</sub> c <sub>0</sub> , 5 <sub>1</sub> 6 <sub>1</sub> 8 <sub>1</sub> c <sub>0</sub> ]	4619	(-, 8)	
456	[c, t mixed]	4506	(-, 15)		510	7 <sub>1</sub> 8 <sub>2</sub> c <sub>1</sub>	4620	(-, 15)	
459	[7 <sub>1</sub> 8 <sub>1</sub> c <sub>3</sub> + 5 <sub>1</sub> t <sub>6</sub> ]	4514	(-, 12)		511	3 <sub>1</sub> 4 <sub>1</sub> c <sub>0</sub>	4622	(-, 15)	4626
460	[7 <sub>1</sub> 8 <sub>1</sub> c <sub>3</sub> - 5 <sub>1</sub> t <sub>6</sub> ]	4518	(-, 10)		512	3 <sub>1</sub> c <sub>3</sub>	4622	(-, 14)	
465	[c, t mixed]	4529	(-, 8)		515	[8 <sub>1</sub> c <sub>5</sub> - 4 <sub>1</sub> t <sub>6</sub> ]	4629	(-, 18)	
467	[4 <sub>1</sub> 6 <sub>1</sub> c <sub>1</sub> ]	4534	(-, 8)		517	[8 <sub>1</sub> c <sub>5</sub> + 4 <sub>1</sub> t <sub>6</sub> ]	4637	(-, 12)	
470	[3 <sub>1</sub> 7 <sub>2</sub> c <sub>0</sub> ]	4543	(-, 11)		520	[6 <sub>1</sub> 8 <sub>1</sub> c <sub>2</sub> ]	4643	(-, 10)	
472	5 <sub>1</sub> 8 <sub>2</sub> c <sub>0</sub>	4546	(-, 10)		524	[7 <sub>4</sub> c <sub>0</sub> , 6 <sub>1</sub> 7 <sub>3</sub> c <sub>0</sub> , 5 <sub>1</sub> 6 <sub>1</sub> 7 <sub>2</sub> c <sub>0</sub> ]	4646	(-, 11)	
476	[3 <sub>1</sub> 7 <sub>2</sub> c <sub>0</sub> - 6 <sub>3</sub> 7 <sub>2</sub> t <sub>0</sub> ]	4550	(-, 15)		527	4 <sub>2</sub> c <sub>1</sub>	4654	(-, 7)	4672
477	[3 <sub>1</sub> 7 <sub>2</sub> c <sub>0</sub> + 6 <sub>3</sub> 7 <sub>2</sub> t <sub>0</sub> ]	4550	(-, 16)		535	[5 <sub>1</sub> c <sub>5</sub> ]	4671	(-, 7)	
479	[7 <sub>2</sub> c <sub>4</sub> ]	4553	(-, 17)		542	[5 <sub>3</sub> c <sub>0</sub> , 5 <sub>2</sub> 6 <sub>1</sub> c <sub>0</sub> ]	4684	(-, 17)	
480	[7 <sub>2</sub> c <sub>4</sub> ]	4553	(-, 16)		544	[5 <sub>1</sub> 7 <sub>1</sub> 8 <sub>1</sub> c <sub>1</sub> , 6 <sub>1</sub> 7 <sub>1</sub> 8 <sub>1</sub> c <sub>2</sub> ]	4689	(-, 15)	
481	[5 <sub>1</sub> 6 <sub>1</sub> c <sub>2</sub> ]	4557	(-, 16)		547	[c, t mixed]	4697	(-, 14)	
484	7 <sub>4</sub> c <sub>1</sub>	4564	(-, 16)		549	[c, t mixed]	4702	(-, 12)	
485	[5 <sub>1</sub> 6 <sub>7</sub> c <sub>3</sub> , 6 <sub>1</sub> 7 <sub>1</sub> c <sub>3</sub> ]	4565	(-, 16)		550	[c, t mixed]	4702	(-, 12)	

a, b, c see footnotes to Table 3.

†: Revised assignment based on the Supplementary Material of Ref. [28].

\*: Tentative comparison.

Table 6

*Delocalized*-HCOOH: selected vibrationally excited states computed with the GENIUSH-Smolyak approach ( $b = 9$ ) with significant contribution from delocalized torsional basis functions,  $d_0, d_1, d_2$ , and  $d_3$ . The vibrational energy,  $\tilde{\nu}$  in  $\text{cm}^{-1}$ , is referenced to the *trans*-ZPVE.

# <sup>a</sup>	Dominant basis-state contributions <sup>b</sup>				$\tilde{\nu}$	$(\delta_{10}, \delta_8)^c$
252	-0.56 6 <sub>3</sub> 7 <sub>1</sub> t <sub>0</sub>	+0.32 6 <sub>4</sub> 7 <sub>1</sub> t <sub>0</sub>	... +0.20 c <sub>6</sub>	+0.15 d <sub>0</sub>	3914	(2, 5)
253	+0.44 c <sub>6</sub>	+0.37 d <sub>0</sub>	-0.33 7 <sub>1</sub> t <sub>6</sub>		3916	(2, 7)
281	-0.36 d <sub>1</sub>	+0.32 5 <sub>1</sub> t <sub>5</sub>			4036	(2, 7)
284	+0.34 6 <sub>2</sub> 7 <sub>1</sub> t <sub>2</sub>	+0.32 d <sub>0</sub>	-0.30 6 <sub>1</sub> 7 <sub>1</sub> t <sub>4</sub>		4053	(5, 4)
287	+0.41 d <sub>0</sub>	+0.33 7 <sub>1</sub> t <sub>6</sub>	+0.31 5 <sub>1</sub> 6 <sub>1</sub> 7 <sub>1</sub> 8 <sub>1</sub> t <sub>0</sub>		4060	(2, 5)
303	+0.41 d <sub>1</sub>	+0.30 3 <sub>1</sub> 5 <sub>1</sub> 8 <sub>1</sub> t <sub>0</sub>	+0.27 5 <sub>2</sub> 6 <sub>1</sub> t <sub>1</sub>	-0.25 6 <sub>1</sub> t <sub>3</sub>	4112	(2, 4)
309	+0.47 d <sub>1</sub>	-0.27 5 <sub>1</sub> 6 <sub>2</sub> t <sub>1</sub>	-0.27 5 <sub>2</sub> 6 <sub>1</sub> t <sub>1</sub>		4125	(2, 4)
376	-0.33 5 <sub>3</sub> t <sub>1</sub>	+0.30 d <sub>2</sub>	+0.30 5 <sub>1</sub> 6 <sub>1</sub> t <sub>3</sub>		4311	(2, 10)
389	+0.42 4 <sub>1</sub> 5 <sub>1</sub> 7 <sub>1</sub> 8 <sub>1</sub> t <sub>0</sub>	+0.25 4 <sub>1</sub> 7 <sub>1</sub> 8 <sub>1</sub> t <sub>2</sub>	+0.21 d <sub>2</sub>		4340	(2, 6)
399	+0.55 d <sub>3</sub>	+0.22 3 <sub>1</sub> 4 <sub>1</sub> t <sub>2</sub>	+0.21 6 <sub>1</sub> t <sub>6</sub>		4371	(4, 9)

a, b, c see footnotes to Table 3.

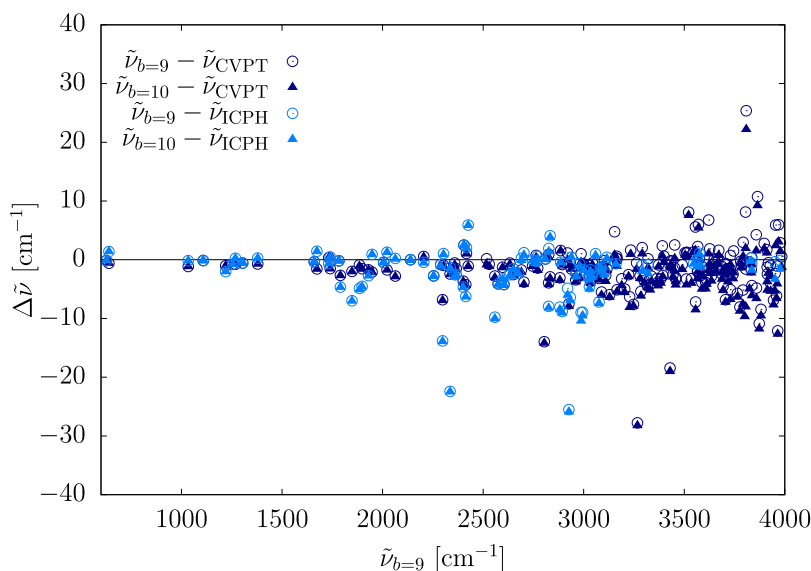


Fig. 12. Comparison of *trans*-HCOOH vibrational energies,  $\tilde{\nu}$  referenced to the zero-point energy, computed with the GENIUSH-Smolyak approach using the  $b = 9$  and 10 basis sets, Eqs. (28) and (29), and the 6th-order canonical van Vleck perturbation theory (CVPT) [30] and the internal-coordinate path Hamiltonian (ICPH) [28] results. The states from the different computations were compared based on the assignment of their wave function (Tables 2–3). The zero-point energies are  $\tilde{\nu}_{ZPVE} = 7351 \text{ cm}^{-1}$  ( $b = 9$  and 10) and  $\tilde{\nu}_{ICPH,ZPV} = 7354 \text{ cm}^{-1}$ .



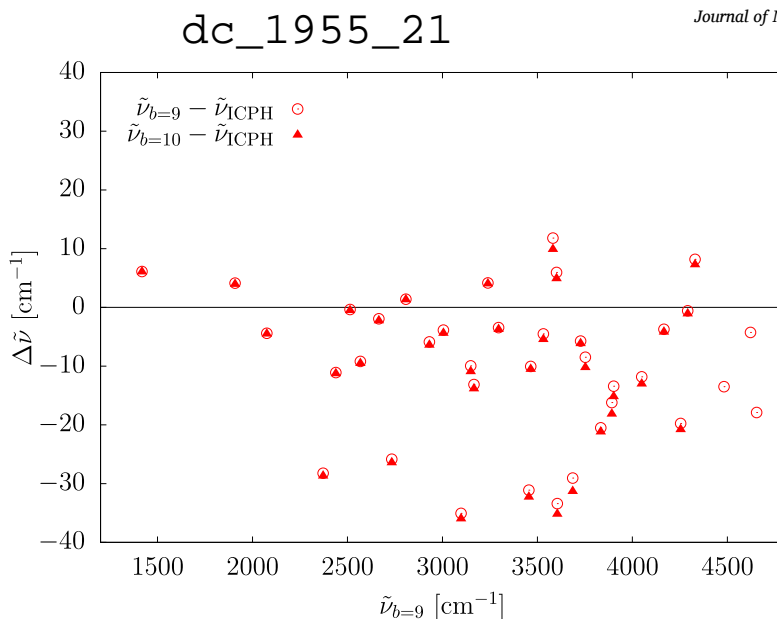


Fig. 13. Comparison of the *cis*-HCOOH vibrational energies,  $\tilde{\nu}$  referenced to the zero-point energy, computed with the GENIUSH-Smolyak approach using the  $b = 9$  and 10 basis sets, Eqs. (28) and (29), and the internal-coordinate path Hamiltonian (ICPH) [28] results. The states from the different computations were compared based on the assignment of their wave function (Tables 4 and 5). The (*trans*)-zero-point energies are  $\tilde{\nu}_{ZPV} = 7351 \text{ cm}^{-1}$  ( $b = 9$  and 10) and  $\tilde{\nu}_{ICPH,ZPV} = 7354 \text{ cm}^{-1}$ .

## References

- [1] D. Lauvergnat, A. Nauts, Exact numerical computation of a kinetic energy operator in curvilinear coordinates, *J. Chem. Phys.* 116 (2002) 8560.
- [2] E. Mátyus, G. Czákó, A.G. Császár, Toward black-box-type full- and reduced-dimensional variational (ro)vibrational computations, *J. Chem. Phys.* 130 (2009) 134112.
- [3] C. Fábri, E. Mátyus, A.G. Császár, Rotating full- and reduced-dimensional quantum chemical models of molecules, *J. Chem. Phys.* 134 (2011) 074105.
- [4] C. Fábri, E. Mátyus, A.G. Császár, Numerically constructed internal-coordinate Hamiltonian with Eckart embedding and its application for the inversion tunneling of ammonia, *Spectrochim. Acta* 119 (2014) 84.
- [5] A. Yachmenev, S.N. Yurchenko, Automatic differentiation method for numerical construction of the rotational-vibrational Hamiltonian as a power series in the curvilinear internal coordinates using the Eckart frame, *J. Chem. Phys.* 143 (2015) 014105.
- [6] D. Lauvergnat, A. Nauts, Quantum dynamics with sparse grids: a combination of Smolyak scheme and cubature. Application to methanol in full dimensionality, *Spectrochim. Acta* 119 (2014) 18.
- [7] A. Nauts, D. Lauvergnat, Numerical on-the-fly implementation of the action of the kinetic energy operator on a vibrational wave function: Application to methanol, *Mol. Phys.* 116 (2018) 3701.
- [8] X.-G. Wang, T. Carrington Jr., Using monomer vibrational wavefunctions to compute numerically exact (12D) rovibrational levels of water dimer, *J. Chem. Phys.* 148 (2018) 074108.
- [9] X.-G. Wang, T. Carrington, A variational calculation of vibrational levels of vinyl radical, *J. Chem. Phys.* 152 (2020) 204311.
- [10] P.M. Felker, Z. Bačić, Weakly bound molecular dimers: Intramolecular vibrational fundamentals, overtones, and tunneling splittings from full-dimensional quantum calculations using compact contracted bases of intramolecular and low-energy rigid-monomer intermolecular eigenstates, *J. Chem. Phys.* 151 (2019) 024305.
- [11] P.M. Felker, Z. Bačić,  $\text{H}_2\text{O}-\text{CO}$  and  $\text{D}_2\text{O}-\text{CO}$  complexes: Intra- and intermolecular rovibrational states from full-dimensional and fully coupled quantum calculations, *J. Chem. Phys.* 153 (2020) 074107.
- [12] Y. Liu, J. Li, P.M. Felker, Z. Bačić,  $\text{HCl}-\text{H}_2\text{O}$  dimer: An accurate full-dimensional potential energy surface and fully coupled quantum calculations of intra- and intermolecular vibrational states and frequency shifts, *Phys. Chem. Chem. Phys.* 23 (2021) 7101.
- [13] G. Avila, T. Carrington, Nonproduct quadrature grids for solving the vibrational Schrödinger equation, *J. Chem. Phys.* 131 (2009) 174103.
- [14] G. Avila, T. Carrington, Using nonproduct quadrature grids to solve the vibrational Schrödinger equation in 12D, *J. Chem. Phys.* 134 (2011) 054126.
- [15] G. Avila, T. Carrington, Using a pruned basis, a non-product quadrature grid, and the exact Watson normal-coordinate kinetic energy operator to solve the vibrational Schrödinger equation for  $\text{C}_2\text{H}_2$ , *J. Chem. Phys.* 135 (2011) 064101.
- [16] G. Avila, E. Mátyus, Toward breaking the curse of dimensionality in (ro)vibrational computations of molecular systems with multiple large-amplitude motions, *J. Chem. Phys.* 150 (2019a) 174107.
- [17] G. Avila, E. Mátyus, Full-dimensional (12D) variational vibrational states of  $\text{CH}_4-\text{F}^-$ : Interplay of anharmonicity and tunneling, *J. Chem. Phys.* 151 (2019b) 154301.
- [18] A. Chen, D. Lauvergnat, ElVibRot-MPI: Parallel quantum dynamics with Smolyak algorithm for general molecular simulation, 2021, arXiv preprint arXiv:2111.13655.
- [19] R. Wodraszka, T. Carrington Jr., A pruned collocation-based multiconfiguration time-dependent Hartree approach using a Smolyak grid for solving the Schrödinger equation with a general potential energy surface, *J. Chem. Phys.* 150 (2019) 154108.
- [20] R. Wodraszka, T. Carrington, A rectangular collocation multi-configuration time-dependent Hartree (MCTDH) approach with time-independent points for calculations on general potential energy surfaces, *J. Chem. Phys.* 154 (2021) 114107.
- [21] T. Carrington, Using collocation to study the vibrational dynamics of molecules, *Spectrochim. Acta* 248 (2021) 119158.
- [22] D. Peláez, K. Sadri, H.-D. Meyer, Full-dimensional MCTDH/MGPF study of the ground and lowest lying vibrational states of the hydroxide  $\text{H}_3\text{O}_2^-$  complex, *Spectrochim. Acta* 119 (2014) 42.
- [23] F. Otto, Y.-C. Chiang, D. Peláez, Accuracy of potfit-based potential representations and its impact on the performance of (ML-)MCTDH, *Chem. Phys.* 509 (2018) 116.
- [24] R.L. Panadé, D. Peláez, Low-rank sum-of-products finite-basis-representation (SOP-FBR) of potential energy surfaces, *J. Chem. Phys.* 153 (2020) 234110.
- [25] T. Halverson, B. Poirier, Large scale exact quantum dynamics calculations: Ten thousand quantum states of acetonitrile, *Chem. Phys. Lett.* 624 (2015a) 37.
- [26] T. Halverson, B. Poirier, One million quantum states of Benzene, *J. Phys. Chem. A* 119 (2015b) 12417.
- [27] J. Sarka, B. Poirier, Hitting the Trifecta: How to simultaneously push the limits of Schrödinger solution with respect to system size, convergence accuracy, and number of computed states, *J. Chem. Theory Comput.* 17 (2021) 7732.
- [28] D.P. Tew, W. Mizukami, Ab initio vibrational spectroscopy of *cis*- and *trans*-formic acid from a global potential energy surface, *J. Phys. Chem. A* 120 (2016) 9815.
- [29] F. Richter, P. Carbonnière, Vibrational treatment of the formic acid double minimum case in valence coordinates, *J. Chem. Phys.* 148 (2018) 064303.
- [30] A. Nejad, E.L. Sibert, The Raman jet spectrum of *trans*-formic acid and its deuterated isotopologs: Combining theory and experiment to extend the vibrational database, *J. Chem. Phys.* 154 (2021) 064301.
- [31] E.B. Wilson Jr., J.C. Decius, P.C. Cross, *Molecular Vibrations: The Theory of Infrared and Raman Vibrational Spectra*, Dover Publications Inc., New York, 1980.
- [32] Wolfram Research, Inc., *Mathematica*, Version 12.1, Champaign, IL, 2020.
- [33] D. Papousek, M.R. Aliev, *Molecular vibrational-rotational spectra*, 1982.
- [34] J. Sarka, A.G. Császár, S.C. Althorpe, D.J. Wales, E. Mátyus, Rovibrational transitions of the methane-water dimer from intermolecular quantum dynamical computations, *Phys. Chem. Chem. Phys.* 18 (2016) 22816.
- [35] J. Sarka, A.G. Császár, E. Mátyus, Rovibrational quantum dynamical computations for deuterated isotopologues of the methane-water dimer, *Phys. Chem. Chem. Phys.* 19 (2017) 15335.

- [36] D. Ferenc, E. Mátyus, Bound and unbound rovibrational states of the methane-argon dimer, *Mol. Phys.* 117 (2019) 1694.
- [37] A. Martín Santa Daría, G. Avila, E. Mátyus, Performance of a black-box-type rovibrational method in comparison with a tailor-made approach: Case study for the methane–water dimer, *J. Chem. Phys.* 154 (2021) 224302.
- [38] A. Martín Santa Daría, G. Avila, E. Mátyus, Fingerprint region of the formic acid dimer: Variational vibrational computations in curvilinear coordinates, *Phys. Chem. Chem. Phys.* 23 (2021) 6526.
- [39] J.C. Light, T. Carrington Jr., Discrete-Variable representations and their utilization, *Adv. Chem. Phys.* 0 (2000) 263–310, (Chapter 14).
- [40] G. Avila, D. Papp, G. Czakó, E. Mátyus, Exact quantum dynamics background of dispersion interactions: Case study for  $\text{CH}_4\cdot\text{Ar}$  in full (12) dimensions, *Phys. Chem. Chem. Phys.* 22 (2020) 2792.
- [41] S.A. Smolyak, Quadrature and interpolation formulas for tensor products of certain classes of functions, in: *Doklady Akademii Nauk*, vol. 148, Russian Academy of Sciences, 1963, pp. 1042–1045.
- [42] F. Heiss, V. Wünschel, Likelihood approximation by numerical integration on sparse grids, *J. Econometrics* 144 (2008) 62.
- [43] M.J. Bramley, T. Carrington Jr., Calculation of triatomic vibrational eigenstates: Product or contracted basis sets, Lanczos or conventional eigensolvers? What is the most efficient combination? *J. Chem. Phys.* 101 (1994) 8494.
- [44] X.-G. Wang, T. Carrington Jr., A finite basis representation Lanczos calculation of the bend energy levels of methane, *J. Chem. Phys.* 118 (2003) 6946.
- [45] T. Carrington Jr., X.-G. Wang, Computing ro-vibrational spectra of van der Waals molecules, *Wiley Interdiscip. Rev. Comp. Mol. Sci.* 1 (2011) 952.
- [46] A. Aerts, P. Carbonnière, F. Richter, A. Brown, Vibrational states of deuterated *trans*- and *cis*-formic acid: DCOOH, HCOOD, and DCOOD, *J. Chem. Phys.* 152 (2020) 024305.



Cite this: DOI: 10.1039/d0cp06289h

# Fingerprint region of the formic acid dimer: variational vibrational computations in curvilinear coordinates†

 Alberto Martín Santa Daría,  Gustavo Avila and Edit Mátyus \*

Curvilinear kinetic energy models are developed for variational nuclear motion computations including the inter- and the low-frequency intra-molecular degrees of freedom of the formic acid dimer. The coupling of the inter- and intra-molecular modes is studied by solving the vibrational Schrödinger equation for a series of vibrational models, from two up to ten active vibrational degrees of freedom by selecting various combinations of active modes and constrained coordinate values. Vibrational states, nodal assignment, and infrared vibrational intensity information is computed using the full-dimensional potential energy surface (PES) and electric dipole moment surface developed by Qu and Bowman [*Phys. Chem. Chem. Phys.*, 2016, **18**, 24835; *J. Chem. Phys.*, 2018, **148**, 241713]. Good results are obtained for several fundamental and combination bands in comparison with jet-cooled vibrational spectroscopy experiments, but the description of the  $\nu_8$  and  $\nu_9$  fundamental vibrations, which are close in energy and have the same symmetry, appears to be problematic. For further progress in comparison with experiment, the potential energy surface, and in particular, its multi-dimensional couplings representation, requires further improvement.

 Received 5th December 2020,  
Accepted 17th February 2021

DOI: 10.1039/d0cp06289h

rsc.li/pccp

## 1. Introduction

In a recent article, Nejad and Suhm reviewed the spectroscopy of the formic acid dimer (FAD)<sup>1</sup> with a focus on the intermolecular vibrational range. The formic acid is the simplest carboxylic acid and its dimer is a prototype for a cyclically arranged pair of hydrogen bonds. The formic acid dimer has been studied in spectroscopy experiments for decades, but the rotational and temperature effects made the detection of the precise vibrational band positions challenging.<sup>1</sup>

Coupling infrared and Raman spectrometers to jet-cooled helium beams seeded with a small amount of molecules in the gas phase made it possible to gain precise information on the vibrational dynamics of molecular complexes and clusters.<sup>2–5</sup> In particular, all intermolecular vibrational fundamentals and several overtone and combination bands of FAD<sup>6–10</sup> have been assigned over the past 16 years with an experimental uncertainty on the order of 1 cm<sup>-1</sup>. The amount and the quality of the experimental data call for detailed and high-level quantum dynamics computations.<sup>1</sup>

A detailed quantum dynamics computation relies on advanced methodology from three areas of theoretical chemistry: (a) electronic

structure methodology that provides good approximate solutions to the electronic Schrödinger equation at a series of nuclear configurations over the coordinate range relevant for the nuclear motion; (b) high-dimensional fitting or interpolation methods that build a potential energy surface (function) from the electronic energies available at points; and (c) rovibrational methodology that provides solution to the (ro)vibrational Schrödinger equation. A full-dimensional *ab initio* potential energy surface for the formic acid dimer is already available in the literature (parts a & b) developed by Qu and Bowman (QB16-PES),<sup>11</sup> and this allows us to focus on the solution of the vibrational Schrödinger equation.

Regarding the QB16-PES, it was obtained as a least-squares fit of a permutationally invariant potential energy function for the 10-atomic formic acid dimer to 13475 CCCD(T)-F12a/haTZ electronic energies. Qu and Bowman used a maximum of fourth order polynomials in the fitting and they report an 11 cm<sup>-1</sup> ‘energy-weighted’ root-mean-squared deviation and an absolute error of about 14 cm<sup>-1</sup> for their points below 4400 cm<sup>-1</sup>. The global minimum structure of the PES has C<sub>2h</sub> point-group symmetry and the corresponding harmonic frequencies are in reasonable agreement with earlier theoretical and experimental work.

Qu and Bowman<sup>12</sup> performed full (24)-dimensional vibrational configuration interaction (VCI) computations with the MULTIMODE computer program using the normal-coordinate representation of the kinetic energy operator (KEO) and a 4-mode-representation of QB16-PES. They write about the low-frequency

Institute of Chemistry, ELTE Eötvös Loránd University, Pázmány Péter sétány 1/A, 1117 Budapest, Hungary. E-mail: edit.matyus@ttk.elte.hu

† Electronic supplementary information (ESI) available. See DOI: 10.1039/d0cp06289h

vibrational energies (below 1000 cm<sup>-1</sup>) obtained in the VCI computations that the energies are ‘slightly’ up-shifted most likely due to the use of rectilinear normal coordinates, which are usually not well suited for describing floppy degrees of freedom, and possible deficiencies in the fitted PES. Otherwise, they estimate the VCI energies to be converged within about 10 cm<sup>-1</sup>.<sup>12</sup>

In the present work, we focus on the low-frequency range and study the role of the coordinate choice for this specific system. Is it necessary to use curvilinear coordinates to describe well the fingerprint range or normal coordinates are also appropriate?

In the next section (Section II), we define curvilinear internal coordinate vibrational models for FAD with focusing on the intermolecular dynamics. Then (Section III), the computed vibrational states are analysed and compared with the experimental data. Section IV is about an assessment of the kinetic and the potential energy representations using internal and normal coordinates. The article ends (Section V) with a summary of the results, conclusions, and outlook for possible future work.

## II. Theoretical and computational details

In the present work, the quantum dynamical computations were carried out using the GENIUSH<sup>13,14</sup> computer program. The general rovibrational Hamiltonian implemented<sup>15–20</sup> in this program is

$$\begin{aligned} \hat{H} = & \frac{1}{2} \sum_{k=1}^D \sum_{l=1}^D \tilde{g}^{-1/4} \hat{p}_k G_{kl} \tilde{g}^{1/2} \hat{p}_l \tilde{g}^{-1/4} \\ & + \frac{1}{2} \sum_{k=1}^D \sum_{a=1}^3 \left( \tilde{g}^{-1/4} \hat{p}_k G_{k,D+a} \tilde{g}^{1/4} + \tilde{g}^{1/4} G_{k,D+a} \hat{p}_k \tilde{g}^{-1/4} \right) \hat{J}_a \\ & + \frac{1}{2} \sum_{a=1}^3 G_{D+a,D+a} \hat{J}_a^2 \\ & + \frac{1}{2} \sum_{a=1}^3 \sum_{b>a}^3 G_{D+a,D+b} [\hat{J}_a, \hat{J}_b]_+ + \hat{V} \end{aligned} \quad (1)$$

where  $\hat{J}_a$  ( $a = 1(x), 2(y), 3(z)$ ) are the body-fixed total angular momentum operators and  $\hat{p}_k = -i\partial/\partial q_k$  with the  $q_k$  ( $k = 1, 2, \dots, D$ ) internal coordinates. The  $G_{kl} = (\mathbf{g}^{-1})_{kl}$  coefficients and  $\tilde{g} = \det(\mathbf{g})$  are determined from the  $\mathbf{g}$  matrix, defined as follows,

$$g_{kl} = \sum_{i=1}^N m_i \mathbf{t}_{ik}^T \mathbf{t}_{il}; \quad k, l = 1, 2, \dots, D+3 \quad (2)$$

where

$$\mathbf{t}_{ik} = \frac{\partial \mathbf{r}_i}{\partial q_k}; \quad k, l = 1, 2, \dots, D \quad (3)$$

$$\mathbf{t}_{i,D+a} = \mathbf{e}_a \times \mathbf{r}_i; \quad a = 1(x), 2(y), 3(z) \quad (4)$$

and  $\mathbf{r}_i$  are the body-fixed Cartesian coordinates for the  $i$ -th atom and  $\mathbf{e}_a$  represent the body-fixed unit vectors.

$D \leq 3N - 6$  is the number of the active vibrational dimensions in the system. If  $D < 3N - 6$ , then this definition of the kinetic energy operator (KEO) corresponds to imposing rigorous geometrical constraints for the fixed part of the system, and the results depend only on the constrained geometry, but they are independent on the actual coordinate representation of the constrained moiety.<sup>13</sup> This procedure is sometimes referred to as ‘reduction in the  $\mathbf{g}$  matrix’ that can be contrasted with ‘the reduction in the  $\mathbf{G}$  matrix’ (that is also common and) for which the results would depend on the actual coordinate representation of the constrained fragments.

Regarding the present system, the formic acid dimer has  $N = 10$  atoms and  $3N - 6 = 24$  vibrational degrees of freedom. A fully coupled, variational computation is currently out of reach for such a high number of degrees of freedom, except for a highly efficient normal-coordinate based representation that have been performed for FAD<sup>11,21–23</sup> and other systems of similar size.<sup>24,25</sup> Solution methods for high-dimensional semi-rigid systems are in a far more advanced stage than methods for solving systems with (more than 1–2) floppy degrees of freedom. Several floppy degrees of freedom in a system are typically strongly coupled and in this case one has to rely on a direct product representation for which the computational cost scales exponentially with the number of the degrees of freedom. Efficient computational schemes (grid and basis reduction, contraction) exploit the weak coupling of modes or groups of modes. There are successful efforts in the community<sup>26</sup> for solving high(er)-dimensional systems with several floppy modes. In a series of recent work,<sup>27–29</sup> we developed and used a computational scheme in which the floppy part is fully coupled and we exploit efficient grid and basis truncation schemes for the semi-rigid part. As a result, the cost of the computation scales exponentially with the number of floppy and polynomially with the number of semi-rigid degrees of freedom.

This work is about an exploratory, first application of the curvilinear methodology for FAD, a series of reduced-dimensional curvilinear internal coordinate models are defined and we solve the corresponding vibrational Schrödinger equation. For a specific coordinate choice, the GENIUSH program automatically computes the KEO coefficients over a grid, and uses the matrix representation of the Hamiltonian (eqn (1)) constructed with discrete variable representation (DVR)<sup>30</sup> for the active vibrational degrees of freedom. The lowest-energy eigenvalues and corresponding eigenvectors are computed using an iterative Lanczos algorithm.<sup>31,32</sup>

### A. Curvilinear internal coordinates and body-fixed frame

The GENIUSH program uses the  $\mathbf{t}$ -vector representation to construct the  $\mathbf{g}$ , and then the  $\mathbf{G}$  matrices appearing in the KEO, eqn (2)–(4). To compute the vibrational  $\mathbf{t}$ -vectors, eqn (3), it is necessary to define the Cartesian coordinates in the body-fixed frame,  $\mathbf{r}_i$ , with respect to the internal coordinates,  $q_k$ . Based on this definition (added to the program as a subroutine), the coordinate derivatives, the KEO coefficients, and the Hamiltonian matrix terms are constructed in an automated fashion. Any coordinates can be set to be constrained, to a fixed value provided by the user, or active, for which an appropriate coordinate range and DVR must be defined.

dc\_1955\_21

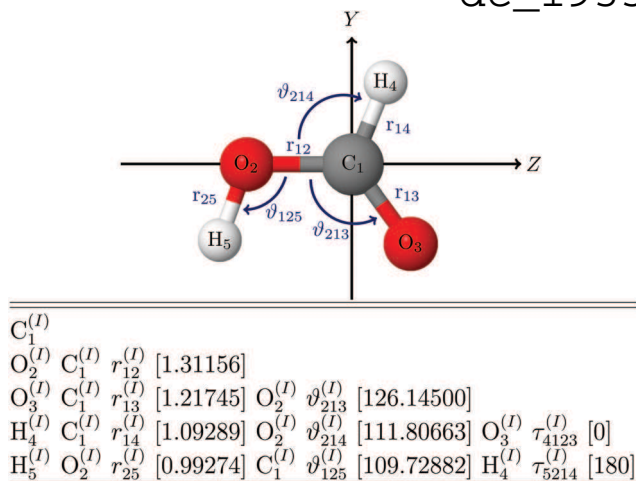


**Fig. 1** Internal coordinate definition of the formic acid monomer. The same internal coordinate definition is used for both monomers,  $I = A$  and  $B$ , within the dimer. For the global minimum of the dimer, the values of the monomer coordinates, in Å for the distances and in degree for the angles, are shown in brackets.

First, we define the monomer structures using a Z-matrix-type notation. These coordinates belong to the intramolecular modes that are set as active or fixed simultaneously in both monomers to respect the compositional symmetry of the system. Next, we define the coordinates that describe the relative position and orientation of the two monomers similarly to ref. 33–35.

The monomer coordinate definition is summarized in Fig. 1. The coordinate axes and the molecular plane are attached to the OCO fragment in both monomers and the following algorithm is implemented to define the KEO:

(1) To define the intra-monomer coordinates, the Cartesian coordinates of both monomers are defined as a function of the interatomic distances,  $r_{ij}$ , angles,  $\vartheta_{ijk}$ , and torsion angles,  $\tau_{ijkl}$  according to the following expressions (see also Fig. 1):

$$\begin{aligned} \tilde{r}_{C_1}^{(I)} &= \underline{0}; \quad \tilde{r}_{O_2}^{(I)} = \begin{pmatrix} 0 \\ 0 \\ -r_{12} \end{pmatrix}; \quad \tilde{r}_{O_3}^{(I)} = \begin{pmatrix} 0 \\ r_{13} \sin(\pi + \vartheta_{213}) \\ r_{13} \cos(\pi + \vartheta_{213}) \end{pmatrix}; \\ \tilde{r}_{H_4}^{(I)} &= \begin{pmatrix} r_{14} \sin(\pi - \vartheta_{214}) \sin \tau_{4123} \\ r_{14} \sin(\pi - \vartheta_{214}) \cos \tau_{4123} \\ r_{14} \cos(\pi - \vartheta_{214}) \end{pmatrix}; \quad \tilde{r}_{H_5}^{(I)} = \begin{pmatrix} r_{25} \sin \vartheta_{125} \sin \tau_{5214} \\ r_{25} \sin \vartheta_{125} \cos \tau_{5214} \\ r_{25} \cos \vartheta_{125} \end{pmatrix} \end{aligned} \quad (5)$$

where  $I = A, B$  labels the monomers.

(2) Shift to the monomer center of mass (CM) for each monomer:

$$\tilde{r}_j^{(I)} := \tilde{r}_j^{(I)} - \tilde{r}_{CM}^{(I)}; \quad j = 1, \dots, 5 \quad (6)$$

Up to this point, both monomers have identical positions.

(3) To define the inter-molecular coordinates, we rotate both monomers from their original orientation using the rotation matrices  $\underline{O}_1(0, \theta, \phi)$  and  $\underline{O}_2(\alpha, \beta, \gamma)$  parameterized with five Euler

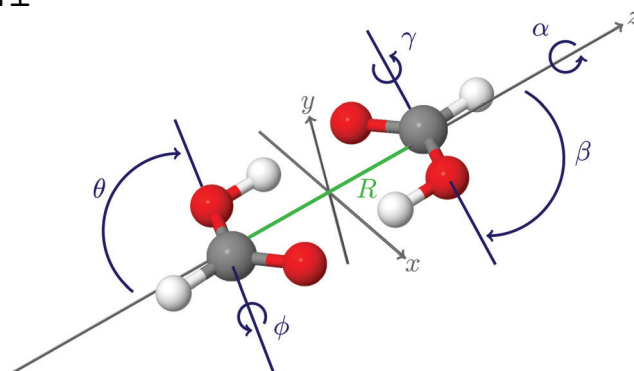


**Fig. 2** Definition of the intermolecular coordinates,  $(R, \theta, \phi, \alpha, \beta, \gamma)$ , shown for the equilibrium geometry of the dimer.

angles,  $(\theta, \phi, \alpha, \beta, \gamma)$ , and we shift monomer  $B$  by  $R$  in the positive direction along the  $z$  axis (Fig. 2):

$$\begin{aligned} \underline{r}_j^{(A)} &:= \underline{O}_1(0, \theta, \phi) \underline{r}_j^{(A)}; \quad \underline{r}_j^{(B)} := \underline{O}_2(\alpha, \beta, \gamma) \underline{r}_j^{(B)} + \begin{pmatrix} 0 \\ 0 \\ R \end{pmatrix} \\ R &\in [0, \infty), \quad \theta, \beta \in [0, \pi], \quad \phi, \alpha, \gamma \in [0, 2\pi) \end{aligned} \quad (7)$$

4. Shift to the dimer center of mass:

$$\tilde{r}_j^{(I)} := \underline{r}_j^{(I)} - \underline{r}_{CM}^{(AB)} \quad (8)$$

5. (optional) Change of the body fixed frame of the dimer: the overall dimer can be rotated to a new body-fixed frame, for example, to the Eckart frame.

The curvilinear nature of the coordinates results in singularities in the KEO. We have defined the coordinates so that the singularities (most importantly, at  $\cos \theta = \pm 1$  and  $\cos \beta = \pm 1$ ) of the KEO are possibly far from the equilibrium structure and the dynamically important coordinate range. For example, it would be a more natural choice to align the C–H bond of both monomers along the  $z$  axis, but then the equilibrium structure of the dimer would correspond to  $\theta = 0$  ( $\cos \theta = 1$ ) where the KEO has a singularity. For this reason, we align the C=O bond in both monomers along the  $z$  axis (Fig. 1 and 2) and perform the  $\underline{O}_1(0, \theta, \phi)$  and  $\underline{O}_2(\alpha, \beta, \gamma)$  rotation from this initial orientation. As a result the values of the angles at the global minimum (Table 1) are far from the singularities of the KEO.

Throughout this work, we used the atomic masses  $m(\text{H}) = 1.007825m_u$ ,  $m(\text{D}) = 2.014000m_u$ ,  $m(\text{C}) = 12m_u$ , and  $m(\text{O}) = 15.994915m_u$ .<sup>36</sup>

## B. Vibrational models and matrix representation

For a start, the constrained coordinates were fixed at their equilibrium value of the dimer's global minimum. Regarding the active coordinates, their initial range was determined from inspection of 1-dimensional cuts of the QB16-PES (Fig. 3). Based on these 1D cuts, we may expect that the fingerprint

Table 1 Coordinate intervals and representations

Coordinate	Equilibrium value	DVR			PO-DVR
		Type	#	Interval	#
$R$ [Å]	3.007879	Laguerre	300	[2.0,4.5]	7
$\cos\theta$	-0.333027	Legendre	101	[10,150]	9
$\phi$ [°]	270	Fourier	101	[200,350]	9
$\alpha$ [°]	180	Fourier	101	[90,270]	11
$\cos\beta$	0.333027	Legendre	101	[30,170]	9
$\gamma$ [°]	90	Fourier	101	[10,160]	9
$\tau_{5214}^{A,B}(\text{HOCO})$ [°]	180	Fourier	101	[120,250]	9
$\vartheta_{213}^{A,B}(\text{OCO})$ [°]	126.145	Fourier	101	[90,160]	9

region can be well described. For every coordinate, we performed a 1D vibrational computation using the 1D (unrelaxed) potential energy cut over a broad, physically meaningful interval (highlighted in orange in the figure) that is not affected by an unphysical behavior of the PES. For this 1D model, we employed a large number of a discrete variable representation (DVR) points<sup>30</sup> scaled to the selected interval. These computations were used to define potential-optimized DVRs (PO-DVR).<sup>37,38</sup>

This construction (and the semi-rigid properties of the system) allowed us to retain only a small fraction of grid points for the multi-dimensional vibrational computations. Table 1

summarizes the coordinate parameters (minimum value and interval), the DVR grid type and the number of points, as well as the number of PO-DVR points that were found to be sufficient to converge the multi-dimensional variational computations presented in this work within  $0.01 \text{ cm}^{-1}$ . This convergence threshold is orders of magnitude better than the fitting error reported for the PES, but we used this threshold to make sure that all states appearing in our energy list are true (converged) states corresponding to the vibrational model.

The reported computations were not very expensive, even the largest one finished within 1–2 days using 24 cores. At the same time, the largest computations required a large amount of memory ( $\sim 1 \text{ TB}$ ), since we used a simple direct product representation and all eigenvectors for the reported states were generated simultaneously in memory. For higher-dimensional computations, we plan to exploit the Smolyak scheme<sup>39–41</sup> recently implemented in GENIUSH<sup>27,28</sup> (and perhaps start further developments).

### III. Analysis of the computed vibrational states

By inspecting the harmonic frequencies of FAD (listed in the ESI†), we may think that the inter- and intra-molecular dynamics

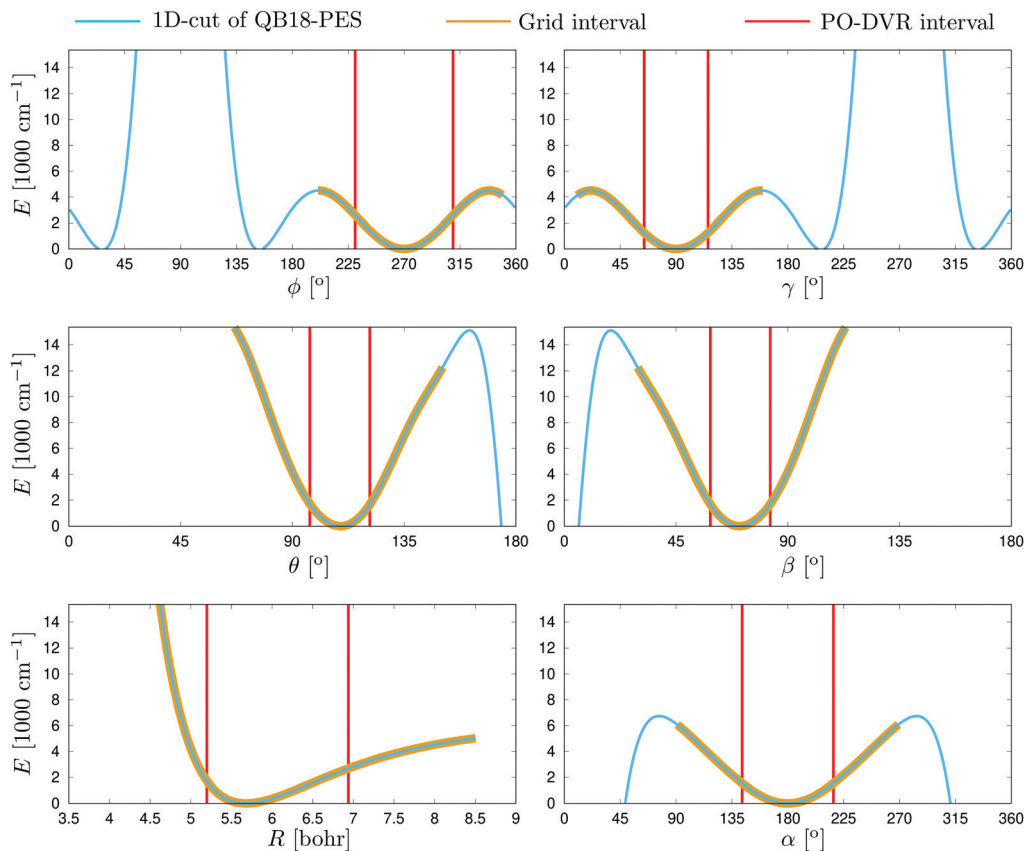


Fig. 3 1-Dimensional cuts of the QB16-PES along the intermolecular coordinates. The intervals used in the 1-dimensional DVR computations are highlighted in orange and the PO-DVR points used in the multi-dimensional vibrational computations are located within the intervals surrounded by the red lines.

**Table 2** Monomer structural parameters:  $r_{\text{eq}}$ , equilibrium value at the global minimum (GM) and  $\langle r \rangle_0^{(2D)}$  averaged structural parameter for the ground-state wave function of the 2D model in FAD

	$r_{25}^{(A,B)}(\text{O-H})^a$ [Å]	$r_{13}^{(A,B)}(\text{C=O})$ [Å]	$r_{12}^{(A,B)}(\text{C-O})$ [Å]	$\vartheta_{213}^{(A,B)}(\text{OCO})$ [°]
$r_{\text{eq}}$ (GM)	0.99274	1.21745	1.31156	126.14500
$\langle r \rangle_0^{(2D)}$	1.01790	1.22136	1.31625	126.18119

<sup>a</sup> Restricted to the anharmonic well, not accounting for tunneling.

are not perfectly separated. Based on the energetic ordering, it may be necessary to include at least the OCO bending,  $\vartheta_{213}^{(A,B)}$ , and/or the HOCO torsional modes,  $\tau_{5214}^{(A,B)}$ , to have a correct description of the intermolecular dynamics.

For this reason, we present (Table 3) the lowest-energy vibrational energies computed with GENIUSH using the 6D( $\mathcal{I}$ ) intermolecular, the 8D( $\mathcal{I}b$ ) intermolecular-bending, the 8D( $\mathcal{I}t$ ) intermolecular-torsional, and the 10D( $\mathcal{I}tb$ ) intermolecular-bending-torsional models and the full QB16-PES. For exploratory reasons, we have constructed other reduced dimensionality models as well, *e.g.*, by including the anharmonic O-H stretching modes, but they did not seem to qualitatively change the intermolecular vibrational energy pattern (we note that the O-H tunneling effects may be accounted for using the same methodology, but it is left for future work). We have also studied the effect of the precise value of the constrained structure by using the equilibrium,  $r_{\text{eq}}$ , or vibrationally averaged,  $\langle r \rangle_0$ , parameters (Table 2). Since we observed only minor shifts (a few  $\text{cm}^{-1}$ ), we continue the discussion for the results obtained with using  $r_{\text{eq}}$  values for the constraints.

Adding the HOCO torsional modes to the active degrees of freedom appears to be qualitatively important in the present case. At the same time, the OCO bending modes have only a small effect on the energy pattern. We do not provide a detailed assignment for all 6D, 8D, and 10D vibrational computations,

but we list (Table 3) the computed vibrational energies together with the infrared intensities,

$$A(\tilde{\nu}_f \leftarrow \tilde{\nu}_0)/(\text{km mol}^{-1}) = 2.506562213 [(\tilde{\nu}_f - \tilde{\nu}_0)/\text{cm}^{-1}] \sum_{\alpha=x,y,z} [|\langle \psi_f | \mu_\alpha | \psi_0 \rangle|^2 / \text{Debye}^2] \quad (9)$$

to facilitate comparison of the various computed and experimental vibrational band origins (VBOs). For the VBOs observed by Raman spectroscopy, we obtain zero infrared intensity (numerically near zero) due to the spatial symmetry of the system. In the jet-cooled experiments, we may assume that initially only the vibrational ground state is populated, so we compute only the transition intensity for excitation to the final state ('f') only from the ground state ('0'). The  $\mu_\alpha$  ( $\alpha = x,y,z$ ) electric dipole moment was evaluated using the QB18-DMS<sup>22</sup> and the body-fixed frame defined in Section IIA.

For the 8D( $\mathcal{I}t$ ) vibrational model, we provide a detailed assignment in Table 4 for the computed vibrational states below  $350 \text{ cm}^{-1}$  (the first 18 vibrational states above the zero-point vibration). The computed vibrational states were assigned based on their nodal structure. Example wave function plots are shown in Fig. 4, in which a clean nodal structure can be observed for the case of the fundamental, the first, the second, and the third overtone of the  $\nu_{16}$  intermolecular twist vibration. Further wave function plots used for the assignment are deposited in the ESI.†

We see a less clear nodal pattern for the case of the close-lying states with 191 and  $208 \text{ cm}^{-1}$  vibrational energies, nodal features along the  $R$  intermolecular stretching appear in both states. The latter state appears to have a more pronounced stretching character, although making a decision between the in-plane bending ( $\nu_9$ ) and intermolecular stretching ( $\nu_8$ ) would be ambiguous based on these results. The two modes belong to the same,  $A_g$ , irreducible representation (irrep) of the  $C_{2h}$  point group,

**Table 3** Vibrational energies, in  $\text{cm}^{-1}$ , and vibrational transition intensities, in  $\text{km mol}^{-1}$ , with respect to the zero-point vibration computed with GENIUSH using internal coordinate KEOs and the QB16-PES<sup>11</sup> and QB18-DMS.<sup>22</sup> The intensity values are shown in the parentheses and only values larger than  $0.05 \text{ km mol}^{-1}$  are shown, otherwise a '0' entry is printed

#	6D( $\mathcal{I}$ ) [ $\mathcal{I}$ ]	8D( $\mathcal{I}b$ ) [ $\mathcal{I}\&\vartheta_{213}^{A,B}$ ]	8D( $\mathcal{I}t$ ) [ $\mathcal{I}\&\tau_{4213}^{A,B}$ ]	10D( $\mathcal{I}tb$ ) [ $\mathcal{I}\&\tau_{4123}^{A,B}\&\vartheta_{213}^{A,B}$ ]
1	76 (3.2)	75 (5.7)	70 (2.3)	70 (2.3)
2	152 (0)	151 (0.1)	141 (0)	140 (0)
3	194 (0)	192 (0)	162 (7.6)	161 (16.6)
4	211 (0)	208 (0)	191 (0)	189 (0)
5	227 (0)	226 (0)	208 (0)	205 (0)
6	232 (0.2)	230 (1.0)	211 (0)	210 (0)
7	258 (33.0)	256 (32.9)	233 (0)	231 (0.1)
8	271 (0)	268 (0.1)	239 (0)	238 (0)
9	286 (0)	283 (0)	253 (50.3)	252 (31.9)
10	302 (0)	300 (0)	262 (0.1)	259 (0.2)
11	308 (0)	306 (0)	277 (0)	274 (0)
12	333 (0)	330 (0)	280 (0)	278 (0)
13	344 (0)	341 (0)	303 (0)	301 (0)
14	348 (0)	345 (0)	310 (0.6)	308 (0.8)
15	361 (0)	357 (0)	323 (0)	321 (0)
16	376 (0)	373 (0)	325 (0)	323 (0)
17	384 (0)	381 (0)	332 (0)	329 (0)
18	386 (0)	381 (0)	347 (0)	343 (0)

**Table 4** Assignment and comparison with literature data of the vibrational states obtained with the 8D( $\mathcal{I}t$ ) vibrational model in GENIUSH and the QB16 PES<sup>11</sup> and QB18 DMS<sup>22</sup>

#	$\tilde{\nu}_{8D(\mathcal{I}t)}$ [cm <sup>-1</sup> ]	$A_{8D(\mathcal{I}t)}$ [km mol <sup>-1</sup> ]	Assignment	$\tilde{\nu}_{8D(\mathcal{I}t)} - \tilde{\nu}_{\text{HO}}^a$ [cm <sup>-1</sup> ]	$\tilde{\nu}_{\text{expt}} - \tilde{\nu}_{8D(\mathcal{I}t)}$ [cm <sup>-1</sup> ]	$\tilde{\nu}_{\text{expt}}$ [cm <sup>-1</sup> ]
1	70	(2.3)	$\nu_{16}$ (A <sub>u</sub> , twist)	0	-1	69.2 <sup>7</sup>
2	141	(0.0)	$2\nu_{16}$		-2	139 <sup>9</sup>
3	162	(7.6)	$\nu_{15}$ (A <sub>u</sub> , oop bend)	-5	6	168.5 <sup>7</sup>
4	191	(0)	$\nu_9/\nu_8$ (A <sub>g</sub> , ip bend/stre)	21(!)	-30	161 <sup>9</sup>
5	208	(0)	$\nu_8/\nu_9$ (A <sub>g</sub> , stre/ip bend)	-1	-14	194 <sup>9</sup>
6	211	(0)	$3\nu_{16}$			
7	233	(0)	$\nu_{15} + \nu_{16}$			
8	239	(0)	$\nu_{12}$ (B <sub>g</sub> , oop lib)	-15	3	242 <sup>9</sup>
9	253	(50.3)	$\nu_{24}$ (B <sub>u</sub> , ip lib)	-22	11	264 <sup>1,5</sup>
10	262	(0.1)	$\nu_9 + \nu_{16}$			
11	277	(0)	$\nu_8 + \nu_{16}$			
12	280	(0)	$4\nu_{16}$			
13	303	(0)	$\nu_{15} + 2\nu_{16}$			
14	310	(0.6)	$\nu_{12} + \nu_{16}$		1	311 <sup>10</sup>
15	323	(0)	$\nu_{24} + \nu_{16}$			
16	325	(0)	$2\nu_{15}$		11	336 <sup>9</sup>
17	332	(0)	$\nu_9 + 2\nu_{16}$			
18	347	(0)	$\nu_8 + 2\nu_{16}$			

<sup>a</sup> The lowest harmonic frequencies,  $\tilde{\nu}_{\text{HO}}$  corresponding to the QB16-PES are listed in column A of Table 5.

and thus their mixing is allowed (and a mixing effect has been observed already in lower-level electronic structure computations<sup>1</sup>). In comparison with the experimental results, we observe a strong and most likely erroneous blueshift. The erroneous behavior is indicated by the strong, positive ‘anharmonicity correction’ (deviation of the variational energy from the harmonic oscillator energy) that indicates a problem in the theoretical description.

We can identify all experimentally observed fundamental vibrations, overtone, and combination bands in this range, except for the 319 cm<sup>-1</sup> peak tentatively assigned to the  $2\nu_9$  (A<sub>g</sub>) band in ref. 9. This VBO may be missing from our energy

list shown up to 347 cm<sup>-1</sup> due to the erroneous blueshift of the  $\nu_9$  fundamental vibration in the computations. Of course, the computed energy list contains a few more combination and overtone bands that have not been observed in experiment yet.

So, apart from the erroneous  $\nu_9/\nu_8$  system, the 8D( $\mathcal{I}t$ ) computational results appear to be in a reasonable, although not spectacularly good, agreement with experiment.

Switching on the OCO bending modes, resulting in the 10D( $\mathcal{I}tb$ ) model, does not change much the computed results. On the contrary, by freezing both the bending and the torsional degrees of freedom at their equilibrium values, resulting in the

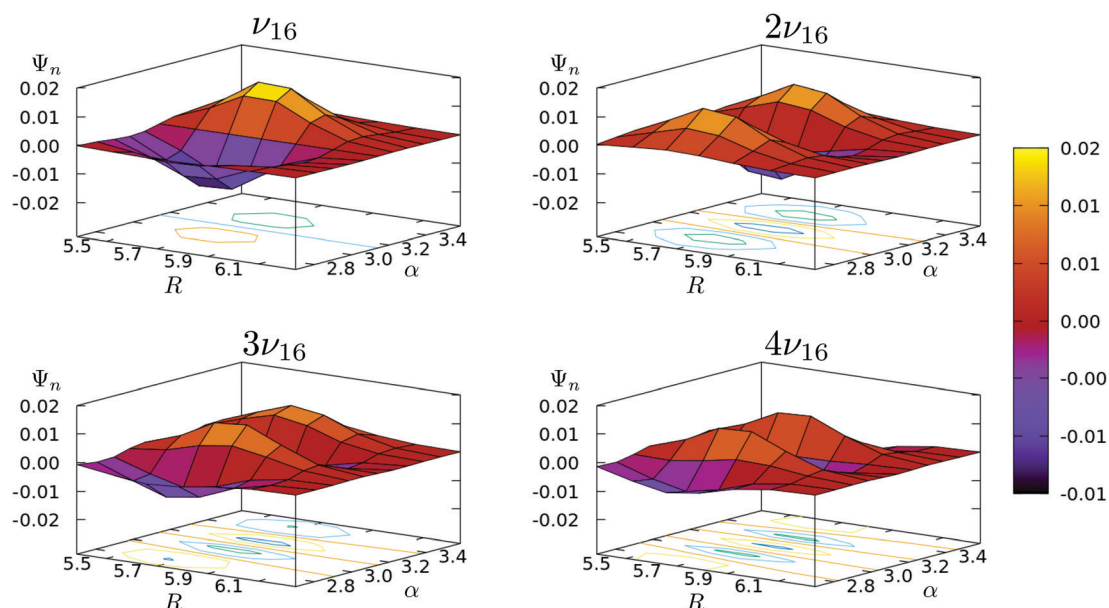


**Fig. 4** Example wave function plots (all quantities shown in atomic units) obtained in the 8D( $\mathcal{I}t$ ) computations with GENIUSH and the QB16-PES.



dc\_1955\_21

6D( $\mathcal{I}$ ) model, we obtain a qualitatively different energy pattern and the problematic blue-shifts appear to be even more pronounced (Table 3). We find this result surprising, we would have expected that already the 6D( $\mathcal{I}$ ) intermolecular model is qualitatively correct and it can be further improved by adding the low-frequency intramolecular modes. To better understand the origin of this behavior, we performed a couple of test calculations using different KEOs that are reported and analyzed in Section IV.

In summary, 8D( $\mathcal{I}t$ ) appears to be the simplest vibrational model for which we get meaningful results with the present QB16 PES, but the results are far from perfect. For this reason we constrained the discussion to the first 18 states of the parent isotopologue obtained with this single model. The vibrational energies obtained for the symmetrically substituted isotopologues with the 8D( $\mathcal{I}t$ ) KEO and the QB16-PES are listed in Table 6 of the Appendix without further analysis. Later on, more states can be computed and analysed using the 8D, 10D (or perhaps even 12D) vibrational models and the most appropriate values for the constrained geometrical parameters can be determined, but we think that it is important first to clarify the origin of the erroneous blueshifts observed for some of the fundamental vibrations.

## IV. Assessment of the KEO and the PES representations

In order to understand better the erroneous results obtained with curvilinear KEOs and the QB16-PES, we performed a number of test computations (Table 5).

First of all, we computed the normal coordinates and harmonic frequencies corresponding to the global minimum structure of the QB16-PES (the normal coordinate parameters are deposited as ESI†). The harmonic frequencies are listed in the A column of Table 5. Next, we have implemented the harmonic potential energy model (HO) in the GENIUSH program, and it can be evaluated with any types of internal coordinates and grid representations. This offers a simple, alternative PES representation to the full QB16-PES that is used in our DVR computations.

Regarding the KEO, we have implemented the (rectilinear) normal coordinates of the QB16-PES as active coordinates in GENIUSH. The vibrational energies obtained for the 6D normal coordinate KEO, in which the six lowest-energy normal modes are active and all other normal coordinates fixed at the '0' value, are shown in columns B and C. The 'B' column can be reproduced from combinations of the harmonic frequencies listed in column A. Column C contains a converged 6D normal coordinate computation on the full QB16-PES. It is interesting to note that these energies are close to the 24-dimensional normal coordinate VCI computations (converged to  $\sim 10$  cm<sup>-1</sup>) of ref. 12 using a 4-mode representation of the QB16-PES. It is also necessary to note that the 'C' column is quite different from the 'E' and 'F' columns which correspond to 6D curvilinear KEOs and the full QB16-PES. This deviation may indicate (a) the deficiency of the

Table 5 Assessment of the PES and the kinetic energy representations: vibrational energies, in cm<sup>-1</sup>, measured from the zero-point vibrational energy (ZPVE)

KEO:	HO <sup>a</sup>		Q <sup>(6D)b</sup>		$\xi^{(6D)c}$		Q <sup>(6D)d</sup>	Q <sup>(24D)e</sup>	Q <sup>(24D)e</sup>
	HO	HO	Full	HO	Full	Full	4MR	4MR	
Label <sup>f</sup>	A	B	C	D	E	F	VSCF <sup>12</sup>	VCI <sup>12</sup>	
ZPVE		573	638	562	682	682	n.a.	n.a.	
$\nu_{16}$	70	70	110	68	76	76	103	96	
$2\nu_{16}$		140	175	136	152	152	171	178	
$\nu_9$	167	167	203	163	194	194	204	209	
$\nu_{15}$	170	170	230	166	211	211	250	213	
$\nu_8$	209	209	269	203	227	227	277	273	
$3\nu_{16}$		211	275	209	232	232	303	286	
$\nu_{16} + \nu_9$		237	288	231	258	258			
$\nu_{16} + \nu_{15}$		241	313	234	271	271			
$\nu_{12}$	254	254	320	239	286	286			
$\nu_{24}$	275	275	353	270	302	302			
		279	358	275	308	308			
		281	378	277	333	333			
		308	387	297	344	344			
		311	390	301	348	348			

<sup>a</sup> Harmonic oscillator model approximation corresponding to the QB16-PES. <sup>b</sup> 6D computation with GENIUSH using the QB16-PES normal coordinates in the KEO with a harmonic oscillator model PES (HO) or with the full QB16-PES (full). The VBOs are converged within 0.01 cm<sup>-1</sup> with (15,15,13,13,13,13) unscaled Hermite-DVR points. <sup>c</sup> 6D computation with GENIUSH using the curvilinear internal coordinates defined in Section IIA in the KEO with a harmonic oscillator model PES (HO) or with the full QB16-PES (full). The energies are converged with (11,11,11,11,11,11) PO-DVR points defined in Table 1. <sup>d</sup> 6D computation with GENIUSH using curvilinear normal coordinates defined in the KEO with the full QB16-PES. The VBOs are converged within 0.01 cm<sup>-1</sup> using (15,15,15,15,15,15) number of unscaled Hermite-DVR points. <sup>e</sup> 24D normal coordinate computation with a 4-mode representation of the QB16-PES, ref. 12. <sup>f</sup> Assignment corresponding to columns A and B. For the other columns, analysis of the wave function would be necessary for the assignment.

rectilinear normal coordinates to describe floppy degrees of freedom; and/or (b) an erratic behavior of the PES that is manifested differently for the different grid representations.

Regarding the 6D curvilinear KEOs (columns D, E, and F), the results obtained with the HO-model PES (column D) are close and slightly redshifted compared to the fully harmonic normal coordinate results (columns A and B), and the erroneous blueshift of the  $\nu_9/\nu_8$  fundamentals is missing. This provides an additional check for our curvilinear KEO definition and suggests that the unphysical deviation of the 6D–8D–10D energies (Section III) from the experimental values may originate from an unphysical behavior of the PES representation in the coupling of these modes.

Finally, we mention that an, in principle, numerically efficient representation of the intermolecular dynamics of FAD, described as a single-well system, is provided by curvilinear normal coordinates. Curvilinear normal coordinates are obtained as the linear combination of the internal coordinates defined in Section IIA that diagonalize the GF matrix (the coordinate definition and the linear combination coefficients are provided in the ESI†).

All in all, for further progress, it is necessary to have an improved PES. For the fingerprint region an improvement of

the intermode coupling PES representation appears to be particularly important.

## V. Conclusion and outlook

Variational vibrational computations are reported for the fingerprint region of the formic acid dimer (FAD) using curvilinear kinetic energy operator representations and the QB16-PES. Besides the intermolecular coordinates, the lowest-frequency monomer vibrations have been included resulting in a series of vibrational models with 6, 8, and 10 active dimensions, while keeping all other degrees of freedom in the system rigid.

This work was initiated by a conjecture (also mentioned by Qu and Bowman in ref. 11, 21 and 23) that perhaps normal coordinates are not well suited and one should rather use curvilinear coordinates to describe the fingerprint region of FAD. We hoped that by using curvilinear coordinates, it becomes possible to resolve discrepancy of earlier theory (with normal coordinates) and experiment. During our vibrational study we obtained good results for several fundamental and combination bands in comparison with jet-cooled vibrational spectroscopy experiment, but noticed that there was a problem with the  $\nu_8$  and  $\nu_9$  fundamental vibrations. These vibrations have always been difficult to describe accurately (already on the harmonic level as it was pointed out by Nejad and Suhm<sup>1</sup>), because they are close in energy and have the same symmetry. These fundamental vibrations are obtained from our variational computations with an erroneous blueshift and the series of computations with different vibrational models developed in this work suggest that for further progress in comparison with experiments, improvement of the PES is necessary.

Relying on the increasing computational resources, further development in the computational methodology, and assuming that an improved potential energy surface will become available soon, we can foresee a curvilinear treatment with more than 10 fully-coupled degrees of freedom, or studying the tunneling dynamics in the fingerprint range in the vibrational or rovibrational spectrum. An interesting alternative future direction will be the computation of tunnelling splitting effects in the monomer stretching spectrum<sup>42,43</sup> that was computationally studied using an extension of the reaction surface Hamiltonian<sup>44,45</sup> and also with 7-dimensional curvilinear vibrational models by Luckhaus.<sup>46,47</sup> Further progress in that direction also requires an improved PES representation up to a beyond the monomer stretching range.

## Conflicts of interest

There are no conflicts to declare.

## Appendix: vibrational energies of the symmetrically deuterated isotopologues

**Table 6** Vibrational band origins, in  $\text{cm}^{-1}$ , referenced to the zero-point vibrational energy (ZPVE) of the parent and the three symmetrically deuterated isotopologues of the formic acid dimer computed with the GENIUSH program using the 8D( $\mathcal{I}$ t) KEO and the QB16-PES

#	(HCOOH) <sub>2</sub>	(DCOOD) <sub>2</sub>	(HCOOD) <sub>2</sub>	(DCOOH) <sub>2</sub>
0	1533	1240	1280	1493
1	70	70	70	70
2	141	135	140	138
3	162	140	157	140
4	191	186	187	191
5	208	205	208	205
6	211	207	210	208
7	233	207	227	209
8	239	209	237	210
9	253	245	251	248
10	262	256	257	261
11	277	270	278	275
12	280	274	279	277
13	303	276	297	279
14	310	277	307	279
15	323	278	313	279
16	325	314	320	317
17	332	319	327	327
18	347	326	341	331
19	350	339	347	342
20	351	341	348	344
21	368	341	363	346
22	372	343	366	347
23	380	345	372	348
24	381	346	377	348
25	389	347	383	349
26	392	371	389	380
27	395	379	392	385
28	397	382	393	389
29	401	389	397	394

## Acknowledgements

We thank Joel Bowman and Chen Qu for sending to us their formic acid dimer PES and DMS. We thank the financial support of the Swiss National Science Foundation (PROMYS Grant, No. IZ11Z0\_166525).

## References

- 1 A. Nejad and M. A. Suhm, Concerted Pair Motion Due to Double Hydrogen Bonding: The Formic Acid Dimer Case, *J. Indian Inst. Sci.*, 2020, **100**, 1.
- 2 T. Häber, U. Schmitt and M. A. Suhm, FTIR-spectroscopy of molecular clusters in pulsed supersonic slit-jet expansions, *Phys. Chem. Chem. Phys.*, 1999, **1**, 5573.
- 3 Y. Liu, M. Weimann and M. A. Suhm, Extension of panoramic cluster jet spectroscopy into the far infrared: Low frequency modes of methanol and water clusters, *Phys. Chem. Chem. Phys.*, 2004, **6**, 3315.
- 4 R. W. Larsen, P. Zielke and M. A. Suhm, Hydrogen-bonded OH stretching modes of methanol clusters: A combined IR and Raman isotopomer study, *J. Chem. Phys.*, 2007, **126**, 194307.
- 5 M. A. Suhm and F. Kollipost, Femtosecond single-mole infrared spectroscopy of molecular clusters, *Phys. Chem. Chem. Phys.*, 2013, **15**, 10702.

dc\_1955\_21

- 6 M. Herman, R. Georges, M. Hepp and D. Hurtmans, High resolution Fourier transform spectroscopy of jet-cooled molecules, *Int. Rev. Phys. Chem.*, 2000, **19**, 277.
- 7 R. Georges, M. Freytes, D. Hurtmans, I. Kleiner, J. Vander Auwera and M. Herman, Jet-cooled and room temperature FTIR spectra of the dimer of formic acid in the gas phase, *Chem. Phys.*, 2004, **305**(1–3), 187–196.
- 8 P. Zielke and M. A. Suhm, Raman jet spectroscopy of formic acid dimers: low frequency vibrational dynamics and beyond, *Phys. Chem. Chem. Phys.*, 2007, **9**, 4528–4534.
- 9 Z. Xue and M. A. Suhm, Probing the stiffness of the simplest double hydrogen bond: The symmetric hydrogen bond modes of jet-cooled formic acid dimer, *J. Chem. Phys.*, 2009, **131**(5), 054301.
- 10 F. Kollipost, R. W. Larsen, A. V. Domanskaya, M. Nörenberg and M. A. Suhm, Communication: The highest frequency hydrogen bond vibration and an experimental value for the dissociation energy of formic acid dimer, *J. Chem. Phys.*, 2012, **136**, 151101.
- 11 C. Qu and J. M. Bowman, An ab initio potential energy surface for the formic acid dimer: zero-point energy, selected anharmonic fundamental energies, and ground-state tunneling splitting calculated in relaxed 1–4-mode subspaces, *Phys. Chem. Chem. Phys.*, 2016, **18**, 24835–24840.
- 12 C. Qu and J. M. Bowman, Quantum approaches to vibrational dynamics and spectroscopy: is ease of interpretation sacrificed as rigor increases?, *Phys. Chem. Chem. Phys.*, 2019, **21**, 3397–3413.
- 13 E. Mátyus, G. Czakó and A. G. Császár, Toward black-box-type full- and reduced-dimensional variational (ro)vibrational computations, *J. Chem. Phys.*, 2009, **130**, 134112.
- 14 C. Fábri, E. Mátyus and A. G. Császár, Rotating full- and reduced-dimensional quantum chemical models of molecules, *J. Chem. Phys.*, 2011, **134**, 074105.
- 15 R. Meyer and H. H. Günthard, Internal Rotation and Vibration in  $\text{CH}_2 = \text{CCl-CH}_2\text{D}$ , *J. Chem. Phys.*, 1969, **50**, 353.
- 16 R. Meyer, Flexible models for intramolecular motion, a versatile treatment and its application to glyoxal, *J. Mol. Spectrosc.*, 1979, **76**, 266.
- 17 D. Luckhaus, 6D vibrational quantum dynamics: Generalized coordinate discrete variable representation and (a)diabatic contraction, *J. Chem. Phys.*, 2000, **113**, 1329.
- 18 D. Luckhaus, The vibrational spectrum of HONO: Fully coupled 6D direct dynamics, *J. Chem. Phys.*, 2003, **118**, 8797.
- 19 D. Lauvergnat and A. Nauts, Exact numerical computation of a kinetic energy operator in curvilinear coordinates, *J. Chem. Phys.*, 2002, **116**, 8560.
- 20 S. N. Yurchenko, W. Thiel and P. Jensen, Theoretical ROVibrational Energies (TROVE): A robust numerical approach to the calculation of rovibrational energies for polyatomic molecules, *J. Mol. Spectrosc.*, 2007, **245**, 126.
- 21 C. Qu and J. M. Bowman, IR Spectra of  $(\text{HCOOH})_2$  and  $(\text{DCOOH})_2$ : Experiment, VSCF/VCI, and Ab Initio Molecular Dynamics Calculations Using Full-Dimensional Potential and Dipole Moment Surfaces, *J. Phys. Chem. Lett.*, 2018, **9**(10), 2604–2610.
- 22 C. Qu and J. M. Bowman, High-dimensional fitting of sparse datasets of CCSD(T) electronic energies and MP2 dipole moments, illustrated for the formic acid dimer and its complex IR spectrum, *J. Chem. Phys.*, 2018, **148**(24), 241713.
- 23 C. Qu and J. Bowman, Quantum and classical IR spectra of  $(\text{HCOOH})_2$ ,  $(\text{DCOOH})_2$  and  $(\text{DCOOD})_2$  using ab initio potential energy and dipole moment surfaces, *Faraday Discuss.*, 2018, **212**, 33–49.
- 24 P. S. Thomas and T. Carrington Jr, An intertwined method for making low-rank, sum-of-product basis functions that makes it possible to compute vibrational spectra of molecules with more than 10 atoms, *J. Chem. Phys.*, 2017, **146**(20), 204110.
- 25 P. S. Thomas, T. Carrington Jr, J. Agarwal and H. F. Schaefer III, Using an iterative Eigensolver and intertwined rank reduction to compute vibrational spectra of molecules with more than a dozen atoms: Uracil and naphthalene, *J. Chem. Phys.*, 2018, **149**(6), 064108.
- 26 X. G. Wang and T. Carrington, Using monomer vibrational wavefunctions to compute numerically exact (12D) rovibrational levels of water dimer, *J. Chem. Phys.*, 2018, **148**, 074108; P. M. Felker and Z. Bacic, Weakly bound molecular dimers: Intramolecular vibrational fundamentals, overtones, and tunneling splittings from full-dimensional quantum calculations using compact contracted bases of intramolecular and low-energy rigid-monomer intermolecular eigenstates, *J. Chem. Phys.*, 2019, **151**, 024305; P. M. Felker and Z. Bacic, HDO–CO Complex: D–Bonded and H–Bonded Isomers and Intra- and Intermolecular Rovibrational States from Full-Dimensional and Fully Coupled Quantum Calculations, *J. Phys. Chem. A*, 2021, **125**, 980–989.
- 27 G. Avila and E. Mátyus, Toward breaking the curse of dimensionality in (ro)vibrational computations of molecular systems with multiple large-amplitude motions, *J. Chem. Phys.*, 2019, **150**, 174107.
- 28 G. Avila and E. Mátyus, Full-dimensional (12D) variational vibrational states of  $\text{CH}_4\text{-F}^-$ : interplay of anharmonicity and tunneling, *J. Chem. Phys.*, 2019, **151**, 154301.
- 29 G. Avila, D. Papp, G. Czakó and E. Mátyus, Exact quantum dynamics background of dispersion interactions: case study for  $\text{CH}_4\text{-Ar}$  in full (12) dimensions, *Phys. Chem. Chem. Phys.*, 2020, **22**, 2792.
- 30 J. C. Light and T. Carrington Jr, Discrete Variable Representations and Their Utilization, *Adv. Chem. Phys.*, 2000, **114**, 263–310.
- 31 C. Lanczos, An Iteration Method for the Solution of the Eigenvalue Problem of Linear Differential and Integral Operators, *J. Res. Natl. Bur. Stand.*, 1950, 255–282.
- 32 E. Mátyus, J. Šimunek and A. G. Császár, On the variational computation of a large number of vibrational energy levels and wave functions for medium-sized molecules, *J. Chem. Phys.*, 2009, **131**, 074106.
- 33 J. Sarka, A. G. Császár, S. C. Althorpe, D. J. Wales and E. Mátyus, Rovibrational Transitions of the Methane-water Dimer from Intermolecular Quantum Dynamical Computations, *Phys. Chem. Chem. Phys.*, 2016, **18**, 22816.
- 34 J. Sarka, A. G. Császár and E. Mátyus, Rovibrational quantum dynamical computations for deuterated isotopologues of the methane-water dimer, *Phys. Chem. Chem. Phys.*, 2017, **19**, 15335.
- 35 M. P. Metz, K. Szalewicz, J. Sarka, R. Tóbiás, A. G. Császár and E. Mátyus, Molecular dimers of methane clathrates:

dc\_1955\_21

- ab initio potential energy surfaces and variational vibrational states, *Phys. Chem. Chem. Phys.*, 2019, **21**, 13504.
- 36 J. E. Sansonetti, W. C. Martin and S. L. Young, *Handbook of Basic Atomic Spectroscopic Data*, version 1.1.2, 2005, p. 52, <http://physics.nist.gov/Handbook>.
- 37 H. Wei and J. T. Carrington, The discrete variable representation of a triatomic Hamiltonian in bond length-bond angle coordinates, *J. Chem. Phys.*, 1992, **97**, 3029.
- 38 J. Echave and D. C. Clary, Potential optimized discrete variable representation, *Chem. Phys. Lett.*, 1992, **190**, 225.
- 39 G. Avila and J. T. Carrington, Nonproduct quadrature grids for solving the vibrational Schrödinger equation, *J. Chem. Phys.*, 2009, **131**(17), 174103.
- 40 G. Avila and J. T. Carrington, Using nonproduct quadrature grids to solve the vibrational Schrödinger equation in 12D, *J. Chem. Phys.*, 2011, **134**(5), 054126.
- 41 G. Avila and J. T. Carrington, Using a pruned basis, a non-product quadrature grid, and the exact Watson normal-coordinate kinetic energy operator to solve the vibrational Schrödinger equation for  $C_2H_4$ , *J. Chem. Phys.*, 2011, **134**(6), 064101.
- 42 F. Madeja and M. Havenith, High resolution spectroscopy of carboxylic acid in the gas phase: Observation of proton transfer in  $(DCOOH)_2$ , *J. Chem. Phys.*, 2002, **117**, 7162.
- 43 M. Ortlieb and M. Havenith, Proton Transfer in  $(HCOOH)_2$ : An IR High-Resolution Spectroscopic Study of the Antisymmetric C-O Stretch, *J. Phys. Chem. A*, 2007, **111**, 7355.
- 44 G. L. Barnes and E. L. Sibert III, The effects of asymmetric motions on the tunneling splittings in formic acid dimer, *J. Chem. Phys.*, 2008, **129**, 164317.
- 45 G. L. Barnes, S. M. Squires and E. L. Sibert, Symmetric Double Proton Tunneling in Formic Acid Dimer: A Diabatic Basis Approach, *J. Phys. Chem. B*, 2007, **112**, 595.
- 46 D. Luckhaus, Concerted Hydrogen Exchange Tunneling in Formic Acid Dimer, *J. Phys. Chem. A*, 2006, **110**, 3151.
- 47 D. Luckhaus, Hydrogen exchange in formic acid dimer: tunnelling above the barrier, *Phys. Chem. Chem. Phys.*, 2010, **12**, 8357–8361.

# Performance of a black-box-type rovibrational method in comparison with a tailor-made approach: Case study for the methane–water dimer

Cite as: J. Chem. Phys. **154**, 224302 (2021); doi: [10.1063/5.0054512](https://doi.org/10.1063/5.0054512)

Submitted: 19 April 2021 • Accepted: 24 May 2021 •

Published Online: 10 June 2021



View Online



Export Citation



CrossMark

Alberto Martín Santa Daría,  Gustavo Avila, and Edit Mátyus<sup>a)</sup> 

## AFFILIATIONS

Institute of Chemistry, ELTE Eötvös Loránd University, Pázmány Péter sétány 1/A, 1117 Budapest, Hungary

<sup>a)</sup> Author to whom correspondence should be addressed: [edit.matyus@ttk.elte.hu](mailto:edit.matyus@ttk.elte.hu)

## ABSTRACT

The present work intends to join and respond to the excellent and thoroughly documented rovibrational study of X. G. Wang and T. Carrington, Jr. [J. Chem. Phys. **154**, 124112 (2021)] that used an approach tailored for floppy dimers with an analytic dimer Hamiltonian and a non-product basis set including Wigner  $D$  functions. It is shown in the present work that the GENIUSH black-box-type rovibrational method can approach the performance of the tailor-made computation for the example of the floppy methane–water dimer. Rovibrational transition energies and intensities are obtained in the black-box-type computation with a twice as large basis set and in excellent numerical agreement in comparison with the more efficient tailor-made approach.

Published under an exclusive license by AIP Publishing. <https://doi.org/10.1063/5.0054512>

## I. INTRODUCTION

Electronic structure theory has general program packages that work for  $n$  electrons, where  $n$  is defined by the user together with the configuration of the clamped nuclei.

Will computational (ro)vibrational spectroscopy methodology reach this level of automatization? Does it need to reach this and why? One may argue that careful gas-phase spectroscopy measurements conducted in order to explore the structure and internal dynamics of molecular systems typically assume months or even years of systematic experimental work (development of sample preparation, source and detector architectures, uncertainty estimation, error control, etc.). It is not a typically high-throughput field studying one molecule after the other at an extraordinary pace. At the same time, the experiments may produce large sets of precise data that provide a highly detailed characterization of the quantum dynamical features of the system.

Regarding computational molecular rovibrational spectroscopy, it is a natural aim for a mathematically formulated theory to have an approach, an algorithm, and a computer program that is

generally applicable, limited “only” by the available computational resources. For solving the rovibrational Schrödinger equation, it should be a general  $N$ -particle approach, where  $N$  is the number of atomic nuclei (although for the moment only finite many  $N$  possible values are computationally feasible). In this field, it is another necessary condition to allow the user to specify the internal coordinates and the body-fixed frame best suited for the computations.

Development of Ref. 1, following earlier work in the field,<sup>2–6</sup> was led by this idea in spite of the fact that there were already excellent approaches available specifically designed for special types of molecular systems (with a given number of nuclei and specific coordinates); the list includes, for example, Refs. 7–15. The numerical advantage of an  $N$ -particle method was not at all obvious over the performance of the tailor-made approaches. For semi-rigid systems, the Eckart–Watson Hamiltonian<sup>16</sup> was available as a general  $N$ -particle Hamiltonian, for which efficient solution techniques have been developed using basis pruning.<sup>17,18</sup> If basis pruning can be efficiently realized, then grid pruning techniques, developed in Refs. 19 and 20, can be employed to milder the curse of dimensionality. Most recently, basis and grid pruning techniques have been used to

describe efficiently the semi-rigid part of floppy complexes in full dimensionality.<sup>21–23</sup>

Floppy molecular systems with multiple large-amplitude motions were and are still an open challenge for the field, so it was natural to ask the following questions about a novel black-box-type approach: (1) Can the black-box-type rovibrational approach tackle floppy systems? (2) Can we come close in efficiency to tailor-made approaches for floppy systems? Although singular regions can be explored numerically, there are difficulties connected to the selection and use of good basis functions and integration grids without an analytic knowledge of the kinetic energy operator (KEO) and its matrix elements.<sup>21</sup> (3) Is it possible to continue using the simpler direct product basis and grid representations for a start, which can be pruned perhaps at a next stage of the development (or is it necessary to group the coordinates in a certain fashion and use specifically coupled basis functions)?

In the present work, we will show for the example of the methane–water (MW) dimer that the answer to all three questions, (1)–(3), is “yes.”

We use the methane–water dimer as an example system because Wang and Carrington<sup>24</sup> recently reported and carefully documented their work using a tailor-made dimer Hamiltonian, Wigner  $D$  basis functions, and the symmetry adapted Lanczos eigensolver for computing rovibrational transitions of this dimer. They have carefully compared their computational results with earlier black-box-type rovibrational computations carried out for this system<sup>25–27</sup> and pointed out that even the excessively large direct-product basis and grid provided insufficiently converged rovibrational energies,<sup>25–27</sup> with inaccuracies on the order of 0.05–1.5  $\text{cm}^{-1}$ . Since the publication of the first applications of the GENIUSH program for molecular dimers, we have gathered more experience in treating floppy complexes, and using this development and experience, we wish to complement this comparison.

The methane–water dimer is also a chemically and spectroscopically important example. It is the simplest model for water–hydrocarbon interactions, and there are high-resolution far-infrared<sup>28</sup> and microwave spectroscopic data<sup>29</sup> available for the system, while the analysis of the congested spectrum was difficult and only partially possible by effective Hamiltonians.

In this work, we will show that using an order of magnitude *smaller* but better basis and grid representation than in earlier work,<sup>25–27</sup> we can converge the rovibrational energies to  $10^{-3} \text{ cm}^{-1}$  with a basis and grid that is “only” twice as large as the coupled basis used by Wang and Carrington.<sup>24</sup>

The tailor-made approach remains to be more efficient, but not by orders of magnitude. The efficiency of the GENIUSH computation can be further enhanced by exploiting part of the rich symmetry features<sup>30</sup> of this particular complex. We think that the level of convergence achieved in this work is much beyond the range of the typical approximations underlying the current computational rovibrational spectroscopy framework (quality of the potential energy surface, Born–Oppenheimer, and non-relativistic approximations).

Finally, we may ask whether we can expect any fundamental or numerical advantage from developing general rovibrational approaches, apart from fulfilling a mathematical “necessity.”

First of all, we may aim for automatically defining internal coordinates that are optimal or near optimal for a particular computation (system and energy range).

Furthermore, for a floppy molecular system, a fundamental and numerically important open problem is finding the optimal body-fixed frame or at least a body-fixed frame that is good enough or better than another one. For small-amplitude vibrations, the Eckart frame is known to be an excellent choice in minimizing the rotational and vibrational problem for low-energy rovibrational states, and thus, it allows us to use the  $J = 0$  vibrational eigenfunctions as a basis for  $J > 0$  computation<sup>31</sup> in the same energy range. For higher excited semi-rigid systems and especially for floppy systems, we do not have any practical approach for finding a good or at least a “better” frame and it may be the numerical KEO approach used also in the GENIUSH program that will allow us to optimize the molecular frame “on-the-fly” over a grid.<sup>32</sup>

Having this perspective in mind, after a short theoretical introduction (Sec. II), we report rovibrational energies (Secs. III and IV), transitions, and line strengths (Secs. V–VII) for the example of methane–water obtained with the numerical KEO approach of GENIUSH and using the potential energy surface (PES) developed by Akin-Ojo and Szalewicz (AOSz05 PES).<sup>33</sup>

## II. THEORETICAL DESCRIPTION AND COMPUTATIONAL DETAILS

The quantum dynamical computations were carried out by using the GENIUSH<sup>1,34</sup> computer program. This program package has been used already to study a number of semi-rigid and floppy molecular systems,<sup>21–23,25–27,30,35–40</sup> so here we only shortly summarize the theoretical background. The general rovibrational Hamiltonian,<sup>2–6,41</sup>

$$\hat{H} = \frac{1}{2} \sum_{k=1}^D \sum_{l=1}^D \hat{g}^{-1/4} \hat{p}_k G_{kl} \hat{g}^{1/2} \hat{p}_l \hat{g}^{-1/4} + \frac{1}{2} \sum_{k=1}^D \sum_{a=1}^3 (\hat{g}^{-1/4} \hat{p}_k G_{k,D+a} \hat{g}^{1/4} + \hat{g}^{1/4} G_{k,D+a} \hat{p}_k \hat{g}^{-1/4}) \hat{J}_a + \frac{1}{2} \sum_{a=1}^3 G_{D+a,D+a} \hat{J}_a^2 + \frac{1}{2} \sum_{a=1}^3 \sum_{b>a}^3 G_{D+a,D+b} [\hat{J}_a, \hat{J}_b]_+ + \hat{V}, \quad (1)$$

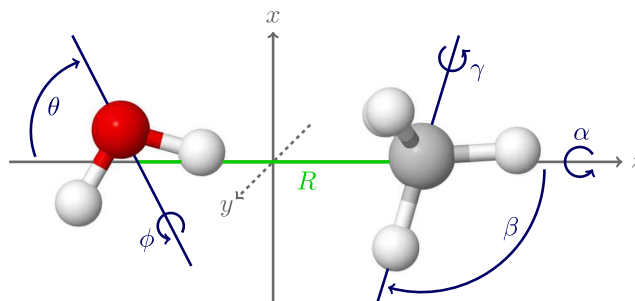


FIG. 1. Definition of the intermolecular coordinates ( $R, \theta, \phi, \alpha, \beta, \gamma$ ) of the  $\text{CH}_4\text{--H}_2\text{O}$  dimer.

is implemented in the GENIUSH program. In Eq. (1),  $\hat{J}_a$  [ $a = 1(x), 2(y), 3(z)$ ] are the body-fixed total angular momentum operators and  $\hat{p}_k = -i\partial/\partial q_k$  with the  $q_k$  ( $k = 1, 2, \dots, D$ ) internal coordinates. The  $G_{kl} = (\mathbf{g}^{-1})_{kl}$  coefficients and  $\tilde{g} = \det(\mathbf{g})$  are determined from the rovibrational  $\mathbf{g} \in \mathbb{R}^{(D+3) \times (D+3)}$  matrix, defined as follows:

$$g_{kl} = \sum_{i=1}^N m_i \mathbf{t}_{ik}^T \mathbf{t}_{il}, \quad k, l = 1, 2, \dots, D+3, \quad (2)$$

with

$$\mathbf{t}_{ik} = \frac{\partial \mathbf{r}_i}{\partial q_k}, \quad k, l = 1, 2, \dots, D, \quad (3)$$

$$\mathbf{t}_{i,D+a} = \mathbf{e}_a \times \mathbf{r}_i, \quad a = 1(x), 2(y), 3(z), \quad (4)$$

where  $\mathbf{r}_i$  are the body-fixed Cartesian coordinates for the  $i$ th atom and  $\mathbf{e}_a$  represent the body-fixed unit vectors.

In the CH<sub>4</sub>-H<sub>2</sub>O dimer, the intermolecular degrees of freedom ( $D = 6$ , Fig. 1) are defined with the following internal coordinates: the  $R \in [0, \infty)$  distance between the centers of mass of the monomers; two angles,  $\cos \theta \in [-1, 1]$  and  $\phi \in [0, 2\pi)$ , to describe the orientation of H<sub>2</sub>O; and three angles,  $\alpha \in [0, 2\pi)$ ,  $\cos \beta \in [-1, 1]$ , and  $\gamma \in [0, 2\pi)$ , to describe the orientation of CH<sub>4</sub>. The monomer structures are fixed at the effective vibrational structures used for the development of the PES in Ref. 33 and

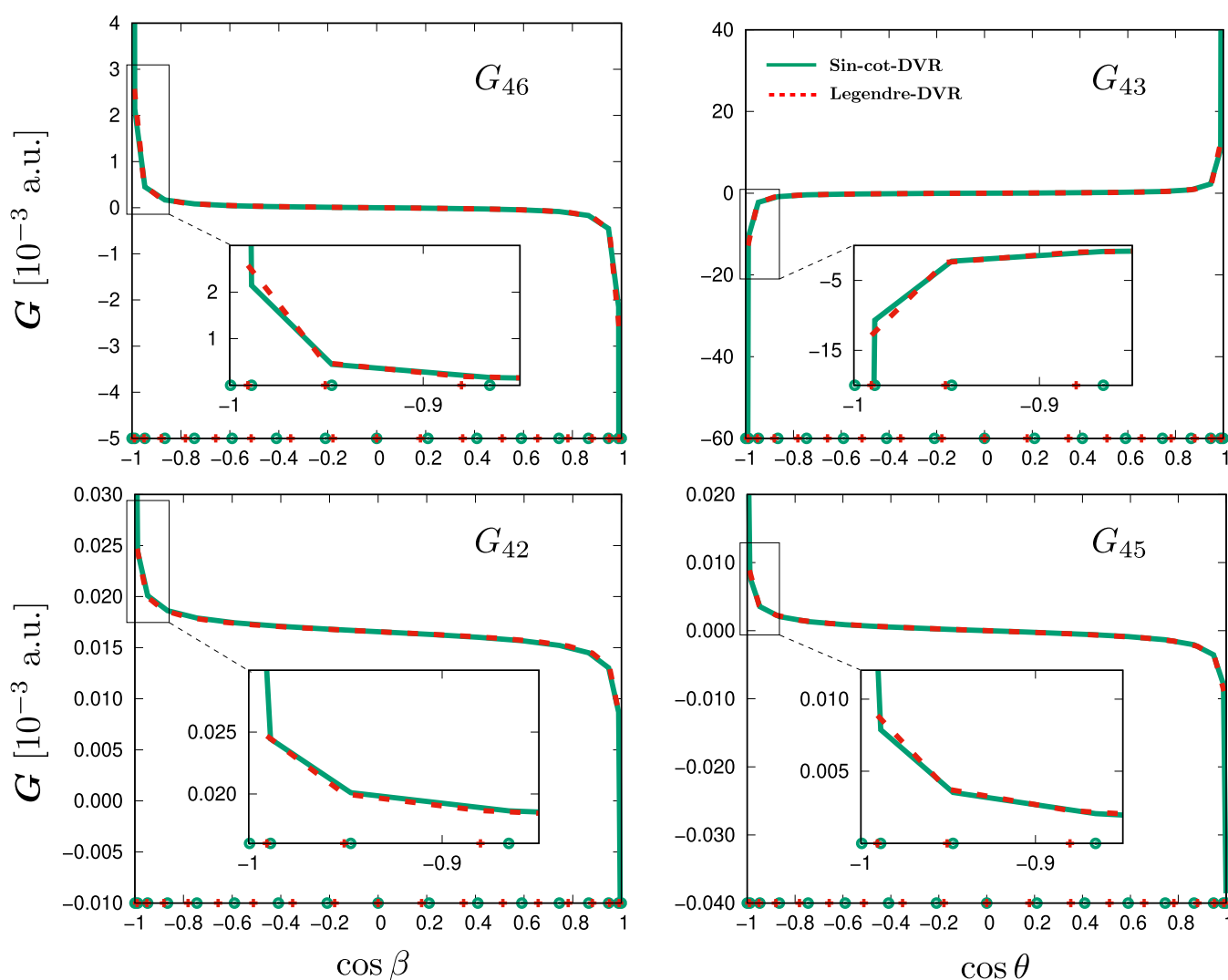


**FIG. 2.** Selected elements of the  $\mathbf{G}$  matrix shown along the singular coordinates,  $\cos \beta$  and  $\cos \theta$  (while all other coordinates are fixed). The Legendre and cot-DVR grid points (17 of each) are plotted on the  $x$  axis of each inset. Both sets of points approach the  $\pm 1$  singular points, but the cot-DVR points have a higher density near the singularities.

in earlier rovibrational computations.<sup>24,25</sup> For completeness, we repeat here the values of the constrained (bond length, angle) values, which are [ $r(\text{O-H}) = 0.971\,625\,7\text{ \AA}$ ,  $\alpha(\text{H-O-H}) = 104.69^\circ$ ] and [ $r(\text{C-H}) = 1.099\,122\text{ \AA}$ ,  $\cos\alpha(\text{H-C-H}) = -1/3$ ] for the water and the methane fragments, respectively. We used the same atomic masses as in Refs. 24 and 25:  $m(\text{H}) = 1.007\,825\text{ m}_u$ ,  $m(\text{C}) = 12\text{ m}_u$ , and  $m(\text{O}) = 15.994\,915\text{ m}_u$ . Since we use the same PES, constrained coordinates, and nuclear (atomic) mass values as Ref. 24 (and also Ref. 25), the direct comparison of the results is possible.

In the present work, the matrix representation of the Hamiltonian is constructed using a direct product discrete variable representation (DVR)<sup>42</sup> for the vibrational degrees of freedom. For our curvilinear coordinate representation (Fig. 1), the KEO has singularities at  $\cos\theta = \pm 1$  and  $\cos\beta = \pm 1$ . Plain Legendre DVR can be used for these coordinates, but the convergence of the (ro)vibrational energies is slow and an excessive number of grid points is needed even for a moderate level of convergence.<sup>25,27,38</sup> The representation is fundamentally correct since we have repulsive singularities in the KEO (Fig. 2), but it is computationally inefficient. (We note that while in Fig. 2 both positive and negative singular values can be seen, the integrals are always positive.) This behavior was correctly pointed out by Wang and Carrington in Ref. 24. The direct product basis and grid with Legendre DVR used in the GENIUSH computations,<sup>25,27,38</sup> which was 20 times larger than the coupled basis representation with Wigner  $D$  functions of Wang and Carrington,<sup>24</sup> were sufficient to converge the rovibrational states in the ZPV splitting range only with a convergence error as large as  $0.44\text{ cm}^{-1}$  and an erroneous split for some of the degenerate levels. At the same time, we note that this split did not hinder the unambiguous molecular symmetry group assignment of the GENIUSH results using the coupled-rotor decomposition scheme.<sup>26</sup>

This convergence problem was intriguing for a full (12)-dimensional computation of the methane-argon complex studied by two of us.<sup>21</sup> In order to make the 12D computation feasible, the more efficient cot-DVR developed by Schiffel and Manthe<sup>43</sup> was used for the singular coordinate (which was the second Euler angle in that system). The cot-DVR was developed by Schiffel and Manthe<sup>43</sup> to have a more efficient representation of the quantum mechanical motion along the singular coordinate (we note that the

**TABLE I.** Coordinate intervals and representations used in the GENIUSH rovibrational computations.

Coord.	GM <sup>a</sup>	DVR		No. points
		Type	Interval	
$R(\text{\AA})$	3.464	PO-Laguerre <sup>b</sup>	(2.5,6.0)	15
$\theta^\circ$	116.190	Cot-DVR <sup>c</sup>	[0, 180]	17
$\phi^\circ$	90.000	Fourier	[0, 360]	15
$\alpha^\circ$	297.460	Fourier	[0, 360]	9
$\beta^\circ$	113.050	Cot-DVR <sup>c</sup>	[0, 180]	17
$\gamma^\circ$	293.010	Fourier	[0, 360]	23

<sup>a</sup>Internal coordinate values for the global minimum (GM) structure of the AOSz05 PES.<sup>33</sup>

<sup>b</sup>Potential-optimized DVR using 300 points.

<sup>c</sup>The cot-DVR was constructed with two sine functions.

singularity is present only for  $K \neq 0$  in the  $|J, K\rangle$  basis representation of Ref. 43). The first practical application for a “multi”-dimensional molecule of cot-DVR was reported by Wang and Carrington.<sup>44</sup> The cot-DVR procedure uses a polynomial series of cosine, and optionally also sine, functions to build a DVR. In the present work, we obtained the best results when two sine functions were also included. The “final” computational parameters are summarized in Table I.

### III. ENERGY LEVELS AND CONVERGENCE TESTS

First, the convergence of the results has been tested with respect to the number of grid points for every coordinate using a series of reduced-dimensional ( $D < 6$ ) and full-dimensional ( $D = 6$ ) computations. Table II highlights the  $10^{-3}\text{ cm}^{-1}$  convergence of the first 20 vibrational states for the selected grid parameters (Table I).

In Table II, we can observe a small  $10^{-3}\text{ cm}^{-1}$  artificial split of some of the triply degenerate levels, which is due to the fact that the underlying grid and basis do not respect the full symmetry of the dimer; hence, certain symmetry features are converged numerically by enlargement of the grid. At the same time, at this level of convergence, we felt important to check three additional computational parameters that are listed in the following paragraphs and summarized in Table III.

**TABLE II.** Convergence test of the vibrational ( $J = 0$ ) energy levels, in  $\text{cm}^{-1}$ , referenced to the zero-point vibrational energy in the methane-water dimer computed with the GENIUSH program and the AOSz05 PES.<sup>33</sup>

$J0.n$	$\tilde{\nu}^a$	$\delta^{(-2)b}$	$\delta^{(+2)c}$
$N_b$ :	$1.4 \cdot 10^7$	$5.6 \cdot 10^6$	$5.9 \cdot 10^7$
1	206.810	0.001	0
2	4.764	0.001	0
3	4.764	0.001	0
4	4.765	-0.001	0.001
5	6.992	0.002	0
6	11.250	0.002	0
7	11.251	0.003	0.001
8	11.251	0	0
9	29.033	-0.001	0
10	29.034	-0.001	0.001
11	29.034	-0.001	0
12	32.636	0.003	0
13	32.637	0	0
14	32.637	0	0
15	32.711	0.002	0
16	32.712	0.001	0.001
17	32.712	0.001	0
18	34.410	0	0
19	35.920	0	0
20	35.920	0	0

<sup>a</sup>Obtained with the (15, 17, 15, 9, 17, 23) grid documented in Table II.

<sup>b</sup> $\delta^{(-2)} = \tilde{\nu} - \tilde{\nu}^{(-2)}$ , where  $\tilde{\nu}^{(-2)}$  was obtained with the same type of grid as in (a), but with fewer points (13, 15, 13, 9, 15, 21).

<sup>c</sup> $\delta^{(+2)} = \tilde{\nu} - \tilde{\nu}^{(+2)}$ , where  $\tilde{\nu}^{(+2)}$  was obtained with the same type of grid as in (a), but with more points (17, 19, 17, 11, 19, 25).



**TABLE III.** Testing the computational setup in GENIUSH for the first twenty vibrational ( $J = 0$ ) energy levels, in  $\text{cm}^{-1}$ , of MW and using the AOSz05 PES. The first energy value corresponds to the zero-point vibrational energy (ZPVE), and the other values are relative to the ZPVE.

$J0.n$	$\tilde{\nu}_0$	NumStep <sup>a</sup>	PESsym <sup>b</sup>	CompAlg <sup>c</sup>
1	206.810 21	$4 \times 10^{-6}$	$1 \times 10^{-8}$	$1 \times 10^{-5}$
2	4.763 83	$4 \times 10^{-6}$	$3 \times 10^{-7}$	$7 \times 10^{-6}$
3	4.764 00	$4 \times 10^{-6}$	$3 \times 10^{-7}$	$8 \times 10^{-6}$
4	4.764 64	$1 \times 10^{-5}$	$3 \times 10^{-8}$	$9 \times 10^{-6}$
5	6.991 93	$3 \times 10^{-7}$	$2 \times 10^{-8}$	$5 \times 10^{-6}$
6	11.250 42	$4 \times 10^{-6}$	$3 \times 10^{-7}$	$1 \times 10^{-5}$
7	11.250 51	$4 \times 10^{-6}$	$4 \times 10^{-7}$	$1 \times 10^{-5}$
8	11.251 22	$1 \times 10^{-5}$	$1 \times 10^{-8}$	$4 \times 10^{-6}$
9	29.033 43	$2 \times 10^{-6}$	$6 \times 10^{-8}$	$2 \times 10^{-6}$
10	29.033 61	$2 \times 10^{-6}$	$5 \times 10^{-8}$	$6 \times 10^{-6}$
11	29.033 61	$2 \times 10^{-6}$	$7 \times 10^{-8}$	$6 \times 10^{-6}$
12	32.636 02	$4 \times 10^{-6}$	$3 \times 10^{-8}$	$2 \times 10^{-5}$
13	32.637 12	$3 \times 10^{-6}$	$2 \times 10^{-7}$	$1 \times 10^{-5}$
14	32.637 14	$3 \times 10^{-6}$	$1 \times 10^{-7}$	$9 \times 10^{-6}$
15	32.710 92	$4 \times 10^{-6}$	$2 \times 10^{-8}$	$2 \times 10^{-5}$
16	32.712 10	$4 \times 10^{-6}$	$2 \times 10^{-7}$	$8 \times 10^{-6}$
17	32.712 30	$4 \times 10^{-6}$	$2 \times 10^{-7}$	$8 \times 10^{-6}$
18	34.410 43	$4 \times 10^{-6}$	$6 \times 10^{-8}$	$1 \times 10^{-6}$
19	35.919 68	$2 \times 10^{-6}$	$2 \times 10^{-8}$	$1 \times 10^{-5}$
20	35.919 72	$2 \times 10^{-6}$	$2 \times 10^{-8}$	$1 \times 10^{-5}$

<sup>a</sup> $\tilde{\nu} - \tilde{\nu}_{\text{NumStep}}$ , where  $\tilde{\nu}_{\text{NumStep}}$  was obtained by changing the step size of the numerical finite difference calculation of the vibrational t-vectors in GENIUSH from  $\zeta = 10^{-5}$  a.u. ( $\tilde{\nu}_0$ ) to  $\zeta = 10^{-6}$  a.u. (using quadruple precision in Fortran).

<sup>b</sup> $\tilde{\nu} - \tilde{\nu}_{\text{PESsym}}$ , where  $\tilde{\nu}_{\text{PESsym}}$  was obtained by averaging for every PES points the effect of the identity and the (123) and (132) methane permutations.

<sup>c</sup> $\tilde{\nu} - \tilde{\nu}_{\text{CompAlg}}$ , where  $\tilde{\nu}_{\text{CompAlg}}$  was obtained by generating the  $\mathbf{G}$  matrix elements using a Wolfram Mathematica implementation with 20 digits precision over the entire grid and performing the vibrational calculations with GENIUSH using these KEO coefficients.

### A. Testing the finite difference calculation of the vibrational t-vectors

We have tested the accuracy of the vibrational t-vectors, the  $\mathbf{t}_{ik}$  vectors in Eq. (3), which are the derivatives of the body-fixed Cartesian coordinates with respect to the internal coordinates and are calculated in GENIUSH using finite differences. We have studied the effect of the  $\zeta$  step size in the two-sided difference formula (it was possible to meaningfully use this formula with the current step sizes also near the boundaries for the grid types listed in Table II). The default value for the step size is  $\zeta = 10^{-5}$  a.u.,<sup>1</sup> which we use in our original study, but we have performed computations also with  $\zeta = 10^{-6}$  a.u. The “NumStep” column of Table III shows that the effect of this change for the lowest twenty vibrational states is less than  $10^{-5}$   $\text{cm}^{-1}$ .

### B. PES symmetrization

Wang and Carrington<sup>24</sup> pointed out that there is a small imperfection in the AOSz05 PES<sup>33</sup> with respect to the (123) and (132) permutations of the methane protons, and for this reason, they used a symmetrized version of the PES by averaging over the rotated

geometries (perfect numerical symmetry was critical for them for using the symmetry-adapted Lanczos eigensolver). The “PESsym” column of Table III shows that the effect of this operation is less than  $3 \times 10^{-7}$   $\text{cm}^{-1}$  for the present results.

### C. Generation of the $\mathbf{G}$ matrix over the grid points by increased precision computer algebra

To check the numerical KEO procedure for this example, we generated the  $\mathbf{G}$  matrix values over the entire grid using the Wolfram Mathematica symbolic algebra program<sup>45</sup> using analytic derivatives and with 20 digits precision. Note that we use quadruple precision in the Fortran implementation of GENIUSH for the finite difference calculation of the vibrational t-vectors, but only double precision for the inversion of the  $\mathbf{g}$  matrix. Near the singularities, we have to deal with small (large) values, and for this reason, we had decided to check the calculation procedure. The “CompAlg” column of Table III shows that using an increased precision Mathematica calculation to generate all KEO coefficients has an effect smaller than  $10^{-5}$   $\text{cm}^{-1}$  on the first twenty vibrational states of methane–water.

### IV. COMPARISON WITH WIGNER $D$ BASIS FUNCTION COMPUTATIONS

The dimer Hamiltonian<sup>7</sup> used by Wang and Carrington in Ref. 24 corresponds to a different coordinate choice than ours. It relies on using two full sets of Euler angles (six angles) to describe the monomers’ rotation with respect to the dimer fixed frame, and two additional angles are used to describe the rotational motion. We also define the monomers’ orientation with two sets of Euler angles, but we set the first Euler angle of  $\text{H}_2\text{O}$  to zero, and thus, we can use three angles to describe the rotation of the body-fixed frame (Secs. II and V, see also Fig. 3). The separation of the centers of mass of the monomers is described with the  $R$  distance in both studies. For this angular representation, the KEO can be written in terms of angular momentum operators and the kinetic energy matrix elements can be calculated analytically using Wigner’s  $D$  functions.<sup>7</sup> The Wigner  $D$  functions are non-direct product functions, and they efficiently account for the singularities in the KEO. Wang and Carrington<sup>24</sup> combined this method with the Symmetry Adapted Lanczos (SAL)

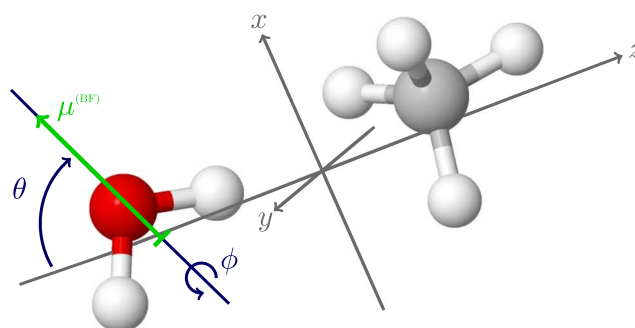


**FIG. 3.** Schematic representation of the dipole moment in the molecule-fixed frame of the  $\text{CH}_4\text{-H}_2\text{O}$  dimer.

**TABLE IV.** Comparison of a representative set of rovibrational energies referenced to the zero-point energy, in  $\text{cm}^{-1}$ , obtained with non-product (NP) and direct-product (DP) basis computations for the methane–water dimer. (The full list is provided in the SOM.)

Label	Sym. <sup>b</sup>	$\tilde{\nu}_{\text{NP}}^{24}$ $3.0 \cdot 10^6$	$\tilde{\nu}'_{\text{DP}}^{25}$ $6.0 \cdot 10^7$	$\tilde{\nu}_{\text{DP}}$ (this work) $1.4 \cdot 10^7$	$\tilde{\nu}_{\text{NP}} - \tilde{\nu}_{\text{DP}}$
J0.1	A <sub>1</sub> <sup>+</sup>	206.810	206.801	206.810	0.000
J0.2		4.765	4.763	4.764	0.001
J0.3	F <sub>2</sub> <sup>+</sup>	4.765	4.764	4.764	0.001
J0.4		4.765	4.764	4.765	0.000
J0.5	A <sub>2</sub> <sup>-</sup>	6.993	6.934	6.992	0.001
J0.18	A <sub>1</sub> <sup>+</sup>	34.413	34.405	34.410	0.003
J0.19	E <sup>+</sup>	35.920	35.880	35.920	0.000
J0.20		35.920	35.880	35.920	0.000
J0.21	E <sup>-</sup>	36.404	36.397	36.404	0.000
J0.22		36.404	36.397	36.405	0.000
J0.23		36.414	36.317	36.412	0.002
J0.24	F <sub>1</sub> <sup>+</sup>	36.414	36.317	36.413	0.001
J0.25		36.414	36.322	36.414	0.000
J0.36	A <sub>1</sub> <sup>+</sup>	48.706	48.685	48.686	0.020
J0.66	A <sub>2</sub> <sup>-</sup>	66.597	66.156	66.598	0.001
J1.1	A <sub>2</sub> <sup>+</sup>	0.289	0.289	0.289	0.000
J1.2		5.047	5.044	5.045	0.001
J1.3	F <sub>1</sub> <sup>+</sup>	5.047	5.044	5.046	0.001
J1.4		5.047	5.045	5.046	0.001
J1.5	A <sub>1</sub> <sup>-</sup>	7.282	7.219	7.281	0.001
J1.38		30.687	30.474	30.687	0.001
J1.39	F <sub>1</sub> <sup>+</sup>	30.687	30.474	30.687	0.001
J1.40		30.687	30.588	30.687	0.001
J1.41		30.688	30.588	30.687	0.001
J1.42	F <sub>2</sub> <sup>+</sup>	30.688	30.633	30.687	0.001
J1.43		30.688	30.633	30.687	0.001
J1.86	A <sub>2</sub> <sup>+</sup>	48.981	48.946	48.961	0.021

<sup>a</sup>Number of basis functions that equals the number of grid points for the DP computations.<sup>b</sup>Symmetry labels corresponding to the character table of Wang and Carrington<sup>24</sup> instead of the table originally proposed by Dore *et al.*<sup>28</sup> used in Refs. 25 and 26.

algorithm to obtain symmetry labels and to make their computations more efficient.

Table IV presents the comparison of three approaches: (a) the analytic dimer Hamiltonian and non-direct product Wigner  $D$  basis functions of Wang and Carrington,<sup>24</sup> (b) GENIUSH with a numerical KEO and the “smaller” direct-product grid using Legendre polynomials for the singular  $\cos \theta$  and  $\cos \beta$  coordinates of Ref. 25, and (c) the present GENIUSH computations with a numerical KEO and a direct-product grid in which the Legendre DVR is replaced with cot-DVR for the singular coordinates.

By replacing the Legendre DVRs with cot-DVRs, we can reduce the number of basis functions from  $60 \times 10^6$  (of the “large” basis and grid<sup>25</sup>) to  $13.4 \times 10^6$ , while the convergence error is reduced from  $\sim 1 \text{ cm}^{-1}$  to  $10^{-3} \text{ cm}^{-1}$ . Our “optimal” basis with  $13.4 \times 10^6$  functions is ca. twice as large as the Wigner  $D$  basis of Wang and Carrington<sup>24</sup> (we note that their  $2.97 \times 10^6$  basis size is for a single parity, while our basis size contains both parity components). Our smaller basis set in Table II includes  $6 \times 10^6$  functions, but it has a somewhat larger convergence error of  $\pm 3 \cdot 10^{-3} \text{ cm}^{-1}$ .

We also note that we observe a  $0.02 \text{ cm}^{-1}$  deviation between our “optimal” basis results (Table IV) and the results of Wang and Carrington<sup>24</sup> for the 36th vibrational state that can be assigned as the stretching fundamental. This convergence error reappears also for  $J = 1$  (J1.86 in Table IV) that corresponds to the rotational excitation of the stretching fundamental vibration. We have checked the convergence of this state also by using tridiagonal Morse functions.<sup>46</sup> Since we have carefully checked the convergence (and other computational parameters) in the present work, we think that this small

**TABLE V.**  $U_{\omega\sigma,\alpha}^{(\Omega)}$  matrix elements for  $\Omega = 1$ .

$(\omega, \sigma)$	$\alpha:$	$x$	$y$	$z$
(1, -1)		$\frac{1}{\sqrt{2}}$	$-\frac{i}{\sqrt{2}}$	0
(1, 0)		0	0	1
(1, 1)		$-\frac{1}{\sqrt{2}}$	$-\frac{i}{\sqrt{2}}$	0

**TABLE VI.** ( $E$ )<sub>1</sub> and ( $E$ )<sub>2</sub> bands of the CH<sub>4</sub>-H<sub>2</sub>O. All transitions are reported in cm<sup>-1</sup> except where it is otherwise stated. ( $J, n$ )' and ( $J, n$ ) label the rovibrational state in our energy lists provided in the SOM, (this w): (this work).  $\Delta\nu = E' - E$ .  $S_0$  is the line strength, Eq. (5), without the spin statistical weight factor.<sup>25</sup>

$(J, n)' \leftarrow (J, n)$	$\Delta\tilde{\nu}_{\text{obs}}$ (MHz) <sup>28</sup>	$\Delta\tilde{\nu}_{\text{obs}}$	$E'$ (this w)	$E$ (this w)	$\Delta\tilde{\nu}$ (this w)	$\Delta\tilde{\nu}^{24}$	$S_0$ (this w)	$S_0^{24}$
Expt.: <sup>28</sup> Table III, ( $E$ ) <sub>1</sub> , $\Sigma \leftarrow \Pi$ band								
0, 21-22 $\leftarrow$ 1, 23-24	532 812.0	17.7727	36.4045	19.3909	17.0136	17.0099	0.155	0.154
1, 53-54 $\leftarrow$ 1, 23-24	541 359.5	18.0578	36.6889	19.3909	17.2980	17.2946	0.232	0.230
2, 75-76 $\leftarrow$ 1, 23-24	558 451.2	18.6279	37.2577	19.3909	17.8668	17.8638	0.074	0.073
1, 53-54 $\leftarrow$ 2, 23-24	524 254.1	17.4872	36.6889	19.9581	16.7309	16.7270	0.232	0.230
2, 75-76 $\leftarrow$ 2, 23-24	541 344.3	18.0573	37.2577	19.9581	17.2996	17.2962	0.393	0.391
Expt.: <sup>28</sup> Table III, ( $E$ ) <sub>2</sub> , $\Delta \leftarrow \Pi$ band								
2, 80-81 $\leftarrow$ 2, 23-24	542 744.8	18.1040	37.5721	19.9581	17.6140	17.6100	0.263	0.262
2, 80-81 $\leftarrow$ 1, 23-24	559 850.8	18.6746	37.5721	19.3909	18.1812	18.1800	0.484	0.482

**TABLE VII.** ( $A/F$ )<sub>1</sub> and ( $A/F$ )<sub>3</sub> bands of CH<sub>4</sub>-H<sub>2</sub>O. See also the caption of Table VI.

$(J, n)' \leftarrow (J, n)$	$\Delta\tilde{\nu}_{\text{obs}}$ (MHz) <sup>28</sup>	$\Delta\tilde{\nu}_{\text{obs}}$	$E'$ (this w)	$E$ (this w)	$\Delta\tilde{\nu}$ (this w)	$\Delta\tilde{\nu}^{24}$	$S_0$ (this w)	$S_0^{24}$
Expt. (Ref. 28): Table IV, ( $A/F$ ) <sub>1</sub> , $\Sigma \leftarrow \Pi$ band								
0, 12-14 $\leftarrow$ 1, 20-22	538 189.8	17.9521	32.6368	14.6152	18.0215	18.0194	0.167	0.166
1, 47-49 $\leftarrow$ 1, 20-22	546 831.5	18.2403	33.0018	14.6152	18.3866	18.3839	0.231	0.230
2, 60-62 $\leftarrow$ 1, 20-22	564 291.7	18.8227	33.5026	14.6152	18.8874	18.8858	0.080	0.080
1, 47-49 $\leftarrow$ 2, 17-19	529 495.8	17.6621	33.0018	15.1903	17.8115	17.8083	0.234	0.232
2, 60-62 $\leftarrow$ 2, 17-19	546 715.2	18.2365	33.5026	15.1903	18.3123	18.3102	0.420	0.417
Predicted in Ref. 24: ( $A/F$ ) <sub>1b</sub> , $\Delta \leftarrow \Pi$ band								
0, 15-17 $\leftarrow$ 1, 17-19	-	-	32.7118	14.6124	18.0994	18.0960	0.155	0.154
1, 44-46 $\leftarrow$ 1, 17-19	-	-	32.9254	14.6124	18.3130	18.3106	0.249	0.248
2, 63-65 $\leftarrow$ 1, 17-19	-	-	33.5818	14.6124	18.9693	18.9667	0.076	0.076
1, 44-46 $\leftarrow$ 2, 20-22	-	-	32.9254	15.1975	17.7279	17.7254	0.251	0.250
2, 63-65 $\leftarrow$ 2, 20-22	-	-	33.5818	15.1975	18.3843	18.3815	0.387	0.384
Expt. (Ref. 28): Table IV, ( $A/F$ ) <sub>3a</sub> , $\Delta \leftarrow \Pi$ band								
2, 66-71 <sup>a</sup> $\leftarrow$ 2, 17-19	564 637.3	18.8343	34.1923	15.1903	19.0020	18.9991	0.217	0.215
2, 66-71 <sup>a</sup> $\leftarrow$ 1, 20-22	581 971.4	19.4125	34.1923	14.6152	19.5770	19.5747	0.392	0.389
Expt. (Ref. 28): Table IV, ( $A/F$ ) <sub>3b</sub> , $\Delta \leftarrow \Pi$ band								
2, 66-71 <sup>a</sup> $\leftarrow$ 2, 20-22	564 437.7	18.8276	34.1925	15.1975	18.9950	18.9919	0.218	0.217
2, 66-71 <sup>a</sup> $\leftarrow$ 1, 17-19	582 013.5	19.4139	34.1925	14.6124	19.5801	19.5771	0.391	0.388
Predicted in Ref. 24: ( $A/F$ ) <sub>3Xa</sub> , $\Delta \leftarrow \Pi$ band								
2, 54-59 <sup>a</sup> $\leftarrow$ 2, 17-19	-	-	32.8319	15.1903	17.6416	17.6405	0.040	0.040
2, 54-59 <sup>a</sup> $\leftarrow$ 1, 20-22	-	-	32.8319	14.6152	18.2167	18.2161	0.075	0.075
Predicted in Ref. 24: ( $A/F$ ) <sub>3Xb</sub> , $\Delta \leftarrow \Pi$ band								
2, 54-59 <sup>a</sup> $\leftarrow$ 2, 20-22	-	-	32.8331	15.1975	17.6357	17.6333	0.042	0.042 <sup>b</sup>
2, 54-59 <sup>a</sup> $\leftarrow$ 1, 17-19	-	-	32.8331	14.6124	18.2207	18.2185	0.074	0.074 <sup>b</sup>

<sup>a</sup>Only three of the six upper states, which are very close in energy (and for this reason, listed together in our tables), give contribution to the  $S_0$  line strength.<sup>b</sup>These two values are interchanged in Ref. 24.

TABLE VIII.  $(A/F)_2$  band of  $\text{CH}_4\text{-H}_2\text{O}$ . See also the caption of Table VI.

$(J, n)' \leftarrow (J, n)$	$\Delta\tilde{\nu}_{\text{obs}}$ (MHz) <sup>28</sup>	$\Delta\tilde{\nu}_{\text{obs}}$	$E'$ (this w)	$E$ (this w)	$\Delta\tilde{\nu}$ (this w)	$\Delta\tilde{\nu}^{24}$	$S_0$ (this w)	$S_0^{24}$
Expt. (Ref. 28): Table V, $(A/F)_2, \Pi \leftarrow \Sigma$ band								
1, 35–37 $\leftarrow$ 0, 6–8	562 445.5	18.7612	29.7641	11.2507	18.5134	18.5106	0.319	0.317
1, 32–34 $\leftarrow$ 1, 12–14	553 888.4	18.4757	29.7619	11.5324	18.2294	18.2265	0.480	0.477
1, 35–37 $\leftarrow$ 2, 12–14	536 931.0	17.9101	29.7641	12.0959	17.6682	17.6648	0.161	0.160
2, 45–47 $\leftarrow$ 1, 12–14	571 055.5	19.0484	30.3357	11.5324	18.8033	18.8009	0.477	0.475
2, 42–44 $\leftarrow$ 2, 12–14	553 883.6	18.4756	30.3291	12.0959	18.2332	18.2303	0.799	0.794

difference in the energy list would probably disappear if Wang and Carrington<sup>24</sup> used a slightly larger basis set and grid along the  $R$  intermolecular stretching coordinate.

In our computations (DVR), the number of grid points equals the number of basis functions that is  $13.4 \times 10^6$  for our “optimal” basis. Wang and Carrington used a basis set that includes ca.  $3 \times 10^6$  functions for one parity component (+1 or -1). The size of their integration grid includes ca.  $91 \times 10^6$  points (which can be calculated from the values given in Ref. 24). By exploiting parity, Wang and Carrington reduced the grid size to ca. half of this value (slightly different values correspond to the two parity components). The size of the grid determines the cost of one matrix-vector multiplication during the Lanczos iteration. It is necessary to note that cot-DVR contains quadrature points very close to the singularities (Fig. 2), and for this reason, our Hamiltonian matrix has a very broad spectral range that considerably increases the number of Lanczos iterations.

All in all, the agreement of the two independent computations is remarkable, given the different coordinate representations, the entirely different KEOs and basis sets used to build the Hamiltonian matrix. We have not exploited molecular symmetry

to make the computations for this particular system more efficient, but the symmetry-adapted Lanczos algorithm could also be used in a GENIUSH computation.<sup>30</sup> The tailor-made, non-product Wigner  $D$  basis function computation remains to be the most efficient approach, but the numerical performance of the GENIUSH program (using the cot-DVR of Schiffel and Manthe for the singular bending coordinates) becomes comparable to the specialized approach.

## V. EVALUATION OF THE LINE STRENGTHS

Wang and Carrington<sup>24</sup> also reported the line strength values for the rovibrational transitions using a simple but excellent model for the dimer’s dipole moment. They set the dipole moment for the rigid water molecule to 1 (in arbitrary or “normalized, relative” units); since the rigid methane fragment is a polar, it does not contribute to this quantity. Using this dipole moment representation, they have computed the line strength for the rovibrational transitions and predicted that the global minimum to the secondary minimum transition should be well visible in the far-infrared spectrum. The transition moment or line strength is defined by<sup>47</sup>

TABLE IX.  $(A/F)_4$  band of  $\text{CH}_4\text{-H}_2\text{O}$ . See also the caption of Table VI.

$(J, n)' \leftarrow (J, n)$	$\Delta\tilde{\nu}_{\text{obs}}$ (MHz) <sup>28</sup>	$\Delta\tilde{\nu}_{\text{obs}}$	$E'$ (this w)	$E$ (this w)	$\Delta\tilde{\nu}$ (this w)	$\Delta\tilde{\nu}^{24}$	$S_0$ (this w)	$S_0^{24}$
Expt. (Ref. 28): Table VI, $(A/F)_4, \Pi \leftarrow \Sigma$ band								
1, 26 $\leftarrow$ 0, 5	574 574.9	19.1658	26.3646	6.9919	19.3727	19.3705	0.313	0.311
1, 25 $\leftarrow$ 1, 5	565 794.7	18.8729	26.3621	7.2805	19.0816	19.0792	0.473	0.471
1, 26 $\leftarrow$ 2, 5	548 506.7	18.2962	26.3646	7.8576	18.5070	18.5043	0.160	0.158
2, 34 $\leftarrow$ 1, 5	583 344.0	19.4583	26.9463	7.2805	19.6657	19.6638	0.467	0.464
2, 33 $\leftarrow$ 2, 5	565 694.1	18.8695	26.9386	7.8576	19.0810	19.0787	0.787	0.783
Predicted in Ref. 24: $(A/F)_{4X}, \Pi \leftarrow \Sigma$ band								
1, 69 $\leftarrow$ 0, 5	–	–	43.0625	6.9919	36.0706	36.0682	0.046	0.046
1, 70 $\leftarrow$ 1, 5	–	–	43.0660	7.2805	35.7855	35.7829	0.071	0.071
1, 69 $\leftarrow$ 2, 5	–	–	43.0625	7.8576	35.2049	35.2020	0.024	0.024
2, 101 $\leftarrow$ 1, 5	–	–	43.6042	7.2805	36.3236	36.3213	0.068	0.068
2, 102 $\leftarrow$ 2, 5	–	–	43.6147	7.8576	35.7571	35.7544	0.118	0.118

**TABLE X.** ( $E$ )<sub>3</sub>, ( $E$ )<sub>4</sub>, and ( $E$ )<sub>5</sub> bands of CH<sub>4</sub>-H<sub>2</sub>O. See also the caption of Table VI.

$(J, n)' \leftarrow (J, n)$	$\Delta\tilde{\nu}_{\text{obs}}$ (MHz) <sup>28</sup>	$\Delta\tilde{\nu}_{\text{obs}}$	$E'$ (this w)	$E$ (this w)	$\Delta\tilde{\nu}$ (this w)	$\Delta\tilde{\nu}^{24}$	$S_0$ (this w)	$S_0^{24}$
Expt. (Ref. 28): Table VII, ( $E$ ) <sub>3</sub> , $\Sigma \leftarrow \Pi$ band								
0, 19–20 $\leftarrow$ 1, 15–16	732 385.1	24.4297	35.9197	13.1087	22.8110	22.8098	0.093	0.092
1, 51–52 $\leftarrow$ 1, 15–16	740 778.1	24.7097	36.1856	13.1087	23.0769	23.0757	0.141	0.140
1, 51–52 $\leftarrow$ 2, 15–16	723 657.8	24.1386	36.1856	13.6782	23.0769	22.5057	0.136	0.135
2, 73–74 $\leftarrow$ 1, 15–16	757 561.5	25.2695	36.7175	13.1087	23.6088	23.6078	0.048	0.048
2, 73–74 $\leftarrow$ 2, 15–16	740 443.2	24.6985	36.7175	13.6782	23.0393	23.0378	0.232	0.231
Expt. (Ref. 28): Table VII, ( $E$ ) <sub>4</sub> , $\Sigma \leftarrow \Pi$ band								
2, 88–89 $\leftarrow$ 2, 15–16	821 483.9	27.4018	38.6481	13.6782	24.9700	24.9680	0.212	0.212
2, 88–89 $\leftarrow$ 1, 15–16	838 603.8	27.9728	38.6481	13.1087	25.5395	25.5380	0.396	0.394
Expt. (Ref. 28): Table VII, ( $E$ ) <sub>4</sub> ', $\Sigma \leftarrow \Pi$ band								
2, 90–91 $\leftarrow$ 2, 15–16	821 483.9	27.4018	39.5975	13.6782	25.9193	25.9171	0.005	0.005
2, 90–91 $\leftarrow$ 1, 15–16	838 603.8	27.9728	39.5975	13.1087	26.4888	26.4871	0.001	0.001
1, 58–59* $\leftarrow$ 2, 15–16	–	–	39.0170	13.6782	25.3388	25.3362 <sup>a</sup>	0.001	0.001
1, 58–59* $\leftarrow$ 1, 15–16	–	–	39.0170	13.1087	25.9083	25.9062 <sup>a</sup>	0.001	0.001
Expt. (Ref. 28): Table VII, ( $E$ ) <sub>5</sub> , $\Sigma \leftarrow \Pi$ band								
0, 34–35 $\leftarrow$ 1, 15–16	–	–	48.0961	13.1087	34.9874	34.9863	0.088	0.087
1, 84–85 $\leftarrow$ 1, 15–16	1057 943.1	35.2892	48.3769	13.1087	35.2682	35.2673	0.132	0.132
2, 116–117 $\leftarrow$ 1, 15–16	1074 920.4	35.8555	48.9384	13.1087	35.8297	35.8292	0.044	0.044
2, 116–117 $\leftarrow$ 2, 15–16	1057 801.7	35.2845	48.9384	13.6782	35.2602	35.2592	0.221	0.219

<sup>a</sup>We believe that there were some typos in Table XVIII of Ref. 24. The corrected values and labels are given here in comparison with the values computed in this work.

**TABLE XI.** ( $A/F$ )<sub>5</sub> band of CH<sub>4</sub>-H<sub>2</sub>O. See also the caption of Table VI.

$(J, n)' \leftarrow (J, n)$	$\Delta\tilde{\nu}_{\text{obs}}$ (MHz) <sup>28</sup>	$\Delta\tilde{\nu}_{\text{obs}}$	$E'$ (this w)	$E$ (this w)	$\Delta\tilde{\nu}$ (this w)	$\Delta\tilde{\nu}^{24}$	$S_0$ (this w)	$S_0^{24}$
Expt. (Ref. 28): Table VIII, ( $A/F$ ) <sub>5</sub> , $\Pi \leftarrow \Sigma$ band								
1, 38–40 $\leftarrow$ 0, 2–4	852 462.1	28.4351	30.6867	4.7642	25.9225	25.9223	0.256	0.255
1, 41–43 $\leftarrow$ 1, 2–4	844 268.9	28.1618	30.6873	5.0455	25.6417	25.6413	0.368	0.368
1, 38–40 $\leftarrow$ 2, 2–4	827 031.4	27.5868	30.6867	5.6083	25.0784	25.0774	0.114	0.113
2, 48–50 $\leftarrow$ 1, 2–4	860 602.5	28.7066	31.2548	5.0455	26.2093	26.2092	0.399	0.397
2, 51–53 $\leftarrow$ 2, 2–4	844 500.0	28.1695	31.2568	5.6083	25.6485	25.6479	0.615	0.612
Predicted in Ref. 24: ( $A/F$ ) <sub>5X</sub> , $\Pi \leftarrow \Sigma$ band								
1, 60–62 $\leftarrow$ 0, 2–4	–	–	40.4210	4.7642	35.6569	35.6572	0.105	0.105
1, 63–64 $\leftarrow$ 1, 2–4	–	–	40.4225	5.0455	35.3769	35.3770	0.164	0.164
1, 60–62 $\leftarrow$ 2, 2–4	–	–	40.4210	5.6083	34.8127	34.8123	0.060	0.060
2, 92–94 $\leftarrow$ 1, 2–4	–	–	40.9716	5.0455	35.9261	35.9267	0.150	0.150
2, 95–97 $\leftarrow$ 2, 2–4	–	–	40.9761	5.6083	35.3678	35.3678	0.273	0.271

$$S(J'l' \rightarrow JI) = g_{\text{ns}} \sum_{m,m'} \sum_{A=X,Y,Z} |\langle \Psi_{J'm'l'}^{(\text{rv})} | \mu_A | \Psi_{Jml}^{(\text{rv})} \rangle|^2, \quad (5)$$

where  $g_{\text{ns}}$  is the nuclear spin statistical weight factor and  $\mu_A$  ( $A = X, Y, Z$ ) are the components of the molecular dipole moment in the laboratory-fixed frame. The  $g_{\text{ns}}$  values have been calculated in Ref. 25. We note that Ref. 24 reported the “bare” values of the integrals (without the  $g_{\text{ns}}$  factor), which will be labeled  $S_0 = S/g_{\text{ns}}$  in Tables VI–XIV.

The rovibrational wave functions of the isolated molecule Hamiltonian, Eq. (1), are represented in the GENIUSH program<sup>34</sup> as

$$|\Psi_{Jml}^{(\text{rv})}\rangle = \sum_{v=1}^{N_h} \sum_{k,\tau} c_{v,k,\tau}^{(Jl)} |v\rangle |J, k, m, \tau\rangle, \quad (6)$$

expressed with the  $|v\rangle$  vibrational wave function and the Wang-type symmetric top functions  $|J, k, m, \tau\rangle = d_{+k}^{(\tau)} |J, k, m\rangle + d_{-k}^{(\tau)} |J, -k, m\rangle$ .

Following the work of Owens and Yachmenev, we evaluate the rovibrational integrals for  $\Omega$ -order tensorial properties in the laboratory-fixed frame (LF)<sup>48</sup> as

$$\langle \Psi_{J'm'l'}^{(\text{rv})} | T_A^{(\text{LF})} | \Psi_{Jml}^{(\text{rv})} \rangle = \sum_{\omega=0}^{\Omega} \mathcal{M}_{A\omega}^{(J'm',Jm)} \mathcal{K}_{\omega}^{(J'l',Jl)}, \quad (7)$$

with

$$\begin{aligned} \mathcal{M}_{A\omega}^{(J'm',Jm)} &= (-1)^{m'} \sqrt{(2J'+1)(2J+1)} \\ &\times \sum_{\sigma=-\omega}^{\omega} [U^{(\Omega)}]_{A,\omega\sigma}^{-1} \begin{pmatrix} J & \omega & J' \\ m & \sigma & -m' \end{pmatrix} \end{aligned} \quad (8)$$

and

**TABLE XII.**  $(A/F)_6$  and  $(A/F)_7$  bands of  $\text{CH}_4\text{-H}_2\text{O}$ . See also the caption of Table VI.

$(J, n)' \leftarrow (J, n)$	$\Delta\tilde{\nu}_{\text{obs}}$ (MHz) <sup>28</sup>	$\Delta\tilde{\nu}_{\text{obs}}$	$E'$ (this w)	$E$ (this w)	$\Delta\tilde{\nu}$ (this w)	$\Delta\tilde{\nu}^{24}$	$S_0$ (this w)	$S_0^{24}$
Expt. (Ref. 28): Table IX, $(A/F)_6, \Sigma \leftarrow \Pi$ band								
0, 23–25 $\leftarrow$ 1, 6–8	–	–	36.4131	7.9119	28.5012	28.5020	0.181	0.180
1, 55–57 $\leftarrow$ 1, 9–11	906 722.4	30.2450	36.6984	7.9158	28.7826	28.7837	0.276	0.275
1, 55–57 $\leftarrow$ 2, 6–8	889 393.8	29.6670	36.6984	8.4916	28.2069	28.2075	0.265	0.264
2, 77–79 $\leftarrow$ 1, 6–8	924 003.8	30.8214	37.2689	7.9119	29.3570	29.3583	0.103	0.103
2, 77–79 $\leftarrow$ 2, 9–11	906 302.4	30.2310	37.2689	8.5026	28.7663	28.7672	0.446	0.444
Predicted in Ref. 24: $(A/F)_{6X}, \Sigma \leftarrow \Pi$ band								
0, 9–11 $\leftarrow$ 1, 9–11	–	–	29.0335	7.9158	21.1177	21.118	0.080	0.080
1, 27–29 $\leftarrow$ 1, 6–8	–	–	29.3049	7.9119	21.3930	21.3563	0.117	0.117
1, 27–29 $\leftarrow$ 2, 9–11	–	–	29.3049	8.5026	20.8023	20.8022	0.123	0.122
2, 37–39 $\leftarrow$ 1, 9–11	–	–	29.8476	7.9158	21.9318	21.9325	0.038	0.037
2, 37–39 $\leftarrow$ 2, 6–8	–	–	29.8476	8.4916	21.3560	21.3563	0.194	0.193
Predicted in Ref. 24: $(A/F)_{6Y}, \Sigma \leftarrow \Pi$ band								
0, 26–28 $\leftarrow$ 1, 9–11	–	–	41.1844	7.9158	33.2686	33.2700	0.101	0.100
1, 66–68 $\leftarrow$ 1, 6–8	–	–	41.4639	7.9119	33.5520	33.5535 <sup>a</sup>	0.157	0.156
1, 66–68 $\leftarrow$ 2, 9–11	–	–	41.4639	8.5026	32.9613	32.9624	0.147	0.147
2, 98–100 $\leftarrow$ 1, 9–11	–	–	42.0229	7.9158	34.1071	34.1092	0.055	0.055
2, 98–100 $\leftarrow$ 2, 6–8	–	–	42.229	8.4916	33.5313	33.5330	0.262	0.261
Expt. (Ref. 28): Table IX, $(A/F)_{7a}, \Sigma \leftarrow \Pi$ band								
2, 82–87 <sup>b</sup> $\leftarrow$ 2, 6–8	912 803.3	30.4478	37.6439	8.4916	29.1523	29.1532	0.299	0.297
2, 82–87 <sup>b</sup> $\leftarrow$ 1, 9–11	930 130.4	31.0258	37.6439	7.9158	29.7281	29.7294	0.536	0.533
Expt. (Ref. 28): Table IX, $(A/F)_{7b}, \Sigma \leftarrow \Pi$ band								
2, 82–87 <sup>b</sup> $\leftarrow$ 2, 9–11	912 529.1	30.4387	37.6447	8.5026	29.1421	29.1421	0.309	0.307
2, 82–87 <sup>b</sup> $\leftarrow$ 1, 6–8	930 230.6	31.0292	37.6447	7.9119	29.7328	29.7332	0.530	0.527

<sup>a</sup>A typo in Table XX of Ref. 24 is corrected based on the  $E'$  and  $E''$  level energies given in the paper and checked against the results of this work.

<sup>b</sup>See footnote a to Table VII.

$$\begin{aligned} \mathcal{K}_{\omega}^{(J'J'',J)} &= \sum_{\substack{v,k,\tau \\ v',k',\tau'}} [c_{v'k'\tau'}^{(J'J'')}]^* c_{v k \tau}^{(J)} \sum_{\pm k', \pm k} [d_{k'}^{(\tau')}]^* d_k^{(\tau)} \\ &\times (-1)^{k'} \sum_{\sigma=-\omega}^{\omega} \sum_{\alpha} \begin{pmatrix} J & \omega & J' \\ k & \sigma & -k' \end{pmatrix} \\ &\times U_{\omega\sigma,\alpha}^{(\Omega)} \langle v' | T_{\alpha}^{(\text{BF})} | v \rangle. \end{aligned} \quad (9)$$

The electric dipole moment is a rank-1 tensor (a vector) with  $\Omega = 1$ , and the corresponding  $U$  matrix values are summarized in Table V. For higher-order tensor operators, this matrix can be calculated from lower rank tensors using the following expression:

$$U_{\omega\sigma,A}^{(\Omega)} = \sum_{\sigma_1=-\omega_1}^{\omega_1} \sum_{\sigma_2=-\omega_2}^{\omega_2} \langle \omega_1 \sigma_1 \omega_2 \sigma_2 | \omega \sigma \rangle U_{\omega_1 \sigma_1, B}^{(\Omega_1)} U_{\omega_2 \sigma_2, C}^{(\Omega_2)}, \quad (10)$$

where  $\Omega = \Omega_1 + \Omega_2$ ,  $A = B \otimes C$ , and  $\langle \omega_1 \sigma_1 \omega_2 \sigma_2 | \omega \sigma \rangle$  is the Clebsch–Gordan coefficient.

Regarding the transition dipoles of methane–water, we have first computed the vibrational matrix elements  $\langle v' | \mu_{\alpha}^{(\text{BF})} | v \rangle$  using the H<sub>2</sub>O dipole approximation of Ref. 24, i.e., only the water monomer contributes to the dipole moment of the dimer (Fig. 3). It is shown in Fig. 3 that in our representation this dipole vector points along the  $Z$  axis of the H<sub>2</sub>O monomer frame, and in the dimer's frame, its rotation is described with the  $\theta$  and  $\phi$  angles (although the value of  $\phi$  is irrelevant in this special case). Hence, it was straightforward to implement this (presumably excellent) approximation for the body-(dimer)-fixed dipole moment  $\mu_{\alpha}^{(\text{BF})}$ , calculate its value at a grid point in the body-fixed (dimer's) frame, and then integrate it for pairs of vibrational eigenvectors.

## VI. FAR-INFRARED SPECTRUM

The rovibrational transitions computed in this work are compared in Tables VI–XIII with the transitions computed by Wang and Carrington<sup>24</sup> and with the transitions observed experimentally in the far-infrared range by Dore *et al.*<sup>28</sup> In addition to the 13 experimentally observed vibration–rotation–tunnelling bands reported by Dore *et al.*: ( $E$ )<sub>1</sub>, ( $E$ )<sub>2</sub>, ( $A/F$ )<sub>1</sub>, ( $A/F$ )<sub>2</sub>, ( $A/F$ )<sub>3</sub>, and ( $A/F$ )<sub>4</sub> for *ortho*-H<sub>2</sub>O, ( $E$ )<sub>3</sub>, ( $E$ )<sub>4</sub>, ( $E$ )<sub>5</sub>, ( $A/F$ )<sub>5</sub>, ( $A/F$ )<sub>6</sub>, ( $A/F$ )<sub>7</sub>, and ( $A/F$ )<sub>8</sub> for *para*-H<sub>2</sub>O; Wang and Carrington predicted eight additional bands<sup>24</sup> (and of course computations can predict more): ( $A/F$ )<sub>1b</sub>, ( $A/F$ )<sub>3X</sub>, ( $A/F$ )<sub>4X</sub>, ( $A/F$ )<sub>5X</sub>, ( $A/F$ )<sub>6X</sub>, ( $A/F$ )<sub>6Y</sub>, ( $A/F$ )<sub>8X</sub>, and ( $A/F$ )<sub>8Y</sub>. Tables VI–XIII show that the two computations are in an excellent agreement. Regarding the theory–experiment comparison, we reiterate the early observation,<sup>25</sup> according to which the discrepancies are larger for the transitions including the *para*-H<sub>2</sub>O than the *ortho*-H<sub>2</sub>O species.

## VII. MICROWAVE SPECTRUM

Similarly to the far-infrared high-resolution spectroscopy experiments, a comparison can be made (Table XIV) with microwave observations by Suenram *et al.*<sup>29</sup> In the microwave spectrum, there were four  $\Sigma$  and six  $\Pi$  bands observed at  $\sim 1$  K rotational temperature in the supersonic expansion. There is an excellent agreement with the experimental and also with the computed transitions by Wang and Carrington.<sup>24</sup>

TABLE XIII. ( $A/F$ )<sub>8</sub> band of CH<sub>4</sub>–H<sub>2</sub>O. See also the caption of Table VI.

$(J, n)' \leftarrow (J, n)$	$\Delta\tilde{\nu}_{\text{obs}}$ (MHz) <sup>28</sup>	$\Delta\tilde{\nu}_{\text{obs}}$	$E'$ (this w)	$E$ (this w)	$\Delta\tilde{\nu}$ (this w)	$\Delta\tilde{\nu}^{24}$	$S_0$ (this w)	$S_0^{24}$
Expt. (Ref. 28): Table X, ( $A/F$ ) <sub>8</sub> , $\Pi \leftarrow \Sigma$ band								
1, 30 $\leftarrow$ 0, 1	927 673.3	30.9439	29.5588	0.0000	29.5588	29.5596	0.374	0.372
1, 31 $\leftarrow$ 1, 1	919 166.0	30.6601	29.5646	0.2891	29.2755	29.2762	0.554	0.551
1, 30 $\leftarrow$ 2, 1	901 595.6	30.0740	29.5588	0.8673	28.6915	28.6918	0.179	0.178
2, 40 $\leftarrow$ 1, 1	936 059.3	31.2236	30.1269	0.2891	29.8377	29.5596	0.569	0.566
2, 41 $\leftarrow$ 2, 1	919 232.4	30.6623	30.1444	0.8673	29.2771	29.2777	0.922	0.918
Predicted in Ref. 24: ( $A/F$ ) <sub>8X</sub> , $\Pi \leftarrow \Sigma$ band								
0, 18 $\leftarrow$ 1, 1	–	–	34.4104	0.2891	34.1213	34.1234	0.048	0.048
1, 50 $\leftarrow$ 0, 1	–	–	34.6785	0.0000	34.6785	34.6811	0.046	0.046
1, 50 $\leftarrow$ 2, 1	–	–	34.6785	0.8673	34.3894	33.8133	0.097	0.096
2, 72 $\leftarrow$ 1, 1	–	–	35.2146	0.2891	34.9254	34.9283	0.091	0.090
Predicted in Ref. 24: ( $A/F$ ) <sub>8Y</sub> , $\Pi \leftarrow \Sigma$ band								
0, 36 $\leftarrow$ 1, 1	–	–	48.6856	0.2891	48.3965	48.4168	0.029	0.029
1, 86 $\leftarrow$ 0, 1	–	–	48.9607	0.0000	48.9607	48.9812	0.027	0.027
1, 86 $\leftarrow$ 2, 1	–	–	48.9607	0.8673	48.0934	48.1134	0.061	0.061
2, 118 $\leftarrow$ 1, 1	–	–	49.5105	0.2891	49.2214	49.2419	0.052	0.052

**TABLE XIV.** Rotation–vibration–tunneling transitions of CH<sub>4</sub>–H<sub>2</sub>O observed in microwave spectroscopy experiments.<sup>29</sup> See also the caption of Table VI.

$(J, n)' \leftarrow (J, n)$	$\Delta\tilde{\nu}_{\text{obs}}$ (MHz) <sup>28</sup>	$\Delta\tilde{\nu}_{\text{obs}}$	$E'$ (this w)	$E$ (this w)	$\Delta\tilde{\nu}$ (this w)	$\Delta\tilde{\nu}^{24}$	$S_0$ (this w)	$S_0^{24}$
$A^+, \Sigma$ band:								
1, 1 $\leftarrow$ 0, 1	8 692.96	0.2900	0.2891	0.0000	0.2891	0.2893	0.040	0.040
2, 1 $\leftarrow$ 1, 1	17 383.05	0.5798	0.8673	0.2891	0.5781	0.5785	0.079	0.079
$F^-, \Sigma$ band:								
1, 12–14 $\leftarrow$ 0, 6–8	8 504.65	0.2837	11.5324	11.2507	0.2817	0.2819	0.029	0.029
2, 12–14 $\leftarrow$ 1, 12–14	17 007.87	0.567	12.0959	11.5324	0.5634	0.5639	0.059	0.059
$F^+, \Sigma$ band:								
1, 2–4 $\leftarrow$ 0, 2–4	8 476.93	0.2828	5.0455	4.7642	0.2814	0.2816	0.055	0.055
2, 2–4 $\leftarrow$ 1, 2–4	16 953.03	0.5655	5.6083	5.0455	0.5628	0.5632	0.109	0.109
$A^-, \Sigma$ band:								
1, 5 $\leftarrow$ 0, 5	8 690.39	0.2899	7.2805	6.9919	0.2886	0.2888	0.024	0.024
2, 5 $\leftarrow$ 1, 5	17 378.14	0.5797	7.8576	7.2805	0.5771	0.5774	0.048	0.048
$E^+, \Pi$ band:								
2, 15–16 $\leftarrow$ 1, 15–16	17 120.06	0.5711	13.6782	13.1087	0.5695	0.5700	0.099	0.099
$E^-, \Pi$ band:								
2, 23–24 $\leftarrow$ 1, 23–24	17 105.28	0.5706	19.9581	19.3909	0.5671	0.5676	0.052	0.052
$F^+, \Pi$ band:								
2, 6–8 $\leftarrow$ 1, 6–8	17 421.68	0.5811	8.4916	7.9119	0.5797	0.5800	0.072	0.071
2, 9–11 $\leftarrow$ 1, 9–11	17 607.72	0.5873	8.5026	7.9158	0.5868	0.5873	0.072	0.071
$F^-, \Pi$ band:								
2, 17–19 $\leftarrow$ 1, 17–19	17 396.81	0.5803	15.1903	14.6124	0.5779	0.5780	0.040	0.040
2, 20–22 $\leftarrow$ 1, 20–22	17 516.82	0.5843	15.1975	14.6152	0.5823	0.5828	0.040	0.040

## VIII. SUMMARY, CONCLUSIONS, AND OUTLOOK

The black-box-type rovibrational method implemented in the GENIUSH program package has been extensively tested with respect to the sophisticated dimer Hamiltonian approach that has been tailored for describing the intermolecular dynamics of floppy dimers by Wang and Carrington.<sup>24</sup>

GENIUSH uses a numerical kinetic energy operator approach, user-defined coordinates and body-fixed frame, and direct product basis and grid. The dimer approach of Wang and Carrington uses an analytic kinetic energy operator (non-direct product) coupled basis functions including Wigner's  $D$  functions, and analytic kinetic energy operator matrix elements.

We show for the example of the rovibrational states and transitions of the methane–water dimer that the performance of the black-box-type approach is on the same order of magnitude as that of the tailor-made approach, the latter being more efficient. In our direct-product approach, it is important to use the cot-DVR developed by Schiffel and Manthe<sup>43</sup> (see also Ref. 44) for the singular “bending”

coordinates. Then, we can converge the energy levels on the order of  $10^{-3} \text{ cm}^{-1}$  with a basis set only twice as large as the non-product dimer basis of Wang and Carrington.<sup>24</sup> (For the full assessment of the computational efficiency, we need to add that their integration grid is larger than ours, but the spectral range of our Hamiltonian is larger resulting in a slower convergence of the Lanczos iteration.) The well-converged data allowed us to notice a small convergence error of  $0.02 \text{ cm}^{-1}$  in the intermolecular stretching fundamental vibration energy of Ref. 24.

To compute rovibrational transitions for  $J = 0, 1$ , and 2 rotational quantum numbers, we use a basis set that is ca. twice as large as the non-product dimer basis of Wang and Carrington, and we evaluate rovibrational transition energies and line strengths. Our transition energies are in an agreement of  $10^{-3} \text{ cm}^{-1}$  often just a few  $10^{-4} \text{ cm}^{-1}$  of the energies reported by Wang and Carrington. These deviations are far beyond the theoretical uncertainty of the current rovibrational theoretical framework based on the non-relativistic and the Born–Oppenheimer approximations.



Further progress that we would be happy to witness in the forthcoming years is related to the computation of extensive line lists for floppy systems. An extensive line list that can be useful for simulating molecular interactions<sup>48</sup> or providing datasets<sup>49</sup> to other disciplines includes rotational excitations up to  $J = 20$  and beyond. If we have to solve the full rovibrational problem (from scratch) for every  $J$ , then a factor of 2–3–5 in the vibrational basis can be an important advantage (of the tailor-made method). A more efficient approach would be, however, if we had a method for finding a good body-fixed frame that allows one to efficiently use the vibrational eigenstates (solutions of the  $J = 0$  problem) in the energy range relevant for the dynamics. It may be the numerical KEO approach (also implemented in GENIUSH) that will finally make it possible to optimize the body-fixed frame even for floppy systems.<sup>32</sup>

## SUPPLEMENTARY MATERIAL

See the [supplementary material](#) for the full list of computed rovibrational energies.

## ACKNOWLEDGMENTS

We thank the financial support of the Swiss National Science Foundation (PROMYS Grant, No. IZ11Z0\_166525). We are grateful to Xiao-Gang Wang and Tucker Carrington for the thorough documentation of their work in Ref. 24 and for paying attention to using exactly the same constant parameters as in Ref. 25 that made it possible for us to extensively test and further develop our methodologies. We also thank them for sharing their cot-DVR implementation<sup>44</sup> during our earlier work<sup>21</sup> that allowed us to test our computations also used in the present work.

## DATA AVAILABILITY

The data that support the findings of this study are available within the article and its [supplementary material](#).

## REFERENCES

- E. Mátyus, G. Czakó, and A. G. Császár, "Toward black-box-type full- and reduced-dimensional variational (ro)vibrational computations," *J. Chem. Phys.* **130**, 134112 (2009).
- R. Meyer and H. H. Günthard, "Internal rotation and vibration in  $\text{CH}_2=\text{CCl}-\text{CH}_2\text{D}$ ," *J. Chem. Phys.* **50**, 353 (1969).
- D. Luckhaus, "6D vibrational quantum dynamics: Generalized coordinate discrete variable representation and (a)diabatic contraction," *J. Chem. Phys.* **113**, 1329 (2000).
- D. Luckhaus, "The vibrational spectrum of HONO: Fully coupled 6D direct dynamics," *J. Chem. Phys.* **118**, 8797 (2003).
- D. Lauvergnat and A. Nauts, "Exact numerical computation of a kinetic energy operator in curvilinear coordinates," *J. Chem. Phys.* **116**, 8560 (2002).
- S. N. Yurchenko, W. Thiel, and P. Jensen, "Theoretical rovibrational energies (TROVE): A robust numerical approach to the calculation of rovibrational energies for polyatomic molecules," *J. Mol. Spectrosc.* **245**, 126 (2007).
- G. Brocks, A. van der Avoird, B. T. Sutcliffe, and J. Tennyson, "Quantum dynamics of non-rigid systems comprising two polyatomic fragments," *Mol. Phys.* **50**, 1025 (1983).
- Z. Bacic and J. C. Light, "Theoretical methods for rovibrational states of floppy molecules," *Annu. Rev. Phys. Chem.* **40**, 469 (1989).
- B. T. Sutcliffe and J. Tennyson, "A general treatment of vibration-rotation coordinates for triatomic molecules," *Int. J. Quantum Chem.* **39**, 183 (1991).
- M. J. Bramley and T. Carrington, Jr., "A general discrete variable method to calculate vibrational energy levels of three- and four-atom molecules," *J. Chem. Phys.* **99**, 8519 (1994).
- C. Leforestier, "Grid method for the Wigner functions. Application to the van der Waals system  $\text{Ar}-\text{H}_2\text{O}$ ," *J. Chem. Phys.* **101**, 7357 (1994).
- S. C. Althorpe and D. C. Clary, "Calculation of the intermolecular bound states for water dimer," *J. Chem. Phys.* **101**, 3603 (1994).
- D. H. Zhang, Q. Wu, J. Z. H. Zhang, M. von Dirke, and Z. Bačić, "Exact full-dimensional bound state calculations for  $(\text{HF})_2$ ,  $(\text{DF})_2$ , and  $\text{HFDF}$ ," *J. Chem. Phys.* **102**, 2315 (1995).
- M. Mladenović, "Discrete variable approaches to tetratomic molecules: Part I: DVR(6) and DVR(3) + DGB methods," *Spectrochim. Acta* **58**, 795 (2002).
- X.-G. Wang and T. Carrington, Jr., "Contracted basis Lanczos methods for computing numerically exact rovibrational levels of methane," *J. Chem. Phys.* **121**, 2937 (2004).
- J. K. G. Watson, "Simplification of the molecular vibration-rotation Hamiltonian," *Mol. Phys.* **15**, 479 (1968).
- R. J. Whitehead and N. C. Handy, "Variational calculation of vibration-rotation energy levels for triatomic molecules," *J. Mol. Spectrosc.* **55**, 356 (1975).
- J. M. Bowman, S. Carter, and X. Huang, "Multimode: A code to calculate rovibrational energies of polyatomic molecules," *Int. Rev. Phys. Chem.* **22**, 533 (2003).
- G. Avila and T. Carrington, Jr., "Nonproduct quadrature grids for solving the vibrational Schrödinger equation," *J. Chem. Phys.* **131**, 174103 (2009).
- G. Avila and T. Carrington, Jr., "Using nonproduct quadrature grids to solve the vibrational Schrödinger equation in 12D," *J. Chem. Phys.* **134**, 054126 (2011).
- G. Avila and E. Mátyus, "Toward breaking the curse of dimensionality in (ro)vibrational computations of molecular systems with multiple large-amplitude motions," *J. Chem. Phys.* **150**, 174107 (2019).
- G. Avila and E. Mátyus, "Full-dimensional (12D) variational vibrational states of  $\text{CH}_4\text{-F}^-$ : Interplay of anharmonicity and tunneling," *J. Chem. Phys.* **151**, 154301 (2019).
- G. Avila, D. Papp, G. Czakó, and E. Mátyus, "Exact quantum dynamics background of dispersion interactions: Case study for  $\text{CH}_4\text{-Ar}$  in full (12) dimensions," *Phys. Chem. Chem. Phys.* **22**, 2792 (2020).
- X.-G. Wang and T. Carrington, Jr., "Using nondirect product Wigner  $D$  basis functions and the symmetry adapted Lanczos algorithm to compute the ro-vibrational spectrum of  $\text{CH}_4\text{-H}_2\text{O}$ ," *J. Chem. Phys.* **154**, 124112 (2021).
- J. Sarka, A. G. Császár, S. C. Althorpe, D. J. Wales, and E. Mátyus, "Rovibrational transitions of the methane-water dimer from intermolecular quantum dynamical computations," *Phys. Chem. Chem. Phys.* **18**, 22816 (2016).
- J. Sarka, A. G. Császár, and E. Mátyus, "Rovibrational quantum dynamical computations for deuterated isotopologues of the methane-water dimer," *Phys. Chem. Chem. Phys.* **19**, 15335 (2017).
- M. P. Metz, K. Szalewicz, J. Sarka, R. Tóbiás, A. G. Császár, and E. Mátyus, "Molecular dimers of methane clathrates: *Ab initio* potential energy surfaces and variational vibrational states," *Phys. Chem. Chem. Phys.* **21**, 13504 (2019).
- L. Dore, R. C. Cohen, C. A. Schmuttenmaer, K. L. Busarow, M. J. Elrod, J. G. Loeser, and R. J. Saykally, "Far infrared vibration-rotation-tunneling spectroscopy and internal dynamics of methane-water: A prototypical hydrophobic system," *J. Chem. Phys.* **100**, 863 (1994).
- R. D. Suenram, G. T. Fraser, F. J. Lovas, and Y. Kawashima, "The microwave spectrum of  $\text{CH}_4\text{-H}_2\text{O}$ ," *J. Chem. Phys.* **101**, 7230 (1994).
- C. Fábri, M. Quack, and A. G. Császár, "On the use of nonrigid-molecular symmetry in nuclear motion computations employing a discrete variable representation: A case study of the bending energy levels of  $\text{CH}_5^+$ ," *J. Chem. Phys.* **147**, 134101 (2017).
- E. Mátyus, C. Fábri, T. Szidarovszky, G. Czakó, W. D. Allen, and A. G. Császár, "Assigning quantum labels to variationally computed rotational-vibrational eigenstates of polyatomic molecules," *J. Chem. Phys.* **133**, 034113 (2010).
- G. Avila, A. Martín Santa Daría, and E. Mátyus, "Optimization of the body-fixed frame to minimize rovibrational coupling" (unpublished) (2021).
- O. Akin-Ojo and K. Szalewicz, "Potential energy surface and second virial coefficient of methane-water from *ab initio* calculations," *J. Chem. Phys.* **123**, 134311 (2005).

- <sup>34</sup>C. Fábri, E. Mátyus, and A. G. Császár, “Rotating full- and reduced-dimensional quantum chemical models of molecules,” *J. Chem. Phys.* **134**, 074105 (2011).
- <sup>35</sup>C. Fábri, A. G. Császár, and G. Czakó, “Reduced-dimensional quantum computations for the rotational–vibrational dynamics of  $F^-CH_4$  and  $F^-CH_2D_2$ ,” *J. Phys. Chem. A* **117**, 6975 (2013).
- <sup>36</sup>C. Fábri, E. Mátyus, and A. G. Császár, *Spectrochim. Acta* **119**, 84 (2014).
- <sup>37</sup>D. Papp, J. Sarka, T. Szidarovszky, A. G. Császár, E. Mátyus, M. Hochlaf, and T. Stoecklin, “Complex rovibrational dynamics of the Ar-NO<sup>+</sup> complex,” *Phys. Chem. Chem. Phys.* **19**, 8152 (2017).
- <sup>38</sup>J. Sarka and A. G. Császár, “Interpretation of the vibrational energy level structure of the astructural molecular ion  $H_5^+$  and all of its deuterated isotopomers,” *J. Chem. Phys.* **144**, 154309 (2016).
- <sup>39</sup>D. Ferenc and E. Mátyus, “Bound and unbound rovibrational states of the methane–argon dimer,” *Mol. Phys.* **117**, 1694 (2019).
- <sup>40</sup>A. Martín Santa Daría, G. Avila, and E. Mátyus, “Fingerprint region of the formic acid dimer: Variational vibrational computations in curvilinear coordinates,” *Phys. Chem. Chem. Phys.* **23**, 6526 (2021).
- <sup>41</sup>R. Meyer, “Flexible models for intramolecular motion, a versatile treatment and its application to glyoxal,” *J. Mol. Spectrosc.* **76**, 266 (1979).
- <sup>42</sup>J. C. Light and T. Carrington, Jr., “Discrete variable representations and their utilization,” *Adv. Chem. Phys.* **114**, 263 (2000).
- <sup>43</sup>G. Schiffel and U. Manthe, “On direct product based discrete variable representations for angular coordinates and the treatment of singular terms in the kinetic energy operator,” *Chem. Phys.* **374**, 118 (2010).
- <sup>44</sup>X.-G. Wang and T. Carrington, Jr., “ $K$ -independent vibrational bases for systems with large amplitude motion,” *Mol. Phys.* **110**, 825 (2012).
- <sup>45</sup>Wolfram Research Inc., Mathematica, version 12.1, Champaign, IL, 2020.
- <sup>46</sup>H. Wei and T. Carrington, Jr., “The discrete variable representation of a triatomic Hamiltonian in bond length–bond angle coordinates,” *J. Chem. Phys.* **97**, 3029 (1992).
- <sup>47</sup>S. N. Yurchenko, R. J. Barber, A. Yachmenev, W. Thiel, P. Jensen, and J. Tennyson, “A variationally computed  $T = 300$  K line list for  $NH_3$ ,” *J. Phys. Chem. A* **113**, 11845 (2009).
- <sup>48</sup>A. Owens and A. Yachmenev, “RichMol: A general variational approach for rovibrational molecular dynamics in external electric fields,” *J. Chem. Phys.* **148**, 124102 (2018).
- <sup>49</sup>J. Tennyson, S. N. Yurchenko, A. F. Al-Refaie, E. J. Barton, K. L. Chubb, P. A. Coles, S. Diamantopoulou, M. N. Gorman, C. Hill, A. Z. Lam, L. Lodi, L. K. McKemmish, Y. Na, A. Owens, O. L. Polyansky, T. Rivlin, C. Sousa-Silva, D. S. Underwood, A. Yachmenev, and E. Zak, “The ExoMol database: Molecular line lists for exoplanet and other hot atmospheres,” *J. Mol. Spectrosc.* **327**, 73 (2016), part of Special Issue: New visions of spectroscopic databases, volume II.

## PAPER



Cite this: *Phys. Chem. Chem. Phys.*,  
2020, 22, 2792

# Exact quantum dynamics background of dispersion interactions: case study for CH<sub>4</sub>·Ar in full (12) dimensions†

Gustavo Avila, \*<sup>a</sup> Dóra Papp, \*<sup>b</sup> Gábor Czakó \*<sup>b</sup> and Edit Mátyus \*<sup>a</sup>

A full-dimensional *ab initio* potential energy surface of spectroscopic quality is developed for the van-der-Waals complex of a methane molecule and an argon atom. Variational vibrational states are computed on this surface including all twelve (12) vibrational degrees of freedom of the methane–argon complex using the GENIUSH computer program and the Smolyak sparse grid method. The full-dimensional computations make it possible to study the fine details of the interaction and distortion effects and to make a direct assessment of the reduced-dimensionality models often used in the quantum dynamics study of weakly-bound complexes. A 12-dimensional (12D) vibrational computation including only a single harmonic oscillator basis function (9D) to describe the methane fragment (for which we use the ground-state effective structure as the reference structure) has a 0.40 cm<sup>-1</sup> root-mean-square error (rms) with respect to the converged 12D bound-state excitation energies, which is less than half of the rms of the 3D model set up with the  $\langle r \rangle_0$  methane structure. Allowing 10 basis functions for the methane fragment in a 12D computation performs much better than the 3D models by reducing the rms of the bound state vibrational energies to 0.07 cm<sup>-1</sup>. The full-dimensional potential energy surface correctly describes the dissociation of the system, which together with further development of the variational (ro)vibrational methodology opens a route to the study of the role of dispersion forces in the excited methane vibrations and the energy transfer from the intra- to the intermolecular vibrational modes.

Received 9th August 2019,  
Accepted 20th December 2019

DOI: 10.1039/c9cp04426d

rsc.li/pccp

## I. Introduction

Molecular interactions play an important role in chemistry, biology, and materials science. Through the many-body construction idea<sup>1</sup> of the potential energy surface (PES) of bulk-phase systems the study of molecular interactions is translated to the study of molecular dimers, trimers, and perhaps larger (but still small) clusters.<sup>2–10</sup> Small molecular clusters can be studied in great detail and precision by high-resolution spectroscopic and quantum chemistry and quantum dynamics techniques. A good, ‘first’ description of the quantum dynamical features of

molecular complexes is provided by the rigid-monomer approximation,<sup>11–14</sup> which allows considerable savings both on the PES development and on the quantum dynamics side. To account for monomer-flexibility effects through the PES representation, the application of effective potential energy cuts (for each monomer vibrational state) provides an improved representation over the rigid-monomer approach while retaining the small number of active vibrational degrees of freedom.<sup>15</sup>

At the same time, monomer flexibility ‘effects’ are, of course, non-negligible,<sup>16,17</sup> especially for (a) strongly interacting fragments (with strong monomer distortions);<sup>18–20</sup> (b) higher vibrational excitations; (c) monomer vibrational excitations that may correspond to predissociative states of the complex;<sup>21,22</sup> or (d) for symmetry reasons (*i.e.*, degenerate monomer excitations may show a non-trivial coupling with the intermolecular modes). A full account of monomer flexibility in complexes of polyatomic molecules represents a considerable challenge for the current (ro)vibrational methodologies due to the large number of vibrational degrees of freedom and the typically multi-well character of the potential energy landscape.

A generally applicable, ‘black-box-type’ description of molecular systems with multiple-large amplitude motions is truly challenging, due to (a) the high-dimensionality of the problem,

<sup>a</sup> Institute of Chemistry, ELTE, Eötvös Loránd University, Pázmány Péter sétány 1/A, 1117 Budapest, Hungary. E-mail: Gustavo\_Avila@telefonica.net, matyuse@caesar.elte.hu

<sup>b</sup> MTA-SZTE Lendület Computational Reaction Dynamics Research Group, Interdisciplinary Excellence Centre and Department of Physical Chemistry and Materials Science, Institute of Chemistry, University of Szeged, Rerrich Béla tér 1, Szeged H-6720, Hungary. E-mail: dorapapp@chem.u-szeged.hu, gczako@chem.u-szeged.hu

† Electronic supplementary information (ESI) available: Coefficients of the FullD-2019 PES and normal coordinate coefficients used for the vibrational computations. *Ab initio* energies (in E<sub>h</sub>) and Cartesian structures (in Å) computed and used for the fitting of the PES. See DOI: 10.1039/c9cp04426d

(b) singularities in the kinetic energy operator in the dynamically important region of the coordinate space, (c) a common lack of good zeroth-order models, (d) large basis sets and integration grids being necessary to converge the results, and thus (e) the necessity to attenuate the curse of dimensionality. For semi-rigid molecules there have been efficient methods developed in the past<sup>23</sup> and further major progress has been achieved over the last decade.<sup>24–32</sup> If there is only a single large-amplitude degree of freedom in the system, the reaction-path-Hamiltonian<sup>33</sup> and similar approaches have been successfully used together with semi-rigid techniques.<sup>34,35</sup> There exist efficient, tailor-made approaches developed for particular systems, *e.g.*, for molecular complexes.<sup>4,36</sup> But a general and efficient solution method for systems with multiple large-amplitude motions remains an open problem. For this reason molecular systems with multiple-large amplitude motions represent a current frontier of research in quantum dynamics. The present work contributes to this direction. The family of molecular complexes offers a wide selection of systems with a varying number of large- and small amplitude motions, varying coupling strengths, singularity patterns, *etc.*, and in this way, their study drives methodological development.

In the present work we focus on the floppy, van-der-Waals complex of a methane molecule and an argon atom (with twelve vibrational degrees of freedom), ultimately aiming to reach the predissociative states which belong to the vibrational excitation of the methane fragment, within a full-dimensional vibrational treatment. Due to the weak interactions governing the internal dynamics of the CH<sub>4</sub>-Ar complex, powerful approximations have been introduced in reduced-dimensionality computations, including some methane vibrations, to interpret the high-resolution predissociative spectrum of the complex.<sup>11,37–39</sup> In spite of this earlier experimental and quantum dynamics work (accounting for some methane flexibility) there is not any full-dimensional (12D) potential energy surface available for this system. Hence, the first part of this article is about the development of an *ab initio*, near-spectroscopic quality, full-dimensional PES for CH<sub>4</sub>-Ar. The second part reports the first application of this PES in vibrational computations including all 12 vibrational degrees of freedom using the GENIUSH-Smolyak procedure developed by two of us in ref. 40. Note that in ref. 40, a (3D + 9D) PES was used (only including kinetic couplings in the Hamiltonian) in order to be able to test the developed vibrational methodology. In addition to the development and the first applications of a full-dimensional PES for CH<sub>4</sub>-Ar, we also take the opportunity to test the rigid-monomer (here 3D) approximation(s), widely used in the study of molecular complexes, with respect to the full-dimensional results.

## II. PES development

### A. Computational details

**1. Benchmark dissociation energies.** The geometries of the global (GM) and secondary minima (SM) of the CH<sub>4</sub>-Ar complex are optimized using the explicitly-correlated coupled cluster

singles, doubles, and perturbative triples electronic structure method, CCSD(T)-F12b,<sup>41</sup> with the aug-cc-pVQZ correlation-consistent basis set,<sup>42</sup> followed by harmonic frequency computations at the same level of theory. The resulting equilibrium structures have C<sub>3v</sub> point-group symmetry forming three (GM) and one (SM) ‘H-bond(s)’—or, more precisely, ‘H contacts’, which modulate the dispersion interaction between Ar and CH<sub>4</sub>. To obtain benchmark dissociation energies (*D<sub>e</sub>*) for the GM and SM complexes single-point energy computations are performed at the CCSD(T)-F12b/aug-cc-pVQZ geometries: CCSD(T)-F12b/aug-cc-pV5Z, CCSD(T)<sup>43</sup> and CCSDT(Q)<sup>44</sup> with the aug-cc-pVDZ basis set to obtain post-(T) contributions, and both all-electron (AE) and frozen-core (FC) CCSD(T)-F12b/cc-pCVQZ-F12<sup>45</sup> to determine core-correlation corrections. The FC approach correlates the valence electrons only, whereas in the AE computations the following electrons are also correlated: 1s<sup>2</sup> for C and 2s<sup>2</sup>2p<sup>6</sup> for Ar. All the *ab initio* computations are carried out with the Molpro program package,<sup>46</sup> except the CCSD(T) and CCSDT(Q) computations, which are performed using the MRCC program<sup>47</sup> interfaced to Molpro. The final benchmark *D<sub>e</sub>* values are obtained as

$$D_e(\text{CCSD(T)-F12b/aug-cc-pV5Z}) + \delta[\text{CCSDT(Q)}] + \Delta_{\text{core}}, \quad (1)$$

where

$$\begin{aligned} \delta[\text{CCSDT(Q)}] = & D_e(\text{CCSDT(Q)/aug-cc-pVDZ}) \\ & - D_e(\text{CCSD(T)/aug-cc-pVDZ}) \end{aligned} \quad (2)$$

and

$$\begin{aligned} \Delta_{\text{core}} = & D_e(\text{AE-CCSD(T)-F12b/cc-pCVQZ-F12}) \\ & - D_e(\text{FC-CCSD(T)-F12b/cc-pCVQZ-F12}). \end{aligned} \quad (3)$$

**2. Full-dimensional PES development.** A full-dimensional analytic *ab initio* PES, named FullD-2019 PES, is developed based on 15 995 energy points computed at the CCSD(T)-F12b/aug-cc-pVTZ level of theory at geometries covering the configuration space relevant for the interaction between methane and argon. Note that previous test computations by one of us showed that the standard augmented and F12 correlation-consistent basis sets provide similar accuracy for PES development.<sup>48</sup> The geometries used for the PES development are generated by isotropically positioning the Ar atom around the methane unit while atoms of the equilibrium CCSD(T)-F12b/aug-cc-pVTZ methane structure are also randomly displaced. The C–Ar distance is varied between 4 and 20 bohr, and the atoms of methane are displaced in Cartesian coordinates within an interval of [0, 0.95] bohr. The PES is represented by a polynomial expansion in Morse-like variables of the *r<sub>i,j</sub>* internuclear distances, *y<sub>i,j</sub>* = exp(−*r<sub>i,j</sub>*/*a*) with *a* = 2.0 bohr, and using a compact polynomial basis that is explicitly invariant under permutation of like atoms.<sup>49,50</sup> The highest total polynomial order applied is 7. The total number of fitting coefficients is 9355. A weighted least-squares fit is performed on the energy points, where a certain energy *E* relative to the global minimum has a weight of (*E<sub>0</sub>*/(*E<sub>0</sub>* + *E*)) × (*E<sub>1</sub>*/(*E<sub>1</sub>* + *E*)) with *E<sub>0</sub>* = 0.05 hartree and *E<sub>1</sub>* = 0.5 hartree.

dc\_1955\_21

**Table 1** Benchmark dissociation energies ( $D_e$ ) in  $\text{cm}^{-1}$  corresponding to the global (GM) and secondary minimum (SM) structures of the  $\text{CH}_4\text{-Ar}$  complex obtained from eqn (1) at CCSD(T)-F12b/aug-cc-pVQZ geometries compared to those obtained on the FullD-2019 PES developed in this study

	AVTZ <sup>a</sup>	AVQZ <sup>b</sup>	$\Delta_{5Z}$ <sup>c</sup>	$\Delta_{\text{core}}$ <sup>d</sup>	$\Delta[\text{CCSDT}(\text{Q})]$ <sup>e</sup>	Final <sup>f</sup>	PES <sup>g</sup>
GM	154.38	149.06	+0.47	+1.40	+1.90	152.83	153.13
SM	103.46	96.79	-0.52	+1.22	+2.03	99.52	102.16

<sup>a</sup>  $D_e(\text{CCSD}(\text{T})\text{-F12b/aug-cc-pVTZ})$ , <sup>b</sup>  $D_e(\text{CCSD}(\text{T})\text{-F12b/aug-cc-pVQZ})$ , <sup>c</sup>  $D_e(\text{CCSD}(\text{T})\text{-F12b/aug-cc-pV5Z}) - D_e(\text{CCSD}(\text{T})\text{-F12b/aug-cc-pVQZ})$ , <sup>d</sup>  $D_e(\text{AE-CCSD}(\text{T})\text{-F12b/cc-pCVQZ-F12}) - D_e(\text{FC-CCSD}(\text{T})\text{-F12b/cc-pCVQZ-F12})$ , <sup>e</sup>  $D_e(\text{CCSDT}(\text{Q})/\text{aug-cc-pVDZ}) - D_e(\text{CCSD}(\text{T})/\text{aug-cc-pVDZ})$ , <sup>f</sup>  $D_e(\text{CCSD}(\text{T})\text{-F12b/aug-cc-pV5Z}) + \Delta_{\text{core}} + \delta[\text{CCSDT}(\text{Q})]$ , <sup>g</sup> Energy on the PES when the Ar atom was 57 bohr from the equilibrium structure of methane (the interaction energy is less than  $0.001 \text{ cm}^{-1}$ ) relative to the corresponding minimum energy of the PES.

## B. Results and discussion

**1. Benchmark dissociation energies.** In Table 1, we present the benchmark dissociation energies corresponding to the global and secondary minimum geometries of the  $\text{CH}_4\text{-Ar}$  complex and compare them to the dissociation energies determined on the newly developed analytic FullD-2019 PES. The correction terms listed in Table 1 allow for estimating the accuracy of the benchmark dissociation energies. The extremely fast basis set convergence of the explicitly-correlated CCSD(T)-F12b method, which is manifested in the  $\Delta_{5Z}$  corrections of only  $0.5 \text{ cm}^{-1}$ , ensures that the CCSD(T)-F12b/aug-cc-pV5Z energy is basis-set-converged within about  $0.1\text{--}0.2 \text{ cm}^{-1}$ . The correlation of core electrons increases the dissociation energies by around  $1.5 \text{ cm}^{-1}$ , and has an estimated uncertainty of  $1 \text{ cm}^{-1}$ . The  $\delta[\text{CCSDT}(\text{Q})]$

correlation contributions are also positive values of around  $2 \text{ cm}^{-1}$  with a similar estimated uncertainty of  $1 \text{ cm}^{-1}$ . (The uncertainty estimates consider basis set effects and post-(Q) contributions.) Relativistic effects, not taken into account in this work, are supposed to have a smaller contribution than core correlation. Taken together, the uncertainty of the final benchmark dissociation energies is estimated to be  $\pm 2 \text{ cm}^{-1}$ . The benchmark  $D_e$  values, as shown in Table 1, are well reproduced on the new PES with  $0.3 \text{ cm}^{-1}$  and  $2.6 \text{ cm}^{-1}$  differences in the case of the global and the secondary minima, respectively. In the case of the global minimum the above agreement is even better than expected due to cancellation of errors as it can be seen from the data of Table 1.

**2. Accuracy of the analytic PES.** The newly developed full-dimensional analytic PES of the  $\text{CH}_4\text{-Ar}$  complex, FullD-2019 PES, features extremely low root mean square (rms) fitting deviations, listed in Table 2, with the rms values being lower than  $1 \text{ cm}^{-1}$  up to  $55\,000 \text{ cm}^{-1}$  relative to the global minimum of the PES. In accord with these low rms values the one-dimensional energy curves obtained on the PES during the separation of the Ar atom from methane along the  $C_3$  axes of the global and secondary minimum geometries, see Fig. 1, show excellent agreement with the *ab initio* energies. As also seen in Fig. 1, the asymptotic behavior of the weakly-bound  $\text{CH}_4\text{-Ar}$  system is also well described by the PES. The asymptotic limits are reached at around 15 bohr from both minima. It is worth emphasizing that the fitted PES reproduces the long-range asymptotic behavior of the high-level *ab initio* data without using any switching function based on the traditional  $1/R^6$  dispersion model. Fig. 2 shows that the structural parameters obtained at the minima of the PES agree well with the benchmark CCSD(T)-F12b/aug-cc-pVQZ values. The C–Ar distances are reproduced on the FullD-2019 PES with a difference of 0.003 bohr and 0.029 bohr for the global and the secondary minima, respectively, whereas the C–H bond lengths and the H–C–H angles are practically the same as in the benchmark geometry. Note that the geometry of  $\text{CH}_4$  is just slightly perturbed in the minima relative to the free  $\text{CH}_4$  structure; the deformation energy at the global minimum is only  $0.05 \text{ cm}^{-1}$ . The outstanding accuracy of the FullD-2019 PES is

**Table 2** Number of points and root mean square (rms) deviations of the fitting in the chemically interesting energy ranges of the FullD-2019 PES relative to its global minimum

$E_{\text{rel}}$ range/ $\text{cm}^{-1}$	Number of points	rms/ $\text{cm}^{-1}$
0–11 000	11 727	0.66
11 000–22 000	1073	0.90
22 000–55 000	1582	0.95

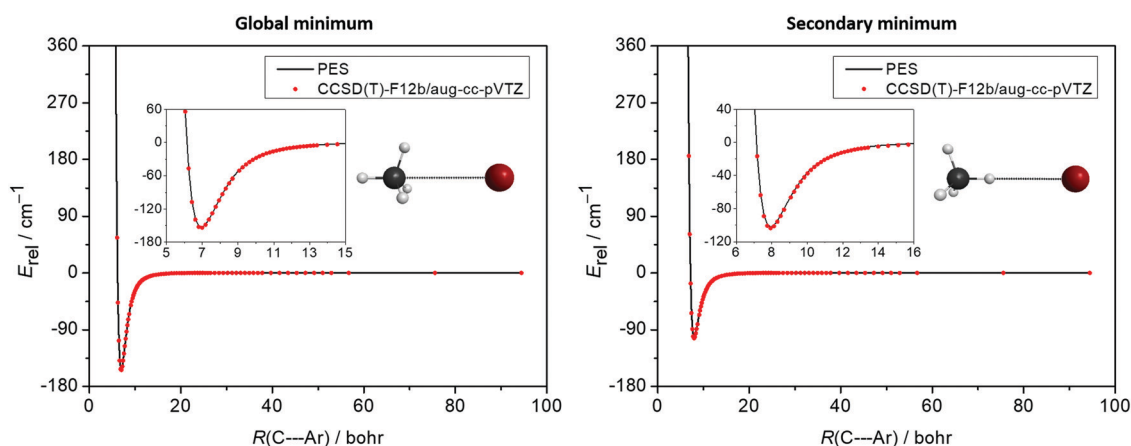


**Fig. 1** Potential energy curves along the  $C_3$  axes of the global (left panel) and secondary (right panel) minimum structures scanning the C–Ar distance of the  $\text{CH}_4\text{-Ar}$  complex (the  $\text{CH}_4$  unit is fixed at its CCSD(T)-F12b/aug-cc-pVTZ equilibrium geometry), and showing a comparison between the direct *ab initio* values and cuts of the FullD-2019 PES. The insets show the potential well regions and the corresponding equilibrium geometries.

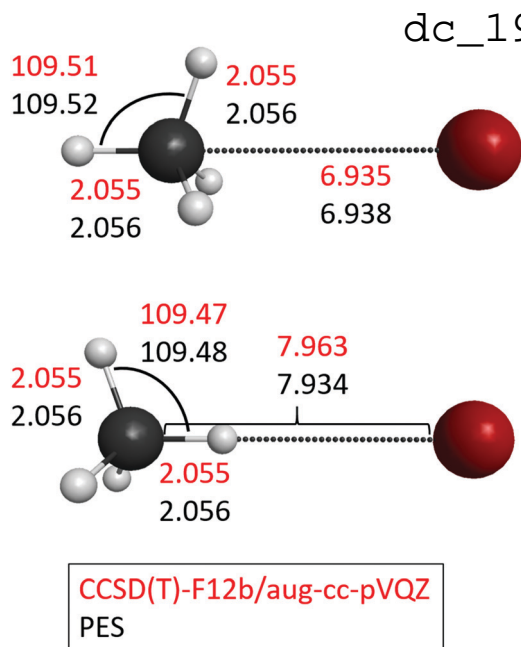


Fig. 2 Geometric parameters of the global (top) and the secondary (bottom) minimum structures of the  $\text{CH}_4\text{-Ar}$  complex obtained at the CCSD(T)-F12b/aug-cc-pVQZ level of theory (red) and on the FullD-2019 PES (black). Bond lengths are given in bohr and bond angles are given in degrees.

also strengthened by the dissociation energies corresponding to the global and secondary minima, reproducing the benchmark values within  $3\text{ cm}^{-1}$  (Table 1). The C–H separation is also scanned on the PES and, as Fig. 3 shows, the FullD-2019 PES describes the C–H stretching motion well up to  $30\,000\text{ cm}^{-1}$  relative to the global minimum. Furthermore, the potential scans (Fig. 1 and 3) show that the PES function is smooth without any artificial oscillations, proving that the large number of fitting parameters does not cause any overfitting problem.

### C. Asymptotic behavior of the PES and comparison with limiting models

The FullD-2019 PES was fitted to *ab initio* points using a permutationally invariant polynomial expansion of Morse variables,

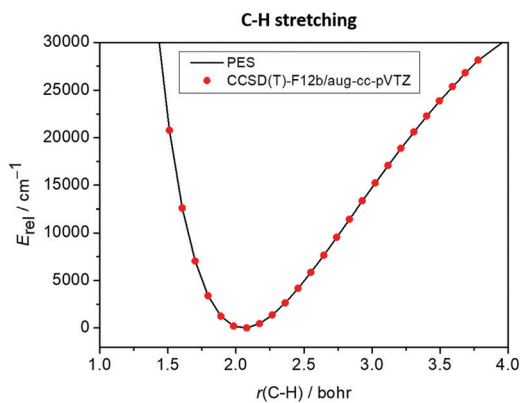


Fig. 3 Potential energy curve along one C–H bond of the CCSD(T)-F12b/aug-cc-pVTZ global minimum geometry while the collinear H atom is separated comparing the direct *ab initio* values and the FullD-2019 PES.

$y_{i,j} = \exp(-r_{i,j}/a)$  (with  $a = 2$  bohr), which are exponential functions of distances for all atom–atom pairs.<sup>49</sup> In the present work, we have included in the fit polynomials of  $y_{i,j}$  up to degree 7. The advantage of using Morse variables over regular distances is that they ensure non-divergent dissociation asymptotes for large  $r_{i,j}$  values. At the same time, one might ask whether the exponentially fast decay of the Morse coordinates allows us to have a correct description of the intermediate range energetics, which, for the present system, is dominated by London dispersion forces, commonly described by a potential energy model, which has not an exponential but a  $1/R^6$ -type limiting behavior.

The low rms values (Table 2) indicate that the fitting function used for the FullD-2019 PES had sufficient flexibility to reproduce excellently the *ab initio* energies, which, of course, automatically capture all ‘interaction effects’. To gain more insight into the short, intermediate, and long-range behavior of the system along the dissociation coordinate, we compare 1D cuts in Fig. 4: the FullD-2019 PES, the Morse potential energy curve, and the best fit of the  $-\sigma/R^6$  model (with  $\sigma$  as a constant, fitted parameter) over the  $R \in [7.5, 15.5]$  bohr intermediate range.

The Morse potential,  $c_0 y_R^0 + c_1 y_R^1 + c_2 y_R^2$ , is a second-order polynomial of the  $y_R$  Morse variable (defined between the carbon and the argon atoms), and it reproduces excellently the PES valley but it decays too fast to the asymptotic limit (Fig. 4). To reproduce well the asymptotic fall, it is necessary to use a higher than second-order polynomial of the Morse variable, and we found that a polynomial including monomials up to the 7th-order, *i.e.*, up to  $y_R^7$ , in the fitting function of the FullD-2019 PES provides an appropriate and automated way to have an excellent overall (short-, intermediate-, and long-range) description of the system.

It is worth pointing out that the difference in the intermediate-range behavior of the Morse (a too fast fall) and

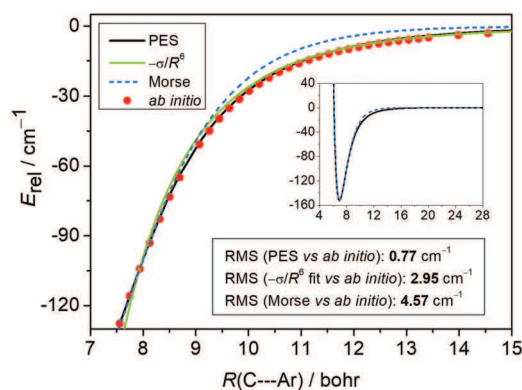


Fig. 4 Long-range interactions: potential energy representations of  $\text{CH}_4\text{-Ar}$  along the dissociation coordinate showing the 1D cut of the FullD-2019 PES;  $-\sigma/R^6$  fit ( $\sigma = 2.59741 \times 10^7\text{ bohr}^6\text{ cm}^{-1}$ ) to the *ab initio* points in the  $[7.5, 15.5]$  bohr range; Morse fit ( $153.928\text{ cm}^{-1}\{1 - \exp[-0.85(R/\text{bohr} - 6.95)]\}^2 - 153.928\text{ cm}^{-1}$ ); and the CCSD(T)-F12b/aug-cc-pVTZ *ab initio* data. The RMS values correspond to the data in the  $[7.5, 15.5]$  bohr interval. The RMS values of the FullD-2019 PES are  $0.53$  and  $0.07\text{ cm}^{-1}$  in the  $[7.5, 95]$  and  $[20, 95]$  bohr range, respectively, whereas the corresponding RMS deviations for the  $-\sigma/R^6$  fits are  $1.96$  and  $0.004\text{ cm}^{-1}$ .

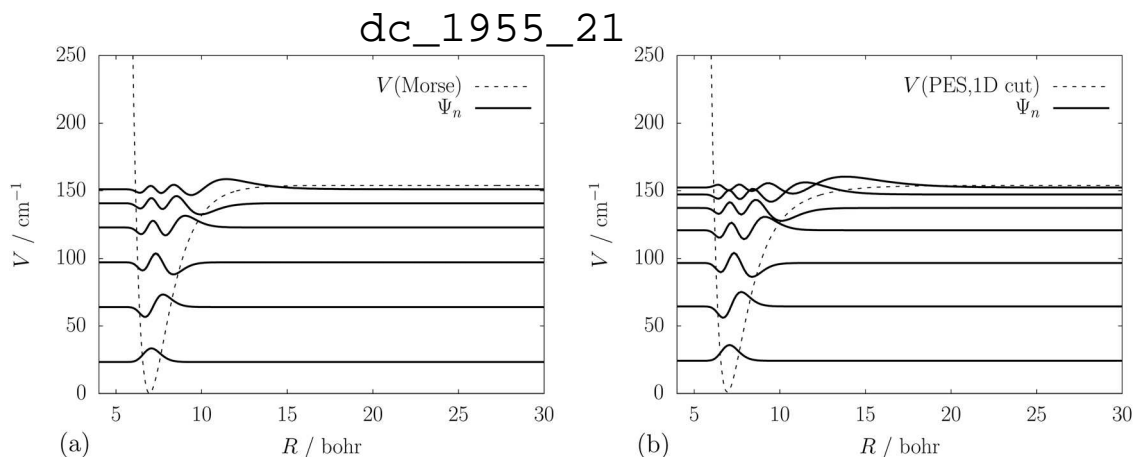


Fig. 5 Vibrational states along the dissociation coordinate (1D model) using (a) the Morse fit, and (b) the 1D cut of the FullID-2019 PES of Fig. 4.

the PES fit (a fall similar to the  $1/R^6$  dispersion model) is manifested also in the vibrational structure (Fig. 5). The FullID-2019 PES supports an additional bound vibrational state and the highest energy wave function has a significant amplitude over a much broader range than the highest energy wave function corresponding to the Morse fit. The significant contribution of higher-order polynomials to the PES representation in the long-range asymptotics is observed also in relation to using Morse tridiagonal basis functions (Section IIIB) to solve the vibrational problem: while the low-energy vibrational states can be converged with a small basis set, the highest-energy bound state requires an excessive number of such functions, indicating that there is an important deviation from the too rapidly decaying Morse character.

### III. Variational vibrational states

Using the newly developed FullID-2019 PES, the bound vibrational states of the methane–argon complex have been computed using the GENIUSH–Smolyak approach.<sup>40</sup> This extension of the GENIUSH program<sup>51,52</sup> makes it possible to discard basis functions as well as points from the direct product basis and grid, using the Smolyak method,<sup>24,25</sup> thereby attenuating the exponential growth of the computational cost with the vibrational dimensionality. This development makes it possible to solve high-dimensional vibrational problems, for which or for, at least, parts of which a good zeroth-order representation can be constructed.

In the case of the  $\text{CH}_4\cdot\text{Ar}$  complex, a good zeroth-order approximation is obtained for the methane fragment by using normal coordinates ( $q_1, q_2, \dots, q_9$ ) and harmonic oscillator basis functions. The relative motion of the fragments is described by spherical polar coordinates, ( $R, \cos\theta, \phi$ ) similarly to ref. 40.

The GENIUSH program requires the definition of the internal coordinates (and the body-fixed, BF, frame) by specifying the Cartesian coordinates in the BF frame with respect to the internal coordinates. The program uses this information to construct the kinetic energy operator (KEO) terms in an

automated fashion.<sup>51</sup> The usual Cartesian coordinate expression of the (generalized) normal coordinates,  $q_j \in (-\infty, \infty)$ , is

$$r_{i\alpha} = c_{i\alpha}^{\text{ref}} + \sum_{j=1}^9 l_{i\alpha,j} q_j, \quad (4)$$

with  $i = 1(\text{H}), 2(\text{H}), 3(\text{H}), 4(\text{H}), 5(\text{C})$  and  $\alpha = 1(\text{x}), 2(\text{y}), 3(\text{z})$ . The  $l_{i\alpha,j}$  linear combination coefficients and the  $c_{i\alpha}^{\text{ref}}$  reference structure can be chosen by convenience (as a special case, they can be obtained from the harmonic analysis of the PES at the equilibrium structure). In the present work, we chose  $c_{i\alpha}^{\text{ref}}$  to reproduce not the equilibrium structure (which could be one of the minima of  $\text{CH}_4\cdot\text{Ar}$  or the isolated  $\text{CH}_4$  minimum), but to reproduce the tetrahedral methane structure for which the C–H distance corresponds to the effective structure of the methane zero-point vibration with  $\rho := r_{\text{eff}} = 2.067337961$  bohr,<sup>40</sup>

$$\begin{aligned} (\mathbf{c}_1^{\text{ref}})^{\text{T}} &= \frac{\rho}{\sqrt{3}}(1, 1, 1) \\ (\mathbf{c}_2^{\text{ref}})^{\text{T}} &= \frac{\rho}{\sqrt{3}}(1, -1, -1) \\ (\mathbf{c}_3^{\text{ref}})^{\text{T}} &= \frac{\rho}{\sqrt{3}}(-1, -1, 1) \\ (\mathbf{c}_4^{\text{ref}})^{\text{T}} &= \frac{\rho}{\sqrt{3}}(-1, 1, -1) \\ (\mathbf{c}_5^{\text{ref}})^{\text{T}} &= (0, 0, 0). \end{aligned} \quad (5)$$

This choice accounts for anharmonicity effects on the structure of the methane fragment already in the coordinate definition. (Note that here we used an effective structure determined in previous work<sup>40</sup> which reproduces the  $B_0$  value corresponding to the methane PES of ref. 53.) Using an effective methane structure corresponding to the ground-state vibration instead of the equilibrium structure for the reference structure of the generalized normal coordinates slightly speeds up the convergence of the vibrational energies with respect to the methane basis. In the ‘complete basis’ limit, the precise reference structure becomes irrelevant, of course.

The Cartesian coordinates of the argon atom are defined with respect to the carbon atom placed at the origin, using the

spherical polar coordinates,  $R \in [0, \infty)$  bohr,  $\cos \theta \in [-1, 1]$ , and  $\phi \in [0, 2\pi)$ ,

$$\begin{aligned} r_{6x} &= R \sin \theta \cos \phi \\ r_{6y} &= R \sin \theta \sin \phi \\ r_{6z} &= R \cos \theta. \end{aligned} \quad (6)$$

In the last step of the coordinate definition, the  $r_{ix}$  Cartesian structure, eqn (4)–(6), is shifted to the center of mass of the methane–argon complex. Throughout this work, atomic masses are used,  $m(\text{H}) = 1.00782503223$  u,  $m(\text{C}) = 12$  u, and  $m(\text{Ar}) = 39.9623831237$  u.<sup>54</sup>

In the forthcoming subsections, we first test cuts of the FullD-2019 PES in lower-dimensional vibrational computations. We report the results of 9D computations carried out for the methane fragment (with the argon atom fixed at a large distance), and observations from 1D ( $R$ ) and 2D ( $\cos \theta, \phi$ ) radial and angular model computations are summarized. The experience gathered from these tests is combined to determine the optimal parameters for the 12D computation, which is presented in the last subsection. It is important to emphasize that in the final computations we include all 12 vibrational degrees of freedom in the variational vibrational treatment, but we chose the coordinates, in particular, the reference structure of the generalized normal coordinate definition, so that they provide an excellent description for the bound atom–molecule vibrations, which are dominated by the methane zero-point state.

### A. Isolated methane vibrations

The energy levels of the methane molecule were computed on the FullD-2019 PES with the argon atom fixed at a 30 bohr distance from the center of mass of the  $\text{CH}_4$  fragment. The atom–molecule interaction is (almost) negligible (less than  $0.05 \text{ cm}^{-1}$ ) at this separation. For the variational computations, we started out from a direct-product basis set of harmonic oscillator functions,  $\phi_{n_1}(q_1) \dots \phi_{n_9}(q_9)$  ( $n_i = 0, 1, \dots, i = 1, \dots, 9$ ), which was pruned according to the simple condition  $n_1 + \dots + n_9 \leq b$ . An integration grid (much) smaller than the naïve direct-product grid was defined using the Smolyak scheme.<sup>24,25</sup> In short, the grid points were chosen to integrate exactly the identity matrix and also polynomials of up to a maximum total degree of 5 with the basis functions included in the pruned basis set.<sup>40</sup> The pruning parameter, the size of the basis, and the size of the Smolyak grid are listed in Table 3. The convergence rate with respect to the basis and grid size and benchmark results for the vibrational energies of  $\text{CH}_4$  are shown in Table 4.

Using the  $b = 10$  basis-pruning parameter, the energies are converged within  $0.01 \text{ cm}^{-1}$  up to (and including) the pentad of  $\text{CH}_4$ . The  $9690.62 \text{ cm}^{-1}$  zero-point vibrational energy (ZPVE) on the FullD-2019 PES is in good agreement with the  $9691.56 \text{ cm}^{-1}$  value corresponding to the T8 force field of Schwenke and Partridge.<sup>55</sup> The root-mean-square (rms) deviation of the converged vibrational excitation energies with respect to their counterparts deduced from experiments<sup>56</sup> is  $2.88 \text{ cm}^{-1}$ , which is excellent given that this is a purely *ab initio* PES, which was developed not specifically for an

Table 3 Basis set and integration grid parameters used to describe the methane fragment

$b^a$	$H^b$	$N_{\text{bas}}^c$	$N_{\text{Smol}}^d$
0	11 <sup>e</sup>	1	163 <sup>e</sup>
1	12 <sup>e</sup>	10	871 <sup>e</sup>
2	13	55	3481
3	14	220	11 833
4	15	715	35 929
5	16	2002	97 561
6	17	5005	241 201
7	18	11 440	556 707
8	19	24 310	1 202 691
9	20	48 620	2 440 227
10	21	92 378	4 718 595

<sup>a</sup> Basis pruning condition,  $n_1 + \dots + n_9 \leq b$ . <sup>b</sup> Grid pruning condition,  $i_1 + \dots + i_9 \leq H$  (for details, see for example ref. 40 and references therein). We chose  $H = D - 1 + b + 3$  (here  $D = 9$ ) to integrate exactly not only the overlap but also polynomials of a maximum degree of 5 with all basis functions included in the pruned basis set. <sup>c</sup> The number of basis functions in the pruned basis set is  $N_{\text{bas}} = (b + 9)!/(b!9!)$ . <sup>d</sup> The number of points in the Smolyak grid corresponding to the selected  $H$  value. <sup>e</sup> When using the FullD-2019 PES with  $b = 0$  ( $b = 1$ ), we observed that  $H = 11$  ( $H = 12$ ) is not sufficient to recover the correct degeneracy of the methane vibrations (especially the E states were affected). So, in the end, we used  $H = 12$  ( $H = 13$ ) and  $N_{\text{Smol}} = 871$  ( $N_{\text{Smol}} = 3481$ ) for  $b = 0$  ( $b = 1$ ).

isolated methane molecule but for the methane–argon complex. Note that these ‘isolated methane’ energies were obtained using the FullD-2019 PES with the argon atom fixed at a large distance from the methane molecule.

Assessment of smaller basis sets (smaller  $b$  values) is important for planning the 12D computations. The bound states of the  $\text{CH}_4\text{-Ar}$  complex are dominated by the zero-point state of methane, hence  $b = 3$  should be an excellent compromise for computing the intermolecular (atom–molecule) states accurately. The computation of predissociative states corresponding to excited vibrational states of methane will require at least  $b = 6$ – $7$ , which assumes further development of the vibrational methodology.

### B. Intermolecular radial representation

There are several possibilities to describe the vibrational motion along the methane–argon distance. One can use  $\mathcal{L}_n^{(\alpha)}$  generalized Laguerre basis functions (with  $\alpha = 2$ )<sup>21,57</sup> or a Morse tridiagonal basis set. The Laguerre basis set may be a better choice for computing predissociative states, whereas the Morse tridiagonal basis set offers a more compact alternative for bound states. In the present work, we used the Morse tridiagonal basis set parameterized with the  $D = 150 \text{ cm}^{-1}$ ,  $\alpha = 0.65$ , and  $\gamma = 0.00033$  values,<sup>18,40,58–60</sup> which gave a good Morse fit to the cut of the FullD-2019 PES at the equilibrium (global minimum) structure of all other coordinates. Since  $\text{CH}_4\text{-Ar}$  is an isotropic complex, this radial basis is expected to perform well over the entire range of the angular coordinates. The convergence tests suggest that 13 Morse functions with 15 quadrature points for  $R$  allow us to converge the 3D( $R, \cos \theta, \phi$ ) and 12D bound-state energies within  $0.01 \text{ cm}^{-1}$ .

### C. Intermolecular angular representation

For the  $\cos \theta$  coordinate, we use sin-cot-DVR (DVR, discrete variable representation) basis functions and points,<sup>61</sup> while



dc\_1955\_21

**Table 4** Convergence of the zero-point and vibrational excitation energies, in  $\text{cm}^{-1}$ , up to and including the pentad of  $\text{CH}_4$  with respect to the (pruned) basis set size using the GENIUSH–Smolyak approach<sup>40</sup> and the FullD-2019 PES with an argon–methane distance fixed at  $R = 30$  bohr. The benchmark energies corresponding to this PES are given in the  $\bar{\nu}(b = 10)$  column

$\Gamma^a$	Label <sup>b</sup>	$A_0^c$	$A_1^c$	$A_2^c$	$A_3^c$	$A_4^c$	$A_5^c$	$A_6^c$	$A_7^c$	$A_8^c$	$A_9^c$	$\bar{\nu}(b = 10)^c$	$\delta^d$	$\bar{\nu}_{\text{exp}}^e$
$A_1$	0000	43.79	42.42	40.06	1.79	0.60	0.52	0.04	0.01	0.01	0.00	9690.62	—	—
$F_2$	0001	—	9.61	7.68	41.19	2.14	0.27	0.54	0.06	0.01	0.01	1310.60	0.16	1310.76
$E$	0100	—	5.76	5.55	39.20	1.76	0.18	0.50	0.04	0.01	0.01	1531.47	1.86	1533.33
$A_1$	0002	—	—	37.74	56.88	43.69	4.60	1.24	0.64	0.11	0.02	2586.02	1.02	2587.04
$F_2$	0002	—	—	29.71	54.22	45.63	3.86	1.12	0.66	0.10	0.02	2613.61	0.65	2614.26
$E$	0002	—	—	19.70	51.49	45.00	3.13	0.94	0.62	0.08	0.01	2623.93	0.69	2624.62
$F_2$	0101	—	—	23.55	51.84	40.55	3.20	0.97	0.56	0.07	0.01	2828.08	2.24	2830.32
$F_1$	0101	—	—	17.14	49.64	43.22	2.87	0.87	0.59	0.07	0.01	2844.38	1.70	2846.08
$A_1$	1000	—	89.70	34.44	66.84	10.68	1.63	1.38	0.27	0.05	0.02	2912.36	4.12	2916.48
$F_2$	0010	—	107.24	38.27	69.89	11.81	1.76	1.50	0.29	0.05	0.03	3014.47	5.02	3019.49
$A_1$	0200	—	—	15.09	49.17	41.73	2.73	0.82	0.56	0.06	0.01	3059.25	4.40	3063.65
$E$	0200	—	—	13.75	47.58	41.39	2.48	0.78	0.55	0.06	0.01	3061.06	4.08	3065.14
rms														2.88

<sup>a</sup> Label of the irreducible representation of the  $T_d$  point group of methane. <sup>b</sup>  $\langle n_1 n_2 n_3 n_4 \rangle$  normal mode label. <sup>c</sup> Deviation from the  $\bar{\nu}(b = 10)$  benchmark value,  $A_k = \bar{\nu}(b = k) - \bar{\nu}(b = 10)$ . <sup>d</sup>  $\delta = \bar{\nu}_{\text{exp}} - \bar{\nu}(b = 10)$ . <sup>e</sup> Vibrational energies deduced from experiments are taken from ref. 56.

Fourier basis functions are used for the  $\phi$  angle. Test computations suggest that 23 sin-cot-DVR functions for  $\cos \theta$  and 21 Fourier functions with 24 quadrature points for  $\phi$  will be sufficient to converge the 3D( $R, \cos \theta, \phi$ ) and 12D vibrational excitation energies better than  $0.01 \text{ cm}^{-1}$ .

#### D. Full-dimensional (12D) vibrational states and comparison with 3D models

All vibrational bound states of the  $\text{CH}_4\text{-Ar}$  complex on the newly developed FullD-2019 PES are listed in Table 5. The intermolecular basis set corresponding to the  $(R, \cos \theta, \phi)$  coordinates is sufficiently large to converge all vibrational excitation energies better than  $0.01 \text{ cm}^{-1}$ . In order to find the smallest necessary intramolecular methane basis set (characterized with the  $b$  basis-pruning parameter), we have carried out 12D computations with an increasing basis set size on the methane fragment corresponding to the  $b = 0, 1, 2,$  and  $3$  value. Concerning the ZPVE, we think that the  $b = 3$  12D result is *ca.*  $1\text{--}2 \text{ cm}^{-1}$  larger (our approach is nearly variational) than the exact result, similarly to the  $b = 3$  ZPVE value of isolated methane (Table 4). Concerning the intermolecular vibrational excitation energies, we could efficiently rely on the cancellation of error in the relative vibrational energies, and thus a rather small methane basis set was sufficient to achieve the  $0.01 \text{ cm}^{-1}$  convergence goal for the excitation energies.

It is interesting to consider the convergence of the excitation energies with respect to  $b$ . The 12D computation with  $b = 0$ , which corresponds to a single(!) basis function on the methane fragment, has an rms error of  $0.40 \text{ cm}^{-1}$ . This rms value is *ca.* half of the rms error of a well-converged 3D computation imposing rigorous geometrical constraints with an  $\langle r \rangle_0$  methane structure (*vide infra*). A 12D computation with  $b = 1$ , which includes 10 basis functions for the methane fragment, has an rms of  $0.07 \text{ cm}^{-1}$ . Finally, our  $0.01 \text{ cm}^{-1}$  convergence goal is achieved for the  $b = 2$  and  $b = 3$  pruning parameter values.

Concerning the computational cost, the  $b = 0$  and  $b = 1$  computations took 10 and 20 hours (using 20 processor cores) and required 6 and 8 GB of memory, respectively. The 12D

$b = 3$  ( $b = 2$ ) computations took 42 (13) days on 50 (20) cores and required 80 (30) GB of memory. As it was indicated already in the footnote to Table 3, we had to use a larger grid size for  $b = 0$  and 1 than we had originally anticipated, which slightly increased the cost of the computation. Furthermore, the condition number of the Hamiltonian matrix in the current representation is very large (due to the application of sin-cot-DVR basis functions, there are grid points which are very close to the singularities of the KEO), which implies an increased number of Lanczos iteration steps. We anticipate reduction of the computational cost with further development.

Table 5 also shows the result of 3D, rigid-monomer computations, in which only the  $R, \cos \theta,$  and  $\phi$  degrees of freedom were treated as active coordinates. The '3D( $\langle r \rangle_0$ )' column corresponds to reduced-dimensionality results in which rigorous geometrical constraints were imposed on the methane's structure (referred to as 'the reduction in the Lagrangian' or 'reduction in the  $g$  matrix' in ref. 51 and constructed automatically in GENIUSH). The methane was fixed at a regular tetrahedral structure with  $\langle r_{\text{C-H}} \rangle_0$ , which we calculated as the expectation value of the C–H distance using the isolated methane's ground-state wave function on the present PES. The vibrational excitation energies of this 3D model have a relatively large,  $0.93 \text{ cm}^{-1}$ , rms with respect to the converged 12D result. Furthermore, this 3D model (erroneously) predicts an additional, triply degenerate, bound state below the dissociation asymptote, which can be explained by the slightly different  $B_0$  value corresponding to this model.

In the '3D( $\langle B \rangle_0$ )' column, we report the bound vibrational energies obtained with an 'adjusted' 3D model. While using the  $\langle r_{\text{C-H}} \rangle_0$  value for defining the 3D cut of the PES, we adjusted the C–H distance in the KEO to reproduce the  $\langle B \rangle_0$  effective rotational constant of this PES in 2D coupled-rotor computations.<sup>13,57</sup> This model reproduces the correct number of bound states and has a smaller,  $0.32 \text{ cm}^{-1}$ , rms than the 3D model with the rigorous geometrical constraints.

In relation to these 3D models, we conclude that a 12D computation performed with a single 9D basis function for methane ( $b = 0$ ) is on a par with the 3D( $\langle B \rangle_0$ ) model. If we allow

dc\_1955\_21

Table 5 All bound-state vibrational energies,  $\tilde{\nu}$  in  $\text{cm}^{-1}$ , of  $\text{CH}_4\text{-Ar}$ , computed with the GENIUSH–Smolyak approach<sup>40</sup> and the FullD-2019 PES developed in the present work

#	Assignment <sup>a</sup>			12D <sup>b</sup>			3D( $\langle B \rangle_0$ ) <sup>c</sup>		3D( $\langle B \rangle_0$ ) <sup>d</sup>		
	$j$	$n_R$	$\Gamma$	$A_0$	$A_1$	$A_2$	$\tilde{\nu}(b=3)$	$\tilde{\nu}_{3D}$	$\delta^e$	$\tilde{\nu}_{3D}$	$\delta^e$
0 <sup>f</sup>	0	0	$A_1$	66.10	40.67	38.32	9754.40	54.30	—	54.38	—
1–3	1	0	$F_2$	0.21	0.03	0.00	8.68	8.65	0.04	8.87	−0.19
4	0	1	$A_1$	0.10	0.01	0.00	29.88	29.80	0.07	29.89	−0.01
5–7	2	0	$F_2$	0.29	0.01	−0.01	31.63	30.84	0.79	31.29	0.35
8–9	2	0	$E$	0.40	0.05	0.01	32.34	31.65	0.69	32.21	0.13
10–12	1	1	$F_2$	0.21	0.02	0.01	45.76	45.27	0.49	45.63	0.13
13	0	2	$A_1$	0.06	0.00	0.01	54.79	54.54	0.26	54.66	0.14
14–16	2	1	$F_2$	0.50	0.05	0.00	56.80	55.92	0.88	56.58	0.22
17–18	2	1	$E$	0.39	0.05	0.02	65.64	64.92	0.72	65.49	0.14
19–21	3	0	$F_2$	0.80	0.08	−0.01	66.08	64.52	1.56	65.72	0.36
22–24	1	2	$F_1$	0.33	0.03	0.01	67.86	66.86	1.00	67.45	0.41
25	0	3	$A_1$	0.30	0.02	0.00	72.62	71.19	1.42	72.02	0.60
26	3	0	$A_1$	0.31	0.02	0.01	75.23	74.63	0.60	74.97	0.26
27–29	2	2	$F_2$	0.29	0.02	0.00	77.73	76.46	1.28	77.11	0.63
30–32	1	3	$F_2$	0.32	0.03	0.01	82.25	81.71	0.54	82.17	0.08
33	0	4	$A_1$	−0.12	−0.01	0.02	87.53	87.06	0.47	87.18	0.35
34–36	1	4	$F_2$	0.23	0.03	0.02	91.42	90.57	0.84	91.07	0.35
37–38	2	4	$E$	0.34	0.04	0.02	91.61	90.80	0.81	91.38	0.23
39	0	5	$A_1$	−0.42	−0.26	0.03	95.44	94.75	0.69	95.02	0.42
40–42	3	3	$F_2$	0.97	0.10	0.00	95.69	94.07	1.61	95.42	0.26
43	0	6	$A_1$	−0.09	0.03	0.03	99.11	98.21	0.90	98.72	0.39
44–46	—	—	—	—	—	—	—	99.32	—	—	—
rms <sup>g</sup>	—	—	—	0.40	0.07	0.01	—	—	0.93	—	0.32

<sup>a</sup> Characterization of the computed states using the 3D wave functions of the 3D( $\langle B \rangle_0$ ) column.  $j$ : angular momentum quantum number of the methane fragment and the relative diatom in the  $[j, j]_{00}$  dominant coupled-rotor (CR) function;<sup>57</sup>  $n_R$ : vibrational excitation along  $R$ ;  $\Gamma$ : irrep label of the  $T_d(M)$  molecular symmetry group of the complex based on the CR assignment and irrep decomposition.<sup>57</sup> <sup>b</sup>  $A_k = \tilde{\nu}(b=k) - \tilde{\nu}(b=3)$ , where  $b$  is the pruning parameter of the methane basis, the intermolecular radial and angular representations are defined in the text, and is sufficient for converging the figures shown in the table. <sup>c</sup> 3D computation using rigorous geometrical constraints with a regular tetrahedral methane structure with  $\langle r_{\text{C-H}} \rangle_0 = 2.093624127$  bohr (used both in the KEO and in the PES). <sup>d</sup> 3D computation using an ‘adjusted’  $r_{\text{fit}}(\text{C-H}) = 2.072988169$  bohr C–H distance in the KEO, which in a 2D coupled-rotor computation<sup>13,57</sup> reproduces the  $\langle B \rangle_0 = 5.212508664$   $\text{cm}^{-1}$  effective rotational constant corresponding to this PES. To define the 3D cut of the PES, we used  $\langle r_{\text{C-H}} \rangle_0$ . <sup>e</sup>  $\delta = \tilde{\nu}(b=3) - \tilde{\nu}_{3D}$ . <sup>f</sup> Zero-point vibration of the complex. The vibrational excitation energies, #; 1, 2, 3, ..., are given with respect to this value. <sup>g</sup> Root-mean-square deviation from the  $\tilde{\nu}(b=3)$  (12D) result.

only 10 functions for the methane fragment ( $b=1$ ) in the 12D computation, the 12D result clearly outperforms the 3D excitation energies, without increasing the computational cost dramatically.

In order to rationalize these numerical observations, we may distinguish between ‘static’ and ‘dynamical’ contributions from the methane’s vibrations to the atom–molecule energy levels. The static contribution is due to the fact that the isolated molecule’s effective (average) structure, due to anharmonicity of methane’s vibrations, is different from the equilibrium structure. In 3D computations, this effect is accounted for by fixing the methane’s structure at an effective structure instead of the equilibrium structure. In 12D computations, we have ‘built in’ this static effect in the coordinate definition (using generalized normal coordinates) in order to speed up convergence with respect to the methane’s basis size.

The dynamical contribution is due to the coupling of the methane’s vibrations with the intermolecular dynamics. This dynamical coupling, which is often small but non-negligible, requires a full-dimensional treatment. In the case of the methane–argon complex, we observe that using only the ground and all singly excited (9D) harmonic oscillator functions captures almost all dynamical effects, but well-converged excitation energies assume at least 220 (9D) harmonic oscillator functions, corresponding to the  $n_1 + n_2 + \dots + n_9 \leq 3$  pruning condition, for the methane fragment.

From a numerical point of view, it is necessary to mention that the 12D and 3D results are close, within 1–2  $\text{cm}^{-1}$ , to the vibrational states reported in ref. 11 (Table 4) on a 3D PES developed using symmetry-adapted perturbation theory and an effective (ro)vibrational Hamiltonian some 20 years ago. The present work reports a fully *ab initio* quantum dynamics study of the system in full dimensionality and its further extension to predissociative states may reveal larger deviations from the effectively designed approach of ref. 11 and 37. There are also experimental results in the predissociative range,<sup>38,39</sup> which will make the comparison more interesting. Furthermore, the methodology recently developed and used in the present work is not designed specifically for very weakly interacting atom–molecule complexes, but it can be used for a greater variety of molecular systems and it fits in a series of recent efforts made for systematic development of general ‘black-box-type’ (ro)vibrational quasi-variational methods, applicable to molecular complexes or any other molecular systems, of high vibrational dimensionality and with multiple large-amplitude motions.

## IV. Summary and conclusions

The present work reports the development of a full-dimensional, near-spectroscopic quality *ab initio* potential energy surface for

dc\_1955\_21

the van-der-Waals complex of the methane molecule and an argon atom. The PES development is accompanied by the computation of all vibrational bound states of this complex including all (12) vibrational degrees of freedom in a near-variational treatment using the GENIUSH program and the Smolyak algorithm. The vibrational excitation energies obtained within a 12D treatment were used to assess traditional 3D (rigid-monomer) approaches. With further development of the quantum dynamics methodology, full-dimensional computations will become more widespread and applicable to floppy molecules or molecular complexes over a broad energy range.

## Conflicts of interest

There are no conflicts of interest to declare.

## Acknowledgements

We thank Xiao-Gang Wang and Tucker Carrington for sharing their well-tested sincot-Legendre-DVR implementation (codvr.f90) with us. G. A. and E. M. acknowledge financial support from a PROMYS Grant (no. IZ11Z0\_166525) of the Swiss National Science Foundation. D. P. and G. C. thank the National Research, Development and Innovation Office-NKFIH, K-125317, the Ministry of Human Capacities, Hungary grant 20391-3/2018/FEKUSTRAT, and the Momentum (Lendület) Program of the Hungarian Academy of Sciences for financial support.

## References

- 1 J. N. Murrell, S. Carter, S. C. Farantos, P. Huxley and A. J. C. Varandas, *Molecular Potential Energy Functions*, New York, Wiley, 1984.
- 2 M. Quack and M. A. Suhm, Potential energy surfaces, quasiadiabatic channels, rovibrational spectra, and intramolecular dynamics of (HF)<sub>2</sub> and its isotopomers from quantum Monte Carlo calculations, *J. Chem. Phys.*, 1991, **95**, 28.
- 3 M. Quack, J. Stohner and M. A. Suhm, Vibrational dynamics of (HF)<sub>n</sub> aggregates from an *ab initio* based analytical (1 + 2 + 3)-body potential, *J. Mol. Struct.*, 1993, **294**, 33.
- 4 G. C. Groenenboom, E. M. Mas, R. Bukowski, K. Szalewicz, P. E. S. Wormer and A. van der Avoird, The pair and three-body potential of water, *Phys. Rev. Lett.*, 2000, **84**, 4072–4075.
- 5 W. Cencek, K. Szalewicz, C. Leforestier, R. van Harreveld and A. van der Avoird, An accurate analytic representation of the water pair potential, *Phys. Chem. Chem. Phys.*, 2008, **10**, 4716–4731.
- 6 Y. Wang and J. M. Bowman, *Ab initio* potential and dipole moment surfaces for water. II. Local-monomer calculations of the infrared spectra of water clusters, *J. Chem. Phys.*, 2011, **134**, 154510.
- 7 G. R. Medders, V. Babin and F. Paesani, A critical assessment of two-body and three-body interactions in water, *J. Chem. Theory Comput.*, 2013, **9**, 1103.
- 8 V. Babin, G. R. Medders and F. Paesani, Development of a “first principles” water potential with flexible monomers. II: Trimer potential energy surface, third virial coefficient, and small clusters, *J. Chem. Theory Comput.*, 2014, **10**, 1599.
- 9 P. Jankowski, G. Murdachaew, R. Bukowski, O. Akin-Ojo, C. Leforestier and K. Szalewicz, *Ab initio* water pair potential with flexible monomers, *J. Phys. Chem. A*, 2015, **119**, 2940–2964.
- 10 U. Góra, W. Cencek, R. Podeszwa, A. van der Avoird and K. Szalewicz, Predictions for water clusters from a first-principles two- and three-body force field, *J. Chem. Phys.*, 2014, **140**, 194101.
- 11 T. G. A. Heijmen, P. E. S. Wormer, A. van der Avoird, R. E. Miller and R. Moszynski, The rotational and vibrational dynamics of argon-methane. I. A theoretical study, *J. Chem. Phys.*, 1999, **110**, 5639.
- 12 J. Sarka, A. G. Császár, S. C. Althorpe, D. J. Wales and E. Mátyus, Rovibrational transitions of the methane-water dimer from intermolecular quantum dynamical computations, *Phys. Chem. Chem. Phys.*, 2016, **18**, 22816.
- 13 J. Sarka, A. G. Császár and E. Mátyus, Rovibrational quantum dynamical computations for deuterated isotopologues of the methane-water dimer, *Phys. Chem. Chem. Phys.*, 2017, **2**, 15335.
- 14 M. P. Metz, K. Szalewicz, J. Sarka, R. Tóbiás, A. G. Császár and E. Mátyus, Molecular dimers of methane clathrates: *ab initio* potential energy surfaces and variational vibrational states, *Phys. Chem. Chem. Phys.*, 2019, **21**, 13504.
- 15 M. Jeziorska, P. Jankowski, K. Szalewicz and B. Jeziorski, On the optimal choice of monomer geometry in calculations of intermolecular interaction energies: Rovibrational spectrum of Ar-HF from two- and three-dimensional potentials, *J. Chem. Phys.*, 2000, **113**, 2957.
- 16 X. G. Wang and T. Carrington, Jr, Using monomer vibrational wavefunctions as contracted basis functions to compute rovibrational levels of an H<sub>2</sub>O-atom complex in full dimensionality, *J. Chem. Phys.*, 2017, **146**, 104105.
- 17 X. G. Wang and T. Carrington, Jr, Using monomer vibrational wavefunctions to compute numerically exact (12D) rovibrational levels of water dimer, *J. Chem. Phys.*, 2018, **148**, 074108.
- 18 G. Avila and E. Mátyus, Full-dimensional (12D) variational vibrational states of CH<sub>4</sub>-F<sup>-</sup>: interplay of anharmonicity and tunneling, *J. Chem. Phys.*, 2019, **151**, 154301.
- 19 C. Fábri, A. G. Császár and G. Czakó, Reduced-dimensional quantum computations for the rotational-vibrational dynamics of F<sup>-</sup>-CH<sub>4</sub> and F<sup>-</sup>-CH<sub>2</sub>D<sub>2</sub>, *J. Phys. Chem. A*, 2013, **117**, 6975.
- 20 R. Wodraszka, J. Palma and U. Manthe, Vibrational Dynamics of the CH<sub>4</sub>-F<sup>-</sup> Complex, *J. Phys. Chem. A*, 2012, **116**, 11249.
- 21 D. Papp, J. Sarka, T. Szidarovszky, A. G. Császár, E. Mátyus and M. Hochlaf, *et al.*, Complex rovibrational dynamics of the Ar-NO<sup>+</sup> complex, *Phys. Chem. Chem. Phys.*, 2017, **19**, 8152–8160.
- 22 P. M. Felker and Z. Bacic, Weakly bound molecular dimers: Intramolecular vibrational fundamentals, overtones, and tunneling splittings from full-dimensional quantum calculations using compact contracted bases of intramolecular

dc\_1955\_21

- and low-energy rigid-monomer intermolecular eigenstates, *J. Chem. Phys.*, 2019, **151**, 024305.
- 23 J. M. Bowman, S. Carter and X. Huang, MULTIMODE: A code to calculate rovibrational energies of polyatomic molecules, *Int. Rev. Phys. Chem.*, 2003, **22**(3), 533–549.
- 24 G. Avila and T. Carrington Jr., Nonproduct quadrature grids for solving the vibrational Schrödinger equation, *J. Chem. Phys.*, 2009, **131**(17), 174103.
- 25 G. Avila and T. Carrington Jr., Using nonproduct quadrature grids to solve the vibrational Schrödinger equation in 12D, *J. Chem. Phys.*, 2011, **134**(5), 054126.
- 26 G. Avila and T. Carrington Jr., Using a pruned basis, a non-product quadrature grid, and the exact Watson normal-coordinate kinetic energy operator to solve the vibrational Schrödinger equation for C<sub>2</sub>H<sub>4</sub>, *J. Chem. Phys.*, 2011, **134**(6), 064101.
- 27 A. Leclerc and T. Carrington, Calculating vibrational spectra with sum of product basis functions without storing full-dimensional vectors or matrices, *J. Chem. Phys.*, 2014, **140**(17), 174111.
- 28 P. S. Thomas and T. Carrington, An intertwined method for making low-rank, sum-of-product basis functions that makes it possible to compute vibrational spectra of molecules with more than 10 atoms, *J. Chem. Phys.*, 2017, **146**(20), 204110.
- 29 T. Halverson and B. Poirier, One million quantum states of benzene, *J. Phys. Chem. A*, 2015, **119**(50), 12417–12433.
- 30 J. Brown and T. Carrington, Using an expanding nondirect product harmonic basis with an iterative eigensolver to compute vibrational energy levels with as many as seven atoms, *J. Chem. Phys.*, 2016, **145**(14), 144104.
- 31 N. K. Madsen, I. H. Godtliebsen, S. A. Losilla and O. Christiansen, Tensor-decomposed vibrational coupled-cluster theory: Enabling large-scale, highly accurate vibrational-structure calculations, *J. Chem. Phys.*, 2018, **148**, 024103.
- 32 A. Baiardi and M. Reiher, Large-scale quantum-dynamics with matrix product states, *J. Chem. Theory Comput.*, 2019, **15**, 3481.
- 33 W. H. Miller, N. C. Handy and J. E. Adams, Reaction path Hamiltonian for polyatomic molecules, *J. Chem. Phys.*, 1980, **72**, 99.
- 34 J. M. Bowman, X. Huang, N. C. Handy and S. Carter, Vibrational levels of methanol calculated by the reaction path version of MULTIMODE, using an *ab initio*, full-dimensional potential, *J. Phys. Chem. A*, 2007, **111**, 7317.
- 35 D. Lauvergnat and A. Nauts, Quantum dynamics with sparse grids: A combination of Smolyak scheme and cubature. Application to methanol in full dimensionality, *Spectrochim. Acta, Part A*, 2014, **119**, 18–25.
- 36 C. Leforestier, *Philos. Trans. R. Soc., A*, 2012, **370**, 2675.
- 37 T. G. A. Heijmen, T. Korona, R. Moszynski, P. E. S. Wormer and A. van der Avoird, *Ab initio* potential-energy surface and rotationally inelastic integral cross sections of the Ar-CH<sub>4</sub> complex, *J. Chem. Phys.*, 1997, **107**, 902.
- 38 R. E. Miller, T. G. A. Heijmen, P. E. S. Wormer, A. van der Avoird and R. Moszynski, The rotational and vibrational dynamics of argon-methane. II. Experiment and comparison with theory, *J. Chem. Phys.*, 1999, **110**, 5651.
- 39 M. Wangler, D. A. Roth, I. Pak, G. Winnewisser, P. E. S. Wormer and A. van der Avoird, The high-resolution spectrum of the Ar-CH<sub>4</sub> complex in the 7 μm region: measurement and *ab initio* calculation, *J. Mol. Spectrosc.*, 2003, **222**(1), 109.
- 40 G. Avila and E. Mátyus, Toward breaking the curse of dimensionality in (ro)vibrational computations of molecular systems with multiple large-amplitude motions, *J. Chem. Phys.*, 2019, **150**, 174107.
- 41 T. B. Adler, G. Knizia and H. J. Werner, A simple and efficient CCSD(T)-F12 approximation, *J. Chem. Phys.*, 2007, **127**, 221106.
- 42 T. H. Dunning, Jr, Gaussian basis sets for use in correlated molecular calculations. I. The atoms boron through neon and hydrogen, *J. Chem. Phys.*, 1989, **90**, 1007.
- 43 K. Raghavachari, G. W. Trucks, J. A. Pople and M. Head-Gordon, A fifth-order perturbation comparison of electron correlation theories, *Chem. Phys. Lett.*, 1989, **157**, 479.
- 44 M. Kállay and J. Gauss, Approximate treatment of higher excitations in coupled-cluster theory, *J. Chem. Phys.*, 2005, **123**, 214105.
- 45 D. E. Woon and T. H. Dunning Jr, Gaussian basis sets for use in correlated molecular calculations. V. Core-valence basis sets for boron through neon, *J. Chem. Phys.*, 1995, **103**, 4572.
- 46 H.-J. Werner, P. J. Knowles, G. Knizia, F. R. Manby and M. Schütz *et al.*, Molpro, version 2015.1, a package of *ab initio* programs, see <http://www.molpro.net>.
- 47 MRCC, a quantum chemical program suite written by M. Kállay, Z. Rolik, I. Ladjánszki, L. Szegedy, B. Ladóczki, J. Csontos and B. Kornis, *J. Chem. Phys.*, 2011, **135**, 104111, See also Z. Rolik, M. Kállay, as well as: [www.mrcc.hu](http://www.mrcc.hu).
- 48 G. Czakó, I. Szabó and H. Telekes, On the choice of the *ab initio* level of theory for potential energy surface developments, *J. Phys. Chem. A*, 2014, **118**, 646.
- 49 B. J. Braams and J. M. Bowman, Permutationally invariant potential energy surfaces in high dimensionality, *Int. Rev. Phys. Chem.*, 2009, **28**, 577.
- 50 J. M. Bowman, G. Czakó and B. Fu, High-dimensional *ab initio* potential energy surfaces for reaction dynamics calculations, *Phys. Chem. Chem. Phys.*, 2011, **13**, 8094.
- 51 E. Mátyus, G. Czakó and A. G. Császár, Toward black-box-type full- and reduced-dimensional variational (ro)vibrational computations, *J. Chem. Phys.*, 2009, **130**, 134112.
- 52 C. Fábri, E. Mátyus and A. G. Császár, Rotating full- and reduced-dimensional quantum chemical models of molecules, *J. Chem. Phys.*, 2011, **134**, 074105.
- 53 X. G. Wang and T. Carrington Jr, Using experimental data and a contracted basis Lanczos method to determine an accurate methane potential energy surface from a least squares optimization, *J. Chem. Phys.*, 2014, **141**(15), 154106.
- 54 J. S. Coursey, D. J. Schwab, J. J. Tsai and R. A. Dragoset, Atomic Weights and Isotopic Compositions (version 4.1), National Institute of Standards and Technology, Gaithersburg, MD, 2015, <http://physics.nist.gov/Comp> last accessed on 12 May 2018.

dc 1955 21

- 55 D. W. Schwenke and H. Partridge, Vibrational energy levels for CH<sub>4</sub> from an *ab initio* potential, *Spectrochim. Acta*, 2001, **57**, 887.
- 56 A. V. Nikitin, M. Rey and V. G. Tyuterev, Rotational and vibrational energy levels of methane calculated from a new potential energy surface, *Chem. Phys. Lett.*, 2011, **501**, 179.
- 57 D. Ferenc and E. Mátyus, Bound and unbound rovibrational states of the methane-argon dimer, *Mol. Phys.*, 2019, **117**, 1694.
- 58 H. Wei and T. Carrington, Jr, The discrete variable representation of a triatomic Hamiltonian in bond length-bond angle coordinates, *J. Chem. Phys.*, 1992, **97**, 3029.
- 59 B. R. Johnson and W. P. Reinhardt, Adiabatic separations of stretching and bending vibrations: Application to H<sub>2</sub>O, *J. Chem. Phys.*, 1986, **85**(8), 4538–4556.
- 60 J. Tennyson and B. T. Sutcliffe, The *ab initio* calculation of the vibrational-rotational spectrum of triatomic systems in the close-coupling approach, with KCN and H<sub>2</sub>Ne as examples, *J. Chem. Phys.*, 1982, **77**(8), 4061–4072.
- 61 G. Schiffel and U. Manthe, On direct product based discrete variable representations for angular coordinates and the treatment of singular terms in the kinetic energy operator, *Chem. Phys.*, 2010, **374**(1), 118–125.

# Full-dimensional (12D) variational vibrational states of $\text{CH}_4\cdot\text{F}^-$ : Interplay of anharmonicity and tunneling

Cite as: J. Chem. Phys. 151, 154301 (2019); doi: 10.1063/1.5124532

Submitted: 15 August 2019 • Accepted: 26 September 2019 •

Published Online: 15 October 2019



View Online



Export Citation



CrossMark

Gustavo Avila<sup>a)</sup>  and Edit Matyus<sup>b)</sup> 

## AFFILIATIONS

Institute of Chemistry, ELTE, Eötvös Loránd University, Pázmány Péter sétány 1/A, 1117 Budapest, Hungary

<sup>a)</sup>Electronic mail: [Gustavo\\_Avila@telefonica.net](mailto:Gustavo_Avila@telefonica.net)

<sup>b)</sup>Electronic mail: [matyuse@caesar.elte.hu](mailto:matyuse@caesar.elte.hu)

## ABSTRACT

The complex of a methane molecule and a fluoride anion represents a 12-dimensional (12D), four-well vibrational problem with multiple large-amplitude motions, which has challenged the quantum dynamics community for years. The present work reports vibrational band origins and tunneling splittings obtained in a full-dimensional variational vibrational computation using the GENIUSH program and the Smolyak quadrature scheme. The converged 12D vibrational band origins and tunneling splittings confirm complementary aspects of the earlier full- and reduced-dimensionality studies: (1) the tunneling splittings are smaller than  $0.02\text{ cm}^{-1}$ ; (2) a single-well treatment is not sufficient (except perhaps the zero-point vibration) due to a significant anharmonicity over the wells; and thus, (3) a full-dimensional treatment appears to be necessary. The present computations extend to a higher energy range than earlier work, show that the tunneling splittings increase upon vibrational excitation of the complex, and indicate non-negligible “heavy-atom” tunneling.

<https://doi.org/10.1063/1.5124532>

## I. INTRODUCTION

The  $\text{CH}_4\cdot\text{F}^-$  complex has been a subject of experimental interest over the past decades. Its infrared spectrum has been recorded and studied in the methane’s stretching region,<sup>1–5</sup> and it has been used as a precursor in anion photoelectron spectroscopy to probe the transition state region of the  $\text{F}+\text{CH}_4$  reaction.<sup>6,7</sup> This experimental activity motivated the computational (ro)vibrational quantum dynamics study of the complex.<sup>8–10</sup> This complex also serves as a good prototype for molecular interactions with relatively large monomer distortions and strong binding.

$\text{CH}_4\cdot\text{F}^-$  has turned out to be challenging for the current (ro)vibrational methodologies due to its high vibrational dimensionality and multiwell, highly anisotropic potential energy landscape. The vibrational states from Refs. 8–10, using the MULTIMODE,<sup>11</sup> the MCTDH,<sup>12,13</sup> and the GENIUSH<sup>14,15</sup> quantum dynamics program packages, respectively, show several (tens of) wavenumbers’ (dis)agreement. In the present work, we aim to resolve this controversy.

There is currently a single, full-dimensional potential energy surface (PES) available for the complex developed by Czako, Braams, and Bowman in 2008,<sup>8</sup> which we will refer to as “CBB08 PES.” The CBB08 PES was obtained by fitting permutationally invariant (up to 6th-order) polynomials to 6547 (plus 3000) electronic energy points of the interaction (plus fragment) region computed at the frozen-core CCSD(T)/aug-cc-pVTZ level of the *ab initio* theory. The root-mean-square deviation (RMSD) of the fitting, within the energy range below  $22\,000\text{ cm}^{-1}$ , was reported to be  $42\text{ cm}^{-1}$ , and in practice, the PES describes the intermolecular region well up to moderate ion-molecule separations.

The equilibrium structure of the complex has  $C_{3v}$  point-group (PG) symmetry with the fluoride binding to one of the apexes of the methane tetrahedron. Since the  $\text{F}^-$  anion can bind to any of the four hydrogens of methane, there are four equivalent minima on the PES, which are separated by “surmountable” barriers, and thus, the molecular symmetry (MS) group is  $T_d(M)$ . The complex is bound by  $D_e = 2434\text{ cm}^{-1}$  on the CBB08 PES,<sup>8</sup> which corresponds to  $D_0 = 2316\text{ cm}^{-1}$  including the zero-point vibrational energy (ZPVE)

correction, and we have found the lowest barrier connecting the equivalent wells to be  $V = 1104 \text{ cm}^{-1}$  (*vide infra*). It is interesting to compare these values with the similar parameters of prototypical systems of hydrogen bonding and tunneling. The prototype of strong hydrogen bond,  $(\text{HF})_2$ , features a dissociation energy of  $D_0 \approx 1050 \text{ cm}^{-1}$ ,<sup>16</sup> which is less than half of the binding energy of  $\text{CH}_4 \cdot \text{F}^-$ . The prototype for (double-well) tunneling, malonaldehyde, has a barrier of  $1410 \text{ cm}^{-1}$ ,<sup>17</sup> which is  $\sim 30\%$  higher than the barrier in  $\text{CH}_4 \cdot \text{F}^-$ , but of course, for estimating the tunneling splitting, one has to consider the effective mass and also the shape (width) of the barrier.

The strong interaction of the methane and the fluoride in  $\text{CH}_4 \cdot \text{F}^-$  is accompanied by a relatively large distortion of the methane fragment. For the interaction (int) region, Table 3 of Ref. 8 reported the equilibrium structure with an elongated C–H bond,  $r_{\text{eq}}^{\text{int}}(\text{C–H}_b) = 1.112 \text{ \AA}$ , for the H, which binds (b) to the  $\text{F}^-$ , while for the other three hydrogens,  $r_{\text{eq}}^{\text{int}}(\text{C–H}) = 1.095 \text{ \AA}$ . The corresponding distorted tetrahedral structure is characterized by the  $\alpha(\text{H–C–H}_b) = 110.46^\circ$  angle. In the  $\text{CH}_4 + \text{F}^-$  channel, the practically isolated (isol) methane molecule is a regular tetrahedron with a C–H equilibrium distance,  $r_{\text{eq}}^{\text{isol}}(\text{C–H}) = 1.090 \text{ \AA}$ .

In the forthcoming sections, we briefly summarize the quantum dynamics methodology used in this work (Sec. II), explain the symmetry analysis and assignment of the vibrational states (Sec. III), and report the vibrational energies obtained in the full- and reduced-dimensionality treatments (Sec. IV). After assessment of the convergence of the vibrational energies, a detailed comparison is provided with the vibrational energies reported in earlier studies.<sup>8–10</sup> The article is concluded (Sec. V) with the computation of tunneling splittings for excited vibrations of the complex up to and slightly beyond the energy range of the barrier separating the equivalent wells.

## II. THEORETICAL AND COMPUTATIONAL DETAILS

The present work is among the first applications of the GENIUSH–Smolyak algorithm and computer program.<sup>18</sup> The GENIUSH–Smolyak approach combines the nonproduct grid (Smolyak) method of Ref. 19, which has been used for several high-dimensional, semirigid molecules<sup>20,21</sup> as well as molecules with a single large-amplitude motion,<sup>22,23</sup> and the numerical kinetic energy operator (numerical KEO) approach of Ref. 14 implemented in the GENIUSH program,<sup>14,15</sup> which includes by now dozens of vibrational-coordinate definitions for floppy systems.<sup>10,14,15,24–30</sup>

Concerning the coordinate definition for the fluoride–methane complex, we used the  $(R, \cos \theta, \phi)$  spherical polar coordinates to describe the relative orientation of the methane fragment and the fluoride ion, and the nine normal coordinates,  $q_1, q_2, \dots, q_9$ , of methane (the coordinate definition is provided in the [supplementary material](#)) to describe its internal vibrations. In the full-dimensional computations, we used the KEO given in Eq. (50) of Ref. 18, which reads for the  $(\xi_1, \xi_2, \xi_3, \dots, \xi_D)$  general coordinates with the special  $\xi_2 = c$  choice

$$\hat{T}^{\text{v}} = -\frac{1}{2} \sum_{j=1}^D \frac{\partial}{\partial c} G_{c,j} \frac{\partial}{\partial \xi_j} - \frac{1}{2} \sum_{i=1, i \neq 2}^D \sum_{j=1}^D G_{i,j} \frac{\partial}{\partial \xi_i} \frac{\partial}{\partial \xi_j} - \frac{1}{2} \sum_{i=1}^D B_i \frac{\partial}{\partial \xi_i} + U, \quad (1)$$

$$B_i = \sum_{k=1, k \neq 2}^D \frac{\partial}{\partial \xi_k} G_{k,i},$$

where  $\mathbf{g} \in R^{(D+3) \times (D+3)}$  is the mass-weighted metric tensor,  $\mathbf{G} = \mathbf{g}^{-1}$ ,  $\tilde{g} = \det \mathbf{g}$ , the extrapotential term

$$U = \frac{1}{32} \sum_{k=1}^D \sum_{l=1}^D \left[ \frac{G_{kl}}{\tilde{g}^2} \frac{\partial \tilde{g}}{\partial \xi_k} \frac{\partial \tilde{g}}{\partial \xi_l} + 4 \frac{\partial}{\partial \xi_k} \left( \frac{G_{kl}}{\tilde{g}} \frac{\partial \tilde{g}}{\partial \xi_l} \right) \right], \quad (2)$$

and the volume element is  $dV = d\xi_1 d\xi_2 \dots d\xi_D$ . In the full-dimensional treatment of  $\text{CH}_4 \cdot \text{F}^-$ ,  $D = 12$  and the coordinates are  $\xi_1 = R, \xi_2 = c = \cos \theta, \xi_3 = \phi, \xi_{3+i} = q_i$  ( $i = 1, 2, \dots, 9$ ). We treat  $c = \cos \theta$  differently from the other coordinates in Eq. (1) in order to avoid a nonsymmetric finite basis representation (FBR) of the Hamiltonian due to inaccurate integration caused by singular terms in the KEO.<sup>18</sup> The Hamiltonian matrix was constructed using a finite basis representation (FBR) for all coordinates except  $c$ , for which the sin-cot discrete variable representation (DVR)<sup>31</sup> was used as is explained in Sec. IV E of Ref. 18. The reduced-dimensionality computations have been carried out with the original GENIUSH program,<sup>14</sup> using the Podolsky form of the KEO (constructed in an automated way for the imposed geometrical constraints), and the Hamiltonian matrix was constructed using DVR.<sup>32</sup> The lowest eigenvalues and eigenfunctions of the Hamiltonian matrix were computed with an iterative Lanczos eigensolver.

Concerning the full-dimensional computations, it is necessary to reiterate some methodological details from Ref. 18 and to specify them for the case of the fluoride–methane complex. First of all, full-dimensional [12-dimensional (12D)] computations were possible for this complex because we used normal coordinates for the methane fragment together with harmonic oscillator basis functions, which provide a good zeroth-order description. Hence, the 9D product basis set of the methane fragment can be pruned,<sup>33</sup> i.e., we can discard high-energy basis functions. We used the simple

$$\sum_{i=1}^9 n_{q_i} \leq b \quad (3)$$

pruning condition for the harmonic oscillator indexes,  $n_{q_i}$ . Since several basis functions are discarded from the methane basis set complying with this condition, it is possible to substantially reduce also the number of quadrature points that are used to calculate the overlap and low-order polynomial integrals with the retained basis functions. Pruning the grid following this observation was first realized by Avila and Carrington<sup>19,20</sup> in vibrational computations using the Smolyak algorithm.

Concerning the 3-dimensional ion–molecule “intermolecular” part, described by the  $R, \cos \theta$ , and  $\phi$  coordinates, we retained the full direct-product basis and grid. For  $R$ , we used a Morse tridiagonal basis set constructed similarly to Ref. 18 but using the  $D_0 = 1975.27 \text{ cm}^{-1}$ ,  $\alpha = 0.9$ , and  $\gamma = 18$  parameter values, which correspond to the 1D cut of the current PES (all other coordinates fixed at their equilibrium value). The  $\cos \theta$  degree of freedom was described with sin-cot-DVR basis functions and quadrature points,<sup>31</sup> while we used Fourier functions for the  $\phi$  angle.

We used large basis sets and grids for the intermolecular degrees of freedom,  $(R, \cos \theta, \phi)$ , both in the 3D and in the 12D computations, which is necessary to ensure that the degeneracies (some of them obtained numerically, only) and tunneling splittings are well converged (*vide infra*). In order to converge the energies with respect to the intramolecular (methane) part of the basis and

**TABLE I.** Vibrational states,  $\bar{\nu}$  in  $\text{cm}^{-1}$ , of  $\text{CH}_4\text{-F}^-$  up to  $730 \text{ cm}^{-1}$  above the zero-point vibrational energy (ZPVE), corresponding to the full-dimensional PES of Ref. 8. Vibrational energies computed in the present work and values taken from the literature are shown together for comparison. The largest computed splitting for each vibrational manifold is given in parenthesis after the vibrational energy value. The most accurate vibrational band origins (from this work) are in column “ $\mathcal{B}_C$ : (25, 4).”

No.	$\Gamma(\text{MS})^{\text{d}}$	$\Gamma(\text{PG})^{\text{e}}$	$n_R^{\text{f}}$	Label <sup>g</sup>	12D GENIUSH–Smolyak (this work)			12D MCTDH	12D MULTIMODE <sup>a,8</sup>	3D GENIUSH <sup>10</sup>	3D GENIUSH (this work)
					$\mathcal{B}_A$ : (23,2) <sup>b,c</sup>	$\mathcal{B}_B$ : (23,3) <sup>b,c</sup>	$\mathcal{B}_C$ : (25,4) <sup>b,c</sup>	B3/B4 <sup>9</sup>			$G_{\text{fit}}^{\text{c,h}}$
					$[3.9 \cdot 10^5]^{\text{b}}$	$[1.6 \cdot 10^6]^{\text{b}}$	$[5.6 \cdot 10^6]^{\text{b}}$				
0–3	$A_1 \oplus F_2$	$A_1^{C_{3v}}$	0	ZPVE	9845.6 (0.0)	9799.1 (0.0)	9791.6 (0.0)	9786.5 (0.5)	9794.7	461.0 (0.0)	378.8 (0.0)
4–7	$A_1 \oplus F_2$	$A_1^{C_{3v}}$	1	$[v_s]$	193.2 (0.0)	193.4 (0.0)	193.6 (0.0)	194.4 (0.1)	201.1	182.5 (0.0)	194.5 (0.0)
8–15	$E \oplus F_1 \oplus F_2$	$E^{C_{3v}}$	0	$[v_b]$	266.3 (0.0)	268.3 (0.0)	267.6 (0.0)	271.7 (1.1)	299.9	284.5 (0.0)	267.7 (0.0)
16–19	$A_1 \oplus F_2$	$A_1^{C_{3v}}$	2	$[2v_s]$	378.0 (0.0)	378.7 (0.0)	379.2 (0.0)	380.6 (0.1)	391	355.8 (0.0)	380.3 (0.0)
20–27	$E \oplus F_1 \oplus F_2$	$E^{C_{3v}}$	1	$[v_s + v_b]$	452.7 (0.0)	454.8 (0.0)	454.3 (0.0)	460.2 (1.3)		458.8 (0.0)	455.2 (0.0)
28–31	$A_1 \oplus F_2$	$A_1^{C_{3v}}$	0	$[2v_b]$	506.7 (0.0)	509.8 (0.0)	509.1 (0.0)	528.7 (0.4)		533.0 (0.1)	509.8 (0.0)
32–39	$E \oplus F_1 \oplus F_2$	$E^{C_{3v}}$	0	$[2v_b]$	523.5 (0.2) <sup>i</sup>	527.0 (0.2) <sup>i</sup>	526.0 (0.0)	545.7 (2.1)		555.3 (0.1)	525.6 (0.0)
40–43	$A_1 \oplus F_2$	$A_1^{C_{3v}}$	3	$[3v_s]$	555.0 (0.0)	556.4 (0.0)	557.5 (0.0)			519.2 (0.0)	556.8 (0.0)
44–51	$E \oplus F_1 \oplus F_2$	$E^{C_{3v}}$	2	$[2v_s + v_b]$	630.3 (0.0)	632.8 (0.0)	632.7 (0.0)				633.6 (0.0)
52–55	$A_1 \oplus F_2$	$A_1^{C_{3v}}$	1	$[v_s + 2v_b]$	685.7 (0.0)	689.0 (0.0)	688.5 (0.0)				690.2 (0.0)
56–63	$E \oplus F_1 \oplus F_2$	$E^{C_{3v}}$	1	$[v_s + 2v_b]$	702.6 (0.2) <sup>i</sup>	706.2 (0.2) <sup>i</sup>	705.5 (0.0)				705.9 (0.0)
64–67	$A_1 \oplus F_2$	$A_1^{C_{3v}}$	4	$[4v_s]$	724.2 (0.0)	726.6 (0.0)	728.5 (0.0)				722.9 (0.0)
RMSD <sup>j</sup>					2.4	0.8	0	11.7	20.3	23.5	1.9

<sup>a</sup>Higher energy vibrations, including the 12 fundamental vibrations, are reported in Ref. 8, but they are beyond the (energy) range of the present GENIUSH–Smolyak computations.

<sup>b</sup> $(N_c, b)$ : short label for indicating the basis set size. The  $N_c$  value gives the number of the sin-cot-DVR functions used for  $\cos \theta$  and  $b$  is the basis pruning parameter,  $\sum_{i=1}^9 n_{q_i} \leq b$ . The  $R$  and  $\phi$  degrees of freedom are described by  $N_R = 8$  Morse tridiagonal and  $N_\phi = 39$  Fourier basis functions, respectively. The overall basis set size,  $[N_R N_c N_\phi (b + 9)!/b!9!]$ , is also shown.

<sup>c</sup>In the vibrational computations, we used atomic masses,  $m(\text{H}) = 1.007\,825\,032\,23 \text{ u}$ ,  $m(\text{C}) = 12 \text{ u}$ , and  $m(\text{F}) = 18.998\,403\,162\,73 \text{ u}$ .<sup>35</sup>

<sup>d</sup>Symmetry assignment (irrep decomposition) in the  $T_d(\text{M})$  molecular symmetry group of the complex.

<sup>e</sup>Symmetry assignment (irrep) within the  $C_{3v}$  point group of the equilibrium structure.

<sup>f</sup>Dominant overlap of the wave function with the  $n_R$ th state of a 1-dimensional vibrational model along the  $R$  degree of freedom (all other coordinates are fixed at their equilibrium value).  $n_R = 0, 1, 2, \dots$  labels the states of this 1D model in an increasing energy order.

<sup>g</sup>Qualitative description based on the nodal structure, overlap with lower-dimensional models, and symmetry assignment. These labels are used to compare the vibrational energies computed in the present work with earlier results.<sup>8–10</sup>

<sup>h</sup>Reduced-dimensionality model with active  $(R, \cos \theta, \phi)$  degrees of freedom fitted to reproduce the 12D GENIUSH–Smolyak  $\mathcal{B}_C$  result. The methane was treated as a regular tetrahedron, and we used  $r_{\text{PES}}(\text{C–H}) = 2.143\,624 \text{ bohr}$  in the PES (to reproduce well the stretches) and  $r_{\text{KEO}}(\text{C–H}) = 2.518\,620 \text{ bohr}$  in the KEO, which was necessary to obtain good bending energies.

<sup>i</sup>These splittings disappear upon increase of the intermolecular basis set.

<sup>j</sup>Root-mean-square deviation of the vibrational excitation energies (ZPVE not included) listed in the table (without considering the splittings) from the 12D GENIUSH–Smolyak  $\mathcal{B}_C$  result.



grid, we have carried out computations with increasing values of the  $b$  parameter,  $b = 2, 3$ , and  $4$ , in the basis pruning condition, Eq. (3), and determined a Smolyak grid that integrates exactly the overlap and fifth-order polynomials with all basis functions retained in the pruned basis.

Table I reports the computed vibrational energies in comparison with literature values. We estimate the vibrational excitation energies from the largest 12D computation, in column  $\mathcal{B}_C$ , to be converged within  $1 \text{ cm}^{-1}$ , and the (apparently very small) tunneling splittings are converged with an uncertainty lower than  $0.05 \text{ cm}^{-1}$ . Note that for  $b = 2$  and  $3$ , we used only 23 sin-cot-DVR basis functions,  $\mathcal{B}_A$  and  $\mathcal{B}_B$ , respectively, which results in a  $0.2\text{--}0.3 \text{ cm}^{-1}$  (artificial) splitting for some higher excited states, but this splitting is reduced to less than  $0.05 \text{ cm}^{-1}$  upon the increase of the basis set, which is reported in column  $\mathcal{B}_C$  of the table (25 sin-cot-DVR basis functions and  $b = 4$  basis-pruning parameter).

Finally, we mention that we were able to put together a “fitted” 3D model that reproduced the 12D GENIUSH–Smolyak vibrational band origins with an RMSD of  $1.9 \text{ cm}^{-1}$  (“ $G_{\text{fit}}$ ” in Table I). “ $G_{\text{fit}}$ ” was obtained by fine-tuning the regular tetrahedral methane structure used in the KEO and in the PES. In this “fitting” procedure, we obtained  $r_{\text{PES}}(\text{C–H}) = 2.143\,624$  bohrs to define the PES cut (which is slightly different from the value used in Ref. 10 and reproduces slightly better the 12D stretching excitations of the complex), but we had to use a (much) larger value in the KEO,  $r_{\text{KEO}}(\text{C–H}) = 2.518\,620$  bohrs (which corresponds to a much smaller effective rotational constant for the methane) to have a good agreement with the vibrational band origins especially for the bending excitations.

Note that “3D( $G_{\text{fit}}$ )” is merely a fitted model, which was designed to reproduce the 12D GENIUSH–Smolyak vibrational band origins and for which we deliberately used two adjustable parameters, the C–H distance in the KEO and in the PES. It differs in this two-parameter adjustment scheme from the “rigorous” 3D reduced-dimensionality treatment (for which only a single structure is selected) used in the first 3D computation of  $\text{CH}_4\text{–F}^-$  in Ref. 10.

### III. SYMMETRY ANALYSIS AND ASSIGNMENT OF THE VIBRATIONAL STATES

First of all, we assigned the computed states to irreducible representations (irreps) of the MS group of the complex. Then, we identified single molecular vibrations classified according to the PG symmetry of the equilibrium structure as groups of states close in energy (slightly) split due to the interaction (spread) of the wave function over the equivalent wells.

At the equilibrium structure of  $C_{3v}$  PG symmetry, one of the hydrogen atoms of the methane binds to the fluoride anion. Any of the four hydrogen atoms of the methane can bind to the fluoride, which gives rise to the four equivalent wells and these wells are connected with “surmountable” barriers. Thereby, the MS group of the complex is  $T_d(M)$ , for which the symmetry analysis of (the global minimum of)  $\text{CH}_4\text{–Ar}$ <sup>34</sup> is almost verbatim adapted.

In order to assign irrep labels to the  $\text{CH}_4\text{–F}^-$  vibrational states computed in the present work, we analyzed the wave function of the 3D fitted model computations (“3D  $G_{\text{fit}}$ ” column in Table I) and the labels were transferred to the 12D results based on the energy ordering (direct analysis of the 12D hybrid DVR-FBR computation would

have been prohibitively expensive). We assigned  $T_d(M)$  molecular symmetry labels to the 3D wave functions by computing their overlap with 2D coupled-rotor (CR) functions, labeled with  $[j, j]_{00}$  ( $j = 0, 1, \dots$ ),<sup>28,34</sup> where  $j$  is the angular momentum quantum number of the methane and the diatom (corresponding to the relative motion of the center of mass of the methane and the fluoride), coupled to a zero total angular momentum state. The characters and the irrep decomposition of the  $\Gamma^{\text{CR}}(j)$  representation spanned by the  $[j, j]_{00}$  coupled-rotor functions in  $T_d(M)$  are<sup>34</sup>

$$\begin{aligned}\Gamma^{\text{CR}}(0) &= A_1, \\ \Gamma^{\text{CR}}(1) &= F_2, \\ \Gamma^{\text{CR}}(2) &= E \oplus F_2, \\ \Gamma^{\text{CR}}(3) &= A_1 \oplus F_1 \oplus F_2, \\ \Gamma^{\text{CR}}(4) &= A_1 \oplus E \oplus F_1 \oplus F_2, \\ \Gamma^{\text{CR}}(5) &= E \oplus F_1 \oplus F_2, \\ \Gamma^{\text{CR}}(6) &= A_1 \oplus A_2 \oplus E \oplus F_1 \oplus 2F_2, \dots\end{aligned}\quad (4)$$

The (hindered) relative rotation of the molecule and the ion over the four wells gives rise to tunneling splittings of the vibrations, which can be classified by  $C_{3v}$  point-group labels of the symmetry of the local minima. (If there was no interaction between the wells, each vibrational state would be 4-fold degenerate due to this feature.) The MS group species within the tunneling manifold of the vibrational modes classified by the PG symmetries (irreps) are<sup>34</sup>

$$\begin{aligned}\Gamma(A_1^{C_{3v}}) &= A_1 \oplus F_2, \\ \Gamma(A_2^{C_{3v}}) &= A_2 \oplus F_1, \\ \Gamma(E^{C_{3v}}) &= E \oplus F_1 \oplus F_2.\end{aligned}\quad (5)$$

Note that we use the  $C_{3v}$  superscript for the PG irreps, i.e.,  $A_1^{C_{3v}}$ ,  $A_2^{C_{3v}}$ , and  $E^{C_{3v}}$ , in order to distinguish them from the MS group irreps, which are labeled with  $A_1$ ,  $A_2$ ,  $E$ ,  $F_1$ , and  $F_2$ . The result of this analysis for the computed vibrational wave functions is summarized in the “ $\Gamma(\text{MS})$ ” and “ $\Gamma(\text{PG})$ ” columns of Table I, respectively.

The fourth column, “ $n_R$ ,” of the table gives the index of the wave function of the 1D model with active  $R$  (all other coordinates fixed at their equilibrium value) for which the 3D wave function has the largest overlap. Hence, “ $n_R$ ” is an index for the excitation along the ion-molecule separation, which we were able to unambiguously assign for all states listed in the table (due to the weak coupling of the radial and angular degrees of freedom in this complex).

We also note that due to the small tunneling splittings, identification of the PG vibrations as a set of states of similar character and close in energy comprising the appropriate MS group species, Eq. (5), was also possible without ambiguities for all states listed in the table. (This may be contrasted with the floppy  $\text{CH}_4\text{–Ar}$  complex, for which unambiguous assignment of the PG vibrations beyond the zero-point state of the global minimum was hardly possible.<sup>34</sup>) Once the complete tunneling manifold was assigned and the PG symmetry was found, we attached a qualitative description to the states (listed in column “Label” in Table I) based on the nodal structure

along the ion-molecule separation coordinate  $R$ , i.e.,  $n$ th “stretching” excitation, labeled with  $v_s$ ,  $2v_s$ , etc. Excitations different from pure stretching excitation were termed “bending” in this qualitative description and were labeled with  $v_b$ ,  $2v_b$ , etc., or combinations of stretching and bending,  $v_s + v_b$ . Similar qualitative labels had been provided in earlier studies,<sup>9,10</sup> which we used to compare with our full-dimensional vibrational energies.

#### IV. COMPUTED VIBRATIONAL STATES

The 12D vibrational energies computed in the present work are reported in Table I (column “12D, GENIUSH–Smolyak”), and the best results are listed in column “ $\mathcal{B}_C$ : (25, 4)” of the table. The level of convergence and comparison with earlier work is addressed in the following paragraphs.

We observe a monotonic decrease in the zero-point vibrational energy (ZPVE) upon the increase in the  $b$  basis pruning parameter, which indicates that the computations are almost variational (the sin-cot-DVR basis and grid is large). Our best ZPVE value is  $9791.6\text{ cm}^{-1}$ . It is  $5.1\text{ cm}^{-1}$  larger than the 12D MCTDH result, which the authors of Ref. 9 claim to be a variational upper bound to the exact ZPVE. The 12D MULTIMODE ZPVE<sup>8</sup> is  $3.1\text{ cm}^{-1}$  ( $8.2\text{ cm}^{-1}$ ) larger than the lowest value obtained by us (by Ref. 9 using MCTDH). The totally symmetric ZPV state ( $A_1^{C_{3v}}$ ) is split by the relative rotation of the methane and the fluoride to an  $A_1$  and an  $F_2$  symmetry species, Eq. (5). The  $\mathcal{B}_C$  12D computation (numerically) reproduces the degeneracy of the  $F_2$  state within  $0.001\text{ cm}^{-1}$  and predicts a tunneling splitting (much) smaller than  $0.05\text{ cm}^{-1}$ .

At the same time, the MCTDH result for the ZPV manifold gives four states with energies differing by  $0.1\text{--}0.9\text{ cm}^{-1}$  (up to  $1.2\text{--}3.4\text{ cm}^{-1}$ , depending on the basis set), which suggests that the (intermolecular) basis or integration grid used in Ref. 9 was too small. For higher excited states, the (artificial) splittings increase to  $2\text{ cm}^{-1}$ ,<sup>9</sup> whereas our computations, using a large intermolecular basis set and grid, indicate that the tunneling splittings are smaller than  $0.05\text{ cm}^{-1}$ , and we obtain the triple degeneracies converged (numerically) better than  $0.001\text{ cm}^{-1}$ .

The small tunneling splittings obtained in the present work are in agreement with the earlier, 3D computations including the intermolecular ( $R, \cos\theta, \phi$ ) coordinates as active vibrational degrees of freedom using the GENIUSH program.<sup>10</sup> Although our results confirm the small splittings obtained in the 3D computation of Ref. 10, we observe larger deviations for the vibrational excitation energies (band origins) from the 3D results of Ref. 10. The first 7 vibrational excitations have a  $23.5\text{ cm}^{-1}$  root-mean-square deviation (RMSD) from our best 12D energies, which suggests that monomer (methane) flexibility effects are important.

A better agreement, with an  $11.7\text{ cm}^{-1}$  RMSD, is observed for the first 6 vibrational excitations in comparison with the 12D MCTDH result,<sup>9</sup> which accounts for the flexibility of the methane fragment and the motion of the fluoride over the four wells, but it is affected by incomplete convergence (manifested in the artificial splittings).

The three lowest-energy vibrational fundamentals obtained within a 12D but single-well treatment with MULTIMODE<sup>8</sup> has a (surprisingly) large,  $20.3\text{ cm}^{-1}$  RMSD, which suggests that despite the small tunneling splittings, a multiwell treatment is necessary for which the normal-coordinate representation is inadequate. It should

be noted that the largest deviation,  $32.3\text{ cm}^{-1}$ , is observed for the  $299.9\text{ cm}^{-1}$  vibration, and this is the state that had the worse convergence properties in the MULTIMODE computation (Table 5 of Ref. 8).

These observations suggest that although tunneling (and the corresponding splittings of the vibrational bands) is almost negligible up to  $725\text{ cm}^{-1}$  above ZPVE under an energy resolution of  $0.05\text{ cm}^{-1}$ , there is a non-negligible anharmonicity due to the quantum mechanical motion over the multiple wells. For these reasons, a well converged, full-dimensional variational treatment, carried out in the present work, appears to be necessary to capture all quantum dynamical features of this strongly bound ion-molecule complex.

#### V. EXCITED-STATE TUNNELING MANIFOLDS

For the ZPV and the lower-energy vibrations, we obtained tiny tunneling splittings ( $<0.05\text{ cm}^{-1}$ , Sec. IV). The question arises whether the energy splitting due to tunneling of the heavy fragments (heavier than the hydrogen atom) becomes more significant upon the vibrational excitation of the complex. The symmetry species in the tunneling manifold are specified in Eq. (5), but of course, the symmetry analysis by itself does not provide any information about the level energies and the size of the splittings.

The height of the barrier, separating the energy wells, can be indicative for the energy range above which we may expect larger splittings. Reference 9 estimated the barrier height connecting the equivalent wells to be  $\sim 1270\text{ cm}^{-1}$ , and we have pinpointed a lower barrier height,  $V_{\text{barrier}} = 1104\text{ cm}^{-1}$  at  $(\theta, \phi) = (90^\circ, 45^\circ)$  (see Fig. 2 of Ref. 10),  $R = 5.745$  bohrs, and  $(q_1, q_2, \dots, q_9) = (0, 0, 0, 0, -0.523, 0, 0, 0, -0.524)$ . It is an interesting question what the “most appropriate” value for the barrier height is (which is not an experimental observable) for comparison with our variational (fully anharmonic, multiwell) vibrational energies. In the present work, we have not attempted to include quantum nuclear corrections in the height and will continue using the purely electronic value. So, we expect the appearance of “sizeable” splittings at around  $\sim 1100\text{ cm}^{-1}$  measured from the PES minima, which is  $\sim 700\text{ cm}^{-1}$  above the intermolecular ZPVE (note that the different intermolecular models have somewhat different ZPVEs). Furthermore, it is necessary to remember that the methane’s bending vibration becomes important in the energy range near the isolated methane’s value at  $1311\text{ cm}^{-1}$  (above the ZPVE), which is an obvious limitation for the applicability of the 3D models and approaching this energy range will require a more efficient 12D treatment.

In order to explore the tunneling splittings and their dependence on the vibrational excitation, we have carried out extensive 3D and more limited (up to only lower vibrational excitations) 12D computations with large, (near) saturated angular basis sets (*vide infra*). The tunneling splittings obtained from the different computations are visualized in Figs. 1 and 2, and the energy lists are provided in the supplementary material.

We used the two types of 3D vibrational models to explore the excited-state tunneling manifold. First, we have carried out computations with the 3D reduced-dimensionality model used already in Ref. 10, cited in Table I, which corresponds to imposing rigorous geometrical constraints in the model through the Lagrangian in GENIUSH.<sup>14</sup> The fixed methane regular tetrahedral structure used in this 3D(rig) model was  $r(\text{C-H}) = 1.104\text{ \AA}$ ,<sup>10</sup> a value close to the

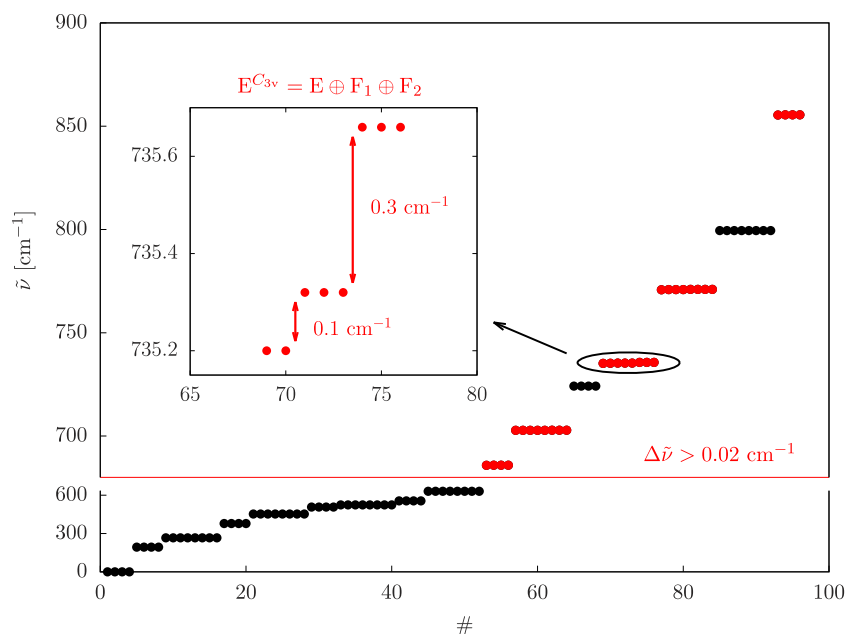


**FIG. 1.** 12D vibrational energies measured from the zero-point vibration. Vibrational levels with tunneling splittings,  $\Delta\tilde{\nu}$ , larger than  $0.02\text{ cm}^{-1}$  are highlighted in red. The position of the vibrational band origins may have an overall uncertainty as large as  $3\text{--}4\text{ cm}^{-1}$ , but the tunneling splittings within a band are converged better than  $0.02\text{ cm}^{-1}$  (see Fig. 2).

isolated methane's  $\langle r(\text{C-H}) \rangle_0$  value. Second, we have carried out computations using the  $3D(G_{\text{fit}})$  model designed (“fitted”) to minimize the RMSD of the vibrational band origins with respect to the 12D GENIUSH–Smolyak results up to  $730\text{ cm}^{-1}$  (Table I). In the largest 3D computations, we used 31 PO-DVR functions<sup>36–38</sup> for  $R$  obtained from  $\mathcal{L}_n^{(\alpha)}$  generalized Laguerre basis functions (with  $\alpha = 2$  and  $n = 0, 1, \dots, 399$ ) and grid points scaled to the  $R \in [2, 5]$  bohrs

interval; 61 sin-cot-DVR functions for the  $\cos\theta$  degree of freedom, which was constructed by extending the  $\cos(m\theta)$  ( $m = 0, \dots, 58$ ) basis set with the  $\sin(\theta)$  and the  $\sin(2\theta)$  functions,<sup>18,31</sup> and 121 Fourier (sine and cosine) functions for the  $\phi$  degree of freedom. This basis is highly saturated and represents a space comparable with the set of the  $Y_j^m(\theta, \phi)$  spherical harmonic functions with  $j = 0, \dots, 60$  and  $m = -j, \dots, j$ . These computations (for both 3D models)

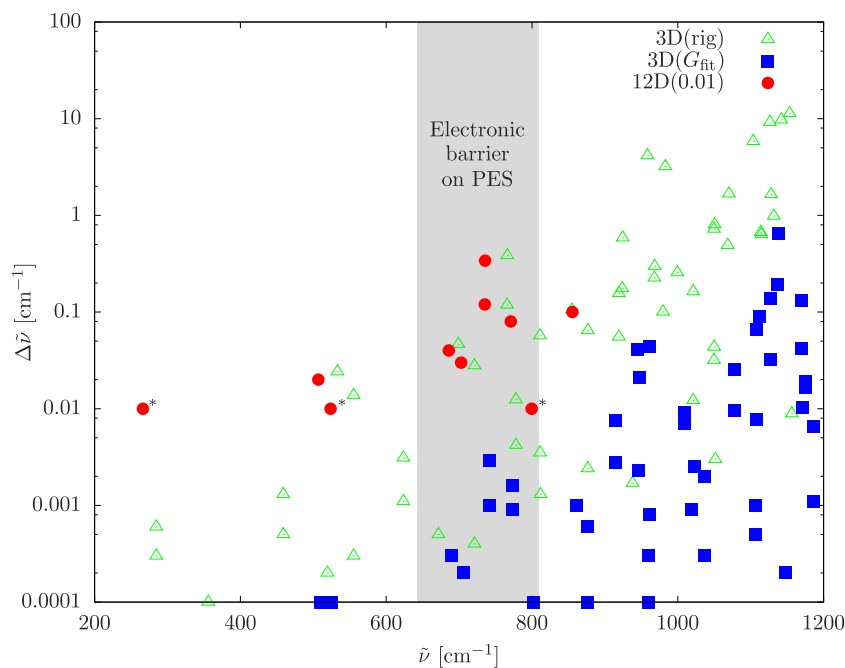


**FIG. 2.** Logarithm of the energy splitting,  $\Delta\tilde{\nu}$  in  $\text{cm}^{-1}$ , among the different symmetry species of the tunneling manifold, Eq. (5), shown with respect to the  $\tilde{\nu}$  energy of the vibrational state measured from the zero-point vibrational energy (ZPVE). The splittings from the rigorous 3D(rig) model, in green triangles, and the fitted 3D( $G_{\text{fit}}$ ) model, in blue squares, are converged with an uncertainty of  $0.0001\text{ cm}^{-1}$ . The 12D tunneling splittings, in red circles, are converged better than  $0.02\text{ cm}^{-1}$  (the splittings smaller than this value may be affected by numerical artifacts and are labeled with \* in the figure). The lowest electronic barrier on the CBB08 PES,  $1104\text{ cm}^{-1}$  above the minimum, measured from the intermolecular ZPVE is indicated with the gray shaded area (note that the intermolecular ZPVEs are different for the different models). The full list of the computed energies is available in the [supplementary material](#).

reproduce the triple degeneracies, which are spatial symmetry features not covered by the DVR grid but obtained numerically, within  $0.0001\text{ cm}^{-1}$  for all computed states.

In the 12D computation of the excited state splittings, we used a large angular representation (relative methane-ion rotation) to tightly converge the splittings, but we had to keep the methane basis small (due to the finite computational resources), which was sufficient to capture methane's flexibility effects on the splittings. So, we chose  $b = 2$  in the pruning condition of the methane basis (9D), and we used 8 tridiagonal-Morse basis functions and 10 Gauss-Laguerre-Morse points for  $R$ ; a large basis and grid for the angular motion including 31 sin-cot-DVR basis functions and points for  $\cos\theta$ ; and 45 Fourier basis functions and 48 trapezoidal points for  $\phi$ . So, this 12D basis set designed for the computation of the tunneling splittings (and henceforth labeled with  $\mathcal{B}_T$ ) included  $(2 + 9)!/2!/9! \times 8 \times 31 \times 45 = 613\,800$  functions, and the 12D Smolyak grid ( $H = 16$ ,  $D = 12$  dimensions) contained  $3481$  (for the  $\text{CH}_4$  monomer)  $\times 10 \times 31 \times 48 = 51\,797\,280$  points to calculate the integrals. The angular part of  $\mathcal{B}_T$  is more than 40% larger than that of  $\mathcal{B}_C$  in Table I, which provides the current benchmark for the vibrational band origins up to  $730\text{ cm}^{-1}$ . Although the uncertainty of the vibrational band origins for  $\mathcal{B}_T$  is  $3\text{--}4\text{ cm}^{-1}$  (due to the small  $b$  value), the 12D tunneling splittings are converged with an uncertainty better than  $0.02\text{ cm}^{-1}$  up to  $856\text{ cm}^{-1}$ , including 96 vibrational states.

The 12D computations show that the tunneling splittings increase upon the vibrational excitation of the complex, and we find several splittings larger than the  $0.02\text{ cm}^{-1}$  uncertainty threshold above  $\sim 680\text{ cm}^{-1}$  measured from the ZPVE (Fig. 1). It is interesting to note that this value is comparable with the value of the electronic barrier separating the equivalent wells, which is  $1104\text{ cm}^{-1}$  from the PES minimum and  $\sim 700\text{ cm}^{-1}$  measured from the intermolecular ZPVE (different models have different ZPVEs).

Figure 2 presents the 12D and the 3D splittings. The 3D( $G_{\text{fit}}$ ) model, which reproduces the known 12D vibrational band origins very well (Table I), predicts tunneling splittings orders of magnitude smaller than the 12D computation (notice the logarithmic scale in Fig. 2). At the same time, the 3D(rig) model (with rigorous geometrical constraints) appears to get the splittings right (currently, we have only a few points to compare), while it has a large error in predicting the vibrational centers (Table I), which may hinder the comparison of the 3D(rig) and 12D splittings at higher energies.

The differences between the different 3D treatments can be rationalized in terms of the difference of the "effective" rotational constant of methane in the computation (the small differences in the PES cut does not affect these results). In the 3D treatments, a "smaller" effective methane rotational constant appears to be necessary to have good vibrational centers, 3D( $G_{\text{fit}}$ ), and a "larger" methane rotational constant is necessary to have good tunneling splittings, 3D(rig). Altogether, these observations suggest that in order to have a correct overall description, it is necessary to explicitly account for the methane's vibrations together with the relative rotation of the methane and the fluoride ion.

## VI. SUMMARY AND CONCLUSIONS

Full-dimensional (12D), near-variational, vibrational states are reported for the strongly bound complex of the methane molecule and the fluoride anion. This is the first application of the recently

developed GENIUSH-Smolyak algorithm and computer program<sup>18</sup> with a fully coupled, high-dimensional potential energy surface.

Benchmark-quality vibrational band origins are computed with energies and tunneling splittings converged better than  $1\text{ cm}^{-1}$  and  $0.05\text{ cm}^{-1}$ , respectively. These computations confirm complementary aspects of earlier studies,<sup>8–10</sup> which relied on different assumptions or approximations about the dynamics of this complex. Regarding controversial aspects of earlier work, we can confirm that tunneling splittings (up to  $730\text{ cm}^{-1}$  above the zero-point energy) are small,<sup>10</sup>  $<0.05\text{ cm}^{-1}$ , but due to the strong binding and significant monomer distortions, a full-dimensional (12D) treatment is necessary.<sup>8,9</sup> Although the tunneling splittings are small, a single-well (normal coordinate) description<sup>8</sup> is not sufficient due to the significant anharmonicity of the multiwell potential energy landscape.<sup>9</sup> Even so, it is necessary to use a large basis set (and grid) to properly describe the relative, hindered rotation of the methane fragment and the fluoride anion.<sup>10</sup>

We also show from 12D computations that the tunneling splittings increase with the vibrational excitation of the complex. Both the 12D and approximate 3D rigid-monomer computations indicate that sizeable tunneling splittings,  $>0.1\text{ cm}^{-1}$ , appear near the "top of the barrier," which separates the equivalent wells. Interestingly, a "fitted" 3D model, which gives excellent vibrational band origins, predicts orders of magnitude smaller splittings than the 12D computation, while the rigorous, reduced-dimensionality 3D model gives reasonable splittings but fails to reproduce the 12D vibrational band energies.

With further progress of the quantum dynamics methodology reported in the present work and a potential energy surface with a broader coverage of the nuclear coordinates (especially, for the ion-molecule separation), it will become possible to study the effect of the methane vibrational excitation on the tunneling dynamics and the intramolecular to intermolecular energy transfer under predissociation.

## SUPPLEMENTARY MATERIAL

Tunneling splittings and vibrational energies obtained from 12D and 3D computations and the definition of normal coordinates of methane are provided in the [supplementary material](#).

## ACKNOWLEDGMENTS

Financial support of the Swiss National Science Foundation through a PROMYS Grant (No. IZ11Z0\_166525) is gratefully acknowledged. We also thank NIIFI for providing us computer time at the Miskolc node of the Hungarian Computing Infrastructure. E.M. is thankful to ETH Zürich for supporting a stay as visiting professor during 2019 and the Laboratory of Physical Chemistry for their hospitality, where part of this work has been completed.

We wish to dedicate this article to Professor Attila Császár on the occasion of his 60th birthday.

## REFERENCES

- <sup>1</sup>D. A. Wild, Z. M. Loh, and E. Bieske, *Int. J. Mass. Spectrom.* **220**, 273 (2002).
- <sup>2</sup>Z. M. Loh, R. L. Wilson, D. A. Wild, E. J. Bieske, and M. S. Gordon, *Aust. J. Chem.* **57**, 1157 (2004).
- <sup>3</sup>Z. M. Loh, L. Wilson, D. A. Wild, J. Bieske, J. M. Lisy, B. Njegic, and M. S. Gordon, *J. Phys. Chem. A* **110**, 13736 (2006).

- <sup>4</sup>D. M. Neumark, *J. Phys. Chem. A* **112**, 13287 (2008).
- <sup>5</sup>T. I. Yacovitch, E. Garand, J. B. Kim, C. Hock, T. Theis, and D. M. Neumark, *Faraday Discuss.* **157**, 399 (2012).
- <sup>6</sup>M. Cheng, Y. Feng, Y. Du, Q. Zhu, W. Zheng, G. Czako, and J. M. Bowman, *J. Chem. Phys.* **134**, 191102 (2011).
- <sup>7</sup>T. Westermann, J. B. Kim, M. L. Weichman, C. Hock, T. I. Yacovitch, J. Palma, D. M. Neumark, and U. Manthe, *Angew. Chem., Int. Ed.* **53**, 1122 (2014).
- <sup>8</sup>G. Czako, B. J. Braams, and J. M. Bowman, *J. Phys. Chem. A* **112**, 7466 (2008).
- <sup>9</sup>R. Wodraszka, J. Palma, and U. Manthe, *J. Phys. Chem. A* **116**, 11249 (2012).
- <sup>10</sup>C. Fábri, A. G. Császár, and G. Czako, *J. Phys. Chem. A* **117**, 6975 (2013).
- <sup>11</sup>J. M. Bowman, S. Carter, and X. Huang, *Int. Rev. Phys. Chem.* **22**, 533 (2003).
- <sup>12</sup>H.-D. Meyer, F. Gatti, and G. A. Worth, *MCTDH for Density Operator* (Wiley-Blackwell, 2009), Chap. 7, pp. 57–62, ISBN: 9783527627400.
- <sup>13</sup>M. Beck, A. Jackle, G. Worth, and H.-D. Meyer, *Phys. Rep.* **324**, 1 (2000).
- <sup>14</sup>E. Mátyus, G. Czako, and A. G. Császár, *J. Chem. Phys.* **130**, 134112 (2009).
- <sup>15</sup>C. Fábri, E. Mátyus, and A. G. Császár, *J. Chem. Phys.* **134**, 074105 (2011).
- <sup>16</sup>M. Quack and M. A. Suhm, *J. Chem. Phys.* **95**, 28 (1991).
- <sup>17</sup>W. Mizukami, S. Habershon, and D. P. Tew, *J. Chem. Phys.* **141**, 144310 (2014).
- <sup>18</sup>G. Avila and E. Mátyus, *J. Chem. Phys.* **150**, 174107 (2019).
- <sup>19</sup>G. Avila and J. T. Carrington, *J. Chem. Phys.* **131**, 174103 (2009).
- <sup>20</sup>G. Avila and J. T. Carrington, *J. Chem. Phys.* **134**, 054126 (2011).
- <sup>21</sup>G. Avila and J. T. Carrington, *J. Chem. Phys.* **135**, 064101 (2011).
- <sup>22</sup>D. Lauvergnat and A. Nauts, *Spectrochim. Acta, Part A* **119**, 18 (2014).
- <sup>23</sup>A. Nauts and D. Lauvergnat, *Mol. Phys.* **116**, 3701 (2018).
- <sup>24</sup>C. Fábri, E. Mátyus, and A. G. Császár, *Spectrochim. Acta* **119**, 84 (2014).
- <sup>25</sup>C. Fábri, J. Sarka, and A. G. Császár, *J. Chem. Phys.* **140**, 051101 (2014).
- <sup>26</sup>J. Sarka and A. G. Császár, *J. Chem. Phys.* **144**, 154309 (2016).
- <sup>27</sup>J. Sarka, A. G. Császár, S. C. Althorpe, D. J. Wales, and E. Mátyus, *Phys. Chem. Chem. Phys.* **18**, 22816 (2016).
- <sup>28</sup>J. Sarka, A. G. Császár, and E. Mátyus, *Phys. Chem. Chem. Phys.* **19**, 15335 (2017).
- <sup>29</sup>C. Fábri, M. Quack, and A. G. Császár, *J. Chem. Phys.* **147**, 134101 (2017).
- <sup>30</sup>I. Simkó, T. Szidarovszky, and A. G. Császár, *J. Chem. Theory Comput.* **15**, 4156 (2019).
- <sup>31</sup>G. Schiffl and U. Manthe, *Chem. Phys.* **374**, 118 (2010).
- <sup>32</sup>J. C. Light and T. Carrington, Jr., *Discrete-Variable Representations and Their Utilization* (John Wiley & Sons, Ltd., 2007), pp. 263–310.
- <sup>33</sup>R. J. Whitehead and N. C. Handy, *J. Mol. Spectrosc.* **55**, 356 (1975).
- <sup>34</sup>D. Ferenc and E. Mátyus, *Mol. Phys.* **117**, 1694 (2019).
- <sup>35</sup>J. S. Coursey, D. J. Schwab, J. J. Tsai, and R. A. Dragoset, *Atomic Weights and Isotopic Compositions (Version 4.1)* (National Institute of Standards and Technology, Gaithersburg, MD, 2015), <http://physics.nist.gov/Comp> (last accessed May 12, 2018).
- <sup>36</sup>H. Wei and T. Carrington, Jr., *J. Chem. Phys.* **97**, 3029 (1992).
- <sup>37</sup>J. Echave and D. C. Clary, *Chem. Phys. Lett.* **190**, 225 (1992).
- <sup>38</sup>V. Szalay, G. Czako, A. Nagy, T. Furtenbacher, and A. G. Császár, *J. Chem. Phys.* **119**, 10512 (2003).

# Toward breaking the curse of dimensionality in (ro)vibrational computations of molecular systems with multiple large-amplitude motions

Cite as: *J. Chem. Phys.* **150**, 174107 (2019); doi: [10.1063/1.5090846](https://doi.org/10.1063/1.5090846)

Submitted: 30 January 2019 • Accepted: 5 April 2019 •

Published Online: 2 May 2019



View Online



Export Citation



CrossMark

Gustavo Avila<sup>a)</sup>  and Edit Mátyus<sup>b)</sup> 

## AFFILIATIONS

Institute of Chemistry, ELTE, Eötvös Loránd University, Pázmány Péter sétány 1/A, Budapest 1117, Hungary

<sup>a)</sup>[Gustavo\\_Avila@telefonica.net](mailto:Gustavo_Avila@telefonica.net)

<sup>b)</sup>[matyus@chem.elte.hu](mailto:matyus@chem.elte.hu)

## ABSTRACT

Methodological progress is reported in the challenging direction of a black-box-type variational solution of the (ro)vibrational Schrödinger equation applicable to floppy, polyatomic systems with multiple large-amplitude motions. This progress is achieved through the combination of (i) the numerical kinetic-energy operator (KEO) approach of Mátyus *et al.* [*J. Chem. Phys.* **130**, 134112 (2009)] and (ii) the Smolyak nonproduct grid method of Avila and Carrington, Jr. [*J. Chem. Phys.* **131**, 174103 (2009)]. The numerical representation of the KEO makes it possible to choose internal coordinates and a body-fixed frame best suited for the molecular system. The Smolyak scheme reduces the size of the direct-product grid representation by orders of magnitude, while retaining some of the useful features of it. As a result, multidimensional (ro)vibrational states are computed with system-adapted coordinates, a compact basis- and grid-representation, and an iterative eigensolver. Details of the methodological developments and the first numerical applications are presented for the CH<sub>4</sub>-Ar complex treated in full (12D) vibrational dimensionality.

Published under license by AIP Publishing. <https://doi.org/10.1063/1.5090846>

## I. INTRODUCTION

Molecular systems with many vibrational degrees of freedom, including multiple fluxional modes, have been challenging for nuclear motion theory (also known as quantum dynamics) for decades. These systems are difficult to handle because (1) they require a curvilinear coordinate representation for which we might not have an analytic kinetic energy operator (KEO) readily available; (2) their wave functions are spread over multiple wells of the potential energy surface (PES); and (3) assume the evaluation of high-dimensional (sometimes singular) integrals due to the multiple, coupled (curvilinear) internal degrees of freedom.

There are important, high-dimensional molecular systems with multiple, large-amplitude motions. For example, molecular complexes belong to this class. Molecular complexes are prototypes for molecular interactions, and they can be probed in high-resolution spectroscopy experiments. Weakly bound complexes have a shallow PES valley, so they exhibit only a few, low-energy transitions between bound states, but they usually have a rich

predissociation spectrum which can be probed in overtone spectroscopy experiments.

The theory of molecular complexes has been restricted to the explicit quantum mechanical description of the intermonomer modes, while the monomers were held fixed, described with some rigid, effective structure.<sup>1,2</sup> An explicit consideration of monomer flexibility effects<sup>3,4</sup> has come to the focus only in recent years.<sup>5–7</sup> This is not surprising: adding the monomer degrees of freedom to the quantum dynamics treatment rapidly increases the vibrational dimensionality, while in molecular complexes, monomer flexibility effects are usually small, so they can be averaged upon a first look at the system. At the same time, the flexibility of monomers, through the kinetic and the potential energy couplings, plays a central role in the energy transfer between the intermolecular and the intramolecular degrees of freedom during the (ro)vibrational and collision dynamics.

Motivation for the present work is provided by these ideas, but we hope that the methodological developments described in this article will become useful for solving the (ro)vibrational Schrödinger

equation of (high-dimensional, floppy) molecular systems, in general.

## II. CURSE OF DIMENSIONALITY IN VIBRATIONAL COMPUTATIONS

We focus in the present work on the variational solution of the Schrödinger equation including the (ro)vibrational Hamiltonian of  $D$  vibrational degrees of freedom,  $\xi = (\xi_1, \dots, \xi_D)$ ,

$$\hat{H}_{\text{vib}}\Psi_i(\xi_1, \dots, \xi_D) = E_i\Psi_i(\xi_1, \dots, \xi_D), \quad (1)$$

where the vibrational wave function is expanded as a linear combination of  $N_{\text{bas}}$  orthogonal basis functions

$$\Psi_i(\xi_1, \dots, \xi_D) = \sum_{n=0}^{N_{\text{bas}}} C_n^i \psi_n(\xi_1, \dots, \xi_D), \quad (2)$$

and the expansion coefficients  $C_n^i$  are obtained as the elements of the eigenvectors of the Hamiltonian matrix. The Hamiltonian matrix elements are computed with some appropriate (multidimensional) integration scheme. If the basis set is well chosen in this finite basis representation (FBR) scheme, the lowest eigenvalues of the Hamiltonian matrix converge to the exact energies by increasing  $N_{\text{bas}}$ . The most common way to build the multidimensional basis functions is to use a direct-product ansatz

$$\psi_n(\xi_1, \dots, \xi_D) = \prod_{\chi=1}^D \psi_{n_\chi}^{(\chi)}(\xi_\chi) \quad (3)$$

constructed from the  $\psi_{n_\chi}^{(\chi)}(\xi_\chi)$  orthogonal basis functions.

### A. Curse of dimensionality due to the multidimensional vibrational basis

By adopting a direct-product basis set, the vibrational wave functions are represented as a linear combination

$$\Psi_i(\xi_1, \dots, \xi_D) = \sum_{n_1=0}^{N_1^{\text{max}}} \dots \sum_{n_D=0}^{N_D^{\text{max}}} C_{n_1, \dots, n_D}^i \prod_{\chi=1}^D \psi_{n_\chi}^{(\chi)}(\xi_\chi), \quad (4)$$

in which the number of terms (multidimensional basis functions) scales exponentially with the vibrational dimensionality,  $N_{\text{bas}} = \prod_{\chi=1}^D (N_\chi^{\text{max}} + 1)$ . For low-dimensional systems, this is not a problem, but many challenging systems are high dimensional. Our example system  $\text{CH}_4\cdot\text{Ar}$  has twelve vibrational degrees of freedom. For a 12-dimensional (12D) problem, if we pick 10 basis functions per coordinate (a reasonable starting point if the coordinates are equally coupled), the number of product basis functions will be  $10^{12}$ . In this representation, we would need to store a vector with  $10^{12}$  elements to represent a single vibrational state, which would require  $\sim 7.3$  TB of memory in double precision arithmetics. For this reason, beyond  $\sim 9$  vibrational dimensions, it is necessary to develop and use methods which attenuate the curse of dimensionality in the basis set.

There are different strategies for breaking the exponential growth of the vibrational basis. The first option is to improve the quality of the basis functions in order to decrease the number of functions per coordinate, at least for a subset of the coordinates. The second option is to find a way to identify and discard the basis functions from the direct-product basis set, which

have little effect on the accuracy of the computed eigenvalues. The first alternative is efficiently realized by the multiconfiguration time-dependent Hartree (MCTDH) method<sup>8,9</sup> and the canonical polyadic (CP) approach<sup>10–12</sup> or in a contracted basis representation obtained by solving reduced-dimensionality eigenproblems.<sup>13–15</sup> The second alternative is achieved by finding physically motivated restrictions on the basis set indices. These restrictions can be as simple as the selection of an appropriate multipolyad,<sup>16,17</sup>  $f(n_1, \dots, n_D) \leq b$ , for which the wave function expansion reads as

$$\Psi_i(\xi_1, \dots, \xi_D) = \sum_{f(n_1, \dots, n_D) \leq b} C_{n_1, \dots, n_D}^i \prod_{\chi=1}^D \psi_{n_\chi}^{(\chi)}(\xi_\chi). \quad (5)$$

This basis-pruning strategy will be used later in this work. More elaborate basis-pruning restrictions are used, for example, in the MULTIMODE program.<sup>18,19</sup>

### B. Curse of dimensionality due to multidimensional integrals

Reducing the number of the multidimensional basis functions solves only half of the problem. In (ro)vibrational computations, multidimensional integrals must be evaluated to construct the Hamiltonian matrix.

There are two common ways to cope with the integral problem. The first option is to expand the Hamiltonian in a Sum-of-Products (SOP) form. For example, the potential energy in a SOP form is

$$\hat{V}(\xi) = \sum_{m_1=0}^{M_1^{\text{max}}} \dots \sum_{m_D=0}^{M_D^{\text{max}}} A_{m_1, \dots, m_D} \prod_{\chi=1}^D \mathcal{V}_{m_\chi}^{(\chi)}(\xi_\chi). \quad (6)$$

Using the SOP form, multidimensional integrals are obtained as the sum of products of 1-dimensional (1D) integrals

$$\begin{aligned} \langle \psi_{n'_\chi}^{(\chi)} | \mathcal{V}_{m_\chi}^{(\chi)} | \psi_{n_\chi}^{(\chi)} \rangle &= \int \psi_{n'_\chi}^{(\chi)}(\xi_\chi) \mathcal{V}_{m_\chi}^{(\chi)}(\xi_\chi) \psi_{n_\chi}^{(\chi)}(\xi_\chi) d\xi_\chi \\ &\approx \sum_{k_\chi=1}^{K_{\text{quad}}} w_{\chi, k_\chi} \psi_{n'_\chi}^{(\chi)}(\xi_{\chi, k_\chi}) \mathcal{V}_{m_\chi}^{(\chi)}(\xi_{\chi, k_\chi}) \psi_{n_\chi}^{(\chi)}(\xi_{\chi, k_\chi}), \end{aligned} \quad (7)$$

which is evaluated with a 1D numerical quadrature using the  $w_{\chi, k_\chi}$  and  $\xi_{\chi, k_\chi}$  quadrature weights and points, respectively, defined for the  $\xi_\chi$  coordinate (in this work, we account for the Jacobian in the wave function). The integrals converge to their exact value upon the increase in the number of quadrature points,  $K_{\text{quad}}$ . The SOP form is useful when a small number of terms are sufficient in Eq. (6) to represent the Hamiltonian. This form is usually employed in MCTDH and in the CP method.<sup>8–12</sup> There are methods which can find an excellent “basis set” for the SOP representation of the Hamiltonian.<sup>20</sup> If the SOP representation, however, requires an excessive number of function evaluations over a multidimensional grid of the vibrational coordinates, the exponential scale-up with the dimension is reintroduced. This feature is related to the fact that a SOP representation of the Hamiltonian can be as expensive as the representation of the multidimensional wave function. In any case, an effective way for attenuating this type of curse of dimensionality was proposed in Ref. 20.

As an alternative to a sum-of-product representation of the Hamiltonian, one can approximate it with a truncated multimode

expansion of  $n$ th-order terms.<sup>12,18,19,21</sup> For example, a five-mode expansion of the potential energy is

$$\begin{aligned}
 V(\xi_1, \dots, \xi_D) = & \sum_{i=1}^D V^i(\xi_i) + \sum_{i=1}^D \sum_{j=i}^D V^{ij}(\xi_i, \xi_j) \\
 & + \sum_{i=1}^D \sum_{j=i}^D \sum_{k=j}^D V^{ijk}(\xi_i, \xi_j, \xi_k) \\
 & + \sum_{i=1}^D \sum_{j=i}^D \sum_{k=j}^D \sum_{l=k}^D V^{ijkl}(\xi_i, \xi_j, \xi_k, \xi_l) \\
 & + \sum_{i=1}^D \sum_{j=i}^D \sum_{k=j}^D \sum_{l=k}^D \sum_{m=l}^D V^{ijklm}(\xi_i, \xi_j, \xi_k, \xi_l, \xi_m). \quad (8)
 \end{aligned}$$

This expansion is exact if  $n = D$ , but under certain circumstances (also depending on the  $\xi_1, \dots, \xi_D$  coordinates), it is very well converged with  $n < D$ . Using this approximation, the integrals are evaluated using a  $D = 1, 2, \dots, n$  dimensional direct-product Gauss quadrature, and thereby, the curse of dimensionality is attenuated.

If we want to use the Hamiltonian directly, without approximating or expanding it, we have to tackle the direct evaluation of multidimensional integrals by the multidimensional quadrature. In this case, the integral of the potential energy over a multidimensional basis set is evaluated as

$$\begin{aligned}
 & \int \dots \int \prod_{\chi'=1}^D \psi_{n_{\chi'}}^{(\chi')}(\xi_{\chi'}) V(\xi_1, \dots, \xi_D) \prod_{\chi=1}^D \psi_{n_{\chi}}^{(\chi)}(\xi_{\chi}) d\xi_1 \dots d\xi_D \\
 & \approx \sum_{K=1}^{K_{\text{quad}}} w_K \prod_{\chi'=1}^D \psi_{n_{\chi'}}^{(\chi')}(\xi_{\chi', k_{\chi'}}) V(\xi_{1, k_1}, \dots, \xi_{D, k_D}) \prod_{\chi=1}^D \psi_{n_{\chi}}^{(\chi)}(\xi_{\chi, k_{\chi}}), \quad (9)
 \end{aligned}$$

where  $w_k$  is the multidimensional quadrature weight for the  $\xi_{\chi, k_{\chi}}$  points; we used the condensed summation index  $K \leftrightarrow (k_1, k_2, \dots, k_D)$ . The integral approaches its exact value as the  $K_{\text{quad}}$  number of points is increased. The most common multidimensional quadrature is the multidimensional direct-product quadrature

$$\begin{aligned}
 & \int \dots \int F(\xi_1, \dots, \xi_D) d\xi_1 \dots d\xi_D \\
 & \approx \sum_{k_1=1}^{K_1^{\text{max}}} \dots \sum_{k_D=1}^{K_D^{\text{max}}} w_{1, k_1} \dots w_{D, k_D} F(\xi_{1, k_1}, \dots, \xi_{D, k_D}), \quad (10)
 \end{aligned}$$

where  $w_{\chi, k_{\chi}}$  and  $q_{\chi, k_{\chi}}$  ( $\chi = 1, \dots, D$ ) are the 1D quadrature weights and points for the  $\chi$ th coordinate, respectively. 1D quadrature rules are most often Gauss (G) quadrature rules, which integrate exactly

$$\int w(\xi) F(\xi) d\xi = \sum_{k=1}^{K_{\text{quad}}^G} w_k^G F(\xi_k^G), \quad \text{for any } F(\xi) = \sum_{n=0}^{2(K_{\text{quad}}^G - 1)} A_n \xi^n, \quad (11)$$

and  $d = 2(K_{\text{quad}}^G - 1)$  is called the (1D) accuracy of the Gauss quadrature.

A multidimensional direct-product quadrature integration suffers from a similar curse of dimensionality problem as a multidimensional direct-product basis set: the number of quadrature

points,  $K_{\text{quad}} = \prod_{\chi=1}^D K_{\chi}^{\text{max}}$ , increases exponentially with the vibrational dimensionality. To continue the 12D example from Sec. II A in which we had 10 basis functions per coordinate, we choose 13 quadrature points per coordinate (a reasonable value) to evaluate the integrals. Then, the number of points in a direct-product grid is  $2.33 \times 10^{13}$ . Storage of this many double-precision numbers would require 170 TB.

As it was explained earlier, the curse of dimensionality in the basis set can be attenuated by identifying and discarding the product basis functions, which are not necessary for the desired precision of the vibrational states. Then, we may think about attenuating the curse of dimensionality in the quadrature grid by using grids which have a nonproduct structure. In general terms, the application of nonproduct quadrature grids can be justified if the integrand  $I(\xi_1, \dots, \xi_D)$  is smooth, i.e., it can be expanded with respect to a pruned, product basis set,

$$I(\xi_1, \dots, \xi_D) = \sum_{f(n_1, \dots, n_D) \leq b} \mathcal{I}_{n_1, \dots, n_D} \prod_{\chi=1}^D \Phi_{n_{\chi}}^{(\chi)}(\xi_{\chi}). \quad (12)$$

For smooth functions, it makes sense to distinguish between *necessary* product basis functions

$$\prod_{\chi=1}^D \Phi_{n_{\chi}}^{(\chi)}(\xi_{\chi}), \quad \text{with } f(n_1, \dots, n_D) \leq b, \quad (13)$$

and *non-necessary* product basis functions

$$\prod_{\chi=1}^D \Phi_{n_{\chi}}^{(\chi)}(\xi_{\chi}), \quad \text{with } f(n_1, \dots, n_D) > b. \quad (14)$$

The total number of necessary and non-necessary product basis functions scales exponentially with the dimension, and this is the reason why the total number of product quadrature grid points, which integrate the overlap of all these functions exactly, also scales exponentially with the dimension. If we need to integrate accurately only the *necessary* product basis functions, the number of which does not grow exponentially with the dimensionality, it is possible to find a multidimensional quadrature, which integrates exactly only the necessary basis functions and which does not grow exponentially with the dimension. In such an approach, the curse of dimensionality in the integration grid can be attenuated, i.e.,

$$\begin{aligned}
 & \int \dots \int F(\xi_1, \dots, \xi_D) d\xi_1 \dots d\xi_D \approx \sum_{m=1}^{K_{\text{quad}}} w_m F(\xi_{1, m_1}, \dots, \xi_{D, m_D}), \\
 & \text{with } K_{\text{quad}} \ll \prod_{\chi=1}^D K_{\chi}^{\text{max}}, \quad (15)
 \end{aligned}$$

during the course of the evaluation of the Hamiltonian terms (without approximating by some expansion). Optimal nonproduct quadratures exist for special cases; two of them are explained in the following paragraphs.

### 1. An optimal, two-dimensional, nonproduct quadrature

The most popular nonproduct quadrature grid is probably the Lebedev quadrature designed to integrate spherical harmonics.<sup>22</sup>



Lebedev grids are used in density functional theory,<sup>23</sup> and they have been used also in rovibrational computations.<sup>24</sup> In particular, if we want to obtain the exact value of all integrals, related to the overlap of the spherical harmonics functions, by numerical integration

$$\int_0^\pi d\theta \int_0^{2\pi} d\phi Y_{l,m}(\theta, \phi) Y_{l',m'}(\theta, \phi) \sin(\theta),$$

with  $l, l' \leq l^{\max}$  and  $m, m' \leq m^{\max}$ , (16)

we would need to use a total number of  $2(l^{\max} + 1)^2$  grid points in the two-dimensional direct-product grid composed of Gauss–Legendre quadrature points for the  $\theta$  and Gauss–Chebyshev (first kind) quadrature points for the  $\phi$  coordinate. Note that in the expansion of the  $Y_{l,m}(\theta, \phi) Y_{l',m'}(\theta, \phi) \sin(\theta)$  integrand in terms of the product-basis functions, one has to comply with the two restrictions  $m \leq l$  and  $m' \leq l'$ . By taking into account these two restrictions, a (smaller) nonproduct quadrature grid, called the Lebedev grid, can be constructed for the numerical integration which includes only

$$N_{\text{Leb}} \sim \frac{4}{3} (l^{\max} + 1)^2 \quad (17)$$

points, instead of the  $2(l^{\max} + 1)^2$  points of the 2D direct-product grid. For example, for  $l^{\max} = 5$ , there are a total number of 36 spherical harmonics functions. To calculate exactly the overlap of these functions, we would need  $2(5 + 1)^2 = 72$  points in the 2D direct-product grid, whereas it is sufficient to use 50 ( $\sim 4/3 \cdot (5 + 1)^2 = 48$ ) Lebedev points.<sup>22</sup> Note that there is not any general formula for the Lebedev quadrature, but the weights and points are tabulated for several two-dimensional maximum accuracy values.

## 2. An optimal, three-dimensional, nonproduct quadrature

Our next example is about the calculation of the exact value of the overlap integrals in a numerical integration scheme for products of harmonic oscillator functions

$$\int_{-\infty}^{\infty} \int_{-\infty}^{\infty} \int_{-\infty}^{\infty} H_l(q_1) H_{l'}(q_1) H_m(q_2) H_{m'}(q_2) H_n(q_3) H_{n'}(q_3) \times e^{-q_1^2 - q_2^2 - q_3^2} dq_1 dq_2 dq_3, \quad (18)$$

$$\text{with the restrictions } l + n + m \leq 4 \text{ and } l' + n' + m' \leq 5, \quad (19)$$

where  $H_n$  is the  $n$ th Hermite polynomial. The smallest, 3D Gauss–Hermite direct-product grid, which recovers the exact value for all these integrals, contains  $5^3 = 125$  points. By explicitly considering the restrictions in Eq. (19), we may realize that there are only 56 different product functions in the integrand. The smallest nonproduct grid (for a maximum multidimensional accuracy of 9), which recovers the exact value of the integrals for the possible integrands, consists of only 77 points.<sup>25</sup> We note that the corresponding Smolyak grid consists of 93 points, which is less than the direct-product grid but more than the optimal nonproduct grid.

In spite of the fact that the optimal multidimensional, nonproduct quadratures use the smallest number of points, they have some handicaps. First, the construction of optimal, nonproduct quadratures may be cumbersome. There are only a limited number of cases for which the optimal multidimensional quadrature is tabulated in the literature (in practice, limited to  $D = 2$  or 3 for the available cases):<sup>25</sup> the points and weights are available only for certain types of polynomials and for limited values of a maximum multidimensional accuracy. Second, optimal nonproduct quadratures lack any structure, which is a serious disadvantage in rovibrational applications.<sup>24</sup> If a nonproduct grid has some structure (reminiscent of a direct-product grid), then it can be used to compute sums over the 1D quadrature points sequentially, which is an important algorithmic element in efficient variational vibrational approaches.

## 3. The Smolyak scheme for nonproduct grids with a structure

There is a simple way to construct nonproduct quadrature grids, first proposed by the Russian mathematician Sergey A. Smolyak. The Smolyak grid may be slightly larger than the optimal nonproduct grid, but it retains some useful features of direct-product grids. The Smolyak scheme was first adopted for solving the (ro)vibrational Schrödinger equation by Avila and Carrington in 2009<sup>16,17</sup> who exploited that the Smolyak grid is built from a sequence of quadrature rules and its special structure makes it possible to compute the potential and kinetic energy matrix-vector products by doing sums sequentially. It is possible to combine the Smolyak algorithm with optimal nonproduct grids of Stroud,<sup>25</sup> i.e., nonproduct Smolyak quadrature grids of high-dimensional systems can be constructed from sequences of Stroud-kind nonproduct quadratures (if the desired Stroud quadrature is available). Although the Stroud–Smolyak grids have less structure, they require fewer points than Smolyak quadratures built from 1D quadrature rules. This direction has been pursued in (ro)vibrational computations by Lauvergnat since 2014.<sup>26</sup>

## III. DEFINITION OF THE (RO)VIBRATIONAL HAMILTONIAN IN GENIUSH

The GENIUSH protocol, as it was proposed in 2009,<sup>27</sup> aimed for the development of a universal and exact procedure for the (near-)variational solution of the (ro)vibrational Schrödinger equation. Its central part is the numerical construction of the kinetic energy terms over a grid—thereby, the burdensome derivation and implementation of the kinetic energy operator for various molecular and coordinate choices were eliminated. The GENIUSH program was developed using the discrete variable representation (DVR),<sup>28</sup> and it suffered from the curse of dimensionality (Sec. II). The present work aims for the elimination of this bottleneck, both with respect to the basis and the grid representations, using the ideas first described by Avila and Carrington in 2009.<sup>16</sup>

### A. Numerical representation of the kinetic-energy operator

The GENIUSH program determines the KEO coefficients numerically, over a grid, from the user's definition of the vibrational

coordinates,  $\xi_i$  ( $i = 1, 2, \dots, D$ ) (and the body-fixed frame definition, which is relevant for rovibrational computations). Arbitrary coordinates and frames can be defined by writing down the Cartesian coordinates (in the body-fixed frame) in terms of the vibrational coordinates,  $\xi_i$  ( $i = 1, 2, \dots, D$ ). From this coordinate conversion subroutine (written by the user if not yet available in the code), the program numerically evaluates the mass-weighted metric tensor,  $\mathbf{g} \in \mathbb{R}^{(D+3) \times (D+3)}$ , from the vibrational and the rotational  $\mathbf{t}$  vectors over the coordinate grid. The vibrational  $\mathbf{t}$  vectors are obtained by two-sided finite differences for which a step size of  $10^{-5}$ – $10^{-7}$  a.u. has been used. In principle, the numerical but exact differentiation scheme of Yachmenev and Yurchenko<sup>29</sup> (using chain rule sequences and the derivatives of “all” possible elementary functions and thereby extending Ref. 30) could also be used to eliminate the numerical differentiation step.

The  $\mathbf{G}$  matrix is calculated by inverting  $\mathbf{g}$ ,  $\mathbf{G} = \mathbf{g}^{-1} \in \mathbb{R}^{(D+3) \times (D+3)}$ , over the grid points of the vibrational coordinates. In this notation, the last three rows and columns of  $\mathbf{g}$  and  $\mathbf{G}$  correspond to the rotational coordinates. The vibrational kinetic-energy operator has usually been written in the Podolsky form<sup>31</sup>

$$\hat{T}_{\text{Pod}}^v = -\frac{1}{2} \sum_{i=1}^D \sum_{j=1}^D \tilde{g}^{-1/4} \frac{\partial}{\partial \xi_i} G_{ij} \tilde{g}^{-1/2} \frac{\partial}{\partial \xi_j} \tilde{g}^{-1/4} \quad (20)$$

with  $\tilde{g} = \det \mathbf{g}$  because it requires the calculation of only first coordinate derivatives. The volume element for this Hamiltonian<sup>27,31,32</sup> and for all its rearranged variants, Eqs. (21), (24), and (51) appearing later in this article, is  $dV = \prod_{i=1}^D d\xi_i$ . Reference 27 also used a general but “rearranged” form of the (ro)vibrational Hamiltonian

$$\hat{T}_{\text{rearr}}^v = -\frac{1}{2} \sum_{i=1}^D \sum_{j=1}^D \frac{\partial}{\partial \xi_i} G_{ij} \frac{\partial}{\partial \xi_j} + U, \quad (21)$$

$$\text{with } U = \frac{1}{32} \sum_{kl=1}^D \left[ \frac{G_{kl}}{\tilde{g}^2} \frac{\partial \tilde{g}}{\partial \xi_k} \frac{\partial \tilde{g}}{\partial \xi_l} + 4 \frac{\partial}{\partial \xi_k} \left( \frac{G_{kl}}{\tilde{g}} \frac{\partial \tilde{g}}{\partial \xi_l} \right) \right], \quad (22)$$

$$= \frac{1}{32} \sum_{kl=1}^D \left[ \frac{G_{kl}}{\tilde{G}^2} \frac{\partial \tilde{G}}{\partial \xi_k} \frac{\partial \tilde{G}}{\partial \xi_l} - 4 \frac{\partial}{\partial \xi_k} \left( \frac{G_{kl}}{\tilde{G}} \frac{\partial \tilde{G}}{\partial \xi_l} \right) \right], \quad (23)$$

which can be further rearranged to

$$\hat{T}_{\text{rearr}}^v = -\frac{1}{2} \sum_{i=1}^D \sum_{j=1}^D G_{ij} \frac{\partial}{\partial \xi_i} \frac{\partial}{\partial \xi_j} - \frac{1}{2} \sum_{j=1}^D B_j \frac{\partial}{\partial \xi_j} + U, \quad (24)$$

$$\text{with } B_j = \sum_{i=1}^D \frac{\partial}{\partial \xi_i} G_{ij}. \quad (25)$$

This last form was used by Lauvergnat and Nauts in their numerical KEO approach.<sup>30</sup> Equations (21)–(25) require third-order derivatives of the coordinates, which are obtained in GENIUSH by using quadruple precision arithmetic to ensure numerical stability for the finite differences. All functions appearing next to the differential operators in Eqs. (20)–(25) have been available from the original implementation,<sup>27</sup> so we were able to change between different KEO representations, which has turned out to be necessary for this work (*vide infra*).

As a first step for implementing the Smolyak algorithm, we had to replace the original DVR implementation with FBR because we

wanted to discard functions from the direct product using simple, physical arguments, e.g., to restrict the basis to a certain (multi) polyad [Eq. (5)].

It is important to notice that the application of the Podolsky form [Eq. (20)] assumes the insertion of multiple (truncated) resolutions of identities in the basis during the construction of the KEO representation. In our earlier DVR applications, this did not cause any problem, but since we are aiming for a compact FBR, an accurate representation of the Podolsky form could be ensured only if an auxiliary basis set was introduced to converge the completeness relation

$$\hat{I} \approx \sum_{n=0}^{N_{\text{max}}} |n\rangle \langle n|. \quad (26)$$

For example, in a 3D FBR computation with a basis set

$$|n_1, n_2, n_3\rangle, \quad 0 \leq n_1 \leq N_1^{\text{max}}, \quad 0 \leq n_2 \leq N_2^{\text{max}}, \quad 0 \leq n_3 \leq N_3^{\text{max}}, \quad (27)$$

the matrix-vector products

$$\begin{aligned} v^1 &= \tilde{g}^{-1/4} v^0, \\ v^2 &= G_{ij} \tilde{g}^{1/2} \frac{\partial}{\partial \xi_j} v^1 \end{aligned} \quad (28)$$

would have to be expanded with respect to a larger, basis

$$\begin{aligned} &|n_1, n_2, n_3\rangle : \\ &0 \leq n_1 \leq N_1^{\text{max}} + m, \quad 0 \leq n_2 \leq N_2^{\text{max}} + m, \quad 0 \leq n_3 \leq N_3^{\text{max}} + m, \end{aligned} \quad (29)$$

where  $m$  is determined by the coordinate-dependence of the  $\tilde{g}^{-1/4}$  and  $G_{ij} \tilde{g}^{1/2}$  multidimensional functions. For the example of the  $\text{H}_2\text{O}$  molecule,  $m = 4$  was found to be sufficient to compute the first fifty vibrational states. So, in this 3D problem, the use of an auxiliary basis set introduces only a modest increase in the computational cost. For a 12D problem, however, an  $m = 4$  choice would increase the basis space by two orders of magnitude!

For this reason, we will use (the rearranged and) the fully rearranged form of the KEO [Eqs. (21)–(24)] which did not require the introduction of any additional (auxiliary) functions in an FBR computation. Further details concerning the matrix representation of the KEO, including a pragmatic “treatment” of the KEO singularities, ubiquitous in floppy systems, will be explained in Sec. IV D.

### 1. Definition of the coordinates for the example of $\text{CH}_4\text{-Ar}$

The vibrational dynamics of the  $\text{CH}_4\text{-Ar}$  complex was described using the  $\xi_1 = R \in [0, +\infty)$ ,  $\xi_2 = \theta \in [0, \pi]$ ,  $\xi_3 = \phi \in [0, 2\pi)$  spherical coordinates, and the nine dimensionless normal coordinates of the isolated  $\text{CH}_4$  molecule,  $\xi_{3+i} = q_i \in (-\infty, +\infty)$  ( $i = 1, \dots, 9$ ). At the reference structure (necessary to define the normal coordinates), methane was oriented in the most symmetric fashion in the Cartesian space with the C atom at the origin (this orientation also ensured that the KEO singularity is not at the equilibrium structure of the complex)

$$\begin{aligned} \text{H}_1 : \mathbf{c}_1^{\text{eq}} &= (r, r, r), \\ \text{H}_2 : \mathbf{c}_2^{\text{eq}} &= (r, -r, -r), \\ \text{H}_3 : \mathbf{c}_3^{\text{eq}} &= (-r, -r, r), \\ \text{H}_4 : \mathbf{c}_4^{\text{eq}} &= (-r, r, -r), \end{aligned} \quad (30)$$

and  $r = r_{\text{CH}}^{\text{eq}} = 2.052\,410\,803$  bohrs was the equilibrium C–H distance corresponding to the PES of Ref. 33. The GENIUSH program evaluates functions appearing in the KEO from a coordinate conversion routine in which the instantaneous (body-fixed) Cartesian coordinates must be specified in terms of the internal coordinates. The Cartesian positions of the carbon and the hydrogen atoms were calculated from the  $q_1, \dots, q_9$  normal coordinate values as

$$\epsilon_i = c_{ie}^{\text{eq}} + \sum_{j=1}^9 l_{eij} q_j, \quad (31)$$

where  $\epsilon = x, y, z$  and  $i = 1, 2, \dots, 5$ , and the Cartesian coordinates of the Ar atom,  $\epsilon_6$  ( $\epsilon = x, y, z$ ), were measured from the center of mass of the methane moiety and were obtained as

$$x_6 = R \sin \theta \cos \phi, \quad y_6 = R \sin \theta \sin \phi, \quad z_6 = R \cos \theta. \quad (32)$$

In the last step of the calculation of the Cartesian coordinates, the center of mass of the complex was shifted to the origin. The orientation of the body-fixed frame corresponding to the coordinates just described corresponds to the orientation of the frame used to define methane's normal coordinates. A more sophisticated choice of the body-fixed frame can be useful to make rovibrational computations efficient. In the present work, however, we focus on the computation of the vibrational states. We used the atomic masses<sup>34</sup>  $m(\text{H}) = 1.007\,825\,032\,23$  u,  $m(\text{C}) = 12$  u, and  $m(\text{Ar}) = 39.962\,383\,123\,7$  u throughout this work.

## 2. Potential energy surface

Due to the lack of any full-dimensional methane-argon potential energy surface, we used the sum of the 3D intermolecular potential energy surface of Refs. 35 and 36 and the 9D methane PES from Wang and Carrington.<sup>33</sup> This setup allows us to study the kinetic coupling of this weakly bound complex. Should a full-dimensional PES become available, the computations can be adapted to it.

## IV. IMPLEMENTATION OF THE SMOLYAK SCHEME IN GENIUSH

### A. Pruning the basis functions

For the example of the  $\text{CH}_4\text{-Ar}$  complex described with the  $(R, \theta, \phi, q_1, \dots, q_9)$  vibrational coordinates defined in Sec. III A 1, we chose the following 1D basis functions:  $\mathcal{L}^{(\alpha)}$  generalized Laguerre basis functions (with  $\alpha = 2$ ) or tridiagonal Morse basis functions for  $R$ ; Legendre basis functions (and variants of them) or Jacobi associated basis functions for  $\theta$ ; Fourier functions, composed of  $\cos(n_\phi \phi)$ ,  $\sin(n_\phi \phi)$ , for  $\phi$ ; and harmonic oscillator functions for the  $q_1, \dots, q_9$  methane normal coordinates. As a result, the direct-product expansion of the vibrational wave function can be written as

$$\begin{aligned} \Psi_i(R, \theta, \phi, q_1, \dots, q_9) &= \sum_{n_R=0}^{N_R^{\text{max}}} \sum_{n_\theta=0}^{N_\theta^{\text{max}}} \sum_{n_\phi=0}^{N_\phi^{\text{max}}} \sum_{n_{q_1}=0}^b \dots \sum_{n_{q_9}=0}^b C_{n_R, n_\theta, n_\phi, n_{q_1}, \dots, n_{q_9}}^i \\ &\times \psi_{n_R}^{(R)}(R) \psi_{n_\theta}^{(\theta)}(\theta) \psi_{n_\phi}^{(\phi)}(\phi) \psi_{n_{q_1}}^{(q_1)}(q_1) \dots \\ &\times \psi_{n_{q_9}}^{(q_9)}(q_9). \end{aligned} \quad (33)$$

This direct-product basis representation, for the typical values of  $N_R^{\text{max}} > 10$ ,  $N_\theta^{\text{max}} > 20$ ,  $N_\phi^{\text{max}} > 15$ , and  $b > 2$ , would include  $> 5.90 \cdot 10^7$  functions. To reduce the basis set size, we prune the basis representation of the methane fragment

$$\begin{aligned} \Psi_i(R, \theta, \phi, q_1, \dots, q_9) &= \sum_{n_R=0}^{N_R^{\text{max}}} \sum_{n_\theta=0}^{N_\theta^{\text{max}}} \sum_{n_\phi=0}^{N_\phi^{\text{max}}} \sum_{n_{q_1} + \dots + n_{q_9} \leq b} \\ &\times C_{n_R, n_\theta, n_\phi, n_{q_1}, \dots, n_{q_9}}^i \psi_{n_R}^{(R)}(R) \psi_{n_\theta}^{(\theta)}(\theta) \psi_{n_\phi}^{(\phi)}(\phi) \\ &\times \psi_{n_{q_1}}^{(q_1)}(q_1) \dots \psi_{n_{q_9}}^{(q_9)}(q_9) \end{aligned} \quad (34)$$

by replacing the 0 and  $b$  lower and upper summation limits of each normal coordinate with the basis-pruning condition

$$n_{q_1} + \dots + n_{q_9} \leq b \quad (b \in \mathbb{N}_0), \quad (35)$$

which we call “standard” pruning. This condition is a natural choice for normal coordinates and harmonic oscillator basis functions, which provide a good “zeroth-order” model. This standard pruning, equivalent to choosing a big polyad of states, allows us to discard basis functions for which the coupling between the intramolecular basis functions (through the full Hamiltonian) is small and for which the zeroth-order energies are very different. The larger the  $b$  value in Eq. (35), the more accurate (higher excited) vibrational states of methane are obtained. (If we focused on the computation of highly excited methane states, it would be better to use a more sophisticated pruning condition.) For the intermolecular basis set  $\Psi_{R, n_R}(R) \Psi_{\theta, n_\theta}(\theta) \Psi_{\phi, n_\phi}(\phi)$ , we do not introduce any pruning because the selected functions are not close to any zeroth-order approximate basis set for this system, so we cannot discard any of the functions based on simple arguments. Nevertheless, standard pruning of the methane part already reduces the basis set substantially. The storage of one vector in the direct-product basis set with 10 basis functions per coordinate would require  $\sim 8$  TB of memory, while using standard pruning [Eq. (35)] reduces this value to 0.39 GB.

### B. Pruning the grid with the Smolyak scheme

The GENIUSH program computes the values of the  $G_{i,j}$ ,  $B_i$ , and  $U$  multidimensional functions of the KEO at multidimensional points of the vibrational coordinates. Since we do not use any interpolation procedure to fit  $G_{i,j}$ ,  $B_i$ , and  $V + U$  to special analytic functions, a multidimensional quadrature grid is necessary to obtain the integrals.

It is straightforward to design nonproduct quadrature grids for the evaluation of the multidimensional integrals of the Hamiltonian operator with the standard basis-pruning condition [Eq. (35)]. For the example of the  $\text{CH}_4\text{-Ar}$  complex (see Sec. III A 1 for the coordinate definition and Sec. IV A for the basis set and the pruning condition), the 12D Smolyak integration operator of order  $H^{16,17}$  is

$$\begin{aligned} \hat{Q}(12, H) &= \sum_{\sigma \mathbf{g}(i) \leq H} \otimes \prod_{\chi}^{12} \Delta \hat{Q}_{\chi}^{i_{\chi}} \\ &= \sum_{\sigma \mathbf{g}(i) \leq H} \Delta \hat{Q}_R^{i_R} \otimes \Delta \hat{Q}_{\theta}^{i_{\theta}} \otimes \Delta \hat{Q}_{\phi}^{i_{\phi}} \otimes \Delta \hat{Q}_{q_1}^{i_{q_1}} \otimes \dots \otimes \Delta \hat{Q}_{q_9}^{i_{q_9}}, \\ &\text{with } i_{\chi} = 1, 2, 3, 4, \dots \text{ and } \chi = 1(R), 2(\theta), \dots, 12(q_9), \end{aligned} \quad (36)$$

and the general grid-pruning condition is

$$\sigma \mathbf{g}(\mathbf{i}) \leq H : g^R(i_R) + g^\theta(i_\theta) + g^\phi(i_\phi) + g^{q_1}(i_{q_1}) + \dots + g^{q_9}(i_{q_9}) \leq H. \quad (37)$$

The  $i_\chi$ th incremental operator is defined as

$$\Delta \hat{Q}_\chi^{i_\chi} = \hat{Q}_\chi^{i_\chi} - \hat{Q}_\chi^{i_\chi-1} \quad (38)$$

with  $\hat{Q}_\chi^0 = 0$ . The action of the  $i_\chi$ th operator,  $\hat{Q}_\chi^{i_\chi}$ , on an  $f$  function is its (numerical, quadrature) integral

$$\hat{Q}_\chi^{i_\chi} f(\xi_\chi) = \sum_{m=1}^{m_\chi(i_\chi)} w_{\chi,m}^{i_\chi} f(\xi_{\chi,m}^{i_\chi}) \quad (39)$$

corresponding to the  $w_{\chi,m}^{i_\chi}$  quadrature weights and  $q_{\chi,m}^{i_\chi}$  quadrature points,  $m = 1, \dots, m_\chi(i_\chi)$ , within the  $i_\chi$ th grid.

We also note that Eq. (36) can be written as a linear combination of the 1D integration operators (instead of using the incremental operators) as

$$\begin{aligned} \hat{Q}(12, H) &= \sum_{\sigma \mathbf{g}(\mathbf{i}) \leq H} C_{\mathbf{i}} \otimes \prod_{\chi=1}^{12} \hat{Q}_\chi^{i_\chi} \\ &= \sum_{\sigma \mathbf{g}(\mathbf{i}) \leq H} C_{i_R, i_\theta, i_\phi, i_{q_1}, \dots, i_{q_9}} \hat{Q}_R^{i_R} \otimes \hat{Q}_\theta^{i_\theta} \otimes \hat{Q}_\phi^{i_\phi} \otimes \hat{Q}_{q_1}^{i_{q_1}} \otimes \dots \otimes \hat{Q}_{q_9}^{i_{q_9}}, \\ &\text{with } i_\chi = 1, 2, 3, 4, \dots \text{ and } \chi = 1(R), 2(\theta), \dots, 12(q_9), \end{aligned} \quad (40)$$

which allows us to better understand the structure of the Smolyak grid. The Smolyak quadrature grid is a linear combination of product quadrature grids with different 1D accuracies, while it has a smaller number of points than the product grid  $\otimes \prod_{i_\chi=1}^{12} \hat{Q}_\chi^{i_\chi}$   $= \hat{Q}_R^{i_R^{\max}} \otimes \hat{Q}_\theta^{i_\theta^{\max}} \otimes \hat{Q}_\phi^{i_\phi^{\max}} \otimes \hat{Q}_{q_1}^{i_{q_1}^{\max}} \otimes \dots \otimes \hat{Q}_{q_9}^{i_{q_9}^{\max}}$ , where  $i_\chi^{\max}$

$$\hat{Q}_\chi^{i_\chi} = \begin{cases} \hat{Q}_\chi^{M_\chi^{\max}}, & \text{for } \chi = R, \theta, \phi, \\ \hat{Q}_\chi^{m_\chi(i_\chi)}, & \text{for } \chi = q_1, \dots, q_9, \\ \text{with } m_\chi(i_\chi) = 1, 3, 3, 7, 9, 9, 9, 9, 17, 19, 19, 19, 31, 33, 41, 41, \dots \end{cases} \quad (43)$$

for  $i_\chi = 1, 2, 3, \dots$ , respectively.

This choice of the integration operators allowed us to use the 12D Smolyak operator for the special case when the first three degrees of freedom are described with a direct-product grid.  $\hat{Q}_R^{M_R^{\max}}$ ,  $\hat{Q}_\theta^{M_\theta^{\max}}$ , and  $\hat{Q}_\phi^{M_\phi^{\max}}$  label the integration operators corresponding to the spherical degrees of freedom, and each of them is constructed with a Gauss quadrature rule with  $M_\chi^{\max}$  points and  $d_\chi = 2M_\chi^{\max} - 1$  maximum accuracy.

The  $\hat{Q}_\chi^{m_\chi(i_\chi)}$  ( $\chi = q_1, \dots, q_9$ ) operators, corresponding to the normal coordinates, are constructed using a nested Hermite quadrature with a maximum degree of  $d_\chi(i_\chi) \geq 2i_\chi - 1$ , and  $d_\chi(i_\chi) = 1, 5, 5, 7, 15, 15, 15, 15, 17, 29, 29, 29, 31, 33, 61, 61, \dots$  for the  $i_\chi = 1, 2, 3, \dots$  sequence of Eq. (43) (also note that the same quadrature is used for each dimensionless normal coordinate). Nesting means

$= H - \sum_{\chi' \neq \chi} g^{\chi'}(1)$  is determined by the smallest value of the pruning function for the other coordinates [Eq. (42)]. If a product basis function,  $f_{n_R}^{(R)}(R) f_{n_\theta}^{(\theta)}(\theta) f_{n_\phi}^{(\phi)}(\phi) f_{n_{q_1}}^{(q_1)}(q_1) \dots f_{n_{q_9}}^{(q_9)}(q_9)$ , can be integrated exactly by the product quadrature grid  $\hat{Q}_R^{i_R} \otimes \hat{Q}_\theta^{i_\theta} \otimes \hat{Q}_\phi^{i_\phi} \otimes \hat{Q}_{q_1}^{i_{q_1}} \otimes \dots \otimes \hat{Q}_{q_9}^{i_{q_9}}$ , that product basis function is also exactly integrated by the Smolyak quadrature grid  $\hat{Q}(12, H)$  because it comprises this smaller product grid.<sup>37</sup>

To ensure accurate integration, we have to tune three factors: (a) the pruning function,  $g^\chi(i_\chi)$  (which must be a monotonic increasing function); (b) the value of  $H$  (the larger, the better); and (c) the number of grid points,  $m_\chi(i_\chi)$ , in the 1D grids determined by the smallest possible Smolyak grid which integrates accurately the Hamiltonian for a selected, pruned, multidimensional basis set.

For the case of CH<sub>4</sub>-Ar, the basis-set pruning condition was (Sec. IV A)

$$\begin{aligned} 0 &\leq n_R \leq N_R^{\max}, \\ 0 &\leq n_\theta \leq N_\theta^{\max}, \\ 0 &\leq n_\phi \leq N_\phi^{\max}, \\ 0 &\leq n_{q_1} + n_{q_2} + n_{q_3} + n_{q_4} + n_{q_5} + n_{q_6} + n_{q_7} + n_{q_8} + n_{q_9} \leq b, \end{aligned} \quad (41)$$

i.e., the intermolecular basis was retained in its product form and pruning was introduced for the methane fragment. The corresponding nonproduct grid includes the intermolecular grid in its product form, and a pruned intramolecular grid is implemented using the following grid-pruning functions:

$$g^\chi(i_\chi) = \begin{cases} 1, & \text{for } \chi = R, \theta, \phi, \\ i, & \text{for } \chi = q_1, \dots, q_9, \quad i = 1, 2, 3, \dots \end{cases} \quad (42)$$

The corresponding  $\hat{Q}_\chi^{i_\chi}$  integration operators are chosen as

that all quadrature points of the quadrature rule  $\hat{Q}_\chi^{i_\chi}$  also appear in the quadrature rule  $\hat{Q}_\chi^{i_\chi+1}$ . It is important that we need to have nested grids to be able to use a Smolyak quadrature efficiently. For this reason, we always use the smallest grid which is nested, e.g., for  $i_\chi = 2$ , we use a three-point quadrature,  $m_\chi(2) = 3$ , in Eq. (43) because there is not any nested, two-point Hermite quadrature. Nested Hermite grids are listed in tables; see, for example, Ref. 38.

In this paragraph, we compare the orders of magnitudes for a direct-product and for a Smolyak grid just defined for the example of CH<sub>4</sub>-Ar. Let us assume that we have a direct-product basis set with  $0 \leq n_R, n_\theta, n_\phi \leq 9$  functions for the spherical degrees of freedom and  $0 \leq n_{q_1} \dots + n_{q_9} \leq b = 3$  for methane's degrees of freedom. The smallest 12D product Gauss grid which gives correctly the overlap integrals for this basis set includes  $10^3 \cdot 4^9 = 2.62 \cdot 10^8$  points.

To integrate the overlap for this basis set exactly, we need to choose  $H = 15$  for the 12D Smolyak grid, which includes  $10^3 \times 871 = 8.71 \cdot 10^5$  points, almost three orders of magnitude less than the 12D direct-product Gauss grid. Certainly, an even more significant reduction in the grid size (in comparison with a direct-product grid) can be achieved if a larger number of degrees of freedom is included in the pruning.<sup>39</sup>

The smallest necessary value of  $H$  can be calculated from the basis-pruning condition and the value of  $b$  as follows. To compute exactly an overlap integral of  $2b$  polynomial degree, it is necessary to have a maximum degree of  $2i_\chi - 1 \geq 2b$ , i.e.,  $i_\chi \geq b + 1/2$ . Then, using the grid-pruning condition [Eq. (43)] and the fact that  $i_\chi \geq 1$ , we must have  $H \geq b + D$ , which makes  $H \geq 3 + 12 = 15$  for a 12D problem with  $b = 3$ . In the numerical applications, we choose an  $H$  value slightly larger than this minimal necessary value:  $H = b + D + 2$  was usually found to be sufficient to converge the results for the example computations (Sec. V).

It is important that the Smolyak algorithm uses nested sequences of quadrature rules. Nesting ensures that the nonproduct grid has a special structure. By exploiting this structure, a multidimensional integral of a multivariable function,  $F(x_1, \dots, x_D)$ , can be rewritten as

$$\begin{aligned} & \int \dots \int F(\xi_1, \dots, \xi_D) d\xi_1 \dots d\xi_D \\ &= \sum_{N=1}^{N^{\max}} W_N F(\xi_{1,k_1}, \dots, \xi_{D,k_D}) \\ &= \sum_{k_1=1}^{k_1^{\max}} \dots \sum_{k_D=1}^{k_D^{\max}} W^S(k_1, \dots, k_D) F(\xi_{1,k_1}, \dots, \xi_{D,k_D}), \end{aligned} \quad (44)$$

where the structure of the Smolyak grid appears in the second equation through the  $k_i^{\max}$  upper summation indexes<sup>16,17</sup>:  $k_1^{\max}$  depends on  $H$ ;  $k_2^{\max}$  depends on  $H$  and  $k_1^{\max}$ ;  $k_3^{\max}$  depends on  $H$  and  $k_1^{\max}, k_2^{\max}$ , etc. It is important to notice that the multidimensional integral [Eq. (44)] can be written in a sequential sum form [the second equation in Eq. (44)] only for structured grids; otherwise, only the first, computationally more demanding, form is applicable.

### C. An efficient matrix-vector product algorithm for computing eigenvalues and eigenvectors with an iterative eigensolver

We develop a method to compute (ro)vibrational states of polyatomic molecules with multiple large-amplitude motions. Probably, the most common way to tackle (ro)vibrational problems is to compute the Hamiltonian matrix elements in FBR and then diagonalize the Hamiltonian matrix following the pioneering work of Whitehead and Handy.<sup>40</sup> For polyatomic molecules and complexes, the size of the basis set, even if we use a pruned, product basis, may be larger than 100 000 ( $10^5$ ), and a corresponding nonproduct quadrature grid would consist of more than 10 000 000 ( $10^7$ ) points. Unless the Hamiltonian matrix is very sparse and the system has a high permutation-inversion symmetry, the “traditional” route of using a direct eigensolver is not feasible for time and memory reasons.

Using iterative eigensolvers is a practical alternative,<sup>41,42</sup> which allows us to compute eigenvalues and eigenvectors without storing or even explicitly computing the Hamiltonian matrix elements. The key algorithmic element in relation with iterative eigensolvers is the efficient multiplication of an input vector with the Hamiltonian matrix.

In this section, we develop an efficient matrix-vector product algorithm in relation with the numerical KEO approach (Sec. III) and the Smolyak scheme (Sec. IV B). The multiplication is made efficient by exploiting the structure of the pruned basis set and the structure of the nonproduct Smolyak grid. Multiplication with the potential energy matrix is carried out as

$$\begin{aligned} v_{N'_{1\dots D}}^{\text{out}} &= \sum_{k_1=1}^{k_1^{\max}} T_{n'_1}^{(1)}(\xi_{1,k_1}) \dots \sum_{k_D=1}^{k_D^{\max}} T_{n'_D}^{(D)}(\xi_{D,k_D}) W_{K_{1\dots D}}^S V(\xi_{K_{1\dots D}}) \\ &\times \sum_{n_D=0}^{n_D^{\max}} T_{n_D}^{(D)}(\xi_{D,k_D}) \dots \sum_{n_1=0}^{n_1^{\max}} T_{n_1}^{(1)}(\xi_{1,k_1}) v_{N_{1\dots D}}^{\text{in}} \end{aligned} \quad (45)$$

with the condensed indexing of the basis labels, grid labels, and multidimensional grid points

$$\begin{aligned} N_{1\dots D} &\leftrightarrow (n_1, n_2, \dots, n_D), & K_{1\dots D} &\leftrightarrow (k_1, k_2, \dots, k_D), \\ \xi_{K_{1\dots D}} &\leftrightarrow (\xi_{1,k_1}, \xi_{2,k_2}, \dots, \xi_{D,k_D}), \end{aligned}$$

respectively.  $T_n(x_k)$  is the value of the basis function with index  $n$  at point  $x_k$ , and  $W^S$  collects the multidimensional quadrature weights. In the Fortran implementation, we use two condensed indexes for the intermediate vectors, labeled with  $K_1 \dots \Delta \leftrightarrow (k_1, \dots, k_\Delta)$  “partial” grid and the corresponding  $N_{\Delta+1}, \dots, D \leftrightarrow (n_{\Delta+1}, \dots, n_D)$  “partial” basis index. The operations are performed in parallel using the OpenMP protocol. The  $n_\chi^{\max}$  and  $k_\chi^{\max}$  values for each coordinate, i.e., the structure of the basis and the grid, are determined from the basis and the grid pruning conditions.

For our present numerical example,  $\text{CH}_4\text{-Ar}$ ,  $D = 12$  and  $\xi = (R, c, \phi, q_1, \dots, q_9)$  (henceforth, we use the short labeling  $c = \cos \theta$ ). According to the basis pruning condition [Eq. (41)], the upper summation indexes for the basis labels are

$$\begin{aligned} n_{\chi_i}^{\max} &= N_{\chi_i}^{\max}, & \text{for } i(\chi_i) &= 1(R), 2(c), 3(\phi), \\ n_{q_{9-i}}^{\max} &= b - \sum_{j=0}^{i-1} n_{q_{9-j}}, & \text{for } i &= 0, 1, \dots, 8. \end{aligned} \quad (46)$$

The grid pruning condition in Eq. (42) determines the structure of the quadrature indexes according to

$$\begin{aligned} k_{\chi_i}^{\max} &= K_{\chi_i}^{\max}, & \text{for } i(\chi_i) &= 1(R), 2(\theta), 3(\phi), \\ k_{q_i}^{\max} &= m_{q_i}(H - (12 - i) - \sum_{j=1}^{i-1} S(k_{q_j})), & \text{for } i &= 1, 2, \dots, 9, \end{aligned} \quad (47)$$

where  $S(k)$  is the index of the smallest quadrature rule in the nested sequence of Hermite quadratures that contains  $k$  points. For the Hermite sequence used in the present work, the  $S(k)$  values are obtained from Eq. (43)

$$\begin{aligned}
 S(1) &= 1, S(2) = 2, S(3) = 2, S(4) = 4, S(5) = 4, S(6) = 4, S(7) = 4, S(8) = 5, \\
 S(9) &= 5, \dots, S(17) = 9, S(18) = 10, S(19) = 10, S(20) = 16, \dots, S(31) = 16, \\
 S(32) &= 17, S(33) = 17, S(34) = 18, S(35) = 18, S(36) = 19, S(37) = 19, \\
 S(38) &= 20, S(39) = 20, S(40) = 21, S(41) = 21.
 \end{aligned} \tag{48}$$

If the FBR method is used for the intermolecular coordinates  $R$ ,  $c$ , or  $\phi$ , we use more grid points than basis functions  $K^{\max} > N^{\max}$  in order to get exact integrals (typically,  $K^{\max} - N^{\max} \approx 5$  was sufficient to achieve convergence). If the DVR scheme is used (due to the reasons explained in Sec. IV D), then we have the same number of points and functions, so  $K^{\max} = N^{\max} + 1$ .

#### D. Singularity concerns and a hybrid DVR-FBR solution

We have numerically identified that KEO we use to describe the  $\text{CH}_4\text{-Ar}$  complex has singularities along the  $\theta$  spherical angle (also related to  $\phi$ ). These singularities appear at  $\theta = 0$  and  $\theta = \pi$  ( $c = \cos \theta = \pm 1$ ), and they represent a considerable challenge for a nonanalytic KEO representation, especially because two kinds of singularities appear

$$\frac{1}{1-c^2} \quad \text{and} \quad \frac{1}{\sqrt{1-c^2}}. \tag{49}$$

This singular property can be discerned from numerical tests with the numerical KEO coefficients and by calculating matrix elements for the  $G_{ij} \partial^2 / \partial \mathcal{R}_i \partial \mathcal{R}_j$  terms using an associated Jacobi basis set,  $J_n^{\alpha, \beta}(c)$ , for example.

An obvious way to avoid these types of singular integrals for analytic KEOs would be to use the 2D spherical harmonics functions for  $\theta$  and  $\phi$ . This option is the way to go for tailor-made approaches, but it would destroy the simplicity and generality of a universal (ro)vibrational approach we are developing, especially if there are several groups of spherical coordinates  $(\theta_i, \phi_i)$   $i = 1, 2, \dots$  in the system.<sup>24</sup> In particular, the application of spherical harmonics would require the development of special matrix-vector product routines for each  $i = 1, 2, \dots$  values.

Another possibility would be to use Jacobi associated functions,  $J_n^{\alpha, \beta}(c)$ , with  $\alpha$  and  $\beta$  close to zero. We could follow this alternative if an analytic KEO and analytic KEO integrals were available.

Since we develop a universal method for numerical KEO representations, we need to find a multidimensional quadrature which allows us to evaluate all the different kinds of integrals appearing in the KEO without knowing its exact, analytic form but knowing only the characteristic singular behavior [Eq. (49)]. Let us use Jacobi associated functions with  $\alpha = \beta = 0.001$  for  $c$ . Then, we have to find a quadrature rule which integrates exactly the following types of integrals simultaneously:

$$\begin{aligned}
 &\int_{-1}^1 J_{n'}^{\alpha, \beta}(c) \frac{1}{1-c^2} J_n^{\alpha, \beta}(c) dc \\
 &\int_{-1}^1 J_{n'}^{\alpha, \beta}(c) \frac{1}{\sqrt{1-c^2}} J_n^{\alpha, \beta}(c) dc \\
 &\int_{-1}^1 J_{n'}^{\alpha, \beta}(c) J_n^{\alpha, \beta}(c) dc
 \end{aligned} \tag{50}$$

with  $0 \leq n, n' \leq N$ . Gauss-quadrature rules exist for each integral in Eq. (50) separately, but there is not any single Gauss quadrature that integrates exactly all three types of integrals, whereas in the numerical KEO, it is not possible to separate different terms of different singular behavior (which we know again from numerical test calculations). Then, the next logical step is to find a (non-Gauss) quadrature rule of  $M$  points that gives exactly all the integrals in Eq. (50) at the same time. We determined such a quadrature using a two-step procedure. First, we optimized the quadrature points with a simplex algorithm and calculated the quadrature weights by solving an overdetermined set of equations; this set of points and weights was refined by optimizing both the quadrature points and weights with the simplex algorithm. Unfortunately, this (non-Gauss) quadrature includes a large number of points ( $K \gg N$ ) (three times as many as a single Gauss-quadrature rule) and some of the points come extremely close to the singular points at  $c = -1$  and  $c = 1$ . Since GENIUSH calculates the  $G_{ij}$  elements through finite differences, the finite step size will place limitations on increasing the number of quadrature points. Due to the large number of points and their accumulation near the singular values, we cannot accept this special quadrature as a practical solution for the problem, but we will use this (non-Gauss) quadrature rule to check the practical ideas we explain in the following paragraphs.

Since we do not have analytic integral expressions and it is not possible to find any compact (Gauss) numerical integration scheme which ensures exact integration, let us consider approximate integrals (which become accurate at the limit of a large number of points). First of all, nonexact integration, due to the singularities, manifests itself in a nonsymmetric matrix representation of the KEO in Eq. (24). Then, instead of aiming for exact integrals (with a compact grid), let us aim for a symmetric matrix representation at the first place. Construction of a symmetric matrix representation is straightforward by using Legendre-DVR (or the variants of it discussed below) and the inherently more symmetric general KEO in Eq. (21) for  $c = \cos(\theta)$ . We will ensure a symmetric representation in the same way as in the original DVR-based GENIUSH implementation<sup>27</sup> (see also Ref. 43 concerning the Legendre polynomials) and in its applications to floppy systems,<sup>44-49</sup> which did not suffer from the present singularity problems but which did suffer from the curse of dimensionality. So, we handle the singular coordinate  $c$  as

we would do it in GENIUSH-DVR; for the rest of the coordinates, we use FBR.

So, instead of using the fully rearranged KEO [Eq. (24)] for which we obtain a nonsymmetric matrix representation due to inexact integration (the off diagonal elements with different basis indexes of  $c$  fail to be equal unless they are exactly integrated), we rewrite the KEO for the  $c$  coordinate into the more symmetric form

$$\hat{T}^v = -\frac{1}{2} \sum_{j=1}^{12} \frac{\partial}{\partial c} G_{c,j} \frac{\partial}{\partial \xi_j} - \frac{1}{2} \sum_{i=1 \neq j}^{12} \sum_{j=1}^{12} G_{i,j} \frac{\partial}{\partial \xi_i} \frac{\partial}{\partial \xi_j} - \frac{1}{2} \sum_{i=1}^{12} B_i \frac{\partial}{\partial \xi_i} + U,$$

$$B_i = \sum_{k=1, \neq 2}^{12} \frac{\partial}{\partial \xi_k} G_{k,i}. \quad (51)$$

Using this KEO and a hybrid DVR( $c$ )-FBR representation, the Hamiltonian matrix is real, symmetric by construction, and the matrix elements for functions with the same  $c$  index are the same as the ones we get using the fully rearranged KEO [Eq. (24)]. We have carried out an additional test for this hybrid DVR-FBR approach. First, we performed a fully FBR computation with the fully rearranged KEO [Eq. (24)] using a Jacobi associated basis set for  $c$  with  $\alpha = 0.01$ ,  $\beta = 0.01$  and a (non-Gauss) quadrature developed to calculate accurately the integrals of Eq. (50). This non-Gauss quadrature included a very large number of points for  $c$ , so we could afford only a small basis and grid for the other degrees of freedom. We repeated the computation using the same, small basis set for the non- $c$  coordinates and DVR with the symmetric KEO [Eq. (51)] for  $c$ . The two computations resulted in the same eigenvalues, which provides a numerical test for our practical DVR-FBR approach (of course, the eigenvalues obtained in this way were different from the converged values due to the smallness of the non- $c$  basis set). So, in this sense, using DVR( $c$ )-FBR and the KEO in Eq. (51) has the correct “limiting” (convergence) behavior, while it ensures a symmetric matrix representation by construction.

### E. Matrix-vector products in the hybrid DVR-FBR

The matrix-vector products in the hybrid DVR-FBR are carried out similarly to Eq. (45). In what follows, we list the necessary changes in comparison with the fully FBR PES multiplication [Eq. (45)] to accommodate the hybrid FBR-DVR representation for the KEO of Eq. (51). We also note that in the hybrid DVR-FBR scheme, the  $W_{K_{1...D}}^S$  Smolyak weights were obtained using a quadrature rule for the  $c$  coordinate with weights equal to one.

1. The matrix-vector product for the potential (and the  $U$  pseudopotential) term is carried out as in Eq. (45), but for the  $c$  coordinate, we make the following replacements:

$$T_{n'_c}^{(c)}(\xi_{c,k_c}) \rightarrow \delta_{n'_c, k_c - 1} \quad \text{and} \quad T_{n_c}^{(c)}(\xi_{c,k_c}) \rightarrow \delta_{n_c, k_c - 1}. \quad (52)$$

2. The matrix-vector product for the  $\frac{\partial}{\partial c} G_{c,c} \frac{\partial}{\partial c}$  term is calculated as in Eq. (45), but for the  $c$  coordinate, we make the following replacements:

$$V(\xi_{K_{1...D}}) \rightarrow G_{c,c}(\xi_{K_{1...D}}),$$

$$T_{n'_c}^{(c)}(\xi_{c,k_c}) \rightarrow -M_{k_c-1, n'_c}, \quad \text{and} \quad T_{n_c}^{(c)}(\xi_{c,k_c}) \rightarrow M_{k_c-1, n_c} \quad (53)$$

with

$$M_{n'_c, n_c} = \int_{-1}^1 \Theta_{n'_c}(c) \frac{d}{dc} \Theta_{n_c}(c) dc, \quad (54)$$

where  $\Theta_{n_c}(c)$  is the  $n_c$ th (cot-, sincot-)Legendre-DVR function with  $K_c^{\max} = N_c^{\max} + 1$  quadrature points (*vide infra*).

3. The matrix-vector product for the  $\frac{\partial}{\partial c} G_{c,\mathcal{R}} \frac{\partial}{\partial \mathcal{R}}$  term, where  $\mathcal{R}$  is not the  $c$  coordinate, is calculated as in Eq. (45) with the following replacements:

$$V(\xi_{K_{1...D}}) \rightarrow G_{\mathcal{R},c}(\xi_{K_{1...D}}),$$

$$T_{n'_c}^{(c)}(\xi_{c,k_c}) \rightarrow -M_{k_c-1, n'_c} \quad \text{and} \quad T_{n_c}^{(c)}(\xi_{c,k_c}) \rightarrow \delta_{n_c, k_c - 1}, \quad (55)$$

$$T_{n_{\mathcal{R}}}^{(\mathcal{R})}(\xi_{\mathcal{R}, k_{\mathcal{R}}}) \rightarrow \frac{d}{d\mathcal{R}} T_{n_{\mathcal{R}}}^{(\mathcal{R})}(\mathcal{R}) \Big|_{\mathcal{R}=\xi_{\mathcal{R}, k_{\mathcal{R}}}}.$$

4. The matrix-vector product for the  $\frac{\partial}{\partial \mathcal{R}} G_{\mathcal{R},c} \frac{\partial}{\partial c}$  term, where  $\mathcal{R}$  is not the  $c$  coordinate, is calculated as in Eq. (45) with the following replacements:

$$V(\xi_{K_{1...D}}) \rightarrow G_{\mathcal{R},c}(\xi_{K_{1...D}}),$$

$$T_{n'_c}^{(c)}(\xi_{c,k_c}) \rightarrow \delta_{n'_c, k_c - 1} \quad \text{and} \quad T_{n_c}^{(c)}(\xi_{c,k_c}) \rightarrow M_{k_c-1, n_c}, \quad (56)$$

$$T_{n'_{\mathcal{R}}}^{(\mathcal{R})}(\xi_{\mathcal{R}, k_{\mathcal{R}}}) \rightarrow \frac{d}{d\mathcal{R}} T_{n'_{\mathcal{R}}}^{(\mathcal{R})}(\mathcal{R}) \Big|_{\mathcal{R}=\xi_{\mathcal{R}, k_{\mathcal{R}}}}.$$

5. The matrix-vector product for the  $G_{\mathcal{R},\mathcal{R}} \frac{\partial^2}{\partial \mathcal{R}^2}$  term, where  $\mathcal{R}$  is not the  $c$  coordinate, is calculated as in Eq. (45) with the following replacements:

$$V(\xi_{K_{1...D}}) \rightarrow G_{\mathcal{R},\mathcal{R}}(\xi_{K_{1...D}}),$$

$$T_{n'_c}^{(c)}(\xi_{c,k_c}) \rightarrow \delta_{n'_c, k_c - 1} \quad \text{and} \quad T_{n_c}^{(c)}(\xi_{c,k_c}) \rightarrow \delta_{n_c, k_c - 1}, \quad (57)$$

$$T_{n_{\mathcal{R}}}^{(\mathcal{R})}(\xi_{\mathcal{R}, k_{\mathcal{R}}}) \rightarrow \frac{d^2}{d\mathcal{R}^2} T_{n_{\mathcal{R}}}^{(\mathcal{R})}(\mathcal{R}) \Big|_{\mathcal{R}=\xi_{\mathcal{R}, k_{\mathcal{R}}}}.$$

6. The matrix-vector product for the  $B_{\mathcal{R}} \frac{\partial}{\partial \mathcal{R}}$  term, where  $\mathcal{R}$  is not the  $c$  coordinate, is calculated as in Eq. (45) with the following changes:

$$V(\xi_{K_{1...D}}) \rightarrow B_{\mathcal{R}}(\xi_{K_{1...D}}),$$

$$T_{n'_c}^{(c)}(\xi_{c,k_c}) \rightarrow \delta_{n'_c, k_c - 1} \quad \text{and} \quad T_{n_c}^{(c)}(\xi_{c,k_c}) \rightarrow \delta_{n_c, k_c - 1}, \quad (58)$$

$$T_{n_{\mathcal{R}}}^{(\mathcal{R})}(\xi_{\mathcal{R}, k_{\mathcal{R}}}) \rightarrow \frac{d}{d\mathcal{R}} T_{n_{\mathcal{R}}}^{(\mathcal{R})}(\mathcal{R}) \Big|_{\mathcal{R}=\xi_{\mathcal{R}, k_{\mathcal{R}}}}.$$

7. The matrix-vector product for the  $G_{\mathcal{R}_s, \mathcal{R}_t} \frac{\partial^2}{\partial \mathcal{R}^2}$  term, where  $\mathcal{R}_s$  and  $\mathcal{R}_t$  are not the  $c$  coordinate, is calculated as in Eq. (45) with the replacements

$$V(\xi_{K_{1...D}}) \rightarrow G_{\mathcal{R}_s, \mathcal{R}_t}(\xi_{K_{1...D}}),$$

$$T_{n'_c}^{(c)}(\xi_{c,k_c}) \rightarrow \delta_{n'_c, k_c - 1} \quad \text{and} \quad T_{n_c}^{(c)}(\xi_{c,k_c}) \rightarrow \delta_{n_c, k_c - 1},$$

$$T_{n_{\mathcal{R}_s}}^{(\mathcal{R}_s)}(\xi_{\mathcal{R}_s, k_{\mathcal{R}_s}}) \rightarrow \frac{d}{d\mathcal{R}_s} T_{n_{\mathcal{R}_s}}^{(\mathcal{R}_s)}(\mathcal{R}_s) \Big|_{\mathcal{R}_s=\xi_{\mathcal{R}_s, k_{\mathcal{R}_s}}} \quad (59)$$

$$\text{and} \quad T_{n_{\mathcal{R}_t}}^{(\mathcal{R}_t)}(\xi_{\mathcal{R}_t, k_{\mathcal{R}_t}}) \rightarrow \frac{d}{d\mathcal{R}_t} T_{n_{\mathcal{R}_t}}^{(\mathcal{R}_t)}(\mathcal{R}_t) \Big|_{\mathcal{R}_t=\xi_{\mathcal{R}_t, k_{\mathcal{R}_t}}}.$$

## F. Analysis and improvements for the intermolecular representation

To test the convergence properties and to determine the optimal basis set and grid sizes for our example system, CH<sub>4</sub>·Ar, we performed reduced-dimensionality computations. Intermolecular (3D) computations were performed with a fixed methane structure corresponding to the effective rotational constant  $B_{v=0} = 5.246\,981\,98\text{ cm}^{-1}$  (and an effective C–H distance of  $\langle R(\text{CH}) \rangle_{v=0} = 1.107\,117\,44$  bohrs) obtained with the ground-state vibrational wave function of CH<sub>4</sub> with pruning condition  $b = 8$  (see Sec. IV G) and using the isolated methane's PES.<sup>33</sup>

### 1. Intermolecular angular representation: Legendre, cot-Legendre, and sincot-Legendre DVRs

Since regions near the singularities [Eq. (49)] are dynamically relevant for the CH<sub>4</sub>·Ar complex, using Legendre DVR for the coordinate  $c = \cos \theta$  is an inefficient choice: more than 120 points are needed to converge all vibrational bound states of CH<sub>4</sub>·Ar (3D) within 0.01 cm<sup>-1</sup>.

In 2010, Schiffel and Manthe<sup>50</sup> proposed more efficient alternatives to Legendre DVR to be used for the type of singularities we have to tackle. First of all, the quadrature is improved by selecting the quadrature points, different from the Legendre points, as the inverse cotangent of the eigenvalues ( $w_i$ ) of the following matrix:

$$P_{n,m} = \int_{-1}^1 L_n(c) \frac{c}{1-c^2} L_m(c) dc, \quad n, m = 0, \dots, N_c^{\max} - 1, \quad (60)$$

$$\epsilon_i = \text{arccot}(w_i), \quad i = 1, \dots, N_c^{\max},$$

where  $L_n(c)$  is the  $n$ th normalized Legendre function. These integrals are calculated exactly using the Gauss–Chebyshev quadrature with a sufficiently large number of points. Using the eigenvectors,  $\mathbf{A}$ , of  $\mathbf{P}$ , the cot-Legendre DVR basis functions are defined as

$$\Theta_n(c) = \sum_{m=0}^{N_c-1} A_{m,n} L_m(c), \quad n = 0, \dots, N_c^{\max} - 1, \quad (61)$$

and the first derivative matrix,  $\mathbf{M}$ , for the cot-Legendre DVR functions is

$$M_{n',n} = \int_{-1}^1 \Theta_{n'}(c) \frac{d}{dc} \Theta_n(c) dc. \quad (62)$$

In our test calculations, it was sufficient to use 50 cot-Legendre DVR points to converge all bound states of CH<sub>4</sub>·Ar in 3D (within 0.01 cm<sup>-1</sup>) (see also Table I).

Schiffel and Manthe<sup>50</sup> continued and proposed further improvements by extending the basis set. They have noticed that some eigenfunctions of the KEO in spherical coordinates have a  $\sin(\theta)$  “component” close to the singularities, so they extended the Legendre basis set with sine functions. Their new basis set included  $L_n(c)$ ,  $n = 0, \dots, N_c^{\max} - s$ , and  $\sin(\theta)$ ,  $\dots$ ,  $\sin(s\theta)$ , where  $s = 2$  was sufficient (and stable without any over-completeness problems, which would occur for larger  $s$  values) in most applications. A corresponding DVR basis set, called

“sincot-Legendre (SCL) DVR basis,” is obtained in the following procedure:

1. Orthogonal basis functions are created from the set  $\{L_n(x), (n = 0, \dots, N_c^{\max} - 2), \sin \theta, \sin 2\theta\}$  by diagonalizing the corresponding overlap matrix  $S^{\text{sin-cos}}$ . The orthogonal basis functions,  $L_n^{\text{sin-cos}}(c)$ , are calculated using the eigenvectors of the overlap matrix.
2. A  $\mathbf{P}^{\text{sin-cos}}$  matrix is introduced with the elements

$$P_{n,m}^{\text{sin-cos}} = \int_{-1}^1 L_n^{\text{sin-cos}}(c) \frac{c}{1-c^2} L_m^{\text{sin-cos}}(c) dc, \quad (63)$$

$$n, m = 0, \dots, N_c^{\max}.$$

The DVR points are the inverse cotangent of the  $w_i$  eigenvalues of  $\mathbf{P}^{\text{sin-cos}}$ . The sincot-Legendre DVR basis functions are obtained from the eigenvectors of the  $\mathbf{P}^{\text{sin-cos}}$  matrix, collected in  $\mathbf{A}^{\text{sin-cos}}$ , as

$$\Theta_n^{\text{sin-cos}}(c) = \sum_{m=0}^{N_c^{\max}} A_{m,n}^{\text{sin-cos}} L_m^{\text{sin-cos}}(c), \quad n = 0, \dots, N_c^{\max}. \quad (64)$$

3. The first derivative matrix,  $\mathbf{M}^{\text{sin-cos}}$ , for sincot-Legendre DVR is

$$M_{n',n}^{\text{sin-cos}} = \int_{-1}^1 \Theta_{n'}^{\text{sin-cos}}(c) \frac{d}{dc} \Theta_n^{\text{sin-cos}}(c) dc. \quad (65)$$

The integrals for the  $\mathbf{S}^{\text{sin-cos}}$ ,  $\mathbf{P}^{\text{sin-cos}}$ , and  $\mathbf{M}^{\text{sin-cos}}$  matrices can be calculated analytically using elementary properties of trigonometric functions, and they were tabulated in Ref. 50.

We used the sincot-Legendre DVR points and the corresponding first derivative matrix elements (as an alternative to Legendre DVR) in the matrix-vector multiplication procedure described in Sec. IV D. Our 3D test computations show that it is sufficient to use 21 sincot-Legendre DVR points for coordinate  $c$  to converge all the bound states within 0.01 cm<sup>-1</sup> for CH<sub>4</sub>·Ar, which is a significant reduction compared to the original Legendre DVR which required more than 120 points. The performance of a few different representations for the  $c$  coordinate is compared in Table I. In all computations, we used the  $\mathcal{L}_n^\alpha$  generalized Laguerre polynomials (with  $\alpha = 2$ ) for  $R$ , scaled to the [2.64, 30] Å interval, and Fourier functions for  $\phi$ . The number of points used for the  $R$ ,  $\cos \theta$ , and  $\phi$  degrees of freedom in the three test sets of the table is

- A<sub>3D</sub>: ( $K_R^{\max}, K_c^{\max}, K_\phi^{\max}$ ) = (81, 101(L), 101) using Legendre (L) DVR for  $c$
- B<sub>3D</sub>: ( $K_R^{\max}, K_c^{\max}, K_\phi^{\max}$ ) = (61, 21(SCL), 17) using sincot-Legendre (SCL) DVR for  $c$
- C<sub>3D</sub>: ( $K_R^{\max}, K_c^{\max}, K_\phi^{\max}$ ) = (61, 31(SCL), 31) using sincot-Legendre (SCL) DVR for  $c$ .

It is important to observe in Table I that the vibrational states are not perfectly converged even with a very large number (more than 100) of Legendre DVR points. On the contrary, almost perfect results are obtained with less than 30 sincot-Legendre DVR points. Another important observation (relevant for the 12D applications in Sec. V) is that we can use fewer Fourier basis functions for  $\phi$  than (sincot-Legendre) functions for  $\theta$  to converge the 3D vibrational energies.



**TABLE I.** Convergence tests for the bound-state vibrational energies of  $\text{CH}_4\text{-Ar}$  (3D) using spherical coordinates,  $(R, \cos \theta, \phi)$ . The vibrational energies,  $\tilde{\nu}$  in  $\text{cm}^{-1}$  and referenced to the ZPVE, were computed with GENIUSH-DVR and the PES of Refs. 35 and 36. The vibrational states are labeled with the (approximate)  $j$  methane angular momentum quantum number, the  $n_R$  radial excitation index, and the  $\Gamma T_d(M)$  irrep label. The  $R$  and  $\phi$  degrees of freedom are described using generalized Laguerre basis functions ( $\mathcal{L}_n^{\alpha=2}$ ) scaled to  $[2.64, 30]$  Å and Fourier functions defined over the  $[0, 2\pi)$  interval, respectively. Legendre or sincot-Legendre DVR is used for  $\cos \theta$ . The number of basis functions and grid points is given for each set as  $(K_R^{\text{max}}, K_c^{\text{max}}, K_\phi^{\text{max}})$ . The test sets  $i = A_{3D}, B_{3D}$ , and  $C_{3D}$  are compared with the “final”, benchmark values of  $F_{3D}$ ,  $\Delta\tilde{\nu}_i = \tilde{\nu}_i - \tilde{\nu}_{F_{3D}}$ .

$n$	$j$	$n_R$	$\Gamma$	cos $\theta$ : Legendre-DVR		cos $\theta$ : sincot-Legendre				
				$A_{3D} : (111,111,31)$		$B_{3D} : (111,21,17)$		$C_{3D} : (111,31,31)$		$F_{3D} : (151,31,31)$
				$\tilde{\nu}_{A_{3D}}$	$\Delta\tilde{\nu}_{A_{3D}}$	$\tilde{\nu}_{B_{3D}}$	$\Delta\tilde{\nu}_{B_{3D}}$	$\tilde{\nu}_{C_{3D}}$	$\Delta\tilde{\nu}_{C_{3D}}$	$\tilde{\nu}_{F_{3D}}$
ZPVE	0	0	$A_1$	51.200	0.000	51.200	0.000	51.200	0.000	51.200
1	1	0	$F_2$	9.107	-0.002	9.109	0.000	9.109	0.000	9.109
2	1	0	$F_2$	9.107	-0.002	9.109	0.000	9.109	0.000	9.109
3	1	0	$F_2$	9.109	0.000	9.109	0.000	9.109	0.000	9.109
4	0	1	$A_1$	29.188	0.000	29.188	0.000	29.188	0.000	29.188
5	2	0	$F_2$	31.384	-0.004	31.388	0.000	31.388	0.000	31.388
6	2	0	$F_2$	31.384	-0.004	31.388	0.000	31.388	0.000	31.388
7	2	0	$F_2$	31.388	0.000	31.388	0.000	31.388	0.000	31.388
8	2	0	$E$	31.942	0.000	31.942	0.000	31.942	0.000	31.942
9	2	0	$E$	31.942	0.000	31.942	0.000	31.942	0.000	31.942
10	1	1	$F_2$	44.570	-0.004	44.573	0.000	44.573	0.000	44.573
11	1	1	$F_2$	44.570	-0.004	44.573	0.000	44.573	0.000	44.573
12	1	1	$F_2$	44.573	0.000	44.573	0.000	44.573	0.000	44.573
13	0	2	$A_1$	53.036	0.000	53.036	0.000	53.036	0.000	53.036
14	2	1	$F_2$	56.228	-0.004	56.232	0.000	56.232	0.000	56.232
15	2	1	$F_2$	56.228	-0.004	56.232	0.000	56.232	0.000	56.232
16	2	1	$F_2$	56.232	0.000	56.232	0.000	56.232	0.000	56.232
17	2	1	$E$	64.046	0.000	64.046	0.000	64.046	0.000	64.046
18	2	1	$E$	64.046	0.000	64.046	0.000	64.046	0.000	64.046
19	3	0	$F_2$	65.825	-0.013	65.837	0.000	65.837	0.000	65.837
20	3	0	$F_2$	65.825	-0.013	65.837	0.000	65.837	0.000	65.837
21	3	0	$F_2$	65.837	0.000	65.837	0.000	65.837	0.000	65.837
22	1	2	$F_1$	66.066	-0.004	66.070	0.000	66.070	0.000	66.070
23	1	2	$F_1$	66.066	-0.004	66.070	0.000	66.070	0.000	66.070
24	1	2	$F_1$	66.070	0.000	66.070	0.000	66.070	0.000	66.070
25	0	3	$A_1$	70.313	0.000	70.313	0.000	70.313	0.000	70.313
26	3	0	$A_1$	73.497	0.000	73.497	0.000	73.497	0.000	73.497
27	2	2	$F_2$	75.340	-0.007	75.347	0.000	75.347	0.000	75.347
28	2	2	$F_2$	75.340	-0.007	75.347	0.000	75.347	0.000	75.347
29	2	2	$F_2$	75.347	0.000	75.347	0.000	75.347	0.000	75.347
30	1	3	$F_2$	80.280	-0.003	80.283	0.000	80.283	0.000	80.283
31	1	3	$F_2$	80.280	-0.003	80.283	0.000	80.283	0.000	80.283
32	1	3	$F_2$	80.283	0.000	80.283	0.000	80.283	0.000	80.283
33	0	4	$A_1$	83.085	0.000	83.085	0.000	83.085	0.000	83.085
34	1	4	$F_2$	88.186	-0.003	88.189	0.000	88.189	0.000	88.189
35	1	4	$F_2$	88.186	-0.003	88.189	0.000	88.189	0.000	88.189
36	1	4	$F_2$	88.189	0.000	88.189	0.000	88.189	0.000	88.189
37	2	4	$E$	88.826	0.000	88.826	0.000	88.826	0.000	88.826
38	2	4	$E$	88.826	0.000	88.826	0.000	88.826	0.000	88.826
39	0	5	$A_1$	89.427	0.000	89.427	0.000	89.427	0.000	89.427

## 2. Intermolecular radial representation: Laguerre and Morse-tridiagonal basis sets

If we choose the  $\mathcal{L}_n^{(\alpha)}$  generalized Laguerre basis functions (with  $\alpha = 2$ ) for the  $R$  radial coordinate, we have to use a large number, more than 30, of basis functions to converge the vibrational bound states. Since in the present work we focus on the computation of bound states, it is better to use tridiagonal Morse basis set.<sup>51-53</sup> The parameters of the Morse function were determined according to the equations in Ref. 51 with  $D = 143.49 \text{ cm}^{-1}$ ,  $\alpha = 0.65$ , and  $\gamma = 0.00033$ . These parameters were adjusted to obtain 13 functions that recover the exact vibrational energies for the bound states of the radial Hamiltonian

$$\hat{H}_R = -\frac{1}{2\mu_{\text{CH}_4\text{Ar}}} \frac{\partial^2}{\partial R^2} + V(R, \theta^{\text{eq}}, \phi^{\text{eq}}), \quad (66)$$

where  $\mu_{\text{CH}_4\text{Ar}}$  is the reduced mass of methane and argon and  $\theta^{\text{eq}}$  and  $\phi^{\text{eq}}$  are the equilibrium values of the 3D PES. Since the  $\text{CH}_4\text{Ar}$  complex is a very isotropic system, the parameters and the radial basis set determined in this way should be useful over the entire range of the  $\theta \in [0, \pi]$  and  $\phi \in [0, 2\pi]$  coordinates.

## G. Analysis of the intramolecular representation: Vibrational states of $\text{CH}_4$

The vibrational basis set used to describe the intramolecular vibrational dynamics, i.e., vibrations of the methane molecule, was constructed from the harmonic oscillator basis set with the standard pruning condition,  $\sum_{k=1}^9 n_{q_k} \leq b$  in Eq. (41), and the Smolyak quadrature with  $\sum_{k=1}^9 g^{q_k}(i_{q_k}) \leq H$  in Eq. (42). Table II

**TABLE II.** Deviation of the vibrational energies,  $\text{cm}^{-1}$ , of the  $\text{CH}_4$  molecule obtained with GENIUSH-Smolyak with a pruned basis and grid, from the tightly converged results of Refs. 33, with increasing the  $b$  and  $H$  values in the basis and the grid pruning conditions, Eqs. (41) and (42), respectively. In general,  $H = b + D + 2 \geq b + D$  was found to be sufficient to converge the results (note that  $D = 9$  for isolated methane). The corresponding number of Smolyak points,  $N_{\text{Smol}}$ , is also shown.

$n$	Deviation from Ref. 33							Reference 33
	2	3	4	5	6	7	8	
$b$ :	2	3	4	5	6	7	8	
$H_{9D}$ :	13	14	15	16	17	18	19	
$N_{\text{Smol}}$ :	3481	11 833	35 929	97 561	241 201	556 707	1 202 691	
ZPV	41.18	2.51	0.66	0.57	0.07	0.02	0.02	9 651.29
1	47.81	44.46	3.03	0.81	0.65	0.09	0.03	10 961.76
2	47.81	44.45	3.03	0.81	0.65	0.09	0.03	10 961.76
3	47.82	44.45	3.03	0.81	0.65	0.09	0.03	10 961.76
4	45.91	42.46	2.97	0.75	0.61	0.08	0.03	11 184.76
5	45.93	42.47	2.97	0.75	0.61	0.08	0.03	11 184.76
6	81.12	57.35	46.15	4.79	1.23	0.74	0.14	12 238.29
7	75.65	55.48	48.12	4.18	1.14	0.77	0.13	12 265.12
8	75.73	55.48	48.11	4.17	1.14	0.77	0.13	12 265.13
9	76.42	55.48	48.11	4.17	1.13	0.77	0.13	12 265.13
10	65.82	53.24	47.43	3.49	1.00	0.72	0.11	12 275.73
11	65.85	53.24	47.43	3.49	1.00	0.72	0.11	12 275.74
12	78.12	53.43	43.26	3.87	1.03	0.66	0.11	12 481.49
13	78.77	53.48	43.26	3.88	1.03	0.66	0.11	12 481.49
14	78.77	53.48	43.27	3.87	1.03	0.66	0.11	12 481.49
15	72.37	51.38	45.63	3.57	0.93	0.69	0.10	12 497.25
16	72.37	51.38	45.65	3.56	0.94	0.69	0.10	12 497.25
17	73.08	51.44	45.65	3.57	0.94	0.69	0.10	12 497.26
18	83.68	72.76	15.82	2.88	1.76	0.47	0.12	12 568.47
19	86.04	74.55	16.18	2.89	1.79	0.48	0.12	12 670.73
20	86.07	74.56	16.18	2.89	1.79	0.48	0.12	12 670.73
21	86.07	74.56	16.18	2.89	1.79	0.48	0.12	12 670.73

shows the convergence of the lowest vibrational states by increasing  $b$  and  $H$ .

As to the 12D computation of  $\text{CH}_4\cdot\text{Ar}$ , the bound states correspond to the zero-point vibrational state (ZPV) of  $\text{CH}_4$ ; we focused on the lowest-energy states of  $\text{CH}_4$ . Of course, more accurate results for the isolated methane molecule can be obtained by increasing the size of the Smolyak grid, which is perfectly feasible for a 9D computation.

In a minimalistic setup (to be transferred for the 12D computations), we chose a representation which allowed us to converge the fundamental vibrational energies within  $1\text{ cm}^{-1}$ . In this representation, the 9D Smolyak grid includes more than 100 000 points, which is approximately an order of magnitude larger than what is necessary for a meaningful representation of the zero-point vibration.

## V. FULL-DIMENSIONAL (12D) RESULTS FOR METHANE-ARGON

All bound-state vibrational energies were computed for the  $\text{CH}_4\cdot\text{Ar}$  complex in full (12D) vibrational dimensionality (Table IV). The basis and the grid representations are selected based on the convergence tests carried out for the intermolecular and intramolecular representations (Secs. IV F and IV G). Concerning the intermolecular representation, it is composed of Morse-tridiagonal basis functions with  $N_R^{\text{max}} = 12$ , sincot-Legendre-DVR basis functions with  $N_c^{\text{max}} = 20$ , and Fourier functions with  $N_\phi^{\text{max}} = 17$ . The number of quadrature points was  $K_R^{\text{max}} = 15$ ,  $K_c^{\text{max}} = 21$ , and  $K_\phi^{\text{max}} = 20$ . As to the methane fragment, we used four different intramolecular representations, with  $b = 0, 1, 2$ , and  $3$  values, which allowed us to check the convergence of the ZPVE and the vibrational energies in the full-dimensional treatment.

Table III gives an overview of the orders of magnitudes of the basis and the grid representations employed in the final 12D computations. The largest computation (set  $D$  in the table) includes 82 002 690 ( $8.20 \cdot 10^7$ ) quadrature points and 1 021 020 ( $1.02 \cdot 10^6$ ) basis functions. The numerical KEO terms [Eq. (51)] and the PES are stored as double precision reals (in Fortran) at every grid point, which amounts to a  $(12 \cdot 13/2 + 12 + 1) \cdot 8.20 \cdot 10^7 = 60$  GB

memory usage. The dimensionality of the Lanczos vectors is determined by the number of basis functions, so one Lanczos vector occupies a negligible amount of 8 MB of memory. To multiply a trial vector with the Hamiltonian matrix took  $\sim 230$  s on 51 processor cores, and we had to perform  $\sim 10\,000$  matrix-vector multiplications to obtain the 40 states reported in Table IV using an in-house Lanczos implementation (it might be possible to reduce the number of matrix-vector products with a Lanczos and a preconditioning algorithm optimized for the present system).

Based on the isolated-methane test computations (Table II), the error in the ZPVE for  $b = 2$  and  $3$  is 41 and  $2.5\text{ cm}^{-1}$ , respectively. The vibrational energies of the complex (referenced to the ZPVE) change less than  $0.01\text{ cm}^{-1}$  by increasing the  $b$  value from 2 to 3; hence, we may accept them as converged for  $b = 3$ . The ZPVE of the complex is probably accurate within a few  $\text{cm}^{-1}$  with  $b = 3$  similarly to the case of the isolated methane (Table II). We only note that a full 12D computation with  $b = 4$  would also be feasible with the current implementation, but it would only change the ZPVE since the vibrational energies were converged already with  $b = 3$ .

We also show the  $b = 0$  results, which correspond to a single harmonic oscillator function for methane (the product of the zeroth harmonic oscillator basis functions for  $q_1, \dots, q_9$ ). Since the present model includes only kinetic coupling (the PES coupling is also probably very small), the deviation of  $\tilde{\nu}_A$  ( $b = 0$ ) and  $\tilde{\nu}_A$  ( $b = 3$ ) is due to the structural differences of methane: the effective structure for the  $b = 0$  ground-state harmonic oscillator basis function is the equilibrium structure, whereas  $b > 0$  accounts for structural distortions due to anharmonicity effects. This change is related to the common wisdom in reduced-dimensionality computations of weakly bound complexes that it is better to use effective (vibrationally averaged) monomer structures than equilibrium monomer structures.<sup>54</sup> In agreement with this prescription, the 3D computation (column  $F_{3D}$  in Table III) performed with an effective methane structure corresponding to the (isolated) ground-state vibration very well reproduces the 12D result (remember that only kinetic coupling is included in the present computation due to the lack of a 12D fully coupled PES).

**TABLE III.** Intramolecular (methane, “Met”) basis set and grid choices used in the 12D  $\text{CH}_4\cdot\text{Ar}$  vibrational computations with the basis and grid pruning conditions  $n_{q_1} + \dots + n_{q_9} \leq b$  and  $i_{q_1} + \dots + i_{q_9} \leq H$ , respectively.  $H = b + D + 2 \geq b + D$  was found to be sufficient to converge the results ( $D = 12$ ). The number of basis functions,  $N$ , and grid points,  $K$ , is also given for the methane (“Met,” “Smol”) for the intermolecular (“Inter”) and for the full (12D) computations.

Label	Intramolecular ( $\text{CH}_4$ , 9D)				Intermolecular (3D)		$\text{CH}_4\cdot\text{Ar}$ (12D)	
	$b$	$H$	$N_{\text{Met}}$	$K_{\text{Smol}}/10^3$	$N_{\text{Inter}}/10^3$	$K_{\text{Inter}}/10^3$	$N_{12D}/10^5$	$K_{12D}/10^7$
A	0	14	1	0.163	4.28	6.30	0.0464	0.113
B	1	15	10	0.871	4.28	6.30	0.464	0.604
C	2	16	55	3.48	4.28	6.30	2.55	2.41
D	3	17	220	11.8	4.28	6.30	10.2	8.20

**TABLE IV.** Vibrational bound-state energies,  $\tilde{\nu}$  in  $\text{cm}^{-1}$ , referenced to the ZPVE of  $\text{CH}_4\text{-Ar}$  computed in full (12D) vibrational dimensionality using the GENIUSH program extended with the Smolyak algorithm in the present work. The potential energy was approximated with the sum of the molecule-atom interaction PES of Refs. 35 and 36 and the isolated methane PES of Ref. 33. The A, B, C, and D basis and grid representations defined in Table III correspond to an increasing  $b = 0, 1, 2,$  and  $3$  value in the methane basis functions' pruning condition [Eq. (41)]. Convergence of the results can be estimated based on the deviation from computation D,  $\Delta\tilde{\nu}_i = \tilde{\nu}_i - \tilde{\nu}_D$  (see also Table II). For comparison, the benchmark 3D computation with a fixed, effective ( $v = 0$ ) methane geometry ( $F_{3D}$ ) is also shown (taken from Table I).

Label	12D						3D (Table I) $\tilde{\nu}_{F_{3D}}$	
	A ( $b = 0$ )		B ( $b = 1$ )		C ( $b = 2$ )			D ( $b = 3$ )
	$\tilde{\nu}_A$	$\Delta\tilde{\nu}_A$	$\tilde{\nu}_B$	$\Delta\tilde{\nu}_B$	$\tilde{\nu}_C$	$\Delta\tilde{\nu}_C$		$\tilde{\nu}_D$
ZPV	9695.262	132.242	9604.164	41.144	9600.706	37.686	9563.019	51.200
1	9.398	0.285	9.139	0.026	9.112	-0.002	9.113	9.109
2	9.398	0.285	9.139	0.026	9.112	-0.002	9.113	9.109
3	9.398	0.285	9.139	0.026	9.112	-0.002	9.113	9.109
4	29.275	0.086	29.197	0.008	29.189	-0.000	29.189	29.188
5	31.970	0.575	31.447	0.052	31.392	-0.003	31.395	31.388
6	31.970	0.575	31.447	0.052	31.392	-0.003	31.395	31.388
7	31.970	0.574	31.447	0.052	31.392	-0.003	31.395	31.388
8	32.687	0.736	32.016	0.066	31.946	-0.004	31.950	31.942
9	32.687	0.736	32.017	0.066	31.946	-0.004	31.950	31.942
10	45.042	0.463	44.620	0.041	44.576	-0.003	44.579	44.573
11	45.042	0.463	44.620	0.041	44.577	-0.003	44.579	44.573
12	45.042	0.463	44.620	0.041	44.577	-0.003	44.579	44.573
13	53.156	0.119	53.048	0.011	53.036	-0.001	53.037	53.036
14	57.039	0.799	56.313	0.073	56.236	-0.005	56.240	56.232
15	57.039	0.799	56.313	0.073	56.236	-0.005	56.240	56.232
16	57.039	0.799	56.313	0.073	56.236	-0.005	56.240	56.232
17	64.807	0.753	64.122	0.068	64.050	-0.004	64.055	64.046
18	64.807	0.753	64.122	0.068	64.050	-0.004	64.055	64.046
19	66.819	0.970	65.989	0.141	65.839	-0.009	65.848	65.837
20	66.819	0.971	65.989	0.141	65.839	-0.009	65.848	65.837
21	66.819	0.970	65.989	0.141	65.839	-0.009	65.848	65.837
22	67.414	1.337	66.143	0.066	66.072	-0.004	66.076	66.070
23	67.414	1.337	66.143	0.067	66.072	-0.004	66.076	66.070
24	67.414	1.337	66.143	0.067	66.072	-0.004	66.077	66.070
25	70.705	0.388	70.360	0.043	70.314	-0.003	70.317	70.313
26	74.623	1.118	73.597	0.092	73.499	-0.006	73.505	73.497
27	76.276	0.920	75.438	0.081	75.351	-0.005	75.356	75.347
28	76.276	0.920	75.438	0.081	75.351	-0.005	75.356	75.347
29	76.276	0.920	75.442	0.086	75.351	-0.005	75.356	75.347
30	80.808	0.517	80.338	0.047	80.287	-0.003	80.290	80.283
31	80.808	0.517	80.338	0.047	80.288	-0.003	80.291	80.283
32	80.808	0.517	80.337	0.047	80.288	-0.003	80.291	80.283
33	83.156	0.067	83.093	0.004	83.088	-0.000	83.088	83.085
34	88.844	0.647	88.255	0.057	88.194	-0.004	88.197	88.189
35	88.844	0.647	88.254	0.056	88.194	-0.004	88.198	88.189
36	88.844	0.647	88.254	0.056	88.194	-0.004	88.198	88.189
37	89.588	0.753	88.903	0.068	88.830	-0.004	88.835	88.826
38	89.588	0.753	88.902	0.067	88.830	-0.004	88.835	88.826
39	89.505	0.017	89.431	-0.057	89.488	0.000	89.488	89.427

## VI. SUMMARY, CONCLUSIONS, AND OUTLOOK

The numerical kinetic-energy operator (KEO) approach as implemented in the GENIUSH program<sup>27</sup> has been extended with the Smolyak algorithm,<sup>16,17</sup> which opens a promising route toward variational (ro)vibrational computations for polyatomic systems with multiple large-amplitude motions.

A direct, variational solution of the (ro)vibrational Schrödinger equation of polyatomic systems (without imposing constraints on the coordinates) is difficult due to the high vibrational dimensionality, which generates an exponential growth in the direct-product basis used to represent the wave functions and an exponential growth in the direct-product grid necessary to calculate integrals of multidimensional operator terms in the Hamiltonian.

If coordinates well-suited for the motions in the system and good zeroth-order basis functions can be found for each coordinate, it is not necessary to use a direct-product basis, but a much smaller, “pruned” basis can be defined, the size of which does not scale exponentially with the number of vibrational degrees of freedom. If it is possible to prune a direct-product basis, it is also possible to find a pruned product grid to calculate integrals. The Smolyak scheme of Avila and Carrington<sup>16,17</sup> makes it possible to define non-product (Smolyak) grids, which are orders of magnitude smaller than a direct-product grid but which retain some of the practical features of a direct-product grid. Most importantly, Smolyak grids can be efficiently used in computing matrix-vector products and efficient matrix-vector products allow us to compute eigenvalues and eigenfunctions with an iterative (Lanczos) eigensolver without storing or even explicitly computing the Hamiltonian matrix elements.

In the present work, the combination of these ideas with the numerical KEO approach of GENIUSH was elaborated and explained for all stages of the vibrational computation of the floppy CH<sub>4</sub>·Ar complex treated in full vibrational dimensionality. Due to the highly fluxional nature of this system, regions of the curvilinear coordinate domains above which the KEO has singularities are dynamically important.

In a fully finite basis representation (FBR) treatment of the numerical KEO, the Hamiltonian matrix fails to be Hermitian due to inaccurate integration of the singularities in general coordinates. As a practical way to avoid these singularity problems in FBR, we proposed to use (efficient) DVRs and an inherently symmetric form of the general KEO for the singular coordinate(s), which ensures a symmetric matrix representation by construction and correct limiting (convergence) behavior at the same time. In practice, this hybrid DVR-FBR treatment allows us to converge all bound vibrational states of CH<sub>4</sub>·Ar.

In general, this hybrid DVR-FBR approach makes it possible to continue using (1) numerical KEOs and (2) general and simple starting product basis sets and grids (both pruned according to physically motivated restrictions) for systems with multiple large-amplitude motions and ultimately to (further) develop a universal, black-box-type (ro)vibrational procedure practical for polyatomic systems. Extension of the algorithm for  $J > 0$  rotational quantum number is straightforward; limitations might be set by the memory requirements and the computational time.

We can foresee future possible improvements of the present procedure to (at least partially) eliminate the current bottlenecks in terms of memory usage (storage of the numerical KEO terms over the grid; see for example Ref. 55) and perhaps also in terms of the computational cost. Furthermore, the present developments, in particular, the fact that the Smolyak grid is several orders of magnitude smaller than the direct product grid, can be combined with the basis-set contraction idea.<sup>7,13,56</sup> With these or other developments, it will become possible to directly access the predissociation spectral range corresponding to the molecule’s fundamental (and lowest overtone) vibrations in weakly or more strongly bound complexes of the size of CH<sub>4</sub>·Ar, i.e., with  $D = 12$  or perhaps beyond this value. In general, a careful choice of the coordinate set, the basis, and the grid representation is required to make full use of the ideas combined, developed, and described in the present work. We hope that these ideas will find applications, beyond the realm of molecular complexes, among high-dimensional molecular systems with multiple large-amplitude motions.

## SUPPLEMENTARY MATERIAL

The definition of the normal coordinates used for the methane fragment is provided in the [supplementary material](#).

## ACKNOWLEDGMENTS

Financial support of the Swiss National Science Foundation through a PROMYS Grant (No. IZ11Z0\_166525) is gratefully acknowledged. We thank PRACE for a Preparatory Access Grant during 2017–2018 and NIFI for allocating computer time at the Hungarian Computing Infrastructure (Miskolc node). Xiao-Gang Wang and Tucker Carrington helped us to get through a difficult stage of the development work by sharing their well-tested sincot-Legendre-DVR implementation (codvr.f90) with us.<sup>57</sup> We are indebted to our colleagues and co-authors, in particular, Tucker Carrington, Attila Császár, and Gábor Czakó, with whom we worked together on Refs. 16 and 27 and also the colleagues who later contributed to the further developments and successful applications of the initial methods over the past 10 years.

## REFERENCES

- X. Huang, B. J. Braams, J. M. Bowman, R. E. A. Kelly, J. Tennyson, G. C. Groenenboom, and A. van der Avoird, *J. Chem. Phys.* **128**, 034312 (2008).
- A. van der Avoird, R. Podeszwa, K. Szalewicz, C. Leforestier, R. van Harrevelt, P. R. Bunker, M. Schnell, G. von Helden, and G. Meijer, *Phys. Chem. Chem. Phys.* **12**, 8219 (2010).
- J. Tennyson and B. T. Sutcliffe, *J. Chem. Phys.* **79**, 43 (1983).
- D. Zhang, Q. Wu, J. Z. H. Zhang, M. Von Dirke, and Z. Bacic, *J. Chem. Phys.* **102**, 2315 (1995).
- C. Leforestier, K. Szalewicz, and A. van der Avoird, *J. Chem. Phys.* **137**, 014305 (2012).
- X.-G. Wang and T. Carrington, Jr., *J. Chem. Phys.* **146**, 104105 (2017).
- X.-G. Wang and T. Carrington, Jr., *J. Chem. Phys.* **148**, 074108 (2018).
- H.-D. Meyer, F. Gatti, and G. A. Worth, “MCTDH for density operator,” in *Multidimensional Quantum Dynamics* (Wiley-Blackwell, 2009), Chap. 7, pp. 57–62.
- M. Beck, A. Jackle, G. Worth, and H.-D. Meyer, *Phys. Rep.* **324**, 1 (2000).
- A. Leclerc and T. Carrington, *J. Chem. Phys.* **140**, 174111 (2014).
- P. S. Thomas and T. Carrington, *J. Chem. Phys.* **146**, 204110 (2017).

- <sup>12</sup>J. M. Bowman, S. Carter, and X. Huang, *Int. Rev. Phys. Chem.* **22**, 533 (2003).
- <sup>13</sup>Z. Bacic and J. C. Light, *Annu. Rev. Phys. Chem.* **40**, 469 (1989).
- <sup>14</sup>J. R. Henderson and J. Tennyson, *Chem. Phys. Lett.* **173**, 133 (1990).
- <sup>15</sup>M. Mladenovic, *Spectrochim. Acta, Part A* **58**, 795 (2002).
- <sup>16</sup>G. Avila and T. Carrington, Jr., *J. Chem. Phys.* **131**, 174103 (2009).
- <sup>17</sup>G. Avila and T. Carrington, Jr., *J. Chem. Phys.* **134**, 054126 (2011).
- <sup>18</sup>T. Halverson and B. Poirier, *J. Phys. Chem. A* **119**, 12417 (2015).
- <sup>19</sup>J. Brown and T. Carrington, *J. Chem. Phys.* **145**, 144104 (2016).
- <sup>20</sup>A. Jackle and H.-D. Meyer, *J. Chem. Phys.* **104**, 7974 (1996).
- <sup>21</sup>B. Ziegler and G. Rauhut, *J. Phys. Chem. A* **123**, 3367 (2019).
- <sup>22</sup>V. I. Lebedev and D. Laikov, *Doklady Mathematics* (Pleiades Publishing, 1999), Vol. 59, pp. 477–481.
- <sup>23</sup>C. W. Murray, N. C. Handy, and G. J. Laming, *Mol. Phys.* **78**, 997 (1993).
- <sup>24</sup>X.-G. Wang and T. Carrington, *J. Chem. Theory Comput.* **2**, 599 (2003).
- <sup>25</sup>A. H. Stroud, *Approximate Calculation of Multiple Integrals* (Prentice-Hall, Englewood Cliffs, NJ, 1971).
- <sup>26</sup>D. Lauvergnat and A. Nauts, *Spectrochim. Acta, Part A* **119**, 18 (2014).
- <sup>27</sup>E. Mátyus, G. Czakó, and A. G. Császár, *J. Chem. Phys.* **130**, 134112 (2009).
- <sup>28</sup>J. C. Light and T. Carrington, Jr., “Discrete-variable representations and their utilization,” in *Advances in Chemical Physics* (John Wiley & Sons, 2007), pp. 263–310.
- <sup>29</sup>A. Yachmenev and S. N. Yurchenko, *J. Chem. Phys.* **143**, 014105 (2015).
- <sup>30</sup>D. Lauvergnat and A. Nauts, *J. Chem. Phys.* **116**, 8560 (2002).
- <sup>31</sup>B. Podolsky, *Phys. Rev.* **32**, 812 (1928).
- <sup>32</sup>E. Mátyus, *J. Chem. Phys.* **149**, 194111 (2018).
- <sup>33</sup>X.-G. Wang and T. Carrington, Jr., *J. Chem. Phys.* **141**, 154106 (2014).
- <sup>34</sup>J. S. Coursey, D. J. Schwab, J. J. Tsai, and R. A. Dragoset, Atomic Weights and Isotopic Compositions (version 4.1), National Institute of Standards and Technology, Gaithersburg, MD, 2015, <http://physics.nist.gov/Comp> (last accessed 12 May, 2018).
- <sup>35</sup>M. Geleijns, N. Halberstadt, J. Millan, P. E. S. Wormer, and A. van der Avoird, *Faraday Discuss.* **118**, 143 (2001).
- <sup>36</sup>M. Geleijns, P. E. S. Wormer, and A. van der Avoird, *J. Chem. Phys.* **117**, 7551 (2002).
- <sup>37</sup>R. Cools, E. Novak, and K. Ritter, *Computing* **62**, 147 (1999).
- <sup>38</sup>Smolyak sparse grid datasets for different dimensions and accuracies can be found at the websites [https://people.sc.fsu.edu/~jburkardt/f\\_src/sandia\\_sgmegg/sandia\\_sgmegg.html](https://people.sc.fsu.edu/~jburkardt/f_src/sandia_sgmegg/sandia_sgmegg.html) and <http://sparse-grids.de>.
- <sup>39</sup>G. Avila and T. Carrington, Jr., *J. Chem. Phys.* **134**, 064101 (2011).
- <sup>40</sup>R. J. Whitehead and N. C. Handy, *J. Mol. Spectrosc.* **55**, 356 (1975).
- <sup>41</sup>J.-P. Brunet, R. A. Friesner, R. E. Wyatt, and C. Leforestier, *Chem. Phys. Lett.* **153**, 425 (1988).
- <sup>42</sup>M. J. Bramley and T. Carrington, Jr., *J. Chem. Phys.* **101**, 8494 (1994).
- <sup>43</sup>H. Wei and T. Carrington, Jr., *J. Chem. Phys.* **101**, 1343 (1994).
- <sup>44</sup>C. Fábri, A. G. Császár, and G. Czakó, *J. Phys. Chem. A* **117**, 6975 (2013).
- <sup>45</sup>E. Mátyus, T. Szidarovszky, and A. G. Császár, *J. Chem. Phys.* **141**, 154111 (2014).
- <sup>46</sup>C. Fábri, J. Sarka, and A. G. Császár, *J. Chem. Phys.* **140**, 051101 (2014).
- <sup>47</sup>J. Sarka and A. G. Császár, *J. Chem. Phys.* **144**, 154309 (2016).
- <sup>48</sup>J. Sarka, A. G. Császár, S. C. Althorpe, D. J. Wales, and E. Mátyus, *Phys. Chem. Chem. Phys.* **18**, 22816 (2016).
- <sup>49</sup>J. Sarka, A. G. Császár, and E. Mátyus, *Phys. Chem. Chem. Phys.* **19**, 15335 (2017).
- <sup>50</sup>G. Schiffl and U. Manthe, *Chem. Phys.* **374**, 118 (2010).
- <sup>51</sup>H. Wei and T. Carrington, Jr., *J. Chem. Phys.* **97**, 3029 (1992).
- <sup>52</sup>B. R. Johnson and W. P. Reinhardt, *J. Chem. Phys.* **85**, 4538 (1986).
- <sup>53</sup>J. Tennyson and B. T. Sutcliffe, *J. Chem. Phys.* **77**, 4061 (1982).
- <sup>54</sup>M. Jeziorska, P. Jankowski, K. Szalewicz, and B. Jeziorski, *J. Chem. Phys.* **113**, 2957 (2000).
- <sup>55</sup>A. Nauts and D. Lauvergnat, *Mol. Phys.* **116**, 3701 (2018).
- <sup>56</sup>S. N. Yurchenko, R. J. Barber, A. Yachmenev, W. Thiel, P. Jensen, and J. Tennyson, *J. Phys. Chem. A* **113**, 11845 (2009).
- <sup>57</sup>X.-G. Wang and T. Carrington, Jr., *Mol. Phys.* **110**, 825 (2012).



Cite this: *Phys. Chem. Chem. Phys.*,  
2017, 19, 15335

# Rovibrational quantum dynamical computations for deuterated isotopologues of the methane–water dimer†

János Sarka, <sup>ab</sup> Attila G. Császár <sup>ab</sup> and Edit Mátyus <sup>\*a</sup>

Rovibrational states of four dimers formed by the light and the heavy isotopologues of the methane and water molecules are computed using a potential energy surface taken from the literature. The general rovibrational energy-level pattern characteristic to all systems studied is analyzed employing two models of a dimer: the rigidly rotating complex and the coupled system of two rigidly rotating monomers. The rigid-rotor model highlights the presence of rovibrational sequences corresponding to formally negative rotational excitation energies, which is explained in terms of the coupled-rotors picture.

Received 31st March 2017,  
Accepted 18th May 2017

DOI: 10.1039/c7cp02061a

rsc.li/pccp

## I. Introduction

Weak molecular interactions are important in many areas of chemistry because they make it possible to break and form molecular assemblies, including macromolecules like proteins, and are involved in the self-organization of materials. Weakly bound systems exhibit several interesting and unusual spectroscopic features. High-resolution spectroscopic measurements, when compared with the results of quantum dynamical computations, provide a stringent test of the quality of potentials modeling the interactions of the monomers in the complexes. For quantum dynamical computations, weakly bound complexes are of further interest because they are usually floppy, highly delocalized systems, which challenge our traditional tools and concepts of molecular structure and dynamics.

The methane–water dimer is a floppy, weakly bound complex. It was subjected to microwave<sup>1</sup> and high-resolution far-infrared<sup>2</sup> spectroscopic experiments some twenty years ago. The elucidation of the observed far-infrared transitions by means of quantum dynamical computations had to wait until last year.<sup>3</sup> The experimentally measured<sup>2</sup> and the computed rovibrational transitions up to  $J = 2,^3$  using an accurate *ab initio* intermolecular potential energy surface (PES),<sup>4</sup> are in excellent agreement, yielding deviations on the order of a few  $\text{cm}^{-1}$ . The rovibrational computations reproduce fine details of and provide an assignment to many experimental features. Most interestingly, the experimentally observed reversed rovibrational sequences

(whereby within the usual molecular picture one would assign a “negative” rotational energy to a vibrational state, a characteristic feature of certain floppy molecular systems<sup>5–11</sup>) were also obtained in the computations.

Ref. 3 left the explanation of these reversed sequences to further work suggesting that perhaps they could be better understood in terms of a coupled-rotor model rather than using the traditional picture of a rotating–vibrating molecule. The purpose of the present study is to work out this idea. In fact, we propose and describe a general algorithm to compute the similarity (overlap) of eigenstates of two coupled rotors with the full intermolecular wave function. This coupled-rotor decomposition (CRD) scheme is generally applicable to any system that can be partitioned into two subsystems. Through the application of the CRD scheme to all four possible combinations of the light and deuterated monomers,  $\text{CH}_4\text{-H}_2\text{O}$ ,  $\text{CH}_4\text{-D}_2\text{O}$ ,  $\text{CD}_4\text{-H}_2\text{O}$ , and  $\text{CD}_4\text{-D}_2\text{O}$ , we gain a general overview of the dynamical properties of the methane–water dimer.

## II. Computational details

The quantum dynamical computations of the present study were carried out using the GENIUSH<sup>12,13</sup> code, which was reviewed in ref. 14 highlighting quantum chemical algorithms and computer codes of the fourth age of quantum chemistry. In GENIUSH, the matrix representation of the Hamiltonian is constructed in the discrete variable representation (DVR)<sup>15</sup> and the kinetic energy operator is evaluated numerically during the course of the computation for the selected internal coordinates and body-fixed frame. An iterative Lanczos algorithm<sup>16</sup> is used to compute the required eigenvalues and eigenvectors. In the present work, our in-house Lanczos implementation was

<sup>a</sup> Institute of Chemistry, Eötvös Loránd University, Pázmány Péter sétány 1/A, Budapest, H-1117, Hungary. E-mail: matyus@chem.elte.hu

<sup>b</sup> MTA-ELTE Complex Chemical Systems Research Group, P.O. Box 32, H-1518 Budapest 112, Hungary

† Electronic supplementary information (ESI) available. See DOI: 10.1039/c7cp02061a

improved and optimized for the determination of a large number of eigenstates. Over the years, a number of tools have been developed supporting the analysis of the computed rovibrational wave functions.<sup>6,17</sup>

Computations with the GENIUSH code feature a series of floppy molecular systems.<sup>5,6,12,13,18–21</sup> For example, molecular systems with reversed rovibrational sequences (hence termed “astructural molecules”) were studied in ref. 5 and 6. A molecular complex with almost fully decoupled degrees of freedom resulting in long-lived resonances was presented in ref. 21. Furthermore, the flexibility of the code makes it possible to model non-adiabatic effects in the rovibrational spectrum by using different rotational and vibrational masses.<sup>22</sup>

Hereby we only shortly summarize the computational parameters and explain any difference compared to our earlier work.<sup>3</sup> In the present study we computed the lowest-energy few dozens rovibrational eigenstates (150 states for  $J = 2$ ) for the four isotopologues of the methane–water dimer with  $J = 0, 1,$  and  $2$  rotational angular momentum quantum numbers utilizing the QCHB15 PES.<sup>23,37</sup>

In the quantum dynamical computations of the dimer, the methane and the water monomer structures are fixed and six active internal coordinates describe the intermolecular dynamics. According to a recent study on the variation of the monomer structures due to non-covalent interactions,<sup>24</sup> this appears to be a fairly good approximation. The active internal coordinates,  $(R, \cos \theta, \phi, \alpha, \cos \beta, \gamma)$ , and the embedding are identical to those of ref. 3, but in this work we use the vibrationally averaged,  $r_0$ , structures of the monomers, summarized in Table 1. These values were made available for the H<sub>2</sub>O and D<sub>2</sub>O isotopologues in ref. 25, whereas for CH<sub>4</sub> and CD<sub>4</sub> we computed them as part of this study using the T8 force field.<sup>26</sup> The atomic masses used throughout this work are  $m(\text{H}) = 1.007825$  u,  $m(\text{D}) = 2.014102$  u,  $m(\text{C}) = 12$  u, and  $m(\text{O}) = 15.994915$  u.

The same DVRs were used for the active degrees of freedom as in ref. 3, which are listed in Table 2 for the sake of completeness. The global minimum (GM) structure of the QCHB15 PES is also given in Table 2. The corresponding  $(A, B, C)/\text{cm}^{-1}$  rotational constants of the (near-symmetric top) dimers used for the wave function analysis are (0.158421, 0.157281, 4.14248) for CH<sub>4</sub>·H<sub>2</sub>O, (0.149861, 0.147929, 3.56864) for CH<sub>4</sub>·D<sub>2</sub>O, (0.138355, 0.137491, 2.28551) for CD<sub>4</sub>·H<sub>2</sub>O, and (0.130425, 0.128981, 2.09921) for CD<sub>4</sub>·D<sub>2</sub>O.

For a short and unambiguous referencing of the various isotopologues and their energy levels, we introduce the notation CH<sub>4</sub>·H<sub>2</sub>O (HH), CH<sub>4</sub>·D<sub>2</sub>O (HD), CD<sub>4</sub>·H<sub>2</sub>O (DH), and CD<sub>4</sub>·

**Table 1** Structural parameters and the corresponding rotational constants of the methane and the water molecules in their ground vibrational state ( $X = \text{O}$  or  $\text{C}$  and  $Y = \text{H}$  or  $\text{D}$ )

	CH <sub>4</sub>	CD <sub>4</sub>	H <sub>2</sub> O	D <sub>2</sub> O
$\langle r_{\text{XY}} \rangle [\text{\AA}]$	1.11002	1.10446	0.97565	0.97077
$\langle \alpha_{\text{YXY}} \rangle [^\circ]$	109.471	109.471	104.430	104.408
$A [\text{cm}^{-1}]$			9.17136	4.80367
$B [\text{cm}^{-1}]$	5.09073	2.57303	14.0667	7.11182
$C [\text{cm}^{-1}]$			26.3538	14.8010

**Table 2** Internal coordinates (Coord.), discrete variable representations (DVR), number of grid points ( $N$ ), and grid intervals used in GENIUSH to compute the rovibrational states of the methane–water dimers

Coord.	Min. <sup>a</sup>	Nuclear motion computations		
		DVR type <sup>b</sup>	$N$	Grid interval
$R [\text{\AA}]$	3.447	PO Laguerre	15	Scaled to [2.5,6.0]
$\theta [^\circ]$	117.72	PO Legendre	14	Scaled to [1,179]
$\phi [^\circ]$	90.00	Exponential	15	Unscaled on [0,360]
$\alpha [^\circ]$	297.65	Exponential	9	Unscaled on [0,360]
$\beta [^\circ]$	112.80	PO Legendre	21	Scaled to [1,179]
$\gamma [^\circ]$	293.52	Exponential	21	Unscaled on [0,360]

<sup>a</sup> Equilibrium geometry in internal coordinates corresponding to the global minimum (GM) of the QCHB15 PES.<sup>23</sup> <sup>b</sup> PO: potential-optimized DVR (optimization of the DVR points for a 1-dimensional model).<sup>27,28</sup>

D<sub>2</sub>O (DD). For the computed (ro)vibrational states of XY ( $X, Y = \text{H}, \text{D}$ ) with  $J = 0, 1,$  and  $2$  we shall use the labels XY- $J0.n$ , XY- $J1.n$ , and XY- $J2.n$ , respectively, where the integer  $n$  enumerates all computed levels (including degeneracies) in an increasing energy order.

### III. Assignment of the computed rovibrational states

The direct solution of the rovibrational Schrödinger equation provides numerically correct (“exact”) energy levels and wave functions, which carry detailed (“all”) information about the system. They can be used to make a direct comparison with experimentally observable transitions, to compute electric dipole transition intensities, *etc.* Although the wave functions carry “all” the information that can be learned about each state, it is usually overly complicated to “read” them and we may prefer to think about the states in terms of some well-established but simpler model. These simpler general descriptions include determination of the irreducible symmetry labels of the states based on the underlying molecular symmetry (MS) group, see, *e.g.*, ref. 29; characterization of the nodal structure (“node counting”), see, *e.g.*, ref. 3, 6, and 21; computation of expectation values of structural parameters, see, *e.g.*, ref. 3; or determination of the similarity (overlap) of the full wave function with wave functions of simple model systems as advocated, *e.g.*, in ref. 17. For this purpose, the harmonic oscillator model of vibrational states and the rigid rotor (RR) model of rotational states are the working horses of molecular spectroscopy.

Another limiting model, relevant to weakly bound dimers including but not limited to the ones studied herein, is obtained by means of the coupling of rotating (rigid) subsystems. In what follows, we define an algorithm, which we call the coupled-rotor decomposition (CRD) scheme, in order to compute the overlap of the full wave function (which might be available only in some grid representations, as is the case in a GENIUSH computation) with the coupled-rotor functions.

#### A. The coupled-rotor decomposition

The development and use of the CRD scheme has been motivated by the interesting energy-level structure of the methane–water



dimer but it is useful for the understanding of the internal dynamics of other floppy systems that can be partitioned into two subsystems.

In order to take a closer look at the model that we would like to use to characterize the full system, we reiterate that it consists of two rigid rotors fixed at a certain distance and the rotors are coupled to some total angular momentum state without being under the influence of any external potential. To assign the wave functions of the full system to states of the coupled, rotating monomers, we define the following three-step numerical approach:

- Step (1): compute the rovibrational states of a 5-dimensional model using the same coordinate and grid representation as for the full model but with a fixed intermonomer separation,  $R$ , and with  $V = 0$ , *i.e.*, without the influence of the PES. In this step the coupled-rotor (CR) eigenfunctions (and eigenvalues) are obtained in exactly the same grid representation for the five angles as in the full computation.

- Step (2): calculate the eigenenergies of the 5D CR system with  $J$  total angular momentum using the expressions derived for dimers in ref. 30 corresponding to some monomer rotational states,  $(j_A j_B)$ , and some coupling. The calculated CR energies are associated with angular momentum labels of the subsystems.

- Step (3): by matching the energies in Steps (1) and (2), the CR eigenfunctions computed in Step (1) in the desired representation are associated with the monomer rotational angular momentum and coupling labels of Step (2).

For Step 2, we reiterate the relevant expressions of ref. 30 to calculate the energy levels of an  $A$ - $B$  coupled-rotor system with  $J$  total angular momentum quantum number:

$$E^{(\text{CR})}(j_A j_B j, J) = E_A^{(\text{RR})}(j_A) + E_B^{(\text{RR})}(j_B) + E_c(j, J) \quad (1)$$

where  $j$  is the internal angular momentum quantum number, which results from the Clebsch–Gordan-type<sup>29</sup> coupling of the angular momenta of  $A$  and  $B$ , and it is thus restricted by the  $|j_A - j_B| \leq j \leq |j_A + j_B|$  condition.  $E_A^{(\text{RR})}(j_A)$  and  $E_B^{(\text{RR})}(j_B)$  are the rigid-rotor energies of the monomers.  $E_c(j, J)$  can be obtained by diagonalizing the  $\mathbf{K} \in \mathbb{R}^{\min(j, J) \times \min(j, J)}$  coupling matrix, the angular part of eqn (42) of ref. 30:

$$K_{\Omega', \Omega} = \frac{\hbar^2}{2\mu R^2} \left[ \delta_{\Omega', \Omega} (J(J+1) + j(j+1) - 2\Omega^2) + \delta_{\Omega', \Omega+1} C_{j\Omega}^+ C_{j\Omega}^+ + \delta_{\Omega', \Omega-1} C_{j\Omega}^- C_{j\Omega}^- \right], \quad (2)$$

where  $C_{jk}^\pm = \sqrt{j(j+1) - k(k \pm 1)}$ ,  $\Omega = -\min(j, J), \dots, \min(j, J)$ , and  $\mu^{-1} = m_A^{-1} + m_B^{-1}$  is the reduced mass of the effective rotating diatom, which connects the centers of mass of the monomers.  $m_A$  and  $m_B$  are the total masses of monomers  $A$  and  $B$ , respectively, and  $\delta_{ij}$  is the Kronecker delta function. Note that since the Hamiltonian of ref. 30 does not contain any mixed radial-angular differential operators, the expressions for a fixed intermonomer distance, eqn (2), can be obtained from eqn (42) of ref. 30 by simply retaining the angular part with some fixed  $R$  value.

The eigenvalues of the  $\mathbf{K}$  coupling matrix, *i.e.*, the coupling energies, disappear at infinite separation of  $A$  and  $B$ . In this case the coupled-rotor energy, eqn (1), is determined completely by the sum of the rigid-rotor energies of the monomers, which we call the free-rotor (FR) energy. It is of interest to note that the eigenvalues of  $\mathbf{K}$  can be obtained analytically. The analytic eigenvalues are provided for a few  $J$  and  $j$  values in the ESI† and the corresponding numerical value of the coupling energy is given for two intermonomer distances for all the four isotopologues studied (Tables S17–S19, ESI†). The CR energy,  $E^{(\text{CR})}(j_A j_B j, J)$  is the sum of the FR energy (Tables S13–S16, ESI†) and the coupling energy (Tables S17–S19, ESI†).

As a result of Steps (1)–(3), the coupled-rotor functions,  $\varphi^{(j)}(j_A j_B j)$  (with explicit  $j_A j_B j$ , and  $J$  labels), are available in the same grid representation for the angular degrees of freedom as the full rovibrational wave function. In the next subsection we define the overlap of  $\varphi^{(j)}(j_A j_B j)$  depending on five angles and the full wave function,  $\Psi^{(J)}$ , which depends on all six intermonomer coordinates.

## B. Numerical evaluation of the CRD overlaps

Since the 6-dimensional wave function is normalized to one, we can write

$$1 = \langle \Psi_n^{(J)} | \Psi_n^{(J)} \rangle_{R, \Omega} \quad (3)$$

$$= \sum_{k=-J}^J \sum_{r=1}^{N_R} \sum_{o=1}^{N_\Omega} \left| \tilde{\Psi}_{n,k}^{(J)}(\rho_r, \omega_o) \right|^2, \quad (4)$$

where  $\tilde{\Psi}$  refers to the DVR representation of the wave function with  $\rho_r$  ( $r = 1, \dots, N_R$ ) grid points along the intermonomer distance,  $R$ , and  $\omega_o$  ( $o = 1, \dots, N_\Omega$ ) grid points in the 5D angular subgrid,  $\Omega = (\cos \theta, \phi, \alpha, \cos \beta, \gamma)$ . Next, the truncated resolution of identity over some finite number of CR functions,  $M$ , is introduced:

$$\mathbf{I}^{(J, 5D)} \approx \sum_{m=1}^M \left| \varphi_m^{(J)} \right\rangle_{\Omega} \cdot \left\langle \varphi_m^{(J)} \right|, \quad (5)$$

which is inserted into eqn (3) and (4):

$$1 = \langle \Psi_n^{(J)} | \Psi_n^{(J)} \rangle \quad (6)$$

$$\approx \sum_{m=1}^M \left\langle \Psi_n^{(J)} | \varphi_m^{(J)} \right\rangle_{\Omega} \cdot \left\langle \varphi_m^{(J)} | \Psi_n^{(J)} \right\rangle_{R, \Omega} \quad (7)$$

$$= \sum_{m=1}^M \left( \sum_{r=1}^{N_R} \left| \sum_{k=-J}^J \sum_{o=1}^{N_\Omega} \tilde{\Psi}_{n,k}^{(J)}(\rho_r, \omega_o) \cdot \tilde{\varphi}_{m,k}^{(J)}(\omega_o) \right|^2 \right). \quad (8)$$

Then, we define the  $(n, m)$ th element of what we call the CRD matrix for the  $J$  total rotational quantum number as

$$\text{CRD}_{nm}^{(J)} = \sum_{r=1}^{N_R} \left| \sum_{k=-J}^J \sum_{o=1}^{N_\Omega} \tilde{\Psi}_{n,k}^{(J)}(\rho_r, \omega_o) \cdot \tilde{\varphi}_{m,k}^{(J)}(\omega_o) \right|^2, \quad (9)$$

where  $\Psi_n^{(J)}$  is the  $n$ th state and  $\varphi_m^{(j)}$  is the  $m$ th CR function.

There are a few important properties of the CRD matrix which immediately follow from eqn (9):

(a) The sum of the elements in each row, *i.e.*, the CRD coefficients corresponding to some  $\Psi_n^{(J)}$  state, is 1 for infinitely many CR functions (as the truncated resolution of identity in eqn (5) becomes exact).

(b) The sum of the elements in each column can be larger than 1, because the same CR state can have a dominant contribution to several  $\Psi_n^{(J)}$  states. For the methane–water dimer, the stretching excitations along the intermonomer separation, enumerated using  $\nu = 0, 1, 2, \dots$ , can have similar angular parts.

(c) The angular momentum coupling rules often allow, depending on the angular momenta of the full system and the subsystems, a large number of CR functions with the same  $(j_A, j_B)$  monomer rotational excitations. The individual contributions of the CR functions might be modest but the full  $(j_A, j_B)$  block can have a substantial contribution to the  $\Psi^{(J)}$  state. Therefore, the final assessment of the contribution (or dominance of some monomer excitation)  $(j_A, j_B)$  must be based on the sum of the CRD coefficients corresponding to all  $(j_A, j_B)$  monomer states.

(d) If the CR functions are determined with monomers infinitely far in space (in practice, fixed at some large  $R$  value), then the CR energy is equal to the FR energy, *i.e.*, the simple sum of the RR energies (Tables S13–S16, ESI†). This limit facilitates the assignment of the monomer rotational states,  $(j_A, j_B)$ , but in this case the coupling and the quantum number corresponding to the rotation of an effective diatom connecting the centers of mass of the monomers cannot be determined.

## IV. Symmetry of the methane–water coupled-rotor functions

While Section III applies to any system that can be partitioned into two subsystems, the symmetry analysis of this section applies only to the methane–water dimer. Nevertheless, a similar symmetry analysis can be carried out for other dimers, as well.

In this section, the characters of the methane–water CR representation are calculated and the representation is decomposed into a direct sum of irreducible representations (irrep decomposition) in the  $G_{48}$  group.<sup>2,3</sup> For convenience, the

symmetry properties of the methane and the water monomer rotor functions are presented first within the  $T_d(M)$  and the  $C_{2v}(M)$  groups, respectively, which is followed by the symmetry analysis of the coupled-rotor functions of the dimer within the  $G_{48}$  group. (For completeness, the character tables are reproduced in the ESI.†)

### a. Methane monomer

Each element of a class has the same character, so we select one operator from each class and determine its character. The spatial rotation equivalent to the permutation–inversion operator is first written in the angle-axis parameterization (Fig. S1, ESI of ref. 3 visualizes the effect of the symmetry operations). Then, the Euler angles,  $a, b$ , and  $c$  (using the  $z-x-z$  and the active convention) are determined from the rotation matrix evaluated with Rodriguez' rotation formula in the angle-axis parameterization. For the symmetry operations (one from each class of  $T_d(M)$ ) the  $(a, b, c)$  Euler angles are as follows: (123):  $(0, 0, 2\pi/3)$ ; (12)(34):  $(\pi/3, \pi, 0)$ ; [(1234)]\*:  $(\pi/6, \pi/2, -\pi/6)$ ; and [(34)]\*:  $(0, \pi, 0)$ . Symmetric (as well as spherical) top rotational functions transform under the action of a rotation operator as:<sup>31–33</sup>

$$\hat{R}(a, b, c)\varphi_{km}^{jM} = \sum_{k'=-j^M}^{j^M} D_{kk'}^{jM}(a, b, c)\varphi_{k'm}^{jM}, \quad (10)$$

where  $D_{km}^j$  is the  $(k, m)$ th element of Wigner's  $D$  matrix corresponding to the  $j$ th irrep of the rotation group, and  $M$  denotes the methane monomer of the dimer. Then, an operator  $\hat{o} \in T_d(M)$ , for which  $\hat{R}(a_o, b_o, c_o)$  is the equivalent rotation, has the following character:

$$\begin{aligned} \chi^{jM} &= \sum_{k=-j^M}^{j^M} \langle \varphi_{km}^{jM} | \hat{o} | \varphi_{km}^{jM} \rangle \\ &= \sum_{k=-j^M}^{j^M} D_{kk}^{jM}(a_o, b_o, c_o) \end{aligned} \quad (11)$$

where we also took advantage of the fact that the rotational functions are orthonormal.

Using these properties the characters of a representation spanned by the  $\{\varphi_{km}^{jM}, (k = -j^M, \dots, j^M)\}$  functions are easily determined. The general expressions and the numerical values for  $j^M = 0, 1, \dots, 5$  are collected in Table 3 (and the table can be

**Table 3** Characters and irrep decomposition of the rotational functions of methane in the  $T_d(M)$  molecular symmetry group

	$E$	(123)	(14)(23)	[(1423)]*	[(23)]*	
	1	8	3	6	6	
$j^M$	$2j^M + 1$	$\sum_{m=-j^M}^{j^M} D_{m,m}^{j^M}(0, 0, \frac{2\pi}{3})$	$\sum_{m=-j^M}^{j^M} D_{m,m}^{j^M}(\frac{\pi}{3}, \pi, 0)$	$\sum_{m=-j^M}^{j^M} D_{m,m}^{j^M}(\frac{\pi}{6}, \frac{\pi}{2}, -\frac{\pi}{6})$	$\sum_{m=-j^M}^{j^M} D_{m,m}^{j^M}(0, \pi, 0)$	Irreps
0	1	1	1	1	1	$A_1$
1	3	0	−1	1	−1	$F_1$
2	5	−1	1	−1	1	$E \oplus F_2$
3	7	1	−1	−1	−1	$A_2 \oplus F_1 \oplus F_2$
4	9	0	1	1	1	$A_1 \oplus E \oplus F_1 \oplus F_2$
5	11	−1	−1	1	−1	$E \oplus 2F_1 \oplus F_2$

**Table 4** Characters and irrep decomposition of the rotational functions of water in the  $C_{2v}(\mathbf{M})$  molecular symmetry group

	$E$	$(ab)$	$E^*$	$[(ab)]^*$
	1	1	1	1
$j_{k_a k_c}^{\text{W}}$	1	$(-1)^{k_a+k_c}$	$(-1)^{k_c}$	$(-1)^{k_a}$

extended straightforwardly to higher  $j^{\text{M}}$  values). The last column of Table 3 gives the irrep decomposition for the numerical examples, which is in agreement with the irrep decomposition of the methane rotational states in the  $T(\mathbf{M})$  group<sup>34,35</sup> and reproduces the results of ref. 36 for the  $T_d(\mathbf{M})$  group.

## b. Water monomer

Table 4 lists the general expressions<sup>29</sup> for the characters of the  $j_{k_a k_c}^{\text{W}}$  rotational states of water (W) in the  $C_{2v}(\mathbf{M})$  group.

## c. Coupled-rotor ansatz

The coupled-rotor ansatz can be understood as coupling (a) the symmetric top eigenfunctions of methane,  $\phi_{km}^{\text{M}}$ ; (b) the asymmetric top eigenfunctions of water,  $\phi_{k_a k_c, m}^{\text{W}}$ , and (c) the eigenfunctions of an effective diatomic rotor,  $Y_A^m$ , which corresponds to the rotation of the displacement vector connecting the centers of mass of the monomers. We denote this coupling scheme by  $\left[ \left[ j^{\text{M}}, j_{k_a k_c}^{\text{W}} \right]_j, A \right]_{JM}$ , which corresponds to the function:

$$\begin{aligned} \Psi_J^{\text{M}} \left( j_k^{\text{M}}, j_{k_a k_c}^{\text{W}}, j, A \right) &= \sum_{\mu \in S_1} \langle j\mu, \Lambda(M-\mu) | JM \rangle \psi_j^\mu Y_A^{M-\mu} \\ &= \sum_{\mu \in S_1} \langle j\mu, \Lambda(M-\mu) | JM \rangle Y_A^{M-\mu} \\ &\quad \times \sum_{m \in S_2} \langle j^{\text{M}} m, j^{\text{W}}(\mu-m) | j\mu \rangle \phi_{km}^{\text{M}} \phi_{k_a k_c, \mu-m}^{\text{W}} \end{aligned}$$

$$\text{with } S_1 = \{ \mu \in \mathbb{N}_0 : |\mu| \leq j \text{ and } |M-\mu| \leq \Lambda \},$$

$$S_2 = \{ m \in \mathbb{N}_0 : |m| \leq j^{\text{M}} \text{ and } |\mu-m| \leq j^{\text{W}} \},$$

$$k = -j^{\text{M}}, \dots, j^{\text{M}}.$$

(12)

The label  $j$  is for the internal angular momentum quantum number resulting from the coupling of the methane and water rotors.

An operator  $\hat{O} \in G_{48}$  can be written as the product of  $\hat{o} \in T_d(\mathbf{M})$ , methane permutation-inversion,  $\hat{p} \in C_i = \{E, E^*\}$  acting on the effective diatom, and  $\hat{q} \in C_{2v}(\mathbf{M})$  water permutation-inversion operators. The character of  $\hat{O} = \hat{o}\hat{p}\hat{q}$  is obtained as the trace of the matrix representation of  $\hat{O}$  over the ansatz defined

$$\begin{aligned} \chi(\hat{O}) &= \sum_{k=-j^{\text{M}}}^{j^{\text{M}}} \left\langle \Psi_J^{\text{M}} \left( j_k^{\text{M}}, j_{k_a k_c}^{\text{W}}, j, A \right) \middle| \hat{O} \Psi_J^{\text{M}} \left( j_k^{\text{M}}, j_{k_a k_c}^{\text{W}}, j, A \right) \right\rangle \\ &= \sum_{k=-j^{\text{M}}}^{j^{\text{M}}} \sum_{\mu' \in S_1'} \sum_{m' \in S_2'} \sum_{\mu \in S_1} \sum_{m \in S_2} \\ &\quad \langle j\mu', \Lambda(M-\mu') | JM \rangle \langle j^{\text{M}} m', j^{\text{W}}(\mu'-m') | j\mu' \rangle \\ &\quad \times \langle j\mu, \Lambda(M-\mu) | JM \rangle \langle j^{\text{M}} m, j^{\text{W}}(\mu-m) | j\mu \rangle \\ &\quad \times \left\langle Y_A^{M-\mu'} | \hat{p} | Y_A^{M-\mu} \right\rangle \left\langle \phi_{km'}^{\text{M}} | \hat{o} | \phi_{km}^{\text{M}} \right\rangle \left\langle \phi_{k_a k_c, \mu'}^{\text{W}} | \hat{q} | \phi_{k_a k_c, \mu-m}^{\text{W}} \right\rangle \\ &= \sum_{k=-j^{\text{M}}}^{j^{\text{M}}} \sum_{\mu' \in S_1'} \sum_{m' \in S_2'} \sum_{\mu \in S_1} \sum_{m \in S_2} \\ &\quad \langle j\mu', \Lambda(M-\mu') | JM \rangle \langle j^{\text{M}} m', j^{\text{W}}(\mu'-m') | j\mu' \rangle \\ &\quad \times \langle j\mu, \Lambda(M-\mu) | JM \rangle \langle j^{\text{M}} m, j^{\text{W}}(\mu-m) | j\mu \rangle \\ &\quad \times (-1)^{pA} \delta_{\mu'\mu} D_{kk}^{\text{M}}(a_o, b_o, c_o) \delta_{m'm} \Gamma_{k_a k_c}^{j^{\text{W}}}(\hat{q}) \delta_{\mu'-m', \mu-m} \\ &= \sum_{\mu \in S_1} \sum_{m \in S_2} \langle j\mu, \Lambda(M-\mu) | JM \rangle^2 \langle j^{\text{M}} m, j^{\text{W}}(\mu-m) | j\mu \rangle^2 \\ &\quad \times (-1)^{pA} \left[ \sum_{k=-j^{\text{M}}}^{j^{\text{M}}} D_{kk}^{\text{M}}(a_o, b_o, c_o) \right] \chi_{k_a k_c}^{\text{W}}(\hat{q}) \\ &= \chi^A(\hat{p}) \chi^{\text{M}}(\hat{o}) \chi_{k_a k_c}^{\text{W}}(\hat{q}) \end{aligned} \tag{13}$$

where  $\chi^A(\hat{p}) = (-1)^{pA}$  is the character of the effective diatomic rotation, with  $p = 1$  for inversion and  $p = 0$  otherwise.  $\chi^{j^{\text{M}}}(\hat{o})$  and  $\chi_{k_a k_c}^{\text{W}}(\hat{q})$  are the characters of the permutation-inversion operations of the methane and water molecules listed in Tables 3 and 4, respectively.

The symmetry rules (Table 5 and Tables S23–S26, ESI†) derived in this section together with the numerically computed CRD tables make it possible to carry out the symmetry assignment of the variationally computed rovibrational states in an automated fashion.

## V. Numerical results and discussion

### A. Rovibrational energy-level pattern of the methane–water dimers

In this section, the computed rovibrational states with  $J = 0, 1$  and 2 are presented for the four studied  $CX_4 \cdot Y_2O$  ( $X, Y = \text{H}, \text{D}$ ) dimers focusing on the zero-point vibrational splitting of the global minimum, ZPV(GM). The computed energy levels are provided in Tables S1–S12 of the ESI.† The energy-level differences can be directly compared with high-resolution spectroscopic measurements, when such measurements will become available for the deuterated isotopologues (the electric

dc 1955\_21

Table 5 Characters and irrep decomposition of the  $\left[ \left[ \begin{smallmatrix} j^M, j^W \\ j^K, j^C \end{smallmatrix} \right]_J, A \right]_J$  coupled-rotor functions which dominate the ZPV(GM) splitting manifold of methane–water with  $J = 0$  in the  $G_{48}$  group (see also Fig. 3 and 4)

$\Gamma$	$E$	(123)	(14)(23)	$[(1423)(ab)]^*$	$[(23)(ab)]^*$	(ab)	(123)(ab)	(14)(23)(ab)	$[(1423)]^*$	$[(23)]^*$	Irreps
	1	8	3	6	6	1	8	3	6	6	
$[[0,0_{00}]_0,0]_0$	1	1	1	1	1	1	1	1	1	1	$A_1^+$
$[[0,1_{11}]_1,1]_0$	1	1	1	1	1	1	1	1	1	1	$A_1^+$
$[[1,0_{00}]_1,1]_0$	3	0	-1	-1	1	3	0	-1	-1	1	$F_2^+$
$[[1,1_{11}]_0,0]_0$	3	0	-1	-1	1	3	0	-1	-1	1	$F_2^+$
$[[1,1_{11}]_1,1]_0$	3	0	-1	1	-1	3	0	-1	1	-1	$F_1^+$
$[[1,1_{11}]_2,2]_0$	3	0	-1	-1	1	3	0	-1	-1	1	$F_2^+$
$[[2,0_{00}]_2,2]_0$	5	-1	1	-1	1	5	-1	1	-1	1	$E^+ \oplus F_2^+$
$[[2,1_{11}]_1,1]_0$	5	-1	1	-1	1	5	-1	1	-1	1	$E^+ \oplus F_2^+$
$[[2,1_{11}]_2,2]_0$	5	-1	1	1	-1	5	-1	1	1	-1	$E^+ \oplus F_1^+$
$[[2,1_{11}]_3,3]_0$	5	-1	1	-1	1	5	-1	1	-1	1	$E^+ \oplus F_2^+$
$[[0,1_{01}]_1,1]_0$	1	1	1	-1	-1	-1	-1	-1	1	1	$A_2^-$
$[[0,1_{10}]_1,1]_0$	1	1	1	1	1	-1	-1	-1	-1	-1	$A_1^-$
$[[1,1_{01}]_0,0]_0$	3	0	-1	1	-1	-3	0	1	-1	1	$F_1^-$
$[[1,1_{01}]_1,1]_0$	3	0	-1	-1	1	-3	0	1	1	-1	$F_2^-$
$[[1,1_{01}]_2,2]_0$	3	0	-1	1	-1	-3	0	1	-1	1	$F_1^-$
$[[1,1_{10}]_0,0]_0$	3	0	-1	-1	1	-3	0	1	1	-1	$F_2^-$
$[[1,1_{10}]_1,1]_0$	3	0	-1	1	-1	-3	0	1	-1	1	$F_1^-$
$[[1,1_{10}]_2,2]_0$	3	0	-1	-1	1	-3	0	1	1	-1	$F_2^-$
$[[2,1_{01}]_1,1]_0$	5	-1	1	1	-1	-5	1	-1	-1	1	$E^- \oplus F_1^-$
$[[2,1_{01}]_2,2]_0$	5	-1	1	-1	1	-5	1	-1	1	-1	$E^- \oplus F_2^-$
$[[2,1_{01}]_3,3]_0$	5	-1	1	1	-1	-5	1	-1	-1	1	$E^- \oplus F_1^-$
$[[2,1_{10}]_1,1]_0$	5	-1	1	-1	1	-5	1	-1	1	-1	$E^- \oplus F_2^-$
$[[2,1_{10}]_2,2]_0$	5	-1	1	1	-1	-5	1	-1	-1	1	$E^- \oplus F_1^-$
$[[2,1_{10}]_3,3]_0$	5	-1	1	-1	1	-5	1	-1	1	-1	$E^- \oplus F_2^-$

dipole selection rules and the spin-statistical weights of HH are discussed in detail in ref. 3).

The zero-point vibrational state, or any other vibrational state symmetric with respect to the symmetry plane of the equilibrium structure, is split into the following direct sum, involving 24 states:<sup>3</sup>

$$\Gamma_{A'} = A_1^+ \oplus E^+ \oplus F_1^+ \oplus 2F_2^+ \oplus A_2^- \oplus E^- \oplus 2F_1^- \oplus F_2^- \quad (14)$$

in the  $G_{48}$  molecular symmetry group. The + and – superscripts refer to the symmetry and anti-symmetry of the spatial wave function with respect to the exchange of the two protons (deuterons) of  $H_2O(D_2O)$ , in agreement with the labeling of ref. 2.

As to the vibrational states, an irrep label can be assigned to the computed vibrational states by visual inspection of one- and two-dimensional cuts of the wave function, as was done in ref. 3 (for multidimensional representations, the trace of the representation matrix had to be taken). In the present work, the CRD decomposition and the symmetry rules derived in the previous section made it possible to carry out the symmetry assignment in an almost automated fashion, which is particularly useful for the assignment of the multi-dimensional irreps.

This automated assignment scheme facilitated the identification of a mistake in our earlier assignment of the 1 and 2 subindices of the triply degenerate irreps of HH.<sup>3</sup> According to the corrected assignment of the ZPV(GM) splitting ( $J = 0$ ), there is an  $F_2^+$  and an  $F_1^-$  state in the lower part and there is an ( $F_1^+$ ,  $F_2^+$ ) pair as well as an ( $F_1^-$ ,  $F_2^-$ ) pair of states in the upper part of the splitting with  $J = 0$  (see Fig. 2–4).

To characterize the rovibrational states (Fig. 3 and 4), we identified the parent vibrational state(s) of each rovibrational state using the rigid-rotor decomposition (RRD) scheme.<sup>17</sup> When the identification of a single parent vibrational state is possible, the rovibrational state can be imagined as some rotational excitation of the parent vibrational state.

The numerical values of the energy levels and the splittings are very different for the four isotopologues studied, but the overall rovibrational pattern and assignment is very similar (recall that the four systems are described on the same PES but have different monomer rotational constants): both the vibrational and the rovibrational energy-level patterns are characterized by a lower and an upper part split into further levels (see Fig. 2–4). As expected, the energy values get smaller when the monomers are replaced with their heavier (deuterated) versions.

More interestingly, all studied methane–water dimers have an unusual feature: there are rotational “excitations” which lead to lower energies than the energy of the vibrational parent state; thus, these rovibrational states appear as a rotational excitation with a negative transition energy. These reversed rovibrational sequences were present in the experimental data reported for  $CH_4\text{-}H_2O^2$  and were also reproduced in the computations of ref. 3. Reversed rovibrational sequences have also been identified computationally in other systems, for example, in  $H_5^+$  (ref. 5) as well as in the  $CH_5^+$  molecular ion.<sup>7–9</sup> These reversed sequences observed in the computations for  $H_5^+$  were explained by a 2-dimensional torsional-rotational model.<sup>5</sup>

dc\_1955\_21

Furthermore, ref. 8, 10 and 11 explained this unusual behavior by treating some large-amplitude motions (LAM) on the same footing as the rotations by going beyond the SO(3) group for these LAM-rotational degrees of freedom.

In the present work, we take a simple strategy to better understand the origin of the splitting pattern and these formally negative-energy rotational excitations: besides the rigid-rotor model, which underlies the assignment and the observation of these reversed sequences, we use the coupled-rotor system as another meaningful model for weakly interacting dimers. The computed coupled-rotor decomposition (CRD, introduced in Section III) tables provide detailed information about the monomers' rotational states and their relative rotation within the rotating dimer. In most of this work, we focus on the assignment of monomer-rotor labels,  $[j^M, j_{k_a, k_c}^W]$ , because the monomer excitations are about an order of magnitude more energetic than the coupling (in particular, the water's rotational constants are much larger than the dimer's rotational constants). For this purpose, it is sufficient to use CRD tables computed with a large intermonomer separation, the one used is  $R_{100} = 100$  bohr. In this case the CR energy is the simple sum of the monomer rotor energies (Tables S13–S19, ESI<sup>†</sup>). To better understand the fine details of the dimer's internal dynamics, we also assigned  $j$  and  $A$  for a few states using CR functions obtained with monomers fixed at the complex's equilibrium distance,  $R = R_{\text{eq}} = 6.5$  bohr. For this  $R$  value the  $j$ -splitting of the CR energies is small but larger than the convergence of our variational results, so the assignment of the  $j$  and  $A$  labels (Section IV) is possible. Fig. 1 presents an example of a complete CR assignment.

The results of the symmetry, RR and CR assignments of the computed rovibrational states for all four isotopologues are collected in Fig. 3 and 4 (detailed results are provided in Tables S1–S12 of the ESI<sup>†</sup>). As a general and important conclusion which becomes transparent from the CRD assignment, the characteristic upper-lower separation of the rovibrational ZPV(GM) manifold corresponds to the  $1_{11} \leftarrow 0_{00}$  and the  $1_{10} \leftarrow 1_{01}$  rotational excitation of the water monomer for states of  $\Gamma^+$  and  $\Gamma^-$  symmetry (para and ortho for HH and DH), respectively. The sub-splittings of both the lower and the upper parts are related to the rotational excitation of the methane monomer with one and two quanta and to the excitation of the relative rotation of the two monomers.

## B. Reversed rovibrational sequences

The RRD assignment of the rovibrational states to their vibrational parents highlighted that certain rotational excitations have “negative” transition energies. These reversed rovibrational sequences are observed for all four isotopologues and they appear within the vibrational bands of certain vibrational symmetries.

The CRD tables show that these negative rotational excitation energies correspond to a  $J + 1 \leftarrow J$  transition in which the water molecule loses rotational energy— $0_{00} \leftarrow 1_{11}$  and  $1_{01} \leftarrow 1_{10}$  for  $\Gamma^+$  and  $\Gamma^-$ , respectively—but due to a different internal coupling of the methane and the water rotors, the total

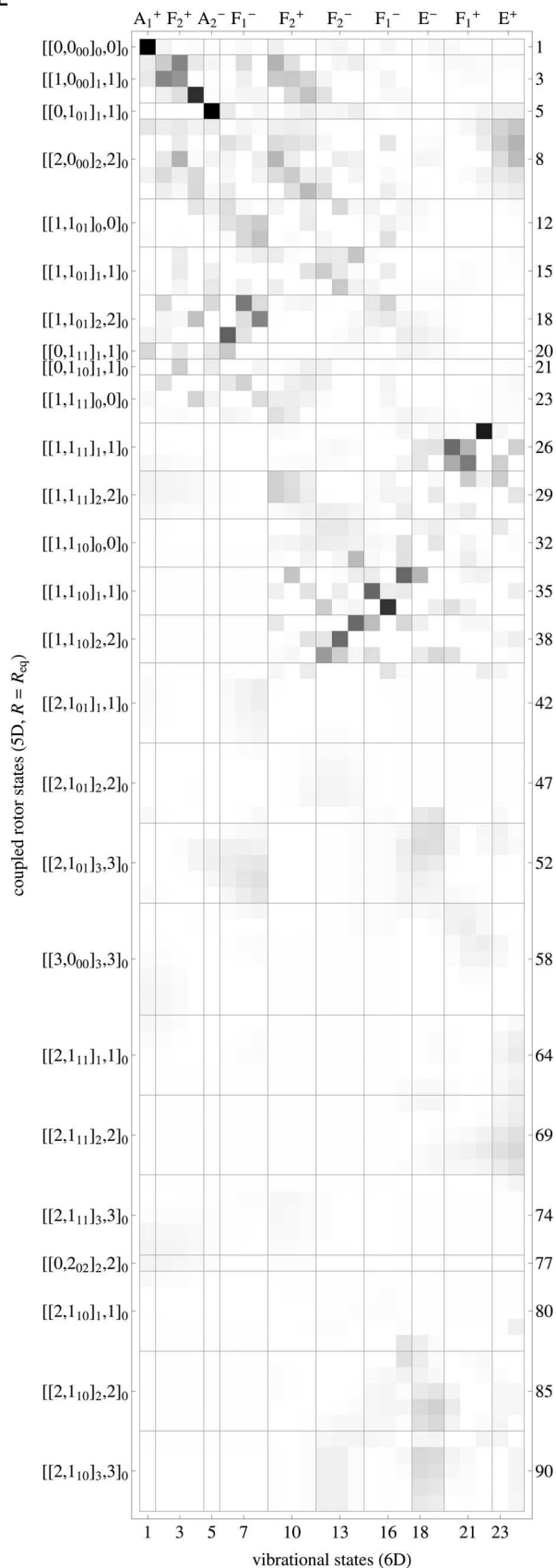


Fig. 1 Coupled-rotor decomposition (CRD) table for  $\text{CH}_4\text{-H}_2\text{O}$  with  $J = 0$ : overlap (eqn (9)) of the 24 lowest-energy vibrational states, which belong to the ZPV(GM) splitting manifold, with the 92 lowest-energy coupled-rotor states.

dc\_1955\_21

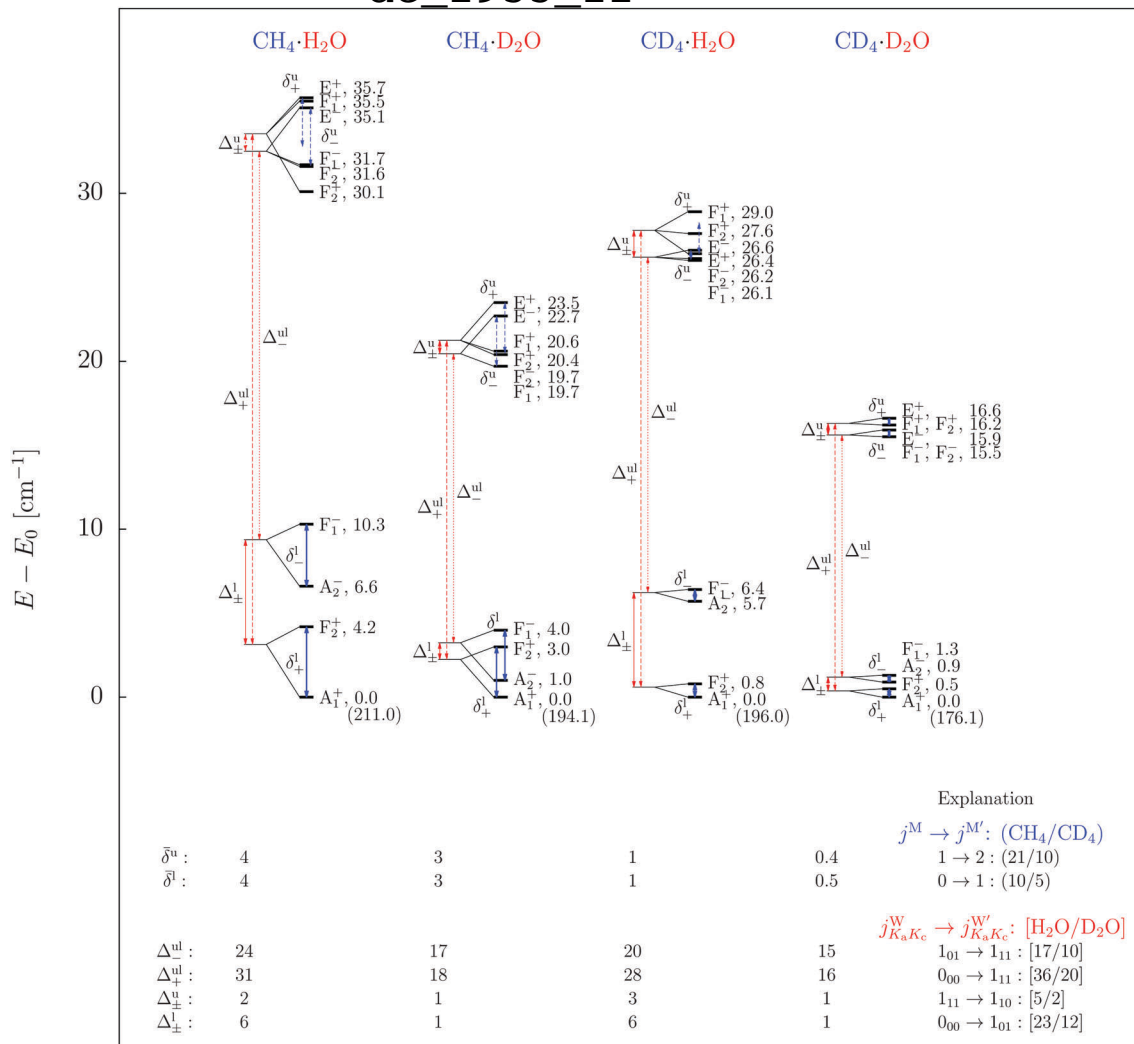


Fig. 2 Zero-point vibrational splitting energies, in  $\text{cm}^{-1}$ , assigned to the global minimum of the four isotopologues studied. The splittings indicated with double-headed arrows are color coded with blue and red referring to the methane and water monomers, respectively.

rotational quantum number increases. This observation is certainly useful and provides an intuitive picture about this phenomenon but it remains to be answered why the lower-energy  $J = 0$  state is “missing” (and is replaced by its higher-energy analogue) in several vibrational bands ( $E^+$ ,  $F_1^+$ ,  $F_2^+$ ,  $E^-$ ,  $F_1^-$ ,  $F_2^-$ ). Is that coupling symmetry forbidden or does this pattern result from a particular mixing of the CR states?

In the case of the  $F_1^+$ -symmetry ZPV(GM) vibration (see Fig. 3) the negative-energy rotational transition is dictated by symmetry rules (Table 5, Tables S23 and S25, ESI<sup>†</sup>). The  $[[1,1_{11}]_1,1]_0$  and  $[[2,1_{11}]_2,2]_0$  states are the lowest-energy CR states of  $F_1^+$  symmetry with  $J = 0$ . They correspond to rotationally excited water, so they are more energetic and appear in the “upper” part of the splitting pattern. At the same time, the  $J = 1$  and 2 rotational excitations of this vibrational state can have contributions from CR states with water in its lowest rotational state,  $0_{00}$ , which lowers the energy of these rovibrational states and makes them appear in the lower part of the splitting. As a result of these symmetry properties, the rotational

excitation of the  $F_1^+$  vibrational state shows up as a “negative-energy” transition.

Unfortunately, the explanation of the reversed rovibrational sequences corresponding to other vibrational states is less straightforward when based on simple symmetry-related arguments (Table 4 and Tables S23–S26, ESI<sup>†</sup>). For example, the  $E^+$  vibrational band has only a “higher-energy” vibrational state but there are both “lower-energy”,  $[2,0_{00}]$ , and “higher-energy”,  $[2,1_{11}]$ , CR functions of  $E^+$  symmetry with  $J = 0$ . In fact, we observe in the numerically computed CRD tables that the lower-energy  $[2,0_{00}]$  CR functions contribute to many states but they do not dominate any of the states. Namely, the  $J = 0$   $E^+$  vibration is assigned to the higher-energy  $[2,1_{11}]$  CR function with some contribution also from  $[2,0_{00}]$ . The HH isotopologue, whose assignment slightly differs from the other three isotopologues, has about equal contributions from both  $[2,1_{11}]$  and  $[2,0_{00}]$ . Similar behavior is observed for the  $F_2^+$ ,  $E^-$ ,  $F_1^-$ , and  $F_2^-$  vibrational bands of the ZPV(GM). The reversed energy ordering results from a particular mixing of CR states with lower-energy

dc\_1955\_21

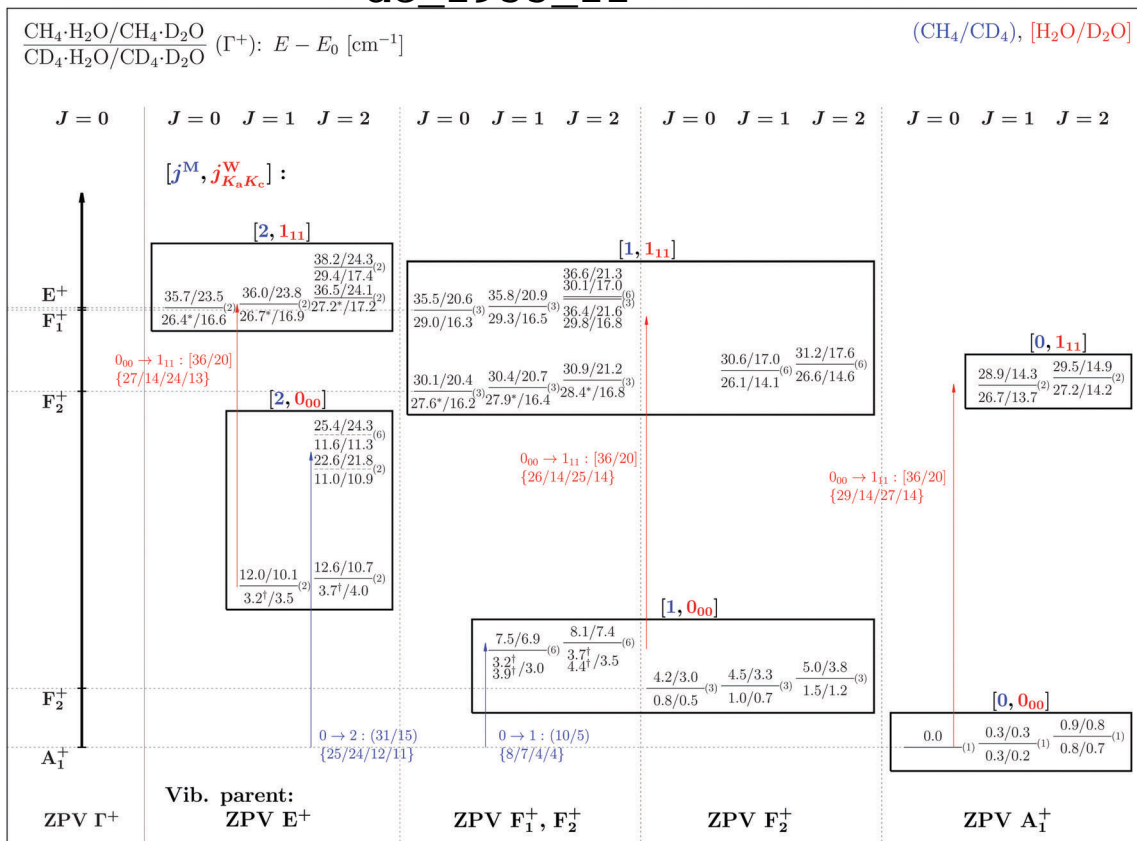


Fig. 3 Summary of the computed  $J = 0, 1$ , and  $2$  rovibrational states of the methane–water dimers with  $\Gamma^+$  symmetry. Levels shown with dashed lines in the ZPV,  $E^+$  column (for all studied isotopologues) correspond to the  $(2,0_{00})$  monomer rotor states of the ZPV rovibrational band but cannot be assigned to a single, dominant vibrational state. The states labelled with \* are characterized by a strong mixing of the  $(1,0_{00})$ ,  $(2,0_{00})$ ,  $(1,1_{11})$ , and  $(2,1_{11})$  monomer rotor states. The states labelled with † exhibit a strong mixing with the  $E^+$  vibrational parent levels in the RRD.

and higher-energy water rather than being due to strict symmetry rules. We also note that for the  $F_2^+$  and  $F_1^-$  states of the ZPV(GM) there are both reversed and normal sequences.

In general, the computed CRD tables show that the higher-energy rovibrational states are dominated by higher-energy CR functions with the  $1_{11}$  and  $1_{10}$  higher-energy rotational states of water in  $\Gamma^+$  and  $\Gamma^-$ , respectively. At the same time, the lower-energy states are dominated by lower-energy CR functions with the  $0_{00}$  and  $1_{01}$  rotational states of water in  $\Gamma^+$  and  $\Gamma^-$ , respectively.

## VI. Summary and outlook

The rovibrational states of four isotopologues of the methane–water dimer have been computed using a six-dimensional intermolecular vibrational model utilizing the GENIUSH code<sup>12,13</sup> and the QCHB15 potential energy surface.<sup>23</sup> The computed rovibrational states (with  $J = 0, 1$ , and  $2$  rotational quantum numbers) were assigned to their parent vibrational state(s) using the rigid-rotor decomposition (RRD) scheme. This assignment highlighted in all four dimers, CH<sub>4</sub>·H<sub>2</sub>O, CH<sub>4</sub>·D<sub>2</sub>O, CD<sub>4</sub>·H<sub>2</sub>O, and CD<sub>4</sub>·D<sub>2</sub>O, the existence of a reversed rovibrational energy ordering, *i.e.*, formally “negative” rotational excitation energies.

In order to better understand the complex rovibrational dynamics of this fluxional, weakly bound complex, we developed the coupled-rotor decomposition (CRD) scheme. The CRD scheme is a general approach to determine the rotational states of the monomers and their relative rotation within a rotating dimer.

For the example of the methane–water dimer, the symmetry properties of the coupled-rotor functions were derived employing the  $G_{48}$  molecular symmetry (MS) group. Together with the numerically computed CRD tables this symmetry classification opens the route to an automated symmetry assignment of the rovibrational states of the dimer, a particularly useful approach for higher excited, multiply degenerate states.

As to the interpretation of the higher-energy states of the methane–water dimer, we can think of a number of challenging, open questions. Is it possible to identify the zero-point splitting manifold of the secondary minimum, ZPV(SM), similarly to the ZPV(GM) studied in the present work? Is the full ZPV(SM) bound or does it spread beyond the first dissociation threshold (which is only  $D_0(\text{HH}) = 152.030$  cm<sup>-1</sup> for CH<sub>4</sub>·H<sub>2</sub>O on the QCHB15 PES<sup>23</sup>). Furthermore, by thinking in terms of the coupled-rotors picture, we may imagine energetic monomer rotational states which bring the system above the dissociation energy. Since the intermolecular angular degrees of freedom are only weakly

dc\_1955\_21

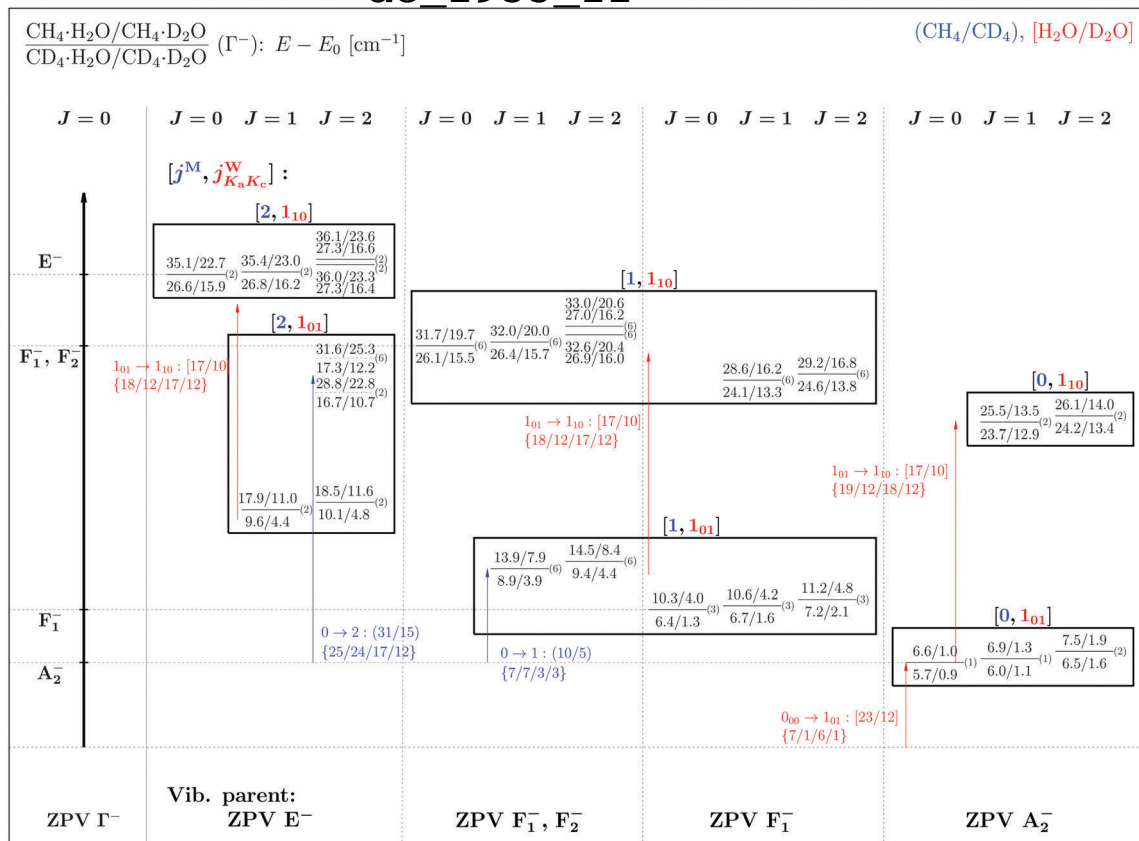


Fig. 4 Summary of the computed  $J = 0, 1$ , and  $2$  rovibrational states of the methane–water dimers with  $\Gamma^-$  symmetry. Levels shown with dashed lines in the ZPV,  $E^-$  column (for all studied isotopologues) correspond to the  $(2,1_{01})$  monomer rotor states but they cannot be assigned to a single, dominant vibrational parent state.

coupled to the intermonomer stretching (the dissociation coordinate), we may expect long-lived quasi-bound states in which the energy is stored in fast spinning monomers. These questions highlight the extremely rich internal-rotational dynamics of this weakly bound dimer, which is worth further experimental and computational investigation. Seemingly all the theoretical tools are at hand to help understanding high-resolution far-infrared spectra of these complexes.

## Acknowledgements

J. S. received support from the ÚNKP-16-3 New National Excellence Program of the Ministry of Human Capacities of Hungary. The work performed by A. G. C. received support from NKFIH (grant no. K119658). E. M. acknowledges financial support from a PROMYS grant (no. IZ11Z0\_166525) of the Swiss National Science Foundation.

## References

- 1 R. D. Suenram, G. T. Fraser, F. J. Lovas and Y. Kawashima, *J. Chem. Phys.*, 1994, **101**, 7230.
- 2 L. Dore, R. C. Cohen, C. A. Schmuttenmaer, K. L. Busarow, M. J. Elrod, J. G. Loeser and R. J. Saykally, *J. Chem. Phys.*, 1994, **100**, 863.
- 3 J. Sarka, A. G. Császár, S. C. Althorpe, D. J. Wales and E. Mátyus, *Phys. Chem. Chem. Phys.*, 2016, **18**, 22816.
- 4 O. Akin-Ojo and K. Szalewicz, *J. Chem. Phys.*, 2005, **123**, 134311.
- 5 C. Fábri, J. Sarka and A. G. Császár, *J. Chem. Phys.*, 2014, **140**, 051101.
- 6 J. Sarka and A. G. Császár, *J. Chem. Phys.*, 2016, **144**, 154309.
- 7 R. Wodraszka and U. Manthe, *J. Phys. Chem. Lett.*, 2015, **6**, 4229.
- 8 H. Schmiedt, P. Jensen and S. Schlemmer, *J. Chem. Phys.*, 2015, **143**, 154302.
- 9 X.-G. Wang and J. T. Carrington, *J. Chem. Phys.*, 2016, **144**, 204304.
- 10 H. Schmiedt, P. Jensen and S. Schlemmer, *Phys. Rev. Lett.*, 2016, **117**, 223002.
- 11 H. Schmiedt, P. Jensen and S. Schlemmer, *Chem. Phys. Lett.*, 2017, **672**, 34.
- 12 E. Mátyus, G. Czako and A. G. Császár, *J. Chem. Phys.*, 2009, **130**, 134112.
- 13 C. Fábri, E. Mátyus and A. G. Császár, *J. Chem. Phys.*, 2011, **134**, 074105.
- 14 A. G. Császár, C. Fábri, T. Szidarovszky, E. Mátyus, T. Furtenbacher and G. Czako, *Phys. Chem. Chem. Phys.*, 2012, **14**, 1085.
- 15 J. C. Light and T. Carrington Jr, *Adv. Chem. Phys.*, 2000, **114**, 263.



dc\_1955\_21

- 16 C. Lanczos, *J. Res. Natl. Bur. Stand.*, 1950, 255–282.
- 17 E. Mátyus, C. Fábri, T. Szidarovszky, G. Czakó, W. D. Allen and A. G. Császár, *J. Chem. Phys.*, 2010, **133**, 034113.
- 18 C. Fábri, E. Mátyus and A. G. Császár, *Spectrochim. Acta*, 2014, **119**, 84.
- 19 C. Fábri, A. G. Császár and G. Czakó, *J. Phys. Chem. A*, 2013, **117**, 6975.
- 20 J. Sarka, D. Lauvergnat, V. Brites, A. G. Császár and C. Léonard, *Phys. Chem. Chem. Phys.*, 2016, **18**, 17678.
- 21 D. Papp, J. Sarka, T. Szidarovszky, A. G. Császár, E. Mátyus, M. Hochlaf and T. Stoecklin, *Phys. Chem. Chem. Phys.*, 2017, **19**, 8152.
- 22 E. Mátyus, T. Szidarovszky and A. G. Császár, *J. Chem. Phys.*, 2014, **141**, 154111.
- 23 C. Qu, R. Conte, P. L. Houston and J. M. Bowman, *Phys. Chem. Chem. Phys.*, 2015, **17**, 8172.
- 24 H. I. Rivera-Arrieta, J. M. Turney and H. F. Schaefer III, *J. Chem. Theory Comput.*, 2017, **13**, 1478.
- 25 G. Czakó, E. Mátyus and A. G. Császár, *J. Phys. Chem. A*, 2009, **113**, 11665.
- 26 D. W. Schwenke and H. Partridge, *Spectrochim. Acta*, 2001, **57A**, 887.
- 27 H. Wei and J. T. Carrington, *J. Chem. Phys.*, 1992, **97**, 3029.
- 28 J. Echave and D. C. Clary, *Chem. Phys. Lett.*, 1992, **190**, 225.
- 29 P. R. Bunker and P. Jensen, *Molecular symmetry and spectroscopy*, NRC Research Press, Ottawa, 2nd edn, 1998.
- 30 G. Brocks, A. van der Avoird, B. T. Sutcliffe and J. Tennyson, *Mol. Phys.*, 1983, **50**, 1025.
- 31 J. T. Hougen, *J. Chem. Phys.*, 1962, **37**, 1433.
- 32 J. T. Hougen, *J. Chem. Phys.*, 1963, **39**, 358.
- 33 O. Álvarez Bajo, R. Lemus, M. Carvajal and F. Pérez-Bernal, *Mol. Phys.*, 2011, **109**, 797.
- 34 Y. Ohshima and Y. Endo, *J. Chem. Phys.*, 1990, **93**, 6256.
- 35 J. M. Hutson, *J. Chem. Phys.*, 1990, **92**, 157.
- 36 R. W. Randall, J. B. Ibboston and B. Howerd, *J. Chem. Phys.*, 1994, **100**, 7042.
- 37 The QCHB15 PES is based on 30467 *ab initio* interaction energies computed at CCSD(T)-F12b/haTZ (aug-cc-pVTZ for the carbon and oxygen atoms, cc-pVTZ for the hydrogen atoms) level of theory and is fitted with a root-mean-square error of 3.5 cm<sup>-1</sup>.



Cite this: *Phys. Chem. Chem. Phys.*,  
2016, **18**, 22816

# Rovibrational transitions of the methane–water dimer from intermolecular quantum dynamical computations†

János Sarka,<sup>ab</sup> Attila G. Császár,<sup>ab</sup> Stuart C. Althorpe,<sup>c</sup> David J. Wales<sup>c</sup> and Edit Mátyus<sup>\*a</sup>

Rovibrational quantum nuclear motion computations, with  $J = 0, 1$ , and  $2$ , are reported for the intermolecular degrees of freedom of the methane–water dimer, where  $J$  is the quantum number describing the overall rotation of the complex. The computations provide the first explanation of the far-infrared spectrum of this complex published in *J. Chem. Phys.*, 1994, **100**, 863. All experimentally reported rovibrational transitions, up to  $J = 2$ , can be assigned to transitions between the theoretically computed levels. The deviation of the experimental and computed rovibrational transitions is  $0.5 \text{ cm}^{-1}$  for the *ortho* and  $2 \text{ cm}^{-1}$  for the *para* species with a variance of  $0.005 \text{ cm}^{-1}$ . In addition to a lower systematic error, the overall agreement of theory and experiment is also better for the *ortho* species (involving *ortho*-H<sub>2</sub>O). Most importantly, for this species all levels of the 24-fold tunneling splitting manifold corresponding to the zero-point vibration (ZPV) are involved in at least one experimentally reported transition. For the *para* species there are a few energy levels in the computed ZPV manifold that are not involved in the reported experimental transitions. Furthermore, computed energy levels are identified that correspond to the ZPV tunneling splitting manifold of the secondary minimum structure of the dimer, which presumably appear in rovibrational transitions in the same energy regime as the observed transitions, but have not been experimentally reported.

Received 6th May 2016,  
Accepted 15th June 2016

DOI: 10.1039/c6cp03062a

www.rsc.org/pccp

## 1 Introduction

A molecular-level representation of materials by an *ab initio* potential energy surface (PES) can be used to make reliable predictions about bulk-phase properties, relevant from biological simulations to technological applications. A universal PES, which can be used from the monomers through the dimer, trimer, *etc.* to the bulk phase, relies on an incremental  $n$ -body expansion, and usually consists of only the monomer PESS, the dimer interaction energy, and the trimer interaction energy contributions.<sup>1–7</sup> Exact quantum dynamical computations of clusters map this PES representation onto transitions between rotational and vibrational energy levels—directly measurable quantities by spectroscopic techniques to high precision. This spectroscopic validation, through the direct comparison of the computed and measured rovibrational

transition energies of the dimer, trimer, and larger clusters, provides a stringent test of this incremental representation of materials.

Complexes of methane and water are important for gas storage, including the naturally captured methane in marine and arctic reservoirs,<sup>8</sup> and transportation. The infrared spectrum of methane clathrate hydrate has been reported in ref. 9 and might find significant astrophysical applications. Recent local-monomer, vibrational self-consistent field, and virtual-state configuration interaction theory computations of CH<sub>4</sub>@(H<sub>2</sub>O)<sub>20</sub><sup>10</sup> show good agreement with the experimental Raman spectrum recorded in the C–H stretch region.<sup>11,12</sup> The methane–water dimer has been studied at high resolution in the microwave<sup>13</sup> and the far-infrared<sup>14</sup> regions of the spectrum; however, a detailed theoretical quantum dynamical characterization of this simplest complex has never been carried out.

The quantum dynamical description of CH<sub>4</sub>·H<sub>2</sub>O is challenging because all intermolecular degrees of freedom correspond to highly delocalized motions, resulting from the fluxional and loosely bound character of the complex. These ‘difficult’ fluxional degrees of freedom play a central role in binding the water and methane molecules. Hence, an exact quantum mechanical description of (at least) the intermolecular degrees of freedom

<sup>a</sup> Institute of Chemistry, Eötvös Loránd University, Pázmány Péter sétány 1/A, H-1117 Budapest, Hungary. E-mail: matyus@chem.elte.hu

<sup>b</sup> MTA-ELTE Complex Chemical Systems Research Group, Eötvös Loránd University, P.O. Box 32, H-1518 Budapest 112, Hungary

<sup>c</sup> Department of Chemistry, University of Cambridge, Lensfield Road, Cambridge, CB2 1EW, UK

† Electronic supplementary information (ESI) available. See DOI: 10.1039/c6cp03062a

is necessary to validate the intermolecular potential energy surface (PES). Such a validation is important for the construction of a universal PES for the  $(\text{CH}_4)_n@(\text{H}_2\text{O})_m$  systems.

In the present article, we describe the direct numerical solution of the rovibrational Schrödinger equation for the dimer with rigid monomers using the *ab initio* PES of ref. 15 (and also report preliminary computations performed with the PES of ref. 6). The computed rovibrational transitions are compared with far-infrared (FIR) spectroscopic measurements.<sup>14</sup> This comparison allows us to directly test the accuracy of the PES representations of the methane–water bimolecular interactions. Understanding the transitions seen in the FIR measurements not only requires the application of the best present-day quantum dynamics techniques pushed to their technical limits, but also the development of several tools for the detailed analysis of the results obtained.

In Section 2, we define the rovibrational Hamiltonian used in this study and explain the details of the numerical solution of the corresponding Schrödinger equation. Section 3.1 lists a few relevant results about the PES of the dimer and Section 3.2 is a summary of the symmetry analysis, provided in full detail in the ESI,<sup>†</sup> which is followed by the presentation and discussion of the computed vibrational energy levels, rovibrational energy levels, and rovibrational transitions in Sections 3.3, 3.4, and 3.5, respectively. The article ends with Section 4, containing a summary and the most important conclusions.

## 2 Numerical solution of the rovibrational Schrödinger equation of the intermolecular degrees of freedom

We have carried out a numerical study of the intermolecular degrees of freedom of the methane–water dimer using the rovibrational quantum dynamics computer program GENIUSH,<sup>16,17</sup> and related wave function analysis tools.<sup>18,19</sup> The program and the related methodology have been used before for a number of floppy,<sup>16,17,20</sup> fluxional,<sup>21</sup> and astructural<sup>19,22</sup> molecules and complexes. In what follows, we summarize the theoretical background and specify the computational parameters used during the present study.

The methane–water complex includes  $N = 8$  atomic nuclei and we describe the intermolecular dynamics by considering  $D = 6$  active degrees of freedom (Fig. 1). The general rovibrational Hamiltonian implemented in GENIUSH<sup>16,17</sup> is

$$\begin{aligned} \hat{H} = & \frac{1}{2} \sum_{k=1}^D \sum_{l=1}^D \tilde{g}^{-1/4} \hat{p}_k G_{kl} \tilde{g}^{1/2} \hat{p}_l \tilde{g}^{-1/4} \\ & + \frac{1}{2} \sum_{k=1}^D \sum_{a=1}^3 (\hat{p}_k G_{k,D+a} + G_{k,D+a} \hat{p}_k) \hat{J}_a \\ & + \frac{1}{2} \sum_{a=1}^3 G_{D+a,D+a} \hat{J}_a^2 \\ & + \frac{1}{2} \sum_{a=1}^3 \sum_{b>a}^3 G_{D+a,D+b} (\hat{J}_a \hat{J}_b + \hat{J}_b \hat{J}_a) + \hat{V}, \end{aligned} \quad (1)$$

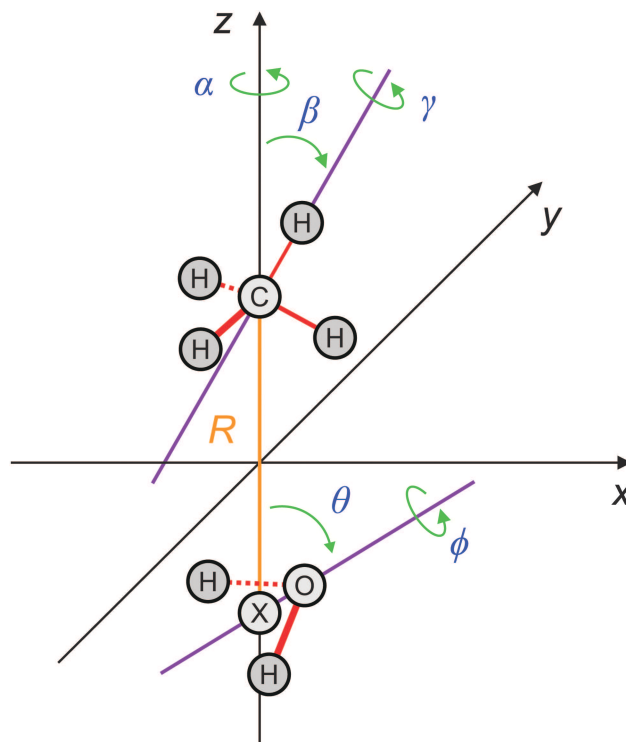


Fig. 1 Internal coordinates ( $R, \theta, \phi, \alpha, \beta, \gamma$ ) and the body-fixed frame ( $x, y, z$ ) employed in the rovibrational computations restricted to intermolecular motions. X labels the center of mass of the water molecule.

where the operators  $\hat{p}_k = -i\partial/\partial q_k$  (in atomic units) correspond to the  $q_k$  ( $k = 1, 2, \dots, D$ ) internal coordinates and  $\hat{J}_a$  ( $a = 1(x), 2(y), 3(z)$ ) are the body-fixed angular momentum operators. The coefficients,  $G_{kl} = (\mathbf{g}^{(\text{inter})})_{kl}^{-1}$  and  $\tilde{g} = \det(\mathbf{g}^{(\text{inter})})$ , are obtained from the reduced-dimensional  $\mathbf{g}$  matrix (which depends also on the structure of the constrained moieties)

$$g_{kl}^{(\text{inter})} = \sum_{i=1}^N m_i \mathbf{t}_{ik}^T \mathbf{t}_{il}, \quad k, l = 1, 2, \dots, D+3 \quad (2)$$

with

$$\mathbf{t}_{ik} = \frac{\partial \mathbf{r}_i}{\partial q_k}, \quad k = 1, 2, \dots, D \quad (3)$$

$$\mathbf{t}_{i,D+a} = \mathbf{e}_a \times \mathbf{r}_i, \quad a = 1(x), 2(y), 3(z) \quad (4)$$

evaluated for the body-fixed Cartesian coordinates,  $\mathbf{r}_i$ , and the unit vectors,  $\mathbf{e}_a$ , of the body-fixed frame. The volume element corresponding to the Hamiltonian, eqn (1), is  $dV = dq_1 dq_2 \dots dq_D d\alpha_1 d\alpha_2 d\alpha_3$ . This intermolecular (reduced-dimensional) quantum Hamiltonian rigorously accounts for the geometrical constraint of the monomer structures for fixed reference geometries, since it is obtained from the classical Lagrangian in which the time derivatives of the monomer structural parameters are set to zero.<sup>16</sup>

The six active internal coordinates visualized in Fig. 1 are defined as follows: the distance of the center-of-mass of the two molecules,  $q_1 = R \in [0, \infty)$ , angles of the spherical polar coordinates  $\rho = (\theta, \phi)$  of  $\text{H}_2\text{O}$ ,  $q_2 = \cos \theta \in [-1, 1]$ ,  $q_3 = \phi \in [0, 2\pi)$ , and the Euler angles for  $\text{CH}_4$ ,  $(\alpha, \beta, \gamma)$  with  $q_4 = \alpha \in [0, 2\pi)$ ,

$q_5 = \cos \beta \in [-1, 1]$ , and  $q_6 = \gamma \in [0, 2\pi]$ . The  $z$  axis of the right-handed  $(x, y, z)$  body-fixed frame is attached to the centers of mass of the two moieties and points from the water towards the methane subunit. We used the same monomer structures (effective ground-state vibrational structures) as in ref. 15, *i.e.*, the fixed structure of the water molecule is defined by  $r(\text{O-H}) = 0.9716257 \text{ \AA}$  and  $\alpha(\text{H-O-H}) = 104.69^\circ$ ,<sup>23</sup> slightly different from the vibrationally averaged parameters two of us computed before,<sup>24</sup>  $\langle r_{\text{OH}} \rangle = 0.97565 \text{ \AA}$  and  $\langle \alpha_{\text{HOH}} \rangle = 104.43^\circ$ . The fixed structure of the methane molecule is a regular tetrahedron,  $\cos \alpha(\text{H-C-H}) = -1/3$ , with  $r(\text{C-H}) = 1.099122 \text{ \AA}$ .<sup>15,25</sup> We used  $m(\text{H}) = 1.007825 \text{ u}$ ,  $m(\text{C}) = 12 \text{ u}$ , and  $m(\text{O}) = 15.994915 \text{ u}$  masses for the atomic nuclei, and the following conversion factors among the different energy units:<sup>26</sup>  $1E_h = 219474.63 \text{ cm}^{-1} = 627.5095 \text{ kcal mol}^{-1}$ , and  $1 \text{ MHz} = 3.335641 \times 10^{-5} \text{ cm}^{-1}$  (the PES of ref. 15 is available in  $\text{kcal mol}^{-1}$  units, we use atomic units during the variational computation, and the experimental results are available in MHz).

In the GENIUSH code the matrix representation of the Hamiltonian is constructed using the discrete variable representation (DVR) for the vibrational degrees of freedom along with symmetrized Wang functions for the rotational degrees of freedom. Table 1 summarizes the parameters of the computations. With these parameters the energy levels (and degeneracies) could be converged to within around  $0.05 \text{ cm}^{-1}$ . The computed energy-level lists for  $J = 0, 1$ , and  $2$  obtained with the AOSz05 PES<sup>15</sup> (the zero of the energy scale is shifted to the energy of the global minimum) are included in the ESI.† In the article we refer to these energy levels with the unambiguous labels  $J0.n$ ,  $J1.n$ , and  $J2.n$  for  $J = 0, 1$ , and  $2$ , respectively, where  $n = 1, 2, \dots$  is an integer that enumerates the energy levels based on their energy order. Tighter convergence (within  $\sim 0.005 \text{ cm}^{-1}$ ) of the degenerate levels can be obtained by using unscaled Legendre DVR points for the  $q_5 = \cos \beta$  degree of freedom; however, a 3–5 times larger grid and about 10 times more CPU are required compared with the computations specified in Table 1.

We have also tested the performance of the more recent PES of ref. 6. The agreement of the vibrational energy levels computed up to *ca.*  $65 \text{ cm}^{-1}$  with the two PESs<sup>6,15</sup> is better than  $1.5 \text{ cm}^{-1}$  and for several levels it is better than  $0.2 \text{ cm}^{-1}$ . This is a very reassuring

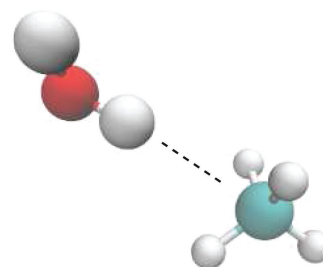
result for the two PESs and the accuracy of the present rovibrational computations. We now present and discuss in detail the results obtained with the AOSz05 PES. (For comparison, the vibrational ( $J = 0$ ) energy levels obtained with both PESs<sup>6,15</sup> and with both the scaled and the unscaled Legendre DVR grids are included in the ESI.†).

### 3 Discussion of the numerical results

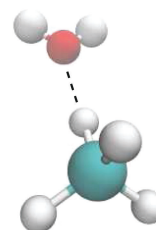
This section presents the most relevant properties of the PES (Section 3.1), a short summary of the symmetry analysis of the dimer (Section 3.2), and a detailed discussion of the numerical results of the quantum dynamical computations including the computed vibrational energy levels (Section 3.3), the computed rovibrational energy levels (Section 3.4), and a comparison of the computed and experimental rovibrational transitions and theoretical predictions for further possible experimental observations (Section 3.5).

#### 3.1 Minima on the AOSz05 PES

The electronic ground-state PES of the methane–water dimer supports two local minima (see Fig. 2 and Table 1), both of  $C_s$  point group symmetry. The secondary minimum (SM) is  $99 \text{ cm}^{-1}$  higher in energy than the global minimum (GM) on the AOSz05 potential energy surface.<sup>15</sup> (The minimum-energy pathway located with OPTIM<sup>27,28</sup> on this PES connecting the global and the secondary minimum structures is shown in Fig. S3 of the ESI.†) In the GM the water molecule is the proton donor, while in the SM the water molecule behaves as an acceptor.



(a) Global minimum (GM)



(b) Secondary minimum (SM)

**Table 1** Internal coordinates (Coord.), discrete variable representations (DVR), number of grid points ( $N$ ), and grid intervals employed during the final variational computations carried out using the GENIUSH code

Coord.	GM <sup>a</sup>	SM <sup>a</sup>	Nuclear motion computations		
			DVR type <sup>b</sup>	$N$	Grid interval
$R$ [Å]	3.464	3.773	PO Laguerre DVR	15	Scaled to [2.5,6.0]
$\theta$ [°]	116.19	22.15 <sup>c</sup>	PO Legendre DVR	14	Scaled to [1,179]
$\phi$ [°]	90.00	0.00	Exponential DVR	15	Unscaled on [0,360]
$\alpha$ [°]	297.46	299.78	Exponential DVR	9	Unscaled on [0,360]
$\beta$ [°]	113.05	70.17	PO Legendre DVR	21	Scaled to [1,179]
$\gamma$ [°]	293.01	240.66	Exponential DVR	21	Unscaled on [0,360]

<sup>a</sup> The values of the internal coordinates are provided for the global minimum (GM) and for the secondary minimum (SM) structures of the AOSz05 PES.<sup>15</sup> <sup>b</sup> PO: potential-optimized DVR, *i.e.*, subsequent optimization of the DVR points with a one-dimensional model. <sup>c</sup> The PES is relatively flat along the  $\theta$  coordinate in the SM well.

**Fig. 2** Equilibrium structures of the AOSz05 potential energy surface.<sup>15</sup> The secondary minimum (SM) is  $99 \text{ cm}^{-1}$  higher in energy than the global minimum (GM).

### 3.2 Symmetry analysis

The feasible permutation-inversion operations of the dimer belong to the  $G_{48}$  molecular symmetry (MS) group.<sup>14</sup> A detailed symmetry analysis, very similar to Dyke's analysis for the water dimer,<sup>29</sup> as well as the character table of  $G_{48}$  are provided in the ESI†. The GM (and also the SM) structure of the underlying PES has  $C_s$  point group symmetry; thus, the dimer has only 24 (instead of 48) distinct, rotationally non-superimposable structures. Therefore (see the ESI†) the zero-point vibration (ZPV) with  $J = 0$  (or any other totally symmetric state) splits into 24 levels, see eqn (S1) (ESI†), characterized by the following symmetry species:

$$\Gamma(\text{ZPV}, J=0) = A_1^+ \oplus E^+ \oplus F_1^+ \oplus 2F_2^+ \oplus A_2^- \oplus E^- \oplus 2F_1^- \oplus F_2^- \quad (5)$$

The + and – superscripts of the irreps differentiate between the symmetric and antisymmetric character of the wave function with respect to the exchange of the two protons of the water molecule. To obtain a total spin-spatial wave function that is antisymmetric with respect to proton exchange, the (+) states have to be combined with the *para* spin function,  $[\alpha(1)\beta(2) - \beta(1)\alpha(2)]/\sqrt{2}$ , while the (–) states have to be combined with one of the *ortho* spin functions,  $\{\alpha(1)\alpha(2), \beta(1)\beta(2), [\alpha(1)\beta(2) + \beta(1)\alpha(2)]/\sqrt{2}\}$ . Hence, we use (+) and *para* or (–) and *ortho* interchangeably.

### 3.3 Vibrational energy levels

Vibrational energy levels computed using the GENIUSH code are visualized at the left of Fig. 3. At the right of the figure we provide the symmetry labels and a qualitative description of the levels up to *ca.*  $65 \text{ cm}^{-1}$ , based on the analysis of the wavefunctions.

The splitting manifold of the ZPV spans  $36.4 \text{ cm}^{-1}$  and separates into a 'lower' and an 'upper' part. The levels can be distinguished by the 'ortho' and 'para' spin states of the water molecule. The upper-lower separation is  $\Delta_o^{\text{ul}} = 23.5 \text{ cm}^{-1}$  for the *ortho* and  $\Delta_p^{\text{ul}} = 29.8 \text{ cm}^{-1}$  for the *para* species. ( $\Delta$  is the difference between the centers of the 'upper' and the 'lower' levels calculated as the degeneracy-weighted average of the corresponding energies.) The large upper-lower separation can be understood in terms of the extremely facile internal rotation of the  $\text{CH}_4$  moiety around the  $\text{O-H} \cdots \text{H}_3\text{C-H}$  hydrogen bond (Fig. 2), which is apparently slightly more hindered for the *ortho* species. The three-fold symmetry of the methane internal rotation,<sup>30</sup> and the corresponding  $A \oplus E$  irreducible decomposition within the  $C_3$  symmetry group, explains the 1 : 2 ratio of the number of levels in the lower and upper parts of the splitting pattern. The lower part covers a range of  $11.2 \text{ cm}^{-1}$  and includes the 'para'  $A_1^+$  and  $F_1^+$  and the 'ortho'  $A_2^-$  and  $F_2^-$  species. The *ortho-para* separation of the degeneracy-weighted average in this lower part is  $\Delta_{\text{op}}^{\text{l}} = 6.5 \text{ cm}^{-1}$ . Interestingly, the same *ortho-para* separation in the upper part of the ZPV manifold is much smaller, only  $\Delta_{\text{op}}^{\text{u}} = 0.2 \text{ cm}^{-1}$ . In general, the upper part is more congested and overlaps with a totally symmetric level that does not fit in this ZPV manifold, since eqn (5) tells us that the ZPV manifold accommodates only a single totally symmetric state. The DVR plots of this 'intruder'

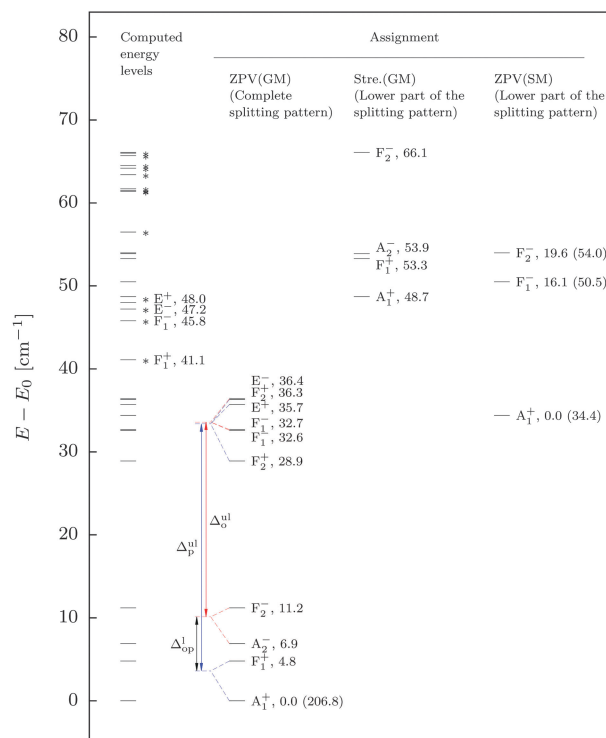


Fig. 3 Vibrational energy levels obtained using the GENIUSH code for the intermolecular degrees of freedom (with rigid monomers). The computed energy levels are shown at the left of the figure, and the symmetry species and characterization are provided at the right, except for those levels labeled with \* (which are left unassigned for the present work). The global minimum (GM) and secondary minimum (SM) structures are shown in Fig. 2. ZPV labels the zero-point vibrational manifold and Stre. stands for stretching fundamental of the intermolecular distance. Definition and discussion of the  $\Delta_{\text{op}}^{\text{l}} = 6.5 \text{ cm}^{-1}$ ,  $\Delta_o^{\text{ul}} = 23.5 \text{ cm}^{-1}$ , and  $\Delta_p^{\text{ul}} = 29.8 \text{ cm}^{-1}$  values are provided in the text.

state (J0.18,  $34.4 \text{ cm}^{-1}$ ) are very similar to the plots of the ground state, whereas the expectation values of some structural parameters markedly differ from those of the ground state (see Fig. 4). Based on these observations we assign this level, as well as the J0.37–39 ( $50.5 \text{ cm}^{-1}$ ), the J0.44–46 ( $54.0 \text{ cm}^{-1}$ ), and the J0.56–57 ( $63.4 \text{ cm}^{-1}$ ) levels, to the zero-point vibrational splitting manifold of the secondary minimum structure, Fig. 2b. The SM has a very shallow potential energy well and accordingly the computed splitting pattern is more diffuse, and we have not attempted to identify all levels in the ZPV(SM).

As well as the ZPV manifolds of the global and the secondary minimum structures, we obtained many more energy levels beyond around  $65 \text{ cm}^{-1}$ . Besides the ZPV(GM) and a few levels from the ZPV(SM), we could unambiguously trace a few levels of the splitting manifold of the intermolecular stretching fundamental by identifying a nodal plane along the  $R$  coordinate in the DVR plots (selected examples are shown in the ESI†). The stretching fundamental vibration is totally symmetric, similar to the ZPV; therefore, the same symmetry species are present in this splitting manifold as in the ZPV manifold, eqn (5). We identified the 'lower part' of this stretching manifold, Stre.  $A_1^+$  ( $48.7 \text{ cm}^{-1}$ , J0.36), Stre.  $F_1^+$  ( $53.3 \text{ cm}^{-1}$ , J0.40–42), Stre.  $A_2^-$

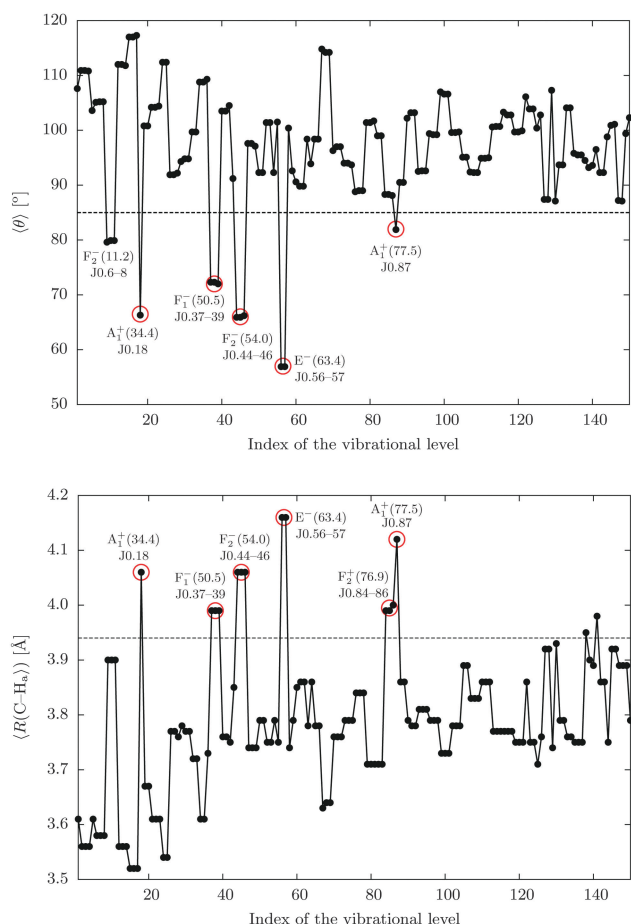


Fig. 4 Expectation values of structural parameters computed with the vibrational wave functions.  $\theta$  is the tilt angle of  $H_2O$  and  $R(C-H_a)$  measures the distance between the carbon nucleus of  $CH_4$  and a hydrogen in  $H_2O$  (the exchange of the two hydrogens is feasible, and thus we obtain the same expectation value for both). These structural parameters have very different values in the equilibrium structures of the two minima (see Fig. 2), and this difference also appears (less markedly) in the expectation values. Vibrational levels that have been assigned to the secondary minimum, based on these structural differences, are highlighted with a red circle.

(53.9  $cm^{-1}$ , J0.43), and Stre.  $F_2^-$  (66.1  $cm^{-1}$ , J0.63,65,66). Indeed, Stre(GM) has a very similar structure to ZPV(GM) but it is characterized by a larger *ortho-para* separation,  $\Delta_{op}^1(\text{Stre}) = 10.9$   $cm^{-1}$ , which might be explained by weaker interactions (and hence 'lower barriers') than in the zero-point energy state. The energy of the lowest-lying state of the stretching fundamental manifold is 48.7  $cm^{-1}$ , only 12  $cm^{-1}$  higher than the energy of the top level of the ZPV(GM) manifold. This is another clear indication of the very weakly bound character of this complex. There are levels that overlap or are even lower in energy than the 'lower' part of the stretching manifold, but left unassigned during the present work (and hence labeled with \* at the left of Fig. 3). Some of these levels could be associated with the ZPV manifold of the secondary minimum and others might belong to some intermolecular bending vibrations. Beyond a certain energy range a conclusive separation of the computed levels between the global minimum well and the

secondary minimum well is probably not possible, because these minima have the same point group symmetry.

### 3.4 Rovibrational energy levels

The rotational constants corresponding to the GM structure, Fig. 2, are  $A = 4.229$   $cm^{-1}$ ,  $B = 0.159$   $cm^{-1}$ , and  $C = 0.158$   $cm^{-1}$ , which indicate an almost perfect prolate symmetric top character. In addition, extremely strong rotational-vibrational mixing is anticipated due to the weak interaction between the two moieties.

The computed rovibrational energy levels with  $J = 0, 1$ , and 2, relevant to the experimental FIR observations,<sup>14</sup> are collected in Fig. 5 and 6 for the *ortho* and the *para* species, respectively. The (ro)vibrational bands in this figure are arranged similarly to Fig. 1 of the experimental paper.<sup>14</sup> A detailed, quantitative comparison of the computed and the experimental transitions is provided in the next subsection.

The most peculiar feature of the rovibrational energy-level manifold is the occasionally reversed ordering of the vibrational and rovibrational levels, *i.e.*, when a  $J = 1$  rovibrational level is lower in energy than its parent vibrational energy level (a parent vibrational level is the dominant vibrational level provided by the rigid rotor decomposition (RRD) analysis of the rovibrational states<sup>18</sup>). This anomalous rovibrational ordering occurs within the  $F_2^-$  (28.9  $cm^{-1}$ , J0.9-11; 36.3  $cm^{-1}$ , J0.21-23),  $E^+$  (35.7  $cm^{-1}$ , J0.19-20),  $F_1^-$  (32.6  $cm^{-1}$ , J0.12-14; 32.7  $cm^{-1}$ , J0.15-17), and  $E^-$  (36.4  $cm^{-1}$ , J0.24-25) bands of the ZPV(GM), and each of these parent vibrational energy levels appear in the 'upper' part of the ZPV(GM) splitting manifold. The reversed statement is also true: all vibrational bands in the 'upper' part of the ZPV(GM) splitting manifold feature anomalous negative rotational 'excitation' energies. This behavior can be understood using the coupled rotors picture: by coupling the rotation of the (rigid) water molecule, the rotation of the (rigid) methane molecule, and the end-over-end rotation of the entire complex.<sup>14,31</sup> The evaluation of the overlap of the exact wave function with these coupled-rotor model functions (for various subsystem angular momenta) is left for future work, and will allow us to make a quantitative assignment to this coupled multiple-rotors model (which is another limiting model along with the common RR model). For the present work, to qualitatively highlight the explained ideas, we defined and constructed energy decomposition tables (see the ESI†), which show the energy contribution of the different terms (and hence different rotors) of the Hamiltonian to the variationally computed (ro)vibrational energy of the complex.

### 3.5 Rovibrational transitions

In addition to the rovibrational energy levels with  $J = 0, 1$ , and 2, Fig. 5 and 6 show the rovibrational transitions that could be identified in the experimental transitions reported in ref. 14. The transitions are labeled with 1,2,... in each band and the same label is used in the corresponding Tables 2-9. There are also experimental observations with higher  $J$  values, which could be explored *via* further computations; however, the results computed with  $J = 0, 1$ , and 2 already highlight the peculiar features (negative rotational excitation energies) of the rovibrational level structure, and also allow us to establish a firm, quantitative comparison

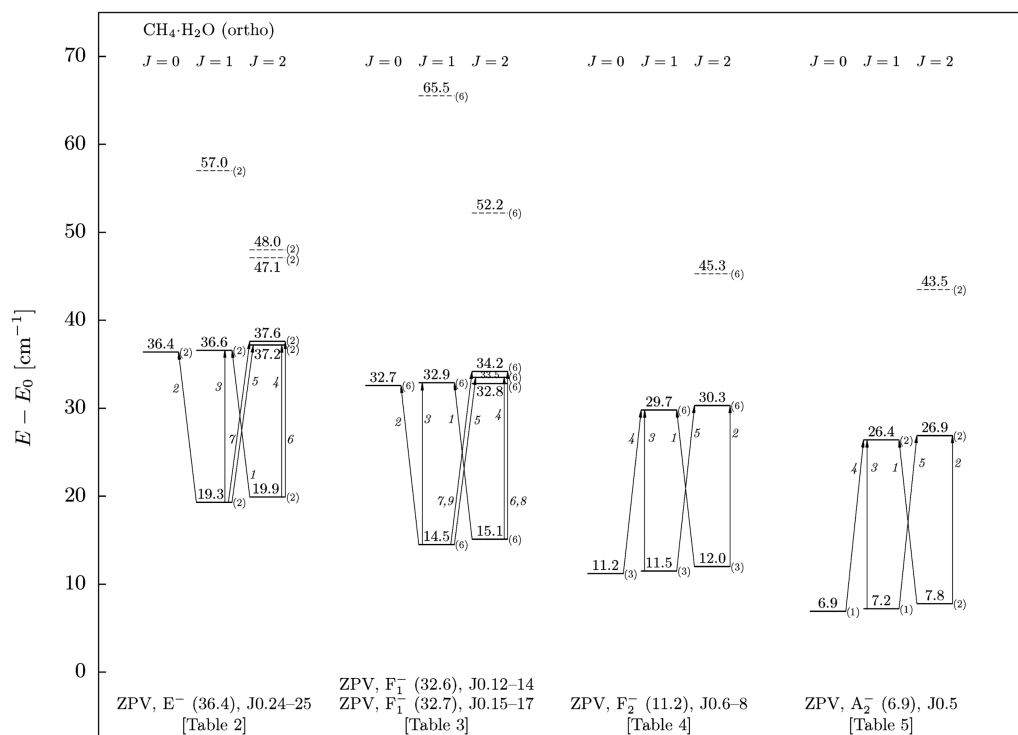


Fig. 5 Rovibrational energy levels, in cm<sup>-1</sup>, and observed<sup>14</sup> and computed transitions of the CH<sub>4</sub>-(*ortho*-H<sub>2</sub>O) dimer with  $J = 0, 1, 2$  (the numbers in italics label the transitions documented in the corresponding tables). The label ( $n$ ) next to each line indicates the number of degenerate or near degenerate energy levels with the average energy given in the figure (rounded to the first decimal place). The dashed lines indicate strongly mixed states with small contributions from the ZPV species in which they are listed.

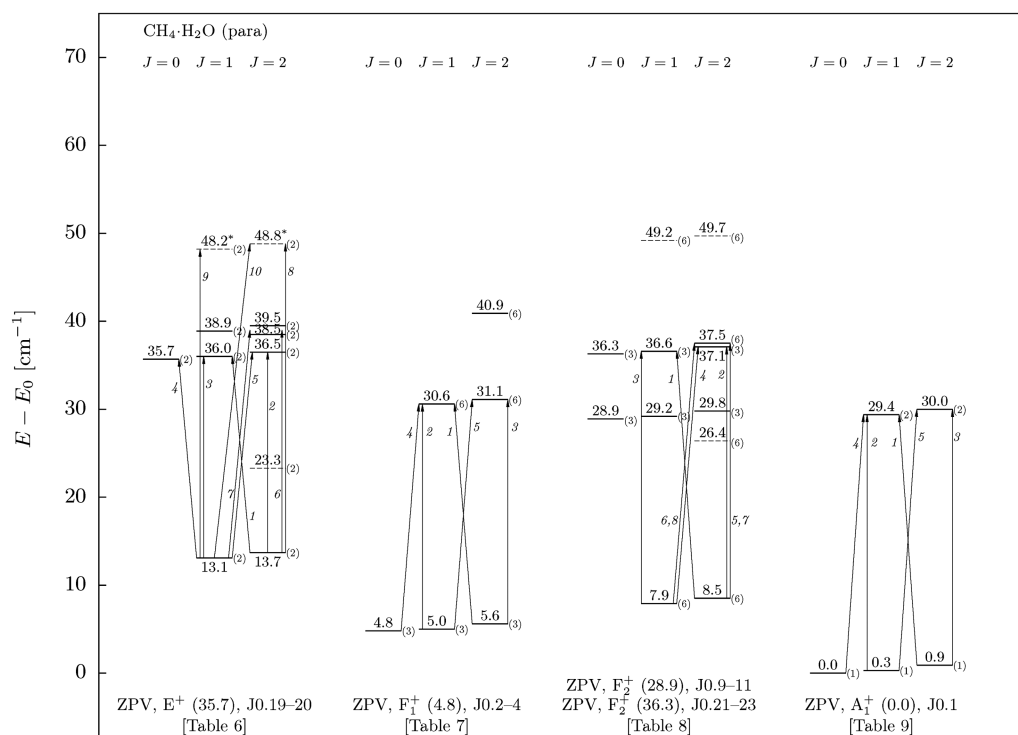


Fig. 6 Rovibrational energy levels, in cm<sup>-1</sup>, and observed<sup>14</sup> and computed transitions of the CH<sub>4</sub>-(*para*-H<sub>2</sub>O) dimer with  $J = 0, 1, 2$  (the numbers in italics identify the lines of the corresponding tables). The label ( $n$ ) next to each line indicates the number of degenerate or near degenerate energy levels with the average energy given in the figure (rounded to the first decimal place). The levels labeled with \* are assignable to the E<sup>+</sup> 48.2 cm<sup>-1</sup> (J0.34–35) vibration. The dashed lines indicate strongly mixed states with small contributions from the ZPV species in which they are listed.

with the experimental results, see Tables 2–9. (The computed rovibrational energy level list is provided in the ESI.†)

Evidently, the observed transitions take place within the rovibrational ZPV(GM) manifold with only three exceptions

**Table 2** Rovibrational transitions assigned to the  $E^-$  36.4  $\text{cm}^{-1}$  (J0.24–25) level of the zero-point vibration

No.	$J' \leftarrow J''$	Expt [MHz]	Expt [ $\text{cm}^{-1}$ ]	$E(J')$ [ $\text{cm}^{-1}$ ]	Label ( $J'$ ) <sup>a</sup>	$E(J'')$ [ $\text{cm}^{-1}$ ]	Label ( $J''$ ) <sup>a</sup>	Calc. [ $\text{cm}^{-1}$ ]	$\delta^b$ [ $\text{cm}^{-1}$ ]
Expt. (ref. 14): Table III, E1, $\Sigma \leftarrow \Pi$ band									
1	1 $\leftarrow$ 2	524254.1	17.5	36.6	J1.56–57	19.9	J2.23–24	16.8	0.7
2	0 $\leftarrow$ 1	532812.0	17.8	36.4	J0.24–25	19.3	J1.23–24	17.0	0.7
3	1 $\leftarrow$ 1	541359.5	18.1	36.6	J1.56–57	19.3	J1.23–24	17.3	0.7
4	2 $\leftarrow$ 2	541344.3	18.1	37.2	J2.78–79	19.9	J2.23–24	17.3	0.7
5	2 $\leftarrow$ 1	558451.2	18.6	37.2	J2.78–79	19.3	J1.23–24	17.9	0.7
Expt. (ref. 14): Table III, E2, $\Delta \leftarrow \Pi$ band									
6	2 $\leftarrow$ 2	542744.8	18.1	37.6	J2.86	19.9	J2.23–24	17.7	0.4
7	2 $\leftarrow$ 1	559850.8	18.7	37.6	J2.86	19.3	J1.23–24	18.2	0.4

<sup>a</sup>  $Jn.i-j$  identifies the levels in the energy-level list provided in the ESI. <sup>b</sup>  $\delta$  is the difference of the experimental and computed transitions. The mean and the sample variance of the deviation in the E1 and E2 bands are  $(\bar{\delta}, \sigma_\delta) = (0.7, 0.002) \text{ cm}^{-1}$  and  $(0.4, 0.003) \text{ cm}^{-1}$ , respectively.

**Table 3** Rovibrational transitions assigned to the  $F_1^-$  32.6  $\text{cm}^{-1}$  (J0.12–14) and 32.7  $\text{cm}^{-1}$  (J0.15–17) levels of the zero-point vibration

No.	$J' \leftarrow J''$	Expt [MHz]	Expt [ $\text{cm}^{-1}$ ]	$E(J')$ [ $\text{cm}^{-1}$ ]	Label ( $J'$ ) <sup>a</sup>	$E(J'')$ [ $\text{cm}^{-1}$ ]	Label ( $J''$ ) <sup>a</sup>	Calc. [ $\text{cm}^{-1}$ ]	$\delta^b$ [ $\text{cm}^{-1}$ ]
Expt. (ref. 14): Table IV, (A/F)1, $\Sigma \leftarrow \Pi$ band									
1	1 $\leftarrow$ 2	529495.8	17.7	32.9	J1.44–49	15.1	J2.17–22	17.8	-0.2
2	0 $\leftarrow$ 1	538189.8	18.0	32.7	J0.12–17	14.5	J1.17–22	18.1	-0.2
3	1 $\leftarrow$ 1	546831.5	18.2	32.9	J1.44–49	14.5	J1.17–22	18.4	-0.2
4	2 $\leftarrow$ 2	546715.2	18.2	33.5	J2.60–65	15.1	J2.17–22	18.4	-0.2
5	2 $\leftarrow$ 1	564291.7	18.8	33.5	J2.60–65	14.5	J1.17–22	19.0	-0.1
Expt. (ref. 14): Table IV, (A/F)3a, $\Delta \leftarrow \Pi$ band									
6	2 $\leftarrow$ 2	564637.3	18.8	34.2	J2.66–71	15.1	J2.17–22	19.1	-0.2
7	2 $\leftarrow$ 1	581971.4	19.4	34.2	J2.66–71	14.5	J1.17–22	19.6	-0.2
Expt. (ref. 14): Table IV, (A/F)3b, $\Delta \leftarrow \Pi$ band									
8	2 $\leftarrow$ 2	564437.7	18.8	34.2	J2.66–71	15.1	J2.17–22	19.1	-0.2
9	2 $\leftarrow$ 1	582013.5	19.4	34.2	J2.66–71	14.5	J1.17–22	19.6	-0.2

<sup>a</sup>  $Jn.i-j$  identifies the levels in the energy level list provided in the ESI. <sup>b</sup>  $\delta$  is the difference between the experimental and computed transitions. The mean and the sample variance of the deviation in the (A/F)1, (A/F)3a, and (A/F)3b bands are  $(\bar{\delta}, \sigma_\delta) = (-0.2, 0.002) \text{ cm}^{-1}$ ,  $(-0.2, 0.001) \text{ cm}^{-1}$ , and  $(-0.2, 0.005) \text{ cm}^{-1}$ , respectively.

**Table 4** Rovibrational transitions assigned to the  $F_2^-$  11.2  $\text{cm}^{-1}$  (J0.6–8) level of the zero-point vibration

No.	$J' \leftarrow J''$	Expt [MHz]	Expt [ $\text{cm}^{-1}$ ]	$E(J')$ [ $\text{cm}^{-1}$ ]	Label ( $J'$ ) <sup>a</sup>	$E(J'')$ [ $\text{cm}^{-1}$ ]	Label ( $J''$ ) <sup>a</sup>	Calc. [ $\text{cm}^{-1}$ ]	$\delta^b$ [ $\text{cm}^{-1}$ ]
Expt. (ref. 14): Table V, (A/F)2, $\Pi \leftarrow \Sigma$ band									
1	1 $\leftarrow$ 2	536931.0	17.9	29.8	J1.32–37	12.0	J2.12–14	17.7	0.2
2	2 $\leftarrow$ 2	553883.6	18.5	30.3	J2.42–47	12.0	J2.12–14	18.3	0.2
3	1 $\leftarrow$ 1	553888.4	18.5	29.8	J1.32–37	11.5	J1.12–14	18.3	0.2
4	1 $\leftarrow$ 0	562445.5	18.8	29.8	J1.32–37	11.2	J0.6–8	18.6	0.2
5	2 $\leftarrow$ 1	571055.5	19.0	30.3	J2.42–47	11.5	J1.12–14	18.9	0.2

<sup>a</sup>  $Jn.i-j$  identifies the levels in the energy-level list provided in the ESI. <sup>b</sup>  $\delta$  is the difference of the experimental and computed transitions. The mean and the sample variance of the deviation are  $(\bar{\delta}, \sigma_\delta) = (0.2, 0.004) \text{ cm}^{-1}$ .

**Table 5** Rovibrational transitions assigned to the  $A_2^-$  6.9  $\text{cm}^{-1}$  (J0.5) level of the zero-point vibration

No.	$J' \leftarrow J''$	Expt [MHz]	Expt [ $\text{cm}^{-1}$ ]	$E(J')$ [ $\text{cm}^{-1}$ ]	Label ( $J'$ ) <sup>a</sup>	$E(J'')$ [ $\text{cm}^{-1}$ ]	Label ( $J''$ ) <sup>a</sup>	Calc. [ $\text{cm}^{-1}$ ]	$\delta^b$ [ $\text{cm}^{-1}$ ]
Expt. (ref. 14): Table VI, (A/F)4, $\Pi \leftarrow \Sigma$ band									
1	1 $\leftarrow$ 2	548506.7	18.3	26.4	J1.25–26	7.8	J2.5	18.6	-0.3
2	2 $\leftarrow$ 2	565694.1	18.9	26.9	J2.33–34	7.8	J2.5	19.1	-0.3
3	1 $\leftarrow$ 1	565694.1	18.9	26.4	J1.25–26	7.2	J1.5	19.1	-0.3
4	1 $\leftarrow$ 0	574574.9	19.2	26.4	J1.25–26	6.9	J0.5	19.4	-0.3
5	2 $\leftarrow$ 1	583344.0	19.5	26.9	J2.33–34	7.2	J1.5	19.7	-0.3

<sup>a</sup>  $Jn.i-j$  identifies the levels in the energy-level list provided in the ESI. <sup>b</sup>  $\delta$  is the difference of the experimental and computed transitions. The mean and the sample variance of the deviation are  $(\bar{\delta}, \sigma_\delta) = (-0.3, 0.003) \text{ cm}^{-1}$ .



**Table 6** Rovibrational transitions assigned to the  $E^+$  35.7  $\text{cm}^{-1}$  (J0.19–20) level of the zero-point vibration

No.	$J' \leftarrow J''$	Expt [MHz]	Expt [ $\text{cm}^{-1}$ ]	$E(J')$ [ $\text{cm}^{-1}$ ]	Label ( $J'$ ) <sup>a</sup>	$E(J'')$ [ $\text{cm}^{-1}$ ]	Label ( $J''$ ) <sup>a</sup>	Calc. [ $\text{cm}^{-1}$ ]	$\delta^b$ [ $\text{cm}^{-1}$ ]
Expt. (ref. 14): Table VII, E3, $\Sigma \leftarrow \Pi$ band									
1	1 $\leftarrow$ 2	723657.8	24.1	36.0	J1.51–52	13.7	J2.15–16	22.3	1.8
2	2 $\leftarrow$ 2	740443.2	24.7	36.5	J2.73–74	13.7	J2.15–16	22.9	1.8
3	1 $\leftarrow$ 1	740778.1	24.7	36.0	J1.51–52	13.1	J1.15–16	22.9	1.8
4	0 $\leftarrow$ 1	732385.1	24.4	35.7	J0.19–20	13.1	J1.15–16	22.6	1.8
5	2 $\leftarrow$ 1	757561.5	25.3	36.5	J2.73–74	13.1	J1.15–16	23.4	1.8
Expt. (ref. 14): Table VII, E4, $\Delta \leftarrow \Pi$ band									
6	2 $\leftarrow$ 2	821483.9	27.4	38.5	J2.88–89	13.7	J2.15–16	24.8	2.6
7	2 $\leftarrow$ 1	838603.8	28.0	38.5	J2.88–89	13.1	J1.15–16	25.4	2.6
or:									
6	2 $\leftarrow$ 2	821483.9	27.4	39.5	J2.90–91	13.7	J2.15–16	25.8	1.6
7	2 $\leftarrow$ 1	838603.8	28.0	39.5	J2.90–91	13.1	J1.15–16	26.4	1.6
Expt. (ref. 14): Table VII, E5, $\Pi \leftarrow \Pi$ band									
8 <sup>c</sup>	2 $\leftarrow$ 2	1057801.7	35.3	48.8	J2.116–117	13.7	J2.15–16	35.1	0.2
9 <sup>c</sup>	1 $\leftarrow$ 1	1057943.1	35.3	48.2	J1.84–85	13.1	J1.15–16	35.1	0.2
10 <sup>c</sup>	2 $\leftarrow$ 1	1074920.4	35.9	48.8	J2.116–117	13.1	J1.15–16	35.7	0.2

<sup>a</sup>  $Jn.i-j$  identifies the levels in the energy-level list provided in the ESI. <sup>b</sup>  $\delta$  is the difference of the experimental and computed transitions. The mean and the sample variance of the deviation in the E3, E4, and E5 bands are  $(\bar{\delta}, \sigma_{\delta}) = (1.8, 0.02) \text{ cm}^{-1}$ ,  $(1.6, 0.002) \text{ cm}^{-1}$ , and  $(0.2, 0.004) \text{ cm}^{-1}$ , respectively. The set of 1–5 transitions has the largest irregularities among all bands studied with a variance as large as  $0.02 \text{ cm}^{-1}$ . <sup>c</sup> The upper level in these transitions is assignable to the  $E^+$  48.2  $\text{cm}^{-1}$  (J0.34–35) vibration.

**Table 7** Rovibrational transitions assigned to the  $F_1^+$  4.8  $\text{cm}^{-1}$  (J0.2–3) level of the zero-point vibration

No.	$J' \leftarrow J''$	Expt [MHz]	Expt [ $\text{cm}^{-1}$ ]	$E(J')$ [ $\text{cm}^{-1}$ ]	Label ( $J'$ ) <sup>a</sup>	$E(J'')$ [ $\text{cm}^{-1}$ ]	Label ( $J''$ ) <sup>a</sup>	Calc. [ $\text{cm}^{-1}$ ]	$\delta^b$ [ $\text{cm}^{-1}$ ]
Expt. (ref. 14): Table VIII, (A/F)5, $\Pi \leftarrow \Sigma$ band									
1	1 $\leftarrow$ 2	827031.4	27.6	30.6	J1.38–43	5.6	J2.2–4	25.0	2.6
2	1 $\leftarrow$ 1	844268.9	28.2	30.6	J1.38–43	5.0	J1.2–4	25.5	2.6
3	2 $\leftarrow$ 2	844500.0	28.2	31.1	J2.48–53	5.6	J2.2–4	25.5	2.6
4	1 $\leftarrow$ 0	852462.1	28.4	30.6	J1.38–43	4.8	J0.2–4	25.8	2.6
5	2 $\leftarrow$ 1	860602.5	28.7	31.1	J2.48–53	5.0	J1.2–4	26.1	2.6

<sup>a</sup>  $Jn.i-j$  identifies the levels in the energy level list provided in the ESI. <sup>b</sup>  $\delta$  is the difference of the experimental and computed transitions. The mean and the sample variance of the deviation are  $(\bar{\delta}, \sigma_{\delta}) = (2.6, 0.01) \text{ cm}^{-1}$ .

**Table 8** Rovibrational transitions assigned to the  $F_2^+$  28.9  $\text{cm}^{-1}$  (J0.9–11) and 36.3  $\text{cm}^{-1}$  (J0.21–23) levels of the zero-point vibration

No.	$J' \leftarrow J''$	Expt [MHz]	Expt [ $\text{cm}^{-1}$ ]	$E(J')$ [ $\text{cm}^{-1}$ ]	Label ( $J'$ ) <sup>a</sup>	$E(J'')$ [ $\text{cm}^{-1}$ ]	Label ( $J''$ ) <sup>a</sup>	Calc. [ $\text{cm}^{-1}$ ]	$\delta^b$ [ $\text{cm}^{-1}$ ]
Expt. (ref. 14): Table IX, (A/F)6, $\Sigma \leftarrow \Pi$ band									
1	1 $\leftarrow$ 2	889393.8	29.7	36.6	J1.53–55	8.5	J2.6–11	28.1	1.6
2	2 $\leftarrow$ 2	906302.4	30.2	37.1	J2.75–77	8.5	J2.6–11	28.6	1.6
3	1 $\leftarrow$ 1	906722.4	30.2	36.6	J1.53–55	7.9	J1.6–11	28.7	1.6
4	2 $\leftarrow$ 1	924003.8	30.8	37.1	J2.75–77	7.9	J1.6–11	29.2	1.6
Expt. (ref. 14): Table IX, (A/F)7a, $\Delta \leftarrow \Pi$ band									
5	2 $\leftarrow$ 2	912803.3	30.4	37.5	J2.80–85	8.5	J2.6–11	29.0	1.4
6	2 $\leftarrow$ 1	930130.4	31.0	37.5	J2.80–85	7.9	J1.6–11	29.6	1.4
Expt. (ref. 14): Table IX, (A/F)7b, $\Delta \leftarrow \Pi$ band									
7	2 $\leftarrow$ 2	912529.1	30.4	37.5	J2.80–85	8.5	J2.6–11	29.0	1.4
8	2 $\leftarrow$ 1	930230.6	31.0	37.5	J2.80–85	7.9	J1.6–11	29.6	1.4

<sup>a</sup>  $Jn.i-j$  identifies the levels in the energy-level list provided in the ESI. <sup>b</sup>  $\delta$  is the difference of the experimental and computed transitions. The mean and the sample variance of the deviation in the (A/F)6, (A/F)7a, and (A/F)7b, bands are  $(\bar{\delta}, \sigma_{\delta}) = (1.6, 0.004) \text{ cm}^{-1}$ ,  $(1.4, 0.003) \text{ cm}^{-1}$ , and  $(1.4, 0.005) \text{ cm}^{-1}$ , respectively.

starting from the ZPV  $E^+$  band (*vide infra*). Anomalous  $J' = 0 \leftarrow J'' = 1$  (and  $J' = 1 \leftarrow J'' = 2$ ) rovibrational transitions are seen both in (the absorption) experiment and theory within the ZPV  $E^-$  (36.4  $\text{cm}^{-1}$ , J0.24–25) and the ZPV  $F_1^-$  (32.6  $\text{cm}^{-1}$ , J0.12–14; 32.7  $\text{cm}^{-1}$ , J0.15–17) bands of the ‘ortho’ species and within the ZPV  $E^+$  (35.7  $\text{cm}^{-1}$ , J0.19–20) and the ZPV  $F_2^+$  (28.9  $\text{cm}^{-1}$ , J0.9–11; 36.3  $\text{cm}^{-1}$ , J0.21–23) bands of the ‘para’ species.

The assignment of the vibrational bands and most rovibrational levels is unambiguous; however, due to the near symmetric prolate character of the complex there are nearly degenerate levels, which cannot be unambiguously assigned based on the computations. This ambiguity could be eliminated if there was an exceedingly accurate potential energy surface available, which could be used to obtain a rovibrational energy level ordering resolved to better than

**Table 9** Rovibrational transitions assigned to the  $A_1^+$  0.0  $\text{cm}^{-1}$  (J0.1) level of the zero-point vibration

No.	$J' \leftarrow J''$	Expt [MHz]	Expt [ $\text{cm}^{-1}$ ]	$E(J')$ [ $\text{cm}^{-1}$ ]	Label ( $J'$ ) <sup>a</sup>	$E(J'')$ [ $\text{cm}^{-1}$ ]	Label ( $J''$ ) <sup>a</sup>	Calc. [ $\text{cm}^{-1}$ ]	$\delta^b$ [ $\text{cm}^{-1}$ ]
Expt. (ref. 14): Table X, (A/F)8 $\Pi \leftarrow \Sigma$ band									
1	1 $\leftarrow$ 2	901595.6	30.1	29.4	J1.30–31	0.9	J2.1	28.6	1.5
2	1 $\leftarrow$ 1	919166.0	30.7	29.4	J1.30–31	0.3	J1.1	29.1	1.5
3	2 $\leftarrow$ 2	919232.4	30.7	30.0	J2.40–41	0.9	J2.1	29.1	1.5
4	1 $\leftarrow$ 0	927673.3	30.9	29.4	J1.30–31	0.0	J0.1	29.4	1.5
5	2 $\leftarrow$ 1	936059.3	31.2	30.0	J2.40–41	0.3	J1.1	29.7	1.5

<sup>a</sup>  $Jn.i-j$  identifies the levels in the energy-level list provided in the ESI. <sup>b</sup>  $\delta$  is the difference of the experimental and computed transitions. The mean and the sample variance of the deviation are  $(\bar{\delta}, \sigma_\delta) = (1.5, 0.007) \text{ cm}^{-1}$ .

0.5  $\text{cm}^{-1}$  (which is perhaps even beyond the accuracy of the common Born–Oppenheimer<sup>32</sup> and non-relativistic approximations<sup>33</sup>). In lieu of a fully resolved list, we assign a rovibrational transition to a sub-manifold of upper and/or lower rovibrational levels (see Fig. 5 and 6), without attempting to make a definitive decision about these non-strictly-degenerate but very-close-lying levels. In these cases, we computed the transition energy as the difference between the centers (energy averages) of the upper and lower sub-manifolds (Tables 2–9). Apart from these very small effects, we can confirm that the rovibrational transitions within a single band have a systematic error (experiment–theory) with an exceedingly small variance, which is on the order of the energy difference of the nearly degenerate levels.

Detailed comparison of the computed and measured rovibrational transitions within the eight experimentally studied main bands (occasionally with a few sub-bands)<sup>14</sup> is provided in Tables 2–9. The mean and the variance of the deviation of experiment and theory is around  $(2, 0.01) \text{ cm}^{-1}$  and  $(0.5, 0.005) \text{ cm}^{-1}$  for the *para* and for the *ortho* species, respectively. In general, the agreement and the consistency (the mean and the variance of the deviation) between experiment and theory is better for the *ortho* species. A possible contributor to the cause of this difference is the 3:1 ratio of the spin-statistical weights and of the corresponding transition intensities.

The largest discrepancies between experiment and theory are observed for the 1–5 rovibrational transitions of the  $E^+$  vibration (Table 6). For the 6–7 transitions of this band (Table 6), we cannot decide unambiguously between two possible upper states, with energies  $38.5 \text{ cm}^{-1}$  and  $39.5 \text{ cm}^{-1}$ . Comparing the systematic error of the computed transitions with the error of the 1–5 transitions, it seems more likely that the upper level of the 6–7 transitions is the one with an energy of  $38.5 \text{ cm}^{-1}$ . The systematic error of the 8–10 transitions (Table 6) is markedly different from the error of the 1–5 transitions. This deviation is explained by the fact that the upper levels of the 8–10 transitions do not belong to the ZPV(GM) splitting manifold, but they are the  $J = 1$  and  $J = 2$  rotational excitations of the  $E^+$   $48.2 \text{ cm}^{-1}$  (J0.34–35) vibration.

Most importantly, all experimentally reported transitions<sup>14</sup> within the  $J = 0, 1, 2$  manifold are identified in our variationally computed dataset. For the *ortho* species (see Fig. 5), all levels within the computed ZPV(GM) manifold (up to  $J = 2$ ) are involved in at least one experimentally reported transition. For the *para* species (see Fig. 6), however, there are a few computed levels within the ZPV(GM) manifold (up to  $J = 2$ ) that are not involved in any experimentally reported transitions

**Table 10** Computed rovibrational energy levels assigned to the ZPV(GM) manifold, which could be observed *via* rovibrational transitions within the same energy range as the experiments of ref. 14 were performed ( $E_0$  is the lowest vibrational energy)

Vibrational band	$J$	$E - E_0$ [ $\text{cm}^{-1}$ ]	Label
$E^+$ ( $35.7 \text{ cm}^{-1}$ , J0.19–20)	1	38.9	J1.58–59
	2	39.5	J2.90–91
$F_1^+$ ( $4.8 \text{ cm}^{-1}$ , J0.2–4)	2	40.9	J2.92–97
$F_2^+$ ( $28.9 \text{ cm}^{-1}$ , J0.9–11) & $F_2^+$ ( $36.3 \text{ cm}^{-1}$ , J0.21–23)	0	28.9	J0.9–11
	0	36.3	J0.21–23
	1	29.2	J1.27–29
	2	29.8	J2.37–39

(there are no arrows starting from or pointing to these levels indicated with a solid line in the figures). These theoretically predicted levels of the ZPV(GM) rovibrational manifold are listed in Table 10 and are awaiting experimental confirmation.

There are also energy levels labeled with a dashed line in Fig. 5 and 6. These levels have a strongly mixed RRD with some minor contribution from the ZPV(GM) vibrational band in which they are shown. We indicated these levels in the figures because they could be observed in transitions under similar conditions as in ref. 14. Furthermore, by counting all energy levels and by including these strongly mixed ones, *i.e.*, summing all ( $n$ ) values shown next to the (solid or dashed) lines in each rovibrational band, we obtain  $2J + 1$  rovibrational levels in total, except for the ZPV  $A_1^+$  ( $0.0 \text{ cm}^{-1}$ , J0.1) with  $J = 2$ . In that case two additional rovibrational levels should appear with rovibrational energies ( $J = 2$ ) larger than  $54.9 \text{ cm}^{-1}$ , *i.e.*, beyond the first 150 energy levels which were computed.

Finally, transitions between the rovibrational levels of the ZPV(GM),  $A_1^+$  ( $0.0 \text{ cm}^{-1}$ , J0.1), and the lowest-lying levels of the ZPV manifold of the secondary minimum, ZPV(SM),  $A_1^+$  ( $34.4 \text{ cm}^{-1}$ , J0.18), could be identified in the experimental spectra, because these transitions lie within the same energy range as the transitions reported in ref. 14. The predicted levels of the secondary minimum,

**Table 11** Computed rovibrational energy levels of the ground-state vibration of the secondary minimum, which could be observed *via* rovibrational transitions within the same energy range as the experiments of ref. 14 were performed ( $E_0$  is the lowest vibrational energy)

Vibrational band	$J$	$E - E_0$ [ $\text{cm}^{-1}$ ]	Label
$A_1^+$ ( $34.4 \text{ cm}^{-1}$ , J0.18)	1	34.7	J1.50
	1	59.3	J1.134–135
	2	35.2	J2.72

which could potentially be observed as upper levels in rovibrational transitions, are listed in Table 11. Locating such transitions would constitute the first experimental confirmation for the existence of a secondary minimum in the methane–water complex, where the methane molecule is the proton donor and the water molecule is the proton acceptor.

## 4 Summary and conclusions

We have computed rovibrational energy levels for the methane–water dimer corresponding to an accurate potential energy surface developed by Akin-Ojo and Szalewicz<sup>15</sup>. The computations exploited the capabilities of the fourth generation<sup>34</sup> quantum chemical code GENIUSH<sup>16,17</sup>. After a careful analysis of the computed states, excellent, quantitative agreement is obtained between the calculated and experimentally reported far-infrared<sup>14</sup> transitions of this complex, which were previously left unassigned. This excellent agreement suggests that the dimer interaction potential energy surfaces available for CH<sub>4</sub>–H<sub>2</sub>O<sup>6,15</sup> can be used with confidence and their combination with the three-body methane–water–water<sup>7</sup> (and the corresponding two- and three-body water–water interaction surfaces<sup>3–5</sup>) opens up new avenues for the study of larger clusters<sup>10</sup> and bulk-phase properties of methane–water mixtures.

Concerning the fine details of the rovibrational spectroscopy of the methane–water dimer, all experimentally reported transitions within the  $J = 0, 1, 2$  rovibrational manifold are identified in our computations. They are assigned to rovibrational energy levels corresponding to the 24-member zero-point vibrational (ZPV) manifold of the global minimum (GM) structure (in which the water molecule is the proton donor and the methane molecule is the acceptor). The exceptions are three transitions whose upper level is higher in energy than the ZPV(GM) manifold. We identified a few rovibrational levels in the computed ZPV(GM) rovibrational splitting manifold, which lie in the same energy range, and thus could potentially be observed under the same experimental conditions, but were not reported in ref. 14.

We have also identified (ro)vibrational energy levels that could only be assigned to the secondary minimum (SM) of the complex, in which the methane molecule is the proton donor and the water molecule is the acceptor. The lower part of the 24-member ZPV(SM) manifold overlaps the upper part of the 24-member ZPV(GM) set; hence, rovibrational transitions ending in levels corresponding to the secondary minimum well might be observed in the same energy range as the transitions reported in ref. 14.

Anomalous, reversed rovibrational-energy level ordering, *i.e.*, negative rotational excitation energy, is observed both in the experimental and in the computed transitions. This observation provides additional confirmation of the excellent agreement between theory and experiment, and, furthermore, indicates that this extremely floppy, astructural<sup>19,22</sup> complex exhibits rich internal quantum dynamics, suggesting that further experimental and theoretical work will be worth pursuing both from fundamental and applied research perspectives.

## Acknowledgements

JS, EM, and AGC acknowledge financial support from the NKFIH (Grant No. NK83583). EM, SCA and DJW acknowledge funding from the UK Engineering and Physical Sciences Research Council (EPSRC). The authors are grateful for the support of the COST Action MOLIM, Molecules in Motion (CM1405).

## References

- 1 J. N. Murrell, S. Carter, S. C. Farantos, P. Huxley and A. J. C. Varandas, *Molecular Potential Energy Functions*, Wiley, New York, 1984.
- 2 B. J. Braams and J. M. Bowman, *Int. Rev. Phys. Chem.*, 2009, **28**, 577.
- 3 Y. Wang and J. M. Bowman, *J. Chem. Phys.*, 2011, **134**, 154510.
- 4 G. R. Medders, V. Babin and F. Paesani, *J. Chem. Theory Comput.*, 2013, **9**, 1103.
- 5 V. Babin, G. R. Medders and F. Paesani, *J. Chem. Theory Comput.*, 2014, **10**, 1599.
- 6 C. Qu, R. Conte, P. L. Houston and J. M. Bowman, *Phys. Chem. Chem. Phys.*, 2015, **17**, 8172.
- 7 R. Conte, C. Qu and J. M. Bowman, *J. Chem. Theory Comput.*, 2015, **11**, 1631.
- 8 T. S. Collett, A. H. Johnson, C. C. Knapp and R. Boswell, Natural Gas Hydrates: A Review, in *Natural gas hydrates—Energy resource potential and associated geologic hazards*, ed. T. S. Collett, A. H. Johnson, C. C. Knapp and R. Boswell, AAPG/NETL/AAPG Foundation/AAPG EMD, 2010, vol. M 89, pp. 146–219.
- 9 E. Dartois and D. Deboffe, *Astron. Astrophys.*, 2008, **490**, L19.
- 10 C. Qu and J. M. Bowman, *J. Phys. Chem. C*, 2016, **120**, 3167.
- 11 A. K. Sum, R. C. Burruss and E. D. Sloan, *J. Phys. Chem. B*, 1997, **101**, 7371.
- 12 H. Ohno, M. Kida, T. Sakurai, Y. Iizuka, T. Hondoh, H. Narita and J. Nagao, *ChemPhysChem*, 2010, **11**, 3070.
- 13 R. D. Suenram, G. T. Fraser, F. J. Lovas and Y. Kawashima, *J. Chem. Phys.*, 1994, **101**, 7230.
- 14 L. Dore, R. C. Cohen, C. A. Schmuttenmaer, K. L. Busarow, M. J. Elrod, J. G. Loeser and R. J. Saykally, *J. Chem. Phys.*, 1994, **100**, 863.
- 15 O. Akin-Ojo and K. Szalewicz, *J. Chem. Phys.*, 2005, **123**, 134311.
- 16 E. Mátyus, G. Czakó and A. G. Császár, *J. Chem. Phys.*, 2009, **130**, 134112.
- 17 C. Fábri, E. Mátyus and A. G. Császár, *J. Chem. Phys.*, 2011, **134**, 074105.
- 18 E. Mátyus, C. Fábri, T. Szidarovszky, G. Czakó, W. D. Allen and A. G. Császár, *J. Chem. Phys.*, 2010, **133**, 034113.
- 19 J. Sarka and A. G. Császár, *J. Chem. Phys.*, 2016, **144**, 154309.
- 20 C. Fábri, E. Mátyus and A. G. Császár, *Spectrochim. Acta*, 2014, **119**, 84–89.
- 21 C. Fábri, A. G. Császár and G. Czakó, *J. Phys. Chem. A*, 2013, **117**, 6975.
- 22 C. Fábri, J. Sarka and A. G. Császár, *J. Chem. Phys.*, 2014, **140**, 051101.

- 23 K. Kuchitsu and L. S. Bartell, *J. Chem. Phys.*, 1962, **36**, 2460.
- 24 G. Czakó, E. Mátyus and A. G. Császár, *J. Phys. Chem. A*, 2009, **113**, 11665.
- 25 M. Nakata and K. Kuchitsu, *J. Chem. Soc. Jpn.*, 1986, 1446.
- 26 E. Cohen, T. Cvitaš, J. Frey, B. Holmström, K. Kuchitsu, R. Marquardt, I. Mills, F. Pavese, M. Quack, J. Stohner, H. Strauss, M. Takami and A. Thor, *Quantities, Units and Symbols in Physical Chemistry (the IUPAC Green Book – 3rd edition)*, RSC Publishing, Cambridge, 2007.
- 27 D. J. Wales, *OPTIM: A program for geometry optimisation and pathway calculations*, <http://www-wales.ch.cam.ac.uk/software.html>.
- 28 L. J. Munro and D. J. Wales, *Phys. Rev. B: Condens. Matter Mater. Phys.*, 1999, **59**, 3969–3980.
- 29 T. R. Dyke, *J. Chem. Phys.*, 1977, **66**, 492.
- 30 V. Szalay, A. G. Császár and M. L. Senent, *J. Chem. Phys.*, 2002, **117**, 6489.
- 31 Y. Ohshima and Y. Endo, *J. Chem. Phys.*, 1990, **93**, 6256.
- 32 E. Mátyus and M. Reiher, *J. Chem. Phys.*, 2012, **137**, 024104.
- 33 O. L. Polyansky, A. G. Császár, S. V. Shirin, N. F. Zobov, P. Barletta, J. Tennyson, D. W. Schwenke and P. J. Knowles, *Science*, 2003, **299**, 539.
- 34 A. G. Császár, C. Fábri, T. Szidarovszky, E. Mátyus, T. Furtenbacher and G. Czakó, *Phys. Chem. Chem. Phys.*, 2012, **14**, 1085.

# Variational vs perturbative relativistic energies for small and light atomic and molecular systems

Cite as: J. Chem. Phys. 157, 094113 (2022); doi: 10.1063/5.0105355

Submitted: 23 June 2022 • Accepted: 27 July 2022 •

Published Online: 6 September 2022



View Online



Export Citation



CrossMark

Dávid Ferenc, Péter Jeszenszki, and Edit Mátyus<sup>a)</sup>

## AFFILIATIONS

Institute of Chemistry, ELTE, Eötvös Loránd University, Pázmány Péter sétány 1/A, Budapest H-1117, Hungary

<sup>a)</sup> Author to whom correspondence should be addressed: [edit.matyus@ttk.elte.hu](mailto:edit.matyus@ttk.elte.hu)

## ABSTRACT

Variational and perturbative relativistic energies are computed and compared for two-electron atoms and molecules with low nuclear charge numbers. In general, good agreement of the two approaches is observed. Remaining deviations can be attributed to higher-order relativistic, also called non-radiative quantum electrodynamics (QED), corrections of the perturbative approach that are automatically included in the variational solution of the no-pair Dirac–Coulomb–Breit (DCB) equation to all orders of the  $\alpha$  fine-structure constant. The analysis of the polynomial  $\alpha$  dependence of the DCB energy makes it possible to determine the leading-order relativistic correction to the non-relativistic energy to high precision without regularization. Contributions from the Breit–Pauli Hamiltonian, for which expectation values converge slowly due to the singular terms, are implicitly included in the variational procedure. The  $\alpha$  dependence of the no-pair DCB energy shows that the higher-order ( $\alpha^4 E_h$ ) non-radiative QED correction is 5% of the leading-order ( $\alpha^3 E_h$ ) non-radiative QED correction for  $Z = 2$  (He), but it is 40% already for  $Z = 4$  ( $\text{Be}^{2+}$ ), which indicates that resummation provided by the variational procedure is important already for intermediate nuclear charge numbers.

Published under an exclusive license by AIP Publishing. <https://doi.org/10.1063/5.0105355>

## I. INTRODUCTION

The non-relativistic quantum electrodynamics (QED) framework, which systematically includes all relativistic and quantum electrodynamics (QED) corrections to the non-relativistic energy with increasing powers of the  $\alpha$  fine structure constant is the current state of the art for small and light atomic and molecular systems.<sup>1–10</sup> Higher precision or higher charge numbers assume the derivation and evaluation of high-order perturbative corrections.

The current state of the art for two-electron systems in the non-relativistic QED framework corresponds to  $\alpha^4 E_h$  order (in atomic units), which is equivalent to  $m\alpha^6$  in natural units.<sup>3,11</sup> The  $\alpha^5 E_h$ -order corrections have been evaluated for triplet states of the helium atom<sup>9</sup> aiming to resolve current discrepancy of theory and experiment.<sup>12–16</sup> The corresponding terms for singlet states have not been completed, yet.

Although the non-relativistic plus relativistic and QED separation has been traditionally (for good reasons) pursued to produce state-of-the-art theoretical values,<sup>8,15,17–23</sup> it is possible to partition the relativistic QED problem differently. The relativistic QED problem of atoms and molecules has two (three) “small” parameters, the

$\alpha$  fine structure constant, the  $Z\alpha$  nuclear charge number multiple of  $\alpha$  (and the electron–nucleus mass ratio, which is not considered in the present work, since the nuclei are fixed). Although  $\alpha = 1/137.035999084 \approx 0.0073^{24}$  is indeed small, resummation of the perturbation series for  $Z\alpha$  would be ideal to cover larger nuclear charge values.

As a starting point for two-electron systems, we consider the Bethe–Salpeter<sup>25</sup> equation, a relativistic QED wave equation. Following Salpeter’s calculation for positronium<sup>26</sup> and Sucher’s calculation for the electronic problem of helium,<sup>27</sup> this equation can be rearranged to an exact equal-times form

$$(H + H_\Delta)\Psi(\mathbf{r}_1, \mathbf{r}_2) = E\Psi(\mathbf{r}_1, \mathbf{r}_2), \quad (1)$$

where  $\mathbf{r}_1, \mathbf{r}_2 \in \mathbb{R}^3$  are the Cartesian coordinates of the two particles,  $H$  is the positive-energy projected two-electron Hamiltonian with instantaneous (Coulomb or Breit) interaction ( $I$ ),

$$H = h_1 + h_2 + \Lambda_{++} I \Lambda_{++}, \quad (2)$$

$h_i = \alpha \mathbf{p}_i + \beta m_i c^2 + U1^{[4]}$  ( $i = 1, 2$ ) labels the one-particle Dirac Hamiltonians in the  $U$  external Coulomb field of fixed nuclei, and

$$H_{\Delta} = \Lambda_{++}I(1 - \Lambda_{++}) - \Lambda_{--}I + H_{\epsilon} \quad (3)$$

is a correction term with  $H_{\epsilon}$ , which contains an integral for the relative energy<sup>27</sup> of two particles, and it carries pair corrections and retardation corrections. Radiative corrections can also be incorporated in  $H_{\epsilon}$ . During the derivation,<sup>26,27</sup> starting out from the interaction of elementary spin-1/2 particles, the two-particle (electron) positive-energy Dirac–Coulomb(–Breit) (DCB) Hamiltonian emerges and  $\Lambda_{++}$  ( $\Lambda_{--}$ ) projects onto the positive-(negative-) energy states of two electrons moving in the external field without electron–electron interactions.

Following Sucher,  $H_{\Delta}$  may be considered as perturbation to the positive-energy projected (also called no-pair) Hamiltonian,  $H$ . So, the present work is concerned with the numerical solution of the

$$H\Psi = E\Psi \quad (4)$$

16-component wave equation for the instantaneous Coulomb (C) and Coulomb–Breit (CB) interactions. The Breit interaction is either included in the variational solution to obtain the no-pair (++) Dirac–Coulomb–Breit (DCB) energy,  $E_{\text{DCB}}^{++}$ , or it is computed as a

$$H(1,2) = \Lambda_{++} \left( \begin{array}{cc|cc} V1^{[4]} + U1^{[4]} & c\sigma_2^{[4]} \cdot \mathbf{p}_2 & c\sigma_1^{[4]} \cdot \mathbf{p}_1 & B^{[4]} \\ c\sigma_2^{[4]} \cdot \mathbf{p}_2 & V1^{[4]} + (U - 2m_2c^2)1^{[4]} & B^{[4]} & c\sigma_1^{[4]} \cdot \mathbf{p}_1 \\ c\sigma_1^{[4]} \cdot \mathbf{p}_1 & B^{[4]} & V1^{[4]} + (U - 2m_1c^2)1^{[4]} & c\sigma_2^{[4]} \cdot \mathbf{p}_2 \\ B^{[4]} & c\sigma_1^{[4]} \cdot \mathbf{p}_1 & c\sigma_2^{[4]} \cdot \mathbf{p}_2 & V1^{[4]} + (U - 2m_{12}c^2)1^{[4]} \end{array} \right) \Lambda_{++}, \quad (6)$$

with  $m_{12} = m_1 + m_2$ ,  $\mathbf{p}_i = -i(\frac{\partial}{\partial r_{ix}}, \frac{\partial}{\partial r_{iy}}, \frac{\partial}{\partial r_{iz}})$  ( $i = 1, 2$ ),  $\sigma_1^{[4]} = (\sigma_x \otimes 1^{[2]}, \sigma_y \otimes 1^{[2]}, \sigma_z \otimes 1^{[2]})$  and  $\sigma_2^{[4]} = (1^{[2]} \otimes \sigma_x, 1^{[2]} \otimes \sigma_y, 1^{[2]} \otimes \sigma_z)$ , where  $\sigma_x, \sigma_y$ , and  $\sigma_z$  are the  $2 \times 2$  Pauli matrices, and  $U = \sum_{i=1}^2 \sum_{a=1}^{N_{\text{nuc}}} q_i Z_a / |\mathbf{r}_i - \mathbf{R}_a|$  is the external Coulomb potential of the nuclei. We note that the operator in Eq. (6) already contains a  $-2m_i c^2$  shift ( $i = 1, 2$ ) for computational convenience and for a straightforward matching of the non-relativistic energy scale.

Regarding the particle–particle interactions in Eq. (6), the Coulomb potential,

$$V = \frac{q_1 q_2}{r_{12}}, \quad (7)$$

is along the diagonal, whereas the  $B^{[4]}$  blocks, corresponding to the Breit potential, can be found on the anti-diagonal of the Hamiltonian matrix,

$$B^{[4]} = G^{[4]} - \frac{q_1 q_2}{2} \sum_{i=1}^3 \sum_{j=1}^3 \sigma_{1_i}^{[4]} \sigma_{2_j}^{[4]} \{ \nabla_1, \nabla_2, r_{12} \}. \quad (8)$$

The first term of  $B^{[4]}$  is called the Gaunt interaction, which reads as

first-order perturbation to the no-pair Dirac–Coulomb (DC) energy ( $E_{\text{DC}}^{++}$ ),

$$\langle B \rangle_{\text{DC}} = \langle \Psi_{\text{DC}}^{++} | B | \Psi_{\text{DC}}^{++} \rangle, \quad (5)$$

and it is labeled  $E_{\text{DC}}^{++}(B) = E_{\text{DC}}^{++} + \langle B \rangle_{\text{DC}}$ .

In 1958, Sucher introduced the non-relativistic (Pauli) approximation to the no-pair DC wave function to arrive at numerical predictions. Using modern computers, we solve the DC and DCB equations numerically to a precision, where comparison with the perturbative treatment (up to the known orders) is interesting and, so far, unexplored. This paper is the concluding part of a series of papers<sup>28–30</sup> which report the development of fundamental algorithmic and implementation details of this program together with the first numerical tests aiming at a parts-per-billion ( $1:10^9$ ) relative precision for the convergence of the variational energy, as well as comparison with benchmark perturbative relativistic corrections.

## II. SIXTEEN-COMPONENT VARIATIONAL METHODOLOGY

The explicit matrix form of the no-pair Dirac–Coulomb–Breit Hamiltonian for two particles is

$$G^{[4]} = -\frac{q_1 q_2}{r_{12}} \sigma_1^{[4]} \cdot \sigma_2^{[4]} = -\frac{q_1 q_2}{r_{12}} \begin{pmatrix} 1 & 0 & 0 & 0 \\ 0 & -1 & 2 & 0 \\ 0 & 2 & -1 & 0 \\ 0 & 0 & 0 & 1 \end{pmatrix}. \quad (9)$$

The  $\Lambda_{++}$  projector is constructed using the electronic states (also called positive-energy states, which is to be understood without the  $-2m_i c^2$  shift) of Eq. (6) by discarding the  $V$  and  $B$  particle–particle interaction terms.

We solve the  $H\Psi = E\Psi$  wave equation with the no-pair Dirac–Coulomb [Eq. (6) without the  $B$  block] and Dirac–Coulomb–Breit operators using a variational-like procedure, a two-particle restricted kinetic balance condition (*vide infra*), and explicitly correlated Gaussian basis functions.<sup>28–30</sup>

For a single particle, the (four-component) wave function can be partitioned to large (l, first two) and small (s, last two) components. A good basis representation is provided by the (restricted) kinetic balance condition<sup>31,32</sup>

$$\psi^s = \frac{\sigma^{[2]} \mathbf{p}}{2mc} \psi^l, \quad (10)$$

connecting the basis function of the small and large components. A block-wise direct product<sup>28,33–36</sup> is commonly used for the two(many)-particle problem, which is used also in Eq. (6). The corresponding block structure of the two-particle wave function, highlighting the large (l) and small (s) component blocks, is

$$\Psi(\mathbf{r}_1, \mathbf{r}_2) = \begin{pmatrix} \psi^{ll}(\mathbf{r}_1, \mathbf{r}_2) \\ \psi^{ls}(\mathbf{r}_1, \mathbf{r}_2) \\ \psi^{sl}(\mathbf{r}_1, \mathbf{r}_2) \\ \psi^{ss}(\mathbf{r}_1, \mathbf{r}_2) \end{pmatrix}. \quad (11)$$

We have implemented<sup>28–30</sup> the simplest two-particle generalization of the restricted kinetic balance, Eq. (10), in the two-particle basis set in the sense of a transformation or metric<sup>31</sup>

$$H_{\text{KB}} = X^\dagger H X, \quad (12)$$

$$X = \text{diag} \left( 1^{[4]}, \frac{(\sigma_2^{[4]} \mathbf{p}_2)}{2m_2 c}, \frac{(\sigma_1^{[4]} \mathbf{p}_1)}{2m_1 c}, \frac{(\sigma_1^{[4]} \mathbf{p}_1)(\sigma_2^{[4]} \mathbf{p}_2)}{4m_1 m_2 c^2} \right).$$

The transformed operators for the DC and the DCB problem are given in Refs. 29 and 30, respectively.

The 16-component wave function is written as a linear-combination of anti-symmetrized<sup>28</sup> spinor functions

$$\Psi(\mathbf{r}_1, \mathbf{r}_2) = \mathcal{A} \sum_{i=1}^{N_b} \sum_{\chi=1}^{16} c_{i\chi} \mathbf{d}_\chi \Theta_i(\mathbf{r}_1, \mathbf{r}_2; \mathbf{A}_i, \mathbf{s}_i), \quad (13)$$

where the spatial part is represented by explicitly correlated Gaussians functions (ECGs),

$$\Theta_i(\mathbf{r}_1, \mathbf{r}_2; \mathbf{A}_i, \mathbf{s}_i) = \exp \left[ -(\mathbf{r} - \mathbf{s}_i)^T (\mathbf{A}_i \otimes 1^{[3]}) (\mathbf{r} - \mathbf{s}_i) \right]. \quad (14)$$

For low  $Z$  systems, it is convenient to work in the  $LS$  coupling scheme. We optimized the ECG parameterization for the ground (and first excited state) by minimization of the ground (and first excited) totally symmetric, non-relativistic singlet energy. To be able to generate (relatively) large basis sets and to achieve good (parts-per-billion relative) convergence of not only the non-relativistic but also the DC(B) and DCB energies, the value of the energy functional, which we minimized, was incremented by a “penalty” term<sup>37,38</sup> that helped us to generate and optimize ECG basis functions that are less linearly dependent (and thus, well represented in double precision arithmetic). The same basis set was used to construct the non-interacting problem [Eq. (6)] without  $V$  and  $B$ , and the positive-energy projector. We used the cutting projection approach and checked some of the results with the complex scaling (CCR) projector.<sup>29</sup> The triplet contributions are estimated to be small (in perturbative relativistic computations, they appear at  $\alpha^4 E_h$  order<sup>3,11</sup>) and will be reported for the present framework in the future.

All computations have been carried out with an implementation of the outlined algorithm (see also Refs. 28–30) in the QUANTEN computer program, used in pre-Born–Oppenheimer, non-adiabatic, and (regularized) perturbative relativistic computations.<sup>18,19,21,39–41</sup> Throughout this work, Hartree atomic units are used and the speed of light is  $c = \alpha^{-1} a_0 E_h / \hbar$ , with  $\alpha^{-1} = 137.035999084$ .<sup>24</sup>

### III. COMPARISON OF THE PERTURBATIVE AND VARIATIONAL ENERGIES

The Dirac–Coulomb–Breit energies,  $E_{\text{DC}}^{++}(\text{B})$  and  $E_{\text{DCB}}^{++}$ , obtained from 16-component computations in this work are compared with perturbation theory results precisely evaluated with well-converged non-relativistic wave functions (taken from benchmark literature values).

The aim of this comparison is threefold.

- First, it is a numerical check, whether the 16-component approach can reproduce the established perturbative benchmarks with a parts-per-billion (ppb) precision, which corresponds to an energy resolution that is relevant for the current experiment–theory comparison.
- Second, it is about understanding the variational results. The 16-component variational computation includes a “resummation” of the perturbation series in  $Z\alpha$  for part of the problem. Identification of the relevant higher-order perturbative corrections provides an additional check for the implementation and for a good understanding of the developed variational relativistic methodology.
- Third, after completion of (a) and (b), we may estimate the importance of missing orders of the perturbative approach, since the 16-component computation provides all  $Z\alpha$  orders for the relevant part of the problem.

The present comparison provides a starting point for further developments aiming at the inclusion of missing “effects”, in particular, contributions from the  $H_\Delta$  term in Eq. (3), including pair correction, retardation, etc., as well as radiative corrections and motion of the nuclei.

#### A. Perturbative energy expressions

The leading,  $\alpha^2 E_h$ , order, often called “relativistic correction” to the non-relativistic energy, is obtained by a perturbative approach, either by the Foldy–Wouthuysen transformation<sup>42</sup> or by Sucher’s approach<sup>27</sup> (in some steps reminiscent of the later Douglas–Kroll transformation<sup>43</sup>) for the Dirac–Coulomb (DC) and Dirac–Coulomb–Breit (DCB) Hamiltonians. The energy up to second order in  $\alpha$  (in atomic units) reads as

$$E_{\text{DCB}}^{(2)} = E_{\text{nr}}^{(0)} + \alpha^2 \langle \Psi_{\text{nr}} | H_{\text{DCB}}^{(2)} | \Psi_{\text{nr}} \rangle = E_{\text{nr}}^{(0)} + \alpha^2 \langle H_{\text{DC}}^{(2)} + H_{\text{B}}^{(2)} \rangle_{\text{nr}}, \quad (15)$$

where  $\Psi_{\text{nr}}$  is the non-relativistic wave function and the  $\langle O \rangle_{\text{nr}} = \langle \Psi_{\text{nr}} | O | \Psi_{\text{nr}} \rangle$  short notation is introduced. Furthermore,

$$H_{\text{DC}}^{(2)} = -\frac{1}{8} \sum_{i=1}^2 (\nabla_i^2)^2 + \frac{\pi}{2} \sum_{i=1}^2 \sum_{A=1}^{N_{\text{nuc}}} Z_A \delta(\mathbf{r}_{iA}) - \pi \sum_{i=1}^2 \sum_{j>i}^2 \delta(\mathbf{r}_{ij}), \quad (16)$$

$$H_{\text{B}}^{(2)} = H_{\text{OO}} + 2\pi \sum_{i=1}^2 \sum_{j>i}^2 \delta(\mathbf{r}_{ij}), \quad (17)$$

with

$$H_{\text{OO}} = -\sum_{i=1}^2 \sum_{j>i}^2 \frac{1}{2r_{ij}} \left( \mathbf{p}_i \mathbf{p}_j + \frac{\mathbf{r}_{ij} (\mathbf{r}_{ij} \mathbf{p}_i) \mathbf{p}_j}{r_{ij}^2} \right). \quad (18)$$

To obtain precise correction values, regularization techniques<sup>41,44,45</sup> have been used to pinpoint the value of the

non-relativistic expectation value of the singular terms,  $\delta(\mathbf{r}_{iA})$ ,  $\delta(\mathbf{r}_{ij})$ , and  $(\nabla_i^2)^2$ .

Furthermore, we have noticed in earlier work<sup>29,30</sup> that the “non-radiative QED” corrections of the perturbative scheme are “visible” at the current ppb convergence level already for  $Z = 1$ . For this reason, we collect the relevant positive-energy corrections from Sucher’s work<sup>27</sup> in the following paragraphs. It is important to point out that these terms contribute to the  $\alpha^3 E_h$ -order perturbative corrections, but provide only part of the full correction at this order, which was first derived by Araki<sup>46</sup> and Sucher.<sup>27</sup>

### 1. Leading-order non-radiative QED corrections ( $\alpha^3 E_h$ ) to the no-pair energy

The two-Coulomb-photon exchange correction [p. 52, Eq. (3.99)<sup>27</sup>] is

$$\varepsilon_{CC}^{++} = -\left(\frac{\pi}{2} + \frac{5}{3}\right) \langle \delta(\mathbf{r}_{12}) \rangle_{\text{nr}} \approx -3.237 \langle \delta(\mathbf{r}_{12}) \rangle_{\text{nr}}. \quad (19)$$

The correction due to one (instantaneous) Breit photon exchange with resummation for the Coulomb ladder [p. 80, Eq. (5.64)<sup>27</sup>] is

$$\varepsilon_{CB}^{++} = 4\left(\frac{\pi}{2} + 1\right) \langle \delta(\mathbf{r}_{12}) \rangle_{\text{nr}} \approx 10.283 \langle \delta(\mathbf{r}_{12}) \rangle_{\text{nr}}. \quad (20)$$

We note that this correction corresponds to the unretarded (Breit) part of the transverse photon exchange (Ref. 27 uses the Coulomb gauge for this part), and the retardation correction to this term is evaluated separately (not considered in this work).

Finally, the correction due to the exchange of two (retarded) transverse photons according to Sucher [p. 93, Eq. (6.9b++)<sup>27</sup>] is

$$\varepsilon_{TT}^{++} = -\frac{\pi}{2} \langle \delta(\mathbf{r}_{12}) \rangle_{\text{nr}} \approx -1.571 \langle \delta(\mathbf{r}_{12}) \rangle_{\text{nr}}. \quad (21)$$

It is necessary to note that this term includes retardation effects, whereas our computation, does not. For this reason, the comparison of this term with the results of the variational DCB computation is only approximate and not fully quantitative.

In summary, the following  $\alpha^3 E_h$ -order perturbative energies will be used for comparison with the DC(B) and DCB 16-component computations,

$$\begin{aligned} E_{\text{DC(B)}}^{(3)} &= E_{\text{DCB}}^{(2)} + \alpha^3 (\varepsilon_{CC}^{++} + \varepsilon_{CB}^{++}) \\ &= E_{\text{DCB}}^{(2)} + \alpha^3 \left( \frac{3\pi}{2} + \frac{7}{3} \right) \langle \delta(\mathbf{r}_{12}) \rangle_{\text{nr}} \\ &\approx E_{\text{DCB}}^{(2)} + \alpha^3 7.046 \langle \delta(\mathbf{r}_{12}) \rangle_{\text{nr}}, \end{aligned} \quad (22)$$

where we note that  $E_{\text{DCB}}^{(2)} = E_{\text{DC(B)}}^{(2)}$  ( $\alpha^2 E_h$  order), and

$$\begin{aligned} E_{\text{DCB}}^{(3)} &\approx E_{\text{DCB}}^{(2)} + \alpha^3 (\varepsilon_{CC}^{++} + \varepsilon_{CB}^{++} + \varepsilon_{TT}^{++}) \\ &= E_{\text{DCB}}^{(2)} + \alpha^3 \left( \pi + \frac{7}{3} \right) \langle \delta(\mathbf{r}_{12}) \rangle_{\text{nr}} \\ &\approx E_{\text{DCB}}^{(2)} + \alpha^3 5.475 \langle \delta(\mathbf{r}_{12}) \rangle_{\text{nr}}, \end{aligned} \quad (23)$$

where, in particular, the single Breit and two-transverse corrections sum to

$$(\varepsilon_{CB}^{++} + \varepsilon_{TT}^{++}) \alpha^3 = \left( 4 + \frac{3\pi}{2} \right) \langle \delta(\mathbf{r}_{12}) \rangle_{\text{nr}} \alpha^3 \approx 8.712 \langle \delta(\mathbf{r}_{12}) \rangle_{\text{nr}} \alpha^3. \quad (24)$$

### B. Sixteen-component, variational results

Table I shows the 16-component, no-pair DC(B) and DCB energies computed in this work and their comparison with the  $\alpha^2 E_h$ - and  $\alpha^3 E_h$ -order perturbative results. The DC(B) and DCB energies reported in this table differ from our earlier work.<sup>28,30</sup> [The entries of the earlier reported tables for the Breit energies were in an error due to a programming mistake during the construction of the 16-component submatrices for pairs of ECG functions. It did not affect the DC (singlet) energies,<sup>29</sup> but affected the energies including the Breit interaction.<sup>30</sup>]

According to Table I, the deviation of the variational results from the  $\alpha^2 E_h$ -order energies is on the order of a few 10 nE<sub>h</sub>

**TABLE I.** The no-pair DC energy with first-order perturbative Breit correction,  $E_{\text{DC(B)}}^{++}$  in  $E_h$ , and the no-pair DCB energy,  $E_{\text{DCB}}^{++}$  in  $E_h$ . The differences from the  $\alpha^2 E_h$ - and  $\alpha^3 E_h$ -order perturbative energies,  $\delta^{(2)}$  and  $\delta^{(3)}$  in nE<sub>h</sub>, are also shown. Ground-state energies are reported, unless otherwise indicated. For up to  $Z = 2$  systems, all digits are significant, for Li<sup>+</sup> (Be<sup>2+</sup>) the last one (two) digits are estimated to be uncertain.

	$E_{\text{DC(B)}}^{++}$	$\delta_{\text{DC(B)}}^{(2)}$ <sup>a</sup>	$\delta_{\text{DC(B)}}^{(3)}$ <sup>a</sup>	$E_{\text{DCB}}^{++}$	$\delta_{\text{DC(B)}}^{(2)}$ <sup>a</sup>	$\delta_{\text{DC(B)}}^{(3)}$ <sup>a</sup>	$\delta_{\text{DCB}}^{(3)}$ <sup>a</sup>
H <sub>2</sub> <sup>b</sup>	-1.174 486 622	45	1	-1.174 486 635	32	-14	-4
H <sub>3</sub> <sup>b</sup>	-1.343 847 366	50	0	-1.343 847 381	35	-21	-4
HeH <sup>++b</sup>	-2.978 807 919	261	-16	-2.978 808 003	177	-100	-38
H <sup>-</sup>	-0.527 756 279	74	0	-0.527 756 281	5	-2	-1
He (2S) <sup>c</sup>	-2.146 082 355	13	-11	-2.146 082 363	5	-19	-13
He (1S) <sup>c</sup>	-2.903 828 032	279	-13	-2.903 828 121	190	-102	-37
Li <sup>+</sup>	-7.280 540 978	1300	-161	-7.280 541 443	835	-626	-301
Be <sup>2+</sup>	-13.657 788 729	3175	-995	-13.657 790 100	1804	-2366	-1436

<sup>a</sup>  $\delta_x^{(n)} = E_x^{++} - E_x^{(n)}$  with  $n = 2, 3$  and  $x$  stands for DC(B) or DCB. The expressions for  $E_x^{(n)}$  are listed in Eqs. (15)–(23), and the reference non-relativistic energy and integral values are collected in Table S13. We note that  $\delta_{\text{DC(B)}}^{(2)} = \delta_{\text{DCB}}^{(2)}$ .

<sup>b</sup> Electronic ground state for the nuclear–nuclear distance,  $R_{\text{eq}} = 1.4, 1.65,$  and  $1.46$  bohrs for H<sub>2</sub>, H<sub>3</sub><sup>+</sup>, and HeH<sup>+</sup>, respectively.

<sup>c</sup> 1S and 2S are used for 1 and 2<sup>1</sup>S<sub>0</sub>, respectively.



for  $Z = 1$ , whereas it is a few  $100 nE_h$  already for  $Z = 2$ . For a better comparison, it is necessary to include the  $\alpha^3 E_h$ -order (non-radiative QED) corrections to the perturbative energy. The relevant terms correspond to the two-Coulomb-photon,  $\varepsilon_{CC}^{++}$  [Eq. (19)], the Coulomb–Breit-photon,  $\varepsilon_{CB}^{++}$  [Eq. (20)], and the Breit–Breit-photon exchange corrections (for the positive-energy states). The last correction can be approximated with the (more complete) two-transverse photon exchange correction [Eq. (21)] (that is available from Ref. 27).

It was shown in Ref. 29 that inclusion of the  $\alpha^3 E_h$ -order, positive-energy Coulomb-ladder correction,  $\varepsilon_{CC}^{++}$ , in the perturbative energy closes the gap between the perturbative and variational energies for the lowest  $Z$  values. Most importantly, for the present work, inclusion of  $\varepsilon_{CC}^{++}$  and  $\varepsilon_{CB}^{++}$  reduces the deviation for the no-pair DC  $\langle B \rangle$  energy from the perturbative value to near  $0 nE_h$  for  $Z = 1$  and to  $\sim 10 nE_h$  for  $Z = 2$ .

Regarding the variational DCB energy, there is a non-negligible remainder between the variational,  $E_{DCB}^{++}$ , and perturbative energies,  $E_{DCB}^{(3)}$  [Eq. (23)], a few  $nE_h$  for  $Z = 1$  and a few tens of  $nE_h$  for  $Z = 2$ . This small, remaining deviation must be due to the fact that the 16-component computation reported in this work (a) does not include retardation, but (b) includes “effects” beyond  $\alpha^3 E_h$  order.

First of all,  $E_{DCB}^{++}$  includes the exchange of two and more (unretarded) Breit photons. To constrain the number of Breit photon exchanges, instead of the variational DCB computation, we can consider perturbative corrections due to the Breit interaction to the 16-component DC wave function. The first-order correction,

$$\langle B \rangle_{DC,n} = \langle \Psi_{DC,n}^{++} | X^\dagger B(1,2) X | \Psi_{DC,n}^{++} \rangle, \quad (25)$$

corresponds to a single Breit-photon exchange (in addition to the Coulomb ladder), while the first- and second-order perturbative corrections,<sup>30</sup>

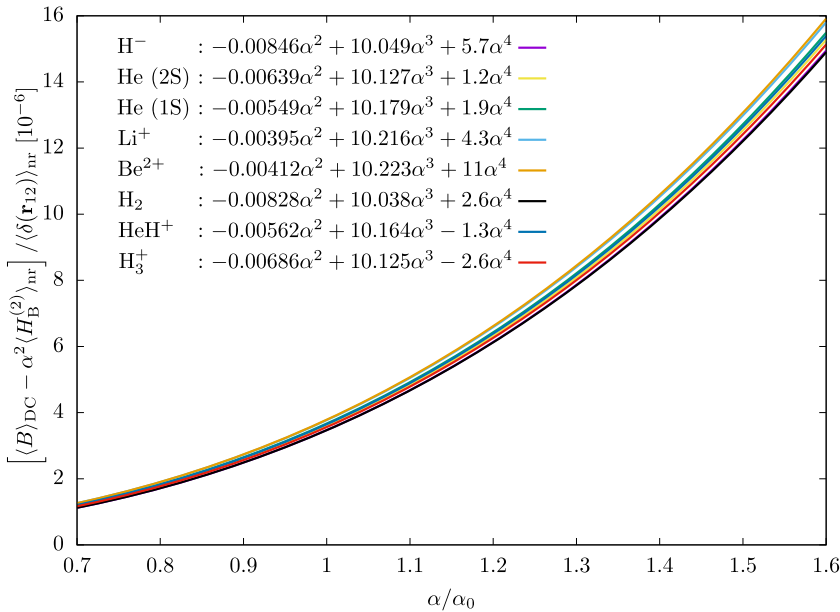


**FIG. 1.** Dependence of the Breit correction to the no-pair DC energy,  $\langle B \rangle_{DC}$ , on the  $\alpha$  coupling constant of the electromagnetic interaction. Hartree atomic units are used and  $\alpha_0$  labels  $1/137.035999084$ .<sup>24</sup> The data points, used for fitting the polynomials, were computed at the  $\alpha = 1/(\alpha_0 + n)$ ,  $n = -50, \dots, 50$  values. The  $\langle H_B^{(2)} \rangle_{nr}$  and  $\langle \delta(r_{12}) \rangle_{nr}$  values used to prepare this figure were calculated by “direct” integration (without regularization, Table S14).

$$\mathcal{P}_n^{(2)}\{B\} = \langle B \rangle_{DC,n} + \sum_{i \neq n} \frac{|\langle \Psi_{DC,i}^{++} | X^\dagger B(1,2) X | \Psi_{DC,n}^{++} \rangle|^2}{E_{DC,i}^{++} - E_{DC,n}^{++}}, \quad (26)$$

account for the effect of one- and two- (non-crossing) Breit photons.

We have numerically observed that  $E_{DC}^{++} + \mathcal{P}_n^{(2)}\{B\}$  reproduces  $E_{DCB}^{++}$  within a few  $nE_h$  (Tables S1–S8), which indicates that the energy is dominated by at most two Breit-photon exchanges in all systems studied in this work (up to  $Z = 4$ ).

In Table I, a relatively good agreement can be observed with the  $\alpha^3 E_h$ -order perturbative energies for  $Z = 1$  and 2, but we observe a larger deviation between the 16-component and perturbative results for  $Z = 3$  and 4, which indicates that inclusion of higher-order perturbative corrections would be necessary for a good (better) agreement. The non-radiative, singlet part of the  $\alpha^4 E_h$  correction (after canceling divergences) has been reported for both He (1S) and (2S) to be  $-11 nE_h$ ,<sup>3</sup> which is in an excellent agreement with the  $\delta_{DC(B)}^{(3)} = -11$  and  $-13 nE_h$  values in Table I. It is necessary to note that the comparison is only approximate, since the perturbative value contains contributions also from other “effects”. We note that  $\alpha^4 E_h$ -order computations have been reported in Ref. 47 for  $Z = 3$  and 4 ( $Li^+$  and  $Be^{2+}$ ) ground states, but we could not separate the non-radiative QED part from the given data.

To disentangle the contribution of the different  $\alpha$  orders, and hence, to have a more direct comparison with the perturbative results, we have studied the  $\alpha$  dependence of  $E_{DC}^{++}\langle B \rangle$  and  $E_{DCB}^{++}$ .

#### IV. FINE-STRUCTURE CONSTANT DEPENDENCE OF THE DIRAC-COULOMB-BREIT ENERGIES

The 16-component DC  $\langle B \rangle$  and DCB computations have been repeated with slightly different values used for the  $\alpha$  coupling constant of the electromagnetic interaction (Figs. 1 and 2). A quartic polynomial of  $\alpha$  was fitted to the computed series of  $E_{DC}^{++}\langle B \rangle(\alpha)$

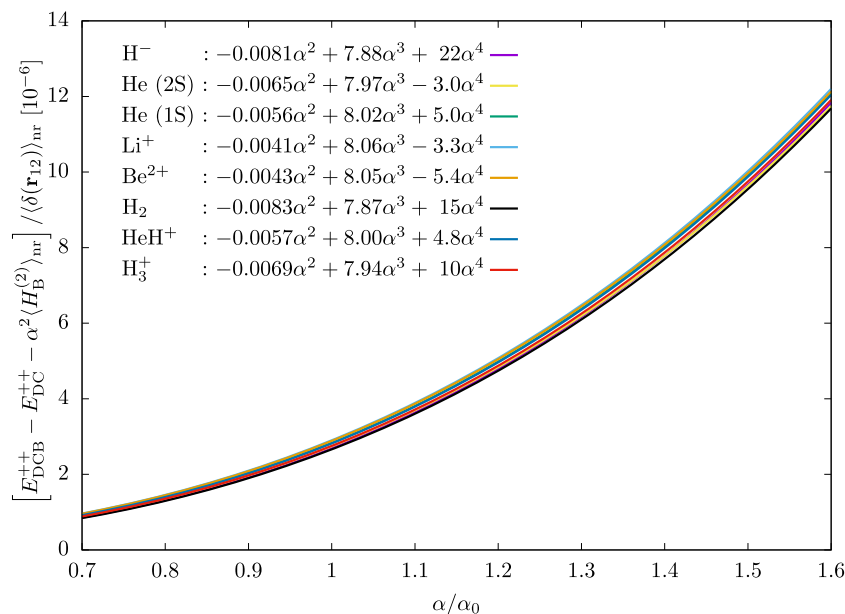


**FIG. 2.** Dependence of the no-pair DCB and DC energy difference on the  $\alpha$  coupling constant of the electromagnetic interaction. Hartree atomic units are used and  $\alpha_0$  labels 1/137.035999084.<sup>24</sup> The data points, used for fitting the polynomials, were computed at the  $\alpha = 1/(\alpha_0 + n)$ ,  $n = -50, \dots, 50$  values. The  $\langle H_B^{(2)} \rangle_{nr}$  and  $\langle \delta(r_{12}) \rangle_{nr}$  values used to prepare this figure were calculated by “direct” integration (without regularization, Table S14).

and  $E_{DCB}^{++}(\alpha)$  energies. The fitted coefficients of the  $\alpha$  polynomial can be directly compared with the perturbative corrections [Eqs. (15)–(23)], corresponding to the same order in  $\alpha$ . We call this approach the  $\alpha$ -scaling procedure (to the analysis of the 16-component results).

### A. Comparison of the $\alpha^3 E_h$ contributions

For a start, we note that the “ $\alpha$ -scaling” procedure was already successfully used for  $E_{DC}^{++}(\alpha)$  in Ref. 29 and resulted in two important observations. First, the  $\alpha^3 E_h$ -order term of the polynomial fitted to the  $E_{DC}^{++}(\alpha)$  points,

$$c_3 \alpha^3 = -3.26(1) \langle \delta(r_{12}) \rangle_{nr} \alpha^3, \quad (27)$$

is in an excellent agreement with Sucher’s positive-energy two-Coulomb-photon correction,  $\varepsilon_{CC}^{++}$  [Eq. (19)].<sup>27</sup>

Regarding the Breit term, a similar  $\alpha$ -scaling procedure resulted in contradictory observations in Ref. 30. It has turned out very recently that the contradictory observations were caused by a programming error in the construction of the DC(B) matrix. After noting and correcting this error, we have recomputed all reported values. The (singlet) DC energies<sup>28,30</sup> did not change, but the DC(B) and DCB energies<sup>28,30</sup> were affected. In the present work, we report the recomputed values and enlarged the basis sets for some of the systems, so it is possible now to achieve a (sub-)ppb-level of relative precision for the variational energy, including the Breit interaction.

First of all, both the  $E_{DC}^{++}(B)(\alpha)$  and  $E_{DCB}^{++}(\alpha)$  data points (corresponding to a series of slightly different  $\alpha$  values) can be fitted well

**TABLE II.**  $H^-(1S)$ : Convergence of the quartic  $\alpha$  polynomial coefficients (only significant digits shown) obtained by fitting to 16-component energy computations (see also Figs. 1 and 2 of this work and Fig. 3 of Ref. 29).  $N_b$  is the number of the ECG basis functions.

Fit:	$\frac{E_{DC}^{++} - \alpha^2 \langle H_B^{(2)} \rangle_{nr}}{\langle \delta(r_{12}) \rangle_{nr}}$ $c_2 \alpha^2 + c_3 \alpha^3 + c_4 \alpha^4$			$\frac{\langle B \rangle_{DC} - \alpha^2 \langle H_B^{(2)} \rangle_{nr}}{\langle \delta(r_{12}) \rangle_{nr}}$ $b_2 \alpha^2 + b_3 \alpha^3 + b_4 \alpha^4$			$\frac{E_{DCB}^{++} - E_{DC}^{++} - \alpha^2 \langle H_B^{(2)} \rangle_{nr}}{\langle \delta(r_{12}) \rangle_{nr}}$ $\tilde{b}_2 \alpha^2 + \tilde{b}_3 \alpha^3 + \tilde{b}_4 \alpha^4$		
	$c_2$	$c_3$	$c_4$	$b_2$	$b_3$	$b_4$	$\tilde{b}_2$	$\tilde{b}_3$	$\tilde{b}_4$
$N_b$									
300	0.003 4	−0.9	−115	−0.009 4	3.25	264	−0.005 1	1.72	228
400	0.008 53	−3.32	−19.7	−0.014 79	9.891	7.0	−0.013 59	7.534	31.9
500	0.000 01	−3.262	−23.1	−0.008 15	10.050	5.7	−0.008 113	7.878	21.5
600	−0.000 03	−3.26	−23.2	−0.008 46	10.049	5.7	−0.008 106	7.877	21.5
Sucher <sup>27 a</sup>		−3.237			10.283			8.712	
$\Delta^b$		−0.02			−0.234			−0.835	

<sup>a</sup>Reference 27:  $c_{3,Su58} = -(\frac{\pi}{2} + \frac{5}{3}) \approx -3.237$ ;  $b_{3,Su58} = 4(\frac{\pi}{2} + 1) \approx 10.283$ ; and  $\tilde{b}_{3,Su58} = 4 + \frac{3\pi}{2} \approx 8.712$ .

<sup>b</sup> $\Delta$ : deviation of the  $\alpha^3 E_h$ -order coefficient of this work and of Sucher’s analytic expressions.<sup>27</sup>

with a quartic polynomial of  $\alpha$ . For practical numerical reasons, we did not fit a general, fourth-order polynomial directly to  $E_{\text{DC}}^{++}(\text{B})(\alpha)$ , but we subtracted a good approximate value for the “large” leading-order ( $\alpha^2 E_{\text{h}}$ ) relativistic correction, i.e.,  $\langle B \rangle_{\text{DC}} - \alpha^2 \langle H_{\text{B}}^{(2)} \rangle_{\text{nr}}$ . We emphasize that the second term,  $\alpha^2 \langle H_{\text{B}}^{(2)} \rangle_{\text{nr}}$ , is a simple quadratic function of  $\alpha$ , since the  $\langle H_{\text{B}}^{(2)} \rangle_{\text{nr}}$  non-relativistic Breit correction is independent of  $\alpha$  in atomic units. To bring the several systems studied in this work to the same scale, we divided the difference by  $\langle \delta(\mathbf{r}_{12}) \rangle_{\text{nr}}$  (Fig. 1). For the generation of the figure and the  $\alpha$  polynomials, we used the  $\langle H_{\text{B}}^{(2)} \rangle_{\text{nr}}$  and  $\langle \delta(\mathbf{r}_{12}) \rangle_{\text{nr}}$  values evaluated “directly” (without regularization) in the (largest) spatial ECG basis set used for the 16-component computations (Table S14).

From a computational point of view, it was the most difficult to have a stable  $\alpha$  fit for  $\text{H}^-$  in double precision arithmetic (due to the smallness of  $\langle \delta(\mathbf{r}_{12}) \rangle_{\text{nr}}$ ), and for this reason, we show the convergence of the fitted coefficients with respect to the basis set size in Table II. For all other systems studied in this work, the fitting was numerically more robust.

The  $\alpha^3 E_{\text{h}}$ -order term in  $\langle B \rangle_{\text{DC}}(\alpha)$  (Fig. 1) is obtained from the cubic term of the fit,

$$b_3 \langle \delta(\mathbf{r}_{12}) \rangle_{\text{nr}} \alpha^3 = 10.1(2) \langle \delta(\mathbf{r}_{12}) \rangle_{\text{nr}} \alpha^3, \quad (28)$$

which is in an excellent agreement with the perturbative correction due to a single Breit photon in addition to the Coulomb ladder (for the positive-energy states),  $\epsilon_{\text{CB}}^{++} \alpha^3 + \epsilon_{\text{BB}}^{++} \alpha^3$  [Eq. (20)]. As to  $E_{\text{DCB}}^{++}(\alpha)$  (Fig. 2), we obtain the  $\alpha^3 E_{\text{h}}$ -order term as

$$\tilde{b}_3 \langle \delta(\mathbf{r}_{12}) \rangle_{\text{nr}} \alpha^3 = 8.98(25) \langle \delta(\mathbf{r}_{12}) \rangle_{\text{nr}} \alpha^3. \quad (29)$$

This value can be compared with the  $\alpha^3 E_{\text{h}}$ -order positive-energy correction of the one- and two-Breit photon exchanges (in addition to the Coulomb ladder),  $\epsilon_{\text{CB}}^{++} \alpha^3 + \epsilon_{\text{BB}}^{++} \alpha^3$ . Instead of the exchange of two Breit-photons, Sucher reported the exchange of two transverse (retarded) photons [Eq. (21)] and  $(\epsilon_{\text{CB}}^{++} + \epsilon_{\text{TT}}^{++}) \alpha^3$  [Eq. (24)], which is in a reasonable agreement with our numerical result for the non-retarded value [Eq. (29)], but the deviation is non-negligible.

We note that the excellent agreement of the variational and corresponding perturbative energies is observed only for the no-pair Hamiltonian, as defined in Secs. I and II with the projector of the non-interacting electrons in the field of the fixed nuclei. Regarding the “bare” (unprojected) DC(B) operators, or the positive-energy projected DC(B) operator with different projectors (free-particle or modified  $Z$  values), none of them resulted in a good numerical

agreement with the well-established perturbative expressions of the “non-relativistic” QED operators.

After all, this numerical observation is not so surprising, if we consider the emergence of the no-pair Dirac–Coulomb–Breit operator (with unretarded electron–electron interaction) from the Bethe–Salpeter QED wave equation following the calculation of Salpeter<sup>26</sup> and Sucher.<sup>27</sup> In this context, a historical note about the Breit equation<sup>48</sup> (eigenvalue equation for DCB without positive-energy projection, “bare” DCB) may also be relevant as it was pointed out by Douglas and Kroll.<sup>43</sup> When Breit used his equation in a perturbative procedure, he had to omit an “extra” term to have good agreement with experiment. This erroneous term was shown by Brown and Ravenhall<sup>49</sup> to correspond to a contribution from negative-energy intermediate states, which, according to Dirac’s hole theory, had to be discarded.

## B. Leading-order, $\alpha^2 E_{\text{h}}$ , relativistic corrections without regularization

The  $\alpha^2 E_{\text{h}}$ -order term obtained from the DC computation with an ECG spatial basis set (optimized for the non-relativistic energy to a ppb relative precision) reproduced the regularized, perturbative benchmark DC energy to a ppb precision.<sup>29</sup> At the same time, the error of the perturbative DC energy by direct integration in the ECG basis was an order of magnitude larger.<sup>29,41</sup>

In the present work, we observe a similar improvement for the  $\alpha^2 E_{\text{h}}$ -order contribution obtained from the  $\alpha$  polynomial fit to the variational  $E_{\text{DC}}^{++}(\text{B})$  and  $E_{\text{DCB}}^{++}$  energies in comparison with the perturbative DCB energy (expectation value of the Breit–Pauli Hamiltonian).

This behavior is highlighted in Table III (see also Tables S9–S12), in which the  $\alpha^2 E_{\text{h}}$  energies obtained from the  $\alpha$ -scaling approach are compared with perturbative values obtained by direct or regularized integration. The improvement can be explained by the fact that the “singular” operators of the Breit–Pauli Hamiltonian are implicitly included in the 16-component Dirac–Coulomb–Breit operator, for which the eigenvalue equation is solved variationally, i.e., the linear combination coefficients of the kinetically balanced ECG basis set are relaxed in a variational manner. Thereby, the relativistic corrections are not *a posteriori* computed as expectation values, but they are automatically included in the variational energy computation.

To generate Figs. 1 and 2 and the fitted  $\alpha$  polynomials, we used the “own basis” value (direct evaluation) of  $\langle \delta(\mathbf{r}_{12}) \rangle_{\text{nr}}$  and  $\langle H_{\text{B}}^{(2)} \rangle_{\text{nr}}$

**TABLE III.** Leading-order ( $\alpha^2 E_{\text{h}}$ ) relativistic corrections from the variational procedure without regularization:  $\alpha^2 E_{\text{DCB}}^{(2)}$ : leading-order DCB energy obtained by direct evaluation;  $O_{\alpha^2}[E_{\text{DC(B)}}^{++}]$  and  $O_{\alpha^2}[E_{\text{DCB}}^{++}]$ :  $\alpha^2 E_{\text{h}}$ -order fitted terms to the DC(B) and DCB energies. Deviations are listed, in  $nE_{\text{h}}$ , from the regularized reference value,  $\alpha^2 E_{\text{DCB,rg}}^{(2)}$  (Table S13).

	$\text{H}^-$	He (2S)	He (1S)	$\text{Li}^+$	$\text{Be}^{2+}$	$\text{H}_2$	$\text{H}_3^+$	$\text{HeH}^+$
$\alpha^2 E_{\text{DCB}}^{(2)} - \alpha^2 E_{\text{DCB,rg}}^{(2)}$	1.7	21	−18	296	766	9.0	9.3	55
$O_{\alpha^2}[E_{\text{DC(B)}}^{++}] - \alpha^2 E_{\text{DCB,rg}}^{(2)}$	0.4	0.5	4.0	13	31	1.1	1.6	1.1
$O_{\alpha^2}[E_{\text{DCB}}^{++}] - \alpha^2 E_{\text{DCB,rg}}^{(2)}$	0.5	0.4	3.2	13	19	1.1	1.6	0.6

**TABLE IV.** Relative importance of the  $\alpha^4 E_h$ - and  $\alpha^3 E_h$ - order contributions to the no-pair Dirac–Coulomb, Breit, and Dirac–Coulomb–Breit energies. The energy contribution is to be understood as  $(a_3 \alpha^3 + a_4 \alpha^4) \langle \delta(r_{12}) \rangle_{nr}$ .

	$E_{DC}^{++}(\alpha)$ Reference 29			$\langle B \rangle_{DC}(\alpha)$ Figure. 1			$E_{DC}^{++}(B)(\alpha)$			$E_{DCB}^{++}(\alpha)$		
	$a_3$	$a_4$	$\frac{a_4 \alpha}{a_3}$ (%)	$a_3$	$a_4$	$\frac{a_4 \alpha}{a_3}$ (%)	$a_3$	$a_4$	$\frac{a_4 \alpha}{a_3}$ (%)	$a_3$	$a_4$	$\frac{a_4 \alpha}{a_3}$ (%)
H <sub>2</sub>	-3.27	-6.59	1	10.04	2.6	0	6.77	-3.99	0	4.60	8.41	1
H <sub>3</sub> <sup>+</sup>	-3.27	-5.27	1	10.13	-2.6	0	6.86	-7.87	-1	4.67	4.73	1
HeH <sup>+</sup>	-3.27	-44.5	10	10.16	-1.3	0	6.89	-45.8	-5	4.73	-39.7	-6
H <sup>-</sup>	-3.26	-23.6	5	10.05	5.7	0	6.79	-17.9	-2	4.62	-1.6	0
He (2S)	-3.26	-470	105	10.13	1.2	0	6.87	-469	-50	4.71	-473	-73
He (1S)	-3.27	-40.3	9	10.18	1.9	0	6.91	-38.4	-4	4.75	-35.3	-5
Li <sup>+</sup>	-3.26	-109	24	10.22	4.3	0	6.96	-105	-11	4.80	-112	-17
Be <sup>2+</sup>	-3.25	-241	54	10.22	11	1	6.97	-230	-24	4.80	-246	-37

(Table S14). Then, using the fitted coefficients and these two integral values, we obtained the leading-order ( $\alpha^2 E_h$ ) relativistic correction (Table III) “carried by” the 16-component DC(B) energy.

All in all, the  $\alpha^2 E_h$ -order contribution to the DCB energy is an order of magnitude more accurate than the perturbative correction by direct integration in comparison with the benchmark, regularized value.

### C. Higher-order ( $\alpha^4 E_h$ ) relativistic corrections

The  $\alpha^4 E_h$ -order contribution to the DC(B) energy increases with an increasing  $Z$  value. Based on the  $\alpha$ -scaling plots, we can observe that the ratio of the  $\alpha^4 E_h$  to  $\alpha^3 E_h$  contribution is 5% and 10% for  $Z = 2$  (ground state) for the DCB and the DC energy, respectively, but this ratio is already 40% and 50% for  $Z = 4$  (ground state). Hence, “resummation” in  $Z\alpha$  of the perturbative series appears to be important for the total energies,  $E_{DC}^{++}$ ,  $E_{DC}^{++}(B)$ ,  $E_{DCB}^{++}$  (Table IV) already for intermediate  $Z$  values.

Regarding the Breit term, the first-order Breit correction to the Coulomb interaction has important contribution at orders  $\alpha^2 E_h$  and  $\alpha^3 E_h$ , but the  $\alpha^4 E_h$ -order contribution to the no-pair energy remains relatively small (for the systems studied in this work).

The only outlier from these observations is He (2S). The large  $a_4 \alpha / a_3$  ratio for the DC (and similarly for the DC(B) and DCB) energy can be understood by noting that the  $\langle \delta(r_{12}) \rangle_{nr}$  factor (Table S13), and thus, the third-order correction, is very small. The third-order DC energy contribution [known to be proportional to  $\langle \delta(r_{12}) \rangle_{nr}$  based on perturbation theory, Eq. (19)] is -11 and -135  $E_h$  for He (2S) and (1S), respectively, whereas the fourth-order terms are comparable, -12  $E_h$  for both He (2S) and (1S).

## V. SUMMARY AND CONCLUSION

Variational and perturbative relativistic energies are computed and compared for two-electron atoms and molecules with low nuclear charge numbers. In general, good agreement of the two approaches is observed. Remaining deviations can be attributed to higher-order relativistic, also called non-radiative quantum electrodynamics (QED), corrections of the perturbative approach that are automatically included in the variational solution of the no-pair

Dirac–Coulomb–Breit (DCB) equation to all orders of the  $\alpha$  fine-structure constant. The analysis of the polynomial  $\alpha$  dependence of the DCB energy makes it possible to determine the leading-order relativistic correction to the non-relativistic energy to high precision without regularization. Contributions from the Breit–Pauli Hamiltonian, for which expectation values converge slowly due the singular terms, are implicitly included in the variational procedure. The  $\alpha$  dependence of the no-pair DCB energy shows that the higher-order ( $\alpha^4 E_h$ ) non-radiative QED correction is 5% of the leading-order ( $\alpha^3 E_h$ ) non-radiative QED correction for  $Z = 2$  (He), but it is 40% already for  $Z = 4$  (Be<sup>2+</sup>), which indicates that resummation provided by the variational procedure is important already for intermediate nuclear charge numbers.

## SUPPLEMENTARY MATERIAL

The [supplementary material](#) contains (1) convergence tables, (2) leading-order corrections from  $\alpha$  scaling, and (3) non-relativistic energies and perturbative corrections.

## ACKNOWLEDGMENTS

Financial support of the European Research Council through a starting grant (No. 851421) is gratefully acknowledged. D.F. thanks a doctoral scholarship from the ÚNKP-21-3 New National Excellence Program of the Ministry for Innovation and Technology from the source of the National Research, Development and Innovation Fund (Grant No. ÚNKP-21-3-II-ELTE-41).

## AUTHOR DECLARATIONS

### Conflict of Interest

The authors have no conflicts to disclose.

### Author Contributions

**Dávid Ferenc:** Formal analysis (equal); Funding acquisition (supporting); Methodology (equal); Software (equal); Validation (equal);

Writing – original draft (equal); Writing – review & editing (equal). **Péter Jeszenszki**: Data curation (equal); Methodology (equal); Software (equal); Visualization (equal); Writing – review & editing (equal). **Edit Mátyus**: Conceptualization (lead); Data curation (equal); Formal analysis (lead); Funding acquisition (lead); Investigation (lead); Methodology (equal); Project administration (lead); Resources (lead); Software (equal); Supervision (lead); Validation (lead); Visualization (equal); Writing – original draft (lead); Writing – review & editing (equal).

#### DATA AVAILABILITY

The data that support the findings of this study are available within the article and its [supplementary material](#).

#### REFERENCES

- <sup>1</sup>H. A. Bethe and E. E. Salpeter, *Quantum Mechanics of One- and Two-Electron Atoms* (Springer, Berlin, 1957).
- <sup>2</sup>T. Kinoshita and M. Nio, *Phys. Rev. D* **53**, 4909 (1996).
- <sup>3</sup>K. Pachucki, *Phys. Rev. A* **74**, 022512 (2006).
- <sup>4</sup>G. Paz, *Mod. Phys. Lett. A* **30**, 1550128 (2015).
- <sup>5</sup>V. Patkóš, V. A. Yerokhin, and K. Pachucki, *Phys. Rev. A* **100**, 042510 (2019).
- <sup>6</sup>M. Haidar, Z.-X. Zhong, V. I. Korobov, and J.-P. Karr, *Phys. Rev. A* **101**, 022501 (2020).
- <sup>7</sup>S. Alighanbari, G. S. Giri, F. L. Constantin, V. I. Korobov, and S. Schiller, *Nature* **581**, 152 (2020).
- <sup>8</sup>V. I. Korobov, J.-P. Karr, M. Haidar, and Z.-X. Zhong, *Phys. Rev. A* **102**, 022804 (2020).
- <sup>9</sup>V. Patkóš, V. A. Yerokhin, and K. Pachucki, *Phys. Rev. A* **103**, 042809 (2021).
- <sup>10</sup>B. M. Henson, J. A. Ross, K. F. Thomas, C. N. Kuhn, D. K. Shin, S. S. Hodgman, Y.-H. Zhang, L.-Y. Tang, G. W. F. Drake, A. T. Bondy, A. G. Truscott, and K. G. H. Baldwin, *Science* **376**, 199 (2022).
- <sup>11</sup>M. Puchalski, J. Komasa, and K. Pachucki, *Phys. Rev. A* **95**, 052506 (2017).
- <sup>12</sup>K. Pachucki, V. Patkóš, and V. A. Yerokhin, *Phys. Rev. A* **95**, 062510 (2017).
- <sup>13</sup>A. Wienczek, K. Pachucki, M. Puchalski, V. Patkóš, and V. A. Yerokhin, *Phys. Rev. A* **99**, 052505 (2019).
- <sup>14</sup>V. A. Yerokhin, V. Patkóš, M. Puchalski, and K. Pachucki, *Phys. Rev. A* **102**, 012807 (2020).
- <sup>15</sup>S. P. Goldman and G. W. F. Drake, *Phys. Rev. Lett.* **68**, 1683 (1992).
- <sup>16</sup>G. Clausen, P. Jansen, S. Scheidegger, J. A. Agner, H. Schmutz, and F. Merkt, *Phys. Rev. Lett.* **127**, 093001 (2021).
- <sup>17</sup>S. Bubin and L. Adamowicz, *Phys. Rev. Lett.* **118**, 043001 (2017).
- <sup>18</sup>D. Ferenc and E. Mátyus, *Phys. Rev. A* **100**, 020501(R) (2019).
- <sup>19</sup>D. Ferenc and E. Mátyus, *J. Chem. Phys.* **151**, 094101 (2019).
- <sup>20</sup>M. Puchalski, J. Komasa, P. Czachorowski, and K. Pachucki, *Phys. Rev. Lett.* **122**, 103003 (2019).
- <sup>21</sup>D. Ferenc, V. I. Korobov, and E. Mátyus, *Phys. Rev. Lett.* **125**, 213001 (2020).
- <sup>22</sup>D. Wehrli, A. Spyszkiewicz-Kaczmarek, M. Puchalski, and K. Pachucki, *Phys. Rev. Lett.* **127**, 263001 (2021).
- <sup>23</sup>Z.-D. Bai, V. I. Korobov, Z.-C. Yan, T.-Y. Shi, and Z.-X. Zhong, *Phys. Rev. Lett.* **128**, 183001 (2022).
- <sup>24</sup>E. Tiesinga, P. J. Mohr, D. B. Newell, and B. N. Taylor, *Rev. Mod. Phys.* **93**, 025010 (2021).
- <sup>25</sup>E. E. Salpeter and H. A. Bethe, *Phys. Rev.* **84**, 1232 (1951).
- <sup>26</sup>E. E. Salpeter, *Phys. Rev.* **87**, 328 (1952).
- <sup>27</sup>J. Sucher, *Energy Levels of the Two-Electron Atom, to Order  $\alpha^3$  Rydberg* (Columbia University, 1958).
- <sup>28</sup>P. Jeszenszki, D. Ferenc, and E. Mátyus, *J. Chem. Phys.* **154**, 224110 (2021).
- <sup>29</sup>P. Jeszenszki, D. Ferenc, and E. Mátyus, *J. Chem. Phys.* **156**, 084111 (2022).
- <sup>30</sup>D. Ferenc, P. Jeszenszki, and E. Mátyus, *J. Chem. Phys.* **156**, 084110 (2022).
- <sup>31</sup>W. Kutzelnigg, *Int. J. Quantum Chem.* **25**, 107 (1984).
- <sup>32</sup>W. Liu, *Mol. Phys.* **108**, 1679 (2010).
- <sup>33</sup>D. S. Tracy and R. P. Singh, *Stat. Neerl.* **26**, 143 (1972).
- <sup>34</sup>Z. Li, S. Shao, and W. Liu, *J. Chem. Phys.* **136**, 144117 (2012).
- <sup>35</sup>S. Shao, Z. Li, and W. Liu, in *Handbook of Relativistic Quantum Chemistry*, edited by W. Liu (Springer, Berlin, Heidelberg, 2017), pp. 481–496.
- <sup>36</sup>B. Simmen, E. Mátyus, and M. Reiher, *J. Phys. B: At., Mol. Opt. Phys.* **48**, 245004 (2015).
- <sup>37</sup>W.-C. Tung, M. Pavanello, and L. Adamowicz, *J. Chem. Phys.* **133**, 124106 (2010).
- <sup>38</sup>S. Bubin and L. Adamowicz, *J. Chem. Phys.* **152**, 204102 (2020).
- <sup>39</sup>E. Mátyus, *Mol. Phys.* **117**, 590 (2019).
- <sup>40</sup>E. Mátyus and D. Ferenc, “Vibronic mass computation for the  $EF-GK-H^1\Sigma_g^+$  manifold of molecular hydrogen”, *Mol. Phys.* (published online, 2022).
- <sup>41</sup>P. Jeszenszki, R. T. Ireland, D. Ferenc, and E. Mátyus, *Int. J. Quantum Chem.* **122**, e26819 (2022).
- <sup>42</sup>K. G. Dyall and K. Faegri, Jr., *Introduction to Relativistic Quantum Chemistry* (Oxford University Press, New York, 2007).
- <sup>43</sup>M. Douglas and N. M. Kroll, *Ann. Phys.* **82**, 89 (1974).
- <sup>44</sup>R. J. Drachman, *J. Phys. B: At., Mol. Opt. Phys.* **14**, 2733 (1981).
- <sup>45</sup>K. Pachucki, W. Cencek, and J. Komasa, *J. Chem. Phys.* **122**, 184101 (2005).
- <sup>46</sup>H. Araki, *Prog. Theor. Phys.* **17**, 619 (1957).
- <sup>47</sup>V. A. Yerokhin and K. Pachucki, *Phys. Rev. A* **81**, 022507 (2010).
- <sup>48</sup>G. Breit, *Phys. Rev.* **34**, 553 (1929).
- <sup>49</sup>G. E. Brown and D. G. Ravenhall, *Proc. R. Soc. London, Ser. A* **208**, 552 (1951).

# On the Breit interaction in an explicitly correlated variational Dirac–Coulomb framework

Cite as: J. Chem. Phys. 156, 084110 (2022); doi: 10.1063/5.0075097

Submitted: 13 October 2021 • Accepted: 5 January 2022 •

Published Online: 23 February 2022



View Online



Export Citation



CrossMark

Dávid Ferenc,  Péter Jeszenszki,  and Edit Mátyus<sup>a)</sup> 

## AFFILIATIONS

ELTE, Eötvös Loránd University, Institute of Chemistry, Pázmány Péter sétány 1/A, Budapest, H-1117, Hungary

<sup>a)</sup> Author to whom correspondence should be addressed: [edit.matyus@ttk.elte.hu](mailto:edit.matyus@ttk.elte.hu)

## ABSTRACT

The Breit interaction is implemented in the no-pair variational Dirac–Coulomb (DC) framework using an explicitly correlated Gaussian basis reported in the previous paper [P. Jeszenszki, D. Ferenc, and E. Mátyus, J. Chem. Phys. 156, 084111 (2022)]. Both a perturbative and a fully variational inclusion of the Breit term are considered. The no-pair DC plus perturbative Breit and the no-pair DC–Breit energies are compared with perturbation theory results including the Breit–Pauli Hamiltonian and leading-order non-radiative quantum electrodynamics corrections for low  $Z$  values. Possible reasons for the observed deviations are discussed.

Published under an exclusive license by AIP Publishing. <https://doi.org/10.1063/5.0075097>

## I. INTRODUCTION

Relativistic effects play an essential role in the quantitative understanding of high-resolution atomic and molecular spectra. For atoms and molecules with a low  $Z$  nuclear charge number, the non-relativistic wave function provides an adequate zeroth-order approximation, and relativistic effects can be treated as perturbation. The most common route for the theoretical determination of energy levels of low- $Z$  atoms and molecules is provided by the non-relativistic quantum electrodynamics (nrQED) framework in which the leading-order relativistic corrections are the well-known Breit–Pauli Hamiltonian terms. The nrQED approach gives excellent agreement with high-resolution spectroscopy measurements for several atomic and molecular systems.<sup>1–4</sup> At the same time, the derivation of the correction operators is tedious in which one has to deal with (cancellation of) divergent terms at higher orders.<sup>4–6</sup> For larger nuclear charge numbers, this approach becomes unsuitable to reach high theoretical accuracy.

An alternative approach is provided by the variational solution of the Dirac–Coulomb (DC) or Dirac–Coulomb–Breit (DCB) equation, which also bears several difficulties. The main complication is caused by the coupling of the positive and negative energy states by the electron–electron interaction known as continuum dissolution or the Brown–Ravenhall disease (BR).<sup>7</sup> The solution to this problem was derived from quantum electrodynamics (QED). Sucher proposed the projection of the Dirac operator to the positive energy

( $E_+$ ) subspace of some non-interacting reference problem.<sup>8,9</sup> This approach, during which the electron–positron pair contribution is eliminated from the Hamiltonian, is referred to as the “no-virtual-pair” approximation, and it is commonly used in modern relativistic quantum chemistry computations.

There are various options for choosing an (effective) one-particle reference problem to define a positive-energy projector. Mittleman argued for a Hartree–Fock (HF) based projector<sup>10</sup> and methods with a single reference determinant are widely used in computations.<sup>11–13</sup> Liu and co-workers pointed out that if the projector is defined with the orbitals of the HF computation, then the positive-energy projected Hamiltonian (and the QED pair corrections to it<sup>14</sup>) can be naturally written in a second-quantized form<sup>15,16</sup> using the same orbitals as a basis. More recently, Almoukhalalati *et al.* considered the choice of a “good” projector for computations including electron correlation.<sup>17</sup> Li and co-workers<sup>18</sup> noted that combination of the orbital-based formalism and explicit correlation (“F12 methods”) is non-trivial, and proposed a “dual basis” approach.

Over the past two decades, methods using explicitly correlated basis functions have been developed and used for solving the DC equation of (helium-like) atoms.<sup>19–22</sup> Explicitly correlated, non-separable basis functions represent a departure from the single-particle picture, and the construction of an  $E_+$  projection operator is not immediately obvious in this framework. For atomic computations, Bylicki, Pestka, and Karwowski proposed to use the complex

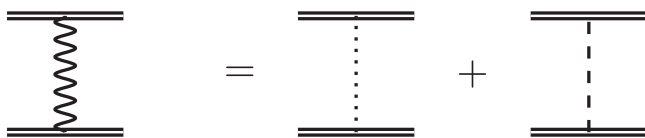


**FIG. 1.** The single-photon exchange diagram in the Coulomb gauge can be separated into an instantaneous Coulomb and a retarded transverse photon exchange contribution.

coordinate rotation (CCR) technique to separate the  $E_+$  subspace of the non-interacting problem in the explicitly correlated basis and employed this projection technique to compute the no-pair Dirac–Coulomb energy for the ground state of helium-like ions (atom) with Hylleraas-type basis functions.<sup>21,23,24</sup>

We have adapted this projector for solving the Dirac–Coulomb and Dirac–Coulomb–Breit models using explicitly correlated Gaussian (ECG) basis sets for atoms and also for molecules. A short account of this work was first given in Ref. 25. The Dirac–Coulomb implementation is reported in detail in Ref. 26 (henceforth, Paper I), and the present work reports theoretical, algorithmic, and numerical details regarding the implementation of the Breit term in the explicitly correlated DC framework of Paper I. No-pair energies computed in this work are reported for the helium atom and for small and light molecules converged to high precision and the results are compared with energies computed in the nrQED framework.

Throughout this work, Hartree atomic units are used and the speed of light is  $c = \alpha^{-1} a_0 E_h / \hbar$  with  $\alpha^{-1} = 137.035\,999\,084$ .<sup>27</sup>

## A. The Breit interaction

The classical Lagrangian and Hamiltonian dynamics of moving charges was studied by Darwin<sup>28</sup> to order  $\mathcal{O}(1/c^2)$ . Breit identified the velocity operator as  $c\boldsymbol{\alpha}$  in relativistic quantum mechanics<sup>29</sup> and

replaced the classical velocity in Darwin’s expression to arrive at the quantum mechanical form for the interaction of two moving charges.<sup>30</sup> A more consistent approach is provided by the derivation of an effective potential from QED scattering amplitudes.<sup>31</sup> The tree-level diagram in the  $S$  matrix of an electron scattering process is the one-photon exchange diagram (Fig. 1). The  $S$  matrix is related to the shift in the energy levels by the Gell-Mann–Low–Sucher formula<sup>32,33</sup> that can be used to calculate the effect of the interaction with the radiation field on the energy levels. The external field of the nuclei can be taken into account exactly within the Furry picture.<sup>34</sup>

The Coulomb gauge, for which the vector potential has a vanishing divergence, is a natural and convenient choice for describing the molecular domain, since, in addition to the instantaneous Coulomb potential, there are only transverse photons present (Fig. 1). The photon propagator in the Coulomb gauge is

$$D_{00}^C(\mathbf{r}_{12}) = \frac{1}{4\pi r_{12}},$$

$$D_{0i}^C = D_{i0}^C = 0, \quad (1)$$

$$D_{ij}^C(\mathbf{r}_{12}, \omega/c) = \int \frac{d^3\mathbf{k}}{(2\pi)^3} \frac{e^{i\mathbf{k}\cdot\mathbf{r}_{12}}}{\omega^2/c^2 - \mathbf{k}^2 + i\epsilon} \left( \delta_{ij} - \frac{k_i k_j}{\mathbf{k}^2} \right),$$

and the corresponding one-photon exchange interaction is (for example, p. 72 of Ref. 35)

$$I^C(\omega/c) = q_1 q_2 \left[ \frac{1}{r_{12}} - \boldsymbol{\alpha}_1 \cdot \boldsymbol{\alpha}_2 \frac{\cos(\omega r_{12}/c)}{r_{12}} + \left\{ (\boldsymbol{\alpha}_1 \cdot \nabla_1) (\boldsymbol{\alpha}_2 \cdot \nabla_2) \frac{\cos(\omega r_{12}/c) - 1}{\omega^2 r_{12}/c^2} \right\} \right], \quad (2)$$

where  $\omega$  is the frequency of the exchanged photon and the gradient operators act only within the braces. We may expand Eq. (2) in terms of  $\omega r_{12}/c$  (for example, p. 253 of Ref. 36),

$$\begin{aligned} \frac{1}{q_1 q_2} I^C(\omega/c) &= \frac{1}{r_{12}} - \frac{\boldsymbol{\alpha}_1 \cdot \boldsymbol{\alpha}_2}{r_{12}} \left[ 1 - \frac{1}{2} \left( \frac{\omega r_{12}}{c} \right)^2 + \dots \right] \\ &+ \left\{ (\boldsymbol{\alpha}_1 \cdot \nabla_1) (\boldsymbol{\alpha}_2 \cdot \nabla_2) \left[ -\frac{1}{2} \left( \frac{\omega r_{12}}{c} \right)^2 + \frac{1}{4!} \left( \frac{\omega r_{12}}{c} \right)^4 - \dots \right] \frac{c^2}{\omega^2 r_{12}} \right\} \\ &= \frac{1}{r_{12}} - \boldsymbol{\alpha}_1 \cdot \boldsymbol{\alpha}_2 \left( \frac{1}{r_{12}} + \mathcal{O}(c^{-2}) \right) + \left\{ (\boldsymbol{\alpha}_1 \cdot \nabla_1) (\boldsymbol{\alpha}_2 \cdot \nabla_2) \left( -\frac{1}{2} r_{12} \right) + \mathcal{O}(c^{-2}) \right\} \\ &= \frac{1}{r_{12}} - \frac{\boldsymbol{\alpha}_1 \cdot \boldsymbol{\alpha}_2}{r_{12}} - \frac{1}{2} \{ (\boldsymbol{\alpha}_1 \cdot \nabla_1) (\boldsymbol{\alpha}_2 \cdot \nabla_2) r_{12} \} + \mathcal{O}(c^{-2}). \end{aligned} \quad (3)$$

If we neglect the  $\mathcal{O}(c^{-2})$  terms, which is often called the zero-frequency or non-retardation approximation, we obtain the sum of the Coulomb and the Breit terms,

$$I^C(0) = \frac{q_1 q_2}{r_{12}} + B(1, 2), \quad (4)$$

$$B(1, 2) = -q_1 q_2 \left[ \frac{\boldsymbol{\alpha}_1 \cdot \boldsymbol{\alpha}_2}{r_{12}} + \frac{1}{2} \{ (\boldsymbol{\alpha}_1 \cdot \nabla_1) (\boldsymbol{\alpha}_2 \cdot \nabla_2) r_{12} \} \right]. \quad (5)$$

If the differentiation is carried out (similarly to the earlier notation, the differential operators act only within the braces), we obtain the more common form for the Breit operator,

$$B(1, 2) = -\frac{q_1 q_2}{2} \left[ \frac{\boldsymbol{\alpha}_1 \cdot \boldsymbol{\alpha}_2}{r_{12}} + \frac{(\boldsymbol{\alpha}_1 \cdot \mathbf{r}_{12})(\boldsymbol{\alpha}_2 \cdot \mathbf{r}_{12})}{r_{12}^3} \right]. \quad (6)$$

It is interesting to note that both the Coulomb and Breit interactions arise from the “zero-frequency approximation” of the exact

one-photon exchange, and this feature suggests that they should be treated on an equal footing, e.g., in a variational procedure.

There has been a long discussion in the literature about the Breit term whether it can be included in a variational procedure or a perturbative treatment should be preferred. It was argued by Bethe and Salpeter in 1957<sup>37</sup> that the Breit interaction should only be used in first-order perturbation theory, since the coupling with negative-energy intermediate states would yield second- and higher-order corrections that are too large. Later, Sucher in 1980<sup>9</sup> pointed out that if the operators are defined with positive-energy projection, then the inclusion of the Breit interaction on the same footing as the Coulomb interaction in a variational scheme is appropriate. The discussion continues also in the numerical quantum chemistry literature based on formal as well as practical considerations and observations.<sup>38–42</sup>

In the first order of perturbation theory, the Breit interaction corresponds to a single transverse photon exchange, meanwhile at higher orders, it describes the consecutive exchange of several transverse photons. If it is included in a variational computation, it accounts for a sum (“ladder”) of all-, i.e., one-, two-, three-, etc., non-retarded transverse photon exchanges.

## II. THE NO-PAIR DIRAC-COULOMB-BREIT EQUATION

In Paper I,<sup>26</sup> we have described in detail a (quasi-)variational procedure for the solution of the no-pair Dirac equation. The no-pair Dirac operator for  $N$  spin-1/2 particles is

$$H(1, 2) = \Lambda_+ \begin{pmatrix} V1^{[4]} + U1^{[4]} & c\sigma_2^{[4]} \cdot \mathbf{p}_2 \\ c\sigma_2^{[4]} \cdot \mathbf{p}_2 & V1^{[4]} + (U - 2m_2c^2)1^{[4]} \\ c\sigma_1^{[4]} \cdot \mathbf{p}_1 & B \\ B & c\sigma_1^{[4]} \cdot \mathbf{p}_1 \end{pmatrix}$$

with  $m_{12} = m_1 + m_2$ ,  $\mathbf{p}_i = -i(\frac{\partial}{\partial r_{ix}}, \frac{\partial}{\partial r_{iy}}, \frac{\partial}{\partial r_{iz}})$  ( $i = 1, 2$ ),  $\sigma_1^{[4]} = (\sigma_x \otimes 1^{[2]}, \sigma_y \otimes 1^{[2]}, \sigma_z \otimes 1^{[2]})$ ,  $\sigma_2^{[4]} = (1^{[2]} \otimes \sigma_x, 1^{[2]} \otimes \sigma_y, 1^{[2]} \otimes \sigma_z)$ , where  $\sigma_x$ ,  $\sigma_y$ , and  $\sigma_z$  are the  $2 \times 2$  Pauli matrices, and  $U = \sum_{i=1}^N \sum_{a=1}^{N_{\text{nuc}}} q_i Q_a / |\mathbf{r}_i - \mathbf{R}_a|$  is the external Coulomb potential of the nuclei. We note that a  $-2m_i c^2$  shift is introduced for both particles in the operator in Eq. (10) in comparison with Eq. (7), which is a commonly used energy-scale shift and serves here practical, computational purposes.

The  $\Lambda_+$  projection operator is constructed from the positive-energy solutions of the reference problem, which is chosen to be the external-field Dirac equation without electron–electron interaction,

$$\sum_{i=1}^N (h_i^{[4N]} + u_i 1^{[4N]}) \phi_k = \epsilon_k \phi_k, \quad \Lambda_+ = \sum_{k \in \{E_+\}} |\phi_k\rangle \langle \phi_k|. \quad (11)$$

The projected Hamiltonian is bounded from below, and it has well-defined bound states, free of the BR problem. Technical details

$$H = \sum_{i=1}^N \Lambda_+ (h_i^{[4N]} + u_i 1^{[4N]}) \Lambda_+ + \sum_{i=1}^N \sum_{j>i}^N \Lambda_+ v_{ij} \Lambda_+, \quad (7)$$

where  $h_i^{[4N]} = 1^{[4]}(1) \otimes \dots \otimes h_i^{[4]}(i) \otimes \dots \otimes 1^{[4]}(N)$  with  $h_i^{[4]} = c\boldsymbol{\alpha}^{[4]} \cdot \mathbf{p} + \beta^{[4]} m_i c^2$  is the free, one-particle Dirac operator,  $u_i = \sum_{a=1}^{N_{\text{nuc}}} q_i Q_a / |\mathbf{r}_i - \mathbf{R}_a|$  is the Coulomb interaction energy with the fixed, point-like nuclei,  $\Lambda_+$  is the  $E_+$ -projection operator, and  $v_{ij}$  is either the Coulomb or the Coulomb–Breit interaction. We use the block-wise direct product, also called the Tracy–Singh product,<sup>18</sup> for convenience.

The many-particle Coulomb and Breit operators have the following form:

$$v_{ij}^{[4N]} = \frac{1}{r_{ij}} 1^{[4N]} + \sum_{k=1}^3 \sum_{l=1}^3 (b_{ij})_{kl} \left[ 1^{[4]}(1) \otimes \dots \otimes (\boldsymbol{\alpha}(i))_k \otimes \dots \otimes (\boldsymbol{\alpha}(j))_l \otimes \dots \otimes 1^{[4]}(N) \right], \quad (8)$$

$$(b_{ij})_{kl} = -\frac{1}{2} \left( \frac{\delta_{kl}}{r_{ij}} + \frac{(\mathbf{r}_{ij})_k (\mathbf{r}_{ij})_l}{r_{ij}^3} \right). \quad (9)$$

The explicit matrix form of the no-pair Dirac–Coulomb–Breit Hamiltonian for two particles is

$$V1^{[4]} + (U - 2m_1c^2)1^{[4]} \begin{pmatrix} c\sigma_1^{[4]} \cdot \mathbf{p}_1 & B \\ B & c\sigma_1^{[4]} \cdot \mathbf{p}_1 \\ c\sigma_2^{[4]} \cdot \mathbf{p}_2 & B \\ B & c\sigma_2^{[4]} \cdot \mathbf{p}_2 \\ c\sigma_1^{[4]} \cdot \mathbf{p}_1 & B \\ B & c\sigma_1^{[4]} \cdot \mathbf{p}_1 \\ c\sigma_2^{[4]} \cdot \mathbf{p}_2 & B \\ B & c\sigma_2^{[4]} \cdot \mathbf{p}_2 \\ V1^{[4]} + (U - 2m_{12}c^2)1^{[4]} \end{pmatrix} \Lambda_+ \quad (10)$$

regarding the projection techniques are explained in Sec. III A and in Paper I.<sup>26</sup>

In Eq. (10), the  $B$  blocks along the anti-diagonal of the matrix represent the Breit potential,

$$B = G - \frac{q_1 q_2}{2} \sum_{i=1}^3 \sum_{j=1}^3 \sigma_{1i}^{[4]} \sigma_{2j}^{[4]} \{ \nabla_{1i} \cdot \nabla_{2j} r_{12} \}. \quad (12)$$

The first term of  $B$  is called the Gaunt interaction, which reads for two particles as

$$G = -\frac{q_1 q_2}{r_{12}} \boldsymbol{\sigma}_1^{[4]} \cdot \boldsymbol{\sigma}_2^{[4]} = -\frac{q_1 q_2}{r_{12}} \begin{pmatrix} 1 & 0 & 0 & 0 \\ 0 & -1 & 2 & 0 \\ 0 & 2 & -1 & 0 \\ 0 & 0 & 0 & 1 \end{pmatrix}. \quad (13)$$



The wave function is expanded over a set of sixteen-component ( $2^N$  for  $N$  particles) basis spinors  $(\mathbf{d}_\chi)_j = \delta_{\chi j}$  with  $N_b$  explicitly correlated Gaussian functions,

$$\Psi(\mathbf{r}_1, \mathbf{r}_2) = \mathcal{A} \sum_{i=1}^{N_b} \sum_{\chi=1}^{16} c_{i\chi} \mathbf{d}_\chi \Theta_i(\mathbf{r}_1, \mathbf{r}_2; \mathbf{A}_i, \mathbf{s}_i), \quad (14)$$

$$\Theta_i(\mathbf{r}_1, \mathbf{r}_2; \mathbf{A}_i, \mathbf{s}_i) = \exp\left[-(\mathbf{r} - \mathbf{s}_i)^T (\mathbf{A}_i \otimes \mathbf{1}^{[3]}) (\mathbf{r} - \mathbf{s}_i)\right], \quad (15)$$

where  $\mathbf{r} = (\mathbf{r}_1, \mathbf{r}_2)^T$  are the coordinates of the particles (electrons),  $\mathbf{s}_i \in \mathbb{R}^6$  and  $\mathbf{A}_i \in \mathbb{R}^{2 \times 2}$  are parameters of the basis functions, and  $\mathcal{A}$  is the anti-symmetrization operator providing the proper permutational symmetry for the relativistic two-fermion wave function.<sup>26</sup>

### A. Kinetic balance

The large and small components of a relativistic four-component basis function must satisfy the relation

$$\psi^s = \frac{\boldsymbol{\sigma}^{[2]} \mathbf{p}}{2mc} \psi^l \quad (16)$$

following from the kinetic balance condition as discussed in Refs. 43 and 44. We use here the simplest two-particle generalization of the one-electron kinetic balance condition and implement the two-electron kinetic balance condition in the sense of a transformation or metric,<sup>43</sup>

$$H_{\text{KB}} = X^\dagger H X, \quad X = \text{diag} \left( \mathbf{1}^{[4]}, \frac{(\boldsymbol{\sigma}_2^{[4]} \mathbf{p}_2)}{2m_2 c}, \frac{(\boldsymbol{\sigma}_1^{[4]} \mathbf{p}_1)}{2m_1 c}, \frac{(\boldsymbol{\sigma}_1^{[4]} \mathbf{p}_1)(\boldsymbol{\sigma}_2^{[4]} \mathbf{p}_2)}{4m_1 m_2 c^2} \right). \quad (17)$$

The two-particle wave function, which corresponds to the block-wise direct product form of the two-electron operators, has the following structure:

$$\Psi(\mathbf{r}_1, \mathbf{r}_2) = \begin{pmatrix} \psi^{ll}(\mathbf{r}_1, \mathbf{r}_2) \\ \psi^{ls}(\mathbf{r}_1, \mathbf{r}_2) \\ \psi^{sl}(\mathbf{r}_1, \mathbf{r}_2) \\ \psi^{ss}(\mathbf{r}_1, \mathbf{r}_2) \end{pmatrix}. \quad (18)$$

The transformed Hamiltonian in Eq. (17) is obtained by using the relationship  $(\boldsymbol{\sigma}^{[4]} \cdot \mathbf{p}) (\boldsymbol{\sigma}^{[4]} \cdot \mathbf{p}) = \mathbf{p}^2 \mathbf{1}^{[4]}$  as

$$H_{\text{KB}} = \begin{pmatrix} D_1 & \frac{\mathbf{p}_2^2}{2m_2} \mathbf{1}^{[4]} & \frac{\mathbf{p}_1^2}{2m_1} \mathbf{1}^{[4]} & B_1 \\ \frac{\mathbf{p}_2^2}{2m_2} \mathbf{1}^{[4]} & D_2 & B_2 & \frac{\mathbf{p}_1^2 \mathbf{p}_2^2}{8c^2 m_1 m_2^2} \mathbf{1}^{[4]} \\ \frac{\mathbf{p}_1^2}{2m_1} \mathbf{1}^{[4]} & B_3 & D_3 & \frac{\mathbf{p}_1^2 \mathbf{p}_2^2}{8c^2 m_1^2 m_2} \mathbf{1}^{[4]} \\ B_4 & \frac{\mathbf{p}_2^2 \mathbf{p}_1^2}{8c^2 m_1 m_2^2} \mathbf{1}^{[4]} & \frac{\mathbf{p}_2^2 \mathbf{p}_1^2}{8c^2 m_1^2 m_2} \mathbf{1}^{[4]} & D_4 \end{pmatrix}, \quad (19)$$

where the diagonal elements are

$$\begin{aligned} D_1 &= V_1^{[4]} + U_1^{[4]}, \\ D_2 &= \frac{(\boldsymbol{\sigma}_2^{[4]} \mathbf{p}_2)(V_1^{[4]} + U_1^{[4]})(\boldsymbol{\sigma}_2^{[4]} \mathbf{p}_2)}{4m_2^2 c^2} - \frac{\mathbf{p}_2^2}{2m_2} \mathbf{1}^{[4]}, \\ D_3 &= \frac{(\boldsymbol{\sigma}_1^{[4]} \mathbf{p}_1)(V_1^{[4]} + U_1^{[4]})(\boldsymbol{\sigma}_1^{[4]} \mathbf{p}_1)}{4m_1^2 c^2} - \frac{\mathbf{p}_1^2}{2m_1} \mathbf{1}^{[4]}, \\ D_4 &= \frac{(\boldsymbol{\sigma}_1^{[4]} \mathbf{p}_1)(\boldsymbol{\sigma}_2^{[4]} \mathbf{p}_2)(V_1^{[4]} + U_1^{[4]})(\boldsymbol{\sigma}_1^{[4]} \mathbf{p}_1)(\boldsymbol{\sigma}_2^{[4]} \mathbf{p}_2)}{16m_1^2 m_2^2 c^4} \\ &\quad - \frac{m_{12}}{8m_1^2 m_2^2 c^2} \mathbf{p}_1^2 \mathbf{p}_2^2 \mathbf{1}^{[4]}. \end{aligned} \quad (20)$$

The anti-diagonal blocks, which carry the magnetic interactions, take the following form in the transformed Hamiltonian,

$$\begin{aligned} B_1 &= \frac{B(\boldsymbol{\sigma}_1^{[4]} \mathbf{p}_1)(\boldsymbol{\sigma}_2^{[4]} \mathbf{p}_2)}{4c^2 m_1 m_2}, \\ B_2 &= \frac{(\boldsymbol{\sigma}_2^{[4]} \mathbf{p}_2)B(\boldsymbol{\sigma}_1^{[4]} \mathbf{p}_1)}{4c^2 m_1 m_2}, \\ B_3 &= \frac{(\boldsymbol{\sigma}_1^{[4]} \mathbf{p}_1)B(\boldsymbol{\sigma}_2^{[4]} \mathbf{p}_2)}{4c^2 m_1 m_2}, \\ B_4 &= \frac{(\boldsymbol{\sigma}_2^{[4]} \mathbf{p}_2)(\boldsymbol{\sigma}_1^{[4]} \mathbf{p}_1)B}{4c^2 m_1 m_2}. \end{aligned} \quad (21)$$

The overlap matrix corresponding to the transformed Hamiltonian, Eq. (17), is

$$S_{\text{KB}} = X^\dagger X = \text{diag} \left( \mathbf{1}^{[4]}, \frac{\mathbf{p}_2^2}{4c^2 m_2^2} \mathbf{1}^{[4]}, \frac{\mathbf{p}_1^2}{4c^2 m_1^2} \mathbf{1}^{[4]}, \frac{\mathbf{p}_1^2 \mathbf{p}_2^2}{16c^4 m_1^2 m_2^2} \mathbf{1}^{[4]} \right). \quad (22)$$

### B. Complex-coordinate rotation for positive-energy projection

The complex-coordinate rotation transformation (CCR), used to define the positive energy projector (Sec. III B 1 of Paper I<sup>26</sup>), scales the coordinates by a complex phase factor

$$x_i \rightarrow x_i e^{i\theta}, \quad (23)$$

$$\frac{\partial}{\partial x_i} \rightarrow \frac{\partial}{\partial x_i} e^{-i\theta}, \quad (24)$$

$$\frac{1}{r_{ij}} \rightarrow \frac{1}{r_{ij}} e^{-i\theta}, \quad (25)$$

and this transformation introduces only a simple complex scaling factor,  $e^{-i\theta}$ ,

$$B^{\text{CCR}}(\theta) = B e^{-i\theta}, \quad (26)$$

in front of the Breit operator and also in front of the Breit matrix elements. In short, the Breit term is dilatation analytic under CCR.

With this single modification in the calculation of the Breit matrix elements, the CCR positive-energy projector for the Dirac–Coulomb part of the problem is constructed and used as described in Paper I<sup>26</sup> (Sec. III B 1).

### C. Variational solution of the no-pair Dirac–Coulomb–Breit equation

We compute variational, no-pair Dirac–Coulomb (DC) and Dirac–Coulomb–Breit (DCB) energies and wave functions by direct diagonalization of the matrix representation of the projected Hamiltonian,

$$\Lambda_+^L \mathbf{H}_{\text{KB}} \Lambda_+^R \mathbf{c}_i = E_i \Lambda_+^L \mathbf{S}_{\text{KB}} \Lambda_+^R \mathbf{c}_i, \quad (27)$$

where  $\mathbf{H}_{\text{KB}}$  and  $\mathbf{S}_{\text{KB}}$  denote the matrix representation of the corresponding operators and  $\mathbf{c}_i$  and  $E_i$  label the expansion coefficient vector and the energy eigenvalue, respectively. It is important to note that the construction of the CCR projector (Secs. III A and III B of Paper I<sup>26</sup>) assumes the solution of a non-Hermitian eigenvalue problem, so we build  $\Lambda_+^L$  and  $\Lambda_+^R$  from the left- and right-handed eigenvectors. For the cutting (or punching) projector (Secs. III B 2 and III B 3 of Paper I<sup>26</sup>), the non-interacting problem is Hermitian, hence we may label  $\Lambda_+ = \Lambda_+^R$ , and then  $\Lambda_+^L = \Lambda_+^\dagger$ .

The Hamiltonian matrix is constructed either for the DC or the DCB operator and provides the positive-energy projected or no-pair DC or DCB energies,  $E_{\text{DC}}^{\text{proj}}$  or  $E_{\text{DCB}}^{\text{proj}}$ , respectively. The non-linear parameters in Eq. (15) were optimized by minimizing the non-relativistic energy. This construction is expected to perform well for low- $Z$  systems. We have carried out test computations for further optimization of the non-linear parameters by minimization of the no-pair DCB energy (for the He, H<sub>2</sub>, HeH<sup>+</sup>, and H<sub>3</sub><sup>+</sup> systems studied in this paper), but no significant improvement was observed.

Further test computations were carried out for the H<sub>2</sub> molecule regarding the contribution of non-relativistic basis functions corresponding to triplet spin states that can mix with the singlet ground state functions ( $LS$  coupling scheme), but the contribution of the triplet basis sector was negligible (<1 nE<sub>h</sub> in the energy). Further details will be reported in future work. Regarding the helium atom, the non-relativistic ground state was computed with choosing  $s = 0$  in the basis functions, Eq. (15). In test computations, this basis set was extended with  $s \neq 0$  functions, but their effect on the DC(B) energy was found to be very small.

All computations were carried out using double precision arithmetic (unless indicated otherwise) using the QUANTEN computer program. QUANTEN is an in-house developed program written using the Fortran90 programming language and contains several analytic ECG integrals, for which recent applications have been reported in Refs. 3 and 45–51.

### D. Perturbative inclusion of the Breit interaction

We have considered not only the variational but also the perturbative inclusion of the Breit interaction in the no-pair Dirac–Coulomb framework. The Rayleigh–Schrödinger perturbative corrections up to the first and second orders take the following form:

$$\langle B \rangle_n = \left\langle \Psi_{\text{DC},n}^{\text{proj}} \left| X^\dagger B(1,2) X \right| \Psi_{\text{DC},n}^{\text{proj}} \right\rangle, \quad (28)$$

$$\mathcal{P}_n^{(2)} \{B\} = \langle B \rangle_n + \sum_{i \neq n} \frac{\left| \left\langle \Psi_{\text{DC},i}^{\text{proj}} \left| X^\dagger B(1,2) X \right| \Psi_{\text{DC},n}^{\text{proj}} \right\rangle \right|^2}{E_{\text{DC},i}^{\text{proj}} - E_{\text{DC},n}^{\text{proj}}}, \quad (29)$$

where  $\Psi_{\text{DC},n}^{(\text{proj})}$  and  $E_{\text{DC},n}^{(\text{proj})}$  are the  $n$ th no-pair DC wave function and energy. Since we calculate perturbative corrections for the no-pair DC problem, Brown–Ravenhall or negative-energy states do not enter the expressions.

Equations (28) and (29) are valid if a Hermitian positive-energy projector (cutting, punching, or determinant projector of Paper I<sup>26</sup>) is used to set up the no-pair DC matrix. During the present work, the reported perturbative results were computed with the cutting projector. The implementation was generalized also for the CCR projector and the tested numerical results agree to all reported digits with the cutting projector values.

The first and second-order perturbative corrections were evaluated for comparison with the no-pair DCB energy, and they (and their good numerical agreement with the variational no-pair DCB energy) are shown in the [supplementary material](#).

## III. NUMERICAL RESULTS AND DISCUSSION

### A. Discussion of the projection techniques

Currently, the most rigorous positive-energy projection approach for methods using explicitly correlated basis functions is based on the complex-coordinate rotation (CCR) technique proposed by Bylicki, Pestka, and Karwowski<sup>23</sup> for the solution of the Dirac–Coulomb problem of atoms. In Paper I,<sup>26</sup> we have generalized this CCR projection approach to molecular computations with the DC Hamiltonian. We adapt the molecular approach to the DCB problem in the present work and report observations in the following paragraphs. The DC(B) Hamiltonian is dilatation analytic for atoms, but not for molecules with fixed nuclei.

We have considered two approaches for molecular computations. The first approach is a non-dilatation analytic (“nda”) approach, which directly accounts for the non-dilatation analytic property of the Hamiltonian due to the Coulomb interaction with the external charges (nuclei).

The second possible approach for molecules relies on a naïve dilatation use of the CCR technique as if the Hamiltonian was dilatation analytic (“da”), i.e., the positions of the fixed nuclei are complex scaled together with the active electronic degrees of freedom. According to Moiseyev,<sup>52</sup> this dilatation analytic approach is also appropriate, but for accurate results, a perturbative correction for the “back rotation” of the nuclear positions is necessary. In Paper I,<sup>26</sup> this perturbative correction was found to be small for the imaginary part of the DC energy (that is 0 for a bound state) and negligibly small for the real part of the DC energy for sufficiently small CCR angles. Any  $\theta$  CCR angle is appropriate for constructing the projector that is sufficiently large for a clear identification of the positive-energy branch of the non-interacting energies (Fig. 1 of Paper I<sup>26</sup>), but not too large for the finite basis set, i.e., the finite basis set error, which increases with  $\theta$ , remains small. The advantage of the “da-CCR” approach is that it does not require the evaluation of complex-valued Coulomb integrals that contain the complex incomplete gamma function, which can be evaluated only with 12-digit precision in our current implementation.

For low- $Z$  systems, studied in the present work, we have found a simple energy cutting projection technique (“cutting”) also appropriate for a (sub-)parts-per-billion (ppb) computation of the DC energy. The cutting approach is technically and numerically the simplest one, and it was always performed as a first test computation.

An overview and comparison of the numerical performance of the projection techniques for the no-pair DCB energy is provided in [Tables I and II](#) for the example of the helium atom and the hydrogen molecule.

[Table I](#) presents the angle dependence of the CCR-projected DCB energies for the ground state of the helium atom and shows also the result of the simple “cutting” projector. For all  $\theta \in [10^{-8}, 10^{-2}]$ , the positive-energy non-interacting states could be separated, and the finite basis error for this interval was sufficiently small, hence the real parts of the DCB energy show a difference less than 1 in  $10^9$  (sub-ppb). The double precision arithmetic is sufficient for achieving ppb precision, but we have performed the computation using quadruple precision to be able to see the details of the numerical behavior of the different projection techniques.

[Table II](#) shows the numerical behavior of the different projection techniques for the example of the ground state of the  $H_2$  molecule. We observe a similar behavior for the nda-CCR and cutting projectors to the da-CCR and cutting projectors for the helium atom ([Table I](#)), respectively. Regarding the da-CCR projector, we used it without the perturbative correction for the back rotation of the nuclei, similarly to the DC problem in [Paper I](#).<sup>26</sup> For sufficiently small CCR angles, the real part of the da-CCR energy is in an excellent numerical agreement with the nda-CCR energy, since the real part for the perturbative back rotation scales with  $\sim \theta^2$  ([Paper I](#)).<sup>26</sup> At the same time, we see a substantial difference in the imaginary part of the da-CCR and nda-CCR energies. This difference can be understood by noticing that the perturbative back rotation for the imaginary part scales with  $\sim \theta$ .

**TABLE I.** Testing the positive-energy projection techniques for the Dirac–Coulomb–Breit energy of the ground state of the helium atom. The CCR angle dependence of the dilatation-analytic energy,  $E_{\text{DCB}}^{\text{da}}$ , is shown in comparison with the energy cutting approach,  $E_{\text{DCB}}^{\text{cutting}}$ . Quadruple precision arithmetic and  $N_b = 300$  ECG functions were used. All energies are in  $E_h$  units.

proj = da( $\theta$ )		
$\theta$	$\text{Re}(E_{\text{DCB}}^{\text{proj}})$	$\text{Im}(E_{\text{DCB}}^{\text{proj}})$
0.000 000 01	−2.903 828 970 048	$7.35 \cdot 10^{-15}$
0.000 000 1	−2.903 828 970 048	$7.35 \cdot 10^{-14}$
0.000 001	−2.903 828 970 048	$7.35 \cdot 10^{-13}$
0.000 01	−2.903 828 970 048	$7.35 \cdot 10^{-12}$
0.000 1	−2.903 828 970 048	$7.35 \cdot 10^{-11}$
0.001	−2.903 828 970 048	$7.35 \cdot 10^{-10}$
0.01	−2.903 828 970 071	$7.35 \cdot 10^{-9}$
0.1	−2.903 828 971 461	$7.47 \cdot 10^{-8}$
0.2	−2.903 828 969 543	$1.50 \cdot 10^{-7}$
0.5	−2.903 829 132 724	$2.56 \cdot 10^{-8}$
proj = cutting		
$E_{\text{DCB}}^{\text{proj}}$	−2.903 828 970 048	0

**TABLE II.** Testing the positive-energy projection techniques for the Dirac–Coulomb–Breit energy of the ground-state of the  $H_2$  molecule with fixed protons ( $R_{\text{pp}} = 1.4$  bohr). The dilatation analytic ( $E_{\text{DCB}}^{\text{da}}$ ), the non-dilatation analytic ( $E_{\text{DCB}}^{\text{nda}}$ ), and the energy cutting ( $E_{\text{DCB}}^{\text{cutting}}$ ) techniques are compared. Quadruple precision arithmetic and  $N_b = 700$  ECG functions were used. All energies are in  $E_h$  units.

$\theta$	$\text{Re}(E_{\text{DCB}}^{\text{proj}})$	$\text{Im}(E_{\text{DCB}}^{\text{proj}})$
	proj = nda( $\theta$ )	
0.000 000 1	−1.174 486 710 978	$5.55 \cdot 10^{-14}$
0.000 001	−1.174 486 710 978	$5.55 \cdot 10^{-13}$
0.000 01	−1.174 486 710 982	$5.55 \cdot 10^{-12}$
0.000 1	−1.174 486 711 397	$5.54 \cdot 10^{-11}$
0.001	−1.174 486 753 444	$4.63 \cdot 10^{-10}$
	proj = da( $\theta$ )	
0.000 000 1	−1.174 486 710 978	$7.14 \cdot 10^{-8}$
0.000 001	−1.174 486 710 978	$7.14 \cdot 10^{-7}$
0.000 01	−1.174 486 710 979	$7.14 \cdot 10^{-6}$
0.000 1	−1.174 486 711 043	$7.14 \cdot 10^{-5}$
0.001	−1.174 486 717 484	$7.14 \cdot 10^{-4}$
proj = cutting		
$E_{\text{DCB}}^{\text{proj}}$	−1.174 486 710 978	0

All in all, the tested positive-energy projection techniques provide the (real part of the) bound-state energy for the example systems (He and  $H_2$ ) with a sub-ppb difference.

## B. Discussion of the numerical results

The energies computed with the inclusion of the Breit correction, [Eq. \(12\)](#), are summarized in [Table III](#). The table collects the results obtained with the largest basis sets for the helium atom and for the ground electronic state of the  $H_2$ ,  $\text{HeH}^+$ , and  $H_3^+$  molecular systems near their equilibrium geometry.

**TABLE III.** The no-pair DC energy with first-order perturbative Breit correction,  $E_{\text{DC}}^{\text{proj}} + \langle B \rangle_{\text{DC}}$  in  $E_h$ , and the no-pair DCB energy,  $E_{\text{DCB}}^{\text{proj}}$  in  $E_h$ . The differences,  $\delta$  and  $\delta'$  in  $nE_h$ , with respect to the non-relativistic energy with the leading-order ( $\alpha^2$ ) perturbative relativistic energy,  $E_{\text{DCB}}^{(2)}$ , [Eq. \(30\)](#), are also shown. The estimated convergence error appears in the last digit.

	$E_{\text{DC}}^{\text{proj}} + \langle B \rangle_{\text{DC}}$	$\{\delta\}^a$	$E_{\text{DCB}}^{\text{proj}}$	$\{\delta'\}^b$
$H_2^c$	−1.174 486 665	{2}	−1.174 486 721	{−54}
$H_3^+c$	−1.343 847 416	{0}	−1.343 847 498	{−82}
$\text{HeH}^+c$	−2.978 808 200	{−20}	−2.978 808 77	{−590}
He ( $1^1S_0$ )	−2.903 828 333	{−22}	−2.903 829 02	{−710}
He ( $2^1S_0$ )	−2.146 082 379	{−11}	−2.146 082 424	{−56}

$$^a \delta = E_{\text{DC}}^{\text{proj}} + \langle B \rangle_{\text{DC}} - E_{\text{DCB}}^{(2)}$$

$$^b \delta' = E_{\text{DCB}}^{\text{proj}} - E_{\text{DCB}}^{(2)}$$

<sup>c</sup>Electronic ground state for nuclear–nuclear distances  $R_{\text{eq}} = 1.4, 1.65,$  and  $1.46$  bohr for  $H_2, H_3^+,$  and  $\text{HeH}^+,$  respectively.

Regarding the convergence details, we consider the no-pair DC plus first-order perturbative Breit energy,  $E_{\text{DC}}^{\text{proj}} + \langle B \rangle_{\text{DC}}$ , converged better than 5–10  $nE_h$  for all systems studied. The no-pair DCB energy,  $E_{\text{DCB}}^{\text{proj}}$ , converged much slower, our largest basis results are probably converged only within 10  $nE_h$  for  $\text{H}_2$ ,  $\text{H}_3^+$ , and  $\text{He } 2^1\text{S}_0$ , but only on the order of  $\sim 100 nE_h$  for  $\text{He } 1^1\text{S}_0$  and  $\text{HeH}^+$ . In Table III, one more digit is shown beyond the converged values and detailed convergence tables are provided in the [supplementary material](#). The parameterization for all basis sets used in these computations was obtained by minimization of the non-relativistic energy.

For small and light systems, the most accurate results (and results in good agreement with the experiment) have been reported using perturbative techniques. For this reason, Table III also shows the deviation ( $\delta$  and  $\delta'$ ) of the computed energies and the leading-order perturbative relativistic energy, i.e., the sum of the non-relativistic energy,  $E_{\text{nr}}$ , and the expectation value of the Breit–Pauli Hamiltonian (the  $\alpha^2$  term) with the non-relativistic wave function,  $\Psi_{\text{nr}}$  (see for example, Ref. 53),

$$E_{\text{DCB}}^{(2)} = E_{\text{nr}} + \alpha^2 \langle \Psi_{\text{nr}} | H_{\text{DC}}^{(2)} + H_{\text{B}}^{(2)} | \Psi_{\text{nr}} \rangle, \quad (30)$$

with

$$H_{\text{DC}}^{(2)} = -\frac{1}{8} \sum_{i=1}^N (\nabla_i^2)^2 + \frac{\pi}{2} \sum_{i=1}^N \sum_{A=1}^{N_{\text{ nuc}}} Z_A \delta(\mathbf{r}_{iA}) - \pi \sum_{i=1}^N \sum_{j>i}^N \delta(\mathbf{r}_{ij}), \quad (31)$$

$$H_{\text{B}}^{(2)} = H_{\text{OO}} + 2\pi \sum_{i=1}^N \sum_{j>i}^N \delta(\mathbf{r}_{ij}), \quad (32)$$

and

$$H_{\text{OO}} = -\sum_{i=1}^N \sum_{j>i}^N \frac{1}{2r_{ij}} \left( \mathbf{p}_i \mathbf{p}_j + \frac{\mathbf{r}_{ij} (\mathbf{r}_{ij} \mathbf{p}_i) \mathbf{p}_j}{r_{ij}^2} \right). \quad (33)$$

We note that the speed of light in Secs. I and II can be written as  $c = \alpha^{-1} a_0 E_h / \hbar$  in Hartree atomic units. In the perturbative expressions, Eqs. (30)–(33), the  $H_{\text{DC}}^{(2)}$ ,  $H_{\text{B}}^{(2)}$ , and  $H_{\text{OO}}$  terms are understood in this context to have units of  $E_h$  (hartree).

We can observe in Table III that the no-pair DCB energy has a very large deviation ( $\delta'$ ), whereas the  $E_{\text{DC}}^{\text{proj}} + \langle B \rangle_{\text{DC}}$  energy has a smaller, but non-negligible, difference ( $\delta$ ) from the  $E_{\text{DCB}}^{(2)}$  leading-order relativistic energy. The sign and the order of magnitude of the deviation are not immediately obvious and motivate further analysis. In Table III of Paper I,<sup>26</sup> we observed that it is necessary to go beyond the leading-order ( $\alpha^2$ ) perturbative correction and include also the  $\alpha^3$ -order non-radiative QED term for the two-Coulomb-photon exchange to have a good agreement with the no-pair Dirac–Coulomb energy. For a better understanding of the Breit results, let us consider the effect of the Breit correction, instead of the full energy.

Table IV shows Breit correction values obtained from different computations. (For the sake of further analysis, we have also included the ground state of  $\text{Li}^+$  and  $\text{Be}^{2+}$  in the table.) First of all, we observe that the bulk of the Breit contribution (first 1–2 significant digits) agree in all computations.

A good agreement is observed even with the  $\langle B_{\omega} \rangle_{\text{MCDF}}$  multi-configuration Dirac–Hartree–Fock value,<sup>56</sup> in which  $B_{\omega}$  includes not only the non-retarded Breit term (as in our work), but also accounts for the frequency dependence of the interaction. Further digits are not available from that computation, but the available information provides us an independent check, assuming that the frequency dependence (and the different projector) has only a small effect on the systems studied. Apart from this set of values, all other values listed in the table correspond to the unretarded Breit interaction, Eq. (6). Regarding the uncertainty of the digits shown in the table, the estimated convergence error appears in the last digit given for  $E_{\text{DCB}}^{\text{proj}} - E_{\text{DC}}^{\text{proj}}$  and  $\langle B \rangle_{\text{DC}}$ . All digits shown for the reference value of  $\alpha^2 \langle H_{\text{B}}^{(2)} \rangle_{\text{nr}}$  are significant, i.e., converged for that quantity.

For  $\langle B \rangle_{\text{P}} = \langle \Psi_{\text{P}} | B | \Psi_{\text{P}} \rangle$ , we show the relevant number of digits of the numerical value obtained with the Pauli wave function constructed from the non-relativistic wave function optimized in this work. The Pauli wave function<sup>8</sup> is an approximation to the no-pair DC wave function, it can be constructed by using Eq. (17) kinetic balance condition and by filling up the appropriate spin-components with the (normalized) non-relativistic wave function in all (ll, ls, sl, and ss) blocks. So, we have evaluated  $\langle B \rangle_{\text{P}}$  by using the

**TABLE IV.** Comparison of the Breit correction, in  $\mu E_h$ , obtained from different computations. The estimated convergence error appears in the last digit. All values correspond to  $\alpha = \alpha_0 = 137.035999084$ .<sup>27</sup>

	$\text{H}^-$	He	$\text{Li}^+$	$\text{Be}^{2+}$	$\text{H}_2$	$\text{H}_3^+$	$\text{HeH}^+$
$E_{\text{DCB}}^{\text{proj}} - E_{\text{DC}}^{\text{proj}}$	0.436	27.61	150.67	449.3	3.033	3.029	25.95
$\langle B \rangle_{\text{DC}}^{\text{a}}$	0.448	28.298	156.354	464.60	3.089	3.111	26.436
$\langle B \rangle_{\text{P}}^{\text{a,b}}$	0.445	28.209	155.907	463.11	3.074	3.095	26.347
$\alpha^2 \langle H_{\text{B}}^{(2)} \rangle_{\text{nr}}^{\text{a,b,25,45,54,55}}$	0.443 5	28.174 9	155.786 1	462.747 1	3.065 5	3.087 7	26.313
$\langle B_{\omega} \rangle_{\text{MCDF}}^{\text{a,c,56}}$	0.4	28	(n.a.)	460	(n.a.)	(n.a.)	(n.a.)

<sup>a</sup> $\langle O \rangle_X$ : the expectation value of the  $O$  operator with the  $X$ : projected Dirac–Coulomb (DC), Pauli (P), non-relativistic (nr), and multi-configuration Dirac–Fock (MCDF) wave function.

<sup>b</sup> $\langle B \rangle_{\text{P}}$  equals (by mathematically equivalent rearrangements)  $\alpha^2 \langle H_{\text{B}}^{(2)} \rangle_{\text{nr}}$ , so the same result is obtained, as if  $\langle H_{\text{B}}^{(2)} \rangle_{\text{nr}}$  was “directly” evaluated in the same basis set as  $\langle B \rangle_{\text{P}}$ . The reference values for  $\langle H_{\text{B}}^{(2)} \rangle_{\text{nr}}$  were obtained by techniques that account for the cusp of the non-relativistic (nr) wave function and enhance the convergence of the expectation value of the singular operator in  $H_{\text{B}}^{(2)}$ , Eq. (32).

<sup>c</sup>Perturbative corrections including the frequency-dependence of the Breit operator taken from Ref. 56. Equation (2) is the relevant equation in this work that contains the sum of the Coulomb and the  $B_{\omega}$  frequency-dependent Breit interactions.

non-relativistic wave function in this way in our sixteen-component Breit implementation. Furthermore, it can be shown that  $\langle \Psi_p | B | \Psi_p \rangle$  can be exactly rearranged to  $\alpha^2 \langle H_B^{(2)} \rangle_{nr} = \alpha^2 \langle \Psi_{nr} | H_B^{(2)} | \Psi_{nr} \rangle$  (normalization of the Pauli wave function gives contribution only at higher  $\alpha$  orders).<sup>8</sup> In our implementation, the  $\langle B \rangle_p = \alpha^2 \langle H_B^{(2)} \rangle_{nr}$  mathematical identity is fulfilled to machine precision, if the same non-relativistic wave function is used in the two computations. Although the same underlying ECG integral routines are used for the evaluation of the two expressions, the two different computations assume the combination of different indices [compare Sec. II on the one hand and Eqs. (32) and (33) on the other], so this was an important check of our Breit implementation.

The  $\langle B \rangle_p$  values reported in the table correspond to the ECG basis that was obtained by minimization of the non-relativistic energy and also used as a “spatial” basis in the no-pair DC and DCB computations. As pointed out, these  $\langle B \rangle_p$  values agree to machine precision with the direct evaluation of  $\alpha^2 \langle H_B^{(2)} \rangle_{nr}$  in the same basis (“own basis”). At the same time, these values are not converged with respect to the basis set size due to the slowly convergent expectation value of the singular operator,  $\delta(\mathbf{r}_{12})$ , which can be most easily identified in Eq. (32), in a Gaussian basis not satisfying the cusp condition.<sup>45</sup> There are special “regularization” techniques<sup>45,57,58</sup> that can be used to improve the convergence of the expectation value for the singular operator,  $\delta(\mathbf{r}_{ij})$  [as well as for other singular operators in  $H_{DC}^{(2)}$  in Eq. (31)].

The well-converged perturbative values are compiled from literature values in the  $\alpha^2 \langle H_B^{(2)} \rangle_{nr}$  line of Table IV. We also note that the  $\alpha^2 \langle H_B^{(2)} \rangle_{nr}$  values for HeH<sup>+</sup> and H<sub>3</sub><sup>+</sup> were taken from Refs. 25 and 45, respectively, and were computed with ECG functions and the so-called integral transformation technique that enhances the convergence by accounting for the missing cusp effects.<sup>45,58</sup> Further numerical details and quantities used to calculate the perturbative corrections are provided in the [supplementary material](#).

After this introduction, we are in a position to compare the  $\alpha^2 \langle H_B^{(2)} \rangle_{nr}$  value, which is a quadratic function in  $\alpha$  ( $\langle H_B^{(2)} \rangle_{nr}$  in Hartree atomic units, which we use in this work, is independent of  $\alpha$ ), with the no-pair, sixteen-component results,  $E_{DCB}^{proj} - E_{DC}^{proj}$  and  $\langle B \rangle_{DC}$ , that contain non-radiative QED contributions, i.e., contributions beyond  $\alpha^2$ . To quantify this dependence, we solved the no-pair DC(B) equation for several  $\alpha$  values in the interval  $\alpha \in [0.7, 1.6] \alpha_0$  with  $\alpha_0 = 1/137.035999084$ .<sup>27</sup> For much smaller  $\alpha$  values, the corrections are too small for our numerical precision, and for much larger  $\alpha$  values, the spatial basis set taken from a non-relativistic optimization procedure is insufficient.

Figure 2 shows the  $\langle B \rangle_{DC}(\alpha) - \alpha^2 \langle H_B^{(2)} \rangle_{nr}$  difference and the  $b_2 \alpha^2 + b_3 \alpha^3 + b_4 \alpha^4$  polynomial fitted to the difference. In each fit, there is a small  $b_2 \alpha^2$  “relativistic offset” that can be attributed to imperfections in the convergence of the  $\langle B \rangle_{DC}$  data. The data are normalized with  $\langle \delta(\mathbf{r}_{12}) \rangle_{nr}$  that brings the values of all helium-like ions ( $Z = 1, 2, 3, 4$ ) and the three molecules (H<sub>2</sub>, HeH<sup>+</sup>, and H<sub>3</sub><sup>+</sup>) to the same scale in the figure. The  $b_3$  coefficients are similar in the different systems, but there is some system dependence that requires further study and, in the first place, better converged  $\langle B \rangle_{DC}$  data. All in all, we may conclude that the leading-order non-radiative QED contribution due to an (unretarded) Breit photon is approximately described by

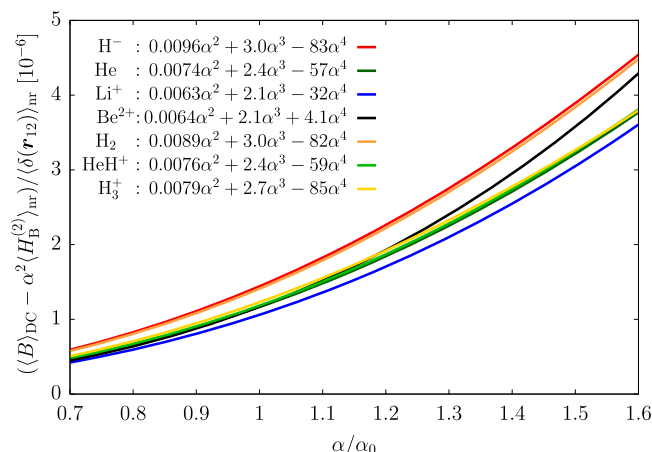


**FIG. 2.** Dependence of the Breit correction to the no-pair DC energy,  $\langle B \rangle_{DC}$ , on the value of the  $\alpha$  coupling constant of the electromagnetic interaction. Hartree atomic units are used and  $\alpha_0$  labels  $1/137.035999084$ .<sup>27</sup> The data points, used for fitting the polynomials, were computed at the  $\alpha = 1/(\alpha_0 + n)$ ,  $n = -50, \dots, 50$  values. The  $\langle H_B^{(2)} \rangle_{nr}$  and the  $\langle \delta(\mathbf{r}_{12}) \rangle_{nr}$  values compiled from Refs. 25, 45, 54, and 55 are listed in Table IV and in the [supplementary material](#).

$$\langle B \rangle_{DC}^{(3)} \approx 2.5\alpha^3 \langle \delta(\mathbf{r}_{12}) \rangle_{nr}. \quad (34)$$

The  $\langle \delta(\mathbf{r}_{12}) \rangle_{nr}$  proportionality is in agreement with Sucher’s result (Chap. V of Ref. 8), but Sucher’s coefficient for the positive-energy contribution (for singlet states) is different, Eq. (5.64) of Ref. 8,

$$\alpha^3 \varepsilon_{CB,unret}^{++} = 4 \left( \frac{\pi}{2} + 1 \right) \alpha^3 \langle \delta(\mathbf{r}_{12}) \rangle_{nr} \approx 10.3\alpha^3 \langle \delta(\mathbf{r}_{12}) \rangle_{nr}. \quad (35)$$

We do not have a conclusive explanation for this discrepancy. It is interesting to note, however, that the single- and double-pair contributions, Eqs. (5.21a)–(5.21b) of Ref. 8, to the (unretarded) expression in Eq. (35) (for singlet states) sum to

$$\alpha^3 \varepsilon_{CB,unret} = (4 - 2 \ln 2) \alpha^3 \langle \delta(\mathbf{r}_{12}) \rangle_{nr} \approx 3.40\alpha^3 \langle \delta(\mathbf{r}_{12}) \rangle_{nr}, \quad (36)$$

and observe that Sucher approximates the intermediate states with free-electron states, while they are one-electron states in the field of the nuclei (without electron–electron interactions) in our computations. Further work, including the pair corrections in our computations, will help in clarifying these aspects.

The  $\alpha^4$ -order contribution is not expected to be well approximated with a constant multiple of  $\langle \delta(\mathbf{r}_{12}) \rangle_{nr}$ . Nevertheless, the  $b_4 \alpha^4$  term is included in the fit (Fig. 2), and we can, indeed, observe a significant variation of  $b_4$  over the different systems studied.

Based on these observation, we can address the good numerical agreement of  $E_{DC}^{proj} + \langle B \rangle_{DC}$  and  $E_{DCB}^{(2)}$  (Table III). The leading-order non-radiative QED correction in  $E_{DC}^{proj}$  (Fig. 3 in Paper I<sup>26</sup>) and in  $\langle B \rangle_{DC}$  have an opposite sign and a similar order of magnitude. The sum of their contribution can be described to leading order in  $\alpha$  as  $(b_3 + c_3) \alpha^3 \approx -\alpha^3 \langle \delta(\mathbf{r}_{12}) \rangle_{nr}$  that corresponds for the physical  $\alpha = \alpha_0$  value to values on the order of  $(-1)$  to  $(-7)$  nE<sub>h</sub> for the hydrogenic systems and  $-40$  nE<sub>h</sub> for the  $Z = 2$  systems. These values, together with the convergence estimates—5 and 10 nE<sub>h</sub> for  $Z = 1$  and  $Z = 2$

systems, respectively—and the observed remaining higher-order contributions in  $E_{\text{DC}}^{\text{proj}}$  (Sec. IV C of Paper I<sup>26</sup>) provide some insight into the numerical agreement of  $E_{\text{DC}}^{\text{proj}} + \langle B \rangle_{\text{DC}}$  and  $E_{\text{DCB}}^{(2)}$  in Table III.

The  $\alpha$  dependence of the no-pair Dirac–Coulomb–Breit energy is much less understood. First of all, it is important to note that the “bulk of the correction” is correct and it is in agreement with other Breit correction results (Table IV). At the same time, we observe a slow convergence of  $E_{\text{DCB}}^{\text{proj}}$  with the basis set size. Furthermore,  $E_{\text{DCB}}^{\text{proj}} - E_{\text{DC}}^{\text{proj}}$  is “much” smaller than  $\langle B \rangle_{\text{DC}}$ , and the absolute value of the deviation is “large” in comparison with the typical deviations of the perturbative theory and experiment. By adding more ECG functions (that is currently limited by the double precision arithmetic that we use), we may expect some further decrease in the  $E_{\text{DCB}}^{\text{proj}}$  energy, i.e., increase in the absolute value of the deviation, due to the (near-)variational property of the no-pair computations and the already good convergence of the  $E_{\text{DC}}^{\text{proj}}$  energy.

It is interesting to note that the second-order Rayleigh–Schrödinger perturbative Breit correction, Eqs. (28) and (29), to the no-pair DC energy practically recovers the no-pair DCB result (the numerical values are provided in the supplementary material). This suggests that the deviation could be understood in terms of a perturbative correction (from the positive energy space) due to the exchange of two (unretarded) Breit photons. Sucher estimated this value to be (for singlet states)  $-\frac{\pi}{2}\alpha^3\langle\delta(r_{ij})\rangle_{\text{nr}}$  in Eq. (6.9b++) of Ref. 8. The sign of the deviation is in agreement with our numerical result, but it is an order of magnitude (!) smaller than the difference found in our computations. The comparison is further complicated by the fact that Sucher approximates the intermediate states with free-electron states. By collecting the pair corrections corresponding to Sucher’s free-electron intermediate-state approximation,<sup>8</sup> we may observe the so-called Araki–Sucher term and a  $\ln\alpha$  dependence. For the example of the helium atom, we have studied the  $\alpha$  dependence of the no-pair DCB and DC energies (Fig. 3). Surprisingly, the fitting coefficients in  $\sum_{n=2}^m t'_n \alpha^n$  change significantly by increasing the maximal polynomial order from  $m=3-4$ . Inclusion of an  $\alpha^3 \ln\alpha$  term did not improve the quality of the fit.

We have repeated all computations using only the Gaunt term, Eq. (13), i.e., solved the no-pair Dirac–Coulomb–Gaunt equation and observed a similar behavior (Fig. 4): (a) relatively slow convergence with respect to the basis set size; (b) failure to find a stable fit of  $\sum_{n=2}^m g_n \alpha^n$  polynomials for  $m=3-4$ .

Since the Dirac–Coulomb–Gaunt and Dirac–Coulomb–Breit wave functions have different coalescence properties,<sup>18</sup> it is unlikely that the similar erratic behavior of the Dirac–Coulomb–Gaunt (DCG) and DCB results (Figs. 3 and 4) is caused by the inexact representation of the coalescence features by the ECG basis set.

For further progress along these lines, it will be necessary to (a) improve the convergence of the no-pair DCB (and DCG) energies by an order of magnitude, (b) compute pair-corrections to the no-pair energies, and (c) test the kinetic balance condition to be able to rule out any deviation caused by an unnoticed “prolapse.” We have not noticed any major sign of prolapse during our no-pair DC computations (Paper I<sup>26</sup>), but it cannot be entirely excluded since the “restricted” kinetic balance, Eq. (16), is only an approximation to the “atomic balance”<sup>59</sup> that would ensure a rigorous variational property for the computation of the non-interacting states used to define the

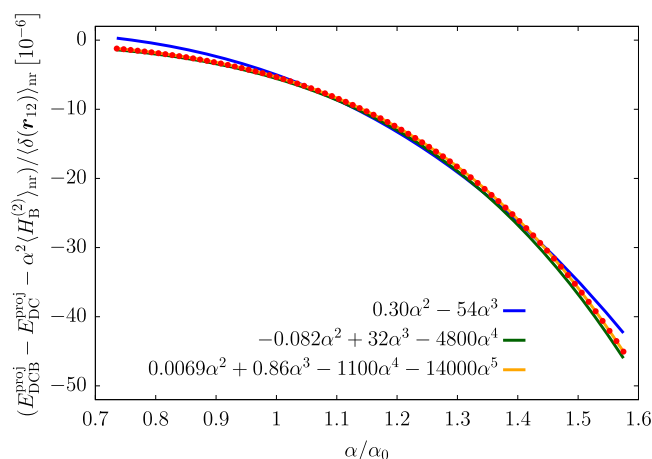


**FIG. 3.** Dependence of the no-pair Dirac–Coulomb–Breit (DCB) energy on the value of the  $\alpha$  coupling constant of the electromagnetic interaction for the example of the ground state of the helium atom. Hartree atomic units are used and  $\alpha_0$  labels  $1/137.035999084$ .<sup>27</sup> The  $\alpha$  dependence of the no-pair Dirac–Coulomb energy,  $E_{\text{DC}}^{\text{proj}}$ , is shown in Fig. 3 of Paper I.<sup>26</sup> The  $\langle H_{\text{B}}^{(2)} \rangle_{\text{nr}}$  and  $\langle \delta(r_{12}) \rangle_{\text{nr}}$  values compiled from Ref. 54 are listed in Table IV and in the supplementary material.

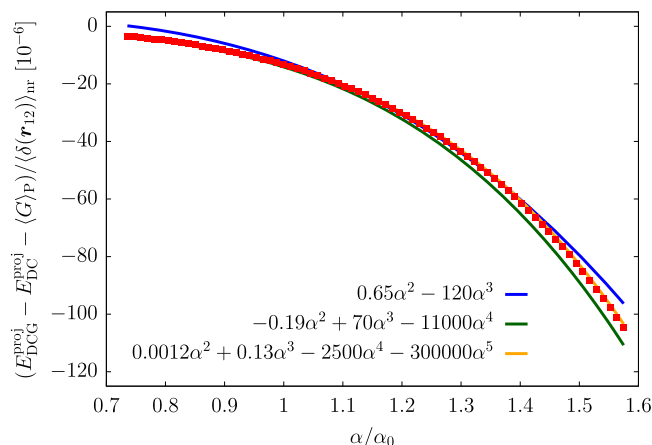


**FIG. 4.** Dependence of the no-pair Dirac–Coulomb–Gaunt (DCG) energy on the value of the  $\alpha$  coupling constant of the electromagnetic interaction for the example of the ground state of the helium atom. Hartree atomic units are used and  $\alpha_0$  labels  $1/137.035999084$ .<sup>27</sup> The  $\alpha$  dependence of the no-pair Dirac–Coulomb energy,  $E_{\text{DC}}^{\text{proj}}$ , is shown in Fig. 3 of Paper I.<sup>26</sup> The leading-order  $\alpha^2$  perturbative value for the Gaunt correction was obtained as  $\langle G \rangle_{\text{P}}$  (using the Pauli approximation and our sixteen-component Gaunt implementation). The  $\langle \delta(r_{12}) \rangle_{\text{nr}}$  value was taken from Ref. 54.

positive-energy projector. It would be prohibitively difficult to use the atomic balance in this work, but we consider testing other types of (approximate) kinetic balance conditions.<sup>22,60</sup>

#### IV. SUMMARY AND CONCLUSION

In summary, the implementation of the Breit interaction operator has been reported in the explicitly correlated no-pair

Dirac–Coulomb framework described in Paper I.<sup>26</sup> Both the variational and the perturbative inclusion of the Breit interaction were considered. Numerical results have been reported for the helium atom and helium-like ions with small nuclear charge numbers as well as for the ground electronic state of the  $H_2$ ,  $HeH^+$ , and  $H_3^+$  molecular systems near their equilibrium configuration.

The numerical results are compared with the leading-order,  $\mathcal{O}(\alpha^2)$ , relativistic energies and the relevant, leading-order,  $\mathcal{O}(\alpha^3)$ , non-radiative quantum electrodynamics corrections that are available from non-relativistic quantum electrodynamics derivations in the literature. Further work is necessary to clarify the origin of the deviation of the variational and perturbative relativistic treatments.

## SUPPLEMENTARY MATERIAL

The [supplementary material](#) contains (a) matrix elements for the Breit operator, (b) convergence tables, and (c) a collection of expectation values for the evaluation of the perturbative formulas.

## ACKNOWLEDGMENTS

Financial support of the European Research Council through a starting grant (Grant No. 851421) is gratefully acknowledged. D.F. is thankful for a doctoral scholarship from the ÚNKP-21-3 New National Excellence Program of the Ministry for Innovation and Technology from the source of the National Research, Development and Innovation Fund (Grant No. ÚNKP-21-3-II-ELTE-41). The authors thank the reviewers for their thoughtful comments that helped them to improve this work (Papers I and II).

## AUTHOR DECLARATIONS

### Conflict of Interest

The authors have no conflicts to disclose.

### DATA AVAILABILITY

The data that support the findings of this study are available within the article and its [supplementary material](#).

## REFERENCES

- M. Germann, S. Patra, J.-P. Karr, L. Hilico, V. I. Korobov, E. J. Salumbides, K. S. E. Eikema, W. Ubachs, and J. C. J. Koelmeij, *Phys. Rev. Res.* **3**, L022028 (2021).
- S. Alighanbari, G. S. Giri, F. L. Constantin, V. I. Korobov, and S. Schiller, *Nature* **581**, 152 (2020).
- D. Ferenc, V. I. Korobov, and E. Mátyus, *Phys. Rev. Lett.* **125**, 213001 (2020).
- M. Puchalski, J. Komasa, P. Czachorowski, and K. Pachucki, *Phys. Rev. Lett.* **117**, 263002 (2016).
- K. Pachucki, *Phys. Rev. A* **74**, 022512 (2006).
- V. Patkóš, V. A. Yerokhin, and K. Pachucki, *Phys. Rev. A* **103**, 042809 (2021).
- G. E. Brown and D. G. Ravenhall, *Proc. R. Soc. London, Ser. A* **208**, 552 (1951).
- J. Sucher, “Energy levels of the two-electron atom, to order  $\alpha^3$  Rydberg; ionization energy of helium,” Ph.D. dissertation (Columbia University, 1958).
- J. Sucher, *Phys. Rev. A* **22**, 348 (1980).
- M. H. Mittleman, *Phys. Rev. A* **24**, 1167 (1981).
- T. Saue, R. Bast, A. S. P. Gomes, H. J. A. Jensen, L. Visscher, I. A. Aucar, R. Di Remigio, K. G. Dyall, E. Eliav, E. Fasshauer, T. Fleig, L. Halbert, E. D. Hedegård, B. Helmich-Paris, M. Iliáš, C. R. Jacob, S. Knecht, J. K. Laerdahl, M. L. Vidal, M. K. Nayak, M. Olejniczak, J. M. H. Olsen, M. Pernpointner, B. Senjean, A. Shee, A. Sunaga, and J. N. P. van Stralen, *J. Chem. Phys.* **152**, 204104 (2020).
- F. A. Parpia, C. Froese Fischer, and I. P. Grant, *Comput. Phys. Commun.* **94**, 249 (1996).
- H. M. Quiney, H. Skaane, and I. P. Grant, *Adv. Quantum Chem.* **32**, 1 (1998).
- W. Liu and I. Lindgren, *J. Chem. Phys.* **139**, 014108 (2013).
- W. Liu, *Phys. Chem. Chem. Phys.* **14**, 35 (2012).
- W. Liu, *Phys. Rep.* **537**, 59 (2014).
- A. Almoukhalalati, S. Knecht, H. J. A. Jensen, K. G. Dyall, and T. Saue, *J. Chem. Phys.* **145**, 074104 (2016).
- Z. Li, S. Shao, and W. Liu, *J. Chem. Phys.* **136**, 144117 (2012).
- G. Pestka, *J. Phys. A: Math. Gen* **31**, 6243 (1998).
- G. Pestka, M. Bylicki, and J. Karwowski, *J. Phys. B: At., Mol. Opt. Phys.* **39**, 2979 (2006).
- G. Pestka and J. Karwowski, *Collect. Czech. Chem. Commun.* **68**, 275 (2003).
- B. Simmen, E. Mátyus, and M. Reiher, *J. Phys. B: At., Mol. Opt. Phys.* **48**, 245004 (2015).
- M. Bylicki, G. Pestka, and J. Karwowski, *Phys. Rev. A* **77**, 044501 (2008).
- G. Pestka, M. Bylicki, and J. Karwowski, *J. Phys. B: At., Mol. Opt. Phys.* **40**, 2249 (2007).
- P. Jeszenszki, D. Ferenc, and E. Mátyus, *J. Chem. Phys.* **154**, 224110 (2021).
- P. Jeszenszki, D. Ferenc, and E. Mátyus, *J. Chem. Phys.* **156**, 084111 (2022).
- E. Tiesinga, P. J. Mohr, D. B. Newell, and B. N. Taylor, *Rev. Mod. Phys.* **93**, 025010 (2021).
- C. G. Darwin, *Philos. Mag.* **39**, 537 (1920).
- G. Breit, *Proc. Nat. Acad. Sci. U. S. A.* **14**, 553 (1928).
- G. Breit, *Phys. Rev.* **34**, 553 (1929).
- P. Indelicato and P. J. Mohr, “Introduction to bound-state quantum electrodynamics,” in *Handbook of Relativistic Quantum Chemistry*, edited by W. Liu (Springer, Berlin, Heidelberg, 2017), pp. 131–241.
- M. Gell-Mann and F. Low, *Phys. Rev.* **84**, 350 (1951).
- J. Sucher, *Phys. Rev.* **107**, 1448 (1957).
- W. H. Furry, *Phys. Rev. A* **81**, 115 (1951).
- I. Lindgren, *Relativistic Many-Body Theory*, Springer Series on Atomic, Optical, and Plasma Physics Vol. 63 (Springer, New York, 2011).
- M. Reiher and A. Wolf, *Relativistic Quantum Chemistry: The Fundamental Theory of Molecular Science*, 2nd ed. (Wiley-VCH, Weinheim, 2015).
- H. A. Bethe and E. E. Salpeter, *Quantum Mechanics of One- and Two-Electron Atoms* (Springer, Berlin, 1957).
- Y.-K. Kim, *Phys. Rev.* **154**, 17 (1967).
- T. Kagawa, *Phys. Rev. A* **12**, 2245 (1975).
- H. M. Quiney, I. P. Grant, and S. Wilson, *J. Phys. B: At., Mol. Opt. Phys.* **20**, 1413 (1987).
- E. Lindroth, A.-M. Martensson-Pendrill, A. Ynnerman, and P. Öster, *J. Phys. B: At., Mol. Opt. Phys.* **22**, 2447 (1989).
- C. Thierfelder and P. Schwerdtfeger, *Phys. Rev. A* **82**, 062503 (2010).
- W. Kutzelnigg, *Int. J. Quantum Chem.* **25**, 107 (1984).
- W. Liu, *Mol. Phys.* **108**, 1679 (2010).
- P. Jeszenszki, R. T. Ireland, D. Ferenc, and E. Mátyus, *Int. J. Quantum Chem.* **e26819** (2021).
- E. Mátyus, *J. Chem. Phys.* **149**, 194111 (2018).
- E. Mátyus, *J. Chem. Phys.* **149**, 194112 (2018).
- D. Ferenc and E. Mátyus, *J. Chem. Phys.* **151**, 094101 (2019).
- E. Mátyus and P. Cassam-Chenaï, *J. Chem. Phys.* **154**, 024114 (2021).
- R. T. Ireland, P. Jeszenszki, E. Mátyus, R. Martinazzo, M. Ronto, and E. Pollak, *ACS Phys. Chem. Au* **2**, 23 (2021).
- D. Ferenc and E. Mátyus, *Phys. Rev. A* **100**, 020501(R) (2019).
- N. Moiseyev, *Non-Hermitian Quantum Mechanics* (Cambridge University Press, Cambridge, 2011).

<sup>53</sup>K. G. Dyall and K. Fægri, Jr., *Introduction to Relativistic Quantum Chemistry* (Oxford University Press, New York, 2007).

<sup>54</sup>G. Drake, "High precision calculations for helium," in *Springer Handbook of Atomic, Molecular, and Optical Physics*, Springer Handbooks, edited by G. Drake (Springer, New York, 2006), pp. 199–219.

<sup>55</sup>M. Puchalski, J. Komasa, and K. Pachucki, *Phys. Rev. A* **95**, 052506 (2017).

<sup>56</sup>F. A. Parpia and I. P. Grant, *J. Phys. B: At., Mol. Opt. Phys.* **23**, 211 (1990).

<sup>57</sup>R. J. Drachman, *J. Phys. B: At., Mol. Opt. Phys.* **14**, 2733 (1981).

<sup>58</sup>K. Pachucki, W. Cencek, and J. Komasa, *J. Chem. Phys.* **122**, 184101 (2005).

<sup>59</sup>M. Lewin and E. Sere, *Proc. London Math. Soc.* **100**, 864 (2010).

<sup>60</sup>V. M. Shabaev, I. I. Tupitsyn, V. A. Yerokhin, G. Plunien, and G. Soff, *Phys. Rev. Lett.* **93**, 130405 (2004).



# Variational Dirac–Coulomb explicitly correlated computations for atoms and molecules

Cite as: J. Chem. Phys. 156, 084111 (2022); doi: 10.1063/5.0075096

Submitted: 13 October 2021 • Accepted: 31 January 2022 •

Published Online: 23 February 2022



View Online



Export Citation



CrossMark

Péter Jeszenszki,  Dávid Ferenc,  and Edit Mátyus<sup>a)</sup> 

## AFFILIATIONS

ELTE, Eötvös Loránd University, Institute of Chemistry, Pázmány Péter sétány 1/A, Budapest H-1117, Hungary

<sup>a)</sup> Author to whom correspondence should be addressed: [edit.matyus@ttk.elte.hu](mailto:edit.matyus@ttk.elte.hu)

## ABSTRACT

The Dirac–Coulomb equation with positive-energy projection is solved using explicitly correlated Gaussian functions. The algorithm and computational procedure aims for a parts-per-billion convergence of the energy to provide a starting point for further comparison and further developments in relation with high-resolution atomic and molecular spectroscopy. Besides a detailed discussion of the implementation of the fundamental spinor structure, permutation, and point-group symmetries, various options for the positive-energy projection procedure are presented. The no-pair Dirac–Coulomb energy converged to a parts-per-billion precision is compared with perturbative results for atomic and molecular systems with small nuclear charge numbers. Paper II [D. Ferenc, P. Jeszenszki, and E. Mátyus, J. Chem. Phys. 156, 084110 (2022).] describes the implementation of the Breit interaction in this framework.

Published under an exclusive license by AIP Publishing. <https://doi.org/10.1063/5.0075096>

## I. INTRODUCTION

For a quantitative description of the high-resolution spectroscopic measurements of atoms<sup>1,2</sup> and molecules,<sup>3,4</sup> calculations of highly accurate energies are required corresponding to an at least parts-per-billion (ppb) relative precision.<sup>5–7</sup> To ensure the ppb level of convergence for atomic and molecular energies, it is necessary to use explicitly correlated basis functions.<sup>6,8–10</sup> Although fast convergence of the energy with respect to the basis set size is ensured, most explicitly correlated functions are highly specialized to the particular system. The integral expressions for the matrix elements typically depend on the number of electrons and nuclei, and new derivations are required for every extra atom and molecule type.<sup>11–13</sup>

Variants of explicitly correlated Gaussian functions (ECGs)<sup>8,14,15</sup> have the advantage that they explicitly contain the interparticle distances, while they preserve the general analytic formulation for a variety of systems.<sup>15–17</sup> In spite of these favorable properties, the ECGs are smooth functions that fail to satisfy the exact particle coalescence properties (cusps) of the non-relativistic wave function<sup>18</sup> and the cuspy or singular coalescence points corresponding to relativistic model Hamiltonians for which the precise properties depend on the particle interaction type.<sup>19,20</sup> For certain non-relativistic quantities, there exist convergence acceleration techniques that account for the missing cusp effects,<sup>21,22</sup> while for

variational relativistic treatments, careful convergence tests and comparison with other specialized methods,<sup>23,24</sup> which account for the singular behavior, are relevant (see also Sec. IV A of this work and Sec. III B of Paper II<sup>25</sup>).

Regarding the physical model, for systems with small  $Z$  nuclear charge numbers, the non-relativistic quantum electrodynamics (QED) (nrQED) approach is commonly used, which includes the  $Z\alpha$  expansion of the Dirac Hamiltonian<sup>5,26–28</sup> and  $\alpha$  is the fine-structure constant. In the nrQED procedure, the relativistic corrections appear in the perturbative terms without any direct account for the interaction of electron correlation with relativistic and QED effects at lowest order. There is another limiting range for which a meaningful expansion can be carried out; the  $1/Z$  expansion is a common choice for high  $Z$  values relevant for heavy elements.<sup>29–32</sup> The “intermediate” range with intermediate  $Z$  is a challenging range for the theory because in this range both the correlation and the relativistic (QED) effects are important.<sup>33,34</sup>

In the present work, we will consider an approach that aims for a treatment of electron correlation and special relativity on the “same footing” and at the same time targets tight convergence for the computed energies. In this way, comparison with results of the nrQED methodology, which can be considered well established for the low- $Z$  range, becomes relevant. In particular, an nrQED calculation is always restricted to a given order of the perturbation theory,

and finding a good estimate for the contributions from higher orders is often challenging.

The Dirac–Coulomb (DC) Hamiltonian is often cited as a starting point to account for special relativity in a many-particle atomic or molecular system. In this model, the direct product of one-particle Dirac operators and the Coulomb interaction between the particles is considered. Energies and wave functions for this seemingly *ad hoc* construct may be obtained by diagonalization of the matrix representation of the Dirac–Coulomb operator. Unfortunately, this simple procedure is problematic: electronic states, which would represent bound states, are “dissolved” in the positron–electron continuum in the infinite basis limit. This problematic behavior is called the “continuum dissolution” or “Brown–Ravenhall (BR) disease.”<sup>35</sup> The usual strategy to have access to these states relies on a positive-energy projection of the operator,<sup>36,37</sup> which eliminates the positron–positron and positron–electron states. Although the projected energies depend on the projector and, hence, on the underlying non-interacting model,<sup>38–40</sup> the final energies and predicted spectroscopic quantities should be independent of these technical details when all relevant QED terms are also accounted for.<sup>37,41,42</sup>

Using a determinant expansion, several approximate<sup>33,43</sup> and *ab initio*<sup>34,44</sup> QED computations have been carried out using the Dirac–Coulomb(–Breit) model used as the zeroth-order Hamiltonian. At the same time, far fewer applications have been reported with explicitly correlated basis functions, partly due to the difficulty caused by the missing one-particle picture in this basis representation. A one-particle basis provides a common and natural starting point for the description of the interaction of elementary particles,<sup>45–48</sup> and it can be used to develop a second quantized framework emphasized by Liu *et al.*<sup>49–52</sup> At the same time, “explicit correlation” is required to accurately describe particle correlation that is important for spectroscopic applications.<sup>5,28,53</sup> Liu *et al.* have considered the explicit correlation as a perturbation in the F12 framework, which required a “dual-basis” generalization of their positive-energy projection approach.<sup>20,49,54</sup>

Apart from our earlier report,<sup>55</sup> the very first and, so far, single implementation of positive-energy projection with an explicitly correlated basis set was based on complex scaling of the particle coordinates.<sup>24</sup> The complex scaling of the non-interacting model results in electronic states that are rotated to a branch in the complex-energy plane that is separated from the electron–positron and positron–positron states. In this way, the (non-interacting) electronic states can be expressed in a non-separable basis, and the corresponding positive-energy functions can be identified. Bylicki, Pestka, and Karwowski<sup>24</sup> proposed and implemented this complex-scaling approach with a (explicitly correlated) Hylleraas basis set and used it to compute the ground-state Dirac–Coulomb energy of the isoelectronic series of the helium atom.

In the present work, we report the detailed theoretical background for the first extension of an explicitly correlated, positive-energy projected approach to molecules.<sup>55</sup> We report the theoretical and algorithmic details for the computation of energies and eigenfunctions of the positive-energy projected or, as it is also called, no-pair DC Hamiltonian. After introduction of the DC model, the methodology is presented for the ECG framework with explanation about the implementation of the permutational and point-group

symmetries. We discuss in detail the positive-energy projection approach for which three alternatives are considered in detail. This paper ends with the presentation and analysis of the numerical results in comparison with perturbative relativistic and QED energies for the example of low- $Z$  atomic and molecular systems.

## II. DIRAC–COULOMB HAMILTONIAN AND DIRAC–SPINOR FOR TWO PARTICLES

### A. Dirac–Coulomb Hamiltonian

To introduce notation, we first consider the eigenvalue equation for the Dirac Hamiltonian (written in Hartree atomic units) of a single electron in interaction with  $N_{\text{nuc}}$  fixed nuclei described as positive point charges,

$$h_{\text{D}}^{[4]} \varphi^{(4)} = E \varphi^{(4)}, \quad (1)$$

$$h_{\text{D}}^{[4]} = \mathbf{c} \boldsymbol{\alpha}^{[4]} \mathbf{p} + \beta^{[4]} m c^2 + 1^{[4]} U, \quad (2)$$

$$U = - \sum_{I=1}^{N_{\text{nuc}}} \frac{Z_I}{|\mathbf{r} - \mathbf{R}_I|}. \quad (3)$$

In the equations,  $\mathbf{r}$  is the position of the electron,  $\mathbf{R}_I$  is the position of the  $I$ th nucleus,  $Z_I$  is the charge of this nucleus,  $1^{[n]}$  is the  $n$ -dimensional unit matrix,  $\varphi^{(4)}$  is a four-component spinor, and  $\boldsymbol{\alpha}^{[4]} = (\alpha_1^{[4]}, \alpha_2^{[4]}, \alpha_3^{[4]})$ . Throughout this work, we use the superscript “ $(n)$ ” and “[ $n$ ]” to label an  $n$ -dimensional vector and an  $(n \times n)$ -dimensional matrix, respectively. The Dirac matrices are chosen according to the usual convention,

$$\alpha_i^{[4]} = \begin{pmatrix} 0^{[2]} & \sigma_i^{[2]} \\ \sigma_i^{[2]} & 0^{[2]} \end{pmatrix}, \quad \beta^{[4]} = \begin{pmatrix} 1^{[2]} & 0^{[2]} \\ 0^{[2]} & -1^{[2]} \end{pmatrix} \quad (4)$$

with the  $\sigma_i^{[2]}$  Pauli matrices,

$$\sigma_1^{[2]} = \begin{pmatrix} 0 & 1 \\ 1 & 0 \end{pmatrix}, \quad \sigma_2^{[2]} = \begin{pmatrix} 0 & -i \\ i & 0 \end{pmatrix}, \quad \text{and} \quad \sigma_3^{[2]} = \begin{pmatrix} 1 & 0 \\ 0 & -1 \end{pmatrix}. \quad (5)$$

The matrix  $0^{[n]}$  is the  $(n \times n)$ -dimensional zero matrix. According to the  $2 \times 2$  block structure of the  $\alpha^{[4]}$  and  $\beta^{[4]}$  matrices, Eq. (4), it is convenient to express the  $\varphi^{(4)}$  spinor with a  $\varphi^{l(2)}$  “large” and a  $\varphi^{s(2)}$  “small” component as

$$\varphi^{(4)}(\mathbf{r}) = \begin{bmatrix} \varphi^{l(2)}(\mathbf{r}) \\ \varphi^{s(2)}(\mathbf{r}) \end{bmatrix}. \quad (6)$$

Both  $\varphi^{l(2)}$  and  $\varphi^{s(2)}$  have two components that can be characterized according to the spin projection on the  $z$  axis ( $+1/2$ :  $\uparrow$  and  $-1/2$ :  $\downarrow$ ),

$$\varphi^{\lambda(2)}(\mathbf{r}) = \begin{bmatrix} \varphi_{\uparrow}^{\lambda}(\mathbf{r}) \\ \varphi_{\downarrow}^{\lambda}(\mathbf{r}) \end{bmatrix}, \quad \lambda = 1 \text{ or } s. \quad (7)$$

The (exact) relation of the large and the small components is obtained from Eqs. (1)–(4),

$$\varphi^{s(2)}(\mathbf{r}) = \frac{c\sigma^{[2]}\mathbf{p}}{E - U + mc^2} \varphi^{l(2)}(\mathbf{r}). \quad (8)$$

To compute low-lying positive-energy states that appear a bit below  $mc^2$ , this relation is commonly approximated by using  $E - U + mc^2 \approx 2mc^2$ ,

$$\varphi^{s(2)}(\mathbf{r}) \approx \frac{\sigma^{[2]}\mathbf{p}}{2mc} \varphi^{l(2)}(\mathbf{r}). \quad (9)$$

It is important to note the symmetry relation (opposite parities) between the large and the small components, which is discussed in Ref. 56.

We use this, so-called “restricted,” kinetic balance condition<sup>56–58</sup> in the sense of a metric,

$$\varphi^{(4)}(\mathbf{r}) = \sum_{i=1}^{N_b} \sum_{q=1}^4 c_{iq} \phi_{iq}^{(4)}(\mathbf{r}), \quad (10)$$

$$\phi_{iq}^{(4)}(\mathbf{r}) = \mathcal{B}^{[4]} 1_q^{(4)} \Theta_i(\mathbf{r}), \quad (11)$$

$$\mathcal{B}^{[4]} = \begin{pmatrix} 1^{[2]} & 0^{[2]} \\ 0^{[2]} & \frac{\sigma^{[2]}\mathbf{p}}{2mc} \end{pmatrix}, \quad (12)$$

where  $c_{iq}$  is a coefficient,  $\Theta_i(\mathbf{r})$  is a spatial function, and  $1_q^{(4)}$  is a four-dimensional vector in which all elements are zero except for the  $q$ th element that is one,  $(1_q^{(4)})_i = \delta_{qi}$ . This relation has a central importance for the construction of a good matrix representation of the Hamiltonian in numerical computations; otherwise, a “variational collapse” would occur caused by an inappropriate representation of the  $\mathbf{p}$  momentum operator in the spinor basis.<sup>57,59,60</sup>

We also note that the rigorous variational property of the physical ground state would be guaranteed in a strict mathematical sense only by the “atomic balance,”<sup>61</sup> which reads as

$$\varphi^{s(2)}(\mathbf{r}) \approx \frac{c\sigma^{[2]}\mathbf{p}}{2mc^2 - U} \varphi^{l(2)}(\mathbf{r}). \quad (13)$$

Unfortunately, application of the atomic balance would result (with practical basis sets) in matrix elements that are difficult (impossible) to integrate analytically, and already, the “restricted” kinetic balance, Eq. (9), provides excellent results. Therefore, in the present work, we will proceed with the “restricted” kinetic balance condition, Eq. (9), and keep in mind the formal mathematical results.

For many-particle systems, several types of kinetic balance conditions have been introduced, which have different advantages depending on the aim of the computation.<sup>57,61–63</sup> Shabaev *et al.* defined the dual kinetic balance condition<sup>46,64</sup> that implements

not only the large–small relation but also the small–large relation. Pestka, Bylicki, and Karwowski<sup>24,65</sup> mentioned an iterative procedure connecting the large and small subspaces. Simmen *et al.* introduced a many-particle, so-called “relativistic” kinetic balance condition<sup>63</sup> by solving the two(many)-electron equations by using the  $E - U + mc^2 \approx 2mc^2$  approximation.

In a many-electron (many-spin-1/2-fermion) system, the Dirac operator for the  $i$ th particle is written in a direct-product form,

$$h_i^{[4^N]} = 1^{[4]}(1) \otimes \dots \otimes h_D^{[4]}(i) \otimes \dots \otimes 1^{[4]}(N), \quad (14)$$

where the particle index is given in parenthesis and  $N$  is the total number of electrons. By assuming instantaneous Coulomb interactions acting between the pairs of particles, we can write down the eigenvalue equation,

$$\mathcal{H}_{\text{DC}}^{[4^N]} |\Psi^{(4^N)}\rangle = E |\Psi^{(4^N)}\rangle, \quad (15)$$

with the Dirac–Coulomb Hamiltonian,

$$\mathcal{H}_{\text{DC}}^{[4^N]} = \sum_{i=1}^N h_i^{[4^N]} + 1^{[4^N]} V, \quad (16)$$

$$V = \sum_{i=1}^N \sum_{i < j}^N \frac{1}{|\mathbf{r}_i - \mathbf{r}_j|}. \quad (17)$$

In the many-particle case, it remains to be convenient to think in terms of the large–small block structure similarly to the one-electron case. The many-particle spinor has in total  $4^N$  components that are now considered in terms of  $2^N$  large–small components and  $2^N$  spin configurations. The block-wise direct product, which allows us to retain the large–small structure, was called the Tracy–Singh product<sup>66</sup> in Refs. 20 and 52 and was later also used in Refs. 55 and 63.

In this paper, we focus on two-electron systems for which the block-wise spinor structure can be written as

$$|\Psi^{(16)}\rangle = \begin{bmatrix} |\psi^{1l(4)}\rangle \\ |\psi^{1s(4)}\rangle \\ |\psi^{s1(4)}\rangle \\ |\psi^{ss(4)}\rangle \end{bmatrix} \quad (18)$$

and

$$|\psi^{\lambda_1\lambda_2(4)}\rangle = \begin{bmatrix} |\psi_{\uparrow\uparrow}^{\lambda_1\lambda_2}\rangle \\ |\psi_{\uparrow\downarrow}^{\lambda_1\lambda_2}\rangle \\ |\psi_{\downarrow\uparrow}^{\lambda_1\lambda_2}\rangle \\ |\psi_{\downarrow\downarrow}^{\lambda_1\lambda_2}\rangle \end{bmatrix}, \quad (19)$$

where  $\lambda_1$  and  $\lambda_2$  can be “l” or “s.” The two-particle Dirac–Coulomb Hamiltonian written in a corresponding block-structure is

$$\mathcal{H}_{\text{DC}}^{[16]} = \begin{pmatrix} (V+U)1^{[4]} & c\sigma_2^{[4]}\mathbf{p}_2 & c\sigma_1^{[4]}\mathbf{p}_1 & 0^{[4]} \\ c\sigma_2^{[4]}\mathbf{p}_2 & (V+U-2m_2c^2)1^{[4]} & 0^{[4]} & c\sigma_1^{[4]}\mathbf{p}_1 \\ c\sigma_1^{[4]}\mathbf{p}_1 & 0^{[4]} & (V+U-2m_1c^2)1^{[4]} & c\sigma_2^{[4]}\mathbf{p}_2 \\ 0^{[4]} & c\sigma_1^{[4]}\mathbf{p}_1 & c\sigma_2^{[4]}\mathbf{p}_2 & [V+U-2(m_1+m_2)c^2]1^{[4]} \end{pmatrix}, \quad (20)$$

where similarly to Eq. (14), the  $\sigma_1^{[4]} = \sigma^{[2]} \otimes 1^{[2]}$  notation is introduced and  $\sigma_2^{[4]} = 1^{[2]} \otimes \sigma^{[2]}$  and the energy scale for the  $i$ th particle is shifted by  $m_i c^2$ . We use during this work the relationship

$$\sigma_1^{[4]}\sigma_2^{[4]} = (\sigma^{[2]} \otimes 1^{[2]})(1^{[2]} \otimes \sigma^{[2]}) = \sigma^{[2]} \otimes \sigma^{[2]}. \quad (21)$$

The exact wave function is expanded in a spinor basis,

$$|\Psi^{(16)}\rangle = \sum_{i=1}^{N_b} \sum_{q=1}^{16} c_{iq} |\Phi_{iq}^{(16)}\rangle, \quad (22)$$

for which the kinetic-balance condition of Eq. (11) can be generalized<sup>57,58</sup> as

$$|\Phi_{iq}^{(16)}\rangle = \mathcal{B}^{[16]} 1_q^{(16)} |\Theta_i\rangle, \quad (23)$$

$$\mathcal{B}^{[16]} = \begin{pmatrix} 1^{[4]} & 0^{[4]} & 0^{[4]} & 0^{[4]} \\ 0^{[4]} & \frac{\sigma_2^{[4]}\mathbf{p}_2}{2m_2c} & 0^{[4]} & 0^{[4]} \\ 0^{[4]} & 0^{[4]} & \frac{\sigma_1^{[4]}\mathbf{p}_1}{2m_1c} & 0^{[4]} \\ 0^{[4]} & 0^{[4]} & 0^{[4]} & \frac{\sigma_1^{[4]}\mathbf{p}_1\sigma_2^{[4]}\mathbf{p}_2}{4m_1m_2c^2} \end{pmatrix}. \quad (24)$$

Additionally,  $|\Theta_i\rangle$  is a floating explicitly correlated Gaussian function,

$$\Theta_i(\mathbf{r}) = \exp[-(\mathbf{r}-\mathbf{s}_i)^T \underline{\mathbf{A}}_i (\mathbf{r}-\mathbf{s}_i)], \quad (25)$$

where  $\mathbf{r} \in \mathbb{R}^6$  is the position vector of the two particles,  $\mathbf{s}_i \in \mathbb{R}^6$  is the “shift” vector, and  $\underline{\mathbf{A}}_i = \mathbf{A}_i \otimes 1^{[3]}$  with  $\mathbf{A}_i \in \mathbb{R}^{2 \times 2}$  is a symmetric, positive-definite parameter matrix.

Multiplying Eq. (15) from the left with  $\langle \Phi_{jp}^{(16)} |$  and using Eqs. (22) and (23), we obtain the matrix eigenvalue equation

$$\sum_{i=1}^{N_b} \sum_{q=1}^{16} \langle \Phi_{jp}^{(16)} | \mathcal{H}_{\text{DC}}^{[16]} | \Phi_{iq}^{(16)} \rangle c_{iq} = E \sum_{i=1}^{N_b} \sum_{q=1}^{16} \langle \Phi_{jp}^{(16)} | \Phi_{iq}^{(16)} \rangle c_{iq}. \quad (26)$$

The explicit form for a matrix element is

$$\begin{aligned} \langle \Phi_{jp}^{(16)} | \mathcal{H}_{\text{DC}}^{[16]} | \Phi_{iq}^{(16)} \rangle &= \langle \Theta_j | 1_p^{(16)T} \mathcal{B}^{[16]\dagger} \mathcal{H}_{\text{DC}}^{[16]} \mathcal{B}^{[16]} 1_q^{(16)} | \Theta_i \rangle \\ &= 1_p^{(16)T} \begin{pmatrix} \langle \Theta_j | \mathcal{W}_{\text{ll}}^{[4]} | \Theta_i \rangle & \frac{1}{2m_2} \langle \Theta_j | p_2^2 | \Theta_i \rangle 1^{[4]} & \frac{1}{2m_1} \langle \Theta_j | p_1^2 | \Theta_i \rangle 1^{[4]} & 0^{[4]} \\ \frac{1}{2m_2} \langle \Theta_j | p_2^2 | \Theta_i \rangle 1^{[4]} & \langle \Theta_j | \mathcal{W}_{\text{ls}}^{[4]} | \Theta_i \rangle & 0^{[4]} & \frac{1}{8m_1m_2c^2} \langle \Theta_j | p_1^2 p_2^2 | \Theta_i \rangle 1^{[4]} \\ \frac{1}{2m_1} \langle \Theta_j | p_1^2 | \Theta_i \rangle 1^{[4]} & 0^{[4]} & \langle \Theta_j | \mathcal{W}_{\text{sl}}^{[4]} | \Theta_i \rangle & \frac{1}{8m_1^2m_2c^2} \langle \Theta_j | p_1^2 p_2^2 | \Theta_i \rangle 1^{[4]} \\ 0^{[4]} & \frac{1}{8m_1m_2c^2} \langle \Theta_j | p_1^2 p_2^2 | \Theta_i \rangle 1^{[4]} & \frac{1}{8m_1^2m_2c^2} \langle \Theta_j | p_1^2 p_2^2 | \Theta_i \rangle 1^{[4]} & \langle \Theta_j | \mathcal{W}_{\text{ss}}^{[4]} | \Theta_i \rangle \end{pmatrix} 1_q^{(16)}, \end{aligned} \quad (27)$$

$$\begin{aligned} \langle \Phi_{jp}^{(16)} | \Phi_{iq}^{(16)} \rangle &= \langle \Theta_j | 1_p^{(16)T} \mathcal{B}^{[16]\dagger} \mathcal{B}^{[16]} 1_q^{(16)} | \Theta_i \rangle \\ &= 1_p^{(16)T} \begin{pmatrix} \langle \Theta_j | \Theta_i \rangle 1^{[4]} & 0^{[4]} & 0^{[4]} & 0^{[4]} \\ 0^{[4]} & \frac{1}{4m_2^2c^2} \langle \Theta_j | p_2^2 | \Theta_i \rangle 1^{[4]} & 0^{[4]} & 0^{[4]} \\ 0^{[4]} & 0^{[4]} & \frac{1}{4m_1^2c^2} \langle \Theta_j | p_1^2 | \Theta_i \rangle 1^{[4]} & 0^{[4]} \\ 0^{[4]} & 0^{[4]} & 0^{[4]} & \frac{1}{16m_1^2m_2^2c^4} \langle \Theta_j | p_1^2 p_2^2 | \Theta_i \rangle 1^{[4]} \end{pmatrix} 1_q^{(16)}, \end{aligned} \quad (28)$$

$$\mathcal{W}_{\parallel}^{[4]} = (V + U)1^{[4]}, \quad (29)$$

$$\mathcal{W}_{\text{ls}}^{[4]} = \frac{1}{4m_2^2c^2} \sum_{ij=1}^3 p_{2i}(V + U)p_{2j}\sigma_{2i}^{[4]}\sigma_{2j}^{[4]} - \frac{1}{2m_2}p_2^21^{[4]}, \quad (30)$$

$$\mathcal{W}_{\text{sl}}^{[4]} = \frac{1}{4m_1^2c^2} \sum_{ij=1}^3 p_{1i}(V + U)p_{1j}\sigma_{1i}^{[4]}\sigma_{1j}^{[4]} - \frac{1}{2m_1}p_1^21^{[4]}, \quad (31)$$

$$\begin{aligned} \mathcal{W}_{\text{ss}}^{[4]} &= \frac{1}{16m_1^2m_2^2c^4} \sum_{ij,k,l=1}^3 p_{1i}p_{2j}(V + U)p_{2k}p_{1l}\sigma_{1i}^{[4]}\sigma_{1l}^{[4]}\sigma_{2j}^{[4]}\sigma_{2k}^{[4]} \\ &\quad - \frac{(m_1 + m_2)}{8m_1^2m_2^2c^2} p_1p_2^21^{[4]}, \end{aligned} \quad (32)$$

where the  $(\sigma^{[4]}\mathbf{p})(\sigma^{[4]}\mathbf{p}) = p^21^{[4]}$  identity was used. In the equations,  $\langle \Theta_i | \mathcal{W}^{[4]} | \Theta_j \rangle$  means that the integral is evaluated for every element of the four-dimensional matrix. Subsection II B describes the implementation of the permutational symmetry for (two) identical spin-1/2 particles.

## B. Implementation of the permutational symmetry

The Dirac–Coulomb Hamiltonian, similarly to its non-relativistic counterpart, is invariant to the permutation of identical particles. At the same time, it is necessary to consider the multi-dimensional spinor structure when we calculate the effect of the particle-permutation operator. For two particles and for the present block structure, it is

$$\mathcal{P}_{12}^{[16]} = (\mathbb{P}_{12}^{\text{ls}[4]} \otimes \mathbb{P}_{12}^{\uparrow\downarrow[4]})P_{12}, \quad (33)$$

where  $P_{12}$  exchanges the particle labels (as in the non-relativistic theory), but due to the multi-dimensional spinor structure, we also have  $\mathbb{P}_{12}^{\text{ls}[4]}$ , which operates on the large–small component space, and  $\mathbb{P}_{12}^{\uparrow\downarrow[4]}$ , which acts on the  $\uparrow\text{--}\downarrow$  spin space, and both of them are represented with the following matrix:

$$\mathbb{P}_{12}^{\text{ls}[4]} = \mathbb{P}_{12}^{\uparrow\downarrow[4]} = \begin{pmatrix} 1 & 0 & 0 & 0 \\ 0 & 0 & 1 & 0 \\ 0 & 1 & 0 & 0 \\ 0 & 0 & 0 & 1 \end{pmatrix}. \quad (34)$$

The permutation operator, Eq. (33), commutes with the Dirac–Coulomb Hamiltonian,<sup>42,52</sup>

$$[\mathcal{H}_{\text{DC}}^{[16]}, \mathcal{P}_{12}^{[16]}] = 0, \quad (35)$$

and, thus, their common eigenfunctions can be identified as bosonic (symmetric) or fermionic (antisymmetric) eigenstates. Since we describe spin-1/2 fermions, it is convenient to work with antisymmetrized basis functions for which we introduce the antisymmetrization operator<sup>42</sup> that reads for the two-particle case as

$$\mathcal{A}^{[16]} = \frac{1}{2}(1^{[16]} - \mathcal{P}_{12}^{[16]}). \quad (36)$$

To define a variational procedure, we combine the antisymmetrized wave function ansatz, the finite basis expansion in Eq. (22), and the eigenvalue equation in Eq. (15). Then, by multiplying the resulting operator eigenvalue equation with  $\langle \Phi_{jp} | \mathcal{A}^{[16]\dagger}$  using Eq. (23), we obtain the matrix-eigenvalue equation

$$\begin{aligned} &\sum_{i=1}^{N_b} \sum_{q=1}^{16} \langle \Phi_{jp}^{(16)} | \mathcal{A}^{[16]\dagger} \mathcal{H}_{\text{DC}} \mathcal{A}^{[16]} | \Phi_{iq}^{(16)} \rangle c_{iq} \\ &= E \sum_{i=1}^{N_b} \sum_{q=1}^{16} \langle \Phi_{jp}^{(16)} | \mathcal{A}^{[16]\dagger} \mathcal{A}^{[16]} | \Phi_i^{(16)} \rangle c_{iq}. \end{aligned} \quad (37)$$

Since  $\mathcal{A}^{[16]\dagger} = \mathcal{A}^{[16]}$ ,  $\mathcal{A}^{[16]}$  is idempotent, and both  $1^{[16]}$  and  $\mathcal{P}_{12}^{[16]}$  commute with the Hamiltonian operator, Eq. (37) can be simplified to

$$\sum_{i=1}^{N_b} \sum_{q=1}^{16} \langle \Phi_{jp}^{(16)} | \mathcal{H}_{\text{DC}} \mathcal{A}^{[16]} | \Phi_{iq}^{(16)} \rangle c_{iq} = E \sum_{i=1}^{N_b} \sum_{q=1}^{16} \langle \Phi_{jp}^{(16)} | \mathcal{A}^{[16]} | \Phi_i^{(16)} \rangle c_{iq}. \quad (38)$$

The permutation operator,  $P_{12}$ , acts only on the  $\mathbf{r}$  spatial coordinates in  $\Theta(\mathbf{r})$  by exchanging the position of the particles. For a floating ECG, the effect of a particle permutation operator  $P_{12}$  translates to a transformation of the ECG parameterization, Eq. (25),<sup>9,15</sup>

$$\begin{aligned} P_{12}\Theta(\mathbf{r}) &= \Theta(P_{12}^{-1}\mathbf{r}) \\ &= \exp\left[\left(P_{12}^{-1}\mathbf{r} - \mathbf{s}_i\right)^{\text{T}} \underline{\mathbf{A}}_i \left(P_{12}^{-1}\mathbf{r} - \mathbf{s}_i\right)\right] \\ &= \exp\left[\left(\mathbf{r} - \underbrace{P_{12}\mathbf{s}_i}_{\mathbf{s}_i^{(12)}}\right)^{\text{T}} \underbrace{P_{12}^{\text{T}}\underline{\mathbf{A}}_i P_{12}}_{\underline{\mathbf{A}}_i^{(12)}} \left(\mathbf{r} - \underbrace{P_{12}\mathbf{s}_i}_{\mathbf{s}_i^{(12)}}\right)\right] \\ &= \exp\left[\left(\mathbf{r} - \mathbf{s}_i^{(12)}\right)^{\text{T}} \underline{\mathbf{A}}_i^{(12)} \left(\mathbf{r} - \mathbf{s}_i^{(12)}\right)\right]. \end{aligned} \quad (39)$$

## C. Implementation of the point-group symmetry

To have an efficient computational approach for molecules with clamped nuclei, it was necessary to make use of the point-group symmetry during the computations. Due to the spinor structure of the Dirac equation, it is necessary to consider the spatial symmetry operations over the spinor space. Each symmetry operation,  $\mathcal{S}^{[16]}$ , will be considered as a composition of a symmetry operator  $S$  acting on the configuration space and an operator  $\mathbb{S}^{[16]}$  acting on the spin part,<sup>42</sup>

$$\mathcal{S}^{[16]} = \mathbb{S}^{[16]}S. \quad (40)$$

In relativistic quantum mechanics, the notation of the spatial symmetry operators is often retained with a modified meaning that includes both spin and spatial symmetry operations. In the present work, we show both the spin and spatial contributions for clarity. The spatial identity, rotation, and inversion symmetry operators for a single particle are generalized with the following operations for the spin-spatial space as<sup>42</sup>

$$\mathcal{E}^{[4]} = 1^{[4]}E, \quad (41)$$

$$C_{na}^{[4]} = 1^{[2]} \otimes \exp\left[-i\frac{\sigma_a^{[2]}\pi}{n}\right] C_{na}, \quad (42)$$

$$\mathcal{I}^{[4]} = \beta^{[4]} I, \quad (43)$$

where  $a$  labels the spatial directions. Furthermore, symmetry operations can be generated using these three symmetry operations. For example, the plane reflection can be obtained as an inversion followed by a two-fold rotation,

$$\mathcal{T}_{ab}^{[4]} = C_{2c}^{[4]} \mathcal{I}^{[4]}, \quad (44)$$

where  $a$ ,  $b$ , and  $c$  label mutually orthogonal spatial directions. Using Euler's formula for the spin part,

$$\exp\left[-i\frac{\sigma_a^{[2]}\pi}{n}\right] = 1^{[2]} \cos\frac{\pi}{n} - i\sigma_a^{[2]} \sin\frac{\pi}{n}, \quad (45)$$

Eq. (44) can be further simplified to

$$\mathcal{T}_{ab}^{[4]} = -i\left(1^{[2]} \otimes \sigma_c^{[2]} C_{2c}\right) \left(\beta^{[4]} I\right). \quad (46)$$

Since we solve the eigenvalue equation in the kinetic-balance metric defined by Eq. (24), it is more convenient to introduce an  $\mathcal{O}_B^{[4]}$  “modified” representation of the symmetry operators,

$$\mathcal{O}_B^{[4]} = \left(\mathcal{B}^{[4]}\right)^{-1} \mathcal{O} \mathcal{B}^{[4]}. \quad (47)$$

It can be shown that both  $\mathcal{E}^{[4]}$  and  $C_{na}^{[4]}$  commute with  $\mathcal{B}^{[4]}$ ; hence,

$$\mathcal{E}_B^{[4]} = \mathcal{E}^{[4]}, \quad (48)$$

$$C_{B,na}^{[4]} = C_{na}^{[4]}, \quad (49)$$

but the inversion and reflection operators simplify to

$$\mathcal{I}_B^{[4]} = 1^{[4]} I, \quad (50)$$

$$\mathcal{T}_{B,ab}^{[4]} = -i\left(1^{[2]} \otimes \sigma_c^{[2]} C_{2c}\right) \mathcal{I}. \quad (51)$$

For two particles, we need to consider the block-wise (Tracy–Singh) direct products,

$$\mathcal{E}_B^{[16]} = 1^{[16]} \mathcal{E}_1 \mathcal{E}_2, \quad (52)$$

$$C_{B,np}^{[16]} = \left(e^{-i\frac{\sigma_1^{[2]}\pi}{n}} \otimes 1^{[2]}\right) \boxtimes \left(1^{[2]} \otimes e^{-i\frac{\sigma_2^{[2]}\pi}{n}}\right) C_{np,1} C_{np,2}, \quad (53)$$

$$\mathcal{I}_B^{[16]} = 1^{[16]} \mathcal{I}_1 \mathcal{I}_2, \quad (54)$$

$$\mathcal{T}_{B,ab}^{[16]} = -\left(\sigma_{c1}^{[2]} \otimes 1^{[2]}\right) \boxtimes \left(1^{[2]} \otimes \sigma_{c2}^{[2]}\right) C_{2c,1} C_{2c,2} \mathcal{I}_1 \mathcal{I}_2, \quad (55)$$

where the subscripts 1 and 2 stand for the particle indices.

A (floating) ECG, Eq. (25), is adapted to the  $\zeta$  irreducible representation of the point group  $G$  by using the projector

$$P_G^{\zeta[16]} = \sum_{\mathcal{O} \in G} \chi_{G\mathcal{O}}^{\zeta} \mathcal{O}^{[16]}, \quad (56)$$

where  $\chi_{G\mathcal{O}}^{\zeta}$  labels the character corresponding to the  $\mathcal{O}^{[16]}$  symmetry operation. In relativistic quantum mechanics, the point groups have to be extended to a double group for an odd number of particles. For the case of two half-spin particles, the simpler, well-known single-group character tables can be used.<sup>42,67</sup>

Due to the  $\underline{A}_i = \mathbf{A}_i \otimes I^{[3]}$  direct-product (“spherical-like”) form of the exponent matrix, the effect of the spatial symmetry operators on the ECG function can be translated to the transformation of the shift vectors (see, for example, Refs. 9 and 68),

$$\begin{aligned} \mathcal{O}\Theta(\mathbf{r}) &= \mathcal{O} \exp\left[(\mathbf{r} - \mathbf{s}_i)^T \underline{A}_i (\mathbf{r} - \mathbf{s}_i)\right] \\ &= \exp\left[\left(\mathbf{r} - \underbrace{\mathcal{O}\mathbf{s}_i}_{\mathbf{s}_i^{\mathcal{O}}}\right)^T \underbrace{\mathcal{O}^T \underline{A}_i \mathcal{O}}_{\underline{A}_i} \left(\mathbf{r} - \underbrace{\mathcal{O}\mathbf{s}_i}_{\mathbf{s}_i^{\mathcal{O}}}\right)\right] \\ &= \exp\left[(\mathbf{r} - \mathbf{s}_i^{\mathcal{O}})^T \underline{A}_i (\mathbf{r} - \mathbf{s}_i^{\mathcal{O}})\right], \end{aligned} \quad (57)$$

which allows for a straightforward evaluation of the effect of the spatial symmetry operators.

In summary, the basis functions used in the computations are obtained by projection of the ECGs with the  $\mathcal{A}^{[16]}$  antisymmetrization and the  $P_G^{\zeta[16]}$  point-group symmetry projection operator, which results in the following generalized eigenvalue equation:

$$\begin{aligned} &\sum_{i=1}^{N_b} \sum_{p=1}^{16} \left\langle \Phi_{jq}^{(16)} \left| \mathcal{H}_{DC}^{[16]} P_G^{\zeta[16]} \mathcal{A}^{[16]} \right| \Phi_{ip}^{(16)} \right\rangle c_{ip} \\ &= E \sum_{i=1}^{N_b} \sum_{p=1}^{16} \left\langle \Phi_{jq}^{(16)} \left| P_G^{\zeta[16]} \mathcal{A}^{[16]} \right| \Phi_{ip}^{(16)} \right\rangle c_{ip}. \end{aligned} \quad (58)$$

Substituting Eqs. (23), (36), and (56) into Eq. (58) and using Eq. (47) and the fact that  $\mathcal{B}^{[16]}$  and  $\left(\mathbb{P}_{12}^{[4]} \otimes \mathbb{P}_{12}^{\dagger[4]}\right) P_{12}$  commute, we obtain the final working equation as

$$\begin{aligned} &\sum_{i=1}^{N_b} \sum_{p=1}^{16} \sum_{\mathcal{O} \in G} \chi_{G\mathcal{O}}^{\zeta} 1_q^{(16)T} \\ &\quad \times \left[ \mathcal{K}_{ji}^{O[16]} \mathbb{O}_B^{[16]} - \mathcal{K}'_{ji}{}^{O[16]} \left(\mathbb{P}_{12}^{[4]} \otimes \mathbb{P}_{12}^{\dagger[4]}\right) \mathbb{O}_B^{[16]} \right] 1_p^{(16)} c_{ip} \\ &= E \sum_{i=1}^{N_b} \sum_{p=1}^{16} \sum_{\mathcal{O} \in G} \chi_{G\mathcal{O}}^{\zeta} 1_q^{(16)T} \\ &\quad \times \left[ \mathcal{S}_{ji}^{O[16]} \mathbb{O}_B^{[16]} - \mathcal{S}'_{ji}{}^{O[16]} \left(\mathbb{P}_{12}^{[4]} \otimes \mathbb{P}_{12}^{\dagger[4]}\right) \mathbb{O}_B^{[16]} \right] 1_p^{(16)} c_{ip}, \end{aligned} \quad (59)$$

$$\mathcal{K}_{ji,qp}^{O[16]} = \left\langle \Theta_j \left| 1_q^{(16)T} \mathcal{B}^{[16]\dagger} \mathcal{H}_{DC}^{[16]} \mathcal{B}^{[16]} 1_p^{(16)} \right| \Theta_i \right\rangle, \quad (60)$$

$$\mathcal{K}'_{ji,qp}{}^{O[16]} = \left\langle \Theta_j \left| 1_q^{(16)T} \mathcal{B}^{[16]\dagger} \mathcal{H}_{DC}^{[16]} \mathcal{B}^{[16]} 1_p^{(16)} O_{P_{12}} \right| \Theta_i \right\rangle, \quad (61)$$

$$S_{ji,qp}^{O[16]} = \left\langle \Theta_j \left| 1_q^{(16)T} \mathcal{B}^{[16]\dagger} \mathcal{B}^{[16]} 1_p^{(16)} O \right| \Theta_i \right\rangle, \quad (62)$$

$$S_{ji,qp}^{O[16]} = \left\langle \Theta_j \left| 1_q^{(16)T} \mathcal{B}^{[16]\dagger} \mathcal{B}^{[16]} 1_p^{(16)} O P_{12} \right| \Theta_i \right\rangle. \quad (63)$$

We note that in Eq. (59), the dimensionality of the final matrix eigenvalue equation to be solved is  $16N_b \times 16N_b$  since the linear combination coefficients are carried in  $c_{ip} \in \mathbb{C}$  ( $i = 1, \dots, N_b$ ,  $p = 1, \dots, 16$ ). For special cases, the matrix representation can be block diagonalized (a special case is described in the [supplementary material](#)).

#### D. Implementation of the Dirac–Coulomb matrix-eigenvalue equation

The working equation, Eq. (59), is implemented in the QUANTEN computer program that is an in-house developed program written using the Fortran90 programming language and contains several analytic ECG integrals. For recent applications of QUANTEN, see Refs. 7, 10, 22, and 69–73. According to Eqs. (39) and (57), the permutation and point-group projection operations can be translated to a parameter transformation of the ECG function and do not require the calculation of (mathematically) new spatial integrals. After construction of the matrices in Eqs. (60)–(63), the point-group symmetry projection is carried out by multiplication with the 16-dimensional (for two electrons) spinor part of the symmetry operator. The summation is performed over the symmetry elements ( $O \in G$ ) of the group according to Eq. (59).

Equation (59) contains both linear ( $c_{ip}$ ,  $i = 1, \dots, N_b$ ,  $p = 1, \dots, 16$ ) and non-linear parameters ( $A_i, s_i$ ,  $i = 1, \dots, N_b$ ) in the basis functions, which can be variationally optimized to improve the (projected or) no-pair relativistic energy [we note also at this point that the currently used kinetic balance condition, Eq. (9), is only an approximation to the mathematically rigorous “atomic” kinetic balance condition, Eq. (8)<sup>74,75</sup>]. The optimal linear parameters are obtained by solving the  $Hc = ESc$ -type generalized eigenvalue equation.

To optimize the non-linear parameters, we minimize the energy (obtained by diagonalization) of the selected (ground or excited) physical state in the spectrum. In contrast to the non-relativistic case, the physical ground-state energy is not the lowest-energy state of the “bare” (unprojected) DC Hamiltonian; lower-energy, often called “positronic” or “negative-energy,” states also appear in the spectrum; hence, the electronic ground state is described by one of the excited states of the eigenvalue equation. Moreover, due to the Brown–Ravenhall disease,<sup>35,76</sup> the electronic ground state appears among the (finite-basis representation of the) electron–positron continuum states. In finite-basis computations and for small nuclear charge numbers, the electronic states are often found to be well separated from the positronic states and only a few positron–electron states “contaminate” the electronic spectrum. In this case, selection of the electronic states is possible based on a threshold energy that can be estimated by a value near (lower than) the non-relativistic energy. We list the computed “bare” DC energies in the [supplementary material](#) (Tables S1–S4), but we consider them only as technical, computational details. The bare DC Hamiltonian is projected and then diagonalized to obtain the physically relevant results, e.g., the ground state energy as the lowest no-pair energy.

The optimization of the non-linear parameters by minimization of the energy for the selected DC state is a central processing unit (CPU)-intensive part in the current implementation. Nevertheless, we ran several refinement cycles of the optimization procedure, but it hardly improved the DC energy in comparison with the DC results obtained with the non-linear (basis) parameters optimized by minimization of the corresponding non-relativistic energy (in low- $Z$  systems). At the same time, it is also worth noting that upon repeated DC energy minimization cycles, the DC energy remained stable, and no sign of a variational collapse or prolapse was observed during the computations, which provides a numerical test (at least for the studied low- $Z$  range) of the current procedure. For these reasons, we may say that the reported no-pair DC energies correspond to a basis set optimized to the non-relativistic energy. If further digits in the low- $Z$  or better results for the higher- $Z$  range are needed, then, the DC optimizer will be further developed.

We have also checked the singlet–triplet mixing by optimizing parameters with relaxing the non-relativistic spatial symmetry as well as by an explicit  $LS$  coupling of spatial functions optimized within their non-relativistic symmetry block and included with the appropriate spin function in the relativistic computation. The triplet contributions were negligibly small for the ground states of the studied low- $Z$  systems. Further details will be reported in the future work.

### III. POSITIVE-ENERGY PROJECTION

#### A. Theoretical aspects and general concepts for the implementation

Due to the Brown–Ravenhall (BR) disease,<sup>35</sup> the negative-energy states of the DC Hamiltonian are eliminated using a projection technique.<sup>37</sup> The fundamental idea of the procedure is based on the solution of the eigenvalue equation of a Hamiltonian without particle–particle (electron–electron) interactions. Without these interactions, the negative- and positive-energy states of the different electrons are not coupled. Therefore, in the non-interacting case, the positive-energy states can be, in principle, selected and used to construct the  $\Lambda^+$  projector as

$$\Lambda^{+[16]} = \sum_{\mu \in E^+} \left| \Psi_{0,\mu}^{(16)} \right\rangle \left\langle \tilde{\Psi}_{0,\mu}^{(16)} \right|. \quad (64)$$

$E^+$  is used to label the physically relevant, “positive-energy” space. In general,  $\left\langle \tilde{\Psi}_{0,\mu}^{(16)} \right|$  is the left eigenvector and  $\left| \Psi_{0,\mu}^{(16)} \right\rangle$  is the right eigenvector of the  $\mu$ th state without particle–particle interactions, and the “0” subindex is used to emphasize that these are non-interacting states. It is necessary to distinguish the left and the right eigenvectors if the underlying non-interacting Hamiltonian is not Hermitian (Sec. III B 1).

We solve the eigenvalue equation of the Dirac–Coulomb Hamiltonian projected onto the positive-energy subspace,

$$\tilde{H}_{DC}^{[16]} = \Lambda^{+[16]} \mathcal{H}_{DC}^{[16]} \Lambda^{+[16]}, \quad (65)$$

where  $\tilde{H}_{DC}^{[16]}$  is the so-called “no-pair” Hamiltonian.<sup>37,42,77</sup>

In order to determine the relativistic energies and wave functions, the matrix representation of the “no-pair” Hamiltonian is constructed over the positive-energy subspace,

$$\tilde{\mathcal{H}}_{\text{DC},\mu\nu}^{[16]} = \left\langle \tilde{\Psi}_{0,\mu}^{(16)} \left| \Lambda^{+[16]} \mathcal{H}_{\text{DC}}^{[16]} \Lambda^{+[16]} \right| \Psi_{0,\nu}^{(16)} \right\rangle = \left\langle \tilde{\Psi}_{0,\mu}^{(16)} \left| \mathcal{H}_{\text{DC}}^{[16]} \right| \Psi_{0,\nu}^{(16)} \right\rangle. \quad (66)$$

After the second equation in Eq. (66), the  $\Lambda^{+[16]}$  projectors have been suppressed since the matrix representation is constructed over the positive-energy eigenfunctions of the non-interacting Hamiltonian. We also note that  $\Lambda^{+[16]}$  was defined with these non-interacting (left- and right-) eigenfunctions, Eq. (64), for which the (bi)orthogonal property applies,

$$\left\langle \tilde{\Psi}_{0,\mu}^{(16)} \left| \Psi_{0,\nu}^{(16)} \right\rangle = \delta_{\mu\nu} 1^{[16]}, \quad (67)$$

where the left and right eigenvectors are understood to be normalized to each other in order to simplify the expressions in Eq. (66).

During the numerical computations, first, the non-interacting problem is solved in the ECG basis. The (left and right) eigenvectors are written as

$$\left| \Psi_{0,\nu}^{(16)} \right\rangle = \sum_{i=1}^{N_b} \sum_{p=1}^{16} c_{\nu,ip}^0 \mathcal{B}^{[16]} 1_p^{(16)} \left| \Theta_i \right\rangle, \quad (68)$$

$$\left\langle \tilde{\Psi}_{0,\mu}^{(16)} \right| = \sum_{j=1}^{N_b} \sum_{p=1}^{16} \tilde{c}_{\mu,jp}^0 \left\langle \Theta_j \right| 1_p^{(16)T} \mathcal{B}^{[16]}, \quad (69)$$

and they are substituted into Eq. (66) to obtain the matrix representation for the no-pair DC Hamiltonian,

$$\tilde{H}_{\text{DC},\mu\nu}^{[16]} = \sum_{ij=1}^{N_b} \sum_{p,q=1}^{16} \tilde{c}_{\mu,iq}^0 c_{\nu,jp}^0 \left\langle \Theta_j \right| 1_q^{(16)T} \mathcal{B}^{(16)} \mathcal{H}_{\text{DC}}^{[16]} \mathcal{B}^{(16)} 1_p^{(16)} \left| \Theta_i \right\rangle. \quad (70)$$

The matrix element  $\left\langle \Theta_j \right| 1_q^{(16)T} \mathcal{B}^{(16)} \mathcal{H}_{\text{DC}}^{[16]} \mathcal{B}^{(16)} 1_p^{(16)} \left| \Theta_i \right\rangle$  is calculated analytically, and the permutation and spatial symmetries are considered according to Secs. II B and II C. The energy and the wave function are obtained by diagonalization of the  $\tilde{H}_{\text{DC}}^{[16]} \in \mathbb{C}^{16N_b \times 16N_b}$  matrix.

In short, the algorithm for computing the no-pair DC energies is as follows:

1. build and diagonalize  $\mathbf{H}_{\text{DC}}^{[16]}$  without the particle–particle interaction and using the ECG basis set,
2. select the  $E^+$ -states,
3. build  $\tilde{\mathbf{H}}_{\text{DC}}^{[16]}$  with particle–particle interaction in the  $E^+$ -subspace using Eq. (70), and
4. diagonalize  $\tilde{\mathbf{H}}_{\text{DC}}^{[16]}$ .

## B. Algorithms for the construction of the positive-energy projector in an explicitly correlated basis

### 1. Projection with the complex-scaling technique

In this section, we adopt the complex-scaling approach, as it was originally proposed by Bylicki, Pestka, and Karwowski<sup>24</sup> for

defining a positive-energy projector, and generalize it to molecules. First of all, similarly to resonance computations,<sup>78–81</sup> complex scaling is employed for the particle coordinates,

$$r_i \rightarrow r_i e^{i\theta}, \quad (71)$$

where  $\theta$  is a real parameter. For atoms,<sup>24</sup> the terms of the Dirac–Coulomb Hamiltonian are rescaled according to the following relations:

$$\sigma_i \frac{\partial}{\partial x_i} \rightarrow \sigma_i \frac{\partial}{\partial x_i} e^{-i\theta}, \quad (72)$$

$$\frac{1}{\sqrt{r^2}} \rightarrow \frac{e^{-i\theta}}{\sqrt{r^2}}, \quad (73)$$

$$\frac{1}{\sqrt{(\mathbf{r}_i - \mathbf{r}_j)^2}} \rightarrow \frac{e^{-i\theta}}{\sqrt{(\mathbf{r}_i - \mathbf{r}_j)^2}}. \quad (74)$$

For molecules, some further considerations are necessary. If the nuclear coordinate is not at the origin, the electron–nucleus interaction operator is not dilatation analytic, i.e.,

$$\frac{1}{\sqrt{(\mathbf{r}_i - \mathbf{R}_l)^2}} \rightarrow \frac{e^{-i\theta}}{\sqrt{(\mathbf{r}_i - \mathbf{R}_l e^{-i\theta})^2}}, \quad (75)$$

and complex integration is required to evaluate the matrix elements. Since the analytic integral expressions are known for  $\theta = 0$ , the expressions can be analytically continued for  $\theta \neq 0$ , similarly to the non-relativistic computations reported in Refs. 80, 82, and 83. Analytic continuation means in this case that the  $\mathbf{R}_l$  nuclear coordinates are replaced with  $\mathbf{R}_l e^{-i\theta}$  in the analytic integral expression. To carry out these types of non-dilatation analytic computations, we have generalized our original (real) ECG integral routines to complex arithmetic to be able to use complex-valued nuclear position vectors.

We have also tested an alternative (at a first sight naive or “wrong”) technique in which the nuclear coordinates are scaled together with the electronic coordinates,

$$\frac{1}{\sqrt{(\mathbf{r}_i - \mathbf{R}_l)^2}} \rightarrow \frac{e^{-i\theta}}{\sqrt{(\mathbf{r}_i - \mathbf{R}_l)^2}}, \quad (76)$$

which obviates the need of using complex arithmetic in the integral routines. However, is this a correct procedure? Well, Moiseyev provides theoretical foundations for this approach<sup>80</sup> within a perturbative framework. Since we have “incorrectly” rotated also the fixed nuclear coordinates, we need to consider a (perturbative) series expansion for the “back rotation” of the nuclear coordinates to the real axis (where they should be since they are treated in this work as fixed external charges),<sup>80</sup>

$$E(\mathbf{R} e^{-i\theta}) = E(\mathbf{R}) + (e^{i\theta} - 1) \sum_I \mathbf{R}_I \frac{\partial E(\mathbf{R}_I)}{\partial \mathbf{R}_A} + \dots, \quad (77)$$

$$\approx E(\mathbf{R}) + i\theta \sum_I \mathbf{R}_I \frac{\partial E(\mathbf{R}_I)}{\partial \mathbf{R}_A} - \theta^2 \sum_I \mathbf{R}_I \frac{\partial E(\mathbf{I})}{\partial \mathbf{R}_A} + \dots \quad (78)$$



Thereby, we may use a dilatation analytic approach with Eq. (76), but then, the resulting energy must be corrected, Eqs. (77) and (78), by accounting for the necessary “back rotation” of the nuclei. At this point, it is important to emphasize that we are interested in the computation of bound states (so, not resonances!), and the complex coordinate scaling is used only to select the positive-energy states computed in an explicitly correlated (non-separable) basis. Therefore,  $\theta$  can take “any” (small) value that is already sufficiently large to distinguish the positive-energy states from the Brown–Ravenhall (electron–positron) states. In practical computations,  $\theta$  is typically of the order of  $\sim 10^{-5}$ , and the “perturbative” correction due to the “back rotation” to the real energy is proportional to  $\theta^2 \sim 10^{-10}$  that gives a (typically) negligible contribution.

For these reasons (and in full agreement with the *a posteriori* analysis of our computational results, Sec. IV), we have

$$\begin{aligned} & \langle \Phi_{jp}^{(16)} | \mathcal{H}_{\text{DC},\theta}^{[16]} | \Phi_i^{(16)} \rangle \\ &= \mathbf{1}_p^{(16)\text{T}} \langle \Theta_j | B^{[16]\dagger} \mathcal{H}_{\text{DC},\theta}^{[16]} B^{[16]} | \Theta_i \rangle d_i^{(16)} \\ &= \mathbf{1}_p^{(16)\text{T}} \begin{pmatrix} \langle \Theta_j | W_{\text{ll},\theta}^{[4]} | \Theta_i \rangle & \frac{e^{-i\theta}}{2m_2} \langle \Theta_j | p_2^2 | \Theta_i \rangle \mathbf{1}^{[4]} & \frac{e^{-i\theta}}{2m_1} \langle \Theta_j | p_1^2 | \Theta_i \rangle \mathbf{1}^{[4]} & 0^{[4]} \\ \frac{e^{-i\theta}}{2m_2} \langle \Theta_j | p_2^2 | \Theta_i \rangle \mathbf{1}^{[4]} & \langle \Theta_j | W_{\text{ls},\theta}^{[4]} | \Theta_i \rangle & 0^{[4]} & \frac{e^{-i\theta}}{8m_1 m_2^2 c^2} \langle \Theta_j | p_1^2 p_2^2 | \Theta_i \rangle \mathbf{1}^{[4]} \\ \frac{e^{-i\theta}}{2m_1} \langle \Theta_j | p_1^2 | \Theta_i \rangle \mathbf{1}^{[4]} & 0^{[4]} & \langle \Theta_j | W_{\text{sl},\theta}^{[4]} | \Theta_i \rangle & \frac{e^{-i\theta}}{8m_1^2 m_2 c^2} \langle \Theta_j | p_1^2 p_2^2 | \Theta_i \rangle \mathbf{1}^{[4]} \\ 0^{[4]} & \frac{e^{-i\theta}}{8m_1 m_2^2 c^2} \langle \Theta_j | p_1^2 p_2^2 | \Theta_i \rangle \mathbf{1}^{[4]} & \frac{e^{-i\theta}}{8m_1^2 m_2 c^2} \langle \Theta_j | p_1^2 p_2^2 | \Theta_i \rangle \mathbf{1}^{[4]} & \langle \Theta_j | W_{\text{ss},\theta}^{[4]} | \Theta_i \rangle \end{pmatrix} d_i^{(16)}, \quad (79) \end{aligned}$$

$$W_{\text{ll},\theta}^{[4]} = (e^{-i\theta} V + U_\theta) \mathbf{1}^{[4]}, \quad (80)$$

$$W_{\text{ls},\theta}^{[4]} = \frac{1}{4m_2^2 c^2} \sum_{ij=1}^3 p_{2i} (e^{-i\theta} V + U_\theta) p_{2j} \sigma_{2i}^{[4]} \sigma_{2j}^{[4]} - \frac{1}{2m_2} p_2^2 \mathbf{1}^{[4]}, \quad (81)$$

$$W_{\text{sl},\theta}^{[4]} = \frac{1}{4m_1^2 c^2} \sum_{ij=1}^3 p_{1i} (e^{-i\theta} V + U_\theta) p_{1j} \sigma_{1i}^{[4]} \sigma_{1j}^{[4]} - \frac{1}{2m_1} p_1^2 \mathbf{1}^{[4]}, \quad (82)$$

$$\begin{aligned} W_{\text{ss},\theta}^{[4]} &= \frac{1}{16m_1^2 m_2^2 c^4} \sum_{ij,k,l=1}^3 p_{1i} p_{2j} (e^{-i\theta} V + U_\theta) p_{2k} p_{1l} \sigma_{1i}^{[4]} \sigma_{1l}^{[4]} \sigma_{2j}^{[4]} \sigma_{2k}^{[4]} \\ &\quad - \frac{(m_1 + m_2)}{8m_1^2 m_2^2 c^2} p_1^2 p_2^2 \mathbf{1}^{[4]}. \quad (83) \end{aligned}$$

If  $U_\theta$  is treated as a non-dilatation analytic operator, it is transformed according to Eq. (75). If it is used in a dilatation analytic procedure, then,  $U_\theta = e^{-i\theta} U$ , Eq. (76). We also note that Eqs. (79)–(83) recover Eqs. (27)–(32) for  $\theta = 0$ .

In what follows, we explain in detail how the complex coordinate rotation affects the non-interacting DC spectrum. Figure 1 highlights an essential feature of the complex-scaled DC energies that makes it possible to unambiguously identify and select the positive-energy states. Figure 1(a) visualizes the energies of the

considered only the zeroth-order term in Eq. (77) and the  $\theta \rightarrow 0$  limit.

If we wanted to compute a resonance state, we cannot consider, in general, the small  $\theta$  limit since a specific finite  $\theta$  value corresponds to the stabilization of the (complex) resonance energy,<sup>80</sup> and in that case, (higher-order) correction terms of the series expansion, (77), would be necessary to obtain good results. Therefore, for resonance computations, the non-dilatation-analytic route, Eq. (75), appears to be the more practical choice although the dilation-analytic approach is also acceptable, in principle.

Using Eqs. (27)–(32), the complex-scaled matrix element for two electrons can be written in the following form (we note that the kinetic balance, Eq. (24), is related to the basis set, and so, it is not included in the complex scaling):

unbound states for a single particle (either free or in interaction with a fixed, positive point charge with a charge number,  $Z < \frac{\sqrt{3}}{2\alpha} 61$ ). In the single-electron spectrum, the “positronic” (negative-energy) and “electronic” (positive-energy) parts can be clearly identified since they are separated by a finite energy gap. If we apply the complex coordinate scaling, Eq. (71), the unbound positron and electron states rotate about different energy “centers” in the complex plane,<sup>84</sup> and they are visualized by the dashed (blue and red) curves in the figure.

If we use a non-separable (explicitly correlated) basis, we also need to consider the behavior of two non-interacting particles [Fig. 1(b)]. In such a basis, we can compute only the two-electron states (of the non-interacting system). The non-interacting, two-electron energy is the sum of the one-electron energies, but the one-electron energies are not obtained explicitly in the computation. Due to the presence of the continuum both in the positronic and in the electronic parts, the two-electron energy spectrum covers the entire real axis [green, solid line in Fig. 1(b)]. Then, we consider the effect of the complex scaling. For “any” finite  $\theta$  angle, three branches appear in the complex plane, depending on the sign of the one-particle contributions to the (non-interacting) two-particle energy. According to the different branches in the complex energy plane, the electron–electron (positive-energy), electron–positron [also called Brown–Ravenhall (BR)], and positron–positron states can be identified.<sup>23,24</sup>

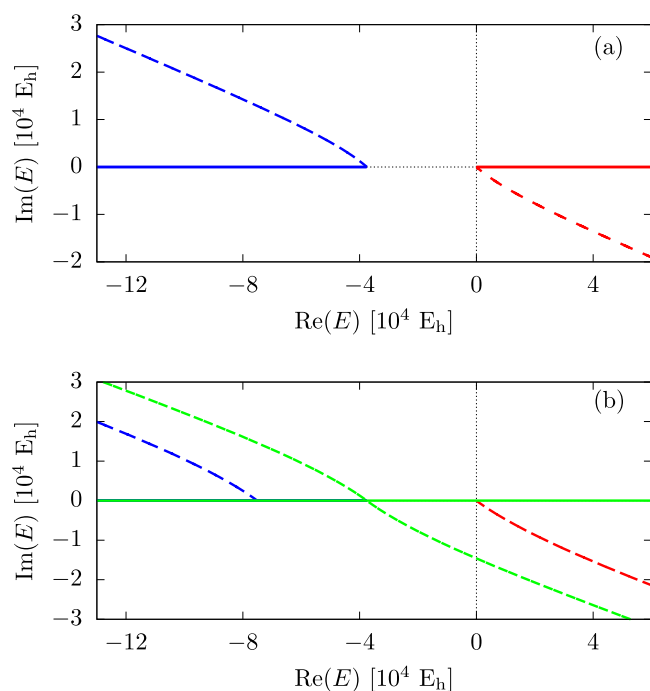


**FIG. 1.** Visualization of the complex-scaling technique to select the positive-energy states of the non-interacting two-electron system: (a) unbound single-particle energies for  $\theta = 0$  (solid) and for some finite  $\theta > 0$  (dashed) values and (b) unbound non-interacting two-particle energies for the same angles. The red, green, and blue colors indicate the electron–electron, electron–positron (or Brown–Ravenhall), and positron–positron states, respectively.

In the next step, the Hamiltonian matrix for the system with interactions is constructed for the  $\theta$  value for which the positive-energy states had been identified and the positive-energy projection can be carried out. In the last step, the “no-pair” energies are obtained by diagonalization of the projected matrix.

Identification of the positive-energy states was automated using the linear relationship<sup>24</sup> that can be derived based on the behavior of the one- and two-electron energies in the complex plane upon the complex scaling of the coordinate,

$$f[\text{Re}(E)] = -\tan \theta \text{Re}(E) + mc^2. \quad (84)$$

The intercept is set to be halfway between the centers of the positron–electron and electron–electron branches, while the slope is parallel with the asymptotic, large  $\text{Re}(E)$ , behavior of the complex eigenvalues.<sup>84</sup> During the selection procedure, state  $\mu$  is identified as a positive-energy state if the  $\text{Im}(E_\mu) > f[\text{Re}(E_\mu)]$  condition is satisfied.

The projected energy was examined for different  $\theta$  values. In general, it was found to be insensitive to the precise value of the  $\theta$  rotation angle until  $\theta$  remained small. For large  $\theta$  values, finite basis set effects become important. For very small  $\theta$ , distinction of the three branches becomes problematic in the finite (double or quadruple) precision arithmetic. At the same time, the results were sensitive to the number of states included in the projector. Therefore, in practice, the selection was carried out according to the linear  $f[\text{Re}(E)]$

relation with the additional constraint to keep the number of positive energy states fixed for every angle.

If we assume that the number of the one-particle positronic and electronic states is equal, the number of the electron–electron states can be fixed to the quarter of the total number of states,  $4N_b$ . We note that in practical computations, the selection of a few points was not entirely unambiguous based on the  $f[\text{Re}(E)]$  linear relation, and this additional “constraint” implemented in the automated procedure was necessary to have consistent results.

In the algorithm, we first sorted the states according to the distance of their (complex) energy from the  $f[\text{Re}(E)]$  line, and then, we kept the first  $4N_b$  states in this list to define the positive-energy space.

## 2. Projection with “cutting” in the energy

For small nuclear charges, the relativistic “effects” are “small” in comparison with the non-relativistic energy. In this case, the positive-, the BR, and the negative-energy regions of the spectrum are well separated in a non-interacting, finite basis computation. In this case, the positive-energy space can be selected, in practice, from the non-interacting, two-electron computation by retaining the non-interacting states with (real) energies (without any complex scaling) that are larger than an estimated energy threshold. We will refer to this projection technique as “cutting” (in the energy spectrum).

The deficiency of this simple approach becomes apparent if the nuclear charge and/or the number of basis functions is increased. Then, there are electron–positron states that contaminate the electron–electron part of the space, and the corresponding BR states may appear as the lowest state of the (imperfectly) projected Hamiltonian. At the same time, we note that this simple “cutting” projector worked remarkably well for most of the low- $Z$  systems studied in this paper and in Paper II.<sup>25</sup> The cutting projector has the advantage that it uses only real integral routines, and due to the hermiticity of the problem, the energy (and the underlying basis set) can be optimized variationally (until contaminant states appear). We used the “cutting” projector for exploratory computations, and we have checked the final results using the, in principle, rigorous complex coordinate rotation (CCR) projection procedure (that confirmed all significant digits of the cutting projection for the studied low- $Z$  systems in this work and in Refs. 25 and 55).

## 3. Projection with “punching” in the energy list

Since the excellent results can be obtained with very small CCR angles (Tables I and II), we have experimented with discarding the states in the  $\theta \rightarrow 0$  limit (followed numerically) for every state labeled a BR state in the CCR projection procedure. In practice, we have discarded all states that have an energy less than an energy threshold, and we “punched out” all higher-energy states from the positive-energy list that corresponded to a state identified as a BR state in the CCR procedure. This “punching” projector ideally combines the good features of cutting (hermiticity) and CCR (rigorous identification of the BR states). Its numerical performance and any disadvantages can be explored for higher- $Z$  systems (where the simple “cutting” projector fails), which is left for future work.

**TABLE I.** Testing the positive-energy projection techniques for the Dirac–Coulomb energy of the ground state of the helium atom: comparison of the dilatation analytic ( $E_{\text{DC}}^{\text{da}}$ ) and the energy cutting ( $E_{\text{DC}}^{\text{cutting}}$ ) techniques.  $N_b = 300$  ECG basis functions are used with double-precision arithmetic. All energy values are in  $E_h$ .

$\theta$	proj = da( $\theta$ )	
	Re( $E_{\text{DC}}^{\text{proj}}$ )	Im( $E_{\text{DC}}^{\text{proj}}$ )
0.000 000 01	−2.903 856 630 628	$1.47 \cdot 10^{-17}$
0.000 000 1	−2.903 856 630 628	$1.47 \cdot 10^{-16}$
0.000 001	−2.903 856 630 628	$1.47 \cdot 10^{-15}$
0.000 01	−2.903 856 630 628	$1.47 \cdot 10^{-14}$
0.000 1	−2.903 856 630 628	$1.47 \cdot 10^{-13}$
0.001	−2.903 856 630 628	$1.46 \cdot 10^{-12}$
0.01	−2.903 856 630 656	$1.61 \cdot 10^{-11}$
0.1	−2.903 856 632 538	$1.29 \cdot 10^{-9}$
0.2	−2.903 856 632 442	$2.62 \cdot 10^{-9}$
0.5	−2.903 856 823 509	$-3.57 \cdot 10^{-7}$
Proj = cutting:	−2.903 856 630 628	0

#### 4. An attempt to perform projection based on a determinant expansion

In Subsection III B 1–3, the positive-energy states were selected directly from the solution of the non-interacting Hamiltonian using ECG basis functions. At the same time, a non-separable, explicitly correlated basis set is not an ideal choice for describing the non-interacting system that is not correlated. States of the non-interacting system are more naturally represented by anti-symmetrized products of one-particle functions, i.e., *determinants*, in which apart from the permutational anti-symmetrization there is no correlation between the electrons. Of course, using determinants

for describing interacting electrons leads to a less accurate representation in comparison with an explicitly correlated basis. For this reason, it appears to be necessary to use two different basis sets, one for describing the interacting and another set for describing the non-interacting states. We outline some early attempts to combine the two worlds, but without reporting any numerical results, because we think that some further considerations will be necessary for an efficient approach. The accuracy of this route is currently limited by the size of the determinant space.<sup>49,54</sup>

Along this route, first, the single-electron Dirac Hamiltonian (corresponding to a fixed nuclear geometry) is solved using a floating Gaussian basis. Then, only those functions are retained for which the one-particle energy belongs to the purely electronic (positive-energy) states,

$$|\varphi_i^{+(4)}\rangle = \sum_{j=1}^{n_b} \sum_{p=1}^4 d_{jip+} \mathcal{B}^{[4]} \mathcal{S}_B^{[4]} \mathbf{1}_p^{(4)} |\chi_j\rangle, \quad (85)$$

where  $|\chi_j\rangle$  is the floating Gaussian function,  $n_b$  is the number of the one-particle basis functions,  $\mathcal{B}^{[4]}$  is a metric tensor corresponding to the kinetic balance condition, Eq. (12), and  $\mathcal{S}_B^{[4]}$  ensures the one-particle spatial symmetry, Eqs. (47)–(51). The two-particle determinant is constructed using the Tracy–Singh product as

$$|\Phi_{ij}^{\text{D}+(16)}\rangle = \mathcal{A}^{[16]} \left( |\varphi_i^{+(4)}\rangle \boxtimes |\varphi_j^{+(4)}\rangle \right). \quad (86)$$

Substituting Eq. (85) into Eq. (86), we can obtain the determinant (D) expansion in the Gaussian spinor basis,

$$|\Phi_{ij}^{\text{D}+(16)}\rangle = \sum_{k,l=1}^{n_b} \sum_{p=1}^{16} d_{kl,ijp+} \mathcal{A}^{[16]} \mathcal{B}^{[16]} \mathcal{S}_B^{[16]} \mathbf{1}_p^{(16)} |X_{kl}\rangle, \quad (87)$$

where the following notation was introduced:

$$|X_{kl}\rangle = |\chi_k\rangle |\chi_l\rangle, \quad (88)$$

**TABLE II.** Testing the positive-energy projection techniques for the Dirac–Coulomb energy of the  $\text{H}_2$  molecule with fixed protons ( $R_{\text{pp}} = 1.4$  bohrs): comparison of the dilatation analytic ( $E_{\text{DC}}^{\text{da}}$ ), non-dilatation analytic ( $E_{\text{DC}}^{\text{nda}}$ ), and energy cutting ( $E_{\text{DC}}^{\text{cutting}}$ ) techniques.  $N_b = 700$  ECG basis functions are used with quadruple-precision arithmetic. All energy values are in  $E_h$ .

$\theta$	proj = nda( $\theta$ )		proj = da( $\theta$ )	
	Re( $E_{\text{DC}}^{\text{proj}}$ )	Im( $E_{\text{DC}}^{\text{proj}}$ )	Re( $E_{\text{DC}}^{\text{proj}}$ )	Im( $E_{\text{DC}}^{\text{proj}}$ )
0.000 000 000 1	−1.174 489 753 666	$4.86 \cdot 10^{-17}$	−1.174 489 753 666	$7.14 \cdot 10^{-11}$
0.000 000 001	−1.174 489 753 666	$4.86 \cdot 10^{-16}$	−1.174 489 753 666	$7.14 \cdot 10^{-10}$
0.000 000 01	−1.174 489 753 666	$4.86 \cdot 10^{-15}$	−1.174 489 753 666	$7.14 \cdot 10^{-9}$
0.000 000 1	−1.174 489 753 666	$4.86 \cdot 10^{-14}$	−1.174 489 753 666	$7.14 \cdot 10^{-8}$
0.000 001	−1.174 489 753 666	$4.86 \cdot 10^{-13}$	−1.174 489 753 666	$7.14 \cdot 10^{-7}$
0.000 01	−1.174 489 753 670	$4.86 \cdot 10^{-12}$	−1.174 489 753 667	$7.14 \cdot 10^{-6}$
0.000 1	−1.174 489 754 085	$4.86 \cdot 10^{-11}$	−1.174 489 753 731	$7.14 \cdot 10^{-5}$
0.001	−1.174 489 796 132	$3.93 \cdot 10^{-11}$	−1.174 489 760 167	$7.14 \cdot 10^{-4}$
0.002	−1.174 489 935 051	$3.80 \cdot 10^{-10}$	−1.174 489 779 671	$1.43 \cdot 10^{-3}$
0.003	−1.174 489 319 219	$-2.21 \cdot 10^{-8}$	−1.174 489 812 176	$2.14 \cdot 10^{-3}$
proj = cutting:	−1.174 489 753 666	0		

$$d_{kl,ijr+} = \sum_{p,q=1}^4 d_{kip+} d_{ljq+} 1_r^{(16)\text{T}} \left[ 1_p^{(4)} \boxtimes 1_q^{(4)} \right]. \quad (89)$$

Multiplying Eq. (87) with an ECG, Eq. (23), from the left, we obtain

$$\begin{aligned} \left\langle \Phi_{qp}^{(16)} \left| \Phi_{ij}^{\text{D}+(16)} \right. \right\rangle &= \sum_{k,l=1}^{n_b} \sum_{q=1}^{16} d_{kl,ijq+} 1_p^{(16)\text{T}} \\ &\times \underbrace{\left\langle \Theta_q \left| \mathcal{B}^{[16]} \mathcal{B}^{[16]} \mathcal{A}^{[16]} \mathcal{S}_B^{[16]} \right| \chi_{kl} \right\rangle}_{S_{q,kl}^{[16]}} 1_q^{(16)}. \quad (90) \end{aligned}$$

Then, we expand  $\left| \Phi_{ij}^{\text{D}+(16)} \right\rangle$  in terms of the ECGs and multiply the expansion from the left with an ECG function, Eq. (23), and obtain an alternative expression for Eq. (90),

$$\begin{aligned} \left\langle \Phi_{qp}^{(16)} \left| \Phi_{ij}^{\text{D}+(16)} \right. \right\rangle &= \sum_{k=1}^{n_b} \sum_{q=1}^{16} c_{ij,kq} 1_p^{(16)\text{T}} \\ &\times \underbrace{\left\langle \Theta_q \left| \mathcal{B}^{[16]} \mathcal{B}^{[16]} \mathcal{A}^{[16]} \mathcal{S}_B^{[16]} \right| \Theta_k \right\rangle}_{S_{q,k}^{[16]}} 1_q^{(16)}. \quad (91) \end{aligned}$$

Since the right-hand sides of Eqs. (90) and (91) are equal, we obtain the expansion coefficients as

$$c_{ij,mr} = \sum_{p=1}^{N_b} \sum_{k,l=1}^{n_b} \sum_{q=1}^{16} d_{kl,ijq+} 1_r^{(16)\text{T}} \left( S^{[16]} \right)_{mp}^{-1} S_{p,kl}^{[16]} 1_q^{(16)}. \quad (92)$$

Using these coefficients, we can define the positive-energy space for the ECG basis while maintaining a Hermitian formulation and at the same time, in principle, accounting for explicit correlation necessary for the ppb convergence for the energy of the interacting system. Equation (91) is critical in this approach that is exact only in the complete basis limit. Moreover, the spaces expanded by the determinants and the ECGs are not the same. Calculating the rest of the space by including the negative-energy solutions in the ECG basis, we have found that it has a non-zero overlap with the positive-energy space. At the same time, this overlap disappears in the complete basis limit. Apparently, there is no unique way to treat this overlapping space. For exploratory computations (not reported in this work), we have used Eq. (92), where the full overlapping space is a part of the positive-energy space.

## IV. NUMERICAL RESULTS

### A. Dirac-Coulomb energy for the helium atom

#### 1. Computational details

The relativistic ground state of helium is dominated by  $1S^e$ -type functions (where “e” is for even parity) that were generated by minimizing the non-relativistic ground-state energy. We used ECG functions, Eq. (25), with  $s = 0$  to represent the spherical symmetry of the  $S^e$ -type functions. For the largest basis set sizes,  $N_b = 300$  and 400, the non-relativistic ground-state energy was converged within 1 nE<sub>h</sub> of the reference value.<sup>85</sup> The computations with these functions were made efficient by making use of the symmetry of the spatial ( $s = 0$ ) and the singlet spin functions (further details are provided in the [supplementary material](#)). We have performed repeated refinement cycles of the basis function parameterization

by minimization of the projected DC energy. Although these refinement cycles improved the projected DC energy for small basis sets, for larger basis set sizes ( $N_b > 200$ ), the change was a fraction of a nE<sub>h</sub>.

Regarding the contribution of  $3P^e$ -type functions, we have generated additional  $s \neq 0$  basis functions selected based on the minimization condition of the no-pair DC energy. The contributions of these functions were less than the current 1 nE<sub>h</sub> convergence goal. Further details regarding the triplet contributions will be reported in future work.

In all computations, we used the speed of light as  $c = \alpha^{-1} a_0 E_h / \hbar$  with  $\alpha^{-1} = 137.035999084$ .<sup>86</sup>

### 2. Comparison of the energy cutting and the CCR projector

During our work, we have noticed (in agreement with Karwowski *et al.*<sup>23,87,88</sup>) that for small  $Z$  values, the positive-, the BR-, and the negative-energy non-interacting states are well separated. Hence, the simple “cutting” projector can be expected to work well.

Table 1 shows the comparison of the projected DC energies obtained with the cutting and the dilatation analytic (da) CCR projector for several rotation angles. Regarding the CCR projector, it is important to note that the no-pair DC Hamiltonian is bounded from below (see also the more detailed and precise discussion in Sec. III), and thus, we can aim to compute bound states. Hence, the complex coordinate rotation is used only to be able to distinguish the different non-interacting “branches.” Any rotation angle is appropriate (and gives the “same” numerical value for the bound-state energy) that is large enough—therefore, we can separate the non-interacting branches and at the same time that is not too large—therefore, the finite basis set error remains small. For the present example (Table 1), “small” means  $\theta \leq 0.01$ . For the different “small”  $\theta$  values, the imaginary part of the energy oscillates around 0 (and by using quadruple precision in the computations, we get numerical values closer to 0). In all computations, the cutting projector could be unambiguously defined. The result of the energy-cutting procedure agrees to 10–11 digits with the da-CCR energy ( $\theta \leq 0.01$ ).

Of course, all results should be understood with respect to the no-pair Hamiltonian that is defined by the selected non-interacting states. Throughout this work, the non-interacting reference system is the one-electron problem in the field of the fixed nucleus (nuclei). We have tested the use of other reference systems. The discussion is left for future work to be considered in relation with the QED (pair-) corrections, e.g., which reference system minimizes the corrections or which one offers the most practical option for the implementation of the corrections.

### 3. Comparison with literature data

The no-pair DC energy obtained in this work for the helium ground state is  $-2.903856631 E_h$ , and it is considered to be converged of the order of 1 nE<sub>h</sub> (see also the [supplementary material](#)). The no-pair DC energy (corresponding to the same non-interacting model) reported by Bylicki, Pestka, and Karwowski<sup>24</sup> is  $-2.90385687 E_h$ . If all digits are significant for helium in Ref. 24, then, the following considerations can be made regarding the deviation from our no-pair DC energy.

On the one hand, Karwowski *et al.* considered the exact relativistic coalescence condition,<sup>19,20</sup> which is not accounted for in the

ECG basis set used in this work. They report the effect of the singularity of the exact DC wave function at the coalescence point to be relevant for the tenth significant digit for the  $Z > 10$  range of heliumlike ions (the “effect” of the coalescence condition was reported only for this  $Z$  range in the paper).<sup>89</sup>

On the other hand, they used an iterative kinetic balance condition that is different from the restricted balance used in the present work. Furthermore, they represented the large–large, large–small, and small–small subspaces by separate basis sets and checked the quality of the representation for the non-relativistic limit by solving the Lévy–Leblond equation.<sup>65</sup>

In our work, the construction of the large–small model spaces and the kinetic balance condition ensured an exact fulfillment of the non-relativistic limit although our kinetic balance condition can be considered as an approximation to the two-particle “relativistic” kinetic balance condition of Ref. 63 that is expected to provide a better representation of the negative-energy states than our balance. The effect of this difference for a positive-energy projected, i.e., no-pair computation remains to be explored in future work.

Furthermore, in a strict mathematical sense, neither the restricted, nor the relativistic,<sup>63</sup> nor the iterative<sup>88</sup> kinetic balance conditions are complete, and only the use of the atomic balance would ensure a rigorous variational property in a strict mathematical sense.<sup>61</sup> This also means that for the projected (no-pair) energies of this work (also Ref. 55) and of Ref. 24, the positive-energy projectors constructed from the “quasi-variational” non-interacting computations may, in principle, contain a very small amount of negative-energy contamination (due to the approximate kinetic balances), resulting in slightly different “quasi-variational” energy values. It is necessary to note, however, that we have never experienced any sign of a variational collapse in our no-pair computations (that would be a clear indication of a negative-energy pollution). At the same time, “prolapse” may occur that would be difficult to notice; nevertheless, it might be responsible for the small deviation of the projected energy of this work and of Ref. 24. To better explore these aspects, we plan to test both the dual balance<sup>46</sup> as well as the relativistic kinetic balance<sup>63</sup> techniques in future work. The implementation of the iterative kinetic balance approach of Karwowski *et al.* does not appear immediately straightforward for us. The application of the rigorous atomic balance does not seem to be feasible neither, in spite of a demonstration of its numerical applicability for a simple system.<sup>74</sup>

Comparison of our no-pair DC energies with respect to precise energy values from the nrQED theory is provided in Sec. IV C.

## B. Dirac–Coulomb energy for the H<sub>2</sub> molecule

### 1. Computational details

The no-pair DC ground state is dominated by the  $^1\Sigma_g^+$  spin-spatial functions, and the contribution of triplet  $^3\Pi_g$  and  $^3\Sigma_g^-$ -type functions is estimated to be smaller than the current  $1\text{ nE}_h$  convergence goal. Further details will be reported in future work. To carry out the computations with the dominant singlet  $\Sigma_g^+$ -type functions, we have fixed the  $s$  shift vectors of the ECGs on the interprotonic axis. In this case, the Hamiltonian matrix can be block diagonalized during the computation. The convergence of the energy with respect to the number of basis functions is shown in the [supplementary material](#).

### 2. Comparison of the energy cutting, dilatation analytic CCR, and non-dilatation analytic CCR projectors

The energies obtained from the non-dilatation analytic and dilatation analytic complex-scaling approaches are compared in Table II. We note that it was necessary to use quadruple precision to observe the smooth behavior at the sub- $\text{nE}_h$  scale as it is shown in the table. The non-dilatation analytic energies of H<sub>2</sub> (for various, small  $\theta$  angles) have a (numerically) zero imaginary part since they correspond to bound states. This behavior is similar to the dilatation analytic computation of the helium atom. At the same time, we have carried out dilatation analytic computations also for the H<sub>2</sub> molecule that can be rigorously interpreted with a perturbative “back” rotation (Sec. III B 1). It is interesting to note that the real parts of the energy of the non-dilatation analytic and dilatation analytic cases agree to 13 significant digits, but the imaginary parts are different. The imaginary part of the dilatation analytic energy is proportional to the  $\theta$  rotation angle, and we would get the correct zero value if we employed the perturbative correction for the “back rotation,” Eq. (78). We note that this perturbative correction for the real part of the energy is proportional to  $\theta^2$  that is very small for small  $\theta$  values. In this example, it was sufficient to use a  $\theta$  value as small as  $10^{-10}$  for the distinction of the positive-energy non-interacting branch from the BR and the negative-energy non-interacting states.

Both the dilatation analytic and the non-dilatation analytic energies agree better than a ppb precision with the energy obtained by the energy “cutting” approach. During the computations, we have observed some numerical sensitivity of the non-dilatation-analytic approach with respect to the  $\theta$  rotation angle. This increased numerical uncertainty probably originates from the higher numerical uncertainty of the complex-valued Coulomb-type integrals. In our current implementation, the complex incomplete gamma function used in the complex Coulomb integrals can be evaluated only with 12 digit precision.

### C. Comparison of the variational no-pair Dirac–Coulomb energy with perturbative results

For the low- $Z$  range of atomic and molecular physics, the most precise computations including relativistic and QED corrections have been obtained by perturbative methods. For this reason, we compare the variational no-pair DC energy computed in this work with the perturbative values. It was observed in Ref. 55 that the variational and leading-order perturbative energies differ substantially already for the lowest  $Z$  systems (see also  $E_{\text{DC}}^{\text{proj}}$  vs  $E_{\text{DC}}^{(2)}$  in Table III).

To better understand the origin of this difference, we consider the various physical contributions in the leading-order (non-radiative) QED corrections,  $\mathcal{O}(\alpha^3)$ , of the perturbative scheme first derived by Araki<sup>92</sup> and Sucher.<sup>36</sup> Sucher<sup>36</sup> reported the contributing terms in detail, and the no-pair correction for the exchange of two Coulomb photons can be identified in his calculation that is present in the current variational treatment. Of course, the variational no-pair computation contains not only two-photon exchanges but also the full “Coulomb ladder” with the complete Dirac kinetic energy operator. Nevertheless, we may expect that the two-photon exchange is the most important, “leading-order” correction to the leading-order perturbative relativistic energy.

**TABLE III.** Comparison of the variational no-pair DC energies,  $E_{\text{DC}}^{\text{proj}}$  in  $E_{\text{h}}$ , computed in this work and the perturbative energies,  $E_{\text{DC}}^{(2)}$  and  $E_{\text{DC}}^{(3)}$  in  $E_{\text{h}}$ , including the  $\alpha^2$ -order Foldy–Wouthuysen DC correction,  $\epsilon_{\text{DC}}^{\text{FW}}$ ,<sup>42</sup> and the  $\alpha^3$ -order no-pair two-photon Coulomb correction,  $\epsilon_{\text{CC}}^{++}$ ,<sup>36</sup> for the example of the ground and the first excited states of the helium atom and for the ground state of the  $\text{H}_2$  molecule ( $R_{\text{pp}} = 1.4$  bohrs) and the  $\text{H}_3^+$  molecular ion ( $R_{\text{pp}} = 1.65$  bohrs). The deviation,  $\delta = E_{\text{DC}}^{\text{proj}} - E_{\text{DC}}^{(n)}$  ( $n = 2$  and  $3$ ), is shown in braces as  $\{\delta/nE_{\text{h}}\}$ . The no-pair energies,  $E_{\text{DC}}^{\text{proj}}$ , are converged of the order of  $2 \text{ nE}_{\text{h}}$ ; further work with quadruple precision arithmetic will be necessary to confirm and improve upon this value.

	He ( $1^1\text{S}_0$ )	He ( $2^1\text{S}_0$ )
$E_{\text{DC}}^{\text{proj}}$	-2.903 856 631	-2.146 084 791
$E_{\text{DC}}^{(2)} = E_{\text{nr}} + \alpha^2 \epsilon_{\text{DC}}^{\text{FW}^{\text{a}}}$	-2.903 856 486 $\{-145\}$	-2.146 084 769 $\{-22\}$
$E_{\text{DC}}^{(3)} = E_{\text{nr}} + \alpha^2 \epsilon_{\text{DC}}^{\text{FW}} + \alpha^3 \epsilon_{\text{CC}}^{++^{\text{a}}}$	-2.903 856 620 $\{-11\}$	-2.146 084 780 $\{-11\}$
$\alpha^4 \epsilon_{\text{non-rad}}^{\text{b}}$	$\{-10.4\}$	$\{-11.2\}$
	$\text{H}_2$	$\text{H}_3^+$
$E_{\text{DC}}^{\text{proj}}$	-1.174 489 754	-1.343 850 527
$E_{\text{DC}}^{(2)} = E_{\text{nr}} + \alpha^2 \epsilon_{\text{DC}}^{\text{FW}^{\text{a}}}$	-1.174 489 733 $\{-21\}$	-1.343 850 503 $\{-24\}$
$E_{\text{DC}}^{(3)} = E_{\text{nr}} + \alpha^2 \epsilon_{\text{DC}}^{\text{FW}} + \alpha^3 \epsilon_{\text{CC}}^{++^{\text{a}}}$	-1.174 489 754 $\{0\}$	-1.343 850 525 $\{-1\}$
$\alpha^4 \epsilon_{\text{non-rad}}^{\text{b}}$	$\{-0.2\}$	$\{\text{n.a.}\}$

<sup>a</sup>We used  $\epsilon_{\text{DC}}^{\text{FW}} = -\frac{1}{8} \sum_{i=1}^N \langle \nabla_i^4 \rangle + \frac{\pi}{2} \sum_{i=1}^N \sum_{A=1}^N Z_A \langle \delta(r_{iA}) \rangle - \pi \sum_{i=1}^N \sum_{j>i}^N \langle \delta(r_{ij}) \rangle$ ,<sup>42</sup> and  $\epsilon_{\text{CC}}^{++} = -(\frac{\pi}{2} + \frac{\pi}{3}) \langle \delta(r_{ij}) \rangle$ .<sup>36</sup> The expectation values used to calculate the correction terms were taken from Refs. 5, 22, 85, and 90.

<sup>b</sup>The full non-radiative correction of order  $\alpha^4$  for He ( $1^1\text{S}_0$  and  $2^1\text{S}_0$ ) and  $\text{H}_2$  (ground state,  $R_{\text{pp}} = 1.4$  bohrs) was taken from Refs. 91 and 5, respectively. (It is not evaluated for  $\text{H}_3^+$  yet.)

In Table III, we compare the no-pair variational and perturbative results for the singlet ground and first excited state of the helium atom and for the ground electronic state of the  $\text{H}_2$  and  $\text{H}_3^+$  molecular systems near their equilibrium configuration. For  $\text{H}_2$  and  $\text{H}_3^+$ , the inclusion of the  $\mathcal{O}(\alpha^3)$  two-photon correction reduces the  $-21$  and  $-24 \text{ nE}_{\text{h}}$  deviation of the variational and perturbative energies to  $0$  and  $-1 \text{ nE}_{\text{h}}$ , respectively. Inclusion of the same correction in the perturbative energy of the  $1^1\text{S}_0$  and  $2^1\text{S}_0$  states of the helium atom reduces the  $-145$  and  $-22 \text{ nE}_{\text{h}}$  deviations to  $-11 \text{ nE}_{\text{h}}$  in both cases.

This remaining, still non-negligible difference of the variational and the perturbative DC energies indicate the importance of the perturbative corrections beyond the  $\mathcal{O}(\alpha^3)$  level. For the ground and the first excited singlet states of helium<sup>91</sup> and for the ground state of the  $\text{H}_2$  molecule,<sup>5</sup> the full  $\mathcal{O}(\alpha^4)$  perturbative correction is also available. For this work, the non-radiative part of the correction is relevant that can be clearly identified in Refs. 5 and 91. Further analysis of the non-radiative perturbative corrections that would allow for a direct comparison of the perturbative terms with our present no-pair energies is not available in Refs. 5 and 91. Nevertheless, we show the full non-radiative part of the  $\mathcal{O}(\alpha^4)$  correction in Table III that allows for a “rough” (probably appropriate in terms of an “order-of-magnitude”) comparison with the remaining difference of the no-pair variational DC energy and the corresponding  $\mathcal{O}(\alpha^3)$  perturbative value. The good numerical agreement of the  $E_{\text{DC}}^{\text{proj}} - E_{\text{DC}}^{(3)}$  difference with  $\alpha^4 \epsilon_{\text{non-rad}}$  in Table III is fortuitous, and further developments are necessary for a direct comparison. Furthermore, we think that the variational energies ( $E_{\text{DC}}^{\text{proj}}$  reported in the table) are converged of the order of  $1 \text{ nE}_{\text{h}}$  for  $\text{H}_2$ , for  $\text{H}_3^+$ , and for the  $2^1\text{S}_0$  state of helium and of the order of  $2 \text{ nE}_{\text{h}}$  for the helium ground state ( $1^1\text{S}_0$ ).

Figure 2 shows the comparison of the perturbative and no-pair variational DC energies for two-electron ions (atom), obtained in this work and in Refs. 24 and 93, over the  $Z = 1, \dots, 26$  range of the nuclear charge number.

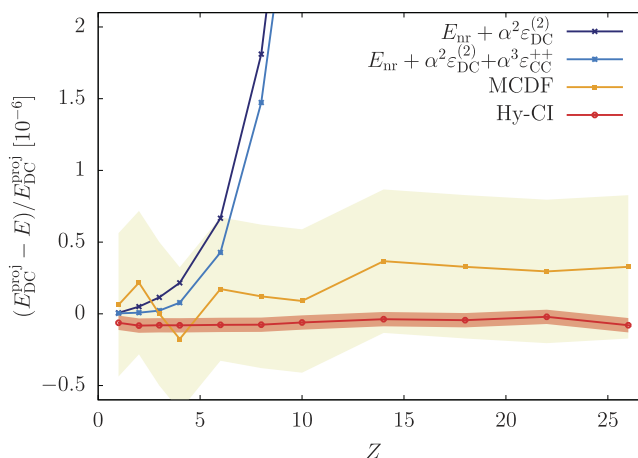


**FIG. 2.** Comparison of the variational no-pair DC energy with perturbative energies for two-electron ions (atom) with respect to the  $Z$  nuclear charge number. The  $E_{\text{DC}}^{\text{proj}}$  energy computed in this work (with a non-relativistically optimized singlet basis set) was used as the reference and literature data are taken from Refs. 24 (Hy-CI) and 93 [multiconfiguration Dirac–Fock (MCDF)]. The perturbative corrections are calculated according to Ref. 36 using expectation values for the operators compiled from Ref. 85 (up to  $Z = 4$ ) or computed in the present work ( $Z > 4$ ) (The data used to prepare this figure is provided in the supplementary material).

Inclusion of the  $\mathcal{O}(\alpha^3)$ -order correction in the perturbative energy reduces the deviation for the lowest  $Z$  values. Nevertheless, the variational-perturbative deviation rapidly increases and indicates the importance of the non-radiative “QED corrections” in the nrQED scheme beyond the  $\mathcal{O}(\alpha^3)$  leading order already in the low  $Z$  range.

The no-pair DC energy can be computed for different  $\alpha$  values that allows us to numerically determine its  $\alpha$  dependence and, thereby, the “leading” and “higher-order” non-radiative QED corrections for the Coulomb interaction and positive-energy states. We have computed  $E_{\text{DC}}^{\text{proj}}(\alpha)$  for 101 different  $\alpha$  values distributed over the  $\alpha \in [0.7, 1.6]\alpha_0$  interval, where  $\alpha_0 = 1/137.035\,999\,084$  is the CODATA18 recommended value.<sup>86</sup> It was possible to fit (Fig. 3) the  $\sum_{n=2}^m c_n \alpha^n$  polynomials to the data points with  $m = 3$  and 4. The  $c_2$  and  $c_3$  coefficients remained stable upon the inclusion of the  $c_4 \alpha^4$  term in the fitted function. It is interesting to note that  $c_4 > c_3$  for all systems studied. For the physically relevant  $\alpha_0$  value, the  $c_4 \alpha^4$  fourth-order term is smaller than the  $c_3 \alpha^3$  third-order contribution. As  $Z$  increases, the relative importance of the higher-order term increases: the fourth-order contribution is only 10% of the third-order term for helium, whereas it is already 50% for  $\text{Be}^{2+}$ . The fitted functions shown in Fig. 3 are “normalized” with  $\langle \delta(\mathbf{r}_{12}) \rangle_{\text{nr}}$  that brings the different systems (helium-isoelectronic ions,  $\text{H}_2$ ,  $\text{H}_3^+$ , and  $\text{HeH}^+$ ) to the same scale in the figure. The third-order contribution is found to be

$$c_3 \alpha^3 = -3.26(1) \langle \delta(\mathbf{r}_{12}) \rangle_{\text{nr}} \alpha^3 \quad (93)$$

in excellent agreement with Sucher’s formal result, which can be found in Eq. (3.99) on p. 52 of Ref. 36,

$$\varepsilon_{\text{CC}}^{++} \alpha^3 = -\left(\frac{\pi}{2} + \frac{5}{3}\right) \langle \delta(\mathbf{r}_{12}) \rangle_{\text{nr}} \alpha^3 \approx -3.24 \langle \delta(\mathbf{r}_{12}) \rangle_{\text{nr}} \alpha^3. \quad (94)$$

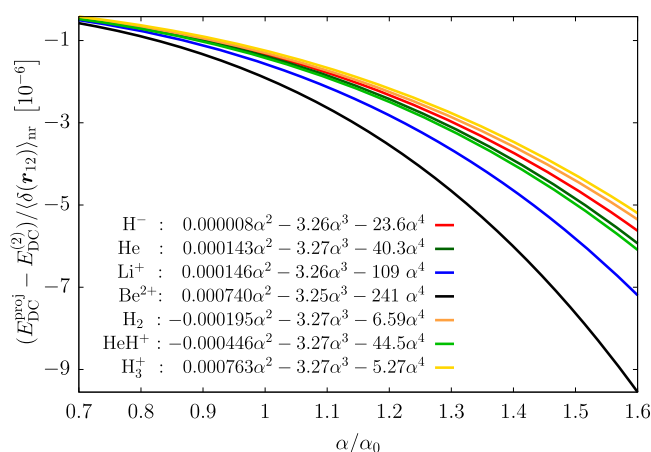


**FIG. 3.** Dependence of the no-pair DC energy,  $E_{\text{DC}}^{\text{proj}}$ , on the value of the  $\alpha$  coupling constant of the electromagnetic interaction. We use Hartree atomic units and  $\alpha_0$  labels  $1/137.035\,999\,084$ .<sup>86</sup> The data points, used for fitting the polynomials, were computed at the  $\alpha = 1/(\alpha_0 + n)$ ,  $n = -50, \dots, 50$ , values. The  $\alpha^2$  leading-order relativistic DC energy values,  $E_{\text{DC}}^{(2)}$ , are compiled from Refs. 22, 55, 85, and 94 (and the contributions are collected in the supplementary material of Paper II).<sup>25</sup>

## V. SUMMARY AND CONCLUSION

Theoretical and algorithmic details are reported for an explicitly correlated, no-pair Dirac–Coulomb framework. Options for positive-energy projection techniques are considered in detail. The computed variational no-pair Dirac–Coulomb energies are compared with the corresponding energy values of the non-relativistic quantum electrodynamics framework for low  $Z$  systems, and it is found that higher-order non-radiative QED corrections become increasingly important for an agreement better than  $1 : 10^9$  beyond  $Z = 1$ . Extension of the present framework with the Breit interaction is reported in Paper II.<sup>25</sup>

## SUPPLEMENTARY MATERIAL

The [supplementary material](#) contains (a) special matrix elements for spherically symmetric and singlet basis functions, (b) convergence of the computed energies, and (c) data for Fig. 2.

## ACKNOWLEDGMENTS

Financial support of the European Research Council through a starting grant (No. 851421) is gratefully acknowledged. D.F. acknowledges a doctoral scholarship from the ÚNKP-21-3 New National Excellence Program of the Ministry for Innovation and Technology from the source of the National Research, Development and Innovation Fund (Grant No. ÚNKP-21-3-II-ELTE-41). We thank the reviewers for their thoughtful comments that helped us to improve this work (Papers I and II).

## AUTHOR DECLARATIONS

### Conflict of Interest

We have no conflict of interest to declare.

## DATA AVAILABILITY

The data that support the findings of this study are available within the article and its [supplementary material](#).

## REFERENCES

- 1 A. Matveev, C. G. Parthey, K. Predehl, J. Alnis, A. Beyer, R. Holzwarth, T. Udem, T. Wilken, N. Kolachevsky, M. Abgrall, D. Rovera, C. Salomon, P. Laurent, G. Grosche, O. Terra, T. Legero, H. Schnatz, S. Weyers, B. Altschul, and T. W. Hänsch, *Phys. Rev. Lett.* **110**, 230801 (2013).
- 2 L. Gurung, T. Babij, S. Hogan, and D. Cassidy, *Phys. Rev. Lett.* **125**, 073002 (2020).
- 3 N. Hölsch, M. Beyer, E. J. Salumbides, K. S. E. Eikema, W. Ubachs, C. Jungens, and F. Merkt, *Phys. Rev. Lett.* **122**, 103002 (2019).
- 4 L. Semeria, P. Jansen, G.-M. Camenisch, F. Mellini, H. Schmutz, and F. Merkt, *Phys. Rev. Lett.* **124**, 213001 (2020).
- 5 M. Puchalski, J. Komasa, P. Czachorowski, and K. Pachucki, *Phys. Rev. Lett.* **117**, 263002 (2016).
- 6 M. Puchalski, J. Komasa, P. Czachorowski, and K. Pachucki, *Phys. Rev. Lett.* **122**, 103003 (2019).
- 7 D. Ferenc, V. I. Korobov, and E. Mátyus, *Phys. Rev. Lett.* **125**, 213001 (2020).
- 8 J. Mitroy, S. Bubin, W. Horiuchi, Y. Suzuki, L. Adamowicz, W. Cencek, K. Szalewicz, J. Komasa, D. Blume, and K. Varga, *Rev. Mod. Phys.* **85**, 693 (2013).
- 9 E. Mátyus and M. Reiher, *J. Chem. Phys.* **137**, 024104 (2012).

- <sup>10</sup>D. Ferenc and E. Mátyus, *J. Chem. Phys.* **151**, 094101 (2019).
- <sup>11</sup>D. M. Fromm and R. N. Hill, *Phys. Rev. A* **36**, 1013 (1987).
- <sup>12</sup>K. Pachucki, *Phys. Rev. A* **86**, 052514 (2012).
- <sup>13</sup>L. M. Wang and Z.-C. Yan, *Phys. Rev. A* **97**, 060501 (2018).
- <sup>14</sup>B. Jeziorski and K. Szalewicz, *Phys. Rev. A* **19**, 2360 (1979).
- <sup>15</sup>Y. Suzuki and K. Varga, *Stochastic Variational Approach to Quantum-Mechanical Few-Body Problems* (Springer, Berlin, Heidelberg; New York, 1998).
- <sup>16</sup>M. Stanke, E. Palikot, and L. Adamowicz, *J. Chem. Phys.* **144**, 174101 (2016).
- <sup>17</sup>M. Stanke, E. Palikot, D. Kędziera, and L. Adamowicz, *J. Chem. Phys.* **145**, 224111 (2016).
- <sup>18</sup>T. Kato, *Commun. Pure Appl. Math.* **10**, 151 (1957).
- <sup>19</sup>W. Kutzelnigg, in *Aspects of Many-Body Effects in Molecules and Extended Systems*, Lecture Notes in Chemistry, edited by D. Mukherjee (Springer, Berlin, Heidelberg, 1989), pp. 353–366.
- <sup>20</sup>Z. Li, S. Shao, and W. Liu, *J. Chem. Phys.* **136**, 144117 (2012).
- <sup>21</sup>K. Pachucki, W. Cencek, and J. Komasa, *J. Chem. Phys.* **122**, 184101 (2005).
- <sup>22</sup>P. Jeszenski, R. T. Ireland, D. Ferenc, and E. Mátyus, *Int. J. Quantum Chem.* (2021).
- <sup>23</sup>G. Pestka, M. Bylicki, and J. Karwowski, *J. Phys. B: At., Mol. Opt. Phys.* **40**, 2249 (2007).
- <sup>24</sup>M. Bylicki, G. Pestka, and J. Karwowski, *Phys. Rev. A* **77**, 044501 (2008).
- <sup>25</sup>D. Ferenc, P. Jeszenski, and E. Mátyus, *J. Chem. Phys.* **156**, 084110 (2022).
- <sup>26</sup>K. Pachucki, U. D. Jentschura, and V. A. Yerokhin, *Phys. Rev. Lett.* **93**, 150401 (2004).
- <sup>27</sup>K. Pachucki, *Phys. Rev. A* **71**, 012503 (2005).
- <sup>28</sup>V. Patkoš, V. A. Yerokhin, and K. Pachucki, *Phys. Rev. A* **103**, 012803 (2021).
- <sup>29</sup>P. J. Mohr, *Phys. Rev. A* **32**, 1949 (1985).
- <sup>30</sup>V. M. Shabaev, *Phys. Rep.* **356**, 119 (2002).
- <sup>31</sup>A. V. Volotka, D. A. Glazov, V. M. Shabaev, I. I. Tupitsyn, and G. Plunien, *Phys. Rev. Lett.* **112**, 253004 (2014).
- <sup>32</sup>V. A. Yerokhin, K. Pachucki, M. Puchalski, Z. Harman, and C. H. Keitel, *Phys. Rev. A* **95**, 062511 (2017).
- <sup>33</sup>P. Indelicato, J. P. Santos, S. Boucard, and J.-P. Desclaux, *Eur. Phys. J. D* **45**, 155 (2007).
- <sup>34</sup>A. V. Malyshev, A. V. Volotka, D. A. Glazov, I. I. Tupitsyn, V. M. Shabaev, and G. Plunien, *Phys. Rev. A* **90**, 062517 (2014).
- <sup>35</sup>G. E. Brown and D. G. Ravenhall, *Proc. R. Soc. London, Ser. A* **208**, 552 (1951).
- <sup>36</sup>J. Sucher, “Energy levels of the two-electron atom to order  $\alpha^3$  Rydberg,” Ph.D. thesis, Columbia University, 1958.
- <sup>37</sup>J. Sucher, *Phys. Rev. A* **22**, 348 (1980).
- <sup>38</sup>J.-L. Heully, I. Lindgren, E. Lindroth, and A.-M. Mårtensson-Pendrill, *Phys. Rev. A* **33**, 4426 (1986).
- <sup>39</sup>M. H. Mittleman, *Phys. Rev. A* **24**, 1167 (1981).
- <sup>40</sup>A. Almoukhalati, S. Knecht, H. J. A. Jensen, K. G. Dyall, and T. Saue, *J. Chem. Phys.* **145**, 074104 (2016).
- <sup>41</sup>J. Sucher, in *Relativistic Effects in Atoms, Molecules, and Solids*, NATO Advanced Science Institutes Series, edited by G. L. Malli (Springer, Boston, 1983), pp. 1–53.
- <sup>42</sup>K. G. Dyall and K. Fægri, *Introduction to Relativistic Quantum Chemistry* (Oxford University Press, New York, 2007).
- <sup>43</sup>V. M. Shabaev, I. I. Tupitsyn, and V. A. Yerokhin, *Comput. Phys. Commun.* **189**, 175 (2015).
- <sup>44</sup>A. V. Volotka, M. Bilal, R. Beerwerth, X. Ma, T. Stöhlker, and S. Fritzsche, *Phys. Rev. A* **100**, 010502 (2019).
- <sup>45</sup>L. N. Labzokskii, *Sov. Phys. JETP* **32**, 94 (1971).
- <sup>46</sup>V. M. Shabaev, I. I. Tupitsyn, V. A. Yerokhin, G. Plunien, and G. Soff, *Phys. Rev. Lett.* **93**, 130405 (2004).
- <sup>47</sup>I. Lindgren, *Relativistic Many-Body Theory*, Springer Series on Atomic, Optical, and Plasma Physics Vol. 63 (Springer, New York, 2011).
- <sup>48</sup>P. Indelicato and P. J. Mohr, in *Handbook of Relativistic Quantum Chemistry*, edited by W. Liu (Springer, Berlin, Heidelberg, 2017), pp. 131–241.
- <sup>49</sup>W. Liu, *Phys. Chem. Chem. Phys.* **14**, 35 (2012).
- <sup>50</sup>W. Liu and I. Lindgren, *J. Chem. Phys.* **139**, 014108 (2013).
- <sup>51</sup>W. Liu, *Phys. Rep.* **537**, 59 (2014).
- <sup>52</sup>S. Shao, Z. Li, and W. Liu, in *Handbook of Relativistic Quantum Chemistry*, edited by W. Liu (Springer, Berlin, Heidelberg, 2017), pp. 481–496.
- <sup>53</sup>W. Cencek and W. Kutzelnigg, *J. Chem. Phys.* **105**, 5878 (1996).
- <sup>54</sup>W. Liu, S. Shao, and Z. Li, in *Handbook of Relativistic Quantum Chemistry*, edited by W. Liu (Springer, Berlin, Heidelberg, 2017), pp. 531–545.
- <sup>55</sup>P. Jeszenski, D. Ferenc, and E. Mátyus, *J. Chem. Phys.* **154**, 224110 (2021).
- <sup>56</sup>W. Liu, *Mol. Phys.* **108**, 1679 (2010).
- <sup>57</sup>W. Kutzelnigg, *Int. J. Quantum Chem.* **25**, 107 (1984).
- <sup>58</sup>K. G. Dyall, *J. Chem. Phys.* **100**, 2118 (1994).
- <sup>59</sup>W. H. E. Schwarz and E. Wechsel-Trakowski, *Chem. Phys. Lett.* **85**, 94 (1982).
- <sup>60</sup>W. Kutzelnigg, *J. Chem. Phys.* **126**, 201103 (2007).
- <sup>61</sup>M. Lewin and É. Séré, *Proc. London Math. Soc.* **100**, 864 (2010).
- <sup>62</sup>W. Kutzelnigg, *Chem. Phys.* **395**, 16 (2012).
- <sup>63</sup>B. Simmen, E. Mátyus, and M. Reiher, *J. Phys. B: At., Mol. Opt. Phys.* **48**, 245004 (2015).
- <sup>64</sup>Q. Sun, W. Liu, and W. Kutzelnigg, *Theor. Chem. Acc.* **129**, 423 (2011).
- <sup>65</sup>G. Pestka and J. Karwowski, in *Explicitly Correlated Wave Functions in Chemistry and Physics*, edited by W. N. Lipscomb, J. Maruani, S. Wilson, and J. Rychlewski (Springer, Dordrecht, The Netherlands, 2003), Vol. 13, pp. 331–346.
- <sup>66</sup>D. S. Tracy and R. P. Singh, *Stat. Neerlandica* **26**, 143 (1972).
- <sup>67</sup>T. Saue and H. J. A. Jensen, *J. Chem. Phys.* **111**, 6211 (1999).
- <sup>68</sup>E. Mátyus, *Mol. Phys.* **117**, 590 (2019).
- <sup>69</sup>E. Mátyus, *J. Chem. Phys.* **149**, 194111 (2018).
- <sup>70</sup>E. Mátyus, *J. Chem. Phys.* **149**, 194112 (2018).
- <sup>71</sup>D. Ferenc and E. Mátyus, *Phys. Rev. A* **100**, 020501 (2019).
- <sup>72</sup>E. Mátyus and P. Cassam-Chenaï, *J. Chem. Phys.* **154**, 024114 (2021).
- <sup>73</sup>R. T. Ireland, P. Jeszenski, E. Mátyus, R. Martinazzo, M. Ronto, and E. Pollak, *ACS Phys. Chem. Au* **2**, 23 (2021).
- <sup>74</sup>J. Dolbeault, M. J. Esteban, and E. Séré, *J. Funct. Anal.* **174**, 208 (2000).
- <sup>75</sup>M. J. Esteban, M. Lewin, and E. Séré, *Bull. Am. Math. Soc.* **45**, 535 (2008).
- <sup>76</sup>J. Karwowski, in *Handbook of Relativistic Quantum Chemistry*, edited by W. Liu (Springer, Berlin, Heidelberg, 2017), pp. 1–47.
- <sup>77</sup>M. Reiher and A. Wolf, *Relativistic Quantum Chemistry: The Fundamental Theory of Molecular Science*, 2nd ed. (Wiley VCH, Weinheim, 2015).
- <sup>78</sup>E. Balslev and J. M. Combes, *Commun. Math. Phys.* **22**, 280 (1971).
- <sup>79</sup>B. Simon, *Ann. Math.* **97**, 247 (1973).
- <sup>80</sup>N. Moiseyev, *Non-Hermitian Quantum Mechanics* (Cambridge University Press, Cambridge, 2011).
- <sup>81</sup>T.-C. Jagau, K. B. Bravaya, and A. I. Krylov, *Annu. Rev. Phys. Chem.* **68**, 525 (2017).
- <sup>82</sup>N. Moiseyev and C. Corcoran, *Phys. Rev. A* **20**, 814 (1979).
- <sup>83</sup>C. W. McCurdy, *Phys. Rev. A* **21**, 464 (1980).
- <sup>84</sup>P. Šeba, *Lett. Math. Phys.* **16**, 51 (1988).
- <sup>85</sup>G. Drake, in *Springer Handbook of Atomic, Molecular, and Optical Physics*, edited by G. Drake (Springer, New York, 2006), pp. 199–219.
- <sup>86</sup>E. Tiesinga, P. J. Mohr, D. B. Newell, and B. N. Taylor, *Rev. Mod. Phys.* **93**, 025010 (2021).
- <sup>87</sup>G. Pestka and J. Karwowski, *Collect. Czech. Chem. Commun.* **68**, 275 (2003).
- <sup>88</sup>G. Pestka, M. Bylicki, and J. Karwowski, *J. Phys. B: At., Mol. Opt. Phys.* **39**, 2979 (2006).
- <sup>89</sup>G. Pestka, M. Bylicki, and J. Karwowski, *J. Math. Chem.* **50**, 510 (2012).
- <sup>90</sup>G. W. Drake, *Can. J. Phys.* **66**, 586 (1988).
- <sup>91</sup>K. Pachucki, *Phys. Rev. A* **74**, 022512 (2006).
- <sup>92</sup>H. Araki, *Prog. Theor. Phys.* **17**, 619 (1957).
- <sup>93</sup>F. A. Parpia and I. P. Grant, *J. Phys. B* **23**, 211 (1990).
- <sup>94</sup>M. Puchalski, J. Komasa, and K. Pachucki, *Phys. Rev. A* **95**, 052506 (2017).



# On the inclusion of cusp effects in expectation values with explicitly correlated Gaussians

Péter Jeszenszki<sup>1</sup> | Robbie T. Ireland<sup>1,2</sup> | Dávid Ferenc<sup>1</sup> | Edit Mátyus<sup>1</sup><sup>1</sup>Institute of Chemistry, ELTE, Eötvös Loránd University, Budapest, Hungary<sup>2</sup>School of Chemistry, University of Glasgow, Glasgow, UK**Correspondence**Edit Mátyus, Institute of Chemistry, ELTE, Eötvös Loránd University, Pázmány Péter sétány 1/A, Budapest H-1117, Hungary.  
Email: edit.matyus@ttk.elte.hu**Funding information**

Erasmus+ Traineeship; H2020 European Research Council, Grant/Award Number: 851421

**Abstract**

This paper elaborates the integral transformation technique and uses it for the case of the non-relativistic kinetic and Coulomb potential energy operators, as well as for the relativistic mass-velocity and Darwin terms. The techniques are tested for the ground electronic state of the helium atom and perturbative relativistic energies are reported for the ground electronic state of the  $H_3^+$  molecular ion near its equilibrium structure.

**KEYWORDS**explicitly correlated Gaussian,  $H_3^+$ , relativistic correction

## 1 | INTRODUCTION

We wish to dedicate this paper to István Mayer's memory. Two of us attended his undergraduate special course (called "speci" among the students) at ELTE that he held until ca. 2010. During our everyday work, we still frequently point to simple calculations and theorems that we have learned from him and from his book [1]. As students, and later, as young researchers, we got to know him as an infinitely patient and supportive person toward the youths and their small things in research. His every reasoning and calculation was simple, because he made them simple and made every small step clear. In this spirit, we work out in detail the theoretical background for a nice technique proposed by Pachucki et al. that makes it possible to correct for the effects of the missing cusp of Gaussian basis functions during the evaluation of the "singular" integrals in the Breit–Pauli Hamiltonian [2]. We imagine presenting this work on a research seminar: we can almost see István Mayer sitting and smiling in the first row of the auditorium and he has several comments and questions. We wonder: what are they?

Pachucki et al. [2] proposed the integral transformation technique to enhance the convergence of the expectation values of terms of the Breit–Pauli Hamiltonian that were known to be difficult to evaluate precisely in the commonly used explicitly correlated Gaussian (ECG) basis sets [3–6].

$$\Theta_i(\mathbf{r}) = \exp\left[-(\mathbf{r} - \mathbf{s}_i)^T \underline{\mathbf{A}}_i (\mathbf{r} - \mathbf{s}_i)\right], \quad (1)$$

where  $\mathbf{r} \in \mathbb{R}^{3n}$  is the position vector of the particles, while  $\mathbf{s}_i \in \mathbb{R}^{3n}$  and  $\underline{\mathbf{A}}_i = \mathbf{A}_i \otimes \mathbf{1}^{[3]}$  with  $\mathbf{A}_i \in \mathbb{R}^{n \times n}$  are parameters of the basis function. The parametrization is selected by minimization of the non-relativistic energy. The advantage of the ECG basis set is that it is an  $n$ -particle basis, for which analytic matrix elements can be derived for almost all physically relevant operators. At the same time, it is also well-known that the Gaussian functions fail to reproduce the analytic properties of the exact non-relativistic wave function at the particle–particle coalescence points (cusps) and in the asymptotic range for large particle–particle separations. The integral transformation technique offers a possibility to correct for the missing cusp effects.

This is an open access article under the terms of the Creative Commons Attribution-NonCommercial-NoDerivs License, which permits use and distribution in any medium, provided the original work is properly cited, the use is non-commercial and no modifications or adaptations are made.

© 2021 The Authors. *International Journal of Quantum Chemistry* published by Wiley Periodicals LLC.

We start the present work by writing out the theoretical background of Pachucki et al. [2] in detail. During this work, we have noticed that the ideas used for the “integral transform” (IT) evaluation of the perturbative relativistic corrections may be more generally applicable. In a nutshell, instead of directly evaluating the expectation value of some physical quantity with the approximate wave function

$$\langle \hat{O} \rangle = \int dr_1 \dots dr_N \Psi(\mathbf{r}_1, \dots, \mathbf{r}_N)^* \hat{O} \Psi(\mathbf{r}_1, \dots, \mathbf{r}_N), \quad (2)$$

it becomes possible to incorporate the effects of the cusp of the exact wave function. An appropriate transformation is defined by introducing  $\mathcal{I}_O$  with variable  $\xi$ , and the integral is calculated in two parts,

$$\langle \hat{O} \rangle = \int_0^{\xi_\Lambda} d\xi \mathcal{I}_O(\xi) + \int_{\xi_\Lambda}^{\infty} d\xi \tilde{\mathcal{I}}_O(\xi), \quad (3)$$

where we introduced the  $\langle \rangle$  notation to emphasize the difference from the standard expectation value labeled with  $\langle \rangle$ . In the short-range part,  $0 \leq \xi \leq \xi_\Lambda$ , the cusp has a negligible effect and it can be accurately computed with an ECG basis. For the long-range part,  $\xi_\Lambda < \xi < \infty$ , the exact cusp condition can be incorporated in the asymptotic tail of the transformed function ( $\tilde{\mathcal{I}}_O(\xi)$ ) by considering the analytic behavior of the wave function near the coalescence points.

In Sections 2 and 3, we work out the theoretical background and the analytic form of the long-range integrand for two types of ITs. Section 4 is about the implementation, technical details and observations. Numerical results are presented for the relativistic calculations in Section 5, for the non-relativistic calculations in Section 6, and the paper ends with a summary and conclusions (Section 7).

## 2 | IT FOR THE COULOMB INTERACTION AND THE DIRAC DELTA OF THE COORDINATE

In this section, we will consider the inclusion of the cusp effect for spatial integrals of operators that can be related to the inverse of the particle-particle distance,  $1/r$ . So, let us first consider the interaction between an electron and a nucleus, which is fixed at the origin. In the matrix-element calculations, the relationship below is commonly used during the evaluation of the Coulomb integrals with Gaussian orbitals [7, 8].

$$\frac{1}{r_i} = \frac{2}{\sqrt{\pi}} \int_0^{\infty} dt e^{-r_i^2 t^2}, \quad (4)$$

where the index  $i$  indicates the index of the electron. This relation can be understood as an IT (we call it  $t$ -transform) generation of  $1/r_i$ . Furthermore, by using

$$-4\pi\delta(\mathbf{r}_i) = \Delta_{\mathbf{r}_i} \frac{1}{r_i}, \quad (5)$$

we can write, following Pachucki et al. [2],

$$\delta(\mathbf{r}_i) = -\frac{1}{2\pi^{3/2}} \int_0^{\infty} dt 2t^2 (3 - 2t^2 r_i^2) e^{-r_i^2 t^2}. \quad (6)$$

So, both operators can be generated by a  $t$ -integral

$$F(\mathbf{r}_i) = \int_0^{\infty} dt f(\mathbf{r}_i, t) e^{-r_i^2 t^2}, \quad (7)$$

where

$$\text{for } F(\mathbf{r}_i) = 1/r_i: f(\mathbf{r}_i, t) = 2/\sqrt{\pi}, \quad (8)$$

dc\_1955\_21

and

$$\text{for } F(\mathbf{r}_i) = \delta(\mathbf{r}_i): f(\mathbf{r}_i, t) = -\pi^{-\frac{3}{2}} t^2 (3 - 2t^2 r_i^2). \quad (9)$$

Then, by generalizing Pachucki et al.'s work for  $\delta(\mathbf{r})$  [2], we re-write the expectation value for  $F(\mathbf{r}_i)$  as

$$\begin{aligned} \langle \Psi | F(\mathbf{r}_i) | \Psi \rangle &= \int d\mathbf{r}_1 \dots d\mathbf{r}_N \Psi(\mathbf{r}_1, \dots, \mathbf{r}_N)^* F(\mathbf{r}_i) \Psi(\mathbf{r}_1, \dots, \mathbf{r}_N) \\ &= \int d\mathbf{r}_1 \dots d\mathbf{r}_N \left[ \int_0^\infty dt f(\mathbf{r}_i, t) e^{-r_i^2 t^2} \right] |\Psi(\mathbf{r}_1, \dots, \mathbf{r}_N)|^2 \\ &= \int_0^\infty dt \int d\mathbf{r}_1 \dots d\mathbf{r}_N f(\mathbf{r}_i, t) e^{-r_i^2 t^2} |\Psi(\mathbf{r}_1, \dots, \mathbf{r}_N)|^2 \\ &= \frac{1}{N} \int_0^\infty dt \int d\mathbf{r}_i f(\mathbf{r}_i, t) e^{-r_i^2 t^2} \rho(\mathbf{r}_i) \end{aligned} \quad (10)$$

where  $\rho(\mathbf{r}_i)$  is the one-electron density function,

$$\rho(\mathbf{r}_i) = N \int \left( \prod_{\substack{j=1 \\ j \neq i}}^N d\mathbf{r}_j \right) |\Psi(\mathbf{r}_1, \dots, \mathbf{r}_N)|^2. \quad (11)$$

Next, we define the IT function for  $F(\mathbf{r}_i)$  as

$$\mathcal{I}_{F(\mathbf{r}_i)}(t) = \frac{1}{N} \int d\mathbf{r}_i f(\mathbf{r}_i, t) e^{-r_i^2 t^2} \rho(\mathbf{r}_i), \quad (12)$$

which can be substituted back into Equation (10),

$$\langle \Psi | F(\mathbf{r}_i) | \Psi \rangle = \int_0^\infty dt \mathcal{I}_{F(\mathbf{r}_i)}(t). \quad (13)$$

The integral  $\mathcal{I}_{F(\mathbf{r}_i)}(t)$  can be written in an analytic form for “any” polynomial  $f(\mathbf{r}_i, t)$  of  $r_i$  and  $t$ . In particular,

$$\text{for } F(\mathbf{r}_i) = 1/r_i: \mathcal{I}_{1/r_i}(t) = \frac{2}{\sqrt{\pi}N} \int d\mathbf{r}_i e^{-r_i^2 t^2} \rho(\mathbf{r}_i) \quad (14)$$

and

$$\text{for } F(\mathbf{r}_i) = \delta(\mathbf{r}_i): \mathcal{I}_{\delta(\mathbf{r}_i)}(t) = -\frac{1}{\pi^{\frac{3}{2}}N} \int d\mathbf{r}_i t^2 (3 - 2t^2 r_i^2) e^{-r_i^2 t^2} \rho(\mathbf{r}_i). \quad (15)$$

At first sight, it may seem strange that we introduce these complicated integral expressions, Equations (12)–(15). This is especially true for the integral of Dirac delta that could be immediately obtained from the density at the origin. But, it is difficult to calculate the density at this point, due to the cusp of the wave function. In numerical computations,  $\rho(\mathbf{r}_i)$  is expanded in terms of a finite number of basis functions. The commonly used Gaussian functions are smooth everywhere and they miss the correct description of the cusp [5, 8, 9].

The integral transformation in Equation (12) widens out the effect of the density to a finite interval due to the term  $e^{-r_i^2 t^2}$  (for finite  $t$  values), and over this finite interval, the density can be represented accurately with smooth functions. The original integral value is obtained by integration for  $t \in [0, +\infty)$ . For larger  $t$  values, the Gaussian in Equation (12) becomes narrower and makes the short-range contribution (cusp) more important to  $\mathcal{I}_{F(\mathbf{r}_i)}(t)$ .

In the following paragraphs, it will be shown that for large  $t$  values, the analytic form of the integrand can be deduced from analytic properties of the density near the cusp. To be able to incorporate these analytic results, the full integral is evaluated as the sum of a short-range,  $t \in [0, t_\lambda]$ , and a long-range,  $t \in [t_\lambda, \infty)$ , part (Equation 3):

$$\left\langle \left\langle \frac{1}{r_i} \right\rangle \right\rangle = \int_0^{t_\lambda} \mathcal{I}_{1/r_i}(t) dt + \int_{t_\lambda}^\infty \tilde{\mathcal{I}}_{1/r_i}(t) dt. \quad (16)$$

The short-range part is evaluated by direct integration over the finite interval  $t \in [0, t_\lambda]$  (Appendix A). To calculate the long-range part including the cusp effects, the following considerations are necessary.

## 2.1 | Derivation of the long-range part from the cusp condition

According to Kato's cusp condition [1, 8, 10], the following relations hold for the exact non-relativistic wave function (in Hartree atomic units) for the electron-nucleus and for the electron–electron coalescence points, respectively,

$$\lim_{r_{iA} \rightarrow 0} \left\langle \frac{\partial \Psi}{\partial r_{iA}} \right\rangle_{\vartheta, \varphi} = -Z_A \Psi(r_{iA} = 0) \quad \text{and} \quad \lim_{r_{ij} \rightarrow 0} \left\langle \frac{\partial \Psi}{\partial r_{ij}} \right\rangle_{\vartheta, \varphi} = \frac{1}{2} \Psi(r_{ij} = 0), \quad (17)$$

where  $\langle \rangle_{\vartheta, \varphi}$  indicates averaging for the spherical angles,  $Z_A$  is the nuclear charge number,  $r_{iA}$  is the distance between electron  $i$  and nucleus  $A$ , and  $r_{ij}$  is the distance between electrons  $i$  and  $j$ . These conditions are valid only if the wave function does not have a node at the coalescence point, otherwise, higher derivatives must be considered for a good description of the wave function in this regime [11, 12]. The coalescence condition can be further elaborated by considering the effect of higher derivatives of the wave function [13, 14], which can be also affected by three-particle coalescence conditions [15, 16]. In this paper, we use the simplest, original conditions of Equation (17) that give the following relations [17]:

$$\lim_{r_{iA} \rightarrow 0} \frac{\partial \langle \rho \rangle_{\vartheta, \varphi}}{\partial r_{iA}} = -2Z_A \rho(\mathbf{0}) \quad \text{and} \quad \lim_{r_{ij} \rightarrow 0} \frac{\partial \langle \eta \rangle_{\vartheta, \varphi}}{\partial r_{ij}} = \eta(\mathbf{0}), \quad (18)$$

where  $\rho$  is the one-electron density, Equation (11), and  $\eta$  labels the pair correlation function [18],

$$\eta(\mathbf{r}) = N(N-1) \int \left( \prod_{k=2}^N d\mathbf{r}_k \right) |\Psi(\mathbf{r}_2 + \mathbf{r}, \mathbf{r}_2, \mathbf{r}_3, \mathbf{r}_4, \dots, \mathbf{r}_N)|^2. \quad (19)$$

that can also be understood also as a quantity proportional to the pseudo-particle density corresponding to the relative motion for a pair of electrons [5].

Then, we may consider the expansion of the spherically averaged density and pair correlation function by the coalescence point taken as the origin (0):

$$\langle \rho \rangle_{\vartheta, \varphi}(r) = \rho(\mathbf{0}) - 2Z_A \rho(\mathbf{0})r + \sum_{j=2}^m B_j r^j + \mathcal{O}(r^{m+1}), \quad (20)$$

$$\langle \eta \rangle_{\vartheta, \varphi}(r) = \eta(\mathbf{0}) + \eta(\mathbf{0})r + \sum_{j=2}^m B_j r^j + \mathcal{O}(r^{m+1}). \quad (21)$$

To obtain the asymptotic form of  $\mathcal{I}_{F(r_i)}$ , labeled with  $\tilde{\mathcal{I}}_{F(r_i)}$  (where tilde refers to the fact that it is valid for the asymptotic range), we insert the density expansion, Equation (20), in the definition of the IT function, Equation (12) and integrate out the angular coordinates. We explicitly show the calculation for  $\tilde{\mathcal{I}}_{F(r_i)}$  (and it can be carried out analogously for  $\tilde{\mathcal{I}}_{F(r_{ij})}$  using Equation (21))

for  $t > t_\Lambda$ :

$$\begin{aligned} \tilde{\mathcal{I}}_{F(r_i)}(t) &= \frac{1}{N} \int_0^{2\pi} d\phi \int_{-1}^1 d(\cos\vartheta) \int_0^\infty dr_i r_i^2 f(r_i, t) e^{-r_i^2 t^2} \rho(r_i) \\ &= \frac{1}{N} \int_0^\infty dr_i r_i^2 f(r_i, t) e^{-r_i^2 t^2} 4\pi \langle \rho \rangle_{\vartheta, \varphi}(r_i) \\ &= \frac{4\pi}{N} \int_0^\infty dr_i r_i^2 f(r_i, t) e^{-r_i^2 t^2} \left[ \rho(\mathbf{0}) - 2Z_A \rho(\mathbf{0})r_i + \sum_{j=2}^m B_j r_i^j + \mathcal{O}(r_i^{m+1}) \right], \end{aligned} \quad (22)$$

where for practical reasons, we truncate the expansion after some (“appropriate”)  $m$  value. The one-dimensional integral for  $r_i$  can be evaluated by analytic or numerical integration. For  $F(r_i) = 1/r_i$  with  $f(r_i, t) = 2\pi^{-1/2}$  in Equation (4), we obtain the asymptotic form as

$$\text{for } t > t_\Lambda: \quad \tilde{\mathcal{I}}_{1/r_i}(t) = \frac{1}{t^3 N} \left( 2\pi \rho(\mathbf{0}) - 8\sqrt{\pi} Z_A \rho(\mathbf{0}) \frac{1}{t} + \sum_{j=2}^m B_j^{[1/r_i]} \frac{1}{t^j} \right), \quad (23)$$

dc\_1955\_21

while for  $F(\mathbf{r}_i) = \delta(\mathbf{r}_i)$ ,  $f(\mathbf{r}_i, t) = -t^2(3 - 2t^2r_i^2)\pi^{-3/2}$  in Equation (6), we have

$$\text{for } t > t_\Lambda: \tilde{\mathcal{I}}_{\delta(\mathbf{r}_i)}(t) = \frac{1}{t^2 N} \left( \frac{4Z_A \rho(\mathbf{0})}{\sqrt{\pi}} - \frac{2}{\sqrt{\pi}} \sum_{j=2}^m B_j^{[\delta(\mathbf{r}_i)]} \frac{1}{t^{j-1}} \right). \quad (24)$$

It is interesting to note that the asymptotic tail of the Coulomb interaction, Equation (23), decays faster than that of the Dirac delta, Equation (24), leading to a faster convergence in a finite basis representation. Using Equations (23) and (24), the integral from  $t_\Lambda$  to  $\infty$  is obtained in an analytic form as

$$\int_{t_\Lambda}^{\infty} \tilde{\mathcal{I}}_{1/r_i}(t) dt = \frac{1}{t_\Lambda^2 N} \left( \pi \rho(\mathbf{0}) - \frac{8}{3} \sqrt{\pi} Z_A \rho(\mathbf{0}) \frac{1}{t_\Lambda} + \sum_{j=2}^m \frac{B_j^{[1/r_i]}}{j+2} \frac{1}{t_\Lambda^j} \right), \quad (25)$$

$$\int_{t_\Lambda}^{\infty} \tilde{\mathcal{I}}_{\delta(\mathbf{r}_i)}(t) dt = \frac{1}{t_\Lambda N} \left( \frac{4Z_A \rho(\mathbf{0})}{\sqrt{\pi}} - \frac{2}{\sqrt{\pi}} \sum_{j=2}^m \frac{B_j^{[\delta(\mathbf{r}_i)]}}{j} \frac{1}{t_\Lambda^{j-1}} \right). \quad (26)$$

Although both expressions contain the particle density at the coalescence point,  $\rho(\mathbf{0})/N = \langle \Psi | \delta(\mathbf{r}_i) | \Psi \rangle$ , that is, inaccurately represented in a(n explicitly correlated) Gaussian basis, we can obtain its precise value by using:

$$\frac{1}{N} \rho(\mathbf{0}) = \langle \delta(\mathbf{r}_i) \rangle = \int_0^{t_\Lambda} \mathcal{I}_{\delta(\mathbf{r}_i)}(t) dt + \int_{t_\Lambda}^{\infty} \tilde{\mathcal{I}}_{\delta(\mathbf{r}_i)}(t) dt \quad (27)$$

in an iterative procedure. First, the short-range integral (first term in the right-hand side of Equation (27)) is calculated by a one-dimensional quadrature (since this integrand is too complicated for an analytic evaluation), while the  $B_j$  parameters in the long-range part are obtained by fitting the asymptotic part, Equation (24), to data points. The data set for the fit corresponds to “intermediate”-range  $t$  values (for practical details, see Sections 5, 6, and Appendix D). Then, using  $\rho(\mathbf{0})$ , obtained directly from numerical integration, the  $\tilde{\mathcal{I}}_{\delta(\mathbf{r}_i)}(t)$  asymptotic function can be evaluated. In the last step, we calculate the integrals in Equation (27) that results in an improved value for  $\rho(\mathbf{0})$  and an improved  $\tilde{\mathcal{I}}_{\delta(\mathbf{r}_i)}(t)$  asymptotic form. The iteration converges in a few cycles as it was noted already in Pachucki et al. [2]. Once we have the precise value for  $\rho(\mathbf{0})$ , we can have a good representation for the asymptotic tail of the Coulomb interaction,  $\tilde{\mathcal{I}}_{1/r_i}(t)$  in Equation (23). Then, the integral value for the Coulomb interaction including also the cusp effect can be obtained as:

$$\left\langle \left\langle \frac{1}{r_i} \right\rangle \right\rangle = \int_0^{t_\Lambda} \mathcal{I}_{1/r_i}(t) dt + \int_{t_\Lambda}^{\infty} \tilde{\mathcal{I}}_{1/r_i}(t) dt. \quad (28)$$

For computing  $\langle \delta(\mathbf{r}_{ij}) \rangle$  and  $\langle 1/r_{ij} \rangle$  a similar approach is used, but it is necessary to substitute  $\rho(\mathbf{0})$ ,  $Z_A$ , and  $N$  with  $\eta(\mathbf{0})$ ,  $-1/2$ , and  $N(N-1)$ , respectively in Equations (23)–(26). The final working equations are

for  $t > t_\Lambda$ :

$$\tilde{\mathcal{I}}_{1/r_{ij}}(t) = \frac{1}{t^3 N(N-1)} \left( 2\pi \eta(\mathbf{0}) + 4\sqrt{\pi} \eta(\mathbf{0}) \frac{1}{t} + \sum_{k=2}^m B_k^{[1/r_{ij}]} \frac{1}{t^k} \right), \quad (29)$$

$$\tilde{\mathcal{I}}_{\delta(\mathbf{r}_{ij})}(t) = -\frac{1}{t^2 N(N-1)} \left( \frac{2\eta(\mathbf{0})}{\sqrt{\pi}} + \frac{2}{\sqrt{\pi}} \sum_{k=2}^m B_k^{[\delta(\mathbf{r}_{ij})]} \frac{1}{t^{k-1}} \right), \quad (30)$$

and

$$\int_{t_\Lambda}^{\infty} \tilde{\mathcal{I}}_{1/r_{ij}}(t) dt = \frac{1}{t_\Lambda^3 N(N-1)} \left( \pi \eta(\mathbf{0}) + \frac{4}{3} \sqrt{\pi} \eta(\mathbf{0}) \frac{1}{t_\Lambda} + \sum_{k=2}^m \frac{B_k^{[1/r_{ij}]} }{k+2} \frac{1}{t_\Lambda^k} \right), \quad (31)$$

$$\int_{t_\Lambda}^{\infty} \tilde{\mathcal{I}}_{\delta(\mathbf{r}_{ij})}(t) dt = \frac{1}{t_\Lambda N(N-1)} \left( -\frac{2\eta(\mathbf{0})}{\sqrt{\pi}} - \frac{2}{\sqrt{\pi}} \sum_{k=2}^m \frac{B_k^{[\delta(\mathbf{r}_{ij})]} }{k} \frac{1}{t_\Lambda^{k-1}} \right), \quad (32)$$

with

$$\frac{1}{N(N-1)}\eta(\mathbf{0}) = \langle \delta(\mathbf{r}_{ij}) \rangle, \quad (33)$$

where the precise value of  $\langle \delta(\mathbf{r}_{ij}) \rangle$  is obtained in an iterative procedure, similarly to  $\langle \delta(\mathbf{r}_{iA}) \rangle$ .

### 3 | FOURIER TRANSFORM FOR THE KINETIC ENERGY AND THE MASS-VELOCITY TERMS

To calculate integrals of momentum operators, it is convenient to switch to momentum space. The Fourier transform of an ECG preserves the mathematical form of the function, and we need to consider only the changes in the parameterization. So, the Fourier transform of the basis function in Equation (1) is [2].

$$\bar{\Theta}_i(\mathbf{p}) = |\mathbf{A}|^{-\frac{3}{2}} \exp\left[-(\mathbf{p} - \bar{\mathbf{s}}_i)^T \bar{\mathbf{A}}_i (\mathbf{p} - \bar{\mathbf{s}}_i) + \bar{\mathbf{C}}_i\right], \quad (34)$$

with  $\bar{\mathbf{s}}_i = -2i\mathbf{s}_i\mathbf{A}_i$ ,  $\bar{\mathbf{A}}_i = \frac{1}{4}\mathbf{A}_i^{-1}$ , and  $\bar{\mathbf{C}}_i = -\mathbf{s}_i^T \mathbf{A}_i \mathbf{s}_i$ . For the expectation value of the non-relativistic kinetic ( $k=2$ ) and of the mass-velocity ( $k=4$ ) operators, we have to evaluate

$$\begin{aligned} \langle \Psi | p_1^k | \Psi \rangle &= \int d\mathbf{p}_1 \dots d\mathbf{p}_n p_1^k |\bar{\Psi}(\mathbf{p}_1 \dots \mathbf{p}_n)|^2 \\ &= \frac{1}{N} \int d\mathbf{p}_1 p_1^k \bar{\rho}(\mathbf{p}_1), \end{aligned} \quad (35)$$

where  $\bar{\rho}(\mathbf{p}_1)$  is the momentum density function. The angular part of the integral can be evaluated according to Equation (A14),

$$\langle \Psi | p_1^k | \Psi \rangle = \frac{4\pi}{N} \int_0^\infty dp p^{k+2} \langle \bar{\rho} \rangle_{\vartheta,\varphi}(p) = \int_0^\infty dp \mathcal{I}_{p^k}(p), \quad (36)$$

where  $\langle \bar{\rho} \rangle_{\vartheta,\varphi}(p)$  labels the spherically averaged momentum density. The explicit integrals for  $k=2$  ( $p^2$ ) are evaluated in Equations (A15) and (A16), and the calculation can be, in principle, carried out similarly for  $k=4$ , but we used quadrature integration, because it was fast and sufficiently accurate (Section 5). It is interesting to note that the momentum density is spherically symmetric (second step in Equation (36)), even if  $\mathbf{s}_i \neq 0$ . This observation is connected with the properties of the Fourier transform of the ECG, Equation (34), in which any coordinate-space shift vector appears as purely imaginary vector.

Similarly to the  $t$ -transform (Section 2), the cusp dominating the small-scale behavior in coordinate space is important for the long-range part in the inverse (now momentum) space. To be able to exploit the different characteristics for the two ranges (short and long), the integral is evaluated in two parts,

$$\langle \Psi | p_1^k | \Psi \rangle = \int_0^{p_\Lambda} dp \mathcal{I}_{p^k}(p) + \int_{p_\Lambda}^\infty dp \tilde{\mathcal{I}}_{p^k}(p), \quad (37)$$

where the short-range part corresponds to the first term and is calculated from the ECG representation by direct integration up to some appropriate  $p_\Lambda$  threshold. The long-range part (second term) is determined by the cusp effects, and its analytic properties can be derived for the asymptotic tail. We will label this analytic asymptotic expression by  $\tilde{\mathcal{I}}_{p^k}(p)$  that is derived in the forthcoming subsection.

#### 3.1 | The asymptotic tail of the momentum density

To show the connection of the short-range behavior in coordinate space dominated by the particle-particle coalescence point(s) and the long-range behavior in momentum space, we need to consider a common theorem from numerical analysis [19] which connects the smoothness of a function,  $f(x)$ , with the asymptotic behavior after Fourier transformation,  $\tilde{f}(k) = \int f(x)e^{ikx} dx$ . The smoothness of  $f(x)$  is defined by the number of continuous derivatives. If  $f(x)$  is infinitely differentiable,  $f(x) \in C^\infty$ , or in other words  $f(x)$  is smooth, then  $\tilde{f}(k)$  decays exponentially fast at large  $k$

## dc\_1955\_21

values. If the  $n$ th derivative corresponds to a Dirac delta function, then the first  $n - 2$  derivatives are continuous,  $f(x) \in C^{n-2}$ , and  $\tilde{f}(k)$  decays polynomially with  $1/k^n$  (Appendix B).

We use this theorem, following Kimball [18], to determine the analytic form for the asymptotic tail of the momentum density function,  $\bar{\rho}(\mathbf{p})$

$$\bar{\rho}(\mathbf{p}) = \frac{1}{8\pi^3} \int e^{i\mathbf{p}(\mathbf{r}-\mathbf{r}')} \Gamma(\mathbf{r}', \mathbf{r}) \, d\mathbf{r} \, d\mathbf{r}' \quad (38)$$

with the one-particle density matrix,

$$\Gamma(\mathbf{r}', \mathbf{r}) = N \int \Psi^*(\mathbf{r}', \mathbf{r}_2, \dots, \mathbf{r}_N) \Psi(\mathbf{r}, \mathbf{r}_2, \dots, \mathbf{r}_N) \prod_{i=2}^N d\mathbf{r}_i. \quad (39)$$

By substituting Equation (39) into (38) and by exchanging the order of integration, we arrive at an alternative expression for the momentum density,

$$\bar{\rho}(\mathbf{p}) = N \int \tilde{\Psi}^*(\mathbf{p}, \mathbf{r}_2, \dots, \mathbf{r}_N) \tilde{\Psi}(\mathbf{p}, \mathbf{r}_2, \dots, \mathbf{r}_N) \prod_{i=2}^N d\mathbf{r}_i, \quad (40)$$

$$\tilde{\Psi}(\mathbf{p}, \mathbf{r}_2, \dots, \mathbf{r}_N) = \frac{1}{\sqrt{8\pi^3}} \int e^{-i\mathbf{p}\mathbf{r}} \Psi(\mathbf{r}, \mathbf{r}_2, \dots, \mathbf{r}_N) \, d\mathbf{r}. \quad (41)$$

To describe the asymptotic tail in momentum space, it is sufficient to consider those regions of the wave function for which the singularity occurs for higher-order derivatives (Appendix B). These regions are the points at the position of the nuclei and at the electron–electron coalescence points, where the exact wave function cusps.

Let us focus on a cusp at nucleus A located at  $\mathbf{R}_A$ . Then, we consider the integral form of the cusp condition [11, 20],

$$\text{for } \mathbf{r}_i \approx \mathbf{R}_A: \Psi(\mathbf{r}_1, \mathbf{r}_2, \dots, \mathbf{r}_i, \dots, \mathbf{r}_N) \approx \left\{ 1 - [Z_A + f_A(\vartheta_i, \varphi_i)] \sqrt{(\mathbf{r}_i - \mathbf{R}_A)^2} \right\} \Phi_i(\mathbf{r}_1, \mathbf{r}_2, \dots, \mathbf{r}_i, \dots, \mathbf{r}_N), \quad (42)$$

where  $Z_A$  is the nuclear charge number,  $f_A(\vartheta_i, \varphi_i)$  is an angular term, and  $\Phi(\mathbf{r}_1, \dots, \mathbf{r}_N)$  is a continuous function at least up to its second derivative according to  $\mathbf{r}_i$  at  $\mathbf{R}_A$  for every particle  $i$ . The  $f_A(\vartheta_i, \varphi_i)$  term accounts for the angular dependence (i.e., not generally spherically symmetric) of the wave function around the cusp. A more specific form for  $f_A(\vartheta_i, \varphi_i)$  can be obtained, if we consider the expansion of the one-electron contribution of the wave function around the cusp using the eigenfunctions of the hydrogen atom [1, 11, 20]. As the leading-order contribution of the radial part is related to  $r^\ell$ , where  $\ell$  is the angular momentum quantum number, we can neglect all  $\ell \geq 2$  angular terms for the small  $r$ . So, to describe the non-spherical angular dependence, it is sufficient to consider the linear combinations of the first-order spherical harmonics ( $Y_{1m}(\vartheta, \varphi)$ ,  $m = -1, 0, 1$ ). It is shown in Appendix C that the angular dependence does not have an effect on the large-momentum tail (that corresponds to the short  $r$  range) [1, 11, 20].

In order to examine the non-smoothness of the cusp, let us consider  $\nabla_i^4 \Psi$  (i.e., commonly understood as  $\nabla_i^4 \Psi = (\nabla_i \cdot \nabla_i)^2 \Psi$ ):

$$\nabla_i^4 \Psi = - \left[ \nabla_i^4 Z_A \sqrt{(\mathbf{r}_i - \mathbf{R}_A)^2} \right] \Phi_i + \phi_i, \quad (43)$$

where  $\phi_i$  collects remainder terms that are smooth with respect to  $\mathbf{r}_i$  near  $\mathbf{R}_A$ . (The effect from cusps due to the other particles can be accounted for by summing up the contributions.) If  $\nabla_i^4$  acts on the cusp, a Dirac delta singularity appears,

$$-Z_A \nabla_i^4 \sqrt{(\mathbf{r}_i - \mathbf{R}_A)^2} = -Z_A \nabla_i^2 \frac{2}{\sqrt{(\mathbf{r}_i - \mathbf{R}_A)^2}} = 8\pi Z_A \delta(\mathbf{r}_i - \mathbf{R}_A). \quad (44)$$

For the fourth derivative, the integral in Equation (41) can be evaluated using the properties of Dirac delta in Equation (44), and thus, we obtain the leading-order contribution for large momentum,

$$\text{for } |\mathbf{p}_i| > p_\Lambda: \tilde{\Psi}(\mathbf{r}_1, \dots, \mathbf{p}_i, \dots, \mathbf{r}_N) = \frac{2\sqrt{2}Z_A}{\sqrt{\pi}p_i^4} \Psi(\mathbf{r}_1, \mathbf{r}_2, \dots, \mathbf{R}_A, \dots, \mathbf{r}_N) e^{-i\mathbf{p}_i \mathbf{R}_A} + \mathcal{O}(p_i^{-6}). \quad (45)$$

## dc\_1955\_21

This short calculation demonstrates that it is indeed the cusp that determines the large-momentum behavior. In Equation (45) (valid for large  $p$ ), the next leading order comes with  $p_i^{-6}$ . Although the  $p_i^{-5}$  term can be neglected in the asymptotic tail, further odd powers of  $1/p_i$  are retained to account for (possible) higher-order singularities in the wave function [13–15].

To generalize the calculation to several nuclei and electrons, we consider the following Ansatz which includes the effect of all the cusps of the exact wave function of the many-particle system,

$$\Psi(\mathbf{r}_1, \mathbf{r}_2, \dots, \mathbf{r}_i, \dots, \mathbf{r}_N) = \sum_{i=1}^N \left\{ 1 - \sum_{A=1}^{N_{\text{nuc}}} [Z_A + f_A(\vartheta_i, \varphi_i)] \sqrt{(\mathbf{r}_i - \mathbf{R}_A)^2} + \sum_{j \neq i}^N \left[ \frac{1}{2} + g(\vartheta_{ij}, \varphi_{ij}) \right] \sqrt{(\mathbf{r}_i - \mathbf{r}_j)^2} \right\} \Phi_i(\mathbf{r}_1, \mathbf{r}_2, \dots, \mathbf{r}_i, \dots, \mathbf{r}_N), \quad (46)$$

where  $g(\vartheta_{ij}, \varphi_{ij})$  takes into account the angular dependence of the short-range electron–electron correlation, similarly to the  $f_A(\vartheta_i, \varphi_i)$  term for the electron–nucleus cusp [11, 20]. The calculation of the large-momentum effect of the electron–electron coalescence can be carried out in a similar manner to the electron–nucleus case, Equations (42)–(45), after a coordinate transformation to the center-of-mass and relative motion coordinates including the  $\mathbf{r}_{ij}$  displacement vector. The same arguments apply for the electron–electron cusp as for the electron–nucleus case, with the only difference that the  $Z_A$  nuclear charge number is replaced with  $Z_{ee} = -1/2$ . Then, the asymptotic tail in momentum space for a many-electron–many-nucleus system is obtained as

$$\text{for } |\mathbf{p}_i| > p_\Lambda: \quad \bar{\Psi}(\mathbf{r}_1, \dots, \mathbf{p}_i, \dots, \mathbf{r}_N) = \frac{\sqrt{2}}{\sqrt{\pi} p_i^4} \left[ 2 \sum_{A=1}^{N_{\text{nuc}}} Z_A \Psi(\mathbf{r}_1, \mathbf{r}_2, \dots, \mathbf{R}_A, \dots, \mathbf{r}_N) e^{-i\mathbf{p}_i \cdot \mathbf{R}_A} - \sum_{j \neq i}^N \Psi(\mathbf{r}_1, \mathbf{r}_2, \dots, \mathbf{r}_j, \dots, \mathbf{r}_N) e^{-i\mathbf{p}_i \cdot \mathbf{r}_j} \right] + \mathcal{O}(p_i^{-6}). \quad (47)$$

To obtain the asymptotic tail for the momentum density, we substitute Equation (47) into (40),

for  $|\mathbf{p}| > p_\Lambda$ :

$$\bar{\rho}(\mathbf{p}) = \frac{2}{\pi p^8} \left[ 4 \sum_{A=1}^{N_{\text{nuc}}} Z_A^2 \rho(\mathbf{R}_A) + 4 \sum_{A=1}^{N_{\text{nuc}}} \sum_{B \neq A}^{N_{\text{nuc}}} Z_A Z_B \cos[\mathbf{p}(\mathbf{R}_A - \mathbf{R}_B)] \Gamma(\mathbf{R}_A, \mathbf{R}_B) - 2(N-1) \sum_{A=1}^{N_{\text{nuc}}} Z_A \left( \int e^{i\mathbf{p}(\mathbf{r}_2 - \mathbf{R}_A)} \Psi^*(\mathbf{R}_A, \mathbf{r}_2, \dots, \mathbf{r}_N) \Psi(\mathbf{r}_2, \mathbf{r}_2, \dots, \mathbf{r}_N) \prod_{i=2}^N d\mathbf{r}_i + \text{cc.} \right) + \eta(\mathbf{0}) \right] + \mathcal{O}(p^{-10}), \quad (48)$$

where “+cc.” means complex conjugation of the first term in the parenthesis. The interesting result that the pair correlation function appears in the momentum distribution was first noticed in References [18, 21]. Moreover, it was also found that it leads to a fifth-order cusp in the off-diagonal density matrix in the jellium model [22]. This fifth-order cusp has been derived recently for general atoms and molecules without using the known results from the momentum distribution [23], hence, the asymptotic tail in Equation (48) can be obtained (as an alternative route to the present one) by Fourier-transforming the cusp condition of the off-diagonal density matrix (Equation (20) in Cioslowski [23]).

Furthermore, it can be shown by partial integration that the integral term in Equation (48) is proportional to  $1/p^4$  for high momentum values, and thus, its contribution to the momentum density can be neglected, since it gives contribution only to the  $1/p^{12}$  term.

Next, we can average the momentum density over the momentum orientations, that is, integrate out the angular dependence of the  $\mathbf{p}$  vector and divide by  $4\pi$ , that reads for the second term in the square bracket of Equation (48) as

$$\frac{1}{4\pi} \int_0^{2\pi} d\varphi \int_{-1}^1 d(\cos\vartheta) \cos[\mathbf{p}(\mathbf{R}_A - \mathbf{R}_B)] = \frac{1}{2} \int_{-1}^1 d\cos\vartheta \cos(pR_{AB}\cos\vartheta) = \frac{1}{pR_{AB}} \sin(pR_{AB}), \quad (49)$$

and thereby, we obtain the spherically averaged momentum density,



dc\_1955\_21

$$\begin{aligned} \text{for } p > p_\Lambda: \langle \bar{p} \rangle_{\theta, \varphi}(p) &= \frac{1}{4\pi} \int_0^{2\pi} d\varphi \int_{-1}^1 d(\cos\theta) \bar{p}(\mathbf{p}) \\ &= \frac{2}{\pi p^8} \left[ 4 \sum_{A=1}^{N_{\text{nuc}}} Z_A^2 \rho(\mathbf{R}_A) + 4 \sum_{A=1}^{N_{\text{nuc}}} \sum_{B \neq A}^{N_{\text{nuc}}} Z_A Z_B \frac{\sin(pR_{AB})}{pR_{AB}} \Gamma(\mathbf{R}_A, \mathbf{R}_B) + \eta(\mathbf{0}) \right] + \mathcal{O}(p^{-10}). \end{aligned} \quad (50)$$

### 3.2 | Asymptotic tail of $\mathcal{I}_{p^k}(\mathbf{p})$ and its contribution to $\langle \Psi | p_1^k | \Psi \rangle$

Using the derived large-momentum, asymptotic tail of the momentum density, Equation (50), we can calculate its contribution to the asymptotic tail of  $\mathcal{I}_{p^k}(\mathbf{p})$ , Equations (36) and (37),

for  $p > p_\Lambda$ :

$$\begin{aligned} \tilde{\mathcal{I}}_{p^k}(\mathbf{p}) &= \frac{4\pi}{N} p^{k+2} \langle \bar{p} \rangle_{\theta, \varphi}(p) \\ &= \frac{8}{p^{6-k} N} \left[ 4 \sum_{A=1}^{N_{\text{nuc}}} Z_A^2 \rho(\mathbf{R}_A) + 4 \sum_{A=1}^{N_{\text{nuc}}} \sum_{B \neq A}^{N_{\text{nuc}}} Z_A Z_B \frac{\sin(pR_{AB})}{pR_{AB}} \Gamma(\mathbf{R}_A, \mathbf{R}_B) + \eta(\mathbf{0}) \right] + \sum_{j=1}^m \frac{A_j}{p^{7-k+j}} + \mathcal{O}(p^{-8+k-m}), \end{aligned} \quad (51)$$

where the  $A_j$  coefficients are determined by fitting and  $m$  is chosen to fix the number of additional terms considered in the expansion. In our calculations the typical value for  $m$  was between 4 and 7.

Using these expressions, the contribution from the large-momentum tail to  $\langle \Psi | p_1^k | \Psi \rangle$  in Equation (37), can be calculated. In this paper, we focus on the  $k=2$  and  $k=4$  cases, for which the final expression is

$$\begin{aligned} \int_{p_\Lambda}^{\infty} dp \tilde{\mathcal{I}}_{p^k}(\mathbf{p}) &= \frac{8}{(5-k)p_\Lambda^{5-k} N} \left[ 4 \sum_{A=1}^{N_{\text{nuc}}} Z_A^2 \rho(\mathbf{R}_A) + \eta(\mathbf{0}) \right] \\ &\quad + \frac{32}{N} \sum_{A=1}^{N_{\text{nuc}}} \sum_{B=1}^{N_{\text{nuc}}} Z_A Z_B \Gamma(\mathbf{R}_A, \mathbf{R}_B) G_k(p_\Lambda, R_{AB}) \\ &\quad + \sum_{j=0}^m \frac{A_j}{(6-k+j)p_\Lambda^{6-k+j} N} + \mathcal{O}(p_\Lambda^{-7+k-m}), \end{aligned} \quad (52)$$

with

$$G_2(p_\Lambda, R) = \frac{\cos(Rp_\Lambda)}{2p_\Lambda} + \frac{\sin(Rp_\Lambda)}{2p_\Lambda^2 R} - \frac{R[\pi - 2\text{Si}(Rp_\Lambda)]}{4} \quad \text{for } k=2, \quad (53)$$

$$G_4(p_\Lambda, R) = \frac{R^2 p_\Lambda^2 - 2}{24p_\Lambda^3} \cos(Rp_\Lambda) - \frac{R^2 p_\Lambda^2 - 6}{24R p_\Lambda^4} \sin(Rp_\Lambda) + \frac{R^3 [\pi - 2\text{Si}(Rp_\Lambda)]}{48} \quad \text{for } k=4, \quad (54)$$

where  $\text{Si}(x)$  is the sine integral function [24].

In the numerical calculations,  $\rho(\mathbf{R}_A)$  and  $\eta(\mathbf{0})$  are determined by using the method described in Section 2,

$$\rho(\mathbf{R}_A) = \sum_{i=1}^N \langle \Psi | \delta(\mathbf{r}_i - \mathbf{R}_A) | \Psi \rangle, \quad (55)$$

$$\eta(\mathbf{0}) = \sum_{i=1}^N \sum_{j>i}^N \langle \Psi | \delta(\mathbf{r}_i - \mathbf{r}_j) | \Psi \rangle. \quad (56)$$

The quantity  $\Gamma(\mathbf{R}_A, \mathbf{R}_B)$  is an element of the density matrix, for which the cusp condition is also known [25, 26], but it is handled as a fitting parameter in the present work.

## 4 | COMPUTATIONAL DETAILS

The integral transformed functions  $\mathcal{I}_{\hat{p}^2}$ ,  $\mathcal{I}_{\hat{p}^4}$ ,  $\mathcal{I}_{1/r_{iA}}$ ,  $\mathcal{I}_{1/r_{ij}}$ ,  $\mathcal{I}_{\delta(r_{iA})}$ , and  $\mathcal{I}_{\delta(r_{ij})}$  are shown in Figures 1 and 2 for the example of the ground electronic state of the helium atom (He) and the trihydrogen cation ( $\text{H}_3^+$ ) with protons (p) clamped at an equilateral triangular configuration with  $R_{pp} = 1.65$  bohr.

Up to a certain  $\xi_\Lambda$  value ( $\xi_\Lambda = p_\Lambda$  for momentum operators, and  $\xi_\Lambda = t_\Lambda$  for Coulombic operators), we calculate the short-range integral analytically for  $\mathcal{I}_{\hat{p}^2}$ ,  $\mathcal{I}_{1/r_{iA}}$ ,  $\mathcal{I}_{1/r_{ij}}$ , and by quadrature for  $\mathcal{I}_{\hat{p}^4}$ ,  $\mathcal{I}_{\delta(r_{iA})}$ , and  $\mathcal{I}_{\delta(r_{ij})}$  (for more details see Appendix A). For the long-range part, it is necessary to determine the accurate value of  $\rho(\mathbf{0})$  and  $\eta(\mathbf{0})$ , which is calculated by an iterative procedure using Equations (24), (27), (32), and (33). Then, the long-range part is obtained by fitting the asymptotic tail to data points using Equations (23), (29), and (51) that is followed by the analytic integration of the asymptotic tail, Equations (25), (31), and (52), using the fitted parameters.

It is critical to choose an optimal  $\xi_\Lambda$  value and a good interval for the data used for the fitting of the long-range analytic expression. We have selected these parameters based on the inspection of the integrand evaluated with the approximate wave function (Figures 1 and 2). Close to the origin, the asymptotic expansion fails, but the ECG basis describes well the non-analytic correlation effects in this range. The parameter  $\xi_\Lambda$  must be large enough to ensure that the function  $\mathcal{I}_{F(r)}(\xi_\Lambda)$  can be approximated accurately with the asymptotic expansion. At the same time, it must be small enough to eliminate the major numerical uncertainties from the finite basis expansion. For the spherically symmetric ground state of the helium atom (Figure 1),  $\mathcal{I}(\xi)$  is simple, it decreases monotonically to zero after an initial peak. The asymptotic part can be “easily” identified and fitted to the asymptotic series. The  $\text{H}_3^+$  molecular ion (Figure 2) is a more “complex” system, with more complicated correlation effects, and thus, we need to choose a larger  $\xi_\Lambda$  value to reach the asymptotic regime (which also implies the use of a larger basis set). Further details about the accuracy of the matrix elements depending on the selection of the  $\xi_\Lambda$  value can be found in Section 6.

According to Sections 2.1 and 3.1, the long-range part of the function  $\mathcal{I}(\xi)$  decays polynomially due to the cusp in the exact wave function that is approximated in the computations. At the same time, we may observe in Figure 3 that the approximate  $\mathcal{I}_{p^k}(p)$  ( $k=2,4$ ) function, corresponding to a finite ECG basis set, has artificial oscillations in momentum space and some non-negligible deviations in  $t$ -space. If the full integral is computed by direct integration, the oscillations approximately cancel in the integral, and this explains the practical observation that accurate results can be obtained even with ECGs that fail to satisfy analytic properties of the exact wave function. We aim to obtain more accurate integral values by replacing the oscillatory asymptotic tail with the mathematically correct decaying form corresponding to the cusp.

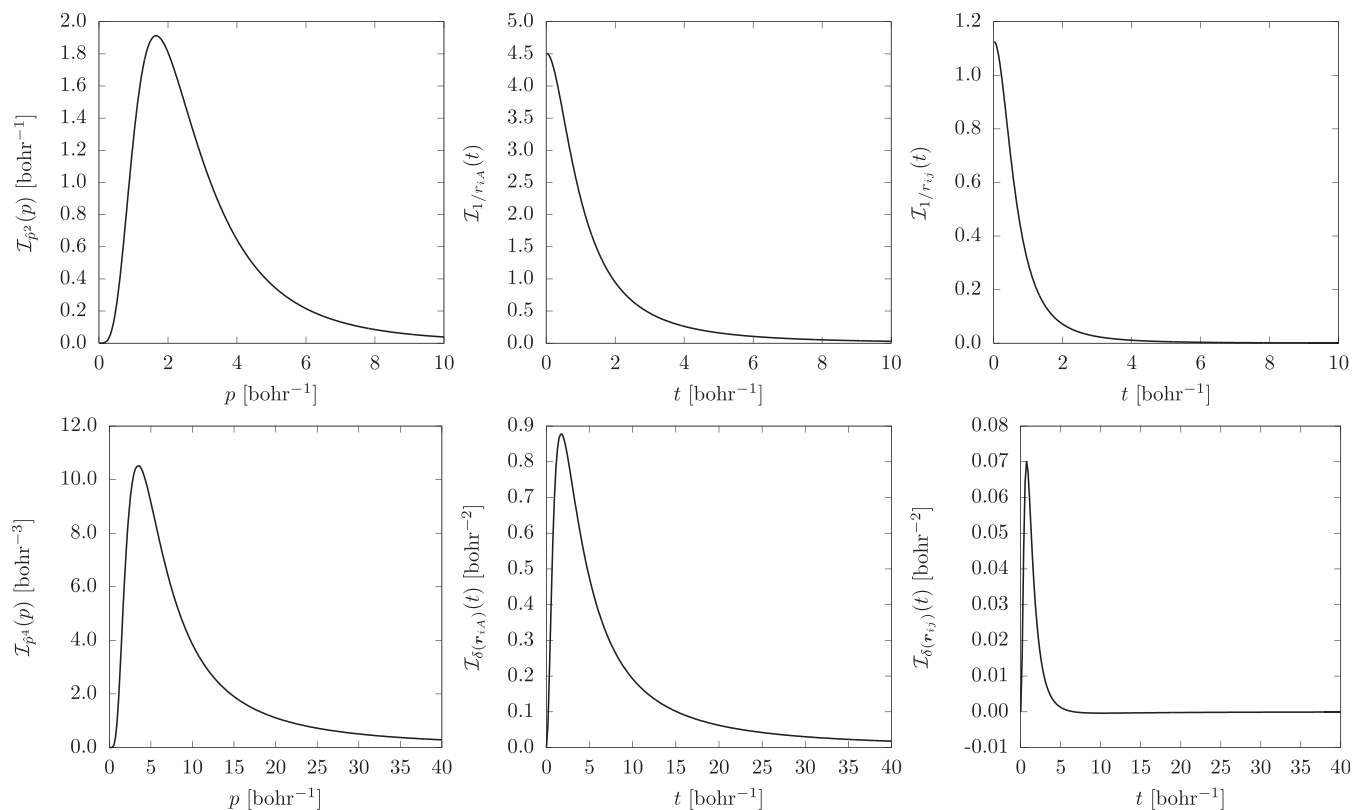


**FIGURE 1** Integral transform (IT) function profile for various operators,  $\mathcal{I}_{\hat{p}^2}$ ,  $\mathcal{I}_{1/r_{iA}}$ ,  $\mathcal{I}_{1/r_{ij}}$ ,  $\mathcal{I}_{\hat{p}^4}$ ,  $\mathcal{I}_{\delta(r_{iA})}$ , and  $\mathcal{I}_{\delta(r_{ij})}$  for the example of the ground electronic state of the helium atom

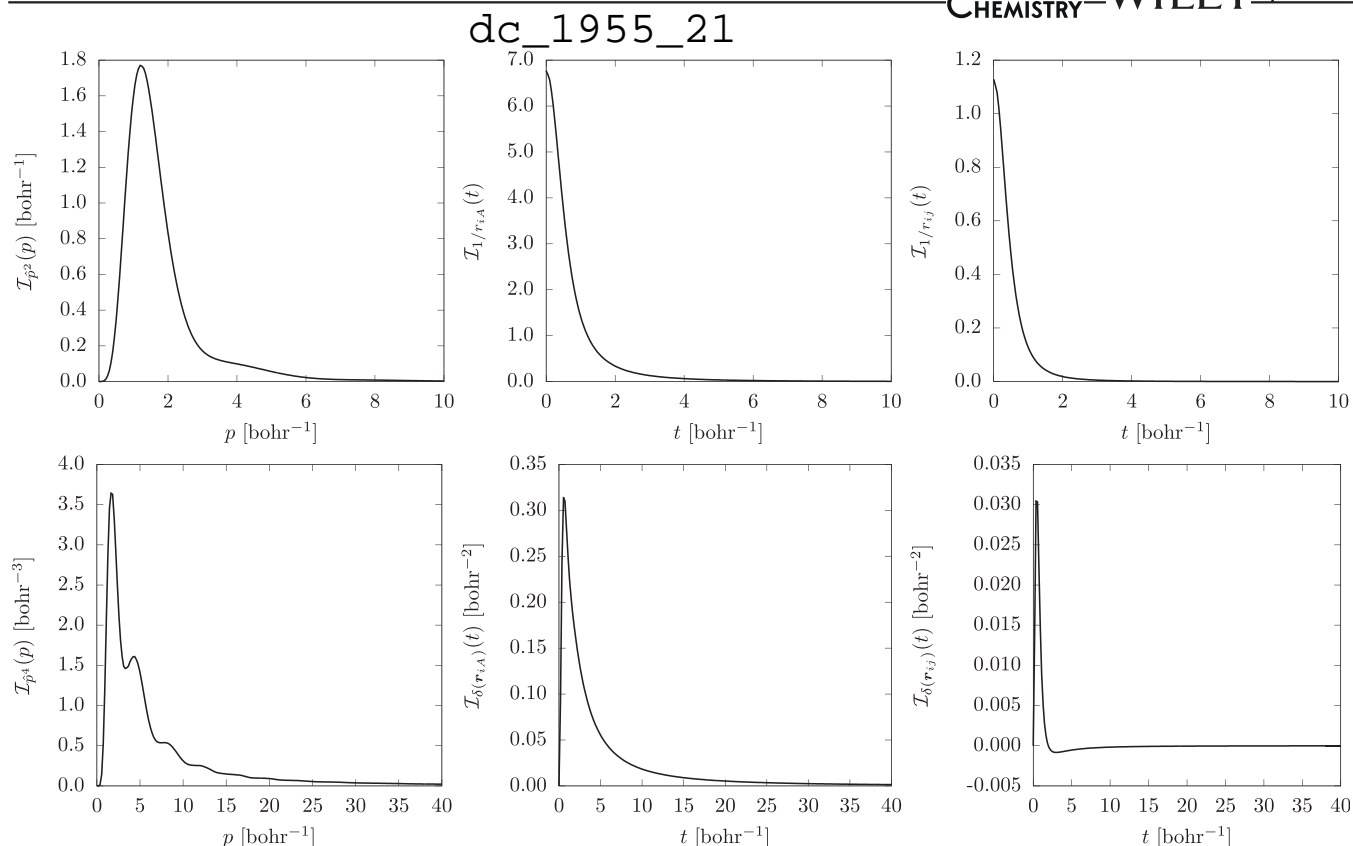


**FIGURE 2** Integral transform (IT) function profile for various operators,  $\mathcal{I}_{\hat{p}^2}$ ,  $\mathcal{I}_{1/r_A}$ ,  $\mathcal{I}_{1/r_B}$ ,  $\mathcal{I}_{\hat{p}^4}$ ,  $\mathcal{I}_{\delta(r_A)}$ , and  $\mathcal{I}_{\delta(r_B)}$  for the example of the ground electronic state of the  $\text{H}_3^+$  with protons (p) clamped at an equilateral triangular configuration with  $R_{pp} = 1.65$  bohr

In practice, the numerical accuracy of the computations is affected by the grids used for the numerical integration (if analytic integration is not possible over the finite, short-range interval) and for the fitting procedure. Our computational strategies are explained in the following sections for the physical operators considered in this work.

## 5 | PERTURBATIVE RELATIVISTIC CORRECTION FOR $\text{H}_3^+$ AT EQUILIBRIUM

For the spectroscopic characterization of compounds of light elements, the leading-order relativistic correction has been traditionally calculated as the expectation value of the Breit–Pauli Hamiltonian with the non-relativistic wave function. The Breit–Pauli Hamiltonian is the leading-order Foldy–Wouthuysen perturbation theory (FWPT) term of the Dirac–Coulomb–Breit Hamiltonian [27–29]. The singular operators that are difficult to evaluate in a Gaussian basis appear already for the leading-order FWPT of the Dirac–Coulomb (DC) operator that reads for the two electrons of  $\text{H}_3^+$  with fixed protons ( $N = 2$  and  $N_{\text{nuc}} = 3$ ) as

$$\hat{H}^{\text{FW}} = \hat{H}_{\text{nonrel}} + \Delta\hat{H}^{\text{FW}} \quad (57)$$

$$c^2\Delta\hat{H}_{\text{DC}}^{\text{FW}} = \underbrace{-\frac{1}{8}\sum_{i=1}^N\nabla_i^4}_{\text{mass-velocity}} + \underbrace{\frac{\pi}{2}\sum_{i=1}^N\sum_{A=1}^{N_{\text{nuc}}}Z_A\delta(\mathbf{r}_{iA})}_{\text{Darwin I}} - \underbrace{\pi\sum_{i=1}^N\sum_{j>i}^N\delta(\mathbf{r}_{ij})}_{\text{Darwin II}}, \quad (58)$$

$$\begin{aligned} c^2\Delta\hat{H}_{\text{DCB}}^{\text{FW}} &= c^2\Delta\hat{H}_{\text{DC}}^{\text{FW}} + \underbrace{2\pi\sum_{i=1}^N\sum_{j>i}^N\delta(\mathbf{r}_{ij})}_{\text{spin-spin}} - \underbrace{\sum_{i=1}^N\sum_{j>i}^N\frac{1}{2r_{ij}}\left(\mathbf{p}_i\mathbf{p}_j + \frac{\mathbf{r}_{ij}(\mathbf{r}_{ij}\mathbf{p}_i)\mathbf{p}_j}{r_{ij}^2}\right)}_{\text{orbit-orbit}} \\ &= -\frac{1}{8}\sum_{i=1}^N\nabla_i^4 + \frac{\pi}{2}\sum_{i=1}^N\sum_{A=1}^{N_{\text{nuc}}}Z_A\delta(\mathbf{r}_{iA}) + \pi\sum_{i=1}^N\sum_{j>i}^N\delta(\mathbf{r}_{ij}) - \sum_{i=1}^N\sum_{j>i}^N\frac{1}{2r_{ij}}\left(\mathbf{p}_i\mathbf{p}_j + \frac{\mathbf{r}_{ij}(\mathbf{r}_{ij}\mathbf{p}_i)\mathbf{p}_j}{r_{ij}^2}\right), \end{aligned} \quad (59)$$

dc\_1955\_21

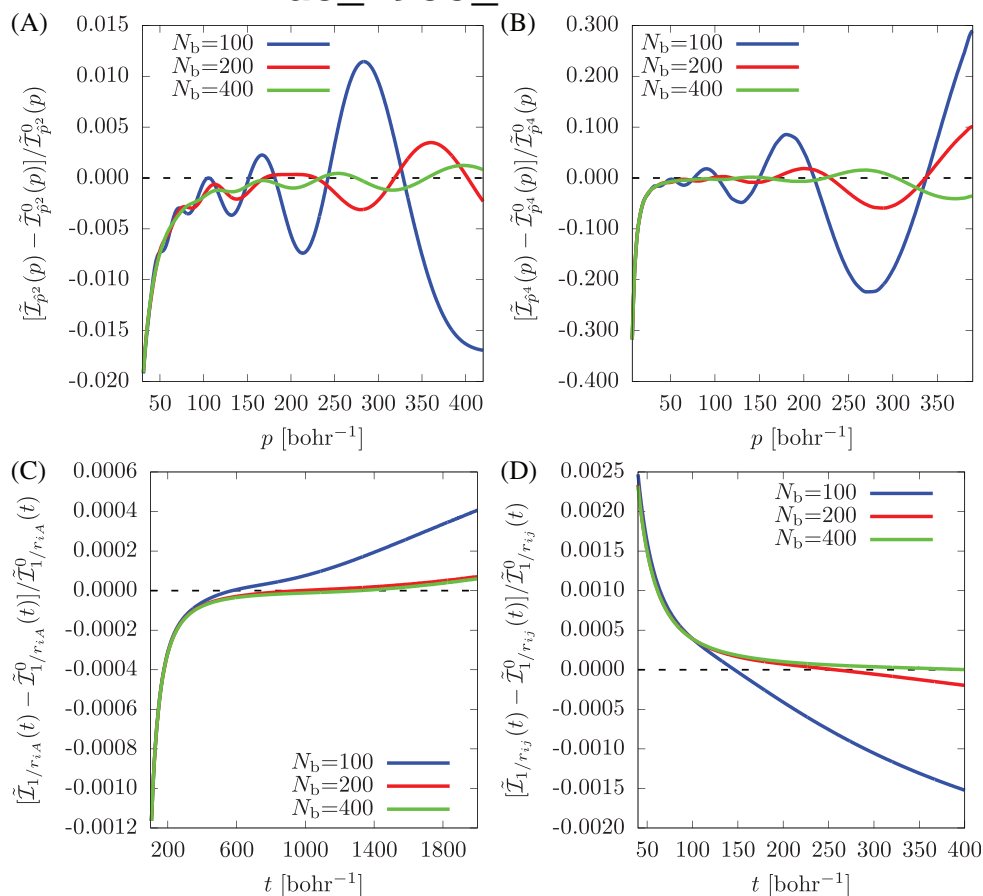


**FIGURE 3** Relative difference in the asymptotic tail of the numerically calculated functions  $\mathcal{I}_{p^2}(p)$ ,  $\mathcal{I}_{p^4}(p)$ ,  $\mathcal{I}_{1/r_{iA}}(t)$ ,  $\mathcal{I}_{1/r_{ij}}(t)$ , and the analytic leading-order expressions of the asymptotic tail,  $\tilde{\mathcal{I}}_{p^k}^0(p) = N^{-1}p^{-2-k}128\pi\rho(\mathbf{0})$ ,  $\tilde{\mathcal{I}}_{1/r_{iA}}^0(t) = N^{-1}t^{-3}(2\pi\rho(\mathbf{0}) - 16\sqrt{\pi}\rho(\mathbf{0})t^{-1})$ , and  $\tilde{\mathcal{I}}_{1/r_{ij}}^0(t) = [N(N-1)]^{-1}t^{-3}2(\pi\eta(\mathbf{0}) + 2\sqrt{\pi}\eta(\mathbf{0})t^{-1})$  for the example of the ground state of the helium atom with an increasing number of explicitly correlated Gaussian (ECG) basis functions ( $N_b$ )

for singlet states.  $\hat{H}_{\text{nonrel}}$  is the non-relativistic Hamiltonian and  $\Delta\hat{H}_{\text{DC}}^{\text{FW}}$  and  $\Delta\hat{H}_{\text{DCB}}^{\text{FW}}$  correspond to the leading-order correction to the non-relativistic energy of the Foldy–Wouthuysen (FW) transformed DC and Dirac–Coulomb–Breit (DCB) Hamiltonians.

We have calculated the expectation value of the mass-velocity and the Darwin terms with the non-relativistic wave function both by direct integration and by the IT technique. IT technique for the example of the simplest polyatomic molecule,  $\text{H}_3^+$  near its equilibrium structure (Table 1). In Table 1, we also show the (non-singular) orbit-orbit term (last term in Equation (59)) by direct integration.

Regarding the computational parameters, the  $\xi_\Lambda = 100 \text{ bohr}^{-1}$  threshold value was appropriate also in this system, similarly to the He and  $\text{H}_2$  computations reported in Pachucki et al. [2]. The short-range integrals were calculated by quadrature. For the Dirac-delta terms, the numerical integration was carried out over three subintervals,  $[0, 1] \text{ bohr}^{-1}$ ,  $[1, 10] \text{ bohr}^{-1}$ , and  $[10, 100] \text{ bohr}^{-1}$ , using 25, 35, and 35 Gauss–Legendre quadrature points. For the mass-velocity term, we have checked the convergence of the integral value over the  $[10, 100] \text{ bohr}^{-1}$  interval using 50, 70, and 100 number of points. The value of the integrand at each grid point is obtained by direct evaluation of the finite basis ECG integral (Appendix A). This setup was sufficient for a parts-per-billion (ppb) convergence of the short-range integral value.

For fitting the long-range part of the integrand, we have considered the  $p > 60 \text{ bohr}^{-1}$  tail that is beyond the range dominated by non-trivial correlation effects (Figure 2). We have carried out the fitting of the asymptotic tail by including additional grid points from the  $[100, 390] \text{ bohr}^{-1}$  interval with  $10 \text{ bohr}^{-1}$  spacing. In each fit, six parameters were included, and the squared sum of residuals was on the order of  $10^{-20}$  (a.u.) for  $\delta(r_{ij})$  and  $\delta(r_{iA})$  and  $10^{-10}$  (a.u.) for the  $p_1^4 + p_2^4$  term. Table 1 collects the terms appearing in the relativistic corrections obtained with direct integration and by the IT technique that reduces the relative error of the expectation value by  $\sim 2$  orders of magnitude.

In Table 2, the leading-order FW–DC and FW–DCB energy is compared with the no-pair variational energy of the corresponding (DC and DCB) operators [31]. In the perturbative DC energy, we observe an error cancelation for the singular terms, hence, the direct and the IT FW–DC energies differ only on the order of  $1 \text{ nE}_h$ . For the FW–DCB energy, due to the spin–spin contribution, Equation (59), there is a  $15 \text{ nE}_h$  deviation between the direct and the IT results. For comparison, we also show the variational DC(B) energies [31] that are not affected by the slow

dc\_1955\_21

**TABLE 1** Expectation value of operator terms in the leading-order Foldy–Wouthuysen perturbative relativistic operators (in atomic units) computed by direct integration (“direct”) and by the integral transformation technique (“IT”) for the ground electronic state of  $H_3^+$  with protons (p) clamped at an equilateral triangular configuration with  $R_{pp} = 1.65$  bohr

$N_b$	$\langle \nabla_1^4 + \nabla_2^4 \rangle$		$\sum_{i=1}^2 \sum_{A=1}^3 \mathbf{Z}_A \langle \delta(\mathbf{r}_i - \mathbf{R}_A) \rangle$		$\langle \delta(\mathbf{r}_1 - \mathbf{r}_2) \rangle$		Orbit-orbit term
	Direct	IT	Direct	IT	Direct	IT	
150	15.428820	15.467265	1.086786273	1.089641891	0.018430054	0.018340790	−0.057219009
200	15.446739	15.467346	1.088110465	1.089651086	0.018407593	0.018336611	−0.057218310
300	15.455982	15.467351	1.088821792	1.089654339	0.018368291	0.018335079	−0.057217628
400	15.456244	15.467368	1.088836952	1.089654512	0.018360864	0.018334828	−0.057217548
500	15.456360	15.467395	1.088843368	1.089654577	0.018358011	0.018334777	−0.057217524
600	15.456386	15.467395	1.088845002	1.089654597	0.018357565	0.018334773	−0.057217520

Note: The basis set size corresponds to the use of  $D_{3h}$  point-group symmetry in the computations.

**TABLE 2** Non-relativistic, perturbative ( $E_{DC}^{FW}$  and  $E_{DCB}^{FW}$ ) and no-pair variational ( $E_{DC}^{npV}$  and  $E_{DCB}^{npV}$ ) relativistic electronic energies, in  $E_h$ , for the ground electronic state of  $H_3^+$  with protons (p) clamped at an equilateral triangular configuration with  $R_{pp} = 1.65$  bohr (see also caption to Table 1)

$N_b$	$E_{nonrel}$	$E_{DC}^{FW}$ (Direct) <sup>a</sup>	$E_{DC}^{FW}$ (IT) <sup>a</sup>	$E_{DC}^{npV}$ [31]	$E_{DCB}^{FW}$ (Direct) <sup>b</sup>	$E_{DCB}^{FW}$ (IT) <sup>b</sup>	$E_{DCB}^{npV}$ [31]
150	−1.343835557	−1.343850435	−1.343850437	−1.343850149	−1.343847315	−1.343847347	−1.343847343
200	−1.343835606	−1.343850488	−1.343850485	−1.343850507	−1.343847376	−1.343847396	−1.343847404
300	−1.343835623	−1.343850501	−1.343850501	−1.343850524	−1.343847402	−1.343847413	−1.343847462
400	−1.343835624	−1.343850502	−1.343850502	−1.343850526	−1.343847405	−1.343847415	−1.343847484
500	−1.343835625	−1.343850502	−1.343850503	−1.343850527	−1.343847406	−1.343847416	−1.343847496
600	−1.343835625	−1.343850502	−1.343850503	−1.343850527	−1.343847406	−1.343847416	−1.343847498

Note: We used the speed of light  $c = \alpha^{-1} a_0 E_h / \hbar$  with  $\alpha^{-1} = 137.035999084$  [30].

<sup>a</sup>Expectation value of  $H_{DC}^{FW}$ , Equations (57) and (58), with the non-relativistic wave function.

<sup>b</sup>Expectation value of  $H_{DCB}^{FW}$ , Equations (57) and (59), with the non-relativistic wave function.

convergence problem of the singular operators. A detailed comparison of the variational and the perturbative FW energies will be provided in future work.

## 6 | AN ATTEMPT TO IMPROVE THE NON-RELATIVISTIC ENERGY WITH THE INTEGRAL TRANSFORMATION TECHNIQUE

According to Sections 2 and 3, the integral transformation technique can be used also for the expectation values of the non-relativistic operators,  $\langle \hat{p}^2 \rangle$ ,  $\langle 1/r_{iA} \rangle$ , and  $\langle 1/r_{ij} \rangle$ . Although these expectation values converge (much) faster than the expectation value of the singular operators appearing in the relativistic corrections, pinpointing their precise value would be useful to have an (even) better estimate of the complete basis limit. In this section, we report observations of some exploratory work for the  $\langle \hat{p}^2 \rangle$  operator for the ground state of the helium atom.

Thanks to the simplicity of the  $\mathcal{I}_{\hat{p}^2}$ ,  $\mathcal{I}_{1/r_{iA}}$ , and  $\mathcal{I}_{1/r_{ij}}$  integrands, the short-range integrals can be obtained in an analytic form (Appendix A). To fit the  $\tilde{\mathcal{I}}_{\hat{p}^2}(\xi)$  asymptotic part, an equidistant grid was used. The start of the fitting interval was determined based on inspection of the integrand functions (Figure 1). On the one hand, we wanted to choose a large  $\xi$  value to avoid fitting to non-trivial correlation features. On the other hand, we wanted to choose a small  $\xi$  value to reduce the finite basis error of the ECG basis set. A short summary about the calculation of the necessary  $\rho(\mathbf{0})$  and  $\eta(\mathbf{0})$  values is provided in Appendix D. Figure 3 shows the relative difference of  $\mathcal{I}_{\hat{p}^2}(\xi)$  represented by the finite basis expansion and by the analytically known leading-order asymptotic part,  $\tilde{\mathcal{I}}_{\hat{p}^2}^0(p) = N^{-1} p^{-2-k} 128\pi\rho(\mathbf{0})$ ,  $\tilde{\mathcal{I}}_{1/r_{iA}}^0(t) = N^{-1} t^{-3} (2\pi\rho(\mathbf{0}) - 16\sqrt{\pi}\rho(\mathbf{0})t^{-1})$ , and  $\tilde{\mathcal{I}}_{1/r_{ij}}^0(t) = [N(N-1)]^{-1} t^{-3} 2(\pi\eta(\mathbf{0}) + 2\sqrt{\pi}\eta(\mathbf{0})t^{-1})$ .

For larger (but not too large, i.e., for which the finite basis representation can be trusted)  $\xi$  values, the relative difference is determined by the contributions beyond the analytic, leading-order terms. The deviation from zero in the asymptotic limit indicates numerical errors, which originate from the finite basis-set approximation.

For the Coulomb terms,  $\tilde{\mathcal{I}}_{1/r_{ij}}$  and  $\tilde{\mathcal{I}}_{1/r_{iA}}$  (Figure 3C,D), this numerical error is monotonic and has non-negligible values beyond some  $t$  value, but by increasing the basis set size, this critical  $t$  threshold is shifted toward larger values.

dc\_1955\_21

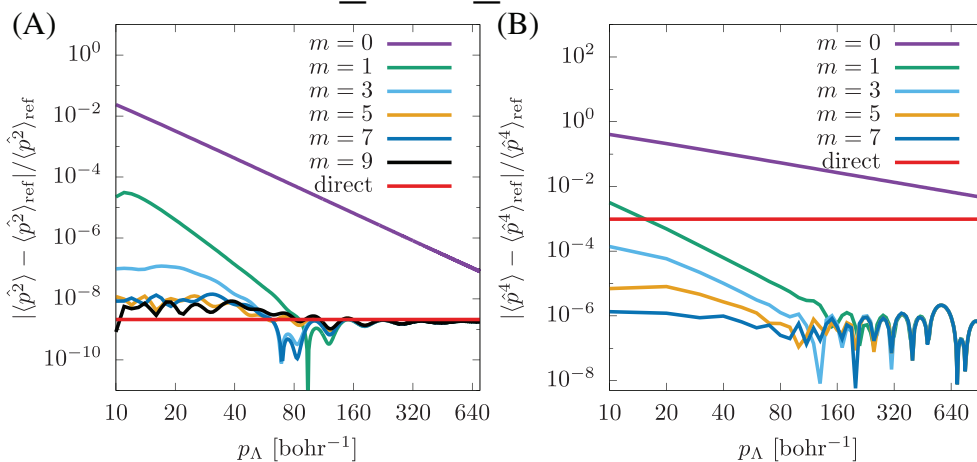


**FIGURE 4** Relative error of  $\langle \hat{p}^2 \rangle$  and  $\tilde{f}(p) = \frac{1}{\sqrt{2\pi}} \int_{-\infty}^{\infty} dx f(x) e^{-ipx}$  for helium, for various  $p_\Lambda$  thresholds and  $m$  terms in fitting function

Equation (52). The result “direct” was obtained by direct integration with explicitly correlated Gaussians (ECGs). The reference values are  $\langle \hat{p}^2 \rangle_{\text{ref}} = 2.903\,724\,377\,034\,119\,5 \text{ bohr}^{-2}$  [32] (using the virial theorem  $\langle \hat{T} \rangle = -E$ ), and  $\langle \hat{p}^4 \rangle_{\text{ref}} = 108.176\,134\,4(8) \text{ bohr}^{-4}$  [2]

Regarding the  $\hat{p}^k$  operators (Figure 3A,B), the Fourier transformation results in oscillations that can be observed for the finite-basis representation of  $\mathcal{I}_{\hat{p}^k}$  over the large momentum range. The oscillation amplitude decreases upon increasing the basis set size. Figure 4 shows the comparison of the direct and the IT integration procedures for  $\hat{p}^2$  and  $\hat{p}^4$ . The computational details for  $\hat{p}^4$  can be found in the Section 4. Regarding  $\hat{p}^2$ , the fit is performed over the  $[10, 90] \text{ bohr}^{-1}$  interval using 1600 equidistant points. Depending on the number of the fitting parameters the squared sum of the residuals varied between  $10^{-11}$  and  $10^{-17}$  (a.u.).

The effect of the choice of the  $p_\Lambda$  threshold value, which separates the short- and the long-range intervals, and the number of the fitted parameters in the long-range part is shown in Figure 4. For both  $\hat{p}^2$  and  $\hat{p}^4$ , the larger the number of the fitted parameters, the better results are observed, especially for smaller  $p_\Lambda$  values. By increasing  $p_\Lambda$ , all curves are close, since the high-order inverse momentum terms have a numerically negligible contribution in this regime. For  $p_\Lambda \rightarrow \infty$ , the contribution from the integral transformation goes to zero, and the direct integration result is recovered. It is also necessary to note that although we achieve a better relative accuracy for  $\langle \hat{p}^2 \rangle$  than for  $\langle \hat{p}^4 \rangle$ , the improvement of  $\langle \hat{p}^2 \rangle$  (IT) over  $\langle \hat{p}^2 \rangle$  (“direct”) is modest. This observation can be contrasted with the two orders of magnitude improvement of  $\langle \hat{p}^2 \rangle$  (IT) over  $\langle \hat{p}^4 \rangle$  (“direct”) that appears to be a robust feature with  $\hat{p}^2$  respect to the choice of  $p_\Lambda$  and the fitting details. For  $\hat{p}^2$ , the “optimal” interval for  $p_\Lambda$  and the fitting details should be very carefully chosen to observe any improvement.

## 7 | SUMMARY AND CONCLUSION

ECGs are often used in atomic and molecular computations, since they incorporate particle-particle correlation and they have analytic integrals for most physically relevant operators. In spite of their advantages, they also have some drawbacks. They fail to describe correctly the particle coalescence points and the asymptotic tail of the exact non-relativistic wave function of Coulomb-interacting point-like particles. This paper was devoted to the study of a possible correction scheme for coalescence properties during computations with Gaussian-type functions.

For this purpose, we have presented the detailed theoretical background of the IT technique originally proposed by Pachucki et al. [2] to enhance the convergence of singular operators appearing in perturbative relativistic corrections. The core idea of the IT technique is to rewrite expectation values of physical quantities with an approximate wave function into a form, for which the cusp effect—characteristic for short ranges in coordinate space—appears in the asymptotic tail of the integrand in an “inverse space” ( $\xi$ ). For momentum-type operators, this transformation is the Fourier transformation and the inverse space is momentum space ( $\xi = p$ ). For Coulomb-type operators this is a “ $t$ -transformation” (for which we are not aware of any common name), and for which the variable in the inverse space was labeled with  $\xi = t$ . Expectation values that contain the cusp effects are obtained by computing the integral as the sum of a short-,  $0 \leq \xi < \xi_\Lambda$ , and a long-range,  $\xi_\Lambda \leq \xi < \infty$ , part. The short-range part is calculated by direct integration with the approximate wave function expressed with ECGs.

We explained in this paper that the effect of the singular derivative of the wave function at the coalescence points, where the exact wave function cusps, appears in the asymptotic tail of the integrand in the inverse space. Using this connection and the analytic cusp conditions, we derived the analytic form of the long-range tail of the integrands for the  $p_i^2$ ,  $1/r_{ij}$ ,  $1/r_{iA}$ -type operators and our derivation reproduced the asymptotic expressions for  $p_i^4$ ,  $\delta(r_{iA})$ , and  $\delta(r_{ij})$  of Pachucki et al. [2]. It is interesting to note that, in the inverse space, the asymptotic tail of the non-relativistic operators ( $p^2$  and  $1/r$ ) decay faster ( $\sim 1/p^4$  and  $\sim 1/t^3$ ), than the tail of the more “singular” operators,  $\hat{p}^4$  and  $\hat{\delta}(r)$ ,  $\sim 1/p^2$  and  $\sim 1/t^2$ , respectively.

## dc\_1955\_21

Exploratory results were reported for the expectation values of the non-relativistic energy operators, for which, in principle, it should be possible to improve upon the non-relativistic energy with the inclusion of the cusp “effect.” The practical realization of this idea appears to be limited, for the moment, by particular details of the fitting procedure of the asymptotic tail.

We also use the IT technique in this work to compute perturbative relativistic corrections for the ground state of  $H_3^+$  near its equilibrium structure. We observe error cancelation among the singular terms in the perturbative Dirac–Coulomb energy, but for the perturbative Dirac–Coulomb–Breit energy the IT technique results in a 15 nE<sub>h</sub> improvement over the direct result. These perturbative relativistic energies pinpointed with the IT technique can be used for a detailed comparison in relation with the variational relativistic result of Jeszenszki et al. [31] that will be reported in future work.

Finally, we would like to mention that the  $\hat{p}^4$ - and  $\delta(r)$ -type singular operators appear not only in the perturbative relativistic theory but also in lower-bound theory due to the presence of the  $\hat{H}^2$  operator [5, 33, 34]. This fact contributes to the observation that the energy lower bounds typically converge slower to the exact energy [5, 34], than the energy upper bound. It would be interesting to use (generalize) the IT technique to the  $\hat{H}^2$  expectation value and variance computations, which may speed up the convergence of the best energy lower bounds [35] and that would open the route to the computation of rigorous theoretical error bars for numerically computed non-relativistic energies.

## ACKNOWLEDGMENTS

The authors thank Gustavo Avila for discussions about the quadrature integration. Financial support of the European Research Council through a Starting Grant (No. 851421) is gratefully acknowledged. Robbie T. Ireland thanks the Erasmus+ program for funding a traineeship at ELTE.

## AUTHOR CONTRIBUTIONS

**Peter Jeszenszki:** Formal analysis; investigation; methodology; software; visualization; writing – original draft; writing – review and editing. **Robbie Ireland:** Investigation; methodology; software; validation; writing – review and editing. **David Ferenc:** Investigation; methodology; software; validation; writing – review and editing. **Edit Mátyus:** Conceptualization; formal analysis; funding acquisition; investigation; methodology; project administration; resources; software; supervision; validation; visualization; writing – original draft; writing – review and editing.

## ENDNOTE

<sup>1</sup> A discontinuous function cannot be differentiated in a rigorous way. However, the differentiation can be generalized using the so-called weak derivative [40], which can be calculated for these functions. This leads to the expected Dirac delta function as the weak derivative of the Heaviside step function.

## DATA AVAILABILITY STATEMENT

The data that support the findings of this study are available from the corresponding author upon reasonable request.

## ORCID

Péter Jeszenszki  <https://orcid.org/0000-0001-8696-6575>

Dávid Ferenc  <https://orcid.org/0000-0002-5193-540X>

Edit Mátyus  <https://orcid.org/0000-0001-7298-1707>

## REFERENCES

- [1] I. Mayer, *Simple Theorems, Proofs, and Derivations in Quantum Chemistry*. Mathematical and Computational Chemistry, Springer US, Boston, MA 2003 <http://link.springer.com/10.1007/978-1-4757-6519-9>
- [2] K. Pachucki, W. Cencek, J. Komasa, *J. Chem. Phys.* **2005**, *122*, 184101.
- [3] B. Jeziorski, K. Szalewicz, *Phys. Rev. A* **1979**, *19*, 2360.
- [4] W. Cencek, J. Rychlewski, *J. Chem. Phys.* **1993**, *98*, 1252.
- [5] Y. Suzuki, K. Varga, *Stochastic Variational Approach to Quantum-Mechanical Few-Body Problems*, Springer-Verlag, Berlin Heidelberg **1998**. <https://www.springer.com/gp/book/9783540651529>.
- [6] J. Mitroy, S. Bubin, W. Horiuchi, Y. Suzuki, L. Adamowicz, W. Cencek, K. Szalewicz, J. Komasa, D. Blume, K. Varga, *Rev. Mod. Phys.* **2013**, *85*, 693.
- [7] S. F. Boys, *Proc. R. Soc. Lond. A* **1950**, *200*, 542.
- [8] T. Helgaker, P. Jørgensen, J. Olsen, *Molecular Electronic-Structure Theory*, John Wiley & Sons, Chichester **2008**.
- [9] C. Hättig, W. Klopper, A. Köhn, D. P. Tew, *Chem. Rev.* **2012**, *112*, 4.
- [10] T. Kato, *Commun. Pure Appl. Math.* **1957**, *10*, 151.
- [11] R. T. Pack, W. B. Brown, *J. Chem. Phys.* **1966**, *45*, 556.
- [12] W. Kutzelnigg, *Int. J. Quantum Chem.* **1994**, *51*, 447.
- [13] V. A. Rassolov, D. M. Chipman, *J. Chem. Phys.* **1996**, *104*, 9908.
- [14] D. P. Tew, *J. Chem. Phys.* **2008**, *129*, 014104.
- [15] S. Fournais, M. Hoffmann-Ostenhof, T. Hoffmann-Ostenhof, T. O. Sorensen, *Commun. Math. Phys.* **2005**, *255*, 183.
- [16] C. R. Myers, C. J. Umrigar, J. P. Sethna, J. D. Morgan, *Phys. Rev. A* **1991**, *44*, 5537.

- [17] E. Steiner, *J. Chem. Phys.* **1963**, 39, 2365.
- [18] J. C. Kimball, *J. Phys. A: Math. Gen.* **1975**, 8, 1513.
- [19] B. Mercier, *An Introduction to the Numerical Analysis of Spectral Methods*, Springer Berlin, Berlin **2014**.
- [20] W. A. Bingel, *Z. Naturforsch* **1963**, 18a, 1249.
- [21] H. Yasuhara, Y. Kawazoe, *Phys. A Stat. Mech. Appl.* **1976**, 85, 416 ISSN 03784371.
- [22] N. H. March, *J. Phys. A: Math. Gen.* **1975**, 8, L133.
- [23] J. Cioslowski, *J. Chem. Phys.* **2020**, 153, 154108.
- [24] F. W. J. Olver, A. B. Olde Daalhuis, D. W. Lozier, B. I. Schneider, R. F. Boisvert, C. W. Clark, B. R. Miller, B. V. Saunders, H. S. Cohl & M. A. McClain NIST Digital Library of Mathematical Functions: Sine and Cosine Integrals, <https://dlmf.nist.gov/6.2#ii> (**2021**). (accessed: 15 March 2021).
- [25] W. L. Clinton, L. J. Massa, *Int. J. Quantum Chem.* **1972**, 6, 519.
- [26] E. Davidson, *Reduced Density Matrices in Quantum Chemistry*, Elsevier Science, St Louis, MO **2014**.
- [27] K. G. Dyall, K. Fægri, *Introduction to Relativistic Quantum Chemistry*, Oxford University Press, New York **2007**.
- [28] M. Reiher, A. Wolf, *Relativistic Quantum Chemistry: The Fundamental Theory of Molecular Science*, 2nd ed., Wiley-VCH, Weinheim, Germany **2015**.
- [29] W. Cencek, W. Kutzelnigg, *J. Chem. Phys.* **1996**, 105, 5878.
- [30] CODATA 2018 Recommended Values of the Fundamental Constants, <https://physics.nist.gov/cuu/Constants/index.html> accessed: February 2021
- [31] P. Jeszenszki, D. Ferenc, E. Mátyus, *J. Chem. Phys.* **2021**, 154, 224110.
- [32] G. Drake, in *Springer Handbook of Atomic, Molecular, and Optical Physics* (Ed: G. Drake), Springer New York, New York, NY **2006**, p. 199.
- [33] D. H. Weinstein, *Proc. Natl. Acad. Sci. USA* **1934**, 20, 529.
- [34] R. Ireland, P. Jeszenszki, E. Mátyus, R. Martinazzo, M. Ronto & E. Pollak ACS Physical Chemistry Au, in press. <https://doi.org/10.1021/acspyschemau.1c00018>
- [35] E. Pollak, R. Martinazzo, *J. Chem. Theory Comput.* **2021**, 17, 1535.
- [36] E. Mátyus, M. Reiher, *J. Chem. Phys.* **2012**, 137, 024104.
- [37] F. W. J. Olver, A. B. Olde Daalhuis, D. W. Lozier, B. I. Schneider, R. F. Boisvert, C. W. Clark, B. R. Miller, B. V. Saunders, H. S. Cohl & M. A. McClain NIST Digital Library of Mathematical Functions: Expansion of plane wave in spherical harmonics, <https://dlmf.nist.gov/10.60#E7> (**2021**). (accessed: 15 March 2021).
- [38] E. W. Weisstein Spherical Bessel Function of the First Kind, <https://mathworld.wolfram.com/SphericalBesselFunctionoftheFirstKind.html> (**2021**). (accessed: 16 August 2021).
- [39] P. Uginčius, *Am. J. Phys.* **1972**, 40, 1690.
- [40] K. S. Ranade, *Fortschr. Phys.* **2015**, 63, 644.

**How to cite this article:** P. Jeszenszki, R. T. Ireland, D. Ferenc, E. Mátyus, *Int. J. Quantum Chem.* **2021**, e26819. <https://doi.org/10.1002/qua.26819>

## APPENDIX A

### NECESSARY GAUSSIAN INTEGRALS FOR THE SHORT-RANGE PART

The approximate wave function is written as a linear combination of antisymmetrized products of  $\chi$  spin and  $\Theta$  ECGs functions,

$$\Psi = \sum_{l=1}^{N_b} c_l \hat{A} \{ \chi_l \Theta_l \} \quad (\text{A1})$$

with the  $\hat{A} = (N_{\text{perm}})^{-\frac{1}{2}} \sum_{p=1}^{N_{\text{perm}}} \varepsilon_p \hat{P}_p$  antisymmetrization operator over the  $N_{\text{perm}}$  possible permutations with  $\varepsilon_p$  parity. Expectation values of a (permutationally invariant)  $\hat{O}$  operator can be calculated as

$$\langle \Psi | \hat{O} | \Psi \rangle = \sum_{l=1}^{N_b} \sum_{J=1}^{N_b} \sum_{p=1}^{N_{\text{perm}}} c_l^* c_J \varepsilon_{lJp} \langle \Theta_l | \hat{O} | \Theta_{Jp} \rangle \quad (\text{A2})$$

where  $\varepsilon_{lJp}$  contains the parity of the permutation and the spin integrals, and we need to calculate matrix elements of  $\hat{O}$  with the ECG functions  $\Theta_l$  and  $\Theta_{Jp}$ . Particle permutation leaves the mathematical form of the ECG unchanged, and assumes transformation of the **A** and **s** parameter arrays (for further details, see, e.g., Mátyus and Reiher [36]).

During the IT procedure, the short-range part of the expectation values is computed by direct integration with the basis functions. For the short-range calculations, the following integrals were used.

### Coulomb integral over the short-range interval

Using the following notations:



dc\_1955\_21

**TABLE A1** Convergence of the density and the pair correlation functions, in bohr<sup>-3</sup>, at the coalescence point for the ground-electronic state of the helium atom computed with the IT technique

$N_b$	$\rho(\mathbf{0})$	$\eta(\mathbf{0})$
100	3.620845647	0.106366877
200	3.620857171	0.106350118
400	3.620858545	0.106348521
Ref. [32]	3.620858636 98(6)	0.106345371 2(2)

Note:  $N_b$  is the number of the basis functions.  $t_\Lambda = 100$  bohr<sup>-1</sup>.

Abbreviation: IT, integral transform.

$$\mathbf{e}_i = \mathbf{A}_i \mathbf{s}_i, \quad (\text{A3})$$

$$\mathbf{e}_{ij} = \mathbf{e}_i + \mathbf{e}_j, \quad (\text{A4})$$

$$\eta_{ij} = \mathbf{s}_i^T \mathbf{A}_i \mathbf{s}_i + \mathbf{s}_j^T \mathbf{A}_j \mathbf{s}_j, \quad (\text{A5})$$

$$\mathbf{A}_{ij} = \mathbf{A}_i + \mathbf{A}_j, \quad (\text{A6})$$

$$\gamma_{ij} = \mathbf{e}_{ij}^T \mathbf{A}_{ij}^{-1} \mathbf{e}_{ij} - \eta_{ij}, \quad (\text{A7})$$

$$(\mathbf{J}_{12})_{kl} = \delta_{1k} \delta_{1l} + \delta_{2k} \delta_{2l} - \delta_{1k} \delta_{2l} - \delta_{2k} \delta_{1l}, \quad k, l = 1, \dots, N \quad (\text{A8})$$

$$\beta_{ij} = \mathbf{e}_{ij}^T \mathbf{A}_{ij}^{-1} \mathbf{J}_{12} \mathbf{A}_{ij}^{-1} \mathbf{e}_{ij}, \quad (\text{A9})$$

$$a_{ij} = \text{Tr}(\mathbf{J}_{12} \mathbf{A}_{ij}^{-1}), \quad (\text{A10})$$

$$S_{ij} = \exp(\gamma_{ij}) \frac{\pi^{\frac{3N}{2}}}{|\mathbf{A}_{ij}|^{3/2}}, \quad (\text{A11})$$

the Coulomb integral for a finite range can be given explicitly as,

$$\begin{aligned} \left\langle \Theta_i \left| \left( \frac{1}{r_{12}} \right)_\Lambda \right| \Theta_j \right\rangle &= \frac{2}{\sqrt{\pi}} \int_0^\Lambda dt \left\langle \Theta_i \left| e^{-r_{12}^2 t^2} \right| \Theta_j \right\rangle \\ &= \frac{2}{\sqrt{\pi}} S_{ij} \int_0^\Lambda dt (1+t^2 a_{ij})^{-3/2} e^{-\frac{\beta_{ij} t^2}{1+t^2 a_{ij}}} \\ &= \frac{S_{ij}}{\sqrt{\pi \beta_{ij}}} \int_0^{\frac{\Lambda^2 \beta_{ij}}{1+\Lambda^2 a_{ij}}} dz z^{-\frac{1}{2}} e^{-z} = \frac{S_{ij}}{\sqrt{\beta_{ij}}} \left[ \left( \frac{\Lambda^2 \beta_{ij}}{1+\Lambda^2 a_{ij}} \right)^{\frac{1}{2}} \right]. \end{aligned} \quad (\text{A12})$$

We note that the  $t$  dependence of the short-range  $\delta(\mathbf{r})$  was integrated by Gauss-Legendre quadrature.

### Momentum integrals

In this subsection, we draft the integration of the angular degrees of freedom for the momentum density, which is used in the second step of Equation (36),

$$\int d\mathbf{p}_1 p_1^k \bar{\rho}(\mathbf{p}_1) = 4\pi \int_0^\infty dp p^{k+2} \langle \bar{\rho} \rangle_{\theta, \phi}(p). \quad (\text{A13})$$

dc\_1955\_21

To work out this step, we write down the integral for two basis functions in Fourier space that is proportional with (where  $a \in \mathbb{R}^+$ ,  $\mathbf{d} \in \mathbb{R}^3$ , and  $d = |\mathbf{d}|$  are constant coefficients containing the exponent matrices and shift vectors of the basis functions)

$$\begin{aligned} \int d\mathbf{p}_1 p_1^k \exp(-ap_1^2 + i\mathbf{d}^T \mathbf{p}_1) &= \int_0^{2\pi} d\phi \int_0^\infty dp p^{2+k} \int_0^\pi d\theta \sin \theta \exp(-ap^2 + i|\mathbf{d}|p \cos \theta) \\ &= 2\pi \int_0^\infty dp p^{k+2} \int_{-1}^1 dz \exp(-ap^2 + idpz) \\ &= \frac{4\pi}{d} \int_0^\infty dp p^{k+1} \sin(dp) e^{-ap^2}. \end{aligned} \quad (\text{A14})$$

We note that  $i\mathbf{d}$  is purely imaginary for any configuration-space shift vectors,  $\mathbf{s} \in \mathbb{R}^{3N}$ , due to Equation (34). The short-range part of the integral in Equation (A14) can be calculated analytically which we show for  $k = 2$ :

$$\begin{aligned} \langle p^2 \rangle_\Lambda &= \frac{4\pi}{d} \int_0^\Lambda dp p^3 e^{-ap^2} \sin(dp) = \frac{4\pi}{d} \partial_a \partial_d \int_0^\Lambda dp e^{-ap^2} \cos(dp) \\ &= \frac{4\pi}{2d} \partial_a \partial_d \int_0^\Lambda dp \left[ e^{-ap^2 + idp} + e^{-ap^2 - idp} \right] \\ &= \frac{\pi^{3/2}}{d\sqrt{a}} \partial_a \partial_d e^{-\frac{d^2}{4a}} \left[ \operatorname{erf}\left(\sqrt{a}\Lambda + \frac{id}{2\sqrt{a}}\right) + \operatorname{erf}\left(\sqrt{a}\Lambda - \frac{id}{2\sqrt{a}}\right) \right] \\ &= \frac{1}{8a^{7/2}d} \left\{ d(6a - d^2) \pi^{\frac{3}{2}} e^{-\frac{d^2}{4a}} \left[ \operatorname{erf}\left(\sqrt{a}\Lambda + \frac{id}{2\sqrt{a}}\right) + \operatorname{erf}\left(\sqrt{a}\Lambda - \frac{id}{2\sqrt{a}}\right) \right] \right. \\ &\quad \left. - 4\pi\sqrt{a}e^{-a\Lambda^2} \left[ 2ad\Lambda \cos(d\Lambda) + (4a + 4a^2\Lambda^2 - d^2) \sin(d\Lambda) \right] \right\}. \end{aligned} \quad (\text{A15})$$

If the ECGs are centered at the origin of the coordinate system, we need to consider the  $d \rightarrow 0$  limit of the general expression:

$$\lim_{d \rightarrow 0} \langle p^2 \rangle_\Lambda = \frac{3\pi^{3/2}}{2a^{5/2}} \operatorname{erf}(\sqrt{a}\Lambda) - \frac{\pi\Lambda}{a^2} (3 + 2a\Lambda^2) e^{-a\Lambda^2}. \quad (\text{A16})$$

## APPENDIX B

### CONNECTION BETWEEN WAVE FUNCTION DERIVATIVES IN REAL SPACE AND THE DECAY RATE OF THE ASYMPTOTIC TAIL IN MOMENTUM SPACE

Let us consider an  $L^2$  integrable function,  $f(x)$ , which decays to zero for  $x \rightarrow \pm\infty$ . Moreover, its  $(k-1)$ th derivative is discontinuous at  $x_0$ , and its  $k$ th derivative at this point is related to the Dirac delta function<sup>1</sup>

$$\frac{d^k f(x)}{dx^k} \sim \delta(x - x_0) A(x), \quad (\text{B1})$$

where  $A(x)$  is a continuous regular function, which describes the  $k$ th derivative everywhere else. Next, let us consider the Fourier transform of  $f(x)$  and its momentum-space properties,

$$\tilde{f}(p) = \frac{1}{\sqrt{2\pi}} \int_{-\infty}^{\infty} dx f(x) e^{-ipx}. \quad (\text{B2})$$

Using partial integration,  $\tilde{f}(p)$  can be expressed with the integral of the derivative of  $f(x)$ ,

$$\tilde{f}(p) = -\frac{1}{\sqrt{2\pi}ip} \underbrace{[f(x)e^{-ipx}]_{-\infty}^{\infty}}_0 + \frac{1}{\sqrt{2\pi}ip} \int_{-\infty}^{\infty} dx \frac{df(x)}{dx} e^{-ipx}, \quad (\text{B3})$$

where the first term in the right hand is zero, since our original condition was  $\lim_{x \rightarrow \pm\infty} f(x) = 0$ . The partial integration can be repeated  $k$  times,

dc\_1955\_21

$$\tilde{f}(p) = \frac{1}{\sqrt{2\pi}} \int_{-\infty}^{\infty} dx f(x) e^{-ipx} = \frac{1}{\sqrt{2\pi}} \left(\frac{-i}{p}\right)^k \int_{-\infty}^{\infty} dx \frac{d^k f(x)}{dx^k} e^{-ipx} = \frac{1}{\sqrt{2\pi}} \left(\frac{-i}{p}\right)^k e^{-ipx_0} A(x_0), \quad (\text{B4})$$

where Equation (B1) is used and we assumed that the Dirac delta predominantly determines the integral expression above. Since  $e^{-ipx_0}$  is bounded,

$$|e^{-ipx_0}| = 1, \quad (\text{B5})$$

in the limit of large  $p$  values,  $\tilde{f}(p)$  decays polynomially,

$$p > p_\Lambda: \tilde{f}(p) \sim \frac{1}{p^k}. \quad (\text{B6})$$

## APPENDIX C

### FOURIER TRANSFORMATION OF $rf(\vartheta, \varphi)$

In this appendix, we consider the effect of the function  $f(\vartheta, \varphi)$  in Equation (42) on the integrand values. The function  $f(\vartheta, \varphi)$  can be written as a linear combination of  $Y_{1m}$  spherical symmetric functions. In what follows we show that the Fourier transform of  $rf(\vartheta, \varphi)$  is local, moreover, its contribution is zero in the asymptotic tail of the kinetic and mass-velocity term integrands. So, we consider

$$h(\mathbf{p}) = \frac{1}{\sqrt{8\pi^3}} \int dr e^{i\mathbf{p}r} r Y_{1m}(\vartheta, \varphi). \quad (\text{C1})$$

In order to perform the Fourier transformation let us expand the plane wave in terms of spherical harmonics [37],

$$e^{i\mathbf{p}r} = 4\pi \sum_{\ell=0}^{\infty} \sum_{m=-\ell}^{\ell} i^\ell j_\ell(pr) Y_{\ell m}^*\left(\frac{\mathbf{p}}{p}\right) Y_{\ell m}\left(\frac{\mathbf{r}}{r}\right), \quad (\text{C2})$$

where  $j_\ell(x)$  is the spherical Bessel function [38]. Substituting Equation (C2) into (C1) and using the orthogonality relation between the spherical harmonics, the angular integral can be evaluated, and we obtain

$$h(\mathbf{p}) = \frac{i}{\sqrt{2\pi}} Y_{1m}^*\left(\frac{\mathbf{p}}{p}\right) \int dr r^3 j_1(pr). \quad (\text{C3})$$

Using the identity,

$$\frac{\partial}{\partial p} j_0(pr) = -r j_1(pr), \quad (\text{C4})$$

which can be checked by substituting the explicit expressions for the spherical Bessel functions [38]. We can rewrite the integral in Equation (C3) as

$$h(\mathbf{p}) = -\frac{i}{\sqrt{2\pi}} Y_{1m}^*\left(\frac{\mathbf{p}}{p}\right) \frac{\partial}{\partial p} \int dr r^2 j_0(pr). \quad (\text{C5})$$

Then, we can recognize one of the identities of the Dirac delta function [39],  $\delta(p) = \frac{2p^2}{\pi} \int dr r^2 j_0(pr)$ ,

$$h(\mathbf{p}) = -\frac{\sqrt{2}i}{\pi^{3/2}} Y_{1m}^*\left(\frac{\mathbf{p}}{p}\right) \frac{\partial}{\partial p} \frac{\delta(p)}{p^2}, \quad (\text{C6})$$

and the differentiation can be performed by using the identity  $\delta(x) = -x\delta'(x)$  for the derivative of the Dirac delta,

dc\_1955\_21

$$h(\mathbf{p}) = \frac{3\sqrt{2}i}{\pi^{3/2}} \frac{\delta(\mathbf{p})}{p^3} Y_{lm}^* \left( \frac{\mathbf{p}}{p} \right). \quad (\text{C7})$$

The appearance of  $\delta(\mathbf{p})$  ensures that the resulting function is localized near the origin (small  $p$  values), and thus, it does not contribute to the large- $p$  asymptotic tail.

## APPENDIX D

### DETERMINATION OF THE $\rho(\mathbf{0})$ AND $\eta(\mathbf{0})$ VALUES FOR THE GROUND STATE OF THE He ATOM

In order to determine accurate values for  $\delta(\mathbf{r}_{iA}) = N^{-1}\rho(\mathbf{0})$  and  $\delta(\mathbf{r}_{ij}) = [N(N-1)]^{-1}\eta(\mathbf{0})$ , the expectation values of  $\delta(\mathbf{r}_{iA})$  and  $\delta(\mathbf{r}_{ij})$  are obtained in an iterative procedure (Section 2). The grid points used in the fitting are selected according to Section 6. For  $\delta(\mathbf{r}_{iA})$  and  $\delta(\mathbf{r}_{ij})$ , the fitting intervals start at 5 bohr<sup>-1</sup>, and at 1 bohr<sup>-1</sup>, respectively, which are sufficient to avoid complicated correlation effects at low  $t$  values (see also Figure 1).

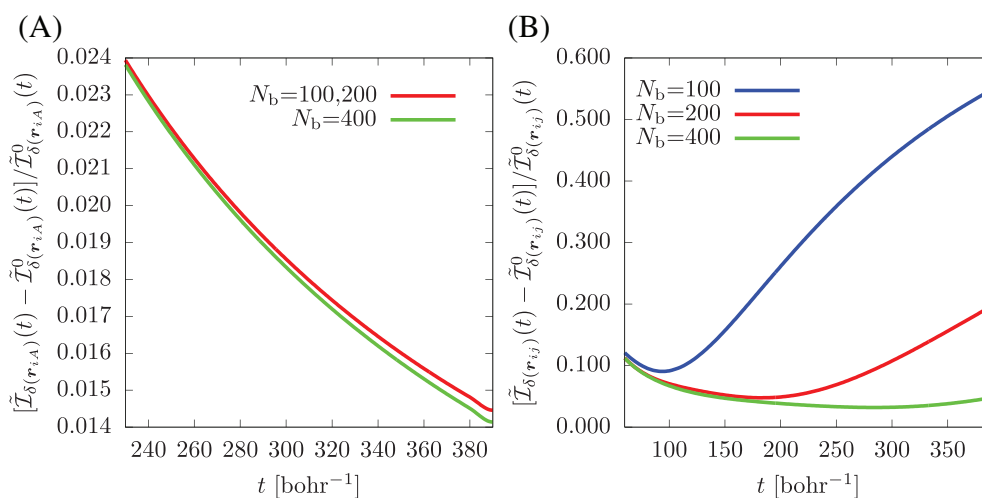


**FIGURE D1** Relative difference in the asymptotic tail of the numerically calculated functions,  $\mathcal{I}_{\delta(\mathbf{r}_{iA})}(t)$  and  $\mathcal{I}_{\delta(\mathbf{r}_{ij})}(t)$ , and the analytic-leading order expressions of the asymptotic tail,  $\tilde{\mathcal{I}}_{\delta(\mathbf{r}_{iA})}^0(t) = 8\rho(\mathbf{0})/(\sqrt{\pi}t^2)$  and  $\tilde{\mathcal{I}}_{\delta(\mathbf{r}_{ij})}^0(t) = -2\eta(\mathbf{0})/(\sqrt{\pi}t^2)$  for the example of the ground state of the helium atom with an increasing number of explicitly correlated Gaussian (ECG) basis functions ( $N_b$ )

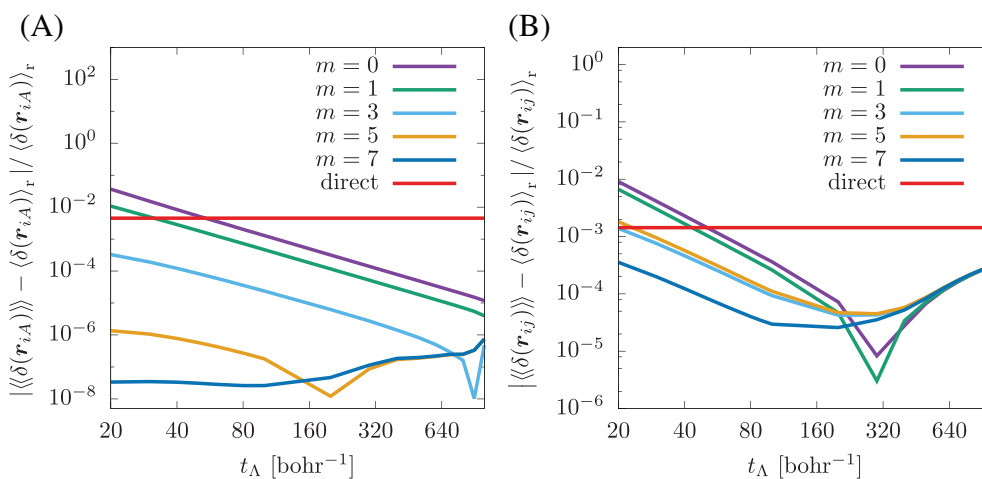


**FIGURE D2** Relative error of  $\langle\delta(\mathbf{r}_{iA})\rangle_r$  and  $\langle\delta(\mathbf{r}_{ij})\rangle_r$  for various  $t_\Lambda$  threshold values and  $m$  terms in the fitting, Equation (24), using 400 explicitly correlated Gaussians (ECGs). The result "direct" was obtained by numerical integration over the entire  $t$  range. The reference values are  $\langle\delta(\mathbf{r}_{iA})\rangle_r = 3.620858637\ 7(3)$  bohr<sup>-1</sup> and  $\langle\delta(\mathbf{r}_{ij})\rangle_r = 0.106345370636(2)$  bohr<sup>-1</sup> [2]

## dc\_1955\_21

For the asymptotic range, the relative deviation of the integrands from the leading-order analytic terms is shown in Figure D1. The function  $\mathcal{I}_{\delta(r_A)}$  appears to be robust with respect to the number of basis functions, while  $\mathcal{I}_{\delta(r_j)}$  is more sensitive to the basis set.

After inspection of these figures, we set  $t_\lambda = 100 \text{ bohr}^{-1}$  for the upper end of the interval used for the fitting, and the beginning of the long-range integral. The  $\rho(\mathbf{0})$  and  $\eta(\mathbf{0})$  values obtained in this computational setup with seven fitting parameters are collected in Table A1.

Figure D2 shows the relative error of  $\langle \delta(r_{iA}) \rangle$  and  $\langle \delta(r_{ij}) \rangle$  in comparison with data available from Pachucki et al. [2]

# Orientalional decoherence within molecules and emergence of the molecular shape

Cite as: J. Chem. Phys. 154, 024114 (2021); doi: 10.1063/5.0036568

Submitted: 9 November 2020 • Accepted: 17 December 2020 •

Published Online: 12 January 2021



View Online



Export Citation



CrossMark

Edit Mátyus<sup>1,a)</sup>  and Patrick Cassam-Chenaï<sup>2,b)</sup> 

## AFFILIATIONS

<sup>1</sup>Institute of Chemistry, Eötvös Loránd University, Pázmány Péter sétány 1/A, 1117 Budapest, Hungary

<sup>2</sup>Université Côte d'Azur, CNRS, LJAD, UMR 7351, 06100 Nice, France

**Note:** This paper is part of the JCP Special Collection in Honor of Women in Chemical Physics and Physical Chemistry.

<sup>a)</sup> Author to whom correspondence should be addressed: [matyus@chem.elte.hu](mailto:matyus@chem.elte.hu)

<sup>b)</sup> Electronic mail: [cassam@unice.fr](mailto:cassam@unice.fr)

## ABSTRACT

The question of classicality is addressed in relation with the shape of the nuclear skeleton of molecular systems. As the most natural environment, the electrons of the molecule are considered as continuously monitoring agents for the nuclei. For this picture, an elementary formalism of decoherence theory is developed and numerical results are presented for few-particle systems. The numerical examples suggest that the electron–nucleus Coulomb interaction is sufficient for inducing a blurred shape with strong quantum coherences in compounds of the lightest elements, H<sub>2</sub>, D<sub>2</sub>, T<sub>2</sub>, and HeH<sup>+</sup>.

Published under license by AIP Publishing. <https://doi.org/10.1063/5.0036568>

## I. INTRODUCTION

We would like to better understand the status of the permanent chemical observables by starting from a fully quantum mechanical description of a molecule, i.e., by including both the electrons and the atomic nuclei in the quantum treatment. The present work is concerned with the recognition of elements of the classical molecular shape. A fundamental difficulty is associated with the fact that the classical shape (unless spherically symmetric) breaks the rotational symmetry of the molecular wave function of an isolated molecule.<sup>1</sup>

There exist quick shortcuts to this problem. First (case I), pieces of information regarding the molecular shape (and structure) can be obtained by fitting an effective model Hamiltonian to the isolated molecule's rotational spectrum.<sup>2</sup> Second (case II), in many chemical experiments, the molecules are in some environment, and the isolated-system symmetries are no longer relevant.

Nevertheless, we remain interested in the original theoretical problem, which had become famous as the molecular structure conundrum:<sup>3–9</sup> We consider an isolated molecule and aim to explore the furthestmost point regarding the molecular shape (and structure) without considering any kind of environment (as in case II) or making any *a priori* assumption on the hierarchical separation in the

spatio-temporal behavior of the internal dynamics to build model Hamiltonians (as in case I).

However, we have mentioned that the classical molecular shape breaks a fundamental symmetry of the isolated quantum system. Hence, how can we expect to see the emergence of a symmetry breaking feature without actually breaking the symmetry?

The core of this work rests on understanding what is quantum, what is classical, and how they are connected. We borrow tools from decoherence theory<sup>10,11</sup> and use them for the molecular problem. Interference is one of the key concepts for understanding quantum behavior. If interference vanishes, then the quantum system has classical-like features. In practical terms, we have to consider the system's reduced density matrix (RDM). If its off-diagonal elements (interference terms) are suppressed in some representation, then the RDM is formally identical with that of a classical mixture (Fig. 1). Based on this mathematical equivalence, we may say that a quantum system resembles a classical statistical ensemble. Science philosophers<sup>12,13</sup> as well as pioneers in decoherence theory<sup>10</sup> have noticed that the suppression of interference between selected states is not a sufficient condition to fully reduce the quantum world to one amenable to a classical treatment. It is a necessary one. In the present work, we will follow this common and fruitful interpretation of the

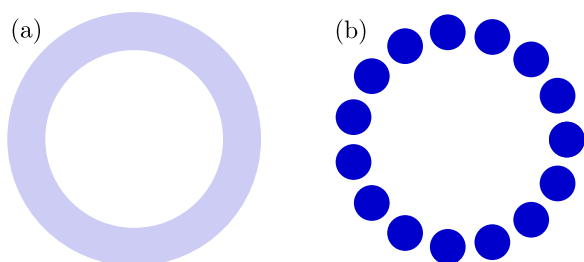


**FIG. 1.** Illustration of a rotationally symmetric object with (a) strong rotational interference and (b) vanishing rotational interference. If the interference vanishes (b), the quantum system resembles a collection of (rotated) classical objects.

quantum-classical relation that is based on the suppression of the interference terms.

Pursuing decoherence ideas for the molecular problem is not new and has always started with the definition of an environment model. Pfeifer<sup>14,15</sup> considered the vacuum state of the electromagnetic field as a general environment to model the localization of enantiomers. This model was later debated for several reasons. Woolley argued<sup>16</sup> that Pfeifer's non-gauge invariant representation and linear approximation in the field operators resulted in an artificial localization. It was also shown that the proposed mechanism fails for non-zero temperature.<sup>17</sup> Zeh argued (p. 387 of Ref. 10) that a non-trivial dressing (on its own) does not guarantee transformation from a superposition to an ensemble.

Independently, Claverie and Jona-Lasinio<sup>18,19</sup> used external random noise to simulate localization in a double-well problem to model molecular chirality. Joos and Zeh studied simple scattering models,<sup>20</sup> and Hornberger and co-workers simulated the stabilization of chiral molecules upon collisions.<sup>21–23</sup> More recently, the change of the environment model parameters was studied on the localization of mesoscopic quantum objects.<sup>24</sup> A systematic and accurate calculation of the decoherence times for molecular processes in interaction with a series of environment models is very interesting and may turn out to be useful for designing better quantum computers (with molecular qubits).

For solving the molecular structure problem, one would like to find the most general possible environment model for a molecule. When we think about the structure of a molecule, we rarely have to specify the corresponding environment. Most probably, this desire led Pfeifer in 1980<sup>14</sup> to pick the electromagnetic vacuum state as an environment.

In the present work, instead of setting out to design the most general environment for a molecule, we will take a closer look at the molecular wave function. We have said that we did not want to introduce any *a priori* dynamical assumptions in the molecular quantum treatment. However, when we have the full molecular wave function at hand, we can, of course, exploit the different properties of the particles during the course of an *a posteriori* analysis of the wave function. Hence, in the present work, we study the spatial coherence or decoherence of the nuclear skeleton induced by the continuous monitoring effect of the electron cloud. This information is encoded in the molecular wave function, and we will write down the formalism that makes this “visible.”

The present study of spatial (de)coherence *within* the molecule adds a missing bit to our earlier understanding<sup>25–30</sup> that followed a path proposed by Claverie and Diner.<sup>5</sup> According to them, elements of the molecular structure can be recognized as nuclear configurations for which the particle density is large. Large values of the particle density certainly indicate configurations that are the most probable, but it does not tell us whether an assembly of particles have the classical-like features that we know about in chemistry.

In Sec. II, we work out the basic decoherence formalism for spatial localization of nuclei in the molecule. Section III makes the formalism specific for the molecular shape, and Sec. IV presents the numerical results computed from molecular wave functions.

## II. MOLECULAR DECOHERENCE THEORY

When a property of a quantum system is measured, the needle of an idealized measuring device points to one of the possible outcome values. In an ideal quantum mechanical description of measurement, the (macroscopic) experimental setup should be included in a quantum treatment.<sup>6,31</sup> The quantum states corresponding to the positions of the measuring needle were termed “pointer states” by Zurek,<sup>32</sup> and their apparent classical behavior is ensured by the decoherence effect of the measuring environment.

Nowadays, the concept of pointer states is used in a more abstract sense without associating an actual experimental setup with them. In the pointer basis representation, the off-diagonal elements of the reduced density matrix, which represent quantum coherence between the states of the system associated with the environment pointer states, are suppressed.

In general, we do not know *a priori* the pointer states of a quantum system in a given environment. For each microscopic environment model, one has to find the proper pointer states that will point to the classical-like (environmentally stabilized) states of the quantum system.<sup>22,32</sup> Localization of macroscopic objects in space (e.g., translational localization) is studied in a so-called “direct representation” using a set of Dirac delta distributions over the configuration space.

By molecular shape (and internal structure), we understand the localization of the nuclei in the three-dimensional space. Hence, our “measuring needles” are functions located in the three-dimensional space (“position basis”). Hence, we will be concerned with the “direct representation” of the density matrix.

Let  $|\Psi\rangle$  be a normalized molecular wave function. The associated (pure-state) density operator is denoted by  $\hat{\rho} = |\Psi\rangle\langle\Psi|$ . Let us multiply  $\hat{\rho}$  from both the left and the right with the resolution of identity written in the position basis of the electrons and the nuclei,  $\chi_r$  and  $\chi_R$ , respectively. Hence, the molecular (pure-state) density operator is written as

$$\begin{aligned} \hat{\rho} &= |\Psi\rangle\langle\Psi| \\ &= \hat{I} \cdot |\Psi\rangle\langle\Psi| \cdot \hat{I} \\ &= \int dr dR |\chi_r\chi_R\rangle\langle\chi_r\chi_R| \cdot |\Psi\rangle\langle\Psi| \cdot \int dr' dR' |\chi_{r'}\chi_{R'}\rangle\langle\chi_{r'}\chi_{R'}| \\ &= \int dr dR dr' dR' |\chi_r\chi_R\rangle\langle\chi_{r'}\chi_{R'}| \Psi(r, R)\Psi^*(r', R'). \end{aligned} \quad (1)$$

Since we are interested in the nuclear structure, we integrate out the electronic degrees of freedom and obtain the nuclear reduced density matrix,

$$\begin{aligned}\hat{\rho}_{\text{nuc}} &= \text{Tr}_{\text{el}} [\hat{\rho}] \\ &= \int d\mathbf{r}'' \langle \chi_{\mathbf{r}''} | \Psi \rangle \langle \Psi | \chi_{\mathbf{r}''} \rangle \\ &= \int d\mathbf{r}'' \langle \chi_{\mathbf{r}''} | \left[ \int d\mathbf{r} dR d\mathbf{r}' dR' |\chi_{\mathbf{r}} \chi_{\mathbf{R}} \rangle \langle \chi_{\mathbf{r}'} \chi_{\mathbf{R}'}| \right. \\ &\quad \left. \times \Psi(\mathbf{r}, R) \Psi^*(\mathbf{r}', R') \right] \chi_{\mathbf{r}''} \rangle \\ &= \int dR dR' |\chi_{\mathbf{R}} \rangle \langle \chi_{\mathbf{R}'}| \int d\mathbf{r}'' \Psi(\mathbf{r}'', R) \Psi^*(\mathbf{r}'', R'),\end{aligned}\quad (2)$$

where the element of the reduced density matrix in the position representation is denoted as

$$\rho_{\text{nuc}}(R, R') = \langle \chi_{\mathbf{R}} | \hat{\rho}_{\text{nuc}} | \chi_{\mathbf{R}'} \rangle = \int d\mathbf{r}'' \Psi(\mathbf{r}'', R) \Psi^*(\mathbf{r}'', R').\quad (3)$$

It is worth making explicit the diagonal and off-diagonal contributions to  $\hat{\rho}_{\text{nuc}}$ ,

$$\begin{aligned}\hat{\rho}_{\text{nuc}} &= \int dR |\chi_{\mathbf{R}} \rangle \langle \chi_{\mathbf{R}}| \rho_{\text{nuc}}(R, R) \\ &\quad + \int dR dR' |\chi_{\mathbf{R}} \rangle \langle \chi_{\mathbf{R}'}| [1 - \delta(R - R')] \rho_{\text{nuc}}(R, R'),\end{aligned}\quad (4)$$

where the second term describes the interference between the nuclear structures at  $R$  and  $R'$ . If the  $\rho_{\text{nuc}}(R, R')$  off-diagonal elements are small, then

$$\hat{\rho}_{\text{nuc}} \approx \int dR |\chi_{\mathbf{R}} \rangle \langle \chi_{\mathbf{R}}| \rho_{\text{nuc}}(R, R),\quad (5)$$

which is mathematically equivalent with the density matrix of a classical mixture of localized structures at  $R$  (a mixed state). According to decoherence theory and based on this mathematical equivalence, we may say that the quantum system has classical features corresponding to the  $\chi_{\mathbf{R}}$  basis representation that becomes a good pointer basis if  $\rho_{\text{nuc}}(R, R') = 0$ . In this case, the  $\chi_{\mathbf{R}}$  basis representation is a pointer basis for the nuclei, and the classical properties associated with a given  $\chi_{\mathbf{R}}$  function are dynamically stable.

We have selected  $\chi_{\mathbf{R}}$  as a basis set over the nuclear configuration space (or more precisely, for practical purposes, a dense mesh of Dirac delta distributions over nuclear configurations) because we would like to study the molecular structure and check whether the interference terms are suppressed between nuclear configurations. It is necessary to study whether and under which circumstances  $\rho_{\text{nuc}}(R, R') \approx 0$  ( $R \neq R'$ ), i.e., the nuclear structure will be dynamically stable as a classical property.

### A. Born-Oppenheimer molecular wave function

It is interesting to note that all arguments are applicable not only for the pre-Born-Oppenheimer molecular wave function but also for the conventional Born-Oppenheimer (BO) product of the electronic and nuclear wave functions,  $\Psi^{[\text{BO}]}(\mathbf{r}, R) = \Psi_{\text{el}}(\mathbf{r}, R) \Psi_{\text{nuc}}(R)$ . In this case, an off-diagonal element of the reduced density matrix is

$$\begin{aligned}\rho_{\text{nuc}}^{[\text{BO}]}(R, R') &= \langle \chi_{\mathbf{R}} | \hat{\rho}_{\text{nuc}} | \chi_{\mathbf{R}'} \rangle \\ &= \int d\mathbf{r}'' \Psi_{\text{el}}^*(\mathbf{r}'', R') \Psi_{\text{nuc}}^*(R') \Psi_{\text{el}}(\mathbf{r}'', R) \Psi_{\text{nuc}}(R) \\ &= \left[ \int d\mathbf{r}'' \Psi_{\text{el}}^*(\mathbf{r}'', R') \Psi_{\text{el}}(\mathbf{r}'', R) \right] \Psi_{\text{nuc}}^*(R') \Psi_{\text{nuc}}(R).\end{aligned}\quad (6)$$

Thus, the interference amplitude between the  $R$  and  $R'$  nuclear structures depends on the overlap of the BO electronic wave functions corresponding to the  $R$  and  $R'$  nuclear configurations.

### B. All-particle molecular wave function

The molecular wave function can be represented as a linear combination of many-particle electron–nucleus basis functions, most commonly using variants of an explicitly correlated Gaussian basis set.<sup>1,33–35</sup> Electrons and nuclei are handled in such a “pre-Born–Oppenheimer” or “all-particle” treatment on an equal footing. The nuclear reduced density matrix is obtained by direct evaluation of the integral in Eq. (3). Due to the equivalent treatment of all particles, it is straightforward to calculate the reduced density matrices corresponding to different kinds of partitioning of the molecule to a subset of ( $a, b, c, \dots$ ) particles as the “system” and the remaining ( $z, y, x, \dots$ ) particles as the “environment.” In the present work, we use the electron–nucleus partitioning.

### III. ORIENTATIONAL LOCALIZATION: THEORETICAL FRAMEWORK

For a start, let us consider a diatomic molecule in its ground rovibronic state with zero total angular momentum. This is a stationary state, and the wave function is spherically symmetric. The one-particle nuclear density,  $\rho_{0,n}(R, R)$ , calculated from this wave function shows that the nuclei (“n”) are within a shell around the molecular center of mass, “0” (see Fig. 1 of Ref. 25 and Fig. 2 of Ref. 26). The two-particle density,  $\rho_{0,nn'}(R, R)$ , is strongly peaked at  $180^\circ$  for the included angle of the position vector of the two nuclei,  $n$  and  $n'$ , measured from the center of mass, “0” (see Fig. 2 of Ref. 26).

The one- and two-particle density functions describe well the internal nuclear structure, but an additional question remains:<sup>1</sup> Does the nuclear structure in the ground-state wave function resemble a shell with strong quantum coherences among the positions [Fig. 2(a)] or a rotating dumbbell with a classical-like shape [Fig. 2(b)]?

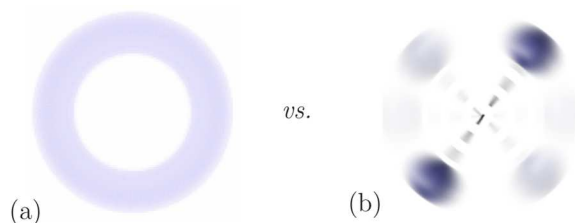


**FIG. 2.** Shell (a) or rotating dumbbell (b)? Reproduced with permission from E. Mátyus, Mol. Phys. 117, 590 (2019). Copyright 2019 Author(s), licensed under a Creative Commons Attribution 4.0 License.



We ask this question within the stationary-state, isolated molecule quantum treatment because we would like to know whether this property is encoded in the molecular wave function itself or it is induced by the environment. This question can be mathematically studied using the arguments and formalism developed in Sec. II.

Hence, we have to assess the orientational coherence or decoherence of the nuclei induced by the electrons. For this purpose, we consider nuclear configurations,  $R$  and  $R'$ , that have the same internal structure and are connected by spatial rotation,  $R' = \hat{O}_\alpha R$ .

To quantify the interference between rotated structures, we will use the  $\{\xi_1, \xi_2, \dots\}$  basis set (Fig. 3) that consists of Dirac delta distributions over a dense mesh in the configuration space of rotated nuclear structures rather than a general  $\chi_R$  configuration basis distributed over the entire configuration space (Sec. II). Hence, our measuring needles are  $\xi_\alpha = \chi_{\hat{O}_\alpha R}$  (Fig. 3). Hence, in Eq. (4), we consider the rotational degrees of freedom for a selected  $R$  nuclear structure (alternatively, the non-rotational part can be integrated out) and write the nuclear reduced density matrix operator corresponding to the rotated structures as

$$\hat{\rho}_{\text{nuc}}^{[\text{rot}]} = \int d\alpha |\xi_\alpha\rangle \langle \xi_\alpha| \rho_{\text{nuc}}(R_\alpha, R_\alpha) + \int d\alpha d\alpha' |\xi_\alpha\rangle \langle \xi_{\alpha'}| [1 - \delta(\alpha - \alpha')] \rho_{\text{nuc}}(R_\alpha, R_{\alpha'}), \quad (7)$$

where  $d\alpha$  collects the volume element for three Euler angles and the integrals are understood with the appropriate integration bounds.  $R_\alpha = \hat{O}_\alpha R$  is a short notation for the rotated structure.

If the off-diagonal elements of the nuclear reduced density matrix for the rotated structures ( $R \neq R_\alpha$ ),

$$\rho_{\text{nuc}}(R, R_\alpha) = \int dr'' \Psi(r'', R) \Psi^*(r'', R_\alpha), \quad (8)$$

are small with respect to the diagonal elements,

$$\rho_{\text{nuc}}(R, R) = \int dr'' \Psi(r'', R) \Psi^*(r'', R), \quad (9)$$

then

$$\hat{\rho}_{\text{nuc}}^{[\text{rot}]} \approx \int d\alpha |\xi_\alpha\rangle \langle \xi_\alpha| \rho_{\text{nuc}}(R_\alpha, R_\alpha), \quad (10)$$

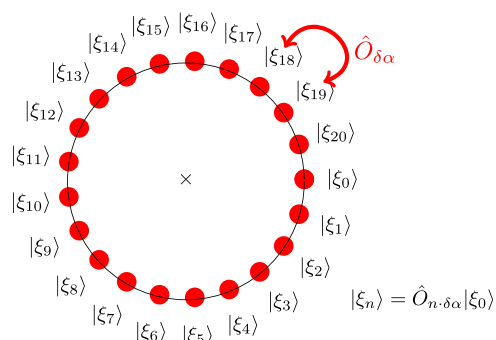


**FIG. 3.** Visual representation of the “orientational basis” that we use to measure the emergence of the shape of the nuclear skeleton: Dirac delta distributions are located at molecular structures connected by rotation (shown in 2D).

i.e., the interference of the rotated nuclear structures is negligible. This nuclear reduced density matrix is mathematically identical with that of a classical mixture of rotated nuclear structures. This case corresponds to Fig. 1(b) in a diatomic molecule, the coherence of the rotated structures vanishes, and we may observe the emergence of a dumbbell-like shape of the nuclear skeleton. If the off-diagonal elements are large with respect to the diagonal ones, then there is a strong interference among the rotated nuclear structures and we cannot observe any new feature emerging beyond (within) the quantum mechanical rotational symmetry. In this case, the shell-like picture of Fig. 1(a) is appropriate. We note that both cases respect the original rotational symmetry of the molecular wave function. Either the classical-like or the quantum-like (as well as all intermediate) cases may be encoded within the molecular wave function depending on the strength of the interparticle interactions. The sole difference is in the suppression or existence of the coherence between pairs of rotated structures within the spherically symmetric molecular wave function.

When do the interference terms get small and the localization of the nuclei by the electrons efficient? It happens if  $\rho_{\text{nuc}}(R, R_\alpha)$  [Eq. (8)] is small. It is easier to understand the meaning of this condition within the Born–Oppenheimer approximation (when it is qualitatively correct), Eq. (6),

$$\rho_{\text{nuc}}^{[\text{BO}]}(R, \hat{O}_\alpha R) = \left[ \int dr'' \Psi_{\text{el}}(r'', R) \Psi_{\text{el}}^*(r'', \hat{O}_\alpha R) \right] \Psi_{\text{nuc}}(R) \Psi_{\text{nuc}}^*(\hat{O}_\alpha R). \quad (11)$$

If the overlap of the BO electronic wave functions corresponding to the rotated nuclear structures is small, then  $\rho_{\text{nuc}}^{[\text{BO}]}(R, R')$  is also small.

#### IV. NUMERICAL STUDY OF ROTATIONAL LOCALIZATION OF THE NUCLEI IN THE MOLECULAR WAVE FUNCTION

We have computed the ground-state wave function for four-particle systems, including the hydrogen molecule ( $\text{H}_2$ ), the positronium molecule ( $\text{Ps}_2$ ), the muonium molecule ( $\mu_2$ ), and other  $\text{H}_2$ -like systems, as well as  $\text{HeH}^+$ , to illustrate the ideas formulated in Secs. II and III.

The molecular wave function was computed using an explicitly correlated Gaussian basis set and the QUANTEN computer program.<sup>1</sup> In the present work, we use a plain explicitly correlated Gaussian (ECG) representation similarly to Refs. 25 and 26 and the center-of-mass-centered translationally invariant coordinates<sup>1,26,35</sup> to evaluate the diagonal and off-diagonal particle densities referenced to the molecular center of mass. We have converged the studied structural density features for the ground state of these systems with zero total angular momentum ( $N = 0$ ), natural parity ( $p = +1$ ), and zero spin for the pair of electrons, protons, and positrons ( $S_e = 0$ ,  $S_p = 0$ ). The corresponding energies were converged within  $\sim 1\%$ , which was sufficient to obtain density plots converged within the resolution of the figures.

To answer the question of Ref. 1 highlighted in Fig. 2, we have calculated the off-diagonal elements of the nuclear reduced density matrix in the rotational basis (Sec. III),  $\rho_{0,n}(R, \hat{O}_\alpha R)$ , where  $\hat{O}_\alpha$  is the

operator for the rotation. The rotation axis goes through the molecular center of mass and  $\vartheta$  parameterizes the rotation angle about this axis. Figure 4 shows the effect of the relative mass and electric charge on the orientational (de)coherence for a series of H<sub>2</sub>-type systems including Ps<sub>2</sub>,  $\mu_2$ , and the deuterium and tritium isotopologs of H<sub>2</sub> and hypothetical (bound) systems with an increased nuclear charge.

We may observe in Fig. 4 that Ps<sub>2</sub> is qualitatively different from the other “homonuclear” systems. Its diagonal “nuclear” (positron) density,  $\rho_{0,n}(R, R)$ , has a maximum at the origin ( $R = 0$  bohr). Regarding the off-diagonal density, it shows a 360° periodicity and has a small local maximum at 180° ( $\pm i \cdot 360^\circ$ ) and shallow local minima at 139° and 221° with a 1% suppression compared to the maximal (diagonal) value.

For  $\mu_2$ , H<sub>2</sub>, D<sub>2</sub>, and T<sub>2</sub>, the diagonal density functions differ, but they all have a maximum (of different values for the different systems) near  $|R| = 0.7$  bohr. Within the resolution of the figure, the off-diagonal density matrix elements normalized with the diagonal density value [shown in Fig. 4(a) for  $|R| = 0.7$  bohr] cannot be distinguished for the four systems that may be surprising at first sight. We may understand this observation by remembering that the

suppression is induced by the electrons’ measuring effect that depends on the electronic structure around the positive particle [Eq. (11)] and this is very similar in the four systems (the BO approximation is qualitatively correct). For this series of systems, the off-diagonal density shows a 180° periodicity and it is minimal at 90° ( $\pm i \cdot 180^\circ$ ). Its minimum value is ~5% smaller than its maximal (diagonal) value.

Regarding the H<sub>2</sub>-like systems with an increased nuclear charge [Fig. 4(b)], we observe a behavior similar to H<sub>2</sub>, but a stronger, up to 8%, suppression at the 90° ( $\pm i \cdot 180^\circ$ ) minima for  $Z = 1.65$ . This observation is in agreement with the fact that the orientational decoherence of the nuclei is induced by the monitoring effect of the electrons, and for an increased nuclear charge, this monitoring effect is stronger due to the stronger interaction (we note that the H<sub>2</sub>-like systems with  $Z \geq 2$  are unbound).

In summary, we may say that all H<sub>2</sub> systems show dominant orientational coherences. Ps<sub>2</sub> is an almost perfect quantum ball with an only 1% maximal suppression among the rotated structures. In the H<sub>2</sub>-like systems, the 180° periodicity and maximal suppression at 90° ( $\pm i \cdot 180^\circ$ ) suggest a symmetric dumbbell shape (within

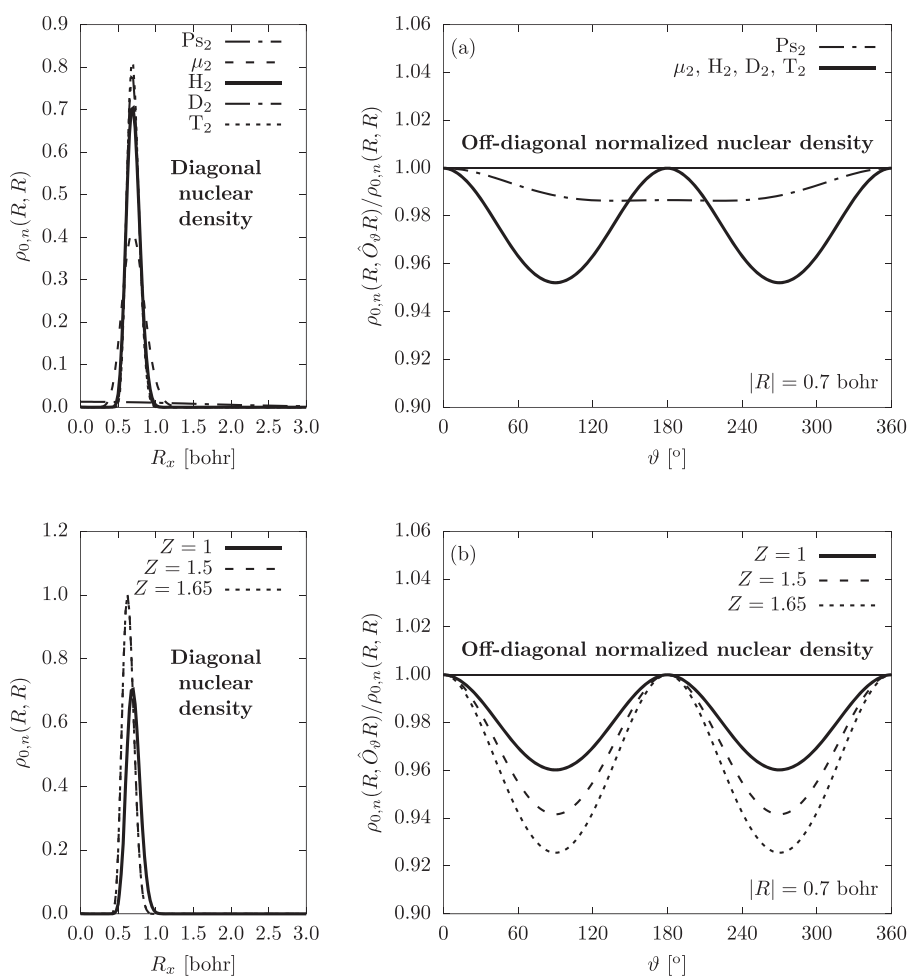


**FIG. 4.** Off-diagonal normalized density matrix elements connecting rotated nuclear structures in H<sub>2</sub>-type systems. The rotation axis for  $\vartheta$  goes through the molecular center of mass that is the origin of the coordinate system used in the calculations. The diagonal density matrix elements are also plotted. (a) Effect of varying the mass of the positively charged particles (“nuclei”),  $m_i/m_e = 1, 206.768, 1836.15, 3670.48,$  and  $5496.92$  for Ps<sub>2</sub>,  $\mu_2$ , H<sub>2</sub>, D<sub>2</sub>, and T<sub>2</sub>, respectively. (b) Effect of varying the electric charge of the proton.

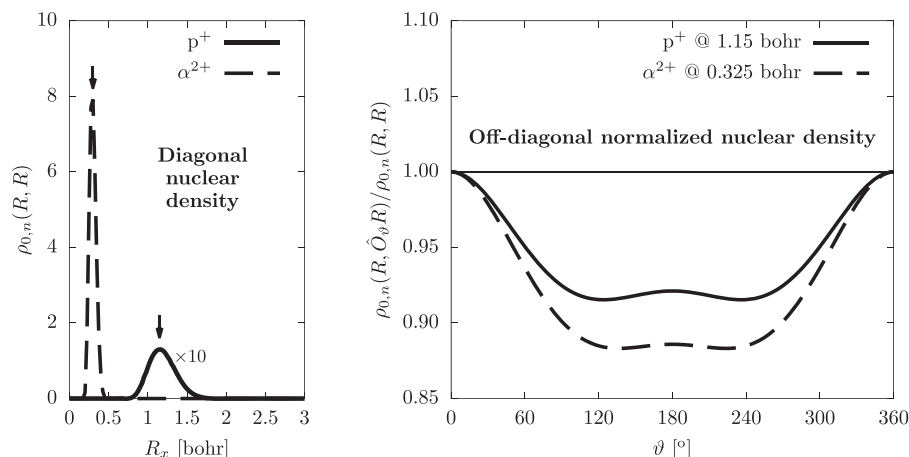


**FIG. 5.** Off-diagonal normalized nuclear density in  $\text{HeH}^+$  connecting rotated nuclear structures. The diagonal nuclear density is also shown.

the spherically symmetric molecular wave function), but due to the small value of the suppression (5%), this dumbbell shape is blurred by quantum coherences.

$\text{HeH}^+$  is a heteronuclear diatomic molecule with an asymmetric dumbbell shape in the BO theory, while its rotational ground-state molecular wave function is, of course, spherically symmetric. The question arises whether this asymmetry can be recognized within the spherically symmetric molecular wave function. Figure 5 shows the diagonal and off-diagonal nuclear density functions. The off-diagonal normalized density functions are plotted for  $|R|$  values that correspond to the diagonal density maximum value for the proton and the alpha particles. The off-diagonal density function is periodic by  $360^\circ$ , and it has equivalent minima at  $\sim 120^\circ (\pm i \cdot 360^\circ)$  and  $\sim 240^\circ (\pm i \cdot 360^\circ)$  and small local maxima at  $180^\circ (\pm i \cdot 360^\circ)$  with an overall 10% suppression for  $\vartheta \in [100^\circ, 300^\circ]$  with respect to the maximal (diagonal) density value.

Figure 6 summarizes the three qualitatively different behaviors observed in this work.  $\text{Ps}_2$  is an almost perfect quantum ball with a maximal 1% suppression among rotated structures, and  $\text{H}_2$  has a symmetric dumbbell shape, while  $\text{HeH}^+$  has an asymmetric dumbbell shape, but both dumbbells are blurred by quantum coherence.

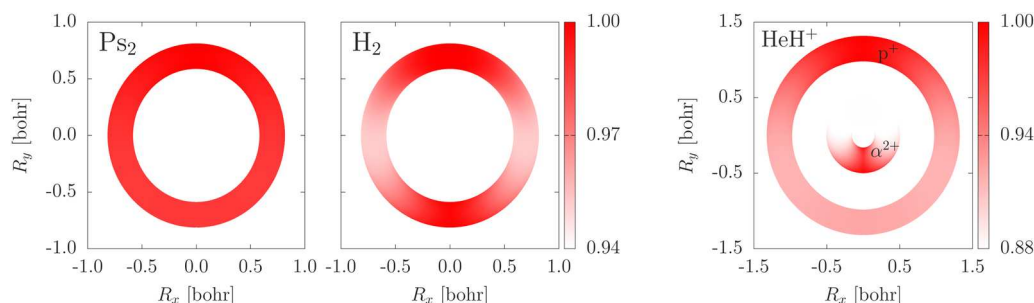


**FIG. 6.** Orientational (de)coherence measured by the suppression of the off-diagonal nuclear density with respect to the diagonal elements,  $\rho_{0,n}(R, \hat{O}_\vartheta R) / \rho_{0,n}(R, R)$ . The xy cut of the three-dimensional function (the width of the shells is arbitrarily chosen to visualize the change of the off-diagonal normalized density with the angle) is shown. The upward (downward) vertical direction corresponds to zero rotation angle  $\vartheta$  for the positron and the proton ( $\alpha$ -particle).

## V. SUMMARY, CONCLUSION, AND OUTLOOK TO FUTURE WORK

This work has been devoted to the study of the emergence of the classical molecular shape of an isolated molecule described by its ground-state rovibronic wave function. To mathematically formulate this paradoxical problem, we have studied the orientational decoherence of the nuclear skeleton under the continuous monitoring effect of the electrons of the molecule, serving as the most natural environment for the nuclei. Orientational (de)coherence is measured by the off-diagonal nuclear reduced density matrix in the (direct) spatial representation.

If the reduced density matrix elements connecting rotated structures are small, then the nuclear reduced density matrix is mathematically equivalent to the classical sum of rotated nuclear structures, and thus, we may say that the nuclei behave as if they formed a classical-like skeleton with a given shape that rotates in space. We have formulated the corresponding equations and computed the nuclear reduced density matrix elements over the nuclear configuration space for a series of  $\text{H}_2$ -type (homonuclear) systems and for the heteronuclear  $\text{HeH}^+$  molecular ion.

We observe a small, 10% maximal suppression of the off-diagonal density connecting rotated nuclear structures (due to the measuring effect of the electrons), and thus, we may say that  $\text{H}_2$  and  $\text{HeH}^+$  have a symmetric and asymmetric dumbbell-like shape, respectively, which is blurred by strong quantum coherences. The decoherence effect in  $\text{Ps}_2$  is almost negligible, and it is seen in this analysis as an almost perfect quantum ball.

We consider molecular rotation and the study of the emergence of the classical molecular shape (in the restricted sense of suppression of interferences) as a prototypical example for the broader problem of reconstruction of isomers, enantiomers, conformers, and rotamers from the molecular wave function (including the electrons and nuclei on an equal footing). Isomerism, handedness, and related phenomena are linked to polyatomic molecules, while already the smallest diatomic molecules have rotational degrees of freedom and they are attached with the picture of a classical shape in chemistry.

The present framework uses a spatial basis for the representation of the nuclear reduced density matrix that can naturally be adapted for studying other space-localized features. Regarding another challenging aspect of the molecular structure problem, the study of the quantum mechanical indistinguishability vs the classical distinguishability of the identical atomic nuclei and implications of the spin-statistics theorem<sup>36,37</sup> will require perhaps a different framework, but almost certainly a different representation for the reduced density matrix.

The developed ideas will gain more practical significance if computations without the Born–Oppenheimer approximation become more widespread, which may happen within a new type of quantum chemistry approach perhaps on the future hardware of quantum computers.<sup>38</sup>

Regarding work for the near future, we can think about extension of the present work in the following directions. A next logical step will be to recover the (two-dimensional) triangular shape of the simplest polyatomic molecule,  $\text{H}_3^+$ , that has an equilateral triangular equilibrium structure in the Born–Oppenheimer theory.  $\text{H}_3^+$  is a system of five spin-1/2 particles (with two electrons and three protons). For this reason, the rovibronic ground state of the five-particle Hamiltonian is not allowed by the Pauli principle. The lowest energy state that is Pauli-allowed has  $N = 1$  rotational angular momentum, and it is the lowest rotationally excited state of the vibrational ground state. The lowest Pauli-allowed state with  $N = 0$  rotational angular momentum is the anti-symmetric stretching fundamental vibration. Hence, the lowest energy  $N = 1$  state appears to be a good candidate for identifying a near equilateral triangular shape (with small distortion due to rovibrational coupling) in the present framework.

We have preliminary results for the ground state of  $\text{H}_2\text{D}^+$ , for which we do not have to deal with complications due to spin statistics, and in its rovibronic ground state ( $N = 0$ ), we observe a ca. maximal 10% suppression among rotated structures. We can observe a planar structure in the off-diagonal density plots, but due to the non-equivalent nuclear masses, the center of mass (the origin of our computations) is not at the geometrical center of the near equilateral triangular shape and this complicates the analysis of the results.

For going beyond planar shapes and possibly studying chiral molecules, one can rely on the BO approximation [Eq. (6)] since the suppression effect is determined by the electronic structure. If

the BO approximation is qualitatively correct for the system, then the overlap of the rotated BO electronic wave functions should provide a good approximation for the suppression effect that one would observe for the off-diagonal nuclear reduced density matrix in the molecular wave function (if the computations were feasible).

## ACKNOWLEDGMENTS

This project was initiated during a Short Term Scientific Mission of the MOLIM COST Action (Grant No. CM1405). E.M. acknowledges financial support from a PROMYS Grant (No. IZ11Z0\_166525) of the Swiss National Science Foundation. We thank one of the reviewers of this article for their insightful comments.

## DATA AVAILABILITY

The data that support the findings of this study are available within the article.

## REFERENCES

- <sup>1</sup>E. Mátyus, *Mol. Phys.* **117**, 590 (2019).
- <sup>2</sup>*Chemistry, Quantum Mechanics and Reductionism: Perspectives in Theoretical Chemistry*, edited by J. Demaison, J. E. Boggs, and A. G. Csaszar (CRC Press, Boca Raton, FL, 2010).
- <sup>3</sup>R. G. Woolley, *Adv. Phys.* **25**, 27 (1976).
- <sup>4</sup>R. G. Woolley and B. T. Sutcliffe, *Chem. Phys. Lett.* **45**, 393 (1977).
- <sup>5</sup>P. Claverie and S. Diner, *Isr. J. Chem.* **19**, 54 (1980).
- <sup>6</sup>H. Primas, *Chemistry, Quantum Mechanics and Reductionism: Perspectives in Theoretical Chemistry* (Springer-Verlag, Berlin, 1981).
- <sup>7</sup>S. J. Weininger, *J. Chem. Educ.* **61**, 939 (1984).
- <sup>8</sup>P.-O. Löwdin, *Pure Appl. Chem.* **61**, 2065 (1989).
- <sup>9</sup>B. T. Sutcliffe and R. G. Woolley, *Phys. Chem. Chem. Phys.* **7**, 3664 (2005).
- <sup>10</sup>*Decoherence and the Appearance of a Classical World in Quantum Theory*, 2nd ed., edited by E. Joos, H. Zeh, C. Kiefer, D. Giulini, J. Kupsch, and I. Stamatescu (Springer-Verlag, Berlin, Heidelberg, 1996, 2003).
- <sup>11</sup>M. Schlosshauer, *Decoherence and the Quantum-To-Classical Transition* (Springer, Berlin, 2007).
- <sup>12</sup>S. Fortin, O. Lombardi, and J. C. M. González, *Found. Chem.* **18**, 225 (2016).
- <sup>13</sup>G. Bacciagaluppi, “The role of decoherence in quantum mechanics,” *The Stanford Encyclopedia of Philosophy* (Fall 2016 Edition), edited by E. N. Zalta, URL: <https://plato.stanford.edu/archives/fall2016/entries/qm-decoherence/>.
- <sup>14</sup>P. Pfeifer, “Chiral molecules: A superselection rule induced by the radiation field,” Ph.D. thesis ETH Zürich, Nr. 6551, ok Gotthard S + D AG, Zürich, 1980.
- <sup>15</sup>P. Pfeifer, “A nonlinear Schrödinger equation yielding the ‘shape of molecules’ by symmetry breaking,” in *Quantum Mechanics in Mathematics, Chemistry and Physics*, edited by K. E. Gustafson and W. P. Reinhardt (Plenum Press, New York, 1981), pp. 255–266.
- <sup>16</sup>R. G. Woolley, *Structure and Bonding* (Springer, 1982), Vol. 52, p. 1.
- <sup>17</sup>A. S. Wightman, *Il Nuovo Cimento B* **110**, 751 (1995).
- <sup>18</sup>P. Claverie and G. Jona-Lasinio, *Phys. Rev. A* **33**, 2245 (1986).
- <sup>19</sup>G. Jona-Lasinio and P. Claverie, *Prog. Theor. Phys. Suppl.* **86**, 54 (1986).
- <sup>20</sup>E. Joos and H. D. Zeh, *Z. Phys. B* **59**, 223 (1985).
- <sup>21</sup>K. Hornberger, *Eur. Phys. Lett.* **77**, 50007 (2007).
- <sup>22</sup>M. Busse and K. Hornberger, *J. Phys. A: Math. Theor.* **43**, 015303 (2009).
- <sup>23</sup>J. Trost and K. Hornberger, *Phys. Rev. Lett.* **103**, 023202 (2009).
- <sup>24</sup>C. Zhong and F. Robicheaux, *Phys. Rev. A* **94**, 052109 (2016).
- <sup>25</sup>E. Mátyus, J. Hutter, U. Müller-Herold, and M. Reiher, *Phys. Rev. A* **83**, 052512 (2011).
- <sup>26</sup>E. Mátyus, J. Hutter, U. Müller-Herold, and M. Reiher, *J. Chem. Phys.* **135**, 204302 (2011).

- <sup>27</sup>E. V. Ludeña, L. Echevarría, X. Lopez, and J. M. Ugalde, *J. Chem. Phys.* **136**, 084103 (2012).
- <sup>28</sup>M. Becerra, V. Posligua, and E. V. Ludeña, *Int. J. Quantum Chem.* **113**, 1584 (2013).
- <sup>29</sup>E. V. Ludeña, P. Iza, M. Cornejo, and D. Zambrano, *Theor. Chim. Acta* **135**, 76 (2016).
- <sup>30</sup>A. Schild, *Front. Chem.* **7**, 424 (2019).
- <sup>31</sup>J. von Neumann, *Mathematical Foundations of Quantum Mechanics* (Princeton University Press, Princeton, NJ, 1955).
- <sup>32</sup>W. H. Zurek, *Phys. Rev. D* **24**, 1516 (1981).
- <sup>33</sup>J. Mitroy, S. Bubin, W. Horiuchi, Y. Suzuki, L. Adamowicz, W. Cencek, K. Szalewicz, J. Komasa, D. Blume, and K. Varga, *Rev. Mod. Phys.* **85**, 693 (2013).
- <sup>34</sup>S. Bubin, M. Pavanello, W.-C. Tung, K. L. Sharkey, and L. Adamowicz, *Chem. Rev.* **113**, 36 (2013).
- <sup>35</sup>E. Mátyus and M. Reiher, *J. Chem. Phys.* **137**, 024104 (2012).
- <sup>36</sup>T. Grohmann and J. Manz, *Mol. Phys.* **116**, 2538 (2018).
- <sup>37</sup>F. Bouakline, *J. Chem. Phys.* **152**, 244308 (2020).
- <sup>38</sup>I. Kassal, S. P. Jordan, P. J. Love, M. Mohseni, and A. Aspuru-Guzik, *Proc. Natl. Acad. Sci. U. S. A.* **105**, 18681 (2008).



# Benchmark potential energy curve for collinear H<sub>3</sub>

Dávid Ferenc, Edit Mátyus\*

ELTE, Eötvös Loránd University, Institute of Chemistry, Pázmány Péter sétány 1/A, Budapest H-1117, Hungary

## ARTICLE INFO

### Keywords:

H<sub>3</sub>  
 ECG  
 MSC:  
 0000  
 1111

## ABSTRACT

A benchmark-quality potential energy curve is reported for the H<sub>3</sub> system in collinear nuclear configurations. The electronic Schrödinger equation is solved using explicitly correlated Gaussian (ECG) basis functions using an optimized fragment initialization technique that significantly reduces the computational cost. As a result, the computed energies improve upon recent orbital-based and ECG computations. Starting from a well-converged basis set, a potential energy curve with an estimated sub-parts-per-billion relative precision is generated for a series of nuclear configurations using an efficient ECG rescaling approach.

## 1. Introduction

This paper is dedicated to the memory of Professor Kuchitsu. The authors did not know Professor Kuchitsu in person, but have learned about his fundamental work on gas-electron diffraction [1] as part of their undergraduate studies, and later, used in their own research [2] molecular structural parameters taken from Kozu Kuchitsu's work [3,4]. The present contribution to the Kuchitsu Special Issue is about a triatomic system, H<sub>2</sub> + H, which, at some point and with further development, may become relevant to Professor Kuchitsu's contribution to the photodissociation dynamics study of triatomics [5].

The simplest chemical reaction H<sub>2</sub> + H → H + H<sub>2</sub>—including its isotopologues—is possibly one of the most exhaustively studied chemical processes [6]. Furthermore, the H<sub>3</sub> system has qualitatively interesting features: a shallow van-der-Waals minimum for collinear nuclear structures and a conical intersection for equilateral triangular configurations. These features impose challenges when investigating the quantum dynamics of the system and require a high-level description of the electronic structure. The first potential energy surface (PES) for collinear H<sub>3</sub> was obtained by Liu in 1973 [7]. Since then, several full-dimensional surfaces have been published [8–14] and refined [15–21] using increasingly accurate quantum chemical methods. More recently, a multireference configuration interaction (MRCI) PES was developed, using a hierarchy of correlation consistent basis sets followed by extrapolation to the complete basis set (CBS) limit [22] with an estimated μE<sub>h</sub> level of precision. This complete configuration interaction (CCI) surface has been the most accurate full-dimensional PES of H<sub>3</sub>, and it was used to resolve long-standing discrepancy of experimental and

theoretical thermal rate constants [23].

The first computation for this system using explicitly correlated Gaussian (ECG) basis functions was performed by Cafiero and Adamowicz [24]. They determined the stationary points of the PES by the simultaneous minimization of the energy with respect to both the nonlinear parameters of the basis functions and the nuclear configuration using analytic gradients. Nevertheless, using only 64 basis functions, they obtained an energy,  $-1.673\,467\,E_h$ , which is above the dissociation threshold,  $E(\text{H}_2) + E(\text{H}) = -1.674\,475\,714\,E_h$ .

In later work, Pavanello, Tung, and Adamowicz carried out methodological developments to improve the convergence of the ECG wave function and energy, and to reduce the computational cost for polyatomic, *i.e.*, H<sub>3</sub><sup>+</sup> and H<sub>3</sub>, systems. Their efforts resulted in the most precise non-relativistic energy for H<sub>3</sub>, so far, near the equilibrium structure [25].

The aim of the present letter is to explore and take the achievable precision further for H<sub>3</sub>, a simple prototype for poly-electronic and poly-atomic molecular systems, using explicitly correlated Gaussian functions.

## 2. Method

The Schrödinger equation (in atomic units) with  $N_{\text{nuc}}$  nuclei clamped at the  $\mathbf{R}$  configuration and  $n_p$  electrons,

$$H\psi(\mathbf{r}; \mathbf{R}) = E(\mathbf{R})\psi(\mathbf{r}; \mathbf{R}) \quad (1)$$

\* Corresponding author.

E-mail address: [edit.matyus@tk.elte.hu](mailto:edit.matyus@tk.elte.hu) (E. Mátyus).

$$H = \frac{1}{2} \sum_{i=1}^{n_p} \mathbf{p}_i^2 - \sum_{a=1}^{N_{\text{nuc}}} \sum_{i=1}^{n_p} \frac{Z_a}{r_{ia}} + \sum_{i<j}^{n_p} \frac{1}{r_{ij}} + \sum_{a<b}^{N_{\text{nuc}}} \frac{Z_a Z_b}{R_{ab}}, \quad (2)$$

is solved for the ground state of  $\text{H}_3$ . The wave function is written as sum of antisymmetrized product of spatial and spin functions,

$$\psi(\mathbf{r}; \mathbf{R}) = \mathcal{A} \sum_{n=1}^{N_b} c_n \phi_n(\mathbf{r}; \mathbf{A}_n, s_n) \chi(\vartheta_n). \quad (3)$$

In the following equations, the spin degree of freedom is explicitly shown if it is directly relevant to the equations. The spatial basis functions,  $\phi_n$ , are expressed with floating ECG functions,

$$\phi_n(\mathbf{r}; \mathbf{A}_n, s_n) = \exp[-(\mathbf{r} - s_n)^T \underline{\mathbf{A}}_n (\mathbf{r} - s_n)], \quad (4)$$

where  $\underline{\mathbf{A}}_n = \mathbf{A}_n \otimes \mathbf{I}_3$ ,  $\mathbf{A}_n \in \mathbb{R}^{n_p \times n_p}$  is the exponent matrix,  $\otimes \mathbf{I}_3$  means direct product with the  $3 \times 3$  unit matrix, and  $\mathbf{r}, s \in \mathbb{R}^{3n_p}$  are the coordinate vectors of the electrons and the Gaussian centers, respectively.  $\mathcal{A}$  is the anti-symmetrization operator, and  $\mathbf{A}$  is parameterized in the  $\mathbf{A} = \mathbf{L}^T \mathbf{L}$  Cholesky-form, with an  $\mathbf{L}$  lower-triangular matrix, to ensure positive definiteness of  $\mathbf{A}$  and square integrability of the basis functions. The  $\text{A}_1$  symmetry (in the  $C_{\infty v}$  point group) of the ground-state wave function is realized by constraining the Gaussian centers to the  $z$  axis.

The  $\chi(\vartheta_n)$  three-particle spin function corresponding to the doublet multiplicity of the ground-state is obtained as a linear combination of the two possible couplings of the elementary, one-electron spin functions  $\sigma(i)_{\frac{1}{2}, \pm \frac{1}{2}}$  to a doublet state [26],

$$\begin{aligned} \chi \left( \vartheta_n \right) &= d_1 \left( \vartheta_n \right) \left[ \left[ \sigma(1)_{\frac{1}{2}} \sigma(2)_{\frac{1}{2}} \right]_{1,0} \sigma(3)_{\frac{1}{2}} \right]_{\frac{1}{2}, \frac{1}{2}} \\ &+ d_2 \left( \vartheta_n \right) \left[ \left[ \sigma(1)_{\frac{1}{2}} \sigma(2)_{\frac{1}{2}} \right]_{0,0} \sigma(3)_{\frac{1}{2}} \right]_{\frac{1}{2}, \frac{1}{2}}, \end{aligned} \quad (5)$$

where the square brackets denote angular momentum coupling, using the Clebsch–Gordan coefficients  $\langle j_1, m_{j_1}, j_2, m_{j_2} | J, M_J \rangle$ . For example, coupling two spin-1/2 particles to a singlet function is labelled as

$$\begin{aligned} &\left[ \sigma(1)_{\frac{1}{2}} \sigma(2)_{\frac{1}{2}} \right]_{0,0} \\ &= \left\langle \frac{1}{2}, \frac{1}{2}, \frac{1}{2}, -\frac{1}{2} \middle| 0, 0 \right\rangle \sigma(1)_{\frac{1}{2}, \frac{1}{2}} \sigma(2)_{\frac{1}{2}, -\frac{1}{2}} \\ &+ \left\langle \frac{1}{2}, -\frac{1}{2}, \frac{1}{2}, \frac{1}{2} \middle| 0, 0 \right\rangle \sigma(1)_{\frac{1}{2}, -\frac{1}{2}} \sigma(2)_{\frac{1}{2}, \frac{1}{2}} \\ &= \frac{1}{\sqrt{2}} (|\uparrow\downarrow\rangle - |\downarrow\uparrow\rangle). \end{aligned} \quad (6)$$

Considering the normalization condition as well, the doublet three-electron spin functions can be parameterized by a single  $\vartheta_n$  parameter as

$$d_1(\vartheta_n) = \sin \vartheta_n \quad \text{and} \quad d_2(\vartheta_n) = \cos \vartheta_n, \quad (7)$$

and  $\vartheta_n$  is optimized together with the nonlinear parameters of the basis set. Although the non-relativistic Hamiltonian, Eq. (2), is spin independent, during the course of the variational solution of Eq. (1), optimization of  $\vartheta_n$  (and the linear combination coefficients of the two possible spin functions, Eq. (5)), provides an additional flexibility for the basis set.

## 2.1. Optimized fragment initialization

The starting basis function parameters are usually generated in a pseudo-random manner, retaining those functions from a trial set that provide the lowest energy expectation value. This generation procedure is followed by extensive refinement of the parameterization based on the variational principle [26]. By increasing the number of electrons, the dimensionality of the parameter space, and hence, the optimization cost increases. To keep the computational cost low, it is useful to consider that the interaction between the electrons of the hydrogen molecule and the electron of the hydrogen atom is weak in the van-der-Waals well or if the two ‘fragments’ are not too close, in general. If the interaction is not too strong, then a  $\psi_I$  initial approximation for the wave function can be written as the product of the wave functions optimized for the ‘fragments’ (atom and molecule for the present example):

$$\begin{aligned} \psi_I^{\text{H}_3}(\mathbf{r}_1, \mathbf{r}_2, \mathbf{r}_3) &= \psi^{\text{H}_2}(\mathbf{r}_1, \mathbf{r}_2) \psi^{\text{H}}(\mathbf{r}_3) \\ &= \sum_{k,l} c_{kl} \phi_k^{\text{H}_2}(\mathbf{r}_1, \mathbf{r}_2) \phi_l^{\text{H}}(\mathbf{r}_3), \end{aligned} \quad (8)$$

which corresponds to an initial parameterization of the three-electron basis set with

$$A_{kl}^I = \begin{pmatrix} \mathbf{A}_k^{\text{H}_2} & 0 \\ 0 & \mathbf{A}_l^{\text{H}} \end{pmatrix}, \quad (9)$$

and the 3-electron  $s$  vectors include the  $s$  vectors shifted according to the configuration of the ‘fragments’ in  $\text{H}_3$ :

$$s_{kl}^I = \begin{pmatrix} s_k^{\text{H}_2} + \mathbf{R}_{\text{CM}}^{\text{H}_2} \\ s_l^{\text{H}} + \mathbf{R}^{\text{H}} \end{pmatrix}, \quad (10)$$

where  $\mathbf{R}_{\text{CM}}^{\text{H}_2}$  is the center of mass of the protons in  $\text{H}_2$ .

This procedure is reminiscent of the monomer contraction method that was first introduced in Ref. [27] for the helium dimer, although there are a few differences. First, we use the fragment (or monomer) basis set only to initialize the many(three)-electron basis, and we run repeated refinement cycles [28,29] using the Powell method [30] for this initial basis. Second, retaining the full direct-product basis optimized for  $\text{H}_2$  and separately for H would be computationally very demanding, so instead, we truncate the direct-product basis according to the following strategy.

The ground-state wave function of the  $\text{H}_2$  molecule was expanded over 1200 ECG functions, yielding  $-1.174475714 E_h$  for the ground state energy, which—compared to the most accurate value obtained by Pachucki  $-1.1744757142204434(5) E_h$  [31]—is converged to a fraction of a  $nE_h$ . The wave function of the hydrogen atom was represented with 10 optimized Gaussian functions, resulting in  $-0.499999332 E_h$  (in comparison with the exact value,  $-0.5 E_h$ ) ground-state energy. Inclusion of all possible combinations of the  $\text{H}_2$  and H basis functions would result in a gigantic, 12 000-term expansion. Such a long expansion would be prohibitively expensive to extensively optimize (refine), and it is unnecessary to have so many functions for reaching a  $1 : 10^9$  (ppb) precision. To reduce the direct-product basis, it would be possible to perform competitive selection over the large basis space or to order (and then truncate) the basis functions based on their importance in lowering the energy [26]. In the present work, we used a very simple construct that does not require any computation: we have generated a set of 1200 functions by appending each  $\text{H}_2$  basis function from the 1200 set with a single H function. Out of the 10 H functions, we have picked one based on the basis index, *i.e.*,

$$\begin{aligned} & \{ \phi_{10n+i}^{\text{H}_2} \phi_i^{\text{H}}; n = 0, 1, \dots, 119, i = 1, 2, \dots, 10 \} \\ & = \{ \phi_1^{\text{H}_2} \phi_1^{\text{H}}, \phi_2^{\text{H}_2} \phi_2^{\text{H}}, \dots, \phi_{10}^{\text{H}_2} \phi_{10}^{\text{H}}, \\ & \quad \phi_{11}^{\text{H}_2} \phi_1^{\text{H}}, \phi_{12}^{\text{H}_2} \phi_2^{\text{H}}, \dots, \phi_{20}^{\text{H}_2} \phi_{10}^{\text{H}}, \\ & \quad \dots \\ & \quad \phi_{1191}^{\text{H}_2} \phi_1^{\text{H}}, \phi_{1192}^{\text{H}_2} \phi_2^{\text{H}}, \dots, \phi_{1200}^{\text{H}_2} \phi_{10}^{\text{H}} \}. \end{aligned} \quad (11)$$

The spin basis functions defined in Eq. (5), were initialized by coupling the two electrons initially localized on the H<sub>2</sub> fragment to a singlet state, *i.e.*,  $d_1(\vartheta_n) = 0$  and  $d_2(\vartheta_n) = 1$  corresponding to  $\vartheta_n = 0$  ( $n = 1, 2, \dots, 1200$ ) in Eqs. (5)–(7). All non-linear parameters, including  $\vartheta_n$ , of the initial basis set were excessively optimized in repeated refinement cycles (Fig. 1). The optimized fragment-based initialization of the basis set, described in this section, allowed saving several weeks (months) of computer time in comparison with Ref. [32] (see also Section 3).

## 2.2. Gaussian-center scaling

Independent variational optimization of the basis set at many points along the PEC (or over the PES) would make the computations very computationally intensive. Kołos and Wolniewicz [33] noted already in 1964 that for a sufficiently large basis set, the  $A_k$  exponents are insensitive to small displacements of the nuclear coordinates. In 1997, Cencek and Kutzelnigg proposed a scaling technique to generate a good initial ECG (re) parameterization for the electronic basis set of diatomics upon small nuclear displacements [34]. They noted that their approach can be generalized beyond diatomics. Pavanello and Adamowicz implemented rescaling the ECG centers (to have a good starting basis set) of H<sub>3</sub><sup>+</sup> upon small nuclear displacements to generate a series of points to represent the 3D PES [32,35–37]. Upon a small  $\Delta R_a$  displacement of the coordinates of the *a*th nucleus,

$$\mathbf{R}_a' = \mathbf{R}_a + \Delta \mathbf{R}_a, \quad (12)$$

the  $s_i \in \mathbb{R}^3$  ECG centers corresponding to the *i*th electron were transformed as

$$s_i' = s_i + \Delta s_i, \quad (13)$$

where  $\Delta s_i$  is expressed as a function of the  $\Delta R_a$  nuclear displacement,

$$\Delta s_i = \frac{1}{W_i} \sum_{a=1}^{N_{\text{nuc}}} w_{ia} \Delta \mathbf{R}_a \quad (14)$$

with  $W_i = \sum_{a=1}^{N_{\text{nuc}}} w_{ia}$ . The  $w_{ia}$  ‘weight’ is a function constructed based on simple arguments. It is chosen to be the distance of the  $s_i$  center and the *a*th nucleus,  $|s_i - \mathbf{R}_a|$  and it is expected to have good limiting properties.

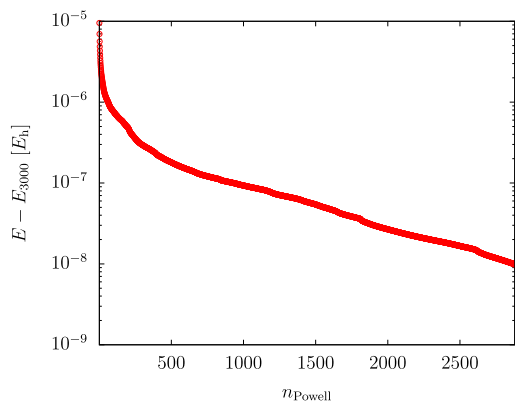


Fig. 1. Convergence of the ground-state energy of H<sub>2</sub>...H during the course of the Powell refinement cycles ( $n_{\text{Powell}}$ ) of  $N_b = 1200$  basis functions initialized using basis functions optimized for the fragments, Eq. (11).  $R_{\text{H}_2} = 1.4$  bohr and  $R_{\text{H}_2 \dots \text{H}} = 6.442$  bohr,  $E_{3000} = -1.674\,561\,687 E_h$ . (See also Table 1.)

First, it must vanish if the  $s_i$  center is very (infinitely) far from the displaced nucleus,  $\lim_{|s_i - \mathbf{R}_a| \rightarrow \infty} w_{ia} = 0$ . Second, the closer the  $s_i$  center to the  $\mathbf{R}_a$  nucleus position, the  $\Delta R_{ia}$  displacement has a larger contribution, *i.e.*, larger  $w_{ia}$  weight, to the  $\Delta s_i$  change.

These conditions allow several possible choices for the weight function. For example, Coulomb-like weights were used in Ref. [32]

$$w_{ia}^{\text{C}} = \frac{1}{|s_i - \mathbf{R}_a|}. \quad (15)$$

After some experimentation with different possible functions, and inspired by the picture that the weight function can be intuitively defined as if there was some attraction between the centers and the nuclear positions by a central field, a Yukawa-like weight function appears to be a good choice

$$w_{ia}^{\text{Y}} = \frac{e^{-\mu|s_i - \mathbf{R}_a|}}{|s_i - \mathbf{R}_a|}, \quad (16)$$

where the parameter  $\mu \in \mathbb{R}^+$  was set to unity in this work. For small nuclear displacements, a parameterization rescaled with Yukawa weights (with  $\mu = 1$ ) provided an energy lower than rescaling with Coulomb weights, Eq. (15).

The rescaling technique with the Yukawa weight function was used to generate the PEC corresponding to the H atom approaching the H<sub>2</sub> molecule with a proton-proton distance fixed at  $R_{\text{H}_2} = 1.4$  bohr. The  $R_{\text{H}_2 \dots \text{H}}$  distance of the hydrogen atom was measured from the center of mass of the H<sub>2</sub> fragment. The starting value was  $R_{\text{H}_2 \dots \text{H}} = 6.442$  bohr, for which an initial basis set was generated using the optimized fragment initialization (Section 2.1) and the representation was improved through several Powell refinement [30] cycles of the non-linear parameters (Fig. 1). Then, initial basis sets were generated by making small  $\Delta R_{\text{H}_2 \dots \text{H}} = \pm 0.1$  bohr displacements, rescaling the centers according to Eq. (14) with Yukawa weights, Eq. (16), followed by 5 entire basis refinement cycles (that took 4 h) before the next step was taken along the series of the nuclear configurations (the positive and the negative displacement series were run in parallel). All computations have been carried out using the QUANTEN computer program [29,38–40].

The energies (Fig. 2) and optimized basis set parameters are deposited in the Supplementary Material.

## 3. Results and discussion

We have carried out extensive single-point computations for the near-equilibrium geometry in the van-der-Waals well with  $R_{\text{H}_2}^{(0)} = 1.4$  bohr and  $R_{\text{H}_2 \dots \text{H}}^{(0)} = 6.442$  bohr first reported in Ref. [24]. This structure is close to

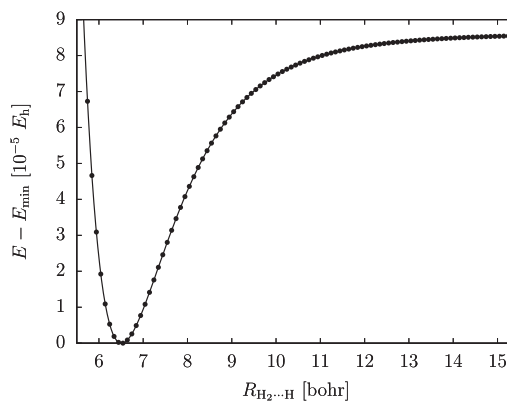


Fig. 2. Potential energy cut of the H<sub>3</sub> system converged in the present work with an estimated sub-ppm precision. Along the curve, the geometry of the H<sub>2</sub> unit is fixed at  $R_{\text{H}_2} = 1.4$  bohr. The lowest-energy datapoint corresponds to  $E_{\text{min}} = -1.674\,561\,899 E_h$  and  $R_{\text{min}} = 6.542$  bohr.



the equilibrium geometry obtained with carefully conducted orbital-based computations [22] (Table 2). The energy of Ref. [24] computed with a small ECG basis is inaccurate, but later, large-scale computations were reported in Ref. [25].

At this geometry, the best energy obtained from the present work with 1200 ECGs (constructed by the initial fragment initialization, Section 2.1, followed by  $n_{\text{Powell}} = 3000$  Powell refinement cycles of the entire basis set) is  $-1.674561687 E_h$  (upper part of Table 1). Table 1 also shows the computed energy values for smaller basis sets that allow assessment of the convergence and extrapolation to the complete basis set (CBS) limit [41].

Direct comparison with Ref. [25] requires further computation, because the extensively optimized energy reported in Ref. [25] appears to belong to a 6.442 bohr distance of the hydrogen atom not from the center of nuclear mass of the  $H_2$  unit, but from the closer proton of  $H_2$ . We think that this nuclear structure was used in Ref. [25], because we obtain good agreement for the energies when we perform the computation at this geometry, shown in the lower part of Table 1, corresponding to  $R_{H_2}^{(0)} = 1.40$  bohr and  $R_{H_2 \dots H} = R_{H_2 \dots H}^{(0)} + R_{H_2}^{(0)}/2 = 6.442$  bohr + 0.700 bohr = 7.142 bohr.

We also note that the best energy value of Ref. [25] computed in 6 months (using 12 CPU cores) was reproduced in this work (corresponding to the structure given in footnote <sup>b</sup> of Table 1) using the optimized fragment initialization technique (Section 2.1) followed by a few Powell refinement cycles in 4 days. The computational benefit of the optimized fragment technique is significant in comparison with a computation [25] constructed from ‘scratch’ immediately for the three-particle problem.

Then, we continued the extensive refinement of the basis parameterization based on the variational principle, and the best result after 3 months computation (using 12 CPU cores) is reported in Table 1. The generation of the points along the PEC was started from this well-optimized parameterization by  $\Delta R_{H_2 \dots H} = \pm 0.1$  bohr increments/decrements (running in parallel) using the rescaling technique (Section 2.1), followed by 5 Powell refinement cycles at every step (before the next step was taken). The entire PEC generation took 13 days using 12 CPU cores.

Finally, it is relevant to compare the ECG energies with the best orbital-based results underlying the CCI PES. For this reason, we have used a single rescaling step from the starting optimized parameterization (upper part of Table 1) to the  $R_{H_2}^{(0)} = 1.4$  bohr and  $R_{H_2 \dots H}^{(0)} = 6.51205$  bohr structure, which was determined to be the global minimum

structure at the MRCI/aug-cc-pV6Z level [22]. The parameter rescaling, with a negligible computational cost, was followed by 5 Powell refinement cycles that took 4 h. Table 2 shows the energy values reported for the MRCI computations corresponding to the aug-cc-pVXZ ( $X = D, T, Q, 5, 6$ ) and the ‘modified’ correlation consistent aug-mcc-pVXZ ( $X = D, T, Q, 5, 6, 7$ ) basis sets [22,19]. The ECG energy is already  $74 \mu E_h$  lower, than the best MRCI value corresponding to the largest (aug-mcc-pV7Z) basis set. Furthermore, we can confirm the estimated  $\mu E_h$  precision of the CBS extrapolated energy from the mcc basis, whereas the extrapolated energy based on the regular correlation consistent basis is slightly lower than our current best estimate [22].

#### 4. Summary, conclusion, and outlook

In summary, we have computed a benchmark-quality one-dimensional segment of the Born–Oppenheimer potential energy surface of the  $H_3$  system for a series of collinear nuclear configurations. The electronic energies are estimated to be converged on the sub-parts-per-million level.

The depth of the van-der-Waals well was predicted to be  $86(1)\mu E_h$  at the  $R_{H_2} = 1.4015$  bohr and  $R_{H_2 \dots H} = 6.51205$  bohr geometry in MRCI computations underlying the currently most precise potential energy surface of  $H_3$  [22]. The variational computations reported in this work and using a (relatively small) explicitly correlated Gaussian basis set confirm this value and improve upon its precision by two orders of magnitude,  $86.54(3)\mu E_h$ . In order to achieve a similar precision for non-collinear nuclear structures, which have a lower order or no point-group symmetry, it will be necessary to use a larger basis set, which is certainly feasible.

Regarding the broader context of this work, (non-) adiabatic perturbation theory [42–46] combined with leading-order relativistic and quantum electrodynamics (QED) corrections [47,48] are expected to provide a state-of-the-art theoretical description for this system. This framework has already been extensively used and tested for the lightest diatomic molecules [49,40]. For the ground-electronic state of the  $H_2$  molecule, the effect of the non-adiabatic-relativistic coupling has also been evaluated and was found to be non-negligible [50]. In this direction, the computation of a precise representation of the electronic wave function is a necessary first step that was demonstrated in this work to be feasible. The adiabatic [51,52], non-adiabatic and (regularized) relativistic and QED corrections can be evaluated at a couple of points using currently existing procedures [46,53,40,54]. At the same time, for a

**Table 1**

Convergence of the non-relativistic, ground-state energy of  $H_3$  near the van-der-Waals equilibrium structure at  $R_{H_2} = 1.4$  bohr and  $R_{H_2 \dots H} = 6.442$  bohr taken from Ref. [24].

$N_b$	Ansatz	$n_{\text{Powell}}$	$E [E_h]$
$R_{H_2} = 1.40$ bohr, $R_{H_2 \dots H} = 6.442$ bohr : <sup>a</sup>			
600	$\{\psi_{10n+i}^{H_2}, \psi_i^{H_1}\}$	2000	-1.674 560 470
800	$\{\psi_{10n+i}^{H_2}, \psi_i^{H_1}\}$	2000	-1.674 561 379
1000	$\{\psi_{10n+i}^{H_2}, \psi_i^{H_1}\}$	2000	-1.674 561 583
1200	$\{\psi_{10n+i}^{H_2}, \psi_i^{H_1}\}$	3000	-1.674 561 687
[Extrapolation to $N_b \rightarrow \infty$ :			-1.674 561 75(3)]
$R_{H_2} = 1.40$ bohr, $R_{H_2 \dots H} = 7.142$ bohr : <sup>b</sup>			
1000	Ref. [25] <sup>c</sup>		-1.674 547 421 00
1200	$\{\psi_{10n+i}^{H_2}, \psi_i^{H_1}\}$	3000	-1.674 547 750

<sup>a</sup>  $R_{H_2} = 1.4$  bohr,  $R_{H_2 \dots H} = 6.442$  bohr, measured from the nuclear center of mass (NCM) of the  $H_2$  unit.

<sup>b</sup>  $R_{H_2} = 1.4$  bohr,  $R_{H_2 \dots H} = 7.142$  bohr (measured from the NCM of the  $H_2$  unit), and corresponds to a 6.442 bohr distance measured from the nearer proton in the  $H_2$  unit.

<sup>c</sup> Geometry <sup>a</sup> is claimed in Ref. [25], but it appears to be <sup>b</sup>. The difference amounts to whether the distance of the hydrogen atom is measured from the NCM or the nearer proton.

**Table 2**

Comparison of energies of various *ab initio* computations. The equilibrium geometry, determined at the MRCI/aug-cc-pV6Z is  $R_{H_2} = 1.4015$  bohr and  $R_{H_2 \dots H} = 6.51205$  bohr [22].

Source	$E [E_h]$
aug-cc-pVDZ <sup>a</sup>	-1.664 339
aug-cc-pVTZ <sup>a</sup>	-1.672 540
aug-cc-pVQZ <sup>a</sup>	-1.673 902
aug-cc-pV5Z <sup>a</sup>	-1.674 332
aug-cc-pV6Z <sup>a</sup>	-1.674 445
aug-mcc-pVTZ <sup>a</sup>	-1.672 553
aug-mcc-pVQZ <sup>a</sup>	-1.673 917
aug-mcc-pV5Z <sup>a</sup>	-1.674 298
aug-mcc-pV6Z <sup>a</sup>	-1.674 430
aug-mcc-pV7Z <sup>a</sup>	-1.674 488
MBE <sup>cc</sup> (3,4 CBS) <sup>b</sup>	-1.674 566
MBE <sup>mcc</sup> (6,7 CBS) <sup>c</sup>	-1.674 562
Present work ( $N_b = 1200$ ) <sup>d</sup>	-1.674 562 264

<sup>b, c</sup> Ref. [22]: extrapolated CBS energy corresponding to the aug-cc-pVXZ ( $X = 3, 4$ ) and aug-mcc-pVXZ ( $X = 6, 7$ ) basis sets, respectively.

<sup>a</sup> Ref. [22]: MRCI energy.

<sup>d</sup> Rescaled from the basis set optimized for the  $(R_{H_2}^{(0)}, R_{H_2 \dots H}^{(0)})$  structure in Table 1 followed by 1000 Powell refinement cycles.

complete description of a polyatomic system like H<sub>3</sub>, these corrections must be computed over hundreds or thousands of nuclear configurations. This requires a fully automated evaluation and error control of all corrections, which may be especially challenging for the singular terms in the relativistic and QED expressions, and this requires further methodological and algorithmic developments that is left for future work.

### Declaration of Competing Interest

The authors declare that they have no known competing financial interests or personal relationships that could have appeared to influence the work reported in this paper.

### Acknowledgment

Financial support of the European Research Council through a Starting Grant (No. 851421) is gratefully acknowledged. DF thanks a doctoral scholarship from the ÚNKP-21-3 New National Excellence Program of the Ministry for Innovation and Technology from the source of the National Research, Development and Innovation Fund (ÚNKP-21-3-II-ELTE-41). We also thank Péter Jeszenszki for discussions about energy extrapolation for ECG basis sets.

### Appendix A. Supplementary material

Supplementary data associated with this article can be found, in the online version, at <https://doi.org/10.1016/j.cplett.2022.139734>.

### References

- [1] K. Kuchitsu, Effect of molecular vibrations on gas electron diffraction. I. Probability distribution function and molecular intensity for diatomic molecules, *Bull. Chem. Soc. Jpn.* 40 (3) (1967) 498–504, <https://doi.org/10.1246/bcsj.40.498>.
- [2] J. Sarka, A.G. Császár, S.C. Althorpe, D.J. Wales, E. Mátyus, Rovibrational transitions of the methane-water dimer from intermolecular quantum dynamical computations, *Phys. Chem. Phys.* 18 (2016) 22816, <https://doi.org/10.1039/C6CP03062A>.
- [3] K. Kuchitsu, L.S. Bartell, Effect of anharmonic vibrations on the bond lengths of polyatomic molecules. I. model of force field and application to water, *J. Chem. Phys.* 36 (9) (1962) 2460–2469, <https://doi.org/10.1063/1.1732909>.
- [4] M. Nakata, K. Kuchitsu, Estimation of equilibrium structure by use of isotopic differences in the rz structure application to several symmetric hydrides, *J. Chem. Soc. Jpn.* 1986 (11) (1986), <https://doi.org/10.1246/nikkashi.1986.1446.1446-1446>.
- [5] T. Nagata, T. Kondow, K. Kuchitsu, G.W. Loge, R.N. Zare, Photodissociation dynamics of triatomic molecules, *Mol. Phys.* 50 (1) (1983) 49–63, <https://doi.org/10.1080/00268978300102161>.
- [6] F.J. Aoiz, L.B. Nares, V.J. Herrero, The H+H<sub>2</sub> reactive system. Progress in the study of the dynamics of the simplest reaction, *Int. Rev. Phys. Chem.* 24 (1) (2005) 119–190, <https://doi.org/10.1080/01442350500195659>.
- [7] B. Liu, Ab initio potential energy surface for linear H<sub>3</sub>, *J. Chem. Phys.* 58 (5) (1973) 1925–1937, <https://doi.org/10.1063/1.1679454>.
- [8] P. Siegbahn, B. Liu, An accurate three-dimensional potential energy surface for H<sub>3</sub>, *J. Chem. Phys.* 68 (5) (1978) 2457–2465, <https://doi.org/10.1063/1.4366018>.
- [9] D.G. Truhlar, C.J. Horowitz, Functional representation of Liu and Siegbahn's accurate ab initio potential energy calculations for H+H<sub>2</sub>, *J. Chem. Phys.* 68 (5) (1978) 2466–2476, <https://doi.org/10.1063/1.4366019>.
- [10] A.J.C. Varandas, F.B. Brown, C.A. Mead, D.G. Truhlar, N.C. Blais, A double many-body expansion of the two lowest-energy potential surfaces and nonadiabatic coupling for H<sub>3</sub>, *J. Chem. Phys.* 86 (11) (1987) 6258–6269, <https://doi.org/10.1063/1.452463>.
- [11] A.I. Boothroyd, W.J. Keogh, P.G. Martin, M.R. Peterson, An improved H<sub>3</sub> potential energy surface, *J. Chem. Phys.* 95 (6) (1991) 4343–4359, <https://doi.org/10.1063/1.461758>.
- [12] A.I. Boothroyd, W.J. Keogh, P.G. Martin, M.R. Peterson, A refined H<sub>3</sub> potential energy surface, *J. Chem. Phys.* 104 (18) (1996) 7139–7152, <https://doi.org/10.1063/1.471430>.
- [13] Y.-S. Wu, J. Anderson, et al., A very high accuracy potential energy surface for H<sub>3</sub>, *Phys. Chem. Chem. Phys.* 1 (6) (1999) 929–937, <https://doi.org/10.1039/A808797K>.
- [14] D.L. Diedrich, J.B. Anderson, Exact quantum Monte Carlo calculations of the potential energy surface for the reaction H+H<sub>2</sub>→H<sub>2</sub>+H, *J. Chem. Phys.* 100 (11) (1994) 8089–8095, <https://doi.org/10.1063/1.466802>.
- [15] M.R.A. Blomberg, B. Liu, The H<sub>3</sub> potential surface revisited, *J. Chem. Phys.* 82 (2) (1985) 1050–1051, <https://doi.org/10.1063/1.448527>.
- [16] C.W. Bauschlicher, S.R. Langhoff, H. Partridge, A reevaluation of the H<sub>3</sub> potential, *Chem. Phys. Lett.* 170 (4) (1990) 345–348, [https://doi.org/10.1016/S0009-2614\(90\)87029-Q](https://doi.org/10.1016/S0009-2614(90)87029-Q).
- [17] H. Partridge, C.W. Bauschlicher, J.R. Stallcop, E. Levin, Ab initio potential energy surface for H-H<sub>2</sub>, *J. Chem. Phys.* 99 (8) (1993) 5951–5960, <https://doi.org/10.1063/1.465894>, arXiv:10.1063/1.465894.
- [18] D.L. Diedrich, J.B. Anderson, An accurate quantum Monte Carlo calculation of the barrier height for the reaction H+H<sub>2</sub>→H<sub>2</sub>+H, *Science* 258 (5083) (1992) 786–788, doi:0.1126/science.258.5083.786.
- [19] S.L. Mielke, B.C. Garrett, K.A. Peterson, The utility of many-body decompositions for the accurate basis set extrapolation of ab initio data, *J. Chem. Phys.* 111 (9) (1999) 3806–3811, <https://doi.org/10.1063/1.479683>.
- [20] K.E. Riley, J.B. Anderson, Higher accuracy quantum Monte Carlo calculations of the barrier for the H+H<sub>2</sub> reaction, *J. Chem. Phys.* 118 (7) (2003) 3437–3438, <https://doi.org/10.1063/1.1527012>.
- [21] H.-X. Huang, Exact Fixed-node Quantum Monte Carlo: Differential Approach, *Chin. J. Chem.* 23 (11) (2005) 1474–1478, <https://doi.org/10.1002/cjoc.200591474>.
- [22] S.L. Mielke, B.C. Garrett, K.A. Peterson, A hierarchical family of global analytic Born-Oppenheimer potential energy surfaces for the H+H<sub>2</sub> reaction ranging in quality from double-zeta to the complete basis set limit, *J. Chem. Phys.* 116 (10) (2002) 4142–4161, <https://doi.org/10.1063/1.1432319>.
- [23] S.L. Mielke, K.A. Peterson, D.W. Schwenke, B.C. Garrett, D.G. Truhlar, J. V. Michael, M.-C. Su, J.W. Sutherland, H+H<sub>2</sub> Thermal Reaction: A Convergence of Theory and Experiment, *Phys. Rev. Lett.* 91 (2003) 063201, <https://doi.org/10.1103/PhysRevLett.91.063201>.
- [24] M. Cafiero, L. Adamowicz, Simultaneous optimization of molecular geometry and the wave function in a basis of Singer's n-electron explicitly correlated Gaussians, *Chem. Phys. Lett.* 335 (5) (2001) 404–408, [https://doi.org/10.1016/S0009-2614\(01\)00086-0](https://doi.org/10.1016/S0009-2614(01)00086-0).
- [25] M. Pavanello, W.-C. Tung, L. Adamowicz, How to calculate H<sub>3</sub> better, *J. Chem. Phys.* 131 (18) (2009) 184106, <https://doi.org/10.1063/1.3257592>.
- [26] Y. Suzuki, K. Varga, *Stochastic Variational Approach to Quantum-Mechanical Few-Body Problems*, Springer-Verlag, Berlin, Heidelberg, 1998.
- [27] W. Cencek, J. Komasa, K. Pachucki, K. Szalewicz, Relativistic Correction to the Helium Dimer Interaction Energy, *Phys. Rev. Lett.* 95 (2005) 233004, <https://doi.org/10.1103/PhysRevLett.95.233004>.
- [28] E. Mátyus, M. Reiher, Molecular structure calculations: a unified quantum mechanical description of electrons and nuclei using explicitly correlated Gaussian functions and the global vector representation, *J. Chem. Phys.* 137 (2012) 024104, <https://doi.org/10.1063/1.4731696>.
- [29] E. Mátyus, Pre-Born–Oppenheimer molecular structure theory, *Mol. Phys.* 117 (5) (2019) 590–609, <https://doi.org/10.1080/00268976.2018.1530461>.
- [30] M.J.D. Powell, The NEWUOA software for unconstrained optimization without derivatives (DAMTP 2004/NA05), Report no. NA2004/08, <http://www.damtp.cam.ac.uk/user/na/reports04.html> (last accessed on January 18, 2013).
- [31] K. Pachucki, Born-Oppenheimer potential for H<sub>2</sub>, *Phys. Rev. A* 82 (2010) 032509, <https://doi.org/10.1103/PhysRevA.82.032509>.
- [32] M. Pavanello, L. Adamowicz, High-accuracy calculations of the ground, 1<sup>1</sup>A<sub>1</sub>' and the 2<sup>1</sup>A<sub>1</sub>', 2<sup>3</sup>A<sub>1</sub>', and 1<sup>1</sup>E' excited states of H<sub>3</sub><sup>+</sup>, *J. Chem. Phys.* 130 (3) (2009) 034104, <https://doi.org/10.1063/1.3058634>.
- [33] W. Kolos, L. Wolniewicz, Accurate Adiabatic Treatment of the Ground State of the Hydrogen Molecule, *J. Chem. Phys.* 41 (12) (1964) 3663–3673, <https://doi.org/10.1063/1.1725796>.
- [34] W. Cencek, W. Kutzelnigg, Accurate adiabatic correction for the hydrogen molecule using the Born-Handy formula, *Chem. Phys. Lett.* 266 (3–4) (1997) 383–387, [https://doi.org/10.1016/S0009-2614\(97\)00017-1](https://doi.org/10.1016/S0009-2614(97)00017-1).
- [35] M. Pavanello, W.-C. Tung, F. Leonarski, L. Adamowicz, New more accurate calculations of the ground state potential energy surface of H<sub>3</sub><sup>+</sup>, *J. Chem. Phys.* 130 (7) (2009) 074105, <https://doi.org/10.1063/1.3077193>.
- [36] L. Adamowicz, M. Pavanello, Progress in calculating the potential energy surface of H<sub>3</sub><sup>+</sup>, *Philos. Trans. R. Soc. A* 370 (1978) (2012) 5001–5013, <https://doi.org/10.1098/rsta.2012.0101>.
- [37] M. Pavanello, L. Adamowicz, A. Alijah, N.F. Zobov, I.I. Mizus, O.L. Polyansky, J. Tennyson, T. Szidarovszky, A.G. Császár, Calibration-quality adiabatic potential energy surfaces for H<sub>3</sub><sup>+</sup> and its isotopologues, *J. Chem. Phys.* 136 (18) (2012) 184303, <https://doi.org/10.1063/1.4711756>.
- [38] D. Ferenc, E. Mátyus, Non-adiabatic mass correction for excited states of molecular hydrogen: Improvement for the outer-well HH<sup>1</sup>Σ<sub>g</sub><sup>+</sup> term values, *J. Chem. Phys.* 151 (9) (2019) 094101, publisher: American Institute of Physics. doi:10.1063/1.51109964.
- [39] D. Ferenc, E. Mátyus, Computation of rovibronic resonances of molecular hydrogen: EF<sup>1</sup>Σ<sub>g</sub><sup>+</sup> inner-well rotational states, *Phys. Rev. A* 100 (2) (2019) 020501, <https://doi.org/10.1103/PhysRevA.100.020501>.
- [40] D. Ferenc, V.I. Korobov, E. Mátyus, Nonadiabatic, Relativistic, and Leading-Order QED Corrections for Rovibrational Intervals of <sup>4</sup>He<sub>2</sub><sup>+</sup> (X<sup>2</sup>Σ<sub>g</sub><sup>+</sup>), *Phys. Rev. Lett.* 125 (2020) 213001, <https://doi.org/10.1103/PhysRevLett.125.213001>.
- [41] P. Kopta, T. Piontek, K. Kurowski, M. Puchalski, J. Komasa, Convergence of Explicitly Correlated Gaussian Wave Functions, in: *EScience on Distributed Computing Infrastructure - vol. 8500*, Springer-Verlag, Berlin, Heidelberg, 2014, pp. 459–474. doi:10.1007/978-3-319-10894-0\_33.
- [42] S. Teufel, *Adiabatic perturbation theory in quantum dynamics*, Springer, 2003.
- [43] G. Panati, H. Spohn, S. Teufel, The time-dependent Born-Oppenheimer approximation, *ESAIM: Math. Mod. Num. Anal.* 41 (2007) 297, <https://doi.org/10.1051/m2an:2007023>.
- [44] K. Pachucki, J. Komasa, Nonadiabatic corrections to the wave function and energy, *J. Chem. Phys.* 129 (2008) 034102, <https://doi.org/10.1063/1.2952517>.

- [45] E. Mátyus, S. Teufel, Effective non-adiabatic Hamiltonians for the quantum nuclear motion over coupled electronic states, *J. Chem. Phys.* 151 (2019) 014113, <https://doi.org/10.1063/1.5097899>.
- [46] E. Mátyus, D. Ferenc, Vibronic mass computation for the EF-GK-HH  $^1\Sigma_g^+$  manifold of molecular hydrogen, *Mol. Phys.* (2022), e2074905, <https://doi.org/10.1080/00268976.2022.2074905>.
- [47] H. Araki, Quantum-electrodynamical corrections to energy-levels of helium, *Prog. of Theor. Phys.* 17 (1957) 619–642, <https://doi.org/10.1143/PTP.17.619>.
- [48] J. Sucher, *Energy levels of the two-electron atom, to order  $\alpha^3$  Rydberg*, Columbia University, 1958.
- [49] J. Komasa, M. Puchalski, P. Czachorowski, G. Łach, K. Pachucki, Rovibrational energy levels of the hydrogen molecule through nonadiabatic perturbation theory, *Phys. Rev. A* 100 (2019) 032519, <https://doi.org/10.1103/PhysRevA.100.032519>.
- [50] P. Czachorowski, M. Puchalski, J. Komasa, K. Pachucki, Nonadiabatic relativistic correction in H<sub>2</sub>, D<sub>2</sub>, and HD, *Phys. Rev. A* 98 (2018) 052506, <https://doi.org/10.1103/PhysRevA.98.052506>.
- [51] S.L. Mielke, D.W. Schwenke, K.A. Peterson, Benchmark calculations of the complete configuration-interaction limit of Born-Oppenheimer diagonal corrections to the saddle points of isotopomers of the H+H<sub>2</sub> reaction, *J. Chem. Phys.* 122 (22) (2005) 224313, <https://doi.org/10.1063/1.1917838>.
- [52] S.L. Mielke, D.W. Schwenke, G.C. Schatz, B.C. Garrett, K.A. Peterson, Functional Representation for the Born-Oppenheimer Diagonal Correction and Born-Huang Adiabatic Potential Energy Surfaces for Isotopomers of H<sub>3</sub>, *J. Phys. Chem. A* 113 (16) (2009) 4479–4488, <https://doi.org/10.1021/jp8110887>.
- [53] K. Pachucki, W. Cencek, J. Komasa, On the acceleration of the convergence of singular operators in Gaussian basis sets, *J. Chem. Phys.* 122 (18) (2005) 184101, <https://doi.org/10.1063/1.1888572>.
- [54] P. Jeszenszki, R.T. Ireland, D. Ferenc, E. Mátyus, On the inclusion of cusp effects in expectation values with explicitly correlated Gaussians, *Int. J. Quant. Chem.* 122 (2022) e26819, [doi:doi.org/10.1002/qua.26819](https://doi.org/10.1002/qua.26819).

# All-order explicitly correlated relativistic computations for atoms and molecules

Cite as: *J. Chem. Phys.* **154**, 224110 (2021); doi: [10.1063/5.0051237](https://doi.org/10.1063/5.0051237)

Submitted: 23 March 2021 • Accepted: 24 May 2021 •

Published Online: 10 June 2021



View Online



Export Citation



CrossMark

Péter Jeszenszki,  Dávid Ferenc,  and Edit Mátyus<sup>a)</sup> 

## AFFILIATIONS

Institute of Chemistry, ELTE, Eötvös Loránd University, Pázmány Péter sétány 1/A, Budapest H-1117, Hungary

<sup>a)</sup> Author to whom correspondence should be addressed: [edit.matyus@ttk.elte.hu](mailto:edit.matyus@ttk.elte.hu)

## ABSTRACT

A variational solution procedure is reported for the many-particle no-pair Dirac–Coulomb and Dirac–Coulomb–Breit Hamiltonians aiming at a parts-per-billion (ppb) convergence of the atomic and molecular energies, described within the fixed nuclei approximation. The procedure is tested for nuclear charge numbers from  $Z = 1$  (hydrogen) to 28 (iron). Already for the lowest  $Z$  values, a significant difference is observed from leading-order Foldy–Wouthusen perturbation theory, but the observed deviations are smaller than the estimated self-energy and vacuum polarization corrections.

Published under an exclusive license by AIP Publishing. <https://doi.org/10.1063/5.0051237>

## I. INTRODUCTION

Precision spectroscopy experiments carried out for small atomic<sup>1–3</sup> and molecular<sup>4,5</sup> systems have been proposed as low-energy tests of the fundamental theory of matter.<sup>6</sup> Atoms and molecules are bound many-body quantum systems held together by electromagnetic interactions usually complemented with some model for the internal nuclear structure. Relativistic quantum electrodynamics is a simple  $U(1)$  gauge theory with a Lagrangian density that, of course, obeys Lorentz invariance of special relativity that is a standard textbook material.<sup>7</sup>

At the same time, the bound states of atoms and molecules are conveniently obtained as eigenstates of some wave equation, most commonly as stationary states of the Galilean invariant Schrödinger equation. Sophisticated techniques have been developed for a numerically exact (14 digit) solution of the three-<sup>8</sup> and four-body Schrödinger equation.<sup>9</sup> “Effects” due to special relativity and the quantized fermion and photon fields are accounted for as perturbation following and considerably extending the pioneer perturbation theory work that was first summarized in a book by Bethe and Salpeter in 1957.<sup>10</sup> Further progress in this direction of research is nowadays called the non-relativistic quantum electrodynamics (nrQED) approach,<sup>11–14</sup> and it is successfully used for light atoms and molecules in comparison with precision spectroscopy experiments. There are sophisticated methods developed for the numerically stable evaluation of the increasingly complex

correction formulas<sup>13,15,16</sup> of the nrQED series expanded in terms of the  $\alpha$  fine-structure constant.

A practical and fully Lorentz covariant wave equation for many-spin-1/2 fermion systems is unknown, except for the two-particle case for which the Bethe–Salpeter (BS) equation<sup>17</sup> (see also Ref. 18) offers a quantum-electrodynamics wave equation by also properly accounting for the relative time of the particles. Beyond two particles, the formulation of a practical (and fully Lorentz covariant) QED wave equation remains to be a challenging problem.<sup>19</sup> Following these observations, the Galilean and Schrödinger wave equation may appear to be a solid starting point for describing the molecular regime combined with the nrQED perturbative scheme that can be related to a perturbative calculation of level shifts from the poles of QED Green’s function.<sup>20–22</sup>

At the same time, the Schrödinger wave equation is known to be an inaccurate starting approximation for atoms and molecules, especially for nuclei beyond the lowest  $Z$  nuclear charge numbers.<sup>23,24</sup> Therefore, a “hybrid model” has been adopted in the quantum chemistry practice by assuming equal times for the particles but using Dirac’s kinetic energy operator for every electron and describing the electron–electron interaction within some (most commonly the Coulomb) approximation,

$$\tilde{H}^{\text{bare}} = \sum_{i=1}^n h_i + \sum_{i=1}^n u_i + \sum_{i=1}^n \sum_{j>i}^n v_{ij}, \quad (1)$$

with  $h_i = 1^{[4]}(1) \otimes \dots \otimes h_i^{[4]}(i) \otimes \dots \otimes 1^{[4]}(n)$  and  $h_i^{[4]} = c\alpha^{[4]} \cdot \mathbf{p} + \beta^{[4]} m_i c^2$ , where  $\alpha_x$ ,  $\alpha_y$ ,  $\alpha_z$ , and  $\beta$  are the standard Dirac matrices. The corresponding wave equation is neither fully Galilean nor Lorentz invariant, but it should serve as a better starting point than the Schrödinger equation. In particular, it would allow us to account for the relativistic “effects” on an equal footing with electron correlation that is important for a good description of the molecular regime. This *ad hoc* construction has mathematical problems due to the non-positive definiteness of the operator.

Sucher proposed<sup>25–28</sup> a no-pair many-particle Hamiltonian based on relativistic QED that is reminiscent to the *naïvely* constructed Hamiltonian in Eq. (1) with the important difference that it is projected with  $\Lambda_+$  to the positive energy states ( $E_+$ ) of a non-interacting reference problem,  $H_0 = \sum_{i=1}^n (h_i + u_i)$ ,

$$H = \sum_{i=1}^N \Lambda_+ (h_i + u_i) \Lambda_+ + \sum_{i=1}^N \sum_{j>i}^N \Lambda_+ v_{ij} \Lambda_+. \quad (2)$$

Sucher explained<sup>25–28</sup> that  $H_0$  can be either the kinetic energy of the free spin-1/2 fermions or some other bound model without fermion–fermion interactions following Furry’s work.<sup>29</sup> This no-pair operator, in some cases called the Brown–Ravenhall (BR) operator,<sup>30</sup> has well-defined mathematical properties, and most importantly, it is bounded from below. The “no-pair” expression refers to the fact that, due to the  $\Lambda_+$  projection, this Hamiltonian does not account for pair creation of the spin-1/2 particles (e.g., electron–positron pairs) of the  $H_0$  non-interacting model, but it operates with a fixed fermion number. This is a natural starting point for describing chemical systems. Pair effects can be accounted for in a next stage of the theoretical treatment.

The present work is about the development and application of a practical variational procedure for solving the

$$H\Psi = E\Psi \quad (3)$$

wave equation for atoms and also molecules on the order of parts-per-billion (ppb) precision. This development is an important step toward providing benchmark theoretical values for precision spectroscopy experiments and also an independent test for the nrQED computations. In further work, we plan to account for the effect of pair creation and for interaction with the photon modes that is necessary for a direct comparison.

There is already, of course, important work in the literature about precise variational relativistic approaches for atoms. Grant and co-workers developed the GRASP computer program to treat atoms especially with high  $Z$  values<sup>31–33</sup> starting out from the Dirac–Hartree–Fock (Dirac HF) framework. Shabaev and co-workers also reported several developments for atoms based on the Dirac HF model as a starting reference. They developed the QED model operator approach<sup>34–36</sup> for computing self-energy corrections, and their most recent applications include the results for resonance states of medium  $Z$  helium-like ions,<sup>37</sup> including the exact one-photon exchange, pair creation, and self-energy corrections. Benchmark results were reported by Bylicki, Pestka, and Karwowski<sup>38</sup> for two-electron atoms using the Dirac–Coulomb (DC) operator, a  $\Lambda_+$  projector similar to ours, and an explicitly correlated Hylleraas basis set.

Regarding the molecular regime, it is necessary to mention the BERTHA<sup>39,40</sup> and the DIRAC<sup>41</sup> program packages that include the implementation of hierarchical quantum chemistry methods starting with the HF approximation and typically aiming for chemical accuracy in the computational results. All atomic and molecular programs listed were based (often implicitly) on the no-pair many-particle Hamiltonians. Probably, the first mention of mean-field projectors is due to Mittleman.<sup>42</sup> It has been argued that mean-field projectors should be favored over free-electron projectors for electronic structure computations,<sup>43</sup> and most recently, an optimal choice beyond a mean-field description was discussed in Ref. 44.

## II. THEORETICAL DEVELOPMENTS

For the present work, we restrict the discussion to two spin-1/2 fermions and the fixed nuclei (“Born–Oppenheimer”) approximation. The restriction on the number of particles can be lifted without conceptual difficulties, and we can foresee applications (with the ppb convergence criterion) to three to four particles. It should also be possible to include spin-1/2 nuclei in the treatment on the same footing as the electrons<sup>45–48</sup> (first assuming point-like, structureless nuclei as if they were elementary spin-1/2 particles). In this case, it appears to be a natural choice to use the finite basis representation of the free-particle projector or to explore some other possible non-interacting reference system specifically designed for the pre-Born–Oppenheimer problem.

For the present description of atoms and molecules with clamped nuclei, it is a natural choice for the definition of the  $\Lambda_+$  projector to use the non-interacting two-electron model that is bound by the external potential of the fixed nuclei (without electron–electron interaction). In our implementation, we can work with other non-interacting models to define the projector, including the finite basis free-electron model or other external field one-electron systems. It remains a question to be explored in future work, which choice will be the most convenient one for further numerical applications and, in particular, for the incorporation of (electron–positron and photon) field interactions.

In this work, we build the  $\Lambda_+ = \sum_n |\varphi_{0,n}^{(+)}\rangle \langle \varphi_{0,n}^{(+)}|$  projector from the  $\varphi_{0,n}^{(+)}$  eigenstates of the atomic or molecular Hamiltonian without electron–electron interactions that have positive energy ( $E_+$ ) and do not belong to the Brown–Ravenhall (BR) continuum (that is uncoupled from the physical  $E_+$  states in the absence of electron–electron interactions).<sup>49–51</sup> The physically relevant  $E_+$  states are separated, in practice, from the BR states using the complex coordinate rotation (CCR) technique following Ref. 38. The non-interacting computation is carried out with the same basis set as the interacting computation because the aim is to select (construct) the  $E_+$  part of the actual basis for the full (interacting) problem. In molecules, due to the interaction potential of the electrons and nuclei, the Hamiltonian is non-dilatation-analytic, but additional considerations allowed for resonance computations by using the CCR technique.<sup>52–54</sup> For the present work, it is important to emphasize that the complex scaling makes it possible to distinguish the positive energy states from the BR and the negative-energy states that is based on the different behavior of their energy in the complex plane upon the complex rotation of the coordinate.

The no-pair Hamiltonian, including the fermion–fermion interactions, reads as

$$\begin{aligned}
 H(1, 2, \dots, n) &= \Lambda_+ \left\{ \sum_{i=1}^n 1^{[4]}(1) \boxtimes \dots \boxtimes \hat{h}_i^{[4]}(i) \boxtimes \dots \boxtimes 1^{[4]}(n) + \sum_{i=1}^n u_i 1^{[4n]} \right. \\
 &+ \sum_{i=1}^n \sum_{j>i}^n \left[ v_{ij} 1^{[4n]} + x_{ij} 1^{[4]}(1) \boxtimes \dots \boxtimes \alpha^{[4]}(i) \boxtimes \dots \right. \\
 &\left. \left. \boxtimes \alpha^{[4]}(j) \boxtimes \dots \boxtimes 1^{[4]}(n) \right] \right\} \Lambda_+, \quad (4)
 \end{aligned}$$

$$H(1, 2) = \Lambda_+ \begin{pmatrix} V1^{[4]} + U1^{[4]} & c\sigma_2^{[4]} \cdot \mathbf{p}_2 \\ c\sigma_2^{[4]} \cdot \mathbf{p}_2 & V1^{[4]} + (U - 2m_2c^2)1^{[4]} \\ c\sigma_1^{[4]} \cdot \mathbf{p}_1 & X^{[4]} \\ X^{[4]} & c\sigma_1^{[4]} \cdot \mathbf{p}_1 \end{pmatrix}$$

with  $m_{12} = m_1 + m_2$ ,  $\mathbf{p}_i = -i(\frac{\partial}{\partial r_{ix}}, \frac{\partial}{\partial r_{iy}}, \frac{\partial}{\partial r_{iz}})$  ( $i = 1, 2$ ),  $\sigma_1^{[4]} = (\sigma_x \otimes 1^{[2]}, \sigma_y \otimes 1^{[2]}, \sigma_z \otimes 1^{[2]})$ , and  $\sigma_2^{[4]} = (1^{[2]} \otimes \sigma_x, 1^{[2]} \otimes \sigma_y, 1^{[2]} \otimes \sigma_z)$ , where  $\sigma_x, \sigma_y$ , and  $\sigma_z$  are the  $2 \times 2$  Pauli matrices. Interactions with the fixed external electric charges (clamped nuclei) are collected in  $U = \sum_{i=1}^n \sum_{a=1}^N q_i Q_a / |r_i - R_a|$ .

The electron–electron interaction appears in the  $4 \times 4$  dimensional  $V1^{[4]}$  and  $X^{[4]}$  blocks. Regarding the matrix representation of the Hamiltonian in the non-interacting two-electron basis, the diagonal  $16 \times 16$  dimensional blocks contain the one-photon exchange terms in leading order, whereas the off-diagonal  $16 \times 16$  blocks (different “in” and “out” energies) assume photon emission or absorption and hence correspond to a process involving at least two photons. In the present work, we describe the electron–electron interaction expressed in the Coulomb gauge and invoke the zero-frequency approximation ( $\omega \approx 0$ ) that gives rise to the Coulomb–Breit (CB) interaction operator. Within this approximation,  $H(1, 2)$  is the no-pair Dirac–Coulomb–Breit (DCB) Hamiltonian that accounts for retardation to leading order, and

$$V1^{[4]} = \frac{q_1 q_2}{r_{12}} 1^{[4]} \quad (6)$$

and

$$X^{[4]} = -\frac{q_1 q_2}{2} \left[ \frac{\sigma_1^{[4]} \cdot \sigma_2^{[4]}}{r_{12}} + \frac{(\sigma_1^{[4]} \cdot \mathbf{r}_{12})(\sigma_2^{[4]} \cdot \mathbf{r}_{12})}{r_{12}^3} \right]. \quad (7)$$

If  $X^{[4]}$  is neglected ( $X^{[4]} = 0^{[4]}$ ), we obtain the Dirac–Coulomb (DC) approximation that corresponds to instantaneous interactions. We note that since both the Coulomb and the Coulomb–Breit approximations are independent of the frequency of the exchanged photons, they can be defined without explicit reference to the underlying “non-interacting”  $\varphi_0^{(+)}$  representation. Thus, the  $\Lambda_+$  projection amounts to simple matrix multiplication with the “bare” (CCR scaled) Dirac Hamiltonian.

To build the matrix representation of the two-electron Hamiltonian, we consider the wave function as a linear combination of

where we use the  $\boxtimes$  “block-wise” direct product<sup>55</sup> (named Tracy–Singh product in Ref. 56 and also used later in Ref. 57) that allows us to work with Pauli’s  $\sigma$  matrices and the “large” and “small” component blocks of the Dirac spinors and  $v_{ij}$  and  $x_{ij}$  describe the interaction (*vide infra*).

In particular, the Hamiltonian operator for two spin-1/2 fermions (for convenience, shifted by  $m_i c^2$  for both  $i = 1$  and 2) takes the following matrix form:

$$\begin{pmatrix} c\sigma_1^{[4]} \cdot \mathbf{p}_1 & X^{[4]} \\ X^{[4]} & c\sigma_1^{[4]} \cdot \mathbf{p}_1 \\ V1^{[4]} + (U - 2m_1c^2)1^{[4]} & c\sigma_2^{[4]} \cdot \mathbf{p}_2 \\ c\sigma_2^{[4]} \cdot \mathbf{p}_2 & V1^{[4]} + (U - 2m_{12}c^2)1^{[4]} \end{pmatrix} \Lambda_+, \quad (5)$$

16-dimensional spinor basis functions,  $\Psi_{i\zeta}^{\lambda} = \Psi_{i\zeta_1\zeta_2}^{\lambda_1\lambda_2}(\mathbf{r}_1, \mathbf{r}_2)$ ,

$$\Psi(\mathbf{r}_1, \mathbf{r}_2) = \sum_{i=1}^{N_b} \sum_{\lambda=\{\text{ll, ls, sl, ss}\}} \sum_{\zeta=\{\uparrow\uparrow, \uparrow\downarrow, \downarrow\uparrow, \downarrow\downarrow\}} c_{i\lambda\zeta} \Psi_{i\zeta}^{\lambda}(\mathbf{r}_1, \mathbf{r}_2). \quad (8)$$

For two identical spin-1/2 fermions, it is necessary to antisymmetrize the spinor basis (now, collecting the  $\lambda_1\lambda_2$  blocks and the  $\zeta_1\zeta_2$  spin components into one vector) that reads as

$$\Psi_i(\mathbf{r}_1, \mathbf{r}_2) = \left\{ 1^{[16]} - \Pi^{[16]} \right\} \Phi_i(\mathbf{r}_1, \mathbf{r}_2), \quad (9)$$

where  $\Pi^{[16]} = P_{\text{ls}}^{[4]} \otimes P_{\uparrow\downarrow}^{[4]} P_{12}$  with the  $P_{\text{ls}}^{[4]} = P_{\uparrow\downarrow}^{[4]} = ((1, 0, 0, 0), (0, 0, 1, 0), (0, 1, 0, 0), (0, 0, 0, 1))$  matrices and  $P_{12}$  is the coordinate exchange operator. Furthermore, it is necessary to ensure spatial symmetry relations between the large (l) and the small (s) components in a finite basis representation of the Dirac operator. To represent the  $(\boldsymbol{\sigma} \cdot \mathbf{p})(\boldsymbol{\sigma} \cdot \mathbf{p}) = p^2$  identity in the finite spinor basis, we use the simplest two-particle kinetic balance (KB) condition<sup>57,58</sup> of the large and small components,

$$\begin{pmatrix} \phi^{\text{ll}} \\ \phi^{\text{ls}} \\ \phi^{\text{sl}} \\ \phi^{\text{ss}} \end{pmatrix} = K_B^{[16]} \begin{pmatrix} \Theta \\ \Theta \\ \Theta \\ \Theta \end{pmatrix}$$

with

$$K_B^{[16]} = \begin{pmatrix} 1^{[4]} & 0^{[4]} & 0^{[4]} & 0^{[4]} \\ 0^{[4]} & \frac{\sigma_2^{[4]} \cdot \mathbf{p}_2}{2m_2c} & 0^{[4]} & 0^{[4]} \\ 0^{[4]} & 0^{[4]} & \frac{\sigma_1^{[4]} \cdot \mathbf{p}_1}{2m_1c} & 0^{[4]} \\ 0^{[4]} & 0^{[4]} & 0^{[4]} & \frac{\sigma_1^{[4]} \cdot \mathbf{p}_1 \sigma_2^{[4]} \cdot \mathbf{p}_2}{4m_1m_2c^2} \end{pmatrix} \quad (10)$$

that allows us to generate the  $\lambda_1\lambda_2 = (\text{ll}, \text{ls}, \text{sl}, \text{ss})$  blocks from the same four-dimensional  $\Theta$  vector in which each element contains

the same spatial function  $\vartheta$ ,  $\Theta^T = (\vartheta, \vartheta, \vartheta, \vartheta)$ . For the  $\vartheta$  spatial basis functions, we use floating explicitly correlated Gaussians (ECGs)

$$\vartheta_i = e^{-(r-s_i)^T (A_i \otimes \mathbb{1}^{[3]})(r-s_i)} \quad (11)$$

that allow for an efficient description of the particle (electron) correlation,<sup>59</sup> and  $A_i \in \mathbb{R}^{n \times n}$  (symmetric, positive definite) and  $s_i \in \mathbb{R}^{3n}$  are parameters optimized by the minimization of the energy. The ECG functions for non-diagonal exponent matrices automatically include fermion correlation, and their integrals for the most important operators can be written in a closed analytic form for a general  $n$  (unlike for Hylleraas-type basis functions), and non-zero shift vectors allow for efficient molecular applications (with symmetry projection). The current DC and DCB implementation is for two electrons (fermions), but we can foresee applications to three and four (maybe even five) particles with the current accuracy goal.

After considering the antisymmetrization and kinetic balance equations [Eqs. (9) and (10)], a  $16 \times 16$  dimensional block of the Hamiltonian and overlap matrices can be written as

$$\langle \Phi_i | O | \Phi_j \rangle = \langle \Theta_i | K_B^\dagger O K_B | \Theta_j \rangle - \langle \Theta_i | K_B^\dagger \Pi O K_B | \Theta_j \rangle, O = H \text{ or } I, \quad (12)$$

for which we have calculated the analytic matrix elements with ECGs, Eq. (11), and implemented the integral expressions in QUANTEN.<sup>60</sup> We obtain the ground state as the lowest-energy (real) eigenvalue of the generalized eigenvalue problem:  $Hc = ESc$  as an upper bound to the exact no-pair energy.

A good starting basis parameterization [Eq. (11)] for the systems studied in this work was obtained by the minimization of the non-relativistic energy to a ppb precision for the largest basis set sizes. For a non-relativistically optimized basis set, we can continue the optimization (minimization) for the no-pair DC energy, but the current implementation is very computation intensive. We intend to develop a more efficient DC optimization strategy in future work that will be important for achieving ppb convergence for high  $Z$  systems ( $Z \sim 100$ ). On the other hand, optimization of the DC energy may be necessary to further converge digits in the low  $Z$  range, but this would require a more efficient application of increased precision arithmetics. The numerical uncertainty of the values reported in this paper is determined by the double precision (8-byte reals) arithmetics used in the optimization procedure.

### III. NUMERICAL RESULTS AND DISCUSSION

In what follows, we report ground (and one example for excited) state energies obtained in the variational procedure implemented in the QUANTEN computer program and using the no-pair DC and DCB Hamiltonians. In all computations, we used the CODATA18 value for the inverse fine-structure constant  $\alpha^{-1} = 137.035999084$ .<sup>61</sup>

Figure 1 shows the excellent agreement of the atomic no-pair DC energies with  $Z = 1$ –26 nuclear charge numbers obtained in our implementation with benchmark literature data: basis set extrapolated multi-configuration Dirac–Fock (MCDF) energies computed by Parpia and Grant<sup>32</sup> and the DC energies of Bylicki, Pestka,

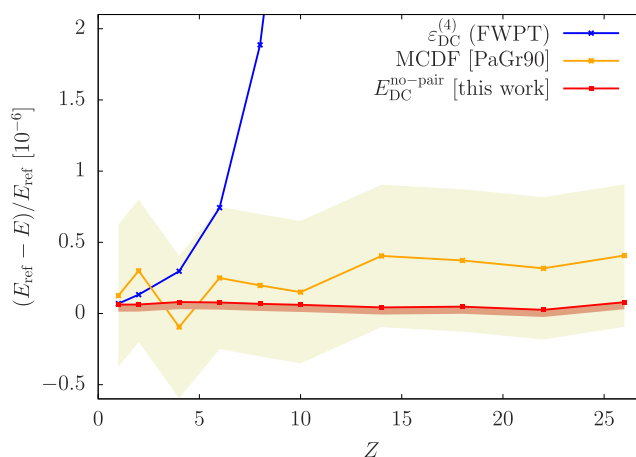


**FIG. 1.** Dirac–Coulomb energy of two-electron helium-like ions. Leading-order perturbative relativistic energy,  $\epsilon_{\text{DC}}^{(4)}$  (for  $Z = 1$ –4 Ref. 64, and for  $4 < Z \leq 26$  this work), extrapolated MCDF result<sup>32</sup> and the no-pair, variational  $E_{\text{DC}}$  energy obtained in the present work.  $E_{\text{ref}}$  is the no-pair variational DC energy in a large Hylleraas basis.<sup>38</sup>

and Karwowski obtained with a large Hylleraas basis set.<sup>38</sup> Using 300–400 ECGs, we observe an at least 8 digit agreement for  $Z = 1$ –26 with the work of Bylicki *et al.* The 30-year-old extrapolated DC results (corresponding to an implicit HF projection) of Parpia and Grant perform remarkably well over the entire range, but they have larger error bounds than Ref. 38 or our work. Foldy–Wouthusen perturbation theory (FWPT) shows a deviation from these results that grows rapidly with  $Z$ . Parpia and Grant also reported the perturbative correction due to the exact one-photon exchange to their MCDF wave function (with large error bounds). A comparison of their work with our no-pair DCB result and with the leading-order FWPT DCB energy,  $\epsilon_{\text{DCB}}^{(4)}$  (expectation value of the Breit–Pauli Hamiltonian), is provided in the [supplementary material](#).

Since no variational reference data (of similar precision) are available for molecular systems, we will compare our results with FWPT energies that are known to high precision. Table I summarizes the numerical results for the ground-state electronic energy of  $\text{H}_2$ ,  $\text{HeH}^+$ , and  $\text{H}_3^+$  with nuclei fixed close to the equilibrium structure (the convergence details are provided in the [supplementary material](#)). Due to the surprisingly large deviation of the leading-order FWPT energies [ $m\alpha^4$ ,  $\epsilon^{(4)}$ ] and our variational values, we have also considered higher-order FWPT energies within the nrQED framework [ $m\alpha^6$ ,  $\epsilon^{(6)}$ ]. Regarding the “poly-electronic” systems, the involved computation of  $\epsilon^{(6)}$  has been carried out so far only for the  $\text{H}_2$  molecule.<sup>16</sup> For a better comparison, we also include the results in the table for the ground and the first excited singlet states of the He atom, the other “poly-electronic” system for which  $\epsilon^{(6)}$  energies are available.<sup>13</sup>

Regarding the electronic ground state of the  $\text{H}_2$  and  $\text{H}_3^+$  hydrogenic compounds, our no-pair variational DC and DCB energy is lower than the leading-order FWPT energy by 21–25  $nE_h$  and 54–92  $nE_h$ , respectively. For the ground state of the  $\text{HeH}^+$  molecular ion and the He atom, our variational DC and DCB energies are

**TABLE I.** Dirac–Coulomb (DC) and Dirac–Coulomb–Breit (DCB) electronic energy, in  $E_h$ , obtained in the present no-pair variational framework.  $\delta^{(4)}$  and  $\delta^{(6)}$  are the difference, in  $nE_h$ , of the no-pair variational energy and the leading and higher-order Foldy–Wouthusen perturbation theory result (compiled from Refs. 13, 16, 62, and 63 or computed in this work), respectively. The nuclei are fixed near their equilibrium position at 1.4, 1.46, and 1.65 bohrs in  $H_2$ ,  $HeH^+$ , and in the equilateral triangular  $H_3^+$ , respectively.

	$E_{DC}$	$\delta_{DC}^{(4)}$	$E_{DCB}$	$\delta_{DCB}^{(4)}$	$\delta_{DCB}^{(6)}$
$H_2$	−1.174 489 754	{−21}	−1.174 486 721(20)	{−54}	{−52}
$He(1^1S)$	−2.903 856 631	{−146}	−2.903 829 024(100)	{−713}	{−660}
$He(2^1S)$	−2.146 084 791(3)	{−22}	−2.146 082 424(3)	{−56}	{−10}
$HeH^+$	−2.978 834 635	{−142}	−2.978 808 818(40)	{−638}	
$H_3^+$	−1.343 850 527(1)	{−25}	−1.343 847 498(10)	{−92}	

lower by 142–146 and 638–713  $nE_h$  than the leading-order FWPT energy. It is interesting to note that these deviations are one to two orders of magnitude larger than the deviation of the exact and perturbative relativistic energy of the ground state, one-electron atomic hydrogen (0.18  $nE_h$ ) and hydrogen-like helium (11  $nE_h$ ).<sup>12</sup>

Higher-order [ $m\alpha^6$ ,  $e^{(6)}$ ] FWPT results can be interpreted within the nrQED framework.<sup>13,16</sup> In the  $m\alpha^6$  expressions of nrQED, it is possible to identify the higher (second) order FWPT correction corresponding to the DCB Hamiltonian. It turns out that this correction contains divergent terms (due to the internal mathematical structure of the nrQED expansion). These divergent terms are canceled with other divergent terms in the one- and two-photon exchange (also approximated at the  $m\alpha^6$  level and expanded with respect to the non-relativistic reference state) in Refs. 13 and 16. Therefore, in the present comparison, we include the higher-order FWPT corrections for the DCB operator after the divergences are canceled within the nrQED expansion. The resulting  $e^{(6)}$  energies are a little bit closer to the variational DCB result than the  $e^{(4)}$  values, but the observed deviation remains large, −52 and −660  $nE_h$  for the ground state of  $H_2$  and  $He$ , respectively. It is interesting to note that for the excited  $1s2s(2^1S)$  state of the helium atom, the agreement of the variational and FWPT energies is much better, and it significantly improves upon inclusion of higher-order PT corrections, and the −56  $nE_h$  deviation of  $e^{(4)}$  reduces to −10  $nE_h$  for  $e^{(6)}$ .

All deviations are smaller than the one-loop self-energy (and vacuum polarization) corrections known from nrQED,<sup>13,16,62,63</sup> so both routes have the potential to provide a useful, quantitative description of experimental observations. We have seen one indication that the differences appear to depend not only on the  $Z$  nuclear charge number but also on the electronic excitation in the system. This connection is not so surprising, after all. From the no-pair variational aspect, it is enough to remember that the generalization of Dirac’s one-electron theory to poly-electron systems is challenging exactly because of the electron–electron interactions.

#### IV. SUMMARY, CONCLUSIONS, AND OUTLOOK

In summary, we have reported the development of an explicitly correlated variational procedure for the no-pair Dirac–Coulomb–Breit Hamiltonian. This procedure was used for atoms and molecules with clamped nuclei, currently with two

but straightforwardly extendable for more than two electrons, using explicitly correlated Gaussian functions and ultimately aiming at a parts-per-billion convergence of the energy. The procedure excellently reproduces literature data for two-electron atoms (ions) and the Dirac–Coulomb model. Larger differences are already observed with respect to Foldy–Wouthusen perturbation theory (FWPT, within the nrQED framework) for atoms and molecules with low  $Z$  values. Our variational DCB energies for the ground state of the  $H_2$ ,  $H_3^+$ , and  $HeH^+$  molecules and the  $He$  atom are lower by 54–92  $nE_h$  (for  $Z = 1$ ) and by 638  $nE_h$  (for  $Z = 2$ ) than the FWPT energies. These deviations are one to two orders of magnitude larger than the difference of the exact Dirac energy and the leading-order perturbation theory result for the one-electron hydrogen-like atoms (0.2 and 11  $nE_h$  for  $Z = 1$  and 2, respectively). Higher-order ( $m\alpha^6$ ) corrections to the FWPT (nrQED) energies, currently available for the  $H_2$  molecule and the  $He$  atom, reduce the deviation a little bit but do not change the order of magnitude of the difference. The only exception in our test set is the excited  $1s2s^1S$  state of the helium atom, for which the difference of the two approaches reduces to “only” 10  $nE_h$  when the higher-order corrections are also included in the FWPT energy (within the nrQED expansion).

At the same time, it is important to note that all listed deviations between the variational and FWPT energies are larger than the electron self-energy predicted within the nrQED approach; hence, our next priority is the calculation of this quantity for the present no-pair Dirac framework. Furthermore, the effect of electron–positron pair creation (vacuum polarization) will be also accounted for. We are working on the inclusion of the exact one-photon exchange to have an improved description of the electron–electron interaction beyond the zero-frequency approximation (Coulomb–Breit).

We think that the developed all-order, variational relativistic approach offers a broad perspective for further developments, and we consider a possible inclusion of two- and multi-photon processes (including absorption and emission), either perturbatively or by an explicit account of the photon field in interaction with the fermionic degrees of freedom.

#### SUPPLEMENTARY MATERIAL

See the [supplementary material](#) for the computed atomic DC and DCB energies and convergence information on the data reported in [Table I](#).



## ACKNOWLEDGMENTS

We wish to dedicate this paper to Markus Reiher, who has long promoted this direction of research, on the occasion of his fiftieth birthday.

Financial support of the European Research Council through a Starting Grant (Grant No. 851421) is gratefully acknowledged.

## DATA AVAILABILITY

The data that support the findings of this study are available within the article and its [supplementary material](#).

## REFERENCES

- <sup>1</sup>A. Matveev, C. G. Parthey, K. Predehl, J. Alnis, A. Beyer, R. Holzwarth, T. Udem, T. Wilken, N. Kolachevsky, M. Abgrall, D. Rovera, C. Salomon, P. Laurent, G. Grosche, O. Terra, T. Legero, H. Schnatz, S. Weyers, B. Altschul, and T. W. Hänsch, "Precision measurement of the hydrogen 1S–2S frequency via a 920-km fiber link," *Phys. Rev. Lett.* **110**, 230801 (2013).
- <sup>2</sup>A. Beyer, L. Maisenbacher, A. Matveev, R. Pohl, K. Khabarova, A. Grinin, T. Lamour, D. C. Yost, T. W. Hänsch, N. Kolachevsky, and T. Udem, "The Rydberg constant and proton size from atomic hydrogen," *Science* **358**(6359), 79 (2017).
- <sup>3</sup>L. Gurung, T. J. Babij, S. D. Hogan, and D. B. Cassidy, "Precision microwave spectroscopy of the positronium  $n = 2$  fine structure," *Phys. Rev. Lett.* **125**, 073002 (2020).
- <sup>4</sup>S. Alighanbari, M. G. Hansen, V. I. Korobov, and S. Schiller, "Rotational spectroscopy of cold and trapped molecular ions in the Lamb–Dicke regime," *Nat. Phys.* **14**, 555 (2018).
- <sup>5</sup>N. Hölsch, M. Beyer, E. J. Salumbides, K. S. E. Eikema, W. Ubachs, C. Jungen, and F. Merkt, "Benchmarking theory with an improved measurement of the ionization and dissociation energies of  $H_2$ ," *Phys. Rev. Lett.* **122**, 103002 (2019).
- <sup>6</sup>M. S. Safronova, D. Budker, D. DeMille, D. Kimball, A. Derevianko, and C. W. Clark, "Search for new physics with atoms and molecules," *Rev. Mod. Phys.* **90**, 025008 (2018).
- <sup>7</sup>M. Kaku, *Quantum Field Theory: A Modern Introduction* (Oxford University Press, New York, NY, 1993).
- <sup>8</sup>V. I. Korobov, "Ro-vibrational states of  $H_2^+$ . Variational calculations," *Mol. Phys.* **116**, 93 (2018).
- <sup>9</sup>K. Pachucki and J. Komasa, "Nonadiabatic rotational states of the hydrogen molecule," *Phys. Chem. Chem. Phys.* **20**, 247 (2018).
- <sup>10</sup>H. A. Bethe and E. E. Salpeter, *Quantum Mechanics of One- and Two-Electron Atoms* (Springer, Berlin, 1957).
- <sup>11</sup>G. P. Lepage, "Two-body bound states in quantum electrodynamics," Ph.D. dissertation; Report No. SLAC-212 UC-34d (SLAC, Stanford University, Stanford, CA, 1978).
- <sup>12</sup>M. I. Eides, H. Grotch, and V. A. Shelyuto, "Theory of light hydrogenlike atoms," *Phys. Rep.* **342**, 63 (2001).
- <sup>13</sup>K. Pachucki, " $\alpha^4\mathcal{R}$  corrections to singlet states of helium," *Phys. Rev. A* **74**, 022512 (2006).
- <sup>14</sup>M. Haidar, Z.-X. Zhong, V. I. Korobov, and J.-P. Karr, "Nonrelativistic QED approach to the fine- and hyperfine-structure corrections of order  $m\alpha^6$  and  $m\alpha^6(m/M)$ : Application to the hydrogen atom," *Phys. Rev. A* **101**, 022501 (2020).
- <sup>15</sup>V. I. Korobov, L. Hilico, and J.-P. Karr, "Calculation of the relativistic Bethe logarithm in the two-center problem," *Phys. Rev. A* **87**, 062506 (2013).
- <sup>16</sup>M. Puchalski, J. Komasa, P. Czachorowski, and K. Pachucki, "Complete  $\alpha^6m$  corrections to the ground state of  $H_2$ ," *Phys. Rev. Lett.* **117**, 263002 (2016).
- <sup>17</sup>H. A. Bethe and E. E. Salpeter, "A relativistic equation for bound-state problems," *Phys. Rev.* **84**, 1232 (1951).
- <sup>18</sup>Y. Nambu, "Force potentials in quantum field theory," *Prog. Theor. Phys.* **5**, 614 (1950).
- <sup>19</sup>A. Jakóvác and A. Patkós, "Bound-state spectra of field theories through separation of external and internal dynamics," in *Gribov-90 Memorial Volume*, edited by Yu L. Dokshitzer, P. Lévai, Á. Lukács, and J. Nyíri (World Scientific, 2021), pp. 359–366.
- <sup>20</sup>M. Gell-Mann and F. Low, "Bound states in quantum field theory," *Phys. Rev.* **84**, 350 (1951).
- <sup>21</sup>J. Sucher, "S-matrix formalism for level-shift calculations," *Phys. Rev.* **107**, 1448 (1957).
- <sup>22</sup>P. J. Mohr, "Quantum electrodynamics perturbation theory," *AIP Conf. Proc.* **189**, 47 (1989).
- <sup>23</sup>K. G. Dyall and K. Faegri, Jr., *Introduction to Relativistic Quantum Chemistry* (Oxford University Press, New York, 2007).
- <sup>24</sup>M. Reiher and A. Wolf, *Relativistic Quantum Chemistry: The Fundamental Theory of Molecular Science*, 2nd ed. (Wiley-VCH, Weinheim, 2015).
- <sup>25</sup>J. Sucher, "Foundations of the relativistic theory of many-electron atoms," *Phys. Rev. A* **22**, 348 (1980).
- <sup>26</sup>J. Sucher, *Foundations of the Relativistic Theory of Many-Electron Systems* (Springer, Boston, MA, 1983), pp. 1–53.
- <sup>27</sup>G. Hardekopf and J. Sucher, "Relativistic wave equations in momentum space," *Phys. Rev. A* **30**, 703 (1984).
- <sup>28</sup>J. Sucher, "Foundations of the relativistic theory of many-electron bound states," *Int. J. Quantum Chem.* **25**, 3 (1984).
- <sup>29</sup>W. H. Furry, "On bound states and scattering in positron theory," *Phys. Rev. A* **81**, 115 (1951).
- <sup>30</sup>G. Hoever and H. Siedentop, "Stability of the Brown–Ravenhall operator," *Math. Phys. Electron. J.* **5**, 76 (2002).
- <sup>31</sup>K. G. Dyall, I. P. Grant, C. T. Johnson, F. A. Parpia, and E. P. Plummer, "GRASP: A general-purpose relativistic atomic structure program," *Comput. Phys. Commun.* **55**, 425 (1989).
- <sup>32</sup>F. A. Parpia and I. P. Grant, "Accurate Dirac–Coulomb energies for the ground states of helium-like atoms," *J. Phys. B: At., Mol. Opt. Phys.* **23**, 211 (1990).
- <sup>33</sup>F. A. Parpia, C. F. Fischer, and I. P. Grant, "GRASP92: A package for large-scale relativistic atomic structure calculations," *Comput. Phys. Commun.* **94**, 249 (1996).
- <sup>34</sup>A. N. Artemyev, V. M. Shabaev, V. A. Yerokhin, G. Plunien, and G. Soff, "QED calculation of the  $n = 1$  and  $n = 2$  energy levels in He-like ions," *Phys. Rev. A* **71**, 062104 (2005).
- <sup>35</sup>V. M. Shabaev, I. I. Tupitsyn, and V. A. Yerokhin, "Model operator approach to the Lamb shift calculations in relativistic many-electron atoms," *Phys. Rev. A* **88**, 012513 (2013).
- <sup>36</sup>V. M. Shabaev, I. I. Tupitsyn, M. Y. Kaygorodov, Y. S. Kozhedub, A. V. Malyshev, and D. V. Mironova, "QED corrections to the  $^2P_{1/2}$ – $^2P_{3/2}$  fine structure in fluorinelike ions: Model Lamb-shift-operator approach," *Phys. Rev. A* **101**, 052502 (2020).
- <sup>37</sup>V. A. Zaytsev, I. A. Maltsev, I. I. Tupitsyn, and V. M. Shabaev, "Complex-scaled relativistic configuration-interaction study of the  $LL$  resonances in heliumlike ions: From boron to argon," *Phys. Rev. A* **100**, 052504 (2019).
- <sup>38</sup>M. Bylicki, G. Pestka, and J. Karwowski, "Relativistic Hylleraas configuration-interaction method projected into positive-energy space," *Phys. Rev. A* **77**, 044501 (2008).
- <sup>39</sup>H. M. Quiney, H. Skaane, and I. P. Grant, "Ab initio relativistic quantum chemistry: Four-components good, two-components bad!," *Adv. Quantum Chem.* **32**, 1 (1998).
- <sup>40</sup>L. Belpassi, M. De Santis, H. M. Quiney, F. Tarantelli, and L. Storchi, "BERTHA: Implementation of a four-component Dirac–Kohn–Sham relativistic framework," *J. Chem. Phys.* **152**, 164118 (2020).
- <sup>41</sup>T. Saue, R. Bast, A. S. P. Gomes, H. J. A. Jensen, L. Visscher, I. A. Aucar, R. Di Remigio, K. G. Dyall, E. Eliav, E. Fasshauer, T. Fleig, L. Halbert, E. D. Hedegård, B. Helmich-Paris, M. Iliaš, C. R. Jacob, S. Knecht, J. K. Laerdahl, M. L. Vidal, M. K. Nayak, M. Olejniczak, J. M. H. Olsen, M. Pernpointner, B. Senjean, A. Shee, A. Sunaga, and J. N. P. van Stralen, "The DIRAC code for relativistic molecular calculations," *J. Chem. Phys.* **152**, 204104 (2020).

- <sup>42</sup>M. H. Mittleman, "Theory of relativistic effects on atoms: Configuration-space Hamiltonian," *Phys. Rev. A* **24**, 1167 (1981).
- <sup>43</sup>J.-L. Heully, I. Lindgren, E. Lindroth, and A.-M. Mrtensson-Pendrill, "Comment on relativistic wave equations and negative-energy states," *Phys. Rev. A* **33**, 4426 (1986).
- <sup>44</sup>A. Almoukhalati, S. Knecht, H. J. A. Jensen, K. G. Dyall, and T. Saue, "Electron correlation within the relativistic no-pair approximation," *J. Chem. Phys.* **145**, 074104 (2016).
- <sup>45</sup>E. Mátyus and M. Reiher, "Molecular structure calculations: A unified quantum mechanical description of electrons and nuclei using explicitly correlated Gaussian functions and the global vector representation," *J. Chem. Phys.* **137**, 024104 (2012).
- <sup>46</sup>E. Mátyus, "On the calculation of resonances in pre-Born–Oppenheimer molecular structure theory," *J. Phys. Chem. A* **117**, 7195 (2013).
- <sup>47</sup>D. Ferenc and E. Mátyus, "Computation of rovibronic resonances of molecular hydrogen:  $EF\ ^1\Sigma_g^+$  inner-well rotational states," *Phys. Rev. A* **100**, 020501(R) (2019).
- <sup>48</sup>E. Mátyus, "Pre-Born–Oppenheimer molecular structure theory," *Mol. Phys.* **117**, 590 (2019).
- <sup>49</sup>G. E. Brown and D. G. Ravenhall, "On the interaction of two electrons," *Proc. R. Soc. London, Ser. A* **208**, 552 (1951).
- <sup>50</sup>G. Pestka, M. Bylicki, and J. Karwowski, "Complex coordinate rotation and relativistic Hylleraas-CI: Helium isoelectronic series," *J. Phys. B: At., Mol. Opt. Phys.* **40**, 2249 (2007).
- <sup>51</sup>J. Karwowski, *Dirac Operator and its Properties* (Springer, Berlin, Heidelberg, 2017), pp. 3–49.
- <sup>52</sup>N. Moiseyev and C. Corcoran, "Autoionizing states of  $H_2$  and  $H_2^-$  using the complex-scaling method," *Phys. Rev. A* **20**, 814 (1979).
- <sup>53</sup>C. W. McCurdy, "Complex-coordinate calculation of matrix elements of the resolvent of the Born–Oppenheimer Hamiltonian," *Phys. Rev. A* **21**, 464 (1980).
- <sup>54</sup>N. Moiseyev, *Non-Hermitian Quantum Mechanics* (Cambridge University Press, Cambridge, 2011).
- <sup>55</sup>D. S. Tracy and R. P. Singh, "A new matrix product and its applications in matrix differentiation," *Stat. Neerl.* **26**, 143 (1972).
- <sup>56</sup>Z. Li, S. Shao, and W. Liu, "Relativistic explicit correlation: Coalescence conditions and practical suggestions," *J. Chem. Phys.* **136**, 144117 (2012).
- <sup>57</sup>B. Simmen, E. Mátyus, and M. Reiher, "Relativistic kinetic-balance condition for explicitly correlated basis functions," *J. Phys. B: At., Mol. Opt. Phys.* **48**, 245004 (2015).
- <sup>58</sup>W. Kutzelnigg, "Basis set expansion of the Dirac operator without variational collapse," *Int. J. Quantum Chem.* **25**, 107 (1984).
- <sup>59</sup>J. Mitroy, S. Bubin, W. Horiuchi, Y. Suzuki, L. Adamowicz, W. Cencek, K. Szalewicz, J. Komasa, D. Blume, and K. Varga, "Theory and application of explicitly correlated Gaussians," *Rev. Mod. Phys.* **85**, 693 (2013).
- <sup>60</sup>QUANTEN, a computer program for the quantum mechanical description of electrons and nuclei, written by D. Ferenc, P. Jeszenszki, I. Hornyák, R. Ireland, and E. Mátyus, see also [www.compchem.hu](http://www.compchem.hu).
- <sup>61</sup>CODATA 2018 recommended values of the fundamental constants at <https://physics.nist.gov/cuu/Constants/index.html>; accessed February 26, 2021.
- <sup>62</sup>G. W. F. Drake, "High precision variational calculations for the  $1s^2\ ^1S$  state of  $H^-$  and  $1s2s\ ^1S$  and  $1s2s\ ^3S$  states of helium," *Nucl. Instrum. Methods Phys. Res., Sect. B* **31**, 7 (1988).
- <sup>63</sup>M. Puchalski, J. Komasa, and K. Pachucki, "Relativistic corrections for the ground electronic state of molecular hydrogen," *Phys. Rev. A* **95**, 052506 (2017).
- <sup>64</sup>G. Drake, *High Precision Calculations for Helium* (Springer, New York, NY, 2006), pp. 199–219.

## Nonadiabatic, Relativistic, and Leading-Order QED Corrections for Rovibrational Intervals of ${}^4\text{He}_2^+$ ( $X^2\Sigma_u^+$ )

Dávid Ferenc<sup>1</sup>, Vladimir I. Korobov<sup>2,\*</sup> and Edit Mátyus<sup>1,†</sup>

<sup>1</sup>*Institute of Chemistry, ELTE, Eötvös Loránd University, Pázmány Péter sétány 1/A, Budapest H-1117, Hungary*

<sup>2</sup>*Bogoliubov Laboratory of Theoretical Physics, Joint Institute for Nuclear Research, Dubna 141980, Russia*



(Received 18 July 2020; accepted 23 September 2020; published 16 November 2020)

The rovibrational intervals of the  ${}^4\text{He}_2^+$  molecular ion in its  $X^2\Sigma_u^+$  ground electronic state are computed by including the nonadiabatic, relativistic, and leading-order quantum-electrodynamics corrections. Good agreement of theory and experiment is observed for the rotational excitation series of the vibrational ground state and the fundamental vibration. The lowest-energy rotational interval is computed to be  $70.93769(10)\text{ cm}^{-1}$  in agreement with the most recently reported experimental value,  $70.937589(23)(60)_{\text{sys}}\text{ cm}^{-1}$  [L. Semeria *et al.*, *Phys. Rev. Lett.* **124**, 213001 (2020)].

DOI: 10.1103/PhysRevLett.125.213001

Few-electron molecules serve as benchmark systems for experimental and theoretical molecular physics and spectroscopy. Recent experimental and theoretical progress of  $\text{H}_2^+$ ,  $\text{H}_2$ , and their isotopologues [1–3] is connected to proposals to test fundamental interactions [4,5] and to refine fundamental physical constants [6,7] using molecular spectroscopy.

This Letter joins this direction and focuses on the five-particle  ${}^4\text{He}_2^+$  molecular ion in its ground electronic state ( $X^2\Sigma_u^+$ ). In addition to testing fundamental aspects, precision spectroscopy of  ${}^4\text{He}_2^+$  in combination with accurate *ab initio* computations has been proposed as an alternative way to determine the polarizability of the helium atom [8,9]. Precise knowledge of this quantity is necessary for a possible new definition of the pressure standard based on counting the number density of a sample of helium gas. There has been experimental progress in the precision spectroscopy of  ${}^4\text{He}_2^+$ , including the measurement of the spin-rotational fine structure [10] and the rotational and rovibrational intervals [9,11–13].

This Letter is concerned with the rotational and rovibrational intervals for which disagreement was observed between the experimental results [9,11–13] and (lower-level) theoretical work [14,15]. The experimental “dataset” includes the rotational intervals for the vibrational ground state  $(0, N^+) - (0, 1)(N^+ = 3, \dots, 19)$  [12] and the rovibrational intervals connecting the ground and the first excited vibrational state  $(1, N^+) - (0, 1)(N^+ = 1, \dots, 13)$  [13] with experimental uncertainties of 0.0008 and  $0.0012\text{ cm}^{-1}$ , respectively. The lowest-energy rotational interval is known more precisely to be  $70.937589(23) \pm 0.000060_{\text{sys}}\text{ cm}^{-1}$  [9].

The most precise theoretical results for molecules can be obtained by including all electrons and nuclei in the nonrelativistic quantum mechanical treatment [2,16–20].

All bound rovibrational and several resonance states of  $\text{H}_2^+$  treated as a three-particle system have been converged with an uncertainty in their nonrelativistic energy better than  $10^{-7}\text{ cm}^{-1}$  [17], and a similar precision has been achieved for selected states of  $\text{H}_2$  treated as a four-particle system [21]. The fundamental vibration energy has been computed for  ${}^3\text{He}^4\text{He}^+$  treated as a five-particle system [22], but the convergence error of this energy appears to be at least 2 orders of magnitude larger than the uncertainty of the currently available experimental value of the parent isotopologue.

To ensure a direct comparison with the experimental dataset, which includes high rotational angular momentum quantum numbers up to  $N^+ = 19$  and a tight control of the numerical (convergence) error, we start out from the Born–Oppenheimer approximation and account for nonadiabatic corrections by perturbation theory [23–27]. The experimental dataset belongs to the ground ( $X^2\Sigma_u^+$ ) electronic state that is well-separated from the electronically excited states over the relevant nuclear configuration range, hence we may expect nonadiabatic perturbation theory to perform well.

There is some evidence of the increasing importance of the nonadiabatic effects with a rotational excitation of  ${}^4\text{He}_2^+$  [12,15], but the nonadiabatic nonrelativistic computation of Ref. [15] was only partially able to account for the discrepancy between theory and experiment for the rotational series. Furthermore, the nonadiabatic corrections (without relativistic and QED effects) increased the deviation of theory and experiment for the fundamental vibration energy [13,15] in comparison to the adiabatic result [14].

This Letter reports a more complete theoretical treatment for the rotational-vibrational intervals of  ${}^4\text{He}_2^+$  ( $X^2\Sigma_u^+$ ), and we account for the nonadiabatic, relativistic and leading-order QED corrections. The error balance of the

computational procedure is analyzed and further contributions, neglected in this Letter, are discussed.

First, we solved the electronic Schrödinger equation for  $n = 3$  electrons and  $N = 2$  fixed nuclei for the  $\phi_0$  ground electronic state (in Hartree atomic units)

$$H_{\text{el}}\phi_0(\mathbf{r}, \mathbf{R}) = E_{\text{el},0}(\mathbf{R})\phi_0(\mathbf{r}, \mathbf{R}) \quad \text{with}$$

$$H_{\text{el}} = -\sum_{i=1}^n \frac{1}{2m_e} \Delta_{\mathbf{r}_i} + \sum_{i=1}^n \sum_{j>i}^n \frac{1}{|\mathbf{r}_i - \mathbf{r}_j|} - \sum_{i=1}^n \sum_{j=1}^N \frac{Z_j}{|\mathbf{r}_i - \mathbf{R}_j|} \quad (1)$$

using floating explicitly correlated Gaussian basis functions and the QUANTEN computer program [19,27].

The rovibrational Hamiltonian corresponding to the ground electronic (“0”th) state and accounting for non-adiabatic coupling up to the second-order terms in  $\varepsilon = (m_e/m_{\text{nuc}})^{(1/2)}$  is [23–27]

$$H_0^{(2)} = \sum_{i,j=1}^{3N} \frac{1}{2} (-i\varepsilon \partial_{R_i}) (\delta_{ij} - \varepsilon^2 M_{ij}) (-i\varepsilon \partial_{R_i}) + E_{\text{el},0} + \varepsilon^2 U_0, \quad (2)$$

where

$$U = \frac{1}{2} \sum_{i=1}^{3N} \langle \partial_{R_i} \phi_0 | \partial_{R_i} \phi_0 \rangle \quad (3)$$

and

$$M_{ij} = 2 \langle \partial_{R_j} \phi_0 | P_0^\perp (\hat{H}_e - E_{\text{el},0})^{-1} P_0^\perp | \partial_{R_i} \phi_0 \rangle, \quad (4)$$

$$P_0^\perp = 1 - |\phi_0\rangle \langle \phi_0|$$

are the diagonal Born–Oppenheimer correction (DBOC) and the mass-correction tensor, respectively.

Rotational-vibrational states of  $\text{He}_2^+$  are computed using this Hamiltonian written in spherical polar coordinates,  $(\rho, \theta, \phi)$ , which leads to the solution of the radial equation [15,27]

$$\left( -\frac{\partial}{\partial \rho} \frac{1}{m_{\text{nuc}}} \left[ 1 - \frac{\mathcal{M}_\rho^\rho}{m_{\text{nuc}}} \right] \frac{\partial}{\partial \rho} + \frac{N^+(N^++1)}{\rho^2} \frac{1}{m_{\text{nuc}}} \left[ 1 - \frac{\mathcal{M}_\Omega^\Omega}{m_{\text{nuc}}} \right] + U(\rho) + E_{\text{el}}(\rho) \right) \chi_{N^+}(\rho) = E_{N^+} \chi_{N^+}(\rho). \quad (5)$$

$\mathcal{M}_\rho^\rho$  and  $\mathcal{M}_\Omega^\Omega$  are the vibrational and rotational mass-correction functions corresponding to the curvilinear representation [27]. The equation is solved for each  $N^+$

rotational angular momentum quantum number using a discrete variable representation [28].

We have computed the  $E_{\text{el}}(\rho)$  potential energy curve over the  $\rho \in [0.992, 3.5]$  bohr interval of the internuclear separation that is necessary to converge the rovibrational states considered in this Letter. As a result, the electronic energy at the equilibrium structure ( $\rho_{\text{eq}} = 2.042$  bohr) is within the  $0.2 \mu\text{E}_h$  error bar of the complete basis set limit estimate by Cencek *et al.* [29]. The newly computed part of the potential energy curve (PEC) improves the earlier PEC [14] by  $0.012 \text{ cm}^{-1}$  ( $59 \text{ nE}_h$ ) at the equilibrium structure and by  $0.034 \text{ cm}^{-1}$  ( $155 \text{ nE}_h$ ) at  $\rho = 3.5$  bohr.

Table I collects the calculated change in the energy intervals using the newly computed and the earlier curves. As a (conservative) estimate for the remaining error due to uncertainties of the PEC, we used the half of the observed change. We think that the uncertainty of the rovibrational intervals due to the uncertainty of the PEC is within a few  $\text{nE}_h$ .

The relativistic effects on the electronic motion are accounted for by incrementing the  $E_{\text{el}} + U$  adiabatic potential energy curve with the expectation value of the spin-independent part of the Breit–Pauli Hamiltonian, including the mass-velocity term, the Darwin terms, and the spin-spin coupling, as well as the orbit-orbit term [34]:

$$E_{\text{rel}}^{(2)} = \alpha^2 \langle \phi_0 | H_{\text{rel}}^{(2)} | \phi_0 \rangle, \quad (6)$$

where

$$H_{\text{rel}}^{(2)} = -\frac{1}{8} \sum_{i=1}^n \mathbf{p}_i^4 + \frac{\pi}{2} \sum_{i=1}^n \sum_{a=1}^N Z_a \delta(\mathbf{r}_{ia}) + \pi \sum_{i=1}^n \sum_{j>i}^n \delta(\mathbf{r}_{ij}) - \frac{1}{2} \sum_{i=1}^n \sum_{j>i}^n \left[ \frac{1}{r_{ij}} \mathbf{p}_i \cdot \mathbf{p}_j + \frac{1}{r_{ij}^3} \mathbf{r}_{ij} (\mathbf{r}_{ij} \cdot \mathbf{p}_i) \cdot \mathbf{p}_j \right]. \quad (7)$$

In order to assess the uncertainty of the computations (Table I), we evaluated the expectation values “directly” for the  $\mathbf{p}_i^4$  and  $\pi \delta(\mathbf{r}_{ix}) = \frac{1}{4} \nabla_{\mathbf{r}_{ix}}^2 (1/r_{ix})$  ( $x = j$  or  $a$ ) operators [31] and by using the integral-transformation technique [30]. Since we have accurate electronic wave functions, we expect that the two routes give very similar rovibrational intervals. Still, the results obtained with the integral-transformation techniques are expected to have a lower uncertainty.

The spin-independent  $\alpha^3$ -order QED correction to the adiabatic potential energy of a diatomic molecule is [34–36]

$$E_{\text{rad}}^{(3)} = \alpha^3 \frac{4}{3} \sum_{i=1}^n \left( \ln \frac{1}{\alpha^2} - \beta_{\text{el}} + \frac{19}{30} \right) \langle \phi_0 | Z \delta(\mathbf{r}_{i1}) + Z \delta(\mathbf{r}_{i2}) | \phi_0 \rangle + \alpha^3 \sum_{i=1}^n \sum_{j>i}^n \left[ \left( \frac{14}{3} \ln \alpha + \frac{164}{15} \right) \langle \phi_0 | \delta(\mathbf{r}_{ij}) | \phi_0 \rangle - \frac{14}{3} Q_{\text{el}} \right], \quad (8)$$

TABLE I. Error balance of the rotational and (ro)vibrational intervals, in  $\text{cm}^{-1}$ , computed in this Letter. The numerical uncertainty of the computed intervals is estimated based on the difference in the intervals obtained with two different datasets.

	Rotational intervals		(Ro)vibrational intervals	
	(0,3)–(0,1)	RMSD <sub>rot</sub>	(1,0)–(0,0)	RMSD <sub>rv</sub>
<i>Numerical uncertainty estimate for the computed terms (<math>\pm\sigma</math>):</i>				
PEC <sup>a</sup>	–0.000 002	0.000 15	–0.003 28*	0.003 37*
DBOC <sup>a</sup>	–0.000 010	0.000 18	–0.000 16	0.000 19
Nadm <sup>b</sup>	–0.000 018	0.000 36	–0.000 13	0.000 24
Relativistic <sup>c</sup>	–0.000 012	0.000 18	0.001 09	0.000 84
$\beta_{\text{el}} (\pm 1\%)^{\text{d}}$	–0.000 032	0.000 22	0.000 12	0.000 63
$\pm\sigma^{\text{e}}$	$\pm 0.000 073$	$\pm 0.001 09$	$\pm 0.003 14$	$\pm 0.003 59$
<i>Estimate for neglected theoretical terms (<math>\Delta_{\text{est}}</math>):</i>				
hQED <sup>f</sup>	–0.000 008	–0.000 15	–0.000 13	–0.000 25
Nad&Rel <sup>g</sup>	–0.000 001	–0.000 02	–0.000 01	–0.000 03
Fsn <sup>h</sup>	–0.000 001	–0.000 02	–0.000 02	–0.000 04
$\Delta_{\text{est}}$	–0.000 010	–0.000 19	–0.000 16	–0.000 31

<sup>a</sup>PEC (DBOC) curve from Ref. [14] and from this Letter.

<sup>b</sup>Nonadiabatic mass computed in Ref. [15] and in this Letter.

<sup>c</sup>Relativistic corrections obtained with the integral transformation technique [30] and the “direct” method [31].

<sup>d</sup>Effect of a hypothetical  $\pm 1\%$  change in  $\beta_{\text{el}}$ .

<sup>e</sup> $\sigma$  is obtained as the sum of the absolute value of the terms.

<sup>f</sup>The effect of the neglected higher-order QED corrections is estimated with the dominant term of  $E^{(4)}$ , Eq. (11).

<sup>g</sup>Estimate for the coupling of the nonadiabatic and relativistic corrections (see also Ref. [32]).

<sup>h</sup>Estimate for the effect of the finite nuclear size [33].

\*We use half of this value for the uncertainty estimate of the present results.

where

$$\beta_{\text{el}} = \frac{\langle \phi_0 | \mathbf{J} (H_0 - E_0) \ln(2(H_0 - E_0)/E_h) \mathbf{J} \phi_0 \rangle}{\langle \phi_0 | [\mathbf{J}, [H_0, \mathbf{J}]] / 2 \phi_0 \rangle} \quad (9)$$

is the (nonrelativistic) Bethe logarithm,  $\mathbf{J} = -\sum_{i=1}^n \mathbf{p}_i$  is the electric current density. A precise evaluation of  $\beta_{\text{el}}$  is a major numerical task, and values can be obtained if the wave function satisfies the electron-nucleus cusp condition [37,38]. The  $Q_{\text{el}}$  term [39,40],

$$Q_{\text{el}} = \lim_{\epsilon \rightarrow 0} \langle \phi_0 | \left[ \frac{\Theta(r_{ij} - \epsilon)}{4\pi r_{ij}^3} + (\ln \epsilon + \gamma_E) \delta(\mathbf{r}_{ij}) \right] \phi_0 \rangle, \quad (10)$$

has been evaluated for  $\text{He}_2^+$  using the integral transformation technique [30] and the floating explicitly correlated Gaussian basis representation.

Concerning the Bethe logarithm, we start with a few numerical observations. Table II presents a compilation of the Bethe logarithm values for the lightest atoms and ions [41–45] to highlight the weak dependence of  $\beta_{\text{el}}$  on the number of electrons but its strong dependence on the nuclear charge  $Z$ . A similar observation applies for molecules described within the adiabatic approximation. Table III shows the value of  $\beta_{\text{el}}(\rho)$  in the ground electronic state of the one-electron  $\text{H}_2^+$  molecular ion and the two-electron  $\text{H}_2$  molecule for selected values of the  $\rho$  internuclear distance. The  $\beta_{\text{el}}(\rho)$  values of  $\text{H}_2^+$  and  $\text{H}_2$  differ in the 4th and 5th significant digit.

These observations suggest that the Bethe logarithm of  $\text{He}_2^+$  ( $X^2\Sigma_u^+$ ) can be well approximated with the Bethe logarithm of the ground electronic state of  $\text{He}_2^{3+}$ . The Bethe logarithm for this one-electron two-center problem was computed using the procedure of Ref. [38]. We estimate the error introduced by the  $\beta_{\text{el},\text{He}_2^+}(\rho) \approx \beta_{\text{el},\text{He}_2^{3+}}(\rho)$  approximation, which we use in this Letter, to be less than 1% over the relevant internuclear range  $\rho \in [0.9, 3.5]$  bohr (Table I).

The effect of higher-order QED corrections is estimated as in Refs. [33,46]:

$$E_{\text{est}}^{(4)} = \alpha^4 \pi \left( \frac{427}{96} - 2 \ln 2 \right) \sum_{i=1}^3 \sum_{a=1}^2 Z_a \delta(\mathbf{r}_{ia}). \quad (11)$$

Table I collects the numerical uncertainty attributed to the rovibrational intervals within the described computational procedure. The present theoretical framework rests

 TABLE II. Dependence of the  $\beta_{\text{el}}$  Bethe logarithm on the  $Z$  nuclear charge and on the  $n$  number of electrons in the ground state of atoms (ions). These data are compiled from Refs. [41–45].

$\beta_{\text{el}} [\text{E}_h]$	H	He	Li
	$Z = 1$	$Z = 2$	$Z = 3$
$n = 1$	2.984 128	4.370 422	5.181 353
$n = 2$	...	4.370 160	5.179 849
$n = 3$	...	...	5.178 28

TABLE III. Comparison of the  $\beta_{\text{el}}(\rho)$  Bethe logarithm for selected  $\rho$  internuclear distances of the one-electron  $\text{H}_2^+$  molecular ion [38] and the two-electron  $\text{H}_2$  molecule [33] in the adiabatic approximation and in their ground electronic states.

$\rho$ [bohr]	0.1	0.2	0.4	0.8	1.5	5.0
$\beta_{\text{el}}(\rho)$ ( $\text{H}_2^+$ ) [ $E_h$ ] [38]	3.763 208	3.525 245	3.284 256	3.100 639	3.023 053	2.995 328
$\beta_{\text{el}}(\rho)$ ( $\text{H}_2$ ) [ $E_h$ ] [33]	3.765	3.526	3.279	3.093 31	3.013 96	2.985 34

on two small parameters, the square root of the electron-to-nucleus mass ratio  $\varepsilon$  and the fine-structure constant  $\alpha$ . The electron-nucleus (nonadiabatic) coupling is accounted for up to  $\varepsilon^2$  order and higher-order contributions are neglected. Relativistic ( $\alpha^2$ ) and leading-order QED ( $\alpha^3$ ) corrections have been included, and an estimate for the  $\alpha^4$ -order terms, Eq. (11), was also computed. We estimate the uncertainty of the rotational-vibrational intervals due to the missing part of  $\alpha^4$  and higher-order QED corrections by the (small) effect of the  $\alpha^4$  estimate (hQED in Table I). We have neglected the nonadiabatic-relativistic (and QED) coupling in this Letter that was found to be important in the  $\text{H}_2$  molecule [32]. An elaborate theoretical and computational study of this coupling for the present system will require further work, but we give an estimate for its magnitude (“Nad&Rel” in Table I). The estimated effect of the finite

nuclear size is also shown in Table I. We used the CODATA18 recommendations for the physical constants and conversion factors throughout the computations.

The computed rotational and (ro)vibrational intervals and corrections are listed in Tables IV and V. Figure 1 visualizes the results and reveals a fine interplay of the various corrections (The potential energy points and all corrections computed and used in this Letter are deposited in the Supplemental Material [47]).

The adiabatic description (“Ad”) with the “empirical mass correction” using  $m_{\text{rot}} = m_{\text{vib}} = m_\alpha + 1.5m_e$  [14] reproduces the fundamental vibration energy almost perfectly, while its deviation from experiment increases with increasing  $N^+$ . By including the rigorous nonadiabatic masses for the rotational and vibrational degrees of freedom [15], the error is reduced for the rotational excitations, but

 TABLE IV. Rotational excitation energies of  $^4\text{He}_2^+$  ( $X^2\Sigma_u^+$ ) in the vibrational ground state.  $\tilde{\nu}_0$ : Born–Oppenheimer description with nuclear masses.  $\delta\tilde{\nu}_{\text{DBOC}}$ : The diagonal Born–Oppenheimer correction.  $\delta\tilde{\nu}_{\text{mveff}}$ : Empirical mass  $m_{\text{rot}} = m_{\text{vib}} = m_\alpha + 1.5m_e$ .  $\delta\tilde{\nu}_{\text{Nad}}$ : Rigorous nonadiabatic mass.  $\delta\tilde{\nu}_{\text{Rel}}$ : Relativistic correction.  $\delta\tilde{\nu}_{\text{QED}}$ : Leading-order QED correction.  $\delta\tilde{\nu}_{\text{hQED}}$ : Estimate for higher-order QED corrections. For the derivation of the error estimates to the computed energies, see Table I.

$N^+$ :	$\tilde{\nu}(0, N^+) - \tilde{\nu}(0, 1)$ [ $\text{cm}^{-1}$ ]			
	3	5	7	9
$\tilde{\nu}_0$	70.960 61	198.427 8	381.954 3	620.898 1
$+\delta\tilde{\nu}_{\text{DBOC}}$	−0.010 28	−0.028 7	−0.055 0	−0.089 1
$+\delta\tilde{\nu}_{\text{mveff}}$	−0.014 46	−0.040 4	−0.077 6	−0.125 8
$+\delta\tilde{\nu}_{\text{mvNad}}$	0.000 45	0.001 3	0.002 6	0.004 4
$+\delta\tilde{\nu}_{\text{Rel}}$	0.002 16	0.006 0	0.011 5	0.018 7
$+\delta\tilde{\nu}_{\text{QED}}$	−0.00078	−0.002 2	−0.004 2	−0.006 8
$+\delta\tilde{\nu}_{\text{hQED}}$	0.000 01	0.000 0	0.000 0	−0.0001
$\tilde{\nu}_{\text{calc}}$	70.937 68(10)	198.363 8(13)	381.831 6(13)	620.699 4(13)
$\tilde{\nu}_{\text{expt}}$ [9,12]	70.937 589(23)(60) <sub>sys</sub>	198.364 7(8)	381.834 6(8)	620.702 1(9)
$\tilde{\nu}_{\text{expt}} - \tilde{\nu}_{\text{calc}}$	−0.00010	0.000 9	0.003 0	0.002 7

$N^+$ :	$\tilde{\nu}(0, N^+) - \tilde{\nu}(0, 1)$ [ $\text{cm}^{-1}$ ]				
	11	13	15	17	19
$\tilde{\nu}_0$	914.426 5	1261.521 5	1660.986 0	2111.450 8	2611.382 6
$+\delta\tilde{\nu}_{\text{DBOC}}$	−0.130 4	−0.178 8	−0.233 6	−0.294 4	−0.360 5
$+\delta\tilde{\nu}_{\text{mveff}}$	−0.184 7	−0.253 8	−0.332 8	−0.420 9	−0.517 7
$+\delta\tilde{\nu}_{\text{mvNad}}$	0.006 9	0.010 1	0.014 1	0.019 1	0.025 2
$+\delta\tilde{\nu}_{\text{Rel}}$	0.027 3	0.037 3	0.048 6	0.061 1	0.074 5
$+\delta\tilde{\nu}_{\text{QED}}$	−0.010 0	−0.013 8	−0.018 1	−0.023 0	−0.028 3
$+\delta\tilde{\nu}_{\text{hQED}}$	−0.0001	−0.0001	−0.0002	−0.0002	−0.0003
$\tilde{\nu}_{\text{calc}}$	914.135 4(13)	1261.122 3(13)	1660.464 0(13)	2110.792 5(13)	2610.575 5(15)
$\tilde{\nu}_{\text{expt}}$ [12]	914.136 7(8)	1261.124 2(8)	1660.462 7(9)	2110.793 2(9)	2610.574 4(9)
$\tilde{\nu}_{\text{expt}} - \tilde{\nu}_{\text{calc}}$	0.001 3	0.001 9	−0.001 3	0.000 7	−0.001 1

TABLE V. Rovibrational excitation energies of  ${}^4\text{He}_2^+$  ( $X\ 2\Sigma_u^+$ ) between the vibrational ground and first excited state. See also the caption to Table IV.

$(v, N^+)''-(v, N^+)'$ :	$\tilde{\nu}(v, N^+)'' - \tilde{\nu}(v, N^+)'$ [ $\text{cm}^{-1}$ ]		
	(1,0)–(0,0)	(1,1)–(0,1)	(1,3)–(0,1)
$\tilde{\nu}_0$	1628.560 0	1628.108 1	1696.808 9
$\delta\tilde{\nu}_{\text{DBOC}}$	−0.022 3	−0.022 2	−0.032 0
$\delta\tilde{\nu}_{\text{mveff}}$	−0.160 2	−0.160 1	−0.173 9
$\delta\tilde{\nu}_{\text{mvNad}}$	0.025 8	0.025 7	0.025 9
$\delta\tilde{\nu}_{\text{Rel}}$	−0.010 2	−0.010 3	−0.008 3
$\delta\tilde{\nu}_{\text{QED}}$	−0.012 0	−0.012 0	−0.012 8
$\delta\tilde{\nu}_{\text{hQED}}$	−0.0001	−0.0001	−0.0001
$\tilde{\nu}_{\text{calc}} = \tilde{\nu}_0 + \sum \delta\tilde{\nu}$	1628.380 9(33)	1627.929 1(39)	1696.607 7(39)
$\tilde{\nu}_{\text{expt}}$ [13]	1628.383 2(12)	1627.931 8(12)	1696.609 6(12)
$\tilde{\nu}_{\text{expt}} - \tilde{\nu}_{\text{calc}}$	0.002 3	0.002 7	0.001 9

$(v, N^+)''-(v, N^+)'$ :	$\tilde{\nu}(v, N^+)'' - \tilde{\nu}(v, N^+)'$ [ $\text{cm}^{-1}$ ]		
	(1,7)–(0,1)	(1,11)–(0,1)	(1,13)–(0,1)
$\tilde{\nu}_0$	1997.857 8	2513.146 5	2848.931 6
$\delta\tilde{\nu}_{\text{DBOC}}$	−0.074 4	−0.145 9	−0.191 6
$\delta\tilde{\nu}_{\text{mveff}}$	−0.233 9	−0.335 7	−0.401 3
$\delta\tilde{\nu}_{\text{mvNad}}$	0.026 9	0.029 3	0.031 2
$\delta\tilde{\nu}_{\text{Rel}}$	0.000 2	0.014 3	0.023 3
$\delta\tilde{\nu}_{\text{QED}}$	−0.016 1	−0.021 6	−0.025 2
$\delta\tilde{\nu}_{\text{hQED}}$	−0.0002	−0.0002	−0.0003
$\tilde{\nu}_{\text{calc}} = \tilde{\nu}_0 + \sum \delta\tilde{\nu}$	1997.560 4(39)	2512.686 7(39)	2848.367 8(39)
$\tilde{\nu}_{\text{expt}}$ [13]	1997.563 3(12)	2512.687 1(12)	2848.369 0(12)
$\tilde{\nu}_{\text{expt}} - \tilde{\nu}_{\text{calc}}$	0.002 9	0.000 4	0.001 2

the fundamental vibration energy shows a large deviation from experiment. Adding the relativistic corrections to this nonadiabatic model reduces the deviation by a factor of two for the fundamental vibration, but it “overcorrects” the rotational excitation energies. By including also the leading-order QED corrections in the theoretical treatment both the fundamental vibration energy, the rotational and the rovibrational excitation energies come in agreement with experiment with root-mean-squared deviations (RMSDs) of 0.001 7 and 0.0019  $\text{cm}^{-1}$ , respectively. The experimental uncertainties of the rotational and rovibrational series is slightly smaller than these values [12,13]; they are 0.000 8 and 0.00012  $\text{cm}^{-1}$ , respectively. The lowest-energy rotational interval, (0,3)–(0,1), has been recently measured more precisely,  $70.937\,589(23) \pm 0.000\,06_{\text{sys}}$  [9], and our theoretical value for this interval is  $70.937\,69(10) \text{ cm}^{-1}$ . For the fundamental vibration, our computational result is  $1628.380\,9(33) \text{ cm}^{-1}$ , which is in agreement with its value derived from experiments,  $1628.383\,2(12) \text{ cm}^{-1}$  [13].

All the rovibrational intervals (Table V) are in agreement with the experimental results within the given uncertainties, although the computational results have almost 3 times larger uncertainties than the experimental ones. We observe some discrepancies for the *rotational* intervals with intermediate  $N^+$  values (especially,  $N^+ = 7, 9$  and 13). We note that the pure rotational intervals have a smaller uncertainty

than the rovibrational ones, since they were much less affected by the PEC improvement (Table I).

We finish the discussion with observations regarding the interplay of the computed corrections (Tables IV and V). First, we point out that  $\delta\tilde{\nu}_{\text{mveff}}$  and  $\delta\tilde{\nu}_{\text{mvNad}}$  together account for the nonadiabatic mass effect.  $\delta\tilde{\nu}_{\text{mveff}}$  is a simple, intuitive, constant mass model ( $m_{\text{rot}} = m_{\text{vib}} = m_{\alpha} + 1.5m_e$ ), and  $\delta\tilde{\nu}_{\text{mvNad}}$  labels the value, which corrects this empirical model to arrive at the rigorous second-order nonadiabatic result. It is interesting to observe, at least for the present example, that  $\delta\tilde{\nu}_{\text{mvNad}}$  has the same order of magnitude but opposite sign as the leading-order QED correction  $\delta\tilde{\nu}_{\text{QED}}$ . The interplay of the corrections changes for the different types of motions, i.e., the relativistic correction has a different sign for the rotational and for the vibrational excitation, whereas the QED contribution is positive in both cases. This interplay of the higher-order correction terms—which we explicitly compute in this Letter—had resulted in cancellation of errors in the lower-order calculations [14] and a seemingly good agreement with the experimental result [13] for this interval.

Rotational and (ro)vibrational intervals have been reported for the three-electron  ${}^4\text{He}_2^+$  ( $X\ 2\Sigma_u^+$ ) molecular ion on a newly computed potential energy curve with nonadiabatic, relativistic, and QED corrections. The computed rotational-vibrational intervals are in good agreement with recent precision

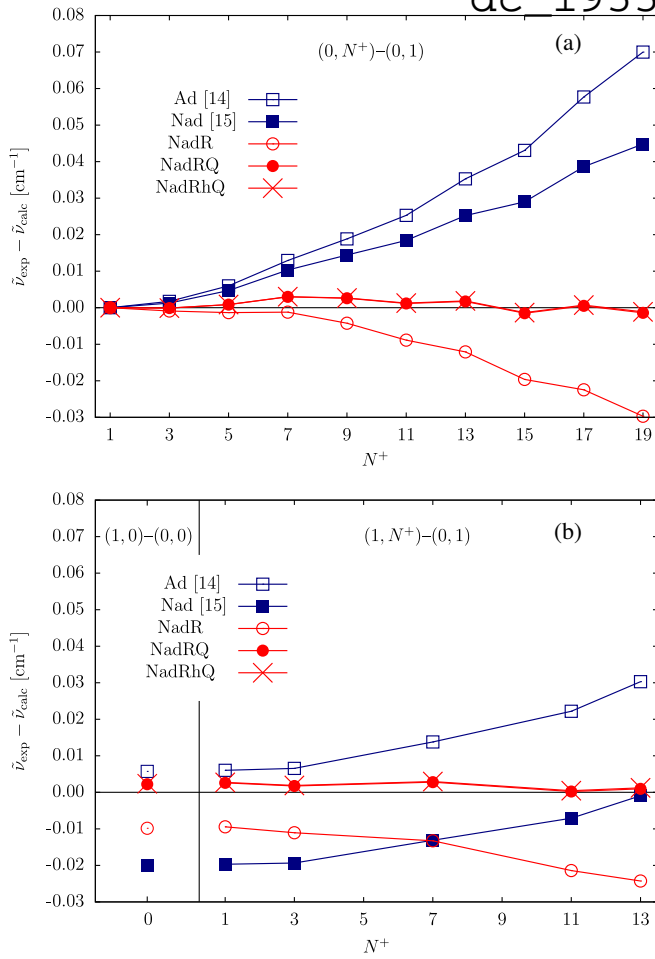


FIG. 1. Deviation of the rotational and (ro)vibrational excitation energies of the  ${}^4\text{He}_2^+$  molecular ion ( $X^2\Sigma_u^+$ ) from experiment [9,12,13].  $(v, N^+)$  labels the  $v$ th vibrational state with the  $N^+$  rotational quantum number. Square: Adiabatic with the  $m_{\text{vib}} = m_{\text{rot}} = m_{\alpha} + 1.5m_e$  empirical mass in the kinetic energy operator. Filled square: Nonadiabatic, i.e., with rigorous rotational and vibrational masses. Circle: Nonadiabatic and relativistic corrections. Filled circle: Nonadiabatic, relativistic, and leading-order QED corrections. Cross: Nonadiabatic, relativistic, leading-order QED with estimates for higher-order QED corrections.

spectroscopy measurements. Further developments, most importantly, a detailed study of the relativistic-nonadiabatic coupling and the extension of the potential energy curve with parts-per-billion uncertainty over large internuclear distances, will challenge precision spectroscopy experiments and contribute to the establishment of primary pressure standards.

D.F. acknowledges the support from the ÚNKP-19-3 New National Excellence Program of the Ministry for Innovation and Technology of Hungary (ÚNKP-19-3-I-ELTE-24). E.M. and D.F. acknowledge the financial support of the Swiss National Science Foundation (PROMYS Grant No. IZ11Z0\_166525) at the beginning of this work and the European Research Council (Starting

Grant No. 851421). E.M. thanks Frédéric Merkt for discussions. V.I.K. acknowledges support from the Russian Foundation for Basic Research under Grant No. 19-02-00058-a.

\*Corresponding author.

korobov@theor.jinr.ru

†Corresponding author.

matyus@chem.elte.hu

- [1] N. Hölsch, M. Beyer, E. J. Salumbides, K. S. E. Eikema, W. Ubachs, C. Jungen, and F. Merkt, Benchmarking Theory with an Improved Measurement of the Ionization and Dissociation Energies of  $\text{H}_2$ , *Phys. Rev. Lett.* **122**, 103002 (2019).
- [2] M. Puchalski, J. Komasa, P. Czachorowski, and K. Pachucki, Nonadiabatic QED Correction to the Dissociation Energy of the Hydrogen Molecule, *Phys. Rev. Lett.* **122**, 103003 (2019).
- [3] S. Alighanbari, G. S. Giri, F. L. Constantin, V. I. Korobov, and S. Schiller, Precise test of quantum electrodynamics and determination of fundamental constants with  $\text{HD}^+$  ions, *Nature (London)* **581**, 152 (2020).
- [4] R. K. Altmann, L. S. Dreissen, E. J. Salumbides, W. Ubachs, and K. S. E. Eikema, Deep-Ultraviolet Frequency Metrology of  $\text{H}_2$  for Tests of Molecular Quantum Theory, *Phys. Rev. Lett.* **120**, 043204 (2018).
- [5] M. S. Safronova, D. Budker, D. DeMille, D. F. J. Kimball, A. Derevianko, and C. W. Clark, Search for new physics with atoms and molecules, *Rev. Mod. Phys.* **90**, 025008 (2018).
- [6] J.-P. Karr, L. Hilico, J. C. J. Koelemeij, and V. I. Korobov, Hydrogen molecular ions for improved determination of fundamental constants, *Phys. Rev. A* **94**, 050501(R) (2016).
- [7] S. Alighanbari, M. G. Hansen, V. I. Korobov, and S. Schiller, Rotational spectroscopy of cold and trapped molecular ions in the Lamb–Dicke regime, *Nat. Phys.* **14**, 555 (2018).
- [8] M. Puchalski, K. Piszczatowski, J. Komasa, B. Jeziorski, and K. Szalewicz, Theoretical determination of the polarizability dispersion and the refractive index of helium, *Phys. Rev. A* **93**, 032515 (2016).
- [9] L. Semeria, P. Jansen, G.-M. Camenisch, F. Mellini, H. Schmutz, and F. Merkt, Precision Measurement in Few-Electron Molecules: The Ionization Energy of Metastable  ${}^4\text{He}_2$  and the First Rotational Interval in  ${}^4\text{He}_2^+$ , *Phys. Rev. Lett.* **124**, 213001 (2020).
- [10] P. Jansen, L. Semeria, and F. Merkt, Determination of the Spin-Rotation Fine Structure of  ${}^4\text{He}_2^+$ , *Phys. Rev. Lett.* **120**, 043001 (2018).
- [11] P. Jansen, L. Semeria, and F. Merkt, High-resolution spectroscopy of  ${}^4\text{He}_2^+$  using Rydberg-series extrapolation and Zeeman-decelerated supersonic beams of metastable  $\text{He}_2$ , *J. Mol. Spectrosc.* **322**, 9 (2016).
- [12] L. Semeria, P. Jansen, and F. Merkt, Precision measurement of the rotational energy-level structure of the three-electron molecule  ${}^4\text{He}_2^+$ , *J. Chem. Phys.* **145**, 204301 (2016).
- [13] P. Jansen, L. Semeria, and F. Merkt, Fundamental vibration frequency and rotational structure of the first excited



- vibrational level of the molecular helium ion ( $\text{He}_2^+$ ), *J. Chem. Phys.* **149**, 154302 (2018).
- [14] W.-C. Tung, M. Pavanello, and L. Adamowicz, Very accurate potential energy curve of the  $\text{He}_2^+$  ion, *J. Chem. Phys.* **136**, 104309 (2012).
- [15] E. Mátyus, Non-adiabatic mass-correction functions and rovibrational states of  $^4\text{He}_2^+$  ( $X^2\Sigma_u^+$ ), *J. Chem. Phys.* **149**, 194112 (2018).
- [16] S. Bubin, M. Pavanello, W.-C. Tung, K. L. Sharkey, and L. Adamowicz, Born–Oppenheimer and non-Born–Oppenheimer, atomic and molecular calculations with explicitly correlated Gaussians, *Chem. Rev.* **113**, 36 (2013).
- [17] V. I. Korobov, Ro-vibrational states of  $\text{H}_2^+$ . variational calculations, *Mol. Phys.* **116**, 93 (2018).
- [18] L. M. Wang and Z.-C. Yan, Relativistic corrections to the ground state of  $\text{H}_2$  calculated without using the Born–Oppenheimer approximation, *Phys. Rev. A* **97**, 060501(R) (2018).
- [19] E. Mátyus, Pre-Born–Oppenheimer molecular structure theory, *Mol. Phys.* **117**, 590 (2019).
- [20] D. Ferenc and E. Mátyus, Computation of rovibronic resonances of molecular hydrogen:  $EF^1\Sigma_g^+$  inner-well rotational states, *Phys. Rev. A* **100**, 020501(R) (2019).
- [21] K. Pachucki and J. Komasa, Nonadiabatic rotational states of the hydrogen molecule, *Phys. Chem. Chem. Phys.* **20**, 247 (2018).
- [22] M. Stanke, S. Bubin, and L. Adamowicz, Fundamental vibrational transitions of the  $^3\text{He}^4\text{He}^+$  and  $^7\text{LiH}^+$  ions calculated without assuming the Born–Oppenheimer approximation and with including leading relativistic corrections, *Phys. Rev. A* **79**, 060501(R) (2009).
- [23] S. Teufel, *Adiabatic Perturbation Theory in Quantum Dynamics*, Lecture Notes in Mathematics (Springer, Berlin, Heidelberg, 2003).
- [24] G. Panati, H. Spohn, and S. Teufel, The time-dependent Born–Oppenheimer approximation, *ESAIM: Math. Model. Num. Anal.* **41**, 297 (2007).
- [25] E. Matyus and S. Teufel, Effective non-adiabatic Hamiltonians for the quantum nuclear motion over coupled electronic states, *J. Chem. Phys.* **151**, 014113 (2019).
- [26] K. Pachucki and J. Komasa, Nonadiabatic corrections to rovibrational levels of  $\text{H}_2$ , *J. Chem. Phys.* **130**, 164113 (2009).
- [27] E. Mátyus, Non-adiabatic mass correction to the rovibrational states of molecules. Numerical application for the  $\text{H}_2^+$  molecular ion, *J. Chem. Phys.* **149**, 194111 (2018).
- [28] J. C. Light and T. Carrington Jr., Discrete-variable representations and their utilization, in *Advances in Chemical Physics* (John Wiley & Sons, Ltd., New York, 2000), pp. 263–310.
- [29] W. Cencek and J. Rychlewski, Benchmark calculations for  $\text{He}_2^+$  and  $\text{LiH}$  molecules using explicitly correlated Gaussian functions, *Chem. Phys. Lett.* **320**, 549 (2000).
- [30] K. Pachucki, W. Cencek, and J. Komasa, On the acceleration of the convergence of singular operators in Gaussian basis sets, *J. Chem. Phys.* **122**, 184101 (2005).
- [31] M. Stanke, E. Palikot, and L. Adamowicz, Algorithms for calculating mass-velocity and Darwin relativistic corrections with  $n$ -electron explicitly correlated Gaussians with shifted centers, *J. Chem. Phys.* **144**, 174101 (2016).
- [32] P. Czachorowski, M. Puchalski, J. Komasa, and K. Pachucki, Nonadiabatic relativistic correction in  $\text{H}_2$ ,  $\text{D}_2$ , and  $\text{HD}$ , *Phys. Rev. A* **98**, 052506 (2018).
- [33] K. Piszczatowski, G. Lach, M. Przybytek, J. Komasa, K. Pachucki, and B. Jeziorski, Theoretical determination of the dissociation energy of molecular hydrogen, *J. Chem. Theory Comput.* **5**, 3039 (2009).
- [34] H. A. Bethe and E. E. Salpeter, *Quantum Mechanics of One- and Two-Electron Atoms* (Plenum Publishing Co., New York, 1977).
- [35] K. Pachucki, Simple derivation of helium Lamb shift, *J. Phys. B* **31**, 5123 (1998).
- [36] K. Pachucki and J. Komasa, Rovibrational levels of  $\text{HD}$ , *Phys. Chem. Chem. Phys.* **12**, 9188 (2010).
- [37] R. Bukowski, B. Jeziorski, R. Moszynski, and W. Kołos, Bethe logarithm and Lamb shift for the hydrogen molecular ion, *Int. J. Quantum Chem.* **42**, 287 (1992).
- [38] V. I. Korobov, L. Hilico, and J.-P. Karr, Calculation of the relativistic Bethe logarithm in the two-center problem, *Phys. Rev. A* **87**, 062506 (2013).
- [39] H. Araki, Quantum-electrodynamical corrections to energy-level of helium, *Prog. Theor. Phys.* **17**, 619 (1957).
- [40] J. Sucher, Energy levels of the two-electron atom to order  $\alpha^3\text{Ry}$ ; Ionization energy of helium, *Phys. Rev.* **109**, 1010 (1958).
- [41] G. W. F. Drake and S. P. Goldman, Bethe logarithms for  $\text{Ps}^-$ ,  $\text{H}^-$ , and heliumlike atoms, *Can. J. Phys.* **77**, 835 (1999).
- [42] V. A. Yerokhin and K. Pachucki, Theoretical energies of low-lying states of light helium-like ions, *Phys. Rev. A* **81**, 022507 (2010).
- [43] V. I. Korobov, Calculation of the nonrelativistic Bethe logarithm in the velocity gauge, *Phys. Rev. A* **85**, 042514 (2012).
- [44] K. Pachucki and J. Komasa, Bethe logarithm for the lithium atom from exponentially correlated Gaussian functions, *Phys. Rev. A* **68**, 042507 (2003).
- [45] Z.-C. Yan, W. Nörtershäuser, and G. W. F. Drake, High Precision Atomic Theory for  $\text{Li}$  and  $\text{Be}^+$ : QED Shifts and Isotope Shifts, *Phys. Rev. Lett.* **100**, 243002 (2008).
- [46] M. Puchalski, J. Komasa, P. Czachorowski, and K. Pachucki, Complete  $m\alpha^6$  Corrections to the Ground State of  $\text{H}_2$ , *Phys. Rev. Lett.* **117**, 263002 (2016).
- [47] See Supplemental Material at <http://link.aps.org/supplemental/10.1103/PhysRevLett.125.213001> for the points computed and used in this Letter for the potential energy and nonadiabatic, relativistic, and QED correction curves.

## Pre-Born–Oppenheimer molecular structure theory

Edit Mátyus 

Institute of Chemistry, ELTE Eötvös Loránd University, Budapest, Hungary

### ABSTRACT

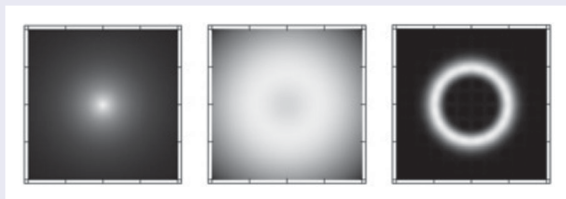
In pre-Born–Oppenheimer (pre-BO) theory a molecule is considered as a quantum system as a whole, including the electrons and the atomic nuclei on the same footing. This approach is fundamentally different from the traditional quantum chemistry treatment, which relies on the separation of the motion of the electrons and the atomic nuclei. A fully quantum mechanical description of molecules has a great promise for future developments and applications. Its most accurate versions may contribute to the definition of new schemes for metrology and testing fundamental physical theories; its approximate versions can provide an efficient theoretical description for molecule-positron interactions and, in general, it would circumvent the tedious computation and fitting of potential energy surfaces and non-adiabatic coupling vectors while it includes also the quantum nuclear motion also often called ‘molecular quantum dynamics’. To achieve these goals, the review points out important technical and fundamental open questions. Most interestingly, the reconciliation of pre-BO theory with the classical chemistry knowledge touches upon fundamental problems related to the measurement problem of quantum mechanics.

### ARTICLE HISTORY

Received 1 March 2018  
Accepted 7 September 2018

### KEYWORDS

pre-Born–Oppenheimer theory; molecular structure in quantum mechanics; rovibronic resonances; explicitly correlated Gaussian functions; stochastic variational method



### 1. Quantum chemistry vs. quantum mechanics and chemistry?



We start this article with a historical overview of the chemical theory of molecular structure and the origins of quantum chemistry, which is followed by methodological details and applications of pre-Born–Oppenheimer theory.

#### 1.1. Historical background: chemical structure, physical structure from organic chemistry experiments

[T]he dominating story in chemistry of the 1860s, 1870s, and 1880s was neither the periodic law, nor the search for new elements, nor the early stages of the study of atoms and molecules as physical entities. It was the maturation, and demonstration of extraordinary scientific and technological power, of the “theory of chemical structure” . . .

ALAN J. ROCKE  
Image and Reality: Kekulé, Kopp, and the Scientific Imagination  
(The University of Chicago Press, Chicago and London, 2010)

During the second half of the 19th century, the pioneering organic chemists generation—represented by Williamson, Kekulé, Butlerov, Crum Brown, Frankland, and Wurtz—had explored an increasing number of chemical transformations in their laboratory experiments and worked towards the establishment of a logical framework for their observations. The ‘first chemistry conference’, held in Karlsruhe on 3 September 1860, resulted in an internationally recognised definition of the atomic masses. This agreement ensured that the same molecular formula was then used for the same substance in all laboratories around the world, and thereby opened the route to the successful development of the theory of chemical structure. The development of the

**CONTACT** Edit Mátyus  matyus@chem.elte.hu  Institute of Chemistry, ELTE Eötvös Loránd University, Pázmány Péter sétány 1/A, Budapest, Hungary

© 2018 The Author(s). Published by Informa UK Limited, trading as Taylor & Francis Group

This is an Open Access article distributed under the terms of the Creative Commons Attribution-NonCommercial-NoDerivatives License (<http://creativecommons.org/licenses/by-nc-nd/4.0/>), which permits non-commercial re-use, distribution, and reproduction in any medium, provided the original work is properly cited, and is not altered, transformed, or built upon in any way.

chemical theory had been surrounded by heated debates about what was reality and what was mere speculation. Contemporary physics (gravitation, electromagnetism) was not able to provide any satisfactory description for molecules. To give a taste of this exciting period, we reproduce a few extracts from Alan J. Rocke's chemical history book [1]:

- Friedrich August Kekulé [von Stradonitz] (1858): 'rational formulas are reaction formulas, and can be nothing more in the current state of science'.
- Friedrich August Kekulé [von Stradonitz] (1859): '[he] rejected the possibility of determining the physical arrangement of the constituent atoms in a molecule from the study of chemical reactions, since chemical reactions necessarily alter the arrangements of the atoms in the molecule'.
- Charles Adolphe Wurtz (1860): '[W]e do not have any means of assuring ourselves in an absolute manner of the arrangement, or even the real existence of the groups which appear in our rational formulas . . . merely express parental ties'.
- Hermann Kolbe (1866): 'Frankly, I consider all these graphical representations . . . as dangerous, because the imagination is thereby given too free rein'.
- Johannes Wislicenus (1869): '[it] must somehow be explained by the different arrangements of their atoms in space'.
- Jacobus Henricus van't Hoff (5 September 1874, 1875): 'La chimie dans l'espace'
- Joseph Achille Le Bel (5 November 1874): physical structure in the 3-dimensional space

### 1.2. Historical background: application of quantum theory to molecules

At the time when Erwin Schrödinger wrote down his famous wave equation [2], the concept of the classical skeleton of the atomic nuclei arranged in the three-dimensional space was already a central idea in molecular science derived from the organic chemists' laboratory experiments. The idea of a separate description of the electrons and the atomic nuclei, i.e. the motion of the atomic nuclei on a potential energy surface (PES), which results from the solution of the electronic problem in the field of fixed external nuclear charges, is usually connected to the work of Born and Oppenheimer in 1927 [3] and perhaps the later references [4,5] are also cited. At the same time, Sutcliffe and Woolley analyze in reference [6] René Marcelin's doctoral dissertation published in 1914 (the author died during World War I), which appears to be the earliest work in which ideas reminiscent of a potential energy surface can be found. Sutcliffe and

Woolley argue that the idea of clamping the atomic nuclei in order to define an electronic problem was attempted already within the framework of The Old Quantum Theory, and later these attempts were taken over (more successfully) to Schrödinger's theory for molecules. In any case, what we usually mean by quantum chemistry gains its equations from a combination of quantum mechanics and the Born–Oppenheimer (BO) approximation (and perhaps corrections to the BO approximation are also included).

### 1.3. Quantum chemistry

The tremendous success of the usual practice might perhaps be best regarded as a tribute to the insight and ingenuity of the practitioners for inventing an effective variant of quantum theory for chemistry.

B. T. Sutcliffe and R. G. Woolley, *J. Chem. Phys.* 137, 22A544 (2012) [7].

The well-known theory applicable to molecules has grown out from the separation of the motion of the electrons and the atomic nuclei. This separation defines two major fields for quantum chemistry, electronic structure theory and the corresponding electronic Hamiltonian (in atomic units):

$$\hat{H}_{\text{el}} = - \sum_{i=1}^{n_e} \frac{1}{2} \Delta_{\mathbf{r}_i} + \sum_{i=1}^{n_e} \sum_{j>i}^{n_e} \frac{1}{|\mathbf{r}_i - \mathbf{r}_j|} - \sum_{i=1}^{n_e} \sum_{n=1}^{n_n} \frac{Z_n}{|\mathbf{r}_i - \mathbf{R}_n|} + \sum_{n=1}^{n_n} \sum_{m>n}^{n_n} \frac{Z_n Z_m}{|\mathbf{R}_n - \mathbf{R}_m|} \quad (1)$$

with the  $\mathbf{r}_i$  electronic and  $\mathbf{R}_n$  nuclear positions and electric charges,  $Z_n$ ; and nuclear motion theory with the Hamiltonian for the motion of the atomic nuclei (or rovibrational Hamiltonian):

$$\hat{H}_{\text{nuc}} = \hat{T}(\rho) + \hat{V}, \quad (2)$$

where  $\hat{T}(\rho)$  is the rovibrational kinetic energy operator and the potential energy,  $\hat{V}$ , which is called the potential energy surface and it is obtained from the eigenvalues of Equation (1) computed at different positions of the atomic nuclei.

Within this framework, a variety of molecular properties are derived from the eigenstates of the electronic Hamiltonian, Equation (1), and an effective combination of the quantum mechanics of electrons with classical electronic properties of identifiable nuclei and quantum mechanics for nuclear motions, Equation (2).

Several chemical concepts gain a theoretical background from this construct, most importantly the potential energy surface (PES) is defined. Its minimum structure (or structures if it has several local minima) defines

the equilibrium structure, which is a purely mathematical construct resulting from the separability approximation but it is usually identified with the classical molecular structure. Then, the nuclei are re-quantised to solve the Schrödinger equation of the atomic nuclei, Equation (2), to calculate rovibrational states, resonances, reaction rates, etc.

The electronic structure and quantum nuclear motion theories have many similar features but each field has its own peculiarities. Most importantly, the spatial symmetries are different: in electronic-structure theory the point-group symmetry is defined by the fixed, classical nuclear skeleton, whereas in nuclear-motion theory the PES depends only on the relative positions of the nuclei in agreement with the translational and rotational invariance of an isolated molecule. Furthermore in electronic-structure theory, the molecular translations and rotations are separated off by fixing the atomic nuclei, and thus the kinetic energy can be written in a very simple form in Cartesian coordinates. In nuclear-motion theory, it is convenient to define a frame fixed to the (non-rigid) body to separate off the translation and to account for the spatial orientation of this frame by three angles [8, 9]. Thereby, in a usual nuclear-motion theory treatment, the coordinates are necessarily curvilinear. In spite of all complications, it was possible to develop automated procedures [10–14], which allow us to efficiently compute hundreds or thousands of rovibrational energy states for small molecules using curvilinear coordinates appropriately chosen for a molecular system [15–17].

#### 1.4. Quantum mechanics and chemistry?

The direct treatment of molecules as few-particle quantum systems is much less explored. Nevertheless, we may think about a molecule as a quantum system as a whole without any *a priori* separation of the particles, which we call pre-Born–Oppenheimer (pre-BO) molecular structure theory (it is also called non-Born–Oppenheimer theory in the literature [18,19]).

The  $(n_p + 1)$ -particle time-independent Schrödinger equation

$$\hat{H}\Psi = E\Psi \quad (3)$$

contains the non-relativistic Hamiltonian

$$\hat{H} = \hat{T} + \hat{V}, \quad (4)$$

which is the sum of the kinetic energy operator

$$\hat{T} = - \sum_{i=1}^{n_p+1} \frac{1}{2m_i} \Delta_{\mathbf{r}_i} \quad (5)$$

and the Coulomb potential energy operator

$$\hat{V} = \sum_{i=1}^{n_p+1} \sum_{j>i}^{n_p+1} \frac{q_i q_j}{|\mathbf{r}_i - \mathbf{r}_j|}, \quad (6)$$

where atomic units are used and  $\mathbf{r}_i$  labels the laboratory-fixed (LF) Cartesian coordinates of the  $i$ th particle. The full molecular Hamiltonian has  $2(n_p + 1)$  parameters, the mass and the electric charge for each particle,  $m_i$  and  $q_i$  ( $i = 1, 2, \dots, n_p + 1$ ), respectively. In addition, the physical solutions must satisfy the spin-statistics theorem, thereby the spins  $s_i$  ( $i = 1, 2, \dots, n_p + 1$ ) (the fermionic or bosonic character) appear as additional parameters. In total, there are  $3(n_p + 1)$  parameters, which define the molecular system. In addition, we may specify the quantum numbers corresponding to the conserved quantities of an isolated molecule: the total angular momentum, its projection to a space-fixed axis, the parity, and the spin quantum numbers labelled with  $N$ ,  $N_z$ ,  $p$ ,  $S_a$ ,  $M_{S_a}$ ,  $S_b$ ,  $M_{S_b}$ , ... (for particle types  $a$ ,  $b$ , etc.), respectively.<sup>1</sup>

It is important to note that the full molecular Hamiltonian,  $\hat{H}$  specified in Equations (4)–(6), has very different mathematical properties from the electronic Hamiltonian,  $\hat{H}_{el}$  in Equation (1). Although the potential energy is the simple Coulomb interaction term both in  $\hat{H}$  and  $\hat{H}_{el}$ , in  $\hat{H}$  all electric charges belong to the quantum system. While, for a neutral molecule  $\hat{H}_{el}$  has an infinite discrete spectrum and the continuous spectrum begins at the first ionisation energy, the  $\hat{H}$  molecular Hamiltonian does not have any discrete spectrum at all unless the overall molecular translation is removed (see for example Refs. [20–22]). In fact,  $\hat{H}$  has the same spatial symmetries as  $\hat{H}_{nuc}$  in nuclear-motion theory. If we separate off the overall translation of the molecule, the translationally invariant molecular Hamiltonian may or may not have any discrete states, if it has, they end at the lowest dissociation threshold, which is generally unknown (see Section 2.7 and Figure 2).

One can introduce new coordinates in  $\hat{H}$ , in order to (a) separate off the overall translational motion, and (b) to describe the internal dynamics more efficiently. The choice of the coordinates (for the kinetic

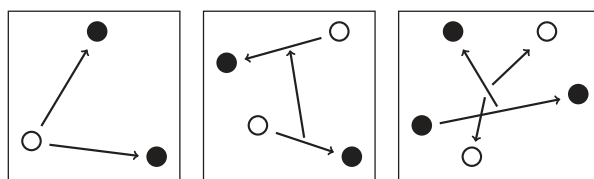


**Figure 1.** Example translationally invariant coordinates: coordinates of relative vectors within the many-particle system.

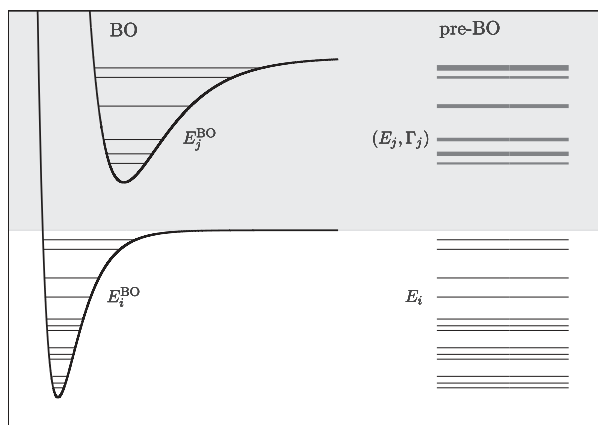


**Figure 2.** The ladder structure of the pre-Born–Oppenheimer (pre-BO) energy levels is visualised in the right. The left of the figure shows the rovibrational states corresponding to their respective potential energy surfaces in the Born–Oppenheimer (BO) approximation. While in the BO picture, the rovibrational states corresponding to the excited electronic state are bound states, the corresponding rovibronic states in pre-BO theory appear as resonances. [Reprinted with permission from E. Mátyus, *J. Phys. Chem. A* 117, 7195 (2013). Copyright 2013 American Chemical Society.]

energy operator) is a question of convenience. We could use some appropriate curvilinear system similarly to nuclear-motion theory. The motivation however for using laboratory-fixed Cartesian coordinates, similarly as in electronic structure theory, is provided by the aim to develop a generally applicable theoretical and computational framework, similarly to the recent electron-nuclear orbital theories [23–30], which have grown out from electronic-structure theory by incorporating (some of the) atomic nuclei in the quantum treatment. Furthermore, (laboratory-fixed) Cartesian coordinates will be the preferred choice for a generalisation to the relativistic regime.

Various direct and highly specialised techniques have been proposed in the literature [31–34] for the solution of the many-particle Schrödinger equation, Equation (4). Our approach, a variational solution method using explicitly correlated Gaussian basis functions (ECGs), is detailed in Section 2. ECGs [35,36] have been successfully used in electronic-structure theory [37] and their application for molecules and in general for few-particle quantum systems has been pioneered by Adamowicz and co-workers [18,19] and Suzuki and Varga [38]. An important year in the development of this field is 1993 when Kinghorn and Poshusta [39] and Kozłowski and Adamowicz [40] published tightly converged ECG-variational results for zero total angular momentum states of the  $\text{Ps}_2 = \{e^+, e^+, e^-, e^-\}$ , which can be thought of as a ‘quasi molecule’. Later, analytic energy gradients

were derived and implemented [41] to speed up the ECG-exponent optimisation, and this development resulted in a highly efficient approach for the computation of ‘real’ diatomic molecules [42,43]. The computational procedures developed by Adamowicz and co-workers have been recently extended to  $N = 1$  and  $N = 2$  total angular momentum quantum numbers (corresponding to natural parity) [44–47].

The diatomic formalism has been extended also to triatomic molecules in Ref. [48]. Practical computations have been carried out using another generally applicable basis set, in which the ECGs can have complex-valued parameters [49,50]. Computations with complex ECG basis functions are presently considered as a promising, practical generalisation towards polyatomic molecules.

Considerable effort has been devoted by Adamowicz and co-workers for the development and evaluation of leading relativistic corrections, the Darwin and mass-velocity terms, computed as expectation values with the non-Born–Oppenheimer wave functions. The original implementation [51] in 2006 was followed by several applications for ground and vibrationally excited states of diatomic molecules [52–57]. The largest diatomic molecule to date for which the ground-state non-Born–Oppenheimer energy (as well as leading relativistic corrections) were computed is the BH molecule including two nuclei and six electrons on the same footing in the quantum mechanical treatment [58].

Suzuki and Varga pioneered the development of flexible basis sets and their applications with the stochastic variational method for many-particle quantum systems with various spatial symmetries and the elegant derivation of the corresponding integral expressions [59–61]. Their formalism was successfully used for the computation of bound, resonance, and scattering states of positronium and excitonic complexes [62–69] with various quantum numbers.

## 2. Variational solution of the electron-nuclear Schrödinger equation with explicitly correlated Gaussian functions

A general  $(n_p + 1)$ -particle variational approach, which we call QUANTEN (QUANTum mechanical treatment of Electrons and atomic Nuclei), was developed in Refs. [20,70] for the solution of the time-independent many-particle Schrödinger equation, Equation (3), to obtain (absolute) molecular energies beyond spectroscopic accuracy<sup>2</sup> corresponding to various non-relativistic quantum numbers,  $N, N_z, p, S_a, M_{S_a}, S_b, M_{S_b}, \dots$ . Our aim was to avoid any *a priori* separation of the different particles, and thus the computational method is applicable over the entire physically

allowed range of the  $3(n_p + 1)$  physical parameters: the  $m_i$  mass, the  $q_i$  electric charge, and the  $s_i$  spin (bosonic or fermionic character) of the particles ( $i = 1, \dots, n_p + 1$ ). Details of the variational procedure are reviewed in the next subsections according to the following aspects:

- (1) Coordinates: translationally invariant (TI) or laboratory-fixed (LF) Cartesian coordinates
  - (2) Hamiltonian: TI and LF forms of the Hamiltonian
  - (3) Basis functions: ECGs with a polynomial prefactor and adapted to the spatial symmetries
  - (4) Matrix elements: analytic expressions with quasi-normalisation and pre-computed quantities using infinite-precision arithmetics
  - (5) Eigensolver: direct diagonalisation using LAPACK library routines, non-orthogonal basis sets, numerical treatment of near-linear dependencies
- (5 + 1) Parameterisation of the basis functions: the enlargement and refinement of the basis set with one function at a time, fast eigenvalue estimator, sampling-importance resampling, random walk or Powell's method for the refinement of the basis functions

## 2.1. Coordinates

Translationally invariant (TI) and centre-of-mass (CM) coordinates are obtained from the LF Cartesian coordinates,  $\mathbf{r}$ , by a linear transformation

$$\begin{pmatrix} \mathbf{x} \\ \mathbf{R}_{\text{CM}} \end{pmatrix} = (\mathbf{U} \otimes \mathbf{I}_3) \mathbf{r} \Leftrightarrow \mathbf{r} = (\mathbf{U}^{-1} \otimes \mathbf{I}_3) \begin{pmatrix} \mathbf{x} \\ \mathbf{R}_{\text{CM}} \end{pmatrix}, \quad (7)$$

where  $\mathbf{R}_{\text{CM}}$  labels the centre-of-mass coordinates and  $\mathbf{x}$  is invariant upon the overall translation of the system, if the constant matrix,  $\mathbf{U} \in \mathbb{R}^{(n_p+1) \times (n_p+1)}$ , has the following properties:

$$\sum_{j=1}^{n_p+1} U_{ij} = 0, \quad i = 1, \dots, n_p \quad \text{and} \quad U_{n_p+1,j} = m_j/m_{\text{tot}}, \quad j = 1, \dots, n_p + 1. \quad (8)$$

( $\mathbf{I}_3$  denotes the  $3 \times 3$  dimensional unit matrix). There are infinitely many possible TI coordinate sets (examples are shown in Figure 1), any two of them,  $\mathbf{x}$  and  $\mathbf{y}$ , are related by a linear transformation:

$$\begin{aligned} \begin{pmatrix} \mathbf{y} \\ \mathbf{R}_{\text{CM}} \end{pmatrix} &= (\mathbf{V}\mathbf{U}^{-1} \otimes \mathbf{I}_3) \begin{pmatrix} \mathbf{x} \\ \mathbf{R}_{\text{CM}} \end{pmatrix} \Leftrightarrow \begin{pmatrix} \mathbf{x} \\ \mathbf{R}_{\text{CM}} \end{pmatrix} \\ &= (\mathbf{U}\mathbf{V}^{-1} \otimes \mathbf{I}_3) \begin{pmatrix} \mathbf{y} \\ \mathbf{R}_{\text{CM}} \end{pmatrix} \end{aligned} \quad (9)$$

with

$$\begin{pmatrix} \mathbf{y} \\ \mathbf{R}_{\text{CM}} \end{pmatrix} = (\mathbf{V} \otimes \mathbf{I}_3) \mathbf{r} \Leftrightarrow \mathbf{r} = (\mathbf{V}^{-1} \otimes \mathbf{I}_3) \begin{pmatrix} \mathbf{y} \\ \mathbf{R}_{\text{CM}} \end{pmatrix}, \quad (10)$$

where  $\mathbf{V}$  satisfies the same conditions as  $\mathbf{U}$  in Equation (8).

## 2.2. Hamiltonian

Translationally invariant energies and wave functions are computed from a translationally invariant Hamiltonian [20], which is obtained from writing the kinetic energy operator in TI Cartesian coordinates, defined in Equations (7) and (8), and by subtracting the kinetic energy operator of the centre of mass. An alternative approach has been proposed in Refs. [22,71], which avoids any transformation of the operators and eliminates the translational contamination from the matrix elements of the  $(n_p + 1)$ -particle kinetic energy operator, Equation (5), during the course of the integral evaluation.

## 2.3. Basis functions

We approximate an eigenfunction corresponding to some spatial  $\lambda = (NM_N p)$  and spin  $\zeta = (S_a, M_{S_a}, S_b, M_{S_b}, \dots)$  quantum numbers as a linear combination of symmetry-adapted basis functions

$$\Psi^{[\lambda, \zeta]} = \sum_{I=1}^{N_b} c_I \Phi_I^{[\lambda, \zeta]}. \quad (11)$$

The  $I$ th basis function is a(n) (anti)symmetrised product of spatial and spin functions for (fermions) bosons

$$\Phi_I^{[\lambda, \zeta]}(\mathbf{r}, \sigma) = \hat{\mathcal{A}}\{\phi_I^{[\lambda]}(\mathbf{r}) \chi_I^{[\zeta]}(\sigma)\} \quad (12)$$

where the (anti)symmetrisation operator is

$$\hat{\mathcal{A}} = (N_{\text{perm}})^{-1/2} \sum_{p=1}^{N_{\text{perm}}} \varepsilon_p \hat{P}_p, \quad (13)$$

and  $N_{\text{perm}}$  is the total number of possible permutations of the identical particles in the system and  $\varepsilon_p$  is  $-1$  if the permutation operator,  $\hat{P}_p$ , contains an odd number of interchanges of identical fermions, otherwise  $\varepsilon_p$  is  $+1$ .

In order to define spatial basis functions, we first introduce geminal (or pair) functions as

$$\varphi(\mathbf{r}_1, \mathbf{r}_2) = \exp\left(-\frac{1}{2}\alpha_{12}|\mathbf{r}_1 - \mathbf{r}_2|^2\right) \quad (14)$$

$$= \exp\left(-\frac{1}{2}\mathbf{r}^T(\mathbf{A} \otimes \mathbf{I}_3)\mathbf{r}\right), \quad (15)$$

with

$$\mathbf{r} = \begin{pmatrix} \mathbf{r}_1 \\ \mathbf{r}_2 \end{pmatrix} \in \mathbb{R}^6 \quad \text{and}$$

$$\mathbf{A} = \begin{pmatrix} \mathbf{A}_{11} & \mathbf{A}_{12} \\ \mathbf{A}_{21} & \mathbf{A}_{22} \end{pmatrix} = \begin{pmatrix} \alpha_{12} & -\alpha_{12} \\ -\alpha_{12} & \alpha_{12} \end{pmatrix} \in \mathbb{R}^{2 \times 2}. \quad (16)$$

The geminal functions are generalised to  $(n_p + 1)$ -particle explicitly correlated Gaussian functions (ECGs) as:

$$\phi(\mathbf{r}; \mathbf{A}) = \prod_{i=1}^{n_p+1} \prod_{j>i}^{n_p+1} \exp\left(-\frac{1}{2}\alpha_{ij}|\mathbf{r}_i - \mathbf{r}_j|^2\right) \quad (17)$$

$$= \exp\left(-\frac{1}{2}\mathbf{r}^T(\mathbf{A} \otimes \mathbf{I}_3)\mathbf{r}\right) \quad (18)$$

with

$$\mathbf{r} = \begin{pmatrix} \mathbf{r}_1 \\ \dots \\ \mathbf{r}_{n_p+1} \end{pmatrix} \in \mathbb{R}^{3(n_p+1)} \quad (19)$$

and

$$A_{ij} = -\alpha_{ij}(1 - \delta_{ij}) + \left(\sum_{k=1, k \neq i}^{n_p+1} \alpha_{ij}\right) \delta_{ij}$$

$$(i, j = 1, \dots, n_p + 1). \quad (20)$$

The matrix form, Equations (15) and (18), makes it apparent that the functions have a general mathematical form for  $(n_p + 1)$  particles. It has been observed (see for example Ref. [20]) that in molecular applications with multiple heavy particles (nuclei), these basis functions are inefficient when sub-spectroscopic accuracy is sought for. In a first attempt to describe atomic nuclei more efficiently, we introduced ECGs with shifted centres, so-called ‘floating ECGs’:

$$\phi(\mathbf{r}; \mathbf{A}, \mathcal{R}) = \exp\left(-\frac{1}{2}(\mathbf{r} - \mathcal{R})^T(\mathbf{A} \otimes \mathbf{I}_3)(\mathbf{r} - \mathcal{R})\right), \quad (21)$$

where  $\mathcal{R}$  can be treated as a fixed or a variational parameter and thereby, it should provide a more efficient description for the atomic nuclei displaced from the origin (Section 3). It turned out however that the convergence rate of a molecular computation became worse with floating ECGs, Equation (21), than with origin-centred ECGs, Equation (18). This behaviour is explained by the fact that  $\phi(\mathbf{r}; \mathbf{A}, \mathcal{R})$  with an arbitrary  $\mathcal{R} \neq 0$  position vector is an eigenfunction of neither the total angular momentum operators,  $\hat{N}^2$  and  $\hat{N}_z$ , nor the parity. In the case of floating ECGs, the spatial symmetries of the eigenfunctions are restored numerically during the course of the

variational optimisation, which results in a substantial increase in the number of required basis functions.

In order to obtain very accurate numerical results for a molecular system, it is necessary to describe displaced atomic nuclei efficiently, and at the same time, account for the spatial symmetries of the system. In principle, it would be possible to project the floating ECGs, Equation (21), onto the irreps of the  $O(3)$  group (numerically). As an alternative, we use explicitly correlated Gaussians in conjunction with the global vector representation (ECG-GVR) [38,59,60]:

$$\phi^{[\lambda]}(\mathbf{r}; \mathbf{A}, \mathbf{u}, K) = \frac{1}{B_{KN}} \int d\hat{\mathbf{e}} Y_N^{M_N}(\hat{\mathbf{e}}) \left\{ \partial_a^{(2K+N)} g(\mathbf{r}; \mathbf{A}, \mathbf{a}\mathbf{u} \otimes \mathbf{e}) \right\}_{a=0, |\mathbf{e}|=1} \quad (22)$$

$$= |\mathbf{v}|^{2K+N} Y_N^{M_N}(\hat{\mathbf{v}}) \exp\left(-\frac{1}{2}\mathbf{r}^T(\mathbf{A} \otimes \mathbf{I}_3)\mathbf{r}\right), \quad (23)$$

which corresponds to an analytic projection of a generator function

$$g(\mathbf{r}; \mathbf{A}, \mathbf{a}\mathbf{u} \otimes \mathbf{e}) = \exp\left(-\frac{1}{2}\mathbf{r}^T(\mathbf{A} \otimes \mathbf{I}_3)\mathbf{r} + \mathbf{a}(\mathbf{u} \otimes \mathbf{e})^T \mathbf{r}\right) \quad (24)$$

with a so-called global vector

$$\mathbf{v} = (\mathbf{u} \otimes \mathbf{e})^T \mathbf{r} = \sum_{i=1}^{n_p+1} u_i \mathbf{r}_i. \quad (25)$$

Further notation used in Equations (22)–(23):  $\partial_a^{(2K+N)} = \partial^{(2K+N)}/\partial a^{(2K+N)}$ ,  $Y_N^{M_N}(\hat{\mathbf{e}})$  is the spherical harmonic function of degree  $N$  and order  $M_N$ ,  $\hat{\mathbf{e}} = (\theta, \phi)$  collects the polar angles characterising the orientation of the unit vector  $\mathbf{e}$ , and

$$B_{KN} = \frac{4\pi(2K+N)!(K+N+1)2^{N+1}}{K!(2K+2N+2)!} \quad (26)$$

with  $K$  and  $N \in \mathbb{N}_0$ . According to Ref. [60], the application of Equation (23) in a variational procedure is equivalent to using a basis set constructed by a hierarchical coupling of the subsystems angular momenta to a total angular momentum state with  $(N, M_N)$ . It is interesting to re-write a floating ECG function into the following form

$$\exp\left(-\frac{1}{2}(\mathbf{r} - \mathcal{R})^T(\mathbf{A} \otimes \mathbf{I}_3)(\mathbf{r} - \mathcal{R})\right)$$

$$= \exp\left(-\frac{1}{2}\mathcal{R}^T(\mathbf{A} \otimes \mathbf{I}_3)\mathcal{R}\right)$$

$$\exp\left(-\frac{1}{2}\mathbf{r}^T(\mathbf{A} \otimes \mathbf{I}_3)\mathbf{r} + \mathcal{R}^T(\mathbf{A} \otimes \mathbf{I}_3)\mathbf{r}\right), \quad (27)$$

which highlights its relation to the generator function of ECG-GVR. Alternatively, an ECG-GVR function can

be written in a form containing a polynomial prefactor, Equation (23), which highlights its effectiveness in describing vibrating molecular systems (at least for two heavy particles).

In the numerical results presented later in this section, we used ECG-GVR-type functions,  $\phi^{[\lambda]}(\mathbf{r}; \mathbf{A}, \mathbf{u}, K)$ , as spatial basis function and optimised all (non-linear) parameters—the  $\alpha_{ij}$  ( $\mathbf{A}$ ) exponents, the  $u_i$  ( $\mathbf{u}$ ), global-vector coefficients, and the  $K \in \mathbb{N}_0$  integer exponent of the polynomial prefactor—variationally. The transformation properties of these functions under TI coordinate transformations are equivalent to a simple transformation of the parameter vectors ( $\mathbf{u}$  in the global vector) and matrices ( $\mathbf{A}$  in the exponent). These transformation properties are conveniently exploited during the course of the analytic evaluation of the integrals (see for example Ref. [20,21,70–73], as well as in an efficient parameterisation scheme of the basis functions [22]). Due to the importance of these transformation relations (for the separation of the translational motion, in integral evaluations, and for efficient computations), we summarise them in the following equations:

$$|v|^{2K+N} Y_N^{MN}(\hat{\mathbf{v}}) \exp\left(-\frac{1}{2} \mathbf{r}^T (\mathbf{A} \otimes \mathbf{I}_3) \mathbf{r}\right) \quad (28)$$

$$= |v|^{2K+N} Y_N^{MN}(\hat{\mathbf{v}}) \exp\left(-\frac{1}{2} \mathbf{x}^T (\mathcal{A}^{(x)} \otimes \mathbf{I}_3) \mathbf{x}\right) \quad (29)$$

$$= |v|^{2K+N} Y_N^{MN}(\hat{\mathbf{v}}) \exp\left(-\frac{1}{2} \mathbf{y}^T (\mathcal{A}^{(y)} \otimes \mathbf{I}_3) \mathbf{y}\right), \quad (30)$$

where

$$\mathbf{A}^{(x)} = \mathbf{U}^{-T} \mathbf{A} \mathbf{U}^{-1} \Leftrightarrow \mathbf{A} = \mathbf{U}^T \mathbf{A}^{(x)} \mathbf{U} \quad \text{and} \quad (31)$$

$$\mathbf{A}^{(x)} = \begin{pmatrix} \mathcal{A}^{(x)} & 0 \\ 0 & c_A \end{pmatrix}$$

$$\mathbf{A}^{(y)} = \mathbf{V}^{-T} \mathbf{A} \mathbf{V}^{-1} \Leftrightarrow \mathbf{A} = \mathbf{V}^T \mathbf{A}^{(y)} \mathbf{V} \quad \text{and} \quad (32)$$

$$\mathbf{A}^{(y)} = \begin{pmatrix} \mathcal{A}^{(y)} & 0 \\ 0 & c_A \end{pmatrix}$$

and

$$\mathbf{A}^{(y)} = (\mathbf{U} \mathbf{V}^{-1})^T \mathbf{A}^{(x)} \mathbf{U} \mathbf{V}^{-1} \Leftrightarrow \quad (33)$$

$$\mathbf{A}^{(x)} = (\mathbf{V} \mathbf{U}^{-1})^T \mathbf{A}^{(y)} \mathbf{V} \mathbf{U}^{-1}.$$

and the global-vector coefficients transform as

$$\mathbf{u} = \mathbf{U}^T \mathbf{u}^{(x)} = \mathbf{V}^T \mathbf{u}^{(y)} \quad \text{and} \quad \mathbf{u}^{(x)} = (\mathbf{U} \mathbf{V}^{-1})^T \mathbf{u}^{(y)}. \quad (34)$$

## 2.4. Evaluation of the matrix elements

Matrix elements of an  $\hat{O}$  operator—e.g. identity, kinetic or potential energy operators,  $\hat{O} = \hat{I}, \hat{T}$  or  $\hat{V}$ , respectively—with the (anti)symmetrised products of the spin and spatial functions, Equations (22) and (23), are obtained by evaluating analytic expressions. In what follows, we summarise the main steps of the derivation of the analytic expressions and a few implementation aspects (further details can be found in Refs. [20,38,61]):

$$\begin{aligned} O_{IJ}^{[\lambda, \zeta]} &= \langle \Phi_I^{[\lambda, \zeta]} | \hat{O} | \Phi_J^{[\lambda, \zeta]} \rangle_{r, \sigma} \\ &= \langle \hat{\mathcal{A}} \{ \phi_I^{[\lambda]} \chi_I^{[\zeta]} \} | \hat{O} | \hat{\mathcal{A}} \{ \phi_J^{[\lambda]} \chi_J^{[\zeta]} \} \rangle_{r, \sigma} \\ &= \sum_{p=1}^{N_{\text{perm}}} \varepsilon_p \langle \phi_I^{[\lambda]} \chi_I^{[\zeta]} | \hat{O} | \hat{P}_p \{ \phi_J^{[\lambda]} \chi_J^{[\zeta]} \} \rangle_{r, \sigma} \\ &= \sum_{p=1}^{N_{\text{perm}}} \varepsilon_p \langle \phi_I^{[\lambda]} | \hat{O} | \hat{P}_p \phi_J^{[\lambda]} \rangle_r \langle \chi_I^{[\zeta]} | \hat{O} | \hat{P}_p \chi_J^{[\zeta]} \rangle_\sigma \\ &= \sum_{p=1}^{N_{\text{perm}}} c_{IJ_p}^{[\zeta]} O_{IJ_p}^{[\lambda]} \end{aligned} \quad (35)$$

with

$$\begin{aligned} c_{IJ_p}^{[\zeta]} &= \varepsilon_p \langle \chi_I^{[\zeta]} | \hat{O} | \hat{P}_p \chi_J^{[\zeta]} \rangle_\sigma \quad \text{and} \\ O_{IJ_p}^{[\lambda]} &= \langle \phi_I^{[\lambda]} | \hat{O} | \phi_J^{[\lambda]} \rangle_r, \end{aligned} \quad (36)$$

which are separate integrals of  $\hat{O}$  with the spin and the spatial functions, respectively. The  $c_{IJ_p}^{[\zeta]}$  term can be obtained by simple algebra (see for example Ref. [20]). The  $O_{IJ_p}^{[\lambda]}$  term contains multidimensional integrals of the spatial functions, Equation (22) and (23), for which analytic expressions are obtained by working out the formal operations in three steps.

*Step 1:* evaluation of the integral with the generator function:

$$I_{O,1}(\mathbf{s}, \mathbf{s}') = \langle g(\mathbf{r}; \mathbf{A}, \mathbf{s}) | \hat{O} | g(\mathbf{r}; \mathbf{A}', \mathbf{s}') \rangle_r \quad (37)$$

*Step 2:* expansion of the angular pre-factors:

$$\begin{aligned} I_{O,2}(\mathbf{e}, \mathbf{e}') &= \{ \partial_a^{2K+N} \partial_{a'}^{2K'+N} I_{O,1}(a\mathbf{u} \otimes \mathbf{e}, a'\mathbf{u}' \otimes \mathbf{e}') \}_{a=a'=0} \quad (38) \\ &\quad |_{|\mathbf{e}|=|\mathbf{e}'|=1} \end{aligned}$$

*Step 3:* evaluation of the angular integrals:

$$\begin{aligned} O^{[\lambda]} &= \frac{1}{B_{KN} B_{K'N}} \\ &\int d\hat{\mathbf{e}} \int d\hat{\mathbf{e}}' (Y_N^{MN}(\hat{\mathbf{e}}))^* Y_N^{MN}(\hat{\mathbf{e}}') I_{O,2}(\mathbf{e}, \mathbf{e}') \end{aligned} \quad (39)$$

The resulting expressions [20, 38, 61] are completely general for basis function with any  $N$  total angular



momentum quantum number and natural parity,  $(-1)^N$  (similar functions and working formulae with unnatural parity,  $(-1)^{N+1}$ , were introduced in Ref. [74]). It is important to mention that details of the computer implementation with finite precision arithmetics of the final expressions are critical in order to ensure the numerical stability and efficiency of molecular applications in which  $N+2K$  are larger than about 5. In particular, we had to introduce the so-called ‘quasi-normalisation’ of the basis functions and pre-compute and tabulate certain coefficients with infinite-precision arithmetics to be able to evaluate the final expressions in double precision arithmetics (this implementation was tested up to ca.  $2K = 40$  and  $N = 5-10$ ) [20].

## 2.5. Computation of bound states

### 2.5.1. Direct diagonalisation

The  $c_I$  linear combination coefficients in Equation (11) are obtained by solving the generalised eigenvalue problem:

$$\mathbf{H}\mathbf{c}_I = E_I\mathbf{S}\mathbf{c}_I. \quad (40)$$

The eigenvalues and eigenvectors are computed by replacing Equation (40) with the symmetric eigenvalue equation

$$\mathbf{H}'\mathbf{c}'_I = E_I\mathbf{c}'_I \quad (41)$$

by using Löwdin's procedure [75]

$$\mathbf{H}' = \mathbf{T}' + \mathbf{V}' \quad (42)$$

with

$$\mathbf{T}' = \mathbf{S}^{-1/2}\mathbf{T}\mathbf{S}^{-1/2} \quad \text{and} \quad \mathbf{V}' = \mathbf{S}^{-1/2}\mathbf{V}\mathbf{S}^{-1/2}. \quad (43)$$

### 2.5.2. Non-linear parameterisation strategy

**2.5.2.1. Parameter selection.** The nonlinear parameters for each basis function are selected and optimised based on the variational principle applicable for the ground and for a finite number of excited states (p. 27–29 of Ref. [38]). In practice, this optimisation strategy translates to the simple rule: the lower the energy, the better the parameter set. The parameter selection is carried out using the stochastic variational method [38], in which new basis functions are generated one by one. Trial values for the parameters of the spatial basis functions, Equation (22),  $K$ ,  $u_i$ ,  $\ln \alpha_{ij}$ , are drawn from discrete uniform, continuous uniform, and normal distributions, respectively. The optimal parameters of each distribution are estimated from short exploratory computations. Due to the one-by-one generation of the basis functions, the updated eigenvalues can be evaluated very efficiently [38] using the known eigenvalues and eigenvectors corresponding

to the old basis set, and this allows a rapid assessment of a trial set.

**2.5.2.2. Refinement.** The refinement of the basis-function parameters generated by the stochastic variational method is necessary if very accurate solutions are required. Similarly to the enlargement of the basis set, the basis functions are refined one after the other with the fast rank-1 eigenvalue update algorithm, which is used also for the selection of a new basis function from a set of randomly generated trials. Refined parameters are found by using Powell's method [76] started from the originally selected parameters for each basis function. The random-walk refinement can be used to adjust the  $K$  integer value (for which the Powell method is not applicable), however in practice it is usually sufficient to generate  $K$  from a discrete uniform distribution spread over a pre-optimised interval and to refine only the continuous variables,  $u_i$  and  $\alpha_{ij}$ . During the course of and at the end of the enlargement of the basis set, every basis function is refined in repeated cycles.

## 2.6. Computation of resonance states

### 2.6.1. Stabilisation technique

The stabilisation of eigenvalues of the real eigenvalue equation, Equation (40), is monitored with respect to the size of the basis set [77,78]. This simple application of the stabilisation method [79–82] allowed us to estimate the energy of long-lived resonances [70]. In order to gain access to the lifetimes (and in general, shorter-lived resonance positions and widths), it is necessary to estimate the box size corresponding to the increasing number of basis functions, which is a non-trivial task with ECG functions.

### 2.6.2. Complex-coordinate-rotation method

The application of the complex-coordinate-rotation method [83] requires the complex scaling of the coordinates according to the  $r \rightarrow re^{i\theta}$  replacement. The scaling rule is rather simple for both the kinetic energy and the Coulomb potential energy operators, and thus the Hamiltonian is scaled according to

$$\hat{H} = \hat{T} + \hat{V} \rightarrow \hat{H}(\theta) = e^{-2i\theta} \hat{T} + e^{-i\theta} \hat{V}. \quad (44)$$

The corresponding matrix equation is written as

$$\tilde{\mathbf{H}}(\theta)\tilde{\mathbf{c}}_i(\theta) = \mathcal{E}_i(\theta)\mathbf{S}\tilde{\mathbf{c}}_i(\theta), \quad (45)$$

which, similarly to its real analogue, Equation (40), is transformed to

$$\tilde{\mathbf{H}}'(\theta)\tilde{\mathbf{c}}'_i(\theta) = \mathcal{E}_i(\theta)\tilde{\mathbf{c}}'_i(\theta) \quad (46)$$

with

$$\begin{aligned}\tilde{\mathbf{H}}'(\theta) &= e^{-2i\theta} \mathbf{S}^{-1/2} \mathbf{T} \mathbf{S}^{-1/2} + e^{-i\theta} \mathbf{S}^{-1/2} \mathbf{V} \mathbf{S}^{-1/2} \\ &= \cos(2\theta) \mathbf{T}' + \cos(\theta) \mathbf{V}' \\ &\quad - i(\sin(2\theta) \mathbf{T}' + \sin(\theta) \mathbf{V}').\end{aligned}\quad (47)$$

The complex symmetric eigenproblem, Equation (46), is solved using LAPACK library routines [84], and the stabilisation point,  $\mathcal{E} = (E, -\Gamma/2)$  with the  $E$  energy and  $\Gamma$  width, in the complex energy plane is identified visually.

Although the complex analogue of the real variational principle [83] states that the exact solution is a stationary point in the complex plane with respect to the variational parameters and the scaling angle, there is not any practical algorithm for using this principle to optimise the basis set and to systematically improve the resonance parameters. The convergence of the resonance parameters is confirmed by achieving reasonable agreement within a series of computations with a varying number of basis functions and parameterisation (see also Section 2.7).

### 2.6.3. Parameterisation strategy

Due to the lack of any practical approach relying on the complex variational principle to select and optimise the non-linear parameters of the basis functions, we relied on the random generation of the parameters from some broad parameter intervals. In addition, we have devised a parameter-transfer approach [70], in which a parameter set optimised based on the real variational principle for bound states with one set of input parameters is transferred to a computation with other input parameters (e.g. different quantum numbers). Note that the spatial symmetries of a basis function are determined by the quantum numbers, Equation (23), and in this sense, the parameters  $K$ ,  $u_i$ , and  $\mathbf{A}$ , are transferable.

## 2.7. Variational results

Quantitative comparison of precision experiments and computations is possible if extremely accurate non-relativistic results are available and they are corrected also for relativistic and quantum electrodynamics (QED) effects. Such corrections have been computed in Ref. [85] for bound states of few-particle systems within a perturbative scheme which started from a very accurate Born–Oppenheimer solution. As an alternative route, efforts have been devoted to the a direct variational solution of the Dirac equation [86,87]. As to an intermediate approach, expectation values of the Breit–Pauli Hamiltonian were computed with the many-particle wave function, i.e. without evoking the BO approximation, to obtain relativistic corrections [88–90]. In the spirit

of this second direction, the present work focuses on the computational methodology of very accurate pre-Born–Oppenheimer energies and wave functions, which provides the starting point for a forthcoming computation of relativistic and QED corrections.

Within the non-relativistic regime, the determination of not only the ground but also the excited states with all possible combinations of the quantum numbers is a challenging task. What makes it particularly challenging is the fact that rovibrational states corresponding to excited electronic states—which can be rigorously defined only within the BO framework—, appear as bound states, whereas the corresponding rovibronic states in pre-BO theory are rigorously obtained as resonances, which are fully coupled to the dissociation continuum of the lower-lying electronic states (Figure 2, see also Section 1.4). This makes the computation and a systematic improvement of excited rovibronic states (with various non-relativistic quantum numbers) a highly challenging task. Nevertheless, if it is successfully realised, not only the energy position but also the predissociative lifetime is obtained, potentially from a full pre-BO computation. The following paragraphs review variational results obtained in a series of computations [20, 70] motivated by these ideas.

**2.7.0.1. Bound and resonances states of the positronium molecule,  $Ps_2 = \{e^+, e^+, e^-, e^-\}$ .** Computation of positronium complexes are extremely challenging for traditional quantum chemistry methods, because of the presence of positively charged light particles. At the same time, positronium complexes are excellent test systems for pre-BO methodological developments [20, 70]. The present ECG-GVR basis set has turned out to be particularly well-suited for positronium systems, which is qualitatively explained by their diffuse, delocalised internal structure in comparison with the localised atomic nuclei in molecular systems. Tightly converged energy levels were computed with basis functions including only low-order polynomial prefactors in Ref. [70]. (Due to the low-order polynomials in the basis functions, Equations (22) and (23), the results were obtained with a modest computational cost and this fact made the positronium complexes excellent systems for testing and developing the pre-BO method.) The basis function parameters were selected by minimising the energy of the lowest-lying state. The resulting basis set was well-suited for not only the lowest-energy bound state but also for a few low-energy resonance states.

The obtained bound-state energies and resonance parameters were in excellent agreement or improved upon the best results available in the literature (see Table 2 of Ref. [70]). We may think that the computed resonance

parameters were more accurate than earlier literature data, because the energies of nearby-lying bound states were improved (lowered) for which the (real) variational principle allows us to make a clear-cut assessment.

**2.7.0.2. Bound and resonances states of the hydrogen molecule,  $H_2 = \{p^+, p^+, e^-, e^-\}$ .** The first variational computations with explicitly correlated Gaussian functions and  $N > 0$  angular momentum quantum numbers carried out for the  $H_2$  molecule as an explicit four-particle system were reported in Refs. [20,70]. Both the ground and certain excited electronic states were considered. We note that exceedingly accurate pure vibrational states of the ground electronic state were computed earlier by the Adamowicz group [91]. Furthermore, very accurate rovibrational states corresponding to the ground electronic state were available from the non-adiabatic perturbation theory computations performed by Pachucki and Komasa [92].

Besides the ground electronic state, we could access electronically excited states by choosing different combinations of the non-relativistic quantum numbers in Ref. [70]. (Note that the electronic states exist only within the BO framework, and they are used here only to label the pre-BO states.) Thereby, we performed independent computations in four different blocks with natural parity:

$$\begin{aligned} \text{'X } ^1\Sigma_g^+ \text{ block': } N \geq 0, p &= (-1)^N, S_p = (1-p)/2, S_e \\ &= 0; \\ \text{'B } ^1\Sigma_u^+ \text{ block': } N \geq 0, p &= (-1)^N, S_p = (1+p)/2, S_e = \\ &0; \\ \text{'a } ^3\Sigma_g^+ \text{ block': } N \geq 0, p &= (-1)^N, S_p = (1-p)/2, S_e = \\ &1; \\ \text{'b } ^3\Sigma_u^+ \text{ block': } N \geq 0, p &= (-1)^N, S_p = (1+p)/2, S_e = \\ &1. \end{aligned}$$

The computations resulted in improved energies for some of the rotational states corresponding to electronically excited states (see Table 3 in Ref. [70]). For the lowest rotational states of the  $B^1\Sigma_u^+$  block, the newly computed energies were lower than those of Ref. [93] by ca.  $0.8 \mu E_h$ . Furthermore, the computed energies improved upon the first and the second rotational states of the  $a^3\Sigma_g^+$  block by a few tens of  $nE_h$  in comparison with the best earlier prediction [94].

In comparison with the positronium molecule, the basis-set parameterisation for the hydrogen molecule has turned out to be computationally far more demanding for the bound states and a really challenging task for the resonances. As to rovibrational (rovibronic) states corresponding to higher excited electronic states, they can be computed within the pre-BO framework

as resonances embedded in the continuum of the lowest-energy electronic state of their respective symmetry block (Figure 3). At present, there is not any existing, practical approach for the optimisation of basis functions for resonance states. Instead, we followed a practical strategy to gain access to some resonance states: we compiled a giant parameter set from all parameters obtained in bound-state optimisations with various combinations of the non-relativistic quantum numbers, and performed a search for resonance states using this large set (parameter-transfer approach). The stabilisation of certain points in the complex plane with respect to the scaling angle are visualised in Figure 3 for the  $X^1\Sigma_g^+$  and  $b^3\Sigma_u^+$  blocks with  $N = 0, 1$ , and 2 angular momentum quantum numbers (reproduced from Ref. [70]).

The  $X^1\Sigma_g^+$  block starts with the bound (ro)vibrational states corresponding to the ground electronic state,  $X^1\Sigma_g^+$ , which are along the real axis up to the first dissociation threshold,  $H(1) + H(1)$ , indicated with a black arrow in each subfigure. Before the start of the second dissociation limit,  $H(1) + H(2)$ , we identify (ro)vibrational (rovibronic) states which are assigned to the  $EF^1\Sigma_g^+$  electronic state (known from BO computations).

As to the  $b^3\Sigma_u^+$  block (see Figure 3), it starts with the first dissociation channel,  $H(1) + H(1)$ , and does not support any bound state (in agreement with our knowledge from BO and post-BO results). Before the  $H(1) + H(2)$  channel opens, we observe a series of vibrational states for  $N=0$ , which were assigned (based on their energies) to the  $e^3\Sigma_u^+$  electronic state. These states are located very close to the real axis, which indicates that they are long-lived resonances. It is interesting to note the appearance of a set of lower-energy states for  $N > 0$ . This set of states were assigned to the vibrational ( $R=0$  rotational angular momentum) and rovibrational ( $R=1$ ) states corresponding to the  $c^3\Pi_u^+$  electronic state (with  $L=1$  orbital angular momentum) for  $N=1$  and 2, respectively. This example highlights the coupling of the electronic orbital ( $\hat{L}$ ) and rotational angular ( $\hat{R}$ ) momenta to the total angular momentum ( $\hat{N}$ ), which is automatically included in our pre-BO approach. We note that the electronic,  $L$ , and rotational,  $R$ , angular momentum quantum numbers are non-exact quantum numbers in the full many-particle quantum treatment, but they are useful labels to describe properties of a state with some  $N$  total angular momentum quantum number.

Mátyus [70] gives a detailed account of the numerical results in comparison with the best available results in the literature: accurate adiabatic computations had been performed by Kołos and Rychlewski for the  $e^3\Sigma_u^+$  state [95], and accurate BO calculations are available for the  $c^3\Pi_u^+$

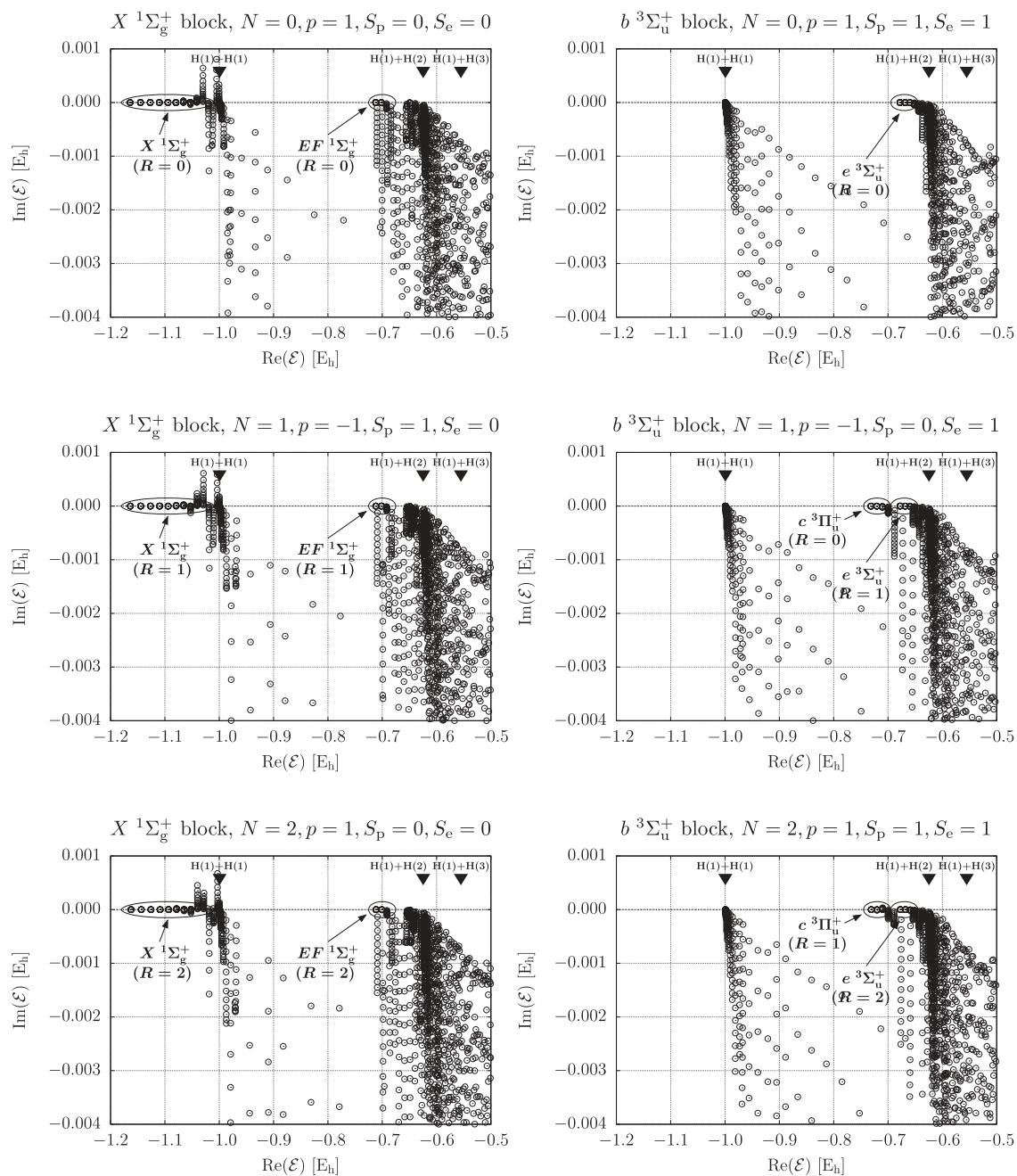


**Figure 3.** Part of the spectrum of the complex-scaled Hamiltonian,  $\mathcal{H}(\theta)$  with  $\theta \in [0.005, 0.065]$  for the  $X^1\Sigma_g^+$  block [ $p = (-1)^N$ ,  $S_p = (1-p)/2$ ,  $S_e = 0$ ] and for the  $b^3\Sigma_u^+$  block [ $p = (-1)^N$ ,  $S_p = (1+p)/2$ ,  $S_e = 1$ ] with  $N = 0, 1$ , and 2 total spatial angular momentum quantum numbers. The black triangles indicate the threshold energy of the dissociation continua corresponding to H(1)+H(1), H(1)+H(2), and H(1)+H(3). [Reprinted with permission from E. Mátyus, J. Phys. Chem. A 117, 7195 (2013). Copyright 2013 American Chemical Society.]

state from the same authors [96]. Mátyus [70] reported the first computational results for rotational excitations corresponding to the  $c^3\Pi_u^+$  electronic state, which can be obtained only by accounting for the coupling of rotational and electronic angular momenta (automatically included in our method).

It is also important to note that the results reviewed in the previous paragraphs provided accurate estimates for the energies. In order to pinpoint the widths and the related lifetimes, it will be necessary to optimise and/or enlarge the basis (and parameter) set. For this purpose, it will be necessary to develop a systematically improvable

basis-set optimisation approach, perhaps relying on the (complex) variational principle, which is applicable for unbound states.

### 3. Molecular structure from quantum mechanics

If the BO approximation is not introduced, the non-relativistic limit can be, in principle, approached arbitrarily close, and when relativistic and QED corrections are also included, computations come close or even challenge precision measurements. It is important to note however that the present-day theoretical foundations for the structure of molecules relies on the BO approximation: the molecular structure is identified with the equilibrium structure, which is defined as a local minimum of the potential energy surface. Interestingly, there is not available any rigorous and practical definition of the molecular structure independent of the BO approximation.<sup>3</sup>

In relation to the separation of the motion of the electrons and the atomic nuclei, which is commonplace in quantum chemistry, Hans Primas points out in his book [97]:

We describe the six degrees of freedom of the ground state of the helium atom (considered as 3-particle problem with the centre-of-mass motion separated) as a problem of two interacting particles in an external Coulomb potential. However, in the case of the molecule  $\text{H}_2^+$  we discuss the very same type of differential equation in an entirely different way, and split the 6 degrees of freedom into 1 vibrational mode, 2 rotational modes, and 3 electronic type degrees of freedom. This qualitatively different description does by no means follow from a purely mathematical discussion.

Following this observation, we would like to study the structure and possible structural changes within a series of three-particle systems including  $\text{H}^- = \{e^-, e^-, e^+\}$  as well as  $\text{H}_2^+ = \{p^+, p^+, e^-\}$ . At the same time, due to the lack of any definition of the molecular structure beyond the BO approximation, we may wonder how to study the structure of a molecular system without introducing the separation of the motion of the electrons and the atomic nuclei?

Observables in quantum mechanics are computed as the expectation value of the appropriate operator with the wave function of the system. It is straightforward to calculate expectation values of structural parameters with the (all-particle) molecular wave function. However, it is important to recognise that if we calculated the carbon nucleus-proton distance in an organic molecule, we would obtain a single  $\langle \Psi | r_{\text{CH}} | \Psi \rangle$  value [98–100] due to the quantum mechanical indistinguishability of identical particles. Another insightful example originates from an attempt to determine the structure of the  $\text{H}_3^+$  molecular

ion from an all-particle computation [98–100]. The calculation of the single expectation value of the HHH angle in  $\text{H}_3^+$  is not sufficient to distinguish between the linear and triangular arrangements of the three protons, since the expectation, i.e. average value,  $\langle \alpha_{\text{HHH}} \rangle = \langle \Psi | \alpha_{\text{HHH}} | \Psi \rangle$ , would be the same either for a linear  $\langle \alpha_{\text{HHH}} \rangle = (0^\circ + 180^\circ + 0^\circ)/3 = 60^\circ$  or for a triangular arrangement,  $\langle \alpha_{\text{HHH}} \rangle = (60^\circ + 60^\circ + 60^\circ)/3 = 60^\circ$  of the three protons.

Even if we considered the molecular Hamiltonian in which the atomic masses tend to infinity would not result in the electronic Hamiltonian,  $\hat{H}_{\text{el}}$ , for which we can define the equilibrium structure, because the infinite-mass limit leaves the nuclear position variables as multiplicative operators, whereas in  $\hat{H}_{\text{el}}$  they are multiplicative constants. Although considering the infinite mass limit may result in useful approximations, it does not provide us a direct mathematical link between the full molecular Hamiltonian,  $\hat{H}$  in Equation (4), and the electronic Hamiltonian,  $\hat{H}_{\text{el}}$  in Equation (1)

The general problem of the reconciliation of the classical molecular structure theory with a full many-particle quantum description has been recognised decades ago and was referred to as the *molecular structure conundrum* [101] (further relevant references include [101–104]).

#### 3.1. Probabilistic interpretation of the wave function

Claverie and Diner suggested in 1980 that appropriate marginal probability density functions calculated from the full wave function could be used to identify molecular structural features in the full electron-nuclear wave function [103]. In other words, structural parameters do not have sharp, dispersionless values, but they are characterised by some probability density function. This idea has been explored for the analytically solvable Hooke–Calogero model of molecules [105–108]. The atoms-in-molecule analysis has been extended to the realm of electron-nuclear quantum theory [109, 110]. Most recently, it was demonstrated that the proton density in methanol obtained from an electron-proton orbital computation (with fixed carbon and oxygen nuclei) can be matched with the spatial configuration obtained from a BO electron-structure calculation [111]. In addition, to the electronic and nuclear densities, flux densities have also been considered in Refs. [112–114].

For the sake of the present discussion, we shall stay with the analysis of (molecular) structure in terms of probability density functions calculated from the full wave function. Further general discussion of obtaining the classical molecular structure from quantum mechanics is provided in Section 3.2. In what follows, one-

and two-particle probability density functions [72,73] are introduced which will be used for the structural analysis later in this section. The probability density of selected particles measured from a ‘centre point’  $P$  fixed to the body is

$$\begin{aligned} D_{P,a_1 a_2 \dots a_n}^{(n)}(\mathbf{R}_1, \mathbf{R}_2, \dots, \mathbf{R}_n) \\ = \langle \Psi | \delta(\mathbf{r}_{a_1} - \mathbf{r}_P - \mathbf{R}_1) \delta(\mathbf{r}_{a_2} - \mathbf{r}_P - \mathbf{R}_2) \dots \\ \delta(\mathbf{r}_{a_n} - \mathbf{r}_P - \mathbf{R}_n) | \Psi \rangle \end{aligned} \quad (48)$$

with  $\mathbf{R}_i \in \mathbb{R}^3$  and the three-dimensional Dirac delta distribution,  $\delta(\mathbf{r})$ . The centre point  $P$  can be the centre of mass (denoted by ‘0’) or another particle. For a single particle, this density function is

$$D_{P,a}^{(1)}(\mathbf{R}_1) = \langle \Psi | \delta(\mathbf{r}_a - \mathbf{r}_P - \mathbf{R}_1) | \Psi \rangle. \quad (49)$$

For  $P = 0$ ,  $D_{0,a}^{(1)}$  is the spatial density of particle  $a$  around the centre of mass (‘0’), while for  $P = b$ ,  $D_{b,a}^{(1)}$  measures the probability density of the displacement vector connecting  $a$  and  $b$ .

Due to the overall space rotation-inversion symmetry,  $D_{P,a}^{(1)}(\mathbf{R}_1)$  is ‘round’ for  $N = 0, p = +1$  and the corresponding radial function is:

$$\rho_{P,a}(R) = D_{P,a}^{(1)}(\mathbf{R}_1) \quad (50)$$

with  $\mathbf{R}_1 = (0, 0, R)$  and  $R \in \mathbb{R}_0^+$ . We normalise the density functions to one (so, they measure the fraction of particles which can be found in an infinitesimally small interval  $dR$  around  $R$ ):

$$4\pi \int_0^\infty dR R^2 \rho_{P,a}(R) = 1. \quad (51)$$

The probability density function for the included  $a$ – $P$ – $b$  angle is obtained by integrating out the radii in the two-particle density measured from a centre point  $P$

$$\Gamma_{P,ab}(\alpha) = \int_0^\infty dR_1 R_1^2 \int_0^\infty dR_2 R_2^2 D_{P,ab}^{(2)}(\mathbf{R}_1, \mathbf{R}_2), \quad (52)$$

with

$$\begin{aligned} D_{P,ab}^{(2)}(\mathbf{R}_1, \mathbf{R}_2) \\ = \langle \Psi | \delta(\mathbf{r}_a - \mathbf{r}_P - \mathbf{R}_1) \delta(\mathbf{r}_b - \mathbf{r}_P - \mathbf{R}_2) | \Psi \rangle. \end{aligned} \quad (53)$$

The centre point,  $P$ , can be the centre of mass ( $P = 0$ ) or another particle ( $P = c$ ). Similarly to  $D_{P,a}^{(1)}(\mathbf{R}_1)$ ,  $D_{P,ab}^{(2)}(\mathbf{R}_1, \mathbf{R}_2)$  is also spherically symmetric for wave functions with  $N = 0, p = +1$ , and its numerical value depends only on the lengths  $R_1 = |\mathbf{R}_1|$ ,  $R_2 = |\mathbf{R}_2|$ , and

the  $\alpha$  included angle of the vectors  $\mathbf{R}_1$  and  $\mathbf{R}_2$  (for non-zero lengths). We normalise the angle density according to

$$8\pi^2 \int_0^\pi d\alpha \sin \alpha \Gamma_{P,ab}(\alpha) = 1. \quad (54)$$

In the next subsections, we continue with the study of the structural features of few-particle (‘atomic’ and ‘molecular’) quantum systems using the ‘radial’ and ‘angular’ probability density functions introduced in the previous equations.

### 3.1.1. Numerical demonstration of the $H^- \rightarrow H_2^+$ transition

Following Hans Primas’ observation (Figure 4) Ref. [72] studied the family of  $\{a^\pm, a^\pm, b^\mp\}$ -type three-particle Coulomb interacting systems with two identical particles and a third one. This family of systems is described with the Hamiltonian

$$\begin{aligned} \hat{H}(m_a, m_b, \mathbf{r}) = & -\frac{1}{2m_a} \Delta_{\mathbf{r}_1} - \frac{1}{2m_a} \Delta_{\mathbf{r}_2} - \frac{1}{2m_b} \Delta_{\mathbf{r}_3} \\ & + \frac{1}{|\mathbf{r}_1 - \mathbf{r}_2|} - \frac{1}{|\mathbf{r}_1 - \mathbf{r}_3|} - \frac{1}{|\mathbf{r}_2 - \mathbf{r}_3|}, \end{aligned} \quad (55)$$

for various  $m_a$  and  $m_b$  mass values and unit charges. (Note that the Hamiltonian is invariant to the inversion of the electric charges.) Furthermore, rescaling the masses by a factor  $\eta$  is equivalent to scaling the energy and shrinking the length by the factor  $\eta$

$$\hat{H}(\eta m_a, \eta m_b, \mathbf{r}) = \eta \hat{H}(m_a, m_b, \eta \mathbf{r}), \quad \forall \eta \in \mathbb{R} \setminus \{0\}. \quad (56)$$

Thereby, it is sufficient to consider only the  $m_a/m_b$  mass ratio to obtain qualitatively different eigenfunctions of Equation (55). It is also known that  $\hat{H}(m_a, m_b, \mathbf{r})$  has at least one bound state for all  $m_a/m_b$  values [115,116].

To numerically study the  $H^- \rightarrow H_2^+$  transition, the ground-state wave functions were computed in Ref. [72] for several  $m_a/m_b$  values using the variational procedure described in Section 2. Figure 5 shows the transition of the particle density,  $D_{0a}^{(1)}$ . It is interesting to note

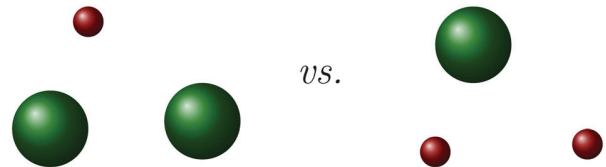


**Figure 4.** For the three-particle He atom and for the three-particle  $H_2^+$  molecular ion ‘we discuss the very same type of differential equation in an entirely different way’ [97] in the standard quantum chemistry approach.

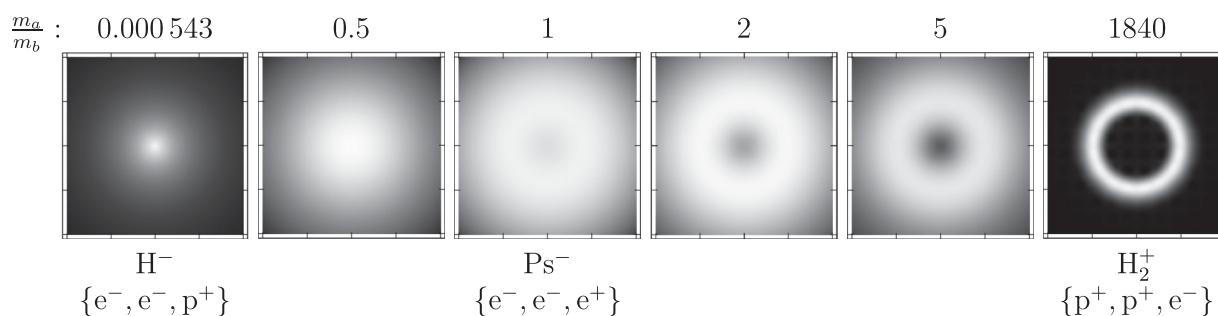


**Figure 5.** Transition of the ground-state particle density,  $D_{0a}^{(1)}$ , by increasing the  $m_a/m_b$  mass ratio in  $\{a^\pm, a^\pm, b^\mp\}$ -type systems [72]. The centre (0) of each plot is the centre of mass.

that the emergence of the particle shell is solely induced by the increase of  $m_a/m_b$  [72,73], while the symmetry-properties of the systems remain unchanged. All systems are ‘round’ in their ground state with  $N=0$  and  $p=+1$ . In Ref. [72] the transition point was numerically estimated to be between 0.4 and 0.8, which also suggests that the positronium anion,  $\text{Ps}^- = \{e^-, e^-, e^+\}$ , has some molecular character. The figure represents the  $\text{H}_2^+$  molecular ion as a shell. We may wonder whether it is possible to identify the relative position of the protons within the shell. For this purpose the angular density function,  $\Gamma_{0,pp'}$ , was calculated in Ref. [73], which demonstrated that the protons are indeed found at around antipodal points of the shell (remember that the centre of each plot is the centre of mass). As to earlier theoretical work, Kinsey and Fröman [117] and later Woolley [102] have anticipated similar results by considering the ‘mass polarisation’ in the translationally invariant Hamiltonian arising due to the separation of the centre of mass (note that the separation of the centre of mass is responsible also

for an important change of the spectral properties of the Hamiltonian discussed in Section 1.4). Furthermore, the proton shell has some finite width, which can be interpreted as the zero-point vibration in the BO picture. Recent work [118–120] has elaborated more on the transition properties and vibrational dynamics of this family of three-particle systems and determined the mass ratio where the transition takes place more accurately.

### 3.1.2. Numerical example for a triangular molecule

In the particle density plots, larger molecules would also be seen as ‘round’ objects in their eigenstates with zero total angular momentum and positive parity ( $N=0, p=+1$ ), and localised particles form shells around the molecular centre of mass. In order to demonstrate a non-trivial arrangement of the atomic nuclei within a molecule, the  $\text{H}_2\text{D}^+ = \{p^+, p^+, d^+, e^-, e^-\}$  molecular ion was studied in Ref. [73]. Interestingly, the qualitative features of the computed density functions (see Figure 6) converged very fast, small basis sets and

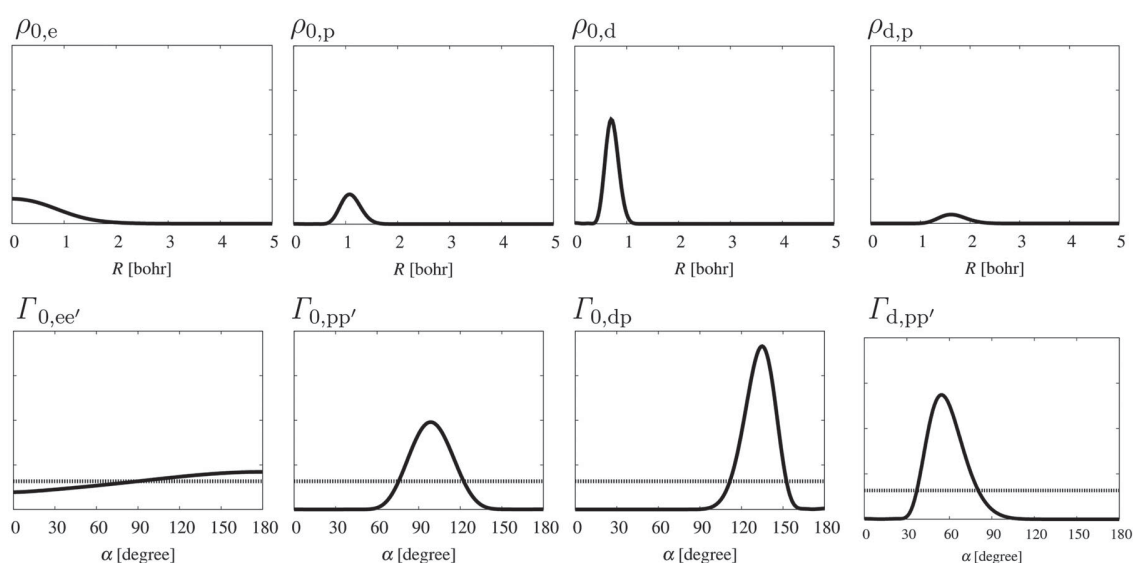


**Figure 6.** Radial,  $\rho_{ab}$ , and angular,  $\Gamma_{a,bc}$ , probability density functions computed for  $\text{H}_2\text{D}^+ = \{e^-, e^-, p^+, p^+, d^+\}$ .

a loose parameterisation was sufficient to observe converged structural features, whereas the energies were far from spectroscopic accuracy.

Figure 6 summarises the particle-density functions which highlight characteristic structural features of the system. First, we can observe the delocalised electron cloud ( $\rho_{0,e}$ ), the proton shell ( $\rho_{0,p}$ ), and the deuteron shell ( $\rho_{0,d}$ ) around the centre of mass (0). The deuteron shell is more peaked and more localised in comparison with the proton shell. (Remember that these plots show the spherically symmetric density along a ray,  $\rho_{ab}$ , and the density functions are normalised to one.)

Next, let's look at the probability density functions for the included angle,  $\Gamma_{0,ab}$ , of two particles measured from the molecular centre of mass ('0'). The dashed line in the plots shows the angular density corresponding to a hypothetical system in which the two particles ( $a$  and  $b$ ) are independent. It is interesting to note that for the two electrons  $\Gamma_{0,ee'}$  shows very small deviation from the (uncorrelated system's) dashed line. At the same time, we see a pronounced deviation from the dashed line for the nuclei,  $\Gamma_{0,pp'}$  and  $\Gamma_{0,pd}$ . These numerical observations are in line with Claverie and Diner's suggestion based on theoretical considerations [103] that molecular structure could be seen in an fully quantum-mechanical description as correlation effects for the nuclei.

As to the included angle of the two protons and the deuteron, the  $\Gamma_{d,pp'}$  probability density function has a maximum at around 60 degrees, which indicates the triangular arrangement of the nuclei. Due to the almost negligible amplitude of  $\Gamma_{d,pp'}$  at around 180 degrees the linear arrangement of the three nuclei (in the ground state) can be excluded. Thus, the structure of  $\text{H}_2\text{D}^+$  derived from our pre-BO numerical study is in agreement with the equilibrium structure (equilateral triangle) known from BO electronic-structure computations.

### 3.2. Classical structure from quantum mechanics

Relying on the probabilistic interpretation of quantum mechanics, the structure of  $\text{H}_2^+$  was visualised as a proton shell (Figure 5) with the protons found at around the antipodal points, and  $\text{H}_2\text{D}^+$  was seen as a proton shell and a deuteron shell within which the relative position of the three nuclei is dominated by a triangular arrangement (Figure 6). This analysis has demonstrated that *elements* of molecular structure can be *recognised* in the appropriate marginal probability densities calculated from the full electron-nuclear wave function. At the same time, a chemist would rather think about  $\text{H}_2^+$  as a (classical) rotating dumbbell (Figure 7) and  $\text{H}_2\text{D}^+$  as a (nearly) equilateral triangle. Although *elements* can be recognised

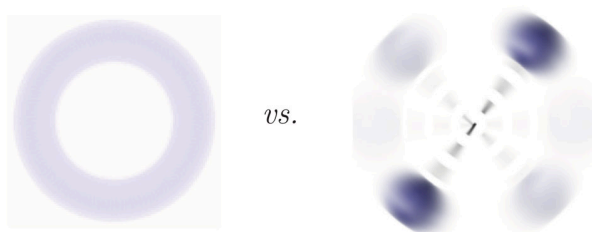


**Figure 7.** Quantum vs. classical structure of molecules: superposition or rotating dumbbell.

in the probability density functions, the link to the classical structure which chemists have used for more than a century to understand and design new reaction pathways for new materials, is not obvious [97,99,100,102,121,122].

In the next couple of paragraphs we briefly outline a promising direction which can offer a resolution to this puzzle. We collect the most relevant aspects and ideas, whereas their detailed exploration is left for future work in this field. In order to recover the classical molecular structure from a fully quantum mechanical treatment, it is necessary to obtain for a molecule

- the shape;
- the handedness: chiral molecules are found exclusively in their left- or right-handed version or in a classical mixture (called racemic mixture) of these mirror images but 'never' in their superposition;
- the individual labelling of the atomic nuclei (distinguishability).

Although it is possible to write down appropriate linear combinations (wave packets) of eigenstates of the full Hamiltonian, which satisfy these requirements at certain moments, we would like to recover these properties as permanent *molecular observables*. (Most recently, Grohmann and Manz [123] have pointed on the fact that it is impossible to form localised superpositions of quantum states of molecular rotors, which would coincide with our (semi)classical picture of methyl groups, due to the different spin part corresponding to the spatial functions which would be necessary for these superpositions.)

A possible resolution of the quantum-classical molecular structure puzzle will start out from the description of the molecule as an open quantum system being in interaction with an environment [124,125]. According to decoherence theory pointer states are selected by the continuous monitoring of the environment. As a result, the system's reduced density matrix (after tracing out the environmental degrees of freedom from the world's density matrix) written in this pointer basis evolves in time



so that its off-diagonal elements decay exponentially with some decoherence time, characteristic to the underlying microscopic interaction process with the environment (radiation or matter). This decay of the off-diagonal elements leads to the suppression of the interference terms between different pointer states, and results in a (reduced) density matrix the form of which corresponds to that of mixed states. Hence, this result can be *interpreted* as the emergence of the classical features in a quantum mechanical treatment.<sup>4</sup> So, decoherence theory allows us to identify pointer states, which are selected and remain stable as a result of the molecule's interaction with its environment.

It is interesting to note that important molecular properties (shape, handedness, atomic labels) break the fundamental symmetries of an isolated quantum system: the rotational and inversion symmetry, as well as the indistinguishability of identical particles. It remains a task to explore on a detailed microscopic level how and why these broken-symmetry states become pointer states of a molecular system.

- (a) *Shape*. Following the pioneering studies which have identified pointer states and confirmed their stability upon translational localisation [126–128] Ref. [129] provides a detailed account of the rotational decoherence of mesoscopic objects induced by a photon-gas environment or massive particles in thermal equilibrium. The qualitative conclusions are similar for the two different environments, but there are differences in the estimated decoherence time and its temperature dependence differ for the two environments. Orientational localisation of the mesoscopic ellipsoid takes place only if there are at least two directions for which the electric polarisabilities are different, and coherence is suppressed exponentially with the angular distance between two orientations.
- (b) *Handedness*. As to the chirality of molecules, the superselection phenomenon has been demonstrated in Ref. [130] by using a master equation [131] which describes the incoherent dynamics of the molecular state in the presence of the scattering of a lighter, thermalised background gas. Experimental conditions are predicted under which the tunnelling dynamics is suppressed between the left and right-handed configurations of  $D_2S_2$ .
- (c) *Individual labelling of the atomic nuclei*. Concerning the distinguishability of atomic nuclei, it remains a challenge to work out the detailed theoretical equations and to estimate the experimental conditions under which the individual labelling of quantum mechanically identical atomic nuclei (e.g. protons) emerges.

#### 4. Summary, conclusions, and future challenges

The direct solution of the full electron-nuclear Schrödinger equation, without the introduction of any kind of separation of the electronic and the nuclear motion, makes it possible to approach the non-relativistic limit arbitrarily close. We call this approach to the molecular problem pre-Born–Oppenheimer (pre-BO) theory in order to emphasise that the usual BO separation is avoided. The article presented details of our pre-BO computational method, which we call QUANTEN (Quantum mechanical treatment of Electrons and atomic Nuclei), using explicitly correlated Gaussian functions and the stochastic variational method with relevant citations to the pioneers of these computational techniques [18,19,38].

We have reviewed numerical results obtained for several bound and a couple of unbound states of three- and four-particle systems with various quantum numbers and with sub-spectroscopic accuracy in the energy. Although these computations are very demanding, they will allow us to test the results provided by more efficient, effective Hamiltonians obtained for example from non-adiabatic perturbation theory [92]. It is also interesting to notice that rovibrational states bound by an excited electronic state within the BO approximation are obtained as resonances within a pre-BO treatment with direct access to not only the energy but also to the finite predissociation lifetime of the state (due to rovibronic couplings). Numerical results demonstrating this idea were discussed for the hydrogen molecule.

At the moment, larger (polyatomic) systems can be addressed with a much reduced accuracy (in the energy) with the various existing pre-BO methods. Indeed, it has been an open problem for many years to define efficient basis functions and/or parameterisation strategies which make a pre-BO treatment amenable for polyatomics with (sub-)spectroscopic accuracy. As soon as polyatomic pre-BO computations of (sub-)spectroscopic accuracy will become possible (even if only a few states of selected non-relativistic quantum numbers can be computed), rigorous variational benchmark values will become available to the effective non-adiabatic theories, which can be efficiently used to compute all rovibrational (rovibronic) bound and many resonance states. At the moment results of these effective non-adiabatic computations can be compared only with experimentally measured spectroscopic transitions for which relativistic (and probably also some QED) correction must be included, which would also need to be validated. Already at the present stage and possibilities of pre-BO theory, less accurate computations of polyatomic molecules shed light to a long-standing problem: the

reconstruction of the chemist's (classical) molecular structure from a fully quantum mechanical description. We reviewed computational results, which allowed us to identify elements of the molecular structure from the full electron-nuclear wave function by inspecting and finding local maxima of appropriately defined marginal probability density functions.

We believe that this, currently less common, route to describe molecular systems, i.e., an equal quantum mechanical treatment of electrons and atomic nuclei, opens up great possibilities and also sets outstanding challenges for future theoretical work and for applications in comparison with the latest experimental developments. To conclude this article, we highlight three important directions to motivate further work in this old-new field of molecular quantum mechanics:

- (1) *Fully quantum mechanical developments for precision spectroscopy of small molecules* The comparison of precision measurements and highly accurate molecular computations for small and light molecules contributes to the testing of fundamental physical constants, e.g. the proton-to-electron mass ratio, the fine structure constant, or to pinpoint fundamental physical quantities, such as the proton radius, and to test fundamental physical theories [132,133]. For a meaningful comparison, it is mandatory to be able to solve the non-relativistic Schrödinger equation very accurately for several (bound and unbound) states of di- and polyatomic molecules and to account for the relativistic as well as QED effects.
- (2) *A hierarchy of approximate pre-BO methods* The idea of including the atomic nuclei in the quantum mechanical treatment of the electrons has been pursued in order to develop a systematically improvable, hierarchy of approximate pre-BO methods [23–29, 134,135]. An appealing feature of a pre-BO treatment is that it allows us to avoid the computation and fitting of the potential energy surface(s) and non-adiabatic coupling vectors (for multiple electronic states). At the moment, it appears to be technically and computationally extremely challenging to devise a practical, accurate, and systematically improvable hierarchy of approximate electron-nuclear methods applicable to larger, polyatomic molecules. Recently, a combination of electronic structure and quantum nuclear motion theory has been suggested [30,136], which aims to combine the best of the two worlds in a practical manner.
- (3) *Chemical observables from a fully quantum mechanical treatment* The definition of molecular structure within a fully quantum mechanical (pre-BO) description of molecules remains to be an unsettled

problem [97,99,100,102,121,122] either for a numerically 'exact' or an approximate treatment. Certainly, the probabilistic interpretation of the molecular wave function and the study of appropriate marginal probability densities provide useful pieces of information about the structure of a molecule. In order to arrive at a quantum molecular theory, in which the molecule is treated quantum mechanically as a whole, and at the same time the known chemical concepts are restored from the theoretical treatment, it is necessary to re-establish the shape, the handedness, and the individual labelling of the identical atomic nuclei. Interestingly, these important chemical properties break the fundamental symmetries of an isolated quantum system. The application of decoherence theory with realistic microscopic models for molecules offers a reasonable starting point for the reconstruction of these known classical chemical properties. The estimation of decoherence time for various environments and interactions has relevance for the practical realisation of quantum control and quantum computing experiments with molecules.

## Notes

1. We use the spectroscopists' notation [137] for the total angular momentum quantum number,  $N$ , instead of  $L$  that is commonly used in the physics literature.
2. The term "spectroscopic accuracy" is not uniquely defined but it is usually used to refer to computations providing vibrational transition wave numbers with an uncertainty better than  $1 \text{ cm}^{-1}$  ( $\approx 4.6 \mu\text{E}_h$ ) and even higher accuracy for rotational transitions.
3. For example, the IUPAC's Compendium of Chemical Terminology ('Gold Book') [138] defines the *equilibrium geometry* in terms of a potential energy surface, but we do not find anything beyond the BO approximation, apart from the definition of the primary, secondary, etc. structures of macromolecules. Interestingly, the *molecular shape* is defined in the Compendium.
4. There is an unsettled discussion concerning the mixed states of open quantum systems in terms of proper vs. improper mixtures, which is related to the quantum measurement problem [139,140].

## Acknowledgements

The author is indebted to Professors Brian Sutcliffe, Markus Reiher, Ulrich Müller-Herold, and Jürg Hutter, as well as to Dr. Benjamin Simmen and Andrea Muolo for their interest, discussions, and joint work over the years on various aspects of this topic.

## Disclosure statement

No potential conflict of interest was reported by the author.

## Funding

Financial support from a PROMYS Grant (no. IZ11Z0\_166525) of the Swiss National Science Foundation is gratefully acknowledged.

## ORCID

Edit Mátyus  <http://orcid.org/0000-0001-7298-1707>

## References

- [1] A.J. Rocke, in *Image & Reality: Kekulé, Kopp, and the Scientific Imagination (Synthesis)*, A Series in the History of Chemistry (The University of Chicago Press, Chicago and London, 2010).
- [2] E. Schrödinger, *Phys. Rev.* **28**, 1049 (1926).
- [3] M. Born and R. Oppenheimer, *Ann. der Phys.* **84**, 457 (1927).
- [4] M. Born, *Nachr. Akad. Wiss. Göttingen, math.-phys. Kl., math.-phys.-chem. Abtlg.* **6**, 1 (1951).
- [5] M. Born and K. Huang, *Dynamical Theory of Crystal Lattices* (Clarendon Press, Oxford, 1954).
- [6] B.T. Sutcliffe and R.G. Woolley, in *The Potential Energy Surface in Molecular Quantum Mechanics* (Springer International Publishing Switzerland, 2013), vol. 27 of *Advances in Quantum Methods and Applications in Chemistry, Physics, and Biology*, *Progress in Theoretical Chemistry and Physics*, pp. 3–40.
- [7] B.T. Sutcliffe and R.G. Woolley, *J. Chem. Phys.* **137**, 22A544 (2012).
- [8] B.T. Sutcliffe, *Coordinate Systems and Transformations*, in *Handbook of Molecular Physics and Quantum Chemistry*, edited by S. Wilson (John Wiley & Sons, Inc., Chichester, 2003a), Vol. 1, pp. 485–500.
- [9] B.T. Sutcliffe, *Molecular Hamiltonians*, in *Handbook of Molecular Physics and Quantum Chemistry*, edited by S. Wilson (John Wiley & Sons, Inc., Chichester, 2003b), Vol. 1, pp. 501–525.
- [10] D. Luckhaus, *J. Chem. Phys.* **113**, 1329 (2000).
- [11] D. Lauvergnat and A. Nauts, *J. Chem. Phys.* **116**, 8560 (2002).
- [12] N. Yurchenko, W. Thiel and P. Jensen, *J. Mol. Spectrosc.* **245**, 126 (2007).
- [13] E. Mátyus, G. Czakó and A.G. Császár, *J. Chem. Phys.* **130**, 134112 (2009).
- [14] C. Fábri, E. Mátyus and A.G. Császár, *J. Chem. Phys.* **134**, 074105 (2011).
- [15] S.N. Yurchenko, J. Tennyson, J. Bailey, M.D.J. Hollis and G. Tinetti, *Proc. Nat. Acad. Sci. USA* **111**, 9379 (2014).
- [16] J. Tennyson, *J. Chem. Phys.* **145**, 120901 (2016).
- [17] T. Carrington, Jr., *J. Chem. Phys.* **146**, 120902 (2017).
- [18] M. Cafiero, S. Bubin and L. Adamowicz, *Phys. Chem. Chem. Phys.* **5**, 1491 (2003).
- [19] S. Bubin, M. Pavanello, W.-C. Tung, K.L. Sharkey and L. Adamowicz, *Chem. Rev.* **113**, 36 (2013).
- [20] E. Mátyus and M. Reiher, *J. Chem. Phys.* **137**, 024104 (2012).
- [21] B. Simmen, E. Mátyus and M. Reiher, *J. Chem. Phys.* **141**, 154105 (2013a).
- [22] A. Muolo, E. Mátyus and M. Reiher, *J. Chem. Phys.* **148**, 084112 (2018).
- [23] H. Nakai, *Int. J. Quant. Chem.* **86**, 511 (2002).
- [24] A.D. Bochevarov, E.F. Valeev and C.D. Sherrill, *Mol. Phys.* **102**, 111 (2004).
- [25] A. Chakraborty, M.V. Pak and S. Hammes-Schiffer, *J. Chem. Phys.* **129**, 014101 (2008).
- [26] T. Ishimoto, M. Tachikawa and U. Nagashima, *Int. J. Quant. Chem.* **109**, 2677 (2009).
- [27] A. Sirjoosingh, M.V. Pak, C. Swalina and S. Hammes-Schiffer, *J. Chem. Phys.* **139**, 034102 (2013).
- [28] N.F. Aguirre, P. Villarreal, G. Delgado-Barrio, E. Posada, A. Reyes, M. Biczysko, A.O. Mitrushchenkov and M.P. de Lara-Castells, *J. Chem. Phys.* **138**, 184113 (2013).
- [29] R. Flores-Moreno, E. Posada, F. Moncada, J. Romero, J. Charry, M. Díaz-Tinoco, S.A. González, N.F. Aguirre and A. Reyes, *Int. J. Quant. Chem.* **114**, 50 (2013).
- [30] P. Cassam-Chenaï, B. Suo and W. Liu, *Phys. Rev. A* **92**, 012502 (2015).
- [31] D.M. Bishop and L.M. Cheung, *Chem. Phys. Lett.* **79**, 130 (1981).
- [32] V.I. Korobov, *Phys. Rev. A* **61**, 064503 (2000).
- [33] J.P. Karr and L. Hilico, *J. Phys. B: At. Mol. Opt. Phys.* **39**, 2095 (2006).
- [34] K. Pachucki, M. Zientkiewicz and V. Yerokhin, *Comput. Phys. Commun.* **208**, 162 (2016).
- [35] J. Rychlewski, ed., *Explicitly Correlated Wave Functions in Chemistry and Physics* (Kluwer Academic Publishers, Dordrecht, 2003).
- [36] J. Mitroy, S. Bubin, W. Horiuchi, Y. Suzuki, L. Adamowicz, W. Cencek, K. Szalewicz, J. Komasa, D. Blume and K. Varga, *Rev. Mod. Phys.* **85**, 693 (2013).
- [37] L. K. F. A. Bischoff and E. F. Valeev, *Chem. Rev.* **112**, 75 (2012).
- [38] Y. Suzuki and K. Varga, *Stochastic Variational Approach to Quantum-Mechanical Few-Body Problems* (Springer-Verlag, Berlin, 1998).
- [39] D.B. Kinghorn and R.D. Poshusta, *Phys. Rev. A* **47**, 3671 (1993).
- [40] P.M. Kozłowski and L. Adamowicz, *Phys. Rev. A* **48**, 1903 (1993).
- [41] D.B. Kinghorn and R.D. Poshusta, *Int. J. Quant. Chem.* **62**, 223 (1997).
- [42] D.B. Kinghorn and L. Adamowicz, *J. Chem. Phys.* **110**, 7166 (1999a).
- [43] D.B. Kinghorn and L. Adamowicz, *Phys. Rev. Lett.* **83**, 2541 (1999b).
- [44] N. Kirnosov, K.L. Sharkey and L. Adamowicz, *J. Phys. B: At. Mol. Opt. Phys.* **48**, 195101 (2015).
- [45] K. Jones, M. Formanek, R. Mazumder, N. Kirnosov and L. Adamowicz, *Mol. Phys.* **114**, 1634 (2016a).
- [46] K. Jones, N. Kirnosov, K.L. Sharkey and L. Adamowicz, *Mol. Phys.* **114**, 2052 (2016b).
- [47] K. Jones, M. Formanek and L. Adamowicz, *Chem. Phys. Lett.* **669**, 188 (2017).
- [48] E. Bednarz, S. Bubin and L. Adamowicz, *Mol. Phys.* **103**, 1169 (2005).
- [49] S. Bubin and L. Adamowicz, *J. Chem. Phys.* **124**, 224317 (2006).
- [50] S. Bubin and L. Adamowicz, *J. Chem. Phys.* **128**, 114107 (2008).
- [51] D. Kedziera, M. Stanke, S. Bubin, M. Barysz and L. Adamowicz, *J. Chem. Phys.* **125**, 084303 (2006).


- [52] M. Stanke, S. Bubin, M. Molski and L. Adamowicz, *Phys. Rev. A* **79**, 032507 (2009).
- [53] S. Bubin, M. Stanke, M. Molski and L. Adamowicz, *Chem. Phys. Lett.* **494**, 21 (2010a).
- [54] S. Bubin, M. Stanke and L. Adamowicz, *Chem. Phys. Lett.* **500**, 229 (2010b).
- [55] S. Bubin, M. Stanke and L. Adamowicz, *J. Chem. Phys.* **134**, 024103 (2011a).
- [56] S. Bubin, M. Stanke and L. Adamowicz, *Phys. Rev. A* **83**, 042520 (2011b).
- [57] S. Bubin, M. Stanke and L. Adamowicz, *J. Chem. Phys.* **135**, 074110 (2011c).
- [58] S. Bubin, M. Stanke and L. Adamowicz, *J. Chem. Phys.* **131**, 044128 (2009).
- [59] K. Varga and Y. Suzuki, *Phys. Rev. C* **52**, 2885 (1995).
- [60] Y. Suzuki, J. Usukura and K. Varga, *J. Phys. B: At. Mol. Opt. Phys.* **31**, 31 (1998).
- [61] T. Joyce and K. Varga, *J. Chem. Phys.* **144**, 184106 (2016).
- [62] J. Usukura, K. Varga and Y. Suzuki, *Phys. Rev. A* **58**, 1918 (1998).
- [63] G. Ryzhikh, J. Mitroy and K. Varga, *J. Phys. B: At. Mol. Opt. Phys.* **31**, 3965 (1998).
- [64] K. Varga, J. Usukura and Y. Suzuki, *Phys. Rev. Lett.* **80**, 1876 (1998).
- [65] J. Usukura, Y. Suzuki and K. Varga, *Phys. Rev. B* **59**, 5652 (1999).
- [66] Y. Suzuki and J. Usukura, *Nucl. Instrum. Methods Phys. Res. B* **171**, 67 (2000).
- [67] I.A. Ivanov, J. Mitroy and K. Varga, *Phys. Rev. Lett.* **87**, 063201 (2001).
- [68] J.Z. Mezei, J. Mitroy, R.G. Lovas and K. Varga, *Phys. Rev. A* **64**, 032501 (2001).
- [69] E.A.G. Armour, J.-M. Richard and K. Varga, *Phys. Rep.* **413**, 1 (2005).
- [70] E. Mátyus, *J. Phys. Chem. A* **117**, 7195 (2013).
- [71] B. Simmen, E. Mátyus and M. Reiher, *Mol. Phys.* **111**, 2086 (2013b).
- [72] E. Mátyus, J. Hutter, U. Müller-Herold and M. Reiher, *Phys. Rev. A* **83**, 052512 (2011a).
- [73] E. Mátyus, J. Hutter, U. Müller-Herold and M. Reiher, *J. Chem. Phys.* **135**, 204302 (2011b).
- [74] Y. Suzuki, W. Horiuchi, M. Orabi and K. Arai, *Few-Body Syst.* **42**, 33 (2008).
- [75] I. Mayer, *Simple Theorems, Proofs, and Derivations in Quantum Chemistry* (Kluwer Academic/Plenum Publishers, New York, 2003).
- [76] M.J.D. Powell, *The NEWUOA Software for Unconstrained Optimization without Derivatives (DAMTP 2004/NA05)*, Report no. NA2004/08. <<http://www.damtp.cam.ac.uk/user/na/reports04.html>> last accessed on January 18, 2013.
- [77] J. Usukura and Y. Suzuki, *Phys. Rev. A* **66**, 010502(R) (2002).
- [78] Y. Suzuki and J. Usukura, *Nucl. Instrum. Methods Phys. Res. B* **221**, 195 (2004).
- [79] A.U. Hazi and H.S. Taylor, *Phys. Rev. A* **1**, 1109 (1970).
- [80] H.S. Taylor and A.U. Hazi, *Phys. Rev. A* **14**, 2071 (1976).
- [81] V.A. Mandelshtam, H.S. Taylor, V. Ryaboy and N. Moiseyev, *Phys. Rev. A* **50**, 2764 (1994).
- [82] J. Müller, X. Yang and J. Burgdörfer, *Phys. Rev. A* **49**, 2470 (1994).
- [83] V.I. Kukulin, V.M. Krasnopolsky and J. Horáček, *Theory of Resonances—Principles and Applications* (Kluwer, Dordrecht, 1988).
- [84] E. Anderson, Z. Bai, C. Bischof, S. Blackford, J. Demmel, J. Dongarra, J. Du Croz, A. Greenbaum, S. Hammarling and A. McKenney, et al., *LAPACK Users' Guide*, 3rd ed. (Society for Industrial and Applied Mathematics, Philadelphia, PA, 1999), ISBN 0-89871-447-8 (paperback).
- [85] K. Piszczatowski, G. Lach, M. Przybytek, J. Komasa, K. Pachucki and B. Jeziorski, *J. Chem. Theo. Comp.* **5**, 3039 (2009).
- [86] B. Simmen, E. Mátyus and M. Reiher, *J. Phys. B* **48**, 245004 (2015).
- [87] B. Simmen, *Developments for a Relativistic Many-1/2-Fermion Theory*, PhD thesis ETH Zürich, Nr. 22363 (2015). <<http://dx.doi.org/10.3929/ethz-a-010398188>> .
- [88] M. Stanke and L. Adamowicz, *J. Phys. Chem. A* **117**, 10129 (2013).
- [89] M. Stanke, J. Jurkowski and L. Adamowicz, *J. Phys. B* **50**, 065101 (2017).
- [90] V.I. Korobov, L. Hilico and J. Karr, *Phys. Rev. A* **74**, 040502(R) (2006).
- [91] S. Bubin and L. Adamowicz, *J. Chem. Phys.* **118**, 3079 (2003).
- [92] K. Pachucki and J. Komasa, *J. Chem. Phys.* **130**, 164113 (2009).
- [93] L. Wolniewicz, T. Orlikowski and G. Staszewska, *J. Mol. Spectrosc.* **238**, 118 (2006).
- [94] L. Wolniewicz, *Mol. Phys.* **105**, 1497 (2007).
- [95] W. Kołos and J. Rychlewski, *J. Mol. Spectrosc.* **143**, 237 (1990).
- [96] W. Kołos and J. Rychlewski, *J. Mol. Spectrosc.* **66**, 428 (1977).
- [97] H. Primas, *Chemistry, Quantum Mechanics and Reductionism: Perspectives in Theoretical Chemistry* (Springer-Verlag, Berlin, 1981).
- [98] M. Cafiero and L. Adamowicz, *Chem. Phys. Lett.* **387**, 136 (2004).
- [99] B.T. Sutcliffe and R.G. Woolley, *Phys. Chem. Chem. Phys.* **7**, 3664 (2005).
- [100] B.T. Sutcliffe and R.G. Woolley, *Chem. Phys. Lett.* **408**, 445 (2005).
- [101] S.J. Weininger, *J. Chem. Educ.* **61**, 939 (1984).
- [102] R.G. Woolley, *Adv. Phys.* **25**, 27 (1976).
- [103] P. Claverie and S. Diner, *Isr. J. Chem.* **19**, 54 (1980).
- [104] J.G.R. Tostes, *Theor. Chim. Acta* **59**, 229 (1981).
- [105] U. Müller-Herold, *J. Chem. Phys.* **124**, 014105 (2006).
- [106] U. Müller-Herold, *Eur. Phys. J. D* **49**, 311 (2008).
- [107] E.V. Ludeña, L. Echevarría, X. Lopez and J.M. Ugalde, *J. Chem. Phys.* **136**, 084103 (2012).
- [108] M. Becerra, V. Posligua, and E.V. Ludeña, *Int. J. Quant. Chem.* **113**, 1584 (2013).
- [109] M. Goli and S. Shahbazian, *Theor. Chim. Acta* **129**, 235 (2011).
- [110] M. Goli and S. Shahbazian, *Theor. Chim. Acta* **131**, 1208 (2012).
- [111] T. Kato and K. Yamanouchi, *Phys. Rev. A* **85**, 034504 (2012).
- [112] J.F. Pérez-Torres, *Phys. Rev. A* **87**, 062512 (2013).

- [113] J.F. Pérez-Torres, J. Phys. Chem. A **119**, 2895 (2015).
- [114] V. Pohl and J.C. Tremblay, Phys. Rev. A **93**, 012504 (2016).
- [115] A. Martin, J.-M. Richard and T.T. Wu, Phys. Rev. A **46**, 3697 (1992).
- [116] A.A. Farajian, K. Esfarjani and Y. Kawazoe, J. Phys. B **32**, 749 (1999).
- [117] A. Fröman and J.L. Kinsey, Phys. Rev. **123**, 2077 (1961).
- [118] F.L. Andrew, W. King and H. Cox, J. Chem. Phys. **139**, 224306 (2013).
- [119] A.W. King, L.C. Rhodes and H. Cox, Phys. Rev. A **93**, 022509 (2016).
- [120] A.L. Baskerville, A.W. King and H. Cox, Phys. Rev. A **94**, 042512 (2016).
- [121] F. Hund, Z. Phys. **43**, 805 (1927).
- [122] P. Cassam-Chenaï, Chem. Phys. Lett. **420**, 354 (2006).
- [123] T. Grohmann and J. Manz, Mol. Phys. **116**, 2538 (2018).
- [124] E. Joos, H. Zeh, C. Kiefer, D. Giulini, J. Kupsch, and I. Stamatescu, *Decoherence and the Appearance of a Classical World in Quantum Theory*, 2nd ed. (Springer-Verlag, Berlin Heidelberg New York, 2003).
- [125] M. Schlosshauer, *Decoherence and the Quantum-to-Classical Transition* (Springer, Berlin, 2007).
- [126] K. Hornberger and J.E. Sipe, Phys. Rev. A **68**, 012105 (2003).
- [127] S.L. Adler, J. Phys. A: Math. Theor. **39**, 14067 (2006).
- [128] M. Busse and K. Hornberger, J. Phys. A: Math. Theor. **43**, 015303 (2009).
- [129] C. Zhong and F. Robicheaux, Phys. Rev. A **94**, 052109 (2016).
- [130] J. Trost and K. Hornberger, Phys. Rev. Lett. **103**, 023202 (2009).
- [131] K. Hornberger, Eur. Phys. Lett. **77**, 50007 (2007).
- [132] J.-P. Karr, S. Patra, J. Koelemeij, J. Heinrich, N. Sillitoe, A. Douillet and L. Hilico, J. Phys.: Conf. Ser. **723**, 012048 (2016).
- [133] W. Ubachs, J. Koelemeij, K. Eikema and E. Salumbides, J. Mol. Spectrosc. **320**, 1 (2016).
- [134] T. Ishimoto, M. Tachikawa and U. Nagashima, J. Chem. Phys. **128**, 164118 (2008).
- [135] A. Sirjoosingh, M.V. Pak, K.R. Brorsen and S. Hammes-Schiffer, J. Chem. Phys. **142**, 214107 (2015).
- [136] P. Cassam-Chenaï, B. Suo and W. Liu, Theor. Chim. Acta **136**, 52 (2017).
- [137] E. Cohen, T. Cvitaš, J. Frey, B. Holmström, K. Kuchitsu, R. Marquardt, I. Mills, F. Pavese, M. Quack, J. Stohner, H. Strauss, M. Takami and A.J. Thor, *Quantities, Units and Symbols in Physical Chemistry* (the IUPAC Green Book - 3rd edition) (RSC Publishing, Cambridge, 2007).
- [138] IUPAC Compendium of Chemical Terminology—the Gold Book. < <https://goldbook.iupac.org/> > last accessed on February 28, 2018..
- [139] S. Fortin, O. Lombardi and J.C.M. González, Found. Chem. **18**, 225 (2016).
- [140] G. Bacciagaluppi, *The Role of Decoherence in Quantum Mechanics*, The Stanford Encyclopedia of Philosophy (Fall 2016 Edition), Edward N. Zalta (ed.). < <https://plato.stanford.edu/archives/fall2016/entries/qm-decoherence/> > last accessed on February 28, 2018.

## Computation of rovibronic resonances of molecular hydrogen: $EF\ ^1\Sigma_g^+$ inner-well rotational states

Dávid Ferenc and Edit Mátyus<sup>\*</sup>

*Institute of Chemistry, ELTE, Eötvös Loránd University, Pázmány Péter sétány 1/A, Budapest, H-1117, Hungary*

 (Received 18 April 2019; published 26 August 2019)

Selected states of the  $EF\ ^1\Sigma_g^+$  electronic manifold of the hydrogen molecule are computed as resonances of the four-body problem. Systematic improvement of the basis representation for the variational treatment is achieved through an energy-tracking optimization procedure. The resulting nonrelativistic energy is converged within a few nano-Hartree, while the predissociative width is found to be negligible at this level of accuracy. The four-particle nonrelativistic energies are appended with relativistic and quantum electrodynamics corrections which close the gap between the experimental observations and earlier theoretical work.

DOI: [10.1103/PhysRevA.100.020501](https://doi.org/10.1103/PhysRevA.100.020501)

The lowest-energy rotational and vibrational states of the ground electronic state of the hydrogen molecule have received much attention over the past decade. We have witnessed several orders of magnitude improvement in terms of accuracy and precision in both experimental [1–4] and theoretical [5,6] frontiers of molecular physics.

The hydrogen molecule has several electronically excited states, and many of them are very interesting on their own, e.g., the famous double-well features caused by avoided crossings. The rovibronic level structure is dominated by nonadiabatic interactions among the states which are not yet fully, quantitatively understood. Meanwhile, many of these electronically excited states have been measured experimentally to high precision [3,7], and rovibronic states corresponding to electronic excitations, e.g., the  $EF$  and  $GK\ ^1\Sigma_g^+$  manifolds, have been used in excitation sequences, resulting in ultraprecise dissociation energy of the lowest rovibrational levels of the ground electronic state [2–4]. Therefore, it is not only of purely theoretical interest to aim for a better and more complete theoretical description of electronically excited states of the hydrogen molecule. In particular, the entire dynamical range of molecular hydrogen, which has already been experimentally studied, spans a  $130\,000\text{ cm}^{-1}$  broad energetic and a 15-bohr-broad structural (proton-proton separation) range and includes a very large number of sharp spectral transitions which can be measured to high precision. For this reason, we think that the computation of a variety of these rovibronic states would offer an excellent testing ground for the numerous small effects, which have been identified during the study of the ground state of  $\text{H}_2$ ; see, for example, Ref. [6]. The present work cannot aim to include all these effects at once, but we wish to provide a good starting point by significantly improving upon earlier theory for the selected states.

$\text{H}_2$  has several challenging excited states, some of them are bound even in the four-body treatment, e.g., the rovibronic levels of  $B\ ^1\Sigma_u^+$ . In the present work, we will look at the first

electronically excited state beyond the ground state, which is the  $EF\ ^1\Sigma_g^+$  state. The Born-Oppenheimer (BO) potential energy curve of  $EF\ ^1\Sigma_g^+$  shows a double-well feature due to an avoided crossing with the nearby  $GK\ ^1\Sigma_g^+$  state (Fig. 1). In a pre-Born-Oppenheimer (pre-BO) description [8–10], all nonadiabatic couplings and effects are automatically included, so we will not use potential energy curves or coupling vectors in the computations, but the curves are useful to look at and we will continue to use the electronic state labels to have a short description and reference for the computed four-particle states. Since all nonadiabatic couplings are included, also the coupling with the  $X\ ^1\Sigma_g^+$  (ground) state continuum is present (we cannot separate it), and thus the  $EF$  states can only be obtained as resonances within the four-body problem [9]. The lower energy vibrations of  $EF$  have been estimated to have a very long predissociative lifetime (much longer than their radiative lifetime) due to their very weak coupling to the dissociation continuum of the  $X\ ^1\Sigma_g^+$  ground electronic state [9,11].

The nonadiabatic manifold, which includes also the  $EF$  state, was computed by Yu and Dressler [12] by explicitly coupling nine electronic states. Yu and Dressler used accurate potential energy curves and nonadiabatic coupling vectors, and their nine-state computation resulted in rovibronic term values within  $0.1\text{--}20\text{ cm}^{-1}$  of experiment. This nine-state computation was a significant improvement upon the earlier five-state study of Quadrelli *et al.* [11], which showed a larger,  $1.3\text{--}120\text{ cm}^{-1}$  deviation from the experimental results. As pointed out by Hölsch *et al.* recently [7], performing a nonadiabatic computation with more than nine fully coupled electronic states for this system is not obvious (one would need to include many more electronic states and probably also the interaction with the  $\text{H}_2^+ + e^-$  ionization continuum) but extension of nonadiabatic perturbation theory could be possible. The effective Hamiltonian for the quantum nuclear motion over coupled electronic states which perturbatively accounts for the effect of the distant electronic states (not included in the fully coupled electronic band) has been recently formulated [13] following Refs. [14,15] and its numerical application, by generalizing the computational approach

<sup>\*</sup>matyus@chem.elte.hu



TABLE I. Variational, nonrelativistic four-particle energy, in  $E_h$ , corresponding to the  $N = 0, 1, \dots, 5$  rotational states of the ground vibrational state in the inner well,  $E0N$ , of the  $EF^1\Sigma_g^+$  electronic state of  $\text{H}_2 = \{e^-, e^-, p^+, p^+\}$ . The term values, in  $\text{cm}^{-1}$ , are given with respect to the rovibronic ground state. To obtain these singlet ( $S_e = 0$ ) states, the parity and the proton spin were chosen to be  $p = (-1)^N$  and  $S_p = (1 - p)/2$ , respectively. The  $E^{(2)}$  nonrelativistic energy is estimated to be converged within a few nano-Hartree.

$N$	$E^{(2)}$	$T^{(2)a}$	$\Delta T_{o-c}^{(2)b}$	$\Delta T_{o-c}^{(2)} [12]$
0	-0.712 197 577	99164.664	0.123	0.320
1	-0.711 908 569	99228.094	0.124	0.321
2	-0.711 332 945	99354.429	0.128	0.304
3	-0.710 475 421	99542.633	0.133	0.312
4	-0.709 342 932	99791.186	0.138	0.32
5	-0.707 944 454	100098.116	0.145	0.33

<sup>a</sup> $T^{(2)} = E^{(2)} - E^{(2)}(X00)$ , where the ground-state, nonrelativistic energy is  $E^{(2)}(X00) = -1.164\,025\,031 E_h$  [6].

<sup>b</sup> $\Delta T_{o-c}^{(2)} = T_o - T_c^{(2)}$  deviation of the observed (o) and computed (c) term values, where  $T_o$  is taken from Ref. [41].

exact, nonrelativistic value. The nonrelativistic term values, the difference of the  $E0N$  energies and the nonrelativistic energy of the ground state ( $X00$ ), reduce the  $0.3 \text{ cm}^{-1}$  deviation of the nine-state nonadiabatic computation of Yu and Dressler [12] to  $0.1 \text{ cm}^{-1}$  and confirm their electronic energy error estimate. Yu and Dressler also estimated the relativistic and QED corrections to be ca.  $0.08 \text{ cm}^{-1}$  for the  $E0N-X00$  terms. This is an average value for the states with different rotational quantum numbers and was compiled from the expectation value of the Breit-Pauli Hamiltonian with the electronic wave function at  $R = 1.9$  bohr [28] and the QED correction of  $\text{H}_2^+$  [29] at the  $R = 1.9$  bohr proton-proton distance, which is near the effective structure of the  $E00$  state. If we correct our nonrelativistic term values with these estimates, then the deviation from experiment reduces to  $(0.035, 0.036, 0.040, 0.045, 0.050, 0.057) \text{ cm}^{-1}$  for  $N = 0, 1, 2, \dots, 5$ , respectively.

We would like to have a more complete account for the relativistic and QED effects and also to possibly know the  $N$  dependence of the correction. For this purpose, we compiled data from the literature [30] and carried out additional computations using the nonrelativistic, pre-BO wave functions computed in the present work. The relativistic, leading, and higher order QED effects (we have explicitly considered estimates up to the so-called  $m\alpha^7$  terms) are calculated as perturbative corrections using the nonrelativistic energy and wave function,  $E^{(2)}$  and  $\psi$ , in terms of increasing orders of the fine-structure constant,  $\alpha$ ,

$$E^{(2..7)} = E^{(2)} + \sum_{k=2}^5 \alpha^k \langle \psi | \mathcal{H}^{(k+2)} | \psi \rangle, \quad (1)$$

where the  $\mathcal{H}^{(k+2)}$  operators are reproduced from the literature in the following paragraphs (with the usual meaning of the symbols and operators, the details can be found in the corresponding references). The underlying integrals, to be described in the following paragraphs, are evaluated so that the uncertainty of each correction term is better than  $0.001 \text{ cm}^{-1}$ .

TABLE II. Perturbative relativistic and QED corrections up to estimates for  $m\alpha^7$  (see text), in  $\text{cm}^{-1}$ , to the  $E0N-X00$  term values of  $\text{H}_2$  reported in Table I. The relativistic and QED corrections are estimated to be accurate within  $10^{-3} \text{ cm}^{-1}$ , which results an overall uncertainty estimate  $\pm 0.005 \text{ cm}^{-1}$  for  $T^{(2..7)}$ .

$N$	$\delta T^{(4)a}$	$\delta T^{(5)b}$	$\delta T^{(6..7)c}$	$\delta T^{(4..7)d}$	$T^{(2..7)e}$	$\Delta T_{o-c}^{(2..7)f}$
0	0.475	-0.351	-0.0027	0.122	99 164.786	0.001
1	0.478	-0.351	-0.0027	0.124	99 228.217	0.001
2	0.482	-0.352	-0.0027	0.127	99 354.557	0.001
3	0.488	-0.353	-0.0027	0.132	99 542.764	0.000
4	0.496	-0.355	-0.0027	0.138	99 791.326	0.000
5	0.506	-0.357	-0.0028	0.146	100 098.265	-0.001

<sup>a</sup>Relativistic correction.

<sup>b</sup>Leading QED correction.

<sup>c</sup> $\delta T^{(6..7)} = \delta T^{(6)} + \delta T^{(7)}$  higher order QED corrections estimated by the dominant contributions to the one-loop term.

<sup>d</sup> $\delta T^{(4..7)} = \delta T^{(4)} + \delta T^{(5)} + \delta T^{(6)} + \delta T^{(7)}$ .

<sup>e</sup> $T^{(2..7)} = T^{(2)} + \delta T^{(4..7)}$ .

<sup>f</sup> $\Delta T_{o-c}^{(2..7)} = T_o - T^{(4..7)}$  deviation of the observed (o) and computed (c) term values, where  $T_o$  is taken from Ref. [41].

To calculate the (spin-independent) relativistic correction, we have started out from the expectation value of the Breit-Pauli Hamiltonian (of the electrons) [31,32]

$$\begin{aligned} \mathcal{H}^{(4)} = & -\frac{1}{8}(\mathbf{p}_1^4 + \mathbf{p}_2^4) + \frac{\pi}{2} \sum_{i=1}^2 \sum_{a=3}^4 \delta(\mathbf{r}_{ia}) \\ & + \pi \delta(\mathbf{r}_{12}) - \frac{1}{2} \left[ \mathbf{p}_1 \frac{1}{r_{12}} \mathbf{p}_2 + \mathbf{p}_1 \cdot \mathbf{r}_{12} \frac{1}{r_{12}^3} \mathbf{r}_{12} \cdot \mathbf{p}_2 \right], \end{aligned} \quad (2)$$

where the electrons are labeled with 1 and 2, while the protons are labeled with 3 and 4. Wolniewicz already calculated the expectation value of  $\mathcal{H}^{(4)}$  with the electronic wave function along a series of nuclear separations [30,33]. We obtained the relativistic correction to each  $E0N$  state by evaluating the expectation value of the BO relativistic correction curve (represented with polynomial fits) with the pre-BO wave functions. To obtain the term corrections,  $\delta T^{(4)}$  (Table II), we used the relativistic correction value,  $-1.652 \text{ cm}^{-1}$ , of the  $X00$  ground state derived from a similar level of theory [32]. Note that this value is  $0.002 \text{ cm}^{-1}$  smaller than the correction calculated directly with the Breit-Pauli Hamiltonian of the electrons and protons and the four-particle wave function of the  $X00$  state [5], which will have to be accounted for when we estimate the uncertainties of the present results.

The leading QED contribution (to the electronic part of the problem) [31,34–36] is

$$\begin{aligned} \mathcal{H}^{(5)} = & \frac{4}{3} \left[ \frac{19}{30} - 2 \ln \alpha - \ln K \right] \sum_{i=1}^2 \sum_{a=3}^4 \delta(\mathbf{r}_{ia}) \\ & + \left[ \frac{164}{15} + \frac{14}{3} \ln \alpha \right] \delta(\mathbf{r}_{12}) - \frac{7}{6\pi} P(1/r_{12}^3) \end{aligned} \quad (3)$$

which we evaluated with accurate electronic wave functions along a series of nuclear configurations. The  $\ln K$  nonrelativistic Bethe logarithm was also treated within the BO



approximation similarly to that in Ref. [37]. The  $\ln K(R)$  values for the  $EF$  electronic state were approximated with the  $\ln K(R)$  function of the ion core of  $EF$ , so we could use the accurate  $\ln K(R)$  values of (the lowest electronic state of)  $H_2^+$  computed by Korobov [25,38]. The Dirac  $\delta$  terms containing the electron-proton and electron-electron displacement vectors were obtained similarly to the Darwin terms of the relativistic correction, i.e., by computing the expectation value of the  $R$ -dependent correction curves with the pre-BO wave function for each  $N$ . The last term in Eq. (3) is the Araki-Sucher (AS) correction, which we computed for the  $EF$  state in the present work using accurate electronic wave functions (obtained within the BO module of QUANTEN using floating ECGs [16,17]) and the integral transformation technique [39]. The AS correction to each  $EON$  state was obtained as the expectation value of the correction curve with the four-particle wave function and was found to be an order of magnitude smaller,  $-0.001 \text{ cm}^{-1}$ , than the correction for the ground state,  $-0.013 \text{ cm}^{-1}$  [6,36]. By summing up all these contributions, we obtain the leading QED correction to the energy, which changes from  $0.385$  to  $0.379 \text{ cm}^{-1}$  as  $N$  increases from  $0$  to  $5$ . To calculate the  $\delta T^{(5)}$  leading QED term corrections listed in Table II, we used the  $0.736 \text{ cm}^{-1}$  value of the ground state compiled from Refs. [6,32].

Higher order QED corrections were estimated at the one-loop level by retaining only those terms which give the dominant corrections at these orders [6,37,40]

$$\mathcal{H}_{\text{est}}^{(6)} = \pi \left( \frac{427}{96} - 2 \ln 2 \right) \sum_{i=1}^2 \sum_{a=3}^4 \delta(\mathbf{r}_{ia}), \quad (4)$$

$$\mathcal{H}_{\text{est}}^{(7)} = -4 \ln^2 \alpha \sum_{i=1}^2 \sum_{a=3}^4 \delta(\mathbf{r}_{ia}). \quad (5)$$

While the  $\mathcal{H}_{\text{est}}^{(6)}$  contribution to the  $EON-X00$  term values is  $-0.003 \text{ cm}^{-1}$ , the  $\mathcal{H}_{\text{est}}^{(7)}$  changes the terms by as little as  $2 \times 10^{-4} \text{ cm}^{-1}$ , which is negligible given the uncertainty of the current evaluation of the relativistic and QED integrals.

The overall  $\delta T^{(4..7)}$  contribution (Table II) of the relativistic, leading, and higher order QED effects increases from  $0.122$  to  $0.146 \text{ cm}^{-1}$  upon the increase of  $N = 0$  to  $5$ . The resulting  $T^{(2..7)}$  term values for  $N = 0, \dots, 5$  show  $\pm 0.001 \text{ cm}^{-1}$  deviations from the experimental values of Ref. [41], which is better (probably fortuitous) than the uncertainty of the present theoretical values, which are thought to be accurate within about  $\pm 0.005 \text{ cm}^{-1}$ .

The experimental values of Ref. [41] are more precise than our theoretical results, and the additional significant

digits surely hide interesting physics, so theory should aim for further improvements. In order to help future work, we close this article with commenting on the possible sources of uncertainties in our work.

First of all, the nonrelativistic energy was obtained in a variational procedure (stabilized for long-lived resonances), and systematic improvement of this value is rather straightforward. The convergence pattern observed in repeated rounds of refinement cycles suggests that the nonrelativistic energy,  $E^{(2)}$ , is converged within  $0.0005 \text{ cm}^{-1}$ . Assessment of the uncertainty of the relativistic and QED corrections is more delicate. In light of the developments of recent years for the rovibronic ground state [5,6,32,40], we think that the largest source of error in our work must be due to the relativistic recoil effect, on the order of a few  $10^{-3} \text{ cm}^{-1}$ , which in simple terms means that (at least) the relativistic corrections should be computed using the full electron-nucleus Breit-Pauli Hamiltonian and the four-particle wave functions [5,6]. Then, in order to pinpoint one or two more digits in the calculations, the current approximations used for the nonrelativistic Bethe-logarithm term will have to be checked and the contribution of the neglected terms in the higher order QED corrections (in particular, the full  $m\alpha^6$  contribution of  $\mathcal{H}^{(6)}$ ) will have to be elaborated.

In the usual perturbative manner, relativistic quantum electrodynamics (and possibly beyond) is adapted to molecular computations, it is necessary to evaluate and sum several, small (and often not so small) contributions (of different signs) on top of a direct, variational, nonrelativistic computation. We think that the extremely rich excited state, rovibronic level structure of the hydrogen molecule (Fig. 1) offers an excellent opportunity to challenge and cross-check the theoretical and computational procedures both in terms of the completeness of the physical description and regarding the error balance of possible uncertainties and inaccuracies. The present work demonstrates that electronically excited states of  $H_2$  can be theoretically described to high precision and, with further improvements, they will provide equally useful and complementary information to the study of the ground electronic state.

We acknowledge financial support from PROMYS Grant No. IZ11Z0\_166525 of the Swiss National Science Foundation. D.F. acknowledges a doctoral scholarship from the New National Excellence Program of the Ministry of Human Capacities of Hungary (ÚNKP-18-3-II-ELTE-133). E.M. is thankful to ETH Zürich for supporting a stay as a visiting professor and to the Laboratory of Physical Chemistry for the hospitality, where part of this work has been completed.

- [1] N. Hölsch, M. Beyer, E. J. Salumbides, K. S. E. Eikema, W. Ubachs, C. Jungen, and F. Merkt, *Phys. Rev. Lett.* **122**, 103002 (2019).  
 [2] J. Liu, E. J. Salumbides, U. Hollenstein, J. C. J. Koelemeij, K. S. E. Eikema, W. Ubachs, and F. Merkt, *J. Chem. Phys.* **130**, 174306 (2009).

- [3] R. K. Altmann, L. S. Dreissen, E. J. Salumbides, W. Ubachs, and K. S. E. Eikema, *Phys. Rev. Lett.* **120**, 043204 (2018).  
 [4] C.-F. Cheng, J. Hussels, M. Niu, H. L. Bethlem, K. S. E. Eikema, E. J. Salumbides, W. Ubachs, M. Beyer, N. Hölsch, J. A. Agner *et al.*, *Phys. Rev. Lett.* **121**, 013001 (2018).  
 [5] L. M. Wang and Z.-C. Yan, *Phys. Rev. A* **97**, 060501(R) (2018).

- [6] M. Puchalski, J. Komasa, P. Czachorowski, and K. Pachucki, *Phys. Rev. Lett.* **122**, 103003 (2019).
- [7] N. Hölsch, M. Beyer, and F. Merkt, *Phys. Chem. Chem. Phys.* **20**, 26837 (2018).
- [8] E. Mátyus and M. Reiher, *J. Chem. Phys.* **137**, 024104 (2012).
- [9] E. Mátyus, *J. Phys. Chem. A* **117**, 7195 (2013).
- [10] E. Mátyus, *Mol. Phys.* **117**, 590 (2019).
- [11] P. Quadrelli, K. Dressler, and L. Wolniewicz, *J. Chem. Phys.* **93**, 4958 (1990).
- [12] S. Yu and K. Dressler, *J. Chem. Phys.* **101**, 7692 (1994).
- [13] E. Matyus and S. Teufel, *J. Chem. Phys.* **151**, 014113 (2019).
- [14] S. Teufel, *Adiabatic Perturbation Theory in Quantum Dynamics*, Lecture Notes in Mathematics (Springer, Berlin, 2003).
- [15] G. Panati, H. Spohn, and S. Teufel, *ESAIM* **41**, 297 (2007).
- [16] E. Mátyus, *J. Chem. Phys.* **149**, 194112 (2018).
- [17] E. Mátyus, *J. Chem. Phys.* **149**, 194111 (2018).
- [18] M. Przybytek, W. Cencek, B. Jeziorski, and K. Szalewicz, *Phys. Rev. Lett.* **119**, 123401 (2017).
- [19] K. Pachucki and J. Komasa, *J. Chem. Phys.* **130**, 164113 (2009).
- [20] Y. Suzuki and K. Varga, *Stochastic Variational Approach to Quantum-Mechanical Few-Body Problems* (Springer-Verlag, Berlin, 1998).
- [21] Y. Suzuki, J. Usukura, and K. Varga, *J. Phys. B: At. Mol. Opt. Phys.* **31**, 31 (1998).
- [22] V. I. Kukulín, V. M. Krasnopolsky, and J. Horáček, *Theory of Resonances—Principles and Applications* (Kluwer, Dordrecht, 1988).
- [23] A. U. Hazi and H. S. Taylor, *Phys. Rev. A* **1**, 1109 (1970).
- [24] V. A. Mandelshtam, H. S. Taylor, V. Ryaboy, and N. Moiseyev, *Phys. Rev. A* **50**, 2764 (1994).
- [25] D. T. Aznabev, A. K. Bekbaev, and V. I. Korobov, *Phys. Rev. A* **98**, 012510 (2018).
- [26] V. I. Korobov, *Nucl. Inst. Meth. Phys. Res. B* **214**, 80 (2004).
- [27] Please see Supplemental Material at <http://link.aps.org/supplemental/10.1103/PhysRevA.100.020501> for more information on theoretical and computational details.
- [28] L. Wolniewicz and K. Dressler, *J. Chem. Phys.* **100**, 444 (1994).
- [29] R. Bukowski, B. Jeziorski, R. Moszynski, and W. Kolos, *Int. J. Quant. Chem.* **42**, 287 (1992).
- [30] L. Wolniewicz, *J. Chem. Phys.* **109**, 2254 (1998).
- [31] H. A. Bethe and E. E. Salpeter, *Quantum Mechanics of One- and Two-Electron Systems* (Springer, Berlin, 1975).
- [32] M. Puchalski, J. Komasa, and K. Pachucki, *Phys. Rev. A* **95**, 052506 (2017).
- [33] The relativistic corrections of the  $EF^1\Sigma_g^+$  state computed by Wolniewicz are taken from the rel98.txt file [<http://www.fizyka.umk.pl/ftp/pub/papers/ifiz/luwo/>]
- [34] J. Araki, *Prog. Theor. Phys.* **17**, 619 (1957).
- [35] J. Sucher, *Phys. Rev.* **109**, 1010 (1958).
- [36] J. Komasa, K. Piszczatowski, G. Lach, M. Przybytek, B. Jeziorski, and K. Pachucki, *J. Chem. Theory Comput.* **7**, 3105 (2011).
- [37] K. Piszczatowski, G. Lach, M. Przybytek, J. Komasa, K. Pachucki, and B. Jeziorski, *J. Chem. Theory Comput.* **5**, 3039 (2009).
- [38] V. I. Korobov, L. Hilico, and J.-P. Karr, *Phys. Rev. A* **87**, 062506 (2013).
- [39] K. Pachucki, W. Cencek, and J. Komasa, *J. Chem. Phys.* **122**, 184101 (2005).
- [40] M. Puchalski, J. Komasa, P. Czachorowski, and K. Pachucki, *Phys. Rev. Lett.* **117**, 263002 (2016).
- [41] G. D. Dickenson, E. J. Salumbides, M. Niu, C. Jungen, S. C. Ross, and W. Ubachs, *Phys. Rev. A* **86**, 032502 (2012).
- [42] L. Wolniewicz, *J. Mol. Spectrosc.* **174**, 132 (1995).
- [43] L. Wolniewicz, *J. Mol. Spectrosc.* **169**, 329 (1995).
- [44] L. Wolniewicz, I. Simbotin, and A. Dalgarno, *Astrophys. J. Suppl. Ser.* **115**, 293 (1998).
- [45] M. Beyer and F. Merkt, *J. Mol. Spectrosc.* **330**, 147 (2016).

# Non-adiabatic mass correction for excited states of molecular hydrogen: Improvement for the outer-well $H\bar{H}^1\Sigma_g^+$ term values

Cite as: J. Chem. Phys. 151, 094101 (2019); doi: 10.1063/1.5109964

Submitted: 14 May 2019 • Accepted: 26 July 2019 •

Published Online: 5 September 2019



Dávid Ferenc and Edit Mátyus<sup>a)</sup>

## AFFILIATIONS

Institute of Chemistry, ELTE, Eötvös Loránd University, Pázmány Péter Sétány 1/A, Budapest H-1117, Hungary

<sup>a)</sup>Electronic mail: [matyus@chem.elte.hu](mailto:matyus@chem.elte.hu)

## ABSTRACT

The mass-correction function is evaluated for selected excited states of the hydrogen molecule within a single-state nonadiabatic treatment. Its qualitative features are studied at the avoided crossing of the  $EF$  with the  $GK$  state and also for the outer well of the  $H\bar{H}$  state. For the  $H\bar{H}$  state, a negative mass correction is obtained for the vibrational motion near the outer minimum, which accounts for most of the deviation between experiment and earlier theoretical work.

Published under license by AIP Publishing. <https://doi.org/10.1063/1.5109964>

## I. INTRODUCTION

This work represents the first steps toward a fully coupled nonadiabatic calculation of the  $EF - GK - H\bar{H}$ -, etc., singlet-gerade manifold of  $H_2$  including the formerly neglected mass-correction terms which appear in the multistate, effective nonadiabatic Hamiltonian recently formulated.<sup>1</sup> Relying on the condition of adiabatic perturbation theory<sup>2</sup> that the electronic band must be separated from the rest of the electronic spectrum by a finite gap over the relevant dynamical range, already a single-state treatment delivers insight into the extremely rich nonadiabatic dynamics of electronically excited hydrogen. Motivated by these ideas and after careful inspection of the singlet-gerade manifold, we have selected the lower-energy region of the  $EF^1\Sigma_g^+$  and the outer well of the  $H\bar{H}^1\Sigma_g^+$  state (Fig. 1), often labeled  $\bar{H}$ , for a single-state nonadiabatic study. After a short summary of the theoretical and computational details, we present the nonadiabatic mass curves and discuss them in relation to earlier theoretical and experimental work.

## II. THEORETICAL AND COMPUTATIONAL DETAILS

### A. Summary of the theoretical background

Let us start with the electronic Schrödinger equation,

$$\hat{H}_{el}\psi_a = E_a\psi_a, \quad (1)$$

including the electronic Hamiltonian (in Hartree atomic units)

$$\hat{H}_{el} = -\frac{1}{2} \sum_{i=1}^{N_{el}} \Delta_{r_i} + \sum_{i=1}^{N_d} \sum_{j>i}^{N_{el}} \frac{1}{|\mathbf{r}_i - \mathbf{r}_j|} - \sum_{i=1}^{N_d} \sum_{k=1}^N \frac{Z_k}{|\mathbf{r}_i - \mathbf{R}_k|} + \sum_{k=1}^N \sum_{l>k}^N \frac{Z_k Z_l}{|\mathbf{R}_k - \mathbf{R}_l|} \quad (2)$$

with the  $r_i$  electronic and the  $\mathbf{R}_k$  nuclear coordinates and  $Z_k$  nuclear charges. In order to approximate the rovibronic energies of the full, electron-nucleus Schrödinger equation accurately, it is necessary to go beyond the Born–Oppenheimer (BO) approximation. In the present work, we explore the selected states within a single-state nonadiabatic treatment, using the second-order, effective Hamiltonian which had been formulated and reformulated in different contexts<sup>3–7</sup> and most recently reproduced as a special case of the multistate effective Hamiltonian.<sup>1</sup> The single-state Hamiltonian has already been used for the ground electronic state of several diatomic molecules,<sup>8–12</sup> in an approximate treatment of the water molecule,<sup>13</sup> and in example single-point computations for polyatomics<sup>7</sup> (for a detailed reference list see Ref. 10).

The second-order or  $\varepsilon^2$  effective Hamiltonian for the quantum nuclear motion over a selected “ $a$ ” electronic state is

$$\hat{H}_{aa}^{(2)} = \frac{1}{2} \sum_{i=1}^{3N} \sum_{j=1}^{3N} (-i\varepsilon\partial_i)(\delta_{ij} - \varepsilon^2 M_{aa,ij})(-i\varepsilon\partial_j) + \varepsilon^2 U_a + E_a, \quad (3)$$

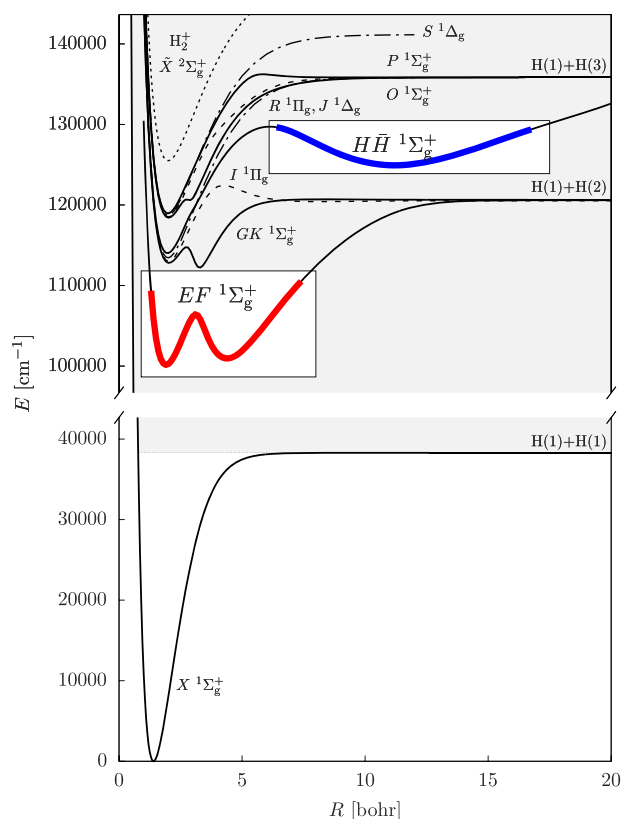


**FIG. 1.** Single-state nonadiabatic treatment for the lower-energy part of the  $EF\ 1\Sigma_g^+$  electronic state, highlighted in red. The results are also obtained within the single-state nonadiabatic framework for the outer well of the  $H\bar{H}\ 1\Sigma_g^+$  electronic state, which is highlighted in blue (see also Table I). The Born–Oppenheimer potential energy curves shown in the figure were compiled from Refs. 33–37.

where  $\varepsilon^2$  is the electron-to-nucleus mass ratio, and in particular, for the  $H_2$  molecule in atomic units, it is  $\varepsilon^2 = 1/m_p$ .  $\partial_i = \partial/\partial R_{k\alpha}$  where  $i = 3(k-1) + \alpha$  [ $k = 1, \dots, N$ ,  $\alpha = 1(x), 2(y), 3(z)$ ] is the partial derivative with respect to the nuclear coordinates.

Besides the nuclear kinetic energy (with constant mass) and the  $E_a$  electronic energy,  $\hat{H}_{aa}^{(2)}$  contains the diagonal Born–Oppenheimer correction (DBOC),

$$\varepsilon^2 U_a = \varepsilon^2 \frac{1}{2} \sum_{i=1}^{3N} \langle \partial_i \psi_a | \partial_i \psi_a \rangle, \quad (4)$$

and the mass correction tensor,

$$\begin{aligned} \varepsilon^2 M_{aa,ij} &= \varepsilon^2 2 \langle \partial_j \psi_a | \mathcal{R}_a | \partial_i \psi_a \rangle \\ &= \varepsilon^2 2 \langle \partial_j \psi_a | (H_{el} - E_a)^{-1} (1 - P_a) | \partial_i \psi_a \rangle, \quad i, j = 1, \dots, 3N, \end{aligned} \quad (5)$$

where the electronic energy,  $E_a$ , and the electronic wave function,  $\psi_a$ , are obtained from solving the electronic Schrödinger equation [Eq. (1)]. For a better understanding of the numerical results, it will be important to remember the appearance of the reduced resolvent,  $\mathcal{R}_a = (H_{el} - E_a)^{-1} (1 - P_a)$  with  $P_a = |\psi_a\rangle\langle\psi_a|$  in the expression of the mass correction tensor. The “effect” of the outlying electronic

states on the quantum nuclear dynamics is accounted for through this reduced resolvent. In addition, note that the term containing  $M_{aa,ij}$  in Eq. (3) is indeed  $\mathcal{O}(\varepsilon^2)$ , since we do not assume small nuclear momenta, hence the action of  $\hat{p}_i = -i\varepsilon\partial_i$  on the nuclear wave function creates an  $\mathcal{O}(1)$  contribution [instead of  $\mathcal{O}(\varepsilon)$ ] (for more details, see, for example, Ref. 1).

The general transformation of the second-order nonadiabatic kinetic energy operator for an  $N$ -atomic molecule—first term in Eq. (3)—to curvilinear coordinates was worked out in Ref. 10. The special transformation for a diatomic molecule described with spherical polar coordinates,  $(\rho, \Omega)$ , which we are using in the present work, had been formulated earlier.<sup>3,6,8,14</sup> Hence, the effective, nonadiabatic, single-state Schrödinger equation for the hydrogen molecule with  $J$  rotational angular momentum quantum number is

$$\begin{aligned} &\left[ -\frac{\partial}{\partial \rho} \frac{1}{m_p} \left( 1 - \frac{(\mathcal{A}_a)^\rho_\rho}{m_p} \right) \frac{\partial}{\partial \rho} + \frac{J(J+1)}{m_p \rho^2} \left( 1 - \frac{(\mathcal{A}_a)^\Omega_\Omega}{m_p} \right) \right. \\ &\quad \left. + \frac{1}{m_p} U_a(\rho) + V_a(\rho) \right] \phi_J(\rho) = E_J \phi_J(\rho) \end{aligned} \quad (6)$$

with the volume element  $d\rho$ . The  $(\mathcal{A}_a)^\rho_\rho$  and  $(\mathcal{A}_a)^\Omega_\Omega$  (coordinate-dependent) coefficients originate from the mass-correction tensor [Eq. (5)] and the coordinate transformation rule from Cartesian coordinates to curvilinear coordinates (see Refs. 10 and 11). Since  $1/(1+y) \approx 1-y$  for small  $y$ , we may write  $1/m_p(1-a/m_p) \approx 1/m_p \cdot 1/(1+a/m_p) = 1/(m_p+a)$ , and in this sense,  $(\mathcal{A}_a)^\rho_\rho$  and  $(\mathcal{A}_a)^\Omega_\Omega$  can be interpreted as the correction to the proton mass for the vibrational and rotational motion, or in short, vibrational and rotational mass corrections, respectively.

## B. Computational details

We used the QUANTEN computer program<sup>10,11,15,16</sup> to accurately solve the electronic Schrödinger equation [Eq. (1)] for the second, third, and fourth singlet gerade electronic states— $EF$ ,  $GK$ , and  $H\bar{H}\ 1\Sigma_g^+$ , respectively—of the hydrogen molecule using floating, explicitly correlated Gaussian functions as spatial functions,

$$f(\mathbf{r}; \mathbf{A}, \mathbf{s}) = \exp\left[-\frac{1}{2}(\mathbf{r}-\mathbf{s})^T (\mathbf{A} \otimes \mathbf{I}_3)(\mathbf{r}-\mathbf{s})\right]. \quad (7)$$

The  $\mathbf{A} \in \mathbb{R}^{2 \times 2}$  and  $\mathbf{s} \in \mathbb{R}^{2 \times 3}$  parameters were optimized variationally for each basis function at every nuclear configuration,  $\mathbf{R}_k$  ( $k = 1, 2$ ), over a fine grid of the  $\rho = |\mathbf{R}_1 - \mathbf{R}_2|$  nuclear separation. For the computational details of the wave function derivatives and the mass correction functions in curvilinear coordinates, see Refs. 10 and 11.

The electronic states we study in this work and the corresponding DBOCs and relativistic corrections have already been computed accurately by Wolniewicz<sup>17</sup> for several proton-proton distances. We have repeated these computations to check the accuracy of the data and to improve it where necessary (*vide infra*). In addition, we have computed the nonadiabatic mass-correction functions in the present work.

The effective nuclear Schrödinger equation for the diatom, Eq. (6), was solved using the discrete variable representation (DVR)<sup>18</sup> and associated Laguerre polynomials,  $L_n^{(\alpha)}$  with  $\alpha = 2$  for the vibrational ( $\rho$ ) degree of freedom. The outer-well

$\tilde{H}$  states were computed by scaling the DVR points to the  $[R_{\min}, R_{\max}] = [6, 20]$  bohr interval.

### III. RESULTS AND DISCUSSION

The nonadiabatic corrections to the vibrational and rotational mass of the proton in the  $EF$  and  $H\bar{H} \ ^1\Sigma_g^+$  electronic states of  $H_2$  are shown in Figs. 2 and 3. These numerical examples highlight qualitative features of the mass-correction functions. The sign and the amplitude of the correction can be understood by remembering that the mass-correction tensor contains the  $\mathcal{R}_a$  reduced resolvent [Eq. (5)].

#### A. The $EF$ state

Concerning the  $EF \ ^1\Sigma_g^+$  state of  $H_2$  below  $\sim 110\,000 \text{ cm}^{-1}$  (below the  $GK$  minima, Fig. 1), the effective vibrational mass of the proton becomes gigantic at the avoided crossing with the  $GK \ ^1\Sigma_g^+$  curve. The large correction value,  $\delta m_{\text{vib}}^{(EF)} = 480 m_e$  near  $R = 3$  bohr, which should be compared with the  $\sim 1836 m_e$  mass of the proton,<sup>38</sup> indicates that it is necessary to go beyond the second-order, single-state nonadiabatic treatment to achieve spectroscopic accuracy. For this purpose, one can consider either using higher-order corrections—the third-order correction formulae can be found in Ref. 1—or including explicit nonadiabatic coupling with the near-lying perturber state(s), in this case  $GK$  (and probably other states), and to use the effective nonadiabatic Hamiltonian of Ref. 1 for a multidimensional electronic subspace. Note that in the single-state treatment, only the  $EF$  state is projected out from the resolvent, Eq. (5), whereas in a multistate treatment, the full explicitly coupled subspace will be projected out, which will result in smaller corrections from electronic states better separated in energy.

With these observations in mind, we have nevertheless checked the rotation-vibration term values obtained within the second-order, single-state nonadiabatic model. We have found that the  $EF$

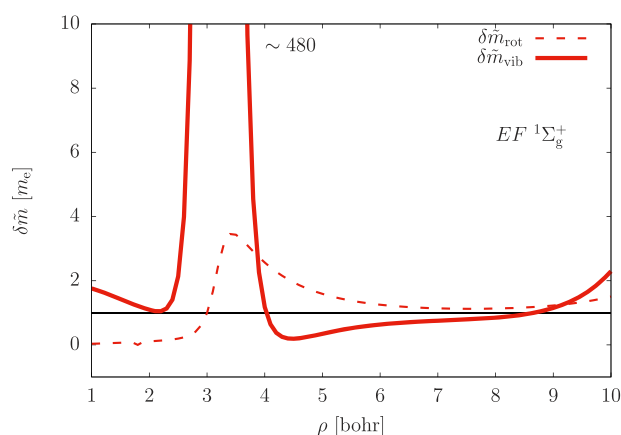


**FIG. 2.** Nonadiabatic mass correction functions to the rotational and the vibrational degrees of freedom,  $\delta\tilde{m}_{\text{rot}}$  and  $\delta\tilde{m}_{\text{vib}}$ , computed for the  $EF \ ^1\Sigma_g^+$  electronic state of the hydrogen molecule.<sup>10,11</sup> (The thin, solid black line indicates the mass of the electron, which together with the proton mass gives the atomic mass.)

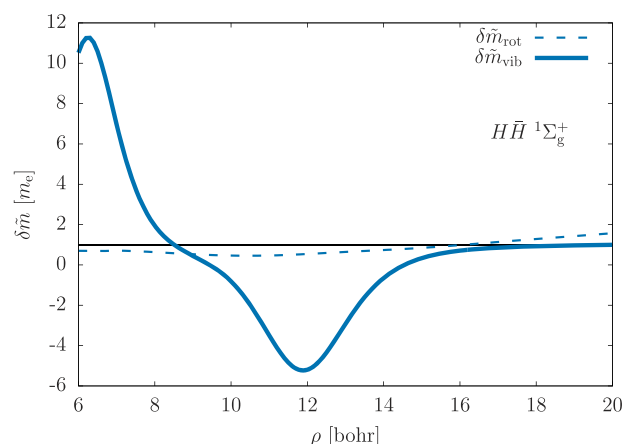


**FIG. 3.** Nonadiabatic mass correction functions to the rotational and the vibrational degrees of freedom,  $\delta\tilde{m}_{\text{rot}}$  and  $\delta\tilde{m}_{\text{vib}}$ , computed for the  $H\bar{H} \ ^1\Sigma_g^+$  electronic state of the hydrogen molecule.<sup>10,11</sup> (The thin, solid black line indicates the mass of the electron, which together with the proton mass gives the atomic mass.)

vibrational term values obtained with the effective masses (Fig. 2) were closer to the experimental values than the constant-mass adiabatic description (using either the nuclear mass of the proton or the atomic mass of hydrogen, which is commonly used as an “empirical” means of modeling nonadiabatic effects). The  $\sim 30\text{--}35 \text{ cm}^{-1}$  root-mean-square deviation of the adiabatic energies from experiment was reduced to  $10 \text{ cm}^{-1}$  when the rigorous nonadiabatic vibrational functions were used instead of the constant (nuclear or atomic) mass. More detailed numerical results will be obtained within a coupled-state nonadiabatic treatment in future work.

#### B. The $H\bar{H}$ state

Next, we have studied the  $H\bar{H}$  state, for which already a single-state model turns out to be useful for spectroscopic purposes, at least for the outer-well states. The inner well of the  $H\bar{H}$  potential energy curve (PEC) gets close to those of several other PECs, and for this reason a single-state treatment is not appropriate here. At the same time, most of the outer-well state energies (below the barrier) can be accurately computed without considering delocalization to the inner well. This behavior was pointed out already several times in the literature,<sup>17,19–22</sup> and we have also checked it for every rovibrational state by solving the rovibrational Schrödinger equation with different  $[R_{\min}, R_{\max}]$  intervals. In particular, we obtained the (adiabatic) inner-well state energies (below the barrier) with an accuracy better than  $0.01 \text{ cm}^{-1}$  even if we used the restricted  $[R_{\min}, R_{\max}] = [6, 20]$  bohr interval. This behavior was observed with using either constant (e.g., nuclear or atomic) or coordinate-dependent, nonadiabatic masses. The few exceptions (states near the top of the barrier which separate the inner and the outer wells) are shown in gray in Table I.

The experimental term values for the outer-well rotation-vibration states of the  $H\bar{H}$  electronic state were first reported in 1997<sup>23</sup> and also later in 1999 together with an improved theoretical treatment.<sup>19,20</sup> The computations were carried out on an

TABLE I. Term values and deviation from experiment, in  $\text{cm}^{-1}$ , for the outer-well rovibrational states of the  $H\bar{H}^1\Sigma_g^+$  electronic state of the hydrogen molecule.

$v$	$J = 0$				$J = 1$				$J = 2$			
	$T_{\text{nad}}^{\text{b}}$	$T_{\text{obs}} - T_{\text{calc}}^{\text{a}}$			$T_{\text{nad}}^{\text{b}}$	$T_{\text{obs}} - T_{\text{calc}}^{\text{a}}$			$T_{\text{nad}}^{\text{b}}$	$T_{\text{obs}} - T_{\text{calc}}^{\text{a}}$		
		nad <sup>c</sup>	ad <sub>H</sub> <sup>d</sup>	ad <sub>p</sub> <sup>e</sup>		nad <sup>c</sup>	ad <sub>H</sub> <sup>d</sup>	ad <sub>p</sub> <sup>e</sup>		nad <sup>c</sup>	ad <sub>H</sub> <sup>d</sup>	ad <sub>p</sub> <sup>e</sup>
0	122 883.4		n.a. <sup>f</sup>		122 885.3		n.a. <sup>f</sup>		122 889.1		n.a. <sup>f</sup>	
1	123 234.5		n.a. <sup>f</sup>		123 236.4		n.a. <sup>f</sup>		123 240.2		n.a. <sup>f</sup>	
2	123 575.8	0.1 <sup>g</sup>	1.1 <sup>g</sup>	0.9 <sup>g</sup>	123 577.7	0.0 <sup>g</sup>	1.0 <sup>g</sup>	0.8 <sup>g</sup>	123 581.5	0.2 <sup>g</sup>	1.1 <sup>g</sup>	0.9 <sup>g</sup>
3	123 907.5	-0.2	1.1	0.8	123 909.4	-0.2	1.1	0.8	123 913.3	-0.2	1.1	0.8
4	124 229.9	-0.2	1.3	0.9	124 231.8	-0.2	1.3	0.9	124 235.7	-0.3	1.2	0.8
5	124 543.0	-0.3	1.4	0.9	124 544.9	-0.3	1.4	0.9	124 548.8	-0.3	1.4	0.9
6	124 847.2	-0.2	1.6	1.1	124 849.1	-0.2	1.6	1.0	124 853.0	-0.2	1.6	1.0
7	125 142.5	-0.2	1.7	1.1	125 144.5	-0.2	1.7	1.1	125 148.4	-0.2	1.7	1.1
8	125 429.3	-0.2	1.8	1.2	125 431.3	-0.1	1.8	1.2	125 435.1	-0.2	1.8	1.1
9	125 707.6	-0.1	1.9	1.2	125 709.6	-0.1	2.0	1.3	125 713.5	-0.1	1.9	1.2
10	125 977.6	-0.1	1.9	1.2	125 979.5	-0.1	2.0	1.2	125 983.4	-0.1	1.9	1.2
11	126 239.1	-0.1	1.9	1.1	126 241.1	-0.1	2.0	1.2	126 245.0	-0.2	1.9	1.1
12	126 492.4	-0.2	1.9	1.1	126 494.4	-0.2	1.9	1.0	126 498.3	-0.2	1.9	1.0
13 <sup>h</sup>	126 737.1	-0.2	1.8	0.9	126 739.1	-0.2	1.8	0.9	126 743.1	-0.3	1.8	0.9
14 <sup>h</sup>	126 972.9	-0.5	1.5	0.6	126 975.0	-0.5	1.5	0.6	126 979.1	-0.6	1.4	0.5
15 <sup>h</sup>	127 199.3	-1.8	0.2	-0.8	127 201.4	-1.7	0.3	-0.7	127 205.6	-1.5	0.4	-0.5
$v$	$J = 3$				$J = 4$				$J = 5$			
	$T_{\text{nad}}^{\text{b}}$	$T_{\text{obs}} - T_{\text{calc}}^{\text{a}}$			$T_{\text{nad}}^{\text{b}}$	$T_{\text{obs}} - T_{\text{calc}}^{\text{a}}$			$T_{\text{nad}}^{\text{b}}$	$T_{\text{obs}} - T_{\text{calc}}^{\text{a}}$		
		nad <sup>c</sup>	ad <sub>H</sub> <sup>d</sup>	ad <sub>p</sub> <sup>e</sup>		nad <sup>c</sup>	ad <sub>H</sub> <sup>d</sup>	ad <sub>p</sub> <sup>e</sup>		nad <sup>c</sup>	ad <sub>H</sub> <sup>d</sup>	ad <sub>p</sub> <sup>e</sup>
0	122 894.9		n.a. <sup>f</sup>		122 902.5		n.a. <sup>f</sup>		122 912.0		n.a. <sup>f</sup>	
1	123 246.0		n.a. <sup>f</sup>		123 253.6		n.a. <sup>f</sup>		123 263.2		n.a. <sup>f</sup>	
2	123 587.3	0.0 <sup>g</sup>	1.0 <sup>g</sup>	0.8 <sup>g</sup>	123 595.0	0.4 <sup>g</sup>	1.4 <sup>g</sup>	1.2 <sup>g</sup>	123 604.6	-0.3 <sup>g</sup>	0.7 <sup>g</sup>	0.5 <sup>g</sup>
3	123 919.1	-0.2	1.0	0.7	123 926.8	-0.2	1.1	0.7	123 936.4	0.0 <sup>g</sup>	1.3 <sup>g</sup>	0.9 <sup>g</sup>
4	124 241.5	-0.2	1.2	0.9	124 249.2	-0.3	1.2	0.8	124 258.8	-0.2	1.3	0.9
5	124 554.6	-0.2	1.4	1.0	124 562.3	-0.3	1.4	0.9	124 572.0	-0.2	1.4	0.9
6	124 858.8	-0.2	1.6	1.1	124 866.5	-0.2	1.6	1.0	124 876.2	-0.2	1.6	1.0
7	125 154.2	-0.1	1.8	1.2	125 161.9	-0.2	1.7	1.1	125 171.6	-0.2	1.7	1.1
8	125 441.0	-0.2	1.8	1.2	125 448.7	-0.2	1.8	1.1	125 458.4	-0.2	1.8	1.2
9	125 719.3	-0.1	1.9	1.2	125 727.0	-0.1	1.9	1.2	125 736.7	-0.1	1.9	1.2
10	125 989.3	-0.1	2.0	1.2	125 997.0	-0.1	1.9	1.2	126 006.8	-0.1	1.9	1.2
11	126 250.9	-0.1	2.0	1.2	126 258.7	-0.2	1.9	1.1	126 268.5	-0.1	1.9	1.1
12	126 504.2	-0.2	1.9	1.0	126 512.1	-0.2	1.9	1.0	126 522.0	-0.2	1.9	1.0
13 <sup>h</sup>	126 749.1	-0.3	1.8	0.9	126 757.1	-0.3	1.8	0.9	126 767.1	-0.3	1.8	0.9
14 <sup>h</sup>	126 985.2	-0.4	1.6	0.7	126 993.4	-0.6	1.4	0.5	127 003.6	-0.4	1.7	0.7
15 <sup>h</sup>	127 211.9	-1.3	0.7	-0.3	127 220.4	-0.9	1.1	0.1	127 230.8			

<sup>a</sup> Deviation of experiment and theory. The  $T_{\text{obs}}$  experimental term values were taken from Refs. 20 and 23.

<sup>b</sup> Calculated term value,  $T_{\text{nad}} = E_{\text{nad}} - E_0$ , referenced to the ground-state energy,  $E_0$ .<sup>31,32</sup>  $E_{\text{nad}}$  was obtained by solving Eq. (6) using the rigorous nonadiabatic masses computed in the present work (Fig. 3) and using the relativistic and diagonal Born–Oppenheimer corrections of Refs. 17 and 19, as well as the radiative corrections and an improved PEC computed in this work.

<sup>c</sup>  $T_{\text{calc}} = T_{\text{nad}}$ .

<sup>d</sup>  $T_{\text{calc}} = T_{\text{adH}} = E_{\text{adH}} - E_0$ , where  $E_{\text{adH}}$  was obtained as  $E_{\text{nad}}$  but using the constant, atomic mass of hydrogen for  $m_p$  and approximating the mass-correction functions by zero.

<sup>e</sup>  $T_{\text{calc}} = T_{\text{adp}} = E_{\text{adp}} - E_0$ , where  $E_{\text{adp}}$  was obtained as  $E_{\text{adH}}$  but using the constant, nuclear mass of the proton for  $m_p$ .

<sup>f</sup> Experimental data not available.

<sup>g</sup> Note that the experimental uncertainty is an order-of-magnitude larger for these term values than for the others.

<sup>h</sup> Neglect of delocalization to the inner well introduces an at least  $0.1 \text{ cm}^{-1}$  error in the computed energy.

accurate, adiabatic PEC including relativistic corrections and were also appended with an estimate for the quantum electrodynamics (QED) effects.<sup>17,20</sup> The resulting term values were in  $\sim 1 \text{ cm}^{-1}$  (dis)agreement with experiment (of  $\sim 0.04 \text{ cm}^{-1}$  uncertainty), which was attributed to the neglect of nonadiabatic effects.

We have repeated the rovibrational computations using the potential energy, diagonal Born–Oppenheimer correction, relativistic correction curves computed, and the QED correction estimated by Wolniewicz,<sup>17</sup> but we used the nonadiabatic mass correction functions for the rotational and the vibrational degrees of freedom computed in the present work (Fig. 3). We obtained a somewhat better agreement with the experimental results; the 1–1.2  $\text{cm}^{-1}$  deviation of theory and experiment of Ref. 20 was reduced to 0.3–0.4  $\text{cm}^{-1}$  (the computed values are larger than the experimental ones).

In order to identify the origin of the remaining discrepancy, we refined the potential energy curve using the QUANTEN program, which resulted in a few tenths of  $\text{cm}^{-1}$  reduction for  $R > 10$  bohr (the improved electronic energies are deposited in the [supplementary material](#)). Next, we have checked the accuracy of the earlier relativistic corrections and found them to be sufficient for the present purposes. We have also explicitly evaluated the leading-order QED correction [see, for example, Eq. (3) of Ref. 24] instead of approximating it with the QED correction value of  $\text{H}^-$  proposed by Wolniewicz.<sup>17</sup> For this purpose, we used the one- and two-electron Darwin integrals already available from the relativistic computations<sup>17</sup> and approximated the nonrelativistic Bethe-logarithm with  $\ln k_0 \approx 3$  based on its value for the ground state of the hydrogen atom (remember the strong  $\text{H}^- + \text{H}^+$  ion-pair character of the outer well and the observation that  $\ln k_0$  is not very sensitive to the number of electrons<sup>25</sup>). We also computed the Araki–Sucher term for the  $\text{H}\bar{\text{H}}$  state in the present work, although it gives an almost negligible contribution at the current level of precision. Based on these computations, the radiative correction curve takes values between 0.27 and 0.29  $\text{cm}^{-1}$  over the outer well of  $\text{H}\bar{\text{H}}$ , and thus, we confirm the earlier estimate using the  $\text{H}^-$  value.<sup>17</sup>

As a summary, we collect in Table I the best rovibrational term values (“ $T_{\text{nad}}$ ” column) and their deviation from experiment (“nad” column) resulting from the computations carried out within the present work. Inclusion of the nonadiabatic masses in the rovibrational treatment and further refinement of the potential energy curve reduces the earlier  $\sim 1$ –1.5  $\text{cm}^{-1}$  deviation to  $\sim 0.1$ –0.2  $\text{cm}^{-1}$ . The  $v \geq 14$  states are shown in gray in the table, because for these states, tunneling to the inner well has an important effect on the energy and an “isolated” outer-well treatment is not sufficient for these states. We also note that the experimental term values for the  $v = 2$  states with  $N = 0, 1, \dots, 4$  and the  $v = 2$  and 3 states for  $N = 5$  are an order-of-magnitude less accurate than for the other states.<sup>20,23</sup>

In the table, we also compare with experiment the adiabatic energies (a) computed rigorously with the nuclear masses (“ $\text{ad}_p$ ” column)—these values are almost identical to the values in Table VI of Ref. 20—and (b) with the hydrogenic atomic mass (“ $\text{ad}_H$ ” column), which is often used to capture some nonadiabatic effects in the spectrum. In the present case, this atomic-mass model does not perform well, which can be understood by noting that the rigorous nonadiabatic (vibrational) correction to the nuclear mass is negative over most of the outer well.

Finally, we mention that Andersson and Elander,<sup>21</sup> by extending earlier work of Yu and Dressler,<sup>26</sup> solved the coupled-state

equations, including the coupling of the six lowest-energy  $^1\Sigma_g^+$  states, and also studied the outer-well region of  $\text{H}\bar{\text{H}}$ . They found that it was necessary to include all six  $^1\Sigma_g^+$  states to converge the  $\bar{H}$  vibrational energies better than 0.1  $\text{cm}^{-1}$ , whereas the 15th and 16th vibrational states ( $v = 14$  and 15 in Table I) changed by 0.12 and 24.11  $\text{cm}^{-1}$  between the five- and six-state treatment. Although their computed values are off by 10–35  $\text{cm}^{-1}$  from experiment, probably due to the fact that they used less accurate potential energy curves, their results seem to underline the general observation that the many-state Born–Oppenheimer (BO) expansion converges relatively slowly with respect to the number of electronic states.

#### IV. SUMMARY AND CONCLUSIONS

Due to the slow convergence of the Born–Oppenheimer (BO) expansion with respect to the number of electronic states, it is important to think about the truncation error when one is aiming to compute highly accurate molecular rovibrational (rovibronic) energies. Direct truncation introduces an error of  $\mathcal{O}(\varepsilon)$  in the rovibronic energies, where  $\varepsilon = (m_e/m_{\text{nuc}})^{1/2}$  is the square root of the electron-to-nucleus mass ratio.<sup>1,2,27</sup> This truncation error can be made lower order in  $\varepsilon$  by using adiabatic perturbation theory.<sup>2,27</sup> For an isolated electronic state, the first-order corrections can be made to vanish. The second-order nonadiabatic effective Hamiltonian, used in the present work, reproduces eigenvalues of the full electron-nucleus Hamiltonian with an error of  $\mathcal{O}(\varepsilon^3)$ , but it contains corrections both to the potential energy as well as to the kinetic energy of the atomic nuclei,<sup>1</sup> which give rise to effective coordinate-dependent masses to the different types of motions.

In particular, we have found a nontrivial, negative mass-correction to the vibrational mass of the proton in the outer well of the  $\text{H}\bar{\text{H}}$   $^1\Sigma_g^+$  electronic state. This negative value, i.e., an effective vibrational mass smaller than the nuclear mass, is dominated by the interaction with the  $\text{H}(1) + \text{H}(2)$  dissociation channel to which  $\text{H}\bar{\text{H}}$  gets close near its outer minimum. Of course, the precise value of the mass correction is the result of an interplay of the interaction of the nuclear dynamics on  $\text{H}\bar{\text{H}}$  with all the other (discrete and continuous) electronic states. It is interesting to note that, whereas the vibrational mass shows this special behavior for  $\text{H}\bar{\text{H}}$ , the nonadiabatic value of the rotational mass remains close to the atomic mass of the hydrogen (proton plus electron, see Fig. 3). Due to these properties,  $\text{H}\bar{\text{H}}$  makes a counterexample to the simple, empirical recipe according to which small nonadiabatic effects can be “approximately modeled” by using (near) the atomic mass value for vibrations and the nuclear mass for rotations.<sup>28–30</sup> In the case of the outer well of  $\text{H}\bar{\text{H}}$ , the vibrational mass is better approximated by the nuclear mass, while the rotational mass equals the atomic mass to a good approximation. Using the rigorous nonadiabatic, mass-correction functions computed in the present work, the nonadiabatic rovibrational energies are  $\sim 1 \text{ cm}^{-1}$  ( $2 \text{ cm}^{-1}$ ) larger than the energies obtained using the nuclear (atomic) mass. This, together with the relativistic and radiative corrections as well as with a minor, 0.1–0.2  $\text{cm}^{-1}$  improvement for the outer-well electronic energies, allows us to achieve a 0.1–0.2  $\text{cm}^{-1}$  agreement, an order of magnitude better than earlier theory, with experiment.<sup>20,23</sup>

All in all, we have demonstrated that small, nonadiabatic corrections in the (high-resolution) spectrum can be efficiently

described using the effective nonadiabatic Hamiltonian which accounts for the truncation error in the electronic space perturbatively. For the particular case of the outer well of the  $HH^+ \Sigma_g^+$  electronic state, the discrepancy of earlier theoretical work with experiment can be accounted for by a nontrivial decrease in the effective, nonadiabatic vibrational mass of the protons as they pass along near-lying electronic states.

### SUPPLEMENTARY MATERIAL

Improved Born–Oppenheimer electronic energies computed in the present work are listed in the [supplementary material](#) for the [6.60, 20.10] bohr interval of the  $R$  proton-proton separation. For  $R < 6.60$  bohr, we used the energies of Ref. 19.

### ACKNOWLEDGMENTS

We acknowledge financial support from a PROMYS Grant (No. IZ11Z0\_166525) of the Swiss National Science Foundation. D.F. acknowledges a doctoral scholarship from the New National Excellence Program of the Ministry of Human Capacities of Hungary (Grant No. ÚNKP-18-3-II-ELTE-133). E.M. thanks ETH Zürich for a visiting professorship during 2019 and the Laboratory of Physical Chemistry for their hospitality, where part of this work has been completed.

### REFERENCES

- <sup>1</sup>E. Mátyus and S. Teufel, *J. Chem. Phys.* **151**, 014113 (2019).
- <sup>2</sup>S. Teufel, *Adiabatic Perturbation Theory in Quantum Dynamics*, Lecture Notes in Mathematics (Springer-Verlag, Berlin, Heidelberg, New York, 2003).
- <sup>3</sup>R. M. Herman and A. Asgharian, *J. Mol. Spectrosc.* **19**, 305 (1966).
- <sup>4</sup>R. M. Herman and J. F. Ogilvie, *Adv. Chem. Phys.* **103**, 187 (1998).
- <sup>5</sup>D. W. Schwenke, *J. Chem. Phys.* **114**, 1693 (2001).
- <sup>6</sup>K. Pachucki and J. Komasa, *J. Chem. Phys.* **130**, 164113 (2009).
- <sup>7</sup>A. Scherrer, F. Agostini, D. Sebastiani, E. K. U. Gross, and R. Vuilleumier, *Phys. Rev. X* **7**, 031035 (2017).
- <sup>8</sup>P. R. Bunker, C. J. McLarnon, and R. E. Moss, *Mol. Phys.* **33**, 425 (1977).
- <sup>9</sup>K. Pachucki and J. Komasa, *J. Chem. Phys.* **129**, 034102 (2008).
- <sup>10</sup>E. Mátyus, *J. Chem. Phys.* **149**, 194111 (2018).
- <sup>11</sup>E. Mátyus, *J. Chem. Phys.* **149**, 194112 (2018).
- <sup>12</sup>M. Przybytek, W. Cencek, B. Jeziorski, and K. Szalewicz, *Phys. Rev. Lett.* **119**, 123401 (2017).
- <sup>13</sup>D. W. Schwenke, *J. Phys. Chem. A* **105**, 2352 (2001).
- <sup>14</sup>P. R. Bunker and R. E. Moss, *Mol. Phys.* **33**, 417 (1977).
- <sup>15</sup>E. Mátyus and M. Reiher, *J. Chem. Phys.* **137**, 024104 (2012).
- <sup>16</sup>E. Mátyus, *Mol. Phys.* **117**, 590 (2019).
- <sup>17</sup>L. Wolniewicz, *J. Chem. Phys.* **109**, 2254 (1998).
- <sup>18</sup>J. C. Light and T. Carrington, Jr., *Adv. Chem. Phys.* **114**, 263 (2000).
- <sup>19</sup>L. Wolniewicz, *J. Chem. Phys.* **108**, 1499 (1998).
- <sup>20</sup>E. Reinhold, W. Hogervorst, W. Ubachs, and L. Wolniewicz, *Phys. Rev. A* **60**, 1258 (1999).
- <sup>21</sup>S. Andersson and N. Elander, *Phys. Rev. A* **69**, 052507 (2004).
- <sup>22</sup>S. C. Ross, T. Yoshinari, Y. Ogi, and K. Tsukiyama, *J. Chem. Phys.* **125**, 133205 (2006).
- <sup>23</sup>E. Reinhold, W. Hogervorst, and W. Ubachs, *Phys. Rev. Lett.* **78**, 2543 (1997).
- <sup>24</sup>D. Ferenc and E. Mátyus, “Precise computation of rovibronic resonances of molecular hydrogen:  $EF^+ \Sigma_g^+$  inner-well rotational states,” *Phys. Rev. A* (to be published); e-print [arXiv:1904.08609](https://arxiv.org/abs/1904.08609).
- <sup>25</sup>V. I. Korobov, *Mol. Phys.* **116**, 93 (2018).
- <sup>26</sup>S. Yu and K. Dressler, *J. Chem. Phys.* **101**, 7692 (1994).
- <sup>27</sup>G. Panati, H. Spohn, and S. Teufel, *ESAIM: Math. Modell. Numer. Anal.* **41**, 297 (2007).
- <sup>28</sup>O. L. Polyansky and J. Tennyson, *J. Chem. Phys.* **110**, 5056 (1999).
- <sup>29</sup>L. G. Diniz, J. R. Mohallem, A. Alijah, M. Pavanello, L. Adamowicz, O. L. Polyansky, and J. Tennyson, *Phys. Rev. A* **88**, 032506 (2013).
- <sup>30</sup>E. Mátyus, T. Szidarovszky, and A. G. Császár, *J. Chem. Phys.* **141**, 154111 (2014).
- <sup>31</sup>L. M. Wang and Z.-C. Yan, *Phys. Rev. A* **97**, 060501(R) (2018).
- <sup>32</sup>M. Puchalski, A. Spyszkievicz, J. Komasa, and K. Pachucki, *Phys. Rev. Lett.* **121**, 073001 (2018).
- <sup>33</sup>L. Wolniewicz, *J. Mol. Spectrosc.* **174**, 132 (1995).
- <sup>34</sup>L. Wolniewicz, *J. Mol. Spectrosc.* **169**, 329 (1995).
- <sup>35</sup>L. Wolniewicz and K. Dressler, *J. Chem. Phys.* **100**, 444 (1994).
- <sup>36</sup>L. Wolniewicz, I. Simbotin, and A. Dalgarno, *Astrophys. J., Suppl. Ser.* **115**, 293 (1998).
- <sup>37</sup>M. Beyer and F. Merkt, *J. Mol. Spectrosc.* **330**, 147 (2016).
- <sup>38</sup>See <http://physics.nist.gov/cuu/Constants> for in the computations we used the precise values of the CODATA14 constants and conversion factors (last accessed May 3, 2019).



# Effective non-adiabatic Hamiltonians for the quantum nuclear motion over coupled electronic states

Cite as: J. Chem. Phys. 151, 014113 (2019); doi: 10.1063/1.5097899

Submitted: 29 March 2019 • Accepted: 7 June 2019 •

Published Online: 3 July 2019



View Online



Export Citation



CrossMark

Edit Mátyus<sup>1,a)</sup>  and Stefan Teufel<sup>2,b)</sup> 

## AFFILIATIONS

<sup>1</sup>Institute of Chemistry, ELTE, Eötvös Loránd University, Pázmány Péter sétány 1/A, H-1117 Budapest, Hungary

<sup>2</sup>Fachbereich Mathematik, Universität Tübingen, Auf der Morgenstelle 10, 72076 Tübingen, Germany

<sup>a)</sup>Electronic mail: [matyus@chem.elte.hu](mailto:matyus@chem.elte.hu)

<sup>b)</sup>Electronic mail: [stefan.teufel@uni-tuebingen.de](mailto:stefan.teufel@uni-tuebingen.de)

## ABSTRACT

The quantum mechanical motion of the atomic nuclei is considered over a single- or a multidimensional subspace of electronic states which is separated by a gap from the rest of the electronic spectrum over the relevant range of nuclear configurations. The electron-nucleus Hamiltonian is block-diagonalized up to  $\mathcal{O}(\epsilon^{m+1})$  through a unitary transformation of the electronic subspace, and the corresponding  $n$ th-order effective Hamiltonian is derived for the quantum nuclear motion. Explicit but general formulas are given for the second- and the third-order corrections. As a special case, the second-order Hamiltonian corresponding to an isolated electronic state is recovered which contains the coordinate-dependent mass-correction terms in the nuclear kinetic energy operator. For a multidimensional, explicitly coupled electronic band, the second-order Hamiltonian contains the usual Born–Oppenheimer terms and nonadiabatic corrections, but generalized mass-correction terms appear as well. These, earlier neglected terms, perturbatively account for the outlying (discrete and continuous) electronic states not included in the explicitly coupled electronic subspace.

Published under license by AIP Publishing. <https://doi.org/10.1063/1.5097899>

## I. INTRODUCTION

Molecules are central paradigms of chemistry. They acquire unique features as physical objects due to the three orders of magnitude difference in the mass of their constituent particles, the electrons and the atomic nuclei.

Significant improvements in the energy resolution of spectroscopy experiments,<sup>1,2</sup> developed or adapted for the molecular domain, provide us with new pieces of information which can be deciphered, if a similarly precise and accurate theoretical description becomes available. For this purpose, it is necessary to reconsider the usual approximations used in quantum chemistry, in particular, the Born–Oppenheimer (BO) and the nonrelativistic approximations. These two approximations give rise to “effects” which play a role at the presently available experimental energy resolution. Further “effects” may also be visible; for example, the interaction between the molecule and the quantized photon field is more and more

appreciated as significant corrections to the molecular energy at this resolution.<sup>3</sup> Molecules have a large number of sharp spectral transitions, which can be measured experimentally to high precision. The interplay of the many small (or often not so small) effects (may) show up differently for the transitions between the different dynamical domains, so we cannot rely on the cancellation of the small effects, but their explicit computation,<sup>3–5</sup> and hence further development of molecular quantum theory, is necessary.

As to the coupling of the quantum mechanical motion of the electrons and the atomic nuclei benchmark, energies and wave functions can be obtained by the explicit, variational solution of the few-particle Schrödinger equation.<sup>6–16</sup> We call this direction pre-Born–Oppenheimer (pre-BO) theory because it completely avoids the BO separation, nor does it evoke the concept of a potential energy surface (PES). Obviously, a pre-BO computation captures “all” nonadiabatic “effects.” Although all bound and low-lying resonance states of the three-particle  $\text{H}_2^+ = \{p^+, p^+, e^-\}$  molecular ion

have been recently reported to an outstanding precision,<sup>17</sup> already for four- and five-particle systems,<sup>15</sup> the explicit many-particle solution is typically limited to a few selected states due to the increased computational cost and other methodological challenges.

In order to compute (reasonably) accurate energies and wave functions over a broad dynamical range, we look for effective nonadiabatic Hamiltonians.

There is a vast literature about dominant nonadiabatic features,<sup>18–20</sup> such as conical intersections, the geometric phase effect, or Jahn–Teller systems. Practical diabaticization procedures<sup>19,21,22</sup> have been developed which make it possible to couple close-coming electronic states (to a good approximation) without the explicit knowledge of nonadiabatic coupling vectors, which are tedious to compute and burdensome to interpolate for larger systems. These effects are sometimes called first-order nonadiabatic effects and represent qualitatively important features for the molecular dynamics.

In the case of an isolated electronic state, the dynamics is well described using a single potential energy surface. In order to obtain more accurate results, one would need to couple an increasing number of electronic states. These additional, explicitly coupled states would give small but non-negligible contributions to the molecular energy when studied under high resolution. Tightly converging the rovibrational (rovibronic) energy by increasing the number of explicitly coupled electronic states is impractical (or impossible, since one would need to include also continuum electronic states).

A correction which is often computed is the diagonal Born–Oppenheimer correction (DBOC), which gives a mass-dependent contribution to the potential energy surface (PES). It has been (empirically) observed that in rovibrational computations carried out on a single potential energy surface, it is “better” (in comparison with experiments) to use the atomic mass, especially for heavier atoms, instead of the nuclear mass, which would have been rigorously dictated by the BO approximation. The difference between the atomic and the nuclear mass is small; it is the mass of the electrons. This empirical adjustment of the mass of the nuclei used in the rovibrational kinetic energy operator has been supplemented with the argument that attaching the electron mass to the nuclear mass approximately accounts for small, “secondary” nonadiabatic effects.<sup>23</sup> The empirical adjustment is motivated by the picture that the electrons “follow” the atomic nuclei in their motion.

For an isolated electronic state, the effective rovibrational Hamiltonian including the rigorous mass-correction terms has been derived and rederived in a number of independent and different (perturbative) procedures<sup>24–30</sup> over the past decades and was numerically computed for a few systems.<sup>26,31–38</sup> These mass-correction terms perturbatively account for the effect of all other electronic states on the rovibrational motion.

We would like to have similar perturbative corrections, for a system which is governed by not only a single but by a few close-lying electronic states, which are explicitly, nonadiabatically coupled, but which are distant (separated by a finite gap) from the rest of the (discrete and continuous) electronic states over the relevant range of the nuclear coordinates (Fig. 1).

To the best of our knowledge, the explicit formulas have never been derived for an electronic band which includes multiple electronic states, but all the necessary ideas and techniques have been

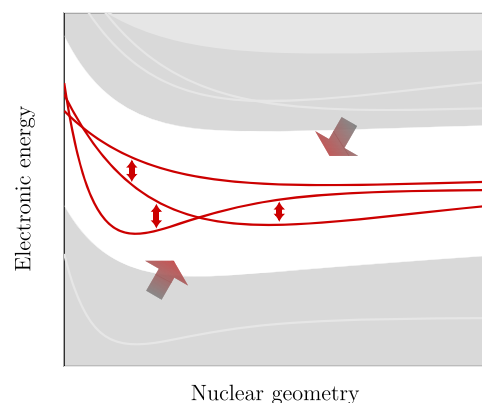


**FIG. 1.** Schematic plot of the electronic energy with respect to the nuclear geometry to visualize the aim of the present work: formulation of an effective nonadiabatic Hamiltonian for the quantum nuclear motion over an explicitly coupled electronic band, which is separated by a gap and decoupled perturbatively from the outlying (discrete or continuous) electronic spectrum.

available in the literature, in particular, in relation with the space-adiabatic theory of quantum mechanics,<sup>39–43</sup> but also other rigorous approaches to compute higher-order corrections to the Born–Oppenheimer approximation have been developed, most notably in Ref. 44. The techniques we use in this article are somewhat reminiscent of Van Vleck perturbation theory and contact transformation often used in chemistry and physics. We use here a compact and powerful notation which will allow us to obtain not only second- but also third-order correction formulas for a single or multidimensional (nonadiabatically coupled) electronic subspace.

We believe that the explicit formulation of the effective nonadiabatic Hamiltonians for coupled electronic states, including the earlier missing kinetic (or mass) correction terms, will be useful for the chemical physics community. Their numerical application assumes the computation of nonadiabatic coupling vectors. Earlier work in which the mass-correction terms were computed for a single electronic state, e.g., Refs. 37 and 38, can be generalized for a multistate band, so numerical applications will probably follow this theoretical work in the near future.

## A. Summary of the main result

At the end of this introduction, we summarize the main result of the paper to help orientation in the rather technical sections to come. In this article, we derive the general form of the effective nonadiabatic Hamiltonian  $\hat{H}^{(2)}$  for a group of  $d$  electronic levels  $E_1(R), \dots, E_d(R)$  that are separated by a gap from the rest of the spectrum. Our analysis implies, for example, that its eigenvalues approximate the eigenvalues of the full molecular Hamiltonian up to order  $\varepsilon^3$ , where  $\varepsilon = \sqrt{\frac{m}{M}}$  is the square root of the mass ratio of electron and nuclear mass. It thus captures *all* second-order contributions. It is important to note that the perturbative expansion is carried out without assuming small nuclear momenta,

so the nuclear kinetic energy  $\|\varepsilon\nabla_R\psi\|^2$  is of order one and not of order  $\varepsilon^2$ .

After choosing  $d$  electronic states  $\psi_1(R), \dots, \psi_d(R)$  that are smooth functions of  $R$  and pointwise form an orthonormal basis of the selected electronic subspace, the projection onto which we denote by  $P(R)$  (i.e., an adiabatic or diabatic basis set for the selected electronic subspace), the effective nonadiabatic Hamiltonian  $\widehat{H}^{(2)}$  takes the form of an operator acting on wave functions on the nuclear configuration space  $\mathbb{R}^{3N}$  that take values in  $\mathbb{C}^d$  and thus can be written as a  $d \times d$ -matrix of operators  $(\widehat{H}^{(2)})_{\alpha\beta}$  acting on functions on  $\mathbb{R}^{3N}$ ,

$$(\widehat{H}^{(2)})_{\alpha\beta} = \sum_{ij=1}^{3N} \left[ \frac{1}{2} (-i\varepsilon\partial_i\mathbf{1} + \varepsilon\mathbf{A}_i)(\delta_{ij}\mathbf{1} - \varepsilon^2\mathbf{M}_{ij})(-i\varepsilon\partial_j\mathbf{1} + \varepsilon\mathbf{A}_j) \right]_{\alpha\beta} + (\mathbf{E} + \varepsilon^2\Phi)_{\alpha\beta}.$$

Here, the boldface objects are  $(d \times d)$  matrix-valued functions on the nuclear configuration space, with  $(\mathbf{1})_{\alpha\beta} := \delta_{\alpha\beta}$  denoting the identity matrix and the others given as follows in terms of the electronic states  $\psi_1(R), \dots, \psi_d(R)$ .

The coefficients of the nonabelian Berry connection are as expected,  $\mathbf{A}_{\alpha\beta,i}(R) = -i\langle\psi_\alpha(R)|\partial_i\psi_\beta(R)\rangle$ . The “diabatic” electronic level matrix becomes  $\mathbf{E}_{\alpha\beta}(R) = \langle\psi_\alpha(R)|H_e(R)|\psi_\beta(R)\rangle$ , where  $H_e(R)$  is the electron Hamiltonian for fixed nuclear configuration  $R$ . The second-order diagonal correction is  $\Phi_{\alpha\beta}(R) = \frac{1}{2}\sum_{i=1}^{3N}\langle\partial_i\psi_\alpha(R)|P^\perp(R)|\partial_i\psi_\beta(R)\rangle$ , where  $P^\perp(R) = 1 - P(R)$  projects on the orthogonal complement of the selected electronic subspace, i.e., on the orthogonal complement of the span of  $\psi_1(R), \dots, \psi_d(R)$ .

While the matrix versions of terms discussed up to now could have been easily guessed from the single band ( $d = 1$ ) case, the determination of the second-order mass correction matrix requires the systematic perturbation approach developed in Sec. IV. The resulting expression is

$$\mathbf{M}_{\alpha\beta,ij} = \sum_{a,b=1}^d \langle\psi_\alpha|P_a(\partial_jP)(\mathcal{R}_a + \mathcal{R}_b)(\partial_iP)P_b|\psi_\beta\rangle,$$

where for better readability, we dropped the argument  $R$  in all the functions. Here,  $\mathcal{R}_a(R) := (H_e(R) - E_a(R))^{-1}P^\perp(R)$  is the reduced resolvent of the level  $E_a(R)$  acting as a bounded operator on the range of  $P^\perp(R)$ , and  $P_a(R)$  is the projection onto the eigenspace of  $H_e(R)$  corresponding to the eigenvalue  $E_a(R)$ . In the special case that  $\psi_1(R), \dots, \psi_d(R)$  form an adiabatic basis set, i.e.,  $H_e(R)\psi_\alpha(R) = E_\alpha(R)\psi_\alpha(R)$  for  $\alpha = 1, \dots, d$ , the expression for the mass correction term simplifies to  $\mathbf{M}_{ab,ij}(R) = \langle\partial_j\psi_a(R)|\mathcal{R}_a(R) + \mathcal{R}_b(R)|\partial_i\psi_b(R)\rangle$ .

## II. HAMILTONIAN, COUPLING PARAMETER, AND OPERATOR ORDERS

### A. Molecular Hamiltonian

The molecular Hamiltonian is the sum of the nuclear kinetic energy acting on the nuclear coordinates  $\bar{R}$ , the electron kinetic energy acting on the electronic coordinates  $r$ , and the Coulomb

interaction terms (in hartree atomic units,  $m_e = \hbar = 1$ ),

$$\widehat{H} = -\sum_{i=1}^N \frac{1}{2m_i} \Delta_{\bar{R}_i} - \sum_{k=1}^n \frac{1}{2} \Delta_{r_k} + V(\bar{R}, r). \quad (1)$$

By absorbing the different masses of the atomic nuclei in the mass-scaled Cartesian coordinates  $R_i = M_i^{-1/2}\bar{R}_i$ , where  $M_i$  are the nuclear masses in atomic mass units,<sup>45</sup> one can rewrite the nuclear kinetic energy operator as

$$-\sum_{i=1}^N \frac{1}{2m_i} \Delta_{\bar{R}_i} = -\varepsilon^2 \sum_{i=1}^N \frac{1}{2M_i} \Delta_{\bar{R}_i} = -\frac{\varepsilon^2}{2} \sum_{i=1}^N \Delta_{R_i} = -\frac{\varepsilon^2}{2} \Delta = -\frac{\varepsilon^2}{2} (\varepsilon\nabla)(\varepsilon\nabla) = -\frac{1}{2} \sum_{j=1}^{3N} (\varepsilon\partial_j)^2, \quad (2)$$

and we label  $\varepsilon^2 = m_e/m_u \ll 1$  the conversion factor between the electronic and the atomic mass scale, which is characteristic of the three orders of magnitude mass difference of the electrons and the atomic nuclei.

Using the common notation  $H_e(R) := -\sum_{k=1}^n \frac{1}{2} \Delta_{r_k} + V(R, r)$  for the electronic Hamiltonian, we can rewrite the electron-nucleus Hamiltonian into the compact form,

$$\widehat{H} = -\frac{\varepsilon^2}{2} \Delta + H_e(R) =: \widehat{K} + H_e(R), \quad (3)$$

which highlights the  $\varepsilon^2$  scale-separation (and coupling) between the electron-nucleus quantum mechanical motion. Also note that capital letters without a hat label operators that are functions of  $R$ , i.e., they act fibrewise (pointwise in  $R$ ) on the electronic Hilbert space, such as  $H_e$ . All other operators (which include differential operators of  $R$ ) are labeled with a wide hat, and the nuclear kinetic energy  $\widehat{K}$  is an example for this type of operators.

### B. Counting operator orders

During the course of this work, we will perform an asymptotic expansion of operators in powers of the small parameter  $\varepsilon$ . Since many of the operators appearing in the calculations are unbounded, we emphasize that we are interested in the action of operators on typical molecular wave functions with energies of order  $\mathcal{O}(1)$ . In particular, the nuclear kinetic energy  $-\frac{\varepsilon^2}{2}\Delta = \frac{1}{2}\widehat{p}^2$  and thus also the nuclear momentum operator  $\widehat{p} = -i\varepsilon\nabla$  are of order  $\mathcal{O}(1)$  (instead of  $\mathcal{O}(\varepsilon)$ , which one could naively think). This is because a typical molecular wave function shows oscillations with respect to the nuclear coordinates on a spatial scale of order  $\varepsilon^{-1}$ , and thus, it has derivatives of order  $\varepsilon^{-1}$ . However, when  $\widehat{p}$  acts on a smooth, perhaps operator-valued, function  $f(R)$  of the nuclear coordinates, we have a quantity  $\mathcal{O}(\varepsilon)$ , indeed,

$$[\widehat{p}, f(R)]\psi = \widehat{p}(f\psi) - f\widehat{p}\psi = (\widehat{p}f)\psi = -i\varepsilon(\nabla f)(R)\psi. \quad (4)$$

These observations will be important to remember for the following calculations.

### III. THE ZERO-TH-ORDER NONADIABATIC HAMILTONIAN: TRUNCATION ERROR AND A STRATEGY FOR REDUCING THIS ERROR

Let  $\{E_a(R), a = 1, \dots, d\}$  be a finite set of eigenvalues of the electronic Hamiltonian  $H_e(R)$  that are isolated by a finite gap<sup>47</sup> from the rest of the spectrum over the relevant range of nuclear configurations and denote by  $P_a(R)$  the corresponding spectral projections. Then,  $P(R) = \sum_{a=1}^d P_a(R)$  projects onto the selected electronic subspace and  $P^\perp := 1 - P$  is the projection onto the orthogonal complement.

The full electron-nucleus Hamiltonian can be written in a block form as

$$\widehat{H} = \begin{pmatrix} P\widehat{H}P & P\widehat{H}P^\perp \\ P^\perp\widehat{H}P & P^\perp\widehat{H}P^\perp \end{pmatrix}, \quad (5)$$

where  $\widehat{H}_p^{(0)} := P\widehat{H}P$  corresponds to the “usual” nonadiabatic Hamiltonian.<sup>48</sup> In numerical computations,  $\widehat{H}_p^{(0)}$  is usually represented over some adiabatic or diabatic basis, whereas the off-diagonal (OD)  $P\widehat{H}P^\perp$  and  $P^\perp\widehat{H}P$  blocks have been neglected in earlier work.

The following calculation shows that the off-diagonal terms are indeed small (remember the gap condition at the beginning of this section), more precisely, of order  $\varepsilon$ :

$$\begin{aligned} P^\perp\widehat{H}P &= P^\perp(\widehat{K} + H_e)P \\ &= P^\perp\widehat{K}P \quad ([P, H_e] = 0) \\ &= P^\perp[\widehat{K}, P]P \quad (PP = P \text{ and } P^\perp P = 0) \\ &= -\frac{\varepsilon}{2}P^\perp[\Delta, P]P \\ &= -\frac{1}{2}P^\perp(\varepsilon^2\Delta P - P\varepsilon^2\Delta)P \\ &= -\frac{1}{2}P^\perp(\varepsilon\nabla \cdot \varepsilon(\nabla P) + \varepsilon(\nabla P) \cdot \varepsilon\nabla)P \\ &= -\frac{\varepsilon}{2}P^\perp(\varepsilon\nabla \cdot P' + P' \cdot \varepsilon\nabla)P \\ &=: -\varepsilon P^\perp\widehat{P}'_\nabla P, \end{aligned} \quad (6)$$

where for any fibered operator  $A$ , we use the abbreviations  $A' := \nabla A$ , and the symmetrized directional derivative of  $A$  is

$$\widehat{A}'_\nabla := \frac{1}{2}(\varepsilon\nabla \cdot A' + A' \cdot \varepsilon\nabla) = \frac{1}{2}(\widehat{p} \cdot A' + A' \cdot \widehat{p}), \quad (7)$$

i.e.,  $A'$  is again a fibered operator, while  $\widehat{A}'_\nabla$  is a first-order differential operator in the nuclear coordinates of  $\mathcal{O}(1)$ . For the upper-right off-diagonal block, we find similarly

$$P\widehat{H}P^\perp = \varepsilon P\widehat{P}'_\nabla P^\perp. \quad (8)$$

Hence, the off-diagonal part of the nuclear kinetic energy operator  $\widehat{K}$  is of order  $\varepsilon$  and we introduce the abbreviation

$$\widehat{Q} := \frac{1}{\varepsilon}(P\widehat{K}P^\perp + P^\perp\widehat{K}P) = P\widehat{P}'_\nabla P^\perp - P^\perp\widehat{P}'_\nabla P, \quad (9)$$

which, as explained above, is an operator of  $\mathcal{O}(1)$ . Using  $\widehat{Q}$  and the properties of  $P$  and  $P^\perp$ , the off-diagonal blocks of the Hamiltonian are written in the compact form,

$$P^\perp\widehat{H}P = \varepsilon P^\perp\widehat{Q}P \quad \text{and} \quad P\widehat{H}P^\perp = \varepsilon P\widehat{Q}P^\perp, \quad (10)$$

which are both of  $\mathcal{O}(\varepsilon)$ , and thus,

$$\widehat{H} = \begin{pmatrix} \widehat{H}_p^{(0)} & \varepsilon P\widehat{Q}P^\perp \\ \varepsilon P^\perp\widehat{Q}P & P^\perp\widehat{H}P^\perp \end{pmatrix} = \begin{pmatrix} \widehat{H}_p^{(0)} & 0 \\ 0 & P^\perp\widehat{H}P^\perp \end{pmatrix} + \mathcal{O}(\varepsilon). \quad (11)$$

This expression confirms the well-known fact that the off-diagonal nonadiabatic couplings are small (for a group of bands separated by a gap from the rest of the electronic spectrum). As a consequence, the spectrum of  $\widehat{H}_p^{(0)}$  provides an  $\mathcal{O}(\varepsilon)$  approximation, at least locally in energy, to the spectrum of  $\widehat{H}$ . More precisely, within a neighborhood of order  $\varepsilon$  around any spectral value of  $\widehat{H}_p^{(0)}$ , there is also a spectral value of the full Hamiltonian  $\widehat{H}$ .<sup>49</sup>

To obtain a better approximation, we replace the projection  $P$  by a slightly “tilted” projection  $\widehat{\Pi}$  such that the off-diagonal terms in the block-decomposition of  $\widehat{H}$  with respect to  $\widehat{\Pi}$  are of lower order, namely,

$$\widehat{H} = \begin{pmatrix} \widehat{\Pi}\widehat{H}\widehat{\Pi} & \widehat{\Pi}\widehat{H}\widehat{\Pi}^\perp \\ \widehat{\Pi}^\perp\widehat{H}\widehat{\Pi} & \widehat{\Pi}^\perp\widehat{H}\widehat{\Pi}^\perp \end{pmatrix} = \begin{pmatrix} \widehat{H}_p^{(n)} & 0 \\ 0 & \widehat{\Pi}^\perp\widehat{H}\widehat{\Pi}^\perp \end{pmatrix} + \mathcal{O}(\varepsilon^{n+1}), \quad (12)$$

for some  $n \geq 1$ . The projection  $\widehat{\Pi}$  is obtained from  $P$  through a near-identity unitary transformation,

$$\widehat{\Pi} = e^{i\varepsilon\widehat{S}} P e^{-i\varepsilon\widehat{S}}, \quad (13)$$

where the generator  $\widehat{S} \approx \widehat{A}_1 + \varepsilon\widehat{A}_2 + \varepsilon^2\widehat{A}_3 + \dots$  will be determined exactly by the condition that the off-diagonal elements in Eq. (12) are of order  $\varepsilon^{n+1}$ . The  $n$ th-order effective Hamiltonian  $\widehat{H}_p^{(n)}$  obtained in this way will give an  $\mathcal{O}(\varepsilon^{n+1})$  approximation to the spectrum of  $\widehat{H}$ . The physical picture behind the projection  $\widehat{\Pi}$  is the following. The range of the adiabatic projection  $P$  is spanned by states of the form  $\Psi(R, r) = \varphi(R)\psi_a(R, r)$ , where  $\psi_a(R, r)$  are eigenstates of the electronic Hamiltonian  $H_e(R)$  for the clamped nuclear configuration  $R$ ,  $H_e(R)\psi_a(R, \cdot) = E_a(R)\psi_a(R, \cdot)$ . However, since the nuclei are also moving, the molecular eigenstates are only approximately but not exactly of this local product form. Loosely speaking, the state of the electrons depends also on the momenta of the nuclei. This effect is taken care of by slightly tilting the projection  $P$  into the projection  $\widehat{\Pi}$ .

For computing eigenvalues of the  $n$ th-order effective Hamiltonian  $\widehat{H}_p^{(n)}$ , it will be more appropriate to consider the unitarily equivalent (and thus isospectral) operator,

$$\widehat{\mathcal{H}}_p^{(n)} := e^{-i\varepsilon\widehat{S}}\widehat{H}_p^{(n)}e^{i\varepsilon\widehat{S}} = e^{-i\varepsilon\widehat{S}}\widehat{\Pi}\widehat{H}\widehat{\Pi}e^{i\varepsilon\widehat{S}} = P e^{-i\varepsilon\widehat{S}}\widehat{H}e^{i\varepsilon\widehat{S}}P, \quad (14)$$

which, by choosing a basis representation for  $P$ , will provide an  $n$ th-order effective Hamiltonian for the quantum nuclear motion corresponding to the selected electronic subspace. The eigenvectors of  $\widehat{H}_p^{(n)}$  and  $\widehat{\mathcal{H}}_p^{(n)}$  are related by the unitary transformation  $e^{i\varepsilon\widehat{S}}$ .

#### IV. CALCULATION OF THE $n$ TH-ORDER TRANSFORMATION MATRIX

We would like to achieve an  $\mathcal{O}(\epsilon^{n+1})$  block diagonalization of the electron-nucleus Hamiltonian by conjugating it with an appropriate unitary operator  $e^{i\widehat{S}}$ , a strategy that is somewhat reminiscent of what is known in chemical physics as Van Vleck perturbation theory and contact transformation. The actual procedure we use is known as adiabatic perturbation theory in the mathematical literature<sup>39–42</sup> but was applied before in physics also in the context of the Born–Oppenheimer approximation in Ref. 43. While the quoted references, with the exception of Ref. 41, used pseudodifferential calculus and are therefore quite technical and demanding, our approach is rather elementary and uses a general and compressed notation. As a consequence, we are able to derive with relatively little effort explicit expressions not only for  $\widehat{H}_p^{(2)}$  but also for  $\widehat{H}_p^{(3)}$  and not only for a single but for a finite number of coupled electronic states. Note that  $\widehat{H}_p^{(2)}$  for a single electronic state was explicitly calculated earlier, e.g., in Refs. 24, 29, 30, 40, 41, and 43, although in some cases without carefully paying attention to the subtleties of counting operator orders in relation with the nuclear momenta (see Sec. II B).

The simplicity and generality of our derivation is based on the concept and simple algebraic properties of diagonal and off-diagonal operators and an explicit expression for the inverse of the quantum Liouvillian (*vide infra*) acting on operators which do not contain nuclear differential operators.

#### A. Technical preliminaries

Before constructing  $\widehat{S}$  and  $\widehat{H}_p^{(n)}$ , we introduce the concept of (off)diagonal operators and the (inverse) Liouvillian as well as some of their properties, which will become useful during the course of the calculations. Further useful relationships are collected in the Appendix.

#### 1. Diagonal and off-diagonal operators

We define the diagonal (D) and the off-diagonal (OD) parts of a linear operator  $\widehat{A}$  with respect to the orthogonal projections  $P$  and  $P^\perp = 1 - P$  as

$$\widehat{A}^D := P\widehat{A}P + P^\perp\widehat{A}P^\perp \quad \text{and} \quad \widehat{A}^{\text{OD}} := P\widehat{A}P^\perp + P^\perp\widehat{A}P, \quad (15)$$

respectively. From this definition, a number of simple relationships follow immediately. For example, it holds for all operators  $\widehat{A}$

and  $\widehat{B}$  that

$$[\widehat{A}^D, P] = [\widehat{A}^D, P^\perp] = 0 \quad \text{and} \quad [\widehat{A}^{\text{OD}}, P] = P^\perp\widehat{A}P - P\widehat{A}P^\perp, \quad (16)$$

and

$$[\widehat{A}^D, \widehat{B}^D]^{\text{OD}} = 0, \quad [\widehat{A}^D, \widehat{B}^{\text{OD}}]^D = 0, \quad \text{and} \quad [\widehat{A}^{\text{OD}}, \widehat{B}^{\text{OD}}]^{\text{OD}} = 0. \quad (17)$$

Finally, note that  $\widehat{Q}$  defined in Eq. (9) is related to the off-diagonal part of the nuclear kinetic energy as

$$\widehat{K}^{\text{OD}} = \epsilon\widehat{Q}. \quad (18)$$

#### 2. Commutators, the quantum Liouvillian, and its inverse

Given an operator  $\widehat{B}$ , let us define the linear mapping

$$\widehat{A} \mapsto \mathcal{L}_{\widehat{B}}(\widehat{A}) := -i[\widehat{B}, \widehat{A}], \quad (19)$$

whenever the commutator is well defined (for the operators we consider in this work, no problems with operator domains occur). For  $\widehat{B} = H_e$ , we call this mapping the quantum Liouvillian of  $\widehat{A}$ ,

$$\mathcal{L}_{H_e}(\widehat{A}) = -i[H_e, \widehat{A}]. \quad (20)$$

Since  $H_e$  commutes with  $P$  and  $P^\perp$ , the Liouvillian  $\mathcal{L}_{H_e}$  preserves (off)diagonality, i.e.,

$$\mathcal{L}_{H_e}(\widehat{A}^D) = \mathcal{L}_{H_e}(\widehat{A})^D \quad \text{and} \quad \mathcal{L}_{H_e}(\widehat{A}^{\text{OD}}) = \mathcal{L}_{H_e}(\widehat{A})^{\text{OD}}. \quad (21)$$

Furthermore,  $\mathcal{L}_{H_e}$  is invertible on the space of fibered off-diagonal operators (labeled without any hat). Explicitly, for  $B := B^{\text{OD}}$ , its inverse is

$$\mathcal{I}_{H_e}(B) = i \sum_{a=1}^d (\mathcal{R}_a B P_a - P_a B \mathcal{R}_a), \quad (22)$$

where

$$\mathcal{R}_a(R) := (H_e(R) - E_a(R))^{-1} P^\perp(R) \quad (23)$$

is the reduced resolvent (with the nuclear coordinate dependence shown explicitly). Note that, due to the gap condition,  $(H_e(R) - E_a(R))^{-1}$  is indeed a bounded operator when restricted to states in the orthogonal complement of the range of  $P(R)$ .

In the following lines, we check that Eq. (22) is indeed the inverse Liouvillian on off-diagonal fibered operators, but we carry out this calculation for a general operator,  $\widehat{B}$ , which may contain also the nuclear momentum operator (highlighted with a hat in the notation),

$$\begin{aligned} \mathcal{L}_{H_e}(\mathcal{I}_{H_e}(\widehat{B})) &= -i \left[ H_e, i \sum_a (\mathcal{R}_a \widehat{B} P_a - P_a \widehat{B} \mathcal{R}_a) \right] \\ &= \sum_a [H_e, (\mathcal{R}_a \widehat{B} P_a - P_a \widehat{B} \mathcal{R}_a)] \\ &= \sum_a [H_e - E_a, (\mathcal{R}_a \widehat{B} P_a - P_a \widehat{B} \mathcal{R}_a)] + \sum_a (\mathcal{R}_a [E_a, \widehat{B}] P_a - P_a [E_a, \widehat{B}] \mathcal{R}_a) \\ &= \sum_a (P^\perp \widehat{B} P_a + P_a \widehat{B} P^\perp) + \sum_a (\mathcal{R}_a [E_a, \widehat{B}] P_a - P_a [E_a, \widehat{B}] \mathcal{R}_a) \\ &= \widehat{B}^{\text{OD}} + \sum_a (\mathcal{R}_a [E_a, \widehat{B}] P_a - P_a [E_a, \widehat{B}] \mathcal{R}_a), \end{aligned} \quad (24)$$

where  $E_a(R)$  is the electronic energy. For off-diagonal, fibered operators  $\mathcal{S}_{H_e}$  is indeed the (exact) inverse of  $\mathcal{L}_{H_e}$  since  $[E_a, B] = 0$ . Otherwise, it is an approximation to the inverse with an error depending on the value of the commutator  $[E_a, \widehat{B}]$ . For example, if  $\widehat{B} = \widehat{K}^{\text{OD}}$ , the commutator in Eq. (24) is  $[E_a(R), \widehat{K}^{\text{OD}}] = \varepsilon[E_a(R), \widehat{Q}]$ , and thus,  $\mathcal{L}_{H_e}(\mathcal{S}_{H_e}(\widehat{K}^{\text{OD}})) = \widehat{K}^{\text{OD}} + \mathcal{O}(\varepsilon)$ , so the inverse is obtained with an  $\mathcal{O}(\varepsilon)$  error.

## B. Conditions for making the off-diagonal block of the Hamiltonian lower order

As explained in Sec. III, in order to reduce the off-diagonal coupling between the selected electronic subspace  $P$  and its orthogonal complement  $P^\perp$ , we will choose the self-adjoint operator  $\widehat{S} = \widehat{A}_1 + \varepsilon\widehat{A}_2 + \dots$  such that the off-diagonal part (coupling) within the  $\widehat{\Pi}$ -block decomposition of the Hamiltonian  $\widehat{H}$  [Eq. (12)] is small,

$$\widehat{\Pi}^\perp \widehat{H} \widehat{\Pi} \stackrel{!}{=} \mathcal{O}(\varepsilon^{n+1}). \quad (25)$$

Due to hermiticity, this condition also implies that  $\widehat{\Pi} \widehat{H} \widehat{\Pi}^\perp$  is of  $\mathcal{O}(\varepsilon^{n+1})$ . To construct explicitly the operators  $\widehat{A}_1, \widehat{A}_2, \dots$ , it is more practical to use the unitary transform

$$\begin{aligned} e^{-i\varepsilon\widehat{S}} \widehat{\Pi}^\perp \widehat{H} \widehat{\Pi} e^{i\varepsilon\widehat{S}} &= P^\perp e^{-i\varepsilon\widehat{S}} \widehat{H} e^{i\varepsilon\widehat{S}} P \\ &= P^\perp \widehat{H} P \\ &\stackrel{!}{=} \mathcal{O}(\varepsilon^{n+1}) \end{aligned} \quad (26)$$

of condition (25), where the transformed Hamiltonian is defined as

$$\widehat{\mathcal{H}} = e^{-i\varepsilon\widehat{S}} \widehat{H} e^{i\varepsilon\widehat{S}}. \quad (27)$$

In the language of diagonal and off-diagonal operators, the condition of Eq. (26) is fulfilled if the *off-diagonal part* of the transformed Hamiltonian,  $\widehat{\mathcal{H}}^{\text{OD}} = P^\perp \widehat{\mathcal{H}} P + P \widehat{\mathcal{H}} P^\perp$ , is small,

$$\widehat{\mathcal{H}}^{\text{OD}} \stackrel{!}{=} \mathcal{O}(\varepsilon^{n+1}), \quad (28)$$

which will be our working equation to determine the operators  $\widehat{A}_1, \dots, \widehat{A}_n$  up to the  $(n+1)$ st order in  $\varepsilon$ . Then, using these operators, an explicit expression will be derived for the relevant block of the transformed Hamiltonian, namely, of  $\widehat{\mathcal{H}}_P^{(n)} = P \widehat{\mathcal{H}} P$  as defined in Eq. (14) and explained in Sec. III.

## C. Reduction of the off-diagonal coupling: Determination of $\widehat{A}_1, \dots, \widehat{A}_n$

The transformed electron-nucleus Hamiltonian is expanded in terms of increasing powers of  $\varepsilon$  (see the Appendix) as

$$\begin{aligned} \widehat{\mathcal{H}} &= e^{-i\varepsilon\widehat{S}} \widehat{H} e^{i\varepsilon\widehat{S}} \\ &= \widehat{H} + \varepsilon \mathcal{L}_{\widehat{S}}(\widehat{H}) + \frac{\varepsilon^2}{2} \mathcal{L}_{\widehat{S}}(\mathcal{L}_{\widehat{S}}(\widehat{H})) + \frac{\varepsilon^3}{6} \mathcal{L}_{\widehat{S}}(\mathcal{L}_{\widehat{S}}(\mathcal{L}_{\widehat{S}}(\widehat{H}))) + \dots \end{aligned} \quad (29)$$

For the electronic Hamiltonian, the expansion up to  $\mathcal{O}(\varepsilon^4)$  is

$$\begin{aligned} e^{-i\varepsilon\widehat{S}} H_e e^{i\varepsilon\widehat{S}} &= H_e + \varepsilon \mathcal{L}_{\widehat{A}_1}(H_e) + \varepsilon^2 \left( \mathcal{L}_{\widehat{A}_2}(H_e) + \frac{1}{2} \mathcal{L}_{\widehat{A}_1}(\mathcal{L}_{\widehat{A}_1}(H_e)) \right) \\ &\quad + \varepsilon^3 \left( \mathcal{L}_{\widehat{A}_3}(H_e) + \frac{1}{2} \mathcal{L}_{\widehat{A}_1}(\mathcal{L}_{\widehat{A}_2}(H_e)) + \frac{1}{2} \mathcal{L}_{\widehat{A}_2}(\mathcal{L}_{\widehat{A}_1}(H_e)) \right) \\ &\quad + \frac{1}{6} \mathcal{L}_{\widehat{A}_1}(\mathcal{L}_{\widehat{A}_1}(\mathcal{L}_{\widehat{A}_1}(H_e))) + \mathcal{O}(\varepsilon^4). \end{aligned} \quad (30)$$

Anticipating that commutators of the form  $[\widehat{A}_j, \widehat{K}]$  are of order  $\varepsilon$ , the expansion for the nuclear kinetic energy term up to the same order is

$$\begin{aligned} e^{-i\varepsilon\widehat{S}} \widehat{K} e^{i\varepsilon\widehat{S}} &= \widehat{K} + \varepsilon^2 \mathcal{L}_{\widehat{A}_1}(\frac{1}{\varepsilon} \widehat{K}) + \varepsilon^3 \left( \mathcal{L}_{\widehat{A}_2}(\frac{1}{\varepsilon} \widehat{K}) \right. \\ &\quad \left. + \frac{1}{2} \mathcal{L}_{\widehat{A}_1}(\mathcal{L}_{\widehat{A}_1}(\frac{1}{\varepsilon} \widehat{K})) \right) + \mathcal{O}(\varepsilon^4). \end{aligned} \quad (31)$$

Note that  $\widehat{K} = \widehat{K}^{\text{D}} + \varepsilon\widehat{Q}$ , so its diagonal part is of leading order, while the off-diagonal part is  $\mathcal{O}(\varepsilon)$ .

Thus, the transformed Hamiltonian has an asymptotic expansion in powers of  $\varepsilon$ ,

$$\widehat{\mathcal{H}} = \widehat{h}_0 + \varepsilon \widehat{h}_1 + \varepsilon^2 \widehat{h}_2 + \dots + \varepsilon^n \widehat{h}_n + \mathcal{O}(\varepsilon^{n+1}), \quad (32)$$

with

$$\widehat{h}_0 = \widehat{K} + H_e, \quad (33)$$

$$\widehat{h}_1 = \mathcal{L}_{\widehat{A}_1}(H_e) = -\mathcal{L}_{H_e}(\widehat{A}_1), \quad (34)$$

$$\begin{aligned} \widehat{h}_2 &= \mathcal{L}_{\widehat{A}_2}(H_e) + \frac{1}{2} \mathcal{L}_{\widehat{A}_1}(\mathcal{L}_{\widehat{A}_1}(H_e)) + \mathcal{L}_{\widehat{A}_1}(\frac{1}{\varepsilon} \widehat{K}) \\ &= -\mathcal{L}_{H_e}(\widehat{A}_2) - \frac{1}{2} \mathcal{L}_{\widehat{A}_1}(\mathcal{L}_{H_e}(\widehat{A}_1)) + \mathcal{L}_{\widehat{A}_1}(\frac{1}{\varepsilon} \widehat{K}), \end{aligned} \quad (35)$$

and

$$\begin{aligned} \widehat{h}_3 &= \mathcal{L}_{\widehat{A}_3}(H_e) + \frac{1}{2} \mathcal{L}_{\widehat{A}_1}(\mathcal{L}_{\widehat{A}_2}(H_e)) + \frac{1}{2} \mathcal{L}_{\widehat{A}_2}(\mathcal{L}_{\widehat{A}_1}(H_e)) \\ &\quad + \frac{1}{6} \mathcal{L}_{\widehat{A}_1}(\mathcal{L}_{\widehat{A}_1}(\mathcal{L}_{\widehat{A}_1}(H_e))) + \mathcal{L}_{\widehat{A}_2}(\frac{1}{\varepsilon} \widehat{K}) + \frac{1}{2} \mathcal{L}_{\widehat{A}_1}(\mathcal{L}_{\widehat{A}_1}(\frac{1}{\varepsilon} \widehat{K})) \\ &= -\mathcal{L}_{H_e}(\widehat{A}_3) - \frac{1}{2} \mathcal{L}_{\widehat{A}_1}(\mathcal{L}_{H_e}(\widehat{A}_2)) - \frac{1}{2} \mathcal{L}_{\widehat{A}_2}(\mathcal{L}_{H_e}(\widehat{A}_1)) \\ &\quad - \frac{1}{6} \mathcal{L}_{\widehat{A}_1}(\mathcal{L}_{\widehat{A}_1}(\mathcal{L}_{H_e}(\widehat{A}_1))) + \mathcal{L}_{\widehat{A}_2}(\frac{1}{\varepsilon} \widehat{K}) + \frac{1}{2} \mathcal{L}_{\widehat{A}_1}(\mathcal{L}_{\widehat{A}_1}(\frac{1}{\varepsilon} \widehat{K})). \end{aligned} \quad (36)$$

To reduce the off-diagonal coupling, we will now proceed by induction. Assuming that  $\widehat{A}_1, \widehat{A}_2, \dots, \widehat{A}_{n-1}$  have been chosen such that

$$(\widehat{\mathcal{H}}^{(n-1)})^{\text{OD}} := \left( \sum_{i=0}^{n-1} \varepsilon^i \widehat{h}_i \right)^{\text{OD}} = \sum_{i=0}^{n-1} \varepsilon^i \widehat{h}_i^{\text{OD}} =: \varepsilon^n \widehat{B}_{n-1} \quad (37)$$

is  $\mathcal{O}(\varepsilon^n)$ , we will fix  $\widehat{A}_n$  such that  $(\widehat{\mathcal{H}}^{(n)})^{\text{OD}} = \sum_{i=0}^n \varepsilon^i \widehat{h}_i^{\text{OD}} =: \varepsilon^{n+1} \widehat{B}_n$  is  $\mathcal{O}(\varepsilon^{n+1})$ .

We mention already at this point that fulfillment of this sequence of requirements will fix only the off-diagonal part  $\widehat{A}_i^{\text{OD}}$  of each  $\widehat{A}_i$ . The diagonal parts,  $\widehat{A}_i^{\text{D}}$ , generate merely rotations within the subspaces  $P$  and  $P^\perp$  but do not affect the (de)coupling. Hence, we set  $\widehat{A}_i^{\text{D}} = 0$  ( $i = 1, 2, \dots$ ). With this choice,  $\widehat{A}_1, \widehat{A}_2, \dots, \widehat{A}_n$  are completely determined by the requirement [Eq. (28)].

**Zeroth-order off-diagonal (OD) terms:** The off-diagonal part of  $\widehat{h}_0$  [Eq. (33)],

$$\widehat{h}_0^{\text{OD}} = \widehat{K}^{\text{OD}} = \varepsilon \widehat{Q} =: \varepsilon \widehat{B}_0, \quad (38)$$

is of order  $\varepsilon$ ; hence, decoupling is automatically fulfilled at this order.

**First-order OD terms:** In the next step, we require

$$\begin{aligned} \widehat{h}_0^{\text{OD}} + \varepsilon \widehat{h}_1^{\text{OD}} &= \varepsilon (\widehat{B}_0 + \widehat{h}_1^{\text{OD}}) = \varepsilon (\widehat{Q} - \mathcal{L}_{H_e}(\widehat{A}_1)^{\text{OD}}) \\ &= \varepsilon (\widehat{Q} - \mathcal{L}_{H_e}(\widehat{A}_1^{\text{OD}})) \stackrel{!}{=} \varepsilon^2 \widehat{B}_1, \end{aligned} \quad (39)$$

where we used Eq. (21) and the fact that  $\widehat{A}_1 = \widehat{A}_1^{\text{OD}}$ . This condition can be fulfilled by choosing

$$\widehat{A}_1 := \mathcal{S}_{H_e}(\widehat{Q}). \quad (40)$$

Inserting Eq. (40) back into Eq. (39) and using Eq. (24), we find that

$$\begin{aligned} \varepsilon \widehat{B}_1 &= \widehat{Q} - \mathcal{L}_{H_e}(\mathcal{S}_{H_e}(\widehat{Q})) \\ &= -\sum_a (\mathcal{R}_a[E_a, \widehat{Q}]P_a - P_a[E_a, \widehat{Q}]\mathcal{R}_a), \\ &= -\varepsilon \sum_a (\mathcal{R}_a[E_a, \frac{1}{\varepsilon}\widehat{Q}]P_a - P_a[E_a, \frac{1}{\varepsilon}\widehat{Q}]\mathcal{R}_a) \\ &= -\varepsilon \sum_a E'_a \cdot (\mathcal{R}_a P'_a P_a + P_a P'_a \mathcal{R}_a). \end{aligned} \quad (41)$$

This explicit expression for  $\widehat{B}_1$  will be required for calculating the third-order terms in the effective Hamiltonian  $\widehat{\mathcal{H}}_p^{(3)}$  [see Eqs. (57)–(67)].

**Second-order OD terms:** We require

$$\begin{aligned} \widehat{h}_0^{\text{OD}} + \varepsilon \widehat{h}_1^{\text{OD}} + \varepsilon^2 \widehat{h}_2^{\text{OD}} &= \varepsilon^2 \widehat{B}_1 + \varepsilon^2 \widehat{h}_2^{\text{OD}} \\ &= \varepsilon^2 (\widehat{B}_1 - \mathcal{L}_{H_e}(\widehat{A}_2)^{\text{OD}} - \frac{1}{2} \mathcal{L}_{\widehat{A}_1}(\mathcal{L}_{H_e}(\widehat{A}_1))^{\text{OD}} \\ &\quad + \mathcal{L}_{\widehat{A}_1}(\frac{1}{\varepsilon}\widehat{K})^{\text{OD}}) \\ &= \varepsilon^2 (\widehat{B}_1 - \mathcal{L}_{H_e}(\widehat{A}_2) + \mathcal{L}_{\widehat{A}_1}(\frac{1}{\varepsilon}\widehat{K}^{\text{D}})) \stackrel{!}{=} \varepsilon^3 \widehat{B}_2, \end{aligned} \quad (42)$$

where in the third equality, we used the algebraic relations of Eq. (17). Again, we solve this equation for  $\widehat{A}_2$  using the approximate inverse Liouvillian, Eq. (22),

$$\widehat{A}_2 := \mathcal{S}_{H_e}(\mathcal{L}_{\widehat{A}_1}(\frac{1}{\varepsilon}\widehat{K}^{\text{D}}) + \widehat{B}_1). \quad (43)$$

The explicit expression for the remainder  $\widehat{B}_2$  could be determined, if needed, through the calculation of the  $\mathcal{O}(\varepsilon)$  error term [Eq. (24)] from the approximate inversion,

$$\begin{aligned} \varepsilon \widehat{B}_2 &= \widehat{B}_1 - \mathcal{L}_{H_e}(\widehat{A}_2) + \mathcal{L}_{\widehat{A}_1}(\frac{1}{\varepsilon}\widehat{K}^{\text{D}}) \\ &= \widehat{B}_1 - \mathcal{L}_{H_e}(\mathcal{S}_{H_e}(\mathcal{L}_{\widehat{A}_1}(\frac{1}{\varepsilon}\widehat{K}^{\text{D}}) + \widehat{B}_1)) + \mathcal{L}_{\widehat{A}_1}(\frac{1}{\varepsilon}\widehat{K}^{\text{D}}). \end{aligned} \quad (44)$$

**Third-order OD terms:** By the same reasoning, we require

$$\begin{aligned} \widehat{B}_2 + \widehat{h}_3^{\text{OD}} &= \widehat{B}_2 - \mathcal{L}_{H_e}(\widehat{A}_3)^{\text{OD}} - \frac{1}{2} \mathcal{L}_{\widehat{A}_1}(\mathcal{L}_{H_e}(\widehat{A}_2))^{\text{OD}} \\ &\quad - \frac{1}{2} \mathcal{L}_{\widehat{A}_2}(\mathcal{L}_{H_e}(\widehat{A}_1))^{\text{OD}} - \frac{1}{6} \mathcal{L}_{\widehat{A}_1}(\mathcal{L}_{\widehat{A}_1}(\mathcal{L}_{H_e}(\widehat{A}_1)))^{\text{OD}} \\ &\quad + \mathcal{L}_{\widehat{A}_2}(\frac{1}{\varepsilon}\widehat{K})^{\text{OD}} + \frac{1}{2} \mathcal{L}_{\widehat{A}_1}(\mathcal{L}_{\widehat{A}_1}(\frac{1}{\varepsilon}\widehat{K}))^{\text{OD}} \\ &= \widehat{B}_2 - \mathcal{L}_{H_e}(\widehat{A}_3) - \frac{1}{6} \mathcal{L}_{\widehat{A}_1}(\mathcal{L}_{\widehat{A}_1}(\mathcal{L}_{H_e}(\widehat{A}_1))) \\ &\quad + \mathcal{L}_{\widehat{A}_2}(\frac{1}{\varepsilon}\widehat{K}^{\text{D}}) + \frac{1}{2} \mathcal{L}_{\widehat{A}_1}(\mathcal{L}_{\widehat{A}_1}(\widehat{Q})) \\ &\stackrel{!}{=} \varepsilon \widehat{B}_3, \end{aligned} \quad (45)$$

where we used that the last two terms in the first line are zero (off-diagonal part of diagonal operators). Again, we make the left-hand side of Eq. (45) small by solving the equation for  $\widehat{A}_3$  using the approximate inverse Liouvillian [Eq. (22)],

$$\begin{aligned} \widehat{A}_3 &:= \mathcal{S}_{H_e}(\widehat{B}_2 - \frac{1}{6} \mathcal{L}_{\widehat{A}_1}(\mathcal{L}_{\widehat{A}_1}(\mathcal{L}_{H_e}(\widehat{A}_1))) + \mathcal{L}_{\widehat{A}_2}(\frac{1}{\varepsilon}\widehat{K}^{\text{D}}) \\ &\quad + \frac{1}{2} \mathcal{L}_{\widehat{A}_1}(\mathcal{L}_{\widehat{A}_1}(\widehat{Q}))), \end{aligned} \quad (46)$$

and the remainder term  $\widehat{B}_3$  can be determined by the direct calculation of the  $\mathcal{O}(\varepsilon)$  error of the inversion using Eq. (24).

It is obvious how to continue this induction to arbitrary orders. However, as we are only interested in explicit expressions for the effective Hamiltonians up to third order, we refrain from stating the general induction explicitly.

## D. Second- and third-order Hamiltonians

In this section, we calculate the leading terms in the expansion of the  $n$ th-order effective Hamiltonian,

$$\widehat{\mathcal{H}}_p^{(n)} = \sum_{j=0}^n \varepsilon^j P \widehat{h}_j P + \mathcal{O}(\varepsilon^{n+1}), \quad (47)$$

up to and including  $P \widehat{h}_3 P$ , and thus obtain explicit expressions for the second and the third-order effective Hamiltonians,  $\widehat{\mathcal{H}}_p^{(2)}$  and  $\widehat{\mathcal{H}}_p^{(3)}$ . To this end, we first calculate the diagonal parts  $\widehat{h}_j^{\text{D}}$  and then, in a second step, project onto the range of  $P$ .

**Zeroth-order diagonal (D) terms:**

$$\widehat{h}_0^{\text{D}} = \widehat{K}^{\text{D}} + H_e^{\text{D}} = \widehat{K}^{\text{D}} + H_e. \quad (48)$$

**First-order D terms:** Recalling that  $\widehat{A}_j = \widehat{A}_j^{\text{OD}}$  for all  $j \geq 1$  and the algebraic relations in Eq. (17), we find, in particular, that

$$\widehat{h}_1^{\text{D}} = -\mathcal{L}_{H_e}(\widehat{A}_1)^{\text{D}} = -\mathcal{L}_{H_e}(\widehat{A}_1^{\text{D}}) = 0. \quad (49)$$

**Second-order D terms:** Similarly, since  $\widehat{B}_j = \widehat{B}_j^{\text{OD}}$  for all  $j \geq 1$ , we find

$$\begin{aligned} \widehat{h}_2^{\text{D}} &= -\mathcal{L}_{H_e}(\widehat{A}_2)^{\text{D}} - \frac{1}{2} \mathcal{L}_{\widehat{A}_1}(\mathcal{L}_{H_e}(\widehat{A}_1))^{\text{D}} + \mathcal{L}_{\widehat{A}_1}(\frac{1}{\varepsilon}\widehat{K})^{\text{D}} \\ &= -\frac{1}{2} \mathcal{L}_{\widehat{A}_1}(\mathcal{L}_{H_e}(\widehat{A}_1)) + \mathcal{L}_{\widehat{A}_1}(\widehat{Q}) \\ &= -\frac{1}{2} \mathcal{L}_{\widehat{A}_1}(\widehat{Q} - \varepsilon \widehat{B}_1) + \mathcal{L}_{\widehat{A}_1}(\widehat{Q}) \\ &= \frac{1}{2} \mathcal{L}_{\widehat{A}_1}(\widehat{Q}) + \frac{\varepsilon}{2} \mathcal{L}_{\widehat{A}_1}(\widehat{B}_1). \end{aligned} \quad (50)$$

**Third-order D terms:**

$$\begin{aligned}
\widehat{h}_3^D &= -\mathcal{L}_{H_c}(\widehat{A}_3)^D - \frac{1}{2}\mathcal{L}_{\widehat{A}_1}(\mathcal{L}_{H_c}(\widehat{A}_2))^D - \frac{1}{2}\mathcal{L}_{\widehat{A}_2}(\mathcal{L}_{H_c}(\widehat{A}_1))^D - \frac{1}{6}\mathcal{L}_{\widehat{A}_1}(\mathcal{L}_{\widehat{A}_1}(\mathcal{L}_{H_c}(\widehat{A}_1)))^D + \mathcal{L}_{\widehat{A}_2}(\frac{1}{\epsilon}\widehat{K})^D + \frac{1}{2}\mathcal{L}_{\widehat{A}_1}(\mathcal{L}_{\widehat{A}_1}(\frac{1}{\epsilon}\widehat{K}))^D \\
&= -\frac{1}{2}\mathcal{L}_{\widehat{A}_1}(\mathcal{L}_{H_c}(\widehat{A}_2)) - \frac{1}{2}\mathcal{L}_{\widehat{A}_2}(\mathcal{L}_{H_c}(\widehat{A}_1)) + \mathcal{L}_{\widehat{A}_2}(\widehat{Q}) + \frac{1}{2}\mathcal{L}_{\widehat{A}_1}(\mathcal{L}_{\widehat{A}_1}(\frac{1}{\epsilon}\widehat{K}^D)) \\
&= -\frac{1}{2}\mathcal{L}_{\widehat{A}_1}(\mathcal{L}_{\widehat{A}_1}(\frac{1}{\epsilon}\widehat{K}^D)) + \widehat{B}_1 - \epsilon\widehat{B}_2 - \frac{1}{2}\mathcal{L}_{\widehat{A}_2}(\widehat{Q} - \epsilon\widehat{B}_1) + \mathcal{L}_{\widehat{A}_2}(\widehat{Q}) + \frac{1}{2}\mathcal{L}_{\widehat{A}_1}(\mathcal{L}_{\widehat{A}_1}(\frac{1}{\epsilon}\widehat{K}^D)) \\
&= -\frac{1}{2}\mathcal{L}_{\widehat{A}_1}(\widehat{B}_1) + \frac{1}{2}\mathcal{L}_{\widehat{A}_2}(\widehat{Q}) + \mathcal{O}(\epsilon).
\end{aligned} \tag{51}$$

By combining these expressions, we obtain the second- and the third-order effective Hamiltonians as

$$\widehat{H}_P^{(2)} := P\widehat{K}P + PH_eP + \frac{\epsilon^2}{2}P\mathcal{L}_{\widehat{A}_1}(\widehat{Q})P + \mathcal{O}(\epsilon^3) \tag{52}$$

and

$$\widehat{H}_P^{(3)} := P\widehat{K}P + PH_eP + \frac{\epsilon^2}{2}P\mathcal{L}_{\widehat{A}_1}(\widehat{Q})P + \frac{\epsilon^3}{2}P\mathcal{L}_{\widehat{A}_2}(\widehat{Q})P + \mathcal{O}(\epsilon^4), \tag{53}$$

respectively. We note that in the third-order correction, the  $-\frac{1}{2}\mathcal{L}_{\widehat{A}_1}(\widehat{B}_1)$  remainder from second order cancels the  $\frac{1}{2}\mathcal{L}_{\widehat{A}_1}(\widehat{B}_1)$  third-order term. In Subsection IV E, we continue with inserting the explicit formulas for  $\widehat{A}_1$ ,  $\widehat{A}_2$ , and  $\widehat{Q}$  into the compact expressions of  $\widehat{H}_P^{(2)}$  and  $\widehat{H}_P^{(3)}$  just obtained.

## E. More explicit expressions for the second- and the third-order nonadiabatic Hamiltonian corrections

### 1. Second-order correction

Using the explicit expression for the inverse Liouvillian [Eq. (22)], Eq. (40) yields

$$\widehat{A}_1 = i \sum_{a=1}^d (\mathcal{R}_a \widehat{Q} P_a - P_a \widehat{Q} \mathcal{R}_a). \tag{54}$$

Thus, the  $\mathcal{O}(\epsilon^2)$  correction term of the effective Hamiltonian in Eq. (52) is

$$\begin{aligned}
\frac{\epsilon^2}{2}P\mathcal{L}_{\widehat{A}_1}(\widehat{Q})P &= -\frac{\epsilon^2}{2} \sum_{a,b=1}^d (P_b \widehat{Q} \mathcal{R}_a \widehat{Q} P_a + P_a \widehat{Q} \mathcal{R}_a \widehat{Q} P_b) \\
&= \frac{\epsilon^2}{2} \sum_{a,b=1}^d (P_b P'_\nabla \mathcal{R}_a P'_\nabla P_a + P_a P'_\nabla \mathcal{R}_a P'_\nabla P_b),
\end{aligned} \tag{55}$$

where we inserted Eq. (9) for  $\widehat{Q}$  and used the fact that the reduced resolvent  $\mathcal{R}_a$  acts only in the  $P^\perp$  subspace. [Recall that  $P'_\nabla$  is defined by Eq. (7).] Since the commutator of  $\epsilon\nabla$  in  $P'_\nabla$  with smooth, fibered operators yields higher-order terms in  $\epsilon$ , we can further simplify  $\widehat{H}_P^{(2)}$  to

$$\begin{aligned}
\widehat{H}_P^{(2)} &= P\widehat{K}P + PH_eP + \frac{\epsilon^2}{2} \sum_{j,i=1}^{3N} \sum_{a,b=1}^d (P_b(\epsilon\partial_j)(\partial_j P)\mathcal{R}_a(\partial_i P)(\epsilon\partial_i)P_a + P_a(\epsilon\partial_j)(\partial_j P)\mathcal{R}_a(\partial_i P)(\epsilon\partial_i)P_b) \\
&= P\widehat{K}P + PH_eP + \frac{\epsilon^2}{2} \sum_{j,i=1}^{3N} \sum_{a,b=1}^d (\epsilon\partial_j) (P_b(\partial_j P)\mathcal{R}_a(\partial_i P)P_a + P_a(\partial_j P)\mathcal{R}_a(\partial_i P)P_b) (\epsilon\partial_i) + \mathcal{O}(\epsilon^3) \\
&= P\widehat{K}P + PH_eP + \epsilon^2 \sum_{j,i=1}^{3N} \sum_{a,b=1}^d (\epsilon\partial_j) P_a(\partial_j P) \frac{\mathcal{R}_a + \mathcal{R}_b}{2} (\partial_i P) P_b(\epsilon\partial_i) + \mathcal{O}(\epsilon^3).
\end{aligned} \tag{56}$$

Note, however, that the  $\mathcal{O}(\epsilon^3)$  term does contribute to the third-order effective Hamiltonian and cannot be neglected when computing  $\widehat{H}_P^{(3)}$ .

### 2. Third-order correction

To obtain an explicit expression for the third-order correction, we need to derive an explicit expression for  $\widehat{A}_2$  [Eq. (43)],

$$\widehat{A}_2 = \mathcal{S}_{H_c}(\mathcal{L}_{\widehat{A}_1}(\frac{1}{\epsilon}\widehat{K}^D)) + \mathcal{S}_{H_c}(\widehat{B}_1), \tag{57}$$

which assumes the explicit knowledge of the first-order remainder term  $\widehat{B}_1$  [Eq. (41)], too. The first term in Eq. (57) includes

$$\begin{aligned}
\mathcal{L}_{\widehat{A}_1}(\frac{1}{\epsilon}\widehat{K}^D) &= -i[\widehat{A}_1, \frac{1}{\epsilon}\widehat{K}^D] \\
&= -i \left[ i \sum_{a=1}^d (\mathcal{R}_a \widehat{Q} P_a - P_a \widehat{Q} \mathcal{R}_a), \frac{1}{\epsilon}\widehat{K}^D \right] \\
&= \frac{1}{\epsilon} \sum_{a=1}^d (\mathcal{R}_a \widehat{Q} P_a \widehat{K} P - P^\perp \widehat{K} \mathcal{R}_a \widehat{Q} P_a - P_a \widehat{Q} \mathcal{R}_a \widehat{K} P^\perp \\
&\quad + P\widehat{K}P_a \widehat{Q} \mathcal{R}_a),
\end{aligned} \tag{58}$$



and its inverse Liouvillian [Eq. (22)] is

$$\begin{aligned} \mathcal{I}_{H_\varepsilon}(\mathcal{L}_{\widehat{A}_1}(\frac{1}{\varepsilon}\widehat{K}^D)) &= i \sum_{a,b=1}^d (\mathcal{R}_b \mathcal{L}_{\widehat{A}_1}(\frac{1}{\varepsilon}\widehat{K}^D)P_b - P_b \mathcal{L}_{\widehat{A}_1}(\frac{1}{\varepsilon}\widehat{K}^D)\mathcal{R}_b) \\ &= \frac{i}{\varepsilon} \sum_{b=1}^d (\mathcal{R}_b (\mathcal{R}_a \widehat{Q}P_a \widehat{K} - \widehat{K}\mathcal{R}_a \widehat{Q}P_a)P_b \\ &\quad - P_b (\widehat{K}P_a \widehat{Q}\mathcal{R}_a - P_a \widehat{Q}\mathcal{R}_a \widehat{K})\mathcal{R}_b) \\ &= \frac{i}{\varepsilon} \sum_{a=1}^d (P_a \widehat{Q}\mathcal{R}_a \widehat{K}\mathcal{R}_a - \mathcal{R}_a \widehat{K}\mathcal{R}_a \widehat{Q}P_a) \\ &\quad + \frac{i}{\varepsilon} \sum_{a,b=1}^d (\mathcal{R}_b \mathcal{R}_a \widehat{Q}P_a \widehat{K}P_b - P_b \widehat{K}P_a \widehat{Q}\mathcal{R}_a \mathcal{R}_b). \end{aligned} \quad (59)$$

The inverse Liouvillian of  $\widehat{B}_1$  [Eq. (41)] is

$$\begin{aligned} \mathcal{I}_{H_\varepsilon}(\widehat{B}_1) &= i \sum_{a=1}^d (\mathcal{R}_a \widehat{B}_1 P_a - P_a \widehat{B}_1 \mathcal{R}_a) \\ &= -i \sum_{a,b=1}^d E'_b \cdot (\mathcal{R}_a \mathcal{R}_b P'_b P_a - P_a P_b P'_b \mathcal{R}_a) \\ &= -i \sum_{a=1}^d E'_a \cdot (\mathcal{R}_a \mathcal{R}_a P'_a - P_a P'_a \mathcal{R}_a). \end{aligned} \quad (60)$$

Next, the explicit expression for  $\widehat{A}_2$ , obtained as the sum of Eqs. (59) and (60), is used to expand the third-order correction as

$$\begin{aligned} \frac{1}{2}P \mathcal{L}_{\widehat{A}_2}(\widehat{Q})P &= -\frac{i}{2}P[\widehat{A}_2, \widehat{Q}]P = \frac{1}{2\varepsilon} \sum_{a=1}^d (P\widehat{Q}\mathcal{R}_a \widehat{K}\mathcal{R}_a \widehat{Q}P_a + P_a \widehat{Q}\mathcal{R}_a \widehat{K}\mathcal{R}_a \widehat{Q}P) \\ &\quad - \frac{1}{2\varepsilon} \sum_{a,b=1}^d (P_b \widehat{K}P_a \widehat{Q}\mathcal{R}_a \mathcal{R}_b \widehat{Q}P + P\widehat{Q}\mathcal{R}_b \mathcal{R}_a \widehat{Q}P_a \widehat{K}P_b) \\ &\quad + \frac{1}{2} \sum_{a=1}^d E'_a \cdot (P\widehat{Q}\mathcal{R}_a \mathcal{R}_a P'_a + P_a P'_a \mathcal{R}_a \widehat{Q}P). \end{aligned} \quad (61)$$

By working out the second sum of Eq. (61), we obtain

$$\begin{aligned} \sum_{a,b=1}^d (P_b \widehat{K}P_a \widehat{Q}\mathcal{R}_a \mathcal{R}_b \widehat{Q}P + P\widehat{Q}\mathcal{R}_b \mathcal{R}_a \widehat{Q}P_a \widehat{K}P_b) &= \sum_{a,b=1}^d (P_b [\widehat{K}, P_a] \widehat{Q}\mathcal{R}_a \mathcal{R}_b \widehat{Q}P + P\widehat{Q}\mathcal{R}_b \mathcal{R}_a \widehat{Q}[P_a, \widehat{K}]P_b) \\ &\quad + \sum_{a=1}^d (P_a \widehat{K}\widehat{Q}\mathcal{R}_a \mathcal{R}_a \widehat{Q}P + P\widehat{Q}\mathcal{R}_a \mathcal{R}_a \widehat{K}P_a) \\ &= \sum_{a,b=1}^d (P_b [\widehat{K}, P_a] \widehat{Q}\mathcal{R}_a \mathcal{R}_b \widehat{Q}P + P\widehat{Q}\mathcal{R}_b \mathcal{R}_a \widehat{Q}[P_a, \widehat{K}]P_b) + \sum_{a=1}^d (P_a [\widehat{K}, \widehat{Q}] \mathcal{R}_a \mathcal{R}_a \widehat{Q}P \\ &\quad + P\widehat{Q}\mathcal{R}_a \mathcal{R}_a [\widehat{Q}, \widehat{K}]P_a) + \sum_{a=1}^d (P_a \widehat{Q}\widehat{K}\mathcal{R}_a \mathcal{R}_a \widehat{Q}P + P\widehat{Q}\mathcal{R}_a \mathcal{R}_a \widehat{K}\widehat{Q}P_a) \\ &= \sum_{a,b=1}^d (P_b [\widehat{K}, P_a] \widehat{Q}\mathcal{R}_a \mathcal{R}_b \widehat{Q}P + P\widehat{Q}\mathcal{R}_b \mathcal{R}_a \widehat{Q}[P_a, \widehat{K}]P_b) + \sum_{a=1}^d (P_a [\widehat{K}, \widehat{Q}] \mathcal{R}_a \mathcal{R}_a \widehat{Q}P \\ &\quad + P\widehat{Q}\mathcal{R}_a \mathcal{R}_a [\widehat{Q}, \widehat{K}]P_a) + \sum_{a=1}^d (P_a \widehat{Q}[\widehat{K}, \mathcal{R}_a] \mathcal{R}_a \widehat{Q}P + P\widehat{Q}\mathcal{R}_a [\mathcal{R}_a, \widehat{K}] \widehat{Q}P_a) \\ &\quad + \sum_{a=1}^d (P_a \widehat{Q}\mathcal{R}_a \widehat{K}\mathcal{R}_a \widehat{Q}P + P\widehat{Q}\mathcal{R}_a \widehat{K}\mathcal{R}_a \widehat{Q}P_a), \end{aligned} \quad (62)$$

where the last expression exactly cancels the first term in Eq. (61), and thus, the correction term at third order is

$$\begin{aligned} \frac{1}{2}P \mathcal{L}_{\widehat{A}_2}(\widehat{Q})P &= -\frac{1}{2} \sum_{a,b=1}^d (P_b [\frac{1}{\varepsilon}\widehat{K}, P_a] \widehat{Q}\mathcal{R}_a \mathcal{R}_b \widehat{Q}P + P\widehat{Q}\mathcal{R}_b \mathcal{R}_a \widehat{Q}[P_a, \frac{1}{\varepsilon}\widehat{K}]P_b) - \frac{1}{2} \sum_{a=1}^d (P_a [\frac{1}{\varepsilon}\widehat{K}, \widehat{Q}] \mathcal{R}_a \mathcal{R}_a \widehat{Q}P + P\widehat{Q}\mathcal{R}_a \mathcal{R}_a [\widehat{Q}, \frac{1}{\varepsilon}\widehat{K}]P_a) \\ &\quad - \frac{1}{2} \sum_{a=1}^d (P_a \widehat{Q}[\frac{1}{\varepsilon}\widehat{K}, \mathcal{R}_a] \mathcal{R}_a \widehat{Q}P + P\widehat{Q}\mathcal{R}_a [\mathcal{R}_a, \frac{1}{\varepsilon}\widehat{K}] \widehat{Q}P_a) + \frac{1}{2} \sum_{a=1}^d E'_a \cdot (P\widehat{Q}\mathcal{R}_a \mathcal{R}_a P'_a + P_a P'_a \mathcal{R}_a \widehat{Q}P). \end{aligned} \quad (63)$$

The commutators can be evaluated as

$$[\frac{1}{\varepsilon}\widehat{\mathcal{K}}, P_a] = -\frac{\varepsilon}{2}[\Delta, P_a] = -\frac{1}{2}(\varepsilon\nabla \cdot P'_a + P'_a \cdot \varepsilon\nabla) = -P'_{a\nabla}, \quad (64)$$

and

$$P[\frac{1}{\varepsilon}\widehat{\mathcal{K}}, \widehat{Q}]P^\dagger = -\frac{\varepsilon}{2}P[\Delta, PP'_\nabla P^\dagger - P^\dagger P'_\nabla P]P^\dagger = -PP''_{\nabla^2}P^\dagger + \mathcal{O}(\varepsilon), \quad (65)$$

with  $P''_{\nabla^2} := \varepsilon \sum_{i,j=1}^{3N} \partial_j(\partial_j \partial_i P) \varepsilon \partial_i$ , and

$$P^\dagger[\frac{1}{\varepsilon}\widehat{\mathcal{K}}, \mathcal{R}_a]P^\dagger = -P^\dagger \mathcal{R}'_{a\nabla} P^\dagger. \quad (66)$$

Inserting these identities into Eq. (63), we finally obtain for the third-order correction as

$$\begin{aligned} & \frac{\varepsilon^3}{2} P \mathcal{L}_{\widehat{A}_2}(\widehat{Q})P \\ &= -\frac{\varepsilon^3}{2} \sum_{a,b=1}^d (P_b P'_{a\nabla} P'_\nabla \mathcal{R}_a \mathcal{R}_b P'_\nabla P - PP'_\nabla \mathcal{R}_b \mathcal{R}_a P'_\nabla P'_\nabla P_b) \\ & \quad - \frac{\varepsilon^3}{2} \sum_{a=1}^d (P_a P''_{\nabla^2} \mathcal{R}_a \mathcal{R}_a P'_\nabla P - PP'_\nabla \mathcal{R}_a \mathcal{R}_a P''_{\nabla^2} P_a) \\ & \quad - \frac{\varepsilon^3}{2} \sum_{a=1}^d (P_a P'_\nabla P^\dagger \mathcal{R}'_{a\nabla} \mathcal{R}_a P'_\nabla P - PP'_\nabla \mathcal{R}_a \mathcal{R}'_{a\nabla} P^\dagger P'_\nabla P_a) \\ & \quad + \frac{\varepsilon^3}{2} \sum_{a=1}^d E'_a \cdot (PP'_\nabla \mathcal{R}_a \mathcal{R}_a P'_\nabla P - P_a P' \mathcal{R}_a \mathcal{R}_a P'_\nabla P) + \mathcal{O}(\varepsilon^4). \quad (67) \end{aligned}$$

Note that the first three lines are third order in the nuclear momentum,  $\widehat{p}$ , and the last line is linear in  $\widehat{p}$ .

When looking at the second- and the third-order corrections in Eqs. (56) and (67), one might worry about singular expressions. Indeed, some of the summands become singular near points of the nuclear configuration space at which eigenvalues within the set  $\{E_a | a = 1, \dots, d\}$  cross. At these points, the single spectral projections  $P_a$  might not be differentiable. However, as it can be seen from the original expressions [Eqs. (52) and (53)], for  $\widehat{\mathcal{H}}_p^{(2)}$  and  $\widehat{\mathcal{H}}_p^{(3)}$ , the complete expression (the full sum) remains bounded because the singularities in the different summands cancel each other. This property might require additional care in numerical computations.

## V. BASIS REPRESENTATION AND EFFECTIVE NUCLEAR HAMILTONIANS

By choosing an electronic (e.g., adiabatic or diabatic) basis set  $\{\psi_\alpha, \alpha = 1, \dots, d\}$  for  $P\mathfrak{H}_e$ , one can represent a molecular wave function  $\Psi$  in the range of  $P$ ,  $\Psi \in P\mathfrak{H}$ , as  $\Psi(R, r) = \sum_{\alpha=1}^d \varphi_\alpha(R) \psi_\alpha(R, r)$  (where  $\mathfrak{H}_e$  and  $\mathfrak{H}$  denote the electronic and the molecular Hilbert space, respectively). It is common practice to represent the zeroth-order effective Hamiltonian  $\widehat{\mathcal{H}}_p^{(0)} = \widehat{H}_p^{(0)} = P\widehat{H}P$  as a matrix operator  $\widehat{H}_p^{(0)}$  with respect to such a basis set, which then acts only on the nuclear functions  $(\varphi_1(R), \dots, \varphi_d(R))$ . This yields, in particular, also the Berry phase and the diagonal BO correction terms (see below).

In what follows, we construct the matrix representation also for the second-order Hamiltonian  $\widehat{\mathcal{H}}_p^{(2)}$ . As a special case, the known mass-correction terms for a single, isolated electronic state will be recovered. The basis representation for the third-order correction [Eq. (67)] can be worked out along the same lines.

### A. Basis representation for the second-order, multistate Hamiltonian

Let us choose an electronic (e.g., adiabatic or diabatic) basis set  $\psi_1(R), \dots, \psi_d(R)$  such that  $\psi_\alpha$  are smooth functions of  $R$  and pointwise form an orthonormal basis of the range of  $P(R)$ , i.e.,

$$\langle \psi_\alpha(R) | \psi_\beta(R) \rangle = \delta_{\alpha,\beta} \quad \text{and} \quad P(R) = \sum_{\alpha=1}^d |\psi_\alpha(R)\rangle \langle \psi_\alpha(R)|. \quad (68)$$

Because of the gap condition, such a smooth diabatic basis set always exists at least locally.<sup>50</sup> However, due to possible crossings within the set of eigenvalues  $E_1, \dots, E_d$ , it might **not** be possible to choose  $\psi_1(R), \dots, \psi_d(R)$  as smooth functions of  $R$ , and at the same time, as pointwise eigenfunctions of  $H_e(R)$ , i.e.,

$$H_e(R)\psi_\alpha(R) = E_\alpha(R)\psi_\alpha(R), \quad \alpha = 1, \dots, d \quad (69)$$

is not assumed in general!

Then, the matrix representation of  $\widehat{\mathcal{H}}_p^{(2)}$  [Eq. (56)] over  $\psi_\alpha, \alpha = 1, \dots, d$ , results in a matrix operator  $\widehat{H}_p^{(2)}$  for the quantum nuclear motion with matrix elements,

$$\begin{aligned} (\widehat{H}_p^{(2)})_{\alpha\beta} &= \langle \psi_\alpha | \widehat{\mathcal{H}}_p^{(2)} | \psi_\beta \rangle = \langle \psi_\alpha | \widehat{\mathcal{K}} | \psi_\beta \rangle + \langle \psi_\alpha | H_e | \psi_\beta \rangle \\ & \quad + \frac{\varepsilon^2}{2} \sum_{j,i} \sum_{a,b} (\varepsilon \partial_j) \langle \psi_\alpha | P_a (\partial_j P) (\mathcal{R}_a + \mathcal{R}_b) (\partial_i P) P_b | \psi_\beta \rangle (\varepsilon \partial_i) \\ & \quad + \mathcal{O}(\varepsilon^3). \quad (70) \end{aligned}$$

For the kinetic-energy part, we find

$$\langle \psi_\alpha | \widehat{\mathcal{K}} | \psi_\beta \rangle = -\sum_i \left( \frac{1}{2} (\varepsilon \partial_i)^2 \delta_{\alpha\beta} + \varepsilon \langle \psi_\alpha | \partial_i \psi_\beta \rangle (\varepsilon \partial_i) + \frac{\varepsilon^2}{2} \langle \psi_\alpha | \partial_i^2 \psi_\beta \rangle \right). \quad (71)$$

By introducing the coefficient of the nonabelian Berry-connection

$$\mathbf{A}_{\alpha\beta,i} := -i \langle \psi_\alpha | \partial_i \psi_\beta \rangle = \overline{\mathbf{A}_{\beta\alpha,i}}, \quad (72)$$

we find

$$\begin{aligned} & \left[ \frac{1}{2} (-i\varepsilon \partial_i \mathbf{1} + \varepsilon \mathbf{A}_i)^2 \right]_{\alpha\beta} \\ &= \left[ -\frac{1}{2} (\varepsilon \partial_i)^2 \mathbf{1} - i\varepsilon \mathbf{A}_i (\varepsilon \partial_i) - i \frac{\varepsilon^2}{2} (\partial_i \mathbf{A}_i) + \frac{\varepsilon^2}{2} (\mathbf{A}_i)^2 \right]_{\alpha\beta} \\ &= -\frac{1}{2} (\varepsilon \partial_i)^2 \delta_{\alpha\beta} - \varepsilon \langle \psi_\alpha | \partial_i \psi_\beta \rangle (\varepsilon \partial_i) - \frac{\varepsilon^2}{2} \langle \psi_\alpha | \partial_i^2 \psi_\beta \rangle \\ & \quad - \frac{\varepsilon^2}{2} \langle \partial_i \psi_\alpha | \partial_i \psi_\beta \rangle - \frac{\varepsilon^2}{2} \sum_\gamma \langle \psi_\alpha | \partial_i \psi_\gamma \rangle \langle \psi_\gamma | \partial_i \psi_\beta \rangle. \quad (73) \end{aligned}$$

With  $\langle \psi_\alpha | \partial_i \psi_\gamma \rangle = -\langle \partial_i \psi_\alpha | \psi_\gamma \rangle$ , the last term becomes

$$\begin{aligned} \sum_{\gamma} \langle \psi_{\alpha} | \partial_t \psi_{\gamma} \rangle \langle \psi_{\gamma} | \partial_t \psi_{\beta} \rangle &= - \sum_{\gamma} \langle \partial_t \psi_{\alpha} | \psi_{\gamma} \rangle \langle \psi_{\gamma} | \partial_t \psi_{\beta} \rangle \\ &= - \langle \partial_t \psi_{\alpha} | P | \partial_t \psi_{\beta} \rangle, \end{aligned} \quad (74)$$

and thus, the kinetic-energy term can be written in the form

$$\langle \psi_{\alpha} | \widehat{K} | \psi_{\beta} \rangle = \frac{1}{2} \sum_{i=1}^{3N} \left[ \frac{1}{2} (-i\varepsilon \partial_i \mathbf{1} + \varepsilon \mathbf{A}_i)^2 \right]_{\alpha\beta} + \varepsilon^2 \Phi_{\alpha\beta}, \quad (75)$$

with the matrix-valued Berry-connection coefficient  $\mathbf{A}_i$  and the matrix-valued potential energy correction

$$\Phi_{\alpha\beta}(R) := \frac{1}{2} \sum_{i=1}^{3N} \langle \partial_i \psi_{\alpha}(R) | P^{\perp}(R) | \partial_i \psi_{\beta}(R) \rangle. \quad (76)$$

This latter quantity can be understood as an  $\mathcal{O}(\varepsilon^2)$  correction to the “diabatic” electronic level matrix,

$$\mathbf{E}_{\alpha\beta}(R) := \langle \psi_{\alpha}(R) | H_e(R) | \psi_{\beta}(R) \rangle. \quad (77)$$

Note that  $\mathbf{E}_{\alpha\beta}$  is a diagonal matrix if and only if all  $\psi_{\alpha}$  are eigenvectors of  $H_e$ . Defining the second-order mass-correction term as

$$\mathbf{M}_{\alpha\beta,ij} := \sum_{a,b=1}^d \langle \psi_{\alpha} | P_a(\partial_j P)(\mathcal{R}_a + \mathcal{R}_b)(\partial_i P)P_b | \psi_{\beta} \rangle, \quad (78)$$

the matrix representation of  $\widehat{H}_P^{(2)}$  over  $\psi_{\alpha}$ ,  $\alpha = 1, \dots, d$ , can be compactly written as

$$\begin{aligned} (\widehat{H}_P^{(2)})_{\alpha\beta} &= \sum_{ij=1}^{3N} \left[ \frac{1}{2} (-i\varepsilon \partial_i \mathbf{1} + \varepsilon \mathbf{A}_i) (\delta_{ij} \mathbf{1} - \varepsilon^2 \mathbf{M}_{ij}) (-i\varepsilon \partial_j \mathbf{1} + \varepsilon \mathbf{A}_j) \right]_{\alpha\beta} \\ &\quad + (\mathbf{E} + \varepsilon^2 \Phi)_{\alpha\beta} + \mathcal{O}(\varepsilon^3). \end{aligned} \quad (79)$$

We note that this is the complete second-order nonadiabatic Hamiltonian operator for the nuclear motion. It is important to remember the peculiarities of counting operator orders (Sec. II B), which follow from not making the assumption that the nuclear momenta (when  $-i\varepsilon \partial_R$  acts on the nuclear wave function) are small. Also note that we used Cartesian coordinates scaled with the nuclear mass [Eq. (2)], so the derived expressions can be used also for heteronuclear systems by making this scaling factor explicit in the numerical computations.

In the special case, where  $\psi_1, \dots, \psi_d$  form an adiabatic basis set, i.e., satisfy Eq. (69), the expression for  $\mathbf{M}_{\alpha\beta,ij}$  simplifies to

$$\mathbf{M}_{\alpha\beta,ij} = \langle \partial_j \psi_{\alpha} | \mathcal{R}_{\alpha} + \mathcal{R}_{\beta} | \partial_i \psi_{\beta} \rangle.$$

To see this, one uses that the reduced resolvent [Eq. (23)] contains a projection  $P^{\perp}$ , and

$$(\partial_j P)P^{\perp} = \sum_{\gamma=1}^d \langle \partial_j | \psi_{\gamma} \rangle \langle \psi_{\gamma} | \rangle P^{\perp} = \sum_{\gamma=1}^d |\psi_{\gamma}\rangle \langle \partial_j \psi_{\gamma} | P^{\perp}, \quad (80)$$

and similarly for its adjoint,  $P^{\perp}(\partial_i P) = \sum_{\gamma=1}^d P^{\perp} | \partial_i \psi_{\gamma} \rangle \langle \psi_{\gamma} |$ .

In all our expressions, the nuclear differential operators are written in terms of Cartesian coordinates. The operators can be transformed to curvilinear coordinates, necessary for efficient rovibrational computations, similarly to the transformation of the single-state nonadiabatic Hamiltonian as it was carried out in

Ref. 37 using the Jacobi and the metric tensors of the new coordinates.

For the special case of a single electronic state ( $\psi_1, E_1$ ), we are free to choose a real-valued, normalized electronic wave function  $\psi_1$ . Then, the effective operator of the atomic nuclei [Eq. (79)] simplifies to

$$\begin{aligned} (\widehat{H}_P^{(2)})_{1,1} &= \sum_{ij=1}^{3N} \frac{1}{2} (-i\varepsilon \partial_i) (\delta_{ij} - \varepsilon^2 M_{11,ij}) (-i\varepsilon \partial_j) \\ &\quad + E_1 + \varepsilon^2 \Phi_1 + \mathcal{O}(\varepsilon^3). \end{aligned} \quad (81)$$

So, we assume that  $\psi_1$  is chosen such that  $A_1 = -i \langle \psi_1 | \nabla \psi_1 \rangle = 0$  and find for the mass correction term that

$$M_{11,ij} = 2 \langle \partial_j \psi_1 | \mathcal{R}_1 | \partial_i \psi_1 \rangle = 2 \langle \partial_j \psi_1 | (H_e - E_1)^{-1} (1 - P_1) | \partial_i \psi_1 \rangle. \quad (82)$$

This mass-correction function is identical with that used in Ref. 37, and thus, for a single, isolated electronic state, the known expression of the second-order nonadiabatic Hamiltonian is recovered.

## VI. SUMMARY AND CONCLUSIONS

Molecular wave functions are often approximated on the subspace  $P\mathfrak{H}$  of the full electron-nucleus  $\mathfrak{H}$  Hilbert space, where  $P$  is the electronic subspace which governs the motion of the atomic nuclei.

We have shown that a complete neglect of the complementary electronic subspace  $(1 - P)\mathfrak{H}$  introduces an  $\mathcal{O}(\varepsilon)$  error in the Hamiltonian and also in the molecular spectrum ( $\varepsilon$  is the square root of the electron-to-nucleus mass ratio). We improved upon this  $\mathcal{O}(\varepsilon)$  approximation, by using a near-identity unitary transform of  $P$ ,  $\widehat{P} = e^{i\varepsilon \widehat{S}} P e^{-i\varepsilon \widehat{S}}$ . Terms of the self-adjoint transformation operator  $\widehat{S} = \widehat{A}_1 + \varepsilon \widehat{A}_2 + \varepsilon^2 \widehat{A}_3 + \dots$  were determined for increasing orders of  $\varepsilon$  by making the coupling, and hence the error of the molecular energy,  $\varepsilon$  times smaller at every order. The resulting transformation operators include the momentum operator  $\widehat{p}$  of the atomic nuclei; thereby, the transformed electronic space  $\widehat{P}$ , which makes the coupling lower order, depends not only on the nuclear positions  $R$  but also on the nuclear momenta  $\widehat{p}$ . The transformed electronic states adjusted by  $\widehat{p}$  up to order  $\widehat{p}^n$  achieve a block-diagonalization of  $\widehat{H}$  up to terms of order  $\varepsilon^{n+1}$ . From the transformed,  $\mathcal{O}(\varepsilon^{n+1})$  block-diagonal Hamiltonian, we obtained effective  $n$ th-order Hamiltonians for the quantum nuclear motion. Explicit expressions were derived up to the third-order corrections for a multidimensional electronic subspace.

In particular, the second-order nonadiabatic Hamiltonian contains correction terms quadratic in the nuclear momenta, which may be small near the bottom of the electronic band, but for highly excited states, they can easily dominate the diagonal correction. These kinetic energy correction terms can be identified as a coordinate-dependent correction to the nuclear mass in the nuclear kinetic energy operator. These earlier neglected “mass-correction terms” perturbatively account for the effect of the electronic states not included in the selected, explicitly coupled electronic band. For a single electronic state, the multistate expressions simplifies to the known, second-order Hamiltonian including the mass-correction function.

This perturbative decoupling can be used for isolated (groups of) electronic states, and we believe that at least the second-order, multistate expression will soon gain practical applications in rovibronic and quantum scattering computations. Examples for potential applications include the electronically excited manifold of molecular hydrogen—the first steps toward these applications are reported in Ref. 46—the predissociation dynamics of  $H_3^+$ , in which the interaction of the electronic ground and excited states is thought to play a role, and also the  $H+H_2$  reactive scattering system.

## ACKNOWLEDGMENTS

E.M. acknowledges financial support from the Swiss National Science Foundation through a PROMYS (Grant No. IZ11Z0\_166525).

## APPENDIX: SIMPLE MATHEMATICAL RELATIONS USED IN THIS WORK

### 1. Contact transform of an operator

Transformation of an operator  $\hat{Y}$  with  $e^{i\varepsilon\hat{S}}$  can be expanded in terms of increasing powers of  $\varepsilon$  as

$$\begin{aligned} \hat{Y} &= e^{-i\varepsilon\hat{S}}\hat{Y}e^{i\varepsilon\hat{S}} = \hat{Y} + \varepsilon\mathcal{L}_{\hat{S}}(\hat{Y}) + \frac{\varepsilon^2}{2}\mathcal{L}_{\hat{S}}(\mathcal{L}_{\hat{S}}(\hat{Y})) \\ &+ \frac{\varepsilon^3}{6}\mathcal{L}_{\hat{S}}(\mathcal{L}_{\hat{S}}(\mathcal{L}_{\hat{S}}(\hat{Y}))) + \dots \end{aligned} \quad (A1)$$

### 2. Commutator operations with diagonal and off-diagonal operators

$$[\hat{X}^D, \hat{Y}]^D = [\hat{X}^D, \hat{Y}^D] \quad \text{and} \quad [\hat{X}^D, \hat{Y}]^{OD} = [\hat{X}^D, \hat{Y}^{OD}], \quad (A2)$$

$$[\hat{X}^{OD}, \hat{Y}]^D = [\hat{X}^{OD}, \hat{Y}^{OD}] \quad \text{and} \quad [\hat{X}^{OD}, \hat{Y}]^{OD} = [\hat{X}^{OD}, \hat{Y}^D]. \quad (A3)$$

For the example of the diagonal  $H_e$  and the off-diagonal  $\hat{A}_i$ , we have collected the following identities (relevant for the calculations in the manuscript):

$$\mathcal{L}_{H_e}(\hat{A}_i)^D = 0, \quad (A4)$$

$$\mathcal{L}_{H_e}(\hat{A}_i)^{OD} = \mathcal{L}_{H_e}(\hat{A}_i), \quad (A5)$$

$$\mathcal{L}_{\hat{A}_j}(\mathcal{L}_{H_e}(\hat{A}_i))^D = \mathcal{L}_{\hat{A}_j}(\mathcal{L}_{H_e}(\hat{A}_i)), \quad (A6)$$

$$\mathcal{L}_{\hat{A}_j}(\mathcal{L}_{H_e}(\hat{A}_i))^{OD} = 0, \quad (A7)$$

$$\mathcal{L}_{\hat{A}_k}(\mathcal{L}_{\hat{A}_j}(\mathcal{L}_{H_e}(\hat{A}_i)))^D = 0, \quad (A8)$$

$$\mathcal{L}_{\hat{A}_k}(\mathcal{L}_{\hat{A}_j}(\mathcal{L}_{H_e}(\hat{A}_i)))^{OD} = \mathcal{L}_{\hat{A}_k}(\mathcal{L}_{\hat{A}_j}(\mathcal{L}_{H_e}(\hat{A}_i))). \quad (A9)$$

### 3. Commutator expressions

$$[\hat{K}, A] = -\frac{\varepsilon}{2}[\Delta, A] = -\frac{\varepsilon}{2}(\varepsilon\nabla \cdot A' + A' \cdot \varepsilon\nabla) = -\varepsilon A'_{\nabla} = \mathcal{O}(\varepsilon). \quad (A10)$$

## REFERENCES

- M. Beyer, N. Hölsch, J. A. Agner, J. Deiglmayr, H. Schmutz, and F. Merkt, *Phys. Rev. A* **97**, 012501 (2018).
- C.-F. Cheng, J. Hussels, M. Niu, H. L. Bethlem, K. S. E. Eikema, E. J. Salumbides, W. Ubachs, M. Beyer, N. Hölsch, J. A. Agner *et al.*, *Phys. Rev. Lett.* **121**, 013001 (2018).
- K. Piszczatowski, G. Lach, M. Przybytek, J. Komasa, K. Pachucki, and B. Jeziorski, *J. Chem. Theory Comput.* **5**, 3039 (2009).
- M. Puchalski, J. Komasa, and K. Pachucki, *Phys. Rev. A* **95**, 052506 (2017).
- L. M. Wang and Z.-C. Yan, *Phys. Rev. A* **97**, 060501 (2018).
- Y. Suzuki and K. Varga, *Stochastic Variational Approach to Quantum-Mechanical Few-Body Problems* (Springer-Verlag, Berlin, 1998).
- M. Cafiero, S. Bubín, and L. Adamowicz, *Phys. Chem. Chem. Phys.* **5**, 1491 (2003).
- S. Bubín, F. Leonarski, M. Stanke, and L. Adamowicz, *Chem. Phys. Lett.* **477**, 12 (2009).
- E. Mátyus and M. Reiher, *J. Chem. Phys.* **137**, 024104 (2012).
- E. Mátyus, *J. Phys. Chem. A* **117**, 7195 (2013).
- S. Bubín, M. Pavanello, W.-C. Tung, K. L. Sharkey, and L. Adamowicz, *Chem. Rev.* **113**, 36 (2013).
- J. Mitroy, S. Bubín, W. Horiuchi, Y. Suzuki, L. Adamowicz, W. Cencek, K. Szalewicz, J. Komasa, D. Blume, and K. Varga, *Rev. Mod. Phys.* **85**, 693 (2013).
- K. Pachucki and J. Komasa, *Phys. Chem. Chem. Phys.* **20**, 247 (2018).
- A. Muolo, E. Mátyus, and M. Reiher, *J. Chem. Phys.* **148**, 084112 (2018).
- A. Muolo, E. Mátyus, and M. Reiher, *J. Chem. Phys.* **149**, 184105 (2018).
- E. Mátyus, *Mol. Phys.* **117**, 590 (2019).
- V. I. Korobov, *Mol. Phys.* **116**, 93 (2018).
- C. A. Mead and D. G. Truhlar, *J. Chem. Phys.* **77**, 6090 (1982).
- T. Pacher, L. S. Cederbaum, and H. Köppel, *J. Chem. Phys.* **89**, 7367 (1988).
- D. R. Yarkony, *Rev. Mod. Phys.* **68**, 985 (1996).
- A. Viel and W. Eisfeld, *J. Chem. Phys.* **120**, 4603 (2004).
- T. Karman, A. van der Avoird, and G. C. Groenenboom, *J. Chem. Phys.* **144**, 121101 (2016).
- W. Kutzelnigg, *Mol. Phys.* **105**, 2627 (2007).
- P. R. Bunker and R. E. Moss, *Mol. Phys.* **33**, 417 (1977).
- P. R. Bunker and R. E. Moss, *J. Mol. Spectrosc.* **80**, 217 (1980).
- M. Aubert-Frecon, G. Hadinger, and S. Ya Umanskii, *J. Phys. B: At., Mol. Opt. Phys.* **27**, 4453 (1994).
- D. W. Schwenke, *J. Chem. Phys.* **114**, 1693 (2001).
- D. W. Schwenke, *J. Phys. Chem. A* **105**, 2352 (2001).
- K. Pachucki and J. Komasa, *J. Chem. Phys.* **130**, 164113 (2009).
- A. Scherrer, F. Agostini, D. Sebastiani, E. K. U. Gross, and R. Vuilleumier, *Phys. Rev. X* **7**, 031035 (2017).
- P. R. Bunker, C. J. McLarnon, and R. E. Moss, *Mol. Phys.* **33**, 425 (1977).
- K. L. Bak, S. P. A. Sauer, J. Oddershede, and J. F. Ogilvie, *Phys. Chem. Chem. Phys.* **7**, 1747 (2005).
- F. Holka, P. G. Szalay, J. Fremont, M. Rey, K. A. Peterson, and V. G. Tyuterev, *J. Chem. Phys.* **134**, 094306 (2011).
- K. Pachucki and J. Komasa, *J. Chem. Phys.* **137**, 204314 (2012).
- S. P. A. Sauer, H. J. A. Jensen, and J. F. Ogilvie, *Adv. Quantum Chem.* **48**, 319 (2005).
- M. Przybytek, W. Cencek, B. Jeziorski, and K. Szalewicz, *Phys. Rev. Lett.* **119**, 123401 (2017).
- E. Mátyus, *J. Chem. Phys.* **149**, 194111 (2018).
- E. Mátyus, *J. Chem. Phys.* **149**, 194112 (2018).
- A. Martínez and V. Sordani, *C. R. Math.* **334**, 185 (2002).
- S. Teufel, *Adiabatic Perturbation Theory in Quantum Dynamics*, Lecture Notes in Mathematics (Springer, 2003).
- G. Panati, H. Spohn, and S. Teufel, *ESAIM: Math. Modell. Numer. Anal.* **41**, 297 (2007).

<sup>42</sup>A. Martinez and V. Sordani, *Twisted Pseudodifferential Calculus and Application to the Quantum Evolution of Molecules* (American Mathematical Society, 2009).

<sup>43</sup>S. Weigert and R. G. Littlejohn, *Phys. Rev. A* **47**, 3506 (1993).

<sup>44</sup>G. A. Hagedorn, *Commun. Math. Phys.* **116**, 23 (1988).

<sup>45</sup>E. Cohen, T. Cvitaš, J. Frey, B. Holmström, K. Kuchitsu, R. Marquardt, I. Mills, F. Pavese, M. Quack, J. Stohner *et al.*, *Quantities, Units and Symbols in Physical Chemistry*, The IUPAC Green Book, 3rd ed. (RSC Publishing, Cambridge, 2007).

<sup>46</sup>D. Ferenc and E. Mátyus, “Non-adiabatic mass correction for excited states of molecular hydrogen: Improvement for the outer-well  $H\bar{H}^1\Sigma_g^+$  term values,” e-print [arXiv:1905.05525](https://arxiv.org/abs/1905.05525) (submitted).

<sup>47</sup>A precise formulation of the gap assumption is as follows. We say that there is a gap of size  $g > 0$  in the relevant region  $\Omega \subset \mathbb{R}^{3N}$  of nuclear configuration space if there are two continuous functions  $f_{\pm} : \Omega \rightarrow \mathbb{R}$  such that  $\text{dist}(f_{\pm}(R), \sigma(H_e(R))) \geq g/2$  such that the interval  $I(R) := [f_-(R), f_+(R)]$  satisfies  $I(R) \cap \sigma(H_e(R)) = \{E_1(R), \dots, E_d(R)\}$ . Then, all correction terms (Berry phase, diagonal correction, and effective mass) are asymptotically small as  $\varepsilon \rightarrow 0$  when choosing any smooth diabatic basis  $\{\psi_1(R), \dots, \psi_d(R)\}$ . In a real problem, of course,  $\varepsilon$  is fixed by the physical parameters and smallness of the correction terms is an indicator of a sufficiently large spectral gap.

<sup>48</sup>Note that we follow here the physical chemistry terminology in which a description is called nonadiabatic if it concerns more than one electronic states which are coupled among each other. Compare this terminology with the mathematics’ naming conventions, in which BO or “adiabatic” is commonly used for a description in which a (single or multidimensional) electronic subspace is not coupled with the rest of the electronic spectrum.

<sup>49</sup>One simple way to see this is as follows: Let  $\psi$  be a normalized eigenfunction of  $\widehat{H}_p^{(0)}$ , i.e.,  $(\widehat{H}_p^{(0)} - E)\psi = 0$  and  $\|\psi\| = \|P\psi\| = 1$ . Then,  $\chi := (\widehat{H} - E)\psi$  has norm  $\|\chi\| = \varepsilon\|P^{\perp}\widehat{Q}\psi\|$  of order  $\varepsilon$ , and thus,  $\|(\widehat{H} - E)^{-1}\frac{\chi}{\|\chi\|}\| = \frac{\|\psi\|}{\|\chi\|} \gtrsim \frac{1}{\varepsilon}$ . Hence,  $\text{dist}(E, \text{spec}(\widehat{H})) = \frac{1}{\|(\widehat{H} - E)^{-1}\|} \lesssim \varepsilon$ . For spectral values in the continuous spectrum of  $\widehat{H}_p^{(0)}$ , one can use the same argument with a Weyl sequence instead of an eigenfunction.

<sup>50</sup>Strictly speaking, such a smooth diabatic basis set exists over each contractible subset  $\Omega \subseteq \mathbb{R}^{3N}$  of the nuclear configuration space  $\mathbb{R}^{3N}$  on which the gap condition is satisfied. This is because the gap condition implies that the projections  $P(R)$  define a smooth rank- $d$  vector bundle over  $\Omega$ , and a vector bundle over a contractible set always allows for a global trivialization, that is, for a diabatic basis set as above.

# $H_3^+$ as a five-body problem described with explicitly correlated Gaussian basis sets

Cite as: J. Chem. Phys. 151, 154110 (2019); doi: 10.1063/1.5121318

Submitted: 23 July 2019 • Accepted: 17 September 2019 •

Published Online: 18 October 2019



Andrea Muolo,<sup>1</sup>  Edit Mátyus,<sup>2,a)</sup>  and Markus Reiher<sup>1,b)</sup> 

## AFFILIATIONS

<sup>1</sup>ETH Zürich, Laboratory of Physical Chemistry, Vladimir-Prelog-Weg 2, 8093 Zürich, Switzerland

<sup>2</sup>Institute of Chemistry, ELTE, Eötvös Loránd University, Pázmány Péter sétány 1/A, 1117 Budapest, Hungary

<sup>a)</sup>Electronic mail: [matyuse@caesar.elte.hu](mailto:matyuse@caesar.elte.hu)

<sup>b)</sup>Electronic mail: [markus.reiher@phys.chem.ethz.ch](mailto:markus.reiher@phys.chem.ethz.ch)

## ABSTRACT

Various explicitly correlated Gaussian (ECG) basis sets are considered for the solution of the molecular Schrödinger equation with particular attention to the simplest polyatomic system,  $H_3^+$ . Shortcomings and advantages are discussed for plain ECGs, ECGs with the global vector representation, floating ECGs and their numerical projection, and ECGs with complex parameters. The discussion is accompanied with particle density plots to visualize the observations. In order to be able to use large complex ECG basis sets in molecular calculations, a numerically stable algorithm is developed, the efficiency of which is demonstrated for the lowest rotationally and vibrationally excited states of  $H_2$  and  $H_3^+$ .

Published under license by AIP Publishing. <https://doi.org/10.1063/1.5121318>

## I. INTRODUCTION

Recent progress in the experimental energy resolution<sup>1,2</sup> of spectroscopic transitions of small molecules urges theoretical and computational methods to deliver orders of magnitude more accurate molecular energies than ever before. The current and near future energy resolution of experiments allow for a direct assessment of relativistic quantum electrodynamics effects and beyond them, as soon as calculations with a low uncertainty become available. For small molecules, composed of just a few electrons and a few nuclei, this endeavor should be realistic within the near future. A remarkable experiment–theory concourse has been unfolding for the three-particle  $H_2^+$  molecular ion<sup>3,4</sup> and for the four-particle  $H_2$  molecule.<sup>1,5–7</sup> In addition, there are promising initial results for the five-particle  $He_2^{+8–11}$  for which an explicit five-particle treatment, at least for the lowest vibrational and rotational excitations, should be possible.<sup>12</sup>

$H_3^+$  is also a five-particle system, but it is a polyatomic system. In comparison with atoms and diatomic molecules, there has been very little progress achieved for polyatomics over the past two decades regarding an accurate description of the coupled quantum mechanical motion of the electrons and the atomic nuclei. In addition to

the variational treatment considered in the present work, nonadiabatic perturbation theory offers an alternative route for closing the gap between theory and experiment. The single-state nonadiabatic Hamiltonian has been known for a long time<sup>13–18</sup> and has been used a few times in practice,<sup>10,19,20</sup> while the general working equations for the effective nonadiabatic nuclear Hamiltonian for multiple, coupled electronic states have been formulated only recently.<sup>21</sup>

We have already worked on the development of explicitly correlated Gaussian (ECG) *Ansätze* in relation with the variational solution of polyatomics (electrons plus nuclei). In 2018, we proposed to use (numerically) projected floating ECGs, which allowed us to approach the best estimate obtained on a potential energy surface (PES) for the Pauli-allowed ground state within  $70\text{ cm}^{-1}$  ( $31\text{ cm}^{-1}$  with basis set extrapolation).<sup>22</sup>

The present work starts with an overview of the advantages and shortcomings of the different ECG representations together with proton density plots which highlight important qualitative features. Then, we develop an algorithm which ensures a numerically stable variational optimization of extensive sets of ECGs with complex parameters, another promising *Ansatz* for molecular calculations,<sup>23,24</sup> and demonstrate its applicability for the lowest

rotational and vibrational states of  $\text{H}_2$  and  $\text{H}_3^+$ . Our focus in this work is on the convergence of density distributions for which a smaller number of basis functions is sufficient than what would be required to observe energy convergence.

## II. EXPLICITLY CORRELATED GAUSSIANS

We consider the solution of the time-independent Schrödinger equation (in Hartree atomic units) including all electrons and atomic nuclei, in total  $N_p$  particles, of the molecule,

$$\left[ -\sum_{i=1}^{N_p} \frac{1}{2m_i} \Delta_{\mathbf{r}_i} + \sum_{i=1}^{N_p} \sum_{j>i}^{N_p} \frac{Z_i Z_j}{|\mathbf{r}_i - \mathbf{r}_j|} \right] \Psi = E\Psi, \quad (1)$$

with electric charges  $Z_i$  and  $Z_j$  and positions  $\mathbf{r}_i$  and  $\mathbf{r}_j$ . The exact quantum numbers of the molecular energies and wave functions,  $E$  and  $\Psi$ , are the total angular momentum quantum numbers,  $N$  and  $M_N$ , the parity,  $p$ , and the spin quantum numbers for each particle type,  $S_a, M_{S_a}, S_b, M_{S_b}, \dots$

We obtain increasingly accurate approximations to the  $\Psi$  molecular wave function by using a linear combination of antisymmetrized products of (many-particle) spatial,  $\psi_i^{[N, M_N, p]}$ , and spin,  $\chi_i^{[S_a, M_{S_a}, S_b, M_{S_b}, \dots]}$ , functions,

$$\Psi^{[N, M_N, p, S_a, M_{S_a}, S_b, M_{S_b}, \dots]} = \sum_{i=1}^{N_b} c_i \hat{\mathcal{A}} \left\{ \psi_i^{[N, M_N, p]} \chi_i^{[S_a, M_{S_a}, S_b, M_{S_b}, \dots]} \right\}, \quad (2)$$

where  $N_b$  is the number of basis functions and  $\hat{\mathcal{A}}$  is the antisymmetrization operator for fermions (we would need to symmetrize the product for bosonic particles). The nonlinear parameters of the spatial and the spin functions are optimized based on the variational principle,<sup>25,26</sup> and the  $c_i$  coefficients are determined by solving the linear variational problem in a given basis set.

Concerning the construction of the basis set, explicitly correlated Gaussian (ECG) functions have been successfully used as spatial basis functions for a variety of chemical and physical problems.<sup>26,27</sup> In what follows, we consider various ECG basis sets aiming at an accurate solution that can approach spectroscopic accuracy of the molecular Schrödinger equation [generally defined as obtaining (ro)vibrational state energies within better than a  $1 \text{ cm}^{-1}$  uncertainty]. A precise description of vibrational states of di- and polyatomic molecules assumes the use of basis functions which have sufficient flexibility to describe the nodes of the wave function along the interparticle distances, sharp peaks corresponding to the localization of the nuclei displaced from the center of mass, and allow us to obtain efficiently the solutions corresponding to the exact quantum numbers of this nonrelativistic problem.

Concerning the spin functions, we use the spin functions of two and three identical spin-1/2 fermions (electrons and protons) with the spin quantum numbers  $(S, M_S) = (0, 0)$  and  $(S, M_S) = (1/2, 1/2)$ , respectively, formulated according to Refs. 25 and 28.

In the case of  $\text{H}_3^+$ , the mathematically lowest-energy (ground electronic, zero-point vibrational) state of the Schrödinger equation with  $N = 0$  and  $p = +1$  is not allowed by the Pauli principle (for the  $S_e = 0$  electrons' and  $S_p = 1/2$  protons' spin states), or in short,

the nonrotating vibrational and electronic ground state of  $\text{H}_3^+$  is spin forbidden.<sup>29,30</sup> The lowest-energy, Pauli-allowed state is the vibrational ground state ( $v = 0$ ) with  $N = 1$  and  $p = -1$  (the first rotationally excited state). The lowest-energy state with  $N = 0$  is the  $(0, 1^1)$  fundamental vibration,<sup>29</sup> which corresponds to asymmetric distortions (antisymmetric for the proton exchange) with respect to the equilateral triangular equilibrium structure.

For the assessment and visualization of the results obtained with the different spatial basis sets, we use particle density functions, which are very useful in analyzing the qualitative properties of the molecular wave function.<sup>31–33</sup> We will focus on properties of the proton ( $p$ ) density (measured from the center-of-mass, CM, position),

$$D_{p, \text{CM}}(\mathbf{R}) = \langle \Psi | \delta(\mathbf{r}_p - \mathbf{r}_{\text{CM}} - \mathbf{R}) | \Psi \rangle. \quad (3)$$

### A. Plain ECG, polynomial ECG, and ECG-GVR

Plain ECG-type functions,

$$\psi_{\text{ECG}}(\mathbf{A}; \mathbf{r}) = \exp[-\mathbf{r}^T (\mathbf{A} \otimes \mathbf{I}_3) \mathbf{r}] \quad (4)$$

with the collective position vector  $\mathbf{r} = (\mathbf{r}_1, \mathbf{r}_2, \dots, \mathbf{r}_{N_p})$  and the  $\mathbf{A} \in \mathbb{R}^{N_p \times N_p}$  symmetric matrix, have been successfully used to describe atoms and positron-electron complexes (with  $N = 0$  total angular momentum quantum number and  $p = +1$  parity).<sup>25</sup> To describe the localization and vibrational excitation of atomic nuclei, a linear combination of several plain ECG functions is necessary, which makes their use in molecular calculations very inefficient. The slow convergence of plain ECGs for the lowest-energy  $N = 0$  state of  $\text{H}_3^+$  is shown with respect to ECG-GVR (*vide infra*) in Fig. 1 [compare Figs. 1(a) and 1(b)].

Explicitly correlated Gaussians with the global vector representation (ECG-GVR) have been originally proposed by Suzuki, Usukura, and Varga in 1998.<sup>34</sup> These functions represent a general form of ECGs with polynomial prefactors. When several ECG-GVR functions are used in a variational procedure, molecular states can be converged with a total angular momentum quantum number,  $N$ , and natural parity,  $p = (-1)^N$ ,

$$\psi_{\text{ECG-GVR}}^{[N, M_N]}(\mathbf{r}; \mathbf{A}, \mathbf{u}, K) = Y_{NM_N}(\hat{\mathbf{v}}) |\mathbf{v}|^{2K+N} \exp[-\mathbf{r}^T (\mathbf{A} \otimes \mathbf{I}_3) \mathbf{r}], \quad (5)$$

where the "global vector"  $\mathbf{v}$  is a linear combination of particle coordinates,

$$\mathbf{v} = u_1 \mathbf{r}_1 + u_2 \mathbf{r}_2 + \dots + u_{N_p} \mathbf{r}_{N_p} = (\mathbf{u} \otimes \mathbf{I}_3)^T \mathbf{r}, \quad (6)$$

and  $\hat{\mathbf{v}}$  contains the spherical polar angles corresponding to the unit vector  $\mathbf{v}/|\mathbf{v}|$ . The integer value  $K$  and the global vector coefficient  $\mathbf{v}$  may be unique to all basis functions and are determined variationally.

The general ECG-GVR basis set can be very well used to converge the ground- and excited states of atoms, positron-electron complexes, as well as diatomic molecules (for which plain ECGs would be inefficient) with various total angular momentum quantum numbers  $N$ .<sup>28,35–38</sup> It is important to stress, however, that higher vibrational excitations, heavier nuclei, or higher  $N$  values require the use of higher-order polynomials in front of the ECG, which make the

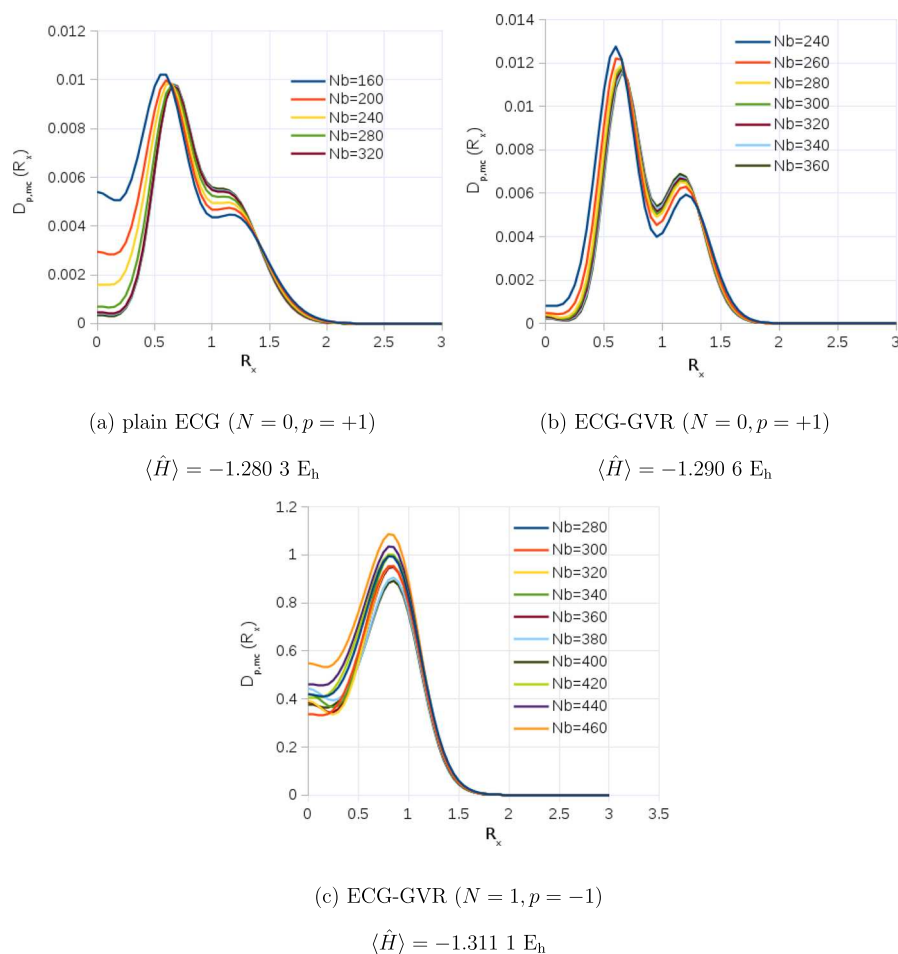


**FIG. 1.** Proton probability density for  $H_3^+ = \{p^+, p^+, p^+, e^-, e^-\}$  ( $S_e = 0, S_p = 1/2$ ) obtained with plain ECG for ( $N = 0, p = +1$ ) in (a) and with ECG-GVR functions for ( $N = 0, p = +1$ ) in (b) and ( $N = 1, p = -1$ ) in (c). The density is shown along a ray measured from the center of mass,  $D(R_x, 0, 0)$ , which is sufficient as the overall space rotation-inversion leaves the system invariant ( $N = 0, p = +1$ ). In the ECG-GVR calculations, the maximal order for the polynomial prefactor was  $2K_{\max} = 20$ . The reference energy values obtained by us on a PES are  $E_{\text{PES}}(N = 0, p = +1) = -1.311950 E_h$  and  $E_{\text{PES}}(N = 1, p = -1) = -1.323146 E_h$ <sup>39</sup> (note that the latter value corresponds to the lowest-energy Pauli-allowed state). All quantities in the figure are given in atomic units.

integral evaluation and the entire calculation computationally more demanding.

For  $N = 0$ , an ECG-GVR with the special parameterization  $u_i = 1, u_j = -1$ , and  $u_k = 0$  ( $k \neq i, j$ ) simplifies to an ECG with a single (even-power) polynomial prefactor,

$$\begin{aligned} \psi_{\text{ECG-r}}^{[0,0]}(\mathbf{r}; \mathbf{A}, K) &= |\mathbf{r}_i - \mathbf{r}_j|^{2K} \exp[-\mathbf{r}^T (\mathbf{A} \otimes I_3) \mathbf{r}], \\ &= r_{ij}^{2K} \exp[-\mathbf{r}^T (\mathbf{A} \otimes I_3) \mathbf{r}], \end{aligned} \quad (7)$$

which has been successfully used to describe vibrations of diatomic molecules by Adamowicz and co-workers.<sup>40–42</sup>

In spite of the success of these types of basis functions for atoms and diatoms, the ECG-GVR *Ansatz* was found to be inefficient<sup>22</sup> [comparable to the single-polynomial ECG *Ansatz*, Eq. (7)<sup>43</sup>] to converge the five-particle energy of  $H_3^+$  within spectroscopic accuracy. Even the proton density can be hardly converged (Fig. 1), while the energy has uncertainties (much) larger than  $1 \text{ mE}_h$ . The proton density for the lowest-energy  $N = 0$  state has two peaks, which may be qualitatively correct, since this state (if converged) corresponds to the antisymmetric fundamental vibration, which should feature two peaks in the proton density measured from the

center of mass. The two peaks appear already in the plain ECG calculation [Fig. 1(a)], but plain ECG densities have even larger uncertainties. A further increase in the basis set (toward convergence) is hindered by near-linear dependency problems, which is an indication of insufficient flexibility in the mathematical form of the basis functions.

Figure 1(c) shows the (convergence of the) proton density obtained with ECG-GVR functions for the lowest-energy rotational ( $N = 1$ ) state which corresponds to the lowest-energy Pauli-allowed state of the system. Notice the significant amount of density at the origin (center of mass) and the large deviations of results obtained with different basis set sizes, which must be artifacts due to incomplete convergence (compare with Figs. 3 and 5). The “best” (lowest) five-particle energy, we obtained with an ECG-GVR representation for the lowest-energy state ( $N = 1$ ), is  $1.8 \text{ mE}_h$  larger than the best estimate on a potential energy surface (PES).<sup>22</sup>

Hence, the slow convergence of the energy and the density in the ECG-GVR *Ansatz* is related to the fact that these functions are not flexible enough to efficiently describe the triangular arrangement (and vibrations) of the protons in  $H_3^+$  and the spherical symmetry



of the system at the same time.<sup>22</sup> In principle, it would be possible to define ECG-GVRs with multiple global vectors which could give a better account of the rotational and the multiparticle clustering effects in a polyatomic molecule, but the formalism would be very involved.

## B. ECGs with three pre-exponential polynomials

We note in passing that, in 2005, Bednarz, Bubin, and Adamowicz proposed an ECG *Ansatz* for  $H_3^+$ ,<sup>43</sup>

$$\psi_{\text{ECG-3r}}^{[0,0]}(\mathbf{r}; \mathbf{A}, k_{12}, k_{13}, k_{23}) = r_{12}^{2k_{12}} r_{13}^{2k_{13}} r_{23}^{2k_{23}} \exp[-\mathbf{r}^T (\mathbf{A} \otimes I_3) \mathbf{r}], \quad (8)$$

by including polynomial prefactors for all three proton-proton distances,  $r_{ij} = |\mathbf{r}_i - \mathbf{r}_j|$  ( $i, j = 1, 2, 3, j > i$ ). The integral expressions have been formulated, but to our best knowledge, they have never been used in practical calculations due to their very complicated form and numerical instabilities.<sup>44</sup>

## C. Floating ECGs with explicit projection

Floating ECGs (FECGs),

$$\psi_{\text{FECG}}(\mathbf{A}, \mathbf{s}; \mathbf{r}) = \exp[-(\mathbf{r} - \mathbf{s})^T (\mathbf{A} \otimes I_3) (\mathbf{r} - \mathbf{s})], \quad (9)$$

offer the flexibility to choose (optimize) not only the exponents but also the centers,  $\mathbf{s} \in \mathbb{R}^{N_p \times 3}$ , which allows one to efficiently describe localization of the heavy particles in polyatomics. At the same time, the FECG functions with arbitrary,  $\mathbf{s} \neq 0$ , centers do not transform as the irreducible representations (irreps) of the three-dimensional rotation-inversion group,  $O(3)$ , and therefore, they are neither eigenfunctions of the total squared angular momentum operator,  $\hat{N}^2$ , nor eigenfunctions of space inversion (parity). Although these symmetry properties are numerically recovered during the course of the variational optimization converging to the exact solution [see Figs. 2(a)–2(c), 3(a), and 3(b)], it is extremely inefficient (impractical) for molecular calculations to recover the continuous symmetry numerically.

To speed up the slow convergence in the FECG *Ansatz* due to the broken spatial symmetry, we proposed in 2018<sup>22</sup> to project the floating ECG basis functions onto irreps of  $O(3)$ ,

$$\psi_{\text{p-FECG}}^{[N,p]}(\mathbf{A}, \mathbf{s}; \mathbf{r}) = \frac{1}{4\pi} \int \left[ D_{M_N M_N}^{(N)}(\Omega) \right]^* \hat{R}(\Omega) \frac{1}{2} (1 + p \cdot \hat{i}) \times \exp[-(\mathbf{r} - \mathbf{s})^T (\mathbf{A} \otimes I_3) (\mathbf{r} - \mathbf{s})] d\Omega, \quad (10)$$

where  $\Omega$  collects parameterization of the 3-dimensional rotation, e.g., in terms of three Euler angles,  $D_{M_N M_N}^{(N)}(\Omega)$  is the  $(M_N, M_N)$ th element of the  $N$ th-order Wigner  $D$  matrix, and  $\hat{R}(\Omega)$  is the corresponding three-dimensional rotation operator.  $p$  is the parity, +1 or -1, and  $\hat{i}$  is the 3-dimensional space-inversion operator. Both the  $\hat{R}$  rotational and the  $\hat{i}$  space-inversion operators act on the particle coordinates,  $\mathbf{r}$ , but the mathematical form of the ECGs allowed us to translate their action onto the transformation of the ECG parameters,  $\mathbf{A}$  and  $\mathbf{s}$ .<sup>22,28</sup>

For the projected basis functions, the integral expressions of the nonrelativistic operators are in general not known analytically, and for this reason, we have carried out an approximate, numerical projection in Ref. 22. Using numerically projected floating ECGs, we

achieved to significantly improve upon the five-particle energy for  $H_3^+$  and to approach the current best estimate (on a potential energy surface) for the Pauli-allowed ground state within  $70 \text{ cm}^{-1}$  (with extrapolation within  $31 \text{ cm}^{-1}$ ).

Properties of (unprojected, symmetry-breaking) and (approximately) projected FECGs are shown for the example of the proton density of  $H_2$  and  $H_3^+$  in Figs. 2 and 3, respectively. At the beginning of an unprojected calculation, the proton density first localizes at around three (two) lobes which corresponds to the localization of the protons in  $H_3^+$  (and  $H_2$ ), exhibiting small-amplitude vibrations in a fixed orientation (which can be understood as a superposition of several eigenstates with different  $N$ ,  $M_N$ , and  $p$  values). Then, during the course of the variational increase in the basis set, the spherical symmetry is recovered, but the triangular (dumbbell-like) relative configuration of the protons in  $H_3^+$  (in  $H_2$ ) is also described within the proton shells (not shown in the figures). Numerical projection reconstructs the expected spherical symmetry directly, without the need of variational optimization, as it is shown in Figs. 3(c), 3(d), and 2(d).

To construct the density plots, we had to evaluate the proton density at several points in space, which is demanding for  $H_3^+$  with the current projection scheme. For this reason, the largest basis set used for the density plot [Fig. 3(d)] is smaller than the best one obtained during the convergence of the five-particle energy in Ref. 22. Projected FECGs are promising candidates for solving  $H_3^+$  as a five-particle problem, and we anticipate further progress along this line in the future.

## D. Complex ECGs

In 2006, Bubin and Adamowicz<sup>23</sup> proposed to use ECGs with complex parameters (CECGs),

$$\psi_{\text{CECG}}(\mathbf{C}; \mathbf{r}) = \exp[-\mathbf{r}^T (\mathbf{C} \otimes I_3) \mathbf{r}], \quad (11)$$

to describe vibrational ( $N = 0$ ,  $p = +1$ ) states of molecules.  $\mathbf{C} = \mathbf{A} + i\mathbf{B} \in \mathbb{C}^{N_p \times N_p}$  is a complex-valued matrix with the real, symmetric matrices,  $\mathbf{A}$  and  $\mathbf{B}$ . To ensure square integrability,  $\psi$  must decay to zero at large distances. Furthermore, to have a positive definite  $\psi$ ,  $\mathbf{A}$  must be positive definite. Most physical operators have very simple integrals in this basis set, and the integrals can be evaluated with a small number of operations (i.e., at low computational cost), which does not increase with increasing the number of nodes of the basis function (unlike for ECG-GVR or polynomial ECG). The rich nodal structure of CECGs, introduced by the  $\mathbf{B}$  imaginary part of the exponent, can be understood through the Euler identity,  $e^{-(a+ib)r^2} = e^{-ar^2} [\cos(br^2) - i \sin(br^2)]$ .

In 2008, Bubin and Adamowicz<sup>24</sup> proposed to extend CECGs for computing  $N = 1$  states of diatomics with

$$\psi_{z\text{CECG}}(\mathbf{C}; \mathbf{r}) = \rho_z \exp[-\mathbf{r}^T (\mathbf{C} \otimes I_3) \mathbf{r}], \quad (12)$$

using  $\rho_z = (\mathbf{r}_{n_1} - \mathbf{r}_{n_2})_z$ , which is the  $z$ -component of the displacement vector between the two nuclei,  $n_1$  and  $n_2$ . This *Ansatz* yields a very good description for the first rotationally excited state of a diatomic molecule (the electrons' contribution to the total angular momentum is almost negligible).

The analytic matrix elements for the overlap, kinetic energy, Coulomb potential energy, and particle density (together with the

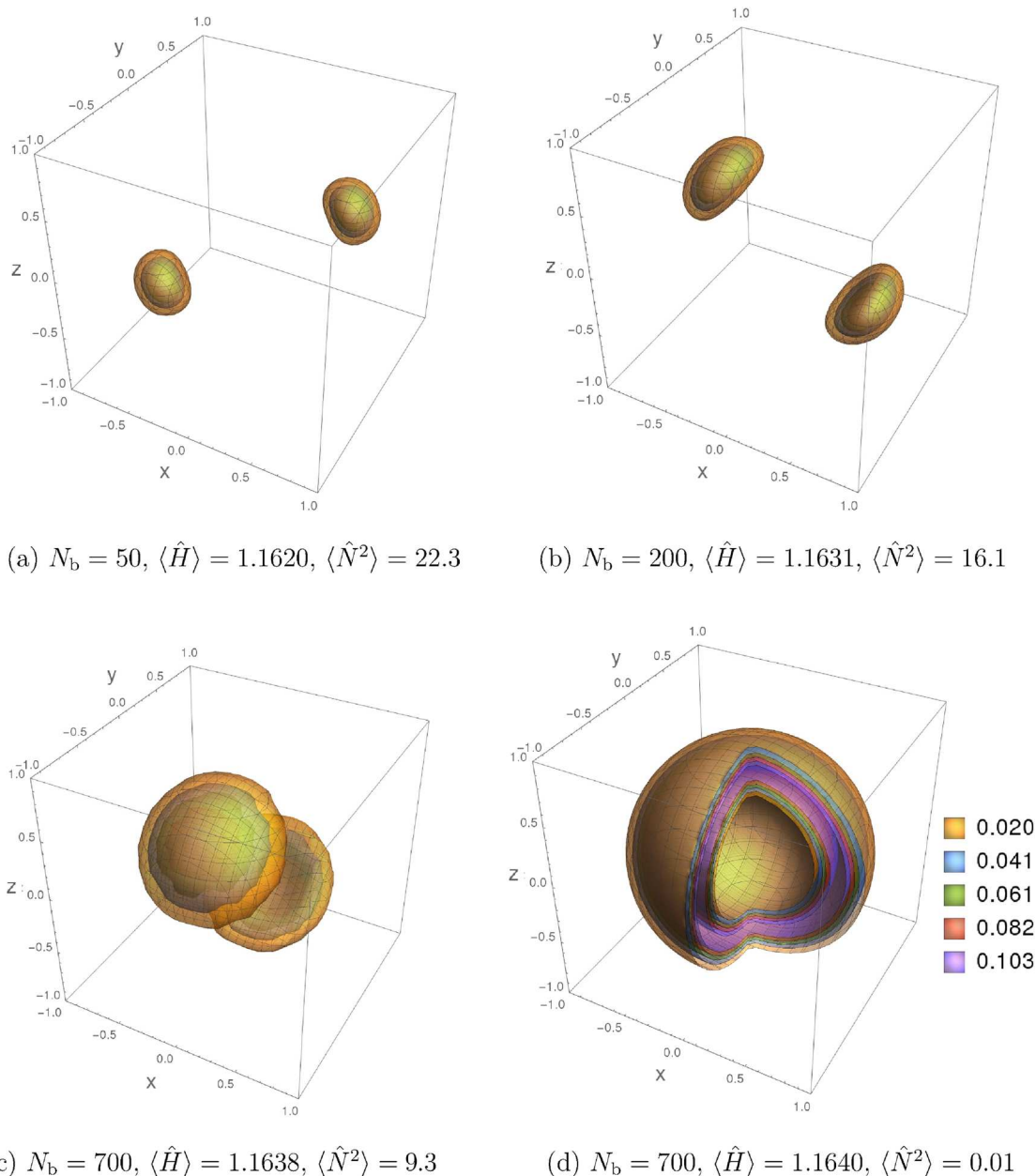


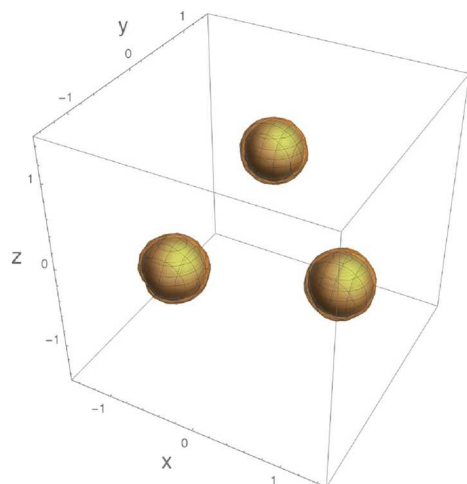
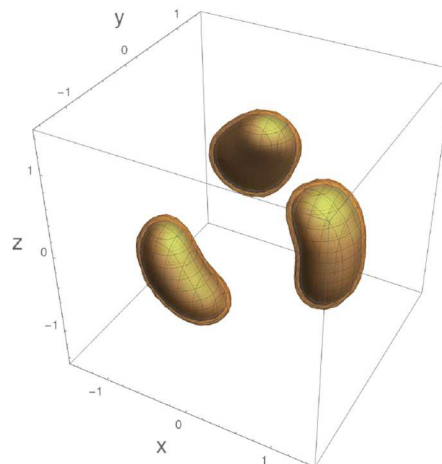
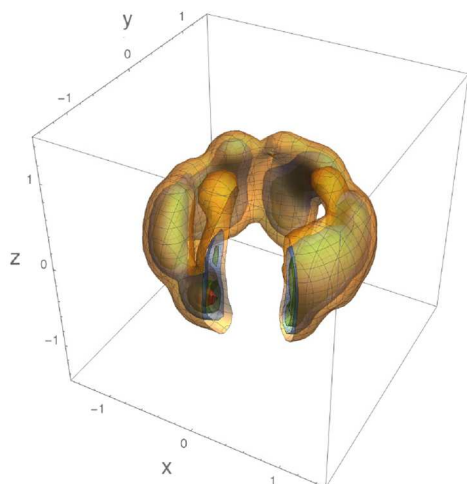
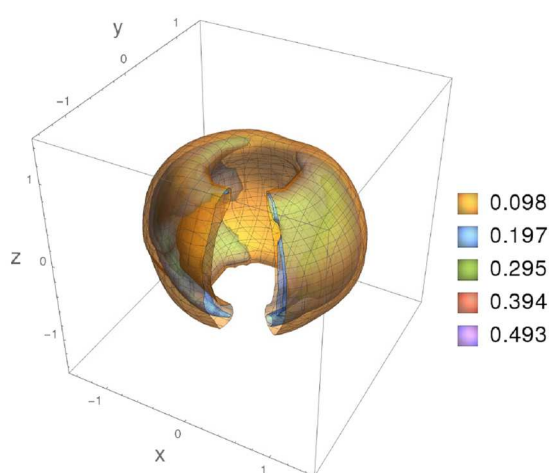
**FIG. 2.** Proton probability density for the ground state of  $H_2 = \{p^+, p^+, e^-, e^-\}$  ( $S_a = 0$ ,  $S_p = 0$ ) obtained with floating ECGs. (a)–(c) Nonprojected (symmetry breaking) FEGCs with 50, 200, and 700 basis functions, respectively; (d) FEGC basis functions numerically projected onto the ( $N = 0$ ,  $p = +1$ ) irrep of  $O(3)$  using 22 quadrature points for each Euler angle (see Ref. 22 for details).  $N_b$  is the number of basis functions. The energy and the square of the total angular momentum operator are  $\langle \hat{H} \rangle = -1.164\,025\,031\,E_h$ <sup>17</sup> and  $\langle \hat{N}^2 \rangle = 0$ , respectively. All quantities in the figure are given in atomic units.

energy gradients with respect to the  $C$  matrix parameters) have been derived by Bubin and Adamowicz, and the expressions can be found in Refs. 23 and 24.

Widespread application of the CECG basis-function family is hindered by the fact that matrix operations (matrix inversion,

etc.) are more affected by numerical instabilities in finite (double) precision complex arithmetics when compared to real arithmetics.

Earlier this year, Varga proposed<sup>45</sup> a numerically stable implementation of the CECG functions, through real combinations,

(a)  $N_b = 240$ ,  $\langle \hat{H} \rangle = -1.3170$ ,  $\langle \hat{N}^2 \rangle = 30.5$ (b)  $N_b = 2250$ ,  $\langle \hat{H} \rangle = -1.3181$ ,  $\langle \hat{N}^2 \rangle = 21.1$ (c)  $N_b = 240$ ,  $\langle \hat{H} \rangle = -1.3190$ ,  $\langle \hat{N}^2 \rangle = 15.8$ (d)  $N_b = 240$ ,  $\langle \hat{H} \rangle = -1.3201$ ,  $\langle \hat{N}^2 \rangle = 5.6$ 

**FIG. 3.** Proton probability density for the lowest-energy, Pauli-allowed state of  $H_3^+ = \{p^+, p^+, p^+, e^-, e^-\}$ , which is the first rotationally excited state ( $N = 1$ ) of the zero-point vibration. (a) and (b) Nonprojected (symmetry breaking) FECGs with 240 and 2250 basis functions, respectively; (c) and (d) FECGs approximately projected onto the ( $N = 1$ ,  $p = -1$ ) irrep of  $O(3)$  using 4 and 8 quadrature points, respectively, for each Euler angle.<sup>22</sup> For the exact wave function,  $\langle \hat{N}^2 \rangle = 2$  ( $N = 1$ ). All quantities are given in atomic units.

$$\psi_{\text{C-CECG}}(\mathbf{r}; \mathbf{C}) = \frac{1}{2} [\psi_{\text{CECG}}(\mathbf{r}; \mathbf{C}) + \psi_{\text{CECG}}(\mathbf{r}; \mathbf{C}^*)], \quad (13)$$

$$\psi_{\text{S-CECG}}(\mathbf{r}; \mathbf{C}) = \frac{1}{2i} [\psi_{\text{CECG}}(\mathbf{r}; \mathbf{C}) - \psi_{\text{CECG}}(\mathbf{r}; \mathbf{C}^*)], \quad (14)$$

with  $\mathbf{C}^*$  being the complex conjugate of  $\mathbf{C}$ , which allowed him to work with real-valued Hamiltonian and overlap matrices. Furthermore, he also proposed an imaginary-time propagation approach to make the optimization of the complex exponent matrices efficient for the ground state of molecular systems.<sup>45</sup>

### III. ALGORITHM FOR NUMERICALLY STABLE CALCULATIONS WITH COMPLEX ECGS

In this section, we present the key elements of a numerically stable algorithm that we developed for the original (complex) CECG functions.

Following Eq. (12), we define a new CECG basis function by specifying the  $\mathbf{A}$  and  $\mathbf{B} \in \mathbb{R}^{N_p \times N_p}$  real symmetric matrices, which give the complex symmetric matrix,  $\mathbf{C} = \mathbf{A} + i\mathbf{B}$ , in the exponent of the ECG. We work in laboratory-fixed Cartesian

coordinates (LFCCs)<sup>46,47</sup> and use a multichannel optimization procedure, i.e., optimize the coefficient matrices corresponding to different translationally invariant (TI) Cartesian coordinate representations.<sup>47</sup> Owing to the mathematical form of the ECGs, the transformation of the coordinates can be translated to the transformation of the parameter matrix.<sup>28</sup> In all TI representations, the  $A$  and  $B$  matrices are block diagonal, i.e., the TI and the center-of-mass (CM) blocks do not couple. To ensure square integrability, we choose the CM block of  $A$  to have nonzero values on its diagonal. We choose the

same nonzero value for all diagonal entries and for each basis function, the contribution of which is eliminated (subtracted) during the evaluation of the integrals. With this choice for the real part  $A$ , we are free to set the CM block of the imaginary part  $B$  to zero, and  $\psi$ , of course, remains positive definite (due to the nonvanishing CM block of  $A$ ).

In order to obtain  $N = 1$  states, we use CECGs multiplied with the  $z$  coordinate of a “pseudoparticle.” Bubin and Adamowicz used the  $z$  component of the nucleus-nucleus displacement

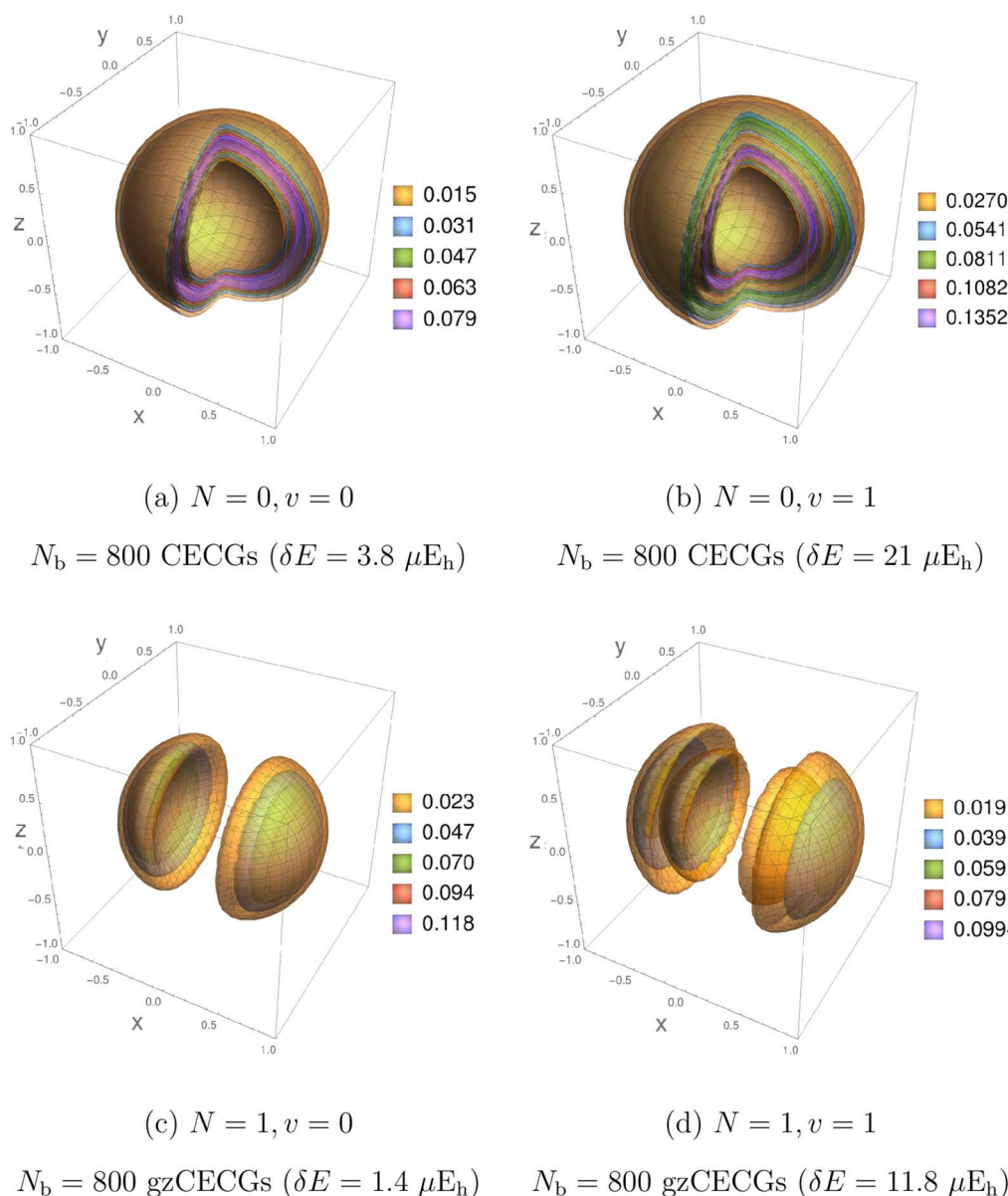


**FIG. 4.** Proton probability density calculated for the ground ( $v = 0, N = 0$ ) in (a) and the lowest rotationally ( $N = 1$ ) and vibrationally ( $v = 1$ ) excited states in (b)–(d) of  $H_2 = \{p^+, p^+, e^-, e^-\}$  ( $S_0 = 0, S_p = (1 - N)/2, \rho = (-1)^N$ ) using (gz)CECG functions. The particle densities are converged within figure resolution; deviation of the energy from benchmark values<sup>17</sup> is given in parentheses. All quantities in the figure are given in atomic units.

vector in diatomic molecules.<sup>24</sup> We do not choose only a single pseudoparticle but pick different particle pairs for the different basis functions (and possibly several other linear combinations of the particle coordinates, inspired by the ECG-GVR idea<sup>48</sup>) to ensure that the contribution of each particle pair to the angular momentum is accounted for. Hence, our general form for complex basis functions, gzCECG, for  $N = 1$ ,  $p = -1$  states is

$$\phi_{\text{gzCECG}}(\mathbf{r}; \mathbf{C}, i) = \rho_z^{(i)}(\mathbf{r}) \exp[-\mathbf{r}^T (\mathbf{C} \otimes \mathbf{I}_3) \mathbf{r}], \quad (15)$$

where  $\rho_z^{(i)}$  is the  $z$  component of the  $i$ th translationally invariant vector, formed as a linear combination of the particle coordinates,

$$\rho_z^{(i)}(\mathbf{r}) = \sum_{j=1}^{N_p} \mathbf{u}_j^{(i)} r_{j,z}. \quad (16)$$

Of course, there are infinitely many such combinations. In the present calculations, we have included all possible pairs of particles, i.e.,  $i$  in Eq. (16) cycles through the possible particle pairs only. For example, there are  $\binom{5}{2} = 10$  possible particle pairs in  $\text{H}_3^+$ , and we consider the following  $\rho_z^{(i)}$ -parameterization ( $i = 1, 2, \dots, 10$ ) in the gzCECG representation:

- (1)  $\mathbf{u}^{(1)} = (1, -1, 0, 0, 0)$ ,
- (2)  $\mathbf{u}^{(2)} = (1, 0, -1, 0, 0)$ ,
- (...)
- (10)  $\mathbf{u}^{(10)} = (0, 0, 0, 1, -1)$ .

A robust and numerically stable implementation of (gz)CECGs has been a challenging task. The overlap and Hamiltonian matrix elements are complex, and the complex generalized eigenvalue

problem quickly becomes unstable when increasing the size of the basis set in a stochastic variational approach. We have studied the nature of these instabilities and have identified two ingredients producing this unstable behavior.

First, an unrestricted optimization of the  $\mathbf{B}$  matrix generates increasingly oscillatory functions, and thus, the basis function decays slowly in the limit  $r \rightarrow \infty$ . This behavior affects a broad region of the parameter space; it happens whenever the imaginary part  $\mathbf{B}$  dominates the real part  $\mathbf{A}$ .

Second, the analytic overlap and Hamiltonian matrix elements require the calculation of the determinant and the inverse of the complex, symmetric matrix  $\mathbf{C}$ , the evaluation of which suffers from loss of precision in floating-point arithmetics, i.e., an ill-conditioned matrix is still invertible, but the inversion is numerically unstable. The quality of the eigenvalues and eigenfunctions of the Hamiltonian matrix (with the complex, nondiagonal overlap matrix) is thereby compromised by ill-conditioned matrices  $\mathbf{C}$ , an undesired feature which can be identified by repeating the calculations with higher-precision arithmetics or by monitoring the range spanned by the eigenvalues of the matrices.<sup>50</sup>

Based on these observations, we propose the following conditions to ensure numerical stability of the variational procedure in finite-precision arithmetics. During the course of the variational selection and optimization of the basis function parameters, we monitor

- (1) the ratio of the diagonal elements of the real and the imaginary parts of  $\mathbf{C} = \mathbf{A} + i\mathbf{B}$ :  $A_{ii}/B_{ii} < \epsilon_{1i}$ ,  $i = 1, \dots, N_p$ ;
- (2) the condition number of  $\mathbf{C}$ :  $\kappa(\mathbf{C}) < \epsilon_2$ ;
- (3) the condition number of the (complex symmetric)  $\mathbf{S}$  overlap and the  $\mathbf{H}$  Hamiltonian matrices:  $\kappa(\mathbf{S}) < \epsilon_{3S}$  and  $\kappa(\mathbf{H}) < \epsilon_{3H}$ .

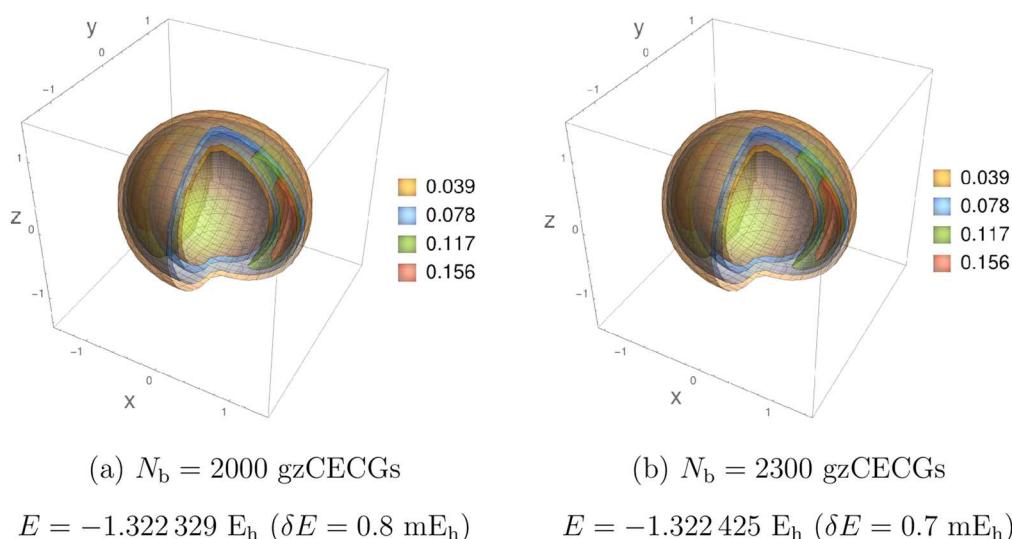


**FIG. 5.** Proton probability density for the lowest-energy, Pauli-allowed state of  $\text{H}_3^+$  ( $N = 1, p = -1, S_e = 0, S_p = 1/2$ ) obtained with 2000 and 2300 gzCECG functions in (a) and (b), respectively. The density is converged within figure resolution [compare plots (a) and (b)], while the deviation of the five-particle energy from the best value obtained on a PES in our earlier work,<sup>22</sup>  $E_{\text{ref}} = -1.323\,146 E_h$ ,<sup>39</sup> is given in parentheses ( $\delta E = E - E_{\text{ref}}$ ). All quantities in the figure are given in atomic units.

For acceptance of a trial basis function as a new basis function in the basis set, these three conditions must be fulfilled in addition to minimization of the energy. In this way, the numerical stability of the computational procedure can be ensured. For the present calculations, carried out using double precision arithmetics, we have found that the same  $\epsilon_{1i} = \epsilon_2 = \epsilon_{3S} = \epsilon_{3H} = \epsilon = 10^{10}$  value for each condition ensures numerical stability for the desired precision, i.e., 6–9 significant digits in the energy. Conditions (1)–(3) and the selected value of  $\epsilon$  have been constantly tested during the calculations by solving the linear variational problem within the actual basis set with increased (quadruple and beyond) precision arithmetics.

The first two conditions ensure that the parameter optimization algorithm avoids the regions which would result in overly oscillatory basis functions at large distances, while the third condition controls the level of linear dependency within the (nonorthogonal) basis set.

The computational bottleneck of the (gz)CECG calculations is related to the solution of the generalized complex eigenvalue problem as it was also noted in Ref. 44. For this reason, we have implemented and used the FEAST eigensolver algorithm,<sup>49</sup> which is a novel, powerful iterative eigensolver for the generalized, complex, symmetric eigenvalue problem.

Figure 4 shows the convergence of the proton density (the energy is also given) for the ground and rotationally and vibrationally excited states of the H<sub>2</sub> molecule ( $S_e = 0$ ,  $S_p = 0$ ). These results were obtained within a few days on a multicore workstation. While the densities are very well converged, the energies can be further improved by subsequent basis-set optimization.

Figure 5 shows our best results obtained for selected states of H<sub>3</sub><sup>+</sup> ( $S_e = 0$ ,  $S_p = 1/2$ ) using the numerically stable gzCECG implementation developed in this work. The proton probability density for the lowest-energy, Pauli-allowed state (zero-point vibration,  $N = 1$ ) is well converged; the difference between Figs. 5(a) and 5(b) can hardly be seen. The best energy is 0.7 mE<sub>h</sub>  $\approx$  153 cm higher than the reference value obtained on a PES.<sup>39</sup>

#### IV. CONCLUSIONS

Explicitly correlated Gaussian basis sets have been an excellent choice when aiming for ultraprecise energies for atoms, electron-positron complexes, and diatomic molecules. However, tight convergence of the energy of H<sub>3</sub><sup>+</sup>, the simplest polyatomic system, by including all electrons and protons in a variational procedure has not yet been achieved.

In this work, we critically assessed explicitly correlated Gaussian (ECG) basis sets for solving the molecular (electrons plus nuclei) Schrödinger equation through the study of the convergence of the energy and the particle (proton) density. These observations will contribute to developments that will eventually allow for the convergence of the five-particle energy of H<sub>3</sub><sup>+</sup> within spectroscopic accuracy, i.e., an uncertainty better than 1 cm<sup>-1</sup> ( $<5 \times 10^{-6}$  E<sub>h</sub>) for the molecular energy.

In 2018, we developed an algorithm for numerically projected floating ECGs<sup>22</sup> to compute the lowest-energy state of H<sub>3</sub><sup>+</sup> in a variational procedure. In the present work, we presented a numerically stable algorithm for another promising basis set for solving H<sub>3</sub><sup>+</sup>,

complex ECGs, which makes it possible to use large basis set sizes in finite precision arithmetics. Although projected floating ECGs provided a somewhat lower energy<sup>22</sup> than complex ECGs (present work) so far, it is currently unclear which type of basis set will finally allow one to reach spectroscopic accuracy for H<sub>3</sub><sup>+</sup> treated as a five-particle system.

Reaching and transgressing this level of uncertainty in a variational computation will make it possible to directly assess effective nonadiabatic mass models and to study relativistic and quantum electrodynamics effects in the high resolutions spectrum. Such calculations are beyond the scope of the present work and therefore deferred to future studies.

#### ACKNOWLEDGMENTS

This work was supported by ETH Zurich. E.M. acknowledges financial support from a PROMYS Grant (No. IZ11Z0\_166525) of the Swiss National Science Foundation and ETH Zürich for supporting a stay as visiting professor during 2019.

#### REFERENCES

- C.-F. Cheng, J. Hussels, M. Niu, H. L. Bethlem, K. S. E. Eikema, E. J. Salumbides, W. Ubachs, M. Beyer, N. Hölsch, J. A. Agner *et al.*, *Phys. Rev. Lett.* **121**, 013001 (2018).
- C. R. Markus and B. J. McCall, *J. Chem. Phys.* **150**, 214303 (2019).
- V. I. Korobov, L. Hilico, and J. P. Karr, *Phys. Rev. Lett.* **118**, 233001 (2017).
- S. Alighanbari, M. G. Hansen, V. I. Korobov, and S. Schiller, *Nat. Phys.* **14**, 555 (2018).
- L. M. Wang and Z.-C. Yan, *Phys. Rev. A* **97**, 060501(R) (2018).
- M. Puchalski, J. Komasa, P. Czachorowski, and K. Pachucki, *Phys. Rev. Lett.* **122**, 103003 (2019).
- N. Hölsch, M. Beyer, E. J. Salumbides, K. S. Eikema, W. Ubachs, C. Jungen, and F. Merkt, *Phys. Rev. Lett.* **122**, 103002 (2019).
- W.-C. Tung, M. Pavanello, and L. Adamowicz, *J. Chem. Phys.* **136**, 104309 (2012).
- L. Semeria, P. Jansen, and F. Merkt, *J. Chem. Phys.* **145**, 204301 (2016).
- E. Mátyus, *J. Chem. Phys.* **149**, 194112 (2018).
- P. Jansen, L. Semeria, and F. Merkt, *J. Chem. Phys.* **149**, 154302 (2018).
- M. Stanke, S. Bubin, and L. Adamowicz, *Phys. Rev. A* **79**, 060501R (2009).
- R. M. Herman and A. Asgharian, *J. Mol. Spectrosc.* **19**, 305 (1966).
- R. M. Herman and J. F. Ogilvie, *Adv. Chem. Phys.* **103**, 187 (1998).
- P. R. Bunker and R. E. Moss, *Mol. Phys.* **33**, 417 (1977).
- P. R. Bunker and R. E. Moss, *J. Mol. Spectrosc.* **80**, 217 (1980).
- K. Pachucki and J. Komasa, *J. Chem. Phys.* **130**, 164113 (2009).
- A. Scherrer, F. Agostini, D. Sebastiani, E. K. U. Gross, and R. Vuilleumier, *Phys. Rev. X* **7**, 031035 (2017).
- D. W. Schwenke, *J. Phys. Chem. A* **105**, 2352 (2001).
- M. Przybytek, W. Cencek, B. Jeziorski, and K. Szalewicz, *Phys. Rev. Lett.* **119**, 123401 (2017).
- E. Mátyus and S. Teufel, *J. Chem. Phys.* **151**, 014113 (2019).
- A. Muolo, E. Mátyus, and M. Reiher, *J. Chem. Phys.* **149**, 184105 (2018).
- S. Bubin and L. Adamowicz, *J. Chem. Phys.* **124**, 224317 (2006).
- S. Bubin and L. Adamowicz, *J. Chem. Phys.* **128**, 114107 (2008).
- Y. Suzuki and K. Varga, *Stochastic Variational Approach to Quantum-Mechanical Few-Body Problems* (Springer-Verlag, Berlin, 1998).
- J. Mitroy, S. Bubin, W. Horiuchi, Y. Suzuki, L. Adamowicz, W. Cencek, K. Szalewicz, J. Komasa, D. Blume, and K. Varga, *Rev. Mod. Phys.* **85**, 693 (2013).
- S. Bubin, M. Pavanello, W.-C. Tung, K. L. Sharkey, and L. Adamowicz, *Chem. Rev.* **113**, 36 (2013).
- E. Mátyus and M. Reiher, *J. Chem. Phys.* **137**, 024104 (2012).

- <sup>29</sup>C. M. Lindsay and B. J. McCall, *J. Mol. Spectrosc.* **210**, 60 (2001).
- <sup>30</sup>P. R. Bunker and P. Jensen, *Molecular Symmetry and Spectroscopy*, 2nd ed. (NRC Research Press, Ottawa, 1998).
- <sup>31</sup>E. Mátyus, J. Hutter, U. Müller-Herold, and M. Reiher, *Phys. Rev. A* **83**, 052512 (2011).
- <sup>32</sup>E. Mátyus, J. Hutter, U. Müller-Herold, and M. Reiher, *J. Chem. Phys.* **135**, 204302 (2011).
- <sup>33</sup>A. Schild, *Front. Chem.* **7**, 424 (2019).
- <sup>34</sup>Y. Suzuki, J. Usukura, and K. Varga, *J. Phys. B: At., Mol. Opt. Phys.* **31**, 31 (1998).
- <sup>35</sup>E. A. G. Armour, J.-M. Richard, and K. Varga, *Phys. Rep.* **413**, 1 (2005).
- <sup>36</sup>K. Varga, J. Usukura, and Y. Suzuki, *Phys. Rev. Lett.* **80**, 1876 (1998).
- <sup>37</sup>E. Mátyus, *J. Phys. Chem. A* **117**, 7195 (2013).
- <sup>38</sup>D. Ferenc and E. Mátyus, *Phys. Rev. A* **100**, 020501(R) (2019).
- <sup>39</sup>These reference values have been computed in our earlier work<sup>22</sup> using the GENIUSH program with the Polyansky–Tennyson mass model and the GLH3P PES by switching off the relativistic corrections. For further details and the relevant references see Ref. 22.
- <sup>40</sup>D. B. Kinghorn and L. Adamowicz, *J. Chem. Phys.* **110**, 7166 (1999).
- <sup>41</sup>S. Bubin and L. Adamowicz, *J. Chem. Phys.* **118**, 3079 (2003).
- <sup>42</sup>M. Cafiero, S. Bubin, and L. Adamowicz, *Phys. Chem. Chem. Phys.* **5**, 1491 (2003).
- <sup>43</sup>E. Bednarz, S. Bubin, and L. Adamowicz, *Mol. Phys.* **103**, 1169 (2005).
- <sup>44</sup>S. Bubin, M. Formanek, and L. Adamowicz, *Chem. Phys. Lett.* **647**, 122 (2016).
- <sup>45</sup>K. Varga, *Phys. Rev. A* **99**, 012504 (2019).
- <sup>46</sup>B. Simmen, E. Mátyus, and M. Reiher, *Mol. Phys.* **111**, 2086 (2013).
- <sup>47</sup>A. Muolo, E. Mátyus, and M. Reiher, *J. Chem. Phys.* **148**, 084112 (2018).
- <sup>48</sup>K. Varga, Y. Suzuki, and J. Usukura, *Few-Body Syst.* **24**, 81 (1998).
- <sup>49</sup>E. Polizzi, *Phys. Rev. B* **79**, 115112 (2009).
- <sup>50</sup>The range of the eigenvalue spectrum is characterized by the so-called condition number. The  $\kappa(M)$  condition number for an  $M$  complex, symmetric matrix is defined as the ratio of the largest to the smallest eigenvalues of  $(M + M^\dagger)/2$ .

# Explicitly correlated Gaussian functions with shifted-center and projection techniques in pre-Born–Oppenheimer calculations

Andrea Muolo,<sup>1</sup> Edit Mátyus,<sup>2,a)</sup> and Markus Reiher<sup>1,a)</sup>

<sup>1</sup>ETH Zürich, Laboratory of Physical Chemistry, Vladimir-Prelog-Weg 2, 8093 Zürich, Switzerland

<sup>2</sup>Institute of Chemistry, Eötvös Loránd University, Pázmány Péter sétány 1/A, 1117 Budapest, Hungary

(Received 31 July 2018; accepted 18 October 2018; published online 13 November 2018)

Numerical projection methods are elaborated for the calculation of eigenstates of the non-relativistic many-particle Coulomb Hamiltonian with selected rotational and parity quantum numbers employing shifted explicitly correlated Gaussian functions, which are, in general, not eigenfunctions of the total angular momentum and parity operators. The increased computational cost of numerically projecting the basis functions onto the irreducible representations of the three dimensional rotation-inversion group is the price to pay for the increased flexibility of the basis functions. This increased flexibility allowed us to achieve a substantial improvement for the variational upper bound to the Pauli-allowed ground-state energy of the  $H_3^+ = \{p^+, p^+, p^+, e^-, e^-\}$  molecular ion treated as an explicit five-particle system. We compare our pre-Born–Oppenheimer result obtained for this molecular ion with rotational-vibrational calculations carried out on a potential energy surface. *Published by AIP Publishing.* <https://doi.org/10.1063/1.5050462>

## I. INTRODUCTION

Energies and wavefunctions of small systems at the low-energy scale can be calculated with very high accuracy. Such calculations serve as a reference for approximate theories and provide results to compare with high precision experimental measurements. The continuous advance of experimental techniques as well as theoretical and computational methods allowed for, e.g., scrutinizing expressions for particle interactions<sup>1–4</sup> and testing extensions to the standard model<sup>5</sup> as solutions to the puzzling experimental results<sup>6,7</sup> of small atoms and molecules and investigating long-range interactions of nuclei with few-ppt uncertainty.<sup>8–13</sup> Three recent examples are (i) relativistic calculations on the  $H_2 = \{p^+, p^+, e^-, e^-\}$  four-particle system leading to a remarkable agreement of its theoretical  $D_0$  dissociation energy<sup>12,13</sup> with experiment,<sup>14</sup> (ii) relativistic calculations on the  $H_2^+ = \{p^+, p^+, e^-\}$  three-particle system<sup>10</sup> that yielded the energy-level structure with a relative accuracy of  $10^{-12}$  and allowed for using this system in metrology as an alternative way to determine fundamental physical constants, and (iii) the transition frequencies of high- $n$  Rydberg states of  $H_2$  belonging to a series converging on the ground state of  $H_2^+$  measured with a relative frequency accuracy of  $10^{-10}$ .<sup>15</sup>

Methods for solving quantum-mechanical few-body problems have been employing the family of explicitly correlated Gaussians (ECG) basis functions.<sup>16–24</sup> Their application is mostly limited to eigenstates of few-electron atoms and diatomic molecules with various total angular momentum values and to natural parity,  $p = (-1)^N$ . A serious difficulty in

molecular applications is obeying the correct rotational symmetry with generally applicable  $N_p$ -particle basis functions. For systems for which nonspherical ( $N > 0$ ) functions are required, the evaluation of the corresponding matrix elements becomes increasingly complicated.

The difficulties can be understood by considering the traditional partial-wave construction of the angular part of the basis functions,

$$\tilde{\theta}_{NM_N}(\mathbf{r}) = \left[ \left[ [\mathcal{Y}_{l_1}(\mathbf{r}_1)\mathcal{Y}_{l_2}(\mathbf{r}_2)]_{N_{12}}\mathcal{Y}_{l_3}(\mathbf{r}_3) \right]_{N_{123}} \cdots \right]_{NM_N}, \quad (1)$$

where  $l_i$  and  $N_i$  are the angular momentum quantum numbers and  $\mathcal{Y}_l(\mathbf{r})$  are the solid spherical harmonics. The expansion length and, hence, the evaluation time of the matrix elements quickly becomes untractable as the number of particles increases.

Different approaches have been developed in the literature to avoid these difficulties. For example, one can restrict the calculation to a special  $N$  value and develop the formalism and efficient computer implementations for that case.<sup>25–30</sup> Alternatively, the angular motion of the few-body system is described by introducing variationally tunable parameters  $u_i$  that depend on the position of the particles and define the so-called global vector,<sup>31,32</sup>

$$\mathbf{v} = \sum_{i=1}^{N_p-1} u_i \mathbf{r}_i. \quad (2)$$

The orbital-rotational motion is then described by the orientation ( $\hat{v} = \mathbf{v}/|\mathbf{v}|$ ) of this global vector as follows:

$$\theta_{NM_N}(\mathbf{r}; \mathbf{u}, K) = |\mathbf{v}|^{2K+N} Y_{NM_N}(\hat{v}). \quad (3)$$

It was shown in Ref. 31 that the global vector representation (GVR), Eq. (3), and the partial wave expansion, Eq. (1), are mathematically equivalent when they are used in a variational procedure in which the  $u_i$  coefficients are selected based on the energy minimization condition.

<sup>a)</sup>Authors to whom correspondence should be addressed: matyus@chem.elte.hu and markus.reiher@phys.chem.ethz.ch



In the present work, a direct projection method is developed in which a general (non-symmetric) ECG basis function is projected onto irreducible representations (irreps) of the  $O(3)$  three-dimensional rotation-inversion group. Our approach relates to the work by Strasburger<sup>33</sup> of reducing unwanted angular momentum contaminations by means of projecting basis functions onto an irrep of a point-group symmetry but exploits the generality of the  $O(3)$  group and does not suffer from deviations of  $\langle N^2 \rangle$  from the exact values of  $N(N+1)$ . In the most straightforward application, the basis function parameters are optimized for the non-projected functions. Then, the linear variational problem is solved with numerically projected basis functions (without any further non-linear optimization). Ideally, the parameter optimization would be carried out for the projected functions but this optimal approach is currently limited by the computationally expensive task of performing the numerical projection at every iteration of the optimization. A hybrid approach consisting of iterations for unprojected functions followed by further steps on projected functions will be described and employed to obtain substantially improved variational upper bounds for the  $H_3^+ = \{p^+, p^+, p^+, e^-, e^-\}$  molecular ion as an explicit five-particle system.

## II. THEORY

### A. Translational symmetry

Symmetries allow for the classification of solutions and also make their approximation more efficient. We briefly introduce basic notation in Secs. II A–II C needed in Secs. II D–II F to present our computational methodology. The translation of a wavefunction  $\Psi(\mathbf{r})$  in the position representation, e.g., a wave packet at  $\mathbf{r} = 0$ , can be represented by an (active) shift  $\mathbf{a}$  achieved by the operation  $\Psi(\mathbf{r}) \rightarrow \Psi(\mathbf{r} - \mathbf{a})$ ; see Fig. 1.

We denote the space translation  $\mathbf{r} \rightarrow \mathbf{r} + \mathbf{a}$  by  $T_{\mathbf{a}}\mathbf{r} = \mathbf{r} + \mathbf{a}$  and the corresponding mapping in the Hilbert space,

$$\begin{aligned} (U_{\mathbf{a}}\Psi)(\mathbf{r}) &= \Psi(\mathbf{r} - \mathbf{a}) \\ &\stackrel{a \text{ small}}{\approx} \Psi(\mathbf{r}) - \mathbf{a} \cdot (\nabla\Psi)(\mathbf{r}) \\ &= (1 - i\mathbf{a} \cdot \mathbf{p})\Psi(\mathbf{r}) \\ &\approx \exp(-i\mathbf{a} \cdot \mathbf{p})\Psi(\mathbf{r}), \end{aligned} \quad (4)$$

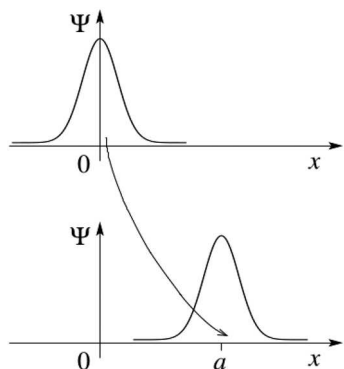


FIG. 1. Active translation of a wavepacket by  $\mathbf{a}$ :  $\Psi(x) \rightarrow \Psi(x - a) = (U_{\mathbf{a}}\Psi)(x)$ .

produces a representation of the (Abelian) group  $G_T = \{T_{\mathbf{a}} | \mathbf{a} \in \mathbb{R}^3\}$  of translation in the Hilbert space of the wavefunction. We denote this representation by  $\mathcal{G} = \{U_{\mathbf{a}} | T_{\mathbf{a}} \in G_T\}$ .

The result in Eq. (4) can be made exact by writing  $\Psi(\mathbf{r} - \mathbf{a})$  in a Taylor series or by integrating with an infinitesimal shift  $\mathbf{a} \rightarrow \mathbf{a} + \delta\mathbf{a}$ ,  $\Psi_{\mathbf{a}+\delta\mathbf{a}} = \Psi_{\mathbf{a}} - (i\delta\mathbf{a} \cdot \mathbf{p})\Psi_{\mathbf{a}}$ , obtaining the differential equation  $\partial_{\mathbf{a}}\Psi_{\mathbf{a}} = -i(\mathbf{p})\Psi_{\mathbf{a}}$ . With the initial condition  $\Psi_0 = \Psi$ , one obtains the solution  $\Psi_{\mathbf{a}} = \exp(-i\mathbf{a} \cdot \mathbf{p})\Psi_0$ . Hence, the translation operator,

$$U_{\mathbf{a}} = \exp(-i\mathbf{a} \cdot \mathbf{p}), \quad (5)$$

describes the active displacement of the wavefunction by  $\mathbf{a}$ , where the momentum operator  $\mathbf{p}$  is the infinitesimal generator of translations. With a Hermitian  $\mathbf{p}$ ,  $U_{\mathbf{a}}$  is unitary,  $\mathcal{G}$  and  $G_T$  are Abelian, continuously connected, isomorphic groups.

### B. Spatial rotations and the $SO(3)$ group

Given an axis of rotation  $\omega$  and an angle  $0 \leq \omega < 2\pi$ , the elements  $R_{\omega} \in SO(3)$  represent 3-dimensional rotations. The corresponding  $U(\Omega)$  unitary representation in the Hilbert space of the many particle wavefunction  $\Psi(\mathbf{r})$  with  $\mathbf{r} \equiv (\mathbf{r}_1 \dots \mathbf{r}_{N_p})^T$  is

$$(U_{\omega}\Psi)(\mathbf{r}) = \Psi\left(\left(\mathbb{1}_{N_p} \otimes R_{\omega}^{-1}\right)\mathbf{r}\right). \quad (6)$$

For small rotations and  $N_p = 1$  with  $R_{\omega}^{-1}\mathbf{r} \sim \mathbf{r} - \omega \wedge \mathbf{r}$ ,

$$\begin{aligned} (U_{\omega}\Psi)(\mathbf{r}) &\approx \Psi(\mathbf{r} - \omega \wedge \mathbf{r}) \\ &= \Psi(\mathbf{r}) - \epsilon_{ijk}\omega_i r_j \partial_k \Psi(\mathbf{r}) + \dots \\ &= [1 - i\omega \cdot \mathbf{l} + \dots]\Psi(\mathbf{r}) \\ &= \exp(-i\omega \cdot \mathbf{l})\Psi(\mathbf{r}), \end{aligned} \quad (7)$$

where the angular momentum operator  $\hat{\mathbf{l}} = -i\mathbf{r} \wedge \nabla$  with  $\hat{\mathbf{r}} = (x, y, z)^T$  and  $\hat{\nabla} = (\nabla_x, \nabla_y, \nabla_z)^T$ .

The representation  $U_{\omega} = \exp(-i\omega \cdot \mathbf{l})$  holds also for large  $\omega$  rotation angles, and the angular momentum operator is the infinitesimal generator of rotation,

$$U_{\omega} = \exp(-i\omega \cdot \mathbf{l}) \in \mathcal{SO}(3), \quad (8)$$

where the group  $SO(3)$  and its representation  $\mathcal{SO}(3)$  in the Hilbert space  $\mathcal{H}$  are isomorphic, non-Abelian, and continuous.

The orthogonal (or rotation-inversion) group  $O(3)$  is the direct product of the special orthogonal group  $SO(3)$  and the group  $C_I = \{\mathcal{E}, \mathcal{I}\}$  including the identity and the inversion operator:  $O(3) = SO(3) \otimes C_I$ . The irreducible representations of  $SO(3)$ , labeled with  $\mathcal{D}^l$ , are  $\dim \mathcal{D}^l = 2l + 1$  dimensional, where  $l \in \mathbb{N}_0$ . The irreducible representations of  $O(3)$  are  $\mathcal{D}^{l\pm}$  with  $\dim \mathcal{D}^{l\pm} = 2l + 1$ . Spherical harmonics functions,  $Y_{lm}$  (of the so-called natural parity), belong to  $\mathcal{D}^{l+}$  if  $l$  is even and to  $\mathcal{D}^{l-}$  if  $l$  is odd. Functions with unnatural parity can be constructed from combinations of spherical harmonics functions (see, for example, Ref. 34).

### C. Rotations and tensors

Let the eigenstate  $|l, m\rangle$  be rotated by  $U_{\omega} = \exp(-i\omega \cdot \mathbf{l})$  by an angle  $|\omega|$  (positive rotation) about the axis defined by  $\hat{\omega}$ .

An arbitrary rotation operator  $\hat{R}$  can then be defined by means of the Euler angles  $\alpha$ ,  $\beta$ ,  $\gamma$  (we use the  $z - y - z$  convention; see also Fig. 2) as<sup>35</sup>

$$\hat{R}(\Omega) \equiv \hat{R}(\alpha, \beta, \gamma) = e^{-i\alpha L_z} e^{-i\beta L_y} e^{-i\gamma L_z}. \quad (9)$$

By definition of an irreducible representation,  $\hat{R}(\Omega)$  leaves the irreducible subspace spanned by  $|l, m'\rangle$  with  $m' = -l, \dots, +l$  invariant,

$$\hat{R}(\Omega)|l, m\rangle = \sum_{m'=-l}^l D_{m'm}^l(\Omega)|l, m'\rangle, \quad (10)$$

where  $D_{m'm}^l(\Omega)$  is the  $(m', m)$ th element of the  $l$ th Wigner D-matrix. Wigner D-matrices define the  $(2l + 1)$ -dimensional irreducible representations of the rotation group,  $SO(3)$ ,

$$D_{m'm}^l(\Omega) \equiv \langle l, m' | \hat{R}(\Omega) | l, m \rangle. \quad (11)$$

The  $D^l(\Omega)$  matrices have a number of important properties.<sup>36</sup> First of all, they are unitary,

$$D^{l\dagger}(\Omega)D^l(\Omega) = D^l(-\Omega)D^l(\Omega) = \mathbb{1}, \quad (12)$$

and also

$$D_{m'm}^{l\dagger}(\Omega) = D_{m'm}^{l\dagger}(\Omega) = D_{m'm}^l(-\Omega). \quad (13)$$

Furthermore, the special case  $D_{mm'}^l(0, \beta, 0) = d_{mm'}^l(\beta)$  is the “small” d-matrix,<sup>36</sup>

$$d_{mm'}^l(\beta) = [(j + m')!(j - m')!(j + m)!(j - m)!]^{1/2}, \quad (14)$$

$$\times \sum_s \left[ \frac{(-1)^s}{(j + m - s)!s!(m' - m + s)!(j - m' - s)!} \right], \quad (15)$$

$$\times \left( \cos \frac{\beta}{2} \right)^{2j+m-m'-2s} \left( \sin \frac{\beta}{2} \right)^{m'-m+2s}. \quad (16)$$

Due to their construction, the  $D_{mm'}^l$  elements appear in the rotation expressions of tensor operators. An irreducible tensor operator,  $T^k$ , of order  $k$  is transformed by its  $2k + 1$  components  $T_q^k$ , with  $q \in \{-k, -k + 1, \dots, k - 1, k\}$  under rotations according to the following equation:

$$R(\Omega) T_q^k R(\Omega)^{-1} = \sum_{q'=-k}^k D_{q'q}^k(\Omega) T_{q'}^k. \quad (17)$$

#### D. Hamiltonian and expansion of the wavefunction

We aim at the variational calculation of the bound states of the many-particle Schrödinger Hamiltonian for  $N_p$  particles

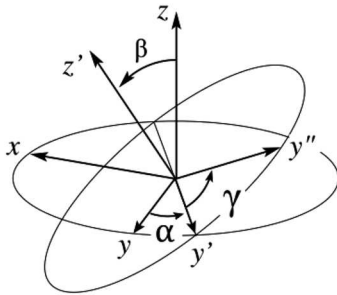


FIG. 2. Euler angles:  $\alpha$  is a rotation about the  $z$  axis and defines  $y'$ ,  $\beta$  is a rotation about  $y'$  and defines  $z'$ , and  $\gamma$  is a rotation about the  $z'$ .

with Cartesian coordinates  $\mathbf{r} = (\mathbf{r}_1, \dots, \mathbf{r}_{N_p})^T$ , masses  $m_i$ , and charges  $q_i$ ,

$$\hat{H} = -\nabla_{\mathbf{r}}^T M \nabla_{\mathbf{r}} + \sum_{i=1}^{N_p} \sum_{j>i}^{N_p} \frac{q_i q_j}{|\mathbf{r}_i - \mathbf{r}_j|}, \quad (18)$$

where  $\nabla_{\mathbf{r}} = (\nabla_{\mathbf{r}_1}, \dots, \nabla_{\mathbf{r}_{N_p}})^T$  collects the 3-dimensional Nabla operators for each particle with  $\nabla_{\mathbf{r}_1} = (\frac{\partial}{\partial r_{1x}}, \frac{\partial}{\partial r_{1y}}, \frac{\partial}{\partial r_{1z}})$ . The entries of the diagonal matrix  $M_{ij} = \delta_{ij} \frac{1}{2m_i}$  absorb the factor  $\frac{1}{2}$ .

The many-particle Schrödinger Hamiltonian, Eq. (18), is invariant to three-dimensional space translation and rotation-inversion of the total many-particle system,

$$[\hat{H}, U_a] = 0 \quad \forall T_a \in G_T, \quad (19)$$

$$[\hat{H}, U_\omega] = 0 \quad \forall R_\omega \in SO(3), \quad (20)$$

$$[\hat{H}, \hat{I}] = 0 \quad \hat{I} \in C_I, \quad (21)$$

and the operators  $\hat{H}$ ,  $U_a \in G_T$ ,  $U_\omega \in SO(3)$ , and  $\hat{I} \in C_I$  have common eigenvectors. This is an important property, which we would like to build in the basis set in order to design an efficient variational procedure for calculating the eigenvalues and eigenfunctions of  $\hat{H}$ .

We approximate eigenfunctions of  $\hat{H}$  in a variational procedure as

$$\Psi(\mathbf{r}) = \sum_{I=1}^{N_b} c_I \chi_I^{S, M_S} \hat{Y} \phi_I^{\text{FECG}}(\mathbf{r}; \{A_I, \mathbf{s}_I\}), \quad (22)$$

where the  $c_I$  are the linear expansion parameters,  $\chi_I^{S, M_S}$  are the spin functions,  $\phi_I^{\text{FECG}}$  are the floating explicitly correlated Gaussians (FECGs), and  $\hat{Y}$  is the Young operator projecting onto the appropriate (anti)symmetric subspace.

A basis function  $\phi_I^{\text{FECG}}$  is defined as

$$\phi_I^{\text{FECG}}(\mathbf{r}; A_I, \mathbf{s}_I) = \exp[-(\mathbf{r} - \mathbf{s}_I)^T A_I (\mathbf{r} - \mathbf{s}_I)], \quad (23)$$

where  $A_I = \bar{A}_I \otimes \mathbb{1}_3$  with  $\bar{A}_I \in \mathbb{R}^{N_p \times N_p}$  exponents and  $\mathbf{s}_I$  positions being optimized variationally.

#### E. Projection onto $O(3)$ irreducible representations

A general FECG function, Eq. (23), is neither invariant to space inversion nor to space rotation. Although this property of the exact eigenfunctions of  $\hat{H}$  is restored in the complete basis set limit, this is unfeasible to approach in practice. Space translation and the description of the translationally invariant properties have been discussed in detail in our earlier work,<sup>37,38</sup> and the results of which are used in the numerical application part of this work.

The broken space rotation-inversion symmetry of an FECG function will be restored by explicit projection onto the irreps of  $O(3)$ .

We first consider the  $N = 0, p = +1$  case (a totally symmetric spherical state) for which the symmetrization of a general FECG function corresponds to averaging over all possible orientations,

$$\phi_I^{\text{FECG}[N=0]} = \int d\Omega \hat{R}(\Omega) \phi_I^{\text{FECG}}(\mathbf{r}; A_I, \mathbf{s}_I), \quad (24)$$

where  $\hat{R}(\Omega)$  denotes an active rotation operator and the angular integration is

$$\int d\Omega \equiv \int_0^{2\pi} d\alpha \int_0^\pi \sin \beta d\beta \int_0^{2\pi} d\gamma. \quad (25)$$

By construction,  $\phi_I^{\text{FECG}[N=0]}$  is an eigenstate of the square of the total angular momentum operator,  $\hat{N}^2$  with  $N = 0$ .

How can we now construct functions from FECGs for  $N > 0$  non-zero angular momentum quantum number? These functions have a more involved angular nodal structure. In general, the overall rotational symmetry can be recovered by projecting the FECG functions onto the  $N$ th irreducible representation of the rotation group corresponding to the total orbital angular momentum  $N$ . We first construct the projection operator,  $\hat{P}^{[N]}$ , used by Broeckhove and Lathouwers and by several other authors,<sup>39–43</sup>

$$\hat{P}^{[N]} = \sum_{M_N=-N}^{M_N=+N} \hat{P}_{M_N M_N}^{[N]}, \quad (26)$$

with

$$\hat{P}_{M_1 M_2}^{[N]} \equiv \int \frac{d\Omega}{4\pi^3} D_{M_1 M_2}^{[N]}(\Omega)^* \hat{R}(\Omega), \quad (27)$$

where  $D_{M_1 M_2}^{[N]}(\Omega)$  is the  $(M_1 M_2)$ th element of the  $N$ th Wigner D-matrix, Eq. (11) (note the convenient extension of notation) and the rotation operators  $\hat{R}(\Omega)$  is expressed in terms of three Euler angles  $\Omega \equiv (\alpha, \beta, \gamma)$ , Eq. (9). In short,  $\hat{P}^{[N]}$  projects any trial function  $\varphi(\mathbf{r})$  onto the eigenspace corresponding to  $N$ , spanned by all eigenfunctions of the  $\hat{N}_z$  component of total angular momentum with quantum number  $M_N \in [-N, +N]$ . Another possible choice for the projection operator is described in Appendix C and follows Löwdin's idea<sup>44</sup> later reconsidered by Shapiro and Crossley.<sup>45,46</sup> A projected FECG function obtained with the  $\hat{P}_{M_1 M_2}^{[N]}$  operator, Eq. (27), for  $N = 0$ ,  $p = +1$  is identical with Eq. (24), which we wrote for simple averaging over all possible orientations [note that  $D_{00}^{[0]}(\Omega) = 1$ ].

Analogously, projection onto the desired irrep of  $C_I$  can be performed through the action of the following projection operator:

$$\hat{P}_{C_I}^{[p]} = \hat{\mathcal{E}} + p\hat{\mathcal{L}}. \quad (28)$$

The irreps of  $O(3)$  can then be accessed by the product of projection operators,

$$\hat{P}_{M_N}^{[N,p]} = \hat{P}_{M_N M_N}^{[N]} \hat{P}_{C_I}^{[p]}. \quad (29)$$

From the definition in Eq. (27), it follows that  $\hat{P}_{M_N}^{[N,p]}$  is idempotent, Hermitian, and commutes with  $\hat{H}$ <sup>39</sup> due to the

rotational invariance of the Hamiltonian,

$$\hat{P}_{M_1}^{[N',p']} \hat{P}_{M_2}^{[N,p]} = \delta_{N'N} \delta_{M_1 M_2} \delta_{p'p} \hat{P}_{M_1}^{[N,p]}, \quad (30)$$

$$\left(\hat{P}_{M_N}^{[N,p]}\right)^2 = \hat{P}_{M_N}^{[N,p]}, \quad \left(\hat{P}_{M_N}^{[N,p]}\right)^\dagger = \hat{P}_{M_N}^{[N,p]}, \quad [\hat{H}, \hat{P}_{M_N}^{[N,p]}] = 0. \quad (31)$$

We rely on these properties during the calculation of the matrix elements for various quantum mechanical operators.

## F. Numerical projection by quadrature

Given an FECG function and a representation of the  $N$ th irrep of the rotation group, we project the FECG function onto the  $M_N$ th subspace by numerically performing the angular integration with Gauss–Legendre quadrature,

$$\begin{aligned} \hat{P}_{M_N}^{[N,p]} \phi_I^{\text{FECG}} &= \int \frac{d\Omega}{4\pi^3} D_{M_N M_N}^{[N]}(\Omega)^* \hat{R}(\Omega) \hat{P}_{C_I}^{[p]} \phi_I^{\text{FECG}} \\ &\approx \sum_{i_1=1}^n \sum_{i_2=1}^n \sum_{i_3=1}^n \omega_{i_1} \omega_{i_2} \omega_{i_3} D_{M_N M_N}^{[N]}(\Omega_{i_1})^* \\ &\quad \times \hat{R}(\Omega_{i_1}) \hat{P}_{C_I}^{[p]} \phi_I^{\text{FECG}}, \end{aligned} \quad (32)$$

with weights

$$\omega_i = \frac{2(1-x_i^2)}{(n+1)^2 [P_{n+1}(x_i)]^2}, \quad (33)$$

where  $x_a \in (-1, +1)$  labels the  $a = (1, 2, \dots, n+1)$  roots of the  $P_n(x)$  Legendre polynomials and  $\Omega_i = (\alpha_i, \beta_i, \gamma_i)$  are the Euler angles at the quadrature points obtained from scaling the  $x_a$  points to the appropriate intervals,  $\alpha, \gamma \in [0, 2\pi)$  and  $\beta \in [0, \pi]$ .

We rearrange the rotated FECG as

$$\begin{aligned} \hat{R}(\Omega) \phi_I^{\text{FECG}}(\mathbf{r}; \bar{A}_I \otimes \mathbb{1}_3, \mathbf{s}_I) &= \phi_I^{\text{FECG}}(U(\Omega)^{-1} \mathbf{r}; \bar{A}_I \otimes \mathbb{1}_3, \mathbf{s}_I) \\ &= \exp\left[-(U(\Omega)^{-1} \mathbf{r} - \mathbf{s}_I)^T (\bar{A}_I \otimes \mathbb{1}_3) (U(\Omega)^{-1} \mathbf{r} - \mathbf{s}_I)\right] \\ &= \exp\left[-(\mathbf{r} - U(\Omega) \mathbf{s}_I)^T (\bar{A}_I \otimes \bar{U}(\Omega)^{-T} \bar{U}(\Omega)^{-1})\right. \\ &\quad \left. \times (\mathbf{r} - U(\Omega) \mathbf{s}_I)\right] \\ &= \phi_I^{\text{FECG}}(\mathbf{r}; A_I, U(\Omega) \mathbf{s}_I), \end{aligned} \quad (34)$$

which means that rotating an FECG in the three-dimensional space is equivalent to a rotation of the shift vector defining its center point,  $\mathbf{s}_I \in \mathbb{R}^{3N_p}$ . It is also important to note that only the parametrization changes [ $\mathbf{s}_I$  is replaced with  $U(\Omega) \mathbf{s}_I$ ], while the mathematical form of the FECG function remains invariant under rotation. Employing the  $(z-y-z)$  convention introduced earlier, the  $U(\Omega)$  rotation matrix is obtained from three consecutive in-plane rotations,

$$\begin{aligned} U(\Omega) &= \mathbb{1}_{N_p} \otimes \bar{U}(\Omega) = \mathbb{1}_{N_p} \otimes \left\{ U_z(\alpha_i) U_y(\beta_j) U_z(\gamma_k) \right\} \\ &= \mathbb{1}_{N_p} \otimes \left\{ \begin{pmatrix} \cos \alpha_i & -\sin \alpha_i & 0 \\ \sin \alpha_i & \cos \alpha_i & 0 \\ 0 & 0 & 1 \end{pmatrix} \cdot \begin{pmatrix} \cos \beta_j & 0 & -\sin \beta_j \\ 0 & 1 & 0 \\ \sin \beta_j & 0 & \cos \beta_j \end{pmatrix} \cdot \begin{pmatrix} \cos \gamma_k & -\sin \gamma_k & 0 \\ \sin \gamma_k & \cos \gamma_k & 0 \\ 0 & 0 & 1 \end{pmatrix} \right\}, \end{aligned} \quad (35)$$

where  $\mathbb{1}_{Np}$  is indicated in order to emphasize that the entire object is rotated (as a rigid body) by  $U(\Omega)$  about the origin. By exploiting the form invariance of FECGs, Eq. (34), and the hermiticity and idempotency of  $\hat{P}_{M_N}^{[N,p]}$ , Eqs. (30) and (31), integrals for a rotationally invariant operator,  $\hat{O}$ , are evaluated as

$$\begin{aligned} & \langle \hat{P}_{M_N}^{[N,p]} \phi_I^{\text{FECG}}(\mathbf{r}; A_I, s_I) | \hat{O} | \hat{P}_{M_N}^{[N,p]} \phi_J^{\text{FECG}}(\mathbf{r}; A_J, s_J) \rangle \\ &= \langle \phi_I^{\text{FECG}}(\mathbf{r}; A_I, s_I) | \hat{O} | \hat{P}_{M_N}^{[N,p]} \phi_J^{\text{FECG}}(\mathbf{r}; A_J, s_J) \rangle \\ &= \int \frac{d\Omega}{4\pi^3} D_{M_N M_N}^{[N]}(\Omega)^* \\ & \quad \times \langle \phi_I^{\text{FECG}}(\mathbf{r}; A_I, s_I) | \hat{O} | \hat{P}_{C_I}^{[p]} \phi_J^{\text{FECG}}(\mathbf{r}; A_J, U(\Omega)s_J) \rangle. \end{aligned} \quad (36)$$

### III. RESULTS

In this section, we explore the projection method for the calculation of rovibrational (rovibronic) states of diatomic systems,  $H_2^+ = \{p^+, p^+, e^-\}$  and  $H_2 = \{p^+, p^+, e^-, e^-\}$ , as well as for the triatomic molecular ion  $H_3^+ = \{p^+, p^+, p^+, e^-, e^-\}$  calculated as three-, four-, and five-particle systems, respectively. The Pauli principle is explicitly imposed on both the electrons and the protons in the basis set, Eq. (22). We label the total proton spin quantum number with  $I_p$  and consider singlet (antiparallel,  $S_e = 0$ ) electron spin states for  $H_2$  and  $H_3^+$ .

The expectation value of the parity,  $\hat{p}$ , and the total angular momentum squared operator,  $\hat{N}^2$ , was evaluated to measure the effectiveness of the numerical projection (the analytic expressions for the  $\langle \phi_I^{\text{FECG}} | \hat{N}^2 | \phi_J^{\text{FECG}} \rangle$  matrix elements are derived in Appendix A). The effect of the overall center-of-mass motion is eliminated during the integral calculations<sup>38</sup> by subtracting the center-of-mass related terms from the expectation values (e.g.,  $\langle \hat{H} \rangle$ ,  $\langle \hat{N}^2 \rangle$ , etc.). In Appendix B, we derive the analytic matrix elements for the squared angular momentum operator, the projection of the angular momentum onto one axis, and the center-of-mass (CM) elimination expressions. All  $\langle \hat{N}^2 \rangle$  and  $\langle \hat{H} \rangle$  in the following tables correspond to translationally invariant expectation values.

To demonstrate the efficiency of the numerical projection method introduced in this work, we first build a small basis set composed of only 3 FECG functions. This test set is parametrized by converging the first four decimal places of the energy expectation value in a variational procedure. Table I collects the results obtained with the projector defined in Eq. (27) with  $N = 0$  and  $N = 1$  and parity  $p = +1$  and  $p = -1$ , respectively, for this small basis set.  $\langle \hat{N}^2 \rangle$  is converged to at least three to four decimal places with 20–50 quadrature points for each Euler angle ( $\alpha$ ,  $\beta$ ,  $\gamma$ ).

If we start with a set of unprojected functions, the plain energy minimization algorithm can build up the ground-state rotational symmetry. In other words, the contributions from states of different symmetry are reduced at each iteration (energy-minimization) step. This observation suggests that the projection after non-linear optimization will perform well for low- $N$  values (or high- $N$  states which have a similar internal structure to the low- $N$  states).

Next, we consider a much larger basis set obtained by optimizing projected functions (optimization after projection)

TABLE I. Expectation values for  $\hat{H}$ ,  $\hat{N}^2$ , and  $\hat{p}$  in atomic units for a small test set with a fixed number of  $N_b = 3$  FECG basis functions for the (Pauli-allowed) ground state of  $H_2^+ = \{p^+, p^+, e^-\}$  with  $I_p = 0$  and  $S_e = \frac{1}{2}$  and  $H_3^+ = \{p^+, p^+, p^+, e^-, e^-\}$  with  $I_p = \frac{1}{2}$  and  $S_e = 0$ . For  $H_2^+$  and  $H_3^+$ , the numerical projection is carried out onto the ( $N = 0, M_N = 0, p = +1$ ) and ( $N = 1, M_N = 0, p = -1$ ) rotation-inversion functions, respectively. The numerical results are shown for an increasing number of quadrature points  $n$  (the same  $n$  value is applied for each Euler angle). The  $n = 0$  case corresponds to unprojected basis functions.

	$n$	$N = 0, M_N = 0, p = +1$			$N = 1, M_N = 0, p = -1$		
		$\langle \hat{H} \rangle$	$\langle \hat{p} \rangle$	$\langle \hat{N}^2 \rangle$	$\langle \hat{H} \rangle$	$\langle \hat{p} \rangle$	$\langle \hat{N}^2 \rangle$
$H_2^+$	0	-0.561 18	0.9766	+39.018	-0.559 18	+0.9766	+39.018
	10	-0.568 76	0.9998	-1.114	-0.565 95	-0.9998	+1.074
	20	-0.568 68	1.0000	-0.002	-0.566 31	-1.0000	+1.997
	30	-0.568 68	1.0000	+0.000	-0.566 29	-1.0000	+2.000
	40	-0.568 68	1.0000	+0.000	-0.566 29	-1.0000	+2.000
$H_3^+$	0	-1.171 64	-0.0000	+86.250	-1.171 64	-0.0000	+86.250
	10	-1.142 64	+1.0144	+124.530	-1.206 78	-0.9996	+5.846
	20	-0.968 46	+0.9952	+104.307	-1.224 68	-0.9999	+3.309
	30	-0.848 55	+1.0003	+2.317	-1.227 17	-0.9999	+2.063
	40	-0.846 98	+1.0000	+0.029	-1.227 35	-1.0000	+2.001
50	-0.846 97	+1.0000	+0.000	-1.227 35	-1.0000	+2.000	

instead of minimizing the energy for unprojected functions and then calculating the energy expectation value for projected functions in a separate step (optimization before projection). In Table II, we show the results for  $H_3^+$  calculated with a moderate basis set size composed of  $N_b = 120$  FECGs. The non-linear parameters of the projected basis functions are generated with the competitive selection method described by Suzuki and Varga,<sup>34</sup> and the selected parameters are refined using Powell's method.<sup>47</sup> The projection is carried out onto the ( $N = 1, M_N = 0, p = -1$ ) irreducible representation of  $O(3)$ . Optimization before projection (Table I) and optimization with projected functions (Table II) shows that non-linear optimization for projected functions requires fewer quadrature points to converge the first two to three decimal places of the  $\langle \hat{N}^2 \rangle$  expectation value. Hence, it is computationally less demanding (a smaller

TABLE II. Energy,  $\hat{H}$ , parity,  $\hat{p}$ , and squared total angular momentum,  $\hat{N}^2$ , expectation values in atomic units for  $H_3^+ = \{p^+, p^+, p^+, e^-, e^-\}$  with a total proton spin  $I_p = \frac{1}{2}$ , and a singlet,  $S_e = 0$ , electronic state obtained with  $N_b = 120$  optimized FECGs basis functions projected onto ( $N = 1, M_N = 0, p = -1$ ). The expectation values correspond to a growing number of quadrature points,  $n$ . The  $n = 0$  row shows the results with unprojected basis functions.

	$\langle \hat{H} \rangle$	$\langle \hat{p} \rangle$	$\langle \hat{N}^2 \rangle$
$n = 0$	-1.315 01	-0.0000	+41.233
$n = 16$	-1.321 20	-1.0001	+2.321
$n = 17$	-1.321 23	-0.9997	+2.116
$n = 18$	-1.321 24	-0.9999	+2.091
$n = 19$	-1.321 27	-0.9999	+2.030
$n = 20$	-1.321 15	-0.9999	+2.036
$n = 21$	-1.321 16	-1.0000	+2.014
$n = 22$	-1.321 28	-1.0000	+2.003
$n = 24$	-1.321 28	-1.0000	+2.001

number of quadrature points is sufficient) to project a larger, more tightly pre-optimized basis set to the rotational-inversion irreducible representation of the ground state ( $N = 0, p = +1$  for  $H_2^+$  and  $N = 1, p = -1$  for  $H_3^+$ ).

Finally, we explore the feasibility of a variational optimization of the numerically projected FECG functions (np-FECG), that is, optimization after projection. The non-linear optimization consists of the generation of a good parameter set by competitive selection,<sup>34</sup> which is refined with Powell's method in repeated cycles. When performing projection on-the-fly, the variational machinery can generate functions that would require a number of quadrature points much higher than 20-25 (see Table I). However, since the computational cost of the numerical integration for the Euler angles by quadratures scales cubically  $n^3$ , there are cases for which the quadrature yields matrix elements that are far off the exact value. We note that we exploit the idempotency of the projector in order to reduce the quadratic scaling with the number of quadrature points to a linear dependence. However, only the exact projector is strictly idempotent. If its numerical representation by quadrature was not accurate enough, which also depends on the basis function parametrization, we encountered variational collapse and unphysical energies. We then employed an adaptive quadrature scheme, in which we dynamically adjusted the number of points and dropped trial functions which would have required a number of quadrature points above a certain

threshold, to achieve a good compromise between robustness and computational expense. This adaptive projection optimization of FECGs remains computationally very demanding and is a practical approach for small-sized basis sets (with about  $10 < N_b < 500$ ). Larger basis sets can be handled only if the number of optimization steps per cycle is dramatically reduced.

To calculate tight variational upper bounds which can serve as pre-Born–Oppenheimer (pre-BO) benchmark values for non-adiabatic models, further improvements in the projection scheme were necessary. The idea behind Gauss quadrature is to choose  $n$  nodes and weights in such a way that polynomials of order  $2n + 1$  are integrated exactly. The difference between quadratures of order  $n$  and  $n + 1$  can be considered as an error estimate but, as the zeros of the Legendre polynomials (nodes of the Gaussian quadrature) are never the same for different orders,  $2n + 1$  function evaluations must be performed. As an alternative, we consider the Gauss–Kronrod quadrature,<sup>48</sup> which is an efficient but nested quadrature scheme. For the variational optimization, we built the basis set with the competitive selection method and then performed every refining step in the space of projected functions. Finally, the quadrature with respect to the angle  $\beta$  was improved by employing Gauss quadrature rules (nodes plus weights) specifically tailored for the weight function  $W(\beta) = \sin \beta$  that is part of the projector operator, as shown in Eq. (25).

TABLE III. Energy, parity, and angular momentum expectation values for the ground states of  $H_2 = \{p^+, p^+, e^-, e^-\}$  and  $H_3^+ = \{p^+, p^+, p^+, e^-, e^-\}$ .  $N_b$  is the number of FECGs projected onto the ( $N = 0, M_N = 0, p = +1$ ) and ( $N = 1, M_N = 0, p = -1$ ) angular momentum states. The entries in italics represent the best 5-particle variational upper bound for  $H_3^+$ ; “ $\infty$ ” denotes the extrapolated result.

$N_b$	$\langle \hat{H} \rangle^a / E_h$	$\langle \hat{H} \rangle_{\text{proj.}}^b / E_h$	$\langle \hat{p} \rangle$	$\langle \hat{p} \rangle_{\text{proj.}}$	$\langle \hat{N}^2 \rangle$	$\langle \hat{N}^2 \rangle_{\text{proj.}}$
$H_2$ ( $I_p = 0, N = 0, M_N = 0, p = +1$ )						
440	-1.162162	-1.163897	+0.999955	+1.000000	+4.513534	+0.000054
600	-1.162358	-1.163927	+0.999952	+1.000000	+3.976680	+0.000060
760	-1.162525	-1.163945	+0.999953	+1.000000	+3.399123	+0.000067
920	-1.162630	-1.163967	+0.999939	+1.000000	+2.954402	+0.000050
1080	-1.162685	-1.163969	+0.999945	+1.000000	+2.785041	+0.000024
1240	-1.162716	-1.163980	+0.999952	+1.000000	+2.722068	+0.000052
1400	-1.162732	-1.163989	+0.999944	+1.000000	+2.686361	+0.000052
1560	-1.162739	-1.163998	+0.999946	+1.000000	+2.640778	+0.000053
Reference 57	/	-1.164025	/	+1	/	0
$H_3^+$ ( $I_p = 1/2, N = 1, M_N = 0, p = -1$ )						
180	-1.316346	-1.321340	-0.000008	-0.999940	+36.105414	+2.001901
420	-1.317690	-1.322344	-0.000174	-0.999961	+28.775371	+2.001383
660	-1.318216	-1.322548	-0.000189	-0.999980	+26.623718	+2.000129
840	-1.318523	-1.322652	-0.000256	-0.999991	+24.868238	+2.000136
1080	-1.318904	-1.322726	-0.000656	-0.999993	+22.316282	+2.000014
1320	-1.319011	-1.322782	-0.001249	-0.999992	+21.117237	+2.000048
1560	<i>-1.319 089</i>	<i>-1.322 826</i>	<i>-0.001249</i>	<i>-0.999 994</i>	<i>+20.843 642</i>	<i>+2.000 055</i>
$\infty$	<i>-1.319 288</i>	<i>-1.323 005</i>	/	/	/	/
Estimate <sup>c</sup>	/	-1.323146	/	(-1)	/	(+2)

<sup>a</sup> $\langle \hat{H} \rangle$  is the lowest eigenvalue of the Hamiltonian obtained with the non-projected FECG basis set.

<sup>b</sup> $\langle \hat{H} \rangle_{\text{proj.}}$  is the lowest eigenvalue of the Hamiltonian obtained with the projected FECG basis set.

<sup>c</sup>Non-adiabatic estimate for the energy of this rotational(-vibrational) state that we obtained with the GENIUSH program. The value of the parity and squared angular momentum for the atomic nuclei is  $\langle \hat{p}_{\text{nuc.}} \rangle = -1$  and  $\langle \hat{R}^2 \rangle = +2$ , respectively. These values are indicated in parentheses because they are not strictly the total parity and total angular momentum values of the five-particle system.

The energy, parity, and total angular momentum expectation values for both unprojected and projected (indicated by subscript “proj.”) basis sets for optimization after projection are shown in Table III and plotted in Fig. 3. The digits of accuracy reported for the projected energy expectation values are reliable since the Gauss-Kronrod scheme iteratively increased the number of integration points until convergence of the first 6 digits was reached. The projected total angular momentum expectation values were calculated with  $n = 26$  fixed number of quadrature points. As the basis set progresses toward lower energies,  $\langle \hat{N}^2 \rangle_{\text{proj.}}$  converges to the expected value. The lowest-energy pre-BO state with  $N = 1$ ,  $p = -1$ , and  $S_p = 1/2$  ( $S_e = 0$ ) corresponds to the  $(J, I_p, p, n) = (1, p, -, 1)$  state using the notation of Ref. 49.

The data listed in Table III allow an extrapolation of the energy to the infinite basis-set size. We considered the inverse power functional form,  $E_h = a + b/N_b$ , and fitted  $a$  and  $b$  to the npFECG energies. The interpolating function is shown in Fig. 3, and the extrapolation to infinite basis-set size is given in Table III.

We report also a non-adiabatic estimate (see Table III) for the energy of this rotational-vibrational state that we calculated with the GENIUSH program<sup>50–52</sup> with the Polyansky–Tennyson model (Moss’ mass for the vibrations and nuclear mass for rotations)<sup>53</sup> and the GLH3P potential energy surface.<sup>54</sup> The GLH3P potential energy surface contains both the diagonal Born–Oppenheimer correction (DBOC) as well as relativistic corrections. As we consider here the non-relativistic Schrödinger Hamiltonian, we removed the relativistic corrections from the potential energy surface for a proper comparison. In order to obtain an absolute energy value, we employed the adiabatic electronic energy (BO plus

DBOC) at the equilibrium structure given in Ref. 55. This non-adiabatic estimate for the total energy is not variational. It is based on a perturbative correction to the BO approximation, resulting in the diagonal BO correction and non-adiabatic (mass-correction) effects, which are included here only with a simple model. Nevertheless, such a setup is usually considered to be accurate within about one wavenumber ( $1 \text{ cm}^{-1}$ ). A direct comparison of a variational and (a rigorous) perturbative treatment was recently presented by Pachucki and Komasa for rotational states of the four-particle hydrogen molecule.<sup>56</sup> For the case of  $\text{H}_3^+$ , the present work represents a significant step toward a variational validation of effective non-adiabatic models for the description of the ground- and, the considerably more complicated, near-dissociation states; such models may be developed to compute hundreds and thousands of rovibrational states and transitions available from experiment.

We now compare the results obtained with our numerically projected FECG basis set with the results obtained for the ECG-GVR ansatz and from the literature. Table IV shows the convergence of the (Pauli-allowed) ground-state energy of  $\text{H}_3^+ = \{p^+, p^+, p^+, e^-, e^-\}$  using ECG-GVR basis functions (see Sec. I) with  $N = 1$  and  $p = -1$ . Our best result obtained with ECG-GVR is  $7.897 \text{ mE}_h$  higher than the best variational upper bound obtained with the numerical projection method (see Table III). The global vector representation is an excellent alternative of the partial-wave decomposition of the wavefunction. Its simplicity and generality allowed the calculation of the lowest-energy  $N = 1$  and  $N = 2$  states for the  ${}^7\text{Li}$  atom and for antiprotonic helium.<sup>31,32</sup> However, the variational reconstruction of the rotational symmetry appears to be cumbersome already for triatomic systems. The slow convergence of the ground-state energy in Table IV shows that the ECG-GVR basis set (with a single global vector) is impractical for calculating variational upper bounds to the ground-state energy of  $\text{H}_3^+$ .

Earlier results with unprojected FECG functions for the ground-state energy of  $\text{H}_3^+$  ( $S_e = 0$  and  $I_p = \frac{1}{2}$ ),  $E_{p-\text{H}_3^+}/E_h = -1.314\,383\,574$ , were reported in Ref. 58, which is  $8.442 \text{ mE}_h$  higher in energy than our best result calculated with numerically projected FECGs (Table III). The numerical projection of FECG functions described in Sec. II F allowed us to substantially improve upon the best variational estimates for  $\text{H}_3^+$ .

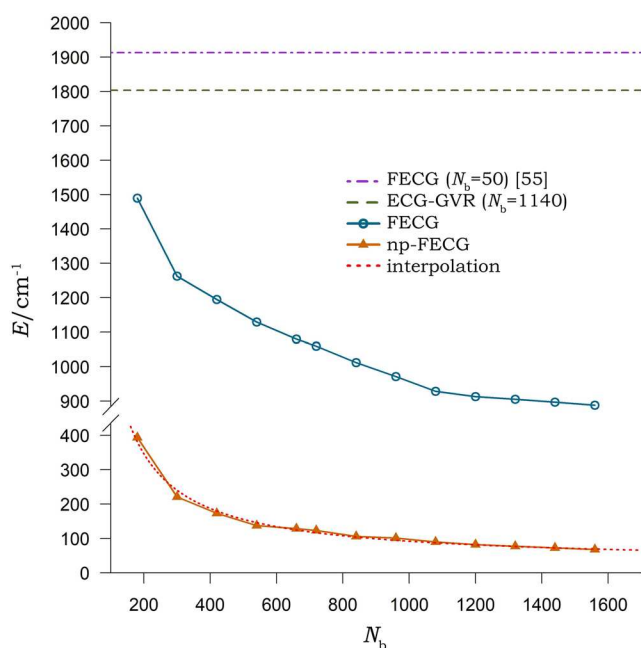


FIG. 3. Energy convergence (in  $\text{cm}^{-1}$ ) with respect to the number of basis functions  $N_b$ , for unprojected and projected basis sets. The non-adiabatic estimate was subtracted from the energies. The dotted line represents the interpolation of the projected FECG energies, while the dashed line shows the best result obtained throughout ECG-GVR functions.

TABLE IV. Convergence of the ground state energy of  $\text{H}_3^+ = \{p^+, p^+, p^+, e^-, e^-\}$  with  $S_e = 0$  and  $I_p = \frac{1}{2}$  with respect to the number of ECG-GVR functions  $N_b$ . The general vector representation is employed to describe the natural parity state ( $N = 1$ ,  $M_N = 0$ ,  $p = +1$ ). The  $K$  exponent of the polynomial prefactor is randomly selected and optimized from the  $\{1, \dots, 20\}$  set.

$N_b$	$\langle \hat{H} \rangle / E_h$	$N_b$	$\langle \hat{H} \rangle / E_h$
60	-1.290269	660	-1.313773
180	-1.304466	780	-1.314465
300	-1.309775	900	-1.314716
420	-1.311816	1020	-1.314850
540	-1.312467	1140	-1.314929

#### IV. CONCLUSIONS

The advantage of explicitly correlated Gaussian functions in calculations on highly accurate (non-relativistic) bound states for few-particle systems is due to the analytic and general  $N_p$ -particle integral expressions available for almost all important operators. Various basis sets with  $N \geq 0$  total spatial angular momentum quantum numbers (isolated systems) have been proposed in the past. The traditional partial-wave expansion as well as the more generally applicable (but in variational approaches equivalent) global vector representation have been used with success. Molecular pre-Born–Oppenheimer calculations, especially for systems with more than two heavy nuclei, have turned out to be challenging because the electronic and the nuclear motion, including rotation-inversion symmetry and correlation effects, have to be efficiently described simultaneously.

In this work, we developed numerical projection techniques for the non-symmetric but flexible basis set of explicitly correlated Gaussian functions with shifted centers. The numerical projection ensures the correct spatial rotation-inversion symmetry of the variational ansatz, while the shifted ECGs are better suited to describe the (de)localization of the atomic nuclei. We presented theoretical as well as technical details for a practical implementation of projected floating ECG functions in a variational pre-Born–Oppenheimer calculation. The first applications of this new numerical approach resulted in an 8.442 mE<sub>h</sub> improvement on the earlier best variational upper bound for the (Pauli-allowed) ground-state energy of the  $H_3^+ = \{p^+, p^+, p^+, e^-, e^-\}$  molecular ion treated as a five-particle system. Further possible improvements on the projection approach and the parametrization of the basis set were discussed in order to provide five-particle variational benchmark values for selected eigenstates of the  $H_3^+$  molecular ion.

#### SUPPLEMENTARY MATERIAL

See [supplementary material](#) for the optimized basis function parameters of  $H_2$  and  $H_3^+$ .

#### ACKNOWLEDGMENTS

This work has been financially supported by ETH Zurich and the Schweizerischer Nationalfonds (No. SNF.169120). EM thanks a PROMYS Grant (No. IZ11Z0.166525) of the SNSF.

#### APPENDIX A: ANGULAR MOMENTUM EXPECTATION VALUES FOR FECG FUNCTIONS

In this section, we derive matrix elements for FECG functions for the squared total spatial angular momentum operator

$$\hat{N}^2 = \hat{N}_x^2 + \hat{N}_y^2 + \hat{N}_z^2, \quad (A1)$$

with  $\hat{N} = \sum_{P=1}^{N_p} \hat{l}^{(P)}$ , which is the sum of angular momentum operators for each particle  $P$ ,

$$\hat{l}^{(P)} = \hat{r}^{(P)} \times \hat{p}^{(P)} = -i \left( \hat{r}^{(P)} \times \hat{\nabla}^{(P)} \right). \quad (A2)$$

With the elementary angular momenta, we re-write the  $\hat{N}^2$  operator as

$$\begin{aligned} \hat{N}^2 &= \sum_{P=1}^{N_p} \hat{l}^{(P)2} + 2 \sum_{P_1 < P_2} \hat{l}^{(P_1)} \hat{l}^{(P_2)} \\ &= - \sum_{P=1}^{N_p} \epsilon_{ijk} \epsilon_{ipq} r_j^{(P)} \nabla_k^{(P)} r_p^{(P)} \nabla_q^{(P)} \\ &\quad - 2 \sum_{P_1 < P_2} \epsilon_{ijk} \epsilon_{ipq} r_j^{(P_1)} \nabla_k^{(P_1)} r_p^{(P_2)} \nabla_q^{(P_2)}, \end{aligned} \quad (A3)$$

where the Levi-Civita symbol  $\epsilon$  is used together with Einstein summation convention over the  $i, j, k, p, q \in \{x, y, z\}$  indices. Then, the  $i$ th component of  $N$  is

$$\hat{N}_i = \sum_{P=1}^{N_p} \hat{l}_i^{(P)} = \frac{1}{i} \epsilon_{ijk} \sum_{P=1}^{N_p} r_j^{(P)} \nabla_k^{(P)} - r_k^{(P)} \nabla_j^{(P)}. \quad (A4)$$

#### 1. $\langle \hat{N}_z \rangle$ for FECG functions

The action of  $\hat{N}_z$  on FECG functions is given by

$$\begin{aligned} \hat{N}_z |\phi\rangle &= \frac{1}{i} \sum_{P=1}^{N_p} \left( r_x^{(P)} \nabla_y^{(P)} - r_y^{(P)} \nabla_x^{(P)} \right) \exp \left[ -s^T A s - r A r + 2r^T A s \right] \\ &= \frac{1}{i} \sum_{P=1}^{N_p} \left( -r_{(P,x)} A_{(P,y)}^T r - r^T A_{(P,y)} r_{(P,x)} + 2r_{(P,x)} A_{(P,y)}^T s \right. \\ &\quad \left. + r_{(P,y)} A_{(P,x)}^T r + r^T A_{(P,x)} r_{(P,y)} - 2r_{(P,y)} A_{(P,x)}^T s \right) \\ &\quad \times \exp \left[ -s^T A s - r^T A r + 2r^T A s \right], \end{aligned} \quad (A5)$$

where  $A_{(P,i)}$  is the column vector of variational parameters corresponding to the  $i$ th component of the position vector  $r_P$ . The pre-exponential terms can be written in a more compact way incorporating the sum over every particle  $P$  in the matrix algebra,

$$\begin{aligned} \hat{N}_z |\phi\rangle &= \left[ -r^T A_{(x,y)} r - r^T A_{(y,x)} r + 2r^T A_{(x,y)} s + r^T A_{(y,x)} r \right. \\ &\quad \left. + r^T A_{(x,y)} r - 2r^T A_{(y,x)} s \right] \exp \left[ -s^T A s - r^T A r + 2r^T A s \right] \\ &= \left( r^T \left( A_{(y,x)} + A_{(x,y)} - A_{(x,y)} - A_{(y,x)} \right) r \right. \\ &\quad \left. + 2r^T \left( A_{(x,y)} - A_{(y,x)} \right) s \right) \exp \left[ -s^T A s - r^T A r + 2r^T A s \right], \end{aligned} \quad (A6)$$

where, given  $(E_{ij})_{xy} = \delta_{ix} \delta_{jy}$ , it is

$$A_{(i,j)} = \bar{A} \otimes E_{ij}. \quad (A7)$$

Given the two symmetric matrices  $\Omega^{(x,y)}$  and  $\omega^{(x,y)}$ ,

$$\Omega^{(x,y)} \equiv A_{(y,x)} + A_{(x,y)} - A_{(x,y)} - A_{(y,x)}, \quad (A8)$$

$$\omega^{(x,y)} \equiv A_{(x,y)} - A_{(y,x)}, \quad (A9)$$

and it can be seen that, when  $A = \bar{A} \otimes \mathbb{1}_3$  is symmetric,  $\Omega^{(x,y)}$  is 0 by construction. This observation greatly simplifies the expectation value calculation  $\langle \hat{N}_z \rangle$ ,

$$\langle \phi_I | \hat{N}_z | \phi_J \rangle = \frac{2}{i} \langle \phi_I | r^T \omega_j^{(x,y)} s_J | \phi_J \rangle, \quad (A10)$$

where the subscript attached to the  $\omega$  matrix indicates that the row exchanging operation is applied to the ket function correlation matrix  $A_J$ . The integration in Eq. (A10) is carried out expressing the appropriate derivatives of  $\phi_J$ , which is followed by the evaluation of the standard overlap integral,

$$\begin{aligned} \langle \phi_I | \hat{N}_z | \phi_J \rangle &= \frac{1}{i} \left( \frac{\partial}{\partial \mathbf{e}} \omega_J^{(x,y)} \mathbf{s}_J \right) \int d\mathbf{r} \\ &\quad \times \exp \left( -\mathbf{s}_I^T A_I \mathbf{s}_I - \mathbf{s}_J^T A_J \mathbf{s}_J - \mathbf{r} A \mathbf{r} + 2\mathbf{r}^T \mathbf{e} \right) \\ &= \frac{1}{i} \left( \frac{\partial}{\partial \mathbf{e}} \omega_J^{(x,y)} \mathbf{s}_J \right) \left( \frac{(2\pi)^{3N_p}}{\det(A)} \right)^{\frac{1}{2}} \\ &\quad \times \exp \left( -\mathbf{s}_I^T A_I \mathbf{s}_I - \mathbf{s}_J^T A_J \mathbf{s}_J + \mathbf{e}^T A^{-1} \mathbf{e} \right) \\ &= \frac{2}{i} \left( \mathbf{e}^T A^{-1} \omega_J^{(x,y)} \mathbf{s}_J \right) \langle \phi_I | \phi_J \rangle, \end{aligned} \quad (\text{A11})$$

with  $A = A_I + A_J$  and  $\mathbf{e} = A_I \mathbf{s}_I + A_J \mathbf{s}_J$ . For the diagonal matrix elements, one finds

$$\begin{aligned} \langle \phi_I | \hat{N}_z | \phi_I \rangle &= \frac{2}{i} \left( \mathbf{s}^T \left[ \mathcal{A} \otimes \begin{pmatrix} 0 & 1 & 0 \\ 0 & 0 & 0 \\ 0 & 0 & 0 \end{pmatrix} - \mathcal{A} \otimes \begin{pmatrix} 0 & 0 & 0 \\ 1 & 0 & 0 \\ 0 & 0 & 0 \end{pmatrix} \right] \mathbf{s} \right) \\ &\quad \times \langle \phi_I | \phi_I \rangle = 0. \end{aligned} \quad (\text{A12})$$

## 2. $\langle \hat{N}^2 \rangle$ for FECG

First, we re-write the integrals by exploiting the Hermiticity of  $\hat{N}$  as

$$\langle \phi_I | \hat{N}^2 | \phi_J \rangle = \langle \hat{N} \phi_I | \hat{N} \phi_J \rangle. \quad (\text{A13})$$

The terms originating from the action of the  $\hat{N}_i = \sum_{p=1}^{N_p} l_i^{(p)}$  on the bra and the ket functions have already been derived in Appendix A 1,

$$\langle \hat{N}_i \phi_I | = -\frac{2}{i} \epsilon'_{ipq} \langle \phi_I | [\mathbf{r}^T \omega_I^{(p,q)} \mathbf{s}_I] \quad (\text{A14})$$

and

$$| \hat{N}_i \phi_J \rangle = +\frac{2}{i} \epsilon'_{ijk} [\mathbf{r}^T \omega_J^{(j,k)} \mathbf{s}_J] | \phi_J \rangle, \quad (\text{A15})$$

where  $\epsilon'_{abc}$  is non-zero only when the corresponding Levi-Civita symbol is equal to +1. Then, the integral in Eq. (A13) becomes

$$\begin{aligned} \langle \hat{N} \phi_I | \hat{N} \phi_J \rangle &= \int \epsilon'_{ijk} \left[ 4 \left( \mathbf{r}^T \omega_I^{(j,k)} \mathbf{s}_I \right) \left( \mathbf{r}^T \omega_J^{(j,k)} \mathbf{s}_J \right) \right] \\ &\quad \times \exp \left( \mathbf{s}_I^T A_I \mathbf{s}_I - \mathbf{s}_J^T A_J \mathbf{s}_J - \mathbf{r}^T \underbrace{(A_I + A_J)}_{\equiv A} \mathbf{r} \right. \\ &\quad \left. + 2\mathbf{r}^T \underbrace{(A_I \mathbf{s}_I + A_J \mathbf{s}_J)}_{\equiv \mathbf{e}} \right) d\mathbf{r}. \end{aligned} \quad (\text{A16})$$

We collect the pre-exponential terms from the integration by writing them in terms of derivatives of  $A$  and  $\mathbf{e}$ . The remaining integrand function is that of the simple  $\langle \phi_I | \phi_J \rangle$  overlap integral given in Eq. (A11) for two FECG functions  $\phi_I$  and  $\phi_J$ ,

$$\langle \hat{N} \phi_I | \hat{N} \phi_J \rangle = \epsilon'_{ijk} \left[ \left( \frac{\partial}{\partial \mathbf{e}} \omega_I^{(j,k)} \mathbf{s}_I \right) \left( \frac{\partial}{\partial \mathbf{e}} \omega_J^{(j,k)} \mathbf{s}_J \right) \right] \langle \phi_I | \phi_J \rangle. \quad (\text{A17})$$

Finally, the integral of  $\hat{N}^2$  with the  $\phi_I$  and  $\phi_J$  functions is obtained as

$$\begin{aligned} \langle \hat{N} \phi_I | \hat{N} \phi_J \rangle &= \epsilon'_{ijk} \left[ \left( \frac{\partial}{\partial \mathbf{e}} \omega_I^{(j,k)} \mathbf{s}_I \right) \left( 2\mathbf{e}^T A^{-1} \omega_J^{(j,k)} \mathbf{s}_J \right) \right] \langle \phi_I | \phi_J \rangle \\ &= \epsilon'_{ijk} \left[ \left( 2\mathbf{s}_I^T \omega_I^{(j,k)T} A^{-1} \omega_J^{(j,k)} \mathbf{s}_J \right) \right. \\ &\quad \left. + \left( 2\mathbf{e}^T A^{-1} \omega_J^{(j,k)} \mathbf{s}_J \right) \left( 2\mathbf{e}^T A^{-1} \omega_I^{(j,k)} \mathbf{s}_I \right) \right] \langle \phi_I | \phi_J \rangle, \end{aligned} \quad (\text{A18})$$

### a. Alternative evaluation of $\langle \phi_I | \hat{N}^2 | \phi_J \rangle$

Instead of exploiting the Hermiticity of  $\hat{N}$ , as in Eq. (A13), we may directly expand  $\hat{N}^2$  as the sum of the square of its components,

$$\langle \phi_I | \hat{N}^2 | \phi_J \rangle = \langle \phi_I | \hat{N}_x^2 + \hat{N}_y^2 + \hat{N}_z^2 | \phi_J \rangle. \quad (\text{A19})$$

Starting from Eq. (A10), we find that by applying the operator  $\hat{N}_z$  on an FECG, the action of another  $\hat{N}_z$  operator produces a lengthy expression,

$$\hat{N}_z^2 | \phi_J \rangle = -2 \left( \mathbf{r}_x \nabla_y - \mathbf{r}_y \nabla_x \right) \left( \mathbf{r}_x A_{J(x,y)} \mathbf{s}_J - \mathbf{r}_y A_{J(y,x)} \mathbf{s}_J \right) | \phi_J \rangle. \quad (\text{A20})$$

However, after simple algebraic manipulations, the following expression is obtained:

$$\hat{N}^2 | \phi_J \rangle = \epsilon'_{ijk} 2 \left( \mathbf{r} A_{J(j,k)} \mathbf{s}_J \right) - 2 \left( \mathbf{r} \omega^{(j,k)} \mathbf{s}_J \right)^2 | \phi_J \rangle. \quad (\text{A21})$$

With this result, we can write the integral as

$$\begin{aligned} \langle \phi_I | \hat{N}^2 | \phi_J \rangle &= \epsilon'_{ijk} \left[ \left( \frac{\partial}{\partial \mathbf{e}} A_{J(k,j)} \mathbf{s}_J \right) - \left( \frac{\partial}{\partial \mathbf{e}} \omega^{(j,k)} \mathbf{s}_J \right)^2 \right] \langle \phi_I | \phi_J \rangle \\ &= \epsilon'_{ijk} \left( 2\mathbf{e}^T A^{-1} A_{J(k,j)} \mathbf{s}_J - 2\mathbf{s}_J \omega_J^{(j,k)T} A^{-1} \omega_J^{(j,k)} \mathbf{s}_J \right. \\ &\quad \left. + 4 \left( \mathbf{e}^T A^{-1} \omega_J^{(j,k)} \mathbf{s}_J \right)^2 \right) \langle \phi_I | \phi_J \rangle, \end{aligned} \quad (\text{A22})$$

where  $A_{J(\text{row})}^{(j,k)}$  is obtained from the  $A_J$  matrix by setting all elements for the  $i$ th coordinate of every particle to zero.

The final results read

$$\hat{N}_i | \phi_J \rangle = \frac{2}{i} \epsilon'_{ijk} \left( \mathbf{r}^T \omega_J^{(j,k)} \mathbf{s}_J \right) | \phi_J \rangle, \quad (\text{A23})$$

$$\hat{N}_i^2 | \phi_J \rangle = \epsilon'_{ijk} \left[ 2 \left( \mathbf{r} A_{J(j,k)} \mathbf{s}_J \right) - 2 \left( \mathbf{r} \omega^{(j,k)} \mathbf{s}_J \right)^2 \right] | \phi_J \rangle. \quad (\text{A24})$$



## APPENDIX B: ELIMINATION OF THE CENTER-OF-MASS CONTRIBUTIONS FROM THE INTEGRAL EXPRESSIONS OF THE SQUARE OF THE TOTAL ANGULAR MOMENTUM OPERATOR

The center of mass (CM) of a system moves like a free particle, and its states are not quantized and not square integrable. We eliminate the contributions from this continuous degree of

freedom,  $\mathbf{r}_{\text{CM}}$ , from the angular momentum integrals derived in Appendix A employing our approach described in Ref. 38.

Generally speaking, the separation of space-translation variables from internal variables is a well understood problem.<sup>59</sup> The CM correction terms for the angular momentum integrals are derived in the following equations.

We start with Eq. (A18),

$$\begin{aligned} \langle \hat{N}^2 \rangle = & \epsilon'_{ijk} \left[ \underbrace{\left( 2\mathbf{s}_I^{(r)T} \omega_I^{(j,k)T} A^{-1} \omega_J^{(j,k)} \mathbf{s}_J^{(r)} \right)}_{\equiv A} + \underbrace{\left( 2\mathbf{e}^{(r)T} A^{-1} \omega_J^{(j,k)} \mathbf{s}_J^{(r)} \right)}_{\equiv B} \underbrace{\left( 2\mathbf{e}^{(r)T} A^{-1} \omega_I^{(j,k)} \mathbf{s}_I^{(r)} \right)}_{\equiv C} \right] \\ & \times \underbrace{\left( \frac{(\det(A_I) \det(A_J))^{1/2}}{\det(A)} \right)^{1/2}}_{\equiv \frac{\langle \phi_I | \phi_J \rangle}{(\langle \phi_I | \phi_I \rangle \langle \phi_J | \phi_J \rangle)^{1/2}}} \exp \left( -\mathbf{s}_I^{(r)T} A_I \mathbf{s}_I^{(r)} - \mathbf{s}_J^{(r)T} A_J \mathbf{s}_J^{(r)} + \mathbf{e}^T A^{-1} \mathbf{e} \right), \end{aligned} \quad (\text{B1})$$

where  $\mathbf{e} = A_I \mathbf{s}_I^{(r)} + A_J \mathbf{s}_J^{(r)}$ , and focus on the pre-exponential terms generated by the  $\hat{N}^2$  operator leaving aside the remaining overlap integral. The superscript ( $r$ ) refers to variational vectors associated with laboratory-fixed Cartesian coordinates (LFCC). The superscript ( $x$ ) denotes variational vectors in transformed translationally invariant Cartesian coordinates (TICC)  $\mathbf{s}^{(x)}$ ,

$$\mathbf{s}^{(r)} = U_x^{-1} \mathbf{s}^{(x)} = U_x^{-1} \mathbf{s}^{(x)} \begin{pmatrix} \mathbf{s}' \\ \mathbf{c}_S \end{pmatrix}, \quad (\text{B2})$$

where  $\mathbf{c}_S$  is a 3-dimensional vector associated with  $\mathbf{r}_{\text{CM}}$  and

$$\bar{A}^{(r)} = U_x^T \bar{A}^{(x)} U_x. \quad (\text{B3})$$

We have

$$A = 2 \left( \mathbf{s}_I^{(x)T} \tilde{\omega}_I^{(j,k)T} U_x A^{-1} U_y^T \tilde{\omega}_J^{(j,k)} \mathbf{s}_J^{(x)} \right), \quad (\text{B4})$$

$$B = 2 \left( \mathbf{s}_I^{(x)T} A_I^{(x)} U_x A^{-1} U_y^T \tilde{\omega}_J^{(j,k)} \mathbf{s}_J^{(x)} + \mathbf{s}_J^{(y)T} A_J^{(y)} U_y A^{-1} U_x^T \tilde{\omega}_I^{(j,k)} \mathbf{s}_I^{(x)} \right), \quad (\text{B5})$$

$$C = 2 \left( \mathbf{s}_I^{(x)T} A_I^{(x)} U_x A^{-1} U_x^T \tilde{\omega}_I^{(j,k)} \mathbf{s}_I^{(x)} + \mathbf{s}_J^{(y)T} A_J^{(y)} U_y A^{-1} U_y^T \tilde{\omega}_J^{(j,k)} \mathbf{s}_J^{(x)} \right), \quad (\text{B6})$$

where  $\tilde{\omega}$  indicates that it is built in the TICC set defined by the  $U_x$  matrix (see also Ref. 38). Next, we recall the results of Ref. 38,

$$U_x \bar{A}_{IJ}^{-1} U_y^T = \begin{bmatrix} \mathcal{A}_{IJ}^{-1} & 0 \\ 0 & \frac{1}{c_{A_I} + c_{A_J}} \end{bmatrix} \quad (\text{B7})$$

and

$$U_x \bar{A}'_{IJ}^{-1} U_x^T = \begin{bmatrix} \mathcal{A}'_{IJ}^{-1} & 0 \\ 0 & \frac{1}{c_{A_I} + c_{A_J}} \end{bmatrix}, \quad (\text{B8})$$

to re-write  $A$ ,  $B$ , and  $C$  as

$$\begin{aligned} A = & 2 \begin{pmatrix} \mathbf{s}'_I \\ \mathbf{c}_{S_I} \end{pmatrix}^T \left[ \begin{pmatrix} \mathcal{A}_I & 0 \\ 0 & c_{A_I} \end{pmatrix} \otimes \mathbb{1}_{jk} \right] \left[ \begin{pmatrix} \mathcal{A}'_{IJ}^{-1} & 0 \\ 0 & \frac{1}{c_{A_I} + c_{A_J}} \end{pmatrix} \otimes \mathbb{1}_3 \right] \\ & \times \left[ \begin{pmatrix} \mathcal{A}_J & 0 \\ 0 & c_{A_J} \end{pmatrix} \otimes \mathbb{1}_{jk} \right] \begin{pmatrix} \mathbf{s}'_J \\ \mathbf{c}_{S_J} \end{pmatrix}, \end{aligned} \quad (\text{B9})$$

$$\begin{aligned} B = & 2 \begin{pmatrix} \mathbf{s}'_I \\ \mathbf{c}_{S_I} \end{pmatrix}^T \left[ \begin{pmatrix} \mathcal{A}_I & 0 \\ 0 & c_{A_I} \end{pmatrix} \otimes \mathbb{1}_3 \right] \left[ \begin{pmatrix} \mathcal{A}'_{IJ}^{-1} & 0 \\ 0 & \frac{1}{c_{A_I} + c_{A_J}} \end{pmatrix} \otimes \mathbb{1}_3 \right] \\ & \times \left[ \begin{pmatrix} \mathcal{A}_J & 0 \\ 0 & c_{A_J} \end{pmatrix} \otimes \mathbb{1}_{jk} \right] \begin{pmatrix} \mathbf{s}'_J \\ \mathbf{c}_{S_J} \end{pmatrix} \\ & + 2 \begin{pmatrix} \mathbf{s}'_J \\ \mathbf{c}_{S_J} \end{pmatrix}^T \left[ \begin{pmatrix} \mathcal{A}_J & 0 \\ 0 & c_{A_J} \end{pmatrix} \otimes \mathbb{1}_3 \right] \left[ \begin{pmatrix} \mathcal{A}'_{IJ}^{-1} & 0 \\ 0 & \frac{1}{c_{A_I} + c_{A_J}} \end{pmatrix} \otimes \mathbb{1}_3 \right] \\ & \times \left[ \begin{pmatrix} \mathcal{A}_I & 0 \\ 0 & c_{A_I} \end{pmatrix} \otimes \mathbb{1}_{jk} \right] \begin{pmatrix} \mathbf{s}'_I \\ \mathbf{c}_{S_I} \end{pmatrix}, \end{aligned} \quad (\text{B10})$$

$$\begin{aligned} C = & 2 \begin{pmatrix} \mathbf{s}'_I \\ \mathbf{c}_{S_I} \end{pmatrix}^T \left[ \begin{pmatrix} \mathcal{A}_I & 0 \\ 0 & c_{A_I} \end{pmatrix} \otimes \mathbb{1}_3 \right] \left[ \begin{pmatrix} \mathcal{A}'_{IJ}^{-1} & 0 \\ 0 & \frac{1}{c_{A_I} + c_{A_J}} \end{pmatrix} \otimes \mathbb{1}_3 \right] \\ & \times \left[ \begin{pmatrix} \mathcal{A}_I & 0 \\ 0 & c_{A_I} \end{pmatrix} \otimes \mathbb{1}_{jk} \right] \begin{pmatrix} \mathbf{s}'_I \\ \mathbf{c}_{S_I} \end{pmatrix} \\ & + 2 \begin{pmatrix} \mathbf{s}'_J \\ \mathbf{c}_{S_J} \end{pmatrix}^T \left[ \begin{pmatrix} \mathcal{A}_J & 0 \\ 0 & c_{A_J} \end{pmatrix} \otimes \mathbb{1}_3 \right] \left[ \begin{pmatrix} \mathcal{A}'_{IJ}^{-1} & 0 \\ 0 & \frac{1}{c_{A_I} + c_{A_J}} \end{pmatrix} \otimes \mathbb{1}_3 \right] \\ & \times \left[ \begin{pmatrix} \mathcal{A}_I & 0 \\ 0 & c_{A_I} \end{pmatrix} \otimes \mathbb{1}_{jk} \right] \begin{pmatrix} \mathbf{s}'_I \\ \mathbf{c}_{S_I} \end{pmatrix}, \end{aligned} \quad (\text{B11})$$

where  $\mathbb{1}_{jk} = E_{kj} - E_{jk}$  and  $E_{ij}$  are  $3 \times 3$  matrices in which only the  $ij$ th element is different from zero and it is equal to 1.

Following the prescriptions of Ref. 38, the CM contributions are eliminated by subtracting the following terms from the  $A$ ,  $B$ , and  $C$  expressions in Eqs. (B9)–(B11):

$$A^{(\text{CM})} = 2 \mathbf{c}_{S_I}^T (c_{A_I} \otimes \mathbb{1}_{jk}) \left( \frac{1}{c_{A_I} + c_{A_J}} \otimes \mathbb{1}_3 \right) (c_{A_J} \otimes \mathbb{1}_{jk}) \mathbf{c}_{S_J}, \quad (\text{B12})$$

$$B^{(\text{CM})} = 2 \mathbf{c}_{S_I}^T (c_{A_I} \otimes \mathbb{1}_3) \left( \frac{1}{c_{A_I} + c_{A_J}} \otimes \mathbb{1}_3 \right) (c_{A_J} \otimes \mathbb{1}_{jk}) \mathbf{c}_{S_J} \\ + 2 \mathbf{c}_{S_J}^T (c_{A_J} \otimes \mathbb{1}_3) \left( \frac{1}{c_{A_I} + c_{A_J}} \otimes \mathbb{1}_3 \right) (c_{A_I} \otimes \mathbb{1}_{jk}) \mathbf{c}_{S_I}, \quad (\text{B13})$$

$$C^{(\text{CM})} = 2 \mathbf{c}_{S_I}^T (c_{A_I} \otimes \mathbb{1}_3) \left( \frac{1}{c_{A_I} + c_{A_J}} \otimes \mathbb{1}_3 \right) (c_{A_I} \otimes \mathbb{1}_{jk}) \mathbf{c}_{S_I} \\ + 2 \mathbf{c}_{S_J}^T (c_{A_J} \otimes \mathbb{1}_3) \left( \frac{1}{c_{A_I} + c_{A_J}} \otimes \mathbb{1}_3 \right) (c_{A_I} \otimes \mathbb{1}_{jk}) \mathbf{c}_{S_I}. \quad (\text{B14})$$

### APPENDIX C: ALTERNATIVE PROJECTION APPROACH

Löwdin proposed two different forms for the angular momentum projection: a sum<sup>45,46</sup> which is derived from a product form.<sup>44</sup> In his original method the projector is considered as a product of annihilation operators that remove all components other than that of the desired symmetry. This iterative process is accomplished by means of the two operators  $\hat{P}_N$  and  $\hat{P}_{M_N}$  acting on an arbitrary function  $\psi$  that is resolved into components  $C_{NM_N} \psi_{NM_N}$  which are eigenfunctions of  $\hat{N}^2$  and  $\hat{N}_z$ ,

$$\psi = \sum_N \sum_{M_N} C_{NM_N} \psi_{NM_N}, \quad (\text{C1})$$

where the summation is over all possible values of  $N$  and  $M_N$  and the wavefunction is written in the basis of mutually orthogonal unit vectors  $\psi_{NM_N}$  spanning the complete Hilbert space. The eigenvalue relations for  $\hat{N}^2$  and  $\hat{N}_z$  may be written in the form

$$[\hat{N}^2 - N(N+1)] \psi_{NM_N} \equiv 0, \quad (\text{C2})$$

$$[\hat{N}_z - M_N] \psi_{NM_N} \equiv 0, \quad (\text{C3})$$

which means that the eigenfunction  $\psi_{NM_N}$  is annihilated by the operator  $[\hat{N}^2 - N(N+1)]$  or  $[\hat{N}_z - M_N]$ . It is therefore possible to select a specific component,  $C_{NM_N} \psi_{NM_N}$ , from  $\psi$  by annihilating all other components. This can be achieved with the following projectors:<sup>44</sup>

$$\hat{P}_N = \prod_{l \neq N} \frac{\hat{N}^2 - l(l+1)}{N(N+1) - l(l+1)}, \quad (\text{C4})$$

$$\hat{P}_{M_N} = \prod_{\mu \neq M_N} \frac{\hat{M}_N - \mu}{M_N - \mu}, \quad (\text{C5})$$

where the numerators are products of Löwdin's elementary annihilation operators over all quantum numbers except those which correspond to the selected value(s). The denominators have been chosen so that the projectors have eigenvalue 1 when acting on the term  $\psi_{NM_N}$ .

Löwdin showed that Eq. (C4) may be rewritten, when acting on an eigenvector of  $N_z$  with eigenvalue  $M_N \geq 0$ , in the so-called sum form,<sup>45</sup>

$$\hat{P}_{NM_N} = \prod_{l \neq N} \frac{(2N+1)(N+M_N)!}{(N-M_N)!} \sum_{l \neq N} \frac{(-1)^l N_-^{N-M_N+k} N_+^{N-M_N+k}}{k!(2N+1+k)!}, \quad (\text{C6})$$

where

$$\hat{N}_\pm = \hat{N}_x \pm i\hat{N}_y \quad (\text{C7})$$

are the usual raising and lowering operators and the subscript  $M_N$  is added to  $P_N$  since Eq. (C6) is valid only when acting on a state of definite  $M_N$ .

For practical applications, the product operators (C4) and (C5) can be restricted to contain only a finite number of factors,  $l_{\text{max}}$ . However, the product series in Eq. (C4) converges quadratically with respect to  $l$  since the  $l$ th term is  $\approx 1$  for sufficiently large  $l$ .<sup>44</sup>

We have not explored the feasibility of a numerical approach based on Eq. (C4) or Eq. (C6) because the expressions for  $\hat{N}_i^n$ , for  $n$  being a positive integer, become lengthy as shown in Appendix A 2 already for  $n = 2$ .

<sup>1</sup>V. I. Korobov, *Phys. Rev. A* **77**, 022509 (2008).

<sup>2</sup>Z.-X. Zhong, Z.-C. Yan, and T.-Y. Shi, *Phys. Rev. A* **79**, 064502 (2009).

<sup>3</sup>J. Komasa, K. Piszczatowski, G. Lach, M. Przybytek, B. Jeziorski, and K. Pachucki, *J. Chem. Theory Comput.* **7**, 3105 (2011).

<sup>4</sup>V. I. Korobov, L. Hilico, and J.-P. Karr, *Phys. Rev. A* **87**, 062506 (2013).

<sup>5</sup>E. J. Salumbides, J. C. J. Koelemeij, J. Komasa, K. Pachucki, K. S. E. Eikema, and W. Ubachs, *Phys. Rev. D* **87**, 112008 (2013).

<sup>6</sup>R. Pohl, R. Gilman, G. A. Miller, and K. Pachucki, *Annu. Rev. Nucl. Part. Sci.* **63**, 175 (2013).

<sup>7</sup>A. Beyer, L. Maisenbacher, A. Matveev, R. Pohl, K. Khabarova, A. Grinin, T. Lamour, D. C. Yost, T. W. Hänsch, N. Kolachevsky, and T. Udem, *Science* **358**, 79 (2017).

<sup>8</sup>Z.-X. Zhong, P.-P. Zhang, Z.-C. Yan, and T.-Y. Shi, *Phys. Rev. A* **86**, 064502 (2012).

<sup>9</sup>J.-P. Karr, L. Hilico, J. C. J. Koelemeij, and V. I. Korobov, *Phys. Rev. A* **94**, 050501 (2016).

<sup>10</sup>V. I. Korobov, L. Hilico, and J.-P. Karr, *Phys. Rev. Lett.* **118**, 233001 (2017).

<sup>11</sup>V. Korobov, *Phys. Rev. A* **74**, 052506 (2006).

<sup>12</sup>L. M. Wang and Z.-C. Yan, *Phys. Rev. A* **97**, 060501(R) (2018).

<sup>13</sup>M. Puchalski, A. Spyszkiwicz, J. Komasa, and K. Pachucki, *Phys. Rev. Lett.* **121**, 073001 (2018).

<sup>14</sup>C. Cheng, J. Hussels, M. Niu, H. L. Bethlem, K. S. E. Eikema, E. J. Salumbides, W. Ubachs, M. Beyer, N. J. Hölsch, J. A. Agner, F. Merkt, L.-G. Tao, S.-M. Hu, and C. Jungen, *Phys. Rev. Lett.* **121**, 013001 (2018).

<sup>15</sup>M. Beyer, N. Hölsch, J. A. Agner, J. Deiglmayr, H. Schmutz, and F. Merkt, *Phys. Rev. A* **97**, 012501 (2018).

<sup>16</sup>S. F. Boys, *Proc. R. Soc. London, Ser. A* **258**, 402 (1960).

<sup>17</sup>K. Singer, *Proc. R. Soc. London, Ser. A* **258**, 412 (1960).

<sup>18</sup>V. I. Kukulin and V. M. Krasnopol'sky, *J. Phys. G: Nucl. Phys.* **3**, 795 (1977).

<sup>19</sup>S. A. Alexander, H. J. Monkhorst, and K. Szalewicz, *J. Chem. Phys.* **85**, 5821 (1986).

<sup>20</sup>W. Cencek and J. Rychlewski, *J. Chem. Phys.* **98**, 1252 (1993).

<sup>21</sup>E. Mátýus, J. Hutter, U. Müller-Herold, and M. Reiher, *Phys. Rev. A* **83**, 052512 (2011).

<sup>22</sup>E. Mátýus, J. Hutter, U. Müller-Herold, and M. Reiher, *J. Chem. Phys.* **135**, 204302 (2011).

<sup>23</sup>S. Bubín, M. Pavanello, W.-C. Tung, K. L. Sharkey, and L. Adamowicz, *Chem. Rev.* **113**, 36 (2013).

<sup>24</sup>J. Mitroy, S. Bubín, W. Horiuchi, Y. Suzuki, L. Adamowicz, W. Cencek, K. Szalewicz, J. Komasa, D. Blume, and K. Varga, *Rev. Mod. Phys.* **85**, 693 (2013).

<sup>25</sup>S. Bubín and L. Adamowicz, *J. Chem. Phys.* **128**, 114107 (2008).

<sup>26</sup>K. L. Sharkey, M. Pavanello, S. Bubín, and L. Adamowicz, *Phys. Rev. A* **80**, 062510 (2009).

<sup>27</sup>K. L. Sharkey, S. Bubín, and L. Adamowicz, *J. Chem. Phys.* **132**, 184106 (2010).

- <sup>28</sup>K. L. Sharkey, S. Bubin, and L. Adamowicz, *J. Chem. Phys.* **134**, 044120 (2011).
- <sup>29</sup>K. L. Sharkey, S. Bubin, and L. Adamowicz, *J. Chem. Phys.* **134**, 194114 (2011).
- <sup>30</sup>K. L. Sharkey, S. Bubin, and L. Adamowicz, *Phys. Rev. A* **83**, 012506 (2011).
- <sup>31</sup>K. Varga, Y. Suzuki, and J. Usukura, *Few-Body Syst.* **24**, 81 (1998).
- <sup>32</sup>Y. Suzuki, J. Usukura, and K. Varga, *J. Phys. B: At., Mol. Opt. Phys.* **31**, 31 (1998).
- <sup>33</sup>K. Strasburger, *J. Chem. Phys.* **141**, 044104 (2014).
- <sup>34</sup>Y. Suzuki and K. Varga, *Stochastic Variational Approach to Quantum-Mechanical Few-Body Problems* (Springer-Verlag, Berlin, 1998).
- <sup>35</sup>M. E. Rose, *Elementary Theory of Angular Momentum* (Wiley, New York, 1957).
- <sup>36</sup>F. Schwabl, *Quantum Mechanics* (Springer, 2007).
- <sup>37</sup>B. Simmen, E. Mátyus, and M. Reiher, *Mol. Phys.* **111**, 2086 (2013).
- <sup>38</sup>A. Muolo, E. Mátyus, and M. Reiher, *J. Chem. Phys.* **148**, 084112 (2018).
- <sup>39</sup>L. F. Lathouwers and E. Duemens, *J. Phys. A: Math. Gen.* **15**, 2785 (1982).
- <sup>40</sup>C. Cerjan, *Numerical Grid Methods and Their Application to Schrödinger's Equation* (Springer, The Netherlands, 1993).
- <sup>41</sup>J. Suarez, S. Farantos, S. Stamatiadis, and L. Lathouwers, *Comput. Phys. Commun.* **180**, 2025 (2009).
- <sup>42</sup>J. O. Corbett, *Nucl. Phys. A* **169**, 426 (1971).
- <sup>43</sup>A. Kerman and N. Onishi, *Nucl. Phys. A* **281**, 373 (1977).
- <sup>44</sup>P. Löwdin, *Rev. Mod. Phys.* **36**, 966 (1964).
- <sup>45</sup>J. Shapiro, *J. Math. Phys.* **6**, 1680 (1965).
- <sup>46</sup>R. J. S. Crossley, *Int. J. Quantum Chem.* **11**, 917 (1977).
- <sup>47</sup>M. J. D. Powell, *The NEWUOA Software for Unconstrained Optimization Without Derivates* (Springer, New York, 2006).
- <sup>48</sup>T. N. L. Patterson, *Math. Comput.* **22**, 847 (1968).
- <sup>49</sup>C. M. Lindsay and B. J. McCall, *J. Mol. Spectrosc.* **210**, 60 (2001).
- <sup>50</sup>E. Mátyus, G. Czakó, and A. G. Császár, *J. Chem. Phys.* **130**, 134112 (2009).
- <sup>51</sup>C. Fábri, E. Mátyus, and A. G. Császár, *J. Chem. Phys.* **134**, 074105 (2011).
- <sup>52</sup>E. Mátyus, T. Szidarovszky, and A. G. Császár, *J. Chem. Phys.* **141**, 154111 (2014).
- <sup>53</sup>O. L. Polyansky and J. Tennyson, *J. Chem. Phys.* **110**, 5056 (1999).
- <sup>54</sup>M. Pavanello, L. Adamowicz, A. Aljiah, N. F. Zobov, I. Mizus, O. L. Polyansky, J. Tennyson, T. Szidarovszky, and A. G. Császár, *J. Chem. Phys.* **136**, 184303 (2012).
- <sup>55</sup>W. Cencek, J. Rychlewski, R. Jaquet, and W. Kutzelnigg, *J. Chem. Phys.* **108**, 2831 (1998).
- <sup>56</sup>K. Pachucki and J. Komasa, *Phys. Chem. Chem. Phys.* **20**, 247 (2018).
- <sup>57</sup>K. Pachucki and J. Komasa, *J. Chem. Phys.* **130**, 164113 (2009).
- <sup>58</sup>M. Caffero and L. Adamowicz, *Chem. Phys. Lett.* **387**, 136 (2004).
- <sup>59</sup>B. T. Sutcliffe, "Coordinate system and transformations," in *Handbook of Molecular Physics and Quantum Chemistry*, edited by S. Wilson (Wiley, Chichester, 2003), Vol. 1, Chap. 31.

# Relativistic kinetic-balance condition for explicitly correlated basis functions

Benjamin Simmen<sup>1</sup>, Edit Mátyus<sup>2,3</sup> and Markus Reiher<sup>1</sup>

<sup>1</sup>ETH Zürich, Laboratorium für Physikalische Chemie, Vladimir-Prelog-Weg 2, 8093 Zürich, Switzerland

<sup>2</sup>Eötvös Loránd University, Institute of Chemistry, PO Box 32, H-1518, Budapest 112, Hungary

E-mail: [matyus@chem.elte.hu](mailto:matyus@chem.elte.hu) and [markus.reiher@phys.chem.ethz.ch](mailto:markus.reiher@phys.chem.ethz.ch)

Received 30 July 2015, revised 22 August 2015

Accepted for publication 26 August 2015

Published 23 October 2015



CrossMark

## Abstract

This paper presents the derivation of a kinetic-balance condition for explicitly correlated basis functions employed in semi-classical relativistic calculations. Such a condition is important to ensure variational stability in algorithms based on the first-quantized Dirac theory of 1/2-fermions. We demonstrate that the kinetic-balance condition can be obtained from the row reduction process commonly applied to solve systems of linear equations. The resulting form of kinetic balance establishes a relation for the  $4^N$  components of the spinor of an  $N$ -fermion system to the non-relativistic limit, which is in accordance with recent developments in the field of exact decoupling in relativistic orbital-based many-electron theory.

Online supplementary data available from [stacks.iop.org/jpb/48/245004/mmedia](http://stacks.iop.org/jpb/48/245004/mmedia)

Keywords: *ab initio* calculations, relativistic molecular physics, explicitly correlated basis functions, geminals, kinetic balance

## 1. Introduction

Most of relativistic quantum chemistry and molecular physics is based on the (first-quantized) Dirac Hamiltonian [1–7]. However, unlike its non-relativistic counterpart, the Dirac Hamiltonian is not bounded from below and measures have to be taken in order to obtain correct lower bounds for the ground- and excited-state energies of bound states. Depending on whether the small components of the one-fermion basis spinors are included or eliminated (by some decoupling approach [8]), methods are classified as four- or two-component methods. Four-component methods rely on the kinetic-balance condition for variational stability. This condition is well-defined for single fermions [9–16] and can therefore easily be applied to orbital-based methods such as the Dirac–Hartree–Fock approach and electron-correlation methods based on it [17–30]. For orbital-based theories with explicit correlation factors, recent work focused on four-component second-order Møller–Plesset perturbation theory with positive-energy-states projection operators in combination with the one-electron kinetic-balance condition [31]. Li

and co-workers have studied coalescence conditions for explicitly correlated four-component wave functions [32] but without addressing the issue of kinetic balance.

A first solution to the full problem of kinetic balance for explicitly correlated trial wave functions was presented by Pestka and co-workers who have published a series of papers investigating the relativistic helium-like two-electron systems treated as a two-electron system in a central potential [33–39]. They have demonstrated that the energy levels associated with the two-fermion Dirac Hamiltonian are in fact resonances with a small imaginary part. The imaginary part, and thus coupling to the continuum, is detectable in the numerical solution for systems with large nuclear charges,  $Z$ , and with a kinetically balanced basis set constructed from a large number of explicitly correlated basis functions. As to the kinetic-balance condition, their solution involves an infinite series of transformations of the individual components of the two-electron 16-spinor, and it remains unclear how this kinetic-balance approach can be extended to systems containing more than two fermions.

In this paper, we extend the pioneering work by Pestka *et al* on He-like atoms [37] and focus our attention on the kinetic balance condition of general,  $N$ -particle, non-separable basis functions. We present a scheme which allows us to

<sup>3</sup> Present address: Department of Chemistry, University of Cambridge, Lensfield Road, Cambridge CB2 1EW, UK.

derive an explicitly correlated kinetic-balance condition based on row reduction and an expression similar to the row-reduced echelon form of the augmented matrix. We begin in section 2 with the presentation of the theoretical background. In section 3, we apply our scheme to a two-electron system. Then, in section 4, we show that the correct non-relativistic limit is obtained. In section 5, we illustrate how the computational cost can be reduced for the  $N$ -fermion case by introducing systematic approximations to a given order in the speed of light. Finally in section 6, we demonstrate the variational stability of explicitly correlated, kinetically balanced trial wave functions for the ground state of the He atom.

## 2. Theoretical background

The relativistic description of electrons based on the many-1/2-fermion Dirac Hamiltonian provides us with a first-quantized, i.e., semi-classical formalism capturing essential aspects of special relativity for molecular matter [1, 3].

### 2.1. The relativistic electron

A single 1/2-fermion, such as an electron, may be described by the Dirac Hamiltonian [40, 41]

$$\mathbf{h}_D = c\boldsymbol{\alpha} \cdot \mathbf{p} + \beta mc^2 + V. \quad (1)$$

The matrices  $\boldsymbol{\alpha} = (\alpha_x, \alpha_y, \alpha_z)$  and  $\beta$  are defined by anti-commutation relations. The most common choice that respects these relations is the standard representation of  $4 \times 4$  matrices,

$$\alpha_i = \begin{bmatrix} \mathbf{0}_2 & \sigma_i \\ \sigma_i & \mathbf{0}_2 \end{bmatrix} \quad \text{with } i \in \{x, y, z\} \quad \text{and} \\ \beta = \begin{bmatrix} \mathbf{1}_2 & \mathbf{0}_2 \\ \mathbf{0}_2 & -\mathbf{1}_2 \end{bmatrix}, \quad (2)$$

where  $\sigma_i$  denotes one of the three Pauli spin matrices and  $\mathbf{1}_2$  is the two-dimensional unit matrix.  $\mathbf{p} = (p_x, p_y, p_z)^T$  is the momentum operator,  $V$  is an operator for the interaction energy due to external potentials,  $m$  is the rest mass of the fermion, and  $c$  is the speed of light.

It is convenient to introduce a block structure for the one-fermion eigenfunction  $\psi(\mathbf{r})$ , the 4-spinor, according to the  $2 \times 2$  super-structure of the four-dimensional  $\alpha_i$  and  $\beta$  matrices in standard representation,

$$\psi(\mathbf{r}) = \begin{bmatrix} \psi^l(\mathbf{r}) \\ \psi^s(\mathbf{r}) \end{bmatrix} = \begin{bmatrix} |l\rangle \\ |s\rangle \end{bmatrix}, \quad (3)$$

where ‘ $l$ ’ denotes the so-called large and ‘ $s$ ’ the corresponding small component. As we develop the entire formalism in the coordinate representation, we follow the common shorthand notation that abbreviates, for instance,  $\psi^l(\mathbf{r}) = \langle \mathbf{r} | \psi^l \rangle$  as  $|\psi^l\rangle$  or just as  $|l\rangle$ . We refer the reader to the review by Esteban, Lewin and Séré [42] and the book by Thaller [43] for a more

detailed mathematical discussion of the Dirac Hamiltonian and its eigenfunctions.

The spectrum of the Dirac Hamiltonian features three distinct parts. The first part comprises the discrete bound states with energies between  $+mc^2$  and  $-mc^2$ . The second part is the positive continuum ranging from  $+mc^2$  to  $+\infty$ . The last part of the spectrum is the negative continuum ranging from  $-mc^2$  to  $-\infty$ . The negative continuum is a source of instabilities in variational calculations where the Rayleigh quotient,

$$E[\mathbf{h}_D, \psi(\mathbf{r})] = \frac{\langle \psi(\mathbf{r}) | \mathbf{h}_D | \psi(\mathbf{r}) \rangle}{\langle \psi(\mathbf{r}) | \psi(\mathbf{r}) \rangle}, \quad (4)$$

is minimized and (usually unwanted) negative-energy continuum solutions can be encountered if no precautions (such as projection onto positive-energy states) are taken into account. For basis-set expansion techniques, Schwarz and co-workers showed that the finite size of ordinary basis sets may pose difficulties [44, 45], which is therefore sometimes called the ‘finite-basis disease’ [46].

An effective means of dealing with the problem of variational collapse is the kinetic-balance condition [9, 10, 12–16] which relates the large and the small component of the 4-spinor:

$$\psi^s(\mathbf{r}) \approx \frac{\boldsymbol{\sigma} \cdot \mathbf{p}}{2mc} \psi^l(\mathbf{r}). \quad (5)$$

The derivation of this relation is straightforward. The Dirac eigenvalue problem

$$(\mathbf{h}_D - E\mathbf{1}_4)\psi(\mathbf{r}) = 0 \quad (6)$$

leads to a set of two linear equations for the two components of the 4-spinor in equation (3). After the energy spectrum has been shifted by  $-mc^2$  to match the non-relativistic energy scale, this system of equations reads

$$(V - E)\psi^l(\mathbf{r}) + c\boldsymbol{\sigma} \cdot \mathbf{p} \psi^s(\mathbf{r}) = 0, \quad (7)$$

$$(V - E - 2mc^2)\psi^s(\mathbf{r}) + c\boldsymbol{\sigma} \cdot \mathbf{p} \psi^l(\mathbf{r}) = 0, \quad (8)$$

where the four-dimensional operator  $V$  was assumed to be a diagonal matrix with the same element  $V$  as diagonal entries. We only need one of the two equations to relate the small component to the large one. Since  $\boldsymbol{\sigma} \cdot \mathbf{p}$  has no multiplicative inverse, it is more convenient to choose the second equation in order to obtain an expression for  $\psi^s(\mathbf{r})$ . After rearranging the terms, we obtain the exact relation for equation (8)

$$\psi^s(\mathbf{r}) = \frac{c\boldsymbol{\sigma} \cdot \mathbf{p}}{(E - V + 2mc^2)} \psi^l(\mathbf{r}). \quad (9)$$

This relation depends on the energy of the system which is not known a priori but is one of the desired results of the problem. Equation (9) can therefore not be applied to our problem. Now,  $(E - V)$  is considered small compared to  $mc^2$

so that we may introduce the approximation

$$E - V + 2mc^2 \approx 2mc^2 \quad (10)$$

to eliminate  $(E - V)$  and arrive at the kinetic-balance condition in equation (5). We note that this approximation step turned out to be unimportant for the construction of variationally stable basis-set expansion techniques applied in four-component orbital-based theories [8, 47], which we assume to remain valid for the  $N$ -particle theory to be developed in this work.

Basis-set expansions which obey equation (5) provide a variationally stable parametrization of a trial wave function for a single fermion. Equation (5) may therefore be formulated in terms of the one-fermion model spaces [14, 37, 48]

$$|l\rangle \in \mathcal{H}^l \quad \text{and} \quad |s\rangle \in (\boldsymbol{\sigma} \cdot \mathbf{p})\mathcal{H}^l \subset \mathcal{H}^s. \quad (11)$$

This one-fermion kinetic-balance condition can be imposed by a transformation [8],

$$U_{\text{KB}}^{(1)} = \begin{bmatrix} U_l^{(1)} & 0_2 \\ 0_2 & U_s^{(1)} \end{bmatrix} = \begin{bmatrix} \mathbf{1}_2 & \mathbf{0}_2 \\ \mathbf{0}_2 & \frac{\boldsymbol{\sigma} \cdot \mathbf{p}}{p} \end{bmatrix} \quad (12)$$

(with  $p = |\mathbf{p}|$ ) on basis functions into which the large component of the one-fermion 4-spinor is expanded. Hence, the model spaces for the large and the small components are generated in terms of this transformation. The advantage of this form of the kinetic-balance condition is that the large-component and small-component model spaces remain normalized. It is also possible to transform the Dirac Hamiltonian and then form identical model spaces for the large and small components. The transformed Dirac Hamiltonian is the so-called modified Dirac Hamiltonian [47] and is the basis of orbital-based exact-decoupling methods [8].

The kinetic-balance condition in equation (5) also ensures the correct non-relativistic (NR) limit for  $c \rightarrow \infty$ . The Rayleigh quotient of equation (4) yields in the limit  $c \rightarrow \infty$  the non-relativistic Schrödinger energy:

$$E_{\text{NR}} = \lim_{c \rightarrow \infty} \frac{\langle \boldsymbol{\psi}(\mathbf{r}) | \mathbf{h}_D - \beta mc^2 | \boldsymbol{\psi}(\mathbf{r}) \rangle}{\langle \boldsymbol{\psi}(\mathbf{r}) | \boldsymbol{\psi}(\mathbf{r}) \rangle} = \frac{\langle \tilde{l} | \frac{p^2}{2m} + V | \tilde{l} \rangle}{\langle \tilde{l} | \tilde{l} \rangle}, \quad (13)$$

where  $|\tilde{l}\rangle$  denotes the (scalar part of the) large component of the spinor after taking the limit.

## 2.2. Many-fermion Dirac Hamiltonian

The relativistic first-quantized many-fermion Hamiltonian (with positive-energy projection not explicitly shown for the

sake of brevity) reads,

$$\mathbf{H}_D^{(N)} = \sum_{i=1}^N \mathbf{h}_D(i) + \mathbf{W}^{(N)} \quad (14)$$

with

$$\mathbf{h}_D(i) = \mathbf{1}_4(1) \otimes \dots \otimes \mathbf{1}_4(i-1) \otimes \mathbf{h}_D \otimes \mathbf{1}_4(i+1) \otimes \dots \otimes \mathbf{1}_4(N), \quad (15)$$

where  $\mathbf{h}_D$  is the one-fermion Dirac Hamiltonian of equation (1) taken for fermion  $i$  and  $\mathbf{W}^{(N)}$  describes the interaction of all pairs of the  $N$  fermions. The wave function for  $N$  non-interacting fermions, i.e.,  $\mathbf{W}^{(N)} = 0$ , can be constructed as the direct product of one-fermion 4-spinors  $\boldsymbol{\psi}_i(\mathbf{r}_i)$ ,

$$\boldsymbol{\Psi}(\mathbf{r}) = \boldsymbol{\psi}_1(\mathbf{r}_1) \otimes \dots \otimes \boldsymbol{\psi}_i(\mathbf{r}_i) \otimes \dots \otimes \boldsymbol{\psi}_N(\mathbf{r}_N), \quad (16)$$

which can be antisymmetrized to fulfill the Pauli principle. Now,  $\mathbf{r} = (\mathbf{r}_1, \dots, \mathbf{r}_N)^T$  collects all  $N$  one-fermion coordinates. In the case of two fermions, we have the direct product of two basis states

$$\boldsymbol{\psi}_1(\mathbf{r}_1) \otimes \boldsymbol{\psi}_2(\mathbf{r}_2) = \begin{bmatrix} \psi_1^{l1}(\mathbf{r}_1) \\ \psi_1^{l2}(\mathbf{r}_1) \\ \psi_1^{s1}(\mathbf{r}_1) \\ \psi_1^{s2}(\mathbf{r}_1) \end{bmatrix} \otimes \begin{bmatrix} \psi_2^{l1}(\mathbf{r}_2) \\ \psi_2^{l2}(\mathbf{r}_2) \\ \psi_2^{s1}(\mathbf{r}_2) \\ \psi_2^{s2}(\mathbf{r}_2) \end{bmatrix} = \begin{bmatrix} \psi_1^{l1}(\mathbf{r}_1)\psi_2^{l1}(\mathbf{r}_2) \\ \psi_1^{l1}(\mathbf{r}_1)\psi_2^{l2}(\mathbf{r}_2) \\ \psi_1^{l1}(\mathbf{r}_1)\psi_2^{s1}(\mathbf{r}_2) \\ \psi_1^{l1}(\mathbf{r}_1)\psi_2^{s2}(\mathbf{r}_2) \\ \psi_1^{l2}(\mathbf{r}_1)\psi_2^{l1}(\mathbf{r}_2) \\ \psi_1^{l2}(\mathbf{r}_1)\psi_2^{l2}(\mathbf{r}_2) \\ \vdots \\ \psi_1^{s2}(\mathbf{r}_1)\psi_2^{s2}(\mathbf{r}_2) \end{bmatrix}. \quad (17)$$

The superscripts ‘ $l$ ’ and ‘ $s$ ’ indicate large and small 2-spinors, respectively, as before. The number attached to these letters indicates the element of a 2-spinor. For instance, the elements of the large-component 2-spinor are denoted as

$$\boldsymbol{\psi}_1^l(\mathbf{r}_1) = \begin{bmatrix} \psi_1^{l1}(\mathbf{r}_1) \\ \psi_1^{l2}(\mathbf{r}_1) \end{bmatrix}. \quad (18)$$

A basis-set expansion of an  $N$ -fermion wave function may be constructed to be consistent with the model space

$$\mathcal{H}^{(N)} = \mathcal{H}^{l\dots l} \oplus \dots \oplus \mathcal{H}^{\lambda_1\dots\lambda_N} \oplus \dots \oplus \mathcal{H}^{s\dots s}, \quad (19)$$

where each  $\mathcal{H}^{\lambda_1\dots\lambda_N}$  is constructed from the one-fermion model spaces,

$$\mathcal{H}^{\lambda_1\dots\lambda_N} = \mathcal{H}^{\lambda_1} \otimes \dots \otimes \mathcal{H}^{\lambda_N}, \quad (20)$$

with  $\lambda_1, \dots, \lambda_N \in \{l, s\}$ . The highlighted spinor components in equation (17) are those contained within the model space

$\mathcal{H}^l$ . We recognize that the wave function in equation (16) and the model space in equation (19) are not compatible since it is not possible to partition equation (16) in terms of the one-fermion model spaces. However, we can reorder the spinor elements of the wave function as

$$\mathbf{P}^T \Psi(\mathbf{r}) = \psi_1(\mathbf{r}_1) \boxtimes \dots \boxtimes \psi_i(\mathbf{r}_i) \boxtimes \dots \boxtimes \psi_N(\mathbf{r}_N) \quad (21)$$

where  $\boxtimes$  is the Tracy–Singh product and  $\mathbf{P}$  is a permutation matrix (see appendix A.1 for further details). Then, our two-spinor example reads

$$\begin{aligned} \psi_1(\mathbf{r}_1) \boxtimes \psi_2(\mathbf{r}_2) &= \begin{bmatrix} \psi_1^l(\mathbf{r}_1) \otimes \psi_2^l(\mathbf{r}_2) \\ \psi_1^l(\mathbf{r}_1) \otimes \psi_2^s(\mathbf{r}_2) \\ \psi_1^s(\mathbf{r}_1) \otimes \psi_2^l(\mathbf{r}_2) \\ \psi_1^s(\mathbf{r}_1) \otimes \psi_2^s(\mathbf{r}_2) \end{bmatrix} \\ &= \begin{bmatrix} \psi_1^{l1}(\mathbf{r}_1) \psi_2^{l1}(\mathbf{r}_2) \\ \psi_1^{l1}(\mathbf{r}_1) \psi_2^{l2}(\mathbf{r}_2) \\ \psi_1^{l2}(\mathbf{r}_1) \psi_2^{l1}(\mathbf{r}_2) \\ \psi_1^{l2}(\mathbf{r}_1) \psi_2^{l2}(\mathbf{r}_2) \\ \psi_1^{s1}(\mathbf{r}_1) \psi_2^{s1}(\mathbf{r}_2) \\ \psi_1^{s1}(\mathbf{r}_1) \psi_2^{s2}(\mathbf{r}_2) \\ \vdots \\ \psi_1^{s2}(\mathbf{r}_1) \psi_2^{s2}(\mathbf{r}_2) \end{bmatrix}. \end{aligned} \quad (22)$$

The spinor components highlighted in equation (22) are those contained within the  $\mathcal{H}^l$  model space as in equation (17). We see that the wave function in equation (22) can be partitioned such that the individual components are part of the different model spaces in equation (19),

$$\begin{aligned} [\mathbf{P}^T \Psi(\mathbf{r})]^{\lambda_1 \dots \lambda_N} &= \psi_1^{\lambda_1}(\mathbf{r}_1) \otimes \dots \\ &\otimes \psi_i^{\lambda_i}(\mathbf{r}_i) \otimes \dots \otimes \psi_N^{\lambda_N}(\mathbf{r}_N), \end{aligned} \quad (23)$$

where  $\lambda_1, \dots, \lambda_N \in \{l, s\}$  as in equation (20) and antisymmetrization will be required.

The Hamiltonian is transformed accordingly (cf. equation (99) in the appendix)

$$\begin{aligned} \mathbf{H}_{DTS}^{(N)} &= \mathbf{P}^T \mathbf{H}_D^{(N)} \mathbf{P} = \sum_{i=1}^N \mathbf{P}^T \mathbf{h}_D(i) \mathbf{P} \\ &+ \mathbf{P}^T \mathbf{W}^{(N)} \mathbf{P} \equiv \sum_{i=1}^N \mathbf{h}_{DTS}(i) + \mathbf{P}^T \mathbf{W}^{(N)} \mathbf{P} \end{aligned} \quad (24)$$

with

$$\begin{aligned} \mathbf{h}_{DTS}(i) &= \mathbf{P}^T \mathbf{h}_D(i) \mathbf{P} = \mathbf{1}_4(1) \boxtimes \dots \boxtimes \mathbf{1}_4(i-1) \\ &\boxtimes \mathbf{h}_D \boxtimes \mathbf{1}_4(i+1) \boxtimes \dots \boxtimes \mathbf{1}_4(N). \end{aligned} \quad (25)$$

The potential-energy operator  $\mathbf{W}^{(N)}$  will be invariant under this transformation if only the instantaneous Coulomb interaction is considered as it is a diagonal matrix with identical entries. The situation is more complicated when magnetic interactions are taken into account. A  $N$ -fermion

wave function for 1/2-fermions can then be partitioned in terms of the model space into  $2^N$  components each of dimension  $2^N$ ,

$$\Psi(\mathbf{r}) = \begin{bmatrix} \Psi^{l\dots l}(\mathbf{r}) \\ \vdots \\ \Psi^{\lambda_1 \dots \lambda_N}(\mathbf{r}) \\ \vdots \\ \Psi^{s\dots s}(\mathbf{r}) \end{bmatrix} = \begin{bmatrix} |l\dots l\rangle \\ \vdots \\ |\lambda_1 \dots \lambda_N\rangle \\ \vdots \\ |s\dots s\rangle \end{bmatrix}. \quad (26)$$

Note that a related reordering of the Hamiltonian similar to equation (24) is key for the quaternion formulation of four-component self-consistent field algorithms [49].

### 3. Two-particle kinetic-balance condition

In this section, we derive the kinetic-balance condition for explicitly correlated basis functions for a system of two fermions. According to equation (19) the model space takes the form

$$\mathcal{H}^{(2)} = \mathcal{H}^l \oplus \mathcal{H}^{ls} \oplus \mathcal{H}^{sl} \oplus \mathcal{H}^{ss}, \quad (27)$$

where the four subspaces are formed from the single-fermion model spaces  $\mathcal{H}^l$  and  $\mathcal{H}^s$ :

$$\mathcal{H}^{ll} = \mathcal{H}^l \otimes \mathcal{H}^l, \quad (28)$$

$$\mathcal{H}^{ls} = \mathcal{H}^l \otimes \mathcal{H}^s, \quad (29)$$

$$\mathcal{H}^{sl} = \mathcal{H}^s \otimes \mathcal{H}^l, \quad (30)$$

$$\mathcal{H}^{ss} = \mathcal{H}^s \otimes \mathcal{H}^s. \quad (31)$$

Each model space in equations (28)–(31) is assigned to one of four components in the 16-component wave function. The structure of the Dirac Hamiltonian has to respect the structure of the Tracy–Singh product (see equation (97) in the appendix) to match the partitioning of the wave function according to equation (26). We then obtain the following block structure for the two-fermion Hamiltonian defined in equation (24):

$$\begin{aligned} \mathbf{H}_{DTS}^{(2)}(\mathbf{r}_1, \mathbf{r}_2) &= \\ &\begin{bmatrix} \mathbf{V} + \mathbf{W} & c(\boldsymbol{\sigma}_2^{(2)} \cdot \mathbf{p}_2) & c(\boldsymbol{\sigma}_1^{(2)} \cdot \mathbf{p}_1) & \mathbf{0}_4 \\ c(\boldsymbol{\sigma}_2^{(2)} \cdot \mathbf{p}_2) & \mathbf{V} + \mathbf{W} - 2m_2 c^2 \mathbf{1}_4 & \mathbf{0}_4 & c(\boldsymbol{\sigma}_1^{(2)} \cdot \mathbf{p}_1) \\ c(\boldsymbol{\sigma}_1^{(2)} \cdot \mathbf{p}_1) & \mathbf{0}_4 & \mathbf{V} + \mathbf{W} - 2m_1 c^2 \mathbf{1}_4 & c(\boldsymbol{\sigma}_2^{(2)} \cdot \mathbf{p}_2) \\ \mathbf{0}_4 & c(\boldsymbol{\sigma}_1^{(2)} \cdot \mathbf{p}_1) & c(\boldsymbol{\sigma}_2^{(2)} \cdot \mathbf{p}_2) & \mathbf{V} + \mathbf{W} - 2m_{12} c^2 \mathbf{1}_4 \end{bmatrix} \end{aligned} \quad (32)$$

where we introduced the four-dimensional unit matrix  $\mathbf{1}_4$  to highlight the dimension and  $\mathbf{V} = [V(\mathbf{r}_1) + V(\mathbf{r}_2)] \mathbf{1}_4$  to yield a four-dimensional representation of the external potential-energy operator. Moreover, we assume that  $\mathbf{V}$  and also the four-dimensional fermion–fermion interaction operator  $\mathbf{W}$  are diagonal, which does not hold if magnetic and retardation effects are considered for the interaction of the two fermions

(hence, we apply the compact notation ‘ $\mathbf{W}$ ’ for a  $4 \times 4$  matrix operator describing the Coulomb interaction of two fermions only). If this assumption is not made, rather complicated expressions will emerge for a magnetically balanced, explicitly correlated basis. In particular, the zero entries in equation (32) that represent the cases with a large and small component in the bracket per fermion would carry the magnetic fermion–fermion interaction (as expressed, for instance, in the Gaunt or Breit operators). As we will later make an assumption that all potential energy contributions are small compared to the rest energies of the fermions, we aim at a kinetic balance condition free of any reference to a potential energy operator in analogy to the orbital-based two-fermion case.

Note that we have also introduced an energy shift of the whole spectrum in equation (32) by  $-m_{12}c^2$  with  $m_{12} = m_1 + m_2$ . Moreover, we absorbed the direct products into  $\sigma_i^{(2)}$  as

$$\sigma_1^{(2)} = (\sigma_x \otimes \mathbf{1}_2, \sigma_y \otimes \mathbf{1}_2, \sigma_z \otimes \mathbf{1}_2)^T, \quad (33)$$

and

$$\sigma_2^{(2)} = (\mathbf{1}_2 \otimes \sigma_x, \mathbf{1}_2 \otimes \sigma_y, \mathbf{1}_2 \otimes \sigma_z)^T. \quad (34)$$

The idea of kinetic balance is to relate the small-component one-fermion model spaces to their large-component one-fermion model spaces in the eigenvalue problem

$$(\mathbf{H}_{DTS}^{(2)} - E\mathbf{1}_6)\Psi(\mathbf{r}_1, \mathbf{r}_2) = 0. \quad (35)$$

This leads to a system of four equations, analogously to equations (7) and (8),

$$0 = (V + W - E\mathbf{1}_4)\Psi^{ll} + c(\sigma_2^{(2)} \cdot \mathbf{p}_2)\Psi^{ls} + c(\sigma_1^{(2)} \cdot \mathbf{p}_1)\Psi^{sl}, \quad (36)$$

$$0 = c(\sigma_2^{(2)} \cdot \mathbf{p}_2)\Psi^{ll} + (V + W - E\mathbf{1}_4 - 2m_2c^2\mathbf{1}_4)\Psi^{ls} + c(\sigma_1^{(2)} \cdot \mathbf{p}_1)\Psi^{ss}, \quad (37)$$

$$0 = c(\sigma_1^{(2)} \cdot \mathbf{p}_1)\Psi^{ll} + (V + W - E\mathbf{1}_4 - 2m_1c^2\mathbf{1}_4)\Psi^{sl} + c(\sigma_2^{(2)} \cdot \mathbf{p}_2)\Psi^{ss}, \quad (38)$$

$$0 = c(\sigma_1^{(2)} \cdot \mathbf{p}_1)\Psi^{ls} + c(\sigma_2^{(2)} \cdot \mathbf{p}_2)\Psi^{sl} + (V + W - E\mathbf{1}_4 - 2m_{12}c^2\mathbf{1}_4)\Psi^{ss}, \quad (39)$$

where we have suppressed the coordinate dependence of the 4-spinors and will continue to do so where convenient. We eliminate one of these four equations because we search for a

relation between the four four-dimensional components of the wave function which we can then apply as a constraint on explicitly correlated basis functions. As in the case of a single fermion, we eliminate the energy  $E$  from the equations by approximating

$$[2m_i c^2 + E]\mathbf{1}_4 - V - W \approx 2m_i c^2 \mathbf{1}_4 \quad (40)$$

where  $m_i \in \{m_1, m_2, m_{12}\}$ . Similarly to the one-fermion case, equation (10), we assume that this approximation remains valid and a variationally stable many-particle basis set can be derived.

We eliminate the first equation, equation (36), from the system of equations since it is the only equation where  $2m_i c^2$  does not occur so that equation (40) cannot be applied. After applying equation (40) to equations (37)–(39), we find the following relations among the four components of the two-fermion wave function:

$$0 \approx c(\sigma_2^{(2)} \cdot \mathbf{p}_2)\Psi^{ll} - 2m_2c^2\Psi^{ls} + c(\sigma_1^{(2)} \cdot \mathbf{p}_1)\Psi^{ss}, \quad (41)$$

$$0 \approx c(\sigma_1^{(2)} \cdot \mathbf{p}_1)\Psi^{ll} - 2m_1c^2\Psi^{sl} + c(\sigma_2^{(2)} \cdot \mathbf{p}_2)\Psi^{ss}, \quad (42)$$

$$0 \approx c(\sigma_1^{(2)} \cdot \mathbf{p}_1)\Psi^{ls} + c(\sigma_2^{(2)} \cdot \mathbf{p}_2)\Psi^{sl} - 2m_{12}c^2\Psi^{ss}. \quad (43)$$

The matrix form of this under-determined system of linear equations can be interpreted as the augmented form of a linear system with a unique solution:

$$\mathbf{A} = \begin{array}{ccc|c} (\sigma_2^{(2)} \cdot \mathbf{p}_2) & -2m_2c\mathbf{1}_4 & \mathbf{0}_4 & -(\sigma_1^{(2)} \cdot \mathbf{p}_1) \{1\} \\ (\sigma_1^{(2)} \cdot \mathbf{p}_1) & \mathbf{0}_4 & -2m_1c\mathbf{1}_4 & -(\sigma_2^{(2)} \cdot \mathbf{p}_2) \{2\} \\ \mathbf{0}_4 & (\sigma_1^{(2)} \cdot \mathbf{p}_1) & (\sigma_2^{(2)} \cdot \mathbf{p}_2) & 2m_{12}c\mathbf{1}_4 \{3\} \end{array} \quad (44)$$

The augmented form of linear systems and row reduction are explained in somewhat more detail in appendix A.2. The number in curly brackets on the right-hand side counts every row. It will be used to express the manipulations in the row reduction below.

There is no row-reduced echelon form for the augmented form in equation (44). The lack of a multiplicative inverse of the differential operator prohibits setting the leading element of each row of the row-reduced echelon form to 1 (see equation (103) in the appendix) and therefore to relate  $\Psi^{ll}(\mathbf{r}_1, \mathbf{r}_2)$ ,  $\Psi^{ls}(\mathbf{r}_1, \mathbf{r}_2)$ , and  $\Psi^{sl}(\mathbf{r}_1, \mathbf{r}_2)$  to  $\Psi^{ss}(\mathbf{r}_1, \mathbf{r}_2)$ . However, we are able to find a similar form with pairwise relations between  $\Psi^{ss}(\mathbf{r}_1, \mathbf{r}_2)$  and the other three components. These individual steps are to be taken in order to obtain this modified row-reduced echelon form:

1. Insert  $(\sigma_1^{(2)} \cdot \mathbf{p}_1)\{1\} - (\sigma_2^{(2)} \cdot \mathbf{p}_2)\{2\}$  into  $\{2\}$ :

$$\begin{array}{ccc|c} (\sigma_2^{(2)} \cdot \mathbf{p}_2) & -2m_2c\mathbf{1}_4 & \mathbf{0}_4 & -(\sigma_1^{(2)} \cdot \mathbf{p}_1) \{1\} \\ \mathbf{0}_4 & -2m_2c(\sigma_1^{(2)} \cdot \mathbf{p}_1) & 2m_1c(\sigma_2^{(2)} \cdot \mathbf{p}_2) & [\mathbf{p}_2^2 - \mathbf{p}_1^2]\mathbf{1}_4 \{2\} \\ \mathbf{0}_4 & (\sigma_1^{(2)} \cdot \mathbf{p}_1) & (\sigma_2^{(2)} \cdot \mathbf{p}_2) & 2m_{12}c\mathbf{1}_4 \{3\} \end{array}$$



2. Insert  $\{2\} + 2m_2c\{3\}$  into  $\{3\}$ :

$$\left[ \begin{array}{ccc|c} (\boldsymbol{\sigma}_2^{(2)} \cdot \mathbf{p}_2) & -2m_2c\mathbf{1}_4 & \mathbf{0}_4 & -(\boldsymbol{\sigma}_1^{(2)} \cdot \mathbf{p}_1) \\ \mathbf{0}_4 & -2m_2c(\boldsymbol{\sigma}_1^{(2)} \cdot \mathbf{p}_1) & 2m_1c(\boldsymbol{\sigma}_2^{(2)} \cdot \mathbf{p}_2) & [\mathbf{p}_2^2 - \mathbf{p}_1^2]\mathbf{1}_4 \\ \mathbf{0}_4 & \mathbf{0}_4 & 2m_{12}c(\boldsymbol{\sigma}_2^{(2)} \cdot \mathbf{p}_2) & \mathbf{p}_2^2 - \mathbf{p}_1^2 + 4m_2m_{12}c^2\mathbf{1}_4 \end{array} \right] \begin{array}{l} \{1\} \\ \{2\} \\ \{3\} \end{array}$$

3. Insert  $-\frac{m_{12}}{m_2}\{2\} + \frac{m_1}{m_2}\{3\}$  into  $\{2\}$ :

$$\left[ \begin{array}{ccc|c} (\boldsymbol{\sigma}_2^{(2)} \cdot \mathbf{p}_2) & -2m_2c\mathbf{1}_4 & \mathbf{0}_4 & -(\boldsymbol{\sigma}_1^{(2)} \cdot \mathbf{p}_1) \\ \mathbf{0}_4 & 2m_{12}c(\boldsymbol{\sigma}_1^{(2)} \cdot \mathbf{p}_1) & \mathbf{0}_4 & [\mathbf{p}_1^2 - \mathbf{p}_2^2 + 4m_1m_{12}c^2]\mathbf{1}_4 \\ \mathbf{0}_4 & \mathbf{0}_4 & 2m_{12}c(\boldsymbol{\sigma}_2^{(2)} \cdot \mathbf{p}_2) & [\mathbf{p}_2^2 - \mathbf{p}_1^2 + 4m_2m_{12}c^2]\mathbf{1}_4 \end{array} \right] \begin{array}{l} \{1\} \\ \{2\} \\ \{3\} \end{array}$$

4. Insert  $(\boldsymbol{\sigma}_1^{(2)} \cdot \mathbf{p}_1)m_{12}\{1\} + m_2\{2\}$  into  $\{1\}$ :

$$\left[ \begin{array}{ccc|c} m_{12}(\boldsymbol{\sigma}_2^{(2)} \cdot \mathbf{p}_2)(\boldsymbol{\sigma}_1^{(2)} \cdot \mathbf{p}_1) & \mathbf{0}_4 & \mathbf{0}_4 & [-m_1\mathbf{p}_1^2 - m_2\mathbf{p}_2^2 + 4m_1m_2m_{12}c^2]\mathbf{1}_4 \\ \mathbf{0}_4 & 2m_{12}c(\boldsymbol{\sigma}_1^{(2)} \cdot \mathbf{p}_1) & \mathbf{0}_4 & [\mathbf{p}_1^2 - \mathbf{p}_2^2 + 4m_1m_{12}c^2]\mathbf{1}_4 \\ \mathbf{0}_4 & \mathbf{0}_4 & 2m_{12}c(\boldsymbol{\sigma}_2^{(2)} \cdot \mathbf{p}_2) & [\mathbf{p}_2^2 - \mathbf{p}_1^2 + 4m_2m_{12}c^2]\mathbf{1}_4 \end{array} \right] \begin{array}{l} \{1\} \\ \{2\} \\ \{3\} \end{array}$$

We arrive at a set of simple pairwise relations between  $\Psi^{ss}(\mathbf{r}_1, \mathbf{r}_2)$  and the other three components

$$\begin{aligned} & -(\boldsymbol{\sigma}_1^{(2)} \cdot \mathbf{p}_1)(\boldsymbol{\sigma}_2^{(2)} \cdot \mathbf{p}_2)m_{12}\Psi^{ll} \\ & = (m_1\mathbf{p}_1^2 + m_2\mathbf{p}_2^2 - 4m_1m_2m_{12}c^2)\Psi^{ss}, \end{aligned} \quad (45)$$

$$\begin{aligned} & -2c(\boldsymbol{\sigma}_1^{(2)} \cdot \mathbf{p}_1)m_{12}\Psi^{ls} \\ & = (\mathbf{p}_2^2 - \mathbf{p}_1^2 - 4m_1m_{12}c^2)\Psi^{ss}, \end{aligned} \quad (46)$$

$$\begin{aligned} & -2c(\boldsymbol{\sigma}_2^{(2)} \cdot \mathbf{p}_2)m_{12}\Psi^{sl} \\ & = (\mathbf{p}_1^2 - \mathbf{p}_2^2 - 4m_2m_{12}c^2)\Psi^{ss}. \end{aligned} \quad (47)$$

Forming the least common multiple from the operators on the left-hand sides of the equations, we can introduce a four-dimensional spinor  $\Theta(\mathbf{r}_1, \mathbf{r}_2)$  related to the  $\Psi^{ss}(\mathbf{r}_1, \mathbf{r}_2)$  component,

$$\Psi^{ss}(\mathbf{r}_1, \mathbf{r}_2) = -2cm_{12}(\boldsymbol{\sigma}_1^{(2)} \cdot \mathbf{p}_1)(\boldsymbol{\sigma}_2^{(2)} \cdot \mathbf{p}_2)\Theta(\mathbf{r}_1, \mathbf{r}_2), \quad (48)$$

insert it into equations (45)–(47) and eliminate identical terms on both sides. Instead of relating the upper component to the lower component, we relate all four four-dimensional

components of the 16-spinor,

$$\Psi(\mathbf{r}) = \begin{bmatrix} \Psi^{ll}(\mathbf{r}) \\ \Psi^{ls}(\mathbf{r}) \\ \Psi^{sl}(\mathbf{r}) \\ \Psi^{ss}(\mathbf{r}) \end{bmatrix} = \begin{bmatrix} |ll\rangle \\ |ls\rangle \\ |sl\rangle \\ |ss\rangle \end{bmatrix} \quad (49)$$

to a common spinor  $\Theta(\mathbf{r}_1, \mathbf{r}_2)$ :

$$\begin{aligned} |ll\rangle & = (m_1\mathbf{p}_1^2 + m_2\mathbf{p}_2^2 - 4m_1m_2m_{12}c^2)\mathbf{1}_4\Theta(\mathbf{r}_1, \mathbf{r}_2) \\ & \equiv U_{ll}^{(2)}\Theta(\mathbf{r}_1, \mathbf{r}_2), \end{aligned} \quad (50)$$

$$\begin{aligned} |ls\rangle & = \frac{(\boldsymbol{\sigma}_2^{(2)} \cdot \mathbf{p}_2)}{2c}(\mathbf{p}_2^2 - \mathbf{p}_1^2 - 4m_1m_{12}c^2)\Theta(\mathbf{r}_1, \mathbf{r}_2) \\ & \equiv U_{ls}^{(2)}\Theta(\mathbf{r}_1, \mathbf{r}_2), \end{aligned} \quad (51)$$

$$\begin{aligned} |sl\rangle & = \frac{(\boldsymbol{\sigma}_1^{(2)} \cdot \mathbf{p}_1)}{2c}(\mathbf{p}_1^2 - \mathbf{p}_2^2 - 4m_2m_{12}c^2)\Theta(\mathbf{r}_1, \mathbf{r}_2) \\ & \equiv U_{sl}^{(2)}\Theta(\mathbf{r}_1, \mathbf{r}_2), \end{aligned} \quad (52)$$

$$\begin{aligned} |ss\rangle & = -m_{12}(\boldsymbol{\sigma}_1^{(2)} \cdot \mathbf{p}_1)(\boldsymbol{\sigma}_2^{(2)} \cdot \mathbf{p}_2)\Theta(\mathbf{r}_1, \mathbf{r}_2) \\ & \equiv U_{ss}^{(2)}\Theta(\mathbf{r}_1, \mathbf{r}_2). \end{aligned} \quad (53)$$

Here, we have introduced the short-hand notation  $U_{ll}^{(2)}$ ,  $U_{ls}^{(2)}$ ,  $U_{sl}^{(2)}$ , and  $U_{ss}^{(2)}$  for the transformation to kinetically balanced components in analogy to the one-fermion case in equation (12). In a subsequent section, we refer to the  $i$ -th term in the prefactor of such expressions as  $d_i^{(N)}$  with  $N = 2$  for the two-fermion case; e.g.,  $d_3^{(N)}$  for  $|sl\rangle$  is then  $-\sigma_1^{(2)} \cdot \mathbf{p}_1 / 2c \times 4m_2m_{12}c^2$ . The physical role of  $\Theta(\mathbf{r}_1, \mathbf{r}_2)$  will become clear when we study the non-relativistic limit (see below). We emphasize that  $\Theta(\mathbf{r}_1, \mathbf{r}_2)$  is in general an explicitly correlated geminal rather than a simple orbital product.

Because of the derivation in equation (48),  $\Psi^{ss}(\mathbf{r}_1, \mathbf{r}_2)$  is uniquely defined by  $\Theta(\mathbf{r}_1, \mathbf{r}_2)$  up to a constant, i.e. the constant of integration. For square-integrable functions, this constant is zero. Hence, cancellation of differential operators is not a problem and all components are uniquely determined by  $\Theta(\mathbf{r}_1, \mathbf{r}_2)$ .

Finally, we consider fermion exchange symmetry (Pauli principle) for the two identical fermions leading to the relations [39]

$$\Psi^{ll}(\mathbf{r}_1, \mathbf{r}_2) = -\Psi^{ll}(\mathbf{r}_2, \mathbf{r}_1), \quad (54)$$

$$\Psi^{ls}(\mathbf{r}_1, \mathbf{r}_2) = -\Psi^{sl}(\mathbf{r}_2, \mathbf{r}_1), \quad (55)$$

$$\Psi^{ss}(\mathbf{r}_1, \mathbf{r}_2) = -\Psi^{ss}(\mathbf{r}_2, \mathbf{r}_1), \quad (56)$$

which have to be fulfilled in addition to the relations in equations (50)–(53).  $\Theta(\mathbf{r}_1, \mathbf{r}_2)$  is antisymmetrized before the components are constructed according to equations (50)–(53) because the operators  $(\sigma_1^{(2)} \cdot \mathbf{p}_1)$  and  $(\sigma_2^{(2)} \cdot \mathbf{p}_2)$  do not commute with the permutation operator which exchanges fermions 1 and 2.

#### 4. The non-relativistic limit

The one-fermion kinetic-balance condition yields the correct non-relativistic limit for  $c \rightarrow \infty$ . This is a key requirement ensuring variational stability. We therefore require any kinetic-balance condition for more than one fermion to yield the correct non-relativistic limit.

Finding the non-relativistic limit for the one-fermion case is fairly trivial. For the two-fermion kinetic-balance condition, this is somewhat more involved. In order to find the correct limit, we rely on de l'Hôpital's rule for limits,

$$\lim_{x \rightarrow y} \frac{f(x)}{g(x)} = \lim_{x \rightarrow y} \frac{f'(x)}{g'(x)}, \quad (57)$$

where  $f'(x)$  and  $g'(x)$  are the derivatives of  $f(x)$  and  $g(x)$  with respect to  $x$ , whereas  $y$  is the limiting value of  $x$ .

The non-relativistic limit of the two-fermion total energy for a wave function kinetically balanced according to equations (50)–(53), can be taken as a limiting case of the Rayleigh quotient

$$E_{\text{NR}} = \lim_{c \rightarrow \infty} \frac{\langle \Psi | \mathbf{H}_{\text{DTS}}^{(2)} | \Psi \rangle}{\langle \Psi | \Psi \rangle}. \quad (58)$$

For the one-electron part in  $\langle \Psi | \mathbf{H}_{\text{DTS}}^{(2)} | \Psi \rangle$  we have

$$\begin{aligned} & \langle \Psi | \sum_{i=1}^2 \mathbf{h}_{\text{DTS}}(r_i) | \Psi \rangle \\ &= \langle ll | c(\sigma_2^{(2)} \cdot \mathbf{p}_2) | ls \rangle + \langle ll | c(\sigma_1^{(2)} \cdot \mathbf{p}_1) | sl \rangle \\ & \quad + \langle ls | c(\sigma_2^{(2)} \cdot \mathbf{p}_2) | ll \rangle - \langle ls | 2m_2c^2 | ls \rangle \\ & \quad + \langle ls | c(\sigma_1^{(2)} \cdot \mathbf{p}_1) | ss \rangle + \langle sl | c(\sigma_1^{(2)} \cdot \mathbf{p}_1) | ll \rangle \\ & \quad - \langle sl | 2m_1c^2 | sl \rangle + \langle sl | c(\sigma_2^{(2)} \cdot \mathbf{p}_2) | ss \rangle \\ & \quad + \langle ss | c(\sigma_1^{(2)} \cdot \mathbf{p}_1) | ls \rangle + \langle ss | c(\sigma_2^{(2)} \cdot \mathbf{p}_2) | sl \rangle \\ & \quad - \langle ss | 2m_{12}c^2 | ss \rangle + \langle \Psi | \mathbf{V} \otimes \mathbf{1}_4 | \Psi \rangle, \end{aligned} \quad (59)$$

where we have not resolved the potential-energy expectation value for convenience. It must now be noted that

$$\begin{aligned} & \langle ls | c(\sigma_2^{(2)} \cdot \mathbf{p}_2) | ll \rangle - \langle ls | 2m_2c^2 | ls \rangle \\ & \quad + \langle ls | c(\sigma_1^{(2)} \cdot \mathbf{p}_1) | ss \rangle = 0, \end{aligned} \quad (60)$$

which can be shown by exploiting equations (45) and (46) to replace  $|ll\rangle$  and  $|ls\rangle$  by expressions for  $|ss\rangle$ . Analogously, we can exploit equations (45)–(47) to show

$$\begin{aligned} & \langle sl | c(\sigma_1^{(2)} \cdot \mathbf{p}_1) | ll \rangle - \langle sl | 2m_1c^2 | sl \rangle \\ & \quad + \langle sl | c(\sigma_2^{(2)} \cdot \mathbf{p}_2) | ss \rangle = 0, \end{aligned} \quad (61)$$

$$\begin{aligned} & \langle ss | c(\sigma_1^{(2)} \cdot \mathbf{p}_1) | ls \rangle \\ & \quad + \langle ss | c(\sigma_2^{(2)} \cdot \mathbf{p}_2) | sl \rangle - \langle ss | 2m_{12}c^2 | ss \rangle = 0. \end{aligned} \quad (62)$$

Hence, we find for the full Hamiltonian with interacting fermions

$$\begin{aligned} \langle \Psi | \mathbf{H}_{\text{DTS}}^{(2)} | \Psi \rangle &= \langle ll | c(\sigma_2^{(2)} \cdot \mathbf{p}_2) | ls \rangle \\ & \quad + \langle ll | c(\sigma_1^{(2)} \cdot \mathbf{p}_1) | sl \rangle + \langle \Psi | (\mathbf{V} + \mathbf{W}) \otimes \mathbf{1}_4 | \Psi \rangle. \end{aligned} \quad (63)$$

We now apply de l'Hôpital's rule to equation (58) by taking the fourth-order derivative with respect to  $c$  of both the numerator and the denominator:

$$\begin{aligned} E_{\text{NR}} &= \lim_{c \rightarrow \infty} \left[ \frac{d^4}{dc^4} \left\{ \langle ll | c(\sigma_1^{(2)} \cdot \mathbf{p}_1) | ls \rangle \right. \right. \\ & \quad + \langle ll | c(\sigma_2^{(2)} \cdot \mathbf{p}_2) | sl \rangle \\ & \quad \left. \left. + \langle \Psi | (\mathbf{V} + \mathbf{W}) \otimes \mathbf{1}_4 | \Psi \rangle \right\} \right] / \left[ \frac{d^4}{dc^4} \langle \Psi | \Psi \rangle \right] \\ &= \lim_{c \rightarrow \infty} \left[ \left( \langle \Theta | 192m_{12}^2m_1^2m_2^2\mathbf{p}_1^2\mathbf{1}_4 \right. \right. \\ & \quad + 192m_{12}^2m_1^2m_2^2\mathbf{p}_2^2\mathbf{1}_4 + 384m_{12}^2m_1^2m_2^2(\mathbf{V} + \mathbf{W}) \\ & \quad \left. \left. + \mathcal{O}(c^{-2}) | \Theta \rangle \right) / (384m_{12}^2m_1^2m_2^2 \langle \Theta | \Theta \rangle) \right]. \end{aligned} \quad (64)$$

The potential energy term,  $\mathbf{V} + \mathbf{W}$ , may also contain contributions depending on  $c$ , but these contributions are of second or higher order in  $c^{-1}$ . When taking the limit, they are

all zero and we find the limit to be a simplified Rayleigh quotient depending on  $\Theta(\mathbf{r}_1, \mathbf{r}_2)$

$$E_{\text{NR}} = \frac{\langle \Theta | \frac{p_1^2}{2m_1} + \frac{p_2^2}{2m_2} + \tilde{V} + \tilde{W} | \Theta \rangle}{\langle \Theta | \Theta \rangle}, \quad (65)$$

where  $\tilde{V}$  and  $\tilde{W}$  are the limiting values with  $c \rightarrow \infty$  for  $V$  and  $W$ , respectively. In equation (65), we obtain the Schrödinger energy and therefore the correct non-relativistic limit. The limit also identifies the four-dimensional spinor  $\Theta(\mathbf{r}_1, \mathbf{r}_2)$  as the non-relativistic two-fermion Schrödinger wave function (note that this function still features a four-dimensional spinor structure as it accounts for the spin of two electrons).

It is interesting to note that the value of the non-relativistic,  $c \rightarrow \infty$ , limit is determined by the leading terms in  $c$  of the three components  $|ll\rangle$ ,  $|ls\rangle$ , and  $|sl\rangle$  in equations (50)–(52) define the non-relativistic limit when we apply de l'Hôpital's rule. These leading terms are

$$|ll\rangle(c^2): \quad -4m_1m_2m_{12}c^2 \Theta, \quad (66)$$

$$|ls\rangle(c): \quad -2m_1m_{12}c(\sigma_2^{(2)} \cdot \mathbf{p}_2) \Theta, \quad (67)$$

and

$$|sl\rangle(c): \quad -2m_2m_{12}c(\sigma_1^{(2)} \cdot \mathbf{p}_1) \Theta. \quad (68)$$

We also note that equations (66)–(68) are related to equation (5). If we apply equation (5) for particles 1 and 2 subsequently to  $\Theta(\mathbf{r})$  and then multiply by  $4m_1m_2m_{12}c^2$ ,

$$\begin{bmatrix} |ll\rangle(c^2) \\ |ls\rangle(c) \\ |sl\rangle(c) \\ |ss\rangle(1) \end{bmatrix} \rightarrow 4m_1m_2m_{12}c^2 \begin{bmatrix} \Theta \\ \frac{(\sigma_2^{(2)} \cdot \mathbf{p}_2)}{2m_2c} \Theta \\ \frac{(\sigma_1^{(2)} \cdot \mathbf{p}_1)}{2m_1c} \Theta \\ \frac{(\sigma_1^{(2)} \cdot \mathbf{p}_1)(\sigma_2^{(2)} \cdot \mathbf{p}_2)}{4m_1m_2c^2} \Theta \end{bmatrix} \quad (69)$$

we obtain the expressions of equations (66)–(68). Hence, we have shown that the one-fermion kinetic-balance condition in equation (5) is sufficient for obtaining the correct non-relativistic limit for a two-fermion system. At first sight, this seems reassuring as obtaining the correct non-relativistic limit has been connected to variational stability for orbital-based theories (see, e.g., [50]). However, the one-fermion kinetic-balance condition may not be sufficient to ensure variational stability in the general case considered here [14, 37, 48]. Accordingly, the non-relativistic limit will then not be a sufficient, albeit a necessary condition for variational stability.

## 5. Kinetic-balance condition for more than two fermions

The derivation presented in section 3 can also be applied to systems of more than two fermions, and thus establishes in its full form a kinetic-balance condition for general (non-separable)  $N$ -particle basis functions. How such a generalization could be achieved for the approach of Pestka and co-workers [14, 37, 48] is not obvious and was not discussed in their papers. In our ansatz, we obtain rather lengthy expressions for three fermions, which we refrain from presenting explicitly for the sake of brevity. The resulting expressions can, however, be expanded into a polynomial with respect to  $c$ . The individual terms  $d_i^{(3)}(c)$  of the prefactor of the 3-fermion 8-spinor  $\Theta(\mathbf{r}_1, \mathbf{r}_2, \mathbf{r}_3)$  feature the important property

$$d_i^{(3)}(c) = k_i^{(3)}(m_1, m_2, m_3) \times c^{(6-u-v-w)} \times (\sigma_1^{(3)} \cdot \mathbf{p}_1)^u (\sigma_2^{(3)} \cdot \mathbf{p}_2)^v (\sigma_3^{(3)} \cdot \mathbf{p}_3)^w \quad (70)$$

where we have omitted to indicate that each  $d_i^{(3)}(c)$  will be different for different sectors  $||ll\rangle$ ,  $||ls\rangle$ ,  $|lss\rangle$ , and so forth and depend on  $u, v, w$ . The positive semi-definite exponents  $u, v, w$  obey the constraints  $0 \leq (u + v + w) \leq 7$  and we have

$$\sigma_1^{(3)} = (\sigma_x \otimes \mathbf{1}_4, \sigma_y \otimes \mathbf{1}_4, \sigma_z \otimes \mathbf{1}_4)^T, \quad (71)$$

$$\sigma_2^{(3)} = (\mathbf{1}_2 \otimes \sigma_x \otimes \mathbf{1}_2, \mathbf{1}_2 \otimes \sigma_y \otimes \mathbf{1}_2, \mathbf{1}_2 \otimes \sigma_z \otimes \mathbf{1}_2)^T, \quad (72)$$

$$\sigma_3^{(3)} = (\mathbf{1}_4 \otimes \sigma_x, \mathbf{1}_4 \otimes \sigma_y, \mathbf{1}_4 \otimes \sigma_z)^T. \quad (73)$$

The multiplicative prefactors  $k_i^{(3)}(m_1, m_2, m_3)$  depend on the masses of the individual fermions and the kinetic-balance conditions simplify significantly if all three fermions have equal masses.

Equation (70) shows that the explicitly correlated kinetic-balance condition for three particles contains the momentum operator to the power of seven, which is unfavorable from a computational point of view. However, we can observe that the power of the momentum operators decreases with increasing orders of  $c$ . The leading terms with respect to  $c$  are the one-fermion kinetic-balance terms and ensure the non-relativistic limit.

For the assessment of the general properties of an  $N$ -fermion kinetic-balance condition, let us first re-write the two-fermion kinetic balance condition, equations (50)–(53), in a general form similar to equation (70):

$$d_i^{(2)}(c) = k_i^{(2)}(m_1, m_2) \times c^{(4-u-v)} (\sigma_1^{(2)} \cdot \mathbf{p}_1)^u (\sigma_2^{(2)} \cdot \mathbf{p}_2)^v, \quad (74)$$

where the multiplicative prefactors  $k_i^{(2)}(m_1, m_2)$  depend on the masses of the two fermions and the positive semi-definite exponents,  $u$  and  $v$ , obey the constraints  $0 \leq (u + v) \leq 3$ .

By comparing the results for two- and three-fermion systems, equations (70) and (74), we obtain for the  $N$ -fermion

case:

$$d_i^{(N)}(c) = k_i^{(N)}(m_1, \dots, m_N) \times c^{(2N-u)} \prod_{j=1}^N (\boldsymbol{\sigma}_j^{(N)} \cdot \mathbf{p}_j)^{u_j} \quad (75)$$

where we skipped the explicit derivation. The power of  $c$ ,  $2N - u$ , and the power of the  $\boldsymbol{\sigma}_j^{(N)} \cdot \mathbf{p}_j$  operator,  $u_j$ , are determined in the kinetic-balance solution by

$$0 \leq u = \sum_{j=1}^N u_j \leq 2N + 1. \quad (76)$$

High powers of the momentum operator is unfortunate from a computational point of view, but with the complete set of kinetic-balance conditions at hand for any set of non-separable  $N$ -particle basis functions, equations (75) and (76), one may introduce a hierarchy of approximate kinetic-balance conditions and investigate their properties systematically.

As an example, we present the approximate kinetic-balance condition for a three-electron system (in Hartree atomic units and with  $m_e = 1$  for the electron mass) where only the leading terms in  $c$  are included:

$$|lll\rangle = \left( 48c^6 \mathbf{1}_8 - 14 \left( (\boldsymbol{\sigma}_1^{(3)} \cdot \mathbf{p}_1)^2 + (\boldsymbol{\sigma}_2^{(3)} \cdot \mathbf{p}_2)^2 + (\boldsymbol{\sigma}_3^{(3)} \cdot \mathbf{p}_3)^2 \right) c^4 \right) \Theta(\mathbf{r}) \equiv U_{lll}^{(3)} \Theta(\mathbf{r}), \quad (77)$$

$$|lls\rangle = (\boldsymbol{\sigma}_3^{(3)} \cdot \mathbf{p}_3) \left( \left( -(\boldsymbol{\sigma}_1^{(3)} \cdot \mathbf{p}_1)^2 - (\boldsymbol{\sigma}_2^{(3)} \cdot \mathbf{p}_2)^2 - 7(\boldsymbol{\sigma}_3^{(3)} \cdot \mathbf{p}_3)^2 \right) c^3 + 24c^5 \mathbf{1}_8 \right) \Theta(\mathbf{r}) \equiv U_{lls}^{(3)} \Theta(\mathbf{r}), \quad (78)$$

$$|lsl\rangle = (\boldsymbol{\sigma}_2^{(3)} \cdot \mathbf{p}_2) \left( \left( -(\boldsymbol{\sigma}_1^{(3)} \cdot \mathbf{p}_1)^2 - 7(\boldsymbol{\sigma}_2^{(3)} \cdot \mathbf{p}_2)^2 - (\boldsymbol{\sigma}_3^{(3)} \cdot \mathbf{p}_3)^2 \right) c^3 + 24c^5 \mathbf{1}_8 \right) \Theta(\mathbf{r}) \equiv U_{lsl}^{(3)} \Theta(\mathbf{r}), \quad (79)$$

$$|lss\rangle = 12(\boldsymbol{\sigma}_2^{(3)} \cdot \mathbf{p}_2)(\boldsymbol{\sigma}_3^{(3)} \cdot \mathbf{p}_3) c^4 \Theta(\mathbf{r}) \equiv U_{lss}^{(3)} \Theta(\mathbf{r}), \quad (80)$$

$$|sll\rangle = (\boldsymbol{\sigma}_1^{(3)} \cdot \mathbf{p}_1) \left( \left( -7(\boldsymbol{\sigma}_1^{(3)} \cdot \mathbf{p}_1)^2 - (\boldsymbol{\sigma}_2^{(3)} \cdot \mathbf{p}_2)^2 - (\boldsymbol{\sigma}_3^{(3)} \cdot \mathbf{p}_3)^2 \right) c^3 + 24c^5 \mathbf{1}_8 \right) \Theta(\mathbf{r}) \equiv U_{sll}^{(3)} \Theta(\mathbf{r}), \quad (81)$$

$$|sls\rangle = 12(\boldsymbol{\sigma}_1^{(3)} \cdot \mathbf{p}_1)(\boldsymbol{\sigma}_3^{(3)} \cdot \mathbf{p}_3) c^4 \Theta(\mathbf{r}) \equiv U_{sls}^{(3)} \Theta(\mathbf{r}), \quad (82)$$

$$|ssl\rangle = 12(\boldsymbol{\sigma}_1^{(3)} \cdot \mathbf{p}_1)(\boldsymbol{\sigma}_2^{(3)} \cdot \mathbf{p}_2) c^4 \Theta(\mathbf{r}) \equiv U_{ssl}^{(3)} \Theta(\mathbf{r}), \quad (83)$$

$$|sss\rangle = -6(\boldsymbol{\sigma}_1^{(3)} \cdot \mathbf{p}_1)(\boldsymbol{\sigma}_2^{(3)} \cdot \mathbf{p}_2)(\boldsymbol{\sigma}_3^{(3)} \cdot \mathbf{p}_3) c^3 \Theta(\mathbf{r}) \equiv U_{sss}^{(3)} \Theta(\mathbf{r}), \quad (84)$$

with the  $\boldsymbol{\sigma}_i^{(3)} \cdot \mathbf{p}_i$  operators defined in equations (71)–(72).  $\Theta(\mathbf{r})$  with  $\mathbf{r} = (\mathbf{r}_1, \mathbf{r}_2, \mathbf{r}_3)^T$  is the non-relativistic limit of  $\Psi(\mathbf{r})$ . We see that the lowest order of  $c$  to consider is 3 due to the  $|sss\rangle$  component. Equations (77)–(84) can be considered as a minimal explicitly correlated kinetic-balance condition for a three-electron system.

## 6. Basis-set expansion and numerical results

In practice, a many-particle wave function can be expanded into a basis set

$$\Psi(\mathbf{r}) = \sum_i \sum_{\lambda \in \Lambda} C_i^\lambda \Phi_i^\lambda(\mathbf{r}) \quad (85)$$

where  $C_i^\lambda$  are the expansion coefficients and  $\Phi_i^\lambda(\mathbf{r})$  are the basis functions.  $\Lambda$  is the set of all component-index strings consisting of  $l$ 's and  $s$ 's according to equation (26), i.e., it is the set of  $2^N$  strings of such indices of length  $N$  for an  $N$ -fermion basis function. For the sake of clarity, we explicitly provide the basis functions for the two-fermion case,

$$\begin{aligned} \Phi_i^{ll} &= \begin{bmatrix} \tilde{\Phi}_i^{ll} \\ 0 \\ 0 \\ 0 \end{bmatrix}, & \Phi_i^{ls} &= \begin{bmatrix} 0 \\ \tilde{\Phi}_i^{ls} \\ 0 \\ 0 \end{bmatrix}, \\ \Phi_i^{sl} &= \begin{bmatrix} 0 \\ 0 \\ \tilde{\Phi}_i^{sl} \\ 0 \end{bmatrix}, & \text{and } \Phi_i^{ss} &= \begin{bmatrix} 0 \\ 0 \\ 0 \\ \tilde{\Phi}_i^{ss} \end{bmatrix}, \end{aligned} \quad (86)$$

where the four-dimensional basis functions  $\tilde{\Phi}_i^{ll}$ ,  $\tilde{\Phi}_i^{ls}$ ,  $\tilde{\Phi}_i^{sl}$ , and  $\tilde{\Phi}_i^{ss}$  are promoted to 16-dimensional functions for a compact notation of the expansion in equation (85); note that we write '0' in equation (86) to indicate four-dimensional null vectors for the sake of brevity. Eventually, these four-dimensional basis functions are to be expressed in terms of basis functions  $\Theta_i$  that represent the common non-relativistic limit  $\Theta$  according to the analysis presented above.

A transformation, similar to that in equation (12) for the one-fermion case, can be formulated for the explicitly correlated kinetic-balance condition in the two-fermion case,

$$U_{\text{KB}}^{(2)} = \begin{bmatrix} \frac{U_{ll}^{(2)}}{|U_{ll}^{(2)}|} & \mathbf{0}_4 & \mathbf{0}_4 & \mathbf{0}_4 \\ \mathbf{0}_4 & \frac{U_{ls}^{(2)}}{|U_{ls}^{(2)}|} & \mathbf{0}_4 & \mathbf{0}_4 \\ \mathbf{0}_4 & \mathbf{0}_4 & \frac{U_{sl}^{(2)}}{|U_{sl}^{(2)}|} & \mathbf{0}_4 \\ \mathbf{0}_4 & \mathbf{0}_4 & \mathbf{0}_4 & \frac{U_{ss}^{(2)}}{|U_{ss}^{(2)}|} \end{bmatrix}, \quad (87)$$

in the notation introduced in equations (50)–(53) and with a normalization introduced for each basis-function component

**Table 1.** Ground-state energy of the two-electron helium atom with fixed nucleus obtained for increasing basis-set sizes.  $\Delta E_R$  and  $\Delta E_{NR}$  are the differences between the calculated relativistic and non-relativistic energies, respectively, with respect to the reference values.  $n$  is the number of basis functions,  $\Theta_i$ , defined in equations (91) and (93). The parameters of the basis functions are deposited in the supplementary data and the value for the speed of light was set to 137.0359895 atomic units.

$n$	$E_R [E_h]$	$\Delta E_R [E_h]$	$E_{NR} [E_h]$	$\Delta E_{NR} [E_h]$
10	-2.89757665	0.00628019	-2.89744422	0.00628016
20	-2.90288205	0.00097479	-2.90275061	0.00097377
50	-2.90382266	0.00003418	-2.90369103	0.00003335
100	-2.90384822	0.00000862	-2.90372140	0.00000298
200	-2.90385566	0.00000118	-2.90372429	0.00000009
300	-2.90385674	0.00000010	-2.90372430	0.00000008
[37]	-2.90385684	[52]	-2.90372438	

according to

$$|U_{ll}^{(2)}\rangle \equiv \sqrt{\langle \tilde{\Phi}_i^{\parallel} | \tilde{\Phi}_i^{\parallel} \rangle} = \sqrt{\langle \Theta_i | U_{ll}^{(2),\dagger} \cdot U_{ll}^{(2)} | \Theta_i \rangle} \quad (88)$$

and so forth for the other  $\lambda$  labels; note that we dropped the basis-function index on the left-hand side for the sake of brevity. Essentially, we normalize each component of each basis function individually to ensure numerical stability when solving the eigenvalue problem. This procedure can be understood as the relativistic counterpart of the quasi-normalization in pre-Born–Oppenheimer theory [51]. Hence, explicit normalization of a trial wave function has to be taken into account when the energy is calculated.

In full analogy to the two-fermion case, we construct  $U_{KB}^{(3)}$  from equations (77)–(84). In general, the  $N$ -fermion trial wave function is expressed in terms of the transformation as

$$\begin{aligned} \Psi(\mathbf{r}) &= \sum_i \begin{bmatrix} C_i^{\parallel\dots l} \frac{U_{ll\dots l}^{(N)}}{|U_{ll\dots l}^{(N)}|} \Theta_i(\mathbf{r}) \\ \vdots \\ C_i^\lambda \frac{U_\lambda^{(N)}}{|U_\lambda^{(N)}|} \Theta_i(\mathbf{r}) \\ \vdots \\ C_i^{ss\dots s} \frac{U_{ss\dots s}^{(N)}}{|U_{ss\dots s}^{(N)}|} \Theta_i(\mathbf{r}) \end{bmatrix} \\ &\equiv \sum_i C_i \cdot [U_{KB}^{(N)} \cdot \Theta_i^{(N)}(\mathbf{r})], \end{aligned} \quad (89)$$

where the  $U_\lambda^{(N)}/|U_\lambda^{(N)}|$  are the entries of the diagonal matrix  $U_{KB}^{(N)}$  normalized by

$$|U_\lambda^{(N)}| \equiv \sqrt{\langle \tilde{\Phi}_i^\lambda | \tilde{\Phi}_i^\lambda \rangle} = \sqrt{\langle \Theta_i | U_\lambda^{(N),\dagger} \cdot U_\lambda^{(N)} | \Theta_i \rangle} \quad (90)$$

(with the index  $i$  dropped for the sake of brevity as before). The vector  $\Theta_i^{(N)}$  contains the non-relativistic limit,  $\Theta_i$ ,  $2^N$  times as entry, i.e.,  $\Theta_i^{(N)} = (\Theta_i, \Theta_i, \dots, \Theta_i)$ .

### 6.1. Numerical results

As an example, we present numerical results for a standard two-electron system: two electrons moving in the central

potential of a helium nucleus within the Born–Oppenheimer approximation. Our starting point is a non-relativistic basis set, which corresponds to  $L = 0$  total spatial angular momentum,  $p = +1$  parity, and  $S = 0$  total electron spin quantum numbers, and which is antisymmetrized according to the Pauli principle:

$$\begin{aligned} \Theta_i(\mathbf{r}) &= \Theta_i'(\mathbf{r}_1, \mathbf{r}_2) \\ &\times \frac{1}{\sqrt{2}} \left[ \begin{pmatrix} 1 \\ 0 \end{pmatrix} \otimes \begin{pmatrix} 0 \\ 1 \end{pmatrix} - \begin{pmatrix} 0 \\ 1 \end{pmatrix} \otimes \begin{pmatrix} 1 \\ 0 \end{pmatrix} \right], \end{aligned} \quad (91)$$

where we introduced the explicit form of the spin functions

$$\alpha = \begin{pmatrix} 1 \\ 0 \end{pmatrix} \quad \text{and} \quad \beta = \begin{pmatrix} 0 \\ 1 \end{pmatrix}. \quad (92)$$

In this notation, the four-dimensional structure of the non-relativistic limit is highlighted in agreement with equation (65). In equation (91), the spatial part can be any non-separable two-particle function and in our calculations it is an explicitly correlated Gaussian function with  $L = 0$  and  $p = +1$ ,

$$\Theta_i'(\mathbf{r}_1, \mathbf{r}_2) = \exp\left(-\frac{1}{2} \mathbf{r}^T (\mathbf{A}_i \otimes \mathbf{1}_3) \mathbf{r}\right), \quad (93)$$

where  $\mathbf{r} = (\mathbf{r}_1, \mathbf{r}_2)^T$  and the elements of the symmetric, positive definite matrix,  $\mathbf{A}_i \in \mathbb{R}^{2 \times 2}$ , are parametrized by

$$\begin{aligned} \{\mathbf{A}_i\}_{kl} &= \delta_{kl} \exp(\alpha_{kl,i}) + 0.1(\delta_{kl} - 1) \exp(-\alpha_{kl,i}) \\ &\text{with } k, l \in \{1, 2\}. \end{aligned} \quad (94)$$

The  $\alpha_{kl,i}$  values are optimized stochastically to minimize the relativistic energy. Trial values for  $\alpha_{kl,i}$  were generated from a normal distribution as in [51] (see also references therein). The optimized parameter values of  $\mathbf{A}_i$  are deposited in the supplementary information.

With equation (89) (see also equations (50)–(53) for the two-particle case) we generate a kinetically balanced basis set from  $\Theta_i(\mathbf{r})$ , equation (91), for the relativistic calculations and

minimize the Rayleigh quotient, equation (4),

$$E[\mathbf{H}_{DTS}^{(2)}, \{\Theta_i(\mathbf{r})\}] = \frac{\left\langle \sum_{ij} \mathbf{C}_i^* \mathbf{C}_j \langle \mathbf{U}_{\text{KB}}^{(2)} \cdot \Theta_i^{(2)}(\mathbf{r}) | \mathbf{H}_{DTS}^{(2)} | \mathbf{U}_{\text{KB}}^{(2)} \cdot \Theta_j^{(2)}(\mathbf{r}) \rangle \right\rangle}{\left\langle \sum_{ij} \mathbf{C}_i^* \mathbf{C}_j \langle \mathbf{U}_{\text{KB}}^{(2)} \cdot \Theta_i^{(2)}(\mathbf{r}) | \mathbf{U}_{\text{KB}}^{(2)} \cdot \Theta_j^{(2)}(\mathbf{r}) \rangle \right\rangle} \quad (95)$$

with respect to the expansion coefficients  $C_i^\lambda$  by solving the generalized eigenvalue problem

$$\mathbf{H}\mathbf{C} = \mathbf{E}\mathbf{S}\mathbf{C}. \quad (96)$$

In equation (96), the Hamiltonian matrix,  $\mathbf{H}$ , has a block structure with  $\mathbf{H}_{ij} = \langle \mathbf{U}_{\text{KB}}^{(2)} \cdot \Theta_i^{(2)}(\mathbf{r}) | \mathbf{H}_{DTS}^{(2)} | \mathbf{U}_{\text{KB}}^{(2)} \cdot \Theta_j^{(2)}(\mathbf{r}) \rangle \in \mathbb{R}^{2^N \times 2^N}$  ( $i, j=1, 2, \dots, n$ ) and similarly the overlap matrix,  $\mathbf{S}$ , contains  $\mathbf{S}_{ij} = \langle \mathbf{U}_{\text{KB}}^{(2)} \cdot \Theta_i^{(2)}(\mathbf{r}) | \mathbf{U}_{\text{KB}}^{(2)} \cdot \Theta_j^{(2)}(\mathbf{r}) \rangle \in \mathbb{R}^{2^N \times 2^N}$  ( $i, j=1, 2, \dots, n$ ) for  $n$  basis functions and for two electrons,  $N=2$ . Accordingly,  $\mathbf{C} \in \mathbb{R}^{n \times 2^{2N}}$  is a matrix containing the expansion coefficients  $C_i^\lambda$  and  $\mathbf{E}$  is an  $(n \times 2^{2N})$ -dimensional diagonal matrix with the energies on its diagonal.

The ground-state energy eigenvalue of the helium atom is obtained from equation (96) by direct solution of the generalized eigenvalue problem in the stochastically optimized basis set (see table 1). The non-relativistic energies, also given in table 1, were obtained from the generalized eigenvalue problem solved for the Schrödinger Hamiltonian in the basis of the non-relativistic basis functions of equation (91), containing the parameters obtained in the relativistic calculations (see the supporting information for details). As it can be seen from the data in table 1, both the relativistic and the non-relativistic energies converge with increasing basis-set size towards the reference data in a variationally stable fashion.

## 7. Conclusions

The kinetic-balance condition for the one-fermion case ensures variational stability in orbital-based approaches to first-quantized relativistic many-fermion theory. In this paper, we derived a kinetic-balance condition for general, non-separable  $N$ -particle basis functions. Similarly to the derivation of a one-particle kinetic-balance condition, we set out from the assumption that the potential energy contributions are small compared to the rest energies of the fermions. We arrived at an  $N$ -particle kinetic balance condition by combining the well-known multiplication properties of the Pauli matrices with the row-elimination approach of solving linear systems of equations. In agreement with the one-fermion case, the  $N$ -particle kinetic-balance condition also ensures that the correct non-relativistic limit is obtained for an infinite speed of light. It had been anticipated, however, that the  $N$ -particle kinetic-balance condition provides better stability when solving the first-quantized Dirac Hamiltonian variationally with an explicitly correlated basis set, and hence

suggested that the requirement of matching the non-relativistic limit is a necessary but not a sufficient condition.

We demonstrated that the variational solution of the Dirac equation is stable for the ground state of the two-fermion helium atom when a relativistic basis set is generated from explicitly correlated Gaussian functions using the  $N$ -particle kinetic balance condition for  $N=2$ .

Concerning the general applicability of our results, the theoretical expressions and our preliminary investigations show that the direct use of the full  $N$ -particle kinetic-balance condition becomes tedious and computationally expensive for more than two fermions. However, it might be possible to reduce the computational cost by systematically eliminating terms of high order in momentum operators from the full expressions and, at the same time, retain variational stability for the solutions. A systematic investigation of the variational stability under such approximations is beyond the scope of the present paper and left for future work.

## Acknowledgments

This work has been supported by the Swiss National Science Foundation SNF (project 200020\_156598). EM thanks the Hungarian Scientific Research Fund (OTKA, NK83583) for financial support.

## Appendix A

### A.1. Tracy–Singh product

The Tracy–Singh product [53] is defined as

$$\mathbf{A}_{\text{tsp}} = \mathbf{B} \boxtimes \mathbf{C} = \left[ (\mathbf{B}_{ij} \otimes \mathbf{C}_{uv}) \right] = \begin{bmatrix} (\mathbf{B}_{11} \otimes \mathbf{C}_{uv}) & \cdots & (\mathbf{B}_{1n} \otimes \mathbf{C}_{uv}) \\ \vdots & & \vdots \\ (\mathbf{B}_{m1} \otimes \mathbf{C}_{uv}) & \cdots & (\mathbf{B}_{mn} \otimes \mathbf{C}_{uv}) \end{bmatrix} \quad (97)$$

where  $\mathbf{B} = [\mathbf{B}_{ij}]$  and  $\mathbf{C} = [\mathbf{C}_{uv}]$  are two matrices of dimension  $(m \times n)$  and  $(p \times q)$ , respectively. They are partitioned block-wise in terms of the matrices  $\mathbf{B}_{ij}$  and  $\mathbf{C}_{uv}$ .  $\mathbf{A}_{\text{tsp}}$  is a matrix of dimension  $(mp \times nq)$ . It is partitioned block-wise with the elements being the matrices  $(\mathbf{B}_{ij} \otimes \mathbf{C}_{uv})$ . The Tracy–Singh product may be considered a more general form of the Kronecker product

$$\mathbf{A}_{\text{kp}} = \mathbf{B} \otimes \mathbf{C} = \left[ (b_{ij} c_{uv}) \right] = \begin{bmatrix} b_{11}\mathbf{C} & \cdots & b_{1n}\mathbf{C} \\ \vdots & & \vdots \\ b_{m1}\mathbf{C} & \cdots & b_{mn}\mathbf{C} \end{bmatrix} \quad (98)$$

where  $b_{ij}$  and  $c_{uv}$  are the matrix elements of  $\mathbf{B}$  and  $\mathbf{C}$ , respectively.  $\mathbf{A}_{\text{kp}}$  is a matrix of dimension  $(mp \times nq)$ . The two matrices  $\mathbf{A}_{\text{tsp}}$  and  $\mathbf{A}_{\text{kp}}$  are identical in the case that  $\mathbf{B}$  and  $\mathbf{C}$  are not partitioned (or partitioned into  $(1 \times 1)$  blocks). Generally the two products are related through a permutation

of the row and column space of either matrix [54–56]

$$\mathbf{P}^T(\mathbf{B}_1 \otimes \dots \otimes \mathbf{B}_n)\mathbf{Q} = \mathbf{B}_1 \boxtimes \dots \boxtimes \mathbf{B}_n \quad (99)$$

where  $\mathbf{P}$  and  $\mathbf{Q}$  are the permutation matrices for the row and the column space and  $n$  is the number of matrices involved. For vectors  $\mathbf{v}_i$ , we find the relation

$$\mathbf{P}^T(\mathbf{v}_1 \otimes \dots \otimes \mathbf{v}_n) = \mathbf{v}_1 \boxtimes \dots \boxtimes \mathbf{v}_n. \quad (100)$$

The partitioning of the matrices and vectors depends on the permutation matrices  $\mathbf{P}$  and  $\mathbf{Q}$ . If all matrices are square and symmetrically partitioned, the two permutation matrices are identical [54]  $\mathbf{P} = \mathbf{Q}$  and the two products are related through a unitary transformation.

### A.2. Row reduction and row reduced echelon form

Systems of linear equations are conveniently solved by first representing them in matrix form

$$\mathbf{A} \cdot \mathbf{x} - \mathbf{b} = 0, \quad (101)$$

where  $\mathbf{A}$  is a matrix containing the linear factors.  $\mathbf{x}$  is a vector and contains the values which are to be determined and  $\mathbf{b}$  is a vector containing the constant factors of the linear system. A reliable method of solving such a linear system is row reduction, i.e., Gaussian elimination. It involves performing a series of operations on the augmented form

$$\mathbf{A}_{\text{aug}} = [\mathbf{A}|\mathbf{b}] \quad (102)$$

until it is in row-reduced echelon form. The row-reduced echelon form is

$$\mathbf{A}_{\text{re}} = [\mathbf{1}|\mathbf{b}'] \quad (103)$$

for systems with a unique solution. Possible operations are permutation of two rows, multiplication of individual rows with a constant scalar factor and evaluating the difference of two rows.

## References

- [1] Reiher M and Wolf A 2015 *Relativistic Quantum Chemistry* 2nd edn (Weinheim: Wiley-VCH)
- [2] Dyall K G and Faegri K 2007 *Introduction to Relativistic Quantum Chemistry* (New York: Oxford University Press)
- [3] Simmen B and Reiher M 2014 Relativistic quantum theory of many-electron systems *Many-Electron Approaches Physics, Chemistry and Mathematics* ed V Blum and L Delle Site (Dordrecht: Springer) pp 3–29
- [4] Barysz M and Ishikawa Y 2010 Relativistic methods for chemists *Challenges and Advances in Computational Chemistry and Physics* 10 (Dordrecht: Springer)
- [5] Hirao K and Ishikawa Y 2004 *Recent Advances in Relativistic Molecular Theory* (Singapore: World Scientific)
- [6] Schwerdtfeger P 2002 *Relativistic Electronic Structure Theory—Fundamentals* (Amsterdam: Elsevier)
- [7] Hess B A 2003 *Relativistic Effects in Heavy-Element Chemistry and Physics* (Chichester: Wiley)
- [8] Peng D and Reiher M 2012 *Theor. Chem. Acc.* **131** 1081
- [9] Lee Y S and McLean A D 1982 *J. Chem. Phys.* **76** 735
- [10] Stanton R E and Havriliak S 1984 *J. Chem. Phys.* **81** 1910
- [11] Kutzelnigg W 1984 *Int. J. Quantum Chem.* **25** 107
- [12] Ishikawa Y, Binning R C and Sando K M 1983 *Chem. Phys. Lett.* **101** 111
- [13] Dyall K G, Grant I P and Wilson S 1984 *J. Phys. B: At. Mol. Phys.* **493** 493
- [14] Pestka G 2004 *Phys. Scripta* **69** 203
- [15] Kutzelnigg W 2007 *J. Chem. Phys.* **126** 201103
- [16] Sun Q, Liu W and Kutzelnigg W 2011 *Theor. Chem. Acc.* **129** 423
- [17] Dyall K G 1994 *Chem. Phys. Lett.* **224** 186
- [18] Jensen H J A, Dyall K G, Saue T and Fægri K Jr 1996 *J. Chem. Phys.* **104** 4083
- [19] Visscher L, Lee T J and Dyall K G 1996 *J. Chem. Phys.* **105** 8769
- [20] Laerdahl J K, Saue T and Fægri K Jr 1997 *Theor. Chem. Acc.* **97** 177
- [21] Thyssen J 2001 Development and application of methods for correlated relativistic calculations of molecular properties *PhD Thesis* University of Southern Denmark, Odense, Denmark
- [22] Visscher L, Eliav E and Kaldor U 2001 *J. Chem. Phys.* **115** 9720
- [23] Fleig T, Olsen J and Visscher L 2003 *J. Chem. Phys.* **119** 2963
- [24] Pernpointner M and Visscher L 2003 *J. Comput. Chem.* **24** 754
- [25] Yanai T, Harrison R J, Nakajima T, Ishikawa Y and Hirao K 2006 *Int. J. Quantum Chem.* **107** 1382
- [26] Fleig T, Jensen H J A, Olsen J and Visscher L 2006 *J. Chem. Phys.* **124** 104106
- [27] Knecht S, Jensen H J A and Fleig T 2010 *J. Chem. Phys.* **132** 014108
- [28] Thyssen J, Fleig T and Jensen H J A 2008 *J. Chem. Phys.* **129** 034109
- [29] Abe M, Gopakumar G, Nakajima T and Hirao K 2008 Relativistic multireference perturbation theory: complete active-space second-order perturbation theory (CASPT2) with the four-component Dirac Hamiltonian *Challenges Adv. Comput. Chem. Phys.* ed J Leszczynski (Dordrecht: Springer) p 157
- [30] Knecht S, Legeza O and Reiher M 2014 *J. Chem. Phys.* **140** 041101
- [31] Ten-no S and Yamaki D 2012 *J. Chem. Phys.* **137** 131101
- [32] Li Z, Shao S and Liu W 2012 *J. Chem. Phys.* **136** 144117
- [33] Pestka G 1998 *J. Phys. A: Math. Gen.* **31** 6243
- [34] Pestka G and Karwowski J 2003 Hylleraas-CI Approach to dirac-coulomb equation *Explicitly Correlated Wave Functions in Chemistry and Physics* ed J Rychlewski (Dordrecht: Kluwer) pp 331–46
- [35] Pestka G, Tatewaki H and Karwowski J 2004 *Phys. Rev. A* **70** 6
- [36] Pestka G, Bylicki M and Karwowski J 2006 *J. Phys. B: At. Mol. Opt. Phys.* **39** 2979
- [37] Pestka G, Bylicki M and Karwowski J 2007 *J. Phys. B: At. Mol. Opt. Phys.* **40** 2249
- [38] Bylicki M, Pestka G and Karwowski J 2008 *Phys. Rev. A* **77** 44501
- [39] Pestka G, Bylicki M and Karwowski J 2012 *J. Math. Chem.* **50** 510
- [40] Dirac P A M 1928 *Proc. Roy. Soc. London A* **117** 610
- [41] Dirac P A M 1928 *Proc. Roy. Soc. London A* **118** 351
- [42] Esteban M J, Lewin M and Séré E 2008 *Bull. Amer. Math. Soc.* **45** 535
- [43] Thaller B 1992 *The Dirac Equation* (Berlin: Springer)
- [44] Mark F and Schwarz W H E 1982 *Phys. Rev. Lett.* **48** 673
- [45] Schwarz W H E and Wallmeier H 1982 *Mol. Phys.* **46** 1045
- [46] Schwarz W H E and Wechsel-Trakowski E 1982 *Chem. Phys. Lett.* **85** 94

- [47] Dyllal K G 1994 *J. Chem. Phys.* **100** 2118
- [48] Pestka G and Karwowski J 2003 *Collect. Czech. Chem. Commun.* **68** 275
- [49] Saue B T, Faegri K, Helgaker T and Gropen O 1997 *Mol. Phys.* **91** 937
- [50] Dyllal K G 2012 *Chem. Phys.* **395** 35
- [51] Mátyus E and Reiher M 2012 *J. Chem. Phys.* **137** 024104
- [52] Freund D E, Huxtable B D and Morgan J D III 1984 *Phys. Rev. A* **29** 980
- [53] Tracy S and Singh P 1972 *Stat. Neerl.* **26** 143
- [54] Wei Y and Zhang F 2000 *Hadron. J. Suppl.* **15** 327
- [55] Horn R A and Mathias R 1992 *Linear Algebr. Appl.* **172** 337
- [56] Wansbeek T 1991 *Linear Algebr. Appl.* **149** 165



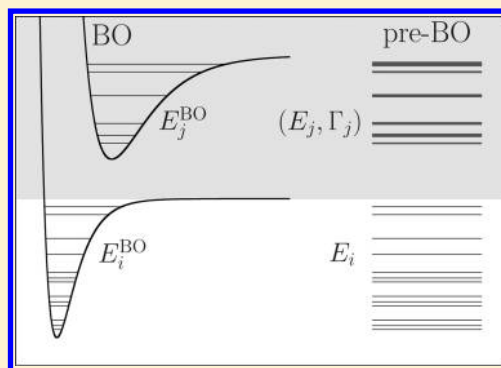
# On the Calculation of Resonances in Pre-Born–Oppenheimer Molecular Structure Theory

Edit Mátyus\*

Laboratory of Molecular Structure and Dynamics, Institute of Chemistry, Eötvös University, P.O. Box 32, H-1518, Budapest 112, Hungary

**S** Supporting Information

**ABSTRACT:** The main motivation for this work is the exploration of rotational–vibrational states corresponding to electronic excitations in a pre-Born–Oppenheimer quantum theory of molecules. These states are often embedded in the continuum of the lower-lying dissociation channel of the same symmetry and thus are thought to be resonances. To calculate rovibronic resonances, the pre-Born–Oppenheimer variational approach of [*J. Chem. Phys.* **2012**, *137*, 024104], based on the usage of explicitly correlated Gaussian functions and the global vector representation, is extended with the complex coordinate rotation method. The developed computer program is used to calculate resonance energies and widths for the three-particle positronium anion,  $\text{Ps}^-$ , and the four-particle positronium molecule,  $\text{Ps}_2$ . Furthermore, the excited bound and resonance rovibronic states of the four-particle  $\text{H}_2$  molecule are also considered. Resonance energies and widths are estimated for the lowest-energy resonances of  $\text{H}_2$  beyond the  $b^3 \sum_u^+$  continuum.



## INTRODUCTION

The present work is devoted to conceptual and computational problems in pre-Born–Oppenheimer (pre-BO) molecular structure theory. Without the Born–Oppenheimer (BO) approximation,<sup>1–3</sup> in a “pre-BO world”, we can gain in accuracy for the numerical results but lose a central paradigm for the well-accustomed concepts of chemistry. The reconstruction or interpretation of many common chemical concepts becomes a real challenge. One of these famous challenges, the problem of the quantum structure of molecules, has been recognized long ago<sup>4–7</sup> and studied by many authors.<sup>8–20</sup>

In the present work we address another challenge, the status of electronically excited rotational–vibrational states in a pre-BO quantum mechanical description. In a pre-BO description there are no electronic states with corresponding potential energy curves or surfaces on which the rotational–vibrational Schrödinger equation could be solved. In addition, rotational–vibrational states corresponding to electronic excitations are often embedded in the lowest-lying dissociation channel of the system (Figure 1) prone to predissociation.<sup>21</sup> These rovibronic states are thus accessible in a pre-BO description only as resonances. These rovibronic resonances are characterized with some energy and width corresponding to a finite nonradiative (predissociative) lifetime. Our aim is to explore how these properties can be calculated in a pre-BO approach.

As for the numerical results, there are practical approaches used for the calculation of quasi-bound states in molecular science.<sup>22–24</sup> The stabilization technique, a very simple computational tool, has been used to identify resonances and to estimate the resonance energy<sup>25–27</sup> and can also be extended

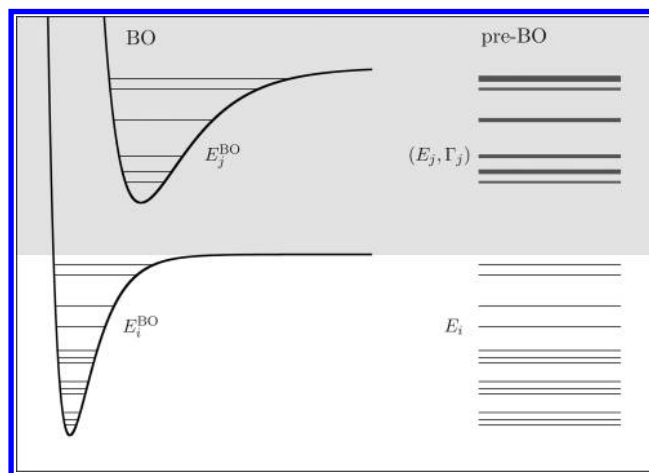


**Figure 1.** Motivation for this work: calculation of rovibronic levels corresponding to electronically excited states, which are bound in the Born–Oppenheimer description but which appear as resonances in pre-Born–Oppenheimer molecular structure theory.

to the calculations of the width.<sup>28–31</sup> The complex coordinate rotation method<sup>32–34</sup> is a neat mathematical approach for the calculation of the resonance energy and width and has been used in several cases,<sup>23,24</sup> for example in rotational–vibrational

**Special Issue:** Joel M. Bowman Festschrift

**Received:** January 30, 2013

**Revised:** May 11, 2013

**Published:** May 15, 2013

calculations on a potential energy surface within the Born–Oppenheimer (BO) theory.<sup>31,35</sup> The usage of complex absorbing potentials<sup>36–38</sup> has been a popular technique in molecular spectroscopy and quantum reaction kinetics with many applications.<sup>39–41</sup> There exist also more involved and specialized approaches, such as the solution of the Faddeev–Merkuriev integral equations.<sup>42,43</sup>

The present work is organized as follows. First, the necessary theoretical framework is described for the variational solution of the Schrödinger equation for bound states of few-particle systems. Then, this approach is extended for the identification and calculation of quasi-bound states. Next, numerical examples are presented for the three-particle  $\text{Ps}^-$  and the four-particle  $\text{Ps}_2$ . Finally, the description of excited bound and resonance rovibronic states of the four-particle  $\text{H}_2$  is explored. In the end, we finish with a summary and outlook.

## ■ THEORY AND COMPUTATIONAL STRATEGY

The Schrödinger equation for an  $(n_p + 1)$ -particle system with  $m_i$  masses and  $q_i$  electric charges assigned to the particles is

$$\hat{H}\Psi = E\Psi \quad (1)$$

with the nonrelativistic quantum Hamiltonian in Hartree atomic units

$$\hat{H} = \hat{T} + \hat{V} = -\sum_{i=1}^{n_p+1} \frac{1}{2m_i} \Delta_{r_i} + \sum_{i=1}^{n_p+1} \sum_{j>i}^{n_p+1} \frac{q_i q_j}{|r_i - r_j|} \quad (2)$$

written in laboratory-fixed Cartesian coordinates  $r = (r_1, r_2, \dots, r_{n_p+1})$ .

In the present work we use the bound-state variational approach of ref 44 and (a) combine it with the stabilization technique to quickly identify long-lived resonances and (b) extend it with the complex coordinate rotation method to calculate resonance energies and widths.

**Variational pre-BO Calculations Using Explicitly Correlated Gaussian Functions and the Global Vector Representation.** The overall translation of the center of mass is eliminated by writing the kinetic energy operator in terms of Jacobi Cartesian coordinates, and the translational kinetic energy of the center of mass is subtracted. As an alternative to this approach, the original laboratory-fixed Cartesian coordinates can be used throughout the calculations without any further coordinate transformation employing a special elimination technique for the overall translation during the evaluation of the matrix elements.<sup>45</sup>

The matrix representation of the translationally invariant Hamiltonian is constructed using a symmetry-adapted basis set defined as follows.

A basis function with the quantum numbers  $\lambda = (N, M_N, p)$  and  $\zeta = (S_w, M_{S_w}, S_b, M_{S_b}, \dots)$  ( $a, b, \dots$  label the particle type) is constructed as

$$\Phi^{[\lambda, \zeta]}(r, \sigma) = \hat{\mathcal{A}}\{\phi^{[\lambda]}(r)\chi^{[\zeta]}(\sigma)\} \quad (3)$$

where  $\hat{\mathcal{A}} = (N_{\text{perm}})^{-1/2} \sum_{i=1}^{N_{\text{perm}}} \epsilon_i \hat{P}_i$  is the symmetrization and antisymmetrization operator for bosonic and fermionic-type particles, respectively.  $\hat{P}_i$  ( $i = 1, 2, \dots, N_{\text{perm}}$ ) is an operator permuting identical particles, and  $\epsilon_i = -1$  if  $\hat{P}_i$  corresponds to an odd number of interchanges of fermions; otherwise,  $\epsilon_i = +1$ . ( $N$  denotes here the total spatial (orbital plus rotational) angular momentum quantum number in agreement with the

recommendations of the International Union of Pure and Applied Chemistry.<sup>46</sup> We note that in ref 44 the symbol  $L$  was used in the same sense. Furthermore,  $p$  is the parity, which we call “natural” if  $p = (-1)^N$  and “unnatural” if  $p = (-1)^{N+1}$ . In this work we restrict the discussion to natural-parity states. The total spin quantum number for particles of type  $a$  is  $S_a$ . For example,  $S_p$  and  $S_e$  denote the total spin quantum numbers for the protons and the electrons, respectively.)

The spatial part of the basis functions with natural parity,  $p = (-1)^N$ , is constructed using explicitly correlated Gaussian functions<sup>47–51</sup> and the global vector representation<sup>52–54</sup> as

$$\phi^{[\lambda]}(r; \alpha, u, K) = |\nu|^{2K+N} Y_{NM_N}(\hat{\nu}) \exp\left(-\frac{1}{2} \sum_{i=1}^{n_p+1} \sum_{j>i}^{n_p+1} \alpha_{ij}(r_i - r_j)^2\right) \quad (4)$$

where the  $\hat{\nu} = \nu/|\nu|$  unit vector points in the direction of the global vector,  $\nu = \sum_{i=1}^{n_p+1} u_i^{(0)} r_i$ ,  $Y_{NM_N}$  denotes the  $N$ th order  $M_N$ th degree spherical harmonic function. The spin function,  $\chi^{[\zeta]}$ , is constructed from elementary spin functions so that the resulting function is an eigenfunction of  $\hat{S}_a^2$  and  $(\hat{S}_a)_z$  for each type of particles ( $a, b, \dots$ ) with the quantum numbers  $\zeta = (S_w, M_{S_w}, S_b, M_{S_b}, \dots)$ .

Then, the resulting  $\Phi^{[\lambda, \zeta]}$  basis function has the quantum numbers of the nonrelativistic quantum theory (it is “symmetry-adapted”) and contains free parameters, which can be optimized for an efficient description of the “internal structure” of a system. The free parameters of the spatial function, eq 4, are  $K$ ;  $\alpha$ ,  $\alpha_{ij}$  ( $i = 1, \dots, n_p + 1, j = i + 1, \dots, n_p + 1$ ); and  $u$ ,  $u_i^{(0)}$  ( $i = 1, \dots, n_p + 1$ ) with the restriction  $\sum_{i=1}^{n_p+1} u_i^{(0)} = 0$ , which guarantees translational invariance. The spin functions used in this work do not contain any free parameters.

We only note here that for the positronium molecule,  $\text{Ps}_2$ , as a special case studied in this work, the entire basis function was additionally adapted to the charge-conjugation symmetry of the electrons and the positrons.<sup>55–57</sup>

The matrix elements of the kinetic and potential energy operators corresponding to the basis functions with natural parity, eqs 3 and 4, were evaluated with the pre-BO program according to ref 44.

Since the basis functions are not orthogonal we have to solve a generalized eigenvalue problem

$$Hc_i = E_i S c_i \quad (5)$$

to find the variationally optimal linear combination of the basis functions with the linear combination coefficients  $c_i$  corresponding to the eigenvalue  $E_i$ . The generalized eigenproblem is solved by introducing  $H' = S^{-1/2} H S^{-1/2}$  and  $c'_i = S^{1/2} c_i$ , which simplifies the eigenvalue equation, eq 5, to  $H'c'_i = E_i c'_i$ . In our computations the Cholesky decomposition of  $S$  for the evaluation of  $S^{-1/2}$  as well as the diagonalization of the real, symmetric transformed Hamiltonian matrix,  $H'$ , were carried out by using the LAPACK library routines.<sup>58</sup>

The computational efficiency and usefulness of the variational approach described depend on the parametrization of the basis functions (the choice of the values of  $K$ ,  $\alpha$ , and  $u_i$  for the basis functions  $I = 1, \dots, N_b$ ). For bound-state calculations we adopted the stochastic variational approach<sup>54,59–62</sup> for the optimization of the basis function parameters. The (quasi-)optimization of the parameter set is a very delicate problem, and our recipe includes the following details:<sup>44</sup> (a) a system-

**Table 1. Identified Bound- and Resonance-State Energies and Resonance Widths, in  $E_{\text{h}}$ , of  $\text{Ps}^- = \{e^-, e^-, e^+\}^a$** 

$(N, p, S_-)^b$	$\text{Re}(\mathcal{E})^c$	$\Gamma/2^c$	$\text{Re}(\mathcal{E}_{\text{ref}})^d$	$\Gamma_{\text{ref}}/2^d$	ref
(0,+1,0)	-0.262 005 070 <sup>c</sup>	0 <sup>c</sup>	-0.262 005 070	0	66
(0,+1,0)	-0.076 030 455	$2.152 \times 10^{-5}$	-0.076 030 442	$2.1517 \times 10^{-5}$	64
(0,+1,0)	-0.063 649 173	$4.369 \times 10^{-6}$	-0.063 649 175	$4.3393 \times 10^{-6}$	64
(0,+1,0)	-0.062 609	$2.5 \times 10^{-5}$	-0.062 550	$5.0 \times 10^{-7}$	42
(0,+1,0)	-0.035 341 85	$3.730 \times 10^{-5}$	-0.035 341 885	$3.7329 \times 10^{-5}$	64
(0,+1,0)	-0.029 845 70	$2.781 \times 10^{-5}$	-0.029 846 146	$2.6356 \times 10^{-5}$	64
(0,+1,0)	-0.028 271	$1.8 \times 10^{-5}$	-0.028 200	$7.5 \times 10^{-6}$	42
(0,+1,0)	-0.020 199	$8.800 \times 10^{-5}$	-0.020 213 921	$6.5026 \times 10^{-5}$	64
(0,+1,1)	-0.063 537 352	$2.132 \times 10^{-9}$	-0.063 537 354	$1.5700 \times 10^{-9}$	64
(0,+1,1)	-0.062 591	$2.6 \times 10^{-7}$	-0.062 550	$2.5 \times 10^{-10}$	42
(0,+1,1)	-0.029 369 87	$1.300 \times 10^{-7}$	-0.029 370 687	$9.3950 \times 10^{-8}$	64
(0,+1,1)	-0.028 21	$1.9 \times 10^{-5}$	-0.028 05	$5.0 \times 10^{-8}$	42
(0,+1,1)	-0.017 071	$6.710 \times 10^{-6}$	-0.017 101 172	$3.5609 \times 10^{-7}$	42

<sup>a</sup>The dissociation threshold energies, in  $E_{\text{h}}$ , accessible for both the  $S_- = 0$  and 1 states are  $E(\text{Ps}(1)) = -1/4 = -0.25$ ,  $E(\text{Ps}(2)) = -1/16 = -0.0625$ , and  $E(\text{Ps}(3)) = -1/36 = -0.0277$ . <sup>b</sup> $N$ ,  $p$ , and  $S_-$ : total spatial angular momentum quantum number, parity, and total spin quantum number of the electrons, respectively. <sup>c</sup> $\text{Re}(\mathcal{E})$  and  $\Gamma$ : resonance energy and width with  $\Gamma/2 = -\text{Im}(\mathcal{E})$  calculated in this work. <sup>d</sup> $\text{Re}(\mathcal{E}_{\text{ref}})$  and  $\Gamma_{\text{ref}}$ : resonance energy width with  $\Gamma_{\text{ref}}/2 = -\text{Im}(\mathcal{E}_{\text{ref}})$  taken from refs 42 and 64. <sup>e</sup>Bound state.

adapted random number generator is constructed using a sampling-importance resampling strategy for the generation of trial parameter sets; (b) the acceptance criterion of the generated trial values is based on the linear independence condition and the energy minimization requirement (relying on the variational principle); (c) the selected parameters are fine-tuned using a simple random walk approach or Powell's method.<sup>63</sup>

Furthermore, once a parameter set has been selected or optimized for a system with some quantum numbers, it can be used, "transferred", to parametrize basis functions for the same system with different quantum numbers ("parameter transfer approach"). It is important to emphasize that the basis functions are not transferred since they have a different mathematical form for different quantum numbers, but only the parameter set is taken over from one calculation to another.

**Calculation of Resonances.** The bound-state pre-BO approach described was extended for the calculation of resonance states as follows. First of all, without any change of the computer program, we looked for the quasi-stabilization of higher-energy eigenvalues (higher than the lowest-energy threshold) of the real eigenvalue problem. This application of the stabilization technique<sup>25–27</sup> is a simple, practical test for identifying possible quasi-bound states and was found to be useful as a first check of the higher-energy eigenspectrum. By making full use of the stabilization theory, both the resonance energies and widths could be calculated from consecutive diagonalization of the (real) Hamiltonian matrix corresponding to increasing number of basis functions, which cover increasing boxes of the configuration space.<sup>28–31</sup>

Instead of using this approach, the complex coordinate rotation method (CCRM)<sup>23,24,32–34</sup> was implemented for the calculation of resonance parameters, energies, and widths. The resonance parameters were determined by identifying stabilization points in the complex plane with respect to the coordinate rotation angle and (the size and parametrization of) the basis set. The localized real part of the eigenvalue,  $\text{Re}(\mathcal{E})$ , was taken to be the resonance energy, and the imaginary part provided the resonance width,  $\Gamma = -2\text{Im}(\mathcal{E})$ , which is inversely proportional to the lifetime,  $\tau = \hbar/\Gamma$ .<sup>22</sup>

**Implementation of the Complex Coordinate Rotation Method for the Coulomb Hamiltonian.** The complex

scaling of the coordinates  $r \rightarrow re^{i\theta}$  translates to the replacement of the Hamiltonian  $\hat{H} = \hat{T} + \hat{V}$  with

$$\hat{\mathcal{H}}(\theta) = e^{-2i\theta}\hat{T} + e^{-i\theta}\hat{V} \quad (6)$$

The matrix representation of  $\hat{\mathcal{H}}(\theta)$  is constructed with the matrices of  $\hat{T}$  and  $\hat{V}$  evaluated by the pre-BO program.<sup>44</sup> Then, the eigenvalue equation for  $\hat{\mathcal{H}}(\theta)$  reads as

$$\mathcal{H}(\theta)v_i(\theta) = \mathcal{E}_i(\theta)Sv_i(\theta) \quad (7)$$

where  $S$  is the overlap matrix of the (linearly independent) set of basis functions.  $S$  is eliminated from the equation similarly to the case of the real generalized eigenproblem, eq 5

$$\mathcal{H}'(\theta)v'_i(\theta) = \mathcal{E}_i(\theta)v'_i(\theta) \quad (8)$$

with

$$\begin{aligned} \mathcal{H}'(\theta) &= e^{-2i\theta}T' + e^{-i\theta}V' \\ &= \cos(2\theta)T' + \cos(\theta)V' - i(\sin(2\theta)T' \\ &\quad + \sin(\theta)V') \end{aligned} \quad (9)$$

and

$$T' = S^{-1/2}TS^{-1/2} \text{ and } V' = S^{-1/2}VS^{-1/2} \quad (10)$$

The complex symmetric eigenvalue problem, eq 8, is solved using the LAPACK library routines.<sup>58</sup>

## NUMERICAL RESULTS

The first numerical applications of our implementation were carried out for the notoriously nonadiabatic positronium anion,  $\text{Ps}^- = \{e^-, e^-, e^+\}$ , and for the positronium molecule,  $\text{Ps}_2 = \{e^-, e^-, e^+, e^+\}$ . The reason for the choice of these systems was of technical nature: we observed in bound-state calculations<sup>44</sup> that it was straightforward to find an appropriate parametrization of the basis set for the positronium complexes. Furthermore, comparison of the results with earlier calculations<sup>27,42,64,65</sup> allowed us to check the developed computational methods and gain experience in the localization of the real and imaginary parts of the complex eigenvalues using the complex coordinate rotation method.

Table 2. Identified Bound- and Resonance-State Energies and Resonance Widths, in  $E_{lv}$ , of  $Ps_2 = \{e^-, e^-, e^+, e^+\}^a$ 

$(N, p, c)^b$	$(S_-, S_+)^c$	$Re(\mathcal{E})^d$	$\Gamma/2^d$	$Re(\mathcal{E}_{ref})^e$	$\Gamma_{ref}/2^e$	ref.
(0,+1,+1)	(0,0)	-0.516 003 789 741 <sup>f</sup>	0 <sup>f</sup>	-0.516 003 790 416	0	69
(0,+1,+1)	(0,0)	-0.329 38	$3.03 \times 10^{-3}$	-0.329 4	$3.1 \times 10^{-3}$	65
(0,+1,+1)	(0,0)	-0.291 7	$2.5 \times 10^{-3}$	-0.292 4	$1.95 \times 10^{-3}$	65
(0,+1,-1)	(0,0)	-0.314 677 072 <sup>f</sup>	0 <sup>f</sup>	-0.314 673 3	0	65
(0,+1,-1)	(0,0)	-0.289 789 3	$7.7 \times 10^{-5}$	-0.289 76	$7 \times 10^{-5}$	65
(0,+1,-1)	(0,0)	-0.279 25	$2.3 \times 10^{-4}$	-0.279 13	$1 \times 10^{-4}$	65
(0,+1,+1)	(1,1)	-0.277 2	$5.4 \times 10^{-4}$	-0.276 55	$1.55 \times 10^{-4}$	65
(0,+1,-1)	(1,1)	-0.309 0	$5.7 \times 10^{-3}$	-0.308 14	$1.2 \times 10^{-4}$	65
(0,+1,-1)	(1,1)	-0.273 3	$2.3 \times 10^{-3}$	-0.273 6	$8.5 \times 10^{-4}$	65
(0,+1, $\pm$ 1)	(1,0)/(0,1)	-0.330 287 505 <sup>f</sup>	0 <sup>f</sup>	-0.330 276 81	0	65
(0,+1, $\pm$ 1)	(1,0)/(0,1)	-0.294 3	$3.1 \times 10^{-3}$	-0.293 9	$2.15 \times 10^{-3}$	65
(0,+1, $\pm$ 1)	(1,0)/(0,1)	-0.282	$2 \times 10^{-3}$	-0.282 2	$8.5 \times 10^{-4}$	65

<sup>a</sup>For the five symmetry blocks with different  $(N, p, c)$  quantum numbers and  $(S_-, S_+)$  labels the lowest accessible thresholds are  $Ps(1S) + Ps(1S)$ ,  $Ps(1S) + Ps(2P)$ ,  $Ps(1S) + Ps(2P)$ ,  $Ps(1S) + Ps(1S)$ , and  $Ps(1S) + Ps(2S,2P)$ , respectively.<sup>68</sup> The corresponding energies, in  $E_{lv}$ , are  $E(Ps(1) + Ps(1)) = -1/2 = -0.5$  and  $E(Ps(1) + Ps(2)) = -5/16 = -0.312 5$ . <sup>b</sup> $N, p$ , and  $c$ : total spatial angular momentum quantum number, parity, and charge-conjugation quantum number, respectively. <sup>c</sup> $S_-$  and  $S_+$ : total spin quantum numbers for the electrons and the positrons, respectively. In the last symmetry block,  $(S_-, S_+) = (0, 1)$  and  $(S_-, S_+) = (1, 0)$  are not good quantum numbers because these spin states are coupled due to the charge-conjugation symmetry of the Hamiltonian. <sup>d</sup> $Re(\mathcal{E})$  and  $\Gamma$ : resonance energy and width with  $\Gamma/2 = -Im(\mathcal{E})$  calculated in this work. <sup>e</sup> $Re(\mathcal{E}_{ref})$  and  $\Gamma_{ref}$ : resonance energy and width with  $\Gamma_{ref}/2 = -Im(\mathcal{E}_{ref})$  taken from ref 65. <sup>f</sup>Bound states.

While for the bound-state calculations the basis function parameters were optimized for the lowest-energy level(s) using the variational principle, this handy optimization criterion was not available in the CCRM calculations. Thus, we used optimized bound-state basis sets and enlarged them with linearly independent basis functions for the estimation of the resonance parameters.

Next, we investigated the calculation of some of the excited states of the  $H_2$  molecule. The construction of a reasonably good parametrization for the basis set has turned out to be a challenge. Nevertheless, we describe the essence of our observations and give calculated resonance energy values and approximate widths for the lowest-lying excited states beyond the  $b^3\Sigma_u^+$  repulsive electronic state embedded in the  $H(1) + H(1)$  continuum.

**$Ps^-$ .** In Table 1 bound- and resonance-state parameters ( $N = 0, p = +1$ ) are collected, which were obtained in this work. The basis sets were generated using the energy minimization and the linear independence conditions using a random number generator setup following the strategy described in ref 44. The parameters for the largest basis sets used during the calculations are given in the Supporting Information. The generated basis sets were apparently large and flexible enough to obtain resonance states not only beyond the first but also beyond the second and the third dissociation channels which correspond to  $Ps(1) + e^-$ ,  $Ps(2) + e^-$ , and  $Ps(3) + e^-$ , respectively. As to the accuracy, the (real) variational principle, directly applicable for bound states, is not useful for the assessment of the resonance parameters. Instead, we used benchmarks available in the literature resulting from extensive three-body calculations using Pekeris-type wave functions with one and two length scales<sup>64</sup> and from the solution of the Fadeev–Mercuriev integral equations for three-body systems.<sup>42</sup>

First of all, the present results and the literature data are in satisfactory agreement. Our results could be certainly improved by running more extensive calculations with larger basis sets. Instead of going in this direction, a careful comparison is carried out with the reference data to learn about the accuracy and convergence behavior of our approach. The results are often in excellent agreement with the benchmarks, but in some

cases the lifetimes are orders of magnitude off. It can be observed that the calculated lifetimes are worse when the real part of the complex energy was determined less accurately (and given to less significant digits in Table 1). The inaccuracy appears in both the real and the imaginary parts and is about of the same order of magnitude compared to the absolute value of the complex energy. Thus, if the widths are expected to be very small and the real part can be determined only to a few digits, the width should be considered only as a rough estimate to its exact value. This observation can be used later in this work also for the assessment of the calculations carried out for the four-particle  $Ps_2$  and  $H_2$ .

**$Ps_2$ .** Our next test case was the four-particle positronium molecule,  $Ps_2 = \{e^-, e^-, e^+, e^+\}$ . Resonances of the positronium molecule have recently attracted attention.<sup>27,65,67</sup>  $Ps_2$  has few bound states, and thus a detailed spectroscopic investigation of its structure and dynamics is possible only through the detection and analysis of its quasi-bound states.

In our list of numerical examples, the positronium molecule is unique because, in addition to the spatial symmetries, its Hamiltonian is invariant under the conjugation of the electric charges. To account for this additional property, the basis functions, eqs 3 and 4, were adapted also to the charge conjugation symmetry.<sup>55–57,65,68</sup> As a result, the total symmetry-adapted basis functions and also the calculated wave functions are not necessarily eigenfunctions for the total spin angular momentum of the electrons or that of the positrons,  $\hat{S}_-^2$  or  $\hat{S}_+^2$ . Nevertheless, the total spatial angular momentum quantum number,  $N$ , the parity,  $p$ , as well as the charge-conjugation parity,  $c = +1$  or  $-1$ , are always good quantum numbers.

The parametrization strategy of the basis set was similar to that used for  $Ps^-$ : we employed (a) the energy minimization condition for the lowest-energy eigenvalue and (b) the linear independence condition for the generation of new basis function parameters. The parameter sets used in the largest calculations are given in the Supporting Information.

The bound and resonance states calculated with  $N = 0$  total spatial angular momentum quantum number and  $p = +1$  parity are collected in Table 2. Considering all possible charge

conjugation and spin functions, we obtained only three bound states in agreement with the literature.<sup>27,65,69</sup> Two of the three calculated bound states substantially improve on the best available results.<sup>65</sup> It is interesting to note that the bound state with  $E = -0.314\,677\,072\,E_h$  ( $c = -1$  and  $(S_-, S_+) = (1, 1)$ ) is bound only due to the charge-conjugation symmetry of the electrons and the positrons. The localization of the energy and width for the lowest-energy resonance state of  $\text{Ps}_2$  is shown in Figure 2. The calculated resonance positions are in good

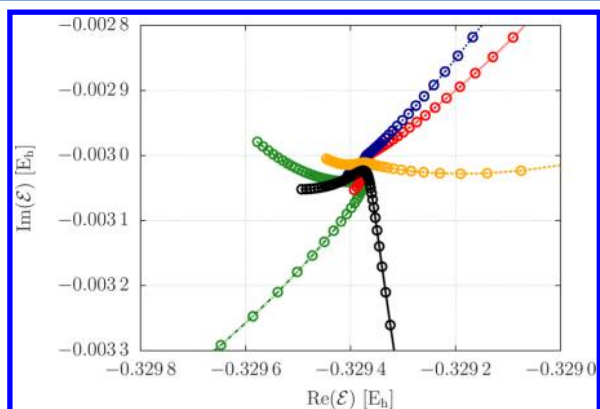


**Figure 2.** Localization of the parameters for the lowest-energy resonance state of  $\text{Ps}_2$  with  $N = 0$ ,  $p = +1$ ,  $c = +1$ , and  $S_- = 0$ ,  $S_+ = 0$ . The stabilization of the trajectories with respect to the rotation angle (circles) and the basis functions (colors) is shown. The stabilization point is located at  $(\text{Re}(\mathcal{E}), \text{Im}(\mathcal{E})) = (-0.329\,38, -0.003\,03)\,E_h$ .

agreement with the literature. In some cases our results might even improve on the best available data,<sup>27,65</sup> although there is no such direct criterion for the assessment of the accuracy of the resonance parameters as the variational principle for bound states.

**Toward the Calculation of Rovibronic Resonances of  $\text{H}_2$ .** Next, our goal was to explore how the lowest-lying resonance states of  $\text{H}_2$  can be calculated in a pre-Born–Oppenheimer quantum mechanical approach. It could be anticipated that one of the major challenges in this undertaking would be the parametrization of the basis functions, which was already in the bound-state calculations more demanding for  $\text{H}_2$  than for  $\text{Ps}_2$ .<sup>44</sup> In the bound-state calculations the optimized parameters were fine-tuned in repeated cycles. The entire parameter selection and optimization procedure relied on the variational principle and the minimization of the energy.

According to the spatial and permutational symmetry properties of the  $\text{H}_2$  molecule, there are four different blocks with natural parity

$$\text{B1: } "X^1\Sigma_g^+ \text{ block}": N \geq 0, p = (-1)^N,$$

$$S_p = (1 - p)/2, S_e = 0$$

$$\text{B2: } "B^1\Sigma_u^+ \text{ block}": N \geq 0, p = (-1)^N,$$

$$S_p = (1 + p)/2, S_e = 0$$

$$\text{B3: } "a^3\Sigma_g^+ \text{ block}": N \geq 0, p = (-1)^N,$$

$$S_p = (1 - p)/2, S_e = 1$$

$$\text{B4: } "b^3\Sigma_u^+ \text{ block}": N \geq 0, p = (-1)^N,$$

$$S_p = (1 + p)/2, S_e = 1$$

which can be calculated in independent runs with our computer program using basis functions with the appropriate quantum numbers, eqs 3 and 4. The lowest-energy levels of the first three blocks correspond to bound states, while the last block starts with the  $\text{H}(1) + \text{H}(1)$  continuum. In the BO picture the  $b^3\Sigma_u^+$  electronic state is repulsive<sup>70</sup> and does not support any bound rotational–vibrational levels (see Figure 3 and Table 3). Then, one of our goals was the identification of the lowest-energy quasi-bound states in the  $b^3\Sigma_u^+$  block.

During the calculation of the lowest-energy resonances of  $\text{Ps}_2$ , the basis function parameters were generated randomly using a system-adapted random number generator.<sup>44</sup> Unfortunately, this simple strategy for the  $\text{H}_2$  resonances was not useful.

The energy minimization criterion for the lowest (few) eigenstates was not useful either since it resulted only in the accumulation of functions near the  $\text{H}(1) + \text{H}(1)$  limit, the lowest-energy levels in the  $b^3\Sigma_u^+$  block, and the higher-lying quasi-bound states were not at all described by the basis sets generated in this way.

Then, our alternative working strategy was the usage of the parameter transfer approach (described in Section “Theory and Computational Strategy” and in ref 44). In this approach a parameter set optimized for a bound state with some quantum numbers, “state  $\mathcal{A}$ ”, is used to parametrize the basis functions corresponding to another set of quantum numbers and used to calculate “state  $\mathcal{B}$ ”. It is important to emphasize that the mathematical form of the basis functions is defined by the selected values of the quantum numbers, eqs 3 and 4, and thus not the basis functions but only the parameters are transferred from one calculation to another. Our qualitative understanding tells us that this parameter-transfer strategy is computationally useful if the internal structures of state  $\mathcal{A}$  and state  $\mathcal{B}$  are more or less similar. By inspecting the orientation chart of  $\text{H}_2$  (Figure 3), our idea was that the combination of the (natural-parity) bound-state optimized parameter sets could provide a parametrization good enough for the identification of the lowest-lying resonance states embedded in the  $b^3\Sigma_u^+$  continuum.

For this purpose, we used the parameters of 2250 basis functions optimized for the lowest-lying bound states with  $N = 0$  and 1 angular momentum quantum number corresponding to the  $X^1\Sigma_g^+$ ,  $B^1\Sigma_u^+$ , and  $a^3\Sigma_g^+$  blocks using the sampling-importance resampling strategy of ref 44 and Powell’s method<sup>63</sup> for the fine-tuning of each basis function. As a result of these calculations, we obtained a parameter set large enough for  $6 \times 2250 = 13\,500$  basis functions. In addition, 1000 basis functions were generated and less tightly optimized for the lowest-energy levels of the  $b^3\Sigma_u^+$  block with  $N = 0$  and 1. Using this large parameter set,  $\mathcal{P}_L$ , 15 500 basis functions were constructed for all possible quantum numbers of the four blocks, B1–B4, with  $N = 0, 1$ , and 2. In each case the resulting basis set was found to be linearly independent. The complete parameter set is given in the Supporting Information. The proton–electron ratio was  $m_p/m_e = 1836.15267247$  throughout the calculations.<sup>71</sup>

**Bound-State Energy Levels.** The lowest-lying energy values obtained with  $\mathcal{P}_L$  for the different quantum numbers are collected in Table 3 and are in good agreement with the best available nonrelativistic results in the literature. The energy values of the  $X^1\Sigma_g^+$  electronic and vibrational ground states

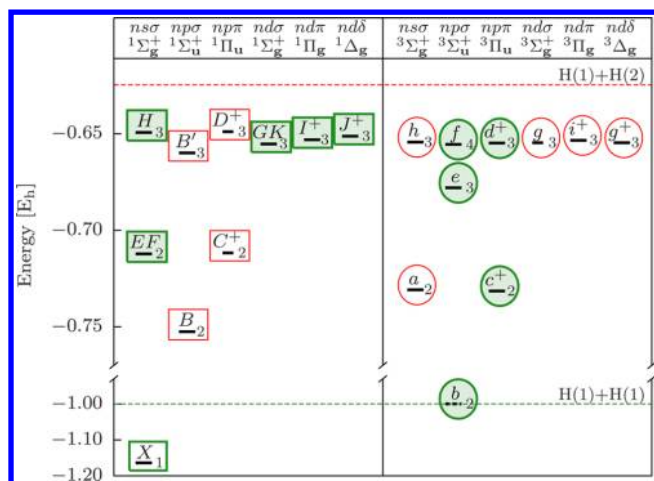


**Figure 3.** Orientation chart for the electronic states of  $H_2$  below the  $H(1) + H(2)$  dissociation threshold (see, for example, Herzberg<sup>78</sup> or Brown and Carrington<sup>79</sup>). The same color (red or green) and shape (rectangle or ellipse) coding indicates those states, which can be obtained in the same pre-Born–Oppenheimer calculation. Empty objects indicate bound states, while filled objects refer to the fact that the corresponding rovibronic states (if there are any) are resonances embedded in the  $H(1) + H(1)$  continuum.

**Table 3. Assessment of the Basis Set Parameterization: The Lowest-Lying Bound-State Energies**

$(N, p, S_p, S_e)^a$	$E/E_h^b$	$\Delta E_{\text{ref}}/\mu E_h^c$	ref	assignment <sup>d</sup>
(0,+1,0,0)	-1.164 025 030	-0.000 6	72	$X^1 \Sigma_g^+$
(1,-1,1,0)	-1.163 485 171	-0.001 4	72	$X^1 \Sigma_g^+$
(2,+1,0,0)	-1.162 410 408	-0.001 9	72	$X^1 \Sigma_g^+$
(0,+1,1,0)	-0.753 027 186	1.383 7	73	$B^1 \Sigma_u^+$
(1,-1,0,0)	-0.752 850 233	1.444 6	73	$B^1 \Sigma_u^+$
(1,+1,1,0)	-0.752 498 022	1.529 1	73	$B^1 \Sigma_u^+$
(0,+1,0,1)	-0.730 825 193	-0.006 9	77	$a^3 \Sigma_g^+$
(1,-1,1,1)	-0.730 521 418	0.008 0	77	$a^3 \Sigma_g^+$
(2,+1,0,1)	-0.729 916 268	0.047 9	77	$a^3 \Sigma_g^+$
(0,+1,1,1)	[-0.999 450 102] <sup>e</sup>	[-5.578]	<i>f</i>	$b^3 \Sigma_u^+$
(1,-1,0,1)	[-0.999 445 835] <sup>e</sup>	[-9.844]	<i>f</i>	$b^3 \Sigma_u^+$
(2,+1,1,1)	[-0.999 439 670] <sup>e</sup>	[-16.010]	<i>f</i>	$b^3 \Sigma_u^+$

<sup>a</sup> $N$ : total spatial angular momentum quantum number;  $p$ : parity,  $p = (-1)^N$ ;  $S_p$  and  $S_e$ : total spin quantum numbers for the protons and the electrons, respectively. <sup>b</sup> $E$ : the energy obtained with the largest parameter set,  $\mathcal{P}_L$ , used in this study corresponding to 15 500 basis functions for each set of quantum numbers (see the text for details and the Supporting Information for the numerical values). The proton–electron ratio was  $m_p/m_e = 1836.152\,672\,47$ . <sup>c</sup> $\Delta E_{\text{ref}} = E_{\text{ref}} - E$  with  $E_{\text{ref}}$  being the best available non-Born–Oppenheimer theoretical energy value in the literature. <sup>d</sup>Born–Oppenheimer electronic state label. Each energy level given here can be assigned to the lowest-energy vibrational level of the electronic state. <sup>e</sup>The lowest-energy eigenvalue of the Hamiltonian obtained for the given set of quantum numbers. <sup>f</sup>The nonrelativistic energy of two ground-state hydrogen atoms,  $E(H(1) + H(1)) = -0.999\,455\,679 E_h$ , was used as reference.

with  $N = 0, 1$ , and  $2$  are larger by only less than  $2 \text{ nE}_h$  than the theoretical results of ref 72.

For all three calculated  $B^1 \Sigma_u^+$   $N = 0, 1, 2$  levels our energy values are lower by more than  $1 \mu E_h$  compared to the results of ref 73 obtained in close-coupling calculations using adiabatic potential energy curves and nonadiabatic couplings for six electronic states. We also note that for the  $N = 0$  lowest-lying vibrational level of  $B^1 \Sigma_u^+$  there is a “variational-perturbational”

estimate given in Table 3 of ref 73, which was anticipated to be more accurate, and thus it was the recommended value for this level in the article, though not a strict upper bound to the exact value. It was obtained not in the six-state close-coupling calculation, but as a result of two-state close-coupling calculations with the potentials and couplings of ref 73, incremented with a nonadiabatic correction term.<sup>74</sup> This term value translates to the energy value  $-0.753\,026\,440 E_h$  based on the explanation given below eq 13 of ref 73. An earlier nonadiabatic estimate<sup>75</sup> (not upper bound) for this energy level was  $-0.753\,027\,31 E_h$  calculated using the adiabatic energy and a correction to the BO potential<sup>76</sup> incremented by a nonadiabatic correction.<sup>74</sup> For comparison, the pre-Born–Oppenheimer energy calculated in the present work (in a fully variational procedure) is  $-0.753\,027\,186 E_h$  (Table 3).

In the case of the  $a^3 \Sigma_g^+$   $N = 1, 2$  energy levels the presented energy values obtained in this work are lower than the lowest energies values published.<sup>77</sup>

On the basis of this overview, we can conclude that the parameter set,  $\mathcal{P}_L$ , performs well for the lowest-lying bound-state energy levels and also contains basis functions optimized for an approximate description of the  $H(1) + H(1)$  continuum. Then, we can hope that the application of this parameter set in the CCRM calculations for the description of the related or just energetically nearby-lying quasi-bound states will be useful.

**Electronically Excited Bound and Resonance Rovibronic States.** In the orientation chart of  $H_2$  (Figure 3), the electronic states are collected below the  $H(1) + H(2)$  dissociation threshold known from the literature<sup>78,79</sup> (only natural-parity states are considered). Although in our calculations there are no potential energy curves corresponding to electronic states, these conventional electronic-state labels help the orientation and the reference to the calculated energy levels. In the figure those states which are coupled by symmetry and calculated in the same block are highlighted similarly (green or red color and oval or rectangular marking) corresponding to the B1–B4 blocks introduced earlier in this section. This coupling is included in the calculations automatically by specifying the total spatial (orbital plus rotational) angular momentum, parity, and spin quantum numbers. The empty ellipses and rectangles indicate bound states, while the shaded signs are for resonance states embedded in their corresponding lowest-lying continuum (here:  $H(1) + H(1)$ ).

We carried out calculations in all four blocks, B1–B4, with  $N = 0, 1$ , and  $2$  total spatial angular momentum quantum numbers, and most of the states indicated in Figure 3 could have been identified using the largest parameter set,  $\mathcal{P}_L$ . Unfortunately, the accuracy of the calculated energies often did not meet the level of spectroscopic accuracy,<sup>80</sup> and thus we collect here only the essence of the calculations.

First of all, the most important qualitative results can be explained by inspecting Figure 4 prepared for the “ $X^1 \Sigma_g^+$  block” and for the “ $b^3 \Sigma_u^+$  block”, B1 and B4. Figure 4 shows a part of the eigenspectrum of the complex scaled Hamiltonian,  $\mathcal{H}(\theta)$  of eq 6, corresponding to small  $\theta$  values,  $\theta \in [0.005, 0.065]$ , and the  $[-1.2, -0.5] E_h$  interval of the real part of the eigenvalues.

In both cases the onset of the  $H(1) + H(1)$  continuum can be observed on the real axes at  $-0.999\,455\,679 E_h$ . In the  $X^1 \Sigma_g^+$  block the bound rovibrational energy levels assignable to the  $X^1 \Sigma_g^+$  electronic state line up on the real axis with  $\text{Im}(\mathcal{E}) = 0$  (deviations from this value are due to the

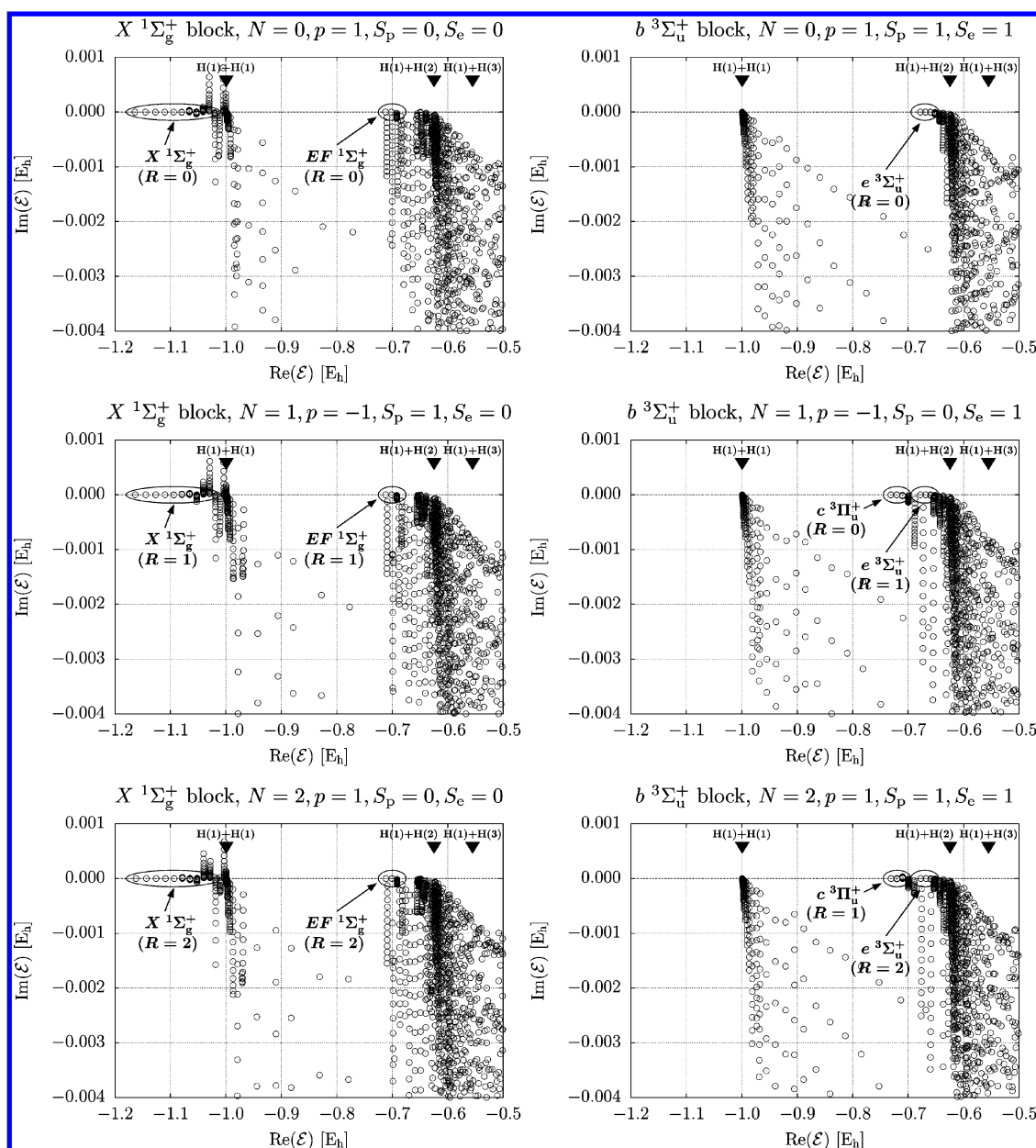


**Figure 4.** Part of the spectrum of the complex scaled Hamiltonian,  $\mathcal{H}(\theta)$ , with  $\theta \in [0.005, 0.065]$  corresponding to the largest basis set used in this work for the  $X^1\Sigma_g^+$  block [ $p = (-1)^N$ ,  $S_p = (1 - p)/2$ ,  $S_e = 0$ ] and for the  $b^3\Sigma_u^+$  block [ $p = (-1)^N$ ,  $S_p = (1 + p)/2$ ,  $S_e = 1$ ] with  $N = 0, 1$ , and  $2$  total spatial angular momentum quantum numbers. The black triangles indicate the threshold energy of the dissociation continua corresponding to  $H(1) + H(1)$ ,  $H(1) + H(2)$ , and  $H(1) + H(3)$ .

incomplete convergence only, and the estimated stabilization points are on the real axis). In the  $b^3\Sigma_u^+$  block, however, we find no states below the  $H(1) + H(1)$  continuum, in agreement with the BO calculations.<sup>70</sup> The next,  $H(1) + H(2)$  threshold corresponds to the energy value  $-0.624\,659\,800 E_h$ . Beyond the  $H(1) + H(1)$  but below the  $H(1) + H(2)$  thresholds stabilization points (with respect to the  $\theta$  rotation angle and the basis set) were observed with small negative imaginary values, which were assigned (based on the real parts of the eigenvalues) to rotational–vibrational levels corresponding to the electronically excited states in their symmetry blocks (see Figure 4 and also Figure 3). The lack of any stabilization points beyond the  $H(1) + H(2)$  threshold can be explained with the limited size and flexibility of the basis set.

It can be observed in Figure 4 in the  $b^3\Sigma_u^+$  block that a group of stabilization points appear for  $N = 1$  and  $2$ , which are not present for  $N = 0$ . These points for  $N = 1$  and  $2$  were assigned to the rotational–vibrational states with  $R = 0$  and  $1$  rotational angular momentum quantum numbers of the  $c^3\Pi_u^+$  electronic state, respectively. This result demonstrates that the coupling of the rotational and orbital angular momenta is automatically included in the calculations by specifying only the total spatial angular momentum quantum number,  $N$ .

Finally, we note that the  $H(1) + H(1)$  continuum does not couple neither to the “ $B^1\Sigma_u^+$  block” nor to the “ $a^3\Sigma_g^+$  block”, and in these cases the lowest-lying continuum corresponds to the  $H(1) + H(2)$  dissociation channel (Figure 3).

*Numerical Results for the Resonance Energies and Widths.* In Table 4 numerical results are given for the

**Table 4.** Identified Resonance-State Energies and Widths, in  $E_h$ , of  $H_2$  in the  $b^3\Sigma_u^+$  Block [ $p = (-1)^N$ ,  $S_p = (1 + p)/2$ ,  $S_e = 1$ ] for  $N = 0, 1$ , and 2

$(N, p, S_p, S_e)^a$	$\text{Re}(\mathcal{E})^b$	$\Gamma/2^b$	$E_{\text{ref,exp}}^c$	$E_{\text{ref,theo}}^d$	assignment <sup>e</sup>
(0,+1,1,1)	[−0.999 450 1] <sup>f</sup> [...]			[−0.999 455 7]	H(1) + H(1) continuum
(0,+1,1,1)	−0.677 947 1	$1 \times 10^{-7}$	−0.677 946 1	−0.677 942 7 <sup>70</sup>	$e^3\Sigma_u^+$ , $R = 0, \nu = 0$
(0,+1,1,1)	−0.668 549 3	$9 \times 10^{-7}$	−0.668 547 8	−0.668 541 0 <sup>70</sup>	$e^3\Sigma_u^+$ , $R = 0, \nu = 1$
(1,−1,0,1)	[−0.999 445 8] <sup>f</sup> [...]			[−0.999 455 7]	H(1) + H(1) continuum
(1,−1,0,1)	−0.731 434 0	$5 \times 10^{-7}$	−0.731 438 8	−0.731 469 1 <sup>82</sup>	$c^3\Pi_u^+$ , $R = 0, \nu = 0$
(1,−1,0,1)	−0.720 72	$2 \times 10^{-7}$	−0.720 782 6		$c^3\Pi_u^+$ , $R = 0, \nu = 1$
	[...]				
(1,−1,0,1)	−0.677 705 5	$2 \times 10^{-7}$	−0.677 704 1	−0.677 698 2 <sup>70</sup>	$e^3\Sigma_u^+$ , $R = 1, \nu = 0$
(1,−1,0,1)	−0.668 32	$1 \times 10^{-6}$	−0.668 319 7	−0.668 309 8 <sup>70</sup>	$e^3\Sigma_u^+$ , $R = 1, \nu = 1$
(2,+1,1,1)	[−0.999 439 7] <sup>f</sup> [...]			[−0.999 455 7]	H(1) + H(1) continuum
(2,+1,1,1)	−0.730 888 2	$9 \times 10^{-7}$	−0.730 888 7		$c^3\Pi_u^+$ , $R = 1, \nu = 0$
(2,+1,1,1)	−0.720 219 0	$<2 \times 10^{-7}$	−0.720 258 0		$c^3\Pi_u^+$ , $R = 1, \nu = 1$
	[...]				
(2,+1,1,1)	−0.677 222 9	$2 \times 10^{-8}$	−0.677 222 2		$e^3\Sigma_u^+$ , $R = 2, \nu = 0$
(2,+1,1,1)	−0.667 863 2	$7 \times 10^{-7}$	−0.667 865 3		$e^3\Sigma_u^+$ , $R = 2, \nu = 1$

<sup>a</sup> $N$ : total spatial angular momentum quantum number;  $p$ : parity,  $p = (-1)^N$ ;  $S_p$  and  $S_e$ : total spin quantum numbers for the protons and electrons, respectively. <sup>b</sup> $\text{Re}(\mathcal{E})$  and  $\Gamma$ : resonance energy and width with  $\Gamma/2 = -\text{Im}(\mathcal{E})$  calculated in this work. The largest basis set contained 15 500 basis functions for each set of quantum numbers. The proton–electron ratio was  $m_p/m_e = 1836.152\,672\,47$ .<sup>71</sup> <sup>c</sup> $E_{\text{ref,exp}}$  experimental reference value, in  $E_h$ , derived as  $E_{\text{exp}} = E_0 + T_{\text{exp}}$  with the ground-state energy ( $X^1\Sigma_g^+$ ,  $N = 0, \nu = 0$ )  $E_0 = -1.164\,025\,030\,E_h$ . All  $T_{\text{exp}}$  values were obtained by correcting the experimental term values of Dieke,<sup>81</sup> with  $-0.000\,681\,7\,E_h = -149.63\text{ cm}^{-1}$  ( $1\,E_h = 219\,474.631\,4\text{ cm}^{-1}$ ), since all triplet term values were too high.<sup>70,90</sup> <sup>d</sup> $E_{\text{ref,theo}}$ : the best available theoretical reference energy values, in  $E_h$ , corresponding to accurate adiabatic calculations for the  $e^3\Sigma_u^+$  levels<sup>70</sup> and to accurate Born–Oppenheimer calculations for the  $c^3\Pi_u^+$  levels.<sup>82</sup> The nonrelativistic energy of two ground-state hydrogen atoms is given in square brackets. <sup>e</sup>Born–Oppenheimer electronic- and vibrational-state labels. The (approximate) rotational angular momentum quantum number,  $R$ , is also given. <sup>f</sup>The lowest-energy eigenvalue of the real Hamiltonian obtained with the largest parameter set and with the given quantum numbers.

“ $b^3\Sigma_u^+$  block”, B4, for the lowest-lying rotational–vibrational levels with  $N = 0, 1$ , and 2 corresponding to the  $e^3\Sigma_u^+$  ( $N = 0, 1, 2$ ) and to the  $c^3\Pi_u^+$  ( $N = 1, 2$ ) electronic-state labels. These rovibronic levels are embedded in the H(1) + H(1) continuum, and thus they are considered as rovibronic resonances.

The real energy values are in satisfactory agreement with the experimental results.<sup>81</sup> We consider however the given imaginary parts as estimates to their accurate values, and all we can conclude at this point is that the obtained imaginary parts are of the order of  $10^{-7}\,E_h$ , which corresponds to a predissociative lifetime,  $\tau = \hbar/\Gamma$ , of the order of 0.2 ns. As it was explained earlier, it is difficult to assess the accuracy of the calculated resonance energies and widths since there is no such simple criterion as the (real) variational principle for bound states. According to our observations in the test calculations for  $\text{Ps}^-$  (Table 1), the relative errors in the real and imaginary parts with respect to the absolute value of the complex energy are similar. The accuracy of the pre-BO real energy values can be estimated here by their comparison with available experimental results. This observation also indicates that the resonance widths given in Table 4 should be considered as rough estimates.

Theoretical energy values are available in the literature calculated by Kolos and Rychlewski<sup>70,82</sup> and are also cited in Table 4. In ref 70 adiabatic rotational–vibrational energy levels were determined for the  $e^3\Sigma_u^+$  electronic state by calculating an accurate adiabatic potential energy curve and solving the corresponding rotational–vibrational Schrödinger equation. The theoretical reference value for the  $c^3\Pi_u^+$ ,  $R = 0, \nu = 0$  level was taken from ref 82, which was obtained by the calculation of an accurate BO potential energy curve and

solving the corresponding vibrational Schrödinger equation. The resulting BO energy could be furthermore corrected for the  $\Lambda$ -doubling, but the numerical value for this correction term was not clearly identifiable in ref 82. It would be interesting to see if nonadiabatic corrections can be calculated to these levels, for example using the recently developed nonadiabatic perturbation theory by Pachucki and Komasa.<sup>72,83</sup>

The lifetimes of rotational–vibrational levels corresponding to the  $e^3\Sigma_u^+$  state were measured in delayed coincidence experiments,<sup>84</sup> which include both the radiative and predissociative decay channels accessible from these levels. In the same work the competition of the two decay channels was investigated using ab initio (full configuration interaction electronic wave functions using Gaussian-type orbitals and an accurate adiabatic potential energy curve<sup>70</sup>) as well as quantum defect theory with a one-channel approximation.<sup>84</sup> According to these calculations the predissociative lifetimes are of the order of 1  $\mu\text{s}$  and 100 ns for the  $\nu = 0$  and  $\nu = 1$  vibrational levels, respectively, for the  $e^3\Sigma_u^+$  state with  $N = 0$ . The lifetimes of the lowest rotational–vibrational levels of the  $c^3\Pi_u^+$  state were calculated using a simple perturbative model, which included the orbit–rotation interaction and used several approximations during the calculations.<sup>85</sup> In a similar perturbative treatment,<sup>86</sup> the orbit–rotational coupling operator was included, and accurate BO potential energy curves were used to describe the  $b^3\Sigma_u^+$  and  $c^3\Pi_u^+$  states.<sup>82,87</sup> According to both the lifetime measurements<sup>88,89</sup> and the calculations<sup>85,86</sup> the predissociative lifetime of the lowest-lying rotational–vibrational levels of  $c^3\Pi_u^+$  is of the order of 1 ns. Unfortunately, calculated energy levels were not reported in any of these theoretical works<sup>84–86</sup> on the predissociative



lifetimes of the  $e^3 \sum_u^+$  and  $c^3 \Pi_u^+$  states, which makes comparison of the results more difficult.

To pinpoint the resonance energies and especially the widths of the rovibronic levels within the rigorous pre-BO framework developed in the present work, further calculations are necessary. Nevertheless, the results shown in Table 4 improve on the best available theoretical values for energy levels published in the literature.<sup>70,82</sup> Furthermore, our primary goal was also completed, as it was demonstrated that in pre-BO calculations (a) electronically excited rovibronic levels are accessible and (b) there are excited rovibronic levels, which are described as bound states in the BO theory but appear as resonances in a pre-BO description, i.e., if the introduction of the BO approximation is completely avoided.

*How to Improve on the Present Results?* First of all, one of the lessons of the present study is that an efficient parametrization of the basis set is one of the main challenges of the calculation of rovibronic resonances in pre-BO theory.

We have shown that the random generation of parameters can be improved using the parameter-transfer approach assuming that there are bound states of comparable internal structure to the quasi-bound states to be calculated. In the case of  $H_2$  the presented calculations could be improved by the tight optimization of parameter sets for the lowest-lying bound states with unnatural parity,  $p = (-1)^{N+1}$ , and by the inclusion of also these parameters in an extended parameter set.

Then another technically straightforward, but computationally more demanding, option is the optimization of parameters not only for the lowest-lying states of a symmetry block but also for more (or all) vibrational and vibronic excited bound states, e.g., for all (ro)vibrational states of  $X^1 \sum_g^+$  up to the  $H(1) + H(1)$  threshold or for all the bound (ro)vibronic energy levels corresponding to the “ $B^1 \sum_u^+$  block” as well as to the “ $a^3 \sum_g^+$  block” up to their lowest-lying correlating threshold,  $H(1) + H(2)$  (see Figure 3).

Finally, a more generally applicable solution to the parametrization problem of resonance states would be the development of a useful and practical application of the complex variational principle for resonances.<sup>24</sup>

## SUMMARY AND OUTLOOK

The present work was devoted to the calculation of rotational–vibrational energy levels corresponding to electronically excited states, which are bound within the Born–Oppenheimer (BO) approximation but appear as resonances in a pre-Born–Oppenheimer (pre-BO) quantum mechanical description.

To calculate resonance energies and widths, corresponding to predissociative lifetimes, the pre-BO variational approach and computer program of ref 44 were extended with the complex coordinate rotation method (CCRM). Similarly to the bound-state calculations, the wave function was written as a linear combination of basis functions which have the non-relativistic quantum numbers (total spatial–rotational plus orbital–angular momentum quantum number, parity, and total spin quantum number for each particle type). The basis functions were constructed using explicitly correlated Gaussian functions and the global vector representation.

This pre-BO resonance approach was first used for the three- and four-particle positronium complexes,  $Ps^- = \{e^-, e^-, e^+\}$  and  $Ps_2 = \{e^-, e^-, e^+, e^+\}$ , respectively. These applications allowed us to test the implementation and gain experience in the identification of resonance parameters. For the dipositronium,

$Ps_2$ , we managed to improve on some of the best available results reported in the literature.

Then, the developed methodology and technology was employed for the four-particle molecule,  $H_2$ . First, the rovibronic states known in the literature were collected and considered which were accessible in our calculations with various sets of (exact) quantum numbers of the nonrelativistic theory. The experimental and theoretical energy values of the literature were also used for the assignment of our calculated energy levels with the common BO terminology of electronic and vibrational state labels.

As to the computational part, we had to find a useful parametrization strategy for the basis functions. Since the bound-state parameter-optimization approach relied on the energy minimization condition and the (real) variational principle, it was not directly applicable for making the CCRM calculations more efficient. A simple and practical solution to the parametrization problem was the parameter-transfer approach, where the basis functions used to describe low-energy resonances of some symmetry were parametrized with optimized parameters of (high-energy) bound states. As a result, a large parameter set was constructed, which was compiled from parameters optimized for different symmetry blocks. The parametrization of basis functions, which have mathematical forms defined by the exact quantum numbers, with this extended parameter set immediately lead to an improvement for the best available energy values available in the literature for the lowest-lying rotational states assigned to the  $B^1 \sum_u^+$  and  $a^3 \sum_g^+$  electronic states.

Then, using this extended parameter set low-energy rovibronic resonances became accessible beyond the  $b^3 \sum_u^+$  repulsive electronic state, embedded in the  $H(1) + H(1)$  continuum. On the basis of these calculations, resonance energies were evaluated, and resonance widths were estimated for the lowest-lying rotational–vibrational levels of the electronically excited  $e^3 \sum_u^+$  and  $c^3 \Pi_u^+$  states. We note here that the coupling of the rotational and orbital angular momenta was automatically included in our computational approach by specifying only the total spatial angular momentum quantum number,  $N$ . Although the presented results improve on the best available (BO and adiabatic) calculations in the literature for these states, to pinpoint the resonance energies and especially the widths more extensive calculations are necessary.

As for further improvements, the major present technical difficulty is the efficient parametrization of the basis set for resonance states. A generally applicable solution to this problem would be a useful application and implementation of a complex analogue for the real variational principle. In the lack of such a general solution, optimization of large parameter sets for bound (excited) states together with the parameter-transfer strategy might be appropriate for the calculation of a larger number and/or more accurate rovibronic resonances of  $H_2$ . In addition to the improvement of the parametrization strategy, a generally applicable analysis tool would also be desirable which provides an assignment for the pre-BO wave function with the common BO electronic- and vibrational-state labels where such an assignment is possible.

## ASSOCIATED CONTENT

### Supporting Information

Additional experimental details. This material is available free of charge via the Internet at <http://pubs.acs.org>.

## ■ AUTHOR INFORMATION

## Corresponding Author

\*E-mail: matyus@chem.elte.hu.

## Notes

The authors declare no competing financial interest.

## ■ ACKNOWLEDGMENTS

E.M. is thankful to Prof. Attila G. Császár and Prof. Markus Reiher for the continuous encouragement and also thanks Benjamin Simmen for discussions. The financial support of the Hungarian Scientific Research Fund (OTKA, NK83583) and an ERA-Chemistry grant is gratefully acknowledged. The computing facilities of HPC-Debrecen (NIIFI) were used during this work.

## ■ REFERENCES

- (1) Born, M.; Oppenheimer, R. Zur Quantentheorie der Molekeln. *Ann. der Phys.* **1927**, *84*, 457–484.
- (2) Born, M. Kopplung der Elektronen- und Kernbewegung in Molekeln und Kristallen. *Nachr. Akad. Wiss. Göttingen, Math.-Phys. Kl.* **1951**, *6*, 1–3.
- (3) Born, M.; Huang, K. *Dynamical Theory of Crystal Lattices*; Clarendon Press: Oxford, 1954.
- (4) Woolley, R. G. Quantum Theory and Molecular Structure. *Adv. Phys.* **1976**, *25*, 27–52.
- (5) Woolley, R. G. Most a Molecule Have a Shape? *J. Am. Chem. Soc.* **1978**, *100*, 1073–1078.
- (6) Woolley, R. G.; Sutcliffe, B. T. Molecular Structure and the Born–Oppenheimer Approximation. *Chem. Phys. Lett.* **1977**, *45*, 393–398.
- (7) Weininger, S. J. The Molecular Structure Conundrum: Can Classical Chemistry Be Reduced to Quantum Chemistry? *J. Chem. Educ.* **1984**, *61*, 939–944.
- (8) Claverie, P.; Diner, S. The Concept of Molecular Structure in Quantum Theory: Interpretation Problems. *Isr. J. Chem.* **1980**, *19*, 54–81.
- (9) Woolley, R. G. Quantum Mechanical Aspects of the Molecular Structure Hypothesis. *Isr. J. Chem.* **1980**, *19*, 30–46.
- (10) Woolley, R. G. Molecular Shapes and Molecular Structures. *Chem. Phys. Lett.* **1986**, *125*, 200–205.
- (11) Cafiero, M.; Adamowicz, L. Molecular Structure in Non-Born–Oppenheimer Quantum Mechanics. *Chem. Phys. Lett.* **2004**, *387*, 136–141.
- (12) Sutcliffe, B. T.; Woolley, R. G. Comment on ‘Molecular Structure in Non-Born–Oppenheimer Quantum Mechanics’. *Chem. Phys. Lett.* **2005**, *408*, 445–447.
- (13) Müller-Herold, U. On the Emergence of Molecular Structure from Atomic Shape in the  $1/r^2$  Harmonium Model. *J. Chem. Phys.* **2006**, *124*, 014105-1–5.
- (14) Müller-Herold, U. On the Transition Between Directed Bonding and Helium-Like Correlation in a Modified Hooke–Calogero Model. *Eur. Phys. J. D* **2008**, *49*, 311–315.
- (15) Ludeña, E. V.; Echevarra, L.; Lopez, X.; Ugalde, J. M. Non-Born–Oppenheimer Electronic and Nuclear Densities for a Hooke–Calogero Three-Particle Model: Non-Uniqueness of Density-Derived Molecular Structure. *J. Chem. Phys.* **2012**, *136*, 084103-1–12.
- (16) Cassam-Chenai, P. A Mathematical Definition of Molecular Structure – Open Problem. *J. Math. Chem.* **1998**, *23*, 61–63.
- (17) Goli, M.; Shahbazian, S. Atoms in Molecules: Beyond Born–Oppenheimer Paradigm. *Theor. Chim. Acta* **2011**, *129*, 235–245.
- (18) Goli, M.; Shahbazian, S. The Two-Component Quantum Theory of Atoms in Molecules (TC-QTAIM): Foundations. *Theor. Chim. Acta* **2012**, *131*, 1208-1–19.
- (19) Mátyus, E.; Hutter, J.; Müller-Herold, U.; Reiher, M. On the Emergence of Molecular Structure. *Phys. Rev. A* **2011**, *83*, 052512-1–5.
- (20) Mátyus, E.; Hutter, J.; Müller-Herold, U.; Reiher, M. Extracting Elements of Molecular Structure from the All-Particle Wave Function. *J. Chem. Phys.* **2011**, *135*, 204302-1–12.
- (21) Harris, R. A. Predissociation. *J. Chem. Phys.* **1963**, *39*, 978–987.
- (22) Kukulin, V. I.; Krasnopolsky, V. M.; Horáček, J. *Theory of Resonances—Principles and Applications*; Kluwer: Dordrecht, 1988.
- (23) Reinhardt, W. P. Complex Coordinates in the Theory of Atomic and Molecular Structure and Dynamics. *Annu. Rev. Phys. Chem.* **1982**, *33*, 223–255.
- (24) Moiseyev, N. Quantum Theory of Resonances: Calculating Energies, Widths and Cross-Sections by Complex Scaling. *Phys. Rep.* **1998**, *302*, 211.
- (25) Hazi, A. U.; Taylor, H. S. Stabilization Method of Calculating Resonance Energies: Model Problem. *Phys. Rev. A* **1970**, *1*, 1109–1120.
- (26) Ho, Y. K. *The Method of Complex Coordinate Rotation and its Applications to Atomic Collision Processes*; North-Holland Publishing Company: Amsterdam, 1983.
- (27) Usukura, J.; Suzuki, Y. Resonances of Positronium Complexes. *Phys. Rev. A* **2002**, *66*, 010502(R)-1–4.
- (28) Mandelshtam, V. A.; Ravuri, T. R.; Taylor, H. S. Calculation of the Density of Resonance States Using the Stabilization Method. *Phys. Rev. Lett.* **1993**, *70*, 1932–1935.
- (29) Mandelshtam, V. A.; Taylor, H. S.; Ryaboy, V.; Moiseyev, N. Stabilization Theory for Computing Energies and Widths of Resonances. *Phys. Rev. A* **1994**, *50*, 2764–2766.
- (30) Müller, J.; Yang, X.; Burgdörfer, J. Calculation of Resonances in Doubly Excited Helium Using the Stabilization Method. *Phys. Rev. A* **1994**, *49*, 2470–2475.
- (31) Ryaboy, V.; Moiseyev, N.; Mandelshtam, V. A.; Taylor, H. S. Resonance Positions and Widths by Complex Scaling and Modified Stabilization Method: van der Waals Complex NeI<sub>2</sub>. *J. Chem. Phys.* **1994**, *101*, 5677–5682.
- (32) Aguilar, J.; Combes, J. M. A Class of Analytic Perturbations for One-Body Schrödinger Hamiltonians. *Commun. Math. Phys.* **1971**, *22*, 269–279.
- (33) Balslev, E.; Combes, J. M. Spectral Properties of Many-Body Schrödinger Operators with Dilatation-Analytic Interactions. *Commun. Math. Phys.* **1971**, *22*, 280–294.
- (34) Simon, B. Quadratic Form Techniques and the Balslev–Combes Theorem. *Commun. Math. Phys.* **1972**, *27*, 1–9.
- (35) Wang, D.; Bowman, J. M. Complex  $L^2$  Calculations of Bound States and Resonances of HCO and DCO. *Chem. Phys. Lett.* **1995**, *235*, 277–285.
- (36) Rom, N.; Engdahl, E.; Moiseyev, N. Tunneling Rates in Bound Systems Using Smooth Exterior Complex Scaling within the Framework of the Finite Basis Set Approximation. *J. Chem. Phys.* **1990**, *93*, 3413–3419.
- (37) Rom, N.; Lipkin, N.; Moiseyev, N. Optical Potentials by the Complex Coordinate Method. *Chem. Phys.* **1991**, *151*, 199–204.
- (38) Riss, U. V.; Meyer, H.-D. Calculation of Resonance Energies and Widths Using the Complex Absorbing Potential Method. *J. Phys. B* **1993**, *26*, 4503–4536.
- (39) Seideman, T.; Miller, W. H. Calculation of the Cumulative Reaction Probability via a Discrete Variable Representation with Absorbing Boundary Conditions. *J. Chem. Phys.* **1992**, *96*, 4412–4422.
- (40) Thompson, W. H.; Miller, W. H. On the “Direct” Calculation of Thermal Rate Constants. II. The Flux-Flux Autocorrelation Function with Absorbing Potentials, with Application to the O+HCl → OH+Cl Reaction. *J. Chem. Phys.* **1997**, *106*, 142–150.
- (41) Miller, W. H. “Direct” and “Correct” Calculation of Canonical and Microcanonical Rate Constants for Chemical Reactions. *J. Phys. Chem. A* **1998**, *102*, 793–806.
- (42) Papp, Z.; Darai, J.; Nishimura, A.; Hlousek, Z. T.; Hu, C.-Y.; Yakovlev, S. L. Faddeev–Mercuriev Equations for Resonances in Three-Body Coulombic Systems. *Phys. Lett. A* **2002**, *304*, 36–42.
- (43) Papp, Z.; Darai, J.; Mezei, J. Z.; Hlousek, Z. T.; Hu, C.-Y. Accumulation of Three-Body Resonances above Two-Body Thresholds. *Phys. Rev. Lett.* **2005**, *94*, 143201-1–4.

- (44) Mátyus, E.; Reiher, M. Molecular Structure Calculations: a Unified Quantum Mechanical Description of Electrons and Nuclei using Explicitly Correlated Gaussian Functions and the Global Vector Representation. *J. Chem. Phys.* **2012**, *137*, 024104–1–17.
- (45) Simmen, B.; Mátyus, E.; Reiher, M. Elimination of the Translational Kinetic Energy Contamination in Pre-Born–Oppenheimer Calculations. *Mol. Phys.* **2013**, DOI: 10.1080/00268976.2013.783938.
- (46) Cohen, E.; Cvitaš, T.; Frey, J.; Holmström, B.; Kuchitsu, K.; Marquardt, R.; Mills, I.; Pavese, F.; Quack, M.; Stohner, J.; et al. *Quantities, Units and Symbols in Physical Chemistry (the IUPAC Green Book - 3rd ed.)*; RSC Publishing: Cambridge, 2007.
- (47) Boys, S. F. The Integral Formulae for the Variational Solution of the Molecular Many-Electron Wave Equation in Terms of Gaussian Functions with Direct Electronic Correlation. *Proc. R. Soc. London A* **1960**, *369*, 402–411.
- (48) Singer, K. The Use of Gaussian (Exponential Quadratic) Wave Functions on Molecular Problems I. General Formulae for the Evaluation of Integrals. *Proc. R. Soc. London A* **1960**, *258*, 412–420.
- (49) Jeziorski, B.; Szalewicz, K. High-Accuracy Compton Profile of Molecular Hydrogen from Explicitly Correlated Gaussian Wave Function. *Phys. Rev. A* **1979**, *19*, 2360–2365.
- (50) Cencek, W.; Rychlewski, J. Many-Electron Explicitly Correlated Gaussian Functions. I. General Theory and Test Results. *J. Chem. Phys.* **1993**, *98*, 1252–1261.
- (51) Rychlewski, J., Ed. *Explicitly Correlated Wave Functions in Chemistry and Physics*; Kluwer Academic Publishers: Dordrecht, 2003.
- (52) Suzuki, Y.; Usukura, J.; Varga, K. New Description of Orbital Motion with Arbitrary Angular Momenta. *J. Phys. B: Atmos. Mol. Opt. Phys.* **1998**, *31*, 31–48.
- (53) Varga, K.; Suzuki, Y.; Usukura, J. Global-Vector Representation of the Angular Motion of Few-Particle Systems. *Few-Body Systems* **1998**, *24*, 81–86.
- (54) Suzuki, Y.; Varga, K. *Stochastic Variational Approach to Quantum-Mechanical Few-Body Problems*; Springer-Verlag: Berlin, 1998.
- (55) Schrader, D. M. Symmetry of Dipositronium,  $\text{Ps}_2$ . *Phys. Rev. Lett.* **2004**, *92*, 043401–1–4.
- (56) Schrader, D. M. Symmetries and States of  $\text{Ps}_2$ . *Nucl. Instrum. Methods Phys. Res., Sect. B* **2004**, *221*, 182–184.
- (57) Schrader, D. M. General Forms of Wave Functions for Dipositronium,  $\text{Ps}_2$ . In *NASA GSFC Science Symposium on Atomic and Molecular Physics*; Bhatia, A. K., Ed.; NASA/CP-2006–214146, Goddard Space Flight Center: Greenbelt, MD, 2007; pp 103–110.
- (58) Anderson, E.; Bai, Z.; Bischof, C.; Blackford, S.; Demmel, J.; Dongarra, J.; Du Croz, J.; Greenbaum, A.; Hammarling, S.; McKenney, A.; et al. *LAPACK Users' Guide*, 3rd ed.; Society for Industrial and Applied Mathematics: Philadelphia, PA, 1999.
- (59) Kukulin, V. I.; Krasnopol'sky, V. M. A Stochastic Variational Method for Few-Body Systems. *J. Phys. G: Nucl. Phys.* **1977**, *3*, 795–811.
- (60) Alexander, S. A.; Monkhorst, H. J.; Szalewicz, K. Random Tempering of Gaussian-Type Geminals. I. Atomic Systems. *J. Chem. Phys.* **1986**, *85*, 5821–5825.
- (61) Alexander, S. A.; Monkhorst, H. J.; Szalewicz, K. Random Tempering of Gaussian-Type Geminals. II. Molecular Systems. *J. Chem. Phys.* **1987**, *87*, 3976–3980.
- (62) Alexander, S. A.; Monkhorst, H. J.; Szalewicz, K. Random Tempering of Gaussian-Type Geminals. III. Coupled Pair Calculations on Lithium Hydride and Beryllium. *J. Chem. Phys.* **1988**, *89*, 355–359.
- (63) Powell, M. J. D. The NEWUOA software for unconstrained optimization without derivatives (DAMTP 2004/NA05), Report no. NA2004/08, <http://www.damtp.cam.ac.uk/user/na/reports04.html> (accessed on January 18, 2013).
- (64) Li, T.; Shakeshaft, R. S-Wave Resonances of the Negative Positronium Ion and Stability of a Systems of Two Electrons and an Arbitrary Positive Charge. *Phys. Rev. A* **2005**, *71*, 052505-1–7.
- (65) Suzuki, Y.; Usukura, J. Stochastic Variational Approach to Resonances of  $\text{Ps}^-$  and  $\text{Ps}_2$ . *Nucl. Instrum. Methods Phys. Res., Sect. B* **2004**, *221*, 195–199.
- (66) Korobov, V. I. Coulomb Three-Body Bound-State Problem: Variational Calculations of Nonrelativistic Energies. *Phys. Rev. A* **2000**, *61*, 064503-1–3.
- (67) DiRienzi, J.; Drachman, R. J. Resonances in the Dipositronium System: Rydberg States. *Can. J. Phys.* **2010**, *88*, 877–883.
- (68) Suzuki, Y.; Usukura, J. Excited States of the Positronium Molecule. *Nucl. Instrum. Methods Phys. Res., Sect. B* **2000**, *171*, 67–80.
- (69) Bubin, S.; Adamowicz, L. Nonrelativistic Variational Calculations of the Positronium Molecule and the Positronium Hydride. *Phys. Rev. A* **2006**, *74*, 052502-1–5.
- (70) Kolos, W.; Rychlewski, J. Adiabatic Potential Energy Curves for the  $b$  and  $e^3\sum_u^+$  States of the Hydrogen Molecule. *J. Mol. Spectrosc.* **1990**, *143*, 237–250.
- (71) <http://physics.nist.gov/cuu/Constants> (CODATA 2006).
- (72) Pachucki, K.; Komasa, J. Nonadiabatic Corrections to Rovibrational Levels of  $\text{H}_2$ . *J. Chem. Phys.* **2009**, *130*, 164113-1–11.
- (73) Wolniewicz, L.; Orlikowski, T.; Staszewska, G.  $^1\Sigma_u$  and  $^1\Pi_u$  States of the Hydrogen Molecule: Nonadiabatic Couplings and Vibrational Levels. *J. Mol. Spectrosc.* **2006**, *238*, 118–126.
- (74) Wolniewicz, L.; Dressler, K. Nonadiabatic Energy Corrections for the Vibrational Levels of the  $B$  and  $B'^1\Sigma_u^+$  States of the  $\text{H}_2$  and  $\text{D}_2$  Molecules. *J. Chem. Phys.* **1992**, *96*, 6053–6064.
- (75) Wolniewicz, L. Lowest Order Relativistic Corrections to the Energies of the  $B^1\Sigma_u$  State of  $\text{H}_2$ . *Chem. Phys. Lett.* **1995**, *233*, 647–650.
- (76) Dressler, K.; Wolniewicz, L. Experiment and Theory of High Resolution Spectra of Rovibronic Molecular States. *Ber. Bunsenges. Phys. Chem.* **1995**, *99*, 246–250.
- (77) Wolniewicz, L. Non-Adiabatic Energies of the  $a^3\Sigma_g^+$  State of the Hydrogen Molecule. *Mol. Phys.* **2007**, *105*, 1497–1503.
- (78) Herzberg, G. *Spectra of Diatomic Molecules*; D. Van Nostrand Company, Inc.: Princeton, NJ, 1950.
- (79) Brown, J.; Carrington, A. *Rotational Spectroscopy of Diatomic Molecules*; Cambridge University Press: Cambridge, 2003.
- (80) The term “spectroscopic accuracy” is not uniquely defined, but it is usually used to refer to calculations providing vibrational transition wave numbers with a certainty of at least  $1\text{ cm}^{-1}$  ( $\approx 4.6\text{ }\mu\text{E}_h$ ) and even better accuracy for calculated rotational transitions.
- (81) Dieke, G. H. The Molecular Spectrum of Hydrogen and Its Isotopes. *J. Mol. Spectrosc.* **1958**, *2*, 494–517.
- (82) Kolos, W.; Rychlewski, J. Ab initio Potential Energy Curves and Vibrational Levels for the  $c$ ,  $I$ , and  $i$  States of the Hydrogen Molecule. *J. Mol. Spectrosc.* **1977**, *66*, 428–440.
- (83) Pachucki, K.; Komasa, J. Nonadiabatic Corrections to the Wave Function and Energy. *J. Chem. Phys.* **2008**, *129*, 034102-1–7.
- (84) Kiyoshima, T.; Sato, S.; Adamson, S. O.; Pazyuk, E. A.; Stolyarov, A. V. Competition Between Predissociative and Radiative Decays in the  $e^3\Sigma_u^+$  and  $d^3\Pi_u^-$  States of  $\text{H}_2$  and  $\text{D}_2$ . *Phys. Rev. A* **1999**, *60*, 4494–4502.
- (85) Chiu, L.-Y. C.; Bhattacharyya, D. K. Lifetimes of Fine Structure Levels of Metastable  $\text{H}_2$  in the  $c^3\Pi_u$  State. *J. Chem. Phys.* **1979**, *70*, 4376–4382.
- (86) Comtet, G.; de Bruijn, D. P. Calculation of the Lifetimes of Predissociative Levels of the  $c^3\Pi_u$  State in  $\text{H}_2$ ,  $\text{HD}$  and  $\text{D}_2$ . *Chem. Phys.* **1985**, *94*, 365–370.
- (87) Kolos, W.; Wolniewicz, L. Potential-Energy Curves for the  $X^1\Sigma_g^+$ ,  $b^3\Sigma_u^+$  and  $C^3\Pi_u$  States of the Hydrogen Molecule. *J. Chem. Phys.* **1965**, *43*, 2429–2441.
- (88) Meierjohann, B.; Vogler, M. Vibrationally Resolved Predissociation of the  $C^3\Pi_u$  and  $e^3\Sigma_u^+$  States of  $\text{H}_2$  by Flight-Time-Difference Spectroscopy. *Phys. Rev. A* **1978**, *17*, 47–51.
- (89) de Bruijn, D. P.; Neuteboom, J.; Los, J. Predissociation of the  $C^3\Pi_u$  State of  $\text{H}_2$ , Populated after Charge Exchange of  $\text{H}_2^+$  with Several Targets at keV Energies. *Chem. Phys.* **1984**, *85*, 233–251.

(90) Miller, T. A.; Freund, R. S. Singlet-Triplet Anticrossings in H<sub>2</sub>. *J. Chem. Phys.* **1974**, *61*, 2160–2162.

# Molecular structure calculations: A unified quantum mechanical description of electrons and nuclei using explicitly correlated Gaussian functions and the global vector representation

Edit Mátyus<sup>a),b)</sup> and Markus Reiher

Laboratory of Physical Chemistry, ETH Zürich, Wolfgang-Pauli-Str. 10, CH-8093 Zürich, Switzerland

(Received 25 April 2012; accepted 14 June 2012; published online 11 July 2012)

We elaborate on the theory for the variational solution of the Schrödinger equation of small atomic and molecular systems without relying on the Born–Oppenheimer paradigm. The all-particle Schrödinger equation is solved in a numerical procedure using the variational principle, Cartesian coordinates, parameterized explicitly correlated Gaussian functions with polynomial prefactors, and the global vector representation. As a result, non-relativistic energy levels and wave functions of few-particle systems can be obtained for various angular momentum, parity, and spin quantum numbers. A stochastic variational optimization of the basis function parameters facilitates the calculation of accurate energies and wave functions for the ground and some excited rotational-(vibrational-)electronic states of  $\text{H}_2^+$  and  $\text{H}_2$ , three bound states of the positronium molecule,  $\text{Ps}_2$ , and the ground and two excited states of the  $^7\text{Li}$  atom. © 2012 American Institute of Physics. [<http://dx.doi.org/10.1063/1.4731696>]

## I. INTRODUCTION

The clamped nuclei or Born–Oppenheimer (BO) approximation<sup>1–3</sup> is one of the central paradigms of present day theoretical and computational chemistry. This paper is devoted to a theoretical approach, which does not rely on this paradigm. A recent overview of such a pre-Born–Oppenheimer or “molecular structure” approach is given in Ref. 4, which also presents one of the central conceptual problems of molecular structure theory: the reconstruction of the classical molecular structure from a fully quantum mechanical description.<sup>4–19</sup> Numerical contributions to this question can be found in Refs. 20–29. In recent work,<sup>25,26</sup> we introduced radial and angular density functions to recognize elements of classical molecular structure in the all-particle quantum theory as strong correlation effects for the nuclei. Using these concepts the atomic-to-molecular transition was observed for a three-particle system by rescaling the relative mass of the particles in the calculations.<sup>25</sup>

In this work, we report on the development of a variational approach for the accurate calculation of energy levels and wave functions of few-particle systems with various angular momentum, parity, and spin quantum numbers. Methodological contributions to this field have a long history in the physicists’ community<sup>30–35</sup> and have found increasing interest in the molecular domain.<sup>36–38</sup> We can only note here that there are also efforts toward chemical and possible biochemical applications of a quantum electrons-nuclei theory.<sup>39–42</sup> Another interesting direction is a variational reduced-density matrix theory for electrons and protons.<sup>43</sup>

Our goal here is the accurate solution of the Schrödinger equation of few-particle systems. We describe electrons and atomic nuclei (or other particles) on equal footing, while focusing on the molecular domain. We are aiming at “spectroscopic accuracy.”<sup>44</sup> This is motivated by high-resolution measurements of the bonding energy of the  $\text{H}_2$  molecule<sup>45,46</sup> and post-Born–Oppenheimer calculations including relativistic and quantum-electrodynamic corrections<sup>47,48</sup> as well as by spectroscopic investigations of the  $\text{H}_3^+$  molecular ion.<sup>49–51</sup> Following the recent methodological developments in Ref. 37 and especially in Refs. 35, 52, and 53, we had to solve some technical issues to be able to use these ideas for our purposes.

The usage of explicitly correlated Gaussian functions considering the pioneering contributions<sup>54–56</sup> since the early work of Boys and Singer,<sup>57,58</sup> the inclusion of polynomial prefactors, and the global vector representation (GVR) (Refs. 35, 53, and 59) appear to be an appealing combination for the construction of a flexible basis set with the required spatial symmetry. This parameterization allows one to include polynomial prefactors in terms of more than one coordinate. However, it was noted in Refs. 60 and 61 that in the case of polynomial prefactors for several coordinates with large exponents instabilities might appear during the integral evaluation in a numerical procedure. Our preliminary tests indicated similar problems for a direct implementation of the formulae in Refs. 35 and 53. At the same time, small exponents in the polynomial prefactors were not sufficient for an efficient calculation of the energy levels of molecular systems. Thus, we decided to rearrange the original formulation<sup>35,53</sup> and make it applicable to molecular systems in practice. This would allow us the variational calculation of energy levels and wave function of molecules with not only zero, for example, Refs. 37, 62, and 63 but also non-zero (rotational or orbital) angular momentum quantum numbers within a pre-Born–Oppenheimer approach.

<sup>a)</sup>Author to whom correspondence should be addressed. Electronic mail: matyus@chem.elte.hu.

<sup>b)</sup>Present address: Institute of Chemistry, Eötvös University, P.O. Box 32, H-1518, Budapest 112, Hungary.

As to the parameterization of the basis functions, a stochastic optimization of the parameters<sup>30,35,64–66</sup> can result in a flexible, on-the-fly adjustment of the basis set to various systems. We shall address the questions how to choose an “appropriate” random number generator for the stochastic optimization and whether this choice has an effect on the efficiency of the procedure.

Finally, for actual calculations, one can use laboratory-fixed (LF) or various translationally invariant Cartesian coordinates, e.g., Radau or Jacobi coordinate sets. Also in this context various questions arise: Which is the best choice? Does this choice have any effect on the convergence rate of the energy? We decided to stick to (laboratory-fixed or translationally invariant) Cartesian coordinates, which allows us to write the Hamiltonian in a simple form, in contrast to the common choice of curvilinear coordinates in BO rotational-vibrational calculations, which results in complicated kinetic energy operators (see, for example, Refs. 67–70).

In Sec. II, we summarize first the necessary theory, and then we describe our solutions to the technical issues raised above. In the paper, we indicate only the main steps of the integral evaluation and our choices made to restore the numerical stability in our calculations, while the lengthy integral formulae are collected in the supplementary material.<sup>71</sup> Based on the methodological details presented in Sec. II, a computer program was developed using the FORTRAN 90 programming language.

To demonstrate the applicability of this program, we report in Sec. III numerical results for rotational(-vibrational) energy levels corresponding to the ground and some electronically excited states of the  $\text{H}_2^+$  and  $\text{H}_2$  molecules; three bound states of the positronium molecule  $\text{Ps}_2$ , and the ground and two excited states of the  $^7\text{Li}$  atom. Finally, we investigate the transferability of the optimized basis function parameters and point out possible directions for future methodological developments.

## II. VARIATIONAL SOLUTION OF THE MANY-PARTICLE SCHRÖDINGER EQUATION

### A. Quantum Hamiltonian and the Pauli principle

The non-relativistic quantum Hamiltonian in Hartree atomic units and expressed in Cartesian coordinates in the LF,  $\mathbf{r}_i$  for  $i = 1, 2, \dots, n_p + 1$  particles, is

$$\hat{H} = \hat{T} + \hat{V} \quad (1)$$

with the kinetic and the potential energy terms

$$\hat{T} = - \sum_{i=1}^{n_p+1} \frac{1}{2m_i} \Delta_{r_i}, \quad (2)$$

$$\hat{V} = \sum_{i=1}^{n_p+1} \sum_{j>i}^{n_p+1} \frac{q_i q_j}{|\mathbf{r}_i - \mathbf{r}_j|}, \quad (3)$$

respectively, where the masses,  $m_i$ , and the electric charges,  $q_i$ , are properties associated to the point-like particles. The physically relevant eigenstates of this Hamiltonian satisfy the Pauli principle, i.e., conditions of the spin-statistics theorem

considering the bosonic or fermionic nature of the particles associated with some spin  $s_i$ .

Instead of re-expressing this Hamiltonian using translational, orientational, and internal coordinates, we use Cartesian coordinates and set up a trial wave function in a variational procedure as a linear combination of symmetry-adapted basis functions, which are angular momentum (total spatial angular momentum, i.e., angular momentum without the spins), parity, and spin eigenfunctions. As a result, the eigenvalues and eigenfunctions are obtained according to the quantum numbers of the non-relativistic theory.

Since we do not want to specify at the outset of the theoretical description the particle types, we simply use  $L$  for total spatial (rotational or orbital) angular momentum quantum number. For the notation of the total spin quantum number for particles  $a$ , we use the symbol  $S_a$ . At a later stage, when the particle types and the system are specified one can adapt the common notations in atomic and molecular spectroscopy (see for example the recommendations of the International Union of Pure and Applied Chemistry, Ref. 72):  $N$  for the total spatial angular momentum without the spins and  $S$  and  $I$  for the electronic and nuclear spin quantum numbers.

### B. Translationally invariant coordinates and Hamiltonian

In order to obtain a translationally invariant wave function,  $\Phi$ , for an  $(n_p + 1)$ -particle system there are two ways to proceed, see, for example, Ref. 20. (A) One can either parameterize the basis functions expressed in terms of LF Cartesian coordinates,  $\mathbf{r} \in \mathbb{R}^{3(n_p+1)}$ , and choose the parameters so that the overall momentum for the wave function is zero, i.e.,  $\hat{\mathbf{P}}_{\text{total}} \Phi = 0$ ; or (B) one can transform the LF Cartesian coordinates to some translationally invariant (TI) set of Cartesian coordinates,  $\mathbf{x} \in \mathbb{R}^{3n_p}$  plus the coordinates of the center of mass (CM),  $\mathbf{R}_{\text{CM}} \in \mathbb{R}^3$  by a linear transformation

$$\begin{pmatrix} \mathbf{x} \\ \mathbf{R}_{\text{CM}} \end{pmatrix} = (\mathbf{U} \otimes \mathbf{I}_3) \mathbf{r} \quad \text{and} \quad \mathbf{r} = (\mathbf{U}^{-1} \otimes \mathbf{I}_3) \begin{pmatrix} \mathbf{x} \\ \mathbf{R}_{\text{CM}} \end{pmatrix} \quad (4)$$

with  $\mathbf{U} \in \mathbb{R}^{(n_p+1) \times (n_p+1)}$ . The coordinates  $\mathbf{x}$  are translationally invariant<sup>73</sup> if

$$\sum_{j=1}^{n_p+1} U_{ij} = 0, \quad i = 1, 2, \dots, n_p \quad (5)$$

and

$$U_{n_p+1,j} = m_j / m_{\text{tot}}, \quad j = 1, 2, \dots, n_p + 1 \quad (6)$$

with  $m_{\text{tot}} = \sum_{j=1}^{n_p+1} m_j$ .

Then, the Hamiltonian is transformed accordingly and after subtracting the kinetic energy of the translational motion of the center of mass,  $\hat{T}_{\text{CM}} = -1/(2m_{\text{tot}}) \Delta_{\mathbf{R}_{\text{CM}}}$ , we have

$$\begin{aligned} \hat{H}' = \hat{H} - \hat{T}_{\text{CM}} = & - \sum_{i=1}^{n_p} \sum_{j=1}^{n_p} M_{ij} \nabla_{x_i}^T \nabla_{x_j} \\ & + \sum_{i=1}^{n_p+1} \sum_{j>i}^{n_p+1} \frac{q_i q_j}{|(\mathbf{f}_{ij} \otimes \mathbf{I}_3)^T \mathbf{x}|} \end{aligned} \quad (7)$$

with  $\nabla_{x_i}^T = (\partial/\partial x_{i1}, \partial/\partial x_{i2}, \partial/\partial x_{i3})$ .  $\mathbf{I}_3 \in \mathbb{R}^{3 \times 3}$  is the unit matrix, the masses are contained in

$$M_{ij} = \sum_{k=1}^{n_p+1} U_{ik} U_{jk} / 2m_k, \quad (8)$$

and the  $k$ th element ( $k = 1, 2, \dots, n_p$ ) of  $\mathbf{f}_{ij}$  is defined as

$$(\mathbf{f}_{ij})_k = (\mathbf{U}^{-1})_{ik} - (\mathbf{U}^{-1})_{jk}. \quad (9)$$

We note that the total spatial angular momentum relative to the center of mass commutes with the translationally invariant Hamiltonian.<sup>20,73,74</sup> In this work, we make use of both the coordinates defined according to (A) and (B). However, we will always apply those that lead to a simpler formulation.

### C. Symmetry-adapted basis functions, parameterization

We apply basis functions constructed as (anti)symmetrized products of spin functions and spatial functions, which are angular momentum and parity eigenfunctions. Thus, the ansatz for some set of quantum numbers  $\lambda = (L, M_L, p)$  and  $\zeta = (S_a, M_{S_a}, S_b, M_{S_b}, \dots)$  ( $a, b, \dots$  denote the particle type) is constructed as

$$\Phi^{[\lambda, \zeta]} = \hat{\mathcal{A}}\{\phi^{[\lambda]} \chi^{[\zeta]}\} \quad (10)$$

with the symmetrization and antisymmetrization operator

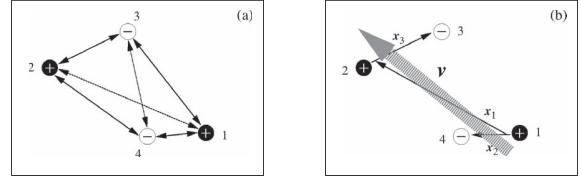
$$\hat{\mathcal{A}} = (N_{\text{perm}})^{-1/2} \sum_{p=1}^{N_{\text{perm}}} \varepsilon_p \hat{P}_p \quad (11)$$

for bosonic and fermionic-type particles, respectively.  $\hat{P}_p \in \mathcal{S}_{n_a} \otimes \mathcal{S}_{n_b} \otimes \dots$  is an operator permuting identical particles and  $\varepsilon_p = -1$  if  $\hat{P}_p$  represents an odd number of interchanges of fermions, otherwise  $\varepsilon_p = +1$ .  $N_{\text{perm}}$  is the number of all possible permutations.

#### 1. Spatial functions

Spatial functions with some  $\lambda = (L, M_L, p)$  can be constructed through the successive coupling of angular momenta of the subsystems within the partial wave decomposition (PWD) formalism. It was shown in Refs. 35, 53, and 59 that there is an alternative and equivalent route, named the global vector representation (GVR), which relies on a linear combination of several basis functions with some global vectors whose orientation as well as the linear combination coefficients are optimized variationally. The resulting function is an angular momentum and parity eigenfunction, while the partial wave contributions, which do not correspond to any “exact” quantum number, are optimized in the variational procedure. In our work, the main advantage of the GVR over the PWD is its simple and direct applicability for many-particle systems with an arbitrary angular momentum quantum number.

Thus, the spatial basis functions (Figure 1) are explicitly correlated Gaussian functions in the form recommended in Refs. 35, 53, and 59, which describe the particle-particle correlation by including products of Gaussian geminals, polynomial prefactors, and an angular function, which is a spherical



Particle-particle interactions,  $\alpha_{ij}$

Angular distribution,  $u_i$

FIG. 1. Visual representation of the inter-particle and the angular parts of the basis functions for a four-particle system: (a) *Particle-particle interactions*: particle-particle displacement vectors and the corresponding geminal exponents,  $\alpha_{ij}$ , are used to describe the inter-particle correlation; (b) *Angular distribution*: “atoms-in-molecule”-type coordinates are used in this example to express the global vector  $\mathbf{v} = u_1 \mathbf{x}_1 + u_2 \mathbf{x}_2 + u_3 \mathbf{x}_3$  with the “inter-atomic” coordinate,  $\mathbf{x}_1 = m_+ / (m_+ - m_-) (\mathbf{r}_2 - \mathbf{r}_1) + m_- / (m_+ - m_-) (\mathbf{r}_3 - \mathbf{r}_4)$  and the “intra-atomic” coordinates,  $\mathbf{x}_2 = \mathbf{r}_4 - \mathbf{r}_1$  and  $\mathbf{x}_3 = \mathbf{r}_3 - \mathbf{r}_2$ . Note that the (anti)symmetrization of the product of the spatial and spin functions guarantees that identical particles enter the description equivalently.

harmonic function of  $L$ th order and  $M_L$ th degree and depends on the orientation of the global vector  $\mathbf{v}$ ,

$$\phi^{[\lambda]}(\mathbf{r}; \boldsymbol{\alpha}, \mathbf{u}, K) = |\mathbf{v}|^{2K+L} Y_{LM_L}(\hat{\mathbf{v}}) \times \exp\left(-\frac{1}{2} \sum_{i=1}^{n_p+1} \sum_{j>i}^{n_p+1} \alpha_{ij} (\mathbf{r}_i - \mathbf{r}_j)^2\right), \quad (12)$$

where  $\hat{\mathbf{v}}$  is a collective label for the spherical angles characterizing the orientation of the unit vector  $\mathbf{v}/|\mathbf{v}|$  with

$$\mathbf{v} = \sum_{i=1}^{n_p+1} \mathbf{u}_i^{(0)} \mathbf{r}_i = (\mathbf{u}^{(0)} \otimes \mathbf{I}_3)^T \mathbf{r} \quad (13)$$

and  $(\mathbf{u}^{(0)})^T = (\mathbf{u}_1^{(0)}, \mathbf{u}_2^{(0)}, \dots, \mathbf{u}_{n_p+1}^{(0)})$ . As to the parameterization corresponding to LF Cartesian coordinates (approach (A)), the  $\sum_{i=1}^{n_p+1} \mathbf{u}_i^{(0)} = 0$  condition is introduced to guarantee zero overall momentum for the basis function.

#### 2. Integral transformation, generator coordinates

During the evaluation of the matrix elements not the original form of the basis functions given in Eq. (12) is used, but it is generated by the integral transformation<sup>53</sup>

$$\phi^{[\lambda]}(\mathbf{r}; \mathcal{A}, \mathbf{u}, K) = \frac{1}{\mathcal{B}_{KLp}} \int d\hat{\mathbf{e}} \eta_{LM_Lp}(\hat{\mathbf{e}}) \times \left\{ \hat{\mathcal{D}}_a^{(2K+L)} g(\mathbf{r}; \mathcal{A}, s(\mathbf{a}, \mathbf{u}, \mathbf{e})) \right\}_{a_i=0, |e_i|=1} \quad (14)$$

with the generating function

$$g(\mathbf{r}; \mathcal{A}, s) = \exp\left(-\frac{1}{2} \mathbf{r}^T (\mathcal{A} \otimes \mathbf{I}_3) \mathbf{r} + s^T \mathbf{r}\right), \quad (15)$$

where  $s \in \mathbb{R}^{3(n_p+1)}$  is also called the generator coordinate and the definition of the symbols are collected in Table I for any  $L, M_L$ , and  $p$  values including both the “natural-parity,”  $p = (-1)^L$ , and the “unnatural-parity,”  $p = (-1)^{L+1}$ , cases.

In this work, we present results obtained using the basis functions with label “A” of Table I, i.e., states with arbitrary angular momentum quantum numbers,  $L$ , and “natural parity,”  $p = (-1)^L$ . We have obtained preliminary results with

TABLE I. Explanation of the notation used in the general definition of basis functions, Eq. (14), with angular momentum  $L$ ,  $M_L$ , and parity  $p$ .

$L$	$p$	$B_{KLp}^a$	$\hat{e}^b$	$\eta_{LM_L p}(\hat{e})^{b,c}$	$s$	$\hat{D}_a^{(K)d}$	Label
$>0$	$(-1)^L$	$B_{KL}$	$\hat{e}_1$	$Y_{LM_L}(\hat{e}_1)$	$a_1 \mathbf{u}_1 \otimes \mathbf{e}_1$	$\partial_{a_1}^K$	A
$>1$	$(-1)^{L+1}$	$B_{01} B_{KL}$	$(\hat{e}_1, \hat{e}_2)$	$[Y_L(\hat{e}_1) Y_1(\hat{e}_2)]_{LM_L}$	$\sum_{i=1}^2 a_i \mathbf{u}_i \otimes \mathbf{e}_i$	$\partial_{a_1}^K \partial_{a_2}$	B
$=0$	$-1$	$B_{01}^2 B_{KL}$	$(\hat{e}_1, \hat{e}_2, \hat{e}_3)$	$[Y_1(\hat{e}_1) Y_1(\hat{e}_2)]_1 Y_1(\hat{e}_3)_{00}$	$\sum_{i=1}^3 a_i \mathbf{u}_i \otimes \mathbf{e}_i$	$\partial_{a_1}^K \partial_{a_2} \partial_{a_3}$	C

<sup>a</sup> $B_{KL} = 4\pi(2K+L)!(K+L+1)!2^{L+1}/[K!(2K+2L+2)!]$  with  $K, L \in \mathbb{N}_0$ .

<sup>b</sup> $\hat{e}_i$  is the collective label for the spherical angles characterizing the orientation of the unit vector  $\mathbf{e}_i$ .

<sup>c</sup> $[Y_{l_1} Y_{l_2}]_{m_l}$  denotes the coupling of the  $l_1$ th and  $l_2$ th spherical harmonics to the  $l$ th order and  $m_l$ th degree spherical harmonic function.

<sup>d</sup> $\kappa = 2K+L$  and the shorthand notation  $\partial_{a_i}^k = \partial^k / \partial a_i^k$  are introduced.

functions of label ‘‘B’’, i.e., ‘‘unnatural-parity’’ basis functions with  $p = (-1)^{L+1}$  for  $L > 0$ , but they are not discussed in the present work.

The generating function  $g(\mathbf{r}; \mathcal{A}, s)$  equals (within a constant factor) an explicitly correlated Gaussian function with shifted origin,  $\mathcal{R} \in \mathbb{R}^{3(n_p+1)}$  (in short, ‘‘floating geminal’’) according to

$$\begin{aligned} f(\mathbf{r}; \mathcal{A}, \mathcal{R}) &= \exp\left(-\frac{1}{2}(\mathbf{r} - \mathcal{R})^T (\mathcal{A} \otimes \mathbf{I}_3)(\mathbf{r} - \mathcal{R})\right) \\ &= \exp\left(-\frac{1}{2}\mathcal{R}^T (\mathcal{A} \otimes \mathbf{I}_3)\mathcal{R}\right) \\ &\quad \times \exp\left(-\frac{1}{2}\mathbf{r}^T (\mathcal{A} \otimes \mathbf{I}_3)\mathbf{r} + \mathcal{R}^T (\mathcal{A} \otimes \mathbf{I}_3)\mathbf{r}\right), \end{aligned} \quad (16)$$

and thus by choosing  $\mathcal{R} = (\mathcal{A}^{-1} \otimes \mathbf{I}_3)s$  so that  $\mathcal{R}^T = s^T (\mathcal{A}^{-1} \otimes \mathbf{I}_3)$  ( $\mathcal{A}$  is symmetric and non-singular), we obtain

$$f(\mathbf{r}; \mathcal{A}, (\mathcal{A}^{-1} \otimes \mathbf{I}_3)s) = \exp\left(-\frac{1}{2}s^T (\mathcal{A}^{-1} \otimes \mathbf{I}_3)s\right) g(\mathbf{r}; \mathcal{A}, s). \quad (17)$$

The functions  $f$  and  $g$  with appropriate exponents  $\mathcal{A}$  describe well particles localized near  $\mathcal{R}$ , which is different from the origin. However, for such an  $\mathcal{R} \neq 0$  vector, they are not parity and angular momentum eigenfunctions. It is the integral transformation of Eq. (14), which restores the space rotation-inversion symmetry of an isolated system for  $g$ .

We note that this approach can be considered as a special application of the more general ‘‘generator coordinate method’’ introduced by Hill and Wheeler in 1953 (Ref. 75) with one of first applications in chemistry during the late 1970s by Lathouwers, van Leuven, and co-workers.<sup>76,77</sup> We also note here that the ansatz introduced in Eq. (12) shows similarities with the ‘‘Hagedorn-type’’ wave packets<sup>78</sup> used, for example, in Ref. 79. Of course, the space rotation-inversion symmetry for floating geminals could be restored numerically in a variational procedure, which was pursued by Adamowicz and Cafiero for  $L = 0$ , for example, in Ref. 22. It would also be interesting to consider this numerical reconstruction of the spatial symmetry for higher  $L$  values, but for the present work we stick to the analytic expressions and employ Eq. (14).

### 3. Linear transformation of the coordinates, channels

The LF Cartesian coordinates,  $\mathbf{r}$ , and various sets of translationally invariant Cartesian coordinates, say  $\mathbf{x}$  or  $\mathbf{y}$ , together with the coordinates of the center of mass,  $\mathbf{R}_{\text{CM}}$ , are related by simple linear transformations

$$\begin{aligned} \begin{pmatrix} \mathbf{x} \\ \mathbf{R}_{\text{CM}} \end{pmatrix} &= (\mathbf{U} \otimes \mathbf{I}_3)\mathbf{r} \text{ and } \mathbf{r} = (\mathbf{U}^{-1} \otimes \mathbf{I}_3) \begin{pmatrix} \mathbf{x} \\ \mathbf{R}_{\text{CM}} \end{pmatrix} \\ \begin{pmatrix} \mathbf{y} \\ \mathbf{R}_{\text{CM}} \end{pmatrix} &= (\mathbf{V} \otimes \mathbf{I}_3)\mathbf{r} \text{ and } \mathbf{r} = (\mathbf{V}^{-1} \otimes \mathbf{I}_3) \begin{pmatrix} \mathbf{y} \\ \mathbf{R}_{\text{CM}} \end{pmatrix} \end{aligned} \quad (18)$$

so that

$$\begin{pmatrix} \mathbf{y} \\ \mathbf{R}_{\text{CM}} \end{pmatrix} = (\mathbf{V}\mathbf{U}^{-1} \otimes \mathbf{I}_3) \begin{pmatrix} \mathbf{x} \\ \mathbf{R}_{\text{CM}} \end{pmatrix}$$

and

$$\begin{pmatrix} \mathbf{x} \\ \mathbf{R}_{\text{CM}} \end{pmatrix} = (\mathbf{U}\mathbf{V}^{-1} \otimes \mathbf{I}_3) \begin{pmatrix} \mathbf{y} \\ \mathbf{R}_{\text{CM}} \end{pmatrix} \quad (19)$$

hold. We thus can easily switch from one set of coordinates to another.

By switching between the coordinates, the mathematical form of the spatial functions remains unchanged and only the parameters have to be transformed. This ‘‘re-parameterization’’ of the basis functions by changing the coordinate representation reads

$$\begin{aligned} \phi^{[x]} &= |\mathbf{v}|^{2K+L} Y_{LM_L}(\hat{\mathbf{v}}) \exp\left(-\frac{1}{2}\mathbf{r}^T (\mathcal{A}^{(0)} \otimes \mathbf{I}_3)\mathbf{r}\right) \\ &= |\mathbf{v}|^{2K+L} Y_{LM_L}(\hat{\mathbf{v}}) \exp\left(-\frac{1}{2}\mathbf{x}^T (\mathcal{A}^{(x)} \otimes \mathbf{I}_3)\mathbf{x}\right) \\ &= |\mathbf{v}|^{2K+L} Y_{LM_L}(\hat{\mathbf{v}}) \exp\left(-\frac{1}{2}\mathbf{y}^T (\mathcal{A}^{(y)} \otimes \mathbf{I}_3)\mathbf{y}\right), \end{aligned} \quad (20)$$

where the exponents

$$(\mathcal{A}^{(0)})_{ij} = -\alpha_{ij}(1 - \delta_{ij}) + \left(\sum_{k=1, k \neq i}^{n_p+1} \alpha_{ik}\right) \delta_{ij} + c_A \frac{m_i}{m_{\text{tot}}} \frac{m_j}{m_{\text{tot}}} \quad (21)$$

are transformed according to

$$\mathcal{A}^{(x)} = \mathbf{U}^{-T} \mathcal{A}^{(0)} \mathbf{U}^{-1} \Leftrightarrow \mathcal{A}^{(0)} = \mathbf{U}^T \mathcal{A}^{(x)} \mathbf{U}$$

and

$$\mathcal{A}^{(y)} = \mathbf{V}^{-T} \mathcal{A}^{(0)} \mathbf{V}^{-1} \Leftrightarrow \mathcal{A}^{(0)} = \mathbf{V}^T \mathcal{A}^{(y)} \mathbf{V}, \quad (22)$$



which also yields the relations

$$\mathcal{A}^{(y)} = (\mathbf{U}\mathbf{V}^{-1})^T \mathcal{A}^{(x)} \mathbf{U}\mathbf{V}^{-1} \quad (23)$$

and

$$\mathcal{A}^{(x)} = (\mathbf{V}\mathbf{U}^{-1})^T \mathcal{A}^{(y)} \mathbf{V}\mathbf{U}^{-1}. \quad (24)$$

Note that

$$\mathcal{A}^{(x)} = \begin{pmatrix} \mathbf{A}^{(x)} & \mathbf{0} \\ \mathbf{0} & c_A \end{pmatrix} \quad \text{and} \quad \mathcal{A}^{(y)} = \begin{pmatrix} \mathbf{A}^{(y)} & \mathbf{0} \\ \mathbf{0} & c_A \end{pmatrix}. \quad (25)$$

Similarly, the global vector can be written as

$$\mathbf{v} = (\mathbf{u}^{(0)} \otimes \mathbf{I}_3)^T \mathbf{r} = (\mathbf{u}^{(x)} \otimes \mathbf{I}_3)^T \mathbf{x} = (\mathbf{u}^{(y)} \otimes \mathbf{I}_3)^T \mathbf{y}, \quad (26)$$

where  $\mathbf{u}^{(0)}$ ,  $\mathbf{u}^{(x)}$ ,  $\mathbf{u}^{(y)}$  obey the transformations  $\mathbf{u}^{(x)} = \mathbf{U}^{-T} \mathbf{u}^{(0)}$ ,  $\mathbf{u}^{(0)} = \mathbf{U}^T \mathbf{u}^{(x)}$ ,  $\mathbf{u}^{(y)} = \mathbf{V}^{-T} \mathbf{u}^{(0)}$ ,  $\mathbf{u}^{(0)} = \mathbf{V}^T \mathbf{u}^{(y)}$ ,  $\mathbf{u}^{(x)} = (\mathbf{U}\mathbf{V}^{-1})^T \mathbf{u}^{(y)}$ , and  $\mathbf{u}^{(y)} = (\mathbf{V}\mathbf{U}^{-1})^T \mathbf{u}^{(x)}$ . Note also that

$$\mathbf{u}^{(x)} = \begin{pmatrix} u^{(x)} \\ c_u \end{pmatrix} \quad \text{and} \quad \mathbf{u}^{(y)} = \begin{pmatrix} u^{(y)} \\ c_u \end{pmatrix} \quad (27)$$

and the zero overall momentum of the basis function in the LF Cartesian representation is guaranteed if  $c_u = 0$ . The condition  $c_u = 0$  is equivalent to the requirement  $\sum_{i=1}^{n_p+1} \mathbf{u}_i^{(0)} = c_u = 0$  according to the properties of the transformation matrix, Eq. (6).

It is convenient to consider various coordinates for the calculations, for at least two reasons. First, the evaluation of the matrix elements can be simplified using a certain type of coordinates. Of course, the Jacobian of the coordinate transformation (here a constant) must be included in the volume element expressed in terms of the transformed coordinates (see Eq. (26) of Ref. 26). Second, different coordinates can represent efficiently different correlations (Figure 2), and thus the parameterization of the wave function expressed in terms of one set of coordinates can be more convenient than in terms of another set of coordinates. Additionally, the action of a permutation operation on the spatial coordinates is equivalent to a linear transformation of the Cartesian coordinates, and thus, its effect on the spatial functions can be accounted for by the transformation of the parameters.

Finally, we note here that since  $\mathbf{A}$  is real symmetric, it is always possible to find some set of translationally invariant coordinates, which corresponds to a diagonal exponent matrix,  $\mathbf{A}'$ , and thus an effective ‘‘one-particle’’ (pseudo-particle) basis function. As the wave function is written as a linear combinations of the basis functions with different exponent matrices, each of these exponent matrices is diagonal in some set of coordinates (‘‘coordinate channels’’), and thus the wave function can be written as a linear combination of this multiple-channel basis set.

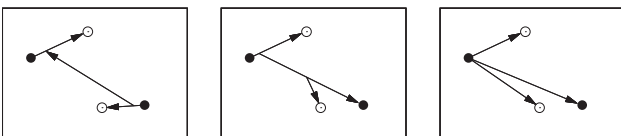


FIG. 2. Examples for translationally invariant Cartesian coordinates for four particles. Every choice can describe different correlations efficiently.

#### 4. Spin functions

In this work, we consider systems in which only the coupling of spin-1/2 particles occur. A spin-1/2 particle can have  $\alpha$  and  $\beta$  spin functions,  $\sigma_{\frac{1}{2}, \frac{1}{2}}(1) = |\uparrow\rangle_\sigma$  and  $\sigma_{\frac{1}{2}, -\frac{1}{2}}(1) = |\downarrow\rangle_\sigma$  corresponding to  $(s_\alpha, m_{s_\alpha}) = (\frac{1}{2}, \frac{1}{2})$  and  $(s_\beta, m_{s_\beta}) = (\frac{1}{2}, -\frac{1}{2})$ , respectively (the subscript  $\sigma$  refers to the spin degree(s) of freedom). For  $n$  identical particles, products of one-particle spin functions (‘‘elementary’’ spin functions or uncoupled basis representations) are coupled to the many-particle spin function,  $\Sigma_{S, M_S}(1, \dots, n)$ , with the total spin quantum numbers  $S$  and  $M_S$ .

The  $\alpha$  and  $\beta$  projections are distributed between the  $n$  particles according to  $n = n_\alpha + n_\beta$  and  $M_S = m_{s_\alpha} n_\alpha + m_{s_\beta} n_\beta$ . Thus, each  $n$ -particle uncoupled basis function,  $\sigma_{\frac{1}{2}, m_{s_1}}(1) \dots \sigma_{\frac{1}{2}, m_{s_n}}(n)$ , which contribute to the  $n$ -particle total spin eigenfunction  $\Sigma_{S, M_S}(1, \dots, n)$ , must contain  $n_\alpha = n/2 + M_S$  and  $n_\beta = n/2 - M_S$  one-particle spin functions,  $\sigma_{\frac{1}{2}, m_{s_i}}(i)$ , which can be written down in all possible permutations, resulting in a total of  $N_s = \binom{n}{n_\alpha} = \binom{n}{n_\beta}$  uncoupled  $n$ -particle basis functions. Then,  $\Sigma_{S, M_S}(1, \dots, n)$  is expressed as a linear combination of the uncoupled basis functions using the Clebsch–Gordan expansion coefficients,  $\langle j_1, m_{j_1}, j_2, m_{j_2} | J, M_J \rangle$ , and the requirement that  $\Sigma_{S, M_S}(1, \dots, n)$  is normalized.

In the present work, we consider only systems with two and three identical spin-1/2 particles, and the spin functions corresponding to the calculated states are constructed as follows (the construction of any other spin function of systems with few spin-1/2 particles can be done similarly).

For two spin-1/2 particles, we use here the  $\Sigma_{0,0}(1, 2)$  (singlet) and the  $\Sigma_{1,0}(1, 2)$  (a triplet) spin functions. Both spin functions have well-known forms, which we present here to introduce notation needed later. For both  $\Sigma_{0,0}(1, 2)$  and  $\Sigma_{1,0}(1, 2)$  holds  $M_S = 0$ , and thus  $n_\alpha = n_\beta = 1$ . The number of uncoupled basis functions is  $N_s = \binom{2}{n_\alpha} = \binom{2}{n_\beta} = 2$ . Then, the total spin function can be obtained as

$$\begin{aligned} \Sigma_{0,0}(1, 2) &= [\sigma_{\frac{1}{2}}(1)\sigma_{\frac{1}{2}}(2)]_{0,0} \\ &= \langle \frac{1}{2}, \frac{1}{2}, \frac{1}{2}, -\frac{1}{2} | 0, 0 \rangle \sigma_{\frac{1}{2}, \frac{1}{2}}(1)\sigma_{\frac{1}{2}, -\frac{1}{2}}(2) \\ &\quad + \langle \frac{1}{2}, -\frac{1}{2}, \frac{1}{2}, \frac{1}{2} | 0, 0 \rangle \sigma_{\frac{1}{2}, -\frac{1}{2}}(1)\sigma_{\frac{1}{2}, \frac{1}{2}}(2) \\ &= \frac{1}{\sqrt{2}} \sigma_{\frac{1}{2}, \frac{1}{2}}(1)\sigma_{\frac{1}{2}, -\frac{1}{2}}(2) - \frac{1}{\sqrt{2}} \sigma_{\frac{1}{2}, -\frac{1}{2}}(1)\sigma_{\frac{1}{2}, \frac{1}{2}}(2) \\ &= \frac{1}{\sqrt{2}} (|\uparrow\downarrow\rangle - |\downarrow\uparrow\rangle), \end{aligned} \quad (28)$$

where  $[\dots]_{jm_j}$  refers to the angular momentum coupling. Similarly, we obtain the triplet spin function as

$$\begin{aligned} \Sigma_{1,0}(1, 2) &= [\sigma_{\frac{1}{2}}(1)\sigma_{\frac{1}{2}}(2)]_{1,0} \\ &= \langle \frac{1}{2}, \frac{1}{2}, \frac{1}{2}, -\frac{1}{2} | 1, 0 \rangle \sigma_{\frac{1}{2}, \frac{1}{2}}(1)\sigma_{\frac{1}{2}, -\frac{1}{2}}(2) \\ &\quad + \langle \frac{1}{2}, -\frac{1}{2}, \frac{1}{2}, \frac{1}{2} | 1, 0 \rangle \sigma_{\frac{1}{2}, -\frac{1}{2}}(1)\sigma_{\frac{1}{2}, \frac{1}{2}}(2) \\ &= \frac{1}{\sqrt{2}} \sigma_{\frac{1}{2}, \frac{1}{2}}(1)\sigma_{\frac{1}{2}, -\frac{1}{2}}(2) + \frac{1}{\sqrt{2}} \sigma_{\frac{1}{2}, -\frac{1}{2}}(1)\sigma_{\frac{1}{2}, \frac{1}{2}}(2) \\ &= \frac{1}{\sqrt{2}} (|\uparrow\downarrow\rangle + |\downarrow\uparrow\rangle). \end{aligned} \quad (29)$$

For three spin-1/2 particles, the  $\Sigma_{\frac{1}{2},\frac{1}{2}}(1, 2, 3)$  (a doublet) spin function has  $M_S = 1/2$ , and thus  $n_\alpha = 2$  and  $n_\beta = 1$  with  $N_s = \binom{n}{n_\alpha} = \binom{n}{n_\beta} = 3$  uncoupled basis functions. Then, the total spin function expressed in terms of the uncoupled spin functions can be obtained by evaluating

$$\begin{aligned} \Sigma_{\frac{1}{2},\frac{1}{2}}(1, 2, 3) = & c_1 [[\sigma_{\frac{1}{2}}(1)\sigma_{\frac{1}{2}}(2)]_1 \sigma_{\frac{1}{2}}(3)]_{\frac{1}{2},\frac{1}{2}} \\ & + c_2 [[\sigma_{\frac{1}{2}}(1)\sigma_{\frac{1}{2}}(2)]_0 \sigma_{\frac{1}{2}}(3)]_{\frac{1}{2},\frac{1}{2}}. \end{aligned} \quad (30)$$

The normalization condition for  $\Sigma_{\frac{1}{2},\frac{1}{2}}(1, 2, 3)$  requires  $c_1^2 + c_2^2 = 1$ , which can be fulfilled by choosing  $c_1 = \sin \vartheta_1$  and  $c_2 = \cos \vartheta_1$  with  $\vartheta_1 \in [-\pi/2, \pi/2]$ , similar to Ref. 35. Then, we couple the one-particle spin functions, insert the corresponding Clebsch–Gordan coefficients, and obtain

$$\begin{aligned} \Sigma_{\frac{1}{2},\frac{1}{2}}(1, 2, 3) &= \sin \vartheta_1 \langle 1, 0, \frac{1}{2}, \frac{1}{2} | \frac{1}{2}, \frac{1}{2} \rangle [\sigma_{\frac{1}{2}}(1)\sigma_{\frac{1}{2}}(2)]_{1,0} \sigma_{\frac{1}{2},\frac{1}{2}}(3) \\ &+ \sin \vartheta_1 \langle 1, 1, \frac{1}{2}, -\frac{1}{2} | \frac{1}{2}, \frac{1}{2} \rangle [\sigma_{\frac{1}{2}}(1)\sigma_{\frac{1}{2}}(2)]_{1,1} \sigma_{\frac{1}{2},-\frac{1}{2}}(3) \\ &+ \cos \vartheta_1 \langle 0, 0, \frac{1}{2}, \frac{1}{2} | \frac{1}{2}, \frac{1}{2} \rangle [\sigma_{\frac{1}{2}}(1)\sigma_{\frac{1}{2}}(2)]_{0,0} \sigma_{\frac{1}{2},\frac{1}{2}}(3) \\ &= \kappa_1(\vartheta_1) \sigma_{\frac{1}{2},\frac{1}{2}}(1)\sigma_{\frac{1}{2},-\frac{1}{2}}(2)\sigma_{\frac{1}{2},\frac{1}{2}}(3) \\ &+ \kappa_2(\vartheta_1) \sigma_{\frac{1}{2},\frac{1}{2}}(1)\sigma_{\frac{1}{2},\frac{1}{2}}(2)\sigma_{\frac{1}{2},-\frac{1}{2}}(3) \\ &+ \kappa_3(\vartheta_1) \sigma_{\frac{1}{2},-\frac{1}{2}}(1)\sigma_{\frac{1}{2},\frac{1}{2}}(2)\sigma_{\frac{1}{2},\frac{1}{2}}(3). \end{aligned} \quad (31)$$

Thus, in short the total spin function can be written as

$$\begin{aligned} \Sigma_{\frac{1}{2},\frac{1}{2}}(1, 2, 3) = & \kappa_1(\vartheta_1) |\uparrow\downarrow\uparrow\rangle + \kappa_2(\vartheta_1) |\uparrow\uparrow\downarrow\rangle \\ & + \kappa_3(\vartheta_1) |\downarrow\uparrow\uparrow\rangle, \end{aligned} \quad (32)$$

where we collected the linear combination coefficients in  $\kappa(\vartheta_1) = (\kappa_1(\vartheta_1), \kappa_2(\vartheta_1), \kappa_3(\vartheta_1))$

$$\kappa_1(\vartheta_1) = \frac{1}{\sqrt{2}} \cos \vartheta_1 - \frac{1}{\sqrt{6}} \sin \vartheta_1, \quad (33)$$

$$\kappa_2(\vartheta_1) = \sqrt{\frac{2}{3}} \sin \vartheta_1, \quad (34)$$

$$\kappa_3(\vartheta_1) = -\frac{1}{\sqrt{2}} \cos \vartheta_1 - \frac{1}{\sqrt{6}} \sin \vartheta_1. \quad (35)$$

If there are several types of identical particles,  $a, b, \dots$  in the system, the total spin function is constructed as

$$\chi_{S, M_S} = \Sigma_{S_a, M_{S_a}}(1, \dots, n_a) \Sigma_{S_b, M_{S_b}}(1, \dots, n_b) \dots \quad (36)$$

and here  $(S, M_S)$  is a collective index for  $(S_a, M_{S_a})$ ,  $(S_b, M_{S_b})$ ,  $\dots$ . Since the total spin function for any particle type  $a$ ,  $\Sigma_{S_a, M_{S_a}}(1, \dots, n_a)$ , can be written as a linear combination of uncoupled many-particle spin functions, the  $\chi_{S, M_S}$  function can also be written in a similar way, and thus for later convenience we introduce the shorthand notation

$$\chi_{S, M_S}(\boldsymbol{\vartheta}) = \sum_{n=1}^{N_s} \kappa_n(\boldsymbol{\vartheta}) |n\rangle_\sigma, \quad (37)$$

where  $|n\rangle_\sigma$  denotes the product of uncoupled many-particle spin functions for each particle type,  $N_s = N_{S_a} N_{S_b} \dots$ ,  $\sigma$  refers to the spin degrees of freedom, and  $\boldsymbol{\vartheta}$  contains the free parameters if there are several ‘‘partial waves.’’ The

value of  $\kappa_n(\boldsymbol{\vartheta})$  is determined by the normalization condition, the Clebsch–Gordan coefficients, and the angular momentum coupling procedure carried out for each particle types similar to Eqs. (28)–(35).

## 5. Permutation of identical particles

For the (anti)symmetrization of the product of the spatial and the spin functions, Eq. (10), we have to evaluate the effect of a permutation operator on this product by acting on both the spatial and the spin ‘‘coordinates’’

$$\begin{aligned} \hat{P}_p \{ \phi^{[\lambda]} \chi^{[\zeta]} \} &= \{ \hat{P}_p \phi^{[\lambda]}(\mathbf{r}) \} \{ \hat{P}_p \chi^{[\zeta]} \} \\ &= \phi^{[\lambda]}(\hat{P}_p^{-1} \mathbf{r}) \sum_{n=1}^{N_s} \kappa_n(\boldsymbol{\vartheta}) \hat{P}_p |n\rangle_\sigma. \end{aligned} \quad (38)$$

To proceed, we construct the matrix representation of  $\hat{P}_p$  for both the elementary (uncoupled) spin functions,  $\mathbf{P}_p^s \in \mathbb{R}^{N_s \times N_s}$ , and for the LF Cartesian coordinates,  $\mathbf{P}_p^r \in \mathbb{R}^{(n_p+1) \times (n_p+1)}$  with

$$\hat{P}_p \mathbf{r} = (\mathbf{P}_p^r \otimes \mathbf{I}_3) \mathbf{r}. \quad (39)$$

Since the effect of  $\hat{P}_p$  is a simple permutation for both the elementary spin functions and the LF Cartesian coordinates, the corresponding matrices contain ‘‘0’’s except for a single ‘‘1’’ element in each row and column. Then, we can write

$$\begin{aligned} \hat{P}_p \{ \phi^{[\lambda]} \chi^{[\zeta]} \} &= \phi^{[\lambda]}((\mathbf{P}_p^r \otimes \mathbf{I}_3)^{-1} \mathbf{r}; \mathbf{u}^{(0)}, \mathcal{A}^{(0)}) \\ &\times \sum_{n=1}^{N_s} ((\mathbf{P}_p^s)^T \boldsymbol{\kappa}(\boldsymbol{\vartheta}))_n |n\rangle_\sigma \\ &= \phi^{[\lambda]}(\mathbf{r}; \mathbf{u}_p^{(0)}, \mathcal{A}_p^{(0)}) \sum_{n=1}^{N_s} (\tilde{\boldsymbol{\kappa}}_p(\boldsymbol{\vartheta}))_n |n\rangle_\sigma, \end{aligned} \quad (40)$$

where the transformation of the spatial function parameters upon the linear transformation,  $\mathbf{P}_p^r$ , of the coordinates was inserted, Eqs. (18)–(27), and for brevity the following notation was introduced:

$$\tilde{\boldsymbol{\kappa}}_p(\boldsymbol{\vartheta}) = (\mathbf{P}_p^s)^T \boldsymbol{\kappa}(\boldsymbol{\vartheta}) \quad (41)$$

and

$$\mathbf{u}_p^{(0)} = (\mathbf{P}_p^r)^T \mathbf{u}^{(0)} \quad \text{and} \quad \mathcal{A}_p^{(0)} = (\mathbf{P}_p^r)^T \mathcal{A}^{(0)} \mathbf{P}_p^r. \quad (42)$$

## D. Overlap and Hamiltonian matrix elements

The matrix element of a spin-independent and permutationally invariant operator,  $\hat{O}$ , for basis functions  $I$  and  $J$  is evaluated as

$$\begin{aligned} O_{IJ}^{[\lambda, \zeta]} &= \langle \Phi_I^{[\lambda, \zeta]} | \hat{O} | \Phi_J^{[\lambda, \zeta]} \rangle_{r, \sigma} \\ &= \langle \hat{\phi} \{ \phi_I^{[\lambda]} \chi_I^{[\zeta]} \} | \hat{O} | \hat{\phi} \{ \phi_J^{[\lambda]} \chi_J^{[\zeta]} \} \rangle_{r, \sigma}. \end{aligned} \quad (43)$$

By exploiting the quasi-idempotency  $\hat{\mathcal{A}}\hat{\mathcal{A}} = (N_{\text{perm}})^{1/2}\hat{\mathcal{A}}$ , the  $(I, J, K)$ th matrix element is

$$\begin{aligned} O_{IJ}^{[\lambda, \zeta]} &= \sum_{p=1}^{N_{\text{perm}}} \varepsilon_p \langle \phi_I^{[\lambda]} \chi_I^{[\zeta]} | \hat{O} | \hat{P}_p \{ \phi_J^{[\lambda]} \chi_J^{[\zeta]} \} \rangle_{r, \sigma} \\ &= \sum_{p=1}^{N_{\text{perm}}} \varepsilon_p \langle \phi_I^{[\lambda]} | \hat{O} | \hat{P}_p \phi_J^{[\lambda]} \rangle_r \langle \chi_I^{[\zeta]} | \hat{P}_p \chi_J^{[\zeta]} \rangle_\sigma \\ &= \sum_{p=1}^{N_{\text{perm}}} c_{IJ_p}^{[\zeta]} O_{IJ_p}^{[\lambda]} \end{aligned} \quad (44)$$

with

$$c_{IJ_p}^{[\zeta]} = \varepsilon_p \langle \chi_I^{[\zeta]} | \hat{P}_p \chi_J^{[\zeta]} \rangle_\sigma, \quad (45)$$

$$O_{IJ_p}^{[\lambda]} = \langle \phi_I^{[\lambda]} | \hat{O} | \hat{P}_p \phi_J^{[\lambda]} \rangle_r. \quad (46)$$

In this work,  $\hat{O}$  will be the unit operator,  $\hat{I}$ , the kinetic energy operator,  $\hat{T}$ , and the potential energy operator,  $\hat{V}$ . Accordingly, the overlap matrix element is

$$S_{IJ}^{[\lambda, \zeta]} = \sum_{p=1}^{N_{\text{perm}}} c_{IJ_p}^{[\zeta]} S_{IJ_p}^{[\lambda]} \quad \text{with} \quad S_{IJ_p}^{[\lambda]} = \langle \phi_I^{[\lambda]} | \hat{P}_p \phi_J^{[\lambda]} \rangle_r. \quad (47)$$

The matrix elements for the kinetic and the potential energy operators are

$$T_{IJ}^{[\lambda, \zeta]} = \sum_{p=1}^{N_{\text{perm}}} c_{IJ_p}^{[\zeta]} T_{IJ_p}^{[\lambda]} \quad \text{with} \quad T_{IJ_p}^{[\lambda]} = \langle \phi_I^{[\lambda]} | \hat{T} | \hat{P}_p \phi_J^{[\lambda]} \rangle_r \quad (48)$$

and

$$V_{IJ}^{[\lambda, \zeta]} = \sum_{p=1}^{N_{\text{perm}}} c_{IJ_p}^{[\zeta]} V_{IJ_p}^{[\lambda]} \quad \text{with} \quad V_{IJ_p}^{[\lambda]} = \langle \phi_I^{[\lambda]} | \hat{V} | \hat{P}_p \phi_J^{[\lambda]} \rangle_r \quad (49)$$

so that

$$H_{IJ}^{[\lambda, \zeta]} = T_{IJ}^{[\lambda, \zeta]} + V_{IJ}^{[\lambda, \zeta]}. \quad (50)$$

Then, we are left with the evaluation of  $S_{IJ_p}^{[\lambda]}$ ,  $T_{IJ_p}^{[\lambda]}$ , and  $V_{IJ_p}^{[\lambda]}$ , i.e., the matrix elements for two spatial functions, Eqs. (12) and (14). The procedure (see, for example, Ref. 35) is somewhat tedious, so we list here only the main steps of the evaluation and collect the explicit formulae in the supplementary material.

A matrix element of operator  $\hat{O}$  is best written using the form of the basis function given with the generating integral equation (14), and it is, with  $\lambda = (L, M_L, p)$ ,

$$\begin{aligned} &\langle \phi^{[\lambda]}(\mathbf{r}; \mathcal{A}, \mathbf{u}, K) | \hat{O} | \phi^{[\lambda]}(\mathbf{r}; \mathcal{A}', \mathbf{u}', K') \rangle_r \\ &= \frac{1}{\mathcal{B}_{KLp} \mathcal{B}_{K'Lp}} \int d\hat{\mathbf{e}} \int d\hat{\mathbf{e}}' \eta_{LM_Lp}^*(\hat{\mathbf{e}}) \eta_{LM_Lp}(\hat{\mathbf{e}}') \\ &\quad \times \{ \hat{\mathcal{D}}_a^{(2K+L)} \hat{\mathcal{D}}_a^{(2K'+L)} \\ &\quad \langle g(\mathbf{r}; \mathcal{A}, s(\mathbf{a}, \mathbf{u}, \mathbf{e})) | \hat{O} | g(\mathbf{r}; \mathcal{A}', s'(\mathbf{a}', \mathbf{u}', \mathbf{e}')) \rangle_{r, a_i=a'_i=0, |e_i|=|e'_i|=1} \} \end{aligned} \quad (51)$$

The definition of the symbols is given in Table I and the integration is carried out over the points of the unit sphere de-

scribed by the spherical angles collected in  $\hat{\mathbf{e}}$  and  $\hat{\mathbf{e}}'$  of the unit vectors  $\mathbf{e}$  and  $\mathbf{e}'$ , respectively.  $\langle \dots \rangle_r$  indicates that the integration has to be carried out for the spatial coordinates  $\mathbf{r}$ .

The evaluation of the integral in Eq. (51) includes the following steps.

- (1) Evaluation of the integral with the generating functions (floating geminals)

$$I_{O,1}(s, s') = \langle g(\mathbf{r}; \mathcal{A}, s) | \hat{O} | g(\mathbf{r}; \mathcal{A}', s') \rangle_r. \quad (52)$$

- (2) Differentiation prescribed by the operators  $\hat{\mathcal{D}}_a^{(2K+L)}$  and  $\hat{\mathcal{D}}_a^{(2K'+L)}$  (see Table I for the definition). Then, the result is expressed in terms of polynomials of scalar products of the unit vectors,  $\mathbf{e}^T \mathbf{e}'$ ,

$$I_{O,2}^{[(L)]}(\mathbf{e}, \mathbf{e}') = \left\{ \hat{\mathcal{D}}_a^{(2K+L)} \hat{\mathcal{D}}_a^{(2K'+L)} I_{O,2}^{[(L)]}(\mathbf{e}, \mathbf{e}') \right\}_{a_i=a'_i=0, |e_i|=|e'_i|=1}. \quad (53)$$

- (3) Evaluation of the angular integrals

$$I_{O,3}^{[\lambda=(L, M_L, p)]} = \frac{1}{\mathcal{B}_{KLp} \mathcal{B}_{K'Lp}} \int d\hat{\mathbf{e}} \times \int d\hat{\mathbf{e}}' \eta_{LM_Lp}^*(\hat{\mathbf{e}}) \eta_{LM_Lp}(\hat{\mathbf{e}}') I_{O,2}^{[(L)]}(\mathbf{e}, \mathbf{e}'), \quad (54)$$

which reads for the natural-parity case,  $p = (-1)^L$ , as

$$I_{O,3}^{[\lambda=(L, M_L, (-1)^L)]} = \frac{1}{\mathcal{B}_{KLp} \mathcal{B}_{K'Lp}} \int d\hat{\mathbf{e}} \times \int d\hat{\mathbf{e}}' Y_{LM_L}^*(\hat{\mathbf{e}}) Y_{LM_L}(\hat{\mathbf{e}}') I_{O,2}^{[(L)]}(\mathbf{e}, \mathbf{e}'). \quad (55)$$

The evaluation of the angular integrals is facilitated by the identity, see p. 87 of Ref. 35, related to the addition theorem of spherical harmonics

$$(\mathbf{e}^T \mathbf{e}')^k = \sum_{l=0}^k B_{\frac{k-l}{2}, l} \sum_{m=-l}^l Y_{lm}^*(\hat{\mathbf{e}}) Y_{lm}(\hat{\mathbf{e}}'), \quad (56)$$

$[(k-l)/2 \in \mathbb{N}_0]$

which is for  $k = 1$

$$\mathbf{e}^T \mathbf{e}' = \frac{4\pi}{3} \sum_{m=-1}^1 Y_{1m}^*(\hat{\mathbf{e}}) Y_{1m}(\hat{\mathbf{e}}'). \quad (57)$$

Further details of the derivation of the overlap, kinetic, and potential energy integrals are given in the supplementary material.

For large  $(2K + L) > 4$  exponents of the  $|\mathbf{v}|^{2K+L}$  polynomial prefactor, Eq. (12), a direct implementation of the integral formulae given in Refs. 35 and 53 resulted in numerical instabilities for a computer program with a finite number representation (double precision in FORTRAN). To restore the numerical stability, we introduced quasi-normalization for the basis functions, which allowed us to cancel some problematic terms. We call the normalization with respect to the spatial function,

$$\Phi^{[\lambda, \zeta]} = (\langle \phi^{[\lambda]} | \phi^{[\lambda]} \rangle_r)^{-1/2} \hat{\mathcal{A}} \{ \phi^{[\lambda]} \chi^{[\zeta]} \}, \quad (58)$$

quasi-normalization. The quasi-normalized and rearranged integral formulae are collected in the supplementary material. Where it was necessary and useful, we used a logarithmic evaluation of products and fractions, e.g.,

$$(a \cdot b)/(c \cdot d) = \text{sign}(ab/cd) \cdot 10^{(\lg a + \lg b - \lg c - \lg d)}, \quad (59)$$

which allowed us to obtain small numbers as ratios and products of large ones. Furthermore, it was possible to factor out the term, see the supplementary material,

$$F_{KL} = \sum_{m=0}^K \frac{2^{2m}(L+m+1)!}{(K-m)!(K-m)!m!(2L+2m+2)!}, \quad (60)$$

whose value for a finite number of  $K$  and  $L$  integer values was pre-calculated with MATHEMATICA.<sup>80</sup> These numbers were stored in a file and are read in by the FORTRAN program.

## E. Multi-stage variational optimization

The wave function for some set of quantum numbers  $\lambda = (L, M_L, p)$  and  $\zeta = (S, M_S)$  is written as a linear combination of  $N_b$  basis functions

$$\begin{aligned} \Psi^{[\lambda, \zeta]}(\mathbf{r}, \boldsymbol{\sigma}) &= \sum_{I=1}^{N_b} c_I \Phi_I^{[\lambda, \zeta]}(\mathbf{r}, \boldsymbol{\sigma}) \\ &= (N_{\text{perm}})^{-1/2} \sum_{I=1}^{N_b} c_I \\ &\quad \times \sum_{p=1}^{N_{\text{perm}}} \hat{P}_p \{ \phi^{[\lambda]}(\mathbf{r}; \boldsymbol{\alpha}_I, \mathbf{u}_I, K_I) \chi^{[\zeta]}(\boldsymbol{\sigma}; \boldsymbol{\vartheta}_I) \}. \end{aligned} \quad (61)$$

The concept of this parameterization is visualized in Figure 3. Since the overlap and the Hamiltonian matrix elements are evaluated analytically (Sec. II D and the supplementary material), we can rely on the variational principle during the course of the selection of the numerical values for the “free parameters” of this ansatz. Thus, the lower the eigenenergy, the better the parameterization is. During the course of the calculations we tightened the optimization criterion of the free parameters and increased the number of the basis functions to obtain a lower energy eigenvalue.

In this work, we solved the generalized linear variational problem corresponding to  $N_b$  basis functions with some fixed

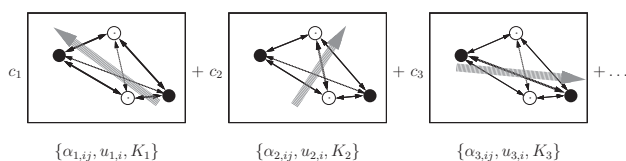


FIG. 3. Visual representation of the parameterization of the wave function for  $H_2$ . The width of the lines of the double-headed arrows, which connect the particles  $i$  and  $j$  is proportional to the value of  $\alpha_{I,ij}$  ( $i = 1, \dots, 4; j = i + 1, \dots, 4$ ), and the orientation of the grey arrows represent the orientation of the global vectors parameterized by  $u_{I,i}$  ( $i = 1, 2, 3$ ) ( $I = 1, 2, \dots, N_b$ ).

$\mathcal{P}_I = (\boldsymbol{\alpha}_I, \mathbf{u}_I, K_I; \boldsymbol{\vartheta}_I)$  parameters

$$\mathbf{H}^{[\lambda, \zeta]} c_i^{[\lambda, \zeta]} = E_i^{[\lambda, \zeta]} S^{[\lambda, \zeta]} c_i^{[\lambda, \zeta]} \quad i = 1, 2, \dots, N_b \quad (62)$$

using the LAPACK “divide and conquer” diagonalizer available in Intel’s Math Kernel Library (MKL).<sup>81</sup> If the parameter set,  $\mathcal{P}_I$ , was selected appropriately (see the discussion below), we did not observe any near-linear dependency problems in finite-precision, 8-byte (double precision in FORTRAN), arithmetics. Near-linear dependency problems were always indicators of an inadequate parameter generation.

The parameters were generated for one basis function after the other in a random procedure.<sup>30,35,64–66</sup> The random generation with a variational selection criterion is a straightforward approach, and this explains our choice here. We have found the description in Ref. 35 the most useful in our work, including the fast eigenvalue estimation procedure of an updated parameter set, described on pp. 27–29 of Ref. 35.

In addition, we have investigated the effect of the coordinate representation and the sampling strategy on the convergence rate of the energy with respect to the computational effort. We have found that both have a crucial impact on the efficiency, and we summarize our observations and our strategy developed as follows.

### 1. Non-linear variational problem

Optimization of the parameters of the basis functions is a delicate problem. For example, for an  $(n_p + 1)$ -particle system there are  $(n_p + 1)n_p/2 + n_p + 1 = (n_p + 1)(n_p + 2)/2$  free parameters,  $\{\boldsymbol{\alpha}_I, \mathbf{u}_I, K_I\}$ , corresponding to each spatial function, Eqs. (12) and (13). If, for example,  $n_p + 1 = 4$ , there are 10 free parameters for each basis function, and thus for 500 basis functions, the ansatz contains 5000 parameters to be optimized. One may suspect that there is a myriad of local minima for such a large number of free parameters. Nevertheless, the variational principle and the physical-chemical intuition served as two major guiding tools for us in the construction of a useful strategy for calculating as low of an energy eigenvalue (and the corresponding wave function) as possible. The actual values of the free parameters at the minimum point are not of primary interest, and there might be several equivalent or at least “almost equivalent” parameterizations due to the non-orthogonality of the basis functions and the multiple equivalent coordinate representations.

During the course of the buildup of the basis set, the free parameters were optimized one after the other. To select a new parameter a large number of trial values were generated randomly, which were then tested using the fast eigenvalue-update procedure of Ref. 35. Then, that trial value was utilized for the extension of the basis set, which provided the lowest energy eigenvalue (or the lowest few energy eigenvalues if vibrational excited states were also of interest). For small to medium-sized basis sets (with typically 50–200 basis functions), we run regular refinement cycles for the already selected parameters, which allowed us to replace an earlier selected parameter with a newly generated and better one, i.e., which corresponded to a lower energy eigenvalue.

In order to select parameters for new spatial and spin functions, we had to generate and test trial values for the

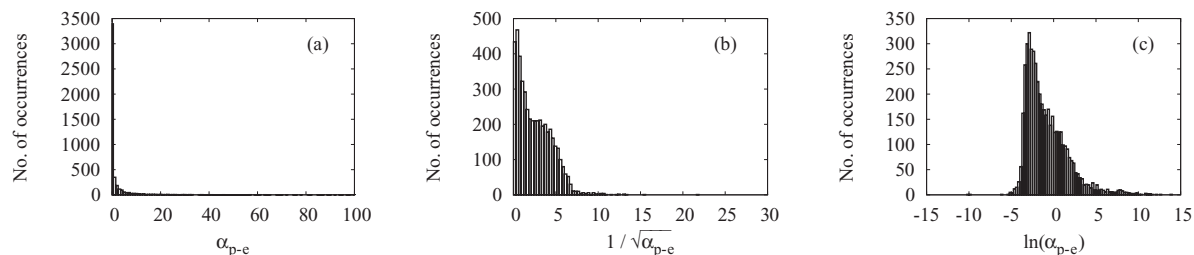


FIG. 4. Optimized basis function parameters for  $H_2$  ( $L = 0$ ,  $p = +1$ ,  $S_p = 0$ ,  $K_{\max} = 10$ ). The  $\alpha_{p-e}$  exponents corresponding to laboratory-fixed Cartesian coordinates were optimized using  $\xi = (\alpha_{p-e})^{-1/2}$  and a random number generator with a uniform continuous distribution of  $\xi \in \mathbf{u}(a_{\min}^{(p-e)}, a_{\max}^{(p-e)})$ . The  $K$  values were generated (not optimized) in a uniform discrete distribution with  $[0, K_{\max}]$ .

$K \in \mathbb{N}_0$  polynomial exponent, the  $\alpha_{ij} \in \mathbb{R}^+$  Gaussian exponents (or the entries of the symmetric  $\mathcal{A}^{(0)}$  or  $\mathcal{A}^{(x)}$  matrices), the  $u_i \in \mathbb{R}$  (or  $\mathbf{u}_i$ ) global vector parameters, and, in the case of the three-fermionic  ${}^7\text{Li}$ , the  $\vartheta_1 \in [-\pi/2, \pi/2]$  spin-function parameter. As to the efficiency of this trial-and-error optimization, we had to address a few technical questions:

1. Shall we sample the parameters corresponding to the laboratory-fixed Cartesian coordinate representation, i.e.,  $\alpha_{ij}$  and  $A_{ij}^{(0)}$ , or is it better to generate first the trial parameters corresponding to some  $\mathbf{x}$  translationally invariant set of coordinates,  $A_{ij}^{(x)}$ ?

In general, which is the most convenient coordinate set for the optimization?

2. Shall we generate random values for the original parameter, say  $\alpha_{ij}$ , or shall we use instead a transformed one, e.g.,  $\sqrt{\alpha_{ij}}$  or  $\ln \alpha_{ij}$ ?

In general, what kind of probability distribution shall we use in the random number generator to generate random trials efficiently for the selected parameterization and coordinate representation?

In the calculations, we used the quasi-random number generators of the Vector Statistical Library available in Intel's MKL.<sup>81</sup> The intrinsic randomness or quasi-randomness of the trials did not play a role here.

The first question is related to the quasi-separability of the many-particle correlation problem to some, coupled, few-particle correlations represented by some coordinate set, Figure 2, and the corresponding geminal basis. The second question addresses the characteristic values and the distribution of the parameters in some representation. In an ideal case, all parameters,  $A_{12}, A_{13}, \dots, u_1, u_2, \dots$  could be optimized independently and the optimal values would be distributed according to some ordinary probability distribution, which is characterized by a few, well-defined parameters. Then, the generation of a trial value according to this probability distribution would be a reasonable first guess, not far from a real minimum point. In practice, a brute-force treatment of a few-particle system can be far from this ideal case, but it can be approached by a good choice of the coordinate set.

Assuming that a coordinate set has been selected, we give an example to our second question in Figure 4, which presents histograms for the optimized values of the proton-electron correlation exponents corresponding to the ground state of the  $H_2$  molecule. As it is apparent from the figure, it is the most practical to sample the distribution of  $\ln \alpha_{p-e}$ , instead of  $\alpha_{p-e}$ .

After exploratory test calculations, we estimated the envelope of the histograms with a normal probability density function parameterized with the sample mean and the unbiased sample variance and used this random distribution in our large-scale calculations to generate “reasonable” trial values for the optimization. In principle, it would be possible to automatize this procedure in the spirit of a sampling-importance-resampling strategy.<sup>82</sup> We note here that the sampling of a uniform continuous distribution for  $\alpha_{ij}$  resulted in a very slow convergence rate and near-linear dependence problems in finite precision arithmetics. In any case, we conclude that the parameterization and the random distribution, which we sample, have a (sometimes dramatic) influence on the convergence rate. At the same time, the convergence is guaranteed, in theory, by the variational principle.

## 2. Basis function generation strategy

We can summarize our basis function generation strategy as follows.

1.  $K$  was generated (not optimized) according to some discrete uniform or discretized normal distribution with the sample mean and the unbiased sample variance determined in test calculations, similar to Refs. 36, 83, and 84.
2. In the case of lithium,  $\vartheta_1$  was generated (not optimized) according to a uniform continuous distribution over the interval  $[-\pi/2, \pi/2]$ .
3. Trial values of  $\ln \alpha_{ij}$  corresponding to LF Cartesian coordinates were generated according to a normal distribution with some sample mean and some unbiased sample variance determined in test calculations. That trial value

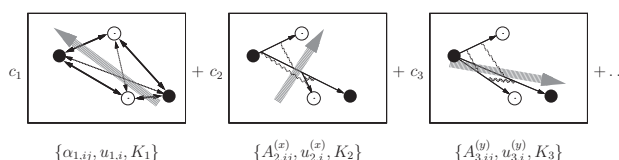


FIG. 5. Visual representation of an ansatz for the  $H_2$  molecule expressed in terms of several coordinates (channels). The Gaussian geminal exponents represented by double-headed arrows and wavy lines correspond to (1) laboratory-fixed Cartesian coordinates; (2) Jacobi coordinates; (3) heavy-particle centered coordinates, respectively, where the different widths of the lines represent the different numerical values of the various exponents. The grey arrows indicate the orientation of the global vectors parameterized by  $u_{1,i}$  ( $i = 1, 2, 3$ ) ( $I = 1, 2, 3, \dots, N_b$ ).

was selected for the construction of the basis function, which provided the lowest energy eigenvalue.

4. Trial values of  $u_i^{(x)}$  ( $i = 1, 2, \dots, n_p$ ) were generated according to a normal distribution with some sample mean and some unbiased sample variance determined in test calculations. That trial value was selected for the construction of the basis function, which provided the lowest energy eigenvalue. Instead of using LF Cartesian coordinates, a set of translationally invariant coordinates,  $\mathbf{x}$ , was selected, which described reasonably well the angular distribution of the particles. In the case of  $H_2$ , the atoms-in-molecule coordinates (Sec. III) were found to provide a useful representation, similar to  $Ps_2$ .<sup>85</sup>

During the extension of the basis set, we regularly run refinement cycles for the already selected Gaussian exponents,  $\alpha_{ij}$ , and the global vector coefficients,  $u_i^{(x)}$ , using the same random number distributions as before, while the values of the  $K$  and  $\vartheta_1$  parameters were kept fixed.

Finally, the  $\alpha_{ij}$  and the  $u_i^{(x)}$  values were further optimized in repeated fine-tuning cycles based on random walks. The fine-tuning was carried out for each  $\alpha_{ij}$  and  $u_i$  parameter one after the other, and was started from the original value of the parameter. A new value was accepted or rejected based on the variational principle. During the random walk, the parameter values were not restricted within any interval, but they were controlled by the definition of a “fine-tuning” radius, which allowed the program to change the parameter value with a certain percentage only, and each random walk sequence was limited by a maximum number of steps.

The optimization of the Gaussian exponents and the global vector parameters were carried out in terms of *different* coordinates. Due to the simple transformation property of the basis functions (and thus the integrals) in terms of a linear transformation of the coordinates, one can use several coordinate representations during the *same* calculation (“re-parameterization”). As a result of this observation, we propose a multiple-coordinate or multiple-channel optimization strategy.

### 3. Multiple-channel optimization

Our optimization strategy needs to answer the questions of how to guess a “good enough” coordinate representation for the optimization procedure and what the best strategy to follow is if there are more than one coordinate representa-

tions which describe important but qualitatively different few-particle correlations?

Since the re-parameterization of the basis functions in terms of various sets of Cartesian coordinates is straightforward, one can optimize (generate and test, refine, and fine-tune) the basis function parameters using several coordinate representations, Figure 5.

A simple application of this multiple-channel optimization strategy is used in our present optimization procedure (steps 1–4), but it can, of course, be generalized by relying on several coordinate representations.

## III. NUMERICAL RESULTS

We have implemented the theory outlined to study the ground and some excited states of  $H_2^+$ ,  $Ps_2$ ,  $H_2$ , and  ${}^7Li$ . As characteristic properties of these systems, the mass, the electric charge, and the spin of the particles as well as the spatial angular momentum and the spin quantum numbers were specified, while we considered states with natural parity only. The virial coefficient,  $\eta = |1 + \langle \Phi | \hat{V} | \Phi \rangle / 2 \langle \Phi | \hat{T} | \Phi \rangle|$ , was evaluated to assess the quality of the calculated wave functions.

During the course of the non-linear optimization the  $\ln \alpha_{ij}$  coefficients were generated and optimized corresponding to the LF Cartesian coordinates where the  $\alpha_{ij}$  parameter is the exponent corresponding to the square of the Cartesian displacement vector between the  $i$ th and  $j$ th particles, Eq. (12). The global vector coefficients were generated and optimized using the translationally invariant coordinates shown in Figure 6.

After the selection and refinement of the  $\alpha_{ij}$  and  $u_i$  parameters, we ran repeated fine-tuning cycles by carrying out random walk sequences, which started from the original value and with a random but less than 10% change of the actual value. A new value was accepted if it lowered the total energy.

Before we discuss the results obtained, we should stress that due to omission of the BO paradigm, no potential energy surface with respect to a subset of coordinates is obtained. Instead, we obtain the total energies and thus all but one are excited states.

### A. $H_2^+$

Figure 7 summarizes our results for  $H_2^+$  and the corresponding BO potential energy curves are also sketched for

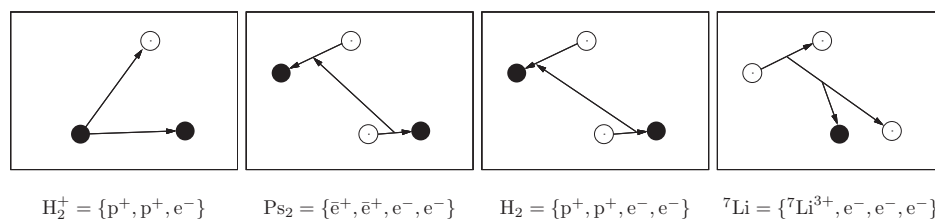


FIG. 6. The translationally invariant Cartesian coordinates used for the optimization of the global vector coefficients. The empty and the full circles represent the electrons and the positively charged particles, respectively.  $H_2^+$ : proton-centered coordinates (similar to heavy-particle centered coordinates<sup>35</sup>);  $Ps_2$  and  $H_2$ : “atoms-in-molecule” coordinates<sup>85</sup> (AIM- $Ps_2$  and AIM- $H_2$ , respectively), where the “inter-atomic” distance vector connects the center-of-mass points of the two “subatoms”;  ${}^7Li$ : Jacobi coordinates.<sup>35</sup>

TABLE II. Calculated energy levels of  $H_2^+ = \{p^+, p^+, e^-\}$ .

$L^a$	$p^a$	$S_p^a$	$E/E_h^b$	$\eta^c$	$\delta E/\mu E_h^d$	Ref.	Assignment <sup>e</sup>
0	1	0	-0.597139059	$1.6 \times 10^{-8}$	-0.004	89, 90	para $\tilde{X}^2\Sigma_g^+ v=0$
0	1	0	-0.587155670	$3.2 \times 10^{-9}$	-0.009	89, 90	para $\tilde{X}^2\Sigma_g^+ v=1$
[...]							
1	-1	1	-0.596873733	$7.9 \times 10^{-9}$	-0.005	89, 90	ortho $\tilde{X}^2\Sigma_g^+ v=0$
1	-1	1	-0.586904311	$9.4 \times 10^{-8}$	-0.010	89, 90	ortho $\tilde{X}^2\Sigma_g^+ v=1$
[...]							
2	1	0	-0.596345202	$1.8 \times 10^{-8}$	-0.004	89, 90	para $\tilde{X}^2\Sigma_g^+ v=0$
2	1	0	-0.586403620	$1.4 \times 10^{-7}$	-0.011	89, 90	para $\tilde{X}^2\Sigma_g^+ v=1$
[...]							
3	-1	1	-0.595557635	$4.1 \times 10^{-10}$	-0.004	90	ortho $\tilde{X}^2\Sigma_g^+ v=0$
3	-1	1	-0.585657606	$1.6 \times 10^{-8}$	-0.006	90	ortho $\tilde{X}^2\Sigma_g^+ v=1$
[...]							
4	1	0	-0.594517166	$2.0 \times 10^{-9}$	-0.003	90	para $\tilde{X}^2\Sigma_g^+ v=0$
4	1	0	-0.584672130	$4.0 \times 10^{-8}$	-0.004	90	para $\tilde{X}^2\Sigma_g^+ v=1$
[...]							
5	-1	1	-0.593231725	$6.4 \times 10^{-9}$	-0.004	88	ortho $\tilde{X}^2\Sigma_g^+ v=0$
5	-1	1	-0.583454791	$1.6 \times 10^{-8}$	-0.005	88	ortho $\tilde{X}^2\Sigma_g^+ v=1$
[...]							
0	1	1	-0.499743489	$1.1 \times 10^{-8}$	-0.014	88	ortho $\tilde{A}^2\Sigma_u^+ v=0$
1	-1	0	-0.499739262	$1.5 \times 10^{-8}$	-0.006	88	para $\tilde{A}^2\Sigma_u^+ v=0$
2	1	1	-0.499731516	$1.9 \times 10^{-8}$	-0.007	88	ortho $\tilde{A}^2\Sigma_u^+ v=0$

<sup>a</sup> $L$ : quantum number of the total angular momentum without the spins;  $p$ : parity;  $S_p$ : total spin quantum number of the protons.

<sup>b</sup> $m_p/m_e = 1836.15267247$ .<sup>86</sup> The dissociation limit is  $E(H(n=1)) = -0.499727840 E_h$ . The wave functions were optimized as a linear combination of  $N_b = 400$  basis functions and for the exponents  $2K$  of the polynomial prefactors the  $K$  values were generated in a normal distribution with mean and variance 5 and 1, respectively, and then the generated value was rounded to the nearest integer.

<sup>c</sup> $\eta = |1 + \langle \Psi | \hat{V} | \Psi \rangle / (2 \langle \Psi | \hat{T} | \Psi \rangle)|$ .

<sup>d</sup> $\delta E = E(\text{Ref.}) - E$ .

<sup>e</sup>The assignment of the ortho ( $S_p = 1$ ) and para ( $S_p = 0$ ) descriptions corresponds to the value of the  $S_p$  quantum number. The electronic state label of the BO theory is assigned based on comparison with the literature.<sup>87,88</sup> There are two energy levels shown corresponding to every set of  $(L, p, S_p)$  quantum numbers in the electronic ground state, which can be assigned to the ground and the first excited vibrational energy levels of the BO theory.

comparison. The calculated numerical values are given in Table II. We used a proton-electron mass ratio of  $m_p/m_e = 1836.15267247$ .<sup>86</sup> The corresponding non-relativistic ground-state energy of the free hydrogen atom, which is the dissociation limit, is  $E(H) = -0.499727840 E_h$ .

The quantum numbers of the non-relativistic theory are  $L$ ,  $p$ , and  $S_p$ . To obtain the various energy levels shown in

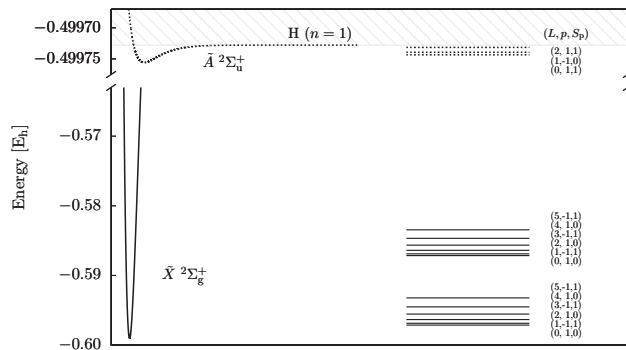


FIG. 7. Calculated all-particle (pre-Born-Oppenheimer) energy levels of  $H_2^+$  (on the right). For comparison, the Born-Oppenheimer potential energy curves are also illustrated (on the left). The dissociation energy corresponds to the ground state energy of the hydrogen atom. The numerical values of the calculated energy levels are given in Table II.  $L$ : Total angular momentum quantum number without the spins,  $p = (-1)^L$ : parity, and  $S_p$ : the total spin quantum number of the protons.

Figure 7, we chose various values for  $L$  and  $S_p$ , and always assumed natural parity,  $p = (-1)^L$ . Due to the Pauli principle for the protons, if the internal part of the wave function is symmetric with respect to the interchange of the two protons for even (odd)  $L$ , the total spin of the protons,  $S_p$  must be 0 (1), i.e., para- $H_2^+$  (ortho- $H_2^+$ ). This case can be assigned to the rotation-vibration energy levels of the electronic ground state,  $\tilde{X}^2\Sigma_g^+$ , of standard BO-based theory. On the other hand, if the internal part of the wave function is antisymmetric with respect to the interchange of the two protons for even (odd)  $L$ ,  $S_p$  must be 1 (0), i.e., ortho- $H_2^+$  (para- $H_2^+$ ). This case corresponds to the electronically excited state,  $\tilde{A}^2\Sigma_u^+$  of BO theory.

The numerical results are compared to literature data, Table II, and the agreement with for example, Refs. 87–90 is good. As to the  $\tilde{A}^2\Sigma_u^+$  states, we obtained only three rotation-only (vibrational ground state) energy levels below the dissociation limit, in agreement with earlier calculations.<sup>87,88</sup>

## B. $Ps_2$

Our second example is the positronium molecule ( $Ps_2$ ), with four particles of equal mass, two of them positively charged and two of them negatively charged. Variational calculations without the adiabatic separation of the positive and

TABLE III. Calculated energy levels of the positronium molecule,  $\text{Ps}_2 = \{\bar{e}^+, \bar{e}^+, e^-, e^-\}$ .

$L^a$	$p^a$	$S_+^a$	$S_-^a$	$E/E_h^b$	$\eta^c$	$\delta E/\mu E_h^d$	Ref.	Assignment <sup>e</sup>
0	1	0	0	-0.5160037887	$3.9 \times 10^{-9}$	-0.0017	97	$0^+ A_1$
0	1	1	0	-0.3302874964	$3.3 \times 10^{-8}$	+10.686	85	$0^+ E$
1	-1	0	0	-0.3344082953	$1.8 \times 10^{-8}$	-0.022	99	$1^- B_2$

<sup>a</sup> $L$ : quantum number of the total angular momentum without the spins;  $p$ : parity;  $S_+$  and  $S_-$ : total spin quantum number of the positrons,  $\bar{e}^+$ , and that of the electrons,  $e^-$ , respectively.

<sup>b</sup> $m_+/m_- = 1$ . The energy of the lowest-lying dissociation threshold is  $E(\text{Ps}(n=1) + \text{Ps}(n=1)) = -1/2 E_h = -0.5 E_h$ , while the second two states belong to a different symmetry block, and the corresponding dissociation threshold is  $E(\text{Ps}(n=1) + \text{Ps}(n=2)) = -5/16 E_h = -0.3125 E_h$ .<sup>85</sup> The wave functions were optimized as a linear combination of  $N_b = 1\,200$  basis functions and the exponents of the polynomial prefactors were  $2K = 0$  or  $2$ , selected randomly.

<sup>c</sup> $\eta = |1 + \langle \Psi | \hat{V} | \Psi \rangle / (2 \langle \Psi | \hat{T} | \Psi \rangle)|$ .

<sup>d</sup> $\delta E = E(\text{Ref.}) - E$ .

<sup>e</sup> $L^p$  and the symmetry labels are taken from Refs. 33 and 85.

negative particles were presented already in 1947 (Ref. 91) and later more accurate calculations for the ground,<sup>33,34,92,93</sup> excited,<sup>85,94,95</sup> and possible metastable states<sup>33,96</sup> followed.

Bound states must lie below the lowest-energy dissociation limit, and the states above are in the continuum. There are however different symmetry blocks or spin states which are not coupled to the continuum of the lowest-lying dissociation products, and thus they can be calculated within the present approach.

We considered here only three states, which are known to be bound.<sup>85</sup> Our  $L = 0$  and  $L = 1$  calculations, Table III, with zero spins agree well with the best available literature data.<sup>97,98</sup> For all three states, we obtain substantially lower energies than those of Ref. 85 and the results could be further improved by extended optimization times. In this work, we have not considered the fourth known bound state, which would become easily accessible to the present approach by considering the charge conjugation symmetry, a special property of this system.

## C. H<sub>2</sub>

Figure 8 summarizes our results for the H<sub>2</sub> molecule and the numerical results are collected in Table IV. With various

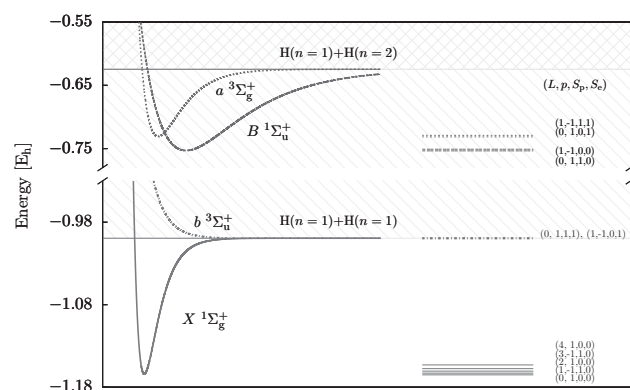


FIG. 8. Calculated all-particle (pre-Born-Oppenheimer) energy levels of H<sub>2</sub> (on the right). For comparison the Born-Oppenheimer potential energy curves are also illustrated (on the left). The lower- and higher-energy dissociation thresholds shown in the figure correspond to two hydrogen atoms in the ground state, and to one hydrogen atom in the ground state and the other in the first excited state, respectively. The numerical values of the calculated energy levels are given in Table IV.  $L$ : quantum number of the total angular momentum without the spins,  $p = (-1)^L$ : parity,  $S_p$ : the total spin quantum number of the protons, and  $S_e$ : the total spin quantum number of the electrons.

selections for the quantum number of the total angular momentum without the spins,  $L$ , the total proton spin,  $S_p$ , and the total electron spin,  $S_e$ , the lowest energy levels of four “types” (symmetries) of states became easily accessible, while we always considered natural parity,  $p = (-1)^L$ . These four “symmetry cases” (or “spin cases”) are

- (1)  $L = 0, 1, \dots, p = (-1)^L, S_e = 0$  (singlet),  $S_p = (1 - p)/2$  (para for even  $L$ , ortho for odd  $L$ );
- (2)  $L = 0, 1, \dots, p = (-1)^L, S_e = 1$  (triplet),  $S_p = (1 - p)/2$  (para for even  $L$ , ortho for odd  $L$ );
- (3)  $L = 0, 1, \dots, p = (-1)^L, S_e = 0$  (singlet),  $S_p = (1 + p)/2$  (ortho for even  $L$ , para for odd  $L$ );
- (4)  $L = 0, 1, \dots, p = (-1)^L, S_e = 1$  (triplet),  $S_p = (1 + p)/2$  (ortho for even  $L$ , para for odd  $L$ ).

The four cases are assigned, based on direct comparison of the calculated energy levels with the literature, to the  $X^1\Sigma_g^+$ ,<sup>47</sup>  $b^3\Sigma_u^+$  (repulsive),<sup>100</sup>  $B^1\Sigma_u^+$ ,<sup>101-106</sup> and  $a^3\Sigma_g^+$  (Refs. 101, 107, and 108) electronic states of the BO theory, respectively. These electronic states are the four lowest ones of the hydrogen molecule.<sup>109</sup> The corresponding potential energy functions are visualized in Figure 8 (for their calculation and applications see, for example, Refs. 47 and 101–106). According to the literature relying on the BO paradigm, there are bound rotation(-vibration) energy levels corresponding to the  $X^1\Sigma_g^+$ ,  $B^1\Sigma_u^+$ , and  $a^3\Sigma_g^+$ , while the  $b^3\Sigma_u^+$  electronic state is repulsive.

In our calculations, we obtained rotation energy levels lower than the corresponding dissociation thresholds in cases (1), (3), and (4) assignable to  $X^1\Sigma_g^+$ ,  $B^1\Sigma_u^+$ , and  $a^3\Sigma_g^+$  electronic states, respectively. Whereas in case (2) the calculated energy levels converged from above to the energy of two ground-state hydrogen atoms,  $E(\text{H}(n=1) + \text{H}(n=1))$  (see Table IV), in agreement with the known results based on the BO theory.<sup>100</sup>

Although the lowest-lying dissociation products are two ground-state hydrogen atoms,  $\text{H}(n=1) + \text{H}(n=1)$  with  $E(\text{H}(n=1) + \text{H}(n=1)) = -0.499727840 E_h$ , the rotation-vibration-electronic wave function can have different symmetry properties upon the interchange of identical particles, which can correspond to higher-lying dissociation thresholds. Although these states have larger energies than the dissociation continuum of the two ground-state hydrogen atoms, they can be calculated within our variational procedure because of their different symmetry (and different spin). Concerning the



TABLE IV. Calculated energy levels of  $\text{H}_2 = \{p^+, p^+, e^-, e^-\}$ .

$L^a$	$p^a$	$S_p^a$	$S_e^a$	$E/E_h^b$	$\eta^c$	$\delta E/\mu E_h^d$	Ref.		Assignment <sup>e</sup>	
0	1	0	0	-1.164025026	$1.4 \times 10^{-8}$	-0.004	62, 63	para	singlet	$X^1\Sigma_g^+$
1	-1	1	0	-1.163485167	$3.2 \times 10^{-9}$	-0.006	47	ortho	singlet	$X^1\Sigma_g^+$
2	1	0	0	-1.162410402	$2.2 \times 10^{-8}$	-0.007	47	para	singlet	$X^1\Sigma_g^+$
3	-1	1	0	-1.160810486	$7.9 \times 10^{-9}$	-0.006	47	ortho	singlet	$X^1\Sigma_g^+$
4	1	0	0	-1.158699660	$6.7 \times 10^{-9}$	-0.006	47	para	singlet	$X^1\Sigma_g^+$
[...]										
0	1	1	1	[-0.999450]	$[6.3 \times 10^{-6}]$	[-5.8]	100	ortho	triplet	$b^3\Sigma_u^+$
1	-1	0	1	[-0.999445]	$[8.9 \times 10^{-6}]$	[-10.4]	100	para	triplet	$b^3\Sigma_u^+$
[...]										
0	1	1	0	-0.753026938	$1.8 \times 10^{-6}$	-0.455	106	ortho	singlet	$B^1\Sigma_u^+$
1	-1	0	0	-0.752848338	$5.9 \times 10^{-6}$	-2.041	106	para	singlet	$B^1\Sigma_u^+$
[...]										
0	1	0	1	-0.730825002	$1.2 \times 10^{-6}$	-0.198	108	para	triplet	$a^3\Sigma_g^+$
1	-1	1	1	-0.730521133	$7.4 \times 10^{-7}$	-0.277	108	ortho	triplet	$a^3\Sigma_g^+$
[...]										

<sup>a</sup> $L$ : quantum number of the total angular momentum without the spins;  $p$ : parity;  $S_p$ : total spin quantum number of the protons;  $S_e$ : total spin quantum number of the electrons.

<sup>b</sup> $m_p/m_e = 1836.15267247$ .<sup>86</sup> The energy of the lowest-lying dissociation threshold is  $E(H(n=1) + H(n=1)) = -0.999455679 E_h$ , while the third and fourth set of states belong to a different symmetry block, and the corresponding dissociation threshold is  $E(H(n=1) + H(n=2)) = -0.624659800 E_h$ . The wave function for the  $X^1\Sigma_g^+$  (for the  $B^1\Sigma_u^+$ ,  $a^3\Sigma_g^+$ ) states was written in terms of a linear combination of  $N_b = 1500$  ( $N_b = 1000$ ) basis functions and the  $K$  values of the “2K” exponents of the polynomial prefactors were generated in a normal distribution with mean and variance 9 and 1, respectively, and the generated value was rounded to the nearest integer.

<sup>c</sup> $\eta = |1 + \langle \Psi | \hat{V} | \Psi \rangle / (2 \langle \Psi | \hat{T} | \Psi \rangle)|$ .

<sup>d</sup> $\delta E = E(\text{Ref.}) - E$ .

<sup>e</sup>The para (ortho) and singlet (triplet) descriptions correspond to  $S_p = 0$  (1) and  $S_e = 0$  (1), respectively. The electronic-state label of the Born–Oppenheimer theory is assigned to the calculated energy levels based on comparison with the literature.<sup>47,100,106,108</sup> In each case, the vibrational ground state is shown, i.e., the lowest energy level corresponding to each set of angular momentum, parity, and spin quantum numbers.

clamped-nucleus analogy, correlation rules between molecular states and dissociation limits were derived by Hund<sup>110,111</sup> and by Wigner and Witmer<sup>112</sup> for homonuclear diatomic molecules, which were later extended by Mulliken<sup>113</sup> (see also Refs. 109 and 114).

As to the technical details of our calculations, we used LF Cartesian coordinates to optimize the logarithm of the basis function exponents,  $\ln \alpha_{ij}$ , while the GVR coefficients were generated first corresponding to the atoms-in-molecule coordinates<sup>85</sup> (see “AIM- $\text{H}_2$ ” in Figure 6). The random number generators were parameterized following the sampling-importance-resampling strategy for the  $X^1\Sigma_g^+$  states. These random distributions (normal distributions with some mean and variance for each  $\ln \alpha_{ij}$  ( $i = 1, 2, \dots, n_p + 1$ ;  $j = i + 1, \dots, n_p + 1$ ) and  $u_i^{(\text{AIM-}\text{H}_2)}$  ( $i = 1, 2, \dots, n_p$ )) were used not only for the  $X^1\Sigma_g^+$  states but also for the generation of the trial parameters for the electronically excited states. Of course, the internal distribution of the particles can be very different in the various electronic states, as it can be anticipated from the very different minimum positions and width of the potential energy curves (Figure 8). Thus, if we reparameterized the random distributions of the random number generators for each electronically excited state (following a sampling-importance-resampling strategy), we could have a more efficient optimization procedure, and thus could calculate lower energy eigenvalues with a similar computational effort. This requires a series of calculations, which we might pursue in a later work.

As to the optimization of the global vector coefficients, the parameter optimization in terms of the AIM coordinates seem to represent the physical idea that the lighter electrons “follow” the heavier protons, and thus provide a rea-

sonable choice for the parameterization of the angular distribution of the particles. Of course, the coordinates of the two electrons and the two protons enter the procedure symmetrically due to the (anti)symmetrization of the trial functions, Eq. (10).

In Table IV, we present the calculated energy values and their comparison with earlier calculations. For  $L = 0$ ,  $S_p = 0$ ,  $S_e = 0$  tightly converged all-particle (“pre-Born–Oppenheimer”) variational calculations<sup>62,63</sup> were used as reference data. For every other energy levels calculations within a pre-Born–Oppenheimer approach were not available, and we compared our results to the results of accurate “post-Born–Oppenheimer” variational-perturbational calculations.<sup>47,101–106</sup> The  $b^3\Sigma_u^+$  energy eigenvalues shown in Table IV converged from above to the energy of two ground-state hydrogen atoms, which we interpret as an indication of the repulsive character of this electronic state in the BO theory.

Although the numerical results reported in Table IV could be improved, our goal is accomplished by demonstrating that rotational energy levels corresponding to the ground and some excited energy levels can be calculated within the presented variational all-particle procedure.

As a next logical question, one may ask if it is possible to calculate rotation(-vibration) energy levels corresponding to higher-lying bound electronic states, for example, to  $e^3\Sigma_u^+$ ,<sup>109</sup> within the present approach. We think that the rotation(-vibration) states, which could be assigned to  $e^3\Sigma_u^+$ ,<sup>109</sup> are embedded in the continuum assignable to the  $b^3\Sigma_u^+$ , and thus could be calculated as resonances with some characteristic energy and finite lifetime within an all-particle approach.

TABLE V. Calculated energy levels of  ${}^7\text{Li} = \{{}^7\text{Li}^{3+}, e^-, e^-, e^-\}$ .

$L^a$	$p^a$	$S_e^a$	$E^b$	$\eta^c$	$\delta E/\mu E_h^d$	Ref.
0	1	1/2	-7.477451901	$1.3 \times 10^{-9}$	-0.029	115
1	-1	1/2	-7.409557349	$8.8 \times 10^{-9}$	-0.410	116
2	1	1/2	-7.334926959	$1.1 \times 10^{-9}$	-0.347	117, 118

<sup>a</sup> $L$ : quantum number of the total angular momentum without the spins;  $p$ : parity;  $S_e$ : total spin quantum number of the electrons.

<sup>b</sup> $m_{{}^7\text{Li}^{3+}}/m_{e^+} = 12\,786.393$  The wave functions were optimized as a linear combination of  $N_b = 1500$  basis functions and the exponents of the polynomial prefactors were  $2K = 0$  or  $2$ , selected randomly.

<sup>c</sup> $\eta = |1 + \langle \Psi | \hat{V} | \Psi \rangle / (2 \langle \hat{T} | \Psi \rangle)|$ .

<sup>d</sup> $\delta E = E(\text{Ref.}) - E$ .

## D. ${}^7\text{Li}$

The last system to be considered is the  ${}^7\text{Li}$  isotopologue of the lithium atom described as a four-particle quantum system with three spin-1/2 fermionic particles (electrons). The numerical results obtained for the doublet electronic states are collected in Table V and agree well with the available literature data.<sup>115–118</sup>

## E. On the transferability of optimized basis function parameters

We should describe our observations concerning the transferability of the non-linear parameters of the basis functions. Assume that there is a set of basis function parameters,  $\mathcal{B}(A)$ , optimized for some system  $A$ , where  $A$  is a collective symbol for the input parameters of a calculation (mass, charge, and spin of the particles, quantum numbers, size of the basis set, etc.). Then, we use  $\mathcal{B}(A)$  to parameterize the basis functions for calculation  $A'$  (with particles of some mass, charge, and spin, quantum numbers, etc.) and solve the linear variational problem only

$$\Psi^{(A')} = \sum_{I=1}^{N_b} c_I \Phi_I^{(A')}[\mathcal{B}_I(A)] \quad (63)$$

to obtain an estimate (an upper bound),  $E^{(A')}[\mathcal{B}(A)]$  to the energy for  $A'$ . We may say that the basis function parameters are transferable from calculation  $A$  to  $A'$  if the energy estimate

$E^{(A')}[\mathcal{B}(A)]$  is close to the energy obtained with optimizing the basis function parameters for system  $A'$ ,  $E^{(A')}[\mathcal{B}(A')]$ .

We emphasize here that we do not transfer the basis functions but only the parameters (geminal exponents, global vector coefficients, polynomial exponents), while the mathematical form of the basis functions is determined by the quantum numbers (spatial and permutational symmetries). This strategy is reminiscent of the vibrational subspace technique for an efficient calculation of rotation-vibration energy levels<sup>119</sup> using pre-calculated vibrational wave functions.

In Table VI, we present examples for such a transfer of the basis function parameters between rotational energy levels of  $\text{H}_2$  ( $X^1\Sigma_g^+$  electronic state) with various  $L$  quantum numbers. In this example, the basis function parameters optimized for a rotational energy level of  $\text{H}_2$  with  $L'$  were used for the parameterization of basis functions for another rotational energy level with  $L$ . Table VI shows that the parameterization transfer between neighboring rotational energy levels,  $L = L' \pm 1$ , gives an estimate within  $0.5 \mu E_h$  of the optimized value. For larger  $|L - L'|$  values, the solution of the linear variational problem only seems to provide less and less good estimates. A qualitative explanation for this observation can be given as follows. For neighboring rotational states, the internal distribution of the particles is similar, and thus the same parameter set can describe both states, while the mathematical form of the basis functions is determined by the quantum numbers, and the flexibility of this ansatz is provided by the linear variational coefficients.

## IV. SUMMARY AND OUTLOOK

The variational solution of the Schrödinger equation of few-particle systems was considered without the introduction of the Born–Oppenheimer approximation. We presented an algorithm and reported some numerical results calculated with a computer program (implemented in FORTRAN 90), which are based on (a) a quantum Hamiltonian expressed in terms of laboratory-fixed or translationally invariant Cartesian coordinates; (b) basis functions constructed with symmetry-adapted explicitly correlated Gaussian functions and polynomial prefactors also using the global vector

TABLE VI. On the transferability of the basis function parameters between different rotational levels of  $\text{H}_2$  corresponding to the  $X^1\Sigma_g^+$  electronic state (see also Table IV). The energy differences,  $\Delta E_L[\mathcal{B}(L')]$ , between the energy obtained via the optimization of the basis function parameters,  $\mathcal{B}(L)$  and four transferred parameter sets,  $\mathcal{B}(L')$ , are given in  $\mu E_h$ .

$L^a$	$E_L[\mathcal{B}(L)]/E_h^{b,c}$	$\Delta E_L[\mathcal{B}(0)]^{b,d}$	$\Delta E_L[\mathcal{B}(1)]^{b,d}$	$\Delta E_L[\mathcal{B}(2)]^{b,d}$	$\Delta E_L[\mathcal{B}(3)]^{b,d}$	$\Delta E_L[\mathcal{B}(4)]^{b,d}$
0	-1.164025026	0.00	-0.06	-1.53	-2.53	-5.03
1	-1.163485167	-0.21	0.00	-0.35	-0.97	-2.54
2	-1.162410402	-0.76	-0.09	0.00	-0.21	-1.01
3	-1.160810486	-1.53	-0.37	-0.29	0.00	-0.23
4	-1.158699660	-2.41	-0.83	-1.05	-0.18	0.00

<sup>a</sup> $L$ : quantum number of the total angular momentum without the spins;  $p = (-1)^L$ : parity;  $S_e = 0$ ; and  $S_p = (1 - p)/2$ . See also the entries of Table IV assigned to the Born–Oppenheimer electronic ground state,  $X^1\Sigma_g^+$ .

<sup>b</sup>The mass ratio is  $m_p/m_e = 1836.15267247$ .

<sup>c</sup> $E_L[\mathcal{B}(L)]$  is the lowest eigenvalue obtained in the non-linear variational optimization, and the optimized basis function parameters are  $\mathcal{B}(L)$ .

<sup>d</sup> $\Delta E_L[\mathcal{B}(L')] = E_L[\mathcal{B}(L)] - E_L[\mathcal{B}(L')]$  ( $L' = 0, 1, 2, 3, 4$ ), where  $E_L[\mathcal{B}(L')]$  is the lowest eigenvalue of the linear variational problem solved for a set of basis functions parameterized with  $\mathcal{B}(L')$ , which was optimized for the angular momentum quantum number ( $L'$ ).

representation;<sup>59</sup> (c) analytic expressions for the calculation of the overlap, the kinetic, and the potential energy integrals following the prescriptions of Refs. 35 and 53; and (d) stochastic variational optimization of the non-linear parameters of the basis functions.

Our work is a practical adaptation of that described in Refs. 35 and 53 for molecular systems with various (rotational or orbital) angular momentum quantum numbers ( $L \geq 0$ ). An accurate calculation of the energy levels of molecular systems required the inclusion of large exponents ( $>4$ ) for the polynomial prefactors in the basis functions. In order to obtain a numerically stable and practical implementation with large exponents, we had to rearrange the integral expressions of Refs. 35 and 53, introduce quasi-normalization for the basis functions, use a logarithmic evaluation of products of polynomials and factorials, and pursue a careful implementation strategy.

It was an advantageous property of the basis functions that upon a linear transformation of the Cartesian coordinates their mathematical form remained unaltered, and only the basis function parameters (Gaussian exponents and global vector coefficients) had to be transformed. We did make use of this simple transformation property during the integral evaluation and the parameter optimization. During the evaluation of the integrals the operators were written in their simplest form in terms of the coordinates.

Clearly, we had to *choose* some set of coordinates for the parameter optimization, but we were able to exploit the ease of re-parameterization of the basis functions in terms of different coordinates. For the systems studied here, we have found the best to generate and optimize the Gaussian exponents corresponding to laboratory-fixed Cartesian coordinates, while for the global vector coefficients some “well-chosen” translationally invariant Cartesian coordinates performed better.

In general, it is not trivial how to choose an appropriate set of coordinates or there might be not only one but several types of correlations in the system, which are represented efficiently by different sets of coordinates. To circumvent this coordinate dilemma, we suggested a multiple-channel optimization strategy for the optimization of the basis function parameters. Indeed, due to the simple transformation property of the basis functions upon a linear transformation of the coordinates, the basis function parameters can be optimized in terms of one or another set of the coordinates during the course of the *same* calculation.

Besides the stochastic optimization (competitive selection and refinement<sup>35</sup>) of the non-linear parameters, we included repeated fine-tuning cycles. In the stochastic optimization procedure, we studied the effect of various random number generators on the efficiency of the procedure, i.e., the convergence rate of the energy with respect to the computational effort, and finally selected a log-normal distribution for each Gaussian exponent and normal distributions for the global vector coefficients. We have proposed a sampling-importance-resampling strategy for the parameterization of the random number distribution, i.e., to be able to choose a reasonably good sample mean and sample variance for the probability distributions.

Our emphasis was on the calculation of energy levels and wave functions with *various* quantum numbers of total spatial angular momentum (rotational and orbital angular momenta of the BO theory), parity, and spin quantum numbers. Though in this work we restricted the presentation to the natural-parity case,  $p = (-1)^L$  only, we have preliminary results for the unnatural parity case,  $p = (-1)^{L+1}$  as well, which might be presented in a later publication.

Although the optimization, especially the “fine-tuning” of the basis function parameters could be certainly improved, our primary goal was here to test the applicability of the procedure, and thus we calculated rotation-vibration energy levels of the molecular  $\text{H}_2^+$  corresponding to the  $\tilde{X}^2\Sigma_g^+$  ground and the  $\tilde{A}^2\Sigma_u^+$  electronically excited states as well as rotational energy levels of  $\text{H}_2$  assigned to the  $X^1\Sigma_g^+$  ground and to the  $B^1\Sigma_u^+$  and  $a^3\Sigma_g^+$  electronically excited states. We also calculated three bound states of the positronium molecule,  $\text{Ps}_2$ , and the  $^7\text{Li}$  atom with various angular momentum quantum numbers.

The assignment of the calculated energy levels to electronic states defined within the Born–Oppenheimer theory was carried out based on the comparison of the calculated energy eigenvalues with the literature. It would be possible to make the assignment based on the analysis of the calculated wave function, which can be explored in a later work. The development of such an assignment tool would allow us to better understand the qualitative meaning of the parameterization of the wave function, and thus could help the improvement of the parameterization strategy and a development of a systematic approximation scheme.

For future work, it would be interesting to calculate rotation-vibration energy levels, for example, for the  $\text{H}_2$  molecule, which can be assigned to higher-lying electronically excited states of the Born–Oppenheimer theory. This undertaking appears not to be a simple, straightforward task in the present all-particle quantum mechanical approach. We believe that these states could be calculated as resonances embedded in the continuum of lower-lying energy levels of the same symmetry.

Finally, we discussed the transferability of the basis function parameters between rotational states of the  $\text{H}_2$  molecule. We have found that between neighboring rotational levels the transferred parameters provided a satisfactory basis set, which—without further optimization of the non-linear parameters—, when used in a linear variational problem to parameterize the basis functions corresponding to the actual quantum numbers, provided a very good approximation to the energy.

## ACKNOWLEDGMENTS

The authors would like to acknowledge discussions with Professor Jürg Hutter and Professor Ulrich Müller-Herold. E.M. acknowledges funding by a two-year ETH Fellowship during 2010–2011. Financial support from the Swiss National Fund (SNF) is also gratefully acknowledged. E.M. also thanks the Hungarian Scientific Research Fund (OTKA, NK83583) and the European Union and the European Social

Fund (TÁMOP-4.2.1/B-09/1/KMR-2010-0003) for financial support during 2012.

- <sup>1</sup>M. Born and R. Oppenheimer, *Ann. Phys.* **84**, 457 (1927).
- <sup>2</sup>M. Born, *Nachr. Akad. Wiss. Goett. II, Math.-Phys. Kl.* **6**, 1 (1951).
- <sup>3</sup>M. Born and K. Huang, *Dynamical Theory of Crystal Lattices* (Clarendon, Oxford, 1954).
- <sup>4</sup>B. T. Sutcliffe and R. G. Woolley, *Phys. Chem. Chem. Phys.* **7**, 3664 (2005).
- <sup>5</sup>R. G. Woolley, *Adv. Phys.* **25**, 27 (1976).
- <sup>6</sup>R. G. Woolley and B. T. Sutcliffe, *Chem. Phys. Lett.* **45**, 393 (1977).
- <sup>7</sup>R. G. Woolley, *J. Am. Chem. Soc.* **100**, 1073 (1977).
- <sup>8</sup>H. Essén, *Int. J. Quantum Chem.* **12**, 721 (1977).
- <sup>9</sup>R. G. Woolley, *Chem. Phys. Lett.* **55**, 443 (1978).
- <sup>10</sup>R. G. Woolley, *Isr. J. Chem.* **19**, 30 (1980).
- <sup>11</sup>P. Claverie and S. Diner, *Isr. J. Chem.* **19**, 54 (1980).
- <sup>12</sup>J. G. R. Tostes, *Theor. Chim. Acta* **59**, 229 (1981).
- <sup>13</sup>S. J. Weininger, *J. Chem. Educ.* **61**, 939 (1984).
- <sup>14</sup>R. G. Woolley, *Chem. Phys. Lett.* **125**, 200 (1986).
- <sup>15</sup>P.-O. Löwdin, *Pure Appl. Chem.* **61**, 2065 (1989).
- <sup>16</sup>B. T. Sutcliffe, *J. Mol. Struct.: THEOCHEM* **259**, 29 (1992).
- <sup>17</sup>B. T. Sutcliffe and R. G. Woolley, *Chem. Phys. Lett.* **408**, 445 (2005).
- <sup>18</sup>B. T. Sutcliffe, *J. Math. Chem.* **44**, 988 (2008).
- <sup>19</sup>N. Sukumar, *Found. Chem.* **11**, 7 (2009).
- <sup>20</sup>A. Fröman and J. L. Kinsey, *Phys. Rev.* **123**, 2077 (1961).
- <sup>21</sup>M. Cafiero and L. Adamowicz, *Chem. Phys. Lett.* **387**, 136 (2004).
- <sup>22</sup>M. Cafiero and L. Adamowicz, *J. Chem. Phys.* **122**, 184305 (2005).
- <sup>23</sup>U. Müller-Herold, *J. Chem. Phys.* **124**, 014105 (2006).
- <sup>24</sup>U. Müller-Herold, *Eur. Phys. J. D* **49**, 311 (2008).
- <sup>25</sup>E. Mátyus, J. Hutter, U. Müller-Herold, and M. Reiher, *Phys. Rev. A* **83**, 052512 (2011).
- <sup>26</sup>E. Mátyus, J. Hutter, U. Müller-Herold, and M. Reiher, *J. Chem. Phys.* **135**, 204302 (2011).
- <sup>27</sup>E. V. Ludeña, L. Echevarría, X. Lopez, and J. M. Ugalde, *J. Chem. Phys.* **136**, 084103 (2012).
- <sup>28</sup>M. Goli and S. Shahbazian, *Theor. Chim. Acta* **129**, 235 (2011).
- <sup>29</sup>M. Goli and S. Shahbazian, *Theor. Chim. Acta* **131**, 1208 (2012).
- <sup>30</sup>V. I. Kukulin and V. M. Krasnopolsky, *J. Phys. G: Nucl. Phys.* **3**, 795 (1977).
- <sup>31</sup>H. Kameyama, M. Kamimura, and Y. Fukushima, *Phys. Rev. C* **40**, 974 (1989).
- <sup>32</sup>M. Kamimura and H. Kameyama, *Nucl. Phys. A* **508**, 17c (1990).
- <sup>33</sup>D. B. Kinghorn and R. D. Poshusta, *Phys. Rev. A* **47**, 3671 (1993).
- <sup>34</sup>A. M. Frolov and V. H. Smith, Jr., *Phys. Rev. A* **55**, 2662 (1997).
- <sup>35</sup>Y. Suzuki and K. Varga, *Stochastic Variational Approach to Quantum-Mechanical Few-Body Problems* (Springer-Verlag, Berlin, 1998).
- <sup>36</sup>D. B. Kinghorn and L. Adamowicz, *Phys. Rev. Lett.* **83**, 2541 (1999).
- <sup>37</sup>M. Cafiero, S. Bubin, and L. Adamowicz, *Phys. Chem. Chem. Phys.* **5**, 1491 (2003).
- <sup>38</sup>Y. Hijikata, H. Nakashima, and H. Nakatsuji, *J. Chem. Phys.* **130**, 024102 (2009).
- <sup>39</sup>H. Nakai, *Int. J. Quantum Chem.* **86**, 511 (2002).
- <sup>40</sup>T. Iordanov and S. Hammes-Schiffer, *J. Chem. Phys.* **118**, 9489 (2003).
- <sup>41</sup>A. D. Bochevarov, E. F. Valeev, and C. D. Sherrill, *Mol. Phys.* **102**, 111 (2004).
- <sup>42</sup>A. Chakraborty, M. V. Pak, and S. Hammes-Schiffer, *J. Chem. Phys.* **129**, 014101 (2008).
- <sup>43</sup>E. Kamarchik and D. A. Mazziotti, *Phys. Rev. A* **79**, 012502 (2009).
- <sup>44</sup>The term “spectroscopic accuracy” is not uniquely defined but it is usually used to refer to calculations providing vibrational transition wave numbers with a certainty of at least  $1\text{ cm}^{-1}$  ( $\approx 4.6\ \mu\text{E}_h$ ) and even better accuracy for calculated rotational transitions.
- <sup>45</sup>J. Liu, E. J. Salumbides, U. Hollenstein, J. C. J. Koelemeij, K. S. E. Eikema, W. Ubachs, and F. Merkt, *J. Chem. Phys.* **130**, 174306 (2009).
- <sup>46</sup>D. Sprecher, C. Jungen, W. Ubachs, and F. Merkt, *Faraday Discuss.* **150**, 51 (2011).
- <sup>47</sup>K. Pachucki and J. Komasa, *J. Chem. Phys.* **130**, 164113 (2009).
- <sup>48</sup>K. Piszczatowski, G. Lach, M. Przybytek, J. Komasa, K. Pachucki, and B. Jeziorski, *J. Chem. Theory Comput.* **5**, 3039 (2009).
- <sup>49</sup>T. Oka, *Phys. Rev. Lett.* **45**, 531 (1980).
- <sup>50</sup>T. Oka, *Faraday Discuss.* **150**, 9 (2011).
- <sup>51</sup>M. Pavanello, L. Adamowicz, A. Alijah, N. F. Zobov, I. I. Mizus, O. L. Polyansky, J. Tennyson, T. Szidarovszky, A. G. Császár, M. Berg, *et al.*, *Phys. Rev. Lett.* **108**, 023002 (2012).
- <sup>52</sup>K. Varga and Y. Suzuki, *Phys. Rev. C* **52**, 2885 (1995).
- <sup>53</sup>Y. Suzuki, J. Usukura, and K. Varga, *J. Phys. B* **31**, 31 (1998).
- <sup>54</sup>B. Jeziorski and K. Szalewicz, *Phys. Rev. A* **19**, 2360 (1979).
- <sup>55</sup>W. Cencek and J. Rychlewski, *J. Chem. Phys.* **98**, 1252 (1993).
- <sup>56</sup>*Explicitly Correlated Wave Functions in Chemistry and Physics*, edited by J. Rychlewski (Kluwer Academic, Dodrecht, 2003).
- <sup>57</sup>S. F. Boys, *Proc. R. Soc. London, Ser. A* **258**, 402 (1960).
- <sup>58</sup>K. Singer, *Proc. R. Soc. London, Ser. A* **258**, 412 (1960).
- <sup>59</sup>K. Varga, Y. Suzuki, and J. Usukura, *Few-Body Syst.* **24**, 81 (1998).
- <sup>60</sup>E. Bednarz, S. Bubin, and L. Adamowicz, *Mol. Phys.* **103**, 1169 (2005).
- <sup>61</sup>M. Cafiero and L. Adamowicz, *Int. J. Quantum Chem.* **107**, 2679 (2007).
- <sup>62</sup>S. Bubin and L. Adamowicz, *J. Phys. Chem.* **118**, 3079 (2003).
- <sup>63</sup>S. Bubin, F. Leonarski, M. Stanke, and L. Adamowicz, *Chem. Phys. Lett.* **477**, 12 (2009).
- <sup>64</sup>S. A. Alexander, H. J. Monkhorst, and K. Szalewicz, *J. Chem. Phys.* **85**, 5821 (1986).
- <sup>65</sup>S. A. Alexander, H. J. Monkhorst, and K. Szalewicz, *J. Chem. Phys.* **87**, 3976 (1987).
- <sup>66</sup>S. A. Alexander, H. J. Monkhorst, and K. Szalewicz, *J. Chem. Phys.* **89**, 355 (1988).
- <sup>67</sup>R. Meyer, *J. Mol. Spectrosc.* **76**, 266 (1979).
- <sup>68</sup>D. Luckhaus, *J. Chem. Phys.* **113**, 1329 (2000).
- <sup>69</sup>D. Lauvergnat and A. Nauts, *J. Chem. Phys.* **116**, 8560 (2002).
- <sup>70</sup>E. Mátyus, G. Czakó, and A. G. Császár, *J. Chem. Phys.* **130**, 134112 (2009).
- <sup>71</sup>See supplementary material at <http://dx.doi.org/10.1063/1.4731696> for the details of the evaluation of the matrix elements for natural-parity states.
- <sup>72</sup>E. Cohen, T. Cvitaš, J. Frey, B. Holmström, K. Kuchitsu, R. Marquardt, I. Mills, F. Pavese, M. Quack, J. Stohner, *et al.*, *Quantities, Units and Symbols in Physical Chemistry (The IUPAC Green Book)*, 3rd ed. (RSC, Cambridge, 2007).
- <sup>73</sup>B. T. Sutcliffe, *Coordinate Systems and Transformations, in Handbook of Molecular Physics and Quantum Chemistry*, edited by S. Wilson (Wiley, Chichester, 2003), Vol. 1, pp. 485–500.
- <sup>74</sup>B. T. Sutcliffe, “Molecular Hamiltonians,” in *Handbook of Molecular Physics and Quantum Chemistry* edited by S. Wilson (Wiley, Chichester, 2003), Vol. 1, pp. 501–525.
- <sup>75</sup>D. L. Hill and J. A. Wheeler, *Phys. Rev.* **89**, 1102 (1953).
- <sup>76</sup>L. Lathouwers, P. van Leuven, and M. Bouten, *Chem. Phys. Lett.* **52**, 439 (1977).
- <sup>77</sup>L. Lathouwers and P. van Leuven, *Adv. Chem. Phys.* **49**, 115 (1982).
- <sup>78</sup>G. A. Hagedorn, *Commun. Math. Phys.* **71**, 77 (1980).
- <sup>79</sup>E. Faou, V. Gradinaru, and C. Lubich, *SIAM J. Sci. Comput. (USA)* **31**, 3027 (2009).
- <sup>80</sup>Wolfram Research, Inc., MATHEMATICA, Version 7.0, Champaign, IL, 2008.
- <sup>81</sup>*Intel’s Math Kernel Library* (2011) can be found in <http://software.intel.com/en-us/articles/intel-math-kernel-library-documentation>.
- <sup>82</sup>S. Marsland, *Machine Learning: An Algorithmic Perspective* (Chapman & Hall, Boca Raton, 2009).
- <sup>83</sup>D. B. Kinghorn and L. Adamowicz, *J. Chem. Phys.* **113**, 4203 (2000).
- <sup>84</sup>C. E. Scheu, D. B. Kinghorn, and L. Adamowicz, *J. Chem. Phys.* **114**, 3393 (2001).
- <sup>85</sup>Y. Suzuki and J. Usukura, *Nucl. Instrum. Methods Phys. Res. B* **171**, 67 (2000).
- <sup>86</sup>See <http://physics.nist.gov/cuu/Constants> for CODATA 2006.
- <sup>87</sup>L. Wolniewicz and T. Orlikowski, *Mol. Phys.* **74**, 103 (1991).
- <sup>88</sup>R. E. Moss, *Mol. Phys.* **80**, 1541 (1993).
- <sup>89</sup>J. P. Karr and L. Hilico, *J. Phys. B* **39**, 2095 (2006).
- <sup>90</sup>V. I. Korobov, *Phys. Rev. A* **74**, 052506 (2006).
- <sup>91</sup>E. A. Hylleraas and A. Ore, *Phys. Rev.* **71**, 493 (1947).
- <sup>92</sup>P. M. Kozłowski and L. Adamowicz, *Phys. Rev. A* **48**, 1903 (1993).
- <sup>93</sup>A. M. Frolov, S. I. Kryuchkov, and V. H. Smith, Jr., *Phys. Rev. A* **51**, 4514 (1995).
- <sup>94</sup>K. Varga, J. Usukura, and Y. Suzuki, *Phys. Rev. Lett.* **80**, 1876 (1998).
- <sup>95</sup>J. Usukura, K. Varga, and Y. Suzuki, *Phys. Rev. A* **58**, 1918 (1998).
- <sup>96</sup>Y. K. Ho, *Phys. Rev. A* **39**, 2709 (1989).
- <sup>97</sup>S. Bubin and L. Adamowicz, *Phys. Rev. A* **74**, 052502 (2006).
- <sup>98</sup>S. Bubin and L. Adamowicz, *J. Chem. Phys.* **128**, 114107 (2008).
- <sup>99</sup>M. Puchalski and A. Czarnecki, *Phys. Rev. Lett.* **101**, 183001 (2008).
- <sup>100</sup>W. Kołos and J. Rychlewski, *J. Mol. Spectrosc.* **143**, 237 (1990).

- <sup>101</sup>W. Kołos and L. Wolniewicz, *J. Chem. Phys.* **48**, 3672 (1968).  
<sup>102</sup>K. Dressler and L. Wolniewicz, *J. Chem. Phys.* **85**, 2821 (1986).  
<sup>103</sup>P. Senn, P. Quadrelli, and K. Dressler, *J. Chem. Phys.* **89**, 7401 (1988).  
<sup>104</sup>L. Wolniewicz and K. Dressler, *J. Chem. Phys.* **96**, 6053 (1992).  
<sup>105</sup>L. Wolniewicz, *Chem. Phys. Lett.* **233**, 647 (1995).  
<sup>106</sup>L. Wolniewicz, T. Orlikowski, and G. Staszewska, *J. Mol. Spectrosc.* **238**, 118 (2006).  
<sup>107</sup>W. Kołos and J. Rychlewski, *J. Mol. Spectrosc.* **169**, 341 (1995).  
<sup>108</sup>L. Wolniewicz, *Mol. Phys.* **105**, 1497 (2007).  
<sup>109</sup>J. Brown and A. Carrington, *Rotational Spectroscopy of Diatomic Molecules* (Cambridge University Press, Cambridge, 2003).  
<sup>110</sup>F. Hund, *Z. Physik* **51**, 795 (1928).  
<sup>111</sup>F. Hund, *Z. Physik* **63**, 719 (1930).  
<sup>112</sup>E. Wigner and E. E. Witmer, *Z. Physik* **51**, 859 (1928).  
<sup>113</sup>R. S. Mulliken, *Phys. Rev.* **36**, 1440 (1930).  
<sup>114</sup>G. Herzberg, *Spectra of Diatomic Molecules* (Van Nostrand, Princeton, New Jersey, 1950).  
<sup>115</sup>M. Stanke, D. Kedziera, S. Bubin, and L. Adamowicz, *J. Chem. Phys.* **127**, 134107 (2007).  
<sup>116</sup>M. Puchalski and K. Pachucki, *Phys. Rev. A* **78**, 052511 (2008).  
<sup>117</sup>K. L. Sharkley, S. Bubin, and L. Adamowicz, *J. Phys. Chem.* **134**, 044120 (2011).  
<sup>118</sup>K. L. Sharkley, S. Bubin, and L. Adamowicz, *Phys. Rev. A* **83**, 012506 (2011).  
<sup>119</sup>C. Fábri, E. Mátyus, T. Furtenbacher, L. Nemes, B. Mihály, T. Zoltáni, and A. G. Császár, *J. Chem. Phys.* **135**, 094307 (2011).